Multivariate Characterisation of Dual Layered Catalysts, Reliability and Durability of Polymer Electrolyte Membrane Fuel Cells

By

Nicholas McCarthy

A Thesis

Submitted in partial fulfilment of the requirements for the award of Degree of Doctor of Philosophy of Loughborough University

31 March 2017

Abstract

Hydrogen fuel cells have held out the promise of clean, sustainable power generation for decades, but have failed to deliver on that potential. Inefficiencies in research and development work can be overcome to increase the rate of new knowledge acquisition in this field. A number of medical and engineering disciplines utilise a wide variety of statistical tools in their research to achieve this same end, but there has been little adoption of such statistical approaches within the fuel cell research community.

This research undertakes a design of experiments (DoE) approach to the analysis of multiply-co-varying (M-ANOVAR) factors by using historic data, and direct experimental work, on a wide variety of polymer electrolyte membrane fuel cells (PEMFCs) cathode gas diffusion media (GDM) and dual layered catalyst structures. This research developed a 'gradient of polarisation regions' approach; a method for making robust numerical comparisons between large numbers of samples based on polarisation curves, while still measuring the more usual peak power of the PEMFC. The assessment of polarisation gradients was completed in a statistically robust fashion that enabled the creation of regression models of GDMs for multiple input and multiple output data sets. Having established the multivariate method; a set of possibly co-varying factors, a DoE approach was used to assess GDM selection, dual layered catalyst structures and degradation of membrane electrode assembly (MEA) performance over time. Degradation studies monopolise resources to be monopolised for protracted periods. M-ANOVAR allows the addition of other factors in the study, and the total efficiency of the degradation experiment is increased. A 20% reduction in the number of samples to be tested was achieved in the case study presented in this thesis (compared to the usual one factor at a time (OFAT) approach). This research highlights the flexibility and efficiency of DoE approaches to PEMFC degradation experimentation.

This research is unique in that it creates catalyst ink formulations where the variation in catalyst loading in each sub-layer of the catalyst layer (CL) was achieved by having a different concentration of the catalyst material on the carbon supports. The final M-ANOVAR analysis indicates a simple average of the individual responses was appropriate for the experiments undertaken.

It was shown that low concentration dual layer catalysts on paper GDMs have improved performance compared to paper GDMs with uniform, single layer catalysts: Demonstrating reduced platinum concentrations to achieve equivalent open cell performance. The time to peak power during testing (how long after starting the test it takes to achieve the maximum performance in the cell) was strongly impacted by GDM selection. Furthermore, there was a strong suggestion that previously published results crediting a change in performance due to a single layer, or multi-layered catalyst structures may, in fact, have been due to the selection of GDM used in the experiment instead.

Acknowledgement

This PhD thesis could not have been completed without the support of the following organisations and individuals.

I gratefully acknowledge the unflagging support of both my supervisors Professor Rui Chen and Dr Alun Owen, who have helped me to achieve a level I never knew I was capable of. To the staff here at the Loughborough University Aeronautical and Automotive Engineering Department who were consistently helpful and made this project possible; I cannot name you all individually, but you have my thanks.

The EPSRC through its funding of the doctoral training centre (DTC) for hydrogen, fuels cells and their applications at the University of Birmingham (EPSRC Grant EP/G037116/1).

The FUTURE vehicles project (EPSRC Grant EP/I038586/1) was also instrumental in ensuring the time and resources were available to undertake the degradation studies.

Dr Ahmad El-Kahrouf of the University of Birmingham, through his sharing of resources and information, was an outstanding contributor to this research. Much of my research would have been impossible without his willingness to share test samples and data in a reciprocal manner.

I would like to take this opportunity to thank my fellow cohort of the Loughborough DTC for their friendship over the years; with a special mention to Dr Ashley Fly for his tuition in Matlab® and his willingness to be a sounding board for my ideas no matter how ridiculous.

Finally, I must thank my wife Julie, my mother Sheila and my son Samuel for their support and love, despite everything, during the years it has taken to get to this point.

Contents

List of Figures

List of Tables

Nomenclature

Symbol	Description
A	Area
A	Electrical current (amps)
bar(a)	Absolute Pressure (1 bar = 100kPa)
bar(g)	Relative Pressure (1 bar = 100kPa)
C	concentration
C	Coulombs
CV	Coefficient of Variance
D_x	Diffusion of species 'x'
D_{eff}	Effective diffusion
df	Degrees of freedom
E	Electron charge ($1.6021766x10^{-19}$ Coulombs)
E	Potential
E_a	Activation Energy
E_{ff}	Effectiveness factor for transport adjacent to catalyst sites
F	Faradays constant (96,487 $C.mol^{-1}$)
F	F-distribution
G	Acceleration due to gravity ($9.8m.s^{-2}$)
gA	Gradient in the activation region of the polarisation curve
gO	Gradient in the Ohmic region of the polarisation curve
gM	Gradient in the mass-loss region of the polarisation curve
G	Gibbs energy
h_{ii}	Leverage of input factors on outputs
H	Enthalpy ($J.kg^{-1}$)
I	Electrical current
i_0	Exchange current density ($A.cm^{-2}$)
i_L	Limiting current
I	$\sqrt{-1}$
J	Joules ($kg.m^2.s^{-2}$)
J_D	Diffusion Flux
K	A constant
K	Kelvin
k_b	Boltzmann's constant ($1.3806452\ x10^{-23}\ \ m^2.kg.s^{-2}.K^{-1}$)
kg	kilograms

M	Meters
mol	NA number of atoms or molecules of a species
N	A number
N	Newtons ($kg.s^{-2}$)
NA	Avogadro's Number (6.022141×10^{23})
P	Pressure (Pascals)
Pa	Pascals (pressure)
P_s	Saturation pressure
P	Partial pressure
Q	Charge
Q	'quartile' 25% of the data in a set
R	Gas constant ($8.314346\ J.K^{-1}.mol^{-1}$)
R^2	Coefficient of determination (μ/σ)
R	Radius
r^2	Pearson's correlation coefficient
S	Entropy ($J.K^{-1}$)
S	Standard deviation of the sample population
s^2	Variance of the sample population
T	Temperature
T_c	Temperature in Centigrade
U	Internal energy (J)
V	Volume (m^3)
$\bar{V}(\hat{y})$	Mean variance of the 'y' estimate
V	Velocity ($m.s^{-1}$)
V_D	Darcy Velocity of diffusion
W	Work ($kg.m^2.s^{-1}$)
$W_{ELECTRICAL}$	Electrical work completed
W	Watts ($J.s^{-1}$)
X	A number
Y	A number
Z	A number

Greek

Symbol	**Description**
A	Charge transfer coefficient

α_c	Chemical activity at the cathode
α_{12}	Active surface area for catalyst agglomerates
β	A constant
χ^2	Chi- Squared
δ	A distance (usually through-plane thickness)
Δ	Change
ε	Perturbation Factor
ε_i	Residual error
η	Thermodynamic efficiency
∇	Gradient
λ_x	Weighted presence of 'x'
λ_{H20}	Saturation constant for ionomers (λ_{H20} = 22 for fully saturated Nafion)
μ	Arithmetic mean
μ_{visc}	Dynamic viscosity
Φ	Thiele Modulus
$\Phi^{(S)}$	Electronic phase potential
Ω	Ohm electrical resistance
ρ	Density
θ	Pore filling factor
τ	Tortuosity ($m.m^{-1}$)
σ	Standard deviation of the entire population
σ^2	Variance of the entire population

Subscripts

Symbol	**Description**
a	Anode
act	Catalyst activation region of the fuel cell performance
Air	Ambient air
Agg	Agglomerate
c	Cathode
Cell	For the whole fuel cell
CI	Confidence Interval
CL	Catalyst Layer
eff	'effective': a calculated value not a single material property
(g)	Gas

H_2	Hydrogen
H_2O	Water
i, j, y or x	Species i, j, y or x
(l)	liquid
m	Mass (kg)
Mass	Mass loss (kinetic) region of the fuel cell performance
Nernst	Nernst potential
soln.	Solution
O2	Oxygen
OCV	Open Circuit Voltage
Ohm	Ohmic region of the fuel cell performance
$\bar{x}$	Arithmetic Mean of 'x'
0	Equilibrium or starting state

Superscript

Symbol	**Description**
o	degrees
Ref	A reference or starting value
'	Transformed data; e.g. a derivative or a transposed matrix
$\hat{x}$	Estimated value of 'x'
$\bar{x}$	Mean value of 'x'

Acronyms

Symbol	**Description**
ANOVA	Analysis of variance
CCM	Catalyst Coated Membrane
CCS	Catalyst Coated Substrate
CV	Coefficient of Variance
DL	Dual Layer
DOF, df	Degrees of freedom
ECSA	Electrochemically Active Surface Area
Fberg	Freudenberg
FFA	Fractional Factorial Analysis
F-test, F-ratio	F distribution relationship

GDE	Gas Diffusion Electrode
GDL	Gas Diffusion Layer
GDM	Gas diffusion Media
HOR	Hydrogen Oxidation Reaction
LSD	Least Significant Difference
MAC	Mixed application Cathode
ManCoVar	Multiple analysis of covariance
M-ANOVA	Multiple analysis of variance
MS	Mean Square
MSE	Mean Squared Error
OA	Orthogonal array
ORR	Oxygen Reduction Reaction
Pt-on-C	Platinum catalyst deposited on carbon particulates
Q-Q	'Quantile-Quantile plot.'
sccm	Standard cubic centimetres per minute
SE	Standard Error
SHE	Standard Hydrogen Electrode
SS	Sum of squares
SSE	Sum of squares of the residuals in a linear fit
St.Dev	Standard deviation
t	Student's t-distribution relationship
VAR	Variance
VIF	Variance inflation factor
WL	Whisker Length
Wt%	Mass present as a percentage of the total mass

1 Introduction

There is a great demand to find alternate energy sources. Energy based on fossil fuels is not sustainable in the long term [1]. The depletion of world resources and concerns about anthropogenic climate change are driving Carbon Dioxide (CO_2) emission reduction policies [2,3]; but despite this, the global demand for energy is predicted to keep growing [4]. Continued growth in the world population is likely, and a predicted increase in industrialisation and living standards in the developing world. The European Union (EU) and G81 leaders have agreed that CO_2 emissions must be cut by 80% to stabilise the atmosphere at 450 parts per million of CO_2 (keeping global warming below the safe level of 2 ^{o}C increase in mean temperature) by 2050[5].

Across a wide spectrum of disciplines and technologies [6-12], many avenues of research are being explored. Some seek to minimise the impact of continued fossil fuel use, some seek to improve energy storage and transmission, and some seek new ways of generating energy. What is undeniable is that the current energy system, with its reliance on fossil fuels, cannot last forever. Research is needed to find a cost-effective replacement for the existing energy supplies.

Polymer Electrolyte Membrane Fuel Cells (PEMFCs) offer the potential of efficient, sustainable power solutions for the future. There has been an expectation in the fuel cell sector of a 'breakthrough' in the near future. Research and Development (R&D) has not progressed as hoped and this anticipated breakthrough has not materialised. Early fuel cells had high platinum catalyst loadings, and this was one of the factors that increased their costs. The increased cost per fuel cell at that time limited sample size for researchers in the past.

Lower concentrations of platinum catalyst loading are now the norm, and membrane electrode assemblies (MEAs) can be manufactured relatively cheaply in comparison to the costs from previous decades. Such cost reductions make multivariate approaches to PEMFC R&D, which is often at their most useful when using larger sample sizes, viable for fuel cell research. This research highlights multi-factor approaches to fuel cell research. If successful, and the methods are adopted in the PEMFC community, research outputs can be accelerated in the future.

One specific area of PEMFC research that has lagged behind other is that of fuel cell durability (as discussed in more detail in Chapter 2). Durability and degradation studies require extensive testing time. Accelerated Stress Testing (AST) has been used to overcome the long durations such experiments can require. However, these ASTs often targeted at a single degradation mechanism, or they provoke a variety of degradation responses with limited understanding of which experimental variables are significant.

A testing regime that can consider multiple input and output factors (also known as variables) at the same time offers the hope of reducing the total time required to test a wide selection of variables. Accelerating the rate of knowledge acquisition even more than AST has so far achieved. There are many possible variables (or factors) that could be considered. These may be process variables such as temperature, pressure of the gas feeds to the PEMFC or some other factor. The structures and components used in the manufacture of PEMFCs are another set of possible variables to consider. This work will focus on some of these key fuel cell components (4 and 6 discuss the selected components in more detail).

A key element in fuel cells and the MEAs at the heart of them is the gas diffusion media (GDM). The GDM is critical for the transport of reactants to the active catalyst sites, the transport of charge into and out of the cell, and water management in the MEA. Variation in performance for different GDMs has been reported in the literature [13,14]. Some of the variability is due to the characteristics of the samples tested. However, due to the many GDM variables (porosity, thickness, types of fibre used, three-dimensional structure, additional coatings, etc.), explaining the variation in fuel cell performance that arises from the GDM performance can be challenging. Some studies have focused on testing GDM properties to achieve a better understanding of GDMs behaviour and the relationship between the different properties [15-18].

Usually, a GDM consists of a fibre substrate that is either constructed directly with carbon fibre or from precursor fibres that are then carbonised (heated at high temperature and pressure in an oxygen free environment). Often the carbon fibres are coated with a polymeric film that is similar to Teflon ® (‘teflonated’). Commonly the carbon fibre GDMs have a Micro-Porous Layer (MPL) painted on one side of the substrate to enhance water transport away from the catalyst layer (CL), and provide a smooth surface with lower electrical and thermal contact resistance for the catalyst layer. Different fibre structures are used for GDMs, namely; woven cloths, fibre papers, and non-woven ‘felts.' The fibre structure of the GDM plays an important role in its function and therefore affects the performance of the cell. Previous work has indicated that woven carbon GDMs have higher power densities [19-21] and are more efficient at higher humidity. In Comparison to woven cloth GDMs, non-woven carbon fibre clothes (known as ‘Papers’ and ‘Felts,' depending on their manufacturing method and resulting structure) are competitive on price, easier to work with, and mechanically stiffer. This research considers GDM degradation, cathode catalyst layer (CL) improvements and GDM structure simultaneously; seeking to discover if the three factors act independently, or if there is a link (known as covariance) between them. To do so an understanding of the various MEA components, and their fabrication methods were developed alongside a detailed examination of the variation (for example due to ambient conditions or the test equipment used) that can cloud the interpretation of experimental results. Yuan et al[22], state that GDM are rarely studied, and that proposed degradation mechanisms are speculative with no “*standard AST protocols on durability and degradation.”*

Antoine et al [23], experimented on variable catalyst concentrations but did not consider the type of GDM the catalyst was applied to as a possible co-varying factor.

By taking a statistical approach (e.g. Multiple Analysis of Variance (M-ANOVAR)), experiments in this research were performed on a reasonable sample size, and provide a robust analysis of GDM, Catalyst Layer (CL) and degradation in a single study.

1.1. Fuel cell structures and principles

Basics structures and topics of fuel cells are covered by several authors [24-26], and a brief summary is given here.

In a fuel cell, the fuel, in this research Hydrogen Gas (H_2), is combined with an oxidant to generate heat and electricity. The H_2 molecules are catalysed to break down into an ionic form (H^+), and the electrons (e^-) formed in the process are collected and utilised for work by transporting them through an external circuit. PEMFCs, using hydrogen and oxygen, work on the following chemical principles.

- Anode = oxidation = loss of electrons = hydrogen side = Hydrogen Oxidation Reaction
- Cathode = reduction = gain of electrons = oxygen (air side) = Oxygen Reduction Reaction

The two half-cell reactions can be written as

$$\text{Anode: } 2H_2 \rightarrow 4H^+ + 4e^- \quad \textbf{(1-1)}$$

$$\text{Cathode: } O_2 + 4H^+ + 4e^- \rightarrow 2H_2O \quad \textbf{(1-2)}$$

see Figure 1 (in which a simplified fuel cell is presented showing gas flow into the fuel cell and the resultant electrical current ‘out’ of the fuel cell) and Figure 2 (in which a simplified schematic of the MEA is presented along with two half-cell reactions that take place on the anode and cathode) for clarification.

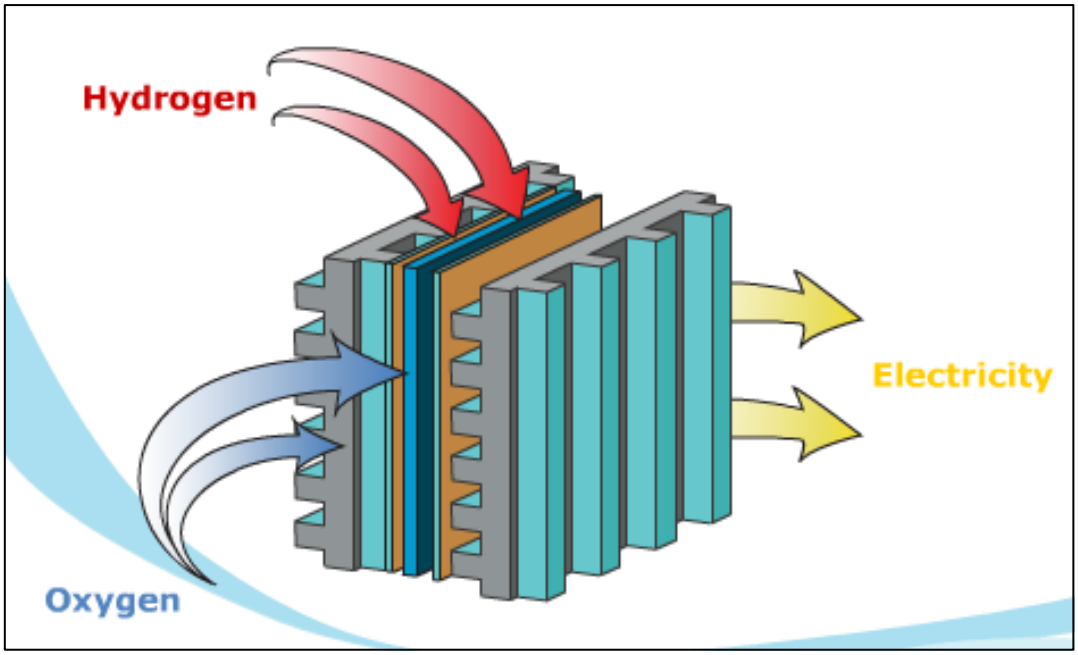

Figure 1: PEM fuel cell image

(Courtesy of Horizon Education Fuel Cell Products)

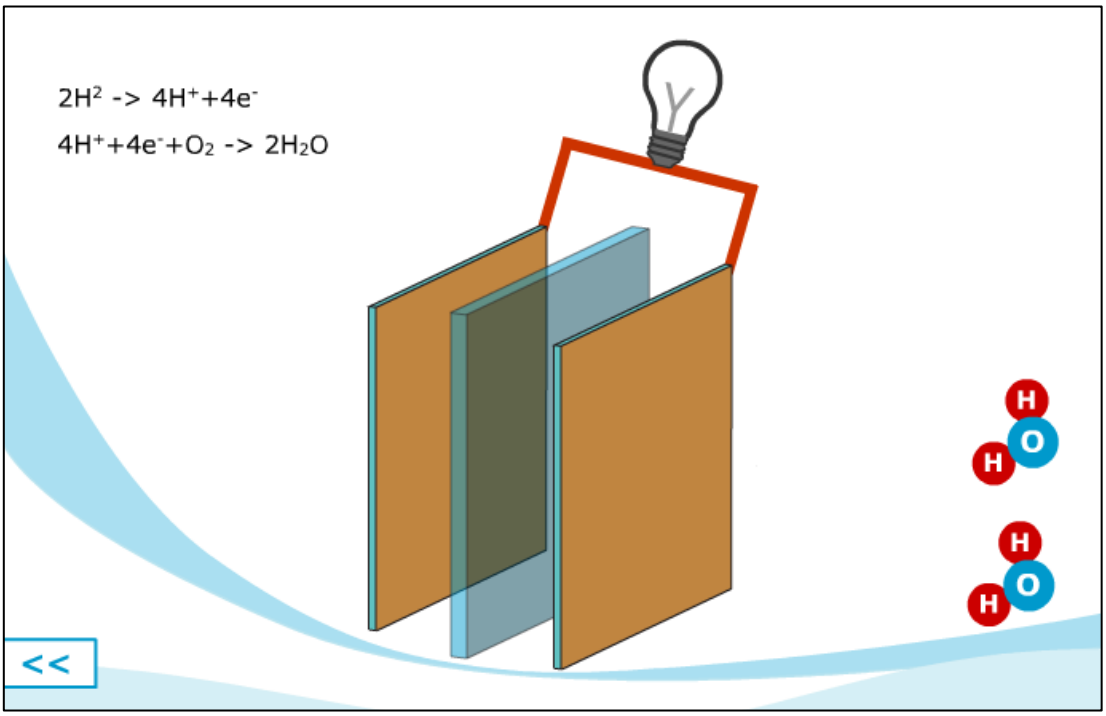

Figure 2: Membrane electrode assembly (MEA)

(Courtesy of Horizon Education Fuel Cell Products)

These two reactions are kept separate from each other by the electrolytic membrane: Usually a fluorinated hydrocarbon similar to Teflon, with a porous structure suitable for the transportation of hydrogen ions. Within the membrane itself, the transport of ions is facilitated not only by the existence of liquid water but also by the transfer from site to site along the chain of chemicals that

make up the membrane itself. The surface of the membrane is supplied with gas by the auspices of the GDM. It should be kept in mind that the full reactions can be more complicated, and it has been argued [24] that incomplete oxidation reactions can give rise to hydroxyl and hydroperoxyl radicle species (.OH and .OOH respectively). These radicle species are highly reactive and are likely to attack all chemical species they come into contact with (the membrane, CL/support, GDM and MPL).

The degree of hydration of the membrane and its adjacent structures are critical; requiring carefully controlled water levels to ensure its efficiency. The catalyst requires a certain degree of humidification to facilitate the transport of reactants, as does the GDM. The Cathode side of the membrane generates water as a reaction product making it liable to flooding, and the anode side of the reaction can dry out excessively, requiring a pre-humidification stage for the gas. Under certain circumstances, the anode side can also become flooded as excess water passes through the membrane and saturates the hydrogen side of the cell (back diffusion) with a significant negative impact on the performance of the cell. Hydration management controls the excess water that forms a liquid within the GDM and the gas flow channels of PEMFCs: Avoiding fuel/oxygen starvation and the cessation of the reaction in flooded areas. It is important to keep in mind that the primary purpose of fuel cells research is the generation of power, and for this reason, a brief section is included on the voltages produced in fuel cells. Thermodynamically (i.e. regarding the conversion of heat and energy) the energy requirements of a system, using standard nomenclatures such as enthalpy, free energy and others is best explained in Figure 3.

-TS →

+PV ↓

U (Internal Energy) U = Energy needed to create the system	F (Helmholtz free energy) F=U-TS F = Energy needed to create a system minus the energy provided by the environment
H (Enthalpy) H=U+pV H = The energy needed to create a system plus the work required to make room for it	G (Gibbs free energy) G = U + PV - TS G = the total energy to create a system and make room for it, minus the energy provided by the environment

Figure 3: Thermodynamic potentials

(Adapted from Babir (2013)[25])

T = Temperature

S = Entropy

P = Pressure

V = volume

The differential equation of enthalpy is

$$\Delta H = T\Delta S + V\Delta P \quad \textbf{(1-3)}$$

For $\Delta P = 0$ (constant pressure) this simplifies to

$$\Delta H = T\Delta S \quad \textbf{(1-4)}$$

In this case ΔH is the same as ΔQ (heat transferred in a reversible process): that is to say, enthalpy is the heat potential of a system under constant pressure conditions, due to the reforming of chemical bonds. On this basis, it is possible to calculate the energy from a series of chemical reactions due to bond formation, based on the initial and final energy states. There are tables of values for each part of the known reactions that can be used to determine this. The potential of a system to perform electrical work is the voltage; the work done is the movement of charge (Q in coulombs) through a potential difference (E in volts) is

$$W_{ELECTRICAL} = EQ \quad (1\text{-}5)$$

If the charge is moved by electrons then

$$Q = nF \quad (1\text{-}6)$$

(n= number of moles of electrons, and F = Faradays constant)

As

$$\Delta G = -dW_{ELECTRICAL} \quad (1\text{-}7)$$

It can be stated that

$$\Delta G = -nfE \quad (1\text{-}8)$$

Gibbs free energy (the extra energy needed to make a system and to make room for it) is the maximum amount of electrical work available from a system:

For an H_2 PEMFC

$$H_2 + (1/2)O_2 \leftrightarrow H_2O \quad (1\text{-}9)$$

It has a Gibbs free energy of -237 kJ/mol under standard conditions for liquid water: Therefore "*the reversible voltage generated under standard-state conditions is thus*" [24], and E^0 is the reversible voltage

$$E^0 = \frac{\Delta\widehat{g^0_{rxm}}}{nF} \tag{1-10}$$

Where

E^0 = (-237,000 J/mol)/((2 mol e^-/ mol of reactants)(96,400 Colombes per mol))

E^0 = +1.23V (the thermodynamically ideal voltage)

The pressure changes in a fuel cell can be significant, as the electrical potential energy available changes with concentration; and concentration and pressure have similar effects when considering gas mixtures. Chemical potential is used to model this. A version of the Nernst equation (discussed in more detail later) can be a useful method of calculating the energy output of fuel cells, but it must be recognised that it does not work with modified temperatures (away from standard) adapted to take into account those changes [24]. In Figure 4 the characteristic 'polarisation curve' showing how the true voltage output differs from the theoretical ideal of 1.23Volts. This image shows both the measured current density (shown in black) at a given load, and also calculates the power density W.cm^2 (shown in red).

Total Voltage output = V

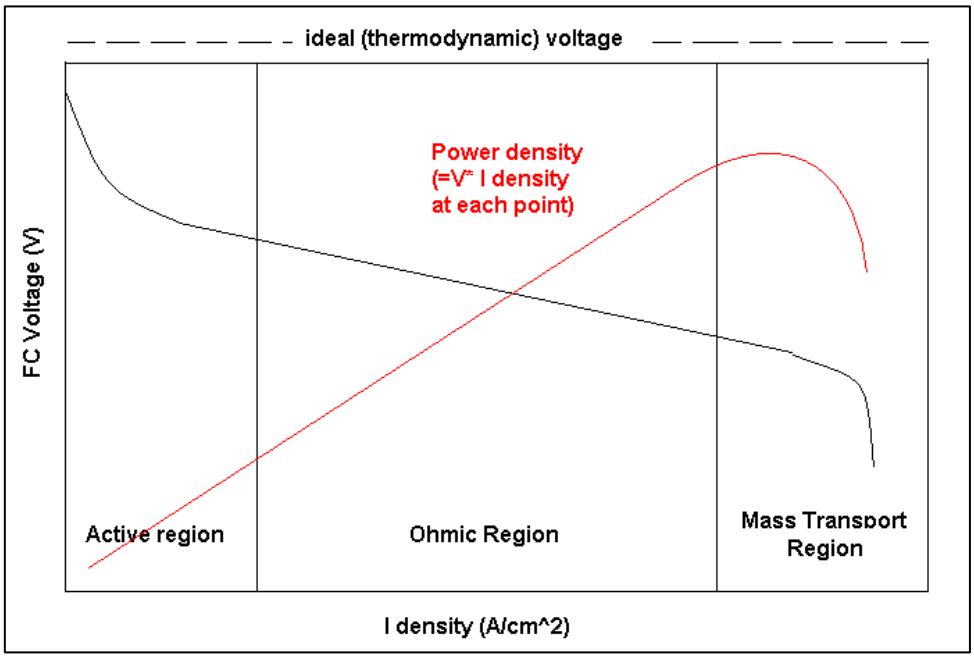

Figure 4: Fuel cell voltages and power density

(Adapted from O'hayre (2009) [24])

1.2. Aims and objectives: Statistics & multivariate analysis

Very large numbers of factors can be considered now in a way that did not use to be possible [27]. The technology exists to generate numeric methods that are suitable for use in very large data sets that do not follow a standard distribution and actively compare disparate methods for defining the sum of squares for a collection of data points. Harrar and Bathke [27] make the generalisation that there is no statistical data analysis method that is "… *uniformly better than the other*[s]…".

When selecting appropriate types of analysis, an objective review of the strengths and weaknesses of various techniques is of course required. So too is a willingness to take a 'first look' at the data with a likely method: Even if by the time the work is completed a better analytical method would have been more suited to the data [28,29]. A well-designed set of experiments is unlikely to miss the key points under investigation [30]. The concepts of a Design of Experiment (DoE) to define operating parameters of primary interest has been used before [31], as has the Box-Behnken approach to experimental design and data analysis [32]. However, they are not always applied correctly with, some authors openly stating "*the maximum voltage, maximum current and maximum voltage efficiency and maximum fuel efficiency*…[should all have undergone]…*transformations"* [33] when they were applying a Box –Behnken method for example. The advent of dedicated computer software to facilitate a wide variety of statistical approaches means that these types of errors should no longer occur in any field of research.

This thesis introduces basic DoE concepts and demonstrates their applicability to standard fuel cell data. This process will reveal information that has not been seen before, and validate the method on known samples. Having done so, they are applied to developed statistical tools for a new set of experiments, namely fuel cell degradation, GDM structure and Dual Layered Catalyst structures.

1.1.1. Aims

The overall aims of this thesis are to:

- Investigate if statistical methods, such DoE and multivariate-ANOVAR (M-ANOVAR) techniques, are applicable in fuel cell research.
- Demonstrate the application of such statistical methods and the reduction in total amount of time taken to conduct ageing and degradation studies in PEMFC research.
- Generate a thesis that will aid future fuel cell research scientists when applying statistical methods to their research.

1.1.2. Objectives

With these aims in mind, the following objectives have been set:

a) Investigate the extent to which DoE and M-ANOVAR have already been utilised in fuel cell ageing/degradation research.
b) Define a preferred statistical approach to apply in the next steps of the research.
c) Identify several areas in PEMFC ageing/degradation research where multiple inputs and multiple output variables can be investigated simultaneously, reducing the total number of experiments required through the use of M-ANOVAR and DoE.
d) Undertake a large scale set of experiments to act as a 'benchmarking' exercise and apply the identified statistical techniques from 'b'.
    - Consider appropriate software for the desired data analysis method.
e) Utilise the 'benchmarking' exercise as an opportunity to validate selected statistical analysis methodology.
f) Undertake a new study in which novel fuel cell assemblies are tested, and the results analysed using the newly validated method.
    - Present this new study as a 'case study' on the use of DoE and M-ANOVAR methods.
    - Demonstrating the reduction in resources required to conduct the experiments.

Objectives 'a' and 'c' are presented as part of the literature review in Chapter 2. Objective 'b' is discussed in depth in Chapter 3. The Benchmarking and validation exercise (objectives 'd' and 'e') are reported in Chapter 4. The final objective (objective f) is achieved in Chapter 6.

1.2. Outline of thesis

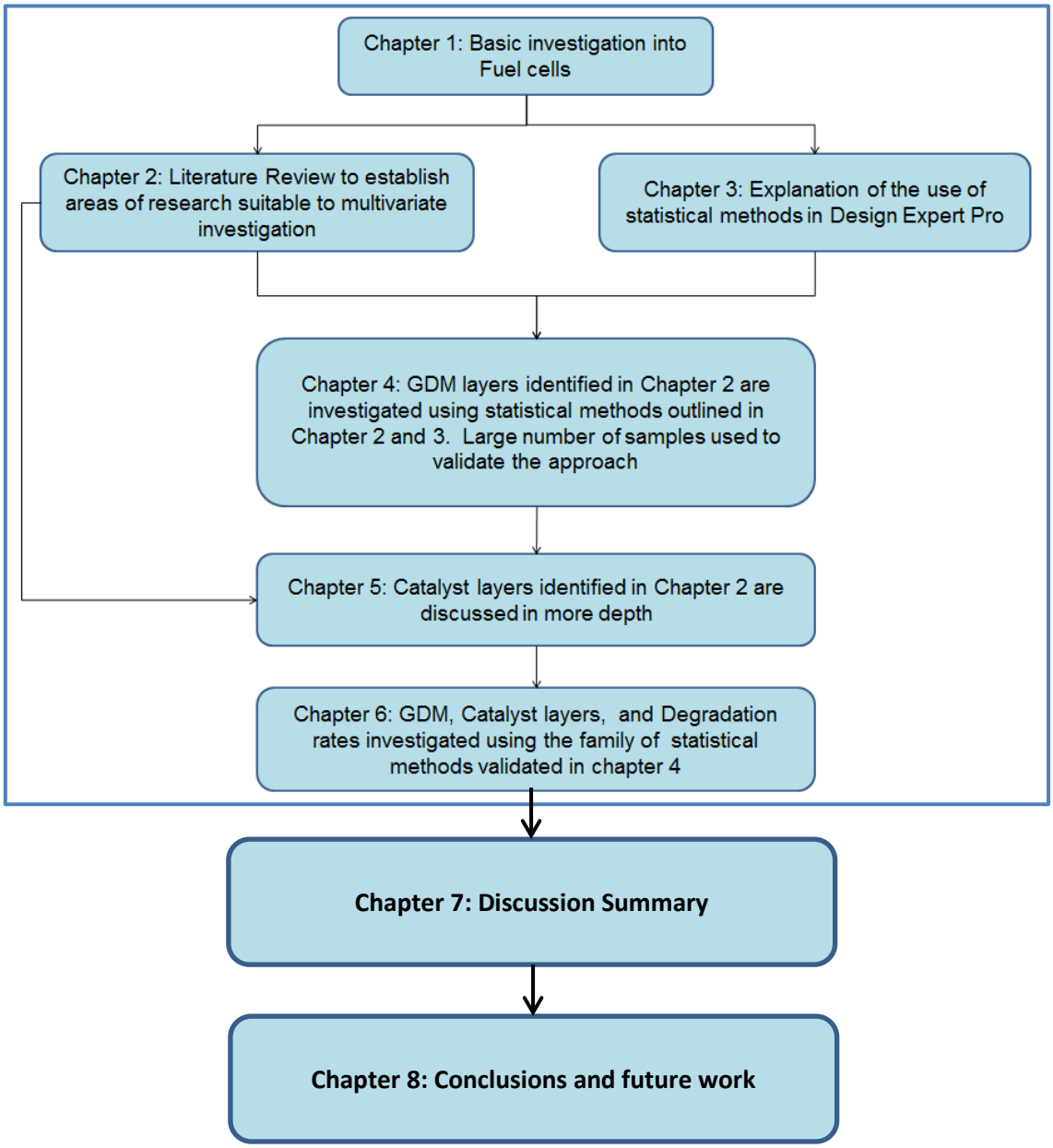

Chapter 1: Introduction. A basic guide to this thesis, fuel cell fundamentals and an introduction to the use of statistical methods in fuel cell research.

Chapter 2: Literature review. Begins with a review of the use of statistical methods as they have been applied in fuel cell research. Having established a knowledge base, this is discussed in more depth in Chapter 3. The literature review then goes on to consider some key factors that impact

PEMFC performance and degradation. Focused primarily on Gas Diffusion Media and Catalyst layers as these two topics are relevant to work that is reported later on in this thesis (see Chapter 4 and Chapter 5).

Chapter 3: Statistical Methods. A more detailed look at the fundamentals of linear regression, and error estimates as they apply to fuel cells. This chapter presents the methods that are applied in software packages that can undertake multiple analysis of variance (M-ANOVAR) assessments of experiential data. It also details several other related methods of statistical analysis and guidance on 'best practice' when applying statistical regression modelling approaches to real experimental data.

Chapter 4: Gas diffusing layers, statistical methods and validation using historic data. A more detailed understanding of GDMs was developed, using a simple two-dimensional numeric model created to highlight its importance. The Multivariate methods discussed in the previous chapter were applied to the GDM experimental data, validated and the results discussed in detail. Test conditions and equipment are detailed, as is the creation of membrane electrode assemblies (MEAs) and the catalyst 'ink' formulations they require. Previously published 'historic' data was combined with experimental results to create a database. An in-depth discussion of the techniques used in the analysis of the data is presented. A covariance between several factors was found to be important; some of which were previously reported in the literature, and some of which were not.

Chapter 5: A discussion on the importance of catalyst layer geometry and a one-dimensional model is presented to highlight some of the important factors in catalyst layer designs. This chapter expands on the literature review undertaken in Chapter 2 and is intended to highlight the important role catalysts play in the successful operation of fuel cells. This chapter introduces key concepts for catalyst layers, such as fuel cell degradation and the loss of catalyst surface area. The Thiele modulus for diffusion in and around catalyst rich carbon substrates and the Butler-Volmer model (adapted from Spiegel 2008 [34]) for catalyst activation are also introduced. The adaptations attempted in the past, to try and understand layered catalyst structures, are briefly discussed. This chapter also reports on a microscopy investigation of layered catalyst materials.

Chapter 6: DoE study on GDM, Catalyst layers and Degradation rates. The original design of experiment cannot be completed, and the interpretation of the results becomes more involved. This event was used as a case study event to demonstrate the flexibility of designed experiment procedures when utilising modern statistical software. No co-varying factors were revealed. It was found that the interplay of GDM structure, and the workloads it can tolerate, does impact the utility of dual layered catalysts and this is discussed in detail.

Chapter 7: A summation of the previous chapters and key findings is presented before the concluding chapter**.**

Chapter 8: Summary of conclusions and future work. The conclusions found in the previous chapters are restated for clarity. Recommendations for future work are made.

Appendices

Appendix 1: - Safety and data sheets & Agglomeration Definition

Appendix 2: The Spiegel model

Appendix 3: Original data tables and analysis

Appendix 4: Additional graphical versions of original data

Appendix 5: Previously published work contributing to this thesis

2 Literature Review

2.1. Introduction to Chapter 2

The flowing literature review considers statistical methods as they have been applied in fuel cell research and related fields such as electrochemistry (see section 2.2). Having established a knowledge base a more detailed discussion of statistical methods, relevant to the work presented in this thesis, is discussed in more depth in Chapter 3. The literature review then goes on to consider some key factors that impact PEMFC performance and degradation over time. Focused primarily on gas diffusion media (section 2.4), and catalyst layers (section 2.5). These two topics are relevant to work that is reported later on in this thesis (see Chapter 4 and Chapter 5). A brief discussion of duty cycles and the impact these can have on the lifetime performance of fuel cells was also considered (section 2.3).

2.2. Statistics & multivariate analysis

An early investigation into the strengths and weaknesses of multivariate methods can be found in the work of Dempster 1971 [35]. Written at the start of the personal computing revolution, it provides basic injunctions to the data analyst "*...to evaluate proposed techniques along dimensions of efficiency and resistance to error, both statistical and computational, and along the dimension of relevance to the substantive scientific enterprise involved*" [35]. The same paper also provides tools such as hierarchical logic trees to formulate research questions. The paper discusses the likelihood (probability) and estimates that the results of a given calculation are at a true maximum or minimum. Such estimates are achieved through the use of iterative calculations, by a computer, to approach the global maxima. The limits of this approach are also highlighted (computer time and the need for normally distributed data for the numeric methods recommended to be valid).

More recent papers [27], attempt to consider very large numbers of factors in a given data set or data sets where the number of samples measured is a very high proportion of the total population. They generate numeric methods that are suitable for use in data sets that do not follow a standard distribution, and actively compare three disparate methods for defining the sum of squares for a collection of data points; considering if Dempster–ANOVAR is as robust as the other available data analysis methods such as the "*…Lawley–Hotelling type, and Bartlett–Nanda–Pillai type"* [27]. Harrar and Bathke (2008) conclude that until the structures of any given correlations are well understood it is not possible to know which system is best suited to a given data analysis task. That is to say at the first attempt it does not matter which method an experimenter first uses to determine if correlations exist between the inputs and outputs of a set of experimental data; any of the three methods will work if applied correctly.

The proofs offered in the paper are based on only two or four variables but with very high numbers of levels for each variable. Harrar and Bathke (2008) compare their non-parametric systems to the data produced by Chatfield et al.[36]. As the data produced was an ordered ranking of 1-5 in terms of resistance to attack in a crab apple population, non-parametric methods were preferred.

The positive correlation between apple scab at different time points indicates that Dempster-ANOVA was the preferred collation technique (negative collections are better suited to the other two methods, and the Lawley – Hotelling test is most robust when dealing with very high numbers of levels).

The Chatfield textbook [29] gives an introduction to the topic for those new to it. It has an open and engaging style and provides a key checklist for all statistical work that is worth remembering, which is paraphrased here.

- Do not analyse any data until what is being measured, and why, is well defined.
- How was the data collected?
- Look at the data structure – is it a continuous field, or can it be logically distributed into groups and sets?
- Initial explorations first – use basic analysis (such as an arithmetic mean, box plots or a plot matrix) before spending time on more complicated analytical methods.
- Use common sense – if the data indicates that a law of thermodynamics no longer applies, it is likely that the data, or its analysis, is flawed.
- Report results in clear, self-explanatory fashion.

It is easy to become lost in the minutiae of complex stacks of data analysis, but at its heart, these rules still apply. Other useful texts exist [28] that can aid in understanding data analysis methods with a clear breakdown of analysis methods, and Manley [28] indicates the similarities and differences between the various types. Clear advice on selecting appropriate types of analysis and the need for the use of multiple analytical methods on a given data set is available [28]; with an objective review of the strengths and weaknesses of various techniques that provide a good grounding in the subject. After following the initial advice, there is an investigation of partial and full factorial analysis methods. Multivariate data, by definition, has several factors that can vary independently, and may also have combined effects. Full factorial methods are known and provide detailed results for analysis. The primary motivation for this research and the basis of the EPSRC funding award was the acceleration of fuel cells research and development. With this in mind, it seems logical to review partial factorial methods as a preference.

While it can be argued that partial factorial analysis runs the risk of missing key data points; others [30] would argue a well-designed set of experiments following the methods such as those developed by Taguchi are unlikely to miss the key points under investigation.

The work by Ranjit Roy (1990) [30] is a highly practical treatise on the use of partial factorial analysis (Taguchi method) in an industrial setting.

Particularly useful is the clear and concise explanation of noise factors, and how these are used to determine the number of replications in an experiential test run. The text gives highly detailed examples on 'orthogonal tables' to design an experimental regime.

The occasional author [31] has reported a design of experiment (Taguchi) approaches to *"… obtain the optimal combination…"* of test parameters. The evolution of the hierarchical trees recommended by Dempster (1971) [35] can be clearly seen in the logic tree for the design of their work plan. This paper by Yu (2008) [31] is notable as a work on fuel cells development that included confidence levels and degree of certainty in their results. It also combined research on Gas Diffusion Media (GDM) degradation, to highlight the interplay between humidification and hydrophobicity (PTFE content from several sources in the Membrane electrode assembly).

By comparison, the paper presented by Carton el at. (2010) [33] attempted to use a Box–Behnken DoE, and by their admission, many of the key output factors from the experiment should all have undergone "*transformations"* [33]. The authors argue that this step could not be conducted, as the transformed data did not follow a standard distribution and that the generated "*responses were not of great importance*" [33]. They discuss results comparing voltages across varying flow field designs with a 0.128V difference. Such work may well be valid, but the failure to include confidence levels and the degree of error calls the results into question. The lack of error assessment compounds the concerns that have been raised by the failure to 'transform' data earlier. It seems clear that the authors lacked the confidence to tackle the nonstandard distribution of data generated.

It should be pointed out that there are other papers where Box-Behnken has been used successfully [32] to produce response surfaces that have optimised experimental procedures in electrochemical analysis techniques. One cannot help but feel that greater preparedness in the experimental design of the work done by Carton and Olabi (2010) [33] would have avoided the complications in data transformations that they experienced. It is hoped that non-parametric methods such as those discussed earlier [27] could be adapted to facilitate the analysis of non-standard data sets.

Other multivariate methods, such as principal component analysis (PCA), have been used [37]. PCA is an optimisation method where certain variables are identified as being more significant than others. PCA approaches may prioritise components that are causal, and given priority. Or PCA may indicate that a new variable can be generated that will encompass several values within a data set (e.g. Width, height and length measurements being combined into a single volume measurement). In this paper, the authors claim to have created a function to map the experimental results that for each of the "*…29 input parameters involve 465 coefficients for each cell*" [37]. These coefficients are part of the

quadratic/linear regression analyses of the data and an attempt to generate a model based on their experimental results. Such results should be treated with a degree of scepticism: The slavish mapping of 465 coefficients to exact match the data fails to recognise the random nature of experimental results. By extension, the validity of all 465 elements in the quadratic equation must be questioned: There are only so many fundamental mechanisms at work within a fuel cell. As a predictive model for fuel cell behaviour, it seems to require a great deal of work for marginal gains in accuracy.

A more rigorous assessment of fuel cell parameters can be found in the numeric modelling fields, and the review by Secanell et al.(2011) [38], of fuel cell optimisation methods, is excellent. The Secanell paper [38] is focused on computer modelling of various fuel cell systems. The optimisation based on algorithms within a simulated (model) environment can reduce, but does not eliminate, the need to perform experimental studies. In this paper, the authors support the notion that, for limited numbers of variables in a 'parametric study', it would be preferred over an optimisation algorithm approach.

It should also be argued that higher numbers of variable and non-parametric also need experimental proofs to validate the numeric models/simulations produced. Secanell et al. (2011), state "… *a parameter estimation technique coupled with a multi-dimensional fuel cell model containing an accurate catalyst layer model still needs to be developed."* [38]. Further practical research would provide the tools needed to quantify the required parameters to create more reliable cell and CL numeric models.

Such a modelling programme requires fundamental experiential work, perhaps utilising some of the novel materials that are identified in the paper, to form the basis of the modelling data. Experimental work becomes especially important when considering the possibility of interaction factors. Novel materials, geometries and adjacent elements within the cell itself (for example if the catalyst and its support are doped on the Gas Diffusion Media – GDM – then factors impacting the integrity of the GDM will impact the integrity of the catalyst structures).

2.3. Degradation and fuel cells

Over time, the output of the cell will reduce. Degradation of the materials that make up the fuel cell is inevitable, and a working life of 5,000 hours for a system suitable for use in domestic automotive markets has yet to be perfected. There are many mechanisms of degradation. Ostwald ripening is the coalescing of smaller particles to form a single larger particle with an overall reduced free energy at the surface of the newly formed larger particle [39]. Ostwald ripening, often referred to as 'agglomeration' (see appendix one) in fuel cell literature, is one example of time dependant degradation.

Wu et al. (2008) [40], produced an excellent review paper on the degradation of fuel cells and highlighted the importance of hydrophobicity (how easily or not the material in question can be 'wetted' by water) in the GDM along with several other factors. There are many excellent review papers on the degradation and failure modes, and their causes, of fuel cells and Table 1 is adapted from two of them ([40] and [41]).

Table 1: Major failure modes of component in PEM fuel cells

Component	Failure mode	Causes
Catalyst, catalyst layer	Loss of activation	Sintering (agglomeration), de-alloying
	Conductivity loss	Carbon support corrosion
	Mass transport rate reduction	Mechanical stress, pore closure
	Poisoning	Contamination
	Decrease in water management	Nafion/PTFE dissolution
	Loss of Pt	Re-distribution of Pt (dissolution)
	Pt Migration	Transport of Pt into the membranes
GDM	Decrease in mass transport	Degradation of backing material (carbon fibre 'cloth') Mechanical stress (pore closure) Changes in hydrophobicity GDM fibre corrosion

(Adapted from (Wu et al. 2008 [40] and Whiteley et al. 2016 [41])

The wettability (hydrophobic or hydrophilic response) of carbon fibre gas diffusion layers is frequently tailored by the addition of varying amounts of water-repellent polymer. Typically this is a PTFE-based polymer [25,42] identical to or very similar to the Nafion of the membrane, catalyst and microporous layers of the MEA. PVDF (Polyvinyl Fluoride) and FEP (Fluorinated Ethylene Propylene) have also been used in the past by other researchers [42]. Table 1 shows that changes in hydrophobicity, one of several major failure modes that occur over time. This change to the hydrophobicity of the GDM leads to a loss in mass transport performance.

This loss in performance seems not to be the case in the paper by Pei et al. (2010) [43]. The Pei paper [43] reported accelerated stress testing regime was shown to result in MEA contact angles of "*124 to 130 degree* [sic]". By the reasoning put forward by Chapuis et al. (2008) [44], this would indicate that hydrophobicity has not been impacted by the accelerated degradation testing undertaken [43]. The three arguments lead one of three possible conclusions:

- The accelerated stress [43] test regime was not correct.
- The model and understanding [44] of the impact of hydrophobicity changes over the lifetime of the cell was not correct.

- The statement that hydrophobicity effects are a significant degradation mechanism in PEMFCs [40] was not correct.

This conflict in the literature is good grounds to consider the GDM in more depth and to develop a design of experiments that can assess the impact of GDMs (with or without hydrophobic coatings) on fuel cell longevity. It is further hoped that such work will provide example experimental design methodologies, and other data analysis techniques, and introduce their use to other fuel cell researchers in accordance with the aims and objectives as stated in section 1.2.

There has already been some outstanding work on fuel cell degradation, though there has been little work completed on the reduction of hydrophobicity, and the subsequent loss of fuel cell performance, that arises from oxidation of the GDL and PTFE degradation [45]. This topic of the degree of degradation of the hydrophobic coating compared to the degradation of the carbon in the GDM more generally needs to be quantified and understood more fully. Hiramitsu et al. (2011) [45] undertake detailed work in this area. Using a wide variety of analytical methods to measure the various properties of the GDM and CL (catalyst layer) and make strong claims as to the importance of hydrophobicity and its impact on GDM/CL longevity, though further work is still required. Table 2 shows the contact angle for a given GDM has been measured both in the 'advancing' and 'receding' position. Hiramitsu et al. [45] report the test results from a sample is inserted into a calibrated container of water, and the contact angle is measured (advancing). The receding measurement is generated when the sample is pulled out again. The 100-hour samples have larger contact angles (hydrophilic), and the authors state that the contact angles for the 6000 hours samples are 5-6 degrees smaller (2.9%) in the advancing contact angle and 11-12 degrees smaller (11.1%) in the receding contact angle; indicating their hydrophobicity increases as they age.

Table 2: Contact angles of GDMs

Contact angles (hydrophobicity) for GDMs		
Homogeneous GDM coating	Advancing contact angle	Receding contact angle
100hrs	172^{O}	108^{O}
6,000 hrs	167^{O}	96^{O}

(Adapted from Hiramitsu et al. (2011) [45])

Unfortunately, no confidence or error bounds are presented. In part, this lack of statistical robustness is complicated by the practical difficulties of creating statistically significant numbers of test cells that can be run for 6,000 hours. Thousand hour test cycles would be a drain on the resources of any laboratory and highlight the need for an accelerated degradation test that can provide reliable results for assessing the impact of GDL/CL hydrophobicity on fuel cell performance over time. The work by Hiramitsu et al. (2011) acknowledge that "*The relation between water management performance of GDL and CL degradation must be verified further*" [45].

It may be possible to improve the hydrophobic properties of GDMs by improving the adhesion and distribution of these PTFE based fibre coatings through the use of a plasma pre-treatment of the carbon fibres before addition of catalyst layers and binders [46]. If this is correct, this once again highlights the importance of PTFE structures in the GDM not only for water management but also for gaining an understanding of the degradation mechanisms involved. Breakdown of PTFE in the MEA has been shown to result in a doubling of the losses in performance compared to the losses accrued as a result of catalyst agglomeration (Ostwald ripening – see section 5.3 for clarification) after 1,000 hours of operation [40] the mechanisms behind such PTFE degradation are not well understood. In part, this is due to the inability to characterise discrete regions of the PTFE network in the fuel cell (though this issue has recently shown some progress [47]).

Improvements in understanding of fuel cell degradation mechanisms have had some headway made in recent years. It has been stated in the Schmittinger and Vahidi (2008) review [48] that there are a wide variety of possible causes of the degradation of fuel cells, and in the GDM in particular. A 6,000-hour study by Hiramitsu et al. (2011) [45], on a limited number of gas diffusion layers, with both homogeneous and inhomogeneous hydrophobic coatings, has been completed. It was concluded that degradation is primarily due to the development of oxidation species in the GDM. Lines of oxygen-rich surface areas, corresponding to the flow channel geometry, provide the evidence for this [45]. Increased concentrations of $C_3F_5O^-$ ions were also detected after the test run. The $C_3F_5O^-$ increase was attributed to the migration of Fluorine species from the electrolyte layer into the GDM itself [45]. However, their work is weakened slightly by the use of two different polymers with different hydrophobic qualities achieved by each process.

Homogenous unbroken PTFE coatings on GDM fibres using a 1wt% (weight percent) of ‘Cytop CTL-109AE’ polymeric solution [45] have been achieved. Compared to a 12wt% solution of PTFE (31-JR) [46], or a 10wt% mixture of PTFE solution. The preferred optimum PTFE loadings are usually cited as being in the order of 15wt% [42] to 20wt% [14]. The exact amount of hydrophobic coating that should be added is still open to some debate, with a range of 15 to 30 weight percent often being cited [25,42], though some authors have considered PTFE loadings as high as 60wt% [49].

There is scope for significant work in designing multivariate experiments to optimise the homogeneity of PTFE layers, and also considering the degree of PTFE layering needed for comparable performance between homogeneous and inhomogeneous systems. It should also be kept in mind that the uniform coating of fibres may indicate a reduction in the control of the hydrophobicity of a given GDM; the advantage of inhomogeneous coating layers is that it can effectively adjust the hydrophobicity by increasing or decreasing the area covered. This 6,000hr study now provides a suitable benchmark to compare a variety of rapid ageing test cycles; and to ascertain if broadly similar results can be achieved by existing, or novel, accelerated test cycles.

Such test cycles can only be validated *"…on available past observed data and statistical models."* [50]. An excellent paper on accelerated ageing protocols by Yuan et al. (2011) [22], points out that degradation mechanisms in the GDM are some of the least studied to date. The proposed mechanisms for degradation have yet to be finalised. Cheng et al. (2007) (reference 52 in Yuan et al. (2011) [22]) that loss of mass transfer is the major degradation effect that occurs in the GDM as a result of changes to GDM surface contact angles and structure. They also point out that accelerated test protocols, almost by definition, target individual structure degradation, and where possible even target individual mechanisms. Sadly for the development of GDM materials, there are no "…*standard AST protocols on durability and degradation issues for GDLs*" [22]. They do however identify two mechanisms of interest:

- Loss of material and changes to pore structure during Hydrogen starvation.
- Changes in hydrophobicity overtime (though often linked back to freeze-thaw cycles).

Yuan et al. (2011) [22] go on to propose four key methods for inducing both of these degradation mechanisms:

- Increased flow rates of reactants.
- Elevated temperatures.
- Constant and very high potential loading of 1.2 Volts and higher during localised fuel starvation.
- Dynamic voltage cycles.

The dynamic voltage changes are the easiest of these to achieve in practice. The above conditions were applied for 200 hours each to small stacks. Two additional factors were also identified:

- Excessive hot pressing during manufacture.
- Excessive stack assembly pressure.

Another element of interest, when considering dynamic loading, is the type of dynamic load applied. US Department of Energy (DOE) single cell/stack testing protocols for transportation applications in both the steady and cycled state are briefly discussed, as is the start-up and shut down cycle developed by the Los-Alamos National Laboratory. Though they have little to say about them other than identifying the need to correlate the drive cycles with "…*systems operating under actual drive cycles*…". The testing of stacks, as opposed to individual cells, is an important consideration in this discussion [51]. How well can single-cell testing be scaled to reflect degradation in a stack? Certain test parameters can be scaled easily such as:

- Tafel slope.
- $E_{OpenCircuit}$.
- Direct current (DC) resistance.

Other factors do not scale well:

- Voltage increase as a result of humidity increases (i.e. up to five cells in a stack voltage increases as a result of humidity increases are scalable, but beyond five cells this is no longer true.
- Mass transport loss.
- Temperature distribution.
- Overall performance (voltage and amps per cm^{-2} in each cell in the stack).
- Humidification of cell membranes.
- Electrochemical surface area (ECSA) of catalyst (catalyst nearest the hydrogen inlet remains most active).

There can be a lack of real life testing [51], with differences between stack and single cell degradation. Other works on ageing and load cycles [34] consider cell stack testing, paying attention to the type of cycling loads being applied and comparisons between them.

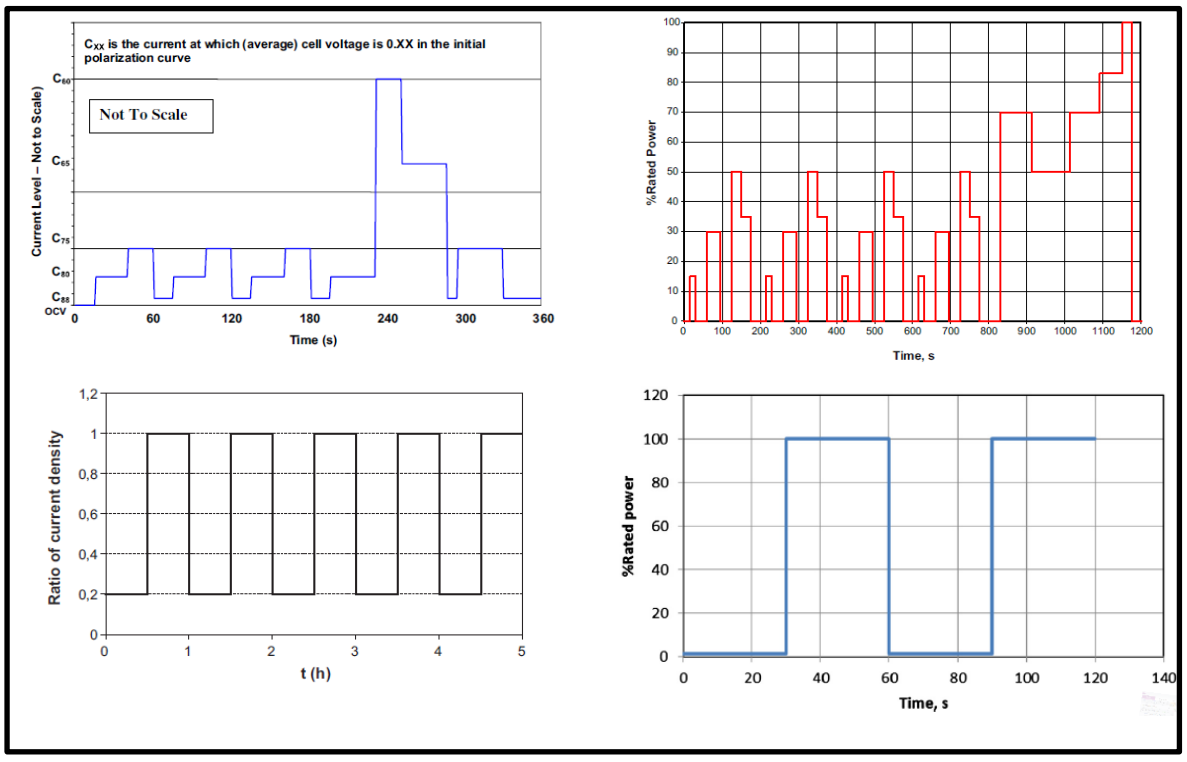

Figure 5: Fuel cell stack duty cycles

(DST Duty Cycle (Top Left), NEDC -ECE squared pulse (Top Right), IEC/FCtestnet Duty Cycle (bottom Left) and FCTT Duty Cycle - wet (bottom right))

Table 3: Duty cycle results

Profile name	Time per cycle, s	Energy, Wh cycle^{-1}	RMS power, W (cycle)	Time at OCV, s (% of cycle at OCV)	Time at full power, s
DST	360	300.1	3734.6	15 (4.2)	20
IEC	3600	5232.3	5959.0	0 (0)[b]	1800
ECE R15	1200	1154.9	4019.6	455 (37.9)	25
FCTT	60	62.2	5193.7	0 (0)[c]	30

[a] The power and energy values are from the 8-kW fuel cell stack used in this study.
[b] The minimum current specified in the IEC protocol is 20% of the maximum current.
[c] The minimum current specified in the FCTT protocol is 0.02 A cm^{-2} (~2% of the maximum current).

(From Bloom, Walker, et al. 2013) [1]

Bloom et al. (2013) [34] state that the causes of degradation require experimentation to identify, and the loss in performance is (in all likelihood) proportional to the duration of the stack being at full power. The authors state that water production is somehow driving this degradation, but fail to identify the mechanisms at play. Figure 5 has been adapted [34] to show four typical 'duty cycles'. Four duty cycles are presented:

- U.S. Department of Energy and US Fuel Cell Council Dynamic Stress Test (DST).
- New European Driving Cycle (NEDC).
- International Electrotechnical Commission and FC Testnet cycle (IEC/FCtestnet).
- US Driving Research and Innovation for Vehicle Efficiency and Energy Sustainability (USDRIVE) Fuel Cell Technical Team (FCTT).

The IEC and FCTT will, along with other works, form the basis of the duty cycle adopted in this work for degradation testing in Chapter 6. Table 3 shows that the time at 'full' power (i.e. peak power) for the square wave duty cycles (IEC and FCTT) is the highest.

Based on the work completed by Bloom et al. (2013) [34], the IEC regime is the one that can be expected to degrade the stack most rapidly. There is little clue about how representative such a drive cycle is for the degradation mechanisms that a working system can expect to experience, as the paper completed research on stacks that were 'end of life' devices. Without fully documented working histories, it becomes difficult to ascribe specific degradation mechanisms.

The work of He et al. (2013) is firmly focused on catalyst systems, and states bonding between the platinum decorated carbon black can have its ability to bond with GDM fibres strengthened. This increased adhesion being achieved by the "… *Nafion content and its humidity level in catalyst layer.*

[1] Figures and tables on this and preceding page reproduced with permission of Argonne National Laboratory.

[thus] …*improving the durability of fuel cells.*" [52] Due consideration must be given to the inclusion or exclusion of hydrophobic coatings, as this will impact results significantly. When hydrophobic coatings are included in a given study, it is acknowledged that coatings are supplied by the manufacturers. The importance of pressing regimes [53] during MEA manufacture are another potential variable that must either be controlled or included in the design parameters of the experiment. Once again many MEAs are tested and compared 'as supplied' by the manufacturer, and it is not always clear to what extent the processing histories of various MEAs are the same, especially when comparing results between different authors.

2.4. Gas diffusion media

The gas diffusion media (GDM) performs multiple tasks with the fuel cell [16,25,54] and is detailed in the following bullet points:

- Supply of reactants.
- Removal of products.
- Structural support to the membrane and catalyst layers.
    - Specific support to catalyst layers in CCS MEAs.
- Control of humidification by inhibiting/accelerating water removal.
    - Tailored in combination with the hydrophobic coating.
- Electrical conductivity.
- Thermal conductivity.

The structure of the gas diffusion layer, its material properties and the application of any coatings to its surface, all contribute to the ability of the GDM to perform these tasks. At this point, it is constructive to discuss various terminologies for GDMs.

- Gas Diffusion Layers (GDL) - this term has two distinct usages:
    - A porous material between the flow field plates and the membrane electrode layer.
    - More specifically a (usually) carbon powder and Nafion® mixture coated onto the surface of the carbon cloth/paper. This carbon and Nafion® mixture, in turn, acts as a support for the catalyst layer (this term is often replaced with the term 'MPL' or Micro Porous Layer, and is also known as the Diffusion layer (DL).
- Gas Diffusion Electrode (GDE) – a GDL that supports, or is in some way electrically connected to, a catalyst layer. The GDE may, or may not, be in conjunction with a micro-porous layer (MPL), and the MPL may be applied to catalysts that have been directly coated onto the membrane itself, to the surface of the MPL closest to the membrane, or to the GDL directly in MEAs that do not have an MPL.

- Gas Diffusion Media (GDM) – a ‘catch all term’ that does not distinguish between GDL and GDE.
- MPL – the microporous layer is a mixture of (usually) carbon powder and Nafion® and is located adjacent to the catalyst layer, the vast majority of them between the carbon cloth/paper and the catalyst layer. This structure is sometimes also known as the GDL (gas diffusion layer), or even simply the DL.

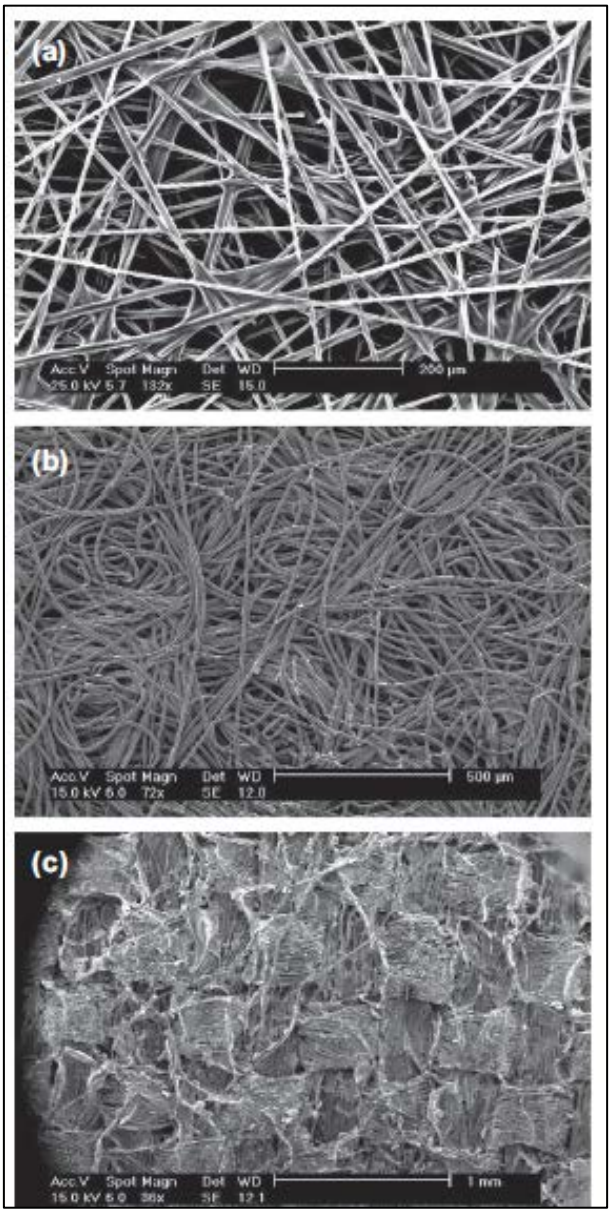

Figure 6: GDM structures

(Comparative carbon papers (a), non-woven (b) and woven (c) GDMs. Reproduced from El-Kharouf and Pollet (2012) [16])

Traditionally GDMs have been classified into two large subgroups: Woven carbon fibre materials (with a three-dimensional interweaving of fibres in a variety of possible patterns), carbon papers that

are deposited layers of carbon fibres that are pressed and sintered together to form a rigid, stratified fibrous matting using a process very similar to that used in paper making. Increased thickness papers can be created directly, or by bonding two or more thinner carbon papers together. Such bonded layers can generate a GDM with a series of stratified layers [55]. See Figure 6 'c' (woven) and 'a' (paper). The internal differences are readily visible and are shown in Figure 7. Typically woven fibres are known to have enhanced performance at high current densities [21] due to improved water removal, though this has been clouded somewhat by the use of GDM with differing levels of hydrophobicity on different GDMs in some research [56].

More recently several authors have begun to distinguish a third category of GDM, colloquially referred to as 'felts' [55,57]. This development in recent years in the third class of carbon materials, the non-woven 'felts', can be further sub categorised in two broadly distinct camps, which can be described as follows:

- Continuous fibre non-woven felts - Displaying a characteristic 'spaghetti-like' macro structure (image 'b' in Figure 6).
- Short fibre felts – Deposited fibres of carbon in a fashion similar to that of the paper manufacturing process. These paper like fibres and layers then undergo an additional process where a degree of three-dimensional fibre structure is introduced through the use of needles (the traditional method for producing true 'felts'). The fibres can also be 'needled' through an air blasting technique. Needling entangles and entwines the fibres that would otherwise form a traditional paper structure. Superficially there is no major difference in the appearance of these needled, or air blasted materials and the paper structures.

The through-plane penetration of fibres in the 'felted' papers may, arguably, have a significant impact on the bulk material properties of the GDM compared to its equivalent paper structure. Assessments of the impact of these structural differences are being published more frequently in the recent past [15,16,55,58-62].

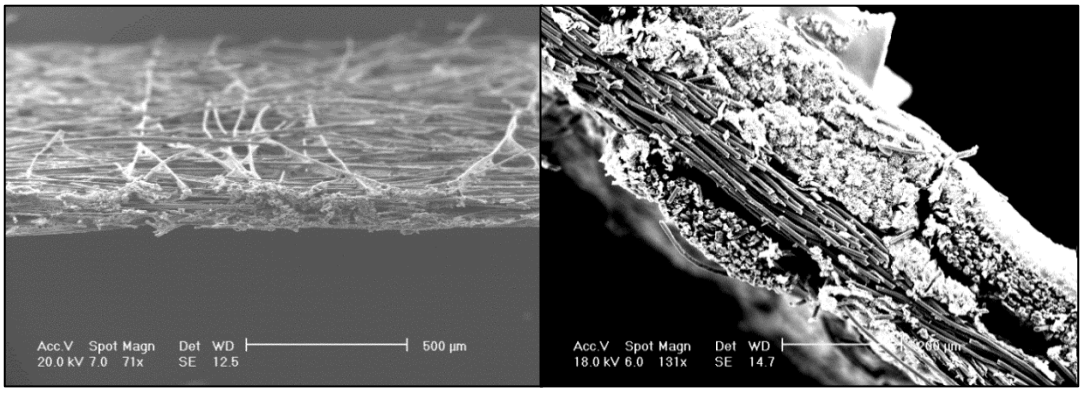

Figure 7: Through-plane section paper

(Paper (Sigracet 25 BC - left) and woven (LT1200W- right))

Many authors [15,16,55,58-62] have characterised the tortuosity, porosity and other characteristics of GDMs. However, there has been a distinct lack of multiple factor interaction analysis; both within the gas diffusion media itself and also for its interaction with adjacent structures such as the catalyst layer (CL). It could be argued for membrane coated catalyst layers (MCLs) that there is unlikely to be a significant effect from the gas diffusion media. However, for catalyst layer manufacturing techniques where the catalyst materials are deposited directly onto the carbon fibre substrate of the GDM (CCS or Catalyst Coated Substrates), it seems likely that multiple factorial effects could be in operation.

Parke et al. (2012) [42] site a variety of authors that have compared carbon paper (TGP-090, Toray) and woven carbon cloth (Panex PWB-3, Zoltek) as GDMs. The woven carbon cloth was found to be superior at higher current densities, and also at variety humidity settings (except for the low humidity condition). Part of the improved performance in carbon cloth material is credited to its bi-modal pore sized distribution [42]. Hydrophobicity is also highlighted as important and is considered optimised in the 15wt% to 30wt% region for PTFE. It has been claimed by Pai et al. (2006) [46] that plasma treatment of the fibres can reduce the optimum PTFE loading to 10wt%. Such low concentrations of PTFE on the fibres, in turn, improve the efficiency of the fuel cell system (fewer pores in the GDM blocked by PTFE) and a 50% improvement in total power output becomes possible.

Typically such PTFE coatings are created by dipping the substrate into a solution of the desired polymer, which is then dried "*above 350 ^{o}C to remove surfactants and uniformly distribute……polymer.*"[42] This drying regime should be kept in mind if the reported improvements after surface activation of fibres are not realised. Unfortunately, these optimised PTFE coated fibres are not commercially available across all GDM structures. Roshendal et al. (2001) [63] provide a model to determine the behaviour of the GDM. GDM models will be considered in more detail in subsequent sections (Chapter 4). Most interesting is that the 'multi-layer' catalyst concentration structures being considered in this paper reveal that, although the idea of the multi-layer catalysts distribution has been well studied, there has been very little practical experimentation to validate them. Furthermore: No comparative degradation study of distributed catalysts structures has been undertaken at this time.

2.5. Catalyst layers

The catalyst layer is arguably the single most critical component of the fuel cell. The separation of O_2 and H_2 molecules, and the recombination of those component atoms into water is facilitated and accelerated by the catalyst materials (usually platinum or an alloy of platinum and other metals). While these processes occur naturally, the rate of a reaction without a catalyst is painfully slow and of no practical use. For this reason optimisation of the catalyst layer has been a major topic of research

in the fuel cell community. Significant gains have been made in the reduction of the required catalyst to achieve a given level of performance, and this research continues to this day.

The 'additional factor' research and development in this area focused primarily on the interactions between the carbon support particles the catalyst it was adhered to. As stated for other topics in fuel cell research this has tended to be 'one factor a time' (OFAT) approach in the past. The CL is not well suited to the identification of more complex interactions. Fortunately, there is a large body of pre-existing knowledge of catalysts in other fields, and a large number of numerical simulations of catalysts both within the fuel cell community, and outside of it.

The 'Dirac-delta distribution' based catalyst optimisation is well known ("*i.e. all the active catalyst should be located at a specific position within the pellet*" [64]), and is regularly used in chemical engineering practice. Obviously, it is not possible to place all the catalyst at a single exact location, and it is arguably counterproductive to do so, but the Dirac-delta function is at the heart of an, idealised and preferred, probable catalyst location. This catalyst distribution is typified by maximising the distribution of catalyst at the point where it will be most effective and then tailing away the catalyst concentration over a relatively small distance [64]. For example, in relation to the specific crystalline plane on the substrate the catalyst is deposited on [65], or the location in a fluidised bed where the major concentration of catalyst materials is deposited [64]. At its simplest, this can be thought of as placing catalyst particles as close to the incoming reactants as possible. Locating each catalyst site in a single cluster on the surface of the catalyst supporting particles, where the surface energy of the supporting particle assists with the bonding of the catalysts, and in some cases with the catalysis itself [65]. It should also be stressed that the pore structure of the catalyst support materials, and its subsequent impact on the flow of reactants, will also impact the ideal location of catalysts. Note that catalyst loading and catalyst activity are not the same – this document will focus primarily on loading. Catalyst optimisation must take into account many measures: effectiveness, selectivity of catalysed reactions, yield, lifetime, reaction kinetics, transport properties, operating conditions, poisoning mechanisms and cost are all important.

In the literature, this full analysis is seldom completed due to its complexity. There is some indication that a Dirac based distribution would be optimal for fuel cell applications, especially if one considers the fuel cell as a membrane reactor [64]. Inert membrane reactors have the catalyst outside of the membrane material itself and are arguably the most frequently used or recommended [64,66-68]: The catalytic membrane reactor (where the membrane itself is part of the reaction) is a category that GDEs could occupy. Szegner et al. (1997) [64] have tackled this problem. They also tackle the issues of functionalised polymer resins, but state that the activities and selectivites of resin based catalysts are operational and system specific (each system needs to be modelled individually). It should be noted that one of the ageing/degradation phenomena encountered in fuel cells is the relocation of catalyst

material from the catalyst support into the membrane itself, and it may be that a combination of models (membrane reactor and functionalised resin) would be required to conceptualise the catalysts system as time passes.

Despite this research in the wider chemical and chemical engineering fields "[t]*here have been limited attempts to optimise the CL parameters mathematically, in spite of numerous modeling* [sic] *efforts"* [68] for fuel cells. A layered structure of catalysts with different catalyst concentrations may make it possible to optimise catalyst loading in fuel cell applications. The catalyst material can be described as an agglomerate particle in which the carbon support material is tightly bound to the platinum (Pt) nanoparticles. This composite pallet is then considered a single unit of catalysed agglomerate [68].

It is perhaps useful to define 'agglomerate' as separate from 'agglomeration'. An agglomerate is a collected mass, ball or cluster [69] of separate things (or phases) and is a generic term. Agglomeration, in terms of catalyst particles, in particular, is the moving together of Pt atoms on the surface of the catalyst support materials, and by extension any other areas where catalysts appear in the fuel cell. It is more correctly referred to as Ostwald ripening (see section 5.3 for clarification). It is typically regarded as one of the degradation mechanisms that results in the loss of the available electrochemically active catalyst surface area (ECSA) of the platinum catalysts [41,70-72]. Figure 8 shows a stylised representation of the agglomerate (i.e. static in time) Pt nanoparticles clustered on and within the carbon substrate that supports them [68]. Figure 9 shows a schematic representation of several of these agglomerate (carbon black and Pt) particles and a simplified distribution on the surface adjacent to the GDM. This assumption of the location of the catalyst is often made in numeric simulations and is discussed in more depth in Chapter 4 and Chapter 5.

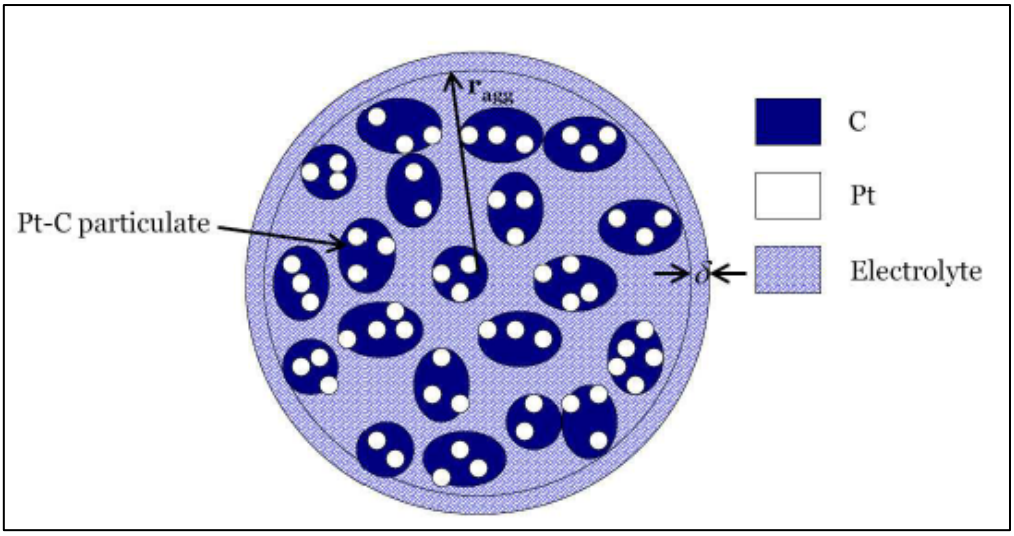

Figure 8: Catalyst agglomerate particle

(From Jain (2009) [68])

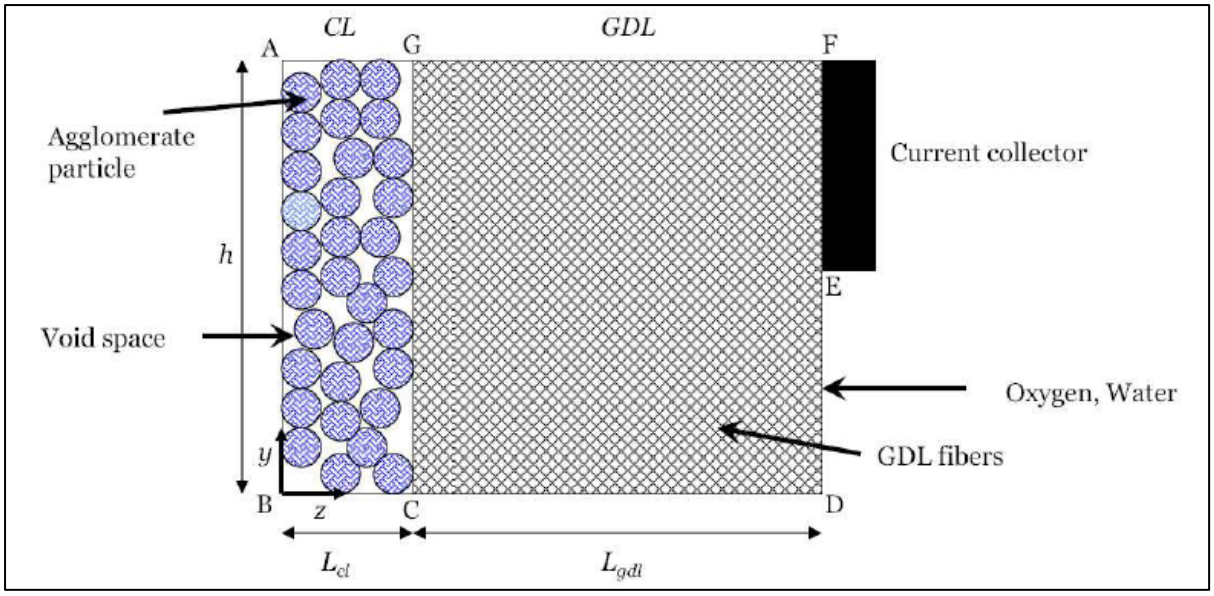

Figure 9: two-dimensional schematic of GDM / CL

(From Jain (2009) [68])

To produce optimal catalyst distribution, it has been proposed to introduce non-homogeneity in the catalyst by utilising a "*multi-zone optimisation…*" [68] and each zone has a unique set of variables linked to adjacent zones with concentration and potential flux. Table 4 shows numeric simulations of catalyst concentrations (in g.cm^{-2}) achieved by [68], with Figure 10 showing the same result graphically (Pt concentration against distance through the thickness of the catalyst layer being shown).

Table 4: Catalyst Distribution Optimisation

N	$I^*(A/cm^2)$	m_{Pt} x 10^4 (g/cm^2) distribution from PEM-CL to CL-GDL interfaces
0	0.0331	1
1	0.0432	0.942 / 0.058
2	0.0467	0.840 / 0.099 / 0.036 / 0.025
3	0.0473	0.588 / 0.234 / 0.078 / 0.037 / 0.022 / 0.016 / 0.013 / 0.012

(g.cm^{-2} (From Jain 2009)) [68])

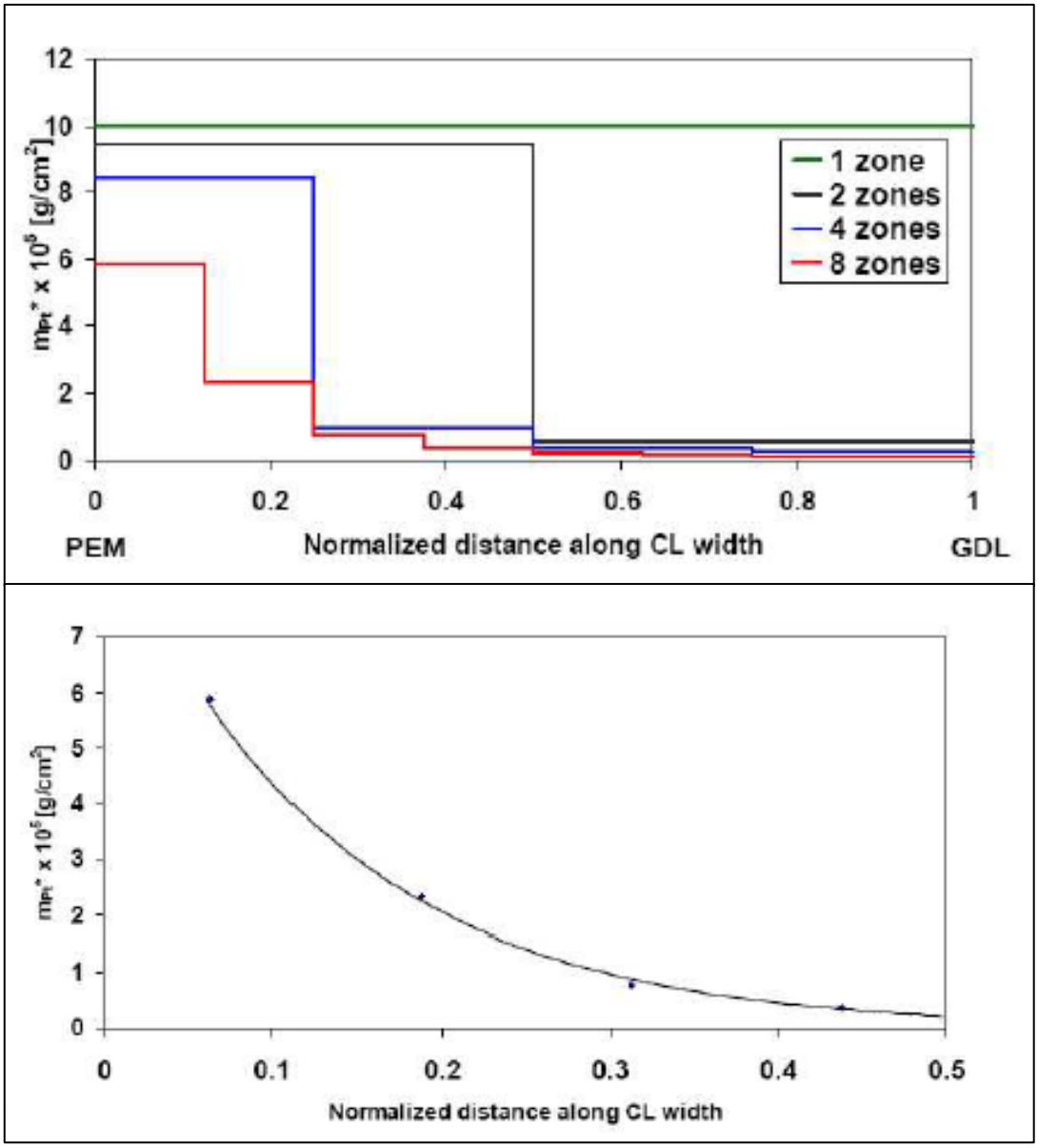

Figure 10: Optimal catalyst distribution

(For 2^N Zones – histogram and fitted curve – at 0.876 Volts.cm^{-2} (From Jain (2009) [68])

Jains' work largely focuses on the thickness of the catalyst layer. Highlighting one of the reasons that layered catalyst structures have been investigated. The activity and utilisation of catalysts are highest adjacent to the membrane surface, and there is no need to have a uniform catalyst concentration in the through-plane thickness of the catalyst Layer (CL) itself. Jains' work agrees with the catalyst distribution considered preferably by some other authors [64]. Experimental verification of this type of numeric model has been few and far between in the literature, though there are some notable exceptions: Antione et al. (2000) [23] confirmed that optimum catalyst deposition was achieved with the Pt particles concentrated at the surface of the membrane.

One limitation in the Antione et al. (2000) [23] work was that they did not consider altering the active area per Platinum doped Carbon (Pt-on-C) particle: Catalyst concentration gradients were achieved by intermixing un-catalysed carbon black particles. Other authors [73,74] have considered the distribution of catalyst and examined it experimentally, but these authors used the addition of Nafion® to reduce catalyst concentration when creating the catalyst ink. This additional Nafion® was intended to reduce Pt concentrations. At the same time performing its usual role of a suspension media for the dispersion and bonding of catalyst in the fuel cell. It is clear that this approach has the advantage of being simple to reproduce in experiments, and strong arguments are made that optimised Nafion® is superior to other methods of dilution.

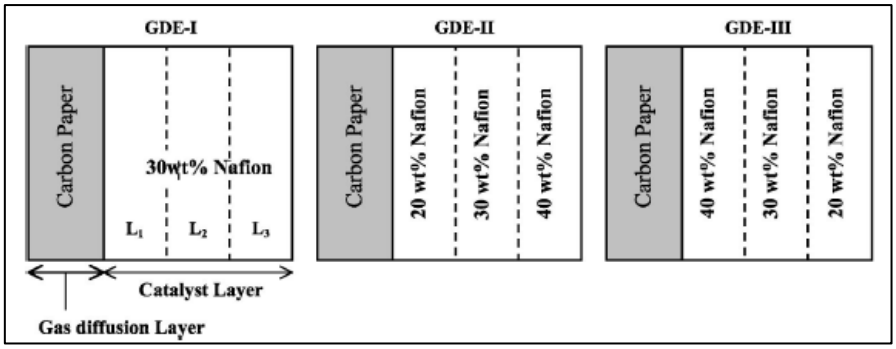

Figure 11: Schematic of GDEs with graded Nafion content in the CL

(GDE-I = uniform 30wt% Nafion®, GDE-II = 20/30/40wt% Nafion®, GDE-III = 40/30/20wt% (Nafion® (From Xie, Navessin et al 2005))

Xie, Navessin, et al. (2005) [73] utilised a 20wt% Pt on Vulcan support carbon and then altered the distribution through ever increasing Nafion® content in the ink formulations as shown in Figure 11. These ink formulation layers were then tested on very small (1.8cm^{-2}) fuel cells. Their key findings indicate that a 30wt% ('GDE-I') distribution of Nafion® in the ink formulation has a significantly higher peak power (in W.cm^{-2}) in comparison to the other formulations.

More sophisticated multivariate approaches are rarer still, but one example has been located; Song, Wang, et al. (2005) [75] stated that the optimum catalyst distribution could be difficult to model numerically when Nafion® and Pt are thought of as a joint system. They instead undertook a statistical approach and considered it as a "…*two-variable optimisation.*…"[75] problem to be solved experimentally. Figure 12 shows the polarisation results (plotting current density against cell potential). In these results, Nafion concentration and Pt loading were varied before the creation of an optimised two-factor model (Figure 13).

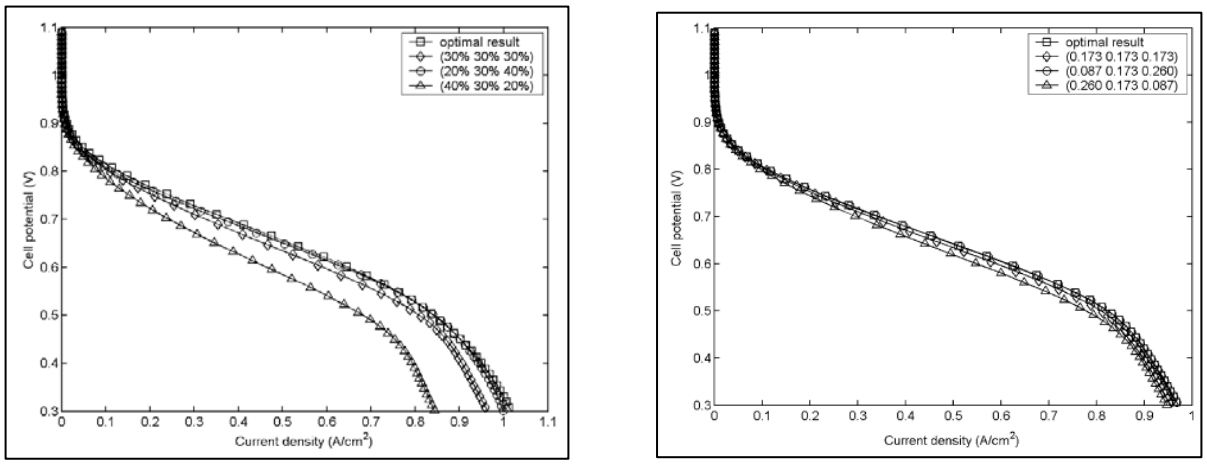

Figure 12: Nafion (left) and Pt (right) variation

(From Song, Wang, et al. 2005) [75])

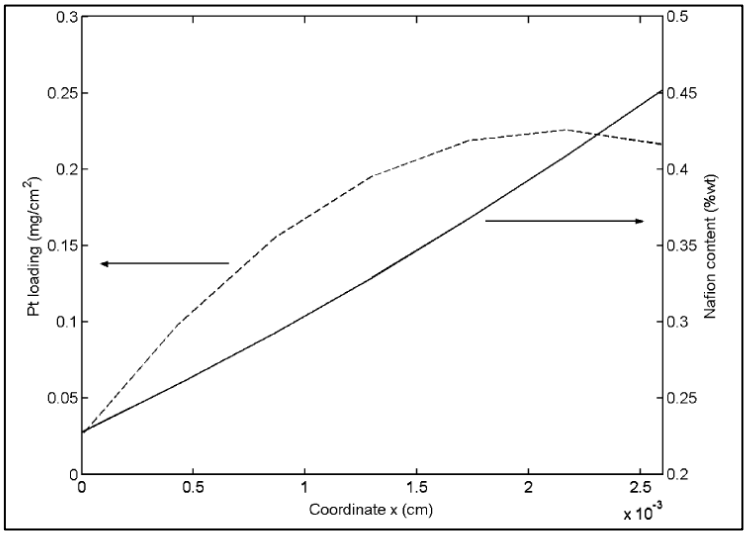

Figure 13: Optimal two-factor model

(From Song, Wang, et al. (2005) [75])

By taking this approach Song, Wang, et al. (2005) [75] showed that the platinum distribution optimisation problem had a convex solution (the dotted line in Figure 13) and the Nafion® optimisation problem had a linear solution. When both Pt and Nafion® from this they concluded that "*….only the optimisation of Nafion*[sic] *content distribution needs to be considered.*" [75]. As far as this goes, it is correct (and agrees with published work that considered single layer catalyst and Nafion® content [76]), based on the data presented. However, the idea that catalyst distribution is not greatly significant calls into question the results universally applied in other systems. Catalyst distribution is of critical importance in optimising performance in any commercial system: Catalyst optimisation is complex, and it is not possible to present all possible factors in a single journal paper. It is suggested here that, if consideration is given to the longevity of the catalyst in the system, the degree to which layered structure CL may either inhibit or accelerate degradation rates may become apparent. Yu et al. (2007) [77] have considered catalyst degradation mechanisms in fuel cells, including ageing on catalyst distributions. The impact of catalysts layers on longevity has been overlooked. For this reason, a degradation study on dual layered catalyst was completed. Based on findings from section 3; a multivariate examination (factoring in two different GDM substrates to coat the catalyst materials onto) will be undertaken, and as discussed in Chapter 6. It is hoped that this will further the understanding of degradation of dual layered catalyst materials and at the same time provide a case study for the effective use of the multivariate design of experiment approach outlined in the following chapters. Additional information on CLs and their importance to PEMFC performance can be found in Chapter 5.

2.6. Degradation of carbon-based gas diffusion media

The work done by Hiramitsu et al. (2011) [45] indicates that the hydrophobic coating can also be used to diminish the degradation of the carbon fibres that make up the GDL. The exposed carbon fibres are, over time, attacked by radical species present in the chemistry of the oxygen reduction reaction (ORR) and the hydrogen reduction reaction (HOR). After 6,000 hours of constant load operation, a noticeable change in the wetting angle of the fibre matting was reported [45], and it is surmised that this is due to changes in the degree of coverage of the hydrophobic polymer on the GDL fibres. It has been reported [57] that significant changes in wettability can occur after much shorter periods of time. The reason for these differences in the durability of hydrophobic coatings is not clear. In either case, the argument indicates that GDMs made with carbon fibres without a hydrophobic coating will suffer a direct attack of the GDM itself more quickly. Such attacks may or may not be the case with catalyst coated substrate (CCS) membrane electrode assemblies (MEAs) in particular, as the act of depositing the ink directly onto the carbon fibre substrate re-introduces PTFE coatings to the fibres.

This approach, of excluding PTFE coatings on the carbon fibres, will be taken in experiments completed for this thesis whenever suitable. If accelerated ageing is detected, then the radical attack is happening throughout the depth of the GDM, and not only adjacent to the catalyst layers. Whatever the case for accelerated carbon corrosion, or not, the mechanisms for it are well understood: C.A. Reiser et al. (2005) [57] commented on the chemical degradation of carbon-based GDM, and their key findings are adapted for reproduction here in Figure 14. Typically this extreme range of voltages (in excess of + 1 Volt or -0.103Volts) in a given system occurs during the start-up / shut-down phase of the duty cycle. During start-up and shut-down there is a depleted hydrogen zone that progresses along the length of the anode channel, and localised exchange currents of hydrogen ions are set up across the membrane. In reversed reactions region the local current is acting at 1.44 volts. The majority of this carbon corrosion is thought to come from the catalyst layer itself [16], but there is some evidence to suggest that the GDM is also involved [57], though at a much-reduced rate compared to the carbon-based catalyst supports.

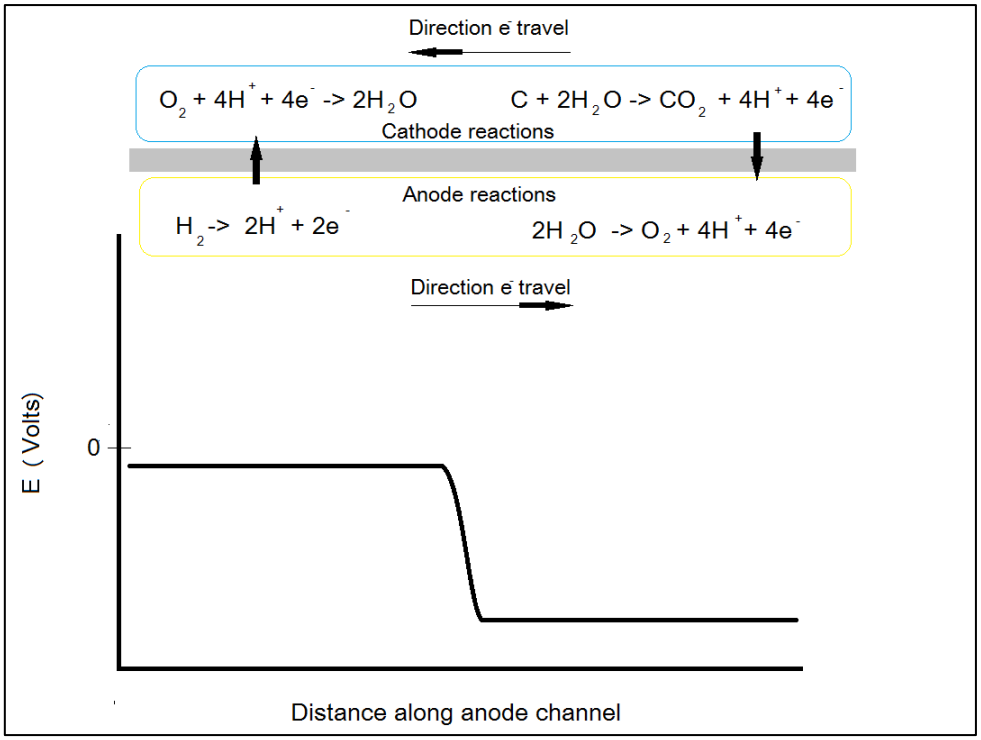

Figure 14: Hydrogen and carbon corrosion

(Adapted from C.A. Reiser et al. (2005) [57])

There are other potentials where the oxidation of carbon occurred, and there will be regions along the channel where these potentials are achieved. Indeed operating the fuel cell at 0.518 Volts (a common potential for constant load experiments) could also accelerate carbon corrosion.

Table 5: Carbon reduction reactions and potentials

$C+2H_2O \rightarrow CO_2 + 4H^+ + 4e^- = 0.207$ V	(2-1)
$C+ H_2O \rightarrow CO2 + 2H^+ + 2e^- = 0.518$ V	(2-2)
$CO+ H_2O \rightarrow CO_2 + 2H^+ + 2e^- = -0.103$ V	(2-3)

(E^0 = Vs standard hydrogen electrode, table adapted from El-Kharouf (2012) [16])

2.7. Key findings

There are a wide variety of factors that influence the performance of PEMFCs over the short and long term. Any future work should ideally consider some of the following factors:

- Unless making comparisons on materials from a single supplier MEAs should, as far as possible, be manufactured 'in house' to limit variability due to manufacturing methods from

different suppliers. This approach will be undertaken as far as reasonably possible with all test samples discussed in this work.

- Hydrophobic coatings have a hugely significant impact on fuel cell performance and ageing.
    - Great care should be taken to normalise hydrophobic coatings in any study, and they may even have to be excluded as a variable as not only wt% PTFE, but also the uniformity of coverage and strength of adhesion for the fibres and PTFE should be quantified and comparable. This will be taken into consideration for the experimental work in in Chapter 6.
- Structural considerations of the GDM carbon fibres are significant, comparisons between non-woven, woven and paper type GDMs may be equally significant as well as discussion around their porosity, pore distribution or through-plane thickness. Chapter 4 and Chapter 6 will both include gross GDM structure (Woven, Paper or non-woven) as a categoric factor to be included in the data analysis.
- Dual layer catalysts have received some attention, but not enough work has been done on their longevity as of the time of writing. Chapter 5 discusses this in more detail, and the experimental study in Chapter 6 includes layered cathode catalyst structures as a variable in the designed experiments.
- There is a probability that one or more of GDM structure, dual layer catalysts and the degradation of the fuel cell are co-varying in some way; especially for CCS manufacturing methods. Chapter 3 will explain in more depth the impact this will have on the design of experiments and the subsequent data analysis of the results. Heaving established an understanding of these issues, the work in Chapter 6 will take this into consideration and provide the case study of applying suitable statistical methods to the work presented in this thesis to achieve at least one of the stated aims in section 1.1.1.
- The extremely high resource demands for degradation studies are exacerbated by ‘one factor at a time’ (OFAT) experiments and so are a prime candidate for showcasing the benefits of multivariate design of experiments approaches to achieve one of the stated aims in section 1.1.1.
- The lack of general usage of multivariate designed experiments reported in the fuel cell literature indicates a need to build up confidence and skill in these types of statistical data analysis tools within the fuel cell research community will achieve one of the stated aims in section 1.1.1.

2.8. Summary of Chapter 2

The review of the literature indicates the investigation of multivariate methods in PEMFC degradation studies is well justified. There are several key gaps and conflicts in the literature that require further experimental study (see sections 2.2, 2.3, 2.5 and 2.7). Notably, the failure to apply statistical methods correctly ([33][37]), and the conflicts in the results presented by different authors on the impact on degradation of fuel cells and the PTFE coatings applied to the GDM ([40], [43], [44]). On the basis of this, and the observations from several authors that there is a lack of data on the performance and degradation of a wide variety of GDMs in the fuel cell literature ([38],[45],[22]); it is suggested that the proposed work in this thesis is justified.

3 Statistical Methods

3.1. Introduction to Chapter 3

Chapter 3 introduces the statistical methods applied to interpret experimental results obtained during the completion of this thesis. In Chapter 4 (notably section 4.4) and Chapter 6 (notably section 6.4), extensive use will be made of the Design Expert Professional V.9 ™ (Design Expert Pro) software. Design Expert Pro is a commercially available statistics and design of experiments software package. While it would be possible to complete the analysis using the software as a 'black box' (i.e. having no understanding of the mathematic at work inside the software), this is not a 'best practice' approach to take. Therefore the multiple linear regression, multiple input and output factors and matrix algebra techniques that are utilised by the software are introduced here in Chapter 3. Developing the understanding of the methods used in the software to analyse the generated experimental data enables a more detailed and thorough interpretation and validation of the multivariate linear regression models that are generated in subsequent chapters. It is hoped that this chapter will shed some light on the 'black box' and clarify the processes going on inside the commercial software.

In chapter 3 a basic understanding of linear regression model development is reported, and its adaptation to be suitable for multiple, co-varying, input factors. The use of blocking and error analysis to remove uncertainty from experimental data was also considered. The information in this section is an amalgamation of knowledge from various sources [30,78-83]. The equations that have been individually referenced in chapter 3 have been amended to share a uniform nomenclature.

Statistical modelling (like all numeric modelling) is typically described as a cycle to gain a better understanding of real world effects. After identifying a topic of interest, estimates of the parameters that control that effect (the 'levers') allows for the creation of models based on those levers. These are in turn validated as the degree of impact on the real world effect is measured and, hopefully, finds an improved system of knowledge to apply. The process then repeats itself continuously to refine and improve understanding of the effect being controlled or modelled.

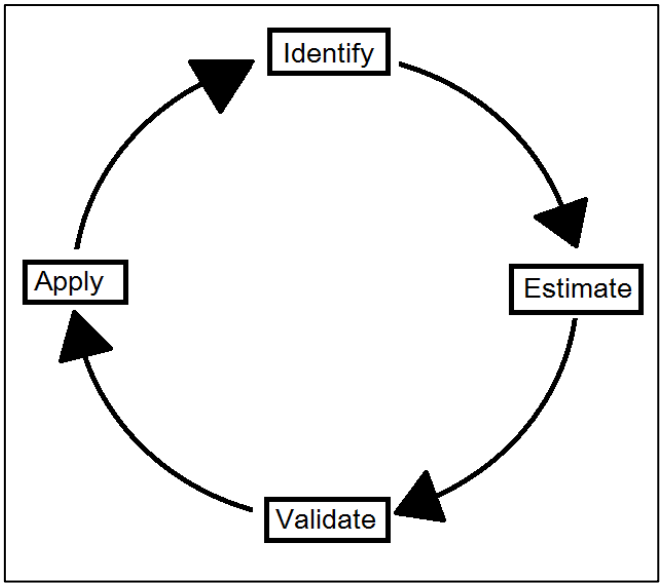

Figure 15: Model Development Process

Applying this concept to regression analysis of experimental data generates a work plan quite quickly:

1. Plot the experimental data.
2. Formulate a model.
3. Test the model.
4. Adapt the model.
5. Finalise the model.

3.2. Linear regression models

At its simplest, a 'one factor at a time' (OFAT) regression, where one variable is measured relative to its impact on another, is a starting point that will enable the fitting of a linear relationship between the two factors [78]. Needless to say, not everything is this simple. If the data fit a straight line perfectly, then a typical straight line plot of results would fit the equation

$$y_i = \beta_0 + \beta_1 x_i \qquad \textbf{(3-1)}$$

[83,83,84]

where 'y_i' is the response for sample 'i' and x_i is the value of the factor for sample i, multiplied by the gradient (β_1) and the straight line intercepts the y axis at a value equal to β_0

However, error and noise always occur, and must be accounted for in the lack of fit for the data to the model.

$$y_i = \beta_0 + \beta_1 x_i + \varepsilon_i \quad \textbf{(3-2)}$$

[78,81,82,85]

where ε_i is the observable error.

Certain assumptions about the errors make more data analysis tools available:

- The true mean error (E) of (ε_i) = 0
- Variance of (ε_i) = σ^2 (a constant)
- The error of each measured point of x is independent of each other (all (ε_i) are independent).
- All (ε_i) are normally distributed i.e.

$$\varepsilon_i \sim N(0, \sigma^2) \quad \textbf{(3-3)}$$

[81]

These assumptions can be represented as the 'statement for the assumption of normality of errors' in the model (3-3).

The true values of the errors in a data set are (almost always) uncertain. The use of a 'hat' [78,81] notation (e.g. $\hat{y}_i$) shows estimates are within the bounds of a system that contains these errors and estimate the best line fit allowing for errors. In other words the error is that of the data measured, and not guaranteed to be exactly the same as the error measured if the entire population of events were measured. The degree of discrepancy between the estimated error value and the true error can be calculated at a later point in the model development cycle. In the first iteration, the assumption is made that the error of the data set measured is equivalent to the error of the entire population.

$$\hat{y}_i = \hat{\beta}_0 + \hat{\beta}_1 x_i \quad \textbf{(3-4)}$$

[78,81,82]

The production of the best line fit is achieved by minimising the residuals (the vertical distances from the estimated line to the actual data points measured). The sum of the squared residuals is used to optimise the fit line (the 'sum of least squares fit' of the residuals) since by construction the mean residual is always zero (i.e. positive and negative residual heights would cancel each other out: therefore the square of the residuals avoids this issue). This value can be noted down as the value of sum squares of the residuals, also known as the sum of squares of the errors (SSE).

$$SSE = \sum_{i=1}^{n} \left[y_l - \left(\hat{\beta}_0 + \hat{\beta}_1 x_i \right) \right]^2 \quad \textbf{(3-5)}$$

[81,83]

where n is the number of samples or sets of observations.

In the first attempt to fit the minimum error, the values are not known. Therefore the results are set to zero and differentiated to locate the minimum values.

$$\frac{\partial SSE}{\partial \hat{\beta}_0} = -2 \sum_{i=1}^{n} \left[y_l - \left(\hat{\beta}_0 + \hat{\beta}_1 x_i \right) \right] \quad \textbf{(3-6)}$$

[80,81]

Solving SSE to find β at minimum

$$\frac{\partial SSE}{\partial \hat{\beta}_1} = -2 \sum_{i=1}^{n} x_i \left[y_l - \left(\hat{\beta}_0 + \hat{\beta}_1 x_i \right) \right] \quad \textbf{(3-7)}$$

[80,81]

Then re-arranging and setting to zero gives

$$\sum_{i=1}^{n} y_i = \sum_{i=1}^{n} \hat{\beta}_0 + \sum_{i=1}^{n} \hat{\beta}_1 x_i \quad \textbf{(3-8)}$$

[81,83]

and

$$\sum_{i=1}^{n} x_i y_i = \sum_{i=1}^{n} \hat{\beta}_0 x_i + \sum_{i=1}^{n} \hat{\beta}_1 {x_i}^2 \quad \textbf{(3-9)}$$

[81,83]

this can then be solved for the lowest values of β *(or* $\hat{\beta}$ in the case of an estimated system)

$$\hat{\beta}_1 = \frac{n \sum x_i y_i - \sum x_i \sum y_i}{n \sum x_i^2 - (\sum x_i)^2} \quad \textbf{(3-10)}$$

[81,83]

$$\hat{\beta}_0 = \frac{\sum y_i}{n} - \hat{\beta}_1 \frac{\sum x_i}{n} \quad \textbf{(3-11)}$$

[79,81,83]

Solving for $\hat{\beta}_0$ and $\hat{\beta}_1$ in this way fits the line equation to the data and allow for error in experimental measurement. This is the foundation of the analysis, and the numerator in (3-10) is expressed as

$$n\sum x_l y_l - \sum x_l \sum y_l = n\left(\sum x_l y_l - n\bar{x}\bar{y}\right) = n\left(\sum (x_l - \bar{x})(y_l - \bar{y})\right) \quad \textbf{(3-12)}$$

[80,81]

and

$$n\left(\sum (x_l - \bar{x})(y_l - \bar{y})\right) = n\, SS_{xy} \quad \textbf{(3-13)}$$

[78]

To reduce the complexity of the notation, 'SS' is used to denote the 'Sum of Squares', with a subscript to define which values (all 'x', all 'y', or a combination of both) are being considered in that sum of squares pairing. The denominator in (3-10) is expressed as

$$n\left(\sum (x_l - \bar{x})^2\right) = n\, SS_{xx} \quad \textbf{(3-14)}$$

[78,81]

where

$$SS_{xx} = \sum (x_l - \bar{x})^2 \quad \textbf{(3-15)}$$

[78,81]

Hence $\hat{\beta}_1$, the gradient of the least squares line of fit, is now determined with this shorter notation

(3-16) (i.e. equation (3-10) is equivalent to (3-16))

$$\hat{\beta}_1 = \frac{n\sum x_i y_i - \sum x_i \sum y_i}{n\sum x_i^2 - (\sum x_i)^2} = \frac{nSS_{xy}}{nSS_{xx}} \quad \textbf{(3-16)}$$

[79,81]

also

$$SS_{yy} = \sum (y_l - \bar{y})^2 \quad \textbf{(3-17)}$$

[79,81]

From which it can be shown (derivation not given for brevity):

$$SSE = SS_{yy} - \beta_1 SS_{xy} \quad \textbf{(3-18)}$$

[81,83]

Recalling the assumption that all errors are normally distributed, then it was possible to assess the model (the linear fit). The term $\hat{\beta}_1 SS_{xy}$ represents the regression sum of squares (variation explained by) the regression model. If this is larger, relative to the SSE, the model may be trusted. But is the model better than a simple mean of the data?

To answer that question, two hypotheses were set:

- H_0 = the mean is good enough, no need to model a line of fit.
- H_1 = the linear equation ($\hat{y}_i = \hat{\beta}_0 + \hat{\beta}_1 x_i$) is a better fit than the mean.

The discussion of analysis of variance (discussed in more detail in section 3.3 and section 3.6) will give more information on this topic. These sums of squares notation are useful in shortening other terms and equations, and the Pearson correlation coefficient ('r' is the expression of linearity of a correlation) is expressed as

$$r = \frac{SS_{xy}}{\sqrt{SS_{xx} SS_{yy}}} \quad \textbf{(3-19)}$$

[78,81,83]

The coefficient of determination or R-squared value is calculated as (3-20)

$$r^2 \cong R^2 = 1 - \frac{SSE}{SS_{yy}} = \frac{SS_{yy} - SSE}{SS_{yy}} \quad \textbf{(3-20)}$$

[79,81,83]

This determines the percentage (expressed as a decimal) of the signal that was accounted for by the model. Variance (s^2) is the most important and useful measure of variability of a sample – while the range only measures two points, the variance measures all points in the system

$$s^2 = \frac{\sum_{i=1}^{n} (Y_i - \bar{Y})^2}{n - 1} \quad \textbf{(3-21)}$$

[81,83]

Sample variance (3-21) [78] is the sum of the deviations from the mean, divided by one less than the total number of points measured. To retain the original units, the sample standard deviation (s) is most often reported [78]:

$$s = \sqrt{\frac{\sum_{i=1}^{n}(Y_i - \bar{Y})^2}{n-1}} \quad \textbf{(3-22)}$$

[78,81]

A typical standard error can also be calculated from the variance, for example

$$SE \cong \sqrt{\frac{s^2}{n}} \quad \textbf{(3-23)}$$

[82,83]

The variance ($\hat{\sigma}^2$) is estimated as

$$\hat{\sigma}^2 = s^2 \cong \frac{SSE}{n-2} \quad \textbf{(3-24)}$$

[81,83,85]

3.3. t-test

The t-Test examines two separate populations (x and y) to determine if they are different, especially for a small data set. The 't' value has often been used to assess the model under investigation for the single case: Until now the question 'is the mean better than the model?' used the F-test (Fisher-Snedecor distribution) [78,81]. With two groups of data, comparison of both means becomes possible, increasing the number of factors that can be examined: the number factors increases to two mean values of multiple inputs. In this case, the t-test can be used, where t = (parameter estimate – assumed parameter value)/standard error of the parameter estimate

$$t = \frac{\bar{y} - k}{\frac{s}{\sqrt{n}}} \quad \textbf{(3-25)}$$

[78,80,81,83]

The F-test compares the 'null hypothesis' (the mean is 'good enough') to an F-distribution and if the two match then the null hypothesis is correct; and the t-test relates to the F-test as equation (3-26) [78].

$$F = t^2 \quad \textbf{(3-26)}$$

[78,81]

Recall as well that the 'p-value' is the probability of generating a t-value as large as the one calculated from the data set. It is also the probability of getting the F-statistic (the F-value) as large as the one calculated from the data set (both cross-referenced to look up tables for their degrees of freedom and

magnitude of confidence interval). In each case, the probability is the same for a given set of data values.

The t-value can be related to the model under investigation to test two hypotheses about the intercept in the model and 'slope' parameter associated with the factor in the model. These hypotheses are:

H_0: $\beta_0 = 0$ and H_1: $\beta_1 = 0$ versus H_1: $\beta_1 \neq 0$

For a single factor case, the t-statistics to test these hypotheses would be

$$t = \frac{\hat{\beta}_0 - \beta_0}{SE(\hat{\beta}_0)} \quad \textbf{(3-27)}$$

[80,83]

or

$$t = \frac{\hat{\beta}_1 - \beta_1}{SE(\hat{\beta}_1)} \quad \textbf{(3-28)}$$

[80,83]

This value can then be compared to the t-distribution (with degrees of freedom = n-2 for a linear model, and n is the number of samples). To go beyond two variables, a similar logic is applied through the use of analysis of variance.

This point of the discussion is an appropriate one to recall that the confidence interval (CI) is defined as:

$$CI = \bar{x} \pm t^* \left(\frac{s}{\sqrt{n}}\right) \quad \textbf{(3-29)}$$

[83]

The traditional practice is to utilise a 'look-up table' of t* values and to apply the desired confidence level of the value of 't' measured. Hence the CI can be declared to be '± CI to 95% confidence' if the 95% column in the lookup table is the value of 't' used [83]. However, modern personal computing has rendered this table based lookup procedure obsolete. Instead, the p-value (the value used to accept or reject a given hypothesis) is calculated directly for each data set. This direct calculation avoids the need to interpolate between pre-generated tables of values when the result does not fall exactly on a particular value.

It was assumed that the distribution of error in the data measurement is normal [83]. To verify this, an assessment of the normality of distribution with 'Quantile-Quantile' (Q-Q) plots was undertaken, utilising the capabilities of the software. A histogram can check this visually but is not a rigorous approach for smaller data sets. Instead, residuals are placed in rank (size) order. Then the calculated theoretical value of the residuals (or quantiles) if they followed a normal distribution (with the limits of the range imposed by the real, measured range of data) can be created. When plotted as a scatter plot 'theoretical quantile values' versus the 'measured quantile values' creates the 'Quantile-Quantile' (Q-Q) plot. The closer the two values plot as a straight line, the more closely the residuals follow a normal distribution. No real-world set of experimental data is ever perfect, and some deviation from the norm is expected.

There is a degree of interpretation to this plot. Standard practice is to follow the 'pencil test' (e.g. Andersom and Whitcomb (2007) [82]), wherein a hardcopy print of the Q-Q graph is created and, if all of data points in the Q-Q plot is sufficiently linear to cover with a pencil, the system is normally distributed. When assessing the linearity of Q-Q plots, it is acknowledged that fewer points will be noisier and less linear. The ANOVA method (discussed later in section 3.6) is quite robust when dealing with distributions that tend away from the norm, and so it can tolerate this degree of estimation in assessing its ability to cope with non-normally distributed data. However, there should be no significant 'S-curve' visible in the Q-Q plot.

If after conducting this test there are still concerns with the degree of normality in the system under investigation, it is often possible to transform the data in some way to make it more normally distributed. These types of transformation are justified as

$$Y \propto Y^a \qquad \textbf{(3-30)}$$

P.R. Nelson in [81]

It is critical to 'undo' this transformation when applying the value to the final empirical model for the predictions to be valid, though modern software for DoE does this automatically. Negative data can be transformed to a positive value (through squaring or the addition of a constant to all data). If required, the data can then be transformed by the application of log scale; the application of an exponential to the data. This approach is only effective if the degree of deviation in the Q-Q plot is quite high.

3.3.1. Weighting and blocking

It is possible to compensate for variation between sets by 'blocking' the results. Each set of samples is tested on several occasions at several values. Comparing between the sets of samples may not be

directly possible due to operational test condition variance, or some other factor. To overcome any such lack of comparability, it is possible to undertake a weighting and blocking exercise. With weighting and blocking, it becomes possible to examine multiple sample families, and average the result across each family, or set, of values. Having done so, this creates a 'mean of means' for those families of results. A more detailed examination of this method is given in section 4.7 and 6.7 where the method was used on experimental data.

3.4. Factorial designs

RA Fisher created full factorial designs [30]. His original book on the subject (*Statistical Methods for Research Workers*) is considered one of the greatest mathematical works of the 20th Century. In the time since it was published in 1925, there have been a vast number of papers and books written on the subject, focusing on the applications, updates and improvements. The partial factorial design seeks to minimise the number of experiments and maximise the amount of information required to generate an equivalent result (for example Genichi Taguchi's methods) [30]. Ranjit Roy (1990) [30] gives an excellent introduction to the topic, and it is the Ranjit Roy (1990) [30] research that forms the central core text for the discussion of these methods in this thesis, as well as drawing on other commonly cited references [81,82,85].

A standard, 'one factor a time' (OFAT) experimental set up is thorough and can be interpreted easily by the methods outlined previously. However, it is inefficient. By having several controllable variables (or factors) in an experimental design at a time, rapid improvements in the efficiency of a set of experiments can be made [30]. As the number of factors increases, the gains in efficiency increase still further. This efficiency improvement is gained by setting the factors of interest at discrete levels, combined with the use of 'orthogonal array' systems, to facilitate planning out the work in advance. Compared to OFAT testing regimes, the use of such repeatable experimental setup and data analysis techniques can reduce the total workload. Such a systemised approach makes it possible for other researchers to reproduce, verify and build on the work completed. The standardisation of test methods increases the rate of development in a given field, and the use of similar analysis by disparate researchers reduces the 'learning curve' when reviewing a new piece of work. For a full factorial design, the number of possible designs is 'N':

$$N = L^m \quad \textbf{(3-31)}$$

[30]

Where L is a number of levels for each factor, m is a number of factors. For example 15 different factors, and desiring to test 2 levels; this would be (2^{15}) = 32,768 tests.

Fractional Factorial Analysis (FFA) can reduce the time and effort needed to implement such a regime, but requires detailed and dedicated mathematical treatment in the design and analysis of the results. The Taguchi-method [30] has standardised the design method that is used in FFA so that "*two engineers conducting tests thousands of miles apart, will always use similar designs and tend to obtain similar results.*" (Taguchi in Roy (1990) [30]). However, FFAs still have several limitations: [30]

- Large numbers of variables are still expensive and time-consuming tests
- Two designs for the same experiment can generate different results
- Designs do not normally allow for the determination of the contribution of each factor
- Interpreting the results for a large number of factors can be difficult

Following the recommendations laid out by Roy (1990) [30] (i.e. the use of standard orthogonal arrays for the design of experiments that are appropriate to the degrees of freedom for the data being analysed) can help to improve the repeatability between researchers. These methods help to diminish the deviation from the 'true' 'real world' value of interest that prompted the experiment in the first place. The use of orthogonal arrays standardise experimental designs and minimise, or at least make it possible to understand and factor out, the uncontrollable factors in a set of experiments. These 'noise factors' are the "*factors influencing a process that cannot be economically controlled*" [30]. Typically these may include things like machine wear or the other environmental factors like the ambient humidity on the day of the test.

3.5. Design of experiment process

Like any method, the design of experiment (DoE) approach has its limitations. The quality of the measurement is a limiting factor, and so the quality of the outputs from the completed DoE is dependent on how well the methods are applied. The orthogonal arrays are most effective [30] when there is the minimum amount of interaction between factors [30]. As the number of interactions between factors (covariance of factors) increases, the size of the orthogonal array (i.e. the total number of experiments and repetitions of experiments to be carried out) also increases, to make it possible to quantify the co-varying factors. Practical, resource driven, circumstances of the experimenter are often the single biggest limitation. It is not uncommon to limit a design of experiments in some way so that it will only (for example) pick up interactions between two of the measured factors. Trying to pick interactions between three factors at a time will exponentially increase the amount of work to be carried out. Another limiting issue is the linearity of the response. As already stated, DoE is ideally intended for linear responses for two factors. With nonlinear systems, the number of test levels to map out the non-linearity must increase (three levels to pick out a parabolic response if that is predicted or five levels for exponential responses). It must be highlighted

that even if factors are non-linear and massively interactive, orthogonal arrays can still be a good starting place, but optimisation estimates will be inaccurate (how inaccurate depends on the degree of nonlinearity and interactions between factors).

Consider a DoE for three factors, each of which has two levels. The following orthogonal array (Table 6, adapted from Roy (1990) [30]) in this case; '-1' refers to the lowest set value for a given factor, and '+1' refers to the highest set value for a given factor.

Table 6: Generic 'Orthogonal array' L4

Experiment number	Factor A	Factor B	Factor C
1	-1	-1	-1
2	-1	+1	+1
3	+1	-1	+1
4	+1	+1	-1

To fully quantify this and determine the amount of experimental noise in the system, a degree of repetition is also desirable. Degrees of freedom (DoF), is calculated by: ((Number of factors -1) + (the number of suspected interactions being studied).

$$DoF = (n_{Factors} - 1) + (n_{2level\_interactions}) \quad \textbf{(3-32)}$$

[30]

The number of experiments (L) for an orthogonal array is given by

$$L = (n_{Factors} - 1) * (n_{2level\_interactions}) \quad \textbf{(3-33)}$$

[30]

In this case, the number of experiments (or rows in the array) is a direct measure of the degrees of freedom; the array must have a number of rows equal to the DoF. It is for this reason that standardised and published arrays are referred to in this matrix identification of 'L' numbers; so L_4 has four rows, L_9 has nine and so on. Once the DoF of the experiment is known, select an orthogonal array (OA) with the same (or greater) degrees of freedom included in the array design. To calculate the effect of a given factor from its results, the following procedure must be followed: The result based on the average of the factor at the high level, and the result based on the average response of the same factor at the low level, is subtracted. This operation calculates the total impact of a single factor on a final result. Combinations of factors must also be taken into account to generate a true picture of

the experimental data to be investigated. By definition, a 'full factorial design' should have enough rows to take into account each factor and each combination of factors. Iteration of this approach for each final result (i.e. each of the 'output' variables) of interest, using the same experimental data (ensuring the results and factors of interest are recorded) is carried out to determine the input variables effect on the output results. This iterative approach generates a numeric value for the impact individual factors have on the investigated output signal; extending the scope of the simple linear regression model [81].

$$Effect = \frac{\sum Y_{+ve}}{n_{+ve}} - \frac{\sum Y_{-ve}}{n_{-ve}} \quad \textbf{(3-34)}$$

[82]

The number of repetitions required in a set of experiments can be determined by an outer array method. In this approach, the likely noise effects (e.g. humidity, ambient temperature, age of material being tested) can be identified and used to produce a supplementary array of experiments. These conditions can then be used to determine the number of repetitions, and noise effects artificially induced as per the outer array design to produce a set of experimental conditions for different repetitions [30].

3.6. ANOVA

The linear regression outputs introduced in section 3.2, and extended in the final equation for a designed experimental orthogonal array approach (equation (3-35) in section 3.5), can be analysed numerically by taking an analysis of variance (ANOVA) approach to summarise the linear regression data as shown in Table 7. In this approach, the total variation in the measured 'Y' values (SSyy as shown in equation (3-17)) is separated into its constituent parts. Part of the Y value is accounted for by the regression model, and the remainder is the residual (the distance between the point on the regression model, and its nearest equivalent 'real world' experimental data point). This topic has been discussed previously and in great depth in section 3.2 and the rest of chapter 3 up to this point. As discussed previously in this chapter, a simple linear system model must test the goodness of fit of the numeric model, and ask the question 'is the model better than a simple average?' [80]. Once again the experimenter must set the two hypotheses that the ANOVA of the linear regression will help to answer by defining the 'F' Value (see equation (3-26) section 3.3):

- H_0 = the mean results is 'good enough', and there is no need to model a line of fit.
- H_1 = the linear equation model is a better fit than the mean.

Recalling the assumption that residuals are normally distributed, this justifies [80,82] the use of a Chi-square relationship (as shown in equation (3-35)) between the experimental results observed and the predicted and results (from either the mean or the linear regression). The Chi- squared result is another test of the 'H0 or H1' probability:

$$\chi^2 = \sum \frac{(Observed - predicted)^2}{Predicted} \quad \textbf{(3-35)}$$

[81,83]

The terms for the regression sum of squares ($\hat{\beta}_1 SS_{xy}$) and the sum of squares of the residuals ($SSE = SS_{yy} - \hat{\beta}_1 SS_{xy}$) were defined in earlier in equations (3-18) and (3-5) respectively. If SSE is divided by the degrees of freedom, this will achieve a chi-square distribution [83], and the same applies to the regression sum of squares (SS_{reg}). Note the ratio of two Chi-Squared distributions follows an F-Probability distribution (Fisher-Snedecor distribution) [83]. Construction of the ANOVA table is now possible each factor of interest (β_n).

Table 7: Generic 'ANOVA' table

ANOVA table				
Source	Sum of squares (SS)	Degrees of freedom	Mean squares	F
Regression	$\hat{\beta}_1 SS_{xy}$	1	SS/DF = MS_r	MS_r/MS_E
Error	$SS_{yy} - \hat{\beta}_1 SS_{xy}$	n-2	SS/DF = MS_E	
Total	SS_{yy}	n-1		

(Adapted from T.P. Ryan and P.R. Nelson Wadsworth (1990) [81])

Generating the F statistic and with reference to the F-distribution on a 1 and n-2 degrees of freedom table, makes it possible to determine if the model is a better fit than the mean. If the calculated F-statistic is greater than the corresponding F-value from the F-distribution; reject H_0 (i.e. reject the idea that 'the mean is better than the model'). ANOVA is a critical component to assessing the outputs from the DoE and orthogonal array approach. It can be adapted to cope with multiple inputs and outputs, handles categorical data well, identifies paired interaction effects and provides confidence levels for the outputs generated [83]. The 'MS' ratio in ANOVA is an assessment of the sum of squares of the residuals in a straight line fit divided by the degrees of freedom of the system. The 'F' statistic creates a ratio of fractions from both the model and the errors from the actual experimental data, to test the robustness of the model.

This approach does require a normally distributed data set, and a linear relationship between the means being measured and their variance together. Though it must be recognised that ANOVA is considered robust when it comes to dealing with non-normal data [83]. While standard ANOVA is not ideal for assessing multiple interactions (two, three or more inputs interacting on two or more outputs), it can be adjusted to look into multiple and co-varying factors (ManCoVar).

3.6.1. ANOVA, sum of squares and F-values

The sum of squares (SS) must be computed for ANOVA analysis, and they are related to the effect of interest. For a two level design, the SS equation is:

$$SS_{Factor} = \frac{N}{4}(Effect^2) \tag{3-36}$$

[82]

Where N is number of runs or rows in the orthogonal array, and Effect = equation (3-34). The sum of squares for a given factor can then be added together. Typically those factors that have the most responses are summed separately, and those factors that have a near zero response are pooled then added as a combined sum; this not just an accounting simplification. Each factor that is included in this 'sum of the sum of squares' contributes to the degrees of freedom in the ANOVA calculation, and as such it would be permissible to add a degree of freedom for each factor included. However, this would not always be a valid way to present the results. To this end, the minor contributing factors (those with a very small effect) are pooled and then presented as a single value in the sum of sum of squares results. Thus they only add a single degree of freedom to the overall calculation. The setting of the level of this pooled value is somewhat arbitrary and should be reported when discussing the results. It is also important to consider the pooled results as residuals with all degrees of freedom included when completing the analysis. The next process in the ANOVA approach is to take the 'mean square' (or MS)

$$MS = \frac{ss}{degF} \tag{3-37}$$

[79,81,83]

The MS value is calculated for each factor of interest, and also for the residual values with all degrees of freedom. The ratio of mean squares for the residuals and the individual factor of interest is known as the F statistic, and again can be used in conjunction with the F distribution to determine the probability of the null hypothesis (i.e. is this measuring something 'real'?). A particular strength of

this approach is the ability to compare all variables simultaneously (the 'model' approach) and also to examine each factor in isolation.

3.6.2. Bonferroni limits

It is perfectly valid to assess multiple effects from several data sets. However with a 5% chance of error (significance level), or a 95% confidence interval (see equation (3-29)), running the risk that one time in 20 will randomly attribute significance to a set of result where it does not belong. To reduce the likelihood of this random error occurring, the 'Bonferroni adjustment' [79] is a rule of thumb whereby the acceptable significance level is decreased, halving it, every time the same data set is used to examine an effect of interest. In fuel cell terms, investigating peak power ($W.cm^{-2}$) with a data set, and at the same time investigate the impact of ageing and degradation (Voltage loss per hour) with that same data set; consider the possibility of increased error through random chance. Where a 95% confidence level is acceptable in $W.cm^{-2}$ case, to achieve an effective 95% confidence level for two interpretations: the researcher would have to set the actual confidence limit to 97.5% in the calculations and when comparing the F- statistic to its corresponding distribution [82].

The Bonferroni adjusted F-value is defined as

$$F_{Bonferroni} = F^*(n) \quad \textbf{(3-38)}$$

[79]

where 'n' is a number of results being generated from a single dataset.

3.6.3.ANOVA summation

I. Calculate the average values for 'high' ('+1') setting results (as per Table 6) and 'low' ('-1') setting results.
II. Sort absolute values of effects into ascending order.
III. Plot effects as half normal or Q-Q residuals to confirm normal distribution.
IV. Calculate each effects sum of squares.
V. Calculate SS.
VI. Calculate SS residuals.
VII. Construct ANOVA analysis.
VIII. Calculate the F-values.
IX. Lookup or calculate the F-values and determine the probability (p-values) for random response.
X. Plot the main effects and interactions.
XI. Interpret and discuss the results in light of scientific understanding of the system.

Using this method produces a series of linear models (for each variable) that contribute to the total measured effect of interest (maximum power in Watts.cm^{-2} for example).

3.7. M-ANOVA and matrix algebra

In the same way that the equation for a straight line is known for a single variable, this logic can be extended to determine multiple factorial contributions [79], including any combined effects detected; this is shown in (3-39)

$$y_i = \beta_0 + \beta_1 x_1 + \beta_2 x_2 + \cdots + \beta_k x_k \quad \textbf{(3-39)}$$

[78-83,85]

Equation (3-39) will produce a model of the system the data is gathered from, though interpreting the physical meaning of the coefficients can be difficult. Another key assumption is that the variables are independent of each other. Once again, the logic for the error associated with the measurement uses the same 'hat' notation to denote a predicted value, and this can be solved for the SSE in a similar (partial derivative) fashion. Obviously, this requires solving multiple simultaneous equations, and a matrix approach is utilised (this is the way programs such as Matlab®, Design-Expert Pro® and 'R' tackle the problem). As an example, a hypothetical demonstration of matrix solution for linear regression is presented:

$$y_i = \beta_0 + \beta_1 x_{1i} + \beta_2 x_{2i} + \cdots + \beta_k x_{ki} + \varepsilon_i \quad \textbf{(3-40)}$$

[81,83]

where i = 1, 2, … n

$$y_1 = \beta_0 + \beta_1 x_{1,1} + \beta_2 x_{2,1} + \cdots + \beta_k x_{k,1} + \varepsilon_1 \quad \textbf{(3-41)}$$

[81]

$$y_2 = \beta_0 + \beta_1 x_{1,2} + \beta_2 x_{2,2} + \cdots + \beta_k x_{k,2} + \varepsilon_2 \quad \textbf{(3-42)}$$

[81]

…

$$y_n = \beta_0 + \beta_1 x_{1,n} + \beta_2 x_{2,n} + \cdots + \beta_k x_{k,n} + \varepsilon_n \quad \textbf{(3-43)}$$

[81]

Next it is possible to define each factorial element as a vector

$$\underline{Y} = \begin{bmatrix} y_1 \\ y_2 \\ \dots \\ y_n \end{bmatrix}, \underline{\beta} = \begin{bmatrix} \beta_1 \\ \beta_2 \\ \dots \\ \beta_n \end{bmatrix}, \qquad \underline{\varepsilon} = \begin{bmatrix} \varepsilon_1 \\ \varepsilon_2 \\ \dots \\ \varepsilon_n \end{bmatrix} \quad \textbf{(3-44)}$$

[80,81,84]

and define the x data as a matrix

$$X = \begin{bmatrix} 1 & x_{1,1} & x_{2,1} & \dots & x_{k,1} \\ 1 & x_{1,2} & x_{2,2} & \dots & x_{k,2} \\ & \dots & \dots & \dots & \dots \\ 1 & x_{1,n} & x_{2,n} & \dots & x_{k,n} \end{bmatrix} \quad \textbf{(3-45)}$$

[79-81,84]

Therefore

$$\underline{Y} = \underline{X}\,\underline{\beta} + \underline{\varepsilon} \quad \textbf{(3-46)}$$

[79-81,84]

Multiplying through with the transform of the '*X*' matrix ($\underline{X}'\,\underline{X}$) will give a new matrix that is the sum of 'x' values with a squared term in the unit matrix location (across the diagonal); numerically equivalent to the SSxx developed earlier in equation (3-14). It is then possible to create a vector from the x matrix and its Y vector ($\underline{X}'\,\underline{Y}$) to generate a sum of x and y value numerically equivalent to SS_{XY} (3-17). This now defines the predicted values that can apply the standard formula in a matrix fashion.

$$\underline{\hat{\beta}} = \begin{bmatrix} \hat{\beta}_0 \\ \hat{\beta}_1 \\ \dots \\ \hat{\beta}_k \end{bmatrix} \quad \textbf{(3-47)}$$

[84]

$$\left(\underline{X}'\underline{X}\right)\underline{\hat{\beta}} = \underline{X}'\underline{Y} \quad \textbf{(3-48)}$$

[79-81]

It is now possible to re-write as the matrix solution estimate of effect

$$\underline{\hat{\beta}} = \left(\underline{X}'\underline{X}\right)^{-1}\ \underline{X}'\underline{Y} \quad \textbf{(3-49)}$$

[79-81]

and the generated matrix of variables becomes the derived factors that fit the experimental data, the matrix equivalent of equations (3-10) and (3-11).

The same relationships exist for the error estimates and all other factors as well (though with additional complications for the covariance matrix and its relationship to the variance). Utilising this matrix approach generates correlation matrices that assess the degree of change in each x_i and

compare it to its neighbours, along with its impact in *y* (the output). Looking at a real world system, there will be some degree of correlation between the various *x* values (in contradiction to the assumption in the previous derivation). This correlation is overcome by setting a maximum threshold of correlation between the *x* values that is acceptable: Typically represented as a matrix plot (values between -0.69 and +0.69 for the correlation between factors is considered a good starting point). Strongly correlated input factors can have a highly adverse effect on the multiple analysis of covariance and the t or F test results they depend upon.

To overcome this weakness arising from strong correlations, if there is a high degree of co-variance in the input arguments, the co-varying data is examined, and the researcher must decide if there is a genuine need to have both data points in the model. A typical example in a fuel cell context is the relationships between temperature, pressure and relative humidity. As temperature varies, the other two factors may also vary, and yet at the root of the problem it may only be the variation of the temperature that is the issue. In this case, it may be beneficial to drop one or more of the variables. This selection process, to determine which variables to remove, can lead to discrepancies between ANOVA models developed by different researchers as they may elect to prioritise different aspects of the model: It is, therefore, essential to state what has been excluded from the analysis when following this approach.

By using this method, a limit on the impact of experimenter selection is created by the process of refining the model within a set of guidelines. This is the principle behind step-wise inclusion or exclusion of various factors. The researcher deliberately eliminates a variable, then re-builds the whole model as a reduced complexity version (i.e. has fewer input variables). The researcher then runs all the significance tests again as already discussed: The 'new' model developed is re-examined to determine how well the reduced complexity model matches to the experimental data [78]. Forward selection is the process of starting with a simple mean, and then comparing each factor at a time to the mean of the data. The researcher can choose to add two factors in a round robin style (e.g. temperature on its own, the temperate and pressure, then temperature and relative humidity; and then compare the model that includes all three factors). After adding the factors of interest the researcher can determine the least number of factors for the best degree of accuracy with the data, adding in the most significant (i.e. the most highly correlated) variables first. Backwards elimination is the reverse of this process, where all factors are included in the model; and the least significant variables are removed one at a time. Elimination is carried on usually until only the significant (i.e. p =>0.05, or a 95% confidence interval – see equation (3 29)) factors are left in the model. Stepwise is a combination of both methods. Stepwise elimination is an extremely labour intensive process but is automated in professional statistical software packages. Design Expert Pro (used in work presented in this thesis) lists all variables and allows the operator to select which variable to remove. This list approach is the preferred option as it allows the reduced complexity model to be created by removing only a single

factor at a time, and so gains a greater understanding of the impact this has on the overall significance of each remaining variable(s).Another important issue when considering multiple co-varying sample data is the assumption that the residuals are also unrelated. If there is covariance in the data, it is highly likely there will be co-variance in the residuals. To overcome this, and maintain the assumptions of normally distrusted residuals, there is a need to create standardised residuals (ε') as follows.

$$\varepsilon' = \frac{\varepsilon_i}{\sigma\left(\sqrt{1-h_{ii}}\right)} \quad \textbf{(3-50)}$$

[85]

where h_{ii} is the summed leverage, or strength of impact on the final result, for each data point. To calculate the 'leverage distance' of all x values is

$$h_{ii} = \left(\frac{1}{n} + \frac{(x_i - \overline{x})}{\sum(x_i - \overline{x})^2}\right) = \left(\frac{1}{n} + \frac{(x_i - \overline{x})^2}{SS_{xx}}\right) \quad \textbf{(3-51)}$$

[81,83,85]

The matrix form of the leverage (H) calculation for is

$$H = (X(X'X)^{-1})\,X' \quad \textbf{(3-52)}$$

Montgomery and Peck in [81]

The h_{ii} is best thought of as the distance of the individual data point from the mean and is termed 'the leverage' [81]. Data points with the highest leverage have the biggest impact on the fit of the model. Note that highly leveraged data points are not outliers. Outliers go beyond even the highly leveraged data points, and they too have a huge impact on the model. The variance ($\hat{\sigma}^2$ = 'Var') of the predicted y values is defined as (F.B. Alt (1990) et al. in Wadsworth (1990) [81]):

$$var(\hat{y}_i) = \left(\frac{1}{n} + \frac{(x_i - \overline{x})}{\sum(x_i - \overline{x})^2}\right)\sigma^2 \quad \textbf{(3-53)}$$

[81,83,85]

so

$$var(\hat{y}_i) = h_{ii}\sigma^2 \quad \textbf{(3-54)}$$

[81,83]

By standardising the residuals in this way, a set of constant variance, normally distributed, errors suitable for the mathematical approach selected is generated. Similarly, the adjusted R-squared estimate for multiple regressions is calculated as well:

$$R^2_{adjusted} = 1 - \frac{(1-R^2)(n-1)}{n-k-1} \equiv R^2 - \frac{k(1-R^2)}{n-k-1} \quad \textbf{(3-55)}$$

[80,81,83]

Recalling that 'k' is the number of factors, and the term in (3-32) can be thought of as the penalty for adapting a simple linear approach to have multiple factors, and so reducing the amount of variation in the response explained by the factors.

$$\frac{k(1-R^2)}{n-k-1} \quad \textbf{(3-56)}$$

[80,81,83]

With this improved method for assessing the coefficient of determination (the goodness of fit to the model); it is possible to assess the overall model, and iterate the model with a backwards elimination process, to sequentially remove the least probable causal input factors.

3.7.1.Non-linear or polynomial applications

It is a relatively simple matter to change the model theory to include non-linear factors: By adding input factors with a power (x^3 for example). Once again care must be taken if the input variables are related (i.e. break the assumption of lack of relationship between them). Second order (quadratic) and third order (cubic), equations are fairly robust to this, and the approach remains valid without changes [85]. Additionally, it is possible to model a factor that is expected to relate to the response in a non-linear manner such as for example where α is a number:

$$(\hat{y}) = \hat{a}e^{\hat{b}x} \quad \textbf{(3-57)}$$

[84]

Convert this to a linear equation by taking logs

$$\log(\hat{y}_i) = \log(\hat{a}) + \hat{\beta}x_i \quad \textbf{(3-58)}$$

[79,81,84]

and

$$\log(\hat{y}_i) = \hat{\beta}_0 + \hat{\beta}_1 x_i \quad \textbf{(3-59)}$$

[79,81,84]

Now it is possible to estimate

$$log_e(\hat{a}) = \hat{\beta} \quad \textbf{(3-60)}$$

[79,84]

$$\hat{a} = e^{\hat{\beta}} \quad \textbf{(3-61)}$$

[84]

and

$$\hat{b} = \hat{\beta}_1 \quad \textbf{(3-62)}$$

[84]

However, the errors in taking this approach now also multiply, for example:

$$exp[log_e(y_i)] = exp[\beta_0 + \beta_1 x_i + \varepsilon_i] \quad \textbf{(3-63)}$$

[81]

$$y_i = exp[\beta_0] \times exp[\beta_1 x_i] \times exp[\varepsilon_i] \quad \textbf{(3-64)}$$

[81]

$$y_i = ae^{bx_i} \times e_i \quad \textbf{(3-65)}$$

where

$$e_i = exp[\varepsilon_i] \quad \textbf{(3-66)}$$

Note that equations (3-65) and (3-66) are the author's explanation. Both equations are required to provide a complete understanding the derivation provided and are based on principles of conversion of logarithmic values as outlined in Croft and Davidson (1997) [84].

Obviously, any transformation that creates a ‘linearized’ form of real world data, suitable for this type of statistical modelling approach, must be reversed before the predicted settings for optimised performance can be applied. Lastly, the linear model regression approach can also be expanded to

cope with data that does not have a normal distribution (generalised linear models), but this approach is not required to explain the results generated in this thesis.

The data generated in all experiments in this thesis (discussed in later in Chapters 4, 5 and 6) correlated well to a linear approximation (i.e. the correlation coefficient of each included data set response – after completing backwards elimination of insignificant input factors) correlates well with the linear regression model (i.e. falls within R = +/- 0.69 as discussed previously in section 3.7 [79-81]).

3.8. Fractional factorials

Having established the fundamentals of ANOVA, and of DoE in previous sections, it is now possible to reduce the complexity of the system of experiments being considered. By limiting the number of multi-factor effects to be investigated, this limits the total number of experiments to complete. By reducing the total number of factors, the total number of experiments is also reduced, and these are referred to as 'fractional factorial designs' or 'partial factorial designs' of experiments.

Conducting these partial factorials saves a great deal of time, but raises the spectre of 'aliasing' the results. What may appear to be a simple single or binary variable effect may be a more complex event of three or more factors in conjunction. Three and four variable interactions are considered rare in the majority of systems [82], but this possibility must still be acknowledged and considered. To understand and quantify the possible aliasing of factors in such reduced complexity DoE, predesigned fractional factorial experiment design tables exist, and these have been codified with Roman numerals as having a set 'resolution'.

This resolution numeral gives an indication of the likely weakness of a given design. The numbers of factors that are mutually aliased are then a sum of the Roman numeral. So a level II fractional factorial design masks two single factors. A level III design masks a binary factor effect with a single factor effect, a level IV masks a single factor effect with a triple factor effect, or two binary effects mask each other, and level V designs have the potential to mask multiple combinations of effects summing five (4+1, 3+2). Keeping in mind the likelihood of triple and quadruple factorial interactions it is obviously preferable to use level five (V) designs if resources permit.

3.9. Response surface methods

Response surface methods (RSM) generate a multi-dimensional 'map' of the experiment under consideration. RSM should only be used once the overall design area is at least partially understood, through the use of ANOVA and similar techniques. Its primary strength is in detecting 'curvatures' in the experimental outputs. As stated previously, basic ANOVA methods assume the output response of a given experiment is linear in the region of interest. At its simplest RSM can be thought of as

adding a third level to the experimental ANOVA method to include central data points (in the notation used previously; set high (+1), central (+/-0) and low (-1)) levels in the factorial designs. These centre points are often replicated to get a better understanding of the natural variation in the experimental setup. It is important to note that this approach is not the same as full factorial three level DoE. The three levels, full factorial, would also include experiments at the zero level for each factor. The difference is best expressed graphically (Figure 16).

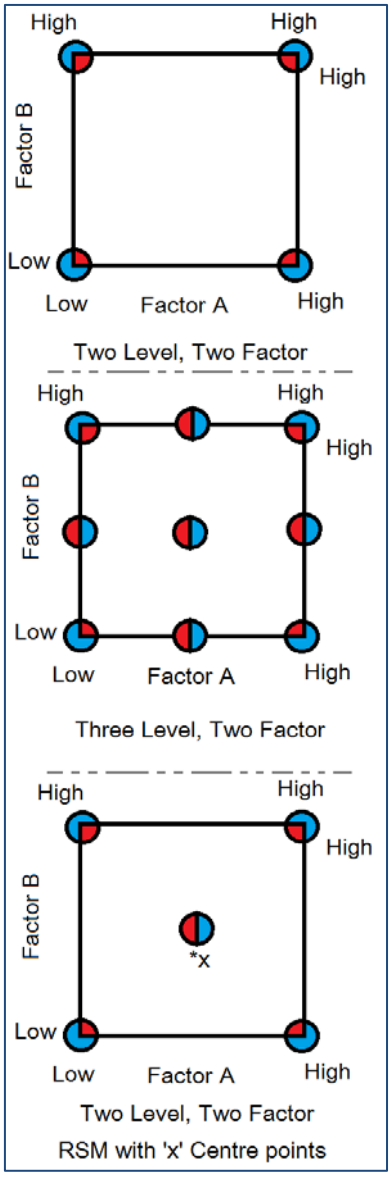

Figure 16: RSM and factorial visual comparison

It must be kept in mind that the hypothetical, three-level full factorial with nine points, will provide a complete understanding of the system, and will be less prone to aliased effects. The RSM, with its centre points, can be considered a compromise between the simpler two level, two-factor DoE, and more resource intensive three level, two factor DoE (with the added benefit of replicated centre points

to provide a robust error estimate and curvature detection facility). The centre points can then be subjected to an F-test approach to determine if there is a curvature to the data. Note that centre points should be conducted in a randomised order, as should all experimental runs if they are also to be used as a measure of the experimental 'noise' of the setup.

$$F = \frac{\left(\bar{y}_{factoral} - \bar{y}_{centre}\right)^2}{\hat{\sigma}^2 \left(\frac{1}{N_{factorial}} + \frac{1}{N_{centre}}\right)} \quad \textbf{(3-67)}$$

[81,83,85]

where

F = F-test for curvature in RSM

$\hat{\sigma}^2$ = the mean square residual in ANOVA analysis

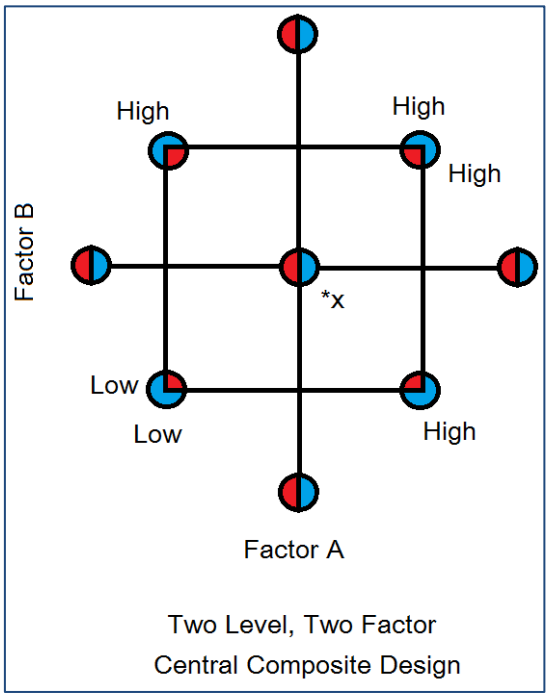

Figure 17: Central Composite Designs

Comparing the F-statistic value to the F-distribution, the greater the significance (i.e. the greater p-value is less than the usual level of 0.05) determines if curvature is present. The stronger the F-test (i.e. the smaller the p-value), the greater the degree of curvature detected. Another strength of the RSM method is that it is amenable to further experimentation. Central composite designs of experiments can be created as the RSM already specified (replicated central points), and if the system does appear to be nonlinear in the central region, additional experimental points can easily be included. In the two-factor system being considered, adding four more points (along each 'face' of

the design square) and, if possible, adding those points outside of the original design region is desirable (though not essential).

This design, and its results, can now fit quadratic equations. However, it is not always practical to go 'outside of the box' in this way for some experimental conditions. To further optimise this approach, the Box-Behnken designs were created by Prof Box and Prof Behnken in the 1960's [86]. These techniques specifically address the issue of incomplete blocks where, for whatever reason, it is not possible to test all factors in all valuable blocks.

A three-factor Box-Behnken design has 17 points (five repeats if the centre point, so 13 unique points) [86] and can fit a 10 factor quadratic; giving it an equivalent power to a three level three factor design that has 27 unique points. The ideal theoretical CCS should have twice as many 'external' factors (i.e. those outside the original design space) as there are factors. The α distance (the length of the arm for the external factors should be the square root of the number of factors) of a 2 factor CCD will often have an α value of 1.414 and five repetitions of the centre point. Some researchers have recommended that the α value should be even higher than this as it creates a rotational symmetry to the design that has subsequent advantages. Some authors state categorically [85], that this rotational symmetry requirement is only of interest in studies with more than five factors, particularly as extending the α length to such a degree will, in most practical applications, vastly reduce the region contained by the main design space of the experiment. There are other considerations when selecting this α length and the degree of rotate-ability of the design. The variance inflation factor (VIF) is one factor that benefits from this change. VIF is the inflation in the error for estimating model coefficients, due to the correlation between terms; yet another penalty applied as a result of forcing a simple linear equation to analyse multiple, possibly co-varying, factors.

$$VIF = \frac{1}{1R^2} \tag{3-68}$$

[85]

where R^2 is the coefficient of determination and can be calculated in several ways

$$R^2 = \frac{SS_{model}}{SS_{cor\,TOTAL}} \cong \frac{\Delta y^2}{(\Delta y + \hat{\sigma}^2)} \tag{3-69}$$

[79,81,83,85]

where SS_{model} (also known as the explained sum of squares or ESS) is

$$SS_{model} = \sum_{i=1}^{n} (\hat{y}_i - \bar{y})^2 \quad \textbf{(3-70)}$$

[81,83,85]

and $SS_{corr\ Total}$ (also known as the total sum of squares) is:

$$SS_{corrTOTAL} = \sum_{i=1}^{n} (y_i - \bar{y})^2 \quad \textbf{(3-71)}$$

[82,85]

$\hat{\sigma}^2$ = estimated standard deviation (from the square root of the residual mean square of the ANOVA analysis). The VIF increases to the point where the ANOVA response for multiple variant (response surface polynomial) factors are no longer trustworthy. When the VIF approaches ten (or greater) serious doubt is cast on the validity of this approach. Once a set of data has been generated, it is possible to calculate the standard error (SE) for the mean of these various individual values in the model: If

$$\hat{y} = \beta_0 + \beta_1 x_i \quad \textbf{(3-72)}$$

[82]

where x_i = is x at the point being predicted

$$SE_{mean(i)} = \hat{\sigma} \sqrt{\frac{1}{n} + \frac{(x_0 - \bar{x})^2}{\sum (x_i - \bar{x})^2}} \quad \textbf{(3-73)}$$

[85]

and the predicted standard error is then

$$SE_{pred} = \sqrt{\hat{\sigma}^2 + (SE_{mean(i)})^2} \quad \textbf{(3-74)}$$

[85]

One point to consider in RSM analysis such as Box-Behnken, or central composite designs, is that some outcomes may be of no interest at the time or physically impossible. So, certain regions or results in the model may well be impossible to calculate. The operational boundaries (upper and lower limits of the designed experimental model's outputs) increase as the number of co-varying factors increases.

Lower limit = C_j

Upper limit = D_j

$$C_j \leq \beta_{1j}x_1 + \beta_{2j}x_2 + \cdots + \beta_{qj}x_q \leq D_j \quad \textbf{(3-75)}$$

[80,85]

where

j= 1,2, … n

and β_{1j} is the scalar constant in the generated linear equation for up to 'q' terms, with the upper and lower limits having various constraints for the designed experiments input arguments.

Returning to the discussion of the α length from earlier, Anderson & Patrick (2005) [85] recommend an α length of the fourth root of the number of factors in the design. Such a fourth root α length will minimise the VIF for larger numbers of factors experimental designs.

3.10. Summary of Chapter 3

This chapter has considered the equations at the heart of the statistical methods utilised in the Design Expert Pro software. This software, and the data analysis methods outlined, will be used in Chapters 4, 5 and 6: Multivariate linear regression models, backwards elimination, and VIF will be used to a large extent. The general DoE for the work in Chapter 6 will be an adaptation of the central composite response method (surface discussed in section 3.9) suitable for use with 'categoric data'.

The methods outlined in Chapter 3 are well understood and recommended best practice in many fields of science and engineering [79,81,83,85]. These methods have model validation built into the procedures they follow. The quantification of residuals and the inherent inclusion of ε values at the most basic stages of the mathematical analysis; ensures that the linear regression models developed have been validated within their stated degree of accuracy, and within the limits and assumptions of the original DoE [79,81,83,85].

4 Data Analysis of Gas Diffusion Media

4.1. Introduction to Chapter 4

Chapter 4 introduces a more detailed study of gas diffusion media (GDM) and provides several numeric simulations to highlight the important role these components play in the performance of fuel cells (see section 4.2). The work on this thesis is focused on the utilisation of designed experiments and their ability to create statistical models of the impact GDMs have on overall cell performance. A visual aid to understanding the mass and heat flow in the GDM of the fuel cell during operation is presented to underline the importance of GDM. Section 4.2 presents a standard numeric model to illustrate the distribution of reactants and products in the cathode GDM. This generic model was used for illustrative purposes in the hope of underlining the importance of the GDM, and also to improve the understanding of the importance that changes to the GDM, and how they will impact the performance of the cathode GDM, and by extension the rest of the fuel cell. In section 4.3 the experimental procedures are outlined in accordance with the statistical methods discussed in Chapter 3. Such a procedural approach is the first step in a comprehensive study of GDM and their impact on the performance of fuel cells: To achieve this, section 4.4 focuses on the comprehensive GDM characterisation work carried out by several authors, most notably Dr Ahmad El-Kharouf [15,16] of the University of Birmingham. The samples tested in this work were originally tested in collaboration with Dr El-Kharouf. The experimental results generated by the author remained the property of the author, and it is this database, combined with the published historic records [15,16] that make up the entire data set analysed in this chapter. This work will be used to assess the validity of the multivariate method outlined in Chapter 3.

4.2. GDM conceptual models

There are several aspects of the GDM to be understood to fully appreciate the importance of its role in the fuel cell. Following the example of Collen Spiegel (2008) [87], a breakdown of some of the major features of the gas diffusion Media is presented. Development of a full fuel cell model is beyond the scope of this thesis, and so the ‘half land half channel’ approach put forward by Spiegel (2008) [87], adapted to reflect the cell geometry and operating conditions used in this study is adopted. The half-land half-channel model simplifies the simulations procedure greatly and still provides a repeatable ‘unitised’ cross section that can be extrapolated over the width of the cathode. This repeatable unit provides a reasonable model of the distribution of reactants and products in the flow channels, and in the GDM itself. As stated previously, a full simulation of working fuel cells is beyond the scope of this thesis. No effort has been made to model the edges of the flow field plate, changes in gas flow due to flow channel geometry, or the impact the wider ‘balance of plant’ has on the performance of the fuel cell (all factors that could be considered weaknesses of the half-land half-channel model).

Figure 18 shows a simplified schematic of the cathode side of a fuel cell in cross section. The 'GDM simulation region' represents the 'half-land', 'half-channel' 'unit' that will be discussed in more detail in the simulation models, and it is defined with more detail Figure 19.

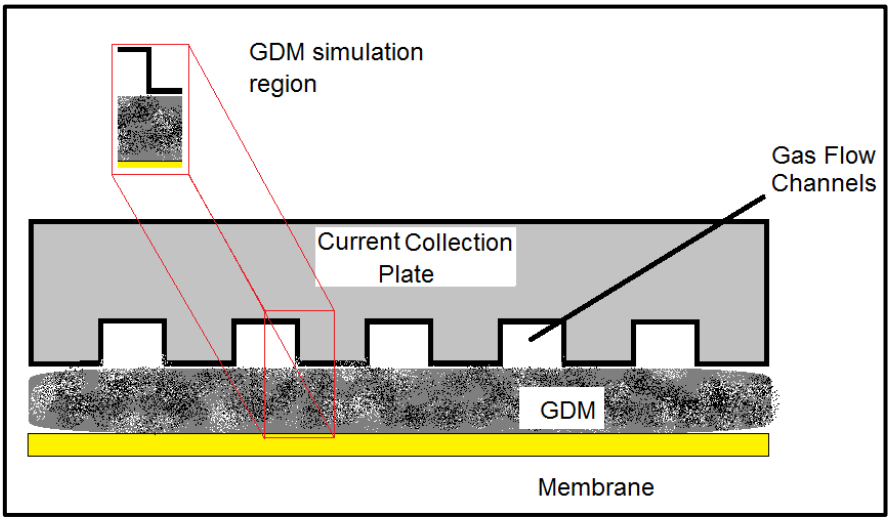

Figure 18: Half 'land' half 'channel' unit for GDM modelling

For modelling purposes, the schematic shown in Figure 18 must be expressed more rigorously as seen in Figure 19. The GDM simulation region in Figure 18 corresponds directly with the region 'd1 and d2' as shown in Figure 19. Figure 19 also shows the key starting assumptions of the initial conditions of the simulation:

- Model assumption.
  - The inlet channel was at higher pressure than the outlet channel.
  - There was no direct mass flow through the GDM (inlet to outlet).
  - There was no pressure differential through the body of the GDM.
  - No liquid H_2O was present in the GDM at the start of the simulation.
  - Catalyst is assumed to be a uniform thin layer on the surface of the membrane.

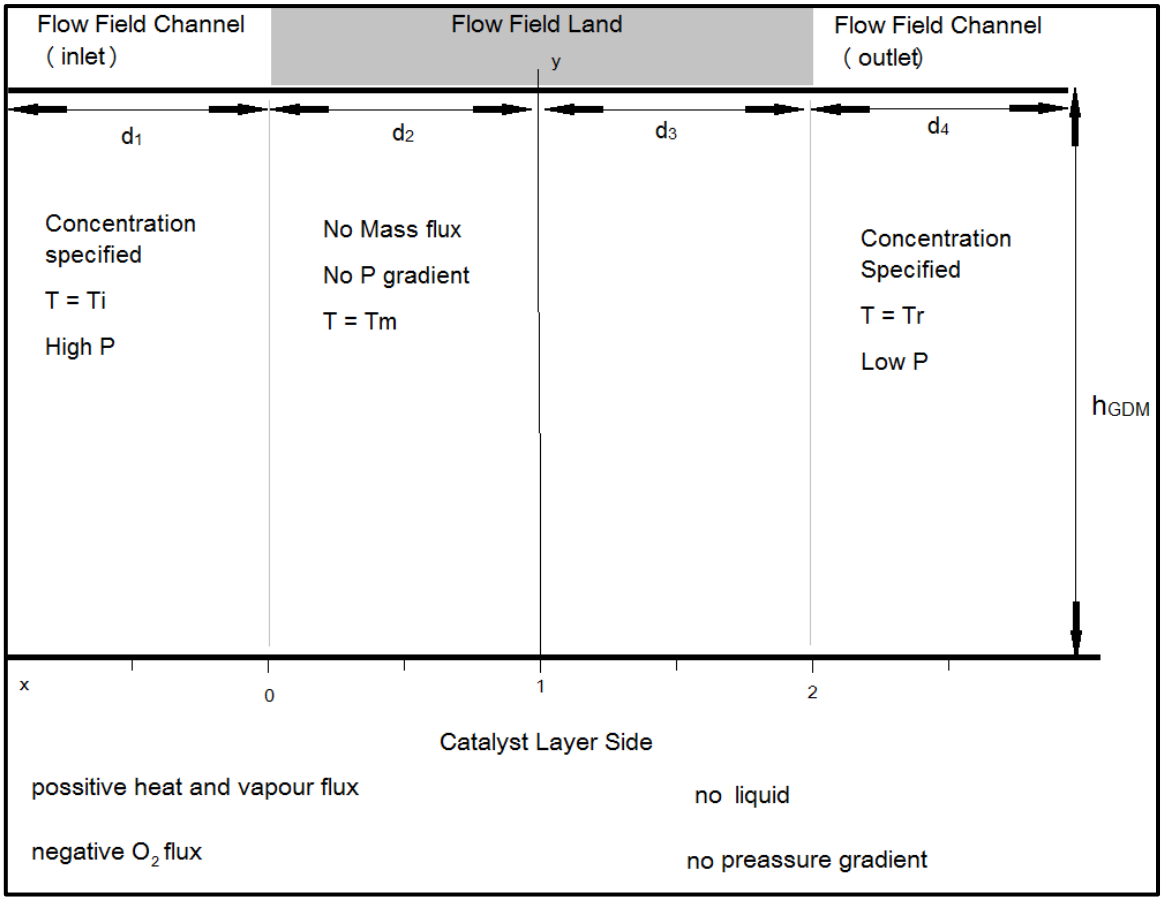

Figure 19: Regions of the GDM (adapted from [87]**)**

The model generated defined the parameters, and produced graphic representation, of the half channel region (regions d_1 and d_2) as shown in Figure 21 through Figure 26. Before initiating any of the subsequent models, a zone of parameters related to the channel dimension (the x plane in all subsequent models) and the thickness of the GDM on the Y axis (where y=zero is the edge of the supposed catalyst layer for a cathode coated membrane in an MEA), were created.

In the case presented, the unit length is dimensionless but could be adapted to any regular cell geometry by treating the actual measured length of 'd' (the half width of the recessed channel) as a single unit value for all other dimensions. A key assumption of this model requires the 'Perturbation factor' be set and is in accordance with the guidance:

$$\varepsilon = h/d_x << 1 \qquad \textbf{(4-1)}$$

where ε is the volume fraction of carbon present in the GDM. Physical properties of the GDM, such as the tortuosity and wettability, were effectively lumped together in the perturbation factor, and the assumptions made about the type mass and heat flow present to simplify the final equations developed to create the model. In the initial simulation ε=0.2

4.2.1. GDM two-dimensional numeric model

The numeric models presented in Chapter 4, have been adapted from work presented by Ms Spiegel [87] who has, in turn, presented work originally developed by Beusher et al. (2004) [88] which is available in the online repository of the Rensselaer Polytechnic Institute.

Porous bodies, such as the GDM, can have fluids flow through them utilising a variety of transport mechanisms. Knudsen (free molecular) flow occurs at low densities of the given species, and this ignores species-species interactions and focuses on the lone molecules of the fluid transported and the environment it is moving through. Viscous flow of the fluid was represented as a continuous field, and collisions between molecules of the species dominates. In ordinary diffusion, mixed species are transported by their interaction with each other and the external forces acting upon them (temperature, pressure and so on). In surface flow, molecules of the species of interest are modelled as moving along the surface of the layer they are adsorbed onto.

This last function was added onto the numeric model to increase its accuracy in well-defined systems. Typically GDMs are said to have pore size distribution that means Knudsen diffusion does not dominate (i.e. pore sizes significantly greater than $0.5\mu m$) [25,87]. Darcy flow velocity (V_{Dacry}) in porous media assumes there is no mixing between species and laminar flow is assumed in accordance with

$$V_{Darcy} = \frac{K_i}{\mu_{visc,i}} (\nabla P - \rho g) \qquad \textbf{(4-2)}$$

Where

$K_i =$ absolute permeability of species *i*

$\mu_{visc,i} =$ Dynamic viscosity of species *i*

$\nabla P =$ Change in preasure

$\rho =$ density of fluid *i*

$g =$ Acceleration due to gravity ($9.8 m.s^{-2}$)

Colleen Spiegel (2008) [87] showed in detail how this is adapted for use in porous media for the phases present in the GDM, and the two-phase form for gaseous water.

$$N_{w,l} = -\frac{K_i}{V_w \, \mu_{visc,i}} \nabla P_l \qquad \textbf{(4-3)}$$

where

$N_{W,l}$ = the volume of pure water in the system in flux

K = absolute permeability of species 'i'

V_w = the velocity of the water

$\mu_{visc,i}$ = the Dynamic viscosity of phase 'i'.

This approach can be further adapted to include transfer between gaseous and liquid phases, but that is far beyond the scope of this thesis. The Steffen-Maxwell equation for diffusion of one gas phase in another is also utilised to model the gas phase transport, especially multi-component gas mixtures, in the GDM [87]. Once again the adaption of this equation for use in the GDM is detailed in the literature [87].

$$\nabla y_i = RT \sum \frac{y_i N_j - y_j N_i}{p D_{ij}^{eff}} \qquad \textbf{(4-4)}$$

Where

∇y_i= the displacement of species *i*

R = Gas Constant (8.313 $J.K^{-1}.mol^{-1}$)

T = Temperature

$N_{'i'}$ = the superficial gas phase flux of species 'i' averaged out over the unit volume area being considered (Note that this area must be much greater than the mean pore size for this approach to be valid).

p = density of fluid system

D_{ij}^{eff} = effective diffusion of species '*i*' in species '*j*'

It is also possible to determine the temperature distribution in the GDM resulting from the exothermic reactions taking place at the surface of a catalysed membrane through the relationship shown in equation (4-5) [87,88]. An initial estimate of the temperature (T^i), based on the distribution of reactant gases and the exothermic nature of their interactions, has to be generated. The calculated T^i value becomes the starting condition of simulations to follow.

$$T^i = \mathbf{R}_{f4} \quad \textbf{(4-5)}$$

The symbol '**R**' denotes the real solutions to all numbers in the set 'f_4'; enabling the initial temperature at a given point within the GDM to be derived (ignoring liquids) and f4 is the transformation function for initial temperature calculation.

$$f_4 = \frac{1}{2} + \frac{1}{\pi} sin^{-1}(f_3) \quad \textbf{(4-6)}$$

$$f_3 = \frac{f_2 - 1}{f_2 + 1} \quad \textbf{(4-7)}$$

and

$$f_2 = \exp(\pi . f_1) \quad \textbf{(4-8)}$$

$$f_1 = z + iy \quad \textbf{(4-9)}$$

where *z* and *y* are coordinates, and *i* is complex.

Once the starting condition (T^i) temperature distribution had been calculated, the proportion of gaseous and liquid water phases was established, and the degree of saturation of pores with liquid water approximated. Utilising the adapted Darcy equation (equation (4–3)), to model the movement of gaseous water through the pores of the GDM ($\tilde{V}_{H2O(g)}$), and factoring in the degree of pore filling taking place as liquid water is produced and moves through the GDM, the velocity of the gaseous water in the system was calculated.

$$\tilde{V}_{H2O(g)} = -\frac{K_{(H2O,gas)}\theta}{\mu_{visc,H2O\ gas}} \nabla \tilde{P} \quad \textbf{(4-10)}$$

where

$\tilde{V}_{H2O(g)}$ = Velcoity of gaseous water in the GDM

$K_{(H2O,gas)}$ = permeability of gaseous water in the GDM

θ = volume fractions of pours taken up with liquid water

$\mu_{visc,H2O\ gas}$ = Dynamic viscosity of gaseous water in the GDM

$\nabla\tilde{P}$ = Pressure gradient

The full derivation of equation (4-10) is inthe literature [87], and the Matlab® code used to reproduce this research (adapted to more accurately represent the FCCA and the experimental operating temperatures used in this research) is available both in [87] and in Appendix 2. T^i, the increase in temperature in the system as a result of ongoing reactions as per equation (4-5), was established. The assumption of an overall uniform temperature in fuel cells breaks down at the scale that is important for GDMs [87]. The deviation away from the mean cell temperature as a result of exothermic reactions is mapped in Figure 20. In Figure 20, the temperature beneath the 'Land' part of the flow geometry (location d2 in Figure 19) and the flow channel (location d1 in Figure 19) as a starting assumption is detailed. The z-axis of Figure 20 shows the deviation from the average temperature of the overall cell operating temperature. The availability of reactant gases and the removal of water (vapour and liquid) are shown with the variation in temperature (z axis (Ti). That change above the mean temperature of the cell was simulated above the catalyst layer (assumed to be a single layer reaction at the base of the region modelled). The heat flow from the reactions primarily accruing within the 'channel region' and the contribution that temperature then makes to the temperature of the GDM directly region beneath the flow field plate.

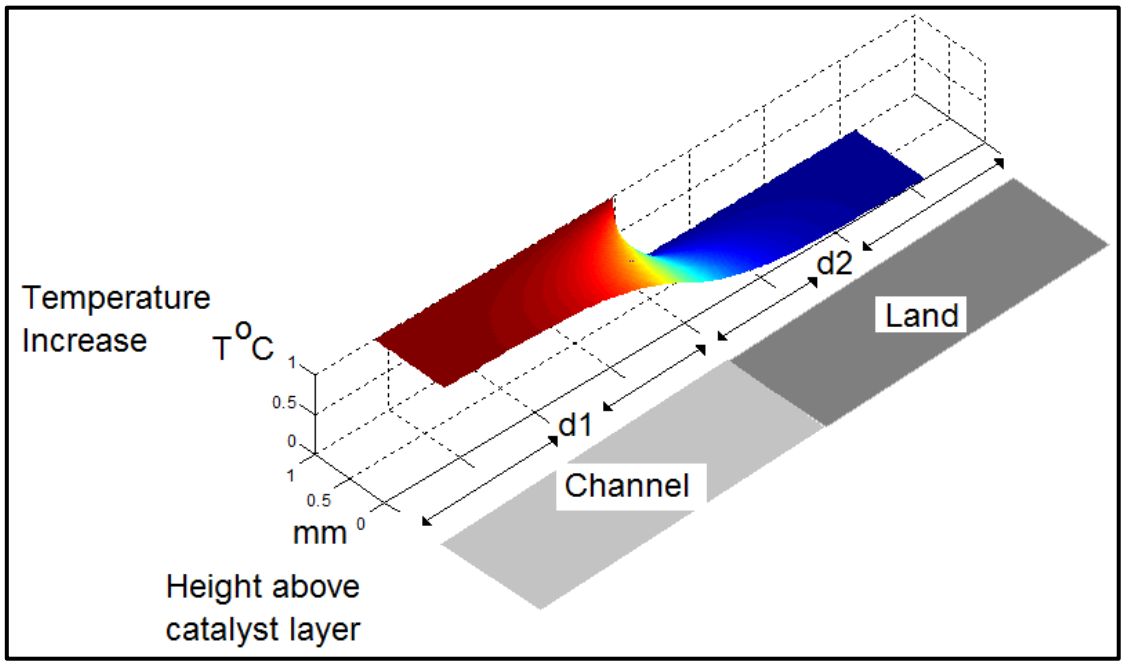

Figure 20: GDM inner layer temperature distribution (half land/half channel)

The variation in the underlying temperature distribution, as a result of exothermic reactions (water formation), was simulated for single 'half channel, channel land' as shown in the inset image of Figure 18. In this instance, the region being modelled is isolated from the rest of the fuel cell prior to

running the rest of the simulation. Note that the peak temperature, after running the simulation through several iterations without simulating additional gas flow, creates a high-temperature region in the channel (d1) at the upper surface of the GDM (Figure 20). Figure 20 shows that peak temperature inside the GDM does not necessarily occur at the membrane surface. This initial temperature profile was run as a simulation until a steady state was achieved. The initial temperature profile shown in Figure 20 now becomes the key assumption of the subsequent simulations in this chapter. This variation will impact the distribution of water as either a liquid or gas and will, in turn, impact the pore filling factor (θ) that changes the percentage availability of open pores in the GDM. As oxygen, water vapour and liquid water enter and exit at the surface of the exposed region of the GDM (simulating the flow of reactant and products along the channel), the simulation continues until a steady state was achieved and the stable distribution of the three phases is presented in Figure 21 through Figure 26. All codes and equations to achieve this were based on the work by Spiegel (2008) [87], and the interested reader is directed there for more detailed explanation of the modelling process.

Having established the boundary conditions (for regions d_1 and d_2 as shown in Figure 19), the assumptions of initial temperature distribution can be applied. It is now possible to visualise a two-dimensional cross section of the GDM for Temperature, O_2 concentration, H_2O vapour distribution and H_2O liquid water saturation in the operating fuel cell, in the steady state.

Once again all codes and equations were based on the work by Spiegel (2008) [87] and have been adapted to reflect the operating geometry and test conditions of the FCCA. In all cases the GDM modelled was a generic one. It is a flaw in this approach that the material properties, wettability and porosity of the GDM are presented largely through a perturbation factor (ε), and not a more detailed understanding of the individual GDMs significant factors such as pore geometry, tortuosity and actual pore size distribution to name just a few. However, such a detailed model is beyond the scope of this thesis. The reduced complexity model presented here is still useful and the developed distributions broadly informative. In Figure 21, the temperature increase above the fuel cell mean temperature in the steady state operation in accordance with equation (4-5), is shown.

Figure 21 shows the temperature distribution through the cathode GDM directly under the flow channel and the land. The x and y axis are in mm. It can be seen that directly under the metallic bipolar plate (x=0 to 1), the ‘land’ of the flow channel structure; there is a significant heat loss, as is to be expected. The region adjacent to the catalyst layer, and underneath the flow channel has the highest temperature concentration as a result of the freely available reaction gases and the exothermic reaction processes modelled.

Figure 22 shows the concentration variation in oxygen through the cathode GDM directly under the flow channel and the land. The x and y axis are in mm. The oxygen concentration in the region (x= -1 to 0) under the flow channel is higher than that under the land (x= 0 to 1).

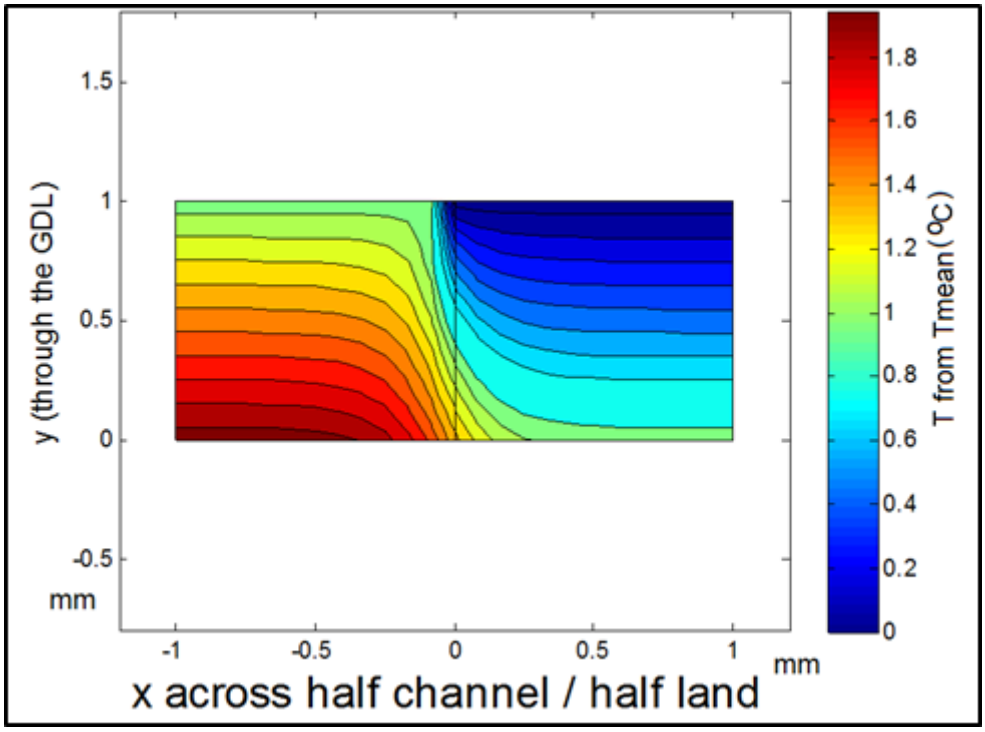

Figure 21: Temperature distribution of working cathode GDM

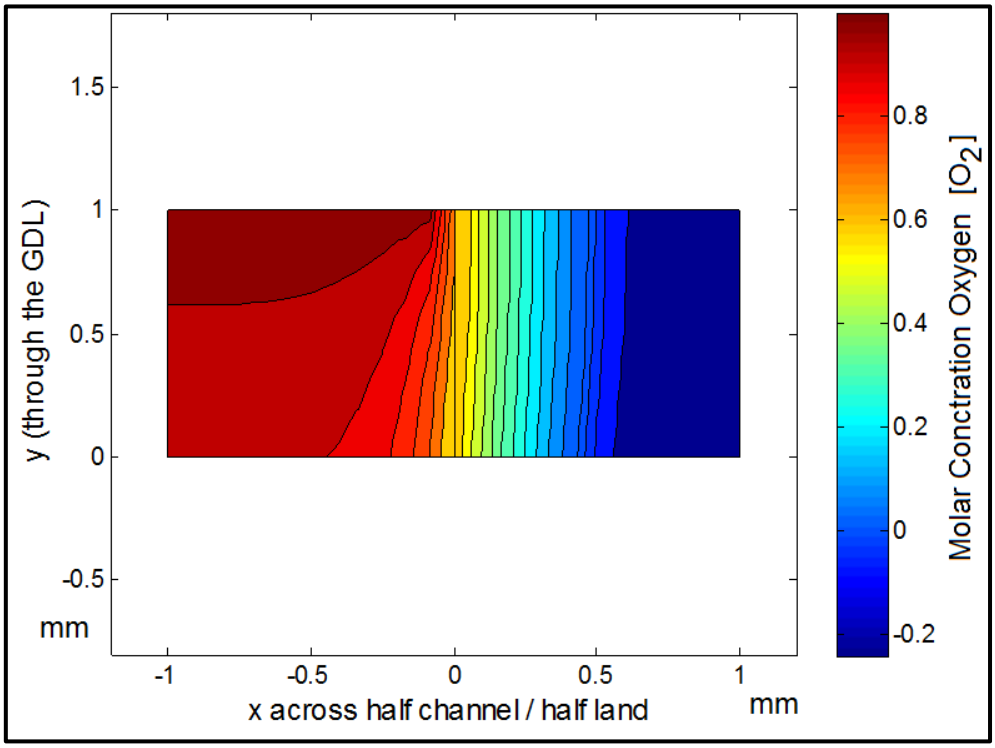

Figure 22: Oxygen concentration distribution of working cathode GDM

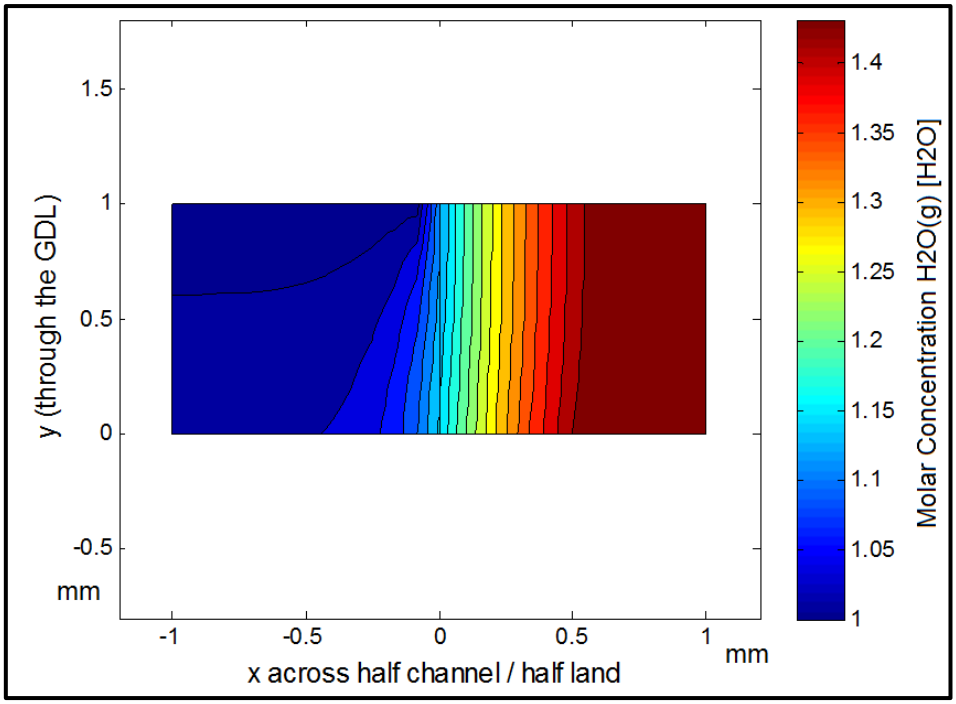

Figure 23: Water vapour distribution of working cathode GDM

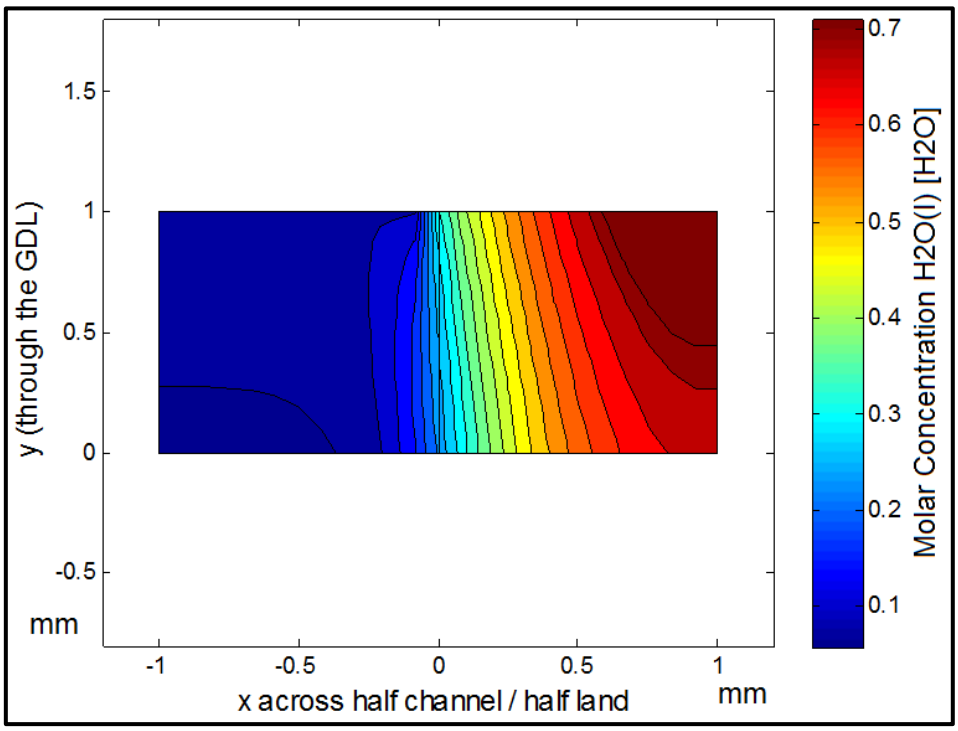

Figure 24: Liquid water distribution of working cathode GDM

Figure 23 shows the concentration variation in gaseous water vapour through the cathode GDM directly under the flow channel and the land. The x and y axis are in mm. Gaseous water vapour was almost the inverse of the distribution of the oxygen concentration.

Figure 24 shows the saturation variation in liquid water through the cathode GDM, directly under the flow channel and the land. The x and y axis are in mm. Liquid water has accumulated in the region directly under the land (x=0 to 1).

These images provide an understanding of the mass flow of reactants and products in various phases through the GDM, and make the importance of the GDM to the overall performance of the fuel cell clear. If the fuel cell saturation distribution of water in the steady state encroaches strongly into the 'd_1' region (x = -1 to x = 0), then there will be a reduction in the estimated pore volume fraction (θ) available for reactant and product species to enter-exit the GDM from the gas flow channel.

4.2.2. GDM degradation and time dependence

The exact mechanisms and failure modes for GDMs are detailed by many other authors already, and the literature has been discussed previously in section 2.3. To summarise the impact GDM ageing can have on liquid water and oxygen concentration shown in Figure 25 and Figure 26, the assumed perturbation factor (ε) has been set to 0.1. Setting ε = 0.1 gave an indication of how sensitive the model is to the assumed porosity and wettability of the system (recall that wettability is a function of PTFE coating mass presence, but increased PTFE reduces the total pore availability). The reduced 'ε' value simulates a more efficient removal of liquid water (saturated H_2O) and this, in turn, allows a more uniform distribution of O_2 directly under the gas flow channel. Therefore, it is clear that changes to the ability to transport water (gaseous or liquid) through the GDM over time will have a significant impact on the GDM performance. GDM degradation mechanisms can be listed as follows [89,90]:

Table 8: GDM degradation mechanisms

Reversible	
Loss of porosity	PTFE ionomer expansion Thermo/mechanical crushing H2O(l) build up
Irreversible	
Diffusion Layer structure alters permeability PTFE coating loss	Carbon Erosion Fibre loss OH radical attack

Regarding the models used in this thesis: As time passes the $\mu_{visc,i}$ (Dynamic viscosity) of liquid water will change within the GDM, as the factors that impact it (such as mean pore size and degree of hydrophobicity) will also alter. The volume fraction of available pores (θ) will also change as the number of pores, their total size and smallest available pore that can be penetrated by various species will alter over time as the cell ages. The exact degree of impact these factors have on the longevity of

fuel cells for specific types of GDM is determined experimentally and is discussed in more detail in Chapter 6 with sections 6.7 and 6.8 being of particular note.

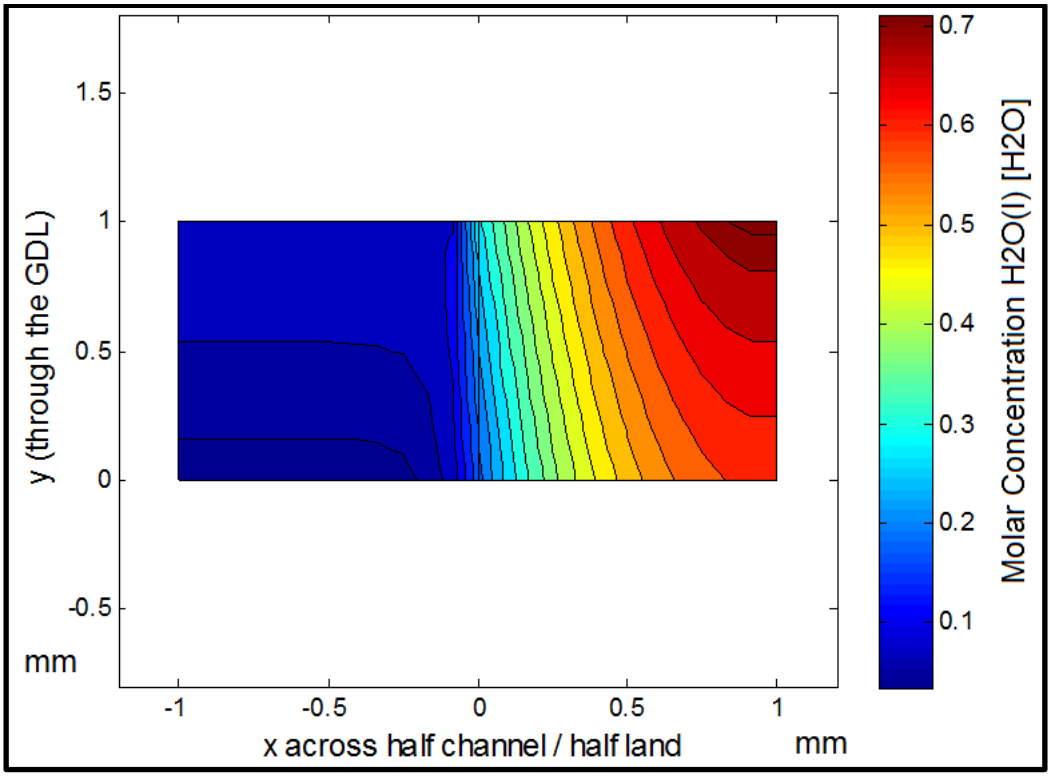

Figure 25: ε=0.1 liquid water distribution of working cathode GDM

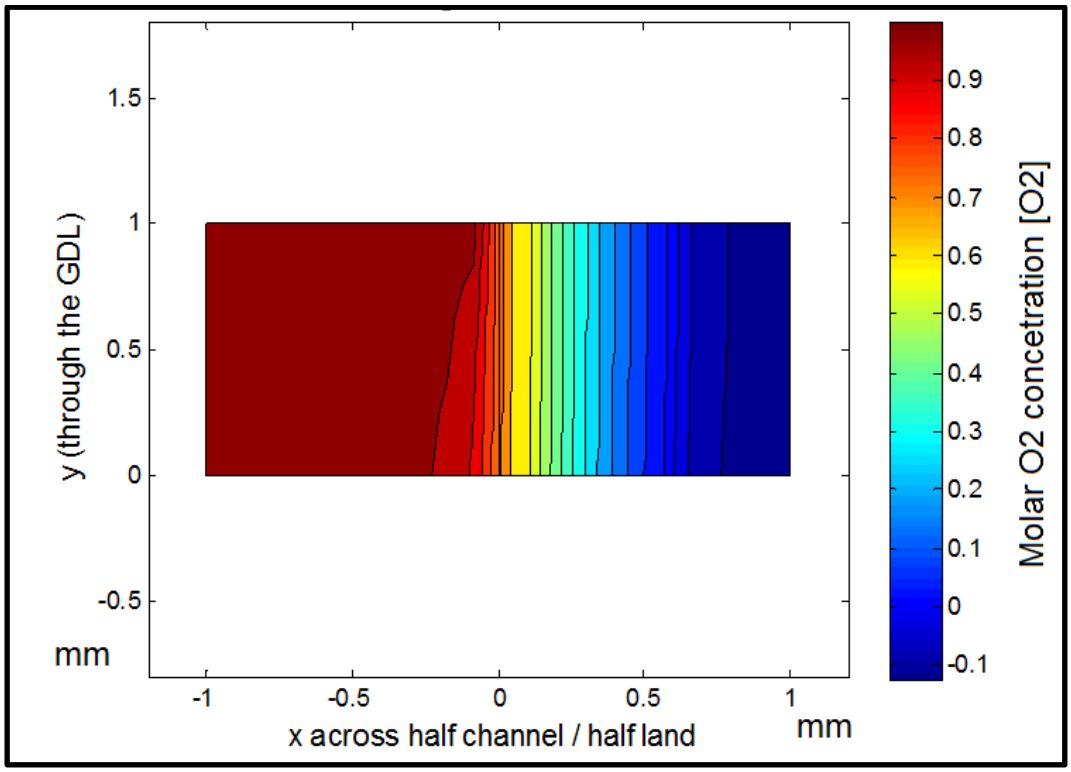

Figure 26: ε=0.1 oxygen concentration distribution of working cathode GDM

Figure 25 shows the concentration variation in oxygen through the cathode GDM directly under the flow channel and the land. The x and y axis are in mm. The oxygen concentration in the region (x= -1 to 0) under the flow channel is higher than under the land. In this case, ε is idealised (ε = 0.1) and demonstrates more uniform oxygen distribution under the channel region (d1 in Figure 19) and at higher concentration than for the reduced performance (i.e. degraded) GDM simulation shown in Figure 22.

Figure 26 shows the saturation variation in liquid water through the cathode GDM, directly under the flow channel and the land. The x and y axis are in mm. Liquid water has accumulated in the region directly under the land (x=0 to 1). In this case, ε is idealised (ε = 0.1) and demonstrates reduced liquid water concentration under the land region (d2 in Figure 19), and at higher concentration than for the reduced performance (i.e. degraded) GDM simulation shown in Figure 24.

It is evident that GDMs are a worthy topic of further investigation and that as the GDM material and structure changes, either by design or over time as a result of degradation; this strongly influences the overall performance of the fuel cell. More detailed numeric modelling and simulation of GDMs is needed in the fuel cell field, and the interested reader is directed to works that focus entirely on numeric simulations of GDMs such as that carried out by Park et al. (2016) [91], and Jinuntuya (2014) [55]. The work in this thesis has retained its focus on multivariate assessment of experimental data.

4.3. Assessment of multivariate methods

The work in this section was undertaken in collaboration with the University of Birmingham Doctoral Training Centre for Hydrogen, Fuels Cells and Their Applications, who provided the materials to manufacture the MEAs tested.

4.3.1. Test conditions

Two sets of parameters were used throughout the testing in this document, as shown in Table 9. Previous experience with the fuel cell component analyser (FCCA - detailed in section 4.3.2) has shown that higher pressure, higher flow rate test settings, generated less variable results. This high-pressure stability is thought to be a peculiarity of the FCCA itself, perhaps due to the lack of inlet gas humidification and the absence of any pre-heating of gas flows. The experimental settings for this research were defined in collaboration with the University of Birmingham and the work being carried out by them into gas diffusion layers and MEA fabrication methodologies. A lower pressure setting was also tested. The low-pressure setting was intended to more accurately simulate the supposed operating conditions of an automotive application, though it must be acknowledged that the FCCA has not always shown repeatable results at these settings. This research was carried out in conjunction with the FUTURE-vehicles project (EPSRC Grant EP/I038586/1).

Table 9: Two sets of fuel cell operating parameters

Setting	High pressure	Low pressure
H_2 flow rate	80 sccm	60 sccm
Air flow rate	200 sccm	150 sccm
Back pressure	2 bar (a)	1.5 bar (a)
Data logging rate	1 Hz	1 Hz
Relative humidity [2]	100%	100%
Cell temperature	75^{O}C (+/- 3^{O}C)	60^{O}C (+/- 3^{O}C)

4.3.2.Fuel Cell Component Analyser

Components were tested on a fuel cell component analyser (FCCA) from Intelligent Energy Ltd. Two of these devices were available and will be referred to as FCCA one or two (FCCA one shown in Figure 27). Each FCCA consists of four test cells with 11.3 cm^2 active area in a circular (disc), geometry (shown in Figure 28) with graphite monopole plates.

Table 10: FCCA specifications

FCCA specifications [3]			
	Min	Nominal	Max
Anode gas mass flow	40 sccm.min^{-1}	100 + sccm.min^{-1}	2,000 sccm.min^{-1}
Cathode gas mass flow	40 sccm.min^{-1}	100 + sccm.min^{-1}	2,000 sccm.min^{-1}
Gas pressure	1bar (g)	3bar(g)	5 bar(g)
Temperature control	Ambient	40^{o}C to 80^{o}C	120^{o}C
Load cell terminals	-	1 Volt	9.9 Volts
Load input	-	1 volt	48 Volts DC
Load current	-	25 Amps / 25 Watts	25Amps /100 Watts
Data collection rate	-	1Hz	-
Ambient temperature	5^{o}C	-	35^{o}C

Each cell consists of a single serpentine flow field, with a 1.6 mm land and a 1mm channel for gas flow. The channels are 1.1mm deep. The FCCAs both operate on a custom Excel™ interface supplied by Intelligent Energy Ltd and a National Instruments® based data acquisition and control system.

[2] Manufacturers operators manual
[3] Manufacturers operators manual

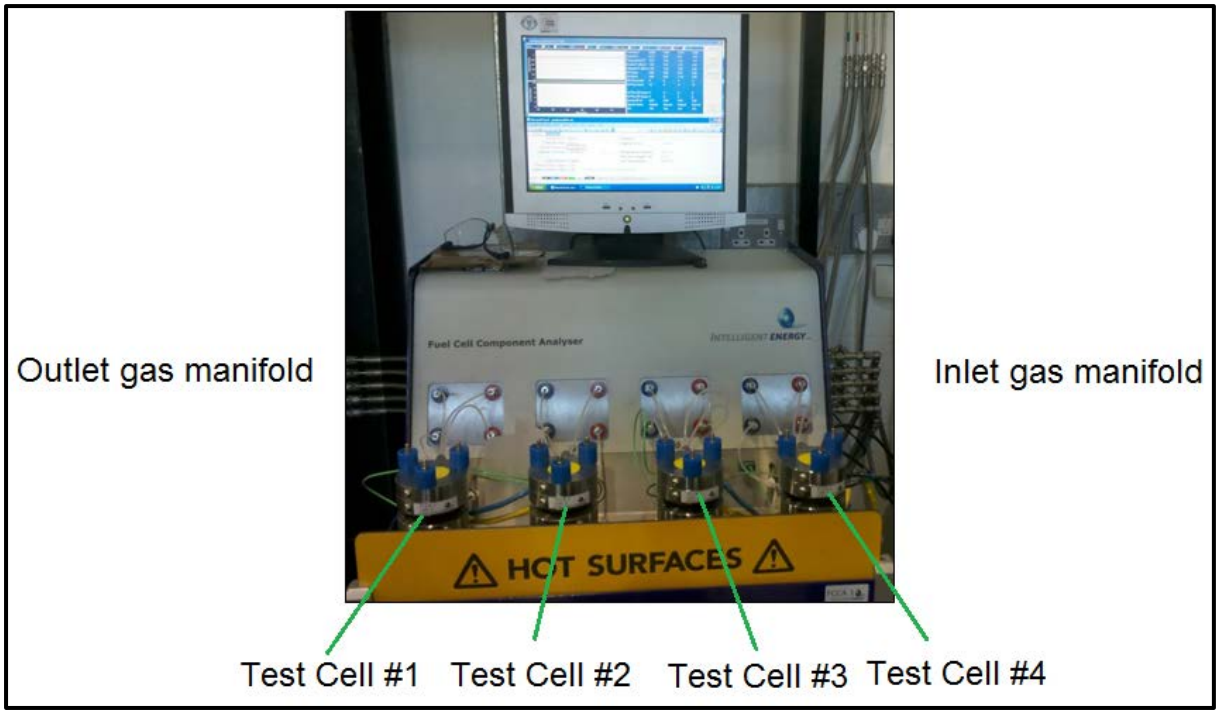

Figure 27: FCCA 1 with EIS on cell #4

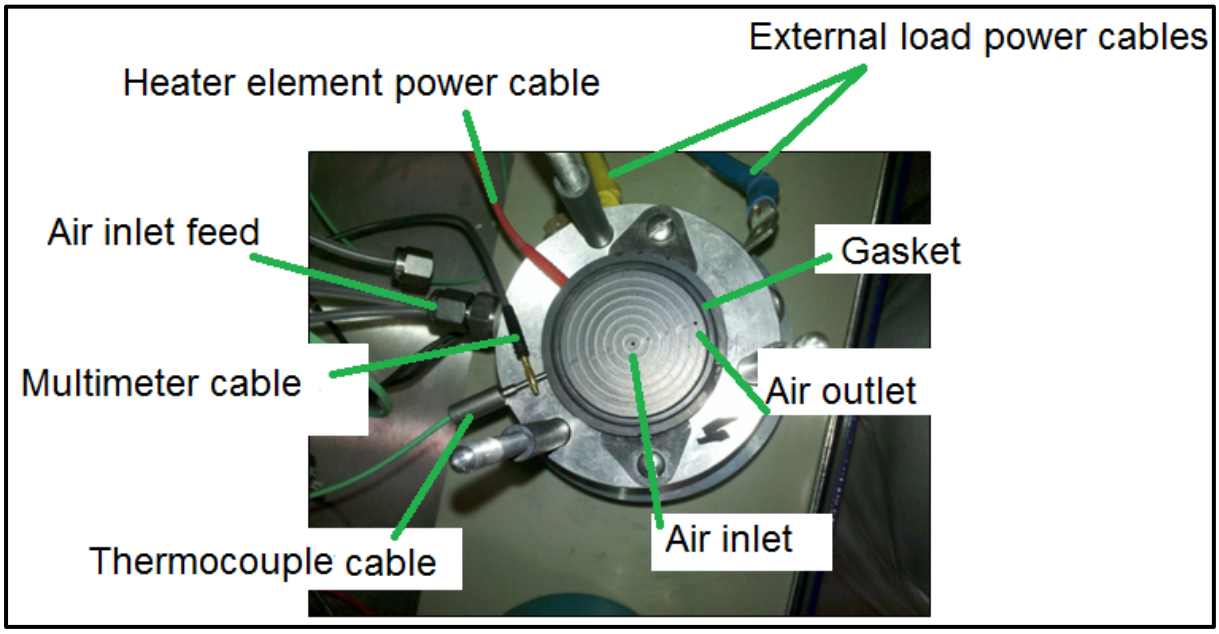

Figure 28: FCCA 1 individual test cell flow field (cathode)

4.3.3.Ink Formulation

The aim of the work in this thesis was focussed on the practical experimentation on GDM. To ensure that all tested MEAs are as uniform in manufacture as possible, and therefore reduce likely sources of experimental variability; it was realised that there was a requirement to manufacture all MEAs in-

house. The GDMs used by several different fuel cell and MEA suppliers are not universally identical. Any commercially manufactured MEAs would have been purchased from several suppliers to achieve the spread of MEAs required for the work completed in Chapter 4 and Chapter 6. However, there were no guarantees that the PTFE based monomers, the cell manufactures heating and pressure regimes, or catalyst ink formulations used by the various manufacturers would be in any way similar. It was, therefore, essential that all MEAs be manufactured in-house, including the catalyst ink required to create electrode surfaces.

All samples were manufactured using the same basic materials (Nafion® membranes, Nafion®-based ionomer). Heating and pressing regimes were uniform across all samples, and the application of catalyst ink was achieved by hand painting. All samples in detailed in Chapter 4 were manufactured by one of three researchers (Nick McCarthy, Amrit Chandan, Ahmad El-Kharouf), and all were manufactured in the fuel cell laboratories at the University of Birmingham. Every effort has been made to ensure samples are of equal quality of manufacture. Catalyst ink formulations are focused on in more detail in section 4.3.3 as they were assessed as being the manufacturing step with the highest risk of error.

Catalyst ink formulations are many and varied, and the ink formulation used in this research was designed to create a catalyst suspension that would maintain its catalyst distribution during the application process. There are various ink formulations in the literature [47,92-94], usually optimised for spray applications. Lacking the ability to spray deposit catalyst ink in the department; these formulations were adapted until the following stable ink manufacturing procedure was perfected. Deionised (DI) water, 30 'weight percent' (30wt%) of platinum (Pt) on carbon (C)[4], 10wt% aqueous Nafion® solution, and 1 molar 2-propanol solution (IPA) were 'sonicated' (agitated in sealed container placed in liquid bath subjected to ultrasonic frequency perturbations) together for one hour. Note the DI water is added to the platinum catalyst first to reduce the possibility of combustion during mixing. The amount aqueous Nafion® solution required in µL = mass of carbon desired (catalyst weight not included) in mg divided by the percentage Nafion® solution strength (expressed as a decimal).

$$Nafion_{soln.}(\mu l) = \frac{m_{Carbon}\,(mg)}{\%_{soln.}(as\ decimal)} \qquad \textbf{(4-11)}$$

The volume of liquid calculated from equation (4-11) was multiplied by 5.31: This is the volume of 2-propanol required to act as a solvent for the ink formulation as shown in equation (4-12).

$$Nafion_{soln.}(\mu l) * 5.31 = 2propanol(\mu l) \qquad \textbf{(4-12)}$$

[4] Carbon black catalyst support was 'Vulcan carbon black' according the to the suppliers.

DI water with a volume equal to 10% of the measured out volume of 2-propanol (isopropanol), as calculated in equation (4-12), was added to the Pt-on-C, to reduce the possibility of combustion during mixing. The whole mixture was sonicated at room temperature for one hour immediately before application. Single layers of ink were painted on and allowed to dry for eight hours (or overnight). The MEAs were then weighed, and the process repeated until the desired catalyst loading was achieved. The ink preparation was sonicated for twenty minutes immediately before application if it has been left static for a significant period (more than three hours).

Note that the amount of carbon relative to mass is a significant factor in the formulations, and the mix ratio for 10wt% Pt on C catalyst powders and 40wt% Pt on C powders were very different. This carbon ratio interacts with the liquid proportions in the ink formulations and necessitated the need to create far larger batches of ink than was originally expected. A great deal of care was exercised in applying the ink iteratively. Additionally, the amount of ink to be applied was further increased to account for wastage and drying that occurs during normal fabrication. Overall a 20% increase of ink to be created (based on the calculations in equations (4-11) and (4-12)) proved to be sufficient. Samples were weighed before painting on the ink and then weighed again several hours later to ensure that the amount of deposited ink (and therefore platinum) is in the correct range of wt% loadings to match the experimental design.

A typical spreadsheet of ink formulation and for a layered catalyst MEA is presented in Table 11. In this instance the data columns were set to achieve a platinum concentration on the surface of the electrode of 0.30mg.cm^{-2}. The column labelled 'Base calculation' gives the values required of each ingredient for a 40wt% Pt-on-C powdered ink at 40wt%. The next three columns each show the measured amounts required (in accordance with equations (4-11) and (4-12) and with an additional 20% to account for wastage) to generate a 10 mg.cm-2 layer for each of three separate weighting of Pt-on-C powdered ink (10wt%, 30wt% and 50wt%).

If these three layers are painted on the sample, the total amount of platinum ink on the electrode would be 0.30mg.cm^{-2}. The spreadsheet presented was used to generate a more complex 'variable concentration' catalyst layer similar to those used in Chapter 6. Simpler, single layers catalyst concentration layers can be created by setting the 'Pt loading desired' row to '0' for any powdered ink loadings surplus to requirements.

				cat layer concentration gradient calculations									
	Base calculations			adjusted by (accounts for wastage)			adjusted by			adjusted by			
				1.20			1.20			1.20			**tot mg/cm^2 achieved**
Pt Loading desired	0.40	mg/cm^2		0.10	mg/cm^2		0.10	mg/cm^2		0.10	mg/cm^2		**0.30**
total active MEA area	1.00	cm^2		11.34	cm^2		11.34	cm^2		11.34	cm^2		
total weight Pt required	0.40	mg of Pt		1.13	mg of Pt		1.13	mg of Pt		1.13	mg of Pt		
Pt loading on carbon	25.00	wt% Pt on Vulcan		10.00	wt% Pt on Vulcan		30.00	wt% Pt on Vulcan		50.00	wt% Pt on Vulcan		
weight of Pt on C to measure out	1.60	mg Pt/C		11.34	mg Pt/C		3.78	mg Pt/C		2.27	mg Pt/C		
(effective Wt of C present)	1.20			10.21			2.65			1.13			
Nafion : C ratio = 1:1													
	10.00	wt% Nafion in soln		10.00	wt% Nafion in soln		10.00	wt% Nafion in soln		10.00	wt% Nafion in soln		
total mass of C present in weighed out sample	1.20	mg		10.21	mg		2.65	mg		1.13	mg		
density of Nafion soln~1													
mass of Nafion solution to weigh out	12.00	mg		102.06	mg		26.46	mg		11.34	mg		
volume of Nafion solution to weigh out	12.00	µL		102.06	µL		26.46	µL		11.34	µL		
add water to catalyst to avoid IPA combustion	6.37	µL		54.14	µL		14.04	µL		6.02	µL		
add IPA to cat/water suspension	63.66	µL		541.43	µL		140.37	µL		60.16	µL		
approx. final solute liquid volume	70.03	µL		595.58	µL		154.41	µL		66.18	µL		
	0.07	mL		0.60	mL		0.15	mL		0.07	mL		
	0.07	cc		0.60	cc		0.15	cc		0.07	cc		
Nafion : Pt ratio				0.90			0.70			0.50			

Table 11: Catalyst ink formulations (10, 30 and 50wt% Pt-on-C)

4.3.4.MEA fabrication

Nafion 212 sheets (manufacturer's data sheet available as Appendix 1) were cut into 60mm by 60mm sections. A 38mm diameter section of gas diffusion layer (GDL) material was cut out from a continuous sheet (surface area of 11.3cm^2), ensuring all cut edges were at least 25mm away from the edge of the as-supplied sheet. Catalyst ink was painted onto the GDL material to create a catalyst coated substrate (CCS) gas diffusion electrode (GDE) as described in 4.3.3. This regime was implemented for both anode and cathode layers. Typical platinum loading in fuel cells was 0.38mg.cm^{-2} (+/- 0.02). Catalyst ink was painted onto the GDM by hand, using an animal hair brush, to avoid cross-contamination from any polymeric bristles (some polymers are incompatible with isopropanol; see Material Safety Data Sheet available in Appendix 1).

4.3.5. Anode GDEs

Anode GDMs were fabricated on Toray diffusion media TGP-H-120 with a 0.30mg.cm^{-2} (+/- 0.02) platinum loading. This material was selected as it was commercially available in quantities sufficient for all experimental samples. The decision was made to maintain a uniform anode catalyst layer and structure, in large part due to the oxygen reduction reaction (OOR) being the rate limiting step for fuel cell systems [24,66,95]. With a relatively high anode catalyst loading and a well-established GDL; it was decided the anode side could be held as a 'constant' for this research.

4.3.6. Cathode GDEs

Cathode GDEs were fabricated in a similar fashion. However, the selection of GDL materials was wider, and a variety of catalyst loadings were manufactured. The overall process of fabrication was largely the same as that used for the anodes, though with differing platinum loadings.

4.3.7. GDM Historic Data Matrix

A large number of samples have been manufactured both by the author, and also by Dr Ahmad el-Kahrouf and Dr Amrit Chandan of the University of Birmingham to facilitate research for their PhD work and to aid in contribution to several publications [15,16].

These samples are all identified with the 'AeK' prefix in their name. Thanks to the shared access to these research samples, it is possible to conduct a 'data-mining' investigation into published, historic information, alongside the polarisation data conducted at Loughborough University, by the author. Note that later samples (identified as 'dual layer','DL', 'fluorescent', 'FL', 'MAC', 'FUTURE' or 'FU') were manufactured in a broadly similar way, by the author.

The electrodes and the membrane were hot pressed using a hydraulic press at 125^{O}C and 1,800kg (15.24cm diameter rams onto a 25.4cm by 25.4cm square platens). The MEA components were protected by a PTFE sheet and wrapped in two layers of aluminium foil. The samples were held flat and stable by a matched pair of 1.6mm thick steel sheets (10cm by 10 cm). All specimens were held at temperature and pressure for two minutes.

A wide variety of MEAs were conditioned and then tested under polarisation conditions. This research was done in collaboration with Ahmed El-Kharouf and Amrit Chandan of UoB as part of the background research that, several months later, went to the publication of their data [15,16]. To undertake the work in a timely fashion, it was agreed to share the manufacturing responsibilities for a large number of MEAs (all work completed at the UoB), and the initial 'conditioning' work for all fuel cells, was carried out at Loughborough University. The ability to undertake conditioning regimes in up to eight fuel cells simultaneously (across the identical test cells of the two FCCA test suites available) were an invaluable resource to complete the work.

After conditioning, the samples were polarised, and the results of this research remain the property of Loughborough University and Mr N. McCarthy. The samples were then returned to the UoB where further characterisation was carried out on a selected number. This additional work at Birmingham was later presented in chapter four of "Polymer Electrolyte Fuel Cell Degradation" [16].

Some 128 samples were made in total, with the 50 materials used to create cathode variation in the sample set. A minimum of two of each sample was created, with additional copies made in Birmingham, for the work undertaken there. A full list of all Birmingham GDM data, including additional data sets from several GDM suppliers, expanded the original data set to include a greater variety of non-woven or non-woven type material. The collected raw data for all test samples can be viewed in spreadsheet form in Appendix (3).

All data on thickness, area weight, bulk density, surface roughness porosity, tortuosity, pore diameter, permeability water contact angle, contact resistance and in-plane resistivity were all gathered from literature [15,16]. All polarisation curve data (temperature, amps, voltage, gas flow rates) were gathered using the built-in data acquisition of the FCCA (see section 4.3.2) by the author.

The fabricated MEAs active surface area was 11.34 cm^{2}. The monopolar plates used were graphite, with a circular, single serpentine flow field. The GDM anode material was held constant: A commercial JM electrode ELE00165 was used with a catalyst loading of 0.4 mg.cm^{-2}. A variety of other GDMs were tested on the cathode side. TKK Pt-on-C catalyst based ink was hand painted on the GDMs to achieve a loading of 0.4 ±0.05 mg.cm^{-2} (as discussed in section 4.3.3 and 4.3.4). Nafion® 212 polymer electrolyte membranes (PEM) were used.

All MEAs were soaked in DI water (resistivity = 18 MΩ.cm) overnight to accelerate the membrane activation process. The MEAs were then randomly assigned to one of seven test chambers for in-situ testing, under the following operating, set point, conditions:

- H_2 flow rate: 80 sccm
- Air flow rate: 200 sccm
- Back pressure: 2 Bar
- Cell temperature: $65^{O}C$ (+/- 5 ^{O}C)
- Data logging rate: 1 Hertz
- Relative humidity: 100% (according to FCCA manufacturer specification)

MEA 'conditioning' was achieved by holding the cells at variable current load to induce a potential of 0.6 ± 0.03 V for three hours. Once completed the MEA was subjected to 25 'rapid' polarisation curves. A three second time step was initiated, with 25 current settings increasing to the maximum current load achievable by the MEA.

As discussed in sections 4.3.3, 4.3.4, 4.3.5 and 4.3.6: All samples were manufactured in the fuel cell laboratories of the University of Birmingham. All three researchers responsible for their manufacture followed a rigorous manufacturing plan with the express intent of minimising experimental variation across all samples. Any created test pieces that were not correctly aligned (anode to cathode), or that failed to meet the desired catalyst loading by +/-0.02mg.cm^{-2} or that were in any other way compromised, were excluded from the study. If possible duplicate samples were manufactured to replace them. Initial 'conditioning' of the samples was carried out by the author at Loughborough University using the FCCA. Any test samples that failed to generate a repeatable polarisation curve after 3 hours of steady state operation and 25 conditioning cycles, were rejected from the study. Where possible such rejected samples were manufactured again. Once again, high standards of manufacture were maintained. The stated conditioning regime had to be completed before samples were put forward for further tests.

Polarisation curve number 25 of the sequence was recorded. A further polarisation curve with a 10 second step time was also carried out and recorded. Polarisation curves were plotted by averaging the V/I values across each time step.

Table 12: Categoric identifiers for GDM analysis

MPL	-
Yes	2
No	1
Structure	-
Non-woven	1
Paper	2
Woven	3
Supplier	-
Ballard	1
E-Tek	2
Freudenberg	3
Sigracet	4
Tenax Toho	5
Toray	6

After collating all the data, Table 12 shows the 'full set' of variables that could be populated. Table 12 represents the input variable where there was sufficient data, across all sets, to conduct the next stage of the analysis. 'Ce-Tech' GDMs were not included in this next stage of the study. While the MEAs were fabricated and tested; there was insufficient background information to characterise the material in the study. Additional samples of GDM (supplied by Tenax-Toho) to offset this reduction in the total number of GDMs available for this stage of the study. Additional non-woven materials were added in from Freudenberg for the same reason.

4.4. Historic data assessment results

Initial investigations included a matrix plot [83] of GDL cathode performance. Since the birth of the personal computing revolution, the recommended method for first assessing what may be multiple co-varying factors is with a matrix scatter plot, as first described by Hartigan (1975) [96]. For any number of variables greater than one, it is possible to pair them and plot them as scatter plot against each other. The matrix scatter plot (matrix plot), allows a rapid visual inspection of multiple variables simultaneously. Its chief strength, is in identifying possible linear relationships between paired variables, and also in identifying categoric data. A matrix plot consists of each variable plotted against each other and then presented as a single overall figure. It is effectively a mosaic of OFAT, two variable, experiments. The matrix plot for the data in this chapter is presented in Figure 29. Matrix plots are a 'first stage analysis' and perform several important functions:

- Clearly defining categoric data (which appear as vertical or horizontal ‘bars’ of data).
- Identifying any strong linear relationships between individual input/output factors.
    - Which in turn makes it possible identify potential ‘pairs of date that may combine to reduce the complexity of study (as discussed in section 2.2).
- Identify any data relationships that are obviously not normally distributed and may require transformation before successful incorporation into the multivariate method (as discussed in section 3.3.1 and 3.7.1).

As discussed in Chapter 3 (sections 3.3, 3.4, 3.6, 3.7 and 3.8), M-ANOVAR and ANOVA techniques are considered robust in dealing with non-normal data distributions, but awareness of the possible impact of this during data analysis is important and must be accounted for. The strongly correlated variables between temperature and the four output variables are a concern for simple ANOVAR analysis. M-ANOVAR techniques (sometimes known as ‘MAnCoVar’) are specifically designed to work with co-varying input-output variables is sets of data, and so this is unlikely to be significant using the data analysis presented.

The matrix plot presented in Figure 29, provides a visual examination of the histograms in the diagonal data displays, and provides an indication that non-normal and categoric data may be present in this data set. Examination of the comparative scatter charts in Figure 29, can be used to identify any strongly correlating sets of data. This set of simple scatter plots for each variable temporarily ignores the differences between individual GDL materials and, in the first instance, visually inspect the data for obvious and significant trends. During the experiment, the mean temperature (Tbar) and the maximum temperature (Tmax) would be expected to correlate strongly, but this was not hugely significant to the experiment as a whole, as the use of multivariate methods overcomes this covariance of input variables. In certain regions, there was a categoric effect that should be factored into all analysis of future results. For example, there was a clear categoric element to the choice of test equipment in the performance of experiments (FCCA 1 or FCCA 2). Cross referencing this to other factors, such as the peak power output (Wmax) and the gradient of the Ohmic region of the polarisation curve (gO); the data appears to be quite uniformly spread. As there was a great deal of information to be processed; computerised analysis was utilised. To aid in this, clearly categoric factors such as the structure, the presence of the MPL, and the identity of the suppliers were identified numerically (as shown in Table 12). It should be noted that a lack of samples in all categories has limited the degree to which E-Tek and Toray samples could be included in all fields.

- **Possible Categoric data in Figure 29:**
    - Relative humidity (RH).
    - PTFE wt% loading (PTFE).
    - Percentage porosity (%pores).
    - One of two possible FCCA units (FCCA).
    - Cell number on each of the 2 FCCA used in the experiment (Cell).
    - Microporous layer presence (MPL).
    - Dew point temperature (dewpntT).
- **Possibly non-normal data in Figure 29:**
    - Mean pressure during polarisation curve testing (Tbar).
    - Ambient Temperature (Tamb).
    - Maximum temperature during polarisation curve (Tmax).
    - Water contact angle (H_2O angle).
    - Measured gas pressure during the polarising curve (Pressure)
    - Gradient of the mass transport loss section of the polarisation curve (gM)
- **Strongly correlating pairs of factors in Figure 29:**
    - Tbar and Tmax.
    - All four output variables correlate with the others (gA, gO, gM, Wmax).

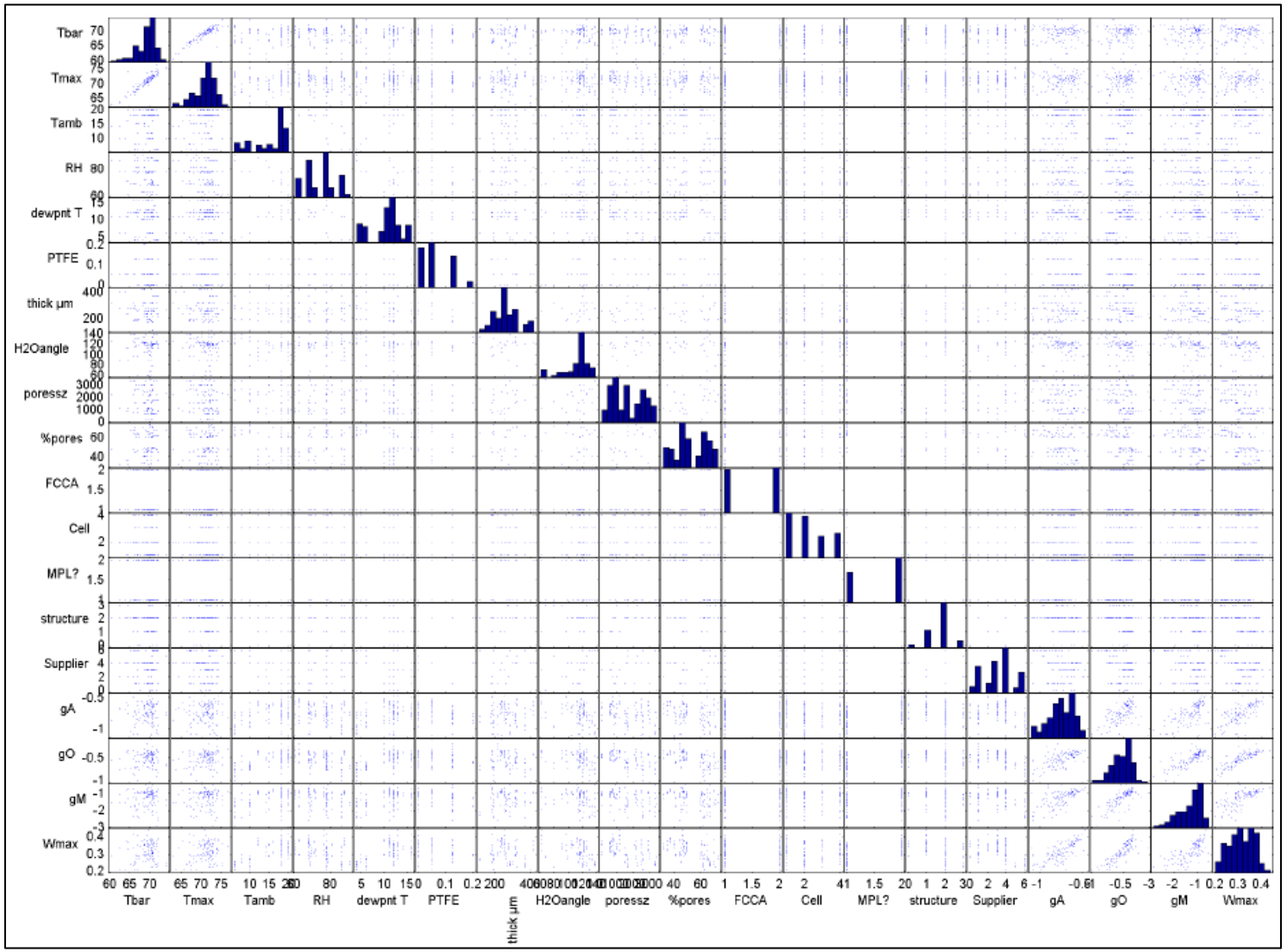

Figure 29: Matrix plot cathode GDL structure

4.4.1.Example results

Full printouts of all data points are available on request, and the base Matlab® code used to generate the following information is included in Appendix 3. Polarisation curves, with individually calculated gradients of the three regions of their curve, were calculated and plotted as shown in Figure 30 and Figure 31: The method used for this approach is explained in more detail in section 4.4.2.

Polarisation curves presented in Figure 30 and Figure 31, and similar images, show the polarisation curve in the top panel, with cell voltage and current density in Amps per centimetre square. Included in the top plot are the gradient of each region of the polarisation curve (activation, Ohmic and mass transfer loss). The lower panel shows the power output generated from the associated polarisation curve as per (4-13). Included on the lower of the two plots shown, are the peak power output of the fuel cell during the polarisation curve (the peak of the plotted curve), and the mean and maximum temperatures of the sample during the 250 seconds it takes complete a polarising curve measurement. This information is required to make a reasonable comparison between individual, or groups, of MEA polarisation curves.

$$Watts = Voltage * Amps \tag{4-13}$$

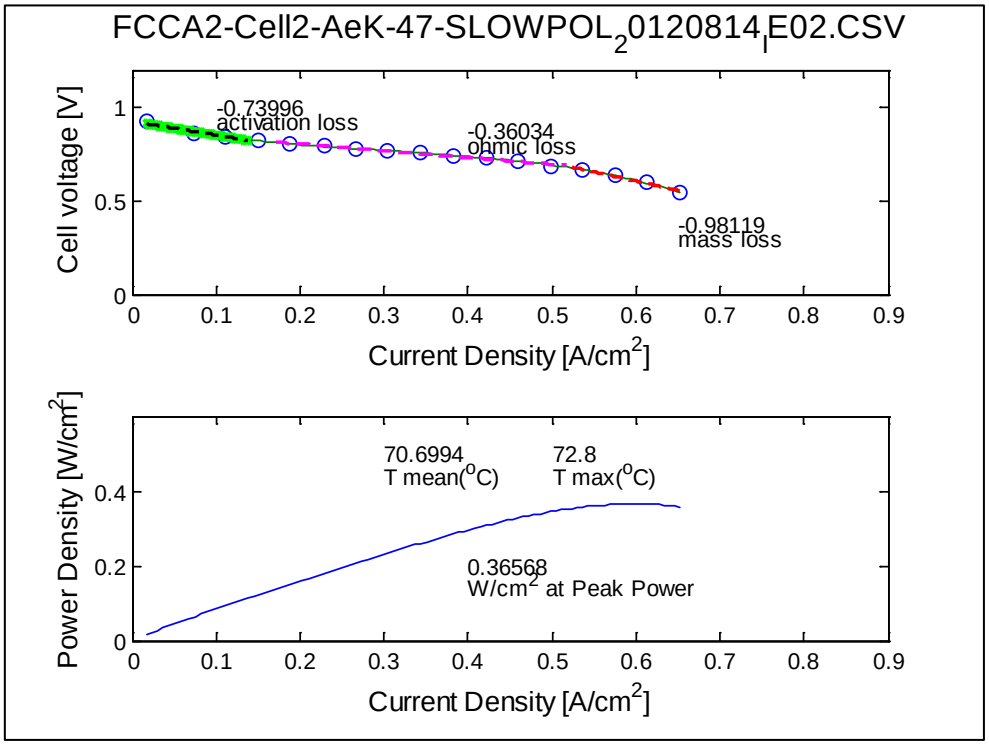

Figure 30: AeK ID 47 non-woven, no MPL

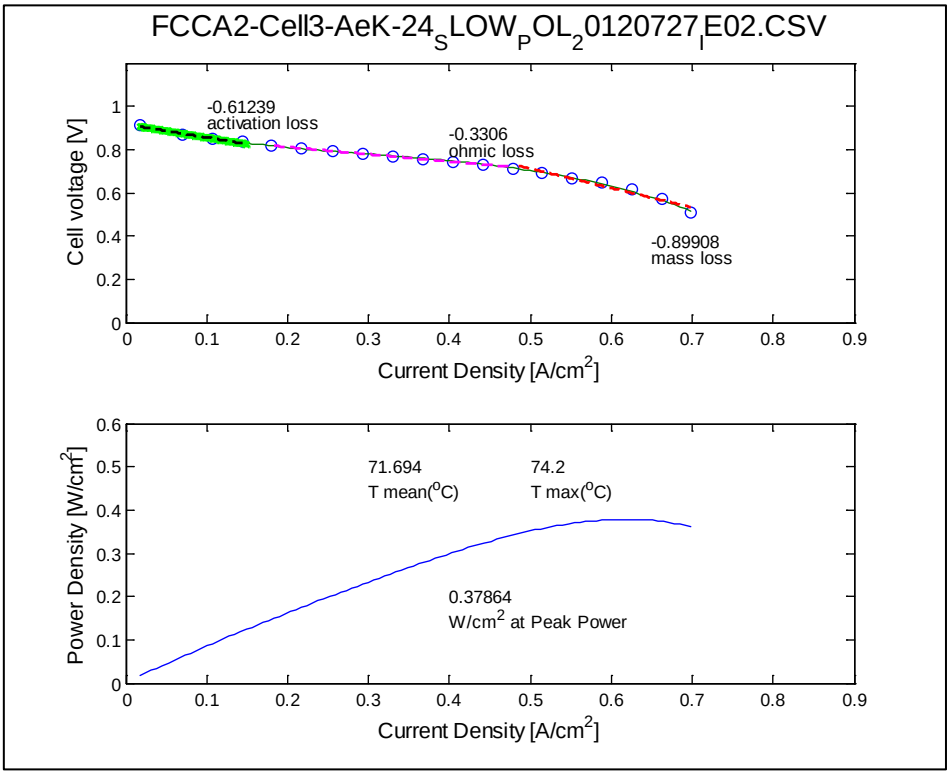

Figure 31: AeK ID 24, non-woven, with MPL

4.4.2. Regional assessment of polarisation curve gradients

The various areas of the polarisation curves have had an assessment of the gradient applied to them individually. Little specific guidance was uncovered in the initial literature review (Chapter 2), on how to make a rigorous comparison of polarisation curves across various samples. There is a long tradition of numeric analysis of polarisation curves in the fields of corrosion and metallurgy [97]. Enumerative comparison of polarisation curves and parameter estimates based on them are less common in fuel cells research, but can be found. Direct comparison of polarisation curves on experimental samples and numeric comparisons between samples and simulated values, has been reported and validated by several other authors [98-100].

Santerelli et al. (2006) [98] make specific use of the gradient of the polarisation curve as a comparator between fuel cells, and this analytical approach adopted in the experimental work reported in this thesis. Santerelli et al. (2006) [98] primarily used this approach to make a comparison between test samples and several numeric simulations, at various temperatures. Santerelli et al. (2006) [98] recommend the approach for high-temperature polarisations (above 50^{o}C); an excellent match for the work completed in this thesis.

Bezmmalinovic et al. (2015) [99], utilised polarisation curve comparison as a method of determining fuel cell degradation, and concluded that numeric comparisons of polarisation curves were a valid experimental technique. Al-Bagdhadadi et al. (2005) [100] recommend a similar approach when using simplified empirical models for reduced complexity "*...system models*"[100]. In this thesis, the technique was extended to several MEAs of different material construction, to make a direct comparison between them suitable for statistical analysis as outlined in Chapter 3.

To rapidly assess a large number of samples, it was felt that a more rigorous approach than visual observation would be needed, but there was not sufficient time available to conduct additional tests on the UoB samples, nor were there sufficient resources to manufacture duplicate test MEAs for additional tests in the future. With this in mind, it was decided to consider the gradient of each region of the curve, similar to the work carried out by previous authors [98-100].

With a well-recognised set of loss regions (activation, Ohmic and mass) [101] in the curve, it was hoped to increase understanding of the impact of cathode GDMs on fuel cell performance by comparing changes in the gradient and the total power output of the MEAs being tested. To that end, the gradient of each discrete region has been calculated separately. Figure 32 gives a graphical representation of the process followed by the software for each polarisation curve analysed. In each case, the gradient in question has been calculated by working from each end, towards the middle. The first measured point of the polarisation curve was assumed to be in the activation loss region of the curve.

An iterative sum of least squares approach (as discussed in Chapter 3), was then taken to determine the point where the gradient of the line changes the most. The length of this region keeps increasing until the fit of a straight line region drops below a certain threshold (the exact level of the goodness of fit can be set by the experimenter). Arguably the activation curve of these samples was far too 'flat'. It was clear that there are multiple effects in this region of the curve. The gradient analysis still required the assessment of the nominal 'activation region' to clearly define the start and end of the Ohmic loss region, for the next part of the analysis. Before calculating the Ohmic loss region, a similar stepwise, least squares curve assessment, was made for the mass transport region. Once again, the end of the data was selected, and the programme worked back along the data until the straight line fit of the various data points fell below the target threshold. The assumption was made that this represented the mass transport loss region of the curve. Having sequentially fit a straight line to each end of the curve, a region was defined as the mass loss section of the curve; another region was defined as the activation loss section. The remainder of the curve is, therefore, the Ohmic loss region to which a linear fit can be applied, and the gradient calculated. Additional data points were excluded from the Ohmic region gradient calculation, to ensure any transition between the regions was avoided.

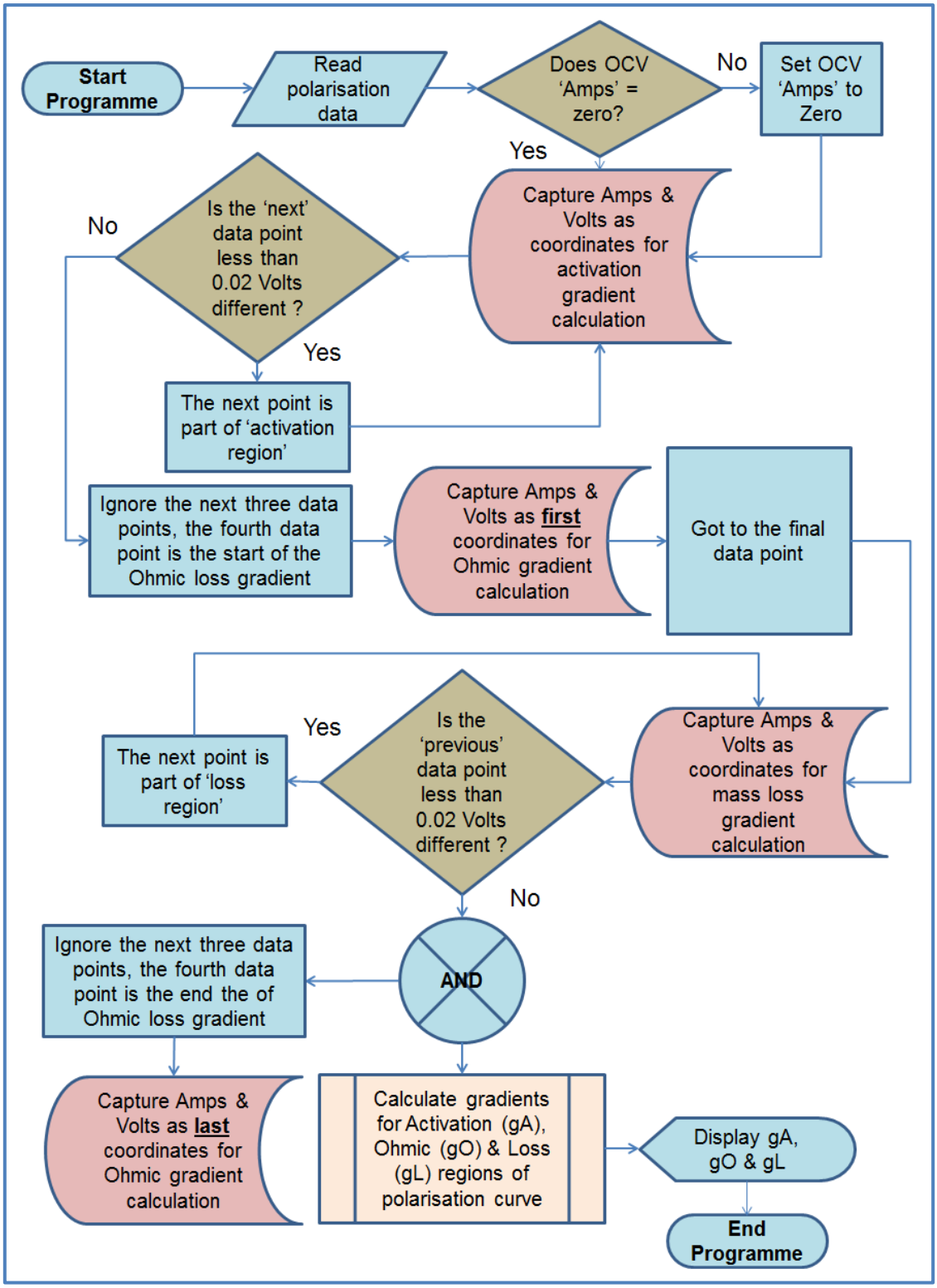

Figure 32: Process chart for 'gradient of regions' assessment of polarisation curves

Three separate best line fits were then labelled 'gA' for the activation region of the polarisation curve (green) 'gO' (pink) for the Ohmic region, and 'gM' (red) for the mass loss region, are shown in Figure 30 and Figure 31. Numeric values for the gradient of each section can now be captured and compared.

When comparing gradients between samples, it must be kept in mind that the gradient of two samples could be identical, while the actual values of the line measured can differ. For this reason, the data should always be considered in light of its corresponding 'peak power' (Wmax), where the Watts.cm^{-2} can provide a fixed and absolute comparison between separate MEAs.

The data gathered from the polarisation curves (examples of which are presented in Figure 30 and Figure 31) were then analysed as collective groups: Figure 33 through Figure 36 show 'box and whisker' plots for the various data sets available. In the box and whisker plots, the red line is the median data point. The lowest line on the basal 'whisker' represents the lowest value that is not estimated to be an outlier. Outliers are determined by the Matlab® 'boxplot' function as follows:

Set the initial condition of the whisker length (W_L)

$$w_L = 1.5 \tag{4-14}$$

If

$$x >> q3+w_L\,(q3-q1) \tag{4-15}$$

then x is an outlier.

If

$$x << q1-w_L\,(q3-q1) \tag{4-16}$$

then x is an outlier.

The 'box' section contains the middle 50% of all data points measured centred on the median value (i.e. all values in the 1st (q1) and 3rd (q3) quartile ranges) [83].

As discussed in Chapter 3, initial investigations of data should be undertaken before proceeding on to more detailed analysis. In this case, the spread of the data in each set was visually represented in Figure 33 through Figure 36. In examining each image, it should be borne in mind that the gradient values (gA, gO & gM) are showing the gradient of each region of the polarisation curve for that group of MEAs. The 'Wmax' on each figure, is a representation of the peak power output in Watts per cm square. As discussed in section 4.4.1, when discussing or comparing polarisation curves it is important to state the relative values of the system being analysed. For the images in Figure 33 through Figure 34 peak power is displayed to provide the context for the gradient values displayed.

In Figure 33, comparative polarisation curve gradients and the peak power, are shown for MEAs with non-woven, paper and woven cathode GDMs. The activation and Ohmic gradients are broadly

equivalent across each type of cathode, and therefore a suitable for comparison between the three cathode types.

In Figure 34, comparative polarisation curve gradients and the peak power, are shown for MEAs with various levels of hydrophobic coating (wt%PTFE) added to them. In this case, the 20wt% PTFE loaded cathode GDM group, has notably depressed gradients compared to the other categories (0%, 5% and 12.5wt% PTFE); but also shows a reduced range of values for the peak power output.

In Figure 35, comparative polarisation curve gradients and the peak power, are shown for MEAs with GDMs supplied by various manufacturers. It is clear to see that the variability of the mass transport gradient for GDMs supplied by Ballard and Toray, were far higher than those for the other samples.

In Figure 36, comparative peak power is shown for all key input variables. In the supplier section, there is a clear drop in the peak power output for supplier number five (Toho-Tenax).

Results on pore sizes are notably missing; especially when considering the relative importance of pore size distributions, pore shape, and the tortuosity of the pore network for the GDMs, and their impact on the effective diffusion rate through the material. As this data was not universally available for all samples, it cannot be included in this stage of the analysis. It should also be pointed out that the apparent reduction in the range of the response as the PTFE increases, was interesting. The increasing PTFE loading shows a distinct reduction in the median maximum power output, but also shows a reduction in the range of the data. This uniformity of response must be viewed with a little caution, though; the number of samples available at 20wt% loading of PTFE was only four individual samples, and all four were supplied by the same manufacturer (Sigracet). In this regard, the apparent reduction in range may simply be due to the use of a single batch from a single supplier. A similar issue needs to be considered for the results of supplier number five (Toho Tenax). Once again, only four samples were included by this manufacturer, an issue exacerbated by the limited number of types of GDM they supplied.

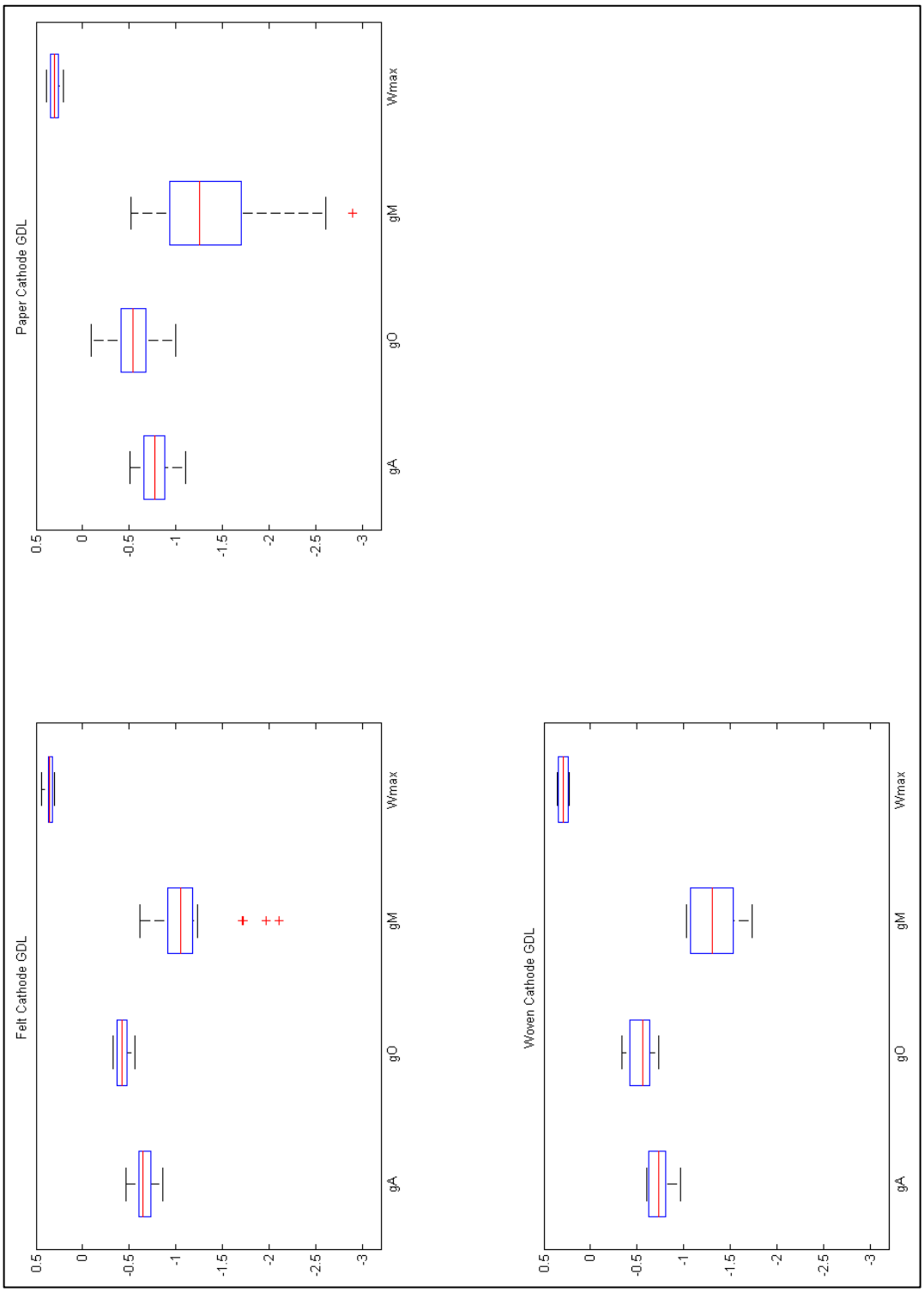

Figure 33: GDL cathode structure outputs

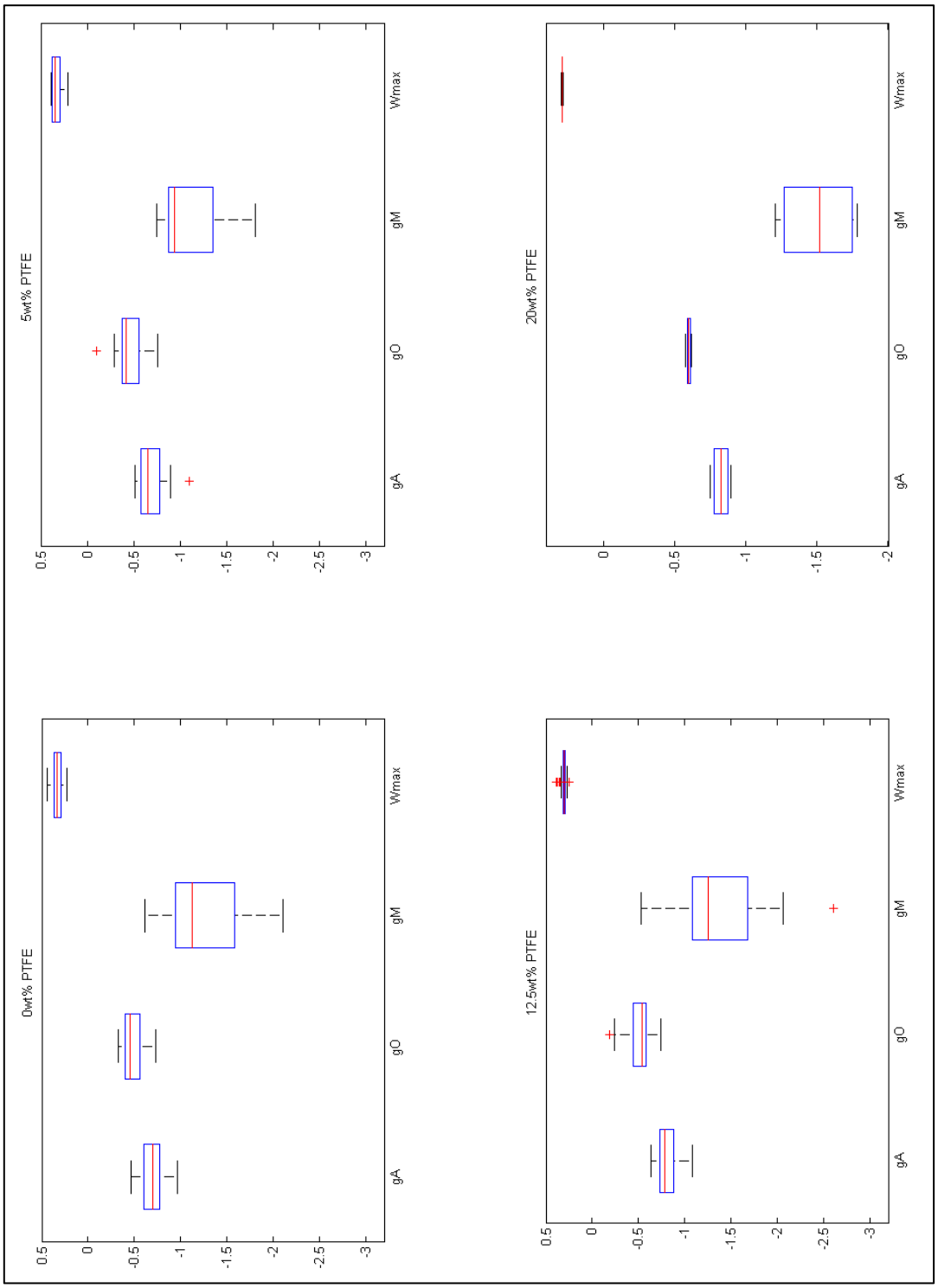

Figure 34: GDL cathode PTFE loading outputs

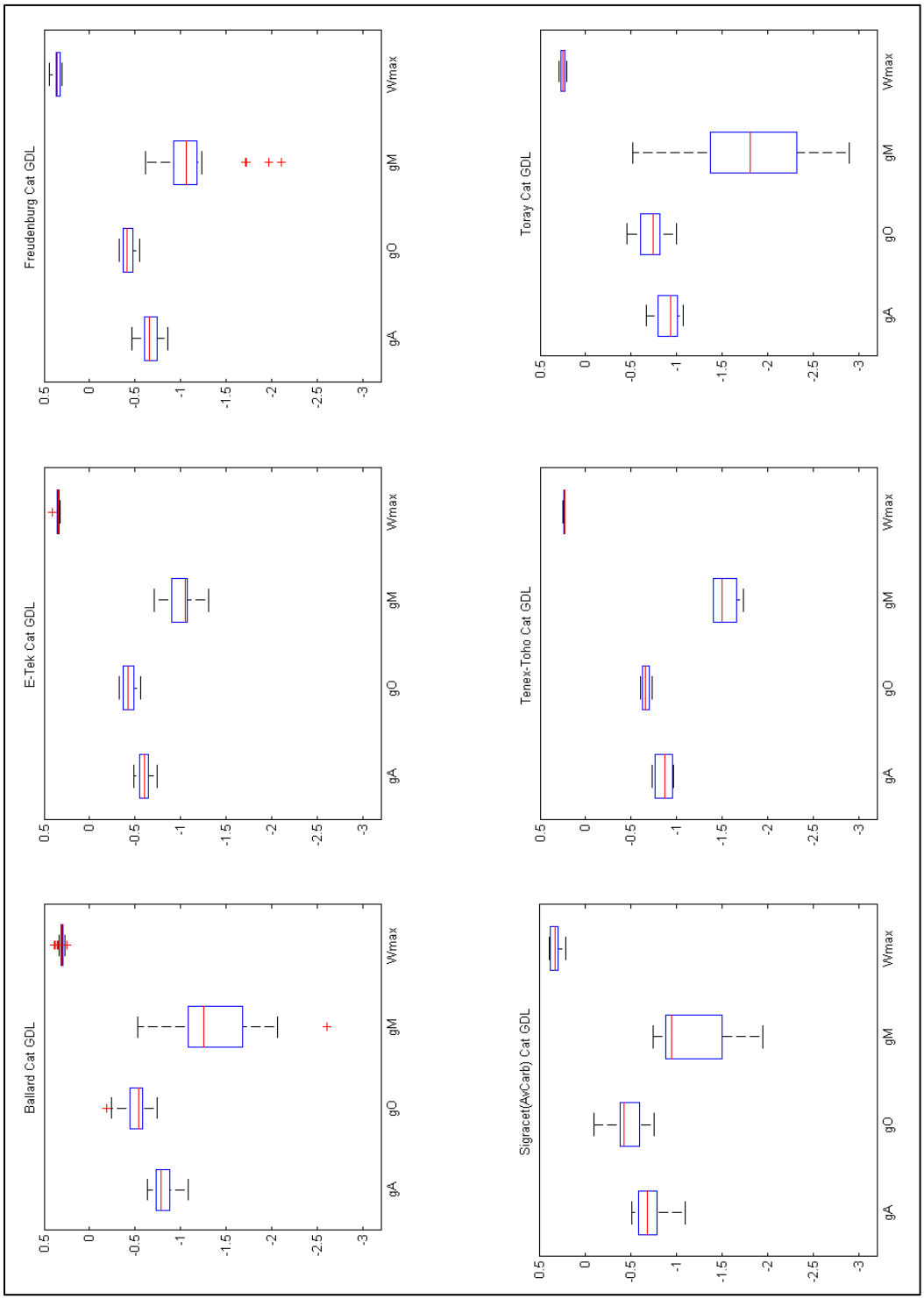

Figure 35: GDL cathode supplier outputs

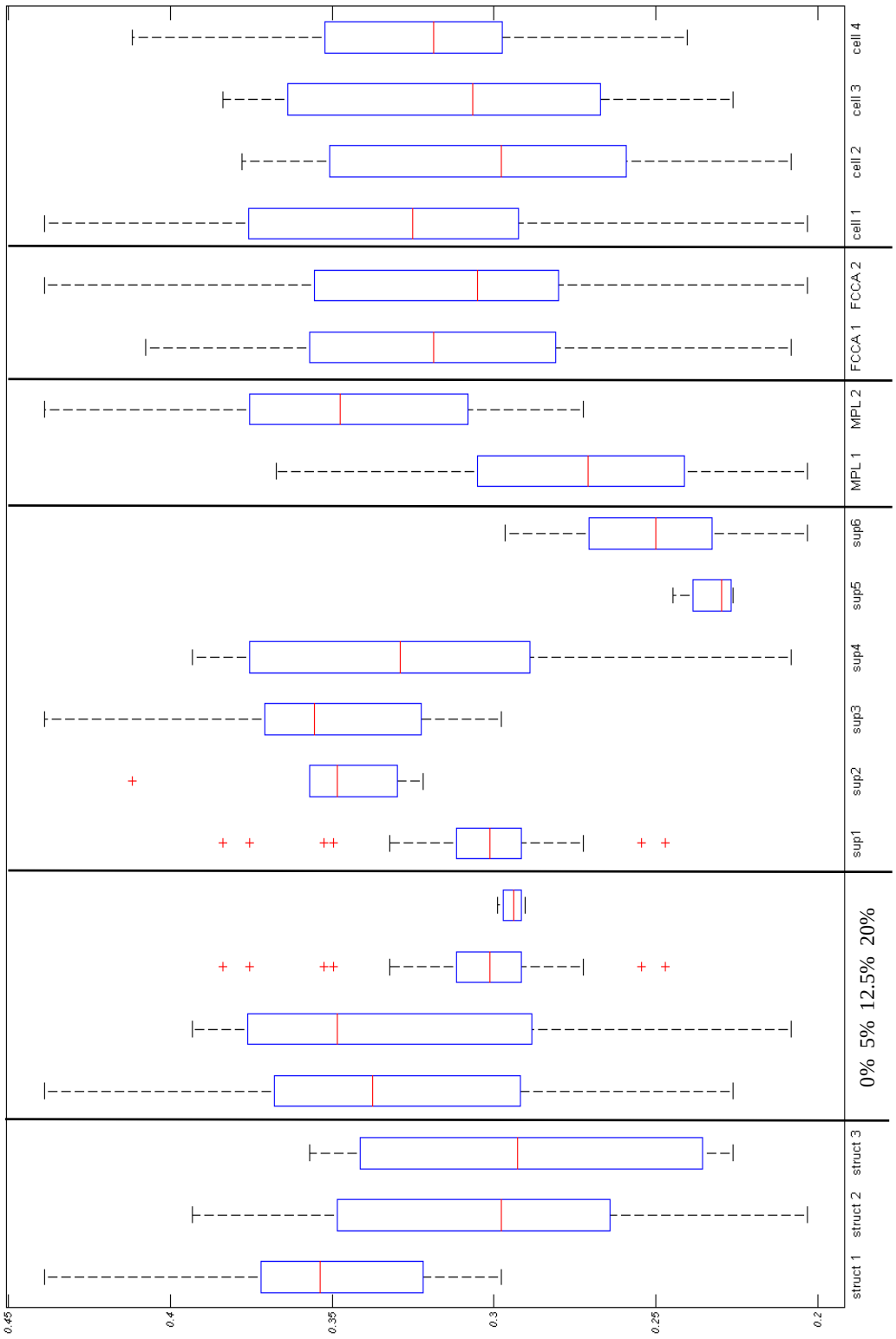

Figure 36: Peak power (Wmax) for all data by 'group'

4.5. Historic data DoE for loss regions and their gradient in cathode GDMs

A more sophisticated analysis of the data can be carried out by using the linear regressions techniques outlined earlier in Chapter 3. The software package Design Expert Pro has been used extensively, and the raw data has been collected from polarisation curves plotted in Matlab®. These two software packages greatly accelerate the time it would otherwise take to complete backwards step regression, and also automates the 'look up table' values for t and F test probability estimations, along with and several other labour intensive actions. All results have been checked for normality via Q-Q plots and were suitable for this type of analysis.

Conducting multiple covariance analysis, allows for the production of a model of the systems for the input variables available and searches for more complex interactions. It should be recalled when viewing this data, that the linear regression functions and the constants associated with them, are not necessarily indicative of physical processes, rather they are statistically derived values that give an indication of the inter-relationships of the input variables analysed.

The variance inflation factors (VIF) below indicates the degree of collinearity in the model factors. The square root of the VIF, is an indication of how much the standard error (deviation away from the 'true' mean) may vary, between sample groups of the same population. If the initial variance is very small, even multiplying it by the root of a very large VIF will still be a small number and so not significant but, as will become clear later in the work completed for this thesis, some of the VIF factors on the untreated data were very large.

That said, a VIF value above ten, indicates care should be taken with the model but does not invalidate it. There are methods available to manipulate the data to counteract the impact of multi-co-linearity in the results, but there is no universal agreement on their utility or application. There is a school of thought that removing the unacceptably high VIF valued factors is a superior approach if any action is needed. [81]

Design Summary											
File Version	8.0.7.1										
Study Type	Response Surface		Runs	126							
Design Type	Historical Data		Blocks	No Blocks							
Design Model	Quadratic		Build Time (ms)	4.23618							
Factor	Name	Units	Type	Subtype	Minimum	Maximum	Coded	Values	Mean	Std. Dev.	
A	Tbar	Deg C	Numeric	Continuous	60.36	73.96	-1.000=60.36	1.000=73.96	69.15	2.26	
B	Tmax	Deg C	Numeric	Continuous	62.90	76.60	-1.000=62.90	1.000=76.60	70.99	2.47	
C	Ambient Tbar	Deg C	Numeric	Continuous	6.00	20.00	-1.000=6.00	1.000=20.00	15.70	4.43	
D	Ambient RHbar	%	Numeric	Continuous	61.00	91.00	-1.000=61.00	1.000=91.00	74.69	8.00	
E	Amb' dew point T	Deg C	Numeric	Continuous	4.00	16.00	-1.000=4.00	1.000=16.00	10.79	3.32	
F	PTFE	wt%	Numeric	Continuous	0.00	0.20	-1.000=0.00	1.000=20.00	0.06	0.06	
G	Thickness	µm	Numeric	Continuous	170.00	420.00	-1.000=110.00	1.000=420.00	262.39	68.93	
H	H2O contact angle	degrees	Numeric	Continuous	61.00	134.00	-1.000=61.00	1.000=138.00	113.28	18.01	
J	Mean Pore sze	um	Numeric	Continuous	158.00	3401.00	-1.000=158.00	1.000=3401.00	1697.83	940.04	
K	Porosity	%	Numeric	Continuous	34.60	73.00	-1.000=31.80	1.000=73.00	52.77	11.94	
L	FCCA		Categoric	Nominal	1	2			Levels: 1 or 2	2.00	
M	Cell		Categoric	Nominal	1	4			Levels: 1, 2, 3, or 4	4.00	
N	MPL		Categoric	Nominal	No	Yes			Levels: Y or N	2.00	
O	structure		Categoric	Nominal	woven	felt			Levels: Non-woven, paper or Woven	3.00	
P	Supplier		Categoric	Nominal	Sigracet	Freudenberg			Levels:B, E, F,S, TT, TO	4.00	
Response	Name	Units	Obs	Analysis	Minimum	Maximum	Mean	Std. Dev.	Ratio	Transformation?	Model
R1	gA		72.00	Polynomial	-1.10	-0.40	-0.73	0.14	2.75	None	R2FI
R2	gO		72.00	Polynomial	-1.71	-0.10	-0.49	0.20	17.65	None	RLinear
R3	gM		72.00	Polynomial	-0.74	-0.10	-0.48	0.13	7.67	None	RQuadratic
R4	Wmax	W	72.00	Polynomial	0.23	0.44	0.32	0.05	1.94	None	RQuadratic

Table 13: Historic data DoE equivalent

Utilising data gathered when assisting the researchers at the University of Birmingham (UoB) with their work, their published results [15,16] and the results they, in turn, have cited from other sources (e.g. manufacturers data), it was now possible to develop an historic data analysis approach to the information at hand. This analysis of pre-existing data, can be thought of as applying a DoE approach to a collection of results, usually from several different authors, after the data has been accumulated. While not an ideal approach to DoE as, by definition, this fails to minimise the number of experiments to gain an answer to the questions: It does, however, make it possible to analyse the published data from other sources and compare it with the experimental inputs, to generate a set of results. Recall that in this case, all polarisation curve results were measured Loughborough University using the FCCA as described previously in section 4.3.2. The 'designed experiments' retroactively created to suit the historic data, are presented here in Table 13.

The result for each gradient (for each 'loss region' of the polarisation curve) and the peak power output, can now be presented. There were 128 separate samples to analyse as requested by the UoB. Not all categories were well represented, and additional materials were added to the data set. Unfortunately, laboratory measured (or well referenced) data could only be provided for a portion of all samples; 76 samples were finally included in this assessment (see Appendix 3). These initial results were the 'backwards optimised' (to generate reduced complexity) M-ANOVA results, as generated by the software. Note that the value 'standard error', is both the deviation away from the 'true' mean of the entire population, and it is at the same time the standard deviation of this data set. The upper and lower bounds indicate where the true mean of the population must lie, with a 95% confidence level. The following results were adapted from the data outputs of the Design Expert Pro software. As is good practice in any statistical analysis, the experimental model was developed iteratively. The first iteration is presented in Annexe 3, and only brief summation of the software outputs is presented in this section.

4.5.1. Activation loss gradient multivariate analysis

It should be noted at this point, that the Q-Q plot for this data deviates away from the preferred line, as can be seen Figure 37. However, the removal of a single outlier data point - Sample ID #30, a Freudenberg non-woven with MPL - corrected this issue. With this in mind, the outlier was included back in the model as its leverage on the overall result was not significant.

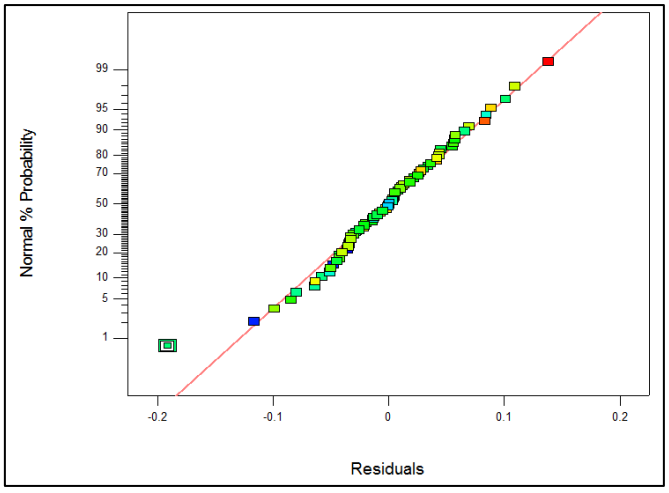

Figure 37: Q-Q plot activation gradient (Ω.cm^2)

4.5.2. Discussion of gA

Certain terms such as 'M = test cell number' are apparatus specific. This information is included, as it helps to quantify the degree of variability caused by the test equipment, the ambient temperature (factor C) interacts quite strongly with several factors. The most significant of which is the porosity (factor K), with a p-value of 0.0025. However, it is not immediately obvious that the interaction between the two was a genuine effect. The ambient temperature should have very little impact on the test MEA itself. It was considered advisable to consider which factors were interacting with the ambient temperature. The interaction between T-bar (factor A) and the average temperature of the Fuel cell during testing and the individual cell conducting the test (factor M) was also a strong one (p-value of 0.005). Once again, there was a temperature and hardware interaction.

Applying knowledge of fuel cell systems; the temperature conditions, both ambient and due to the fuel cell heating, are having an impact on the cell. Combining that knowledge with the interaction with the porosity of the cathode GDM; the most likely explanation is that the clamping forces being experienced were varying, as a result of differential thermal expansion across the material that makes up the fuel cell assembly [24,87,95]. This additional clamping force, results in a change in the degree of 'closing off' of pores in the GDM. Activation losses and mass transport losses are both heavily impacted by pore structure as, by definition, they are reliant on the availability of reactant gas at the catalyst surfaces. However there is a weakness to this argument, in that the clamping pressures experienced in the test apparatus were well within the working range of all GDM and the readings taken; have all been conducted in the 'steady state'.

All test chambers have had the best part of an eight-hour day to reach a stable state, as a result of the conditioning process, before the final polarising curve was taken. The possibility must be considered

that this is a 'balance of plant' issue. The mass flow controllers and other ancillary components that make up the individual test channels on each FCCA, may be out of calibration and so have an exaggerated impact on the results, depending on the ambient conditions in the laboratory. The two possibilities, mass transport loss and balance of plant effects, are not mutually exclusive. It was interesting to note that PTFE content of the fibrous structure of the GDM was registered as 'not significant' (p= 0.1195). This lack of significance was in direct conflict with the literature on the topic [19,49,102-111]. It is suggested that the activation region of the polarisation curve simply does not generate enough water for PTFE content to be of benefit to the system [19,49,102-111].

4.5.3. Ohmic loss gradient multivariate analysis

The Ohmic loss gradient was analysed for co-varying factors in a backwards step, linear regression model. There was a slight 'S' curvature to the data, indicating a slightly flatter distribution: however, the Q-Q plot still passes the 'pencil test', as described in Chapter 3, where all data points can be covered a single 'pencil' width.

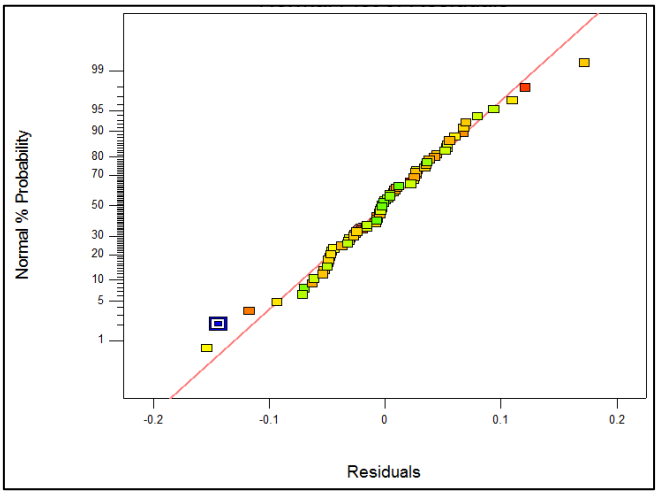

Figure 38: Q-Q plot Ohmic gradient ($\Omega.cm^2$)

4.5.4. Discussion of gO

The reduced order model for the Ohmic loss gradient was identified as the preferred output of the three gradient regions. The rank of significance for the key, lowest p-value, factors changed as the model order was reduced with backwards eliminaiton. A p-value >F probability of 0.00001 (see Table 21) for the PTFE content of the GDM was detected; and identified as the most significant factor in the gO model, which is in keeping with the existing literature as discussed previously (see Chapter2 and section 4.5.2). The p-value>F probability relationship has been discussed in depth in

Chapter 3 (notably in sections 3.3, 3.6 and 3.6.1) and the value generated indicates it is highly unlikely that the null hypothesis (i.e. h_0 = "PTFE connect is not significant") is correct. For the first time significance in the structure (woven, paper or non-woven) in the gradient of the Ohmic loss region is registered. There were no multi-factor effects evidenced by the model, and the significance of test cell or test machine, is to be expected in a region dominated by contact losses and clamping pressures. These results somewhat contradict the previous inference that ambient temperature plays an interactive role on the clamping forces experienced by the system. However, it may be that the resistances across the various test cells (of the eight possible locations) overwhelm any such effect. The pore structure also factors into the Ohmic loss. At first consideration, this may be a little counter-intuitive. However, consider the porosity value (entered as a percentage presence of pores) as an estimate of the solidity, or density, of the system. With higher porosity increasing the gradient of the Ohmic loss region; as there is less material and therefore fewer conductive pathways. For non-wovens, there was a negative gradient modifier generated by the model, whereby the Ohmic loss gradients were further reduced to creat a single statisitcal modle that can include all three GDM types.

Table 14: Numeric designation of GDM structures

Factor	Factor categorical numeric value	Factor modifier
Non-woven	1	-0.13
Paper	2	0.12
Woven	3	0

The requirement for separate numeric values to model the three types of GDM the first key instance in this thesis where it can be categorically stated that there is a quantifiable need for the 'third category' of 'Non-Woven' felt like materials. The evidence is certain (at the 5% level of significance) that the Ohmic losses were reduced for non-woven like material compared to any other carbon fibre based fabric system. Table 14 shows the numeric values assigned to the reduced complexity model developed (see section 4.8.2). Recall that in the automated software calculations, the actual numeric value attributed to the non-wovens (as a first entry data point) will be -1. So the actual impact on the gradient is 0.13: the Ohmic loss region will be less steep for non-woven materials (when taken in isolation from all other possible factors). The software, assigned the exact value required to reduce the sum of squares of the residuals between the actual data points and the predicted data points created by the model. Recall that many factors were included in the final model (see section 4.8.2), and an iterative adjustment of all factors in the model was undertaken by the software: The model value with the lowest error (the lowest sum of squares of the residuals) was presented as the final model. This process was originally introduced in Chapter 3 (most notably in section 3.2).

Interpretation of this was intuitively simple, the planar nature of paper means that through-thickness conductivity of the paper GDM is reduced. The three-dimensional nature of the woven structure facilitates the through-plane conductivity for the system, and the excellent performance of the non-woven (felt like) materials, was somewhat more surprising. A degree of improvement is perhaps expected, but the bettering the performance of the woven materials in this factor, was not.

Non-woven like materials have a number of fibres that penetrate the fabric in the z-direction (i.e. through the plane of the fabric). The exact number of these fibres is limited, and their primary purpose is to improve the structural integrity and stiffness of the non-woven like materials. In this case, it is suggested that the z-direction, though-thickness, fibres are acting as direct electrical conductors from side to side of the GDL; reducing the overall resistance of the MEA. There has been some work completed on a variety of gas diffusion media and assessment of their through plain conductivity [112] to support this suggestion. A systematic analysis of the different types of carbon fibre materials categorised as either paper, woven or non-woven (felt like) GDMs, has been missing from the literature until quite recently [16,24,55]. More information on this topic is coming to light as the modelling community develops more detailed modelling methods and validates them with high energy GDM characterisation techniques [101]. Interpretation of the initial linear regression model developed, is aided by plotting the results as a visual representation. This has been done for Ohmic gradient loss initial value models and is presented in Appendix 3. With more than three factors in the model it is not possible to visualise all vertices at once, but a Porosity, Mean temperature during polarising curve (T-bar), and gradient of the Ohmic loss region (gO) is useful. Analysis of these initial models indicates the lowest possible gradient in this case. This is the most desirable case as the Ohmic region is the area of preferred operation for the vast majority of fuel cell operations. Such Low gradients can be achieved by selecting a paper GDM with a lower porosity, with the non-woven (felt) geometry GDMs performing second best, closely followed by the woven materials.

There was a through-plane thickness and porosity interrelationship, which demonstrates a degree of more complex interaction, with the somewhat surprising finding that minimum porosity is preferable when coupled with very thin GDMs. It is possible that this is, in fact, a reflection on the gasket configuration of the test cell. A reduced complexity modelling step is required before firm conclusions can be drawn, however. While a variety of different thicknesses of GDM were tested, the gasket dimension remains unchanged, and so, for certain thicknesses of the GDM, the compression of the system may be sub-optimal. It is possible that this thickness factor could be removed by optimising the gasket geometry for each GDM. Lin et al. (2010) [58] make a point of limiting their paper selection to a single narrow size range to avoid any such effect. If this interpretation were correct, the optimum Ohmic gradient response would be expected to occur at a single thickness setting at all porosities. In this case, it was clear that the optimum performance at various porosities co-varies with thickness, reducing the likelihood that the lack of optimisation of the sealing gasket

height is the cause of this effect. A literature search on this topic revealed no pre-existing discussions of this effect, indeed the closest like to the topic that could be found [113] was focused on a novel geometry GDM that is not suited to this result. Millichap et al. (2015) [114] state that the primary impact of incorrect gasket geometries will be observed as accelerated degradation effects, and makes no mention of the thickness-porosity-performance relationship detected.

Based on the information available here, and assuming the gasket geometry was not a factor; the through-plane thickness and porosity interaction were present in all cases. Once again on this first iteration model, the paper structure provides the optimum Ohmic Loss region gradient (gO) and the non-woven (felt) structures slightly beating the performance of the woven materials. It is worth stressing once again that this three-factor interaction would be difficult, if not impossible, to detect in the traditional OFAT (one factor at a time) methods of data assessment.

4.5.5. Mass loss gradient multivariate analysis

The mass loss gradient was analysed for co-varying factors in a backwards step linear regression model.

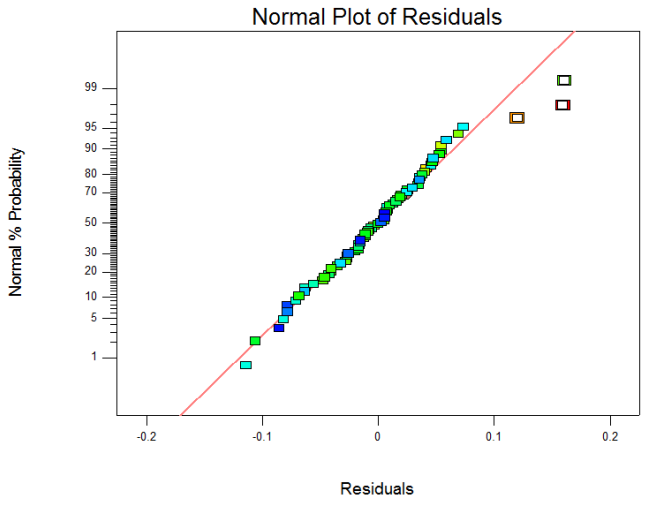

Figure 39: Q-Q plot mass loss gradient ($\Omega.cm^2$)

Figure 39, shows the Q-Q plot for the mass loss gradient. It was clear to see there is a deviation from a straight line in the plot, one that is too extreme to pass the 'pencil' test. The top three data points in Figure 39 do not follow the same distribution as the rest of the data. It is likely that this was caused by a lack of penetration into the mass loss region of the polarisation curve. Recall that the same polarisation regime has been carried out on all test samples, regardless of individual performance. In some cases (see Figure 30 and Figure 31), the polarisation curve has only just begun to 'turn over' into the mass loss region and the true mass loss gradient may not be being detected. The three outliers in Figure 39 could be excluded from the mass loss gradient estimate (gM), but then an argument would have to be made to justify the continued inclusion of the same data points in the previous work.

In this instance, the data for the gM is presented in this thesis for the sake of completeness, with the understanding that the data set presented may not be well suited to this type of analysis.

4.5.6.Discussion of gM

The VIF factor was very high on several of the examined factors. The root VIF figure indicates that the standard error on each figure is much larger than it should be, as a result of the co-linearity of the various factors. As discussed earlier, if the original modifying value for a given variable is small, this is not an issue. In this instance, there were a variety of aliased terms. The model cannot accurately differentiate between the ambient dew point on the day of testing, the supplier, and the interactions between them.

Backwards elimination of the data made no difference to the ranking of the various factors, and so once again this has been left out in this iteration of the model. Applying knowledge of fuel cell systems, it becomes possible to navigate this model and assess its utility or otherwise. The impact of pore closure through heat cycling has already been discussed, as has the possibility of balance of plant effects impacting the results (see sections 4.5.2. and 4.5.4).

The ambient relative humidity had an impact on the final mass transport gradient. As the reactant gas streams for both anode and cathode are fully dehumidified before entering the reaction chambers, it was concluded the machine effects observed were balance of plant issues. M-ANOVAR analysis has the ability to quantify the effects of this and overcome any minor variations between individual samples (as discussed previously in section 3 and 3.7 specifically). The issue of the lack of fit to the Q-Q ‘pencil test’ as discussed in 4.5.5 must cast some doubt on any results or conclusion based on this part of the model.

4.5.7.Maximum power multivariate analysis

The peak power was analysed for co-varying factors in a backwards step linear regression model. Initial findings and conclusions for Wmax are now considered.

Figure 40, shows the Q-Q plot for the peak power model. There was a minor degree of ‘s’ curvature indicating a broadening of the distribution curve. In this case, the data is broadly falling in line and passes the ‘pencil test. The data is well suited to M-ANOVAR type analysis.

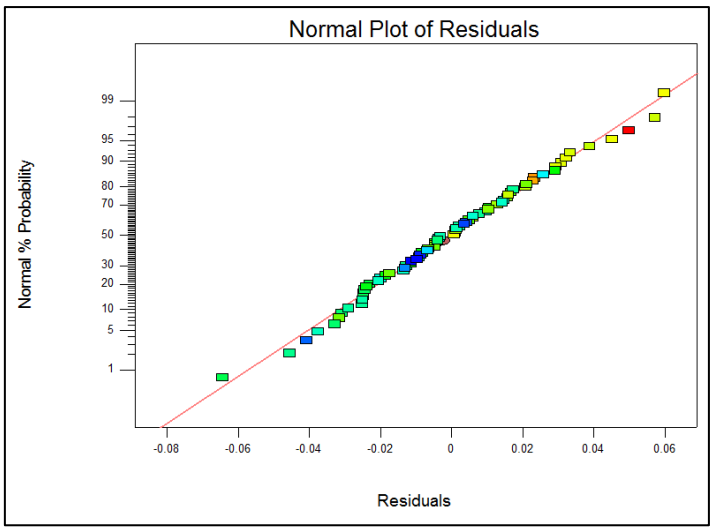

Figure 40: Q-Q plot peak power (w/cm^2)

4.5.8. Wmax Discussion

As stated for the previous models, the VIF factor is an issue to be considered, but the model is still valuable. The balance of plant issues identified previously, remain a factor when comparing individual MEAs tested across various test chambers of both machines, as discussed in previous sections. A slight impact from hydrophobicity input factor was detected and is considered in more depth in this section.

In Figure 41, the initial M-ANOVAR model for non-woven ('felt') GDMs is presented as a response surface graphic (see Chapter 3 for more information on this topic). In this representation, the model has been plotted across the range of all input data points in the experiments conducted, and the resulting power output has been plotted as a response surface. It is not possible to visualise all factors simultaneously. Therefore, the input values for mean temperatures during the polarisation curve and the volume percentage of porosity, are presented along with their impact on peak power (W.cm^{-2}). The top image shows the lowest water contact angle (hydrophilic, achieved with lower PTFE content fibres of the GDM) and the bottom image shows the higher water contact angle (hydrophobic, achieved with a higher PTFE content in the fibres of the GDM).

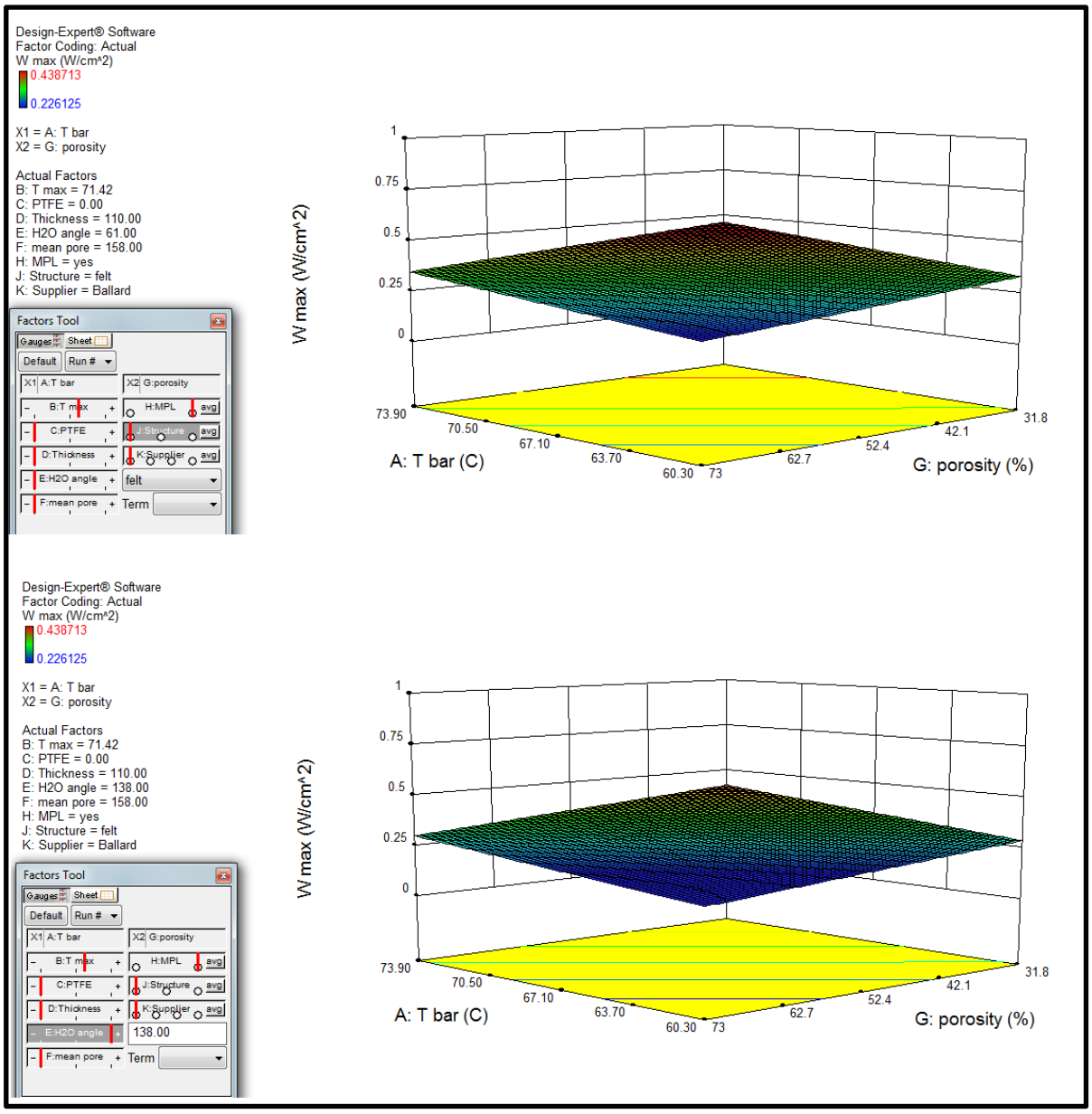

Figure 41: Wmax, temperature, porosity interactions: Felt

(Low (top) and high (bottom) θ felt GDMs)

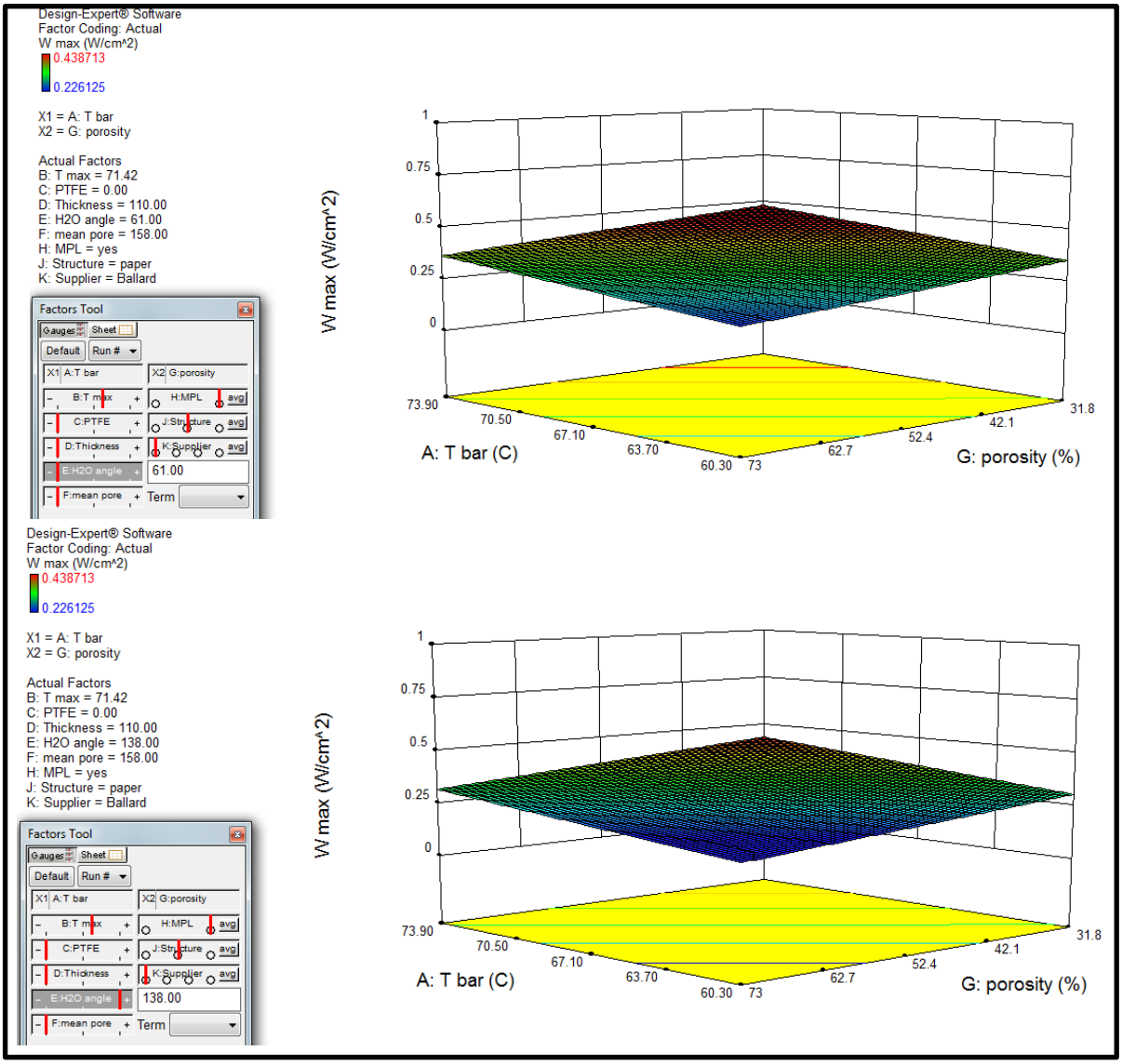

Figure 42: Wmax, temperature, porosity interactions: Paper

(low (top) and high (bottom) θ paper GDMs)

In Figure 42, the initial M-ANOVAR response surface for the model is shown for paper GDMs. Once again hydrophilic results are the top surface plot, hydrophobic results are on the bottom.

In Figure 43, the initial M-ANOVAR response surface for the model is shown for woven GDMs. Once again hydrophilic results are the top surface plot, hydrophobic results are on the bottom.

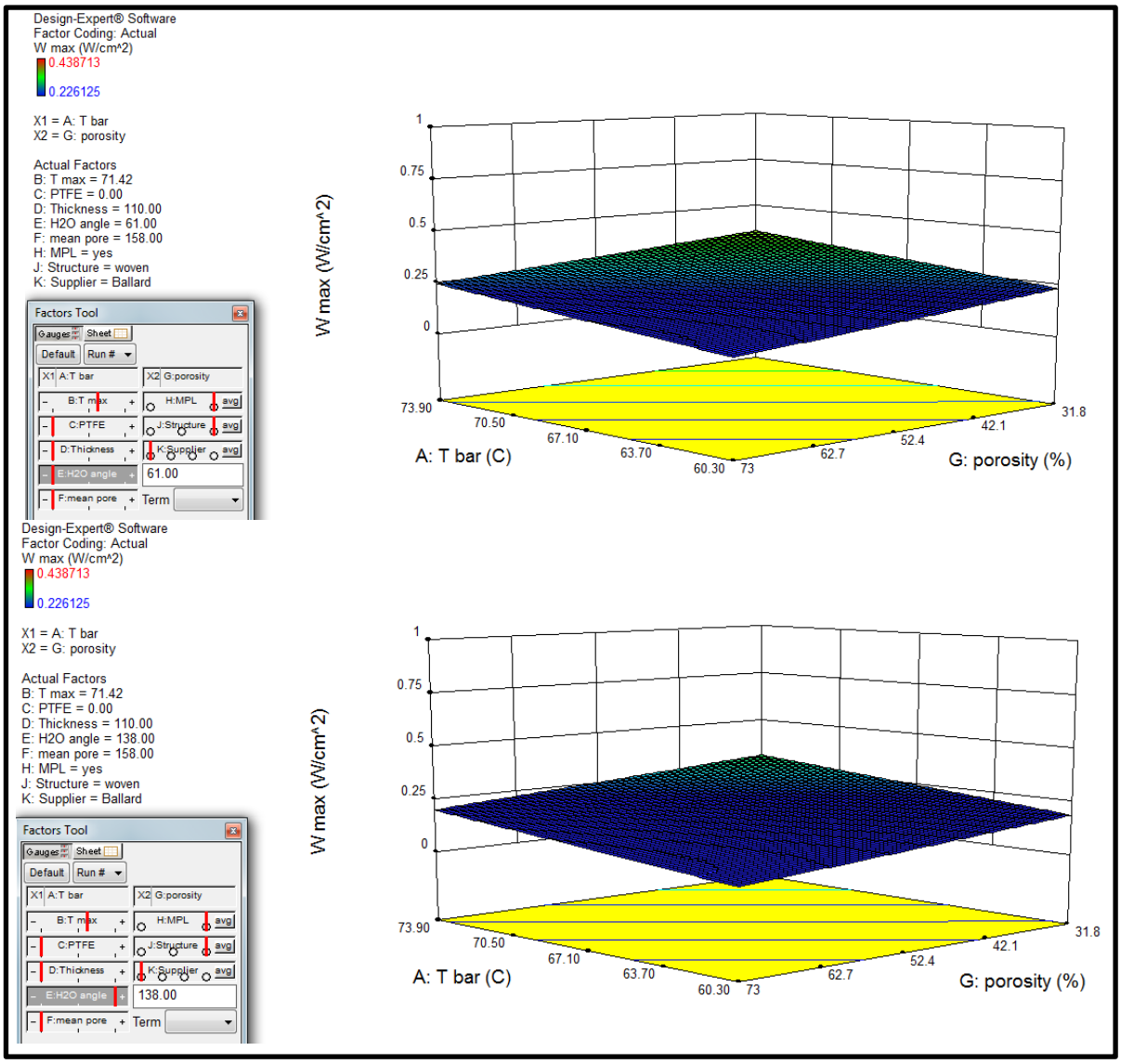

Figure 43: Wmax, temperature, porosity interactions: Woven

(low (top) and high (bottom) θ woven GDMs)

In Figure 41, Figure 42 and Figure 43, it is possible to visualise the outputs from the statistical model and begin to make an analysis of the behaviour of the materials studied. Examining Figure 41, Figure 42 and Figure 43, it was clear that there is a relationship between temperature and porosity that was having an impact on the final power output of the fuel cell. The gains in maximum possible power output, in Watts.cm^{-2}, were modest but statistically significant. In this case, all three classes of materials perform in a broadly similar fashion, with a temperature of operation obviously dominating power output. It can be seen that non-woven (felt) and paper materials were very close in maximum performance (0.439 w/cm^2), with the paper GDM, having a fractionally higher power output.

The woven materials once again fail to provide the maximum performance (~0.400 w/cm^2). All three systems show a hydrophobicity improvement, with low contact angle materials ($\theta = 61^O$), offering improved performance across all porosity and temperature setting in the design space; indicative of

improved water removal. In the materials tested, the maximum PTFE addition was in the order of 20wt% (before the application of catalyst layer inks). It is this value of PTFE loading, with MPL, which equates to the 61^{O} value of water contact angle (θ). It is clear in all three images, but particularly in Figure 41 and Figure 42, that peak power was achieved over a broader range of input settings (in this case porosity and temperature); indicating that the addition of increased hydrophobicity was of benefit across a wider range of porosities.

This increased hydrophobicity corresponds to the range of values for PTFE hydrophobicity treatments most often discussed in the literature [20,45,110,115]. As all GDMs were commercial 'off the shelf' products, no excessively high PTFE loadings (i.e. beyond 30wt% loading) were tested. This method would be ideally suited to identifying the optimum loading for various types of GDMs in the future.

In light of the above, it could be considered that the 'balance of plant' errors are, in fact, an unrelated experimental noise value. The probability of the test apparatus selection being significant was low, however, as the models all have a very high confidence and the data analysis methods selected were specifically designed to detect, and quantify, exactly this kind of test apparatus induced error effect [29,30,35,78-83]. This topic is also discussed further in section 4.7; which shows that the overall impact of machine variability (i.e. the difference between test samples analysed in FCCA 1 and FCCA 2) was a relatively minor contribution to the measured effect. It is likely that the PTFE effect is real, as peak power occurs in the transition region between Ohmic and mass transport loss [24,87]. The water management within the GDL will be at its most critical stage as product water will be produced at ever increasing rates, and in turn saturating the available pores [24,87,95]. It was interesting to note that the relative changes between structures were minimal (see Figure 41, Figure 42 and Figure 43) and that the woven structures perform least well of the three. Typically in the literature, it would be thought that high water content operations were best suited to woven materials [21]. Thus high demand, peak power operation and the consequent increase in water saturation within the cell, would benefit from the reduced tortuosity of woven cloth. Paper GDMs are considered best suited to lower humidity operations, due to the increased path length through the GDM [21], caused by stratification of the fibres in the paper manufacturing process for GDM creation. These findings directly contradict that perception (within the bounds of the space modelled). It is possible that the lack of pre-heating and humidity control on the FCCA test apparatus was a factor in the reduced performance measured for woven materials. Test apparatus that do not pre-treat inlet gases in this way have been shown to have reduced performance, as a result of sub-optimal moisture control [116]. It is, therefore, possible that the degree of flooding in the MEA has not been severe enough or prolonged enough to demonstrate any 'added benefit' usually attributed to the use of a woven GDM [19-21]. In which case these results force us to conclude that woven GDMs are best used in pre-humidified or very high power density (and therefore excessively water generating) PEM FC systems. In PEM FC that do not

operate under such high humidity conditions Paper or Felt GDMs are preferable, based on these results (see Figure 41, Figure 42 and Figure 43).

4.6. Historic data analysis of multiple covariant factors initial findings

It was clear to see that there was a small but measurable test apparatus impact on the final measurements, with both the choice of FCCA, and the individual cell on each FCCA, having a bearing on the gradient of the polarisation curve and the final peak power output. Interestingly the backwards step regression analysis (as discussed in Chapter 3, section 3.6 and section 3.7) for the Ohmic gradient, strips out the test apparatus contribution as not significant. The absolute value attributed to the impact of the cells and the FCCA unit was inflated somewhat by the numeric encoding used for each machine. i.e., cell '1', '2' or '3' have numeric values of -1, 0 or +1 assigned to them, the FCCAs were either 0 for FCCA1 or 1 for FCCA2 in the data matrix constructed by the software. Care should be taken before placing too much emphasis on this source of error. The test apparatus factors re-appear in the backwards regression analysis of the mass transport loss gradient. When making comparisons between individual test cells and identical MEAs under different test conditions, it would be wise to factor in this machine variation, but the overall impact of these factors is relatively small compared to other input variables in the work completed for this thesis. When considering structurally different MEAs where factors such as pore size, PTFE loading and thickness seem to dominate, these machine induced errors can be safely discounted.

The automated backwards regression has, in several cases, failed to remove insignificant terms and further model refinement was required 'by hand'. The models produced are robust and valid (see Table 16 through Table 33) with the model values in all cases. The p-value>F probability value in each case, is displayed as zero to six significant figures for the four modelled output variables (gradients for the activation, Ohmic and mass transport loss regions of polarisation as well as the maximum power output). The design expert pro software is limited to an accuracy of 0.01 in the p-value>F measurement [82,85], and so, at first glance, would seem fair to say in each case the model has CI of (100-0.01) at least 99.99%. Based on this evidence, the gradient of the polarising curve regions was a valid approach to take, and worth pursuing further to optimise the models. Even considering the multiple outputs from a single data set (gA, gO, gM and Wmax) the likely probability of the model being valid is well in excess of 95%. As discussed in section 3.6.2, when considering multiple inputs; the Bonferroni 'rule of thumb' should be applied to more closely estimate the true CI. In this case, it is essential to perform the same calculation for all of the models created from this dataset: with the decrease in CI doubling for each output factor being modelled i.e. gA, gO, gM and Wmax = four separate output factors from a single data set:

$$F_{Bonferroni} = 0.01*(2^4) = 0.16 \quad \textbf{(4-17)}$$

Therefore CI ≈ 98.84%.

It should be stressed that the Design Expert Pro software does not perform this calculation, and the value calculated by equation (4-17) is a closer approximation of the true CI for this data set than that given in Table 16 through Table 33. The point remains however that the models created have very high confidence intervals and easily pass the 95% threshold, and arguably could pass a far higher threshold based on the result of equation (4-17). For the work in this thesis, the phrase 'CI greater than 95%' is used to represent this.

4.7. Further linear regression model refinement

The automated model development in the software has taken the process as far it can. It was clear in all three models that there was a small, but measurable, impact from both the test equipment. The ambient conditions of the day and the H_2O contact angle (hydrophobicity) also have some impact. There was a somewhat difficult to interpret interaction between the MPL and the FCCA test equipment selected (factors 'L' and 'N' in the software generated M-ANOVA results in the appendices). The maximum power measurement was influenced by the selection of an individual test cell, which has a small but measurable bearing on the final result. The machine variability will be removed from the next stage of analysis. While this will slightly increase the overall error of the measurements, as it is anticipated that the model gained will still be valid as discussed in section 4.6. Furthermore, removing the input factors of 'FCCA' and 'Cell Number' opens up the possibility of increasing the overall accuracy of the models generated by replicating 'identical' data points, as discussed previously in sections 2.2, 3.2 and 3.9. Such replication makes the analysis methods available more robust, and more accurate, as the degree of replication increases [81,83,85]. It can be argued that these 'machine' or 'balance of plant' effects as a result of the ambient conditions in the lab, and while they cannot be ignored, they can be acknowledged and dealt with in several ways. A record of the modifying factors for each machine cell can be created, and a 'weighting' or 'blocking' function can be applied to varying degrees of resolution. Table 15 shows the possibility of blocking out the data based on the family of data, and the machine variables (L= FCCA and M = Test cell number). This approach would be recommended for comparisons of very similar MEAs, where the differences between the results were less well defined.

In the broader fuel cell literature, it is not always clear how many different test cells have been used to generate a given set of results. Some published papers may have used one, or several, different test stations without reporting the specifics. This makes a comparison between historic data for different test suites all the more problematic. If a set of experiments were being conducted by several laboratories, before starting the main body of work, a 'Round Robin' benchmarking trial would be

undertaken to define the error. The blocking approach in this section could also be used to normalise across published test results from different experiments reported in the literature [81-83].

The following blocking, or weighting, exercise is intended to provide an understanding of the difference the various test chambers impart (note that maximum power achieved was excluded from this analysis as the units were different, and the results were all of a different order of magnitude). The mean value generated in each column, or family set, was subtracted from the actual value and entered into the weighted set.

Table 15: Blocked results gA, gM and gO

	family 1	family 2	family 3		
	gA	gM	gO	within test mean	within test variance
L	0.0097	0.0640	0.0990	0.0576	0.0020
M1	-0.0686	0.0200	0.0540	0.0018	0.0040
M2	-0.1158	-0.0960	-0.1900	-0.1339	0.0025
M3	-0.0112	0.0230	0.2000	0.0706	0.0128
mean	-0.0465	0.0028	0.0408	-0.0010	=mean of means
difference of means	-0.0455	0.0037	0.0417		
blocked (weighted) values	weighted by difference of mean				
	gA	gM	gO	within test mean (weighted)	within test variance (weighted)
L	0.0552	0.0603	0.0573	0.0576	0.0000
M1	-0.0232	0.0163	0.0123	0.0018	0.0005
M2	-0.0703	-0.0997	-0.2317	-0.1339	0.0074
M3	0.0343	0.0193	0.1583	0.0706	0.0058
mean	-0.0010	-0.0010	-0.0010	-0.0010	= mean of means
difference of means	0.0000	0.0000	0.0000		

Note that this interpretation of the impact of the test equipment, and the ability to quantify the error from the test apparatus in this way, could not have been discovered using the simpler analysis provided by the box plots discussed earlier (see section 4.4). This highlights once again the importance of analysis of variance approaches.

These weighted values for a given data set, were quite significant when taken in isolation: For example, the gO family of values have a 'difference of means' value of 0.0414, over 42% of the FCCA variable 'L'. Recall that the two FCCA values were recorded in the software as '0' and '1', and so the real world impact on the result from FCCA 2 is, 1*0.0573, and the results for FCCA 1 were unmodified (multiplied by zero). These 'balance of plant effects' were only one of several factors included in the result of the model.

Having codified the machine based experimental error, both in this chapter and in section 4.5, it was reasonable to proceed without including them. Future discussions, especially of comparisons between very similar GDMs (i.e. similar porosity and thickness), must acknowledge this test apparatus induced error. It is anticipated the replication of test data points will more than counter the reduction in accuracy caused by the exclusion of machine and ambient conditions. To strip out the machine variation from the evolved models discussed previously, the (M-ANOVA analysis was repeated, excluding those factors that were test apparatus specific. Ignoring the test apparatus error further reduced the complexity of the systems examined, and it was possible to remove the ambient conditions as well. Having gained an understanding of the errors in the test, it becomes possible to produce the next set of linear regression models.

An effort was made to conduct a cubic model ($m.x^3+m.x^2+.m.x+m+c$) that would be capable of identifying higher order interactions if they are present, but the processing time for each result was deemed to be excessive for any minor improvements in accuracy that may be gained. Figure 44 details the estimated processing time for this more complex regression model.

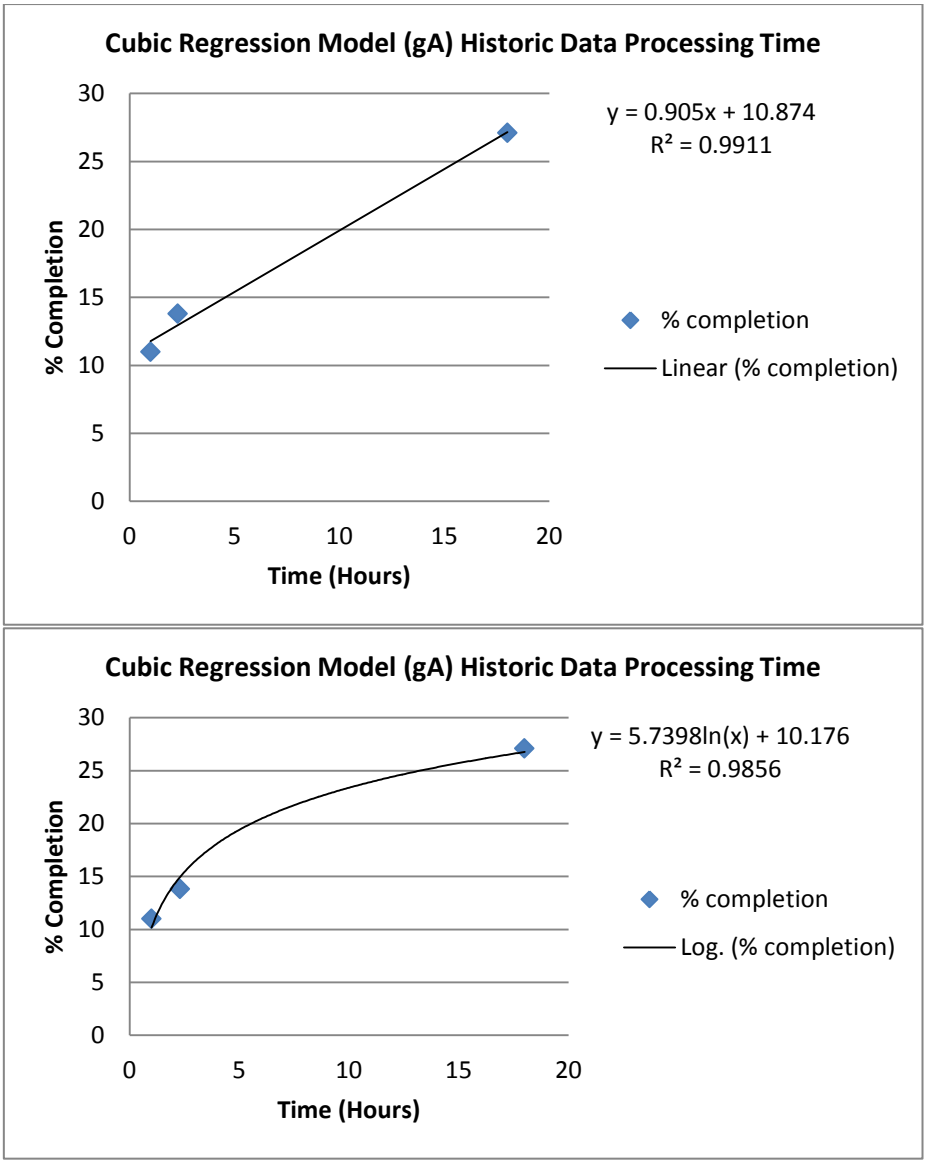

Figure 44: Cubic regression model processing time

(Linear (top) and Logarithmic (bottom))

In light of the likely time taken to run the software for each output variable of interest, not to mention the possibility that the processing time was a logarithmic function, it was decided to discontinue the cubic results before their conclusion. This does mean that higher order interactions (three and four-factor effects) will not be possible to identify, but such events are considered rare, perhaps even non-existent, in most physical systems [82].

The quadratic ($m.x^2+.m.x+m+c$) backwards step regression processed very quickly, and this type of model was therefore selected. In fact, the extreme speed of the operation was aided, in large part, as the backwards optimisation reduced the model to a modified 2FL ('2 factor 2 levels' modified for multiple factors with strong covariance and multiple levels) state, as the least significant factors eliminated first were the higher order interactions.

In the Backwards optimisation, the removal of terms proceeds sequentially, with the highest 'F-test' terms first until only values where F-test gives $p < 0.05$ were left (and any hierarchical subset values were also retained even if they do not pass this test threshold). Once again, the software did not complete this process successfully in all cases. This was due the higher order interactions being flagged as either aliased, or approaching the significant F-test $p<0.05$ threshold, but without sufficient data for the software to categorically keep or dismiss these values. It should be pointed out once more, the modified 2FL model generated, was only suited to identifying 2 level interactions with certainty. All higher-order (three or four factor interactions) were aliased in this design. This analysis can still identify the likelihood of aliased terms and provide an indication of what the aliased terms may be. In this case, for example, all third order terms involving category 'K' (supplier) will be aliased and will not be detectable. The remaining backwards steps (i.e. those not completed by the software) were completed 'by hand' with the following data points being rejected by the author in the order recorded as an alphabetised list below. Note that all models, for all outputs, were run again after the rejection of a single factor, and the process repeated for the next least significant factor still included in the model:

a) B^2 removed for all models.
b) AG interaction removed from the gO and gM models.
c) DE removed from the gA model.

Having completed the steps outlined above, the remaining factors pass the F-test threshold or were retained to preserve hierarchy in the regression. Note that in the reduced complexity gM model, the 'CD' interaction (wt% of hydrophobic PTFE coating and the GDM through-plane thickness (µm) respectively) has been retained as the value of 0.0543, only slightly over the $p < 0.05$ threshold, and both of the hierarchical terms were highly significant in the model.

4.8. Reduced complexity regression model final result

The data was analysed for co-varying factors in a backwards step linear regression model. Note that the following results were taken directly from the Design Expert Pro software. The following text applies to each table, and is adapted from the explanatory output generated by the software (see chapter 3):-

Table 16: Reduced complexity gA regression

- A 2FL M-ANOVAR response surface 2FL classic sum of squares (TypeII).
- F-value = 10.17 (therefore the model is significant).
- CI = is greater than 95%: See section 4.6, equation (4-17).
- Model terms B, C, F, G, J, AB, AJ, BE, BG, CF are significant ((P-value probability > F) is equal to or less 0.05).
- Hierarchy of terms has been retained for factor A and E.

Table 21: Reduced complexity gO regression

- A 2FL M-ANOVAR response surface 2FL classic sum of squares (TypeII).
- F-value = 14.13 (therefore the model significant).
- CI = is greater than 95%: See section 4.6, equation (4-17).
- Model terms B, C, D, G, H, J, DG are significant ((P-value probability > F) is equal to or less 0.05).

Table 26: Reduced complexity gM regression

- A 2FL M-ANOVAR response surface 2FL classic sum of squares (TypeII).
- F-value = 14.13 (therefore the model is significant).
- CI = is greater than 95%: See section 4.6, equation (4-17).
- Model terms B, C, D, G, H, J, CG, DG are significant ((P-value probability > F) is equal to or less 0.05).
- Term CD has been retained ((P-value probability > f) = 0.543).

Table 32: Reduced complexity Wmax regression

- A 2FL M-ANOVAR (i.e. ManCoVar) response surface 2FL classic sum of squares (TypeII).
- F-value = 14.13 (therefore the model is significant).
- CI = is greater than 95%: See section 4.6, and equation (4-17).

- Data underwent power transformation to improve fit: λ= -1.320.
- Model terms A, B, D, E, F, G, AD, AF, CG are significant ((P-value probability > F) is equal to or less 0.05).
- Term C has been retained to maintain hierarchy.
- The term BC has been retained despite the high ((P-value probability > F) as both terms C and B have retained as reviews of appropriate fuel cell literature (see Chapter 2) indicate that PTFE coating and GDM through-plane thickness, and their interaction, are significant in estimating peak power [24,87,95].

More detailed analysis of each model generated is shown in Table 16 through Table 38.

4.8.1. Reduced complexity gA regression model

Table 16: Reduced complexity gA regression

Source	Sum of Squares	df	Mean Square	F Value	p-value Prob > F	
Model	1.01127	14	0.07223	10.17489	0.00000	significant
A-T bar	0.02038	1	0.02038	2.87052	0.09567	
B-T max	0.03544	1	0.03544	4.99203	0.02940	
C-PTFE	0.09850	1	0.09850	13.87470	0.00045	
E-H2O angle	0.00021	1	0.00021	0.02982	0.86351	
F-mean pore	0.03086	1	0.03086	4.34731	0.04156	
G-porosity	0.04459	1	0.04459	6.28116	0.01508	
J-Structure	0.32339	2	0.16169	22.77643	0.00000	
AB	0.06674	1	0.06674	9.40157	0.00331	
AJ	0.12479	2	0.06240	8.78924	0.00047	
BE	0.08768	1	0.08768	12.35130	0.00087	
BG	0.24775	1	0.24775	34.89781	0.00000	
CF	0.10377	1	0.10377	14.61685	0.00033	
Residual	0.40465	57	0.00710			
Cor Total	1.41593	71				

Table 16 shows the M-ANOVAR outputs generated in accordance with the backwards elimination methods outlined in Chapter 3. Backwards elimination reduces the number of terms in the model to those with the most significant, measurable impact on the final result. The model as a whole was significant, and the terms highlighted in green are each significant in their own right. The sum of

squares value indicates the difference between the means of the block presented and the overall mean of the data. The degrees of freedom (df) is associated with the number of model terms and is used in creating the t-distribution (see section 3.3); recall that at df= 30 t-distribution becomes a normal distribution [82]. F-value = model mean square/Residual mean square (see section 3.6.1). P-value probability >F is the probability that the F-value could exist even if the null hypothesises is true (recall that the null hypothesis asks the question; 'Is a simple mean a more accurate model of the systems than the model produced by M-ANOVA analysis?'). The smaller the p-value is, the more likely the M-ANOVAR model is to be correct.

Table 17: Reduced complexity gA summary

Std. Dev.	0.08426	R-Squared	0.71421
Mean	-0.72829	Adj R-Squared	0.64402
C.V. %	11.56910	Pred R-Squared	0.52056
PRESS	0.67885	Adeq Precision	12.10772

Table 17 is the error assessment for the model displayed in Table 16. Std.Dev is the standard deviation of the model, estimated from the square root of the mean of the residual as per equation (3-23). Mean is the overall mean of all data in the model (i.e. the 'null hypothesis' result). C.V. % is the coefficient of variation (the standard deviation from equation (3-24) expressed as a percentage of the mean). PRESS is the 'predicted residual errors sum of squares': the sum of squares of the difference (the residual) between each predicted value in the model compared to its equivalent measured experimental value. R-Squared (R2) is calculated as per equation (3-20). The adjusted and predicted R^2 values are the R^2 values of the model factoring the final number of remaining terms after completing the backwards elimination process to create the reduced complexity model.

$$Adjusted\ R^2 = 1 - \left[\frac{\left(\frac{SSE}{df_{residuals}}\right)}{\left(\frac{SSE + SS_{model}}{df_{residuals} + df_{model}}\right)}\right] \quad \textbf{(4-18)}$$

[85]

Where

$df_{residuals}$ is the degrees of freedom of the residuals given in the M-ANOVAR analysis

df_{model} is the degrees of freedom in the model given by the M-ANOVAR analysis

and

SS_{model} is the sum of squares of the residuals of the model (note that all other terms have been defined previously in 3)

If

Adjusted R^2 = Predicted R^2 +/- 0.2

the model is then considered robust (i.e. not unduly influenced by outliers or values with unusually high leverage) [82,85].

Adequate precision is a measure of the signal to noise ratio of the system, and is calculated as

$$adeq.Precision = \frac{max(\hat{y}) - min(\hat{y})}{\sqrt{\bar{V}(\hat{y})}} \quad \textbf{(4-19)}$$

[85]

Where

$$\bar{V}(\hat{y}) = \frac{1}{n}\sum_{i=1}^{n} V(\hat{y}) = \frac{p.s^2}{n} \quad \textbf{(4-20)}$$

[85]

Where

'$V(\hat{y})$' is the estimated variance based on the estimated values of y (see equation (3-4)).

$\bar{V}(\hat{y})$ is the mean variance of the y estimates.

n is the number of test samples in the experiment.

p is the number of model parameters (including intercept values and any weight/blocking values).

A value of four or greater is desirable for adequate precision and is evidence for the validity of the model created [85].

Table 18: Reduced complexity gA error assessment

Term	Coefficient Estimate	df	Standard Error	95% CI Low	95% CI High	VIF	√VIF
Intercept	-0.84765	1	0.05745	-0.96270	-0.73261		
A-T bar	0.25370	1	0.11865	0.01609	0.49130	13.02502	3.60902
B-T max	-0.19466	1	0.10673	-0.40839	0.01907	11.83006	3.43949
C-PTFE	-0.08596	1	0.03053	-0.14710	-0.02481	3.23129	1.79758
E-H2O angle	-0.08939	1	0.03724	-0.16397	-0.01482	3.30500	1.81797
F-mean pore	0.01736	1	0.03031	-0.04334	0.07806	3.08360	1.75602
G-porosity	-0.00351	1	0.02577	-0.05512	0.04809	2.07640	1.44097
J[1]	0.10671	1	0.06679	-0.02704	0.24045		0
J[2]	0.14368	1	0.06372	0.01608	0.27128		0
AB	-0.23862	1	0.07782	-0.39446	-0.08278	2.28455	1.51147
AJ[1]	0.42807	1	0.12483	0.17810	0.67804		0
AJ[2]	-0.29591	1	0.09735	-0.49084	-0.10098		0
BE	0.40496	1	0.11523	0.17422	0.63569	6.07212	2.46417
BG	0.41116	1	0.06960	0.27179	0.55054	2.10257	1.45002
CF	-0.25819	1	0.06753	-0.39342	-0.12296	8.57950	2.92909

Table 18 continues the error assessment, begun in Table 17. The M-ANOVAR assessment is dealing with multiple co-varying factors, and this has additional impacts on the error assessment for the modified ANOVAR techniques used. The 'coefficient estimate' is the value by which the input value is multiplied, as appropriate (excluding the intercept value). Both 'df' and standard error have repeatedly been discussed in this context already (see comments on Table 16 and Table 17). The two columns labelled 95% CI low, and 95% CI high, show the range that the true coefficient (i.e. the coefficient of a theoretically 'perfect' model) could be found in and still maintain a 95% CI. If the range of these two values goes from negative to positive (i.e. crosses the 'zero' value), it is possible that the true impact of that input factor is zero. As discussed in 3.9, response surface methods are suited to the analysis of co-varying factors, but there is a variance inflation factor (VIF) that should be considered when analysing the data. VIF is calculated as shown in equation (3 68). Values greater than ten indicate significant covariance and the square root of VIF should be used as a multiplier of the standard error for that factor, in the population being studied (i.e. for the experimental data used to create that individual model).

Design Expert Pro does not carry out this procedure or include it in the final coded factors for the model (Table 19 in this case). Therefore VIF is highlighted in Table 18 to demonstrate an

understanding of the likely impact this may have on the final coded model, and to assist in explaining any errors between real world results and those predicted by the model.

Table 19: Reduced complexity gA coded factors

gA	=
-0.8477	
0.2537	* A
-0.1947	* B
-0.0860	* C
-0.0894	* E
0.0174	* F
-0.0035	* G
0.1067	* J[1]
0.1437	* J[2]
-0.2386	* AB
0.4281	* AJ[1]
-0.2959	* AJ[2]
0.4050	* BE
0.4112	* BG
-0.2582	* CF

Table 19 shows the coded factors for the gA model. These numeric values multiply input factors in order to create the model in question. Table 20 further develops this and shows the gradient of the activation region model for each of the three types of GDM.

Final equation in terms of actual factors:-

Table 20: Reduced complexity gA empirical model

Structure	Non-woven	Structure	Paper
gA	=	gA	=
-8.1324		-0.9514	
0.4576	* T bar	0.3511	* T bar
0.0099	* T max	0.0099	* T max
1.9739	* PTFE	1.9739	* PTFE
-0.1094	* H_2O angle	-0.1094	* H_2O angle
0.0002	* mean pore	0.0002	* mean pore
-0.2034	* porosity	-0.2034	* porosity
-0.0051	* T bar * T max	-0.0051	* T bar * T max
0.0015	* T max * H_2O angle	0.0015	* T max * H_2O angle
0.0029	* T max * porosity	0.0029	* T max * porosity
-0.0016	* PTFE * mean pore	-0.0016	* PTFE * mean pore

Structure	woven
gA	=
-2.9613	
0.3752	* T bar
0.0099	* T max
1.9739	* PTFE
-0.1094	* H_2O angle
0.0002	* mean pore
-0.2034	* porosity
-0.0051	* T bar * T max
0.0015	* T max * H_2O angle
0.0029	* T max * porosity
-0.0016	* PTFE * mean pore

4.8.2.Reduced complexity gO regression model

Table 21: Reduced complexity gO regression

Source	Sum of Squares	df	Mean Square	F Value	p-value Prob > F	
Model	0.82243	8	0.10280	14.13478	0.00000	significant
B-T max	0.10010	1	0.10010	13.76340	0.00044	
C-PTFE	0.17685	1	0.17685	24.31529	0.00001	
D-Thickness	0.05755	1	0.05755	7.91321	0.00654	
G-porosity	0.19724	1	0.19724	27.11848	0.00000	
H-MPL	0.04669	1	0.04669	6.41900	0.01379	
J-Structure	0.10839	2	0.05420	7.45161	0.00125	
DG	0.06096	1	0.06096	8.38165	0.00520	
Residual	0.45821	63	0.00727			
Cor Total	1.28063	71				

Table 21 shows the M-ANOVAR outputs generated in accordance with the backwards elimination methods outlined in Chapter 3. Backwards elimination reduces the number of terms in the model, to those that have the most significant, measurable, impact on the final result. The model as a whole is significant, and the terms that are highlighted in green are each significant in their own right. The sum of squares value indicates the difference between the means of the block and the overall mean. The degrees of freedom (df) is associated with the number of model terms and is used in creating the t-distribution (see section 3.3); recall that at df=30 t-distribution becomes a normal distribution [82]. F-value is the model mean square, divided by the Residual mean square (see section 3.6.1). P-value probability >F is the probability that the F-value could exist even if the null hypothesises true (recall that the null hypothesis asks the question; 'Is simple mean is a more accurate model of the systems than the M-ANOVA analysis?'): the smaller this value is the more likely the M-ANOVAR model is to be correct.

Table 22: Reduced complexity gO summary

Std. Dev.	0.08528		R-Squared	0.64220
Mean	-0.48014		Adj R-Squared	0.59677
C.V. %	17.76186		Pred R-Squared	0.55126
PRESS	0.57467		Adeq Precision	14.92902

Table 22 is the error assessment for the model displayed in Table 21: Std.Dev is the standard deviation of the model, estimated from the square root of the mean of the residual as per equation (3 23). Mean is the overall mean of all data in the model (i.e. the 'null hypothesis' result). C.V. % is the coefficient of variation (the standard deviation from equation (3 24) expressed as a percentage of the mean). PRESS is the 'predicted residual errors sum of squares': the sum of squares of the difference (the residual) between each predicted value in the model compared to its equivalent measured experimental value. R-Squared (R2) is calculated as per equation (3 20). The adjusted and predicted R2 values are within 0.2 of each other indicating a robust model. Adequate precision is greater than four indicating the validity of the model is not compromised by outliers or excessive leverage [84].

Table 23: Reduced complexity gO error assessment

Term	Coefficient Estimate	df	Standard Error	95% CI Low	95% CI High	VIF	√VIF
Intercept	-0.6469	1	0.0262	-0.6992	-0.5946		
B-T max	0.1291	1	0.0348	0.0596	0.1986	1.2273	1.10785
C-PTFE	-0.1378	1	0.0279	-0.1936	-0.0819	2.6413	1.625210
D-Thickness	-0.0106	1	0.0419	-0.0942	0.0731	2.8031	1.67424
G-porosity	-0.1391	1	0.0234	-0.1859	-0.0923	1.6726	1.2933
H-MPL	0.0511	1	0.0202	0.0108	0.0914	2.5218	1.58803
J[1]	-0.0221	1	0.0310	-0.0840	0.0398		0
J[2]	0.0941	1	0.0254	0.0434	0.1449		0
DG	0.1476	1	0.0510	0.0457	0.2495	2.2535	1.50118

Table 23 continues the error assessment begun in Table 22. The 'coefficient estimate' is the value by which the input value is multiplied as appropriate (excluding the intercept value). Both 'df' and standard error have repeatedly been discussed in this context already (see comments on Table 16 and

Table 17). The two columns labelled 95% CI low, and 95% CI high, show the range that the true coefficient (i.e. the coefficient of a theoretically 'perfect' model) could be found in and still maintain a 95% CI. If the range of these two values goes from negative to positive (i.e. crosses the 'zero' value), it is possible that the true impact of that input factor is zero. VIF is calculated as shown in equation (3 68). No VIF values greater than ten were generated. Table 24 shows the coded factors for the model. These numeric values multiply input factors to create the model in question. Table 25 further develops this and shows the gradient of the Ohmic loss region model for each of the three types of GDM, with and without an MPL.

Final Equation in Terms of Coded Factors:-

Table 24: Reduced complexity gO coded factors

gO	=
-0.64693	
0.129094	* B
-0.13779	* C
-0.01058	* D
-0.13911	* G
0.051087	* H
-0.02206	* J[1]
0.094138	* J[2]
0.147594	* DG

Final equation in terms of actual factors:-

Table 25: Reduced complexity gO empirical models

MPL	No	MPL	Yes
Structure	Non-woven	Structure	Non-woven
gO	=	gO	=
-0.883		-0.78082	
0.018846	* T max	0.018846	* T max
-1.37787	* PTFE	-1.37787	* PTFE
-0.00249	* Thickness	-0.00249	* Thickness
-0.019	* porosity	-0.019	* porosity
4.62E-05	* Thickness * porosity	4.62E-05	* Thickness * porosity
MPL	No	MPL	Yes
Structure	Paper	Structure	Paper
gO	=	gO	=
-0.7668		-0.66462	
0.018846	* T max	0.018846	* T max
-1.37787	* PTFE	-1.37787	* PTFE
-0.00249	* Thickness	-0.00249	* Thickness
-0.019	* porosity	-0.019	* porosity
4.62E-05	* Thickness * porosity	4.62E-05	* Thickness * porosity
MPL	no	MPL	Yes
Structure	woven	Structure	Woven
gO	=	gO	=
-0.93301		-0.83084	
0.018846	* T max	0.018846	* T max
-1.37787	* PTFE	-1.37787	* PTFE
-0.00249	* Thickness	-0.00249	* Thickness
-0.019	* porosity	-0.019	* porosity
4.62E-05	* Thickness * porosity	4.62E-05	* Thickness * porosity

4.8.3. Reduced Complexity gM Regression model

Table 26: Reduced complexity gM regression

Source	Sum of Squares	df	Mean Square	F Value	p-value Prob > F	
Model	0.86164	10	0.08616	14.12268	0.00000	significant
B-T max	0.07589	1	0.07589	12.43931	0.00080	
C-PTFE	0.17078	1	0.17078	27.99208	0.00000	
D-Thickness	0.06612	1	0.06612	10.83794	0.00166	
G-porosity	0.13682	1	0.13682	22.42524	0.00001	
H-MPL	0.08315	1	0.08315	13.62908	0.00048	
J-Structure	0.08205	2	0.04102	6.72386	0.00230	
CD	0.02350	1	0.02350	3.85136	0.05427	
CG	0.02493	1	0.02493	4.08582	0.04764	
DG	0.02966	1	0.02966	4.86132	0.03125	
Residual	0.37217	61	0.00610			
Cor Total	1.23380	71				

Table 26 shows the M-ANOVAR outputs generated in accordance with the backwards elimination methods outlined in 3. Backwards elimination reduces the number of terms in the model to those that have the most significant, measurable, impact on the final result. The model as a whole is significant, and the terms highlighted green are each significant in their own right. The sum of squares value indicates the difference between the means of the block and the overall mean. Degrees of freedom (df) is associated with the number of model terms and is used in creating the t-distribution (see section 3.3); recall that at df= 30 t-distribution becomes a normal distribution [82]). F-value is equal to model mean square divided by the Residual mean square (see section 3.6.1). P-value probability >F is the probability that the F-value could exist even if the null hypothesises true (recall that the null hypothesis asks the question; 'Is a simple mean is a more accurate model of the systems than the M-ANOVA analysis?'): the smaller this value is the more likely the M-ANOVAR model is to be correct.

Table 27: Reduced complexity gM summary

Std. Dev.	0.07811		R-Squared	0.698358
Mean	-0.47587		Adj R-Squared	0.648909
C.V. %	16.41408		Pred R-Squared	0.588646
PRESS	0.50753		Adeq Precision	14.22369

Table 27 is the error assessment for the model displayed in Table 26. Std.Dev is the standard deviation of the model, estimated from the square root of the mean of the residual, as per equation (3 23). Mean is the overall mean of all data in the model (i.e. the 'null hypothesis' result). C.V. % is the coefficient of variation (the standard deviation from equation (3 24) expressed as a percentage of the mean). PRESS is the 'predicted residual errors sum of squares': the sum of squares of the difference (the residual) between each predicted value in the model compared to its equivalent measured experimental value. R-Squared (R2) is calculated as per equation (3 20). The adjusted and predicted R2 values are within 0.2 of each other indicating a robust model. Adequate precision is greater than four indicating the validity of the model is not compromised by outliers or excessive leverage [84].

Table 28: Reduced complexity gM error assessment

Term	Coefficient		Standard	95% CI	95% CI	VIF	
	Estimate	df	Error	Low	High		√VIF
Intercept	-0.6836	1	0.0326	-0.7487	-0.6185		
B-T max	0.1161	1	0.0329	0.0503	0.1819	1.3086	1.14392
C-PTFE	-0.1581	1	0.0331	-0.2242	-0.0920	4.4080	2.09953
D-Thickness	-0.0833	1	0.0487	-0.1806	0.0140	4.5132	2.12444
G-porosity	-0.1602	1	0.0297	-0.2196	-0.1008	3.2052	1.79031
H-MPL	0.0768	1	0.0208	0.0352	0.1184	3.1988	1.78851
J[1]	0.0006	1	0.0295	-0.0583	0.0595		0
J[2]	0.1005	1	0.0274	0.0457	0.1553		0
CD	-0.1431	1	0.0729	-0.2890	0.0027	2.9804	1.72639
CG	-0.1101	1	0.0545	-0.2190	-0.0012	4.7105	2.17038
DG	0.1064	1	0.0483	0.0099	0.2029	2.4082	1.55183

Table 28 continues the error assessment begun in Table 27. The 'coefficient estimate' is the value by which the input value is multiplied as appropriate (excluding the intercept value).

The ‘df’ and standard error have been discussed in this context already (see comments on Table 16 and Table 17). The two columns labelled 95% CI low, and 95% CI high, show the range that the true coefficient (i.e. the coefficient of a theoretically ‘perfect’ model) could be found in and still maintain a 95% CI. If the range of these two values goes from negative to positive (i.e. crosses the ‘zero’ value), it is possible that the true impact of that input factor was zero. VIF is calculated as shown in equation (3 68). No VIF values greater than ten were generated.

Table 29 shows the coded factors. These numeric values multiply input factors to create the model in question. Table 30 and Table 31 further develops this and shows the gradient of the mass loss region model for each of the three types of GDM. Final Equation in Terms of Coded Factors:

Table 29: Reduced complexity gM coded factors

gM	=
-0.6836	
0.1161	* B
-0.1581	* C
-0.0833	* D
-0.1602	* G
0.0768	* H
0.0006	* J[1]
0.1005	* J[2]
-0.1431	* CD
-0.1101	* CG
0.1064	* DG

Final Equation in Terms of Actual Factors:-

Table 30: Reduced complexity gM empirical models (part 1)

Structure	**Woven no MPL**	**Structure**	**Woven with MPL**
gM	=	gM	=
-1.3972		-1.2436	
0.0169	* T max	0.0169	* T max
3.6668	* PTFE	3.6668	* PTFE
-0.0014	* Thickness	-0.0014	* Thickness
-0.0113	* Porosity	-0.0113	* Porosity
-0.0092	* PTFE * Thickness	-0.0092	* PTFE * Thickness
-0.0534	* PTFE * Porosity	-0.0534	* PTFE * Porosity
0.0000	* Thickness * Porosity	0.0000	* Thickness * Porosity

Table 31: Reduced complexity gM empirical models (part 2)

Structure	**Non-woven No MPL**	**Structure**	**Non-woven with MPL**
gM	=	gM	=
-1.2955		-1.1420	
0.0169	* T max	0.0169	* T max
3.6668	* PTFE	3.6668	* PTFE
-0.0014	* Thickness	-0.0014	* Thickness
-0.0113	* Porosity	-0.0113	* Porosity
-0.0092	* PTFE * Thickness	-0.0092	* PTFE * Thickness
-0.0534	* PTFE * Porosity	-0.0534	* PTFE * Porosity
0.0000	* Thickness * Porosity	0.0000	* Thickness * Porosity
Structure	Paper no MPL	Structure	Paper with MPL
gM	=	gM	=
-1.1957		-1.0421	
0.0169	* T max	0.0169	* T max
3.6668	* PTFE	3.6668	* PTFE
-0.0014	* Thickness	-0.0014	* Thickness
-0.0113	* Porosity	-0.0113	* Porosity
-0.0092	* PTFE * Thickness	-0.0092	* PTFE * Thickness
-0.0534	* PTFE * Porosity	-0.0534	* PTFE * Porosity
0.0000	* Thickness * Porosity	0.0000	* Thickness * Porosity

4.8.4.Reduced complexity Wmax regression model

Table 32: Reduced complexity Wmax regression

Source	Sum of Squares	df	Mean Square	F Value	p-value Prob > F	significant
Model	50.1562	15	3.3437	16.9672	0.0000	
A-Tbar	1.9127	1	1.9127	9.7057	0.0029	
B-PTFE	3.1335	1	3.1335	15.9003	0.0002	
C-Thickness	0.0076	1	0.0076	0.0384	0.8454	
D-H2O Pontact angle	0.8931	1	0.8931	4.5317	0.0377	
E-Porosity	2.1414	1	2.1414	10.8660	0.0017	
F-MPL	3.9728	1	3.9728	20.1590	0.0000	
G-Structure	6.5612	2	3.2806	16.6469	0.0000	
AD	1.5432	1	1.5432	7.8305	0.0070	
AF	2.3428	1	2.3428	11.8880	0.0011	
AG	1.2268	2	0.6134	3.1127	0.0523	
BC	0.0843	1	0.0843	0.4275	0.5159	
CG	1.2925	2	0.6462	3.2792	0.0450	
Residual	11.0360	56	0.1971			
Cor Total	61.1922	71				

Table 32 shows the M-ANOVAR outputs generated with the backwards elimination methods outlined in Chapter 3. This reduces the number of terms in the model to those with the most significant, measurable, impact on the final result. The model as a whole is significant, and the terms highlighted in green are each significant in their own right. The sum of squares value indicates the difference between the means of the block and the overall mean. Degrees of freedom (df) is the associated with the number of model terms and is used in creating the t-distribution (see section 3.3); recall that at df= 30 t-distribution becomes a normal distribution [82]). F-Value is the model mean square divided by the Residual mean square (see section 3.6.1). P-value probability>F is the probability that the F-value could exist even if the null hypothesises true (recall that the null hypothesis asks the question "Is a simple mean is a more accurate model of the systems than the M-ANOVA analysis?"): the smaller this value is the more likely the M-ANOVAR model is to be correct.

Table 33: Reduced complexity Wmax summary

Std. Dev.	0.4439	R-Squared	0.8197
Mean	4.5650	Adj R-Squared	0.7713
C.V. %	9.7246	Pred R-Squared	0.7240
PRESS	16.8885	Adeq Precision	18.3564

Table 33 is the error assessment for the model displayed in Table 32. Std.Dev is the standard deviation of the model, estimated from the square root of the mean of the residual as per equation (3 23). Mean is the overall mean of all data in the model (i.e. the 'null hypothesis' result). C.V. % is the coefficient of variation (the standard deviation from equation (3 24) expressed as a percentage of the mean). PRESS is the 'predicted residual errors sum of squares': the sum of squares of the difference (the residual) between each predicted value in the model compared to its equivalent measured experimental value. R-Squared (R2) is calculated as per equation (3 20). The adjusted and predicted R2 values are within 0.2 of each other indicating a robust model [84]. Adequate precision is greater than four indicating the validity of the model is not compromised by outliers or excessive leverage [84].

Table 34 continues the error assessment begun in Table 33. The 'coefficient estimate' is the value by which the input value is multiplied as appropriate (excluding the intercept value of course). Both 'df' and standard error have repeatedly been discussed in this context already (see comments on Table 16 and Table 17). The two columns labelled 95% CI low, and 95% CI high, show the range that the true coefficient (i.e. the coefficient of a theoretically 'perfect' model) could be found in and still maintain a 95% CI. If the range of these two values goes from negative to positive (i.e. crosses the 'zero' value), it is possible that the true impact of that input factor is zero. VIF is calculated as shown in equation (3 68). Multiple values above ten have been generated. It must be acknowledged that conflict with the literature prompted the inclusion of several factors that would not have been included if judged only on the strict adherence to M-ANOVAR procedures as outlined in Chapter 3.

Table 35 shows the coded factors. These numeric values multiply input factors to create the model in question. Table 36, Table 37 and Table 38 further develop this and show the peak power output (Wmax) model for each of the three types of GDM with and without MPLs. Recall that a power transformation was performed on the data to overcome the increased errors and make the data suitable (i.e. sufficiently linear) for M-ANOVAR analysis. The resultant model requires the undoing of this power transformation to predict the likely power output for a given GDM.

Table 34: Reduced complexity Wmax error assessment

Term	Coefficient Estimate	df	Standard Error	95% CI Low	95% CI High	VIF	Sqrt VIF
Intercept	62.2444	1.0	17.1984	27.7918	96.6970		
A-Tbar	-1.8062	1.0	0.9015	-3.6122	-0.0002	27.0872	5.20453
B-PTFE	55.5994	1.0	17.2658	21.0118	90.1870	3.7217	1.92918
C-Thickness	25.6952	1.0	42.6377	-59.7183	111.1087	107283.0	327.541
D-H2O contact angle	1.0538	1.0	0.3010	0.4508	1.6567	7.7767	2.78867
E-porosity	0.4025	1.0	0.1221	0.1579	0.6470	1.6788	1.29567
F-MPL	0.7444	1.0	0.1315	0.4808	1.0079	3.9613	1.99030
G[1]	3.7022	1.0	1.5144	0.6685	6.7359		0
G[2]	-2.3769	1.0	0.7731	-3.9257	-0.8282		0
AD	-2.1368	1.0	0.7636	-3.6665	-0.6071	11.5664	3.40093
AF	-1.2489	1.0	0.3622	-1.9746	-0.5233	7.7728	2.78797
AG[1]	-0.8959	1.0	1.6612	-4.2236	2.4319		0
AG[2]	1.4188	1.0	0.8485	-0.2809	3.1186		0
BC	27.9149	1.0	42.6924	-57.6082	113.4379	106119.9	325.760
CG[1]	-4.6991	1.0	1.8771	-8.4593	-0.9388		0
CG[2]	1.9920	1.0	1.1676	-0.3470	4.3310		0

Final Equation in Terms of Coded Factors:-

Table 35: Reduced complexity Wmax coded factors

(Wmax)^-1.32	=
62.2444	
-1.8062	* A
55.5994	* B
25.6952	* C
1.0538	* D
0.4025	* E
0.7444	* F
3.7022	* G[1]
-2.3769	* G[2]
-2.1368	* AD
-1.2489	* AF
-0.8959	* AG[1]
1.4188	* AG[2]
27.9149	* BC
-4.6991	* CG[1]
1.9920	* CG[2]

As discussed in section 3.7.1 the output value of the model was a non-linear function, and the result was converted to the appropriate Watts.cm^{-2} value as per equation (3-60).

Table 36: Reduced complexity Wmax empirical models (part 1)

structure	Woven With MPL			Wmax^-1.32	Wmax	
(Wmax)^-1.32	=			10.3451	0.177	W/ cm^2
-22.5055				-22.5055		
0.5984	* Tbar	70	^oC	41.8896		
0.7874	* PTFE	0.10	wt%	0.0787		
-0.0446	* Thickness	250	µm	-11.1593		
0.5755	* H_2O Contact angle	100	^{o}	57.5529		
0.0195	* porosity	60	%	1.1722		
-0.0082	* Tbar * H_2O contact angle	7000		-57.1338		
0.0180	* PTFE * Thickness	25		0.4502		
structure	**Paper With MPL**			Wmax^-1.32	Wmax	
(Wmax)^-1.32	=			4.5851	0.316	W/ cm^2
-62.8852				-62.8852		
0.9388	* Tbar	70	^oC	65.7174		
0.7874	* PTFE	0.10	wt%	0.0787		
-0.0015	* Thickness	250	µm	-0.3673		
0.5755	* H_2O contact angle	100	^{o}	57.5529		
0.0195	* porosity	60	%	1.1722		
-0.0082	* Tbar * H_2O Contact angle	7000		-57.1338		
0.0180	* PTFE * Thickness	25		0.4502		

Table 37: Reduced complexity Wmax empirical models (part 2)

structure	**Non-woven with MPL**			Wmax^-1.32	Wmax	
(Wmax)^-1.32	=			4.7566	0.303	W/ cm^2
-43.8777				-43.8777		
0.6533	* Tbar	70	^oC	45.7280		
0.7874	* PTFE	0.10	wt%	0.0787		
0.0031	* Thickness	250	µm	0.7861		
0.5755	* H_2O Contact angle	100	^{o}	57.5529		
0.0195	* Porosity	60	%	1.1722		
-0.0082	* Tbar * H_2O contact angle	7000		-57.1338		
0.0180	* PTFE * Thickness	25		0.4502		
structure	**woven**			Wmax^-1.32	Wmax	
(Wmax)^-1.32	=			10.7906	0.165	W/ cm^2
3.6535				3.6535		
0.2311	* Tbar	70	^oC	16.1761		
0.7874	* PTFE	0.10	wt%	0.0787		
-0.0446	* Thickness	250	µm	-11.1593		
0.5755	* H_2O Contact angle	100	^{o}	57.5529		
0.0195	* Porosity	60	%	1.1722		
-0.0082	* Tbar * H_2O contact angle	7000		-57.1338		
0.0180	* PTFE * Thickness	25		0.4502		

Table 38: Reduced complexity Wmax model empirical models (part 3)

				Wmax^-1.32	Wmax	
structure	**paper**			5.0306	0.294	W/ cm^2
(Wmax)^-1.32	=					
-36.7262				-36.7262		
0.5715	* Tbar	70	^oC	40.0039		
0.7874	* PTFE	0.10	wt%	0.0787		
-0.0015	* Thickness	250	µm	-0.3673		
0.5755	* H_2O Contact angle	100	^{o}	57.5529		
0.0195	* Porosity	60	%	1.1722		
-0.0082	* Tbar * H_2O contact angle	7000		-57.1338		
0.0180	* PTFE * Thickness	25		0.4502		
structure	**non-woven**			Wmax^-1.32	Wmax	
(Wmax)^-1.32	=			5.2021	0.287	W/ cm^2
-17.7187				-17.7187		
0.2859	* Tbar	70	^oC	20.0145		
0.7874	* PTFE	0.10	wt%	0.0787		
0.0031	* Thickness	250	µm	0.7861		
0.5755	* H_2O contact angle	100	^{o}	57.5529		
0.0195	* Porosity	60	%	1.1722		
-0.0082	* Tbar * H_2O contact angle	7000		-57.1338		
0.0180	* PTFE * Thickness	25		0.4502		

4.9. Reduced complexity regression for GDMs discussion

The reduced complexity regression model, achieved through the use ‘backwards elimination’, has proven to be insignificant to the model ‘F-value’ (as discussed in Chapter 3 and section 4.7). The design space models generated are in good agreement and conform to accepted tolerances with the possible exception of the reduced complexity gA and Wmax models. Both gA and Wmax models have VIF values above 10 (highlighted red in Table 18 and Table 34); For the mean and maximum temperature experienced during the polarisation curve. The square roots of these two factors multiplied by the Standard Error (the deviation away from the actual or true mean), will calculate the actual standard error:

$$SE_{actual} = SE * \sqrt{VIF} \quad \textbf{(4-21)}$$

Using the values from Table 18, the SE for the model from Tbar was possibly increased up to a maximum of

$$SE_{T\text{-}Bar} = 0.119*3.61 = 0.428 \quad \textbf{(4-22)}$$

And SE for T-max was possibly increased up to a maximum of:

$$SE_{T\text{-}Max} = 0.107*3.440 = 0.367 \quad \textbf{(4-23)}$$

Other than these two variables, the remaining factors were much improved over the first generation model, and the reduced complexity values all have far lower VIF values, and all are now under 10.0.

The SE for the model from Tbar was possibly increased up to a maximum of:

$$SE_{T\text{-}Bar} = 0.9015*5.20453 = 4.69 \quad \textbf{(4-24)}$$

Using the values from Table 34, the thickness of the GDM has an alarming high VIF

$$SE_{GDM\ thickness} = 42.6377*327.541 = 13{,}965 \quad \textbf{(4-25)}$$

It should be noted that low-high 95% CI values in Table 34 go from negative to positive, another indication that GDM thickness should not be included as a significant factor in determining total power output for MEAs, in the experimental set up of work completed for this thesis. As discussed previously, the thickness value was left in the model and credited with being significant in determining total resistance across the MEA in other work [24,87,95], and should, therefore, have an impact on the power generated in accordance with Ohm's law as per equation (4-26):

$$V = I.R \quad \textbf{(4-26)}$$

[24,87]

Moreover, as power (Watts) is the product of current and voltage (as shown in Figure 4) it seems reasonable to expect increased thickness and therefore an increase in resistance, to exert some measurable influence on the final power output. However, this was not detected in the M-ANOVAR models created. Using the values from Table 34, the interaction of wt% of PTFE in the GDM, and structure, as detailed in Table 14 has an alarming high VIF:

$$SE_{wt\%\ PTFE\ x\ Structure\ factor} = 42.6924*325.760 = 13{,}907 \quad \textbf{(4-27)}$$

The strict adherence to M-ANOVAR standard methods (as outlined in section 2.2 and Chapter 3) would indicate the removal of terms for GDM thickness and PTFE and Structure interactions from the model. However, as advised in section 2.2, understanding the physical realities of the systems should advise on the inclusion, or otherwise, of a set of factors. As the overall model errors were extremely low (see Table 32), and the factors of GDM thickness and interactions between PTFE content and GDM are of specific interest: These values were retained in the model. Should the validation prove unsuccessful, then the factors could be removed, and validation attempted for a model that does exclude such high VIF factors.

4.10. Validation of reduced complexity models

Classic, mechanistic or theoretical, models are often validated through one or more of several methods. The simple correlation coefficient (R^2, as calculated in equation (3-20)) has been completed for all models as part of the M-ANOVAR analysis [87]. Assessment of the distribution of residuals was a key test for model validation (in the case of M-ANOVAR ensuring all residuals were normally distributed [81,87]), and this was inherent in the M-ANOVAR approaches adopted in work completed for this thesis. This was discussed in more detail in section 2.2, section 3.1 and specifically in equations (3-1) through (3-7) and equation (3-50). As an aid to understanding, reduced complexity model 'Q-Q plots' were used to verify the broadly normal distribution of residuals (Figure 38, Figure 39, and Figure 40). Another key element in the mathematical validation for M-ANOVAR based models, is the confidence interval and the F-values (as discussed in section 2.2, 3.3, 3.6 and 4.6) calculated for the data. Section 4 and the various tabulated results, have reported these values in great detail. By taking the M-ANOVAR approach, the acts of verifying the underlying assumptions are correct and pass key thresholds, such as ensuring sufficiently high F-values; ensures model validation was built into the M-ANOVAR process. Further model validation can be achieved with graphical assessments, and these are included herein.

Base data comparisons are used as a model validation technique, wherein predicted values from the model are plotted against the actual value of the data the model was based on. A linear result indicates a good correlation between the model and real world data [82,85]. There is some debate as to which axis the predicted values should be placed on, if additional data analysis, based on the relationship between predicted and actual results, is to be carried out [117]. However, the degree of linear correlation, regardless of which axis the predicted values is assigned to, remains the same; and the model validation technique remains valid, as a simple visual inspection of the data [117] with an assessment of the R^2 correlation value. Anderson et al. (2007) [82] also state that the exact correlation

is less critical in validating the model and that a broadly equal distribution either side of the 45^{O} line (i.e. the line the data would sit on if there were a perfect 1:1 fit between the model and the real world data) is more important. In Figure 45 through Figure 48, predicted values based on the models presented in section 4.7 (and its various sub-sections) were created that exactly mimic the values for the input data. The results (i.e. gA, gO, gM and Wmax) were plotted as a scatter plot against the actual values recorded during the experiment. This generates the 'predicted versus actual' scatter plot that allows a validation assessment of the model in question.

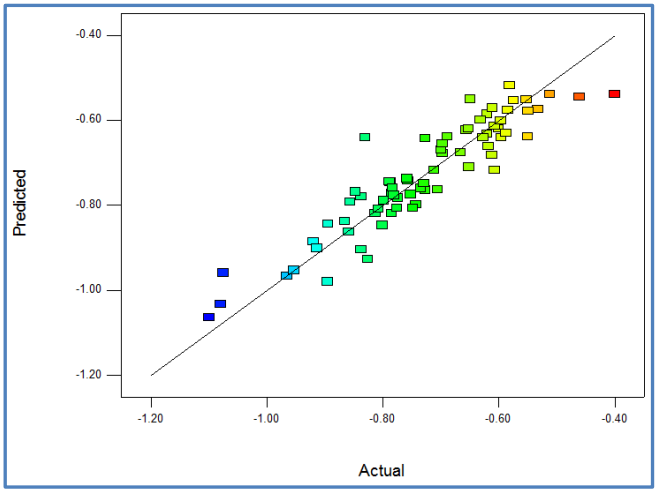

Figure 45: Activation gradient predicted Vs actual validation

Figure 45 demonstrates a strong linear relation between the predicted and actual values of activation loss gradient gA (R^2 = 0.71421 as reported previously in Table 17).

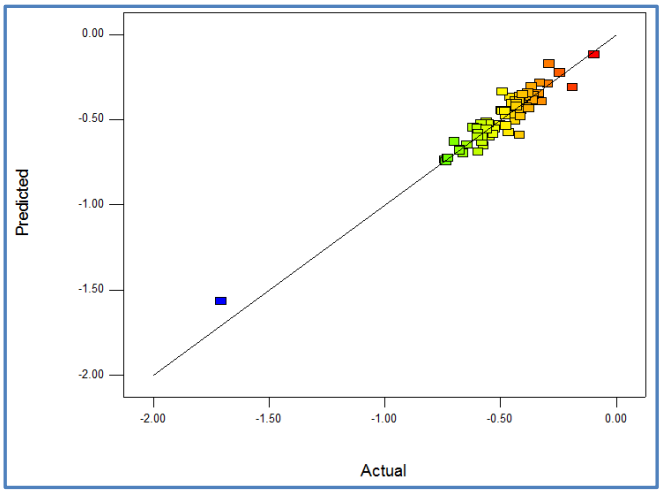

Figure 46: Ohmic gradient predicted Vs actual validation

Figure 46 demonstrates a very strong linear relation between the predicted and actual values of Ohmic loss gradient gO (R^2 = 0.64220 as reported previously in Table 22).

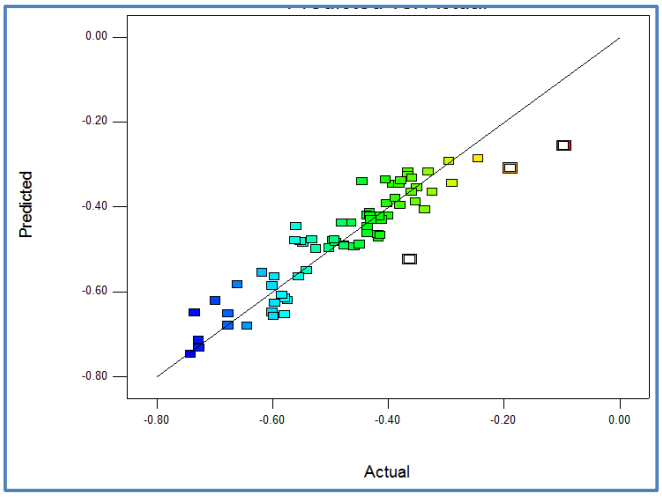

Figure 47: Mass transport gradient predicted Vs actual validation

Figure 47 demonstrates a fair degree linear relation between the predicted and actual values of Mass loss gradient gM (R^2 = 0.69836 as reported previously in Table 27).

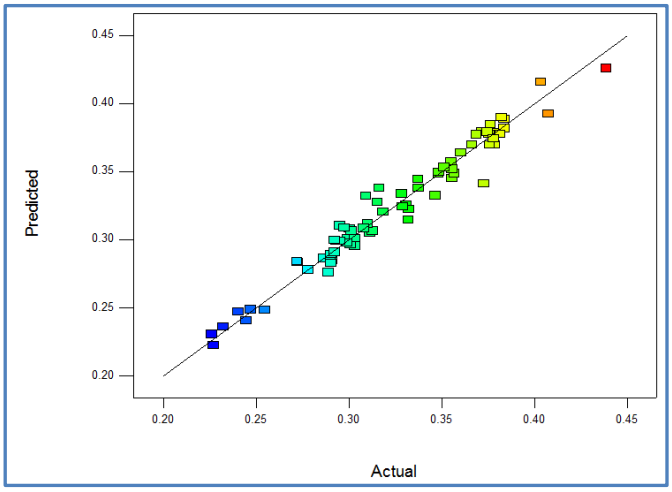

Figure 48: Peak power predicted Vs actual validation

Figure 48 demonstrates a fair degree linear relation between the predicted and actual values of the mass loss gradient gM (R^2 = 0.8197 as reported previously in Table 33).

Lastly, validation of the model can be achieved by the use of forecasting [81,87], in which predictions are made for samples that have not been included in the developed model, and comparisons are then made. Sufficient MEA fabrication materials were retained to manufacture three additional test pieces for model validation through forecasting. These test pieces were randomly assigned places in scheduled experiments. Note that samples 13 and 14 are identical in construction, and variation between them was purely due to experimental error. Input variables for the forecast validation are shown in Table 39.

Table 39: Input variables for reduced complexity model forecast validation

ID	Tbar	Tmax	Wt%PTFE	Thickness	H2O θ	Mean pore µm	% porosity	MPL	Structure
13	70.02	71.7	5	235	112	842	36.5	Yes	paper
14	69.2	73.7	5	235	112	842	36.5	Yes	paper
90	66.09	67	13	180	114	1528	44.9	No	paper

Table 40: Reduced complexity model forecast accuracy assessment

ID = 13	**Forecast**	**Actual**	**Forecast Accuracy**
gA	-1.10388	-0.562377	1.96
gO	-0.26462	-0.327505	0.81
gM	-0.59404	-0.327505	1.81
Wmax (W. cm^{-2})	0.37819	0.390078	0.97
ID = 14	**Forecast**	**Actual**	**Forecast Accuracy**
gA	-1.10388	-0. 562152	1.96
gO	-0.22693	-0. 429273	0.53
gM	-0.56024	-0. 429273	1.31
Wmax (W. cm^{-2})	0.37952	0.375815	1.01
ID = 90	**Forecast**	**Actual**	**Forecast Accuracy**
gA	-0.84852	-0.723662	1.17
gO	-0.61115	-0.690131	0.89
gM	-0.87331	-0.690131	1.27
Wmax (W. cm^{-2})	0.262485	0.254484	1.03

In Table 40 it can be seen that the model performed with a high degree of accuracy in predicting the peak power output ($W.cm^{-2}$), with accuracy values approaching 1 (+/- 0.03). The gradients of the polarising curve were far less accurately modelled. As has been discussed previously (see section 4.4.1, 4.4.2, 4.5.2, 4.5.6 and 4.6), the lack of accuracy for gA and gM were not surprising. The lack of accuracy in the gO (Ohmic loss region gradient) of +/- 0.26 (mean value) was not expected. All previous indications were that gO was correlating reasonably well (see Figure 46) and a forecast accuracy approaching one, was anticipated.

Across the three forecast samples, gO accuracy achieved an average of 0.74. The coefficient of variance (CV) is one method by which the degree of variability around the mean can be quickly and easily quantified and is defined in equation (4 28):

$$CV = \frac{s}{\bar{x}} \tag{4-28}$$

[81,83,85]

The reported accuracy variability of the gO prediction was quite high (CV= 0.254). Therefore, it was concluded that while the prediction centres were close to the population mean, the degree of variability was higher than initially predicted. High reliability (low P-value>F probabilities) were generated for the gO model, as shown in Table 21, Table 22 and Table 23. It is suggested that the most logical explanation of the high variability of the gO model (+/- 26%) is a low trueness. The model for gO is centred close to the 'true value' of gO for a given set of variables, but has a greater range of possible values. This increased range of values is referred to as the trueness [118] of a model. Trueness is best explained by analogy with target shooting (see Figure 49): Consider two models that simulate the location of a shot at a target (the black star in Figure 49). The experiment is then carried out for two different marksmen, each taking four shots at the target.

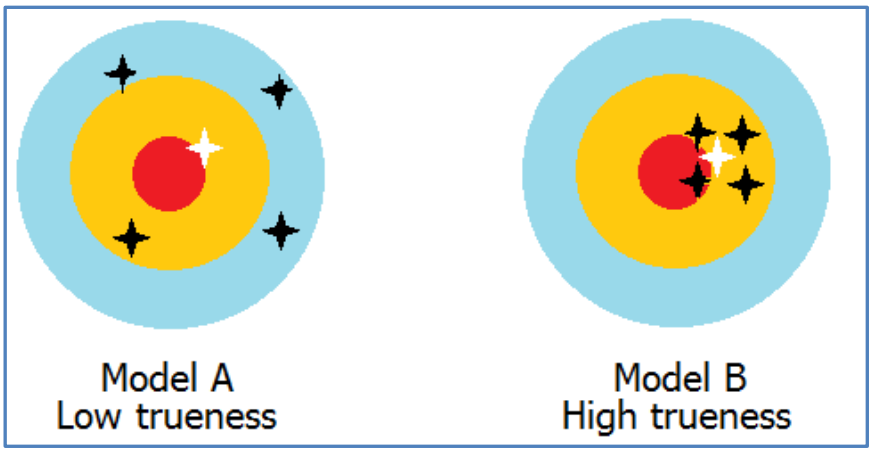

Figure 49: Trueness target analogy

Figure 49 gives an example of this analogy, showing two possible models. Both place the mean position of the actual shots fired (the white star in Figure 49) in the same approximate position. The recorded data for the shots (the black stars in Figure 49) are clustered around the central predicted point. Both are reasonable models and predict reasonably well the mean location of a given shot (the white star in Figure 49), but they have different 'trueness' in terms of their ability to model the degree of variation between individual shots.

The prediction for peak power in $W.cm^{-2}$ had a high degree of trueness, as anticipated by the previous validation exercises outlined so far. Mean accuracy was calculated at 1.003, with CV = 0.030. Returning to the target analogy; the 'marksman' being simulated in the Wmax model clusters its 'shots at the target' much more closely than the 'marksman' for the gradient of the Ohmic loss region.

4.10.1. Repeatability of results

As discussed previously in section 4.6, and demonstrated graphically in Figure 36, repeatability is something of an issue for small numbers of samples. It is clear that many of the categories under investigation had a high degree of variability. So much so, that traditional OFAT attempts to understand the information presented offer limited useful information. It has been shown in previous sections of this thesis (see section 2.2, 3 and 4) that the use of M-ANOVA methods offer the ability to account for multiple variables and their impact on the final result. This is especially true for the Wmax model as recently demonstrated in section 4.10. Great efforts have been undertaken to detail the methods used in the application of M-ANOVAR techniques, and to provide sufficient understanding that future readers of this thesis can apply these statistical methods to other areas of fuel cell research. Therefore, so long as a suitable statistical software package is available (e.g. Matlab ®, R, Minitab®, Maple®, Design Expert Pro® and others), there is no reason why these experiments could not be replicated by other researchers. Even without such bespoke software sufficient detail has been provided that future researchers should be able to conduct M-ANOVAR analysis on their experiments (though replicating these types of calculations by hand or in more widely available spreadsheet software would be extremely labour intensive).

4.10.2. Validation conclusion

The statistical M-ANOVAR model used for this work, was an accurate model of the impact GDMs have on the performance of PEMFCs. Peak power performance can be predicted with greater than 95%CI (see section 4.6) and with a very high degree of trueness (see section 4.10). The gradient of the Ohmic region can also be predicted, though experimental variability was far greater for this prediction (+/- 26%). Attempts to predict the impact GDMs may have on the gradient of the activation and mass transport regions of polarisation curves, is not recommended by the author. Thorough error assessment has been undertaken, and the overall models for each type of GDM (Paper, Non-woven and Woven with or without MPL) all pass the appropriate F-test. It is therefore sugusted that multivariate analysis is a useful tool for modelling GDMs, and PEMFCs. Having established the usefulness of the models, section 4.11 goes on to discuss the outputs generated by the models and to discuss their likely significance in terms of understanding the impact GDM properties can have on the overall performance of PEMFCs.

4.11. Key findings from developed models

Recall from equation (3-26) and Table 7, they key measure for rejecting hypothesis zero (i.e. H_0 = "A simple mean is a better model than the more complex multivariate ANOVAR method") is the F-Test.

The F-distribution, is a family of distribution curves with a shape that varies with the degrees of freedom (the number of data points), of the information being analysed. The F-Test addresses the probability that a more complex model could generate useful answers 'by luck', rather than because the model is correct. Assuming the true answer is a set of random, normally distributed, numbers; it has repeatedly been shown [28,29,78,79,81,83] that the probability of a more complex model being correct by 'accident' reduces as the F-value increases. The F-Test generates a 'critical value' associated with the desired likelihood (usually set at 95% for example) associated with the F-distribution curve for a particular number of degrees of freedom. If the F-value calculated for the model is greater than critical F-Value for that specific F-distribution curve, then the probability threshold has been passed, and it is unlikely that the model is incorrect: Therefore, the researcher can reject H_0, and accept that the more complex model is probably correct (i.e. accept H_1). The more the model F-value exceeds the critical F-Value, the more likely is to be correct. This relationship is shown schematically in Figure 50 for a generic F-distribution, in which the hypothesised 95% level is reached when F is calculated to be 2.5.

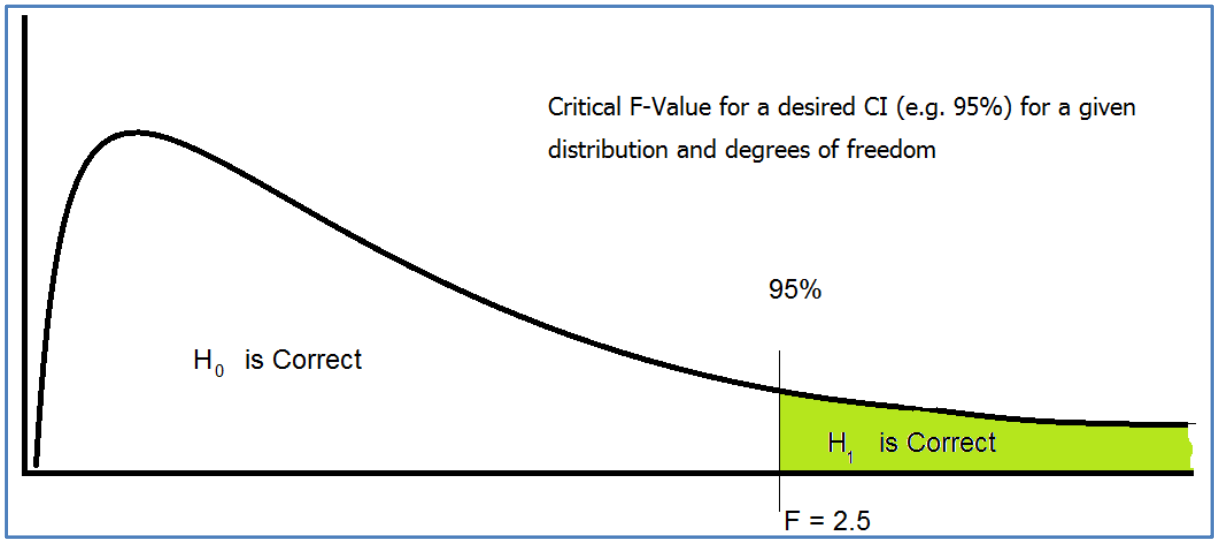

Figure 50: F-test example

The p-value relates to the critical F-value. The p-value is the probability of falsely rejecting a given hypothesis (so smaller P-values are desirable) [82].

Table 41: Summary of reduced complexity models and F-Values

Model	Degrees of freedom	F-Value	P-value*	Model detail can be found in:
gA Model	14	10.17489	0.0000	Table 16
gO Model	8	14.13478	0.0000	Table 21
gM model	10	14.12268	0.0000	Table 26
Wmax Model	15	16.9672	0.0000	Table 32

*Values from Design Expert Pro

The values generated were produced using Design Expert Pro software. Design Expert Pro does not calculate P-values lower than 0.0001 (i.e. a less than 0.01% chance of rejecting H_0 in error).

In each case, the model F-test values indicate a p-value with a less than 0.01% chance of the model not being a suitable way to navigate the design space of the experiments. On the basis of this result, it was concluded that the comparison of cell performance by the 'gradient of polarisation regions' method, is a valid way to make numeric comparisons between polarisation curves (within the +/- 26% error bound). As discussed in sections 3.6.2 and 4.6, and also in equation (4-17); the adaptation of traditional ANOVAR to multiple input and output variables increases the likelihood of error. The probability calculation should be adjusted accordingly. Fortunately, the F-Values generated sit firmly in excess of the 95% confidence limit, and the corresponding p-value>F reported by the software is in actuality no greater 0.0116 (i.e. a 1.16% chance that H_0 was rejected in error) as discussed in 4.6. Therefore the models generated are likely to be useful. It has been shown that the accuracy of the activation and mass transfer loss gradient models was not sufficient. The Ohmic loss gradient can be modelled with a fair degree of accuracy, but the range of likely values was such that caution must be used when using the gO model. The peak power model prediction is extremely accurate (+/- 3%)

There are several key assumptions in this statement:

- The MEAs tested must be of the same overall charge density ($A.cm^{-2}$).
- Comparisons of MEA gradients have only been validated on two very similar test setups.
- It is possible that different fuel cells, gas flow geometries and other factors for different experimental set-ups could have a negative impact on the utility of this method.
- Test conditions, reactant flow rates and all other experimental parameters must match (as far as is possible) to ensure the validity of this approach.
- The gradient measure should always be considered along with an absolute measured value, such as the peak power, to avoid errors caused by shifts in the absolute location of the gradient being considered.

It is possible that the method is, in fact, more robust than these assumptions state, but this requires additional work to validate. Having validated the measured differences between regions for different MEAs, the MEAs tested were analysed. Perturbation plots (see Figure 51 and Figure 52 for examples) were made of the design space, in which the impact of all factors were plotted against an arbitrary scale (the 'desirability' of a given input factor): in this case, all inputs were equally important and have a desirability of '1'.

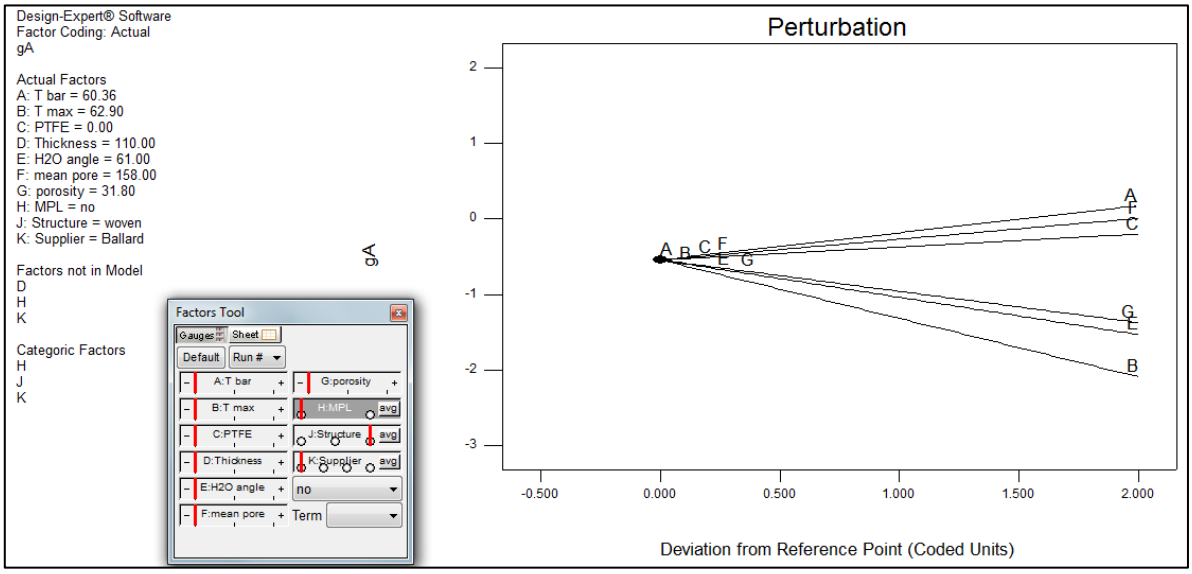

Figure 51: Perturbation graph for reduced complexity model gA

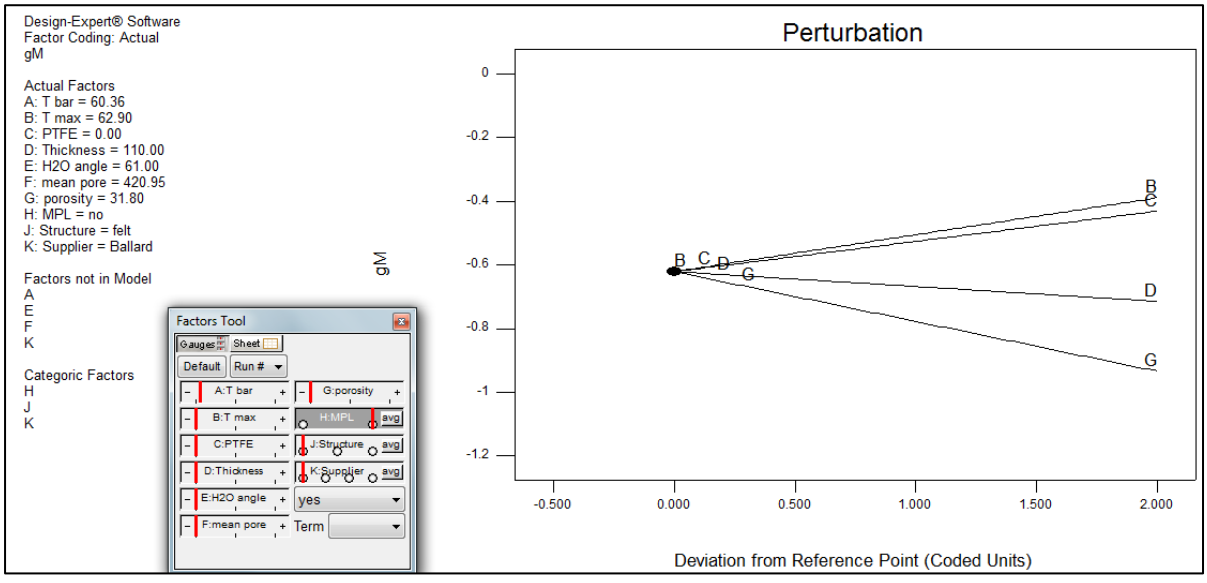

Figure 52: Perturbation graph for optimisation model gM

The perturbation graph (Figure 51 and Figure 52) can be considered a 'one factor at a time' (OFAT) representation of the experimental data. Its primary use is in assigning likely variables as an axis for subsequent surface plots. The lines that deviate away from the horizontal are usually the best choice for applying as an axis in subsequent surface plots [82]. As can be clearly seen in Figure 51 and

Figure 52, the following factors all deviate away from the horizontal and so were well suited to displaying the data in subsequent surface plots (Figure 55 through Figure 60):

- G (% porosity) will be selected for one axis.
- E (H_2O contact angle).
- B (T-max).
- D (through-plane thickness).

The identified input factors were all suitable contenders for the remaining two axes for any surface plots generated. In terms of understanding the overall fuel cell performance, the mean temperature during operation (T-bar) is also of interest, and may be included as a preference to T-max if a useful conclusion can be drawn from the data. It became apparent that the impact of 'T-max' compared to 'T-bar' was a simple upward shift to the overall performance result. In this instance, T-bar was selected as the more representative value of the test conditions realised during the experiments.

While it is possible to analyse the data for all four output factors, gO (gradient of the Ohmic region), and Wmax (peak power output in Watts per cm^2) were focused on as being of the most interest. As shown in Table 40, peak power and, to a lesser extent, the gradient of the Ohmic loss region (gO) were the best suited to the type of M-ANOVAR analysis undertaken in this thesis.

The gradient of the Ohmic region should ideally be as level as possible (close to zero) as the Ohmic region is typically considered the optimum operating condition of a fuel cell system [24]. It is possibel that the gradient of a given region can alter its absolute position along the x-y axis, without it being clearly visible in the analysis.

To overcome this, the $Watts.cm^{-2}$ value provides a fixed point in the data to consider, and is more readily understandable (and comparable) in a fuel cell research context [58]. There were several other points that could have been selected (voltage at set load current for example), but it is thought at this time that the two output variables ('Wmax' and 'gO') were sufficient for this analysis.

4.11.1. Reduced complexity model responses

This model was derived from the following design spaces for each structural GDM type and should be considered valid within these settings. Note that projection beyond this region, increases the error and is not advised. Figure 53 shows the 'design cube' for the gO model created. The model is considered correct within the limits of the factors shown in the cube:

- 110µm > Thickness of GDM > 420µm.
- 31.8% > porosity of GDM > 73%.
- $60.3^{O}C$ > Mean temperature during polarisation test > $73^{O}C$.

Figure 54 shows the ‘design cube’ for the Wmax model created. The model is considered correct with the limits of the factors shown in the cube:

- 110µm > Thickness of GDM > 420µm.
- 31.8% > porosity of GDM > 73%.
- $60.3^{O}C$ > Mean temperature during polarisation test > $73\ ^{O}C$.

Using the model outside of these limits increases the error in an undefined way and is not advised. The numeric values shown adjacent to each corner of the design cube (Figure 53, and Figure 54) are the model outputs, at the extreme values, for each of the displayed factors.

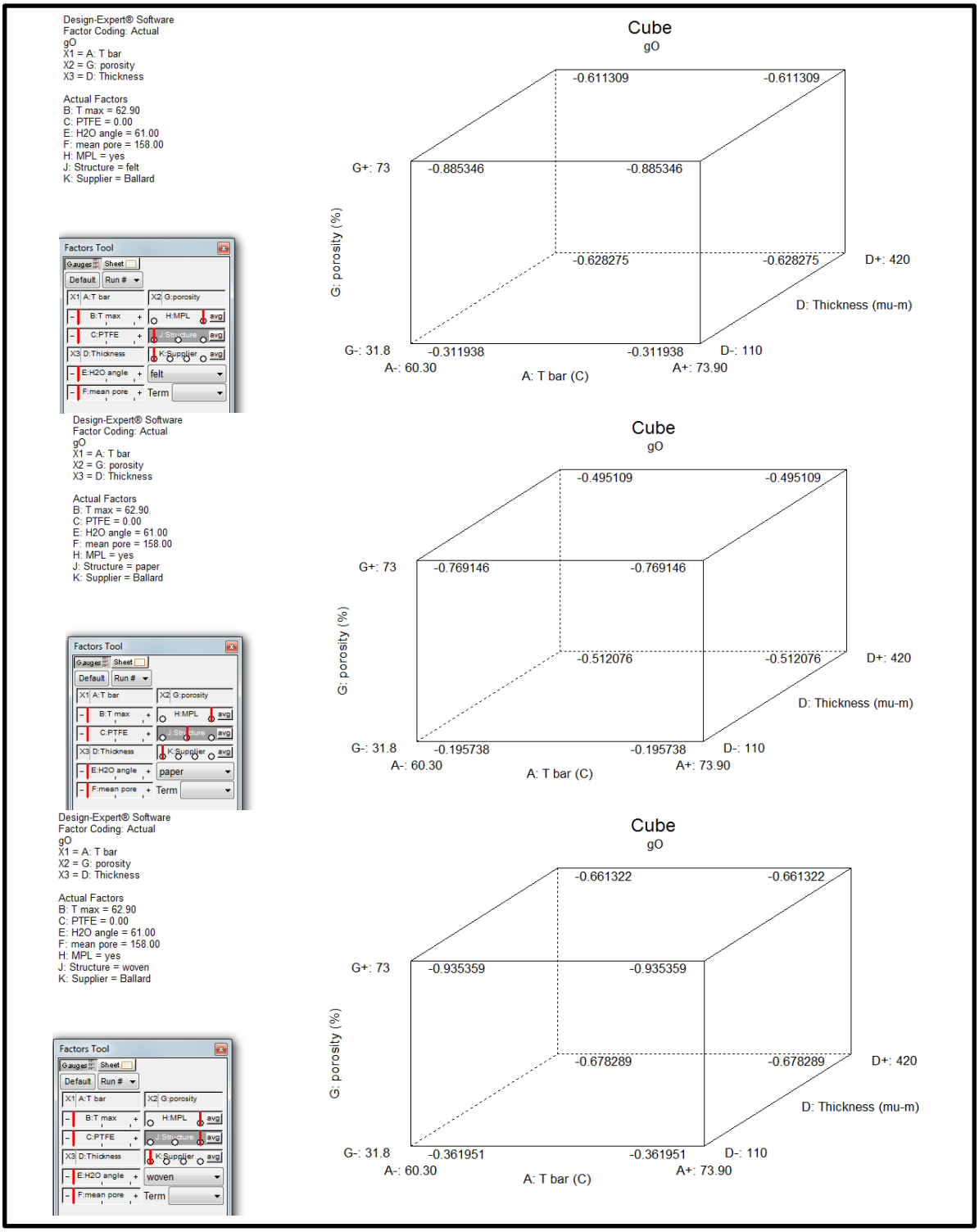

Figure 53: 'Design Cube' for gO models

(non-woven (top), paper (middle) and woven (bottom) GDMs)

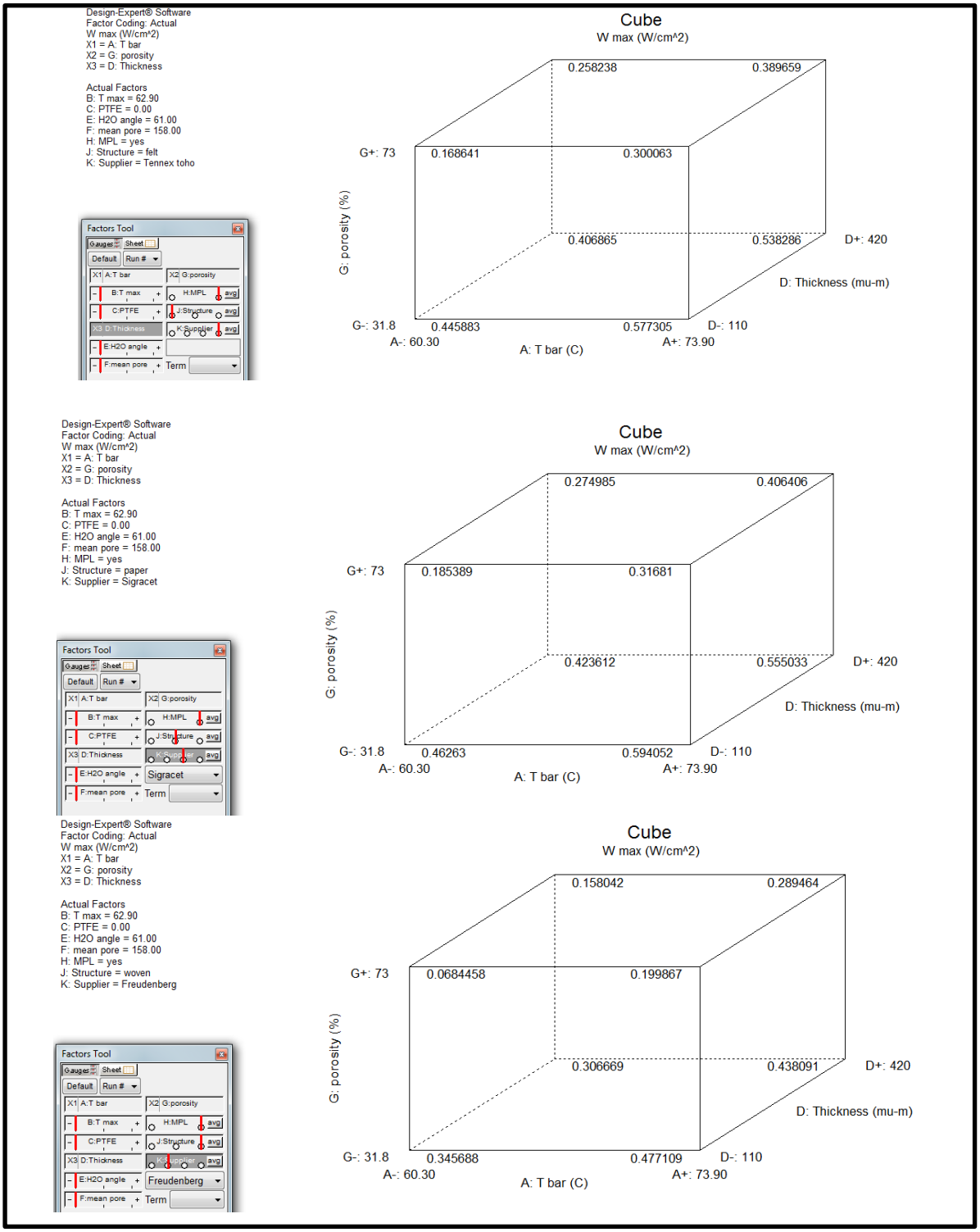

Figure 54: 'Design Cube' for Wmax models

(non-woven (top), paper (middle) and woven (bottom) GDMs)

It is important to bear in mind that there are more than three factors in each model, but it is difficult to visualise this.

4.12. Reduced complexity regression for GDMs conclusion

The backwards step elimination of insignificant terms (detailed in sections 3.7, 3.8, 4.5, 4.6, 4.7 and 4.8), reduced the number of terms in the model (i.e. reduced complexity) without a reduction in the usefulness of the models created as shown in section 4.10. The models have been shown to be robust (i.e. not unduly influenced by extreme values) as Adjusted R2 = Predicted R2 +/- 0.2 [81,84]; this was shown in Table 22 and Table 33 for the gO and Wmax models respectively. Having established the credential of the proposed model the response surface plots generated were used to explore the design space. The response surface plots, shown (Figure 55 through Figure 60), map the developed models (gO model shown in Table 24 with categoric factor detail in Table 25, the Wmax model in Table 35 with categoric factor detail in Table 36, Table 37 and Table 38) across all points, within the limits of the design cube as discussed in section 4.11.1 (Figure 53 and Figure 54). The models graphically represent the result for mean temperature (Tbar) and porosity, and their impact on the model output results (either the gradient of the Ohmic region for gO plots or the peak power result for Wmax plots). The base plane on the response surface plots (Figure 55 through Figure 60) show a yellow field with contour lines to highlight lines of curvature in the response surface. In all cases (Figure 55 through Figure 60) the contour lines are straight, and no measurable curvature was detected. Findings discussed in the initial conclusions in section 4.6 (other than those attributed to machine variables) remain true. It was found that:

- In the gO plots (Figure 55, Figure 57 and Figure 59) the response for porosity dominates across all settings except for through-plane thickness.
- In the Wmax plots (Figure 56, Figure 58 and Figure 60) the response for porosity dominates across all settings except for through-plane thickness.

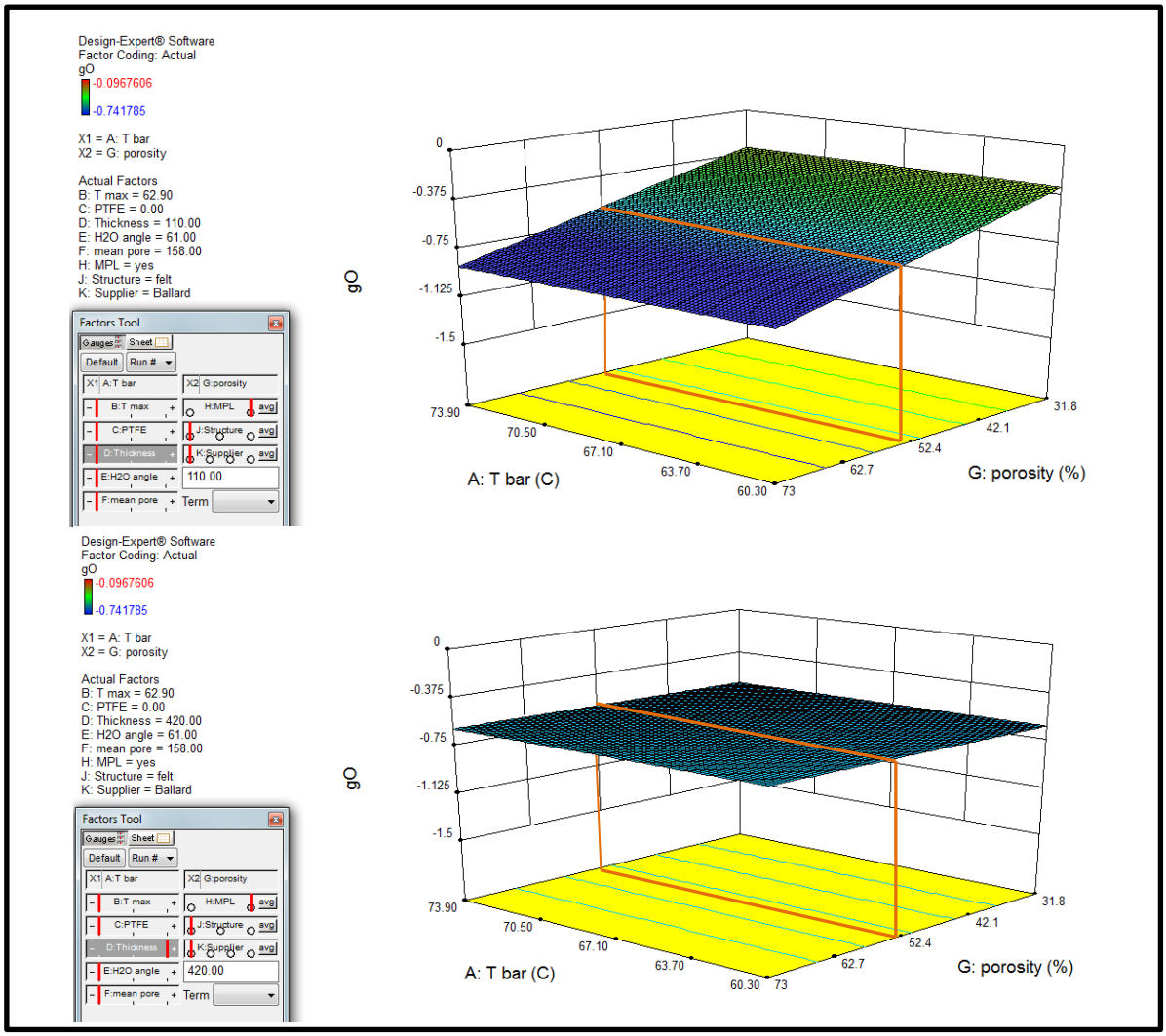

Figure 55: gO Through-thickness 'Felt' interactions

(Through-plane thickness 110 µm (top) and 420µm (bottom))

Examining Figure 55 in more detail, a comparison is made of the impact through-plane thickness of the GDM has on the performance of the Ohmic gradient for 'felt' GDMs. Overall there is a significant change, with lower thickness (110µm 'top') GDMs favouring lower porosity levels. That is to say, an Ohmic loss gradient closer to zero is considered preferable; as this indicates mass transfer losses are less likely to limit the performance of the fuel cell (see section 1.1 and Figure 4 for further clarification). Conversely, thicker through-plane GDMs (420µm 'bottom'), perform equally well across a wide range of porosity values, though fail to achieve the preferred gradient. It is interesting to note there is a 'region of stability' at approximately 53% porosity (highlighted with orange lines in Figure 55), where there is very little change to the gO result.

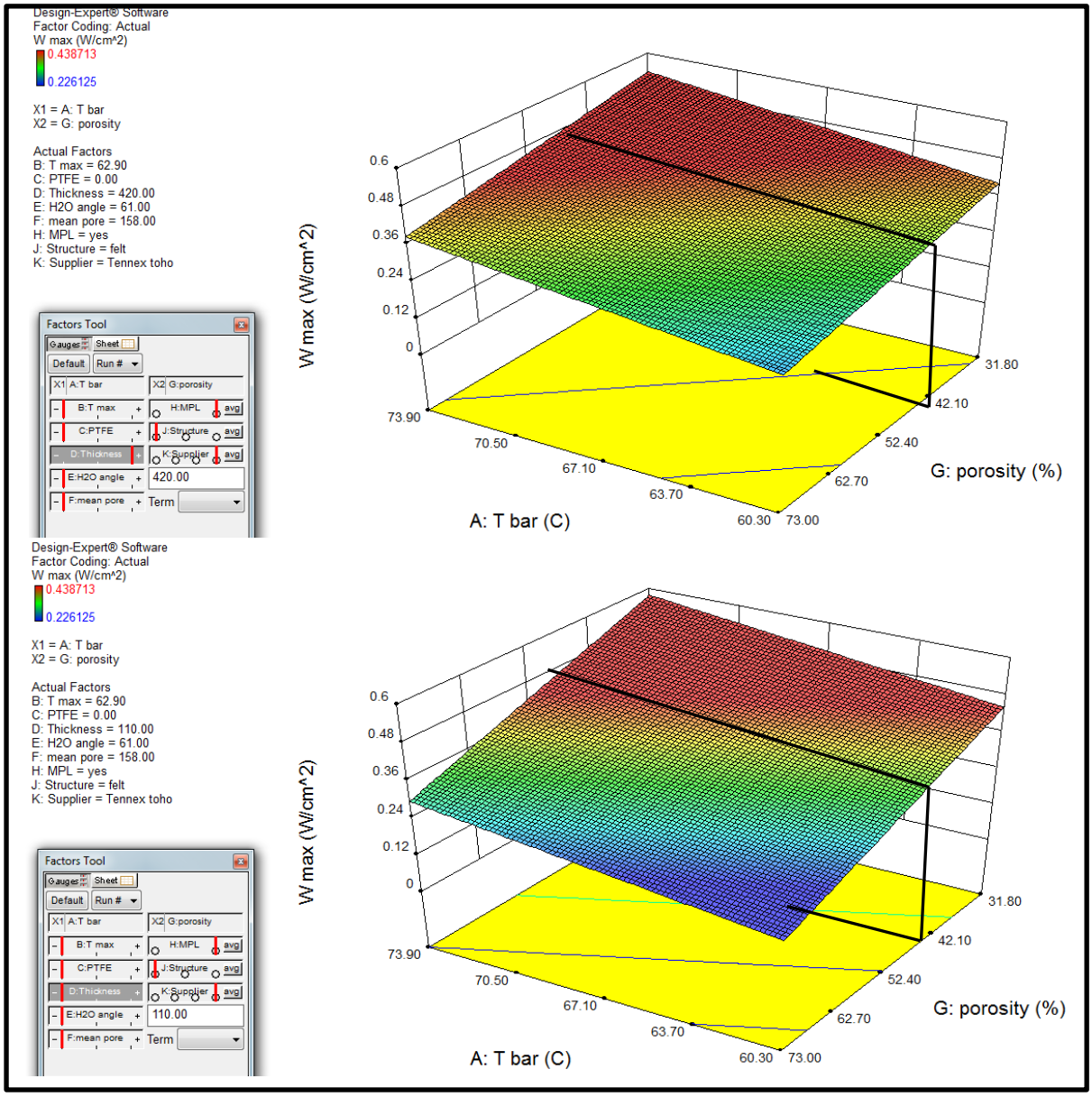

Figure 56: Wmax through-thickness 'Felt' interactions

(Through-plane thickness 110 µm (top) and 420µm (bottom))

Examining Figure 56 in more detail, a comparison is made of the impact through-plane thickness has on the performance of the peak power (in $W.cm^{-2}$) for 'felt' GDMs. Overall, there is a significant change with lower thickness (110µm 'top') GDMs favouring lower porosity levels. That is to say, the maximum achievable peak power is 0.562 $W.cm^{-2}$ (see section 1.1 and Figure 4 for further clarification). It is apparent that the lower thickness model performs less well at very high porosities, with the minimal peak power reading 0.158 $W.cm^{-2}$. Conversely, thicker through-plane GDMs (420µm 'bottom') show a more uniform performance across a wide range of porosity values (maximum = 0.522 $W.cm^{-2}$, minimum = 0.246 $W.cm^{-2}$). It is interesting to note the 'region of stability' (highlighted with orange lines in Figure 55), is also evident, though for the Wmax model,

this region has shifted to a lesser value of porosity of approximately 42.5% (highlighted with black lines in Figure 56).

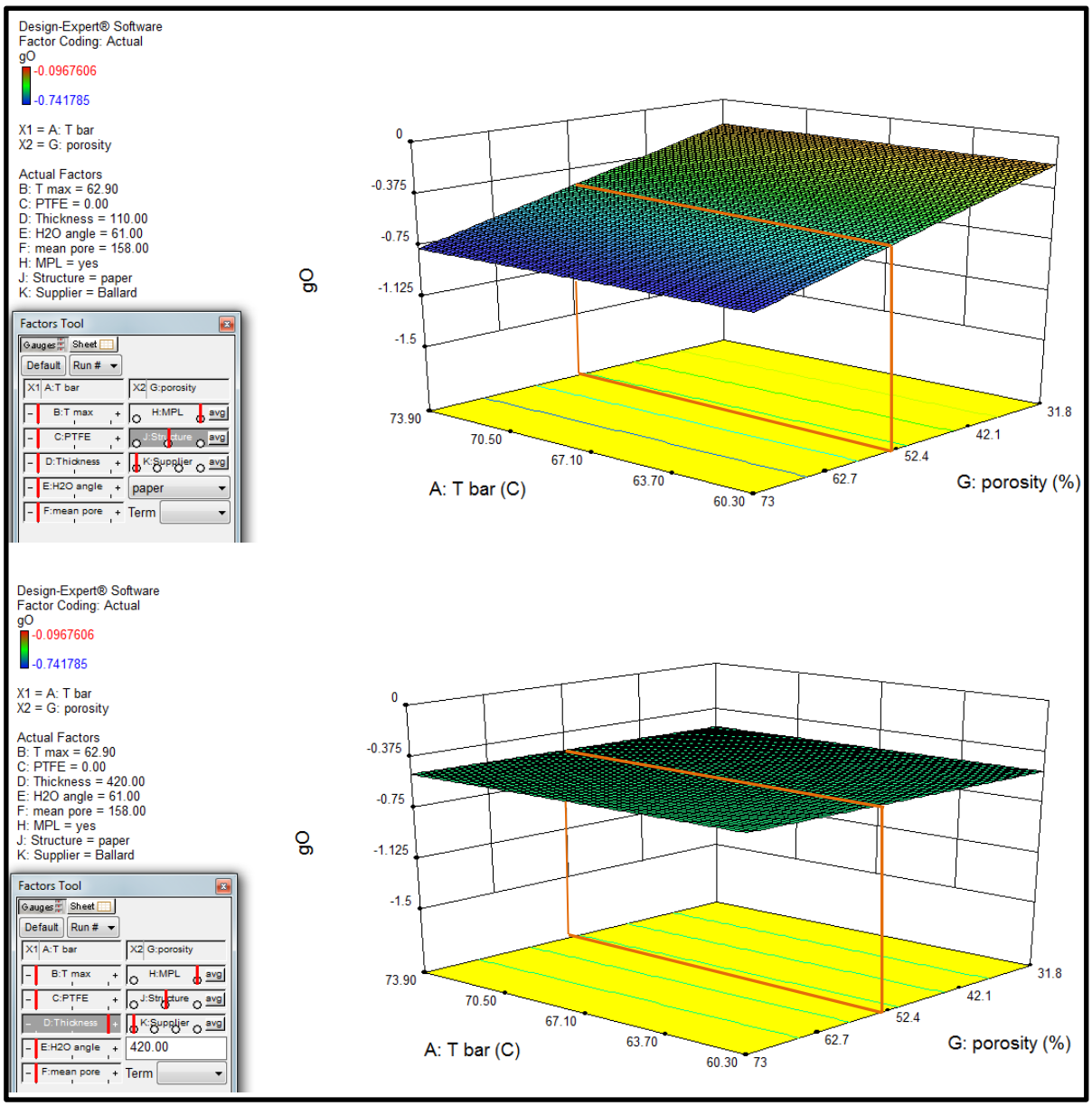

Figure 57: gO Through-thickness Paper interactions

(Through-plane thickness 110 µm (top) and 420µm (bottom))

Examining Figure 57 in detail, a comparison is made of the impact through-plane thickness of the GDM has on the performance of the Ohmic gradient for 'paper' GDMs. Overall, there is a significant change with lower thickness (110µm 'top') GDMs favouring lower porosity levels. That is to say, an Ohmic loss gradient closer to zero is considered preferable; as this indicates mass transfer losses are less likely to limit the performance of the fuel cell (see section 1.1 and Figure 4 for further clarification). Conversely, thicker through-plane GDMs (420µm 'bottom') perform equally well across a wide range of porosity values, though fail to achieve the preferred gradient. It is interesting

to note, there is a 'region of stability' at approximately 53% porosity (highlighted with orange lines in Figure 57), where there is very little change to the gO result.

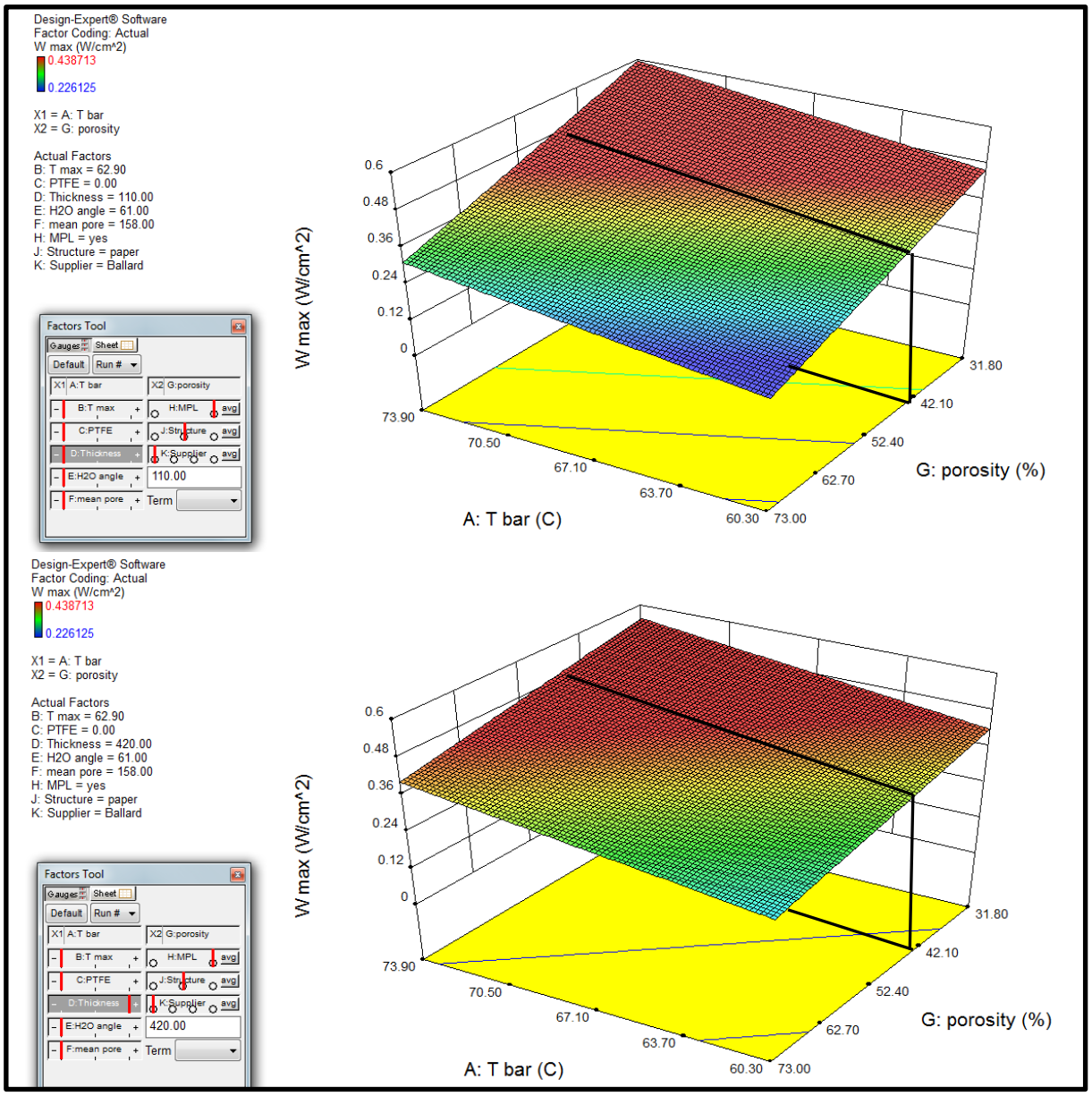

Figure 58: Wmax Through-thickness paper interactions
(Through-plane thickness 110 µm (top) and 420µm (bottom))

In Figure 58, a comparison is made of through-plane thickness of the GDM on peak power (in $W.cm^{-2}$) for 'paper' GDMs. Overall there is a significant change with lower thickness (110µm 'top') GDMs favouring lower porosity levels. That is to say the maximum achievable peak power is 0.592 $W.cm^{-2}$ (see section 1.1 and Figure 4 for further clarification). It is apparent that the lower thickness model performs less well at very high porosities, with the minimal peak power reading 0.190 $W.cm^{-2}$. Conversely, thicker through-plane GDMs (420µm 'bottom'), shows a more uniform performance across a wide range of porosity values (maximum = 0.554 $W.cm^{-2}$, minimum = 0.276 $W.cm^{-2}$). Note

a ‘region of stability’ (highlighted with orange lines in Figure 57), is also evident, though for the Wmax model, this region has shifted to a lesser value of porosity of approximately 42.5% porosity (highlighted with black lines in Figure 58). In the Wmax model for paper GDM, there is also a slight increase in peak power (+0.02 $W.cm^{-2}$) at approximately 42.5% porosity point for thicker 420µm GDMs compared to the thinnest (110 µm) GDMs.

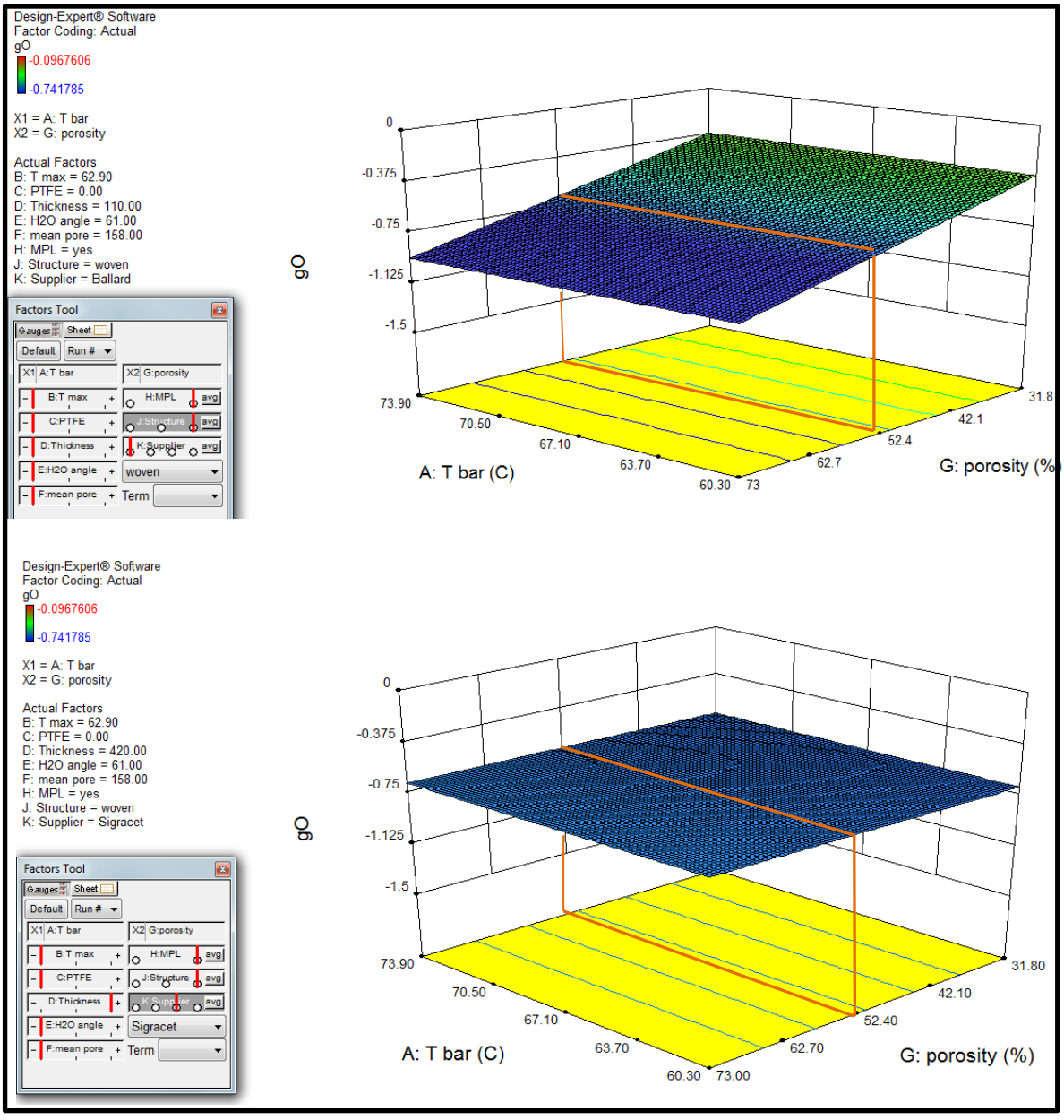

Figure 59: gO through-thickness woven interactions

(Through-plane thickness 110 µm (top) and 420µm (bottom))

Figure 59 details a comparison of through-plane thickness of GDM, on the performance of the Ohmic gradient for ‘paper’ GDMs. Overall, there is a significant change with lower thickness (110µm ‘top’) GDMs favouring lower porosity levels. That is to say, an Ohmic loss gradient closer to zero is considered preferable; as this indicates mass transfer losses are less likely to limit the performance of

the fuel cell (see section 1.1 and Figure 4 for further clarification). Conversely, thicker through-plane GDMs (420µm 'bottom'), perform equally well across a wide range of porosity values, though fail to achieve the preferred gradient. Note there is a 'region of stability' at approximately 52.5% porosity (highlighted with orange lines in Figure 59), where there is very little change to the gO result.

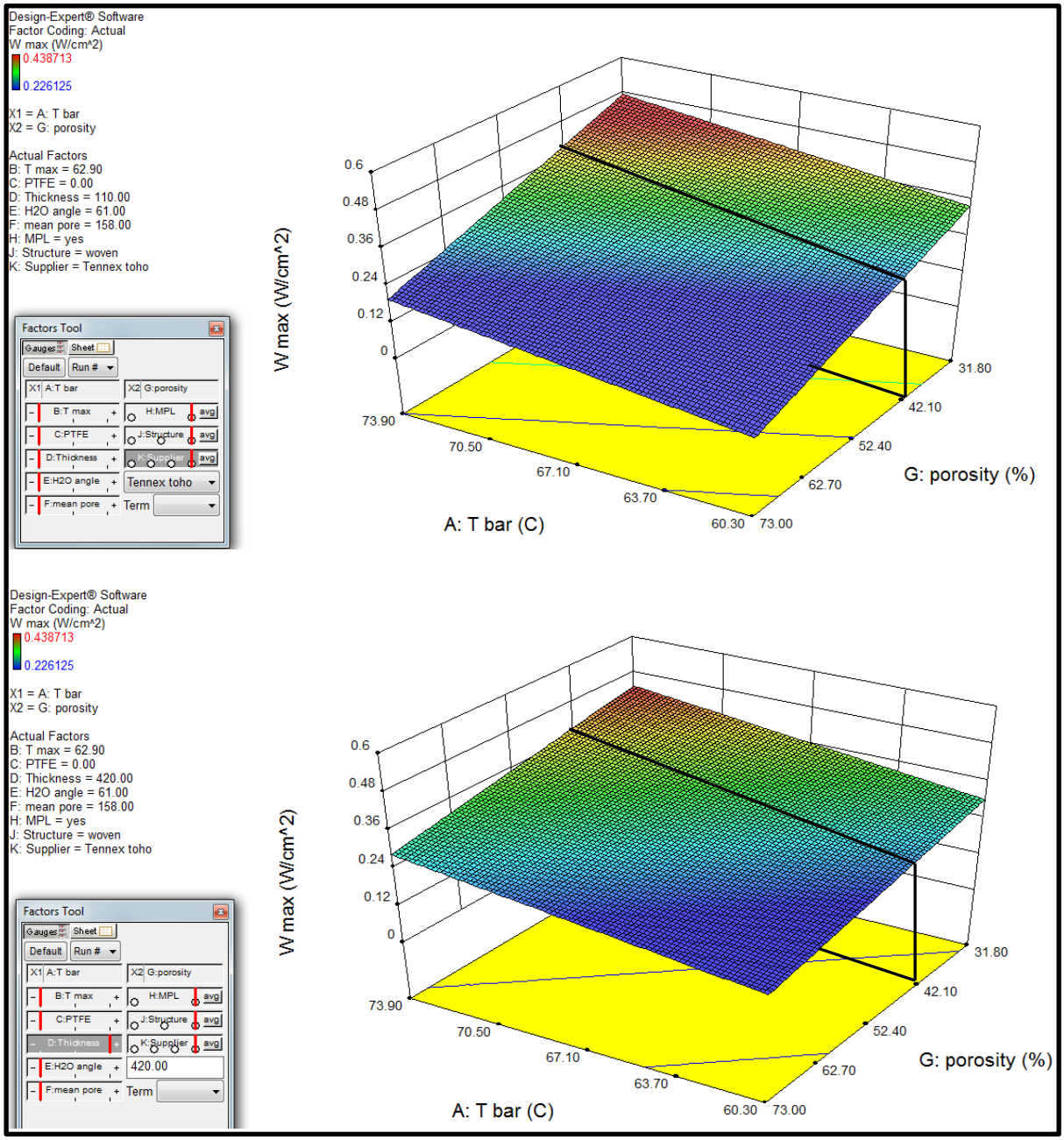

Figure 60: Wmax Through-thickness Woven interactions

(Through-plane thickness 110 µm (top) and 420µm (bottom))

In Figure 60, a comparison is made of through-plane thickness of GDM on peak power 0.48 W.cm^{-2} woven GDMs. Overall, there is a significant change with lower thickness (110µm 'top') GDMs favouring lower porosity levels. That is to say, the maximum achievable peak power is 0.473 W.cm^{-2} (see section 1.1 and Figure 4 for further clarification). It is apparent that the lower thickness model

performs less well at very high porosities, with the minimal peak power reading 0.076 W.cm^{-2}. Conversely, thicker through-plane GDMs (420µm 'bottom') show a more uniform performance across a wide range of porosity values (maximum = 0.436 W.cm^{-2}, minimum = 0.165 W.cm^{-2}). Note the 'region of stability' (highlighted with orange lines in Figure 59) is also evident, though for the Wmax model this region has shifted to a lesser value of porosity; approximately 42% porosity (highlighted with black lines in Figure 60).

The porosity and temperature surface response plots demonstrate a very strong through thickness effect. The peak performance for the Ohmic region (i.e. gO approaches zero) is achieved in all three structures tested, by minimising the through-plane thickness. The impact of porosity on the effect is harder to explain. It can seen that the lower porosity values (less than around 50%) are preferable, perhaps due the increased density of the system.

Even the inclusion of temperature does not significantly alter the effect, despite the well-established links to temperature and performance in every other metric measured. The minimisation of the porosity and through-plane thickness factors, dominates all other considerations. This remains true across all structure types, with woven structures performing moderately worse. Discussions around the impact of pores tend to focus on mass transport through the system. Larger pores require the least amount of pressure to allow water to penetrate [119]. The pore size and capillary pressure relationship is given as:

$$\Delta P = \frac{2\gamma_{water} cos\theta}{r_{pore}} \qquad \textbf{(4-29)}$$

where γ = the surface energy of water, and r_{pore} is the radius of a given pore and θ is the pore filling factor [119] as detailed in section 4.2.1. The resultant pressure value, is the amount pressure required to force water to enter a pore of this size. This concept is the basis of the strong recommendation that a variety of pore sizes is preferential to optimise performance. Smaller pores will remain open for gas flow, while larger pores will dominate liquid water transport. Based on this theory, woven GDMs should dominate performance in most cases. The bimodal pore distribution between threads and the weft-warf of the weave itself, maximises the bimodal pore distribution in an ideal fashion [119]. Other authors have also commented on the importance of pore size and its distribution [120,121], and support this concept; with pore size distribution identified as being more important than either the mean pore size or total porosity in standard GDM materials. It should be observed at this point, that the construction of the 'diffusion layer' proposed in some papers referenced in this section, varies considerably from that used in these experiments; though the central arguments are still valid.

Jordan et al. (2000) [122] comment on the impact of the thickness of diffusion layers, and claim thinner GDMs are important for air based fuel cells (as opposed to oxygen based). However, their work is focused on a porous backing layer between carbon cloths and the catalyst layer, and their use of the term 'thickness' actually relates to the mass loading of this MPL. It may still provide some insight into the results from work in this thesis. Figure 55 through Figure 60 give a graphical representation of the relationship between performance, porosity and thickness of the carbon fibre based GDM for all three structures. The minimal porosity effect for improved performance is true in all materials, for both the gradient of the Ohmic loss region and the absolute peak power. Peak power settings were strongly temperature dependent but otherwise mirror the Ohmic gradient result.

It is interesting to note, the results shown from the peak power models (see Table 35 through Table 38) plotted in Figure 56, Figure 58 and Figure 60 indicate that, in high-demand and maximum-power applications, paper structures would be predicted to outperform the woven material by a significant degree. The non-woven 'felt' class of materials also outperforms the woven structure. This counteracts the usual assumption that the broad pore distribution of woven materials, are better suited to operation regions of the cell where high volumes of liquid water occur. It is possible the high demand state has not been held for long enough period, to trigger the volume of water generation required, to see the direct benefit of the woven pore-size distribution effect. The peak power measurement is an approximately 30-second 'window' of time from the 250 second duration of the polarisation curves that generated this data. Returning to the two-dimensional model from section 4.2.1, the perturbation factor was altered. Perturbation was set to a high value (0.35) to simulate the increased difficulty of liquid mass transport through reduced pores size, and reduced the overall hight of the calculated region to reflect the reduced thickness of the GDM (once again making the assumptions about initial starting temperature as per equation (4-5) and the temperature profile seen in Figure 20). The results for the increased perturbation value and reduced through-plane thickness, are plotted graphically in Figure 61 and Figure 62.

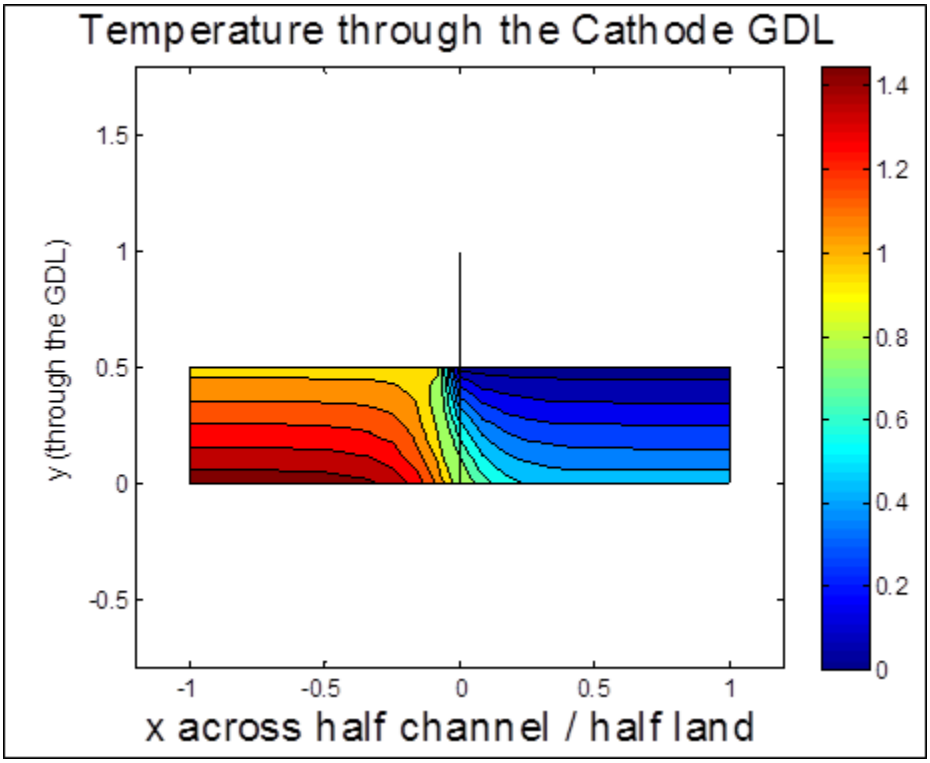

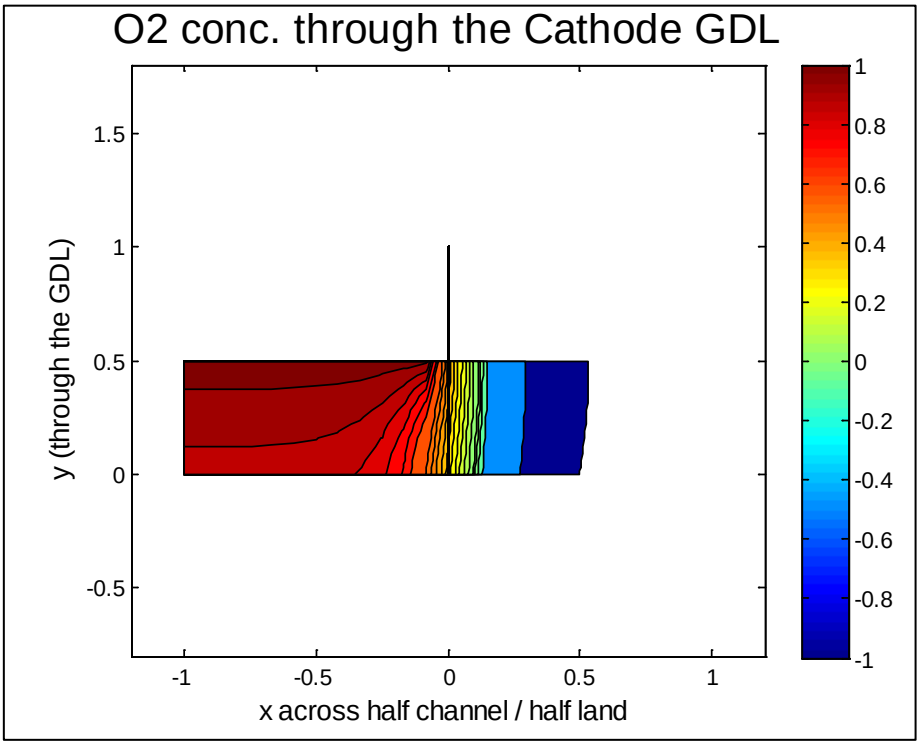

Figure 61: Reduced geometry GDM

(Steady state temperature (top) and O_2 concentration (bottom))

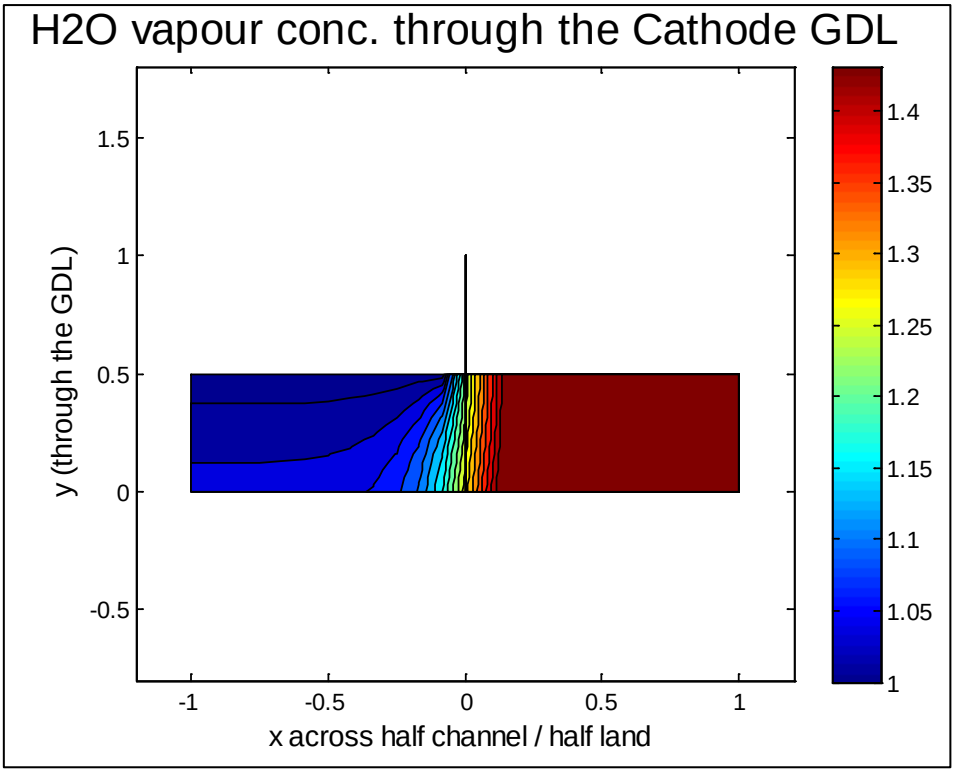

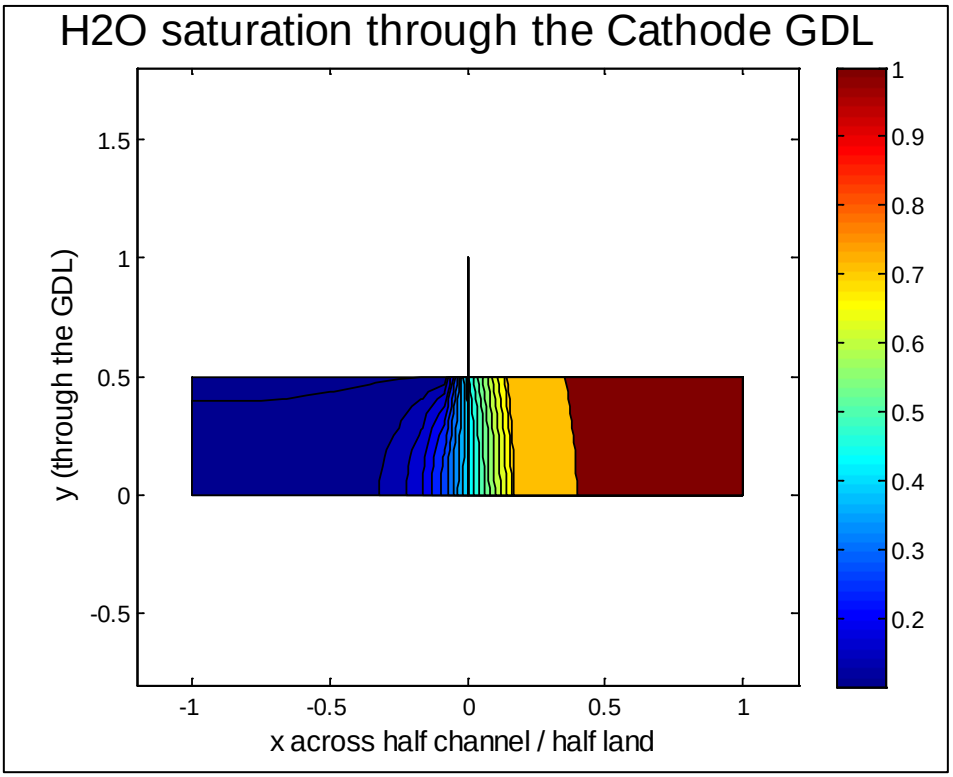

Figure 62: Reduced geometry GDM mass flow

(steady state concentrations for $H_2O_{(g)}$ (top) and $H_2O_{(l)}$ (bottom))

In Figure 62, there is a marked reduction in the O_2 concentration under the land area of the flow channel, and a marked reduction in liquid water retention under the land. The bulk of the gaseous H_2O concentration is distributed over a very narrow region (x = - 0.2 to x = + 0.2) at the channel-land boundary, when compared to the original model (x=- 0.3 to x = + 0.5). The inference being; fewer pores are 100% filled with water in the half-land region, enabling the gaseous water vapour more space to travel through.

This covariance of porosity with through-plane thickness in fibre based GDMs, has not been reported in literature before. The desirability of minimal porosity for both peak power and Ohmic loss region values, is somewhat surprising. As a general rule, pore-size distribution (the ratio of smaller to larger pores of given diameters) is highlighted as being more significant than the total porosity or mean pore size [58,120]; based on the previously discussed assumption of improved speed of water flow from preferential pore filling. It would seem logical that thinner through-plane thickness GDMs would be more desirable. The evidence here broadly supports that hypothesis as it relates to peak power but does not hold true for the gO measurement.

In the gO case, the porosity of around 50% is independent of the thickness. Porosities above this level were positively impacted (gradient approaches closer to zero) by increased GDM thickness. This is in accordance with the findings of Mason et al. (2012) [112], and part of the improved contact resistance between the monopolar plates and the GDM, is a strong contender for the source of this reduced complexity model performance.

The decrease in performance, below the (approximately) 50% porosity figure, is harder to explain. Recall that all samples were clamped to the same torque. An argument could be made that the lower porosity GDM were excessively crushed, closing reactant pathways, as the thickness increase due to its reduced density: If this were indeed the case, the Wmax criteria under the same conditions should experience a proportional and equivivlent decrease as well. This is clearly not the case: Figure 58 and Figure 60 (paer and woven GDM peak power model respectivly, show a slight redcution in peak power as thickness increases, but not to the same degree as that seen for the gO models. Figure 56 actualy deomanstrates a slight increase in peak performance as thickness increases. Consdiering the error bounds f the model, it would have to be arguied that no measurbale change in any of the Wmax GDM models was established with certainty. Therefore, this suports the argumant that reduction in mass flow is unlikely to be the cause of the drop in gO below 50% porosity for higher thickness GDMs.

It could be argued that the anticipated drop would eventually appear if the cell were operated in the steady state at maximum power and the system may eventually converge with the expectations in the literature [112], though the simplified numeric model presented in this thesis does not support this argument.

If the results reported in this thesis are correct, it has not been previously reported that transient loads can, for an unknown but significant period, ignore the effect of pore closure due to excess clamping force. Typically the Bimodal pore distribution of woven materials is cited as the reason why they outperform other GDM structures under high workloads. In testing, this was not the case. It is likely that the relatively short duration at maximum loads in the historic data test (approximately 30 seconds), have revealed there is a period where the non-woven GDM structures can equal, and perhaps even outperform, woven GDMs, even at high loads.

The conclusion from this, is that a properly designed system could optimise the contact resistance, with a suspected loss in long-duration peak power supply; if this were an acceptable operational compromise (for example constant duty cycles with relatively few high-demand periods, such as long-distance transport).

As a corollary to this, GDMs with a total porosity around 40% to 50% may be preferable in a wide variety of applications where thermal-mechanical loading can cycle the clamping force experienced by the GDM. These approximate 45% porosity GDMs, were largely indifferent to the clamping pressure applied to them (based on the findings from completed tests in the experimental design space).

4.13. Summary of Chapter 4

Chapter 4 sought to determine if multivariate data analysis methods could be usefully applied to the study of PEMFCs (and GDMs in particular), to improve understanding of the likely interactions occurring within PEMFCs. To that end, an introduction to a two-dimensional conceptual model of GDMs and their behaviours (originally presented by Spiegel (2008) [87]) was introduced in section 4.2. This was done with the intention of highlighting some of the most important factors governing the performance of GDMs within PEMFCs (according to pre-existing literature and numeric models). A multivariate design of experiments was then detailed in 4.3, along with a wide variety of experimental equipment, procedures and sample preparation methods required to undertake the designed experiments. The key categoric variables in the experiment were detailed (Table 12), and initial scatter plot assessments for all variables were conducted via a matrix plot (Figure 29). Having established the data would, in all likelihood, be suitable for more detailed multivariate analysis, and having verified any likely categorical input factors: Polarisation curve data was captured from a wide variety of GDM samples. A novel automated procedure, to analyse peak power and the gradient of the distinct regions of each polarisation curve, was further detailed.

Initial results were analysed with traditional data interpretation methods, and plotted as box and whisker plots (e.g. see Figure 36). The spread of the data was shown to be such that firm conclusion could not be drawn; and again multivariate methods were recommended. Section 4.5 detailed the

multivariate design of experiments conducted in accordance with the parameters outlined in Table 13. All variables were assessed for normality of residuals and passed Q-Q plot 'pencil tests': confirming the data was well suited to the multivariate methods selected (e.g. see Figure 40). The results were plotted, and initial analysis of the data was completed, in accordance with recommended practice as detailed in section 2.2.

Backwards step elimination was then undertaken to remove extraneous, or insignificant, input factors for the developed M-ANOVAR models as detailed in section 4.7. A detailed examination of error arising from test apparatus was carried out (see Table 15). It was found that while a certain degree of error was measurable, the differences between samples tested were such that it could be safely discounted in this work (i.e. FCCA based apparatus induced error was sufficiently small that it could be ignored). Backwards regression was then concluded, removing equipment factors and the final models, and having had non-significant terms removed from them, were presented in section 4.7 as 'reduced complexity' variants of the models first developed in section 4.5. The models produced were assessed in detail. The models underwent error assessment and determination of any additional impacts on the accuracy of the model as a result of co-varying factors (variance inflation factor analysis). The final models were produced for gA (Table 20), gO (Table 25), gM (Table 30 and Table 31) and Wmax (Table 36, Table 37 and Table 38). Model validation that had been completed in previous sections was highlighted, and graphical and forecasting validation was also completed in section 4.10. It was sugested that the peak power model (referred to as 'Wmax'), was highly suitable for analysing the data. The gradient of the Ohmic loss region of the polarisation curve (referred to as 'gO') gO model was also a useful method for investigating GDM performance, though prone to a greater range of variability in the experimental results. As an example, from Table 25, the associated values for the Ohmic loss gradient model of paper GDMs were:

$$gO_{(paper)} = -0.66462 + (0.018846*Tmax) + (-1.37789*wt\%PTFE_{\text{ as a decimal}}) + (-0.00249*GDMthickness_{\mu m}) + (-0.019*volume\%pores) + (4.62x10^{-5} * GDMthickness_{\mu m} *volume\%pores) \quad \textbf{(4-30)}$$

The equivalent peak power model for paper GDMs is:

$$(Wmax_{(paper)})^{-1.32} = -62.8852 + (0.9388 * T_{mean}) + (0.7874 * wt\%PTFE_{\text{ as a decimal}}) + (-0.0015 * GDMthickness_{\mu m}) + (0.5755 * H_2O\text{-contact anlge}_{degrees}) + (0.0195 * volume\%pores) + (-0.0082 * T_{mean} * H_2O\text{-contact anlge}_{degrees}) + 0.018 * (wt\%PTFE_{\text{ as a decimal}} * GDMthickness_{\mu m}) \quad \textbf{(4-31)}$$

A brief summary of the f-distribution and resultant p-value probability of error was recapped in section 4.11, along with the key assumptions of the models to be analysed. The decision as to which factors to map the response surface plots against, were made using perturbation plots (e.g. Figure 51). The limits of the model design were enumerated both as bullet points, and as 'design cube' results generated by Design Expert Pro (Figure 54).

The conclusions for the chapter were then detailed in section 4.12. It was noted that porosity and through-plane thickness interactions in GDMs have a significant impact on both the peak power performance, and the gradient of the Ohmic loss region. The two-dimensional model reported in section 4.2 was once again utilised and adapted, to closely match the parameters of interest generated from the Wmax and gO models detailed in section 4.11 and 4.12. This then formed the basis of the discussion around likely causes for the various effects, detected in the gO and Wmax reduced complexity M-ANOVAR models.

It was found that while peak power performance occurs for lower porosity GDMs, regardless of type: GDMs have a key porosity value where their performance is more uniform over a variety of through-plane thicknesses. The Ohmic gradient shows a similar trend. In summary, the results are as follows:

- Wmax woven GDMs:
    - Peak power achieved with 110µm thick GDMs at 31.8% porosity (0.473 $W.cm^{-2}$). Stable performance across a wide range of thickness is achieved with approximately 42% porosity GDMs.
- Wmax paper GDMs:
    - Peak power achieved with 110µm thick GDMs at 31.8% porosity (0.592 $W.cm^{-2}$). Stable performance across a wide range of thickness is achieved with approximately 42% porosity GDMs.
- Wmax non-woven GDMs:
    - Peak power achieved with 110µm thick GDMs at 31.8% porosity (0.562 $W.cm^{-2}$). Stable performance across a wide range of thickness is achieved with approximately 42% porosity GDMs.

It should be noted that stable gO performance, across a wide range of GDM thicknesses were noted, at approximately 53% porosity.

5 Expanded Literature Review and Investigation of Catalyst layers

5.1. Introduction to Chapter 5

As has been discussed previously in sections 2.5, 2.7 and 2.8, there is a gap in the literature regarding layered catalyst structures and their longevity. Subsequent chapters consider the interactions between layered catalysts, GDM structure and degradation rates of PEMFCs as a multivariate problem. Chapter 4 has demonstrated the usefulness of M-ANOVAR methods in the study of PEMFCs, specifically in relation to the selection of GDMs to either maximise peak power performance or to select a porosity of GDM that is stable over a wider range of operating conditions. To understand the role layered catalysts play inside PEMFCs; Chapter 5 expands on the literature review (see section 2.5) and presents information on catalyst layers in more depth. It begins with a brief description of simple catalyst layer and agglomerate based models. This is done to aid understanding the importance of the catalyst layer (using a two-dimensional numeric models to highlight the impact of catalyst layers of PEMFC performance). The information presented in Chapter 5 will inform the analysis, discussion and understanding of the results generated in later chapters of this thesis.

5.2. Catalyst layers in PEMFCs

Catalyst layers (CLs) are a region sandwiched between the membrane and the GDM. The CL facilitates Oxygen Reduction Reaction (OOR) on the cathode side, and Hydrogen Oxidation Reactions (HOR) on the anode side of the fuel cell (see Figure 1). Traditionally the CL has been created by nanometre scale catalyst material (e.g. Platinum) that was deposited onto small particles of a supporting substrate. Carbon black has often been used as a substrate, as it is relatively low cost, can be milled down to very small particle sizes and chemically stable in the presence of the platinum catalyst at the majority PEMFC operating conditions [95]. Section 2.5 introduced a literature review of CLs relevant to the wider topic of multivariate factors in PEMFC research. The previous results in Chapter 4 have shown that PEMFCs can be studied using the M-ANOVAR methods discussed previously (section 2.2, 3, section 4.10, section 4.12 and section 4.13). It is important to ensure that the system being studied is understood well enough, so that the results generated by any proposed M-ANOVAR assessment, can be analysed and interpreted successfully. To achieve this, section 5.3 introduces a basic numeric model to highlight the importance of catalyst layers in PEMFCs.

5.2.1. Catalyst layer degradation

There are many suggested sources of degradation in PEMFCs and the literature on degradation mechanisms is extensive; with a large number of authors contributing [16,70,95,99,123-142]. Those of specific interest to layered catalyst structure and multivariate investigation have been discussed previously in section 2.3. The topic of fuel cell degradation is broad, with some degradation

mechanisms, and the test conditions to monitor them, specifically applying to certain components in the fuel cell assembly, and also the operating parameters at the time the degradation event takes place. As degradation is an area of research well served in the literature; this thesis has, instead, focussed on the experimental and statistical methods required to accelerate understanding of the complex interactions that can occur in fuel cell degradation studies. Degradation in fuel cells is not always a straightforward linear effect: Both degradation mechanisms and rates vary over time as the fuel cell operates. The Ostwald ripening (introduced in Chapter 2) rate is far higher when first using new PEMFCs [95]. The newly deposited Pt nano-particles have a very high surface area and so are driven to undergo 'agglomeration' or Ostwald ripening at an accelerated rate. Once the ripening process has progressed for a period, the energetic drive to reduce overall surface area (i.e. the Gibbs free energy of the surface) has significantly reduced, and the rate of ripening will decrease [39]. There are also reversible performance losses, such as excessive water in the fuel cell components [90,95,115,143-146]. These flooding events subside, if conditions are suitable to allow the drying of the components. There are also irreversible degradation effects such as the complete loss of platinum from the fuel cell for a variety of reasons (see Table 42). Part of the complexity of degradation studies in fuel cells is that these, and several other, degradation mechanisms take place simultaneously. The rates of degradation for each mechanism vary over time, and as a result of the duty cycle the fuel cell is required to operate under [57,70,95,99,147-149] (see 2.3 for more detail on this topic). It is the hypothesis of this thesis that material selections, such as the type of GDM, and the manufacturing methods used in fabricating MEAs (i.e. the use of layered catalysts) may also be factors that influences the rate of degradation in fuel cell performance.

There are several key degradation mechanisms that impact the catalyst layer specifically. Once again, there are a great many numbers of authors that have examined this topic in the past [16,70,95,99,123-142]. This thesis has drawn heavily on the information presented by Mench (2012) [95], Whiteley (2016) [90] and Sutharssan et al. (2016) [141], and the key degradation mechanisms for catalyst layers are summarised as follows:

Table 42: Example catalyst layer degradation mechanisms

Reversible degradation				Irreversible degradation			
Degradation	Mechanism	Impact	Notes	Degradation	Mechanism	Impact	Notes
Flooding	H_2O blocks pores	Reduced ECSA	[95], [90]	Poisoning	Chemicals strongly adhere to the surface of the Pt catalyst	Reduced ECSA	e.g. CO, HO^-, HOO^- [95], [90], [141]
Crossover	N_2 passes through the membrane	Reduced H_2 in gas flow channel Reduced ECSA for H_2	[142]	Increased catalyst size	Ostwald ripening – Pt atoms relocate to reduce free surface energy by forming larger particles	Reduced ECSA	Rate reduces as the particles grow over time [95], [90]
Poisoning	Chemicals weakly adhere to the surface of the Pt catalyst	Reduced ECSA	e.g. CO, CO_2 [95], [90]	Pt migration	Relocation of Pt particles	Reduced ECSA	Into the body of the membrane [95], [90]
				Pt loss	Catalyst physically lost from the MEA	Reduced ECSA	Direct loss of Pt or loss as a result of loss of Carbon catalyst support materials [95], [90]

For a more detailed discussion of the time and operational dependence of the large numbers of possible degradation mechanisms, the reader is directed to one of the three primary sources referenced [90,95,141].

5.3. Catalyst layer through-plane thickness models

There have been a wide variety of modelling techniques applied to catalyst layers, and there are many review papers on the topic: Marquis and Coppens (2013) [94] give a good introduction. Agglomerate model approaches become popular in the 1980's, with several notable papers in the field [94].

It is perhaps useful to define agglomerate once again to avoid any possible confusion, please see annex one. It is important to note that the term ‘agglomerate model’ does not, inherently, imply a transient time-dependent model, on the changes in the catalyst layer. In this thesis, it indicates that the type of catalyst being modelled consists of multiple phases clumped together (typically carbon

black and platinum) into a broadly homogenised mass, with an ionically conductive phase at the surface.

It is beyond the scope of this thesis to provide a detailed numeric model of the catalyst layer (CL) and its impact on cell performance, but a basic understanding of the role the CL plays in generating fuel cell outputs is advantageous and so included here. There are many authors [71,72,150-165] who have worked on the topic of CL modelling. Horn-Wen Wu (2016) [166], recently published an extensive review of modelling of transport and performance for fuel cells, and the interested reader is directed there. The key assumption of the two-dimensional agglomerate models presented in Chapter 5, is that the carbon support the platinum catalyst are deposited onto, are treated as a single agglomerated pallet (hence the name) encased in a diffusive media. Usually, this diffusive media is assumed to be Nafion®, but it can also be fluid (gaseous or liquid water). Sun et al. (2005) [164] have produced an excellent two-dimensional model using this approach.

5.3.1. One dimensional agglomerate model catalyst activation

The effectiveness factor can be thought of as the availability of the gas in question (the reactant), to do work at the catalyst sites. It is an interrelationship function, based on the diffusivity properties of the gas in and around the catalyst agglomerates, along with the chemical activity and energy requirements for reactions to occur. In this thesis, a simplified one-dimensional agglomerate model, as reported by Spiegel (2008) [87], is used to gain an appreciation of the factors involved. These equations were originally developed to simulate porous catalysts agglomerate mixtures, but have frequently been used in an unaltered fashion in the modelling of fuel cell catalyst structures (which have typically been fabricated as carbon support structures of unknown porosity, with catalyst layers decorated onto it).

It has been noted [87], that while the activation losses in the polarisation curve are fundamentally diffusion dominated; they are a special case of diffusion in, and adjacent to, the environments of coated catalyst on support structures. It has been common practice to ignore the movement of reactants through the thickness of the CL in the literature [87]. In Chapter 4 for example, the catalyst layer was imagined as little more than a boundary that generated a temperature profile; was one of the assumptions of the two-dimensional model (see section 4.2.1 and Figure 20). The ‘effectiveness factor’ can be thought of as answering the question ‘how well does the reactant gas get into sufficient proximity with the catalyst sites in and around the agglomerate Pt-on-C particles?’

Figure 63 shows the effectiveness factor for anode (H_2) and cathode (O_2) catalysis of molecules to single ions, suitable for transport and reaction inside the MEA. This corresponds to the ‘activation loss’ portion of the polarisation curve as, discussed previously (see sections 1.1 and 2.1). The activation portion of the polarisation curve is modelled using equation (5-1) for the effectiveness factor, plotted against the modelled anticipated current density.

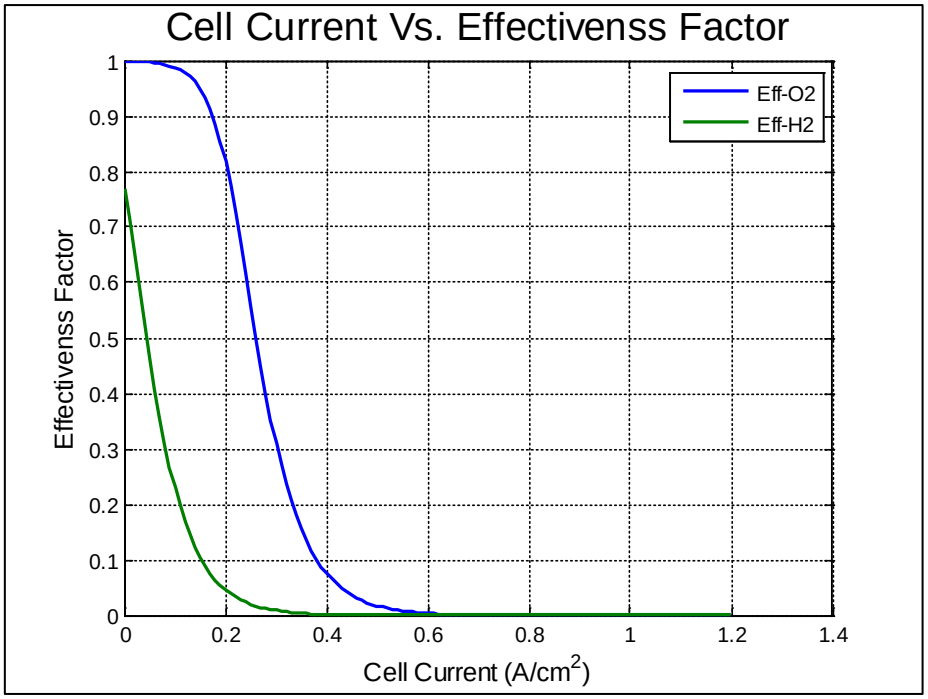

Figure 63: Effectiveness factor

(for reactant gases and agglomerate catalysts (adapted from Spiegel (2008) [87]))

Figure 63 is a simulated plot of the effectiveness factor E_{ff}, for catalysts [87], where E_{ff} is

$$E_{ff} = \frac{1}{3\varphi^2}(3\varphi \coth(3\varphi) - 1) \qquad \textbf{(5-1)}$$

As a Tafel type reaction (first order) [24], resolve this as follows; where φ is the Thiele modulus (for oxygen in this example) from the generalised Thiele Modulus,

$$\varphi = \varsigma \frac{k'}{D_{O2,agg}^{eff}} \qquad \textbf{(5-2)}$$

where $D_{O2,agg}^{eff}$, is the effective diffusion constant for the species (in this case Oxygen) at the surface of an agglomerate particle of support and catalysts material, ς is the effective length of the agglomerate particle (volume, divided by surface area, is approximately equal to the radius of the agglomerate particle, divided by three) and k' is the kinetic portion of the Thiele modulus [87]

$$k' = \frac{a_{1,2}.i_{0,ORR}}{4.F.c_{O2}^{ref}} \, exp\left(-\frac{\alpha_c.F}{R.T}\eta_{ORR,1-2}\right) \qquad \textbf{(5-3)}$$

where $\alpha_{1,2}$ is the active surface of the catalyst and its support structures, c_{O2}^{ref} is the reference concentration value for Oxygen in equilibrium inside, or at the surface of, the catalyst agglomerate

(based on the partial pressure of the oxygen present and the 'Henry's Number' for that species in that specific catalyst agglomerate (a material property) [87]). The exchange current density for the ORR is shown as i_0. It is this use of the Thiele modulus, and the use of equation (5-3), that defines the model as an agglomerate model (i.e. it assumes agglomerate, multiphase, particles compacted together) [86].

The activation loss region of a typical polarisation curve is created using this assumption of catalyst effectiveness for agglomerates. In this case, the 'activation' represents the ability of the reactive gases, in particular hydrogen, which has far greater impact in terms of effectiveness actors, as seen in Figure 63.

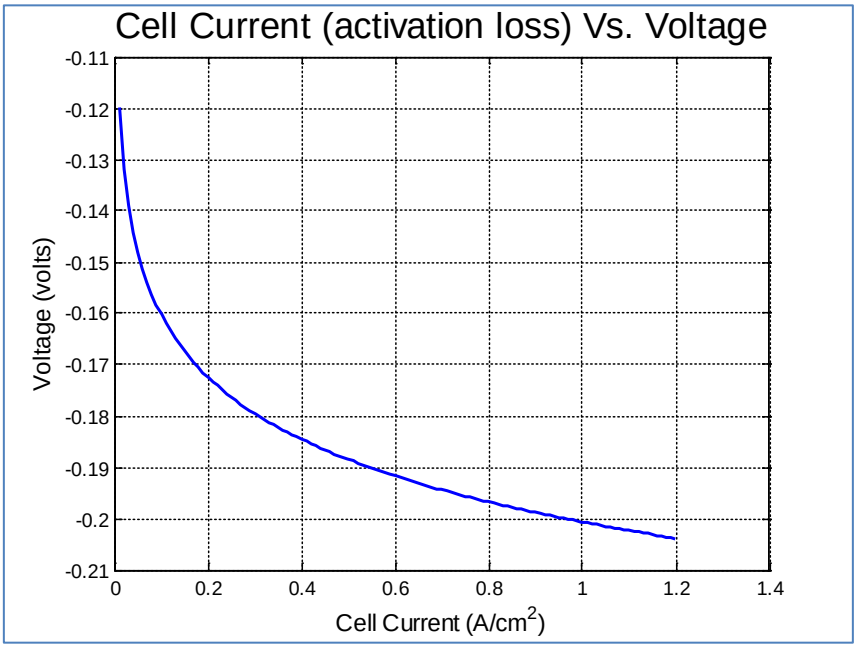

Figure 64: Activation losses in cell potential

(Adapted from Spiegel (2008) [86])

In Figure 64, the activation loss portion of the polarisation curve, as defined by the Butler-Volmer equation [87] (this can also be calculated by the Tafel approach if considering purely one-dimensional problem, as the reaction of the oxygen reduction reaction (ORR) is slow enough that Tafel kinetics are sufficient to simulate it [87]). The generalised Butler-Volmer equation for activation loss, from Spiegel (2008) [87], is:

$$\nabla . i_2 = a_{1,2}(1 - S) . i_{anode} \qquad \textbf{(5-4)}$$

For the (one-dimensional) anode this is

$$i_{anode} = \left[\frac{p_{H2}}{p_{H2}^{ref}} . exp\left(\frac{\alpha_a . F}{R . T} (\Phi_1 - \Phi_2) \right) - exp\left(\frac{-\alpha_a . F}{R . T} (\Phi_1 - \Phi_2) \right) \right] \qquad \textbf{(5-5)}$$

Where pH_2 is the partial pressure of hydrogen, a_a is the anodic charge transfer coefficient, F is Faraday's number, R is the gas constant, T is the temperature, and the Φ values are the Thiele modulus accounting for solid (Φ_1) and liquid (Φ_2) transport properties.

Moreover, for the (one-dimensional) cathode this is:

$$i_{cathode} = \left[\frac{p_{H2}}{p_{H2}^{ref}}.exp\left(\frac{\alpha_a.F}{R.T}\left(\Phi_1 - \Phi_2 - E_{eff}\right)\right)\right] \quad \textbf{(5-6)}$$

Which can be re-arranged to solve the voltage loss due to activation of the catalyst agglomerate as:

$$V_{act,anode} = \left(\frac{R.T}{\alpha_a + \alpha_c}\right) log\left(\frac{i}{i_{HOR}.a_{1,2}.(1-S).(n_{H2}.P_{H2})}\right) \quad \textbf{(5-7)}$$

$$V_{act,cathode} = log\left(\frac{i}{i_{HOR}.a_{1,2}.(1-S).(n_{O2}.P_{AIR})}\right)\left(\frac{R.T}{-\alpha_c.F}\right) \quad \textbf{(5-8)}$$

and the activation loss (plotted in Figure 64) is found by the summation of the two functions:

$$V_{act'loss} = V_{act,anode} + V_{act,cathode} \quad \textbf{(5-9)}$$

It is now possible to create the rest of the polarisation model, using the Butler-Volmer approach to activation loss, along with the Ohmic loss and Fickian (or Darcy) diffusion losses more commonly used [87].

$$V_{polarisation} = E_{Nernst} + V_{act'loss} + V_{Ohm} + V_{mass} \quad \textbf{(5-10)}$$

Where the Nernst Equation [87] is:

$$E_{Nernst} = -\frac{\Delta G_{liquid}}{2.F} - \frac{R.T}{2.F}\, ln\left(\frac{p_{H2O}}{p_{H2}.p_{O2}^{0.5}}\right) \quad \textbf{(5-11)}$$

and Ohms law (V=I/R) provides a simplified model of the resistive losses. Note that this is a highly simplified approach to take to modelling the Ohmic losses, but is suitable for this discussion.

$$V_{mass} = \alpha_1 . i^{k_m} . ln\left(1 - \frac{i}{i_L}\right) \quad \textbf{(5-12)}$$

In this case, α_1 is a system specific constant. Figure 65 utilises α_1 = 0.085 from page 259 of Spiegel (2008) [87]. To apply this method in the model, it is important to set a lower limit of 'zero' for the mass loss equation or the computer code cannot calculate the correct values.

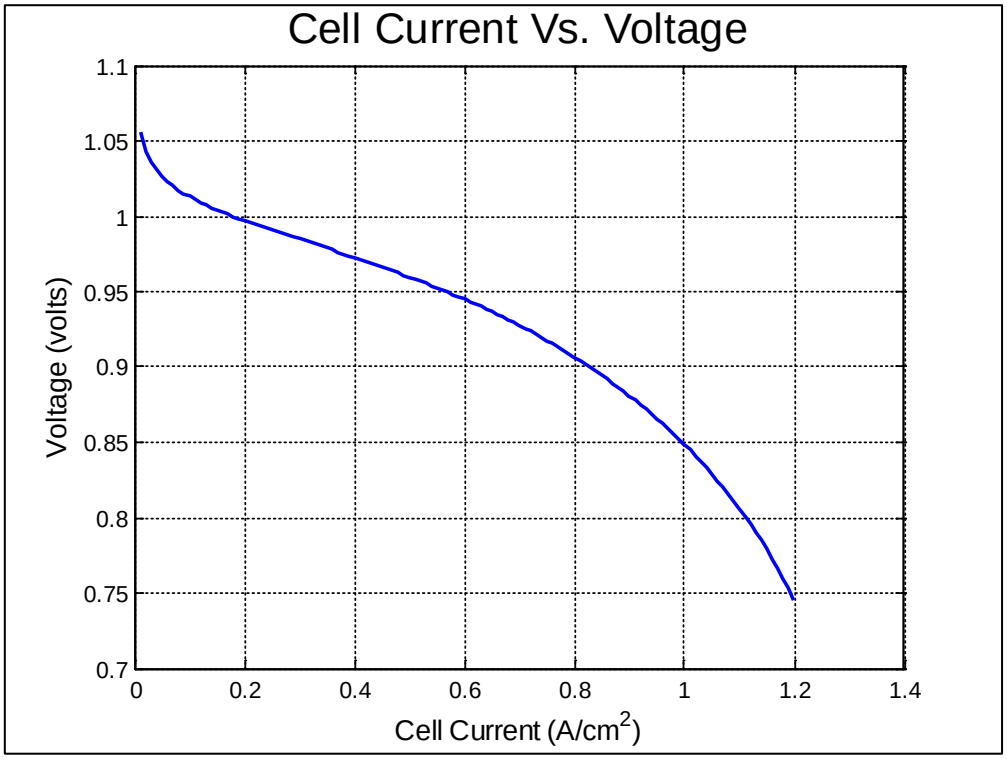

Figure 65: Generic simulated polarisation curve

(Adapted from Spiegel (2008) [87])

Figure 65 shows the idealised polarisation curve, based on equation (5-10) with the (5-11) Nernst potential, and the losses from activation of agglomerate catalyst particles (Thiele modified Butler-Volmer equation (5-9)). Ohmic resistance is calculated from Ohms law [24], and mass transfer losses are dominated by Fickian diffusion effects (equation (5-12)) [87]. The importance of the catalyst sites, in defining the performance of the fuel cell, is evident in the first part of the polarisation curve. The activation losses in the region of A.cm^{-2} 0 to 0.1; are all due to the Thiele-modified accessibility of catalyst sites at the surface of agglomerate particles in the catalyst layer. This dominates the shape of the polarisation curve at in the lower A.cm^{-2} region of the graph (Figure 65). Hopefully, the model, and the mechanisms it is based on, go some way towards explaining the importance of catalyst

structures. The CL determines the overall performance of fuel cells, and it is therefore justified for catalyst materials to have been included as a topic of study in this thesis.

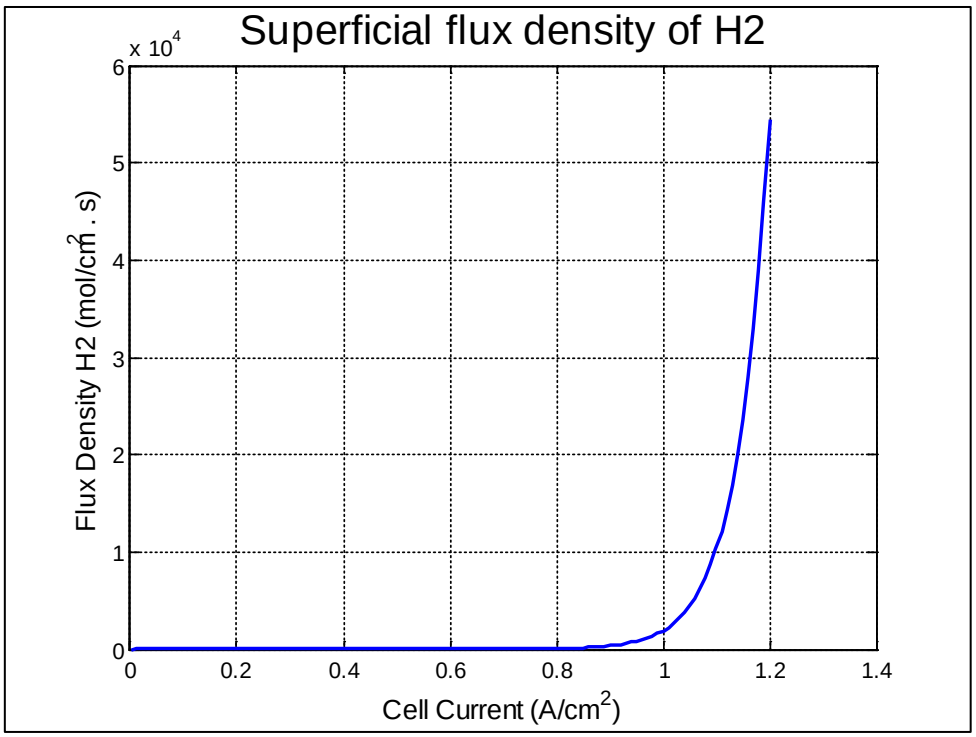

Figure 66: Superficial flux density of hydrogen

(Adapted from Spiegel (2008) [87])

Figure 66 shows the rate of gas flow required across the surface of the catalyst sites, to achieve a certain degree of output (current) in the cells. It is for this reason that a limit on the output of the fuel cells based on the gas flow rate is often encountered. This approach can be extended to apply it to a multi-layered fuel cell catalyst cathode [167,168]. Adapting the Spiegel (2008) [87] model (detailed previously) to match the proposed experimental system in more detail; the following results were achieved by matching the voltage, load and temperature profile.

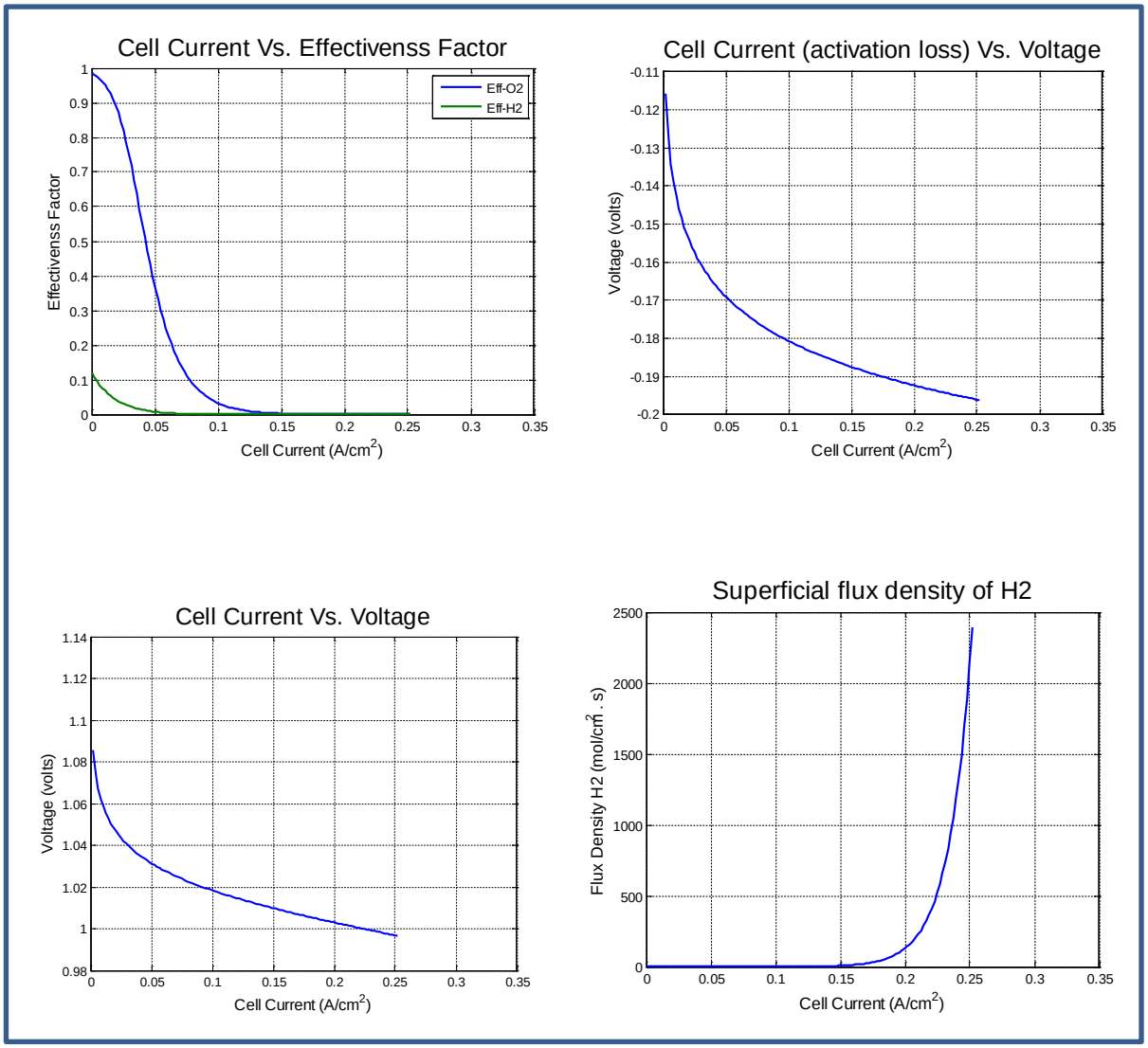

Figure 67: Spiegel model

(Adapted for FCCA: ECSA = 10,000)

In Figure 67 the Spiegel (2008) [86] model, presented in this chapter, was adapted to closely match the experimental setup of the FCCA, and the test samples used in Chapter 4. To achieve broad agreement with the results from experiments, the ECSA value was altered to 10,000, along with the appropriate set of average values for the remainder of the experiments being modelled (see Table 9 in section 4.3.1). Typically, ECSA would be reported in $m^2.g^{-1}$, so it is assumed the Spiegel (2008) [86] model utilises units of $m^2.kg^{-1}$ (though this is not specified in the text). Such a value is in broad agreement with the literature [169].

In comparison to the idealised results generated by the model in Figure 64, Figure 65 and Figure 66: It was found there were significant reductions in hydrogen effectiveness, and the hydrogen flux at catalyst sites (an order of magnitude less than the standard model presented in Figure 66). It is interesting that the model for the polarisation curve (Cell Current Vs. Voltage plot in Figure 67), has failed to demonstrate a mass transport loss region of the polarisation curve. This does not reflect the experimental results generated, in which several samples demonstrated the characteristic mass loss transition in the polarisation result. Ideally, the model would have more closely matched the experimental results generated at the time of the experiments. Despite this lack of ability to adequately model the mass transport loss region, an attempt was made to alter the agglomerate model, by adapting it to two 'sub-layer' catalyst regions as layers one and two. The layered variant model was created in the hopes of more closely matching the experimental results (which were considerably reduced in terms of the overall performance seen here). It was hoped that the activation region of the polarisation model would be sufficiently detailed to still be of use in assessing dual layered catalyst structures.

Spiegel (2008) [87] stated that the effective conductivity of the membrane (σ_m^{eff}) is (electrolyte ionomer content ($\varepsilon_m^{\delta_m} = \varepsilon_m^{1.5}$) multiplied by the conductivity of the membrane σ_m):

$$\sigma_m^{eff} = \varepsilon_m^{1.5}.\sigma_m \qquad \textbf{(5-13)}$$

[87]

also, it has been shown by Springer et al. 1991 [66] that

$$\sigma_m^{eff} = \varepsilon_m^{\delta_m}(0.5139\lambda_{H20} - 0.326)exp\left[1268\frac{1}{303} - \frac{1}{T}\right] \qquad \textbf{(5-14)}$$

[66] [87]

Where ε_m is the conductivity of the membrane, δ_m is the thickness of the membrane, λ_{H20} is the saturation constant of the ionomer (λ_{H2O} =22 for fully saturated Nafion). As there is a geometric constituent in the above equation (i.e. the thickness of the membrane layer $\delta_{m)}$, and, as discussed previously in section 2.5, several authors [68,73,75] have argued that a displacement of the catalyst layer away from the surface of the membrane will impact the performance of the fuel cell. That is to say, the normal assumption of the catalyst layer as an infinitely thin plane is no longer valid. See Figure 10, in Chapter 2 for further clarification. In order account for this, a numerator for the 'reaction surface roughness' (the structure of the electrode) and the platinum loading is also included, and this

impacts the potential of the catalyst layers of phases. This three-dimensional catalyst layer structure is now referred to as the 'electronic phase', and it has a separate electronic phase potential for each separate catalyst layer being considered (from Mukherjee et al. in White (2007) [170]).

$\Phi^{(S)}$ = electronic phase potential

In each layer (i.e. layer 1 or 2) the electrolyte phase potential can be solved as follows

For i = 1 or 2

$$\nabla.\left[\left(\sigma_m^{eff}\right)_i.\nabla.\Phi_i^{(m)}\right]+j_i=0 \qquad \textbf{(5-15)}$$

[87]

The solution for the σ_m^{eff} value can then be fed back into the Thiele modules equation (5-2). Which in turn is used to determine the cathode catalyst layer Φ values (the Thiele modulus accounting for solid (Φ_1) and liquid (Φ_2) transport properties as demonstrated earlier in (5-1) , (5-2) and (5-3) [87]) and the two layer catalyst solution is

$$i_{cathode}=\left(a.i_{0,T}^{ref}\right)_i\left(\frac{p_{O2}}{p_{O2}^{ref}}\right).exp\left(\frac{\alpha_a.F}{R.T}(\Phi_1-\Phi_2-E_0)\right) \qquad \textbf{(5-16)}$$

[87]

The thickness of each sub-layer in the catalyst layer, is determined as a ratio of the overall layer thickness. This is solved for the different thicknesses by dividing the sub-layer thickness by the effective electrolyte monomer content (this is an arbitrary figure assigned to match the model to the desired curve). The effective potential for each layer is the estimated resistance of 'θ' layer (based on ionomer content and the thickness of the layer) multiplied by the estimated current in the region. This current value is assumed to be uniform across all layers and is a simple ratio of the total current, divided by the percentage presence of each layer.

$$E_{cathode,layer\ 1}=R_{cathode,layer\ 1}.i_{cathode,layer\ 1}^{\left(\frac{\delta_{layer\ 1}}{\delta_{total\ thickness}}\right)} \qquad \textbf{(5-17)}$$

It was not possible to measure the CL resistance directly on the samples available and so, based on CL resistance work carried out on freeze-thaw responses [171], which utilised very similar MEA fabrication and operating conditions: The resistance of the individual CLs was estimated as RCL = 20mOhms.cm^2. Combining this information with the findings on catalyst layer thickness, determined using a novel fluorescence microscopy technique (reported by the author previously [47]), the

following information was generated (as shown in Table 43 – the original paper for this work is available in Appendix 5).

Table 43: Catalyst layer location and thickness

	Layer Median point (pixels)			Mean (pixel)	σ (pixels)	SE (pixels)	Mean (µm)	SE (µm)
CL (MAC1)	406	401	388	398.3	9.3	5.4	733	9.9
MPL (MAC2)	178	158	200	178.7	21.0	12.1	329	22.4
	Layer Median point (pixels)			Mean (pixel)	σ (pixels)	SE (pixels)	Mean (µm)	SE (µm)
CL (MAC1)	250	175	260	228.3	46.5	26.8	420	49.6
MPL(MAC2)	350	260	340	316.7	49.3	28.5	583	52.7

Efforts were made to include this adaptation into the existing agglomerate model, but the model is not sensitive enough to alter its outputs based on even the broadest of changes to values such as the size of the agglomerate Pt-Carbon catalyst phase, or the permeation of gas through, and around, these agglomerate phase catalysts structures. It is recognised by many authors [160-162,164,172] that the current agglomerate models, especially simple one-dimensional models, are largely unable to simulate accurately the impact from variations in catalyst layer concentrations and thickness, despite the obvious changes in performance in real world MEAs. There are notable exceptions however: Some authors have made efforts to create one-dimensional models, that attempt to understand the fundamental mechanisms at work in the catalyst layer [167]. However, the creation of new numeric CL models for MEAs falls outside of the aims and objectives of this thesis: this thesis will continue to use the Spiegel models that have already been discussed.

The only 'lever' in the Spiegel (2008) [86] model which makes a significant difference to the behaviour and that can be considered to model the catalyst dispersal, is ECSA (Electrochemically Active Surface Area). ECSA is a catch-all term denoting the total catalyst surface available. Cycling the ECSA from 5,000 to 500 (in steps of 1125) generates the following changes to the model; as shown in Figure 68 through to Figure 72. As discussed previously in this chapter, the model outputs are plotted (in Figure 68 through to Figure 72) for effectiveness factor (top left), the activation loss region of the polarisation curve as calculated from the Thiele modulus modified Butler-Volmer equation (top right), the overall polarisation curve impact; activation and mass transport loss regions (Bottom Left) and the superficial flux density of hydrogen at the catalyst surface (bottom right). These four plots, together, allow the observer to examine the one-dimensional model, to assess what

impact changes in the ECSA have on the theoretically modelled catalyst effectiveness value. This, in turn, should impact activation loss, and the total polarisation curve (activation and mass loss in this case) modelled. The superficial flux density, gives an ability to quantify the changes to the reaction rate for hydrogen in the model, as the ECSA changes. It can be seen from the plotted results of the model (Figure 68 through to Figure 72) that there were significant changes in the anode catalysts effectiveness value; as the ECSA is decreased, anode effectiveness reduces (i.e. catalysts is underutilised). It can also be seen that the hydrogen flux density improves significantly at between ECSA = 500 (Figure 72) and ECSA = 1625 (Figure 71). Thus from the model, as reported by Spiegel (2008) [87] and, assuming degradation is largely due to reductions in ECSA (as discussed in Table 42), it was anticipated a step change in degradation rate for dual layered catalysts would become apparent. Recall that the ECSA reduces over time for a wide variety of degradation mechanisms (see Table 42) and so the sequence of model results shown, can be thought of as providing indicative results of the time-dependent degradation of the system (i.e. in Figure 68 ECSA = 5000 is time step zero, labelled as t_x). This simple one-dimensional model lacks the detail to quantify exact time steps or to identify individual degradation mechanisms.

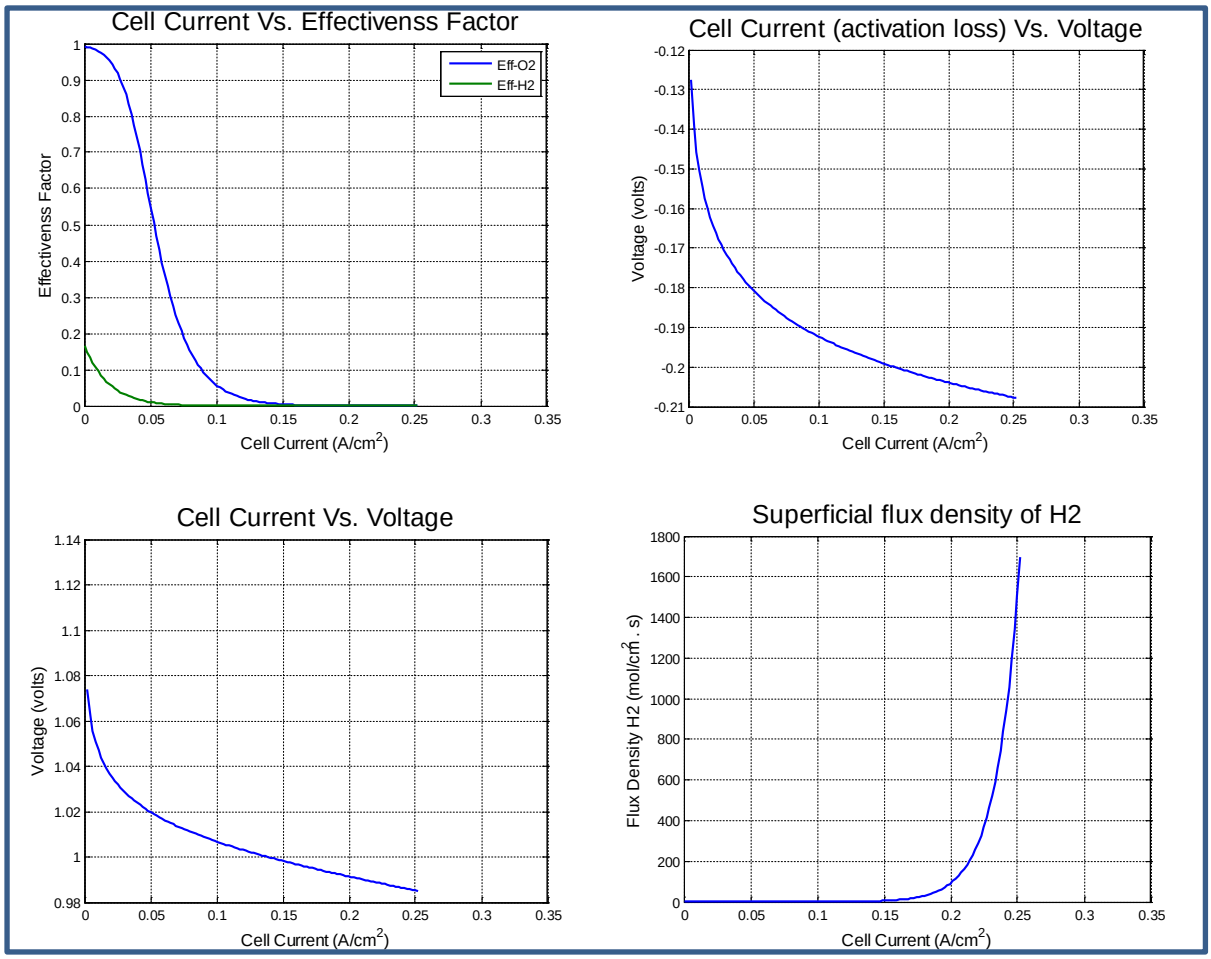

Figure 68: Spiegel model 2 layer cathode catalysts (5000)

(ECSA = 5000 (t_x))

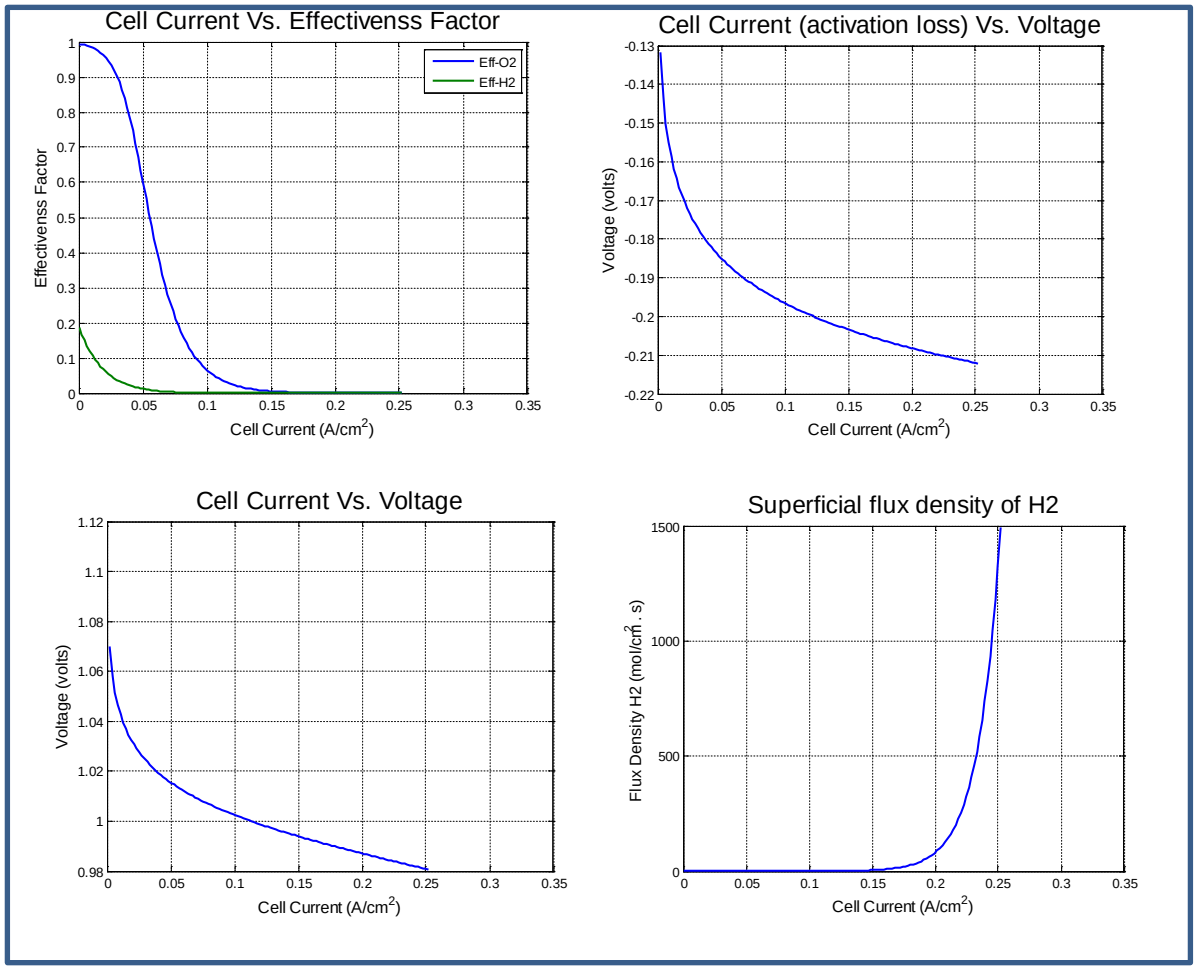

Figure 69: Spiegel model 2 layer cathode catalysts (3875)

(ECSA = 3875 (t_{x+1}))

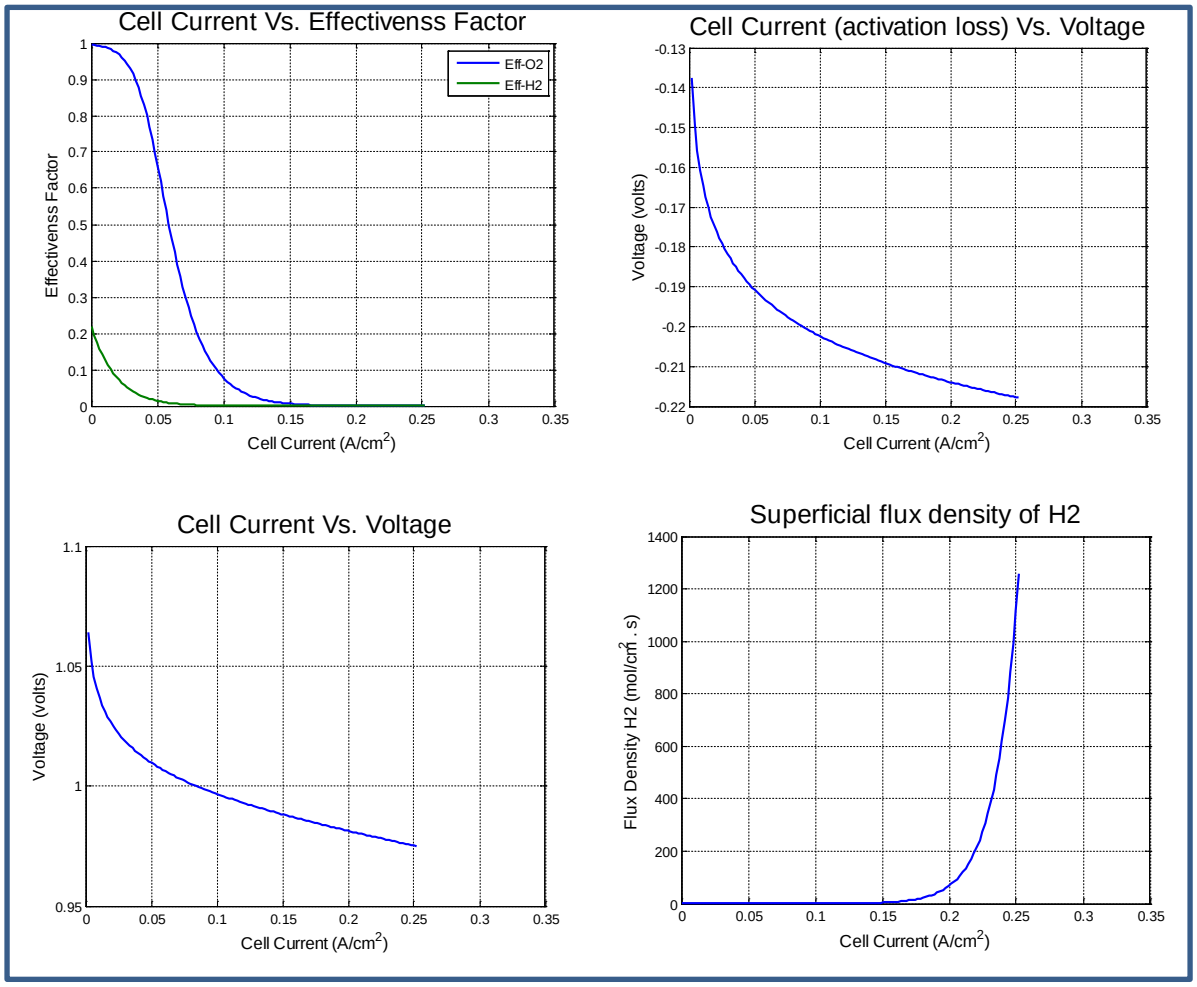

Figure 70: Spiegel model 2 layer cathode catalysts (2750)

(ECSA = 2750 (t_{x+2}))

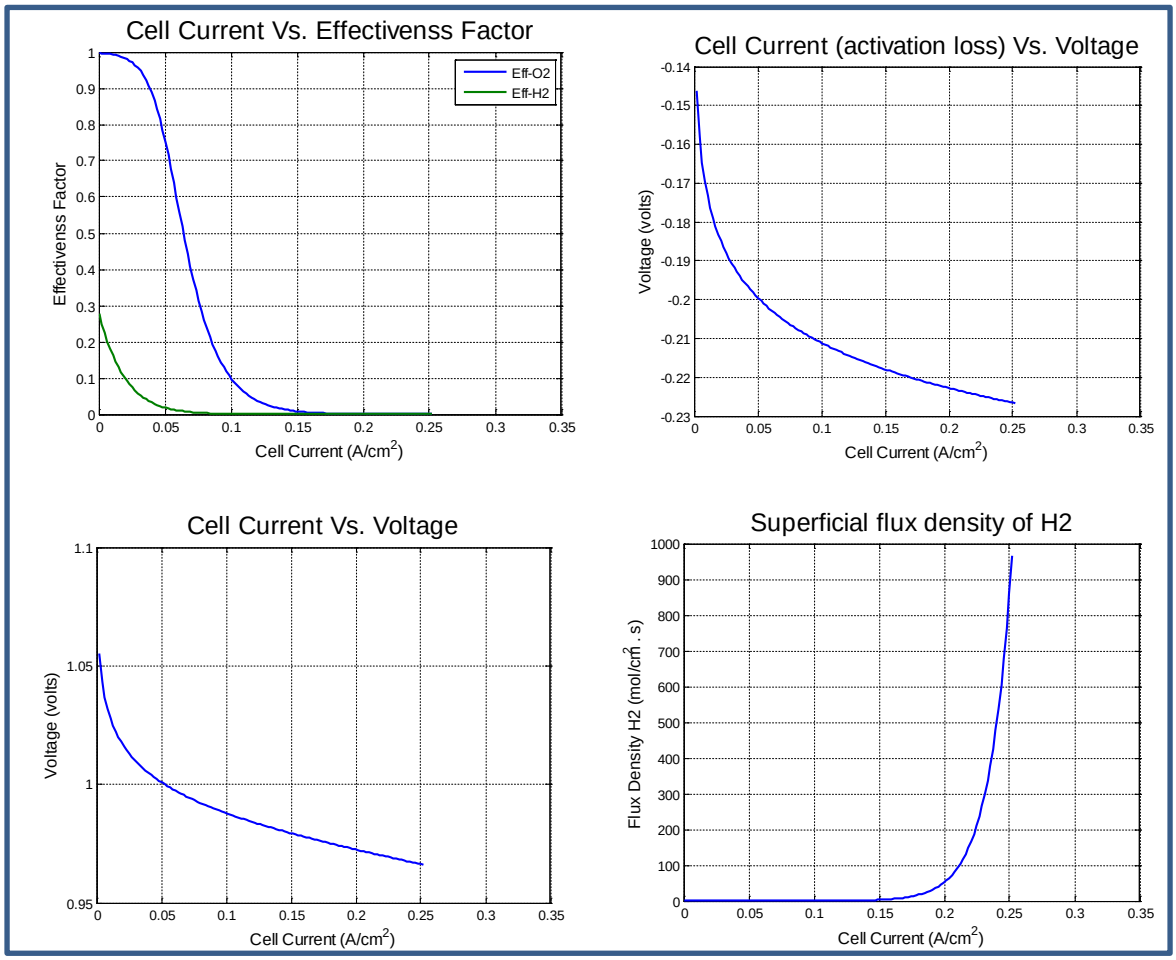

Figure 71: Spiegel model 2 layer cathode catalysts (1625)

(ECSA = 1625 (t_{x+3}))

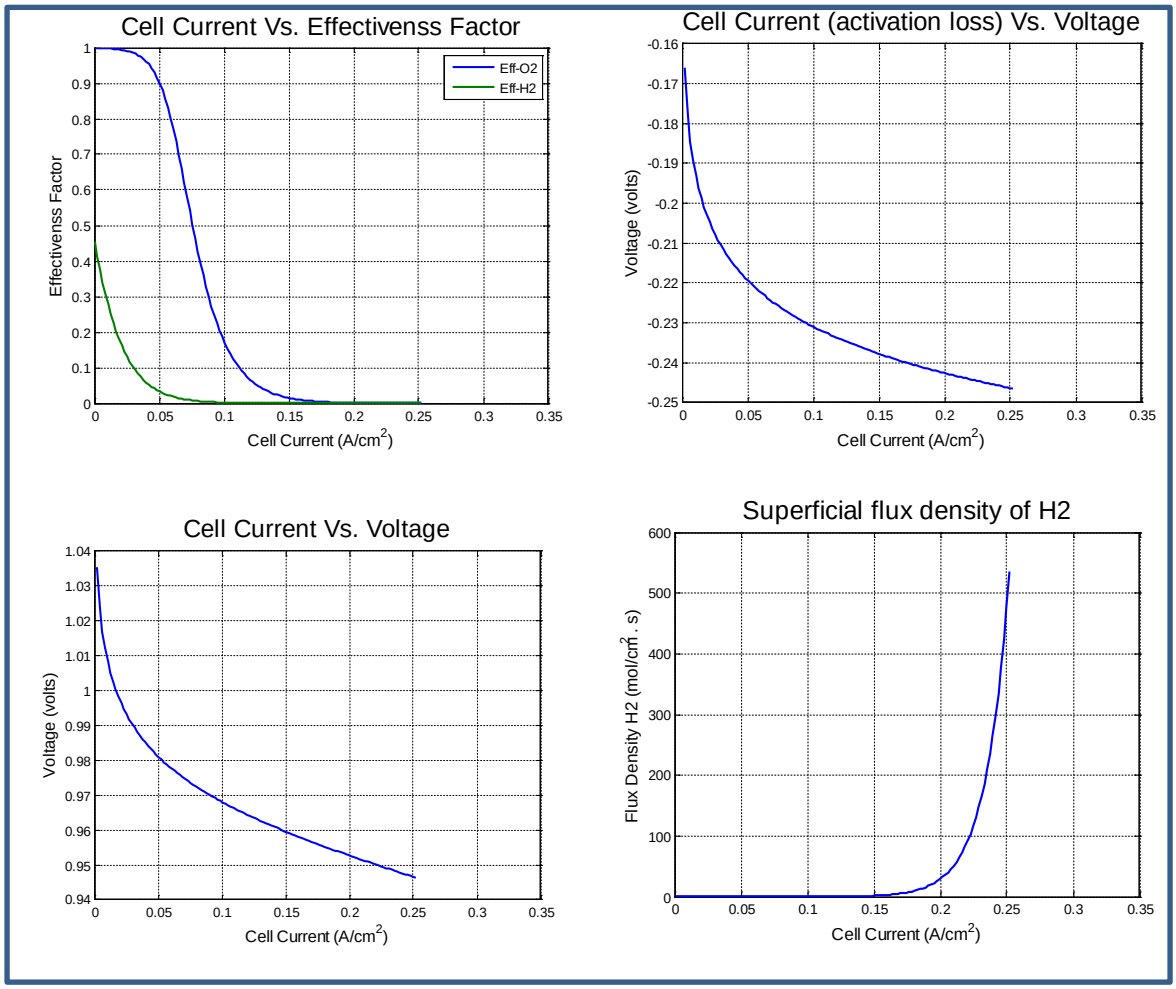

Figure 72: Spiegel model 2 layer cathode catalysts (500)

(ECSA = 500 (t_{x+4}))

Based on the results of this model, it was assumed that any changes in performance, whether an increase for dual layer catalysts at the start of life or changes for dual layer catalysts over the working life, are largely due to the ECSA. As seen in Figure 68 to Figure 71, the decreased ECSA makes a degree of difference to the utilisation of hydrogen, with the lowest values of ECSA increasing the activation losses of the system to a significant degree (especially when compared to the activations loses for Figure 67, where ECSA = 10,000, the effectiveness of the catalyst is low, reflecting an excess of catalyst on electrode). It is also clear in all plots (Figure 68 to Figure 71) that the ECSA is not significantly impacting the cathode side of the model. In this instance, it was concluded, that the rate limits of cathode reaction is either not impacted by catalyst ECSA (which contradicts the literature [24,26,66,95,173]), or that the Spiegel model [87] does not adequately model cathode ECSA effects when modified for dual layered cathode structures using the Thiele modulus. The third possibility is that the fundamental assumption that layering of the catalyst can have a significant

impact on the performance or longevity of fuel cell systems may be in error, which calls into question the work highlighted in the literature review (see section 2.5 and the work [68,73,75] presented there). This discrepancy between model, literature and the findings of the literature review is taken as a justification for the need to conduct additional experimental work on dual layered catalyst structures.

It is difficult, if not impossible, to solve this model for a real system without accurate measurements of the ionomer layer thickness, and its resistance for each discrete catalyst sub-layer. For GDMs that have a preloading of PTFE as a hydrophobic coating on the carbon fibres, it is almost impossible to differentiate between PTFE on the GDM fibres and PTFE-Nafion that is part of the catalyst layer(s). This issue of measuring catalyst sub-layer thickness has been addressed in other published work by the author [47] and summarised in Table 43. Platinum distribution can be tracked through the use of Scanning Electron Microscopy (SEM), but recall that it was established earlier that the Nafion distribution dominates (see section 2.5), and the maximum depth of platinum is not necessarily useful in assigning values to the two separate layers.

For this reason, direct optimisation of the model based on experimental results is extremely difficult and must be done somewhat arbitrarily. While it is true the mass gain for a given layer of added ionomer can be measured, the through-plane thickness of that layer can only be known accurately if it is deposited on a flat, non-porous substrate (such as the Nafion membrane at the heart of the fuel cell). For MEAs that were created by depositing the MPL or the CL directly to the GDM, the true through-plane thickness cannot be known. The utility of the model is further compromised by the fact that not all approaches generate variation in catalysts concentration by altering the loading of PTFE present in the CL.

Based on the literature reviewed to date [168,174,175], improved performance of fuels cells is theoretically and demonstrably possible through the use layered catalyst structures. This improvement is typically accredited to an increased region in which the oxygen reduction reaction (ORR) occurs in the cathode; by effectively increasing the catalyst effectiveness of the cathode[167]. The additional through-plane thickness of the catalyst layers, combined with an optimised catalyst distribution (increased concentration near the membrane surface) has also been cited as a reason for improvements [68,73,75]. This was discussed in detail in the literature review (see section 2.5). Despite acknowledgements that increasing the ratio of ionomer (the ‘electrolyte phase’ in the catalyst layer) “*…retards the electron conduction through the catalytic layer…*”[174], it is precisely by increasing the ionomer content of catalyst ink solutions that has been the standard approach for investigating layered catalyst performance. Another factor that can work against the supposed improvement, is the blocking of porous structures in the GDM when depositing the ionomer rich catalyst inks onto them. However, this can be counterbalanced by the optimisation of proton conduction through the additional ionomer coating on the surface of the agglomerate Pt-carbon black

catalyst phase, which facilitates ionic conduction adjacent to the catalyst sites. It has been shown [174], that with the optimum loading of ionomer, the detrimental impact from pore blocking and reduced electron flow is more than compensated for by other improvements.

The same arguments (increased proton conduction but reduced porosity and electron flow) extend to the optimisation of through-plane thickness of the various layers. This approach has not been researched in great depth, as there are practical limitations in developing accurate measurements of layer thickness that have only recently been overcome [47]. Lastly, Yoon et al. (2003)[174] stated that the operating voltage (expressed as lumped parameter in their paper) is of crucial importance, and that higher voltages were more benefited by dual layer catalyst than lower ones. To date the approach to reducing the amount of catalyst in the secondary layers (those furthest away from the membrane) has been to either:

- Keep the basic formulation for all layers the same, and then increase the effective dilution of the catalyst-bearing particles by increasing the Nafion content in the ink formulation [74],[73].
- To include conductive carbon black particles but without any platinum loading [23].

The research undertaken for this thesis takes a 'middle path' of changing the platinum loading on individual carbon black particles. This middle path was selected as the mimicking of pre-existing work would be of limited interest to the wider fuel cell community, and no literature search identified the catalyst layer concentration variation, achieved through the use of variable mass loading of platinum on carbon black, had ever been undertaken. This constitutes a gap in the knowledge base for layered catalyst structures in fuel cell research. Additionally, the dispersion of active catalyst sites throughout the thickness of the catalyst layers, while maintaining a uniform percentage presence of carbon particles and their conductive pathways; may give rise to novel findings or benefits that have not been identified previously. The inclusion of uniform catalyst layers as a base line will be essential to ensure experimental results can be compared with the results of other authors.

Recall that the aims and objective of this thesis (see section 1.1.1), includes identifying areas where multivariate analysis methods can contribute to the fuel cell field, by analysing multiple input factors simultaneously, with multiple output factors to interpret. The utility and effective performance of layered catalyst structures, achieved through mass variation of platinum loading on catalyst particles is one such factor. The degradation rate of uniform and layered catalyst MEAs is another factor of interest. Considering the impact that GDM structure may have on both performance and degradation rates for MEAs, is the third factor of interest to the wider fuel cell community, and is ideally suited to multivariate analysis. Individually, each of these could be tested as a separate one factor a time (OFAT) set of experiments. This would have several key weaknesses as discussed previously (see section 2.2): The total number of experiments required to test a set of two or more variables, under an

OFAT regime, is greater than the total number of experiments required for the equivalent multivariate set of experiments (i.e. multivariate experiments are more efficient). Secondly, OFAT experiments cannot detect, or quantify, any likely interactions between factors. It has been accepted that catalyst layer thickness is a factor in the effectiveness of the performance of the catalyst layer [66,87,170]. Furthermore, it was recently shown that catalyst coated substrate (CCS) MEA fabrication methods, induce a notable through-plane thickness variation to the CL [47] (see Table 43), that is dependent on the type of substrate the CCS process is applied to. Therefore, the possible interactions between factors are worthy of investigation. The topic aligns well with the aims and objectives of the thesis, and it was decided to proceed with this research on layered catalyst structures using increased platinum presence as the means of varying catalyst concentration levels.

5.3.2. Characterisation of layered catalyst structures

As discussed in section 5.3.1, all carbon supports were loaded with catalyst sites, but the concentration (expressed as a weight percentage) per carbon black (referred to from here on as 'wt%Pt-on-C') particle is not the same. Figure 73 gives a schematic representation of the three styles of catalyst concentration variation that have been proposed in section 5.3.1. These can be summarised as reducing the concentration of catalyst adjacent to the GDM by one of three possible methods:

1) Increased ionomer (typically Nafion) content to effectively 'dilute' the concentration of carbon black/Pt agglomerate particles.
2) Additional carbon-black particles to effectively 'dilute' the concentration of carbon black/Pt agglomerate particles.
3) Two (or more) separate mass loadings (wt%Pt-on-C) of Pt particles on carbon black agglomerate particles –i.e. two separate ink formulations.

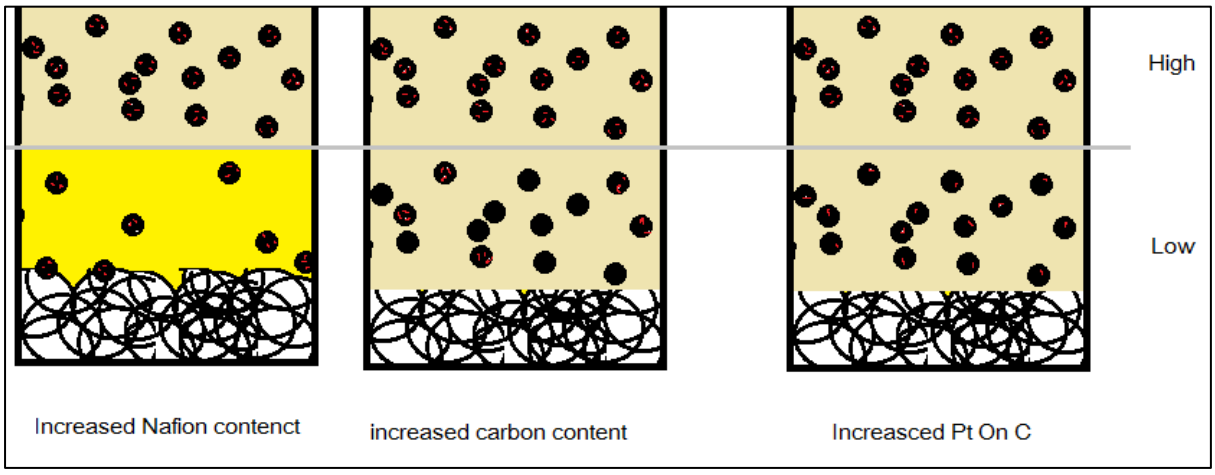

Figure 73: Pt Concentration variants

(Nafion® increase (left), carbon black increase (middle), Pt loading gradient (right))

In work completed for this thesis, approach three is adopted (as discussed in section 5.3.1). Chapter 4 detailed MEA fabrication and ink formulations (see section 4.3.3) previously. The same procedure has been followed for the creation of layered ink structures, with the wt%Pt-on-C of the catalyst agglomerate particles being varied for each layer. The fabrication method and image analysis has been reported previously [47] (see Appendix 5) and is reproduced here for the connivance of the reader.

5.3.3. Scanning electron microscopy and layered catalysts

Basic scanning electron microscope (SEM) images were captured with a Cambridge Instruments (England) Stereoscan 360 Tungsten Filament SEM. More detailed SEM and energy dispersive X-ray spectroscopy (EDS) images were captured using a Leo (Carl Zeiss) 1530VP FEG-SEM (Germany) fitted with an Oxford Instruments X-Max 80 mm EDS detector (England).

To gain an appreciation for the distribution of the catalyst material in the layered catalyst, sections of GDM samples were prepared and coated with layers of catalyst. The first layer applied to the GDM used 10wt%Pt-on-C ink, and the second layer used a 30wt%Pt-on-C ink formulation (ink formulations have been detailed previously in section 4.3.3). A comparative single layer 40wt%Pt-on-C formulation was also examined. The samples shown were painted directly by hand onto Toray TGP-H-120 carbon paper.

Figure 74, shows a cross section of 0.4mg.cm^2 coated carbon paper, with a uniform 50wt% Pt-on-C ink formulation. The ink was applied to the uppermost surface of the GDM substrate, and it is readily apparent that the material has penetrated a significant depth into the body of the GDM. Backscatter imaging (the bottom image in Figure 74) reveals that platinum particles have penetrated through the full thickness of the test piece.

Figure 75, shows the test piece with dual layered catalyst materials (a 10 and 30wt% Pt-on-C ink formulation). The lower concentration catalyst ink was applied first. When judged ‘by eye’, certain regions of the test sample show a degree of stratification. The low concentration layer adjacent at the bottom of the image has 0.1mg of Pt.cm^{-2} achieved with 10wt% Pt-on-C, and the high concentration region closest to the membrane has 0.3mg of Pt.cm^{-2} on 30wt%Pt-on-C. In Figure 75, the platinum coated onto the GDM (CCS method of fabrication) ended up with a distributed layer of ever diminishing catalyst concentration, but with very little control of the effect. Attempts to measure this were inconclusive: Regions of the GDM show a layered distribution in the CL, but when values were averaged over several images, the error in the measurement made this far from conclusive.

To more accurately measure the distribution of the carbon, and attempt to track the various other components in the catalyst inks, a higher resolution FEG-SEM (field emission gun- scanning electron

microscope) with EDS was employed. Figure 76 shows the dual layered ink formulations deposited onto the GDM, with backscatter map of the platinum distribution at high magnification.

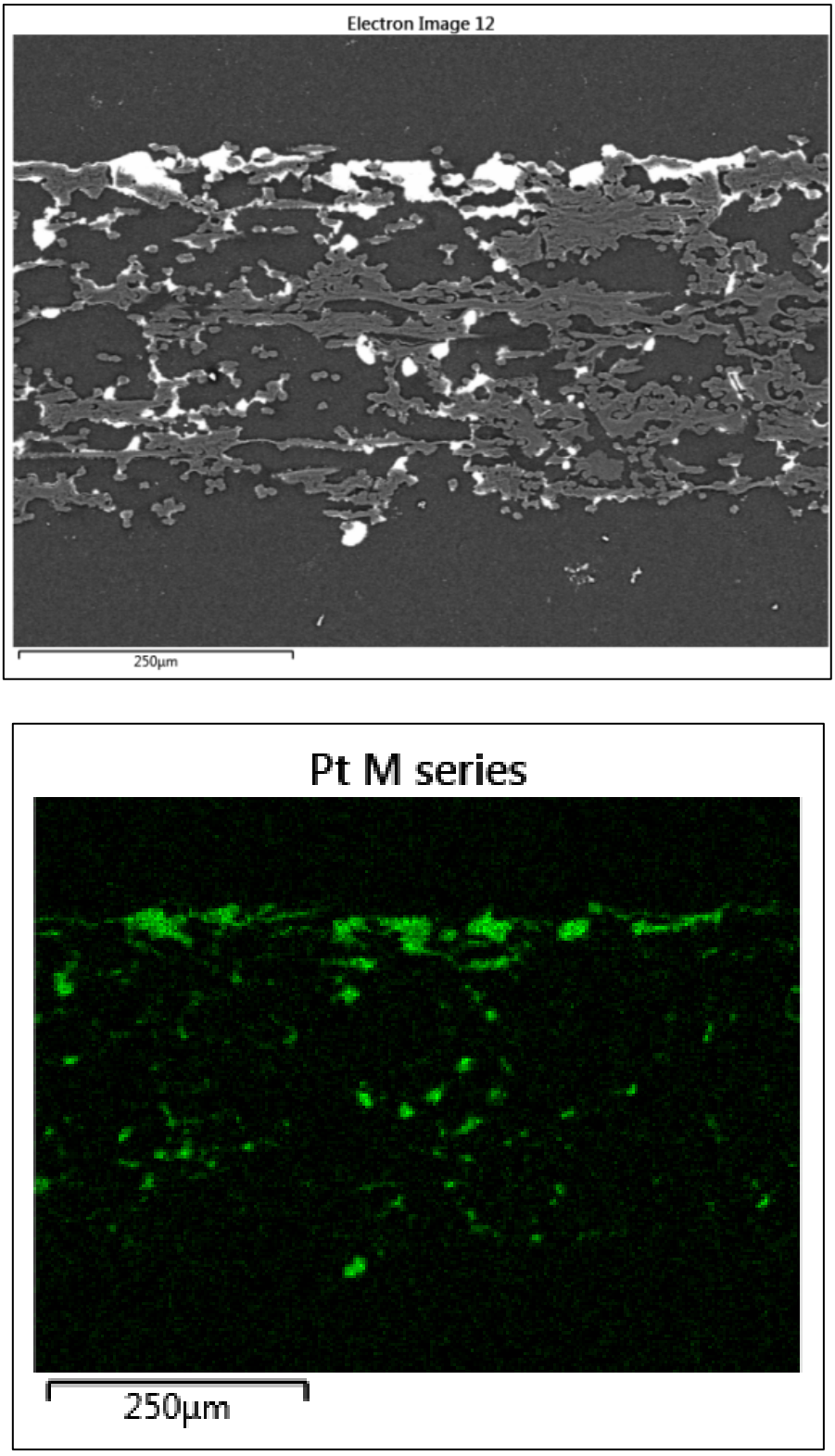

Figure 74: SEM distribution of 50wt% Pt-on-C

(0.4mg.cm^{-2} uniform application SEM (top) and Pt-Map (bottom))

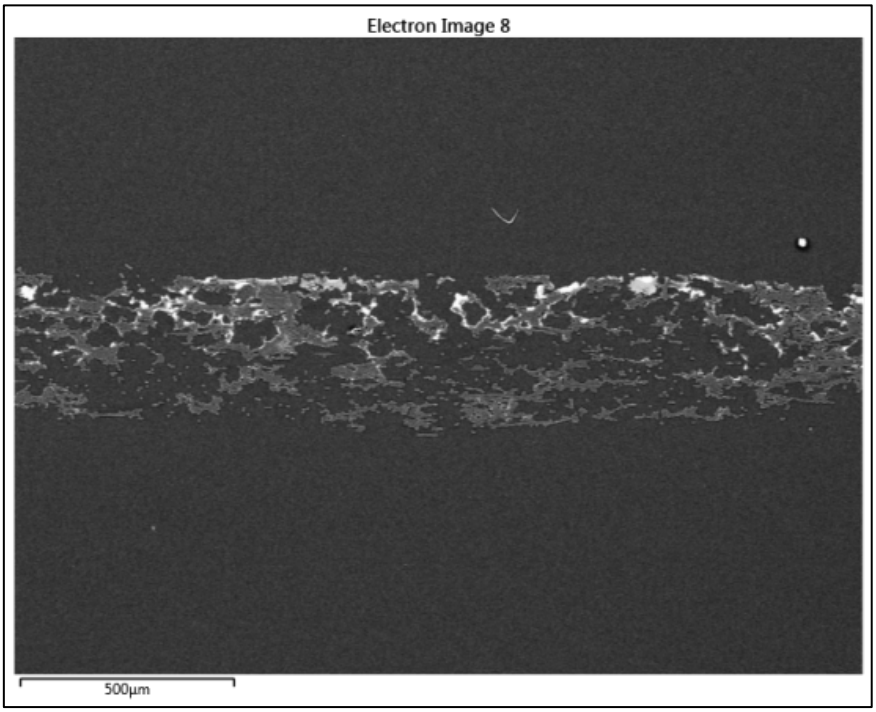

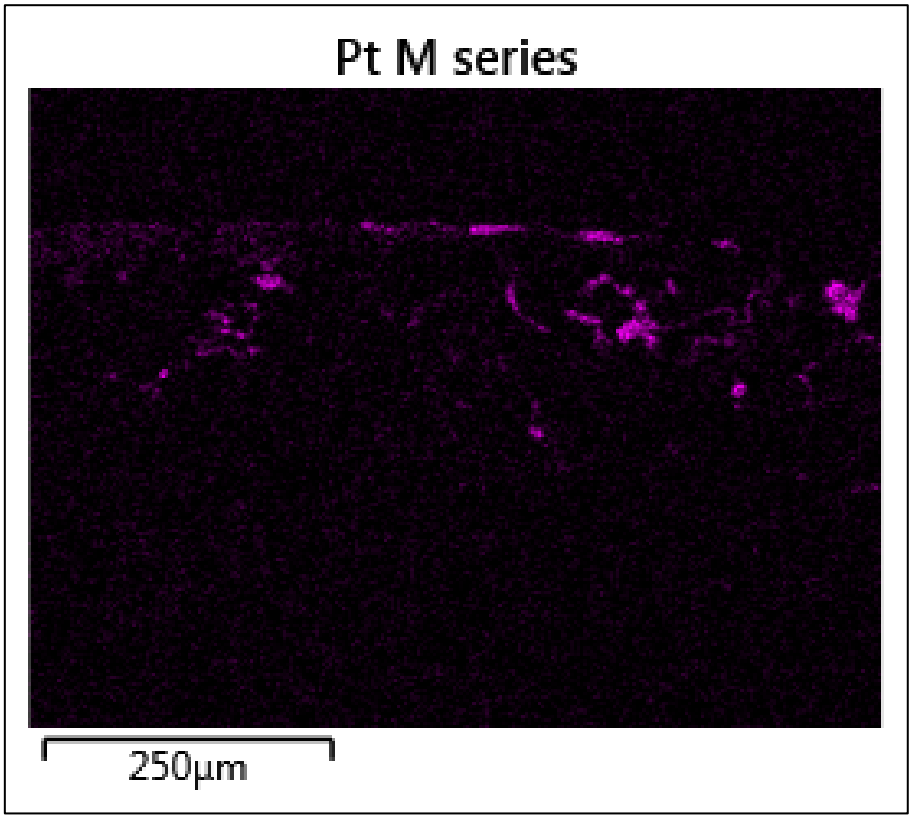

Figure 75: SEM dual layer Pt-on-C catalyst ink

(10wt% and 50wt %)

Figure 75, details initial attempts to investigate the efficacy of dual layer coatings, and it can be seen that changes in the platinum distribution can be made by the simple expedient of reducing the concentration of Pt-on-C. Adapting the technique to allow more time for the layers to dry, the ability to limit the penetration of the platinum into the body of the GDM was improved still further, though a degree of deeper tracking long porous structures was clearly evident. In this case, 10wt% and 30wt% set of ink formulations was used to create the test sample.

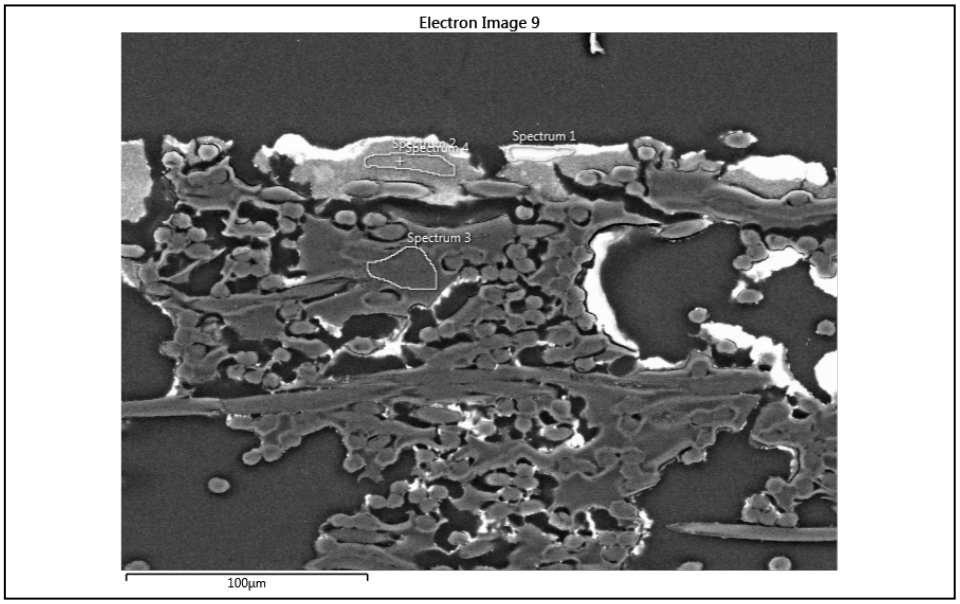

Figure 76: FEG-SEM dual layer Pt-on-C surface

Figure 76 is the FEG-SEM image of the dual layered ink distribution once again. EDS mapping of Pt, Fluorine (F) and Carbon (C) was generated. As the Toray TGP-H-120 paper was an uncoated test piece, the mapping of fluorine atoms by EDS is a useful method for determining if the Pt catalyst and the dispersant ionomer, which was used in the ink formulation, are located in the same regions. This would not be the case for most GDMs, which have extensive fluorine atoms present in the hydrophobic fibre coatings, as discussed previously in Chapter 2 and Chapter 4. Comparison of the Pt and F maps in Figure 77 show that, at this stage of the MEA fabrication process (i.e. before hot pressing), the two elemental maps show broadly similar distributions. Distribution analysis, using a Matlab® image processing toolbox, was used to define the areas of platinum that can be regarded as a single particle of catalyst. The location of those single Pt particles was then measured in pixels, and plotted as a histogram of the centroid-point of each identified cluster of platinum atoms (see Figure 78). It is clearly shown that there is a bi-modal distribution of platinum catalyst sites. It is therefore suggested, that the dual layered catalyst ink technique has been successful in creating stratified concentrations of platinum catalyst sites: a 10wt%Pt-on-C region deeper in the body of the GDM and a 30wt% closer to the surface of the GDM where the ink was originally applied. This work has been reported previously [47].

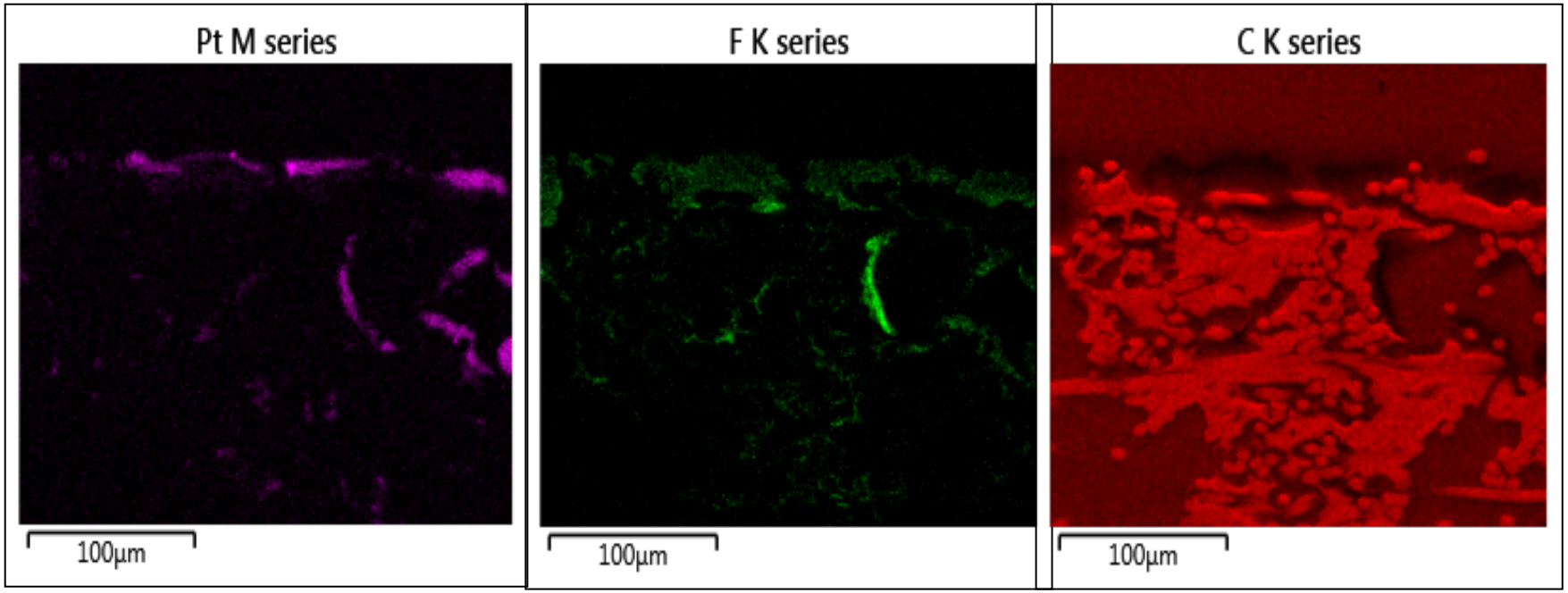

Figure 78: EDS mapping for figure 77

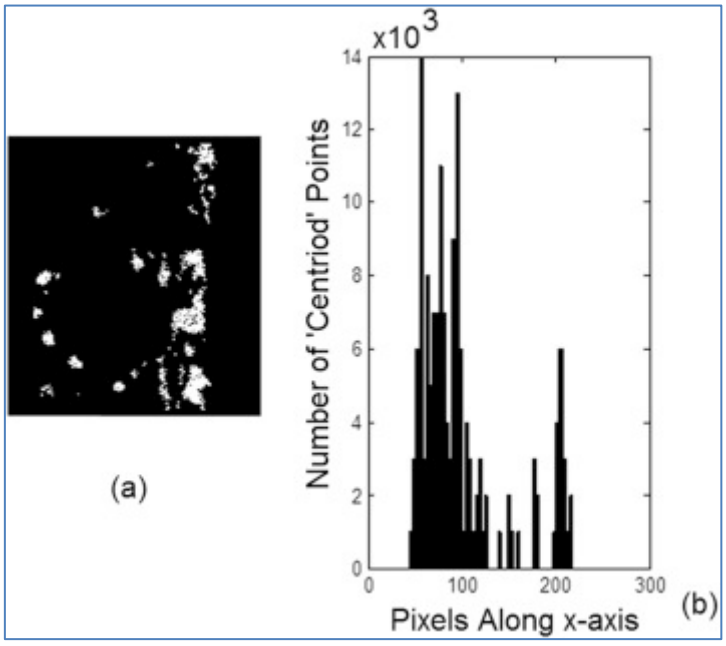

Figure 78: SEM dual layer Pt-on-C platinum distribution

5.4. Gas diffusion media, catalyst layers and degradation

The contribution of overall fuel cell degradation from the catalyst has been established (see section 5.2.1). The importance of the catalyst layer and the likely impacts of dual layered catalyst structures have been discussed in depth (see section 2.5 and section 5.3.1), and it has been confirmed experimentally that a suitable dual layered catalyst MEA fabrication method is possible.

From experience developed during the work completed for this thesis, and bearing in mind discussions from the literature review (see Chapter 2), it is possible to develop a set of research questions for the intended multivariate set of experiments. The attempt to answer these questions would contribute to the achievement of the stated aims and objectives of this thesis (see section 1.1.1 and section 1.1.2). Seven proposed research questions are enumerated below:

I. Will variable wt% loading of Pt-on-C provide an equivalent performance to previous works that used a ‘dilution’ method to reduce the presence of catalyst sites in the low consecration layers?
II. Will reduced Pt loading overall of dual layer catalysts provide performance improvements?
III. When applied as a CCS (catalyst coated substrate) will there be a difference between paper and ‘felt’ cathode GDMs?
IV. Will there be a noticeable difference in degradation rate for dual layer catalyst structures?
V. What impact does constant, square wave (rapid potential transit) or triangular (slower potential transit) load have?

VI. Will degradation be directly proportional to time spent at maximum load in the duty cycle?

VII. What, if any, factors co-vary in this data set?

With a broad set of topics to investigate, the resources spent on long-term degradations studies were justifiable. Consider that a traditional OFAT method to this investigation would need to repeat the experiments once for each of the first six questions just raised, and question seven would be difficult, if not impossible, to answer. The elapsed time to attempt this work would be many times greater, as would the number of test samples required. The M-ANOVAR design of experiments and their results were completed and are discussed in the subsequent chapter (Chapter 6).

5.5. Summary of Chapter 5

Layered catalyst structures were identified in the literature review (see section 2.5), as a possible topic of interest to the fuel cell community, that may also benefit from the multivariate investigation. Having established in Chapter 4 that M-ANOVAR methods can be used to generate useful statistical models for complex fuel cell systems; layered catalyst structures were considered in more detail in Chapter 5.

The initial literature review was expanded upon, with particular attention being paid to the contribution catalyst layers make to the overall degradation of fuel cells in section 5.2 and section 5.3. Having established an improved understanding of layered catalyst and catalyst degradation, a one-dimensional catalyst layer model, created by Spiegel (2008) [87], was reproduced and adapted (as far as was practical and reasonable) to match the experimental apparatus and test conditions available to the author (see section 5.3.1). This included the use of a Thiele modulus based variant of the Butler-Volmer equation (see section 5.3.1) to model layered catalyst structures more closely; and in the process develop a greater understanding of the systems and mechanisms involved in the degradation of fuel cells, specifically as they apply to layered catalyst fuel cells. As discussed previously (see section 2.2 and Chapter 3), any attempt to understand a system through detailed statistical methods (such as the ones proposed in this thesis) must be grounded in an understanding of the fundamentals of the object or process being studied. The re-working of the Spiegel model [87], or any other equivalent model of catalyst layers and their changes to ECSA, is one way of ensuring the researcher has sufficient knowledge to make informed choices, when conducting the subsequent statistical analysis. In accordance with the aims and objectives of this project (see section 1.1.1 and section 1.1.2) this knowledge building exercise has been reported in detail, as an example to the reader of the need to have sufficient understanding of the system being studied. Section 5.3.2 then reported on experimental work undertaken to verify that sufficient capability existed to create layered catalyst, suitable for further experimentation, though attempts to model layered catalyst structures

using the Thiele modified agglomerate Spiegel (2008) [87] model were of limited success: This was in line with the literature on dual layered catalyst systems (see Chapter 2).

Based on the information generated in Chapter 2, Chapter 3, Chapter 4, and previous sections of Chapter 5: Section 5.4 reported a set of un-answered research questions, that were well suited to an M-ANOVAR experimental case study. This is a key achievement of this thesis, in accordance with the aims and objectives reported earlier (see section 1.1.1 and section 1.1.2). These research questions informed the design of experiments for the next stage of the work: The case study of M-ANOVAR methods in a fuel cell context. This work is detailed in Chapter 6.

6 Dual Layer Catalyst Materials, Gas Diffusion Media and Degradation

6.1 Introduction to Chapter 6

As discussed in section 5.4, a series of research questions have been identified, which appear well suited to multivariate investigation. Having established the suitability of the M-ANOVAR approach in Chapter 4 for complex fuel cell research topics, a similar approach was undertaken for the case study presented in Chapter 6.

The original plan for this research was to undertake an investigation into a wide range of variables:

- Dual Layer Catalyst concentration.
- Duty cycles.
- Types of GDM.
- Reactant gas Flow rate.
- Temperature.

However, the inability to conduct long duration studies with gas flows and temperature settings at anything other than those reported in the stoichiometric ratio in Table 45, prevents this from being practical. Therefore the Design of experiments was based on the following input factors:

- Dual layer catalyst concentration on the cathode.
    - Uniform catalyst layer (0.35mg.cm^2 of 30wt%Pt-on-C).
    - High concentration dual layer (0.4 mg.cm^2 of 40wt%Pt-on-C +10wt%Pt-on-C).
    - Low concentration dual layer (0.3 mg.cm^2 of 40wt%Pt-on-C +10wt%Pt-on-C).
- Duty cycles.
    - Constant.
    - Square wave.
- Types of GDM.
    - Paper.
    - Non-woven (felt).

The anticipated output factors are:

- Peak power.
- Degradation rate.
- Gradient of the Ohmic loss region.

6.2 Design of Experiments

In compliance with the information set out earlier (see section 2.2 and Chapter 3), the following design of experiment was developed as shown Table 44. This details the dual layer MEA identifier number (FUDL-MEA#), the standard order the design was originally created in (std), the random order number the samples were tested to avoid any ambient condition or operator induced experimental errors (run), the catalyst loading to be used for the cathode, ($mgPt.cm^{-2}$) the duty-cycle or constant load (load cycle) each MEA will be operated under for the degradation trial, and the type of GDM to be used as the GDL for creating the MEA (cathode GDL).

Table 44: Dual layer degradation DoE

FUDL-MEA#	std	run	mgPt/cm^2	load cycle	cathode GDL
3	10	14	0.3 Low D	-1	Fberg
2	15	1	0.3 Low D	Constant	Fberg
4	12	6	0.3 Low D	1	Fberg
17	14	17	0.35 Uniform	-1	Fberg
18	18	7	0.35 Uniform	Constant	Fberg
19	17	18	0.35 Uniform	1	Fberg
7	11	13	0.4 High D	-1	Fberg
6	16	10	0.4 High D	Constant	Fberg
8	13	16	0.4 High D	1	Fberg
11	1	9	0.3 Low D	-1	Toray
10	6	5	0.3 Low D	Constant	Toray
12	3	2	0.3 Low D	1	Toray
25	5	15	0.35 Uniform	-1	Toray
24	9	12	0.35 Uniform	Constant	Toray
23	8	4	0.35 Uniform	1	Toray
15	2	8	0.4 High D	-1	Toray
14	7	11	0.4 High D	Constant	Toray
16	4	3	0.4 High D	1	Toray

In this case, as shown in Table 44, the load cycle refers to either a constant one amp load or one of two other possible setting. '-1' is a slower, ramped' transit power (triangle wave), and '+1' refers to the rapid transient, 'square wave' setting. The initial concept was to apply the two transient duty cycles in such a way the wavelength would remain the same for both, but the time at maximum/minimum loads would vary.

Additionally, it was considered desirable to keep the number of transients for both duty cycles the same, so that all cells will 'pass through' a given potential region the same number of times. As discussed previously (from section 2.6, Table 5), certain degradation mechanisms occur at key potentials. Moreover, cycled duty loads at multiple potentials, will pass through those key degradation potentials for a varying amount of time. This 'dwell time' at a given potential will, in turn, have a significant impact on the degradation rate of the fuel cell (see Figure 14). To achieve parity between square and triangular wave duty cycles; a reduction of the total wavelength of the square wave duty cycle to only ten seconds, instead of the much longer durations reported by some authors [34], was required.

This reduced wavelength was implemented to provide a more direct comparison between the two duty cycles (square and triangle), and provide a definite answer to the question of the relationship between the time at peak load and MEA degradation. Other authors have adopted similar duration rapid cycles [125,176] with an even shorter square wave cycle time of three seconds. These rapid transit duty cycles accelerate carbon corrosion [70], at the types of potentials normally experienced in a working fuel cell electrode, though most studies focus on the corrosion of catalyst supports rather than the GDM itself. The FCCA is not capable of performing the triangular wave load variation from four to zero amps load in less than ten seconds and so the ten-second wave is adopted as a useful compromise for both the square and triangular duty cycles. This wavelength results in the triangle wave being more of a 'stepped' triangular function, but there is no way to overcome this issue with the test equipment available. The design space of input variables can be easily visualised (Figure 79), with each node on the cube representing an experiment.

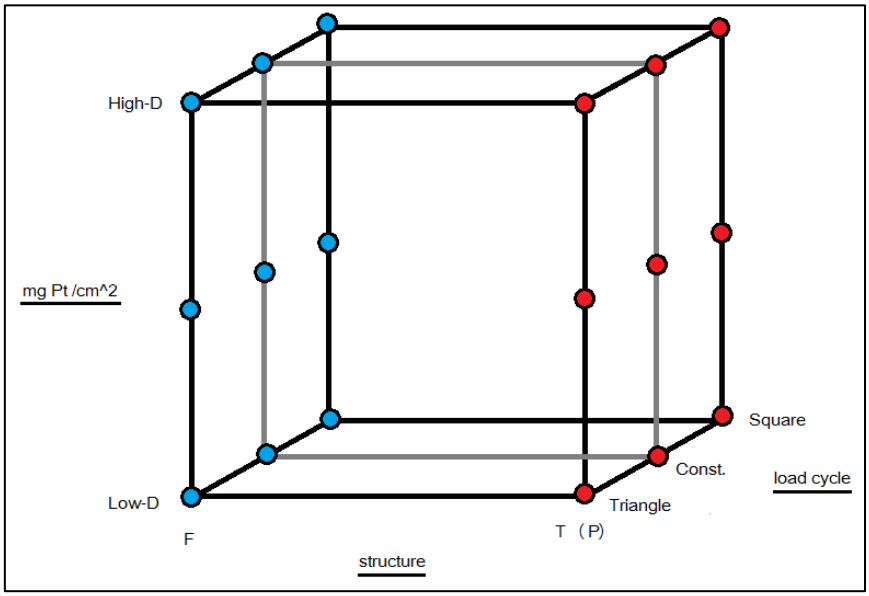

Figure 79: Dual layer DoE 'Design Cube'

Ideally, one or more central points should be replicated inside the design space, but the categoric nature of 'Felt OR Paper' for the GDM structure prevents this. Fortunately, there were a good number of central points in the load cycle and Pt loading axis of the design space that will help to pick up curvature in the system. The principles of categoric factors, and repetition of data points, have been discussed in depth previously in section 2.2, and Chapter 3.

Replication of data points would help to define the error, and additional samples were manufactured to facilitate interim testing. All MEAs were constructed in accordance with the manufacturing procedures outlined previously (see section 4.3.3 and section 5.3.2) with multiple layers of inks: Each layer consisting of 40wt% Pt-on-C and 10wt% Pt-on-C being deposited to create either a high or low concentration 'dual catalyst layer'. All inks were applied 'one layer at a time' and left to dry overnight in a fume cupboard. Uniform catalyst layers for the anode, and the cathode, were fabricated using a 30wt% Pt-on-C. Anode and cathodes were fabricated in accordance with the information shown in previous chapters (see Chapter 2, Chapter 3, and Chapter 4). A full list of anode and cathode MEA Identifier numbers and cathode constructions are available in Appendix 3(Original Data).

Contestant load at one-Amp samples were placed in one of six test cells in either FCCA1 or FCCA2 in a randomised fashion. As the long term testing was taking place, the square and triangular duty cycle Visual Basic for Applications© (VBA) programme was written and tested on a separate computer. When efforts were made to use the working code on the FCCA devices, it was found that it could not be installed as a result of inbuilt security features. As both FCCAs were 'legacy machines'; despite assistance from the manufacturers (Intelligent Energy Ltd.) and the Loughborough University IT department, no solution to this problem could be found short of a complete reinstall of the software. Due to the age of the test apparatus, it was decided not to risk this approach.

As a result, it became possible to only test the cycled loads in one test cell at a time, and with a human operator re-setting the duty cycle after every 13 repetitions of the wavelength. This means that, for the square and triangular duty cycles, the samples could only be tested in normal working hours (eight hours a day), and the total time taken to conduct these tests would be far greater than expected. This made it impossible to complete the work as designed in the time available. To overcome this, a simplified design was developed (exact samples tested correspond to the 'MEA number' from the tables in Appendix 3) as shown in Figure 80.

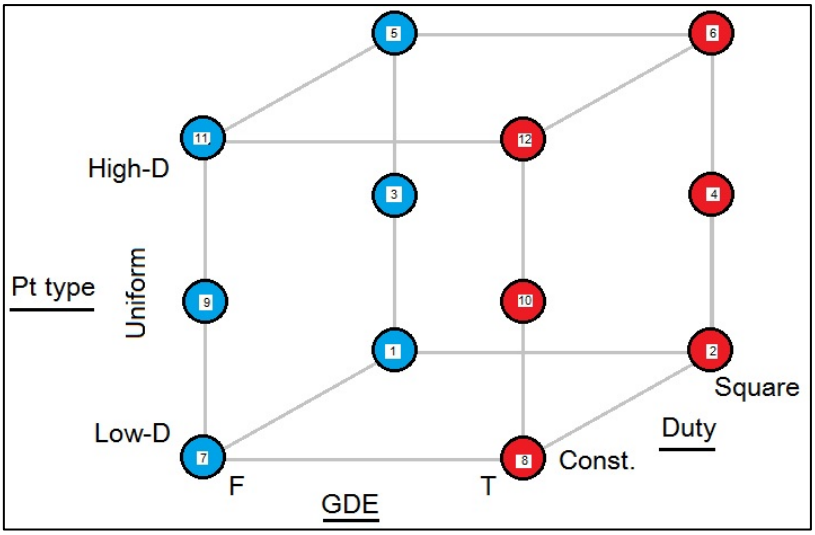

Figure 80: Reduced complexity 'Design Cube'

While this is a far from a desirable set of events, it is an opportunity to demonstrate the flexibility of the designed experiment approach. As long as the investigator is not attempting to examine a very small number of possibly co-varying factors (i.e. an unmodified two factors at two levels design). When real world experimental conditions prevent the original design being undertaken, the existing design can often be modified.

This modification is far easier and simpler to achieve when using dedicated DoE software such as the Design Expert Pro utilised in this research. The reduced complexity design is not as robust as the previous design, and is less able to detect curvature in the design space response. The original short duration square wave with a repeating cycle of five seconds at zero amps followed by a five second four Amps (or maximum available from the cell), was kept. It had been hoped that the software 'lockout' would be solved and it would be possible to return to the original design space that would include a triangular wave load cycle. Unfortunately, this did not prove to be the case in the long run.

6.3 Experimental method

Following the process already outlined (see Chapter 3, Chapter 4 and previous sections of Chapter 6) a series of MEAs were fabricated. Anode fabrication was exactly identical to that already outlined, and all anodes were made from Toray TGP-H-120 paper

Toray TGP-H-120 paper:

- No MPL.
- No Hydrophobic coating.
- 1717 µm mean pore size.
- 370 µm through-plane thickness.
- 61.8% porosity.

Cathode GDMs were either TGP-H-120 (as the anode), or a Freudenberg 'felt' like non-woven.

Freudenberg H23 non-woven[5]:

- No MPL.
- No Hydrophobic coating.
- 1148 µm mean pore size.
- 210 µm through-plane thickness.
- 61% total porosity.

It had been intended to include a woven cathode structure in addition (a Tenax-Toho TCC-3250 was considered as the best match in terms of basic properties), but resource constraints prevented this from being undertaken. The two GDMs selected were broadly similar in many respects, and were the most closely matched available for the two different structures. Therefore any major deviation between peak power out of the two families of GDM (paper and non-woven) should be due to their 'structure' rather than any other factors. Data sheets for both GDMs are available in Appendix 1.

Additional factors, such as reactant gas flow rate and temperature variation, were considered. Unfortunately, initial investigations in these factors soon revealed that long duration (100's of hours), continuous operation, of the test cells at 0.6 Volts using the FCCA apparatus were extremely sensitive to temperature and gas flow: The cells would regularly drop below 0.2 Volts for brief periods of time. This in turn would trigger the automated shutdown sequence of the test apparatus. Automated safety features are a critical part of long duration experimental testing, and cannot be circumvented.

The drop in voltage experienced during the testing at one-Amp constant load samples was, it is suggested, due to a lack of reactants being available at the catalyst sites. It was found that increased gas flow rates eliminate the issue. In light of the fact that increased reactant flow rates eliminated the problem, it is further suggested that this is a 'flooding' event. Flooding occurs when product H_2O is not removed from the CL and GDM sufficiently quickly. The suggested flooding issue will have been exacerbated by the selection of GDMs with no hydrophobic coating or MPL to aid in the water management of the cells. With this in mind, gas flow rates were set for all test conditions:

- H_2 gas.
    - Flow rate 60 sccm (0.06 litres per minute).
    - Pressure = 1.5 bar(a).
- Air.
    - Flow rate.
    - Pressure = 1.5 bar(a) 150 sccm (0.15 litres per minute).

[5] This product has been renamed 'H23' from 'H2315' during the time since this work was started

At a setting of 1 Amp load, voltage was 0.6 Volts (V), and the cell stoichiometry was calculated as [26]:

$$Watts = W = 1 * 0.6 = 06Watts \quad \textbf{(6-1)}$$

O_2 usage

$$O_{2,mol/s} = \frac{W}{4 * VF} \quad \textbf{(6-2)}$$

$$O_{2,kg/s} = \frac{(32 \times 10^{-3})\, W}{4 * VF} \quad \textbf{(6-3)}$$

Using air instead of pure O_2 this becomes:

$$(air)O_{2,kg/s} = \frac{(28.97 \times 10^{-3})\, W}{0.21 * 4 * VF} \quad \textbf{(6-4)}$$

Therefore,

$$(air)O_{2,kg/s} = \frac{(28.97 \times 10^{-3})\, 0.6}{0.21 * 4 * 0.6 * 96487} = 3.57 \times 10^{-6} \quad \textbf{(6-5)}$$

this equates to 1.09×10^{-2} $m^3.hour^{-1}$ which equates to 18.2sccm. For hydrogen the calculation is:

$$H_{2,mol/s} = \frac{i}{2F} \quad \textbf{(6-6)}$$

$$H_{2,mol/s} = \frac{W}{42F} \quad \textbf{(6-7)}$$

$$H_{2,kg/s} = \frac{(2.02 \times 10^{-3})W}{2VF} \quad \textbf{(6-8)}$$

$$H_{2,kg/s} = \frac{(2.02 \times 10^{-3})0.6}{2 * 0.6 * 96487} = 1.05 \times 10^{-8} \quad \textbf{(6-9)}$$

This equates to 3.19x10^{-5} m^3.hour^{-1} which equates to 0.5sccm. Standard cell efficiency is calculated as:

$$Efficiency = \frac{V}{1.48} = \frac{0.6}{1.48} = 0.405 \quad \textbf{(6-10)}$$

The water production rate will theoretically be:

$$H_2O_{kg/s} = \frac{(9.34 \times 10^{-8})W}{V} = \frac{(9.34 \times 10^{-8})0.6}{0.6} = 9.34 \times 10^{-8} \quad \textbf{(6-11)}$$

this equates to 33.6 grams of water per hour produced.

Table 45: Degradation study stoichiometry

Reactant	Utilised volume sccm	Supplied volume Sccm	Stoichiometric Ratio (λ) at 0.08A.cm^{-2}
H_2	0.5	60	112.8
O_2 (21% Air)	18.2	150	8.3

The stoichiometric ratio for hydrogen is extraordinarily high (as shown in Table 45) but, as stated previously, this experimental set up was found to be the only stable configuration over time, for these materials. The relatively small cross section of the GDMs (11.3cm^2 area) means the overall efficiency of the cell will be reduced. The efficiency reduction is due to edge effects, where a significant volume of the cell is adjacent to the outer edge of the disc, this will require additional gas flow to overcome GDM intrusion into the gas channel [177], and this may well factor into the very high stoichiometric requirements as well.

6.4 DoE duel layered catalyst, GDM and degradation results

A full set of all data points is reproduced in this chapter. Each MEA used in these experiments has been individually detailed. Typically, each MEA will have undergone a number of polarisation scans at regular intervals during the degradation test runs. Each polarisation scans change very little between intervals. Therefore, key results from each polarisation scan were reported numerically and plotted graphically to highlight any changes that occur during the degradation trial:

- Initial open cell potential before the polarisation scan ($E_{ocv(i)}$).
- Initial potential at one-Amp (0.08Amps.cm^{-2}) load potential before the polarisation scan ($E1a_{(i)}$).
- Final open cell potential after completing the polarisation scan ($E_{ocv(f)}$).
- Final potential at one-Amp (0.08Amps.cm^{-2}) load after completing the polarisation scan ($E1a_{(f)}$).

6.4.1 MEA ID 02

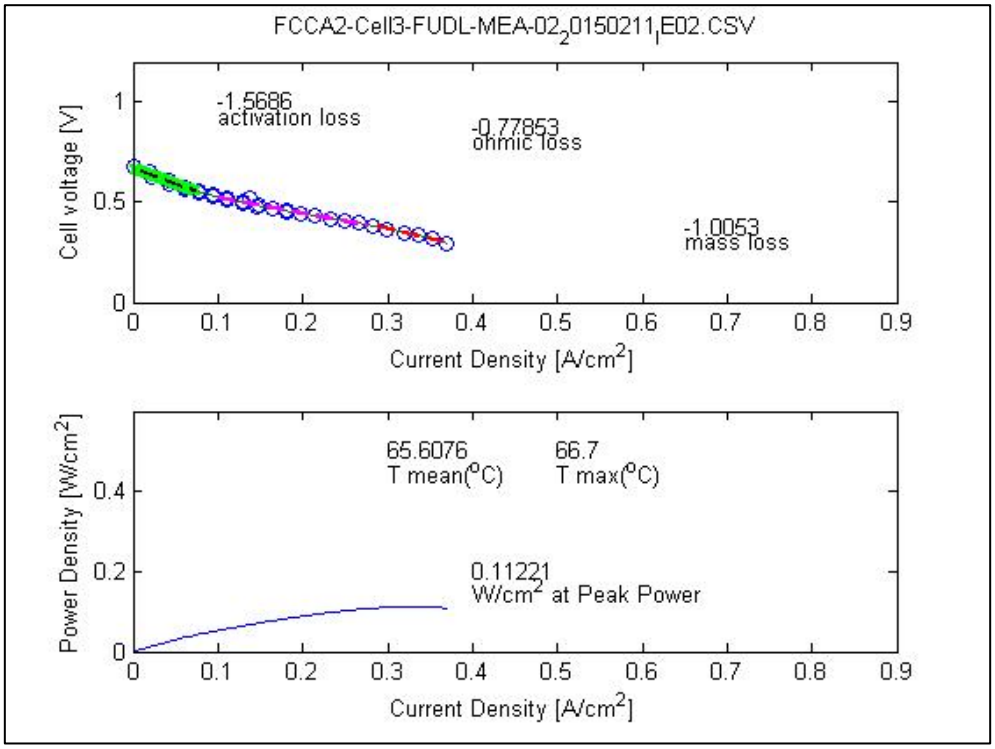

Figure 81: MEA 02 first polarisation curve

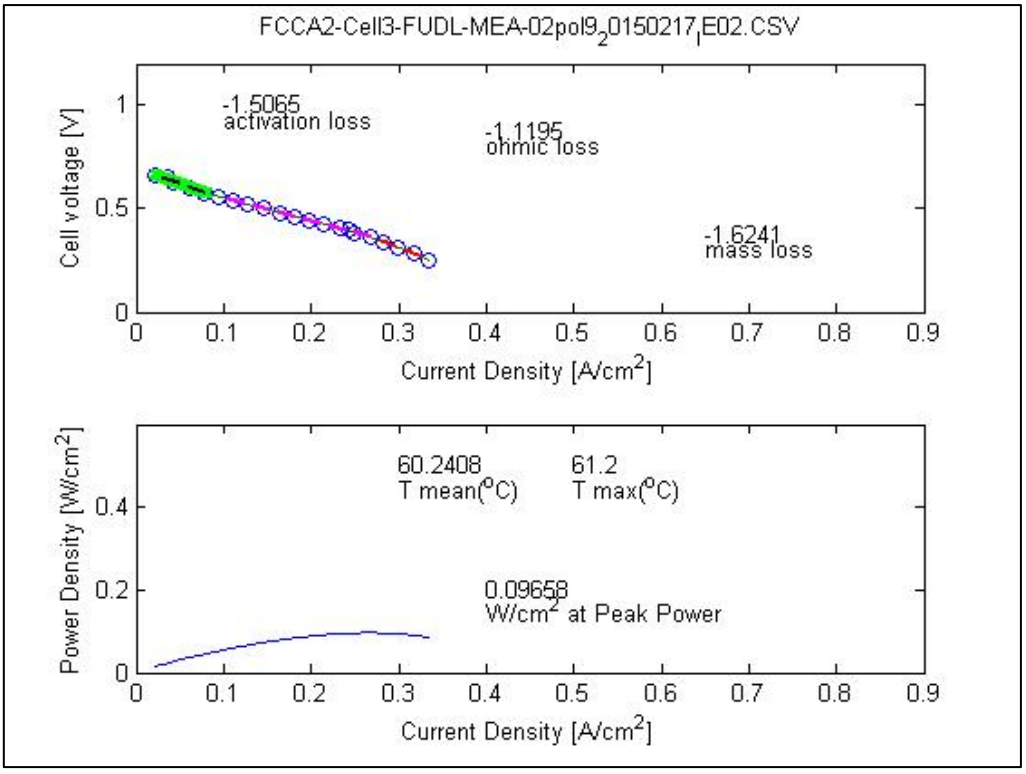

Figure 82: MEA 02 last polarisation curve

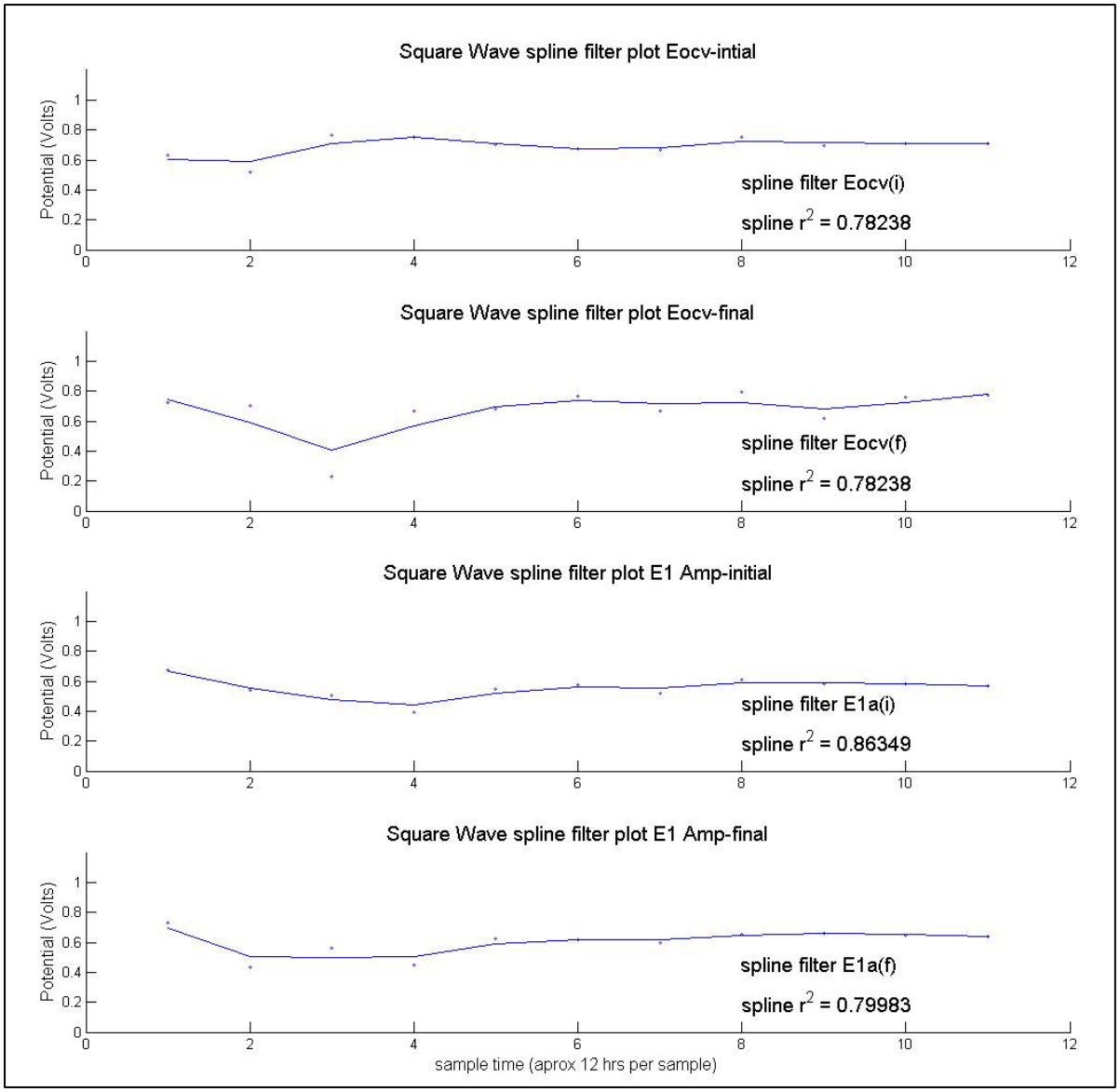

Figure 83: MEA 02 spline fitting for Eocv (i & f), and E1A (i & f)

Figure 81 is the first polarisation scan carried out at the start of the degradation trial on MEA 02. MEA 02 is a Freudenberg cathode GDM with low concentration (0.3mg.cm^{-2}) dual layered catalysts. Figure 82 is the last polarisation scan on MEA 02 after 132 hours of constant operation (24 hours a day) a one-Amp (0.08Amps.cm^{-2}) load. Polarisation scans were taken approximately every 12 hours (exact timing varied depending on the other MEA test samples being tested).

Figure 83 shows the results of the potential measurements on MEA 02 immediately before and after each 12-hour polarisation scan with constant operation. A spline fitting process has been carried out to clearly define a region of linear degradation. This spline fitting operation is explained in more detail in section 6.5.1.

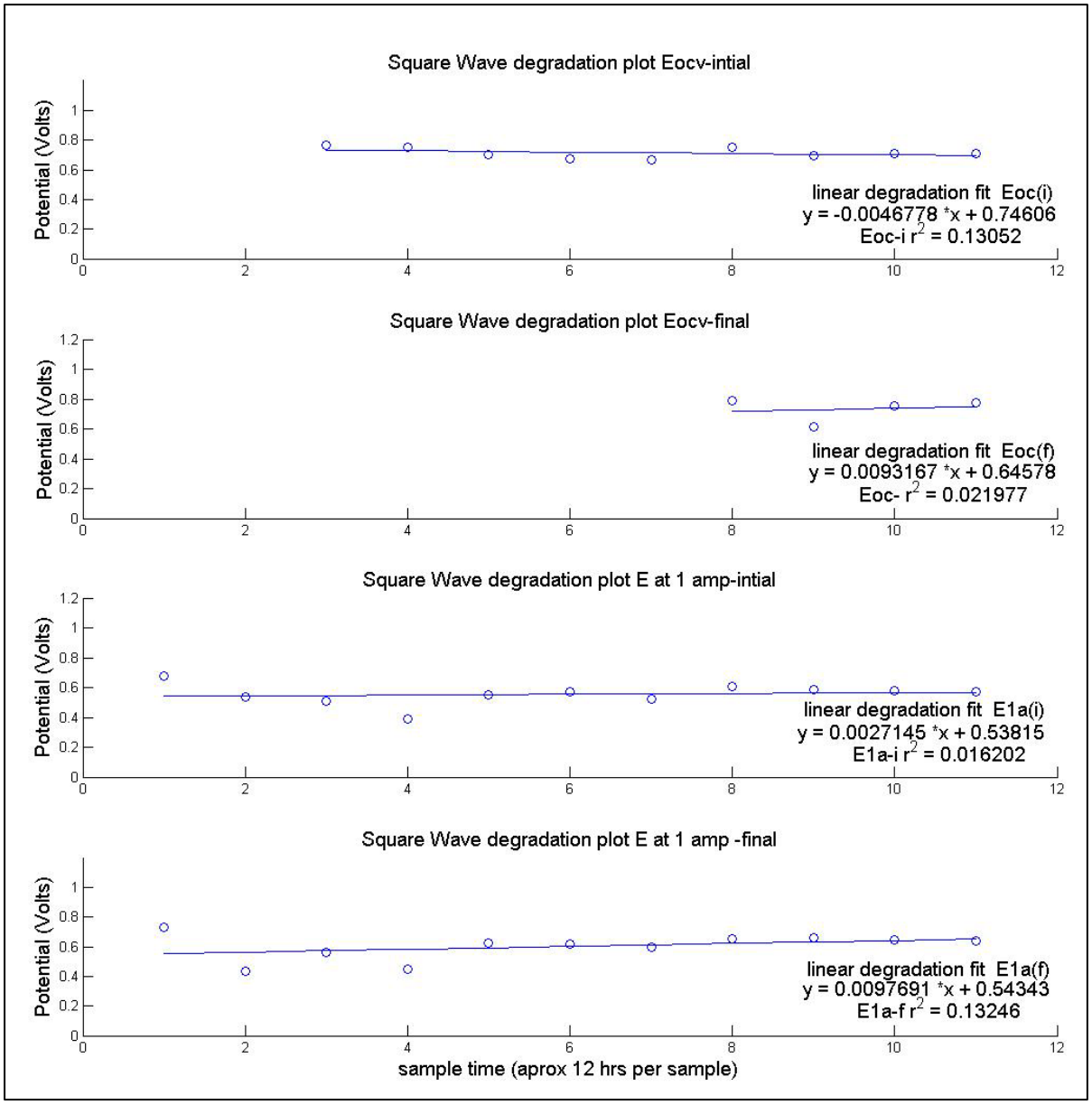

Figure 84: MEA 02 linear degradation region

Figure 84 shows the localised maximum value for each of the potential values identified, with the aid of the spline fitting process in Figure 83, and plots a linear fit to the remaining values until the end of the degradation test run.

6.4.2 MEA ID 04

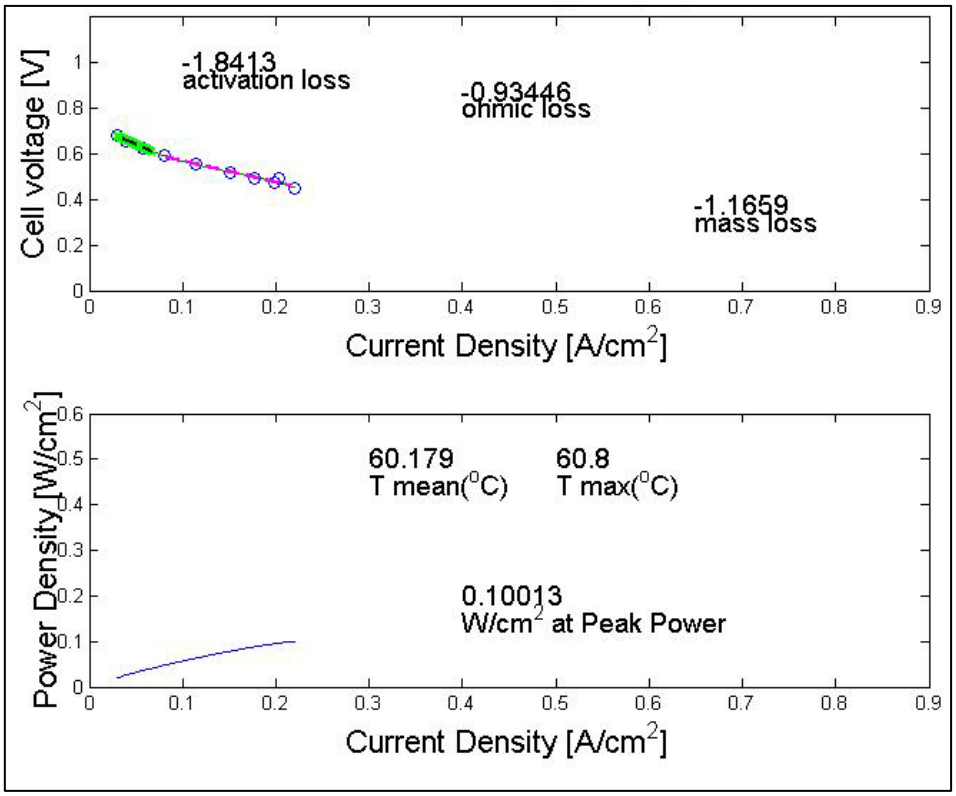

Figure 85: MEA 04 first polarisation curve

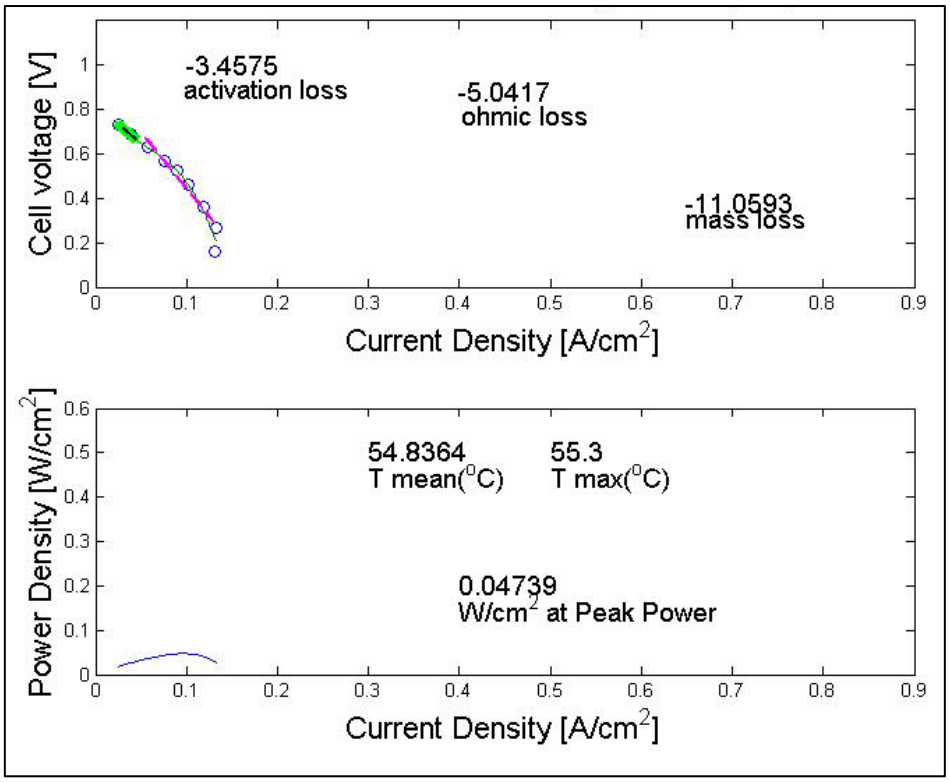

Figure 86: MEA 04 last polarisation curve

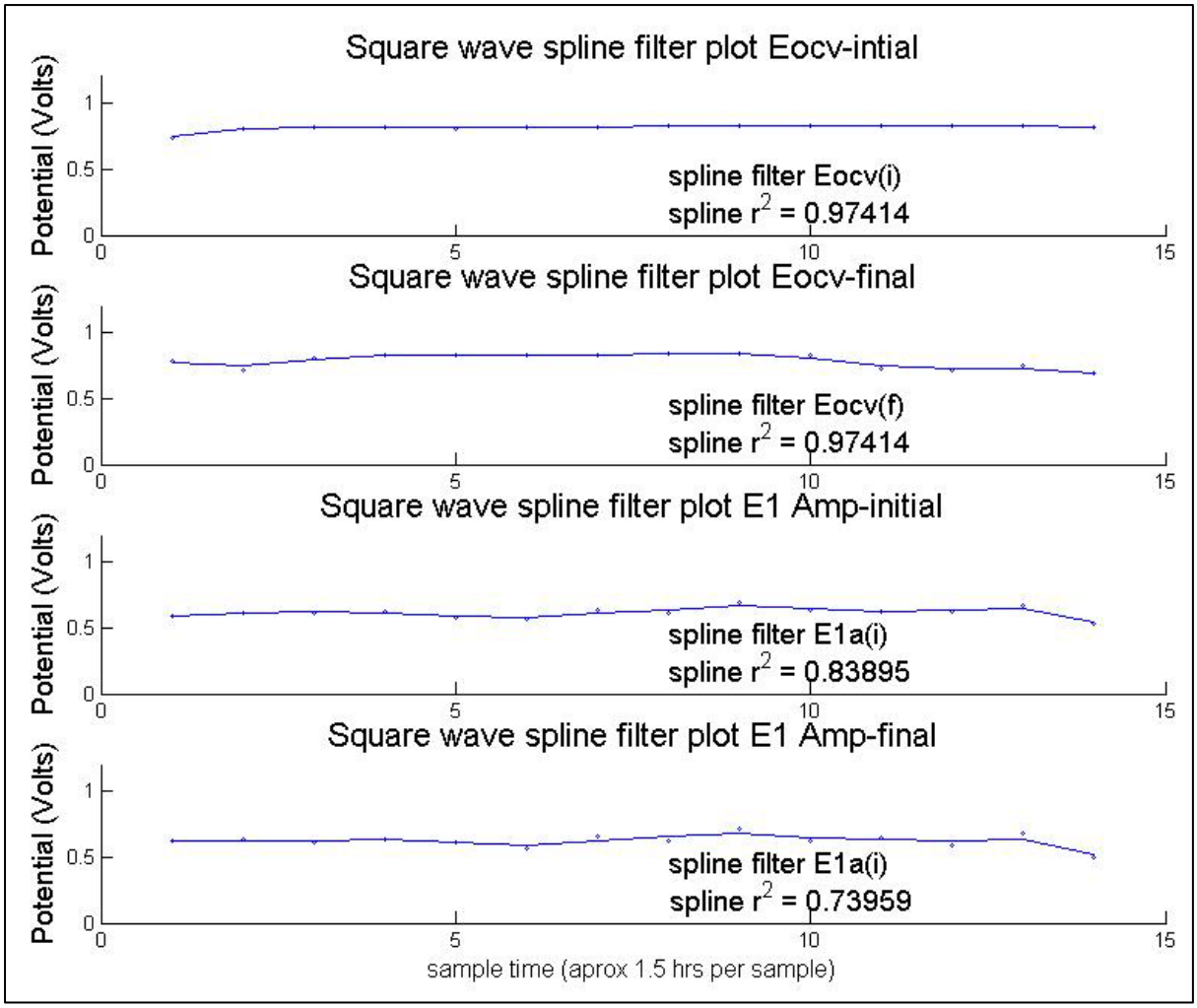

Figure 87: MEA 04 spline fitting for Eocv (i & f), and E1A (i & f)

Figure 85 is the first polarisation scan carried out at the start of the degradation trial on MEA 04. MEA 04 is a Freudenberg cathode GDM with low concentration (0.3mg.cm^{-2}) dual layered catalysts. Figure 86 is the last polarisation scan on MEA 04 after 21 hours of square wave operation (4 Amps to 0.2 Amps cycled every five seconds). Polarisation scans were taken approximately every 1.5 hours (exact timing varied depending on the other MEA test samples being tested).

Figure 87 shows the results of the potential measurements on MEA 04 immediately before and after each 1.5-hour polarisation scan. A spline fitting process has been carried out to clearly define a region of linear degradation. This process is explained in more detail in section 6.5.1.

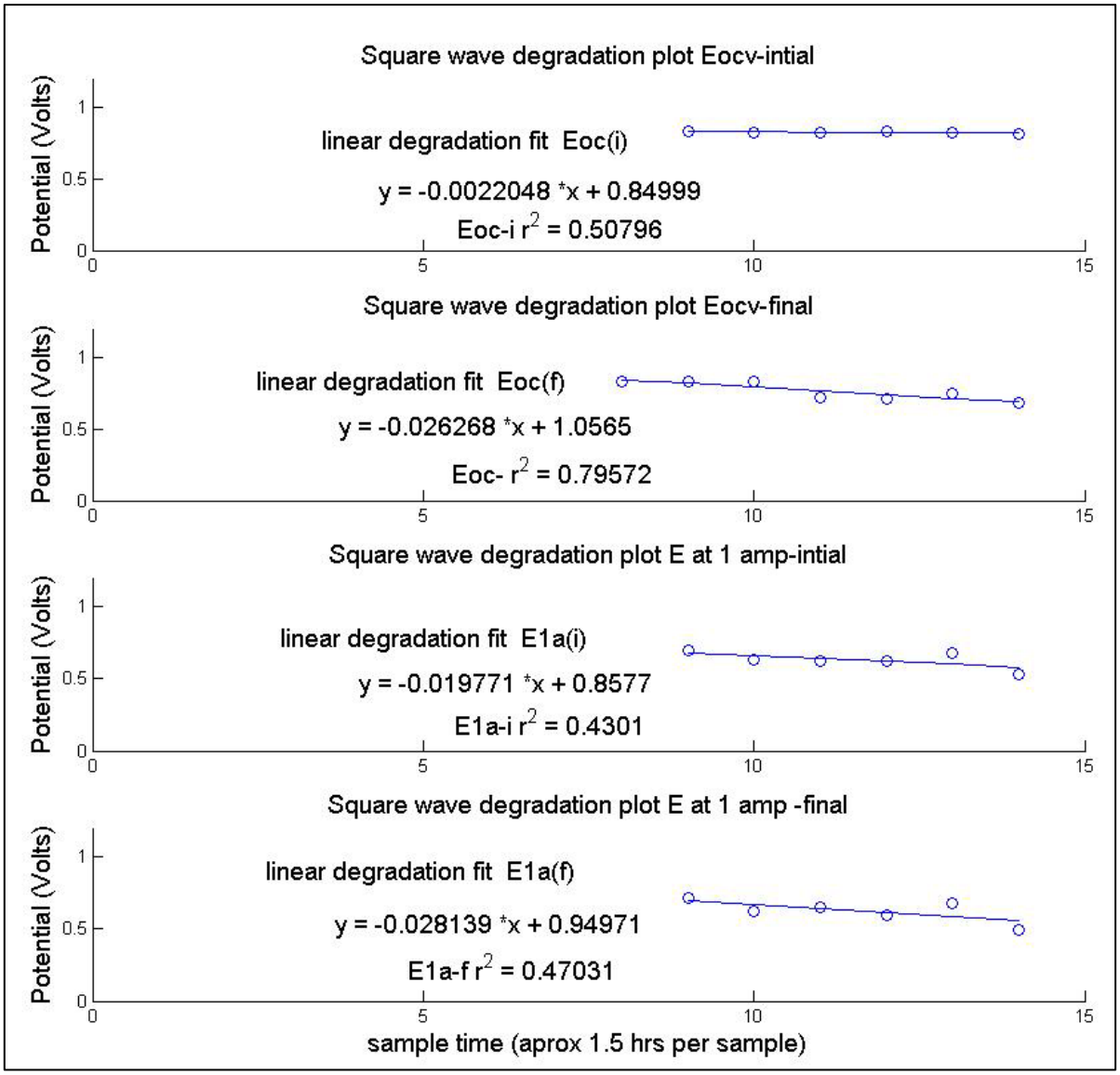

Figure 88: MEA 04 linear degradation region

Figure 88 shows the localised maximum value for each of the potential values, identified with the aid of the spline fitting process in Figure 87, and plots a linear fit to the remaining values until the end of the degradation test run.

6.4.3 MEA ID 06

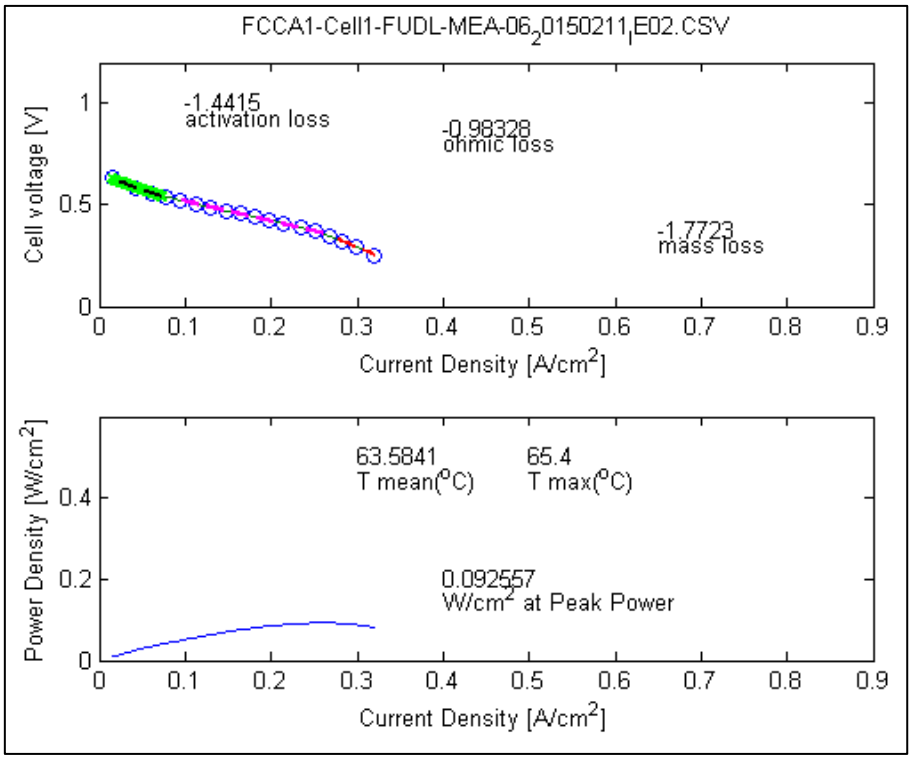

Figure 89: MEA 06 first polarisation curve

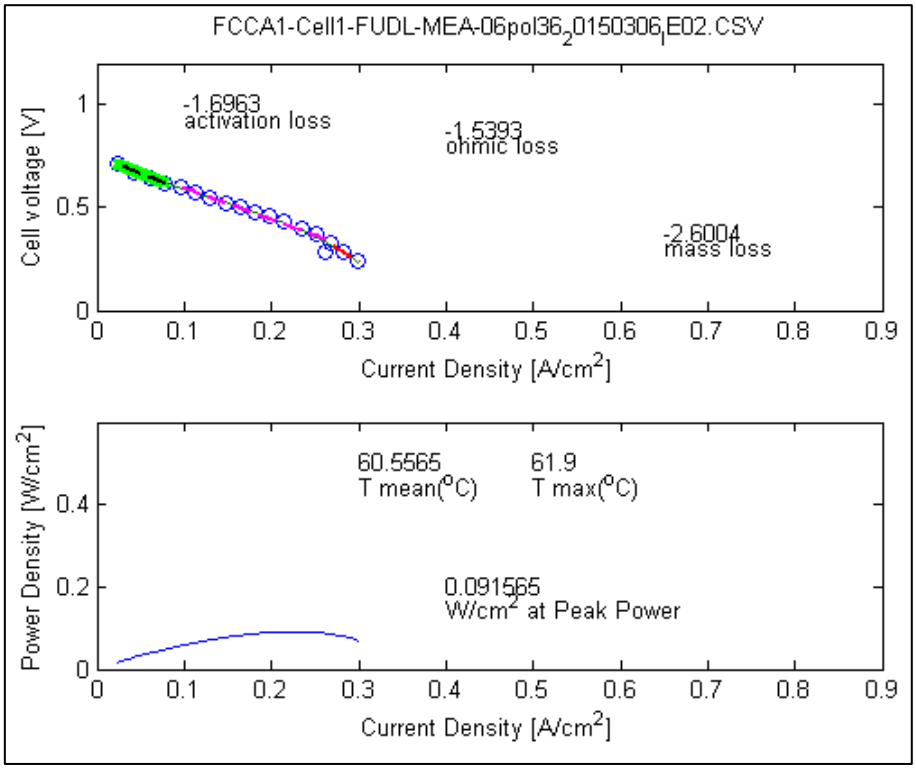

Figure 90: MEA 06 last polarisation curve

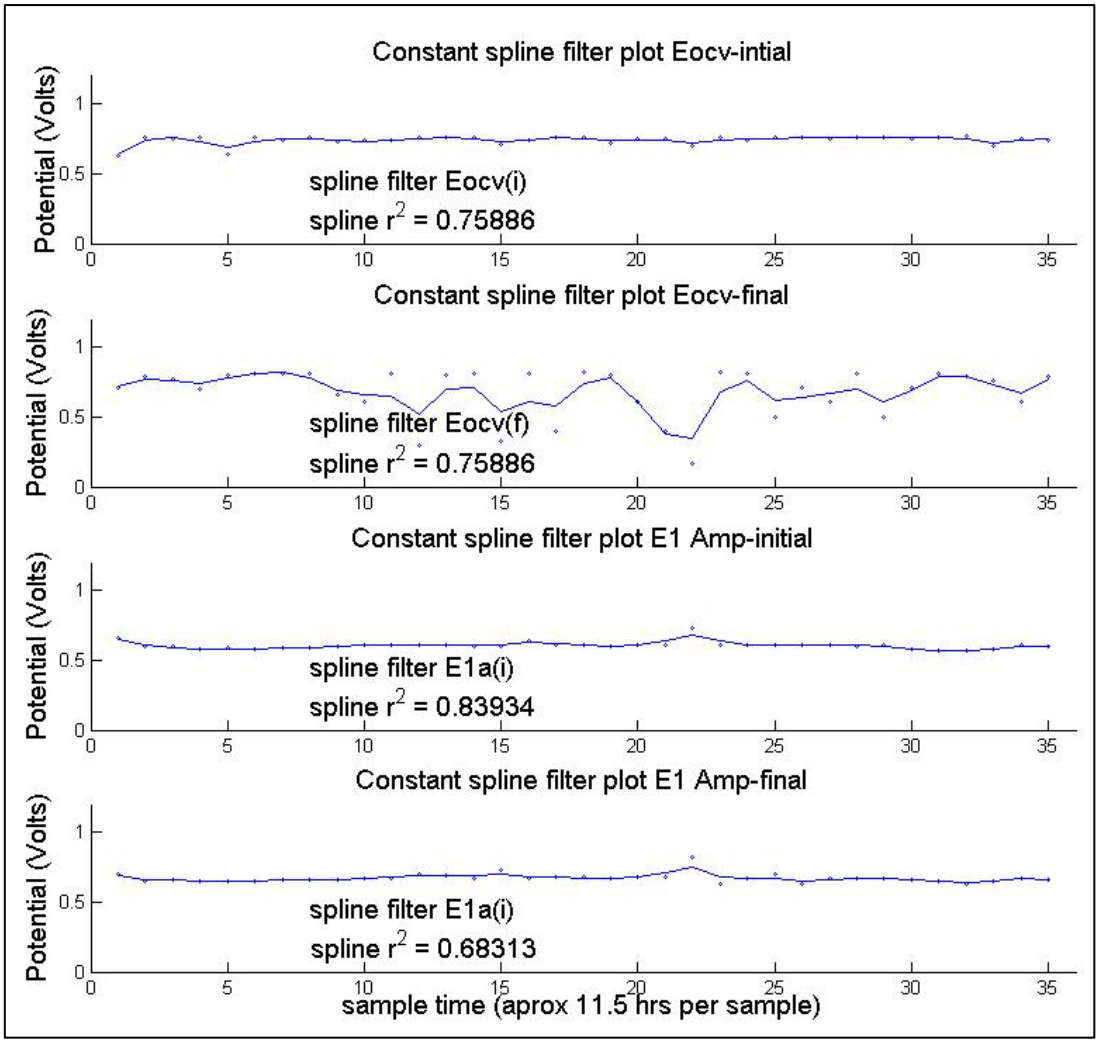

Figure 91: MEA 06 Spline fitting for Eocv (i & f), and E1A (i & f)

Figure 89 shows the first polarisation scan carried out at the start of the degradation trial on MEA 06. MEA 06 is a Freudenberg cathode GDM with high concentration (0.4mg.cm^{-2}) dual layered catalysts. Figure 90 is the last polarisation scan on MEA 06 after 402 hours of constant operation (24 hours a day) a one-Amp (0.08Amps.cm^{-2}) load. Polarisation scans were taken approximately every 11.5 hours (exact timing varied depending on the other MEA test samples being tested).

Figure 91 shows the results of the potential measurements on MEA 06 immediately before and after each 11.5-hour polarisation scan. A spline fitting process has been carried out in order to clearly define a region of linear degradation. This process is explained in more detail in section 6.5.1.

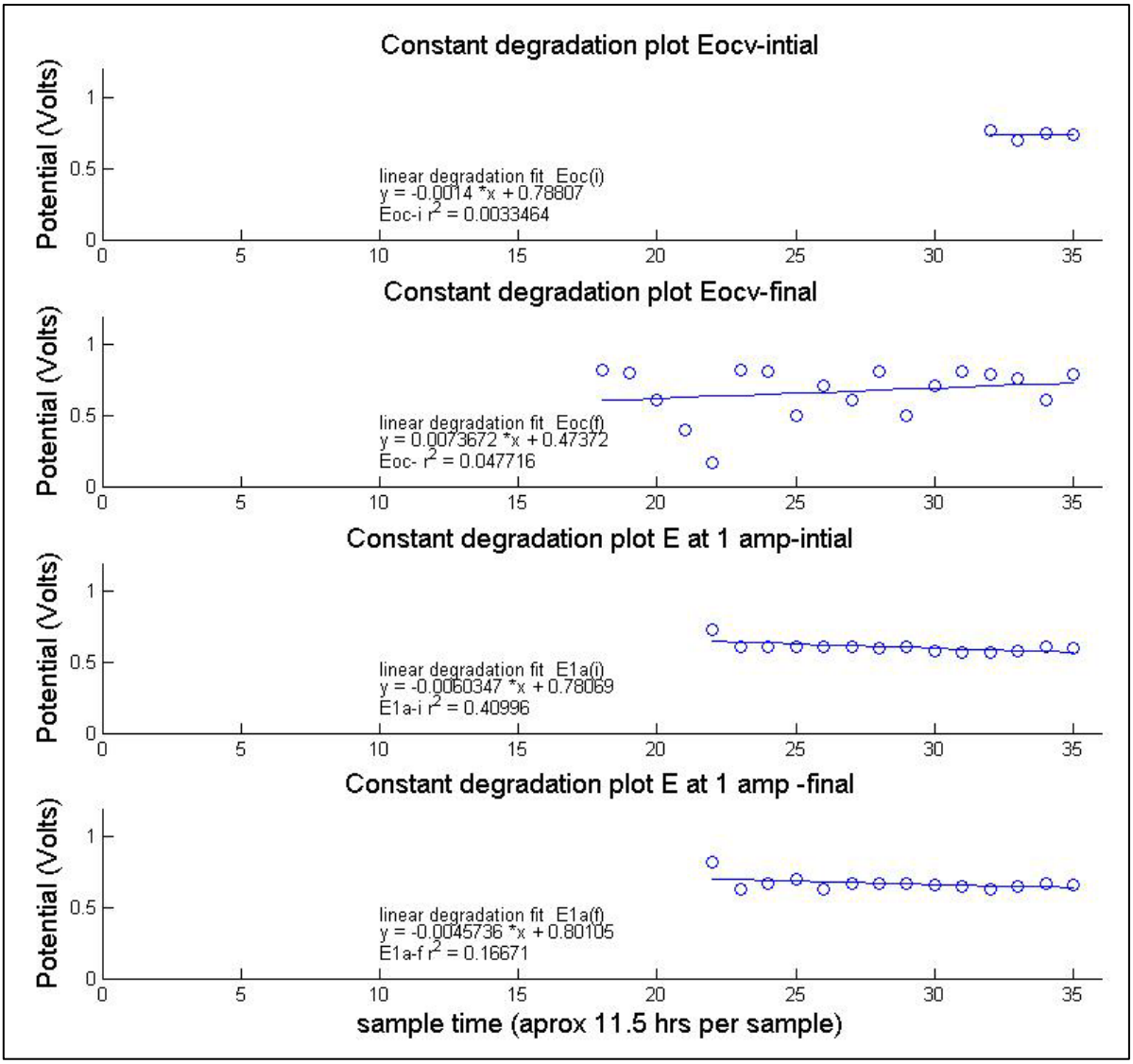

Figure 92: MEA 06 linear degradation region

Figure 92 shows the localised maximum value for each of the potential values, identified with the aid of the spline fitting process in Figure 91, and plots a linear fit to the remaining values until the end of the degradation test run.

6.4.4 MEA ID 08

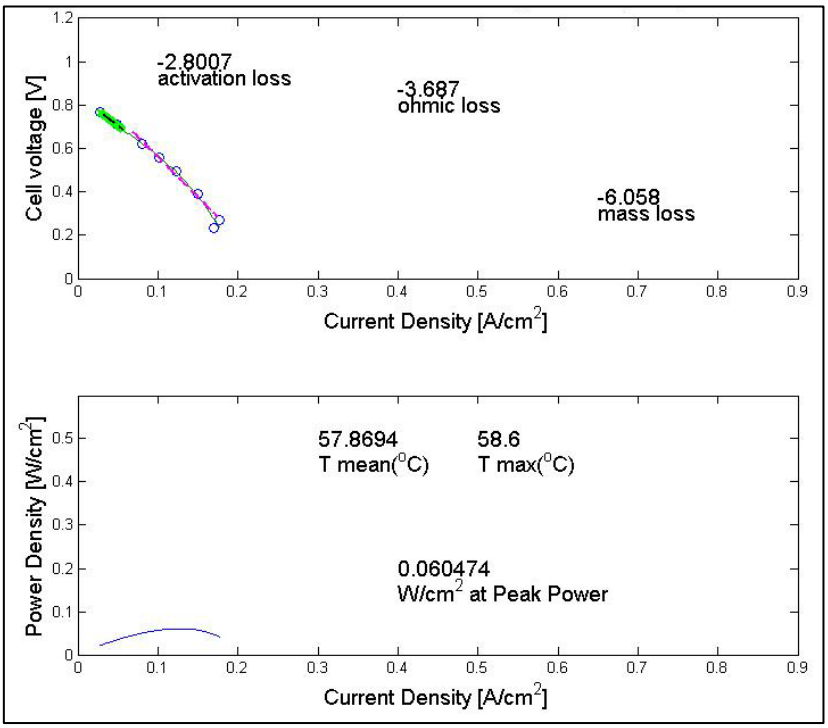

Figure 93: MEA 08 first polarisation curve

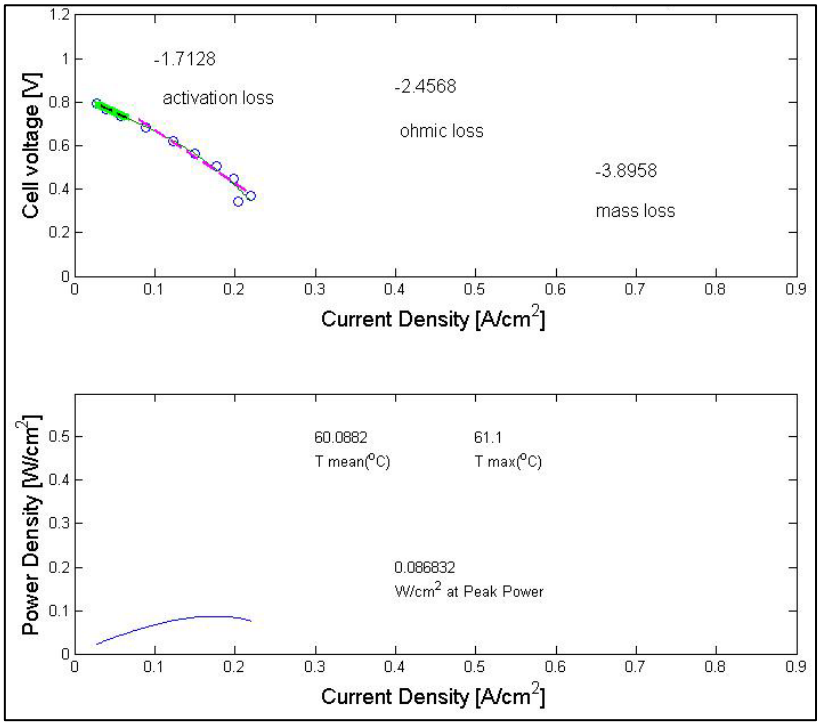

Figure 94: MEA 08 last polarisation curve

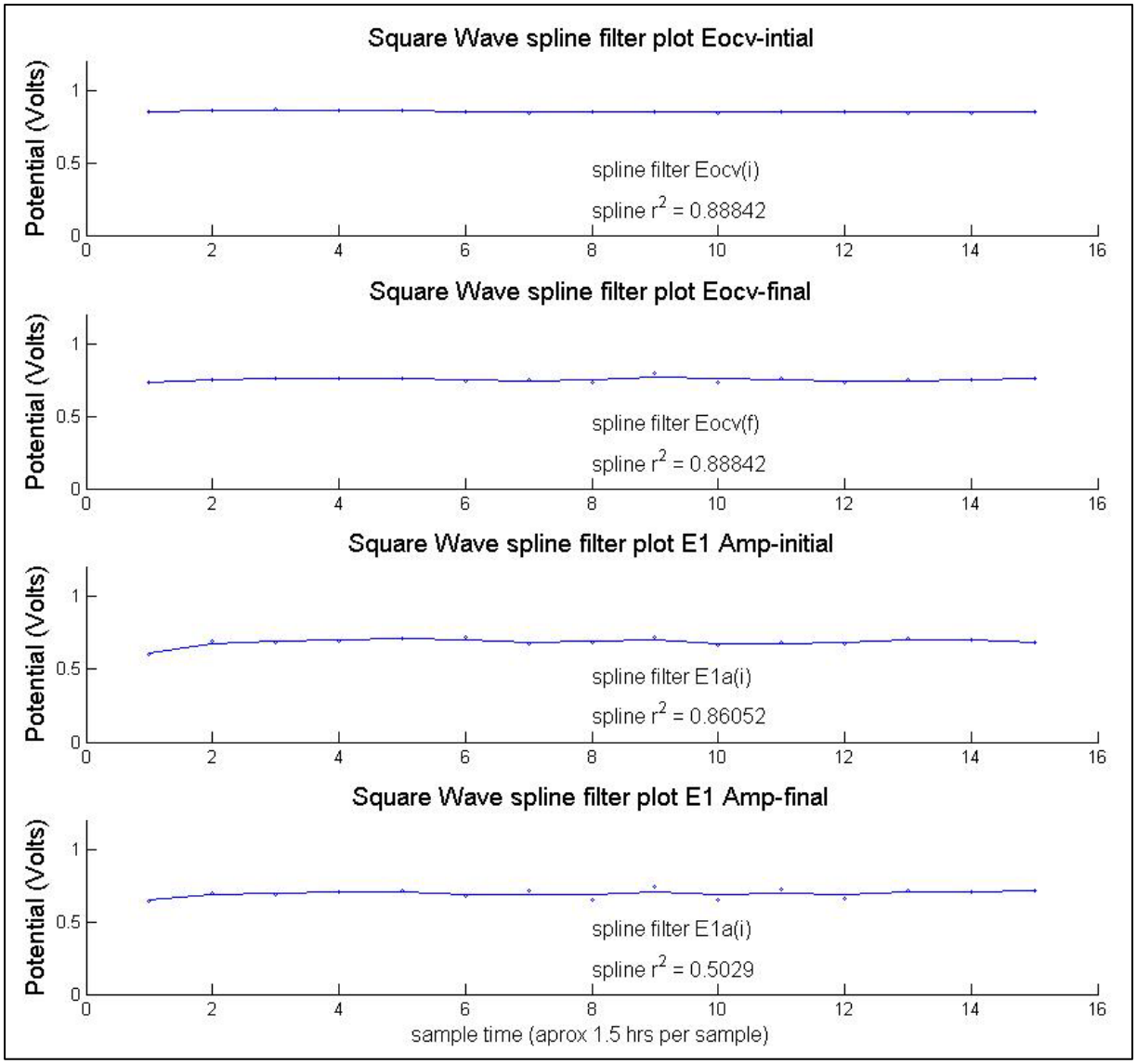

Figure 95: MEA 08 spline fitting for Eocv (i & f), and E1A (i & f)

Figure 93 is the first polarisation scan carried out at the start of the degradation trial on MEA 08. MEA 08 is a Freudenberg cathode GDM with high concentration (0.4mg.cm^{-2}) dual layered catalysts. Figure 94 is the last polarisation scan on MEA 08 after 22.5 hours of square wave operation (4 Amps to 0.2 amps cycled every five seconds). Polarisation scans were taken approximately every 1.5 hours (exact timing varied depending on the other MEA test sample being tested).

Figure 95 shows the results of the potential measurements on MEA 08 immediately before and after each 1.5-hour polarisation scan. A spline fitting process has been carried out in order to clearly define a region of linear degradation. This process is explained in more detail in section 6.5.1.

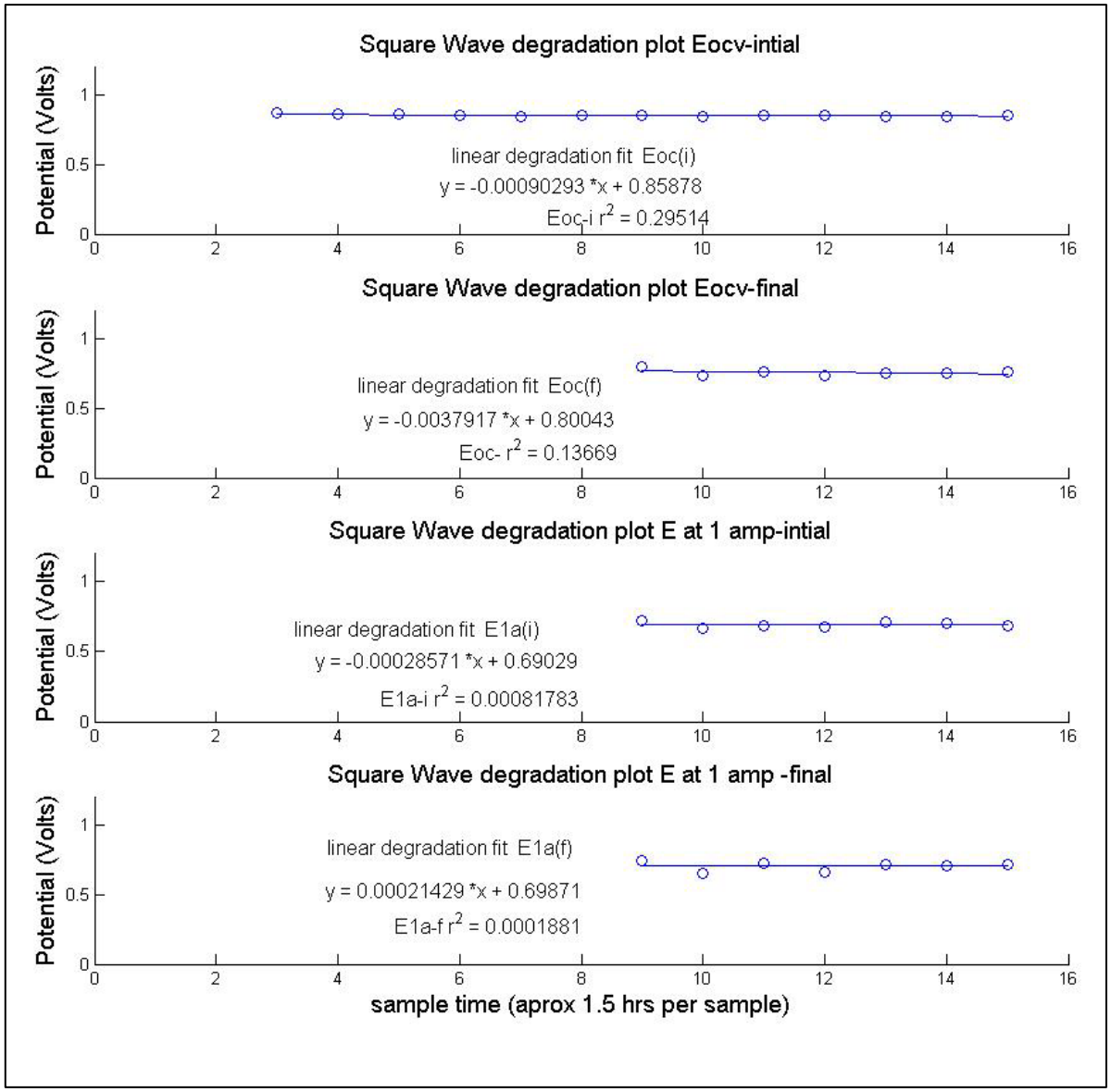

Figure 96: MEA 08 linear degradation region

Figure 96 shows the localised maximum value for each of the potential values, identified with the aid of the spline fitting process in Figure 95, and plots a linear fit to the remaining values until the end of the degradation test run.

6.4.5 MEA ID 10

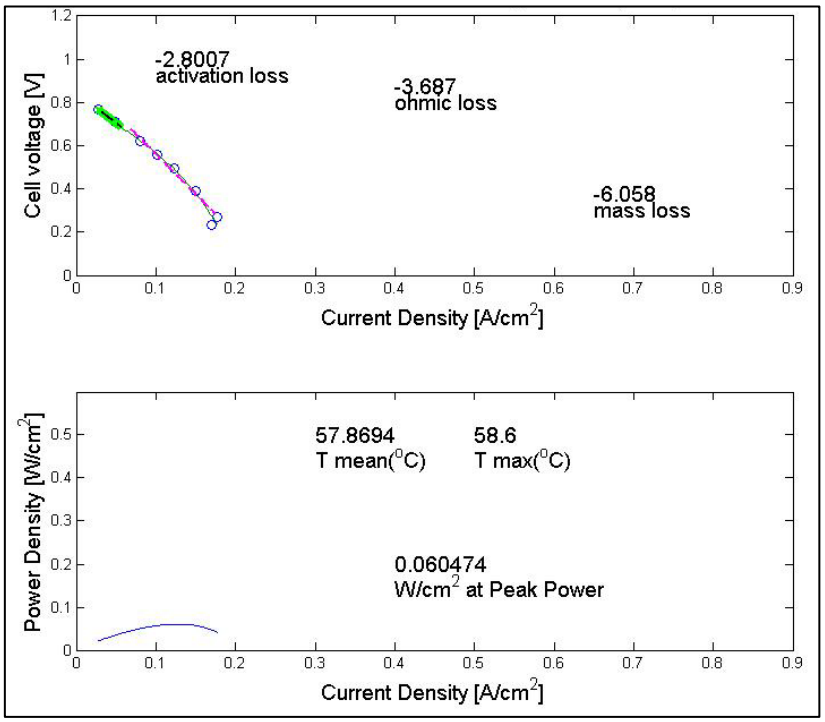

Figure 97: MEA 10 first polarisation curve

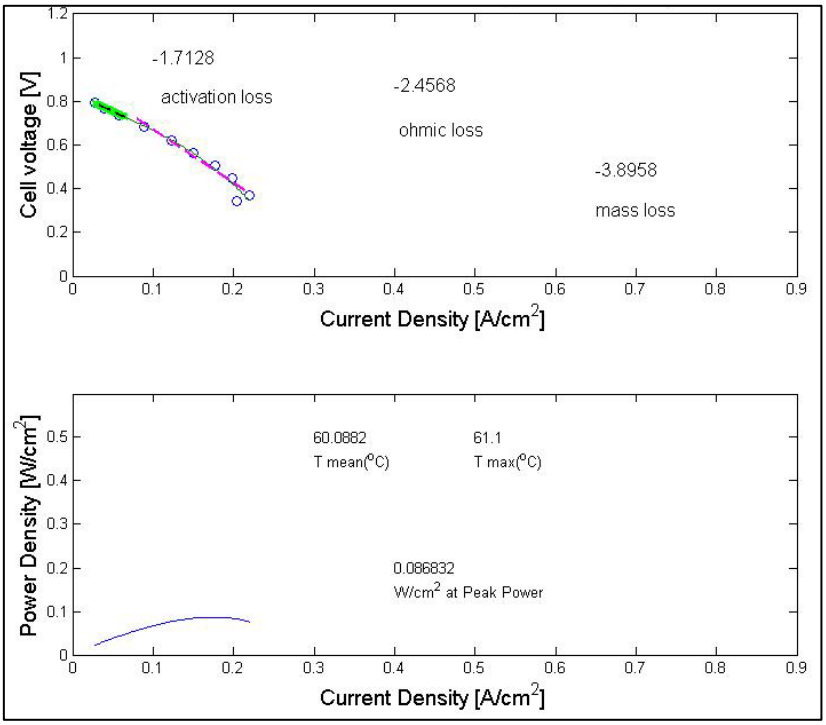

Figure 98: MEA 10 last polarisation curve

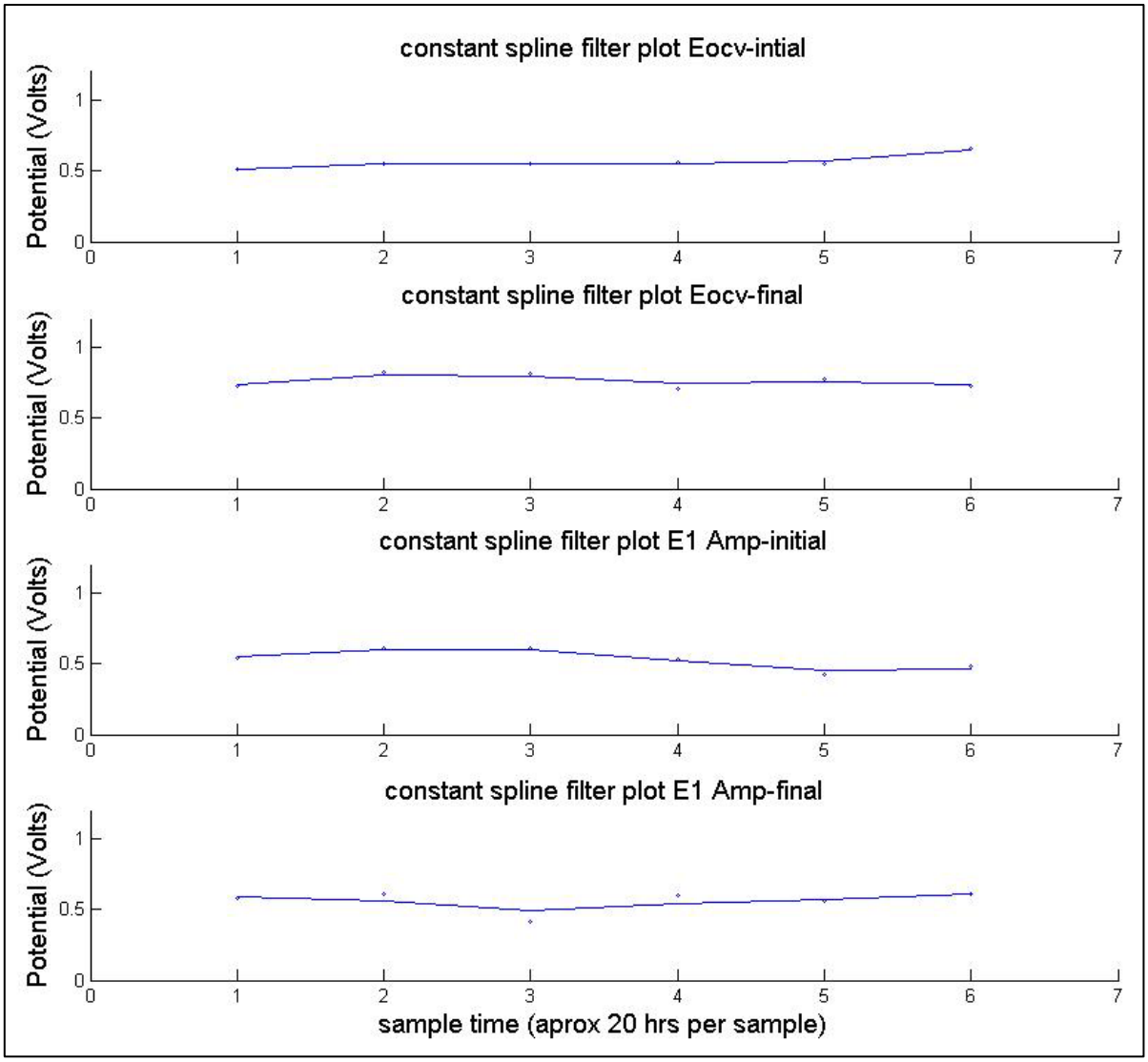

Figure 99: MEA 10 spline fitting for Eocv (i & f), and E1A (i & f)

Figure 97 shows the first polarisation scan carried out at the start of the degradation trial on MEA 10. MEA 10 is a Toray cathode GDM with low concentration (0.3mg.cm^{-2}) dual layered catalysts. Figure 98 is the last polarisation scan on MEA 10 after 120 hours of constant operation (24 hours a day) at one-Amp (0.08Amps.cm^{-2}) load. Polarisation scans were taken approximately every 20 hours (exact timing varied depending on the other MEA test sample being tested).

Figure 99 shows the results of the potential measurements on MEA 10 immediately before and after each 20-hour polarisation scan. A spline fitting process has been carried out in order to clearly define a region of linear degradation. This process is explained in more detail in section 6.5.1.

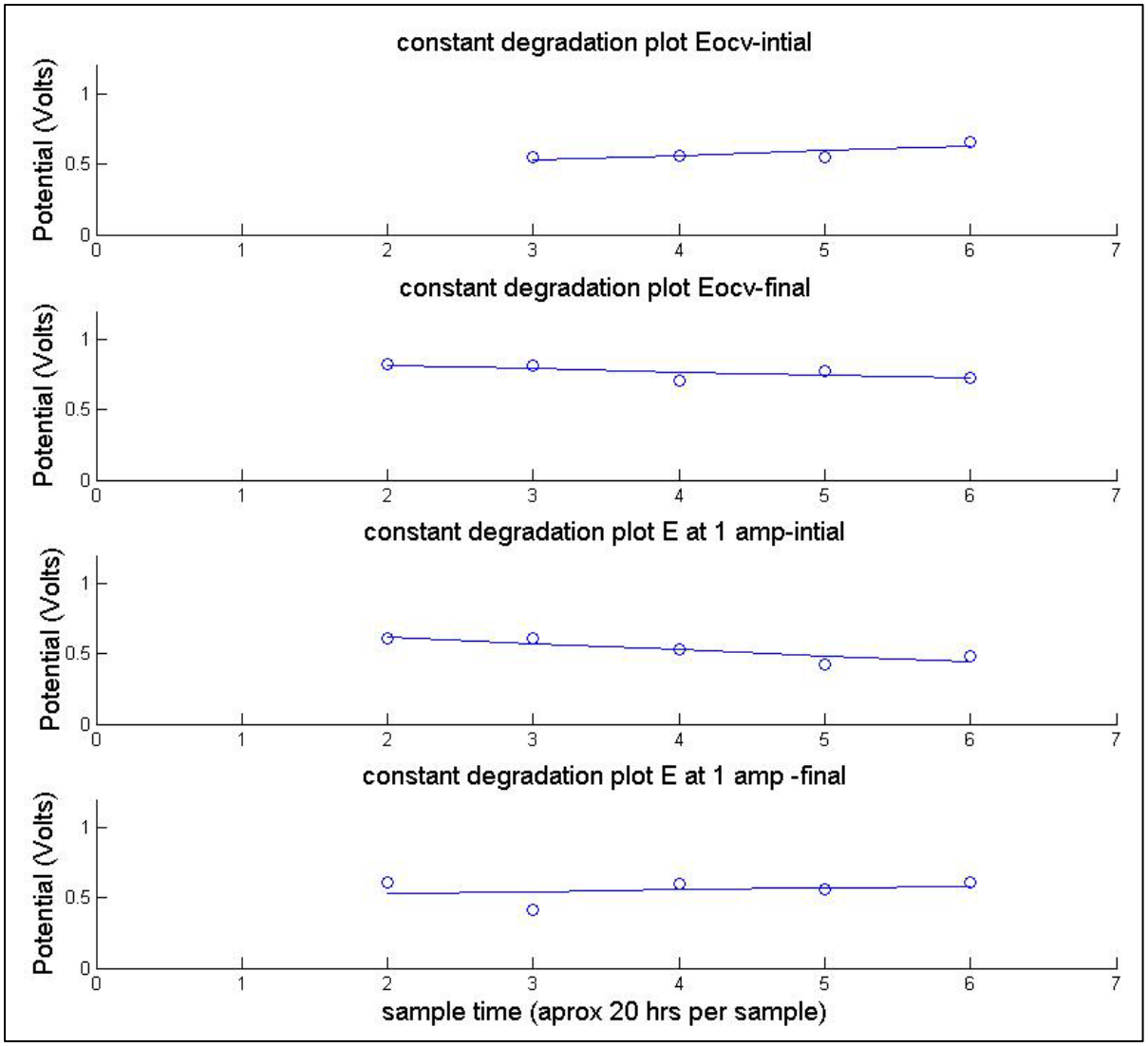

Figure 100: MEA 10 Linear degradation region

Figure 100 shows the localised maximum value for each of the potential values, identified with the aid of the spline fitting process in Figure 99, and plots a linear fit to the remaining values until the end of the degradation test run.

6.4.6 MEA ID 12

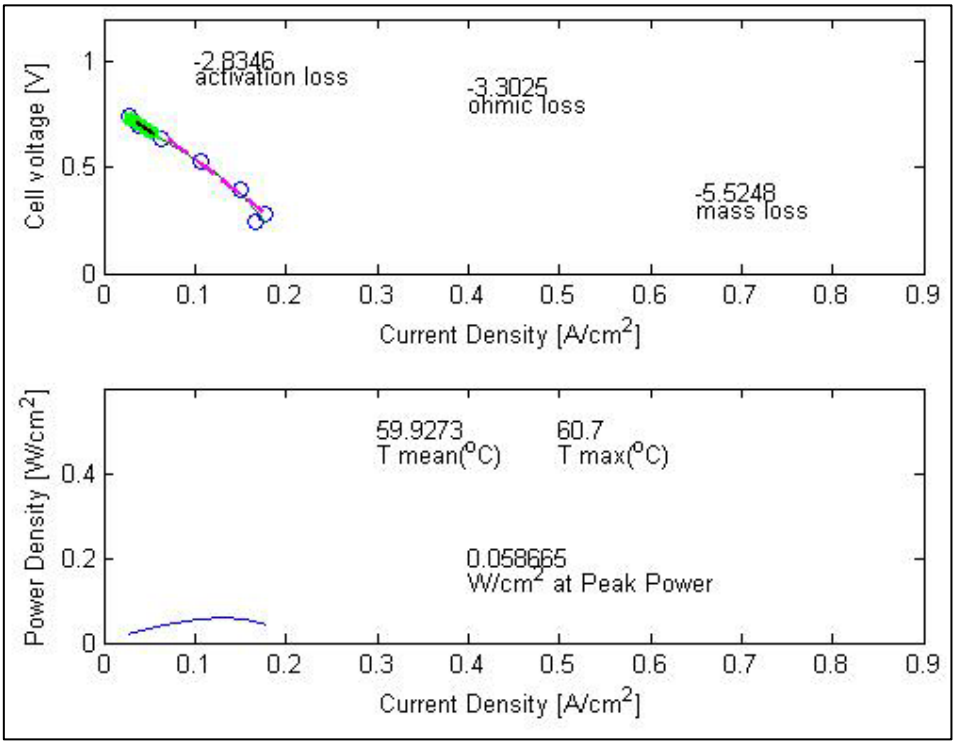

Figure 101: MEA 12 first polarisation curve

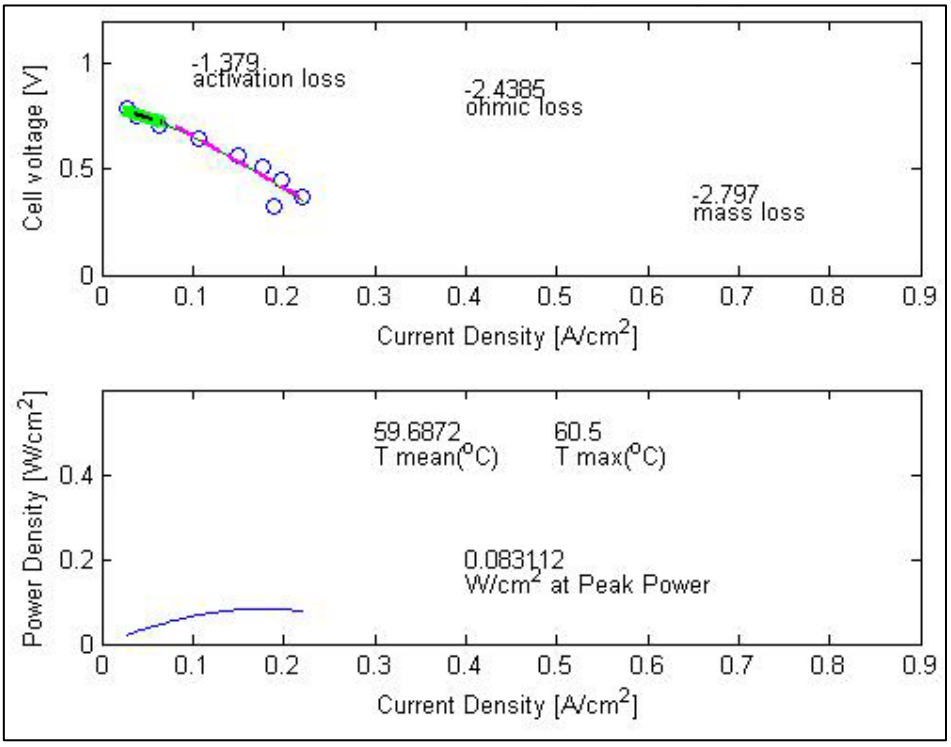

Figure 102: MEA 12 last polarisation curve

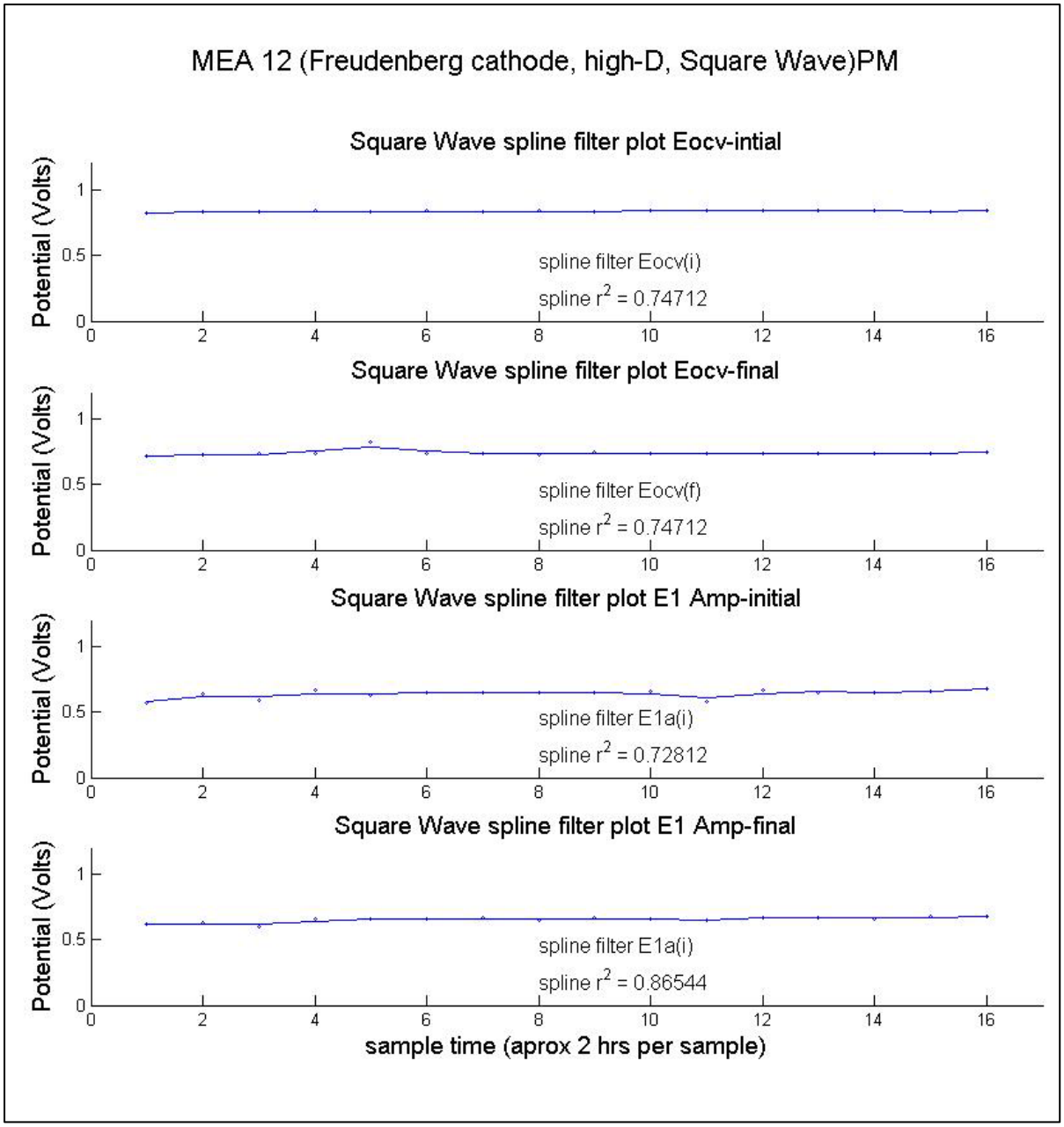

Figure 103: MEA 12 spline fitting for Eocv (i & f), and E1A (i & f)

Figure 101 is the first polarisation scan carried out at the start of the degradation trial on MEA 12. MEA 12 is a Toray cathode GDM with low concentration (0.3mg.cm^{-2}) dual layered catalysts. Figure 103is the last polarisation scan on MEA 12 after 32 hours of square wave operation (4 Amps to 0.2 Amps cycled every five seconds). Polarisation scans were taken approximately every two hours (exact timing varied depending on the other MEA test sample being tested).

Figure 103 shows the results of the potential measurements on MEA 12 immediately before and after each two-hour polarisation scan. A spline fitting process has been carried out in order to clearly define a region of linear degradation. This process is explained in more detail in section 6.5.1.

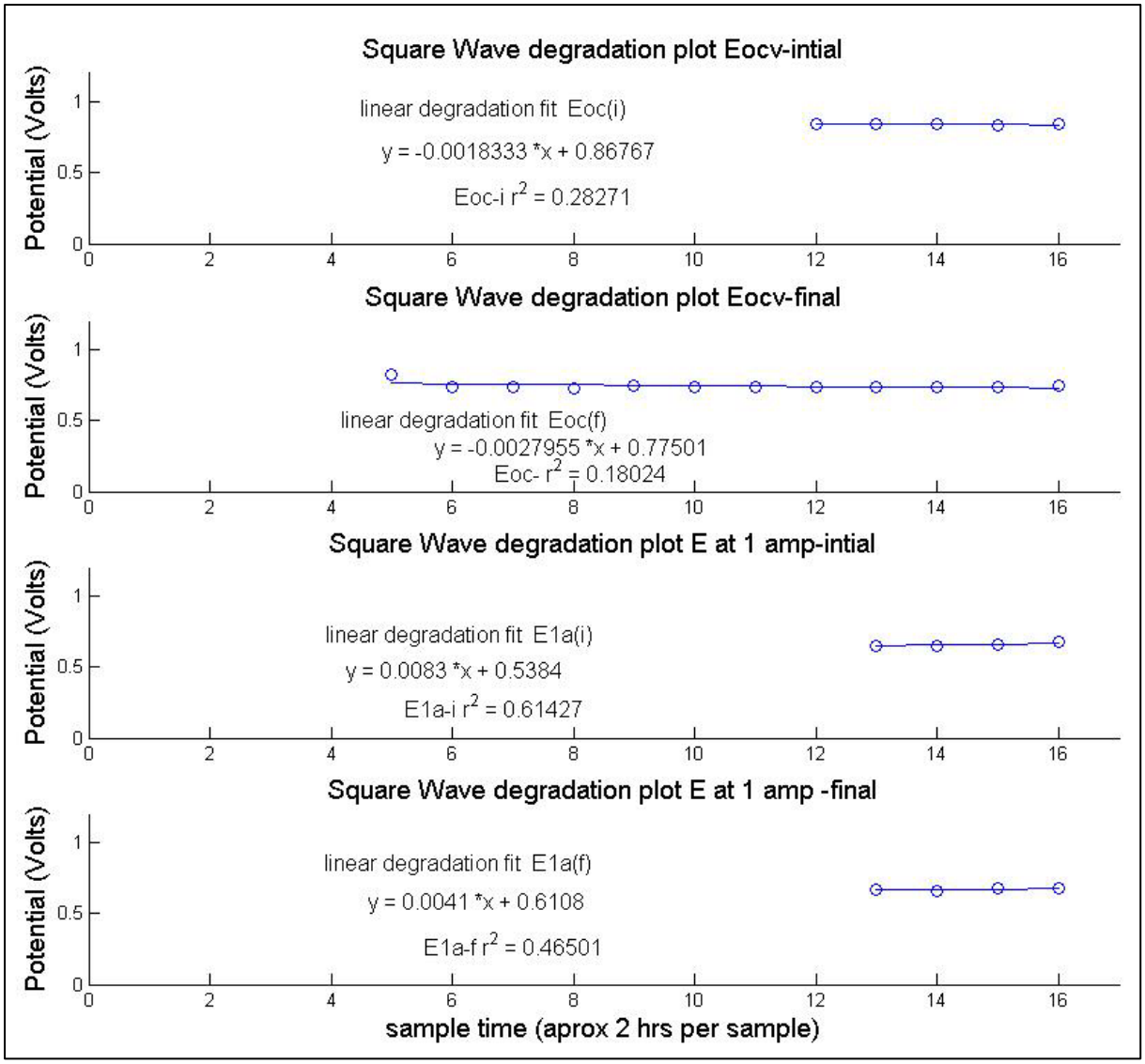

Figure 104: MEA 12 linear degradation region

Figure 104 shows the localised maximum value for each of the potential values, identified with the aid of the spline fitting process in Figure 103, and plots a linear fit to the remaining values until the end of the degradation test run.

6.4.7 MEA ID 14

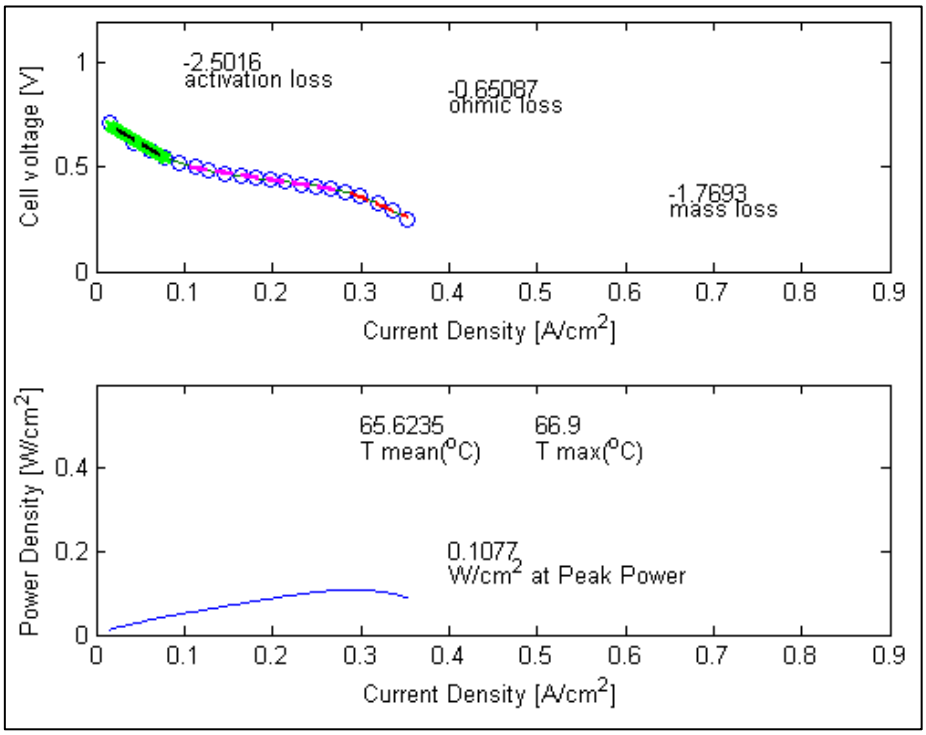

Figure 105: MEA 14 first polarisation curve

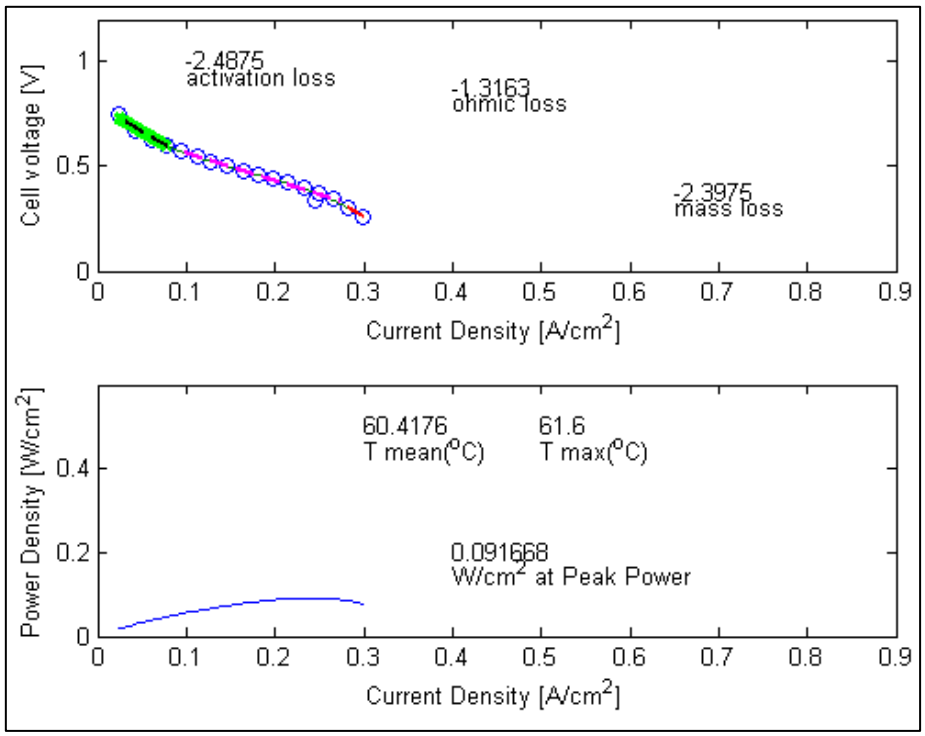

Figure 106: MEA 14 last polarisation curve

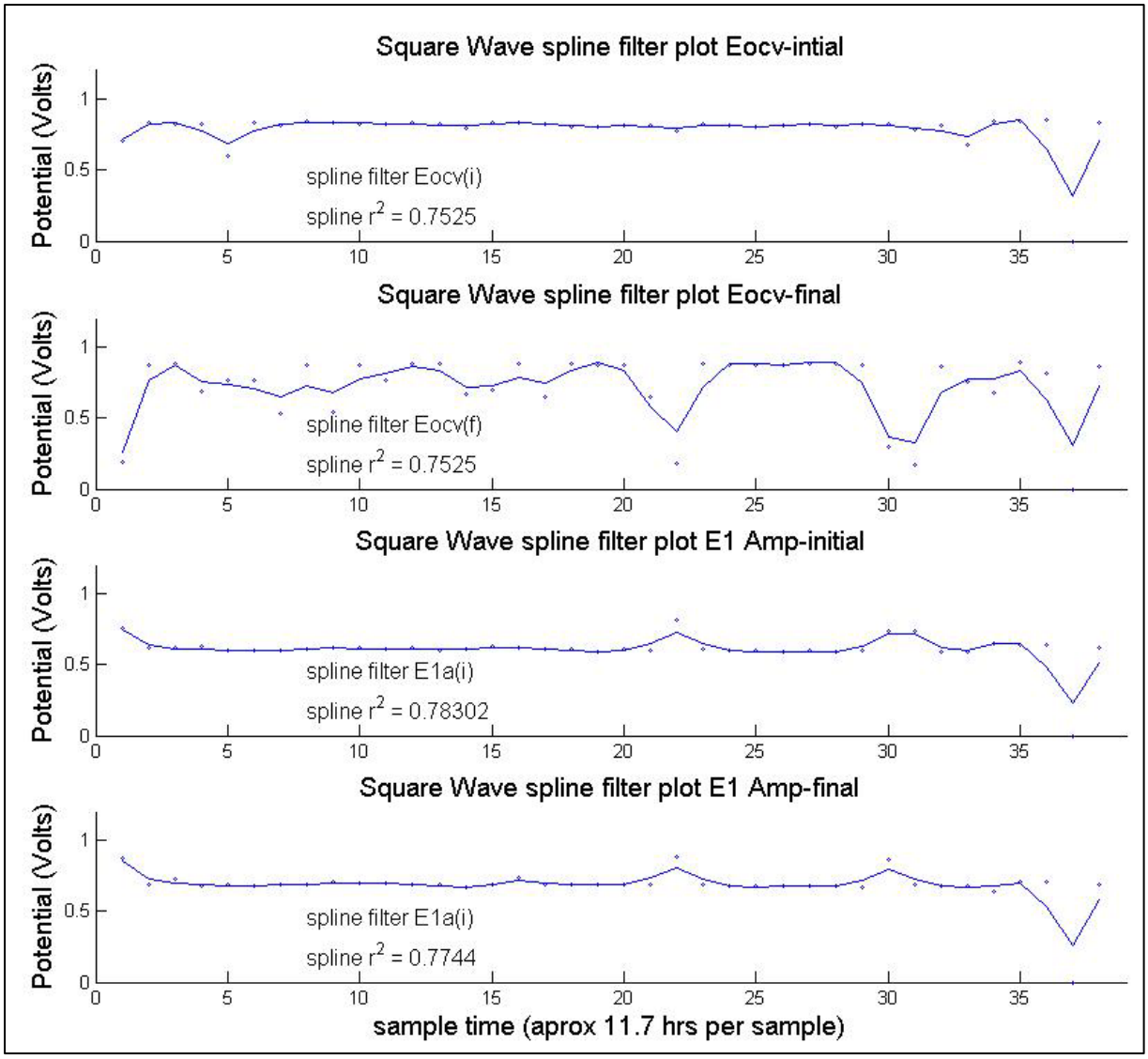

Figure 107: MEA 14 spline fitting for Eocv (i & f), and E1A (i & f)

Figure 105 shows the first polarisation scan carried out at the start of the degradation trial on MEA 14. MEA 14 is a Toray cathode GDM with high concentration (0.4mg.cm^{-2}) dual layered catalysts. Figure 106 is the last polarisation scan on MEA 10 after 444.6 hours of constant operation (24 hours a day) at one-Amp (0.08Amps.cm^{-2}) load. Polarisation scans were taken approximately every 11.7 hours (exact timing varied depending on the other MEA samples being tested).

Figure 107 shows the results of the potential measurements on MEA 14 immediately before and after each 20-hour polarisation scan. A spline fitting process has been carried out in order to clearly define a region of linear degradation. This process is explained in more detail in section 6.5.1.

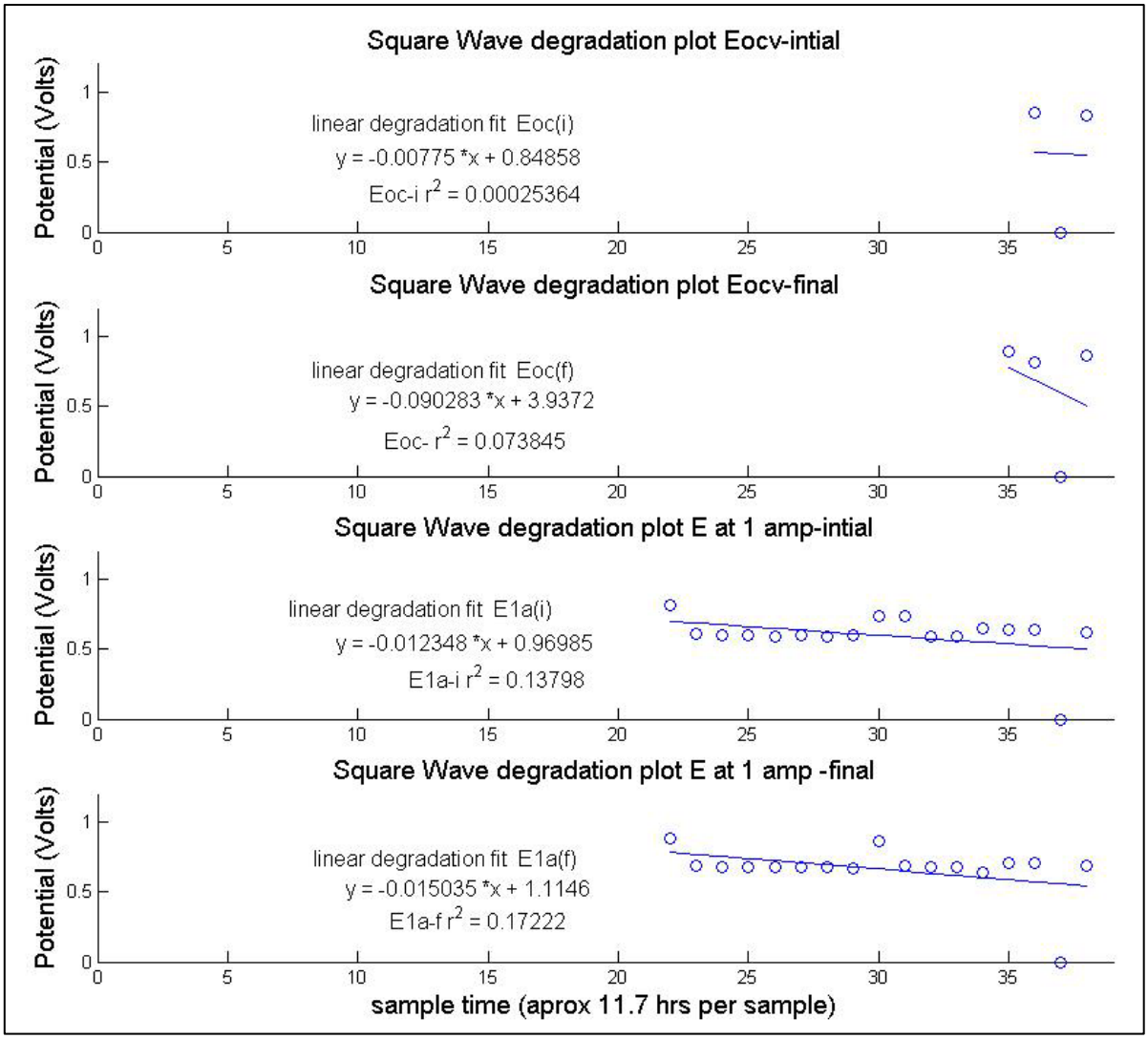

Figure 108: MEA 14 linear degradation region

Figure 108 shows the localised maximum value for each of the potential values, identified with the aid of the spline fitting process in Figure 107, and plots a linear fit to the remaining values until the end of the degradation test run.

6.4.8 MEA ID 16

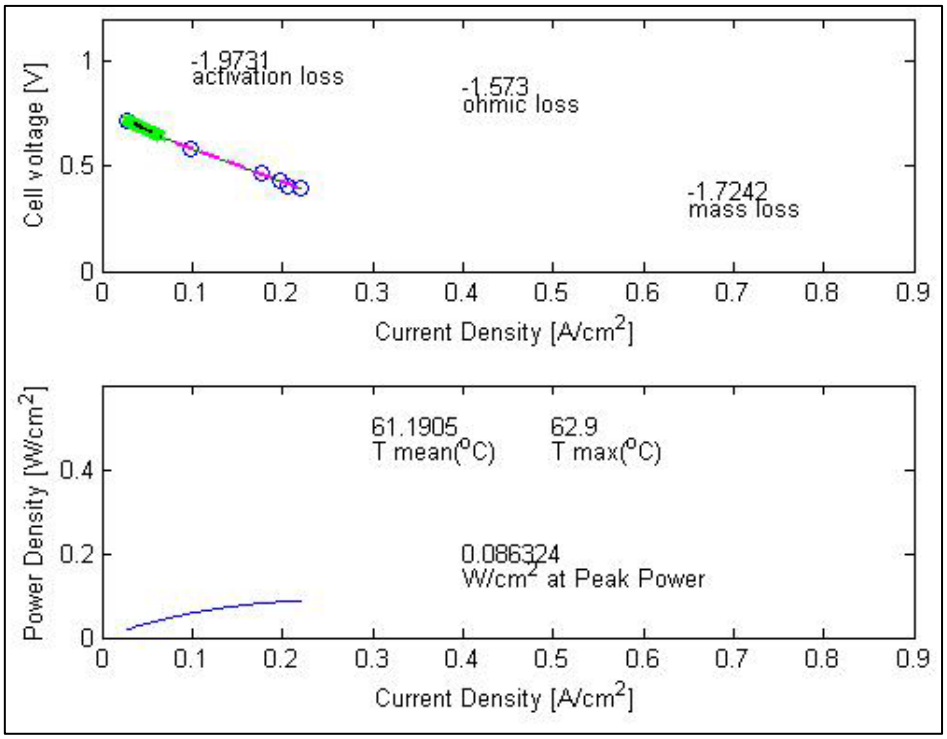

Figure 109: MEA 16 first polarisation curve

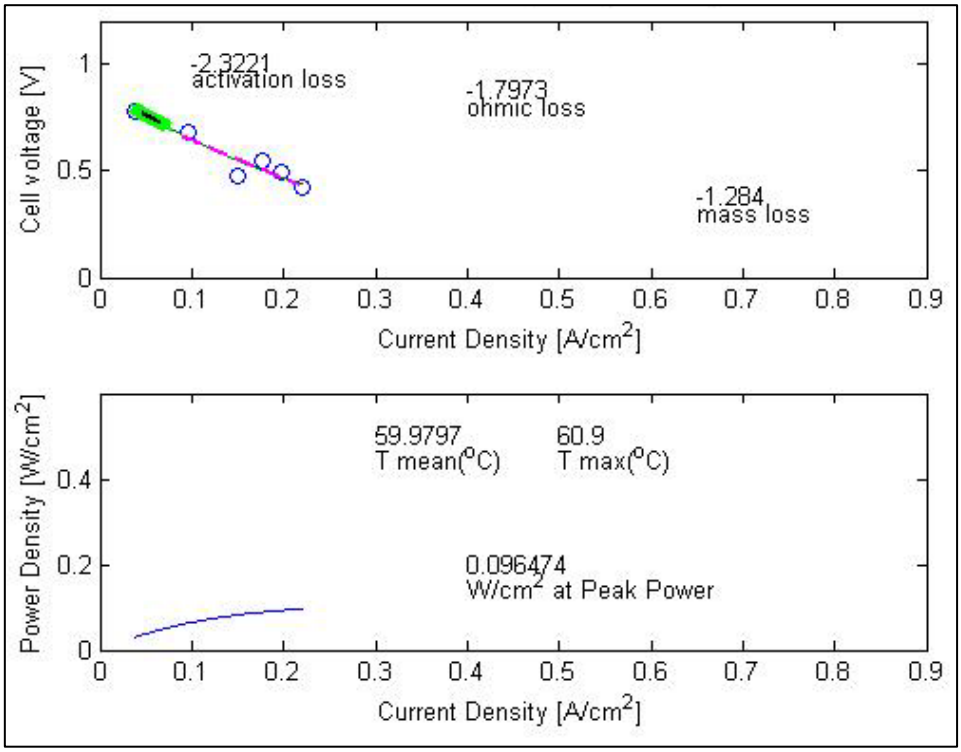

Figure 110: MEA 16 last polarisation curve

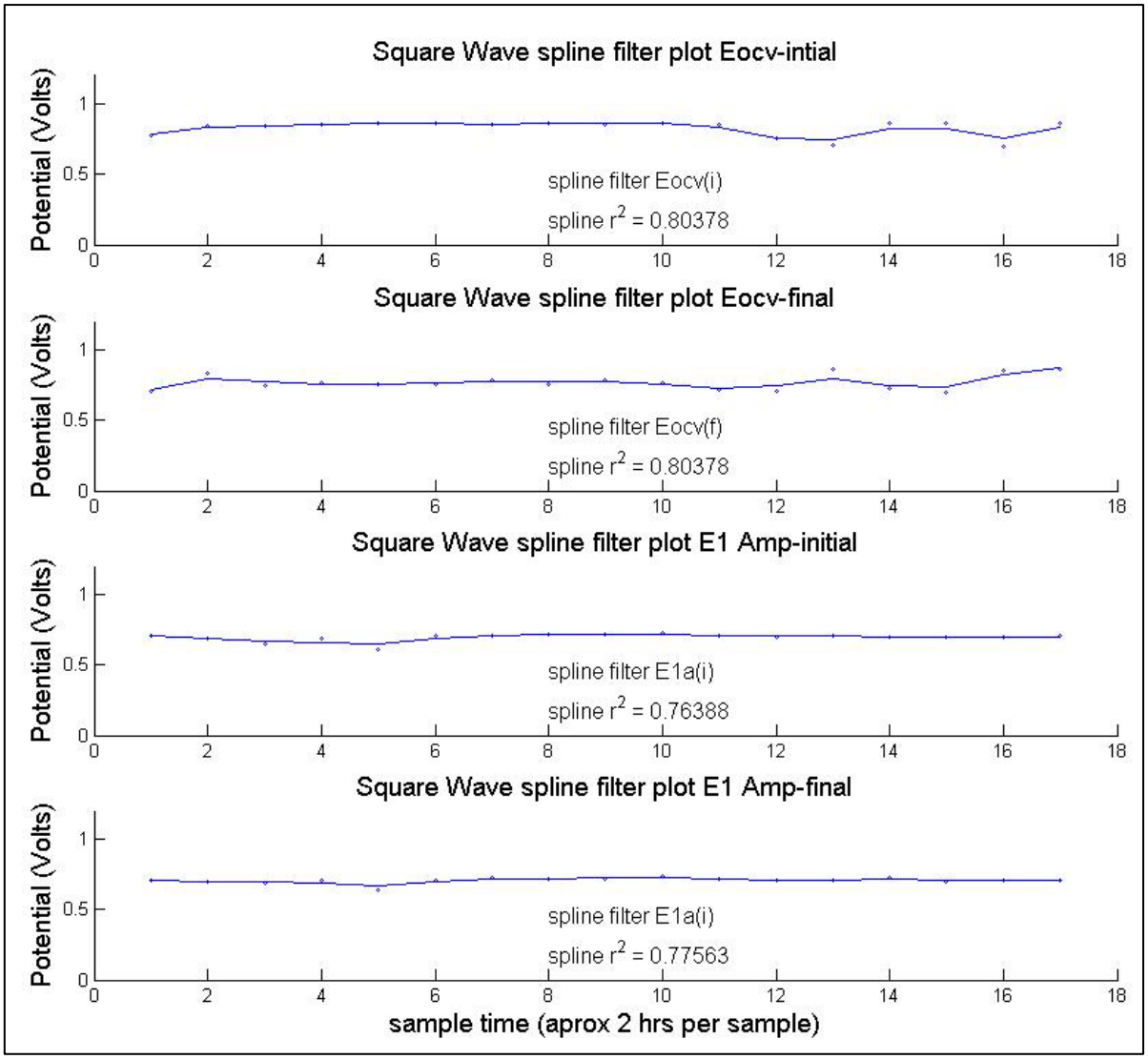

Figure 111: MEA 16 spline fitting for Eocv (i & f), and E1A (i & f)

Figure 109 is the first polarisation scan carried out at the start of the degradation trial on MEA 16. MEA 16 is a Toray cathode GDM with high concentration (0.4mg.cm^{-2}) dual layered catalysts. Figure 110 is the last polarisation scan on MEA 12 after 34 hours of square wave operation (4 Amps to 0.2 Amps cycled every five seconds). Polarisation scans were taken approximately every two hours (exact timing varied depending on the other MEA test sample being tested).

Figure 111 shows the results of the potential measurements on MEA 16 immediately before and after each two-hour polarisation scan. A spline fitting process has been carried out in order to clearly define a region of linear degradation. This process is explained in more detail in section 6.5.1.

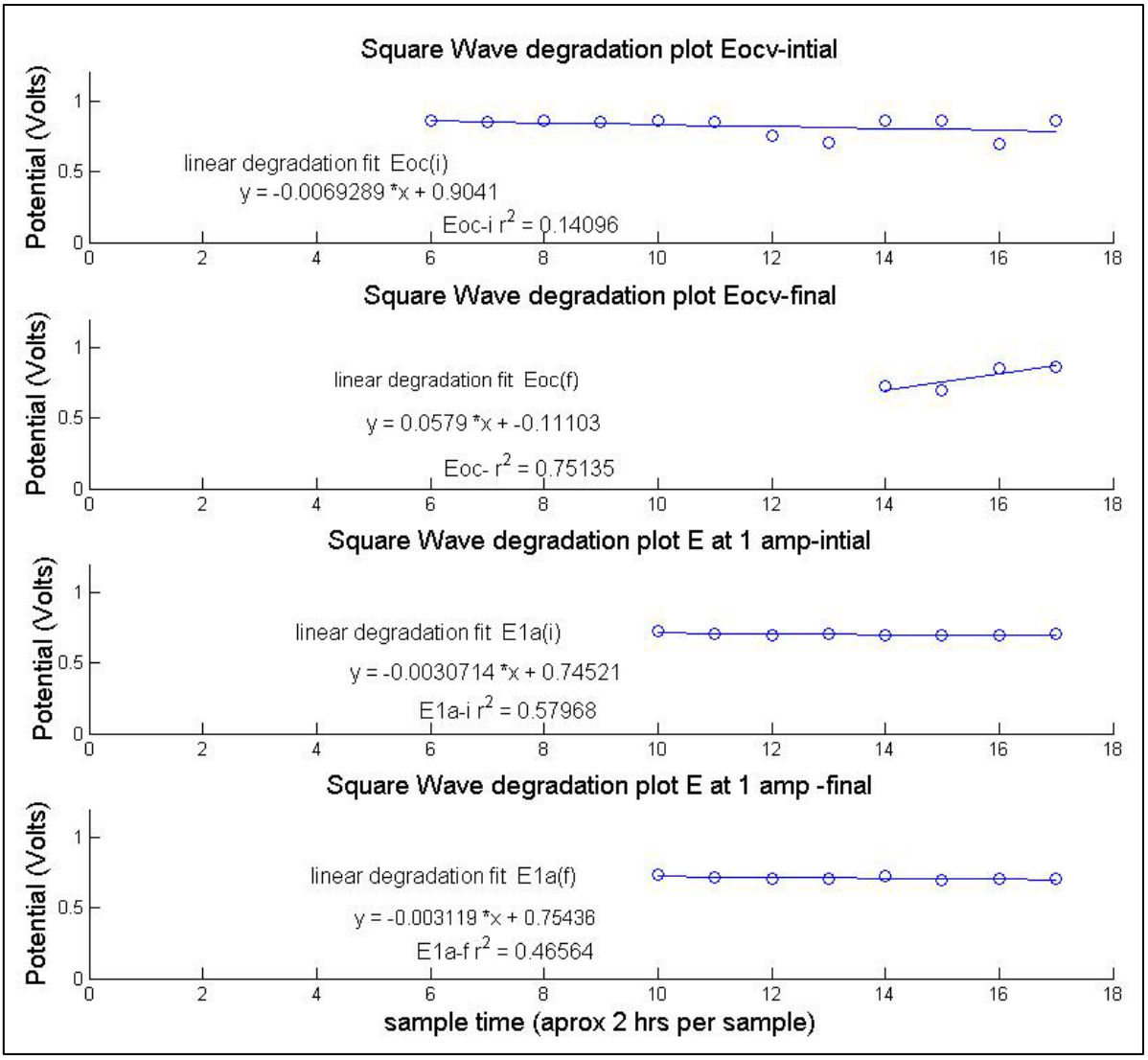

Figure 112: MEA 16 linear degradation region

Figure 112 shows the localised maximum value for each of the potential values, identified with the aid of the spline fitting process in Figure 111, and plots a linear fit to the remaining values until the end of the degradation test run.

6.4.9 MEA ID 18

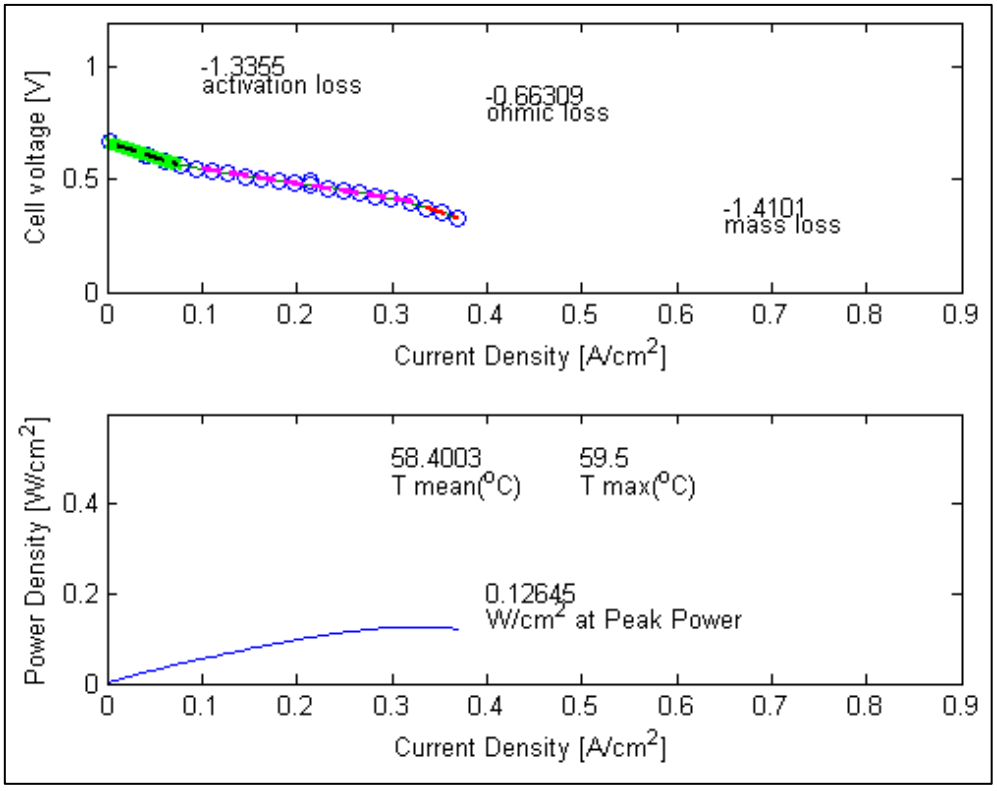

Figure 113: MEA 18 first polarisation curve

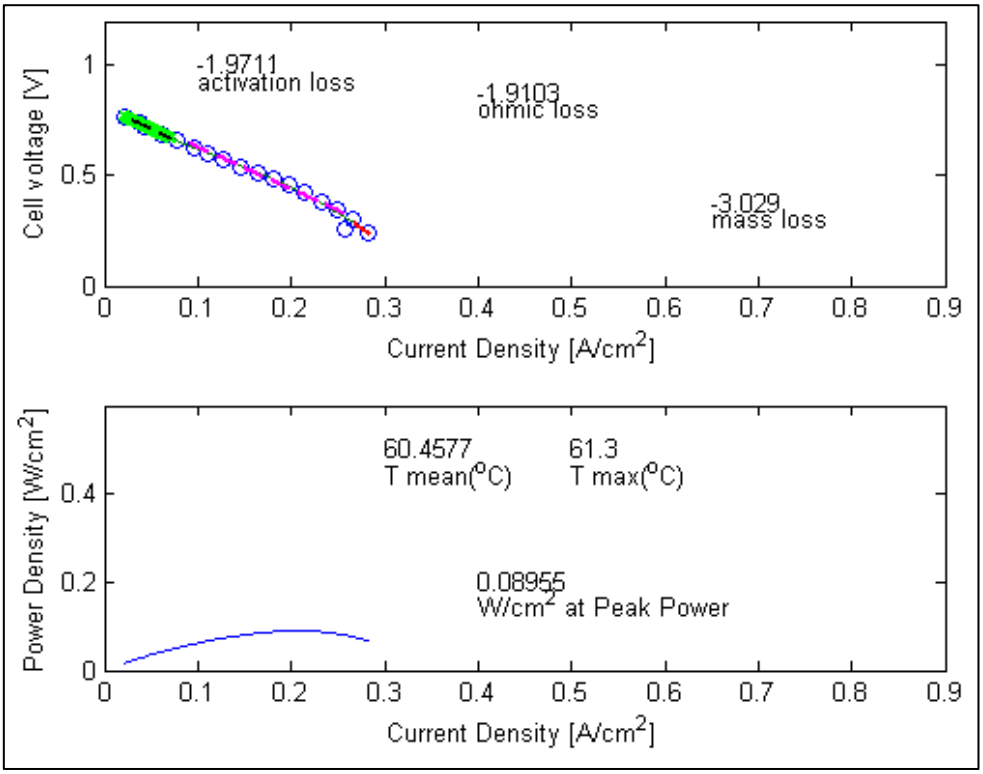

Figure 114: MEA 18 last polarisation curve

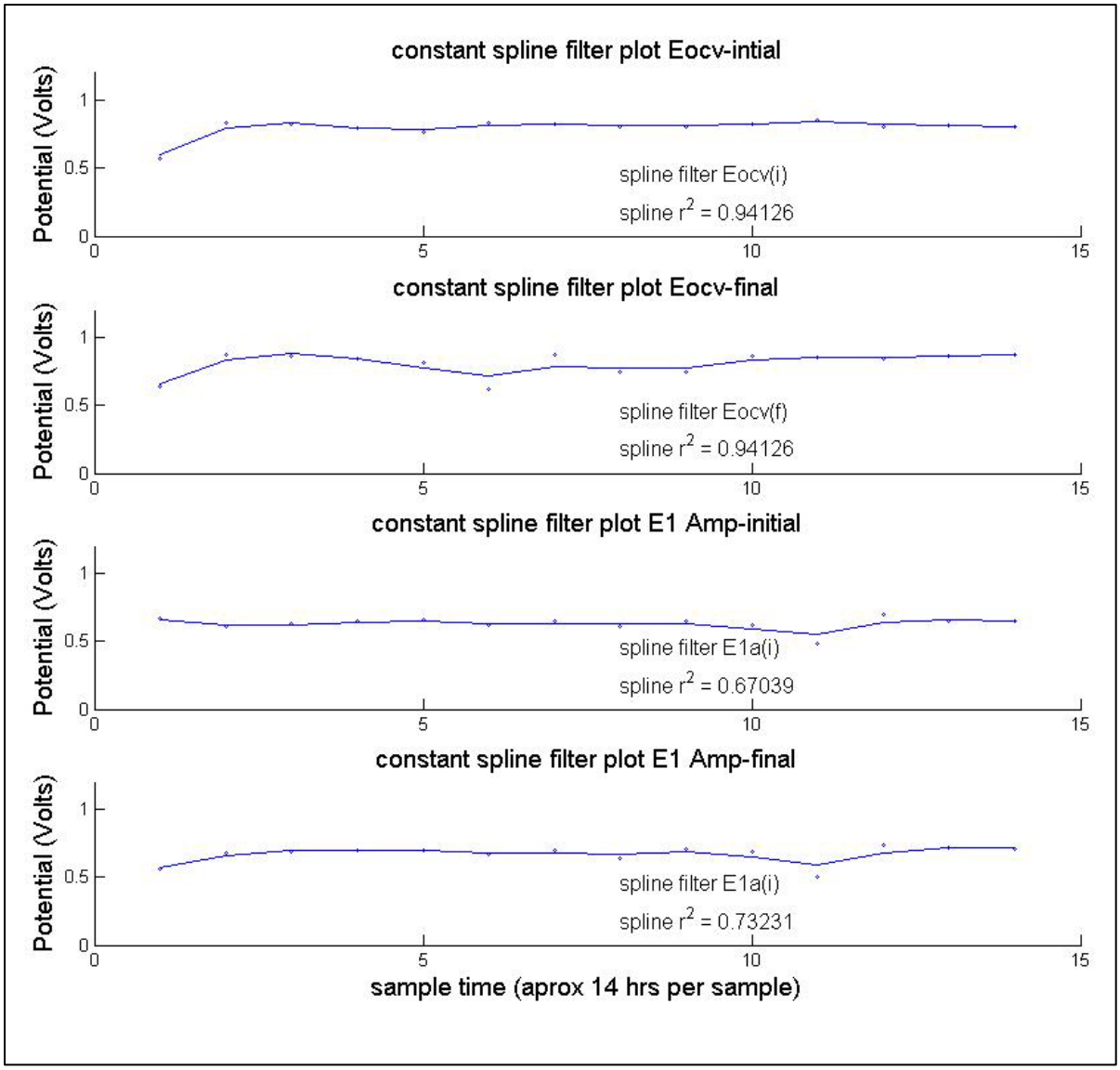

Figure 115: MEA 18 spline fitting for Eocv (i & f), and E1A (i & f)

Figure 113 shows the first polarisation scan carried out at the start of the degradation trial on MEA 18. MEA 18 is a Freudenberg cathode GDM with medium concentration (0.35mg.cm^{-2}) uniform concentration catalyst layer. Figure 114 is the last polarisation scan on MEA 18 after 196 hours of contestant operation (24 hours a day) at a one-Amp (0.08Amps.cm^{-2}) load. Polarisation scans were taken approximately every 14 hours (exact timing varied depending on the other MEA samples being tested).

Figure 115 shows the results of the potential measurements on MEA 14 immediately before and after each 20-hour polarisation scan. A spline fitting process has been carried out in order to clearly define a region of linear degradation. This process is explained in more detail in section 6.5.1.

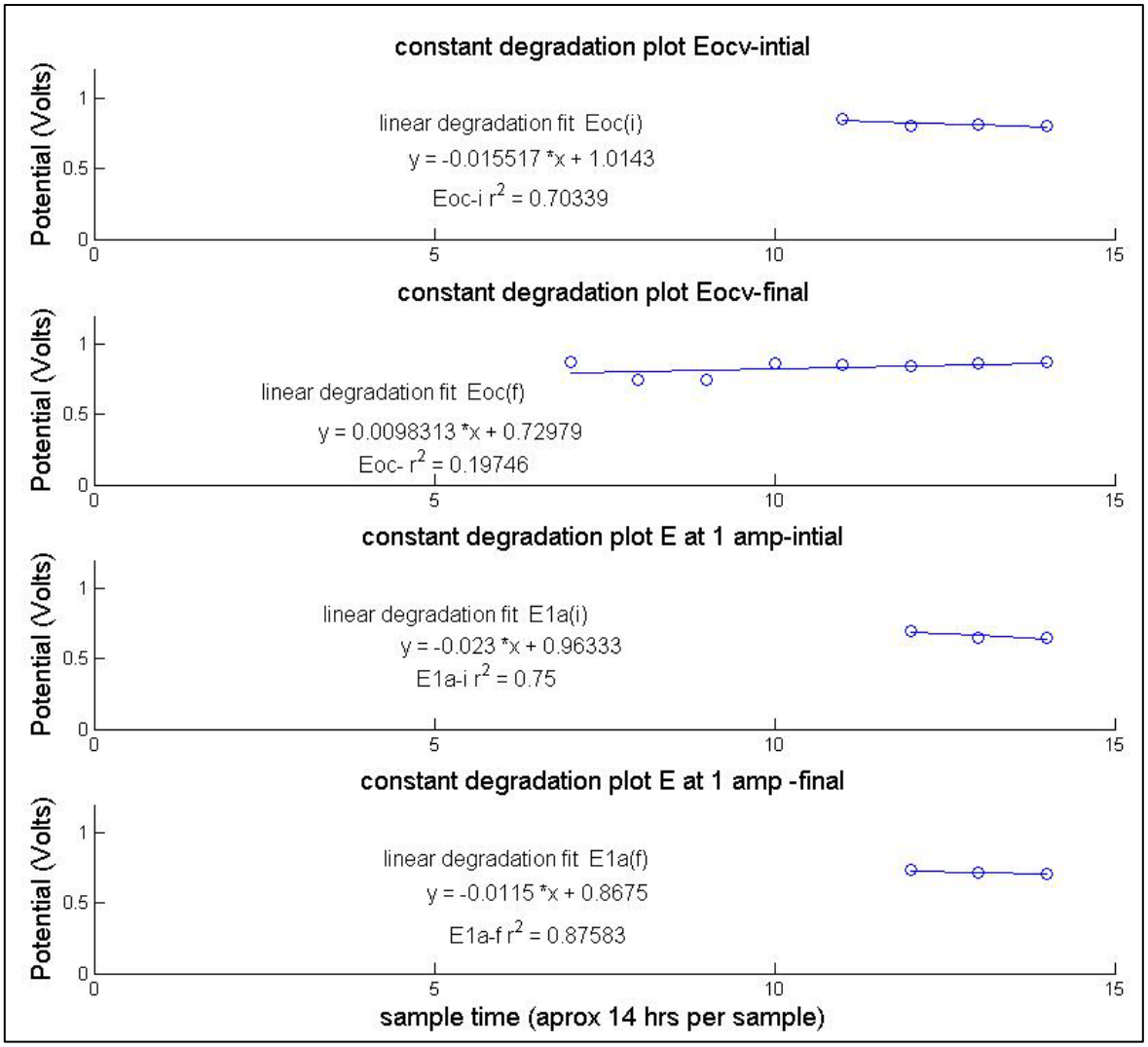

Figure 116: MEA 18 linear degradation region

Figure 116 shows the localised maximum value for each of the potential values, identified with the aid of the spline fitting process in Figure 115, and plots a linear fit to the remaining values until the end of the degradation test run.

6.4.10 MEA ID 19

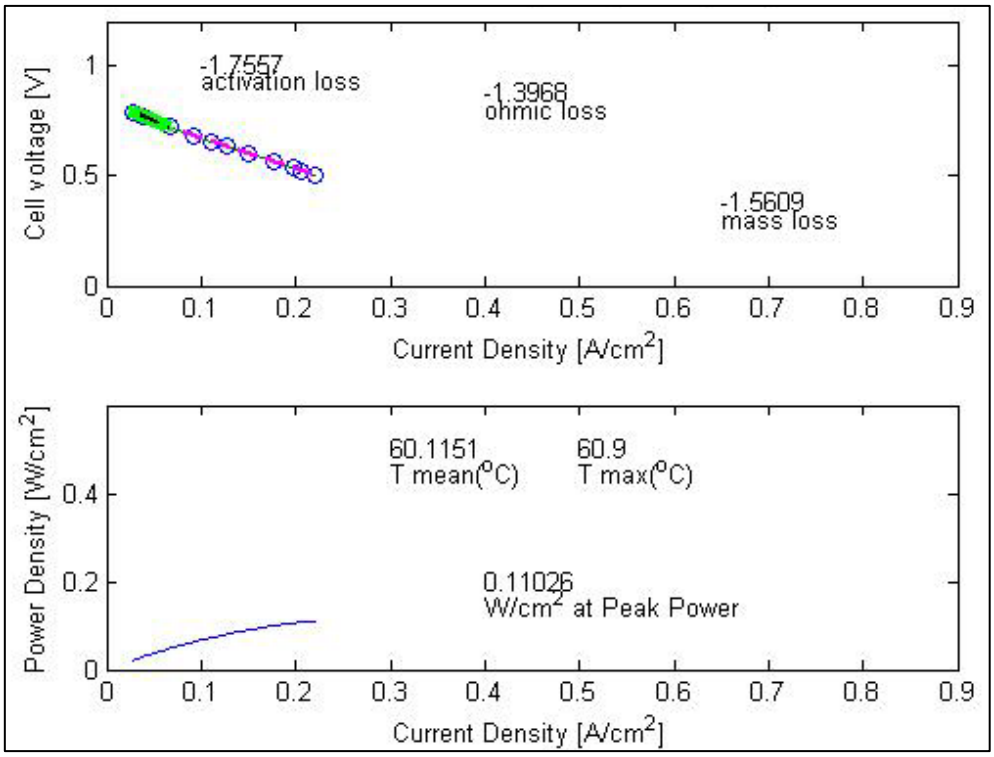

Figure 117: MEA 19 first polarisation curve

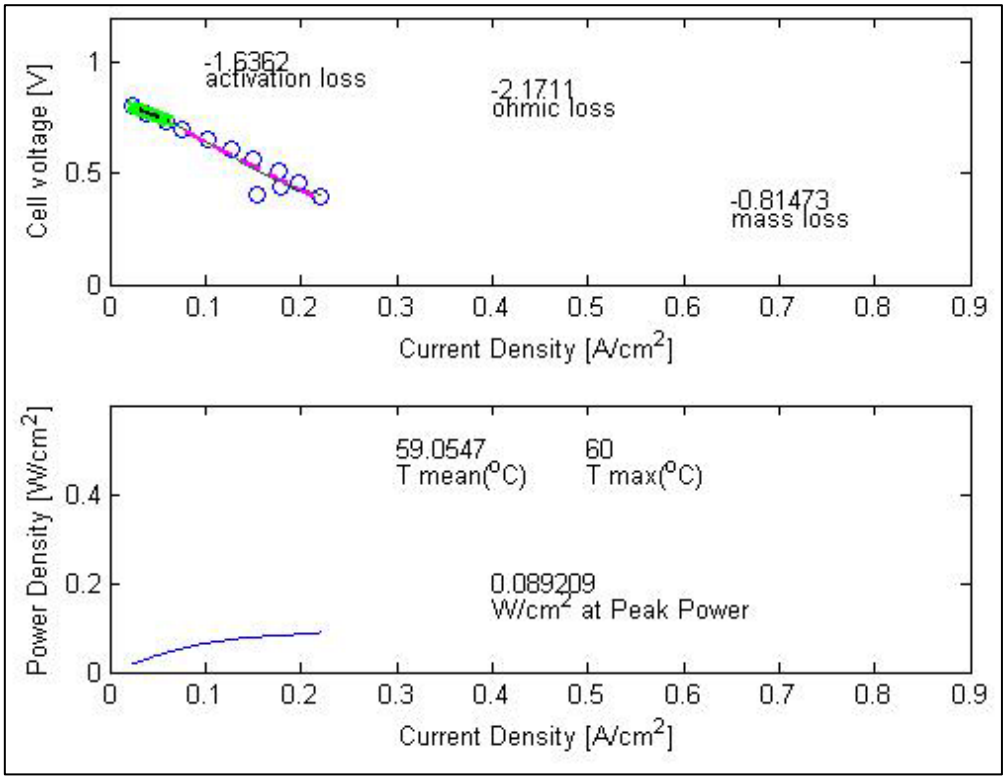

Figure 118: MEA 19 last polarisation curve

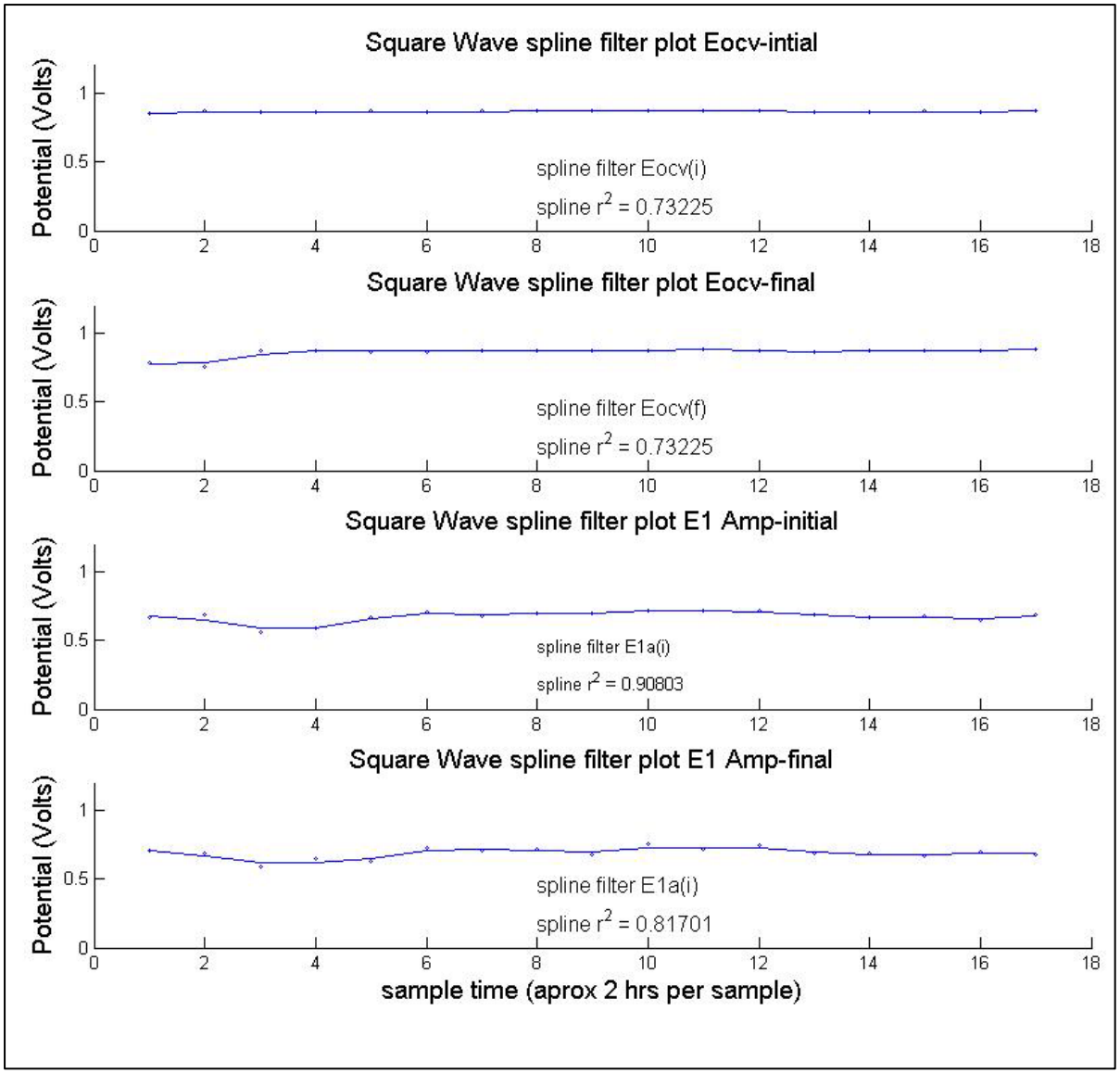

Figure 119: MEA 19 spline fitting for Eocv (i & f), and E1A (i & f)

Figure 117 is the first polarisation scan carried out at the start of the degradation trial on MEA 19. MEA 19 is a Freudenberg cathode GDM with a medium concentration (0.35mg.cm^{-2}) uniform concentration catalyst layer. Figure 118 is the last polarisation scan on MEA 19 after 34 hours of square wave operation (4 Amps to 0.2 Amps cycled every five seconds). Polarisation scans were taken approximately every two hours (exact timing varied depending on the other MEA test samples being tested).

Figure 119 shows the results of the potential measurements on MEA 19 immediately before and after each two-hour polarisation scan. A spline fitting process has been carried out in order to clearly define a region of linear degradation. This process is explained in more detail in section 6.5.1.

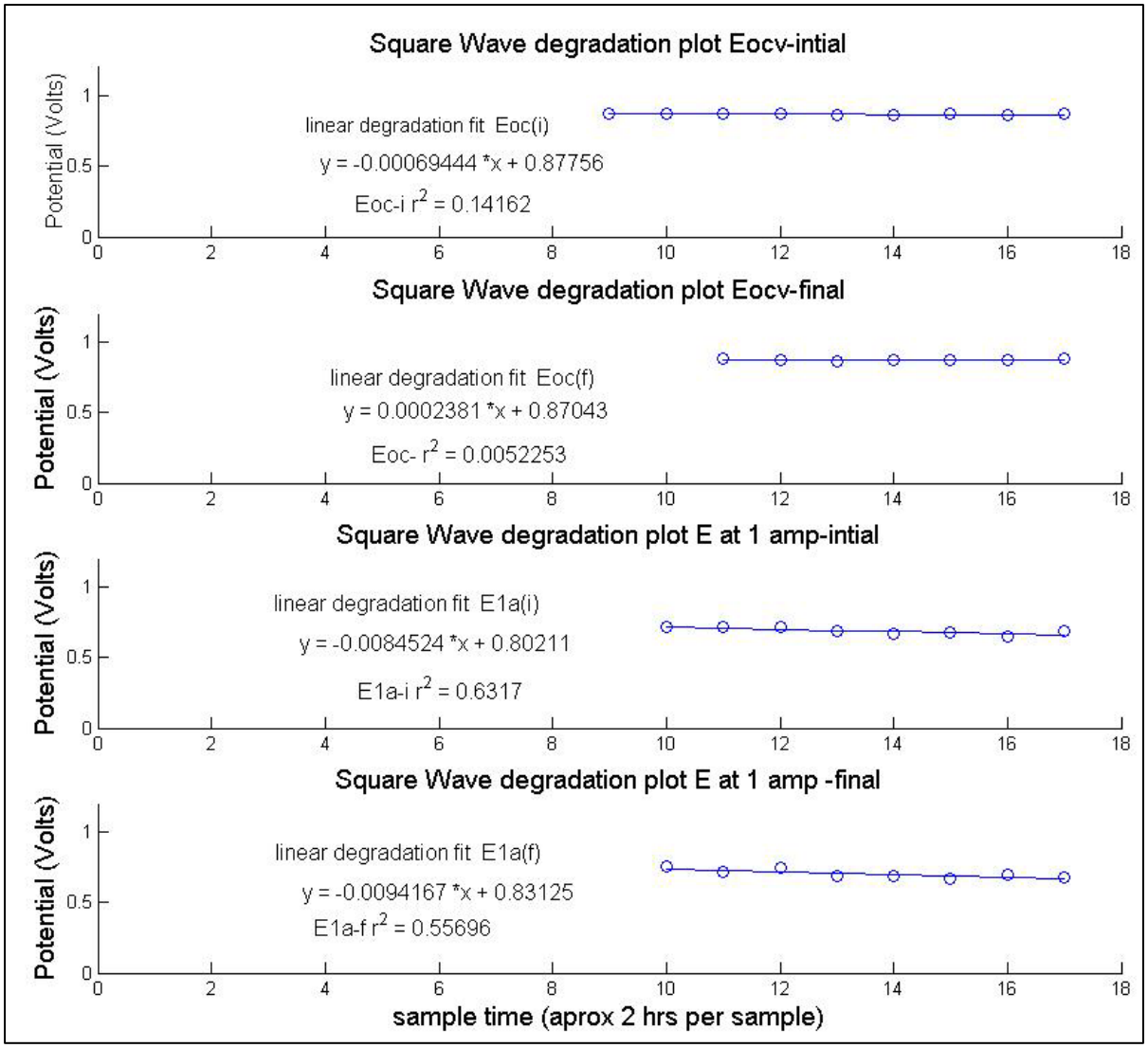

Figure 120: MEA 19 linear degradation region

Figure 120 shows the localised maximum value for each of the potential values, identified with the aid of the spline fitting process in Figure 119, and plots a linear fit to the remaining values until the end of the degradation test run.

6.4.11 MEA ID 23

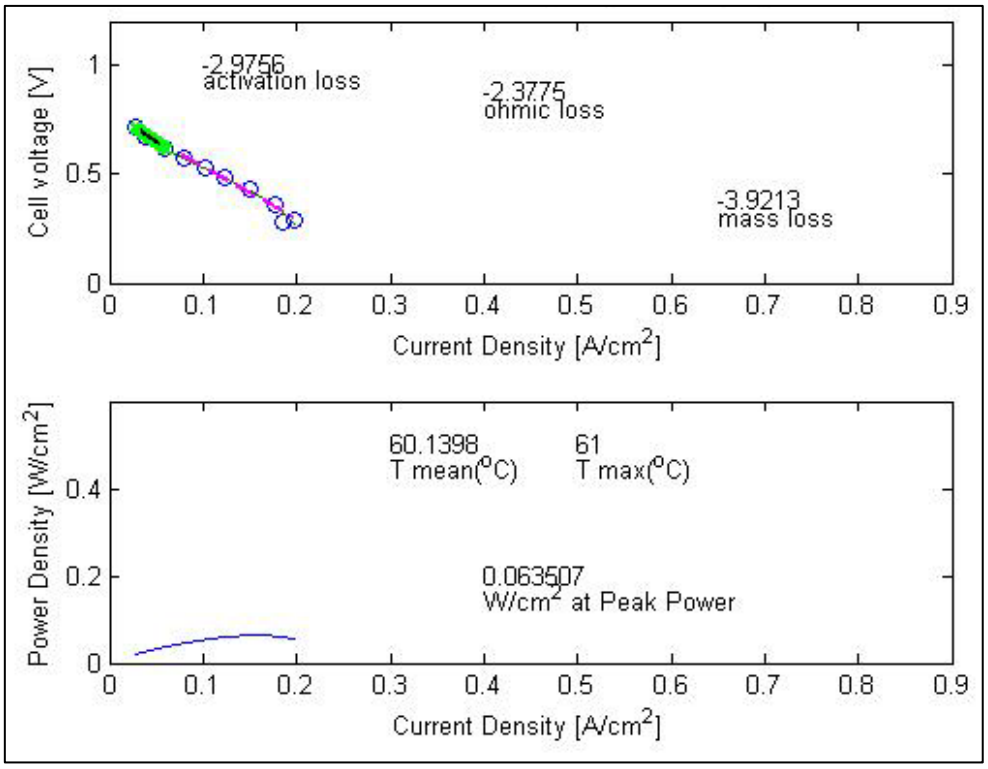

Figure 121: MEA 23 first polarisation curve

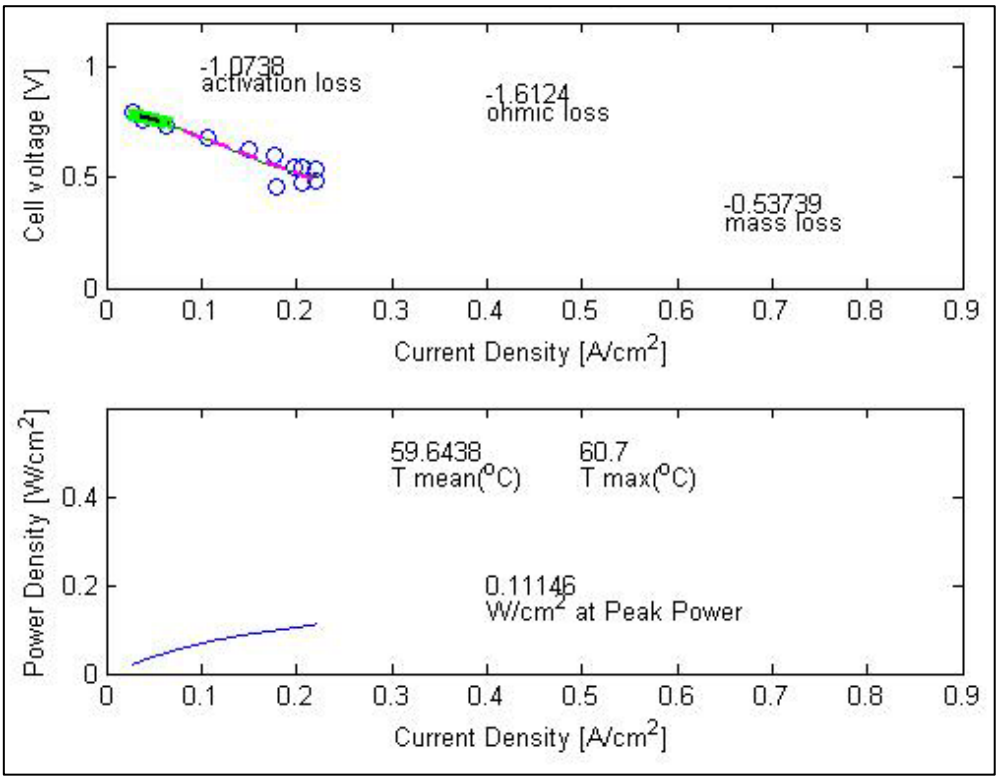

Figure 122: MEA 23 last polarisation curve

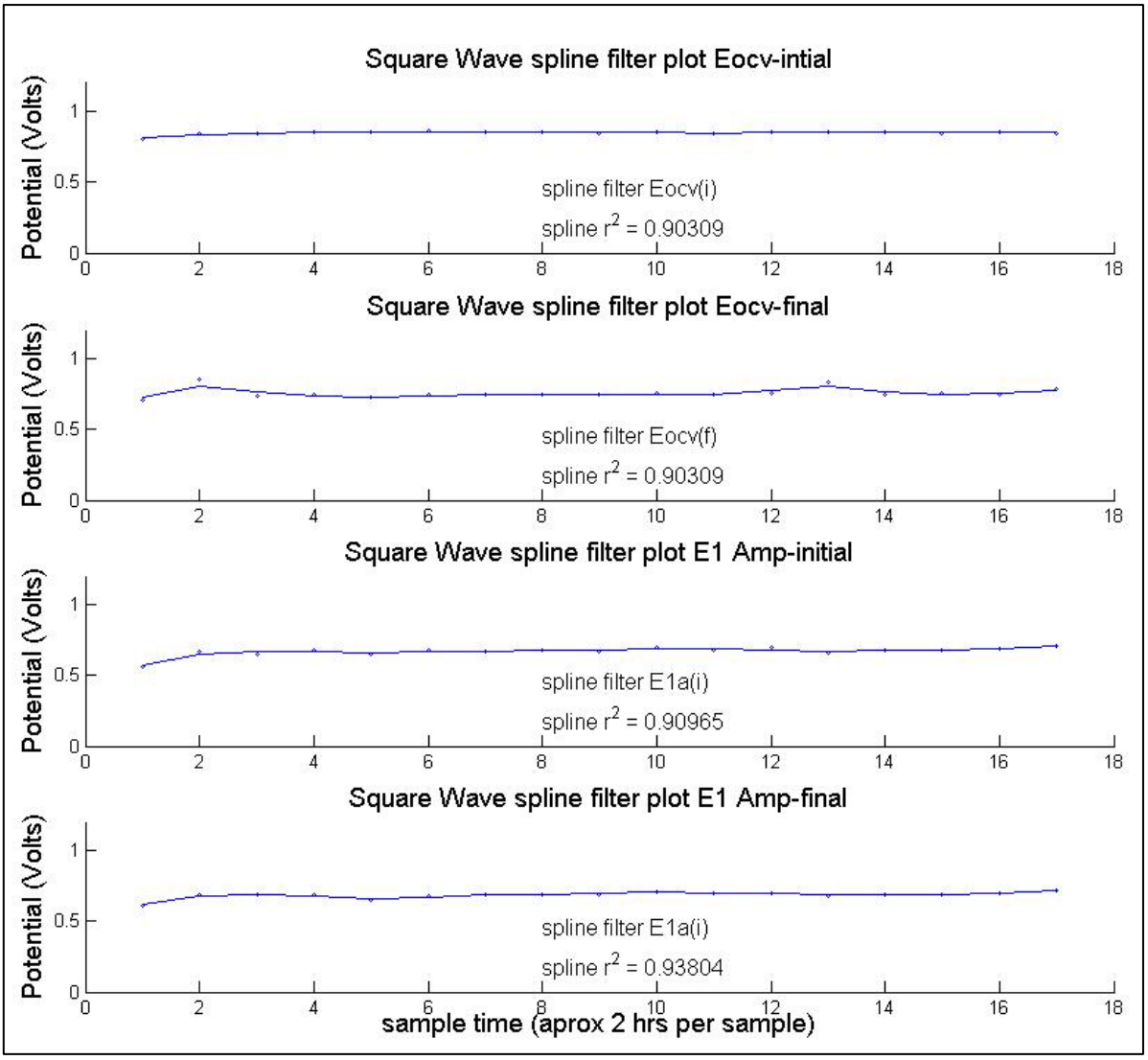

Figure 123: MEA 23 Spline fitting for Eocv (i & f), and E1A (i & f)

Figure 121 is the first polarisation scan carried out at the start of the degradation trial on MEA 23. MEA 23 is a Toray cathode GDM with a medium concentration (0.35mg.cm^{-2}) uniform catalyst layer. Figure 122 is the last polarisation scan on MEA 23 after 34 hours of square wave (4 Amps to 0.2 Amps cycled every five seconds). Polarisation scans were taken approximately every two hours (exact timing varied depending on the other MEA test samples being tested).

Figure 123 shows the results of the potential measurements on MEA 23 immediately before and after each two-hour polarisation scan. A spline fitting process has been carried out in order to clearly define a region of linear degradation. This process is explained in more detail in section 6.5.1.

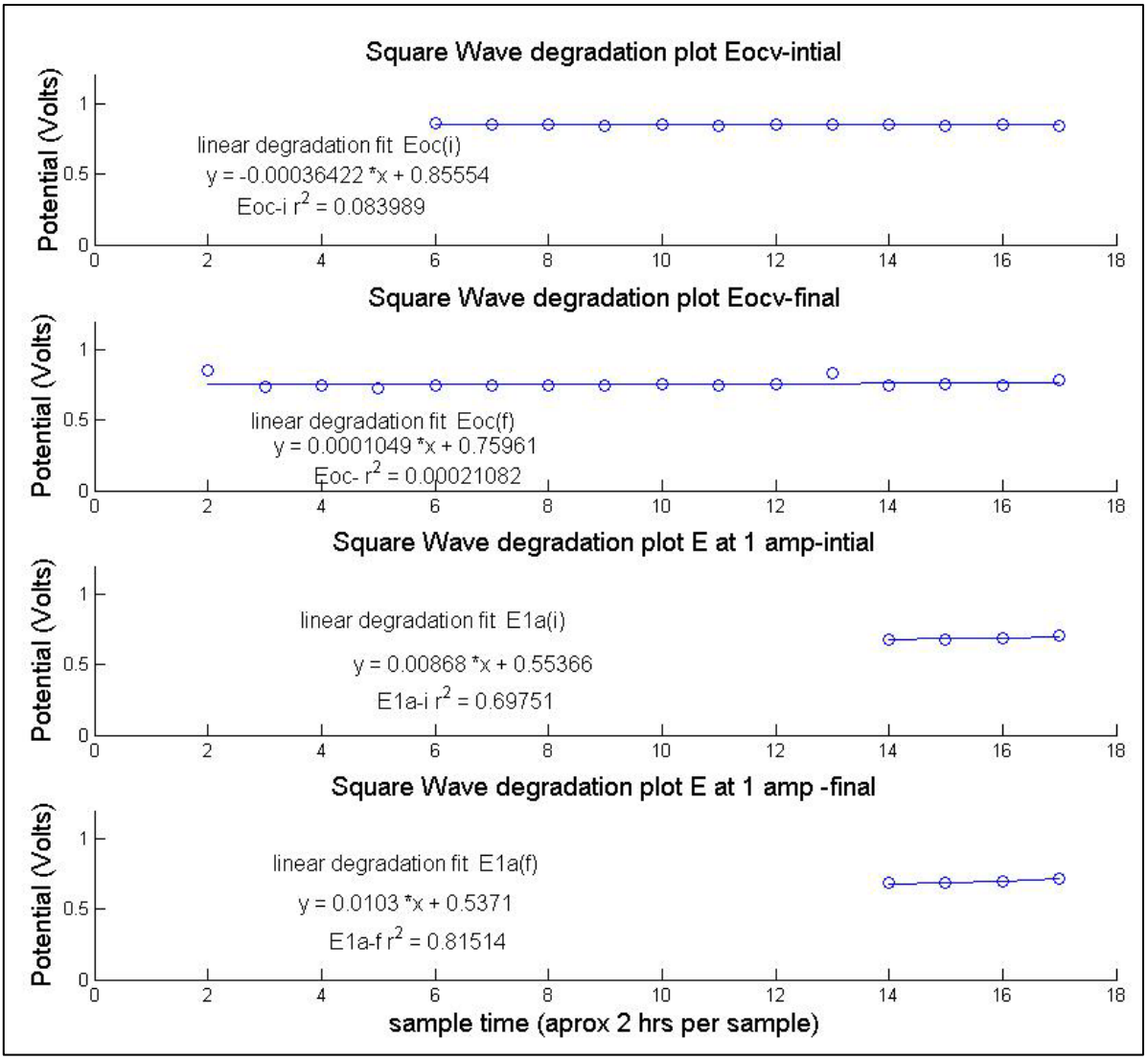

Figure 124: MEA 23 linear degradation region

Figure 124 shows the localised maximum value for each of the potential values, identified with the aid of the spline fitting process in Figure 123, and plots a linear fit to the remaining values until the end of the degradation test run.

6.4.12 MEA ID 24

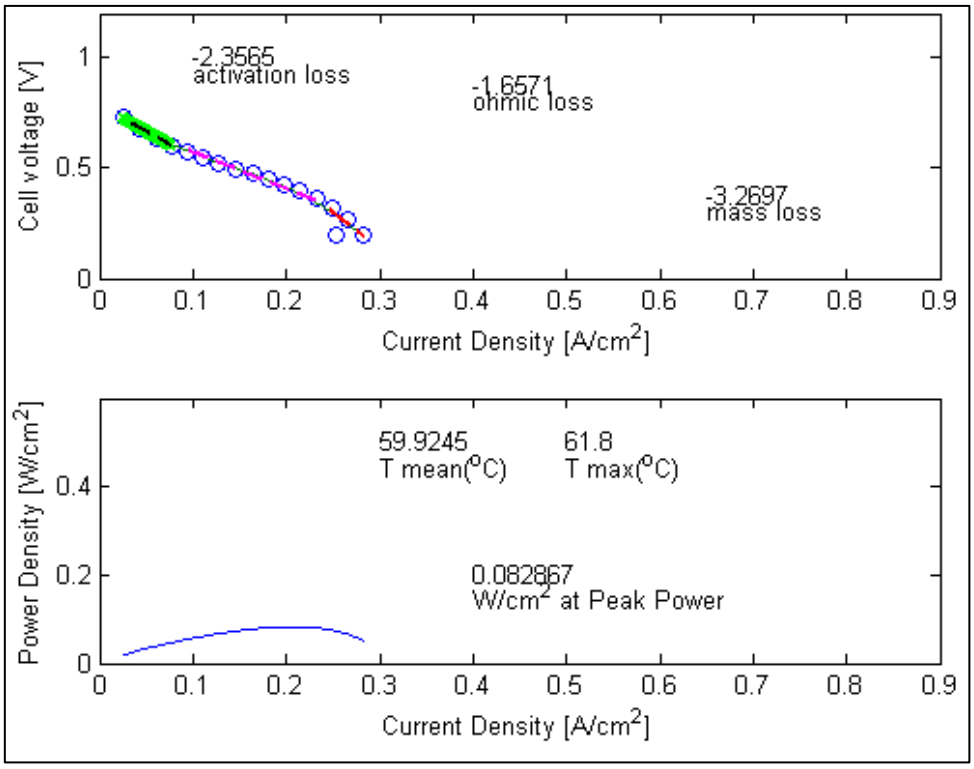

Figure 125: MEA 24 first polarisation curve

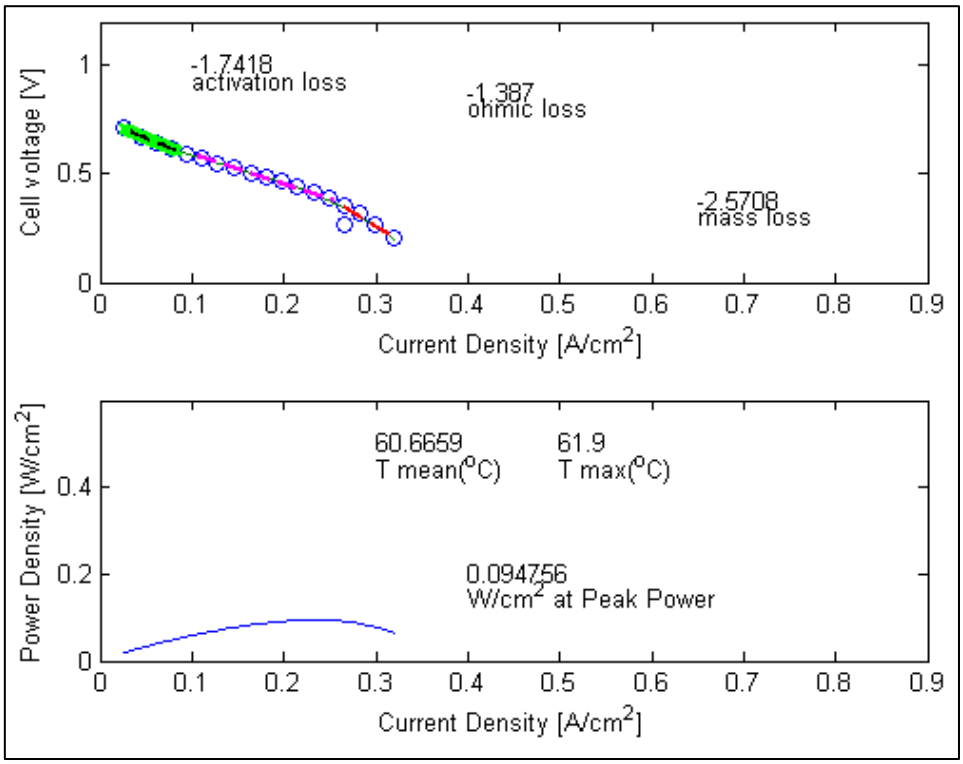

Figure 126: MEA 24 last polarisation curve

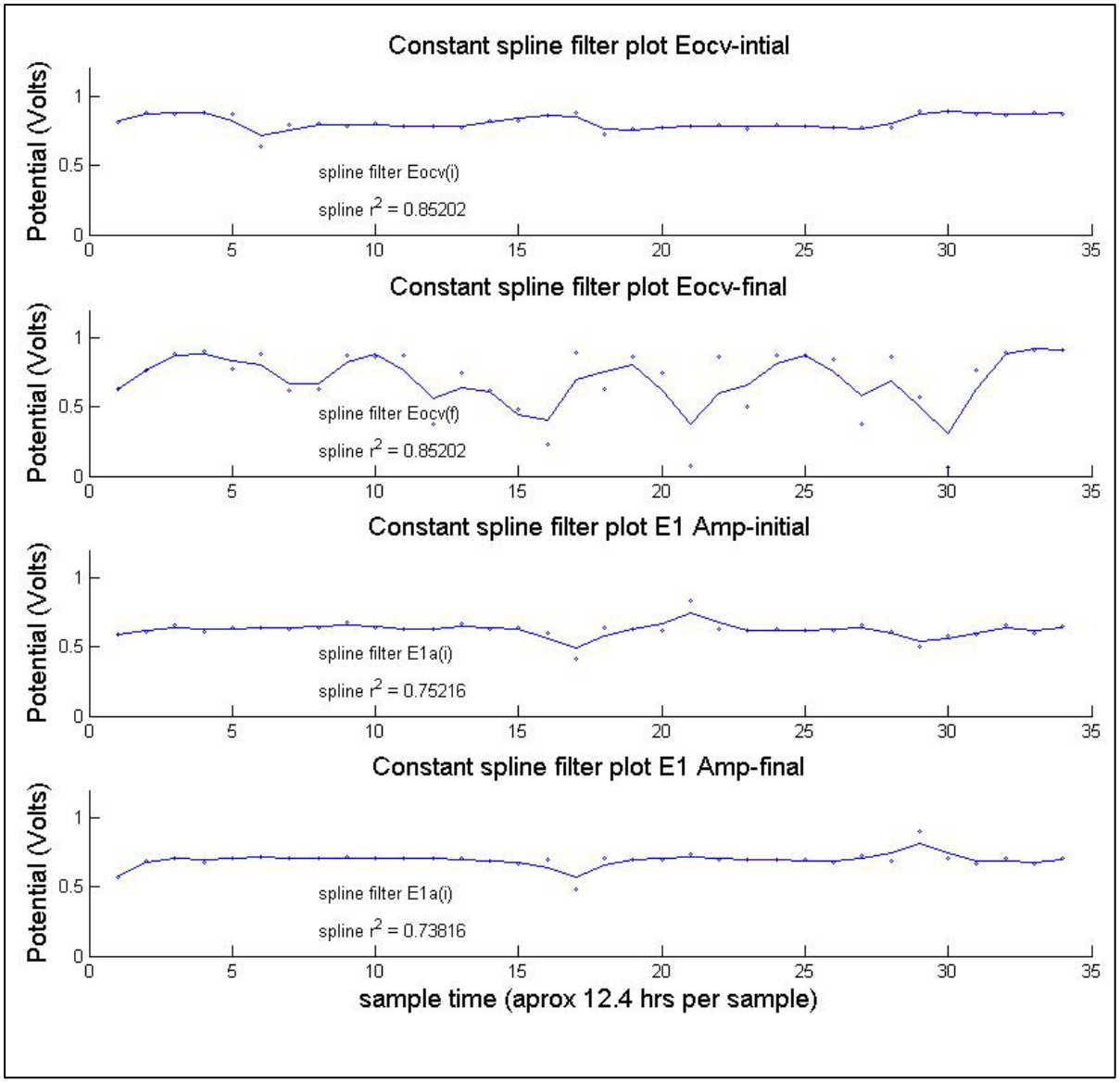

Figure 127: MEA 24 Spline fitting for Eocv (i & f), and E1A (i & f)

Figure 125 shows the first polarisation scan carried out at the start of the degradation trial on MEA 24. MEA 24 is a Toray cathode GDM with a medium concentration (0.35mg.cm^{-2}) Uniform catalyst layer. Figure 126 is the last polarisation scans on MEA 24 after 421 hours of constant operation (24 hours a day) at a one-Amp (0.08Amps.cm^{-2}) load. Polarisation scans were taken approximately every 12.4 hours (exact timing varied depending on the other MEA samples being tested).

Figure 127 shows the results of the potential measurements on MEA 24 immediately before and after each 20-hour polarisation scan. A spline fitting process has been carried out in order to clearly define a region of linear degradation. This process is explained in more detail in section 6.5.1.

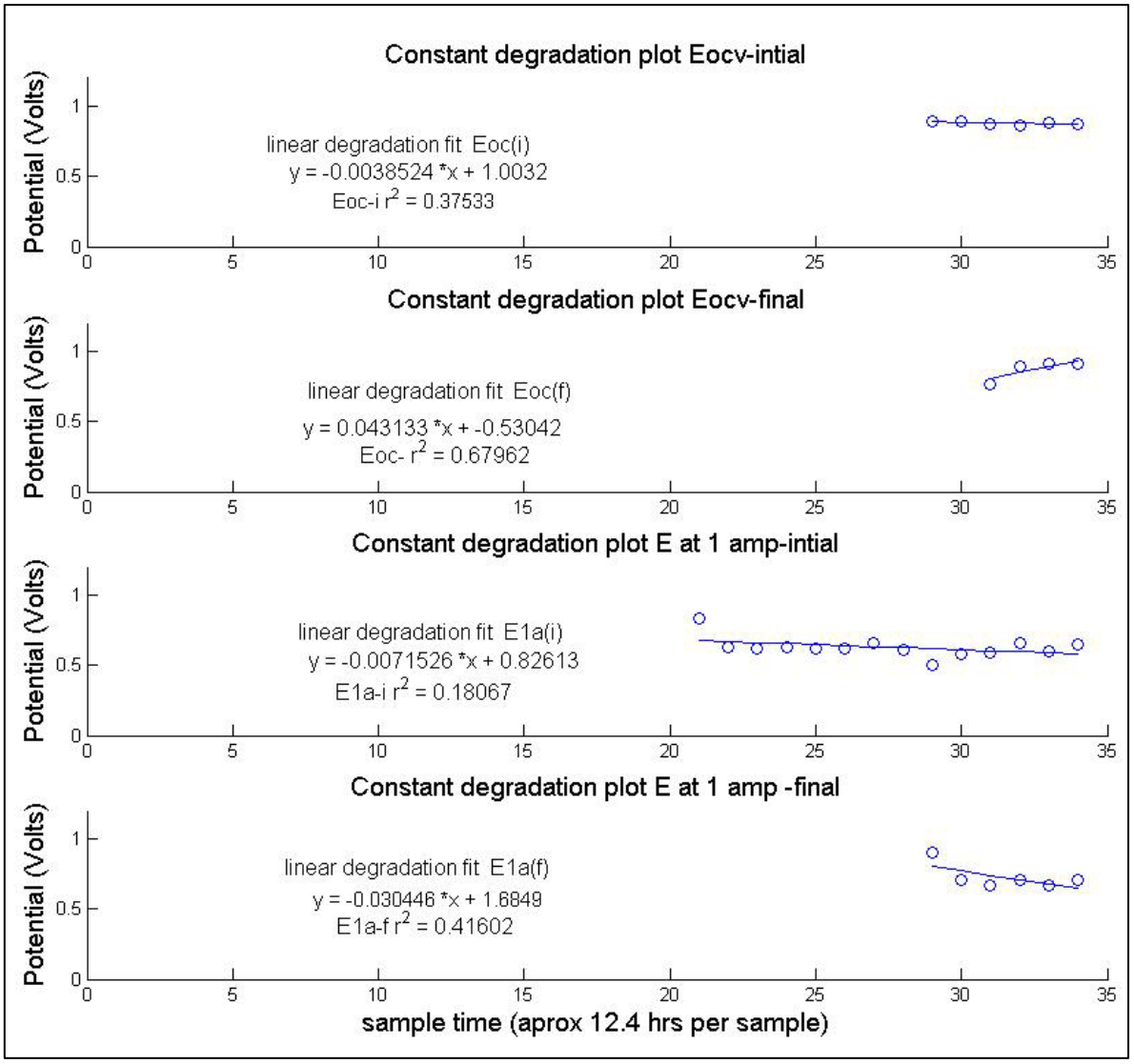

Figure 128: MEA 24 Linear degradation region

Figure 128 shows the localised maximum value for each of the potential values, identified with the aid of the spline fitting process in Figure 127, and plots a linear fit to the remaining values until the end of the degradation test run.

6.5 Analysis and discussion GDM, dual layer catalysts and degradation results

A baseline understanding of the impact of GDMs on fuel cell performance has been developed in this thesis (see Chapter 4). This in turn made it possible to increase the complexity of the information that can be analysed for fuel cell MEAs. The gradient data analysis method used in this study, has been utilised and validated previously, as outlined in section 4.4.2. In many degradation studies, the open cell potential and the potential at a pre-specified load, were also used to measure the degradation output of fuel cell systems [99,124,148]. To that end the E_{ocv} (open cell potential) and E_i (the potential at load current 'i') values were recorded immediately before and after polarisation curves were conducted, at various points in time in the degradation study.

If typical degradation rate responses [148] were to be achieved, then the predicted degradation rate was calculated as follows. From previous work [148] it was anticipated that the potential degradation rate would follow a trend equivivlnt to a 225µV per 'drive cycle' (in Lin et al. (2014) [148] the drive cycle was: 1,200 minutes per driving cycle for up to 200 cycles equates to 4,000 hours of testing). The material tested and the test conditions, in the work by Lin et al. (2014) [148], different slightly (0.2bar(g) operating pressure [148]) from work completed for this thesis, however it was anticipated that it would remain possible to comapre, to some degree, the degradation response generated for samples studied in this thesis.

If similar linear degradation rates to that of Lin et al. (2014) [148] hold true for this experiment, it was anticipated that a measurable degradation rate could be detected in less than forty hours, particularly in the square wave duty cycle. This estimate was based on the conversion of the cyclic degradation rate, reported by Lin et al. (2014) [148], to an hourly rate:

$$1200/60 = 20 \text{ hours}$$

$$225\text{x}10^{-6} \text{ V } /20 = 1.125 \text{ x}10^{-5} \text{ Volts per hour loss.} \qquad (6\text{-}12)$$

Recall the previous arguments [43,45,149] which state that changes in hydrophobicity occur, and the loss of hydrophobic layers open up underlying carbon structures to accelerated degradation. The lack of hydrophobic coating in the selected GDMs, for work completed in this thesis, implies the degradation rate may be even faster than anticipated; if this argument is correct. One factor that may cloud this issue a little is that the CCS method of MEA fabrication may be considered similar to applying a hydrophobic coating to the layer adjacent to the catalyst layer.

In the dual layer MEAs in particular, the low concentration catalyst loading layer is in fact very similar in composition to an MPL. One could even go so far as to describe the low concentration layer as a 'functionalised' MPL, rather than describe it as a true catalyst layer. Having completed the (simplified) design of experiments, basic data interpretations were considered in order to gain an understanding of the overall results. Figure 129 shows that a single linear fit to the data displays the frankly unbelievable result of an ever improving MEA, and this response was the same across all samples. Examining this data, with more a more sophisticated approach than a simple linear regression of the peak power across all polarisation curves, was obviously called for: The degradation of the MEA is not a linear decline, which was evident after completion of the conditioning cycle.

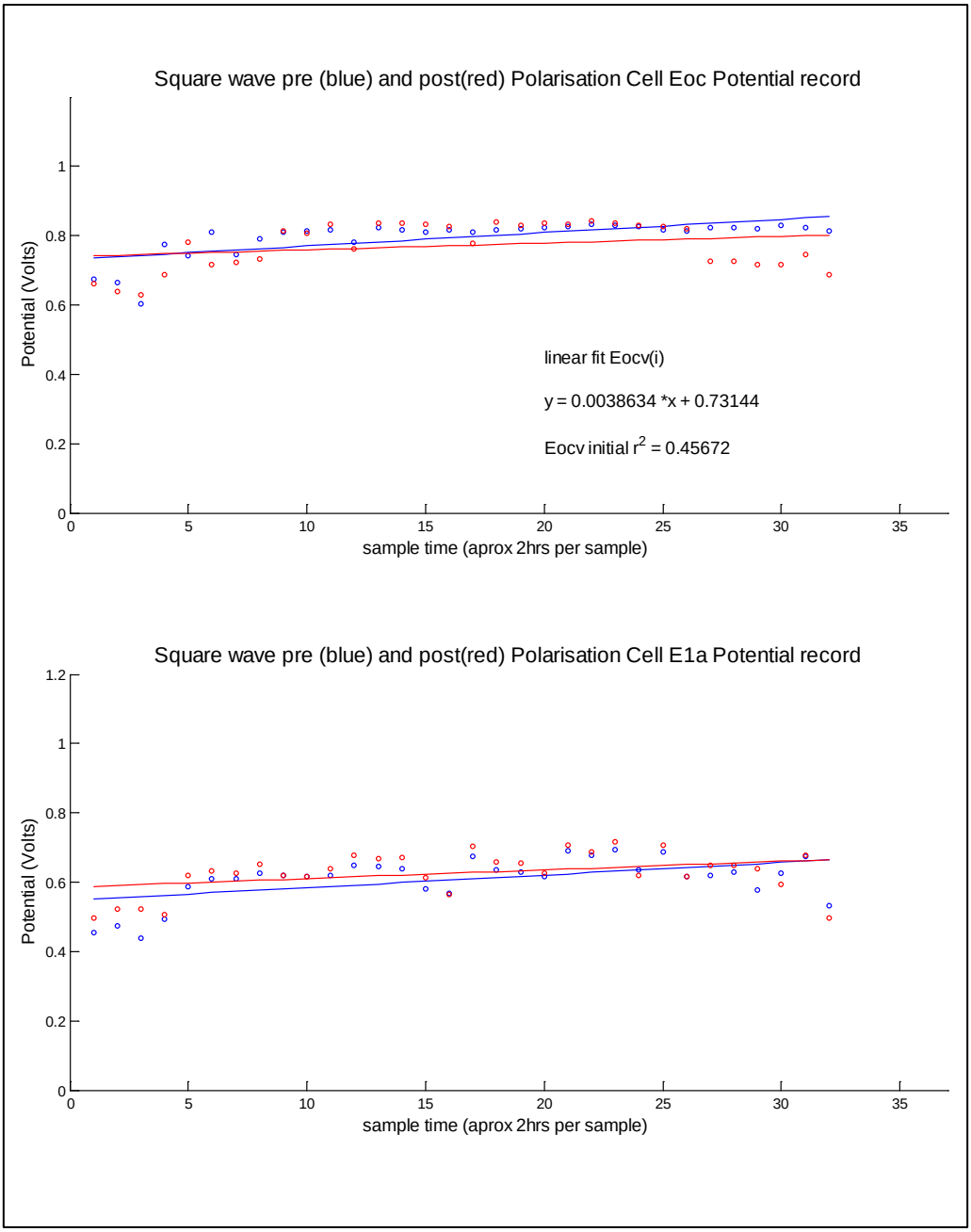

Figure 129: DoE results

Plotting the various values over time, allows an assessment of the degree of degradation of the system. The coefficient of determination (r^2) in Figure 129, is not very high, and visual observation of the data indicates there may be two separate trends. Similar trends are visible for constant load potential measurements before and after polarisation curves (see Figure 138) and the load at one-Amp ($0.08A/cm^2$).

A closer examination raises the possibility that there is an increase in performance up to the midway point, and then a decrease in performance from then onwards. This rising and then falling gradient is not as clearly defined in all samples, and there is often a rise in the cell performance and then a plateau, but not in every case.

Another factor visible in the data; is the tendency for reversible degradation to accrue over the course of a day's testing in the square wave samples. Constant load samples were left to run 24 hours a day. Square wave samples were troublesome to automate and so had to be monitored at all times. As a result of this, it was required that the samples be switched off at the end of each day. A standard 'nitrogen purge' sequence at the start and end of each day was carried out, and the square wave samples had polarisation curves conducted on them four times each day. This increased the number of polarisation curves carried out in anticipation of accelerated ageing for square wave duty cycles (circa 20 hours as discussed above). The first polarisation curve of each day took place after the Nitrogen purge cycle and again, once the system was able to maintain the set temperature.

There is a marked drop across all square wave (e.g. Figure 132 to Figure 130) 'morning' performance. The drop in performance for the very first morning test run on a given square wave sample (Figure 132) was pronounced. The peak load easily hit the 4 Amp mark, and cell Volts drops from 0.38 Volts down to 0.15 limit over a period of 1,000 seconds (approximately 15 minutes). In Figure 133 it can be seen that, after the polarisation curve has been conducted, there was a slight recovery; but not one equivalent to the return to the four amps maximum output seen at the start of the day. The system is set to demand four amps from the working cell, but there was an inbuilt limit on the system that prevents the cell dropping all the way to zero Volts. This hard-wired voltage limit occurs after the cell operates, for more than a second or two, with the cell potential somewhere in the region of 0.15 to 0.2 Volts. There was lower voltage trip limit function in the user interface of the test apparatus, but this was deactivated for the work undertaken in this thesis. The ~0.15 voltage limit is embedded into the setup code elsewhere in the system, and is not reported in the operating manual. As this hard-ware based operating limit was only discovered after testing was started, it was decided to carry on and not attempt to change the hard-encoded machine settings. The same voltage limit condition would apply to all samples tested, and so the results remain comparable.

Note the intermittent gaps in the square wave results that are clearly evident; these were due to human error and were a consequence of the lack of automation for this set of test runs. All key data points have been reported in section 6.4. These raw data plots have not been reported in the main body text; as printing them in legible formats would result in hundreds of pages of largely identical graphs, similar to those in Figure 126 and Figure 132. A full set of all graphical data is available in Appendix 4, which is available as hard copy in the appendices.

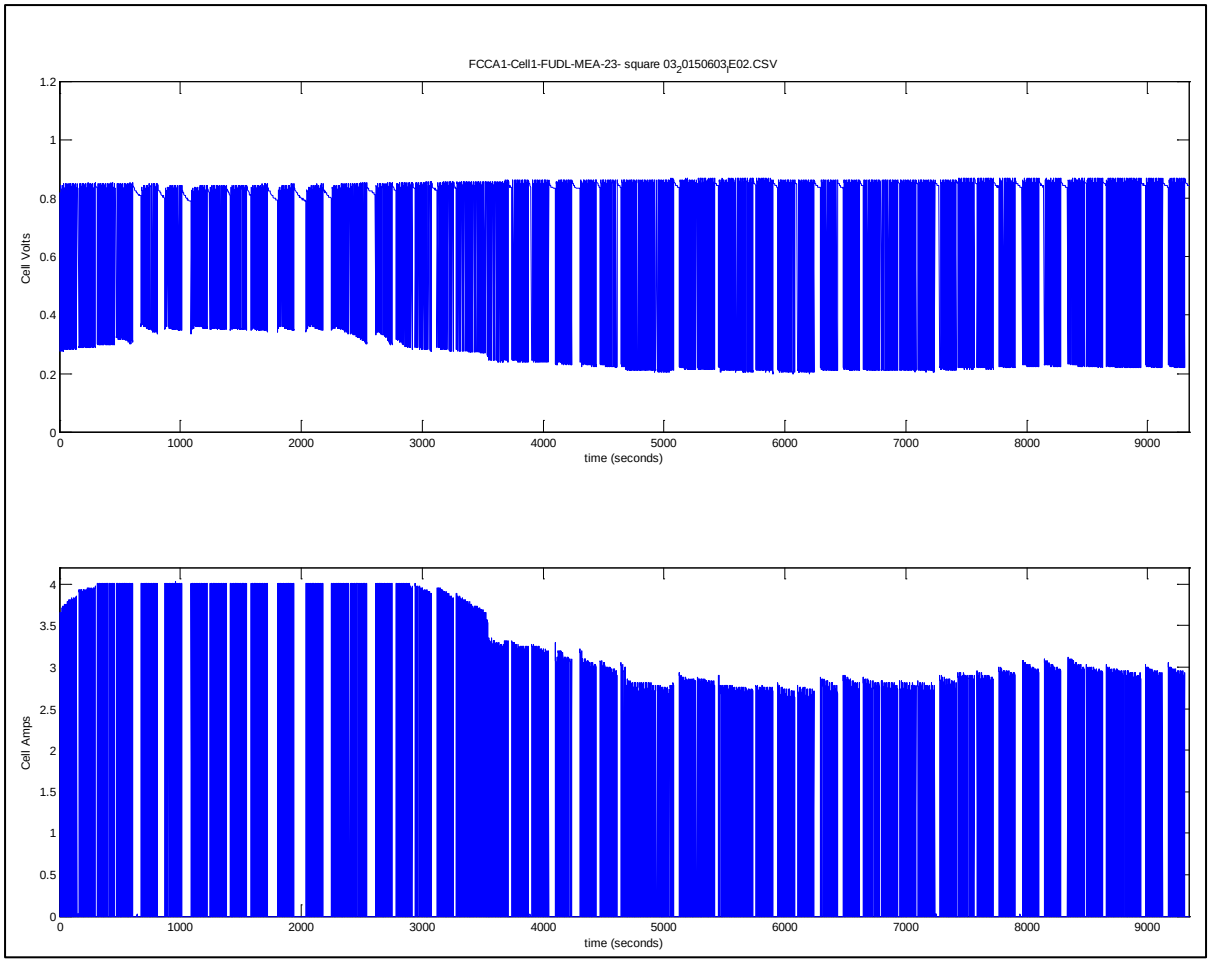

Figure 130: Uniform 0.35mg/cm^2 square wave duty cycles

(Toray AM Day 1)

Figure 130 through Figure 133 show representative square wave duty cycles for a selection of MEAs. Particular attention should be made to the difference in performance on the first day for a given sample (Figure 130 and Figure 132) and the change in behaviour seen in subsequent days (Figure 131, Figure 133), which has been previously identified in Chapter 6 as evidence for reversible degradation.

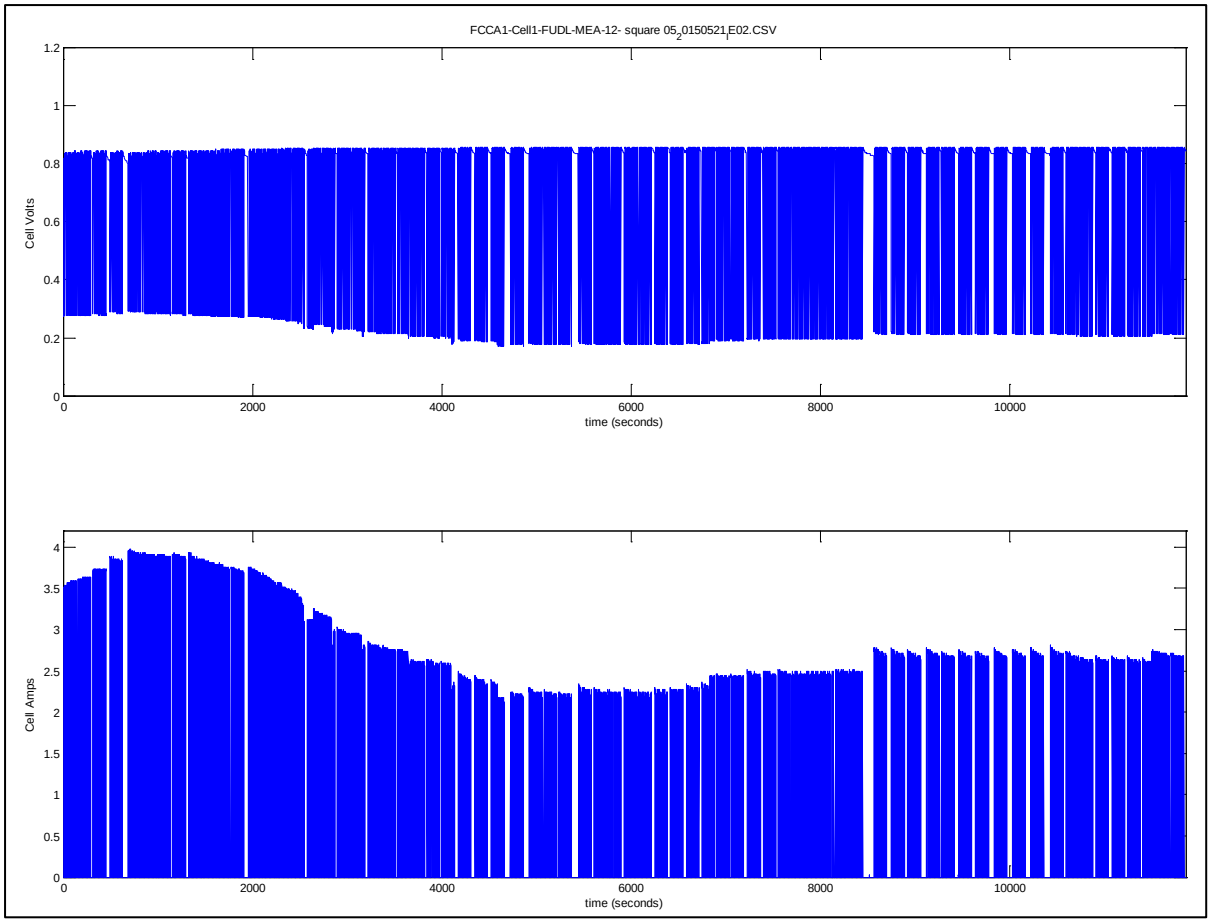

Figure 131: MEA12 low concentration dual layer square wave duty cycle

(Toray, 0.3mg/cm^2 - post N_2 purge day 2)

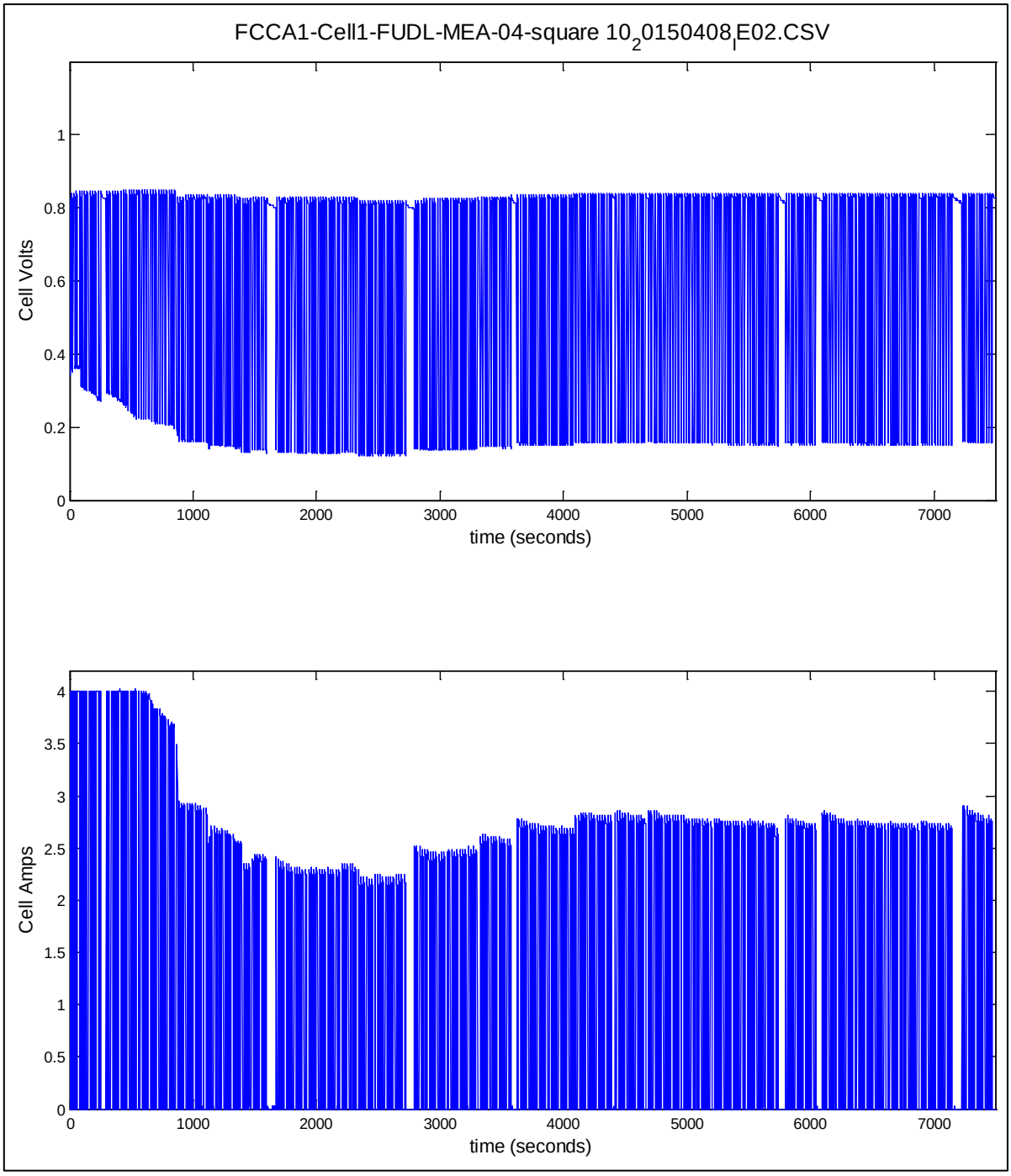

Figure 132: High concentration dual layer square wave duty cycle

(Feudenburg 0.4mg/cm^2 cathode - post morning N_2 purge day 1)

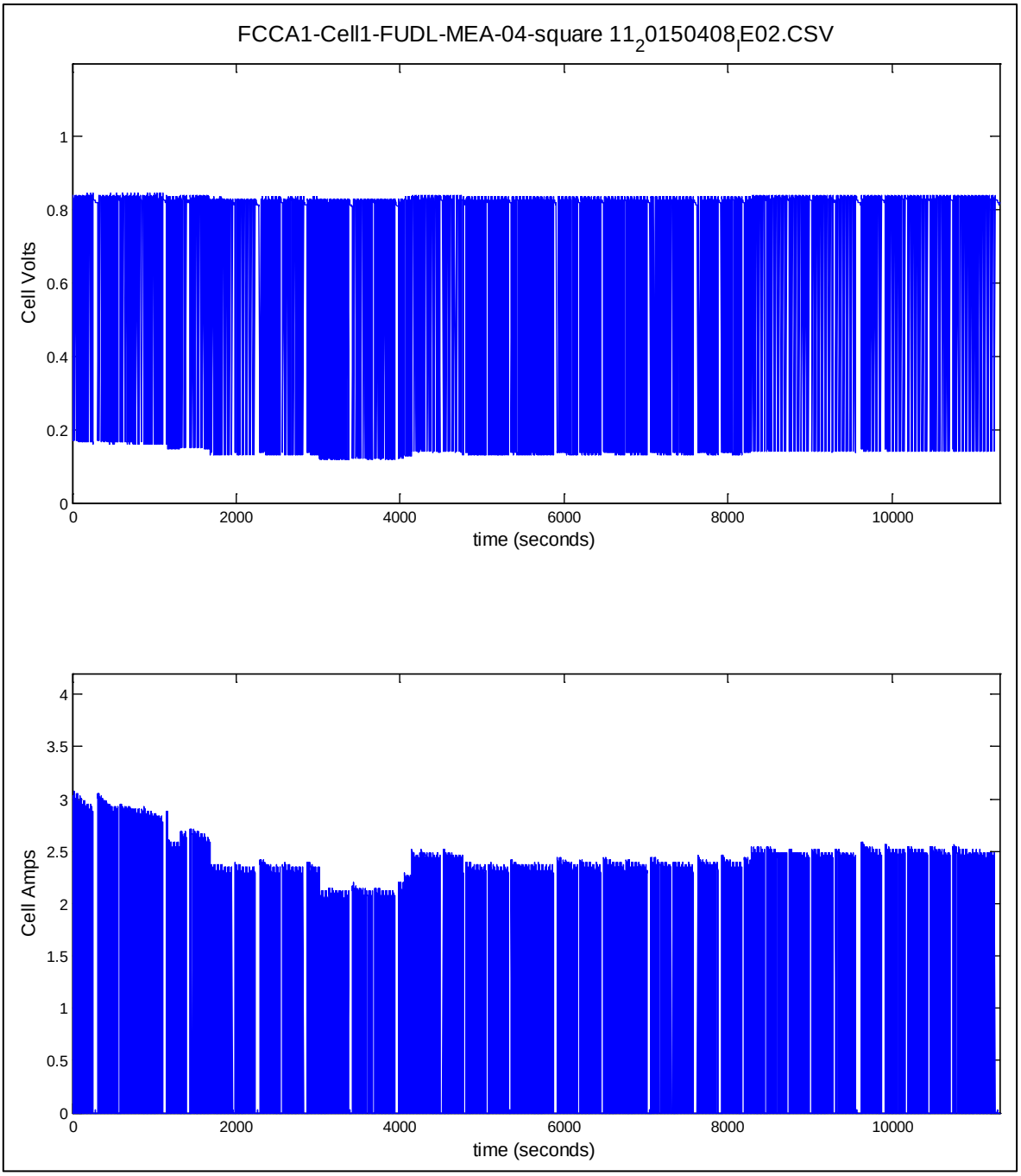

Figure 133: High concentration dual layer square wave duty cycle PM

(Feudenburg 0.4mg/cm^2 day 3)

Subsequent tests show a similar drop in performance each day, though it is not as marked as on the first day for each MEA. Figure 133, the third day of testing after the completion of five nitrogen purging cycles, shows a gradual reduction in output up to the 3,500-second mark. There is then a gradual recovery in total Amps that can be drawn in the 2.5 Amp region.

To reliably detect the performance loss of the cell under study, it was decided to analyse the polarising performance from the same time in the duty cycle each day for the square wave results. With this in mind, it was further decided to focus the analyses in polarisation curves for the same period of each day. This approach is also adopted for constant load samples to ensure the prime data sampling times (am or pm) are comparable across all data sets; even though constant load samples show no evidence of this daily reduction in performance. Figure 134 shows the typical polarisation curve duty cycle applied, and the resultant potential is then measured for each sample.

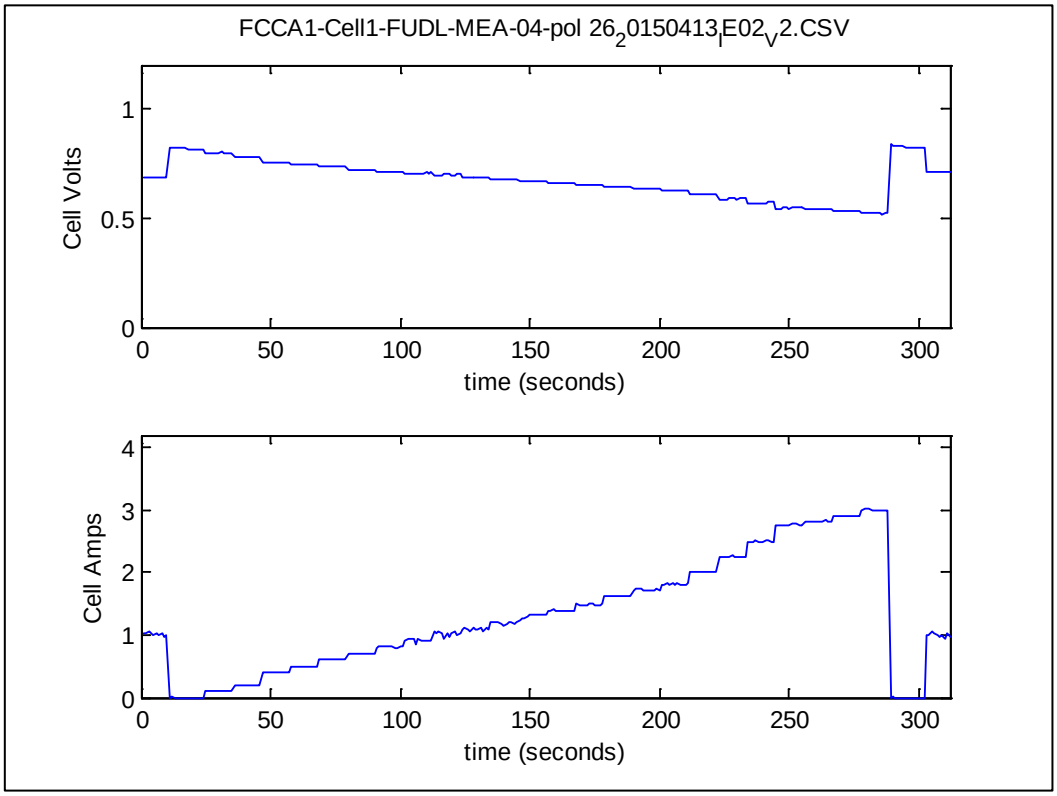

Figure 134: Typical polarisation load

All specimens were subjected to a standard polarising profile, with a ten-second 'hold' at each of the selected steps. The maximum load and step size were kept the same for all polarisation curves. The creation of the polarising curve becomes part of the work history of the cell being studied, and it was for this reason that the absolute polarisation step size was held constant. For some samples tested, this constant step size resulted in failure not take the test cell into the mass transport loss region during measurement. As discussed previously (see Chapter 4), the mass transfer region is not a primary topic of interest due to the inability to model it accurately from the polarisation curve. Therefore, the duplication of identical work cycles was prioritised over gaining information on mass transport losses for all samples.

Peak load during polarisation was set at 3 Amps. The files prepared for analyses were altered slightly, in as much that the overall file length was trimmed at the start and finish of each polarisation test cycle. This was done to simplify the automated data collection form the mat lab code (available in Appendix 3) by ensuring there were exactly ten measurements (i.e. ten seconds of data) before and after the start of the polarisation cycle itself. This ten-second period, at one-Amp, becomes the $E1a_X$ measurement and the adjacent ten-second region with no load, current becomes out Eoc_X reading.

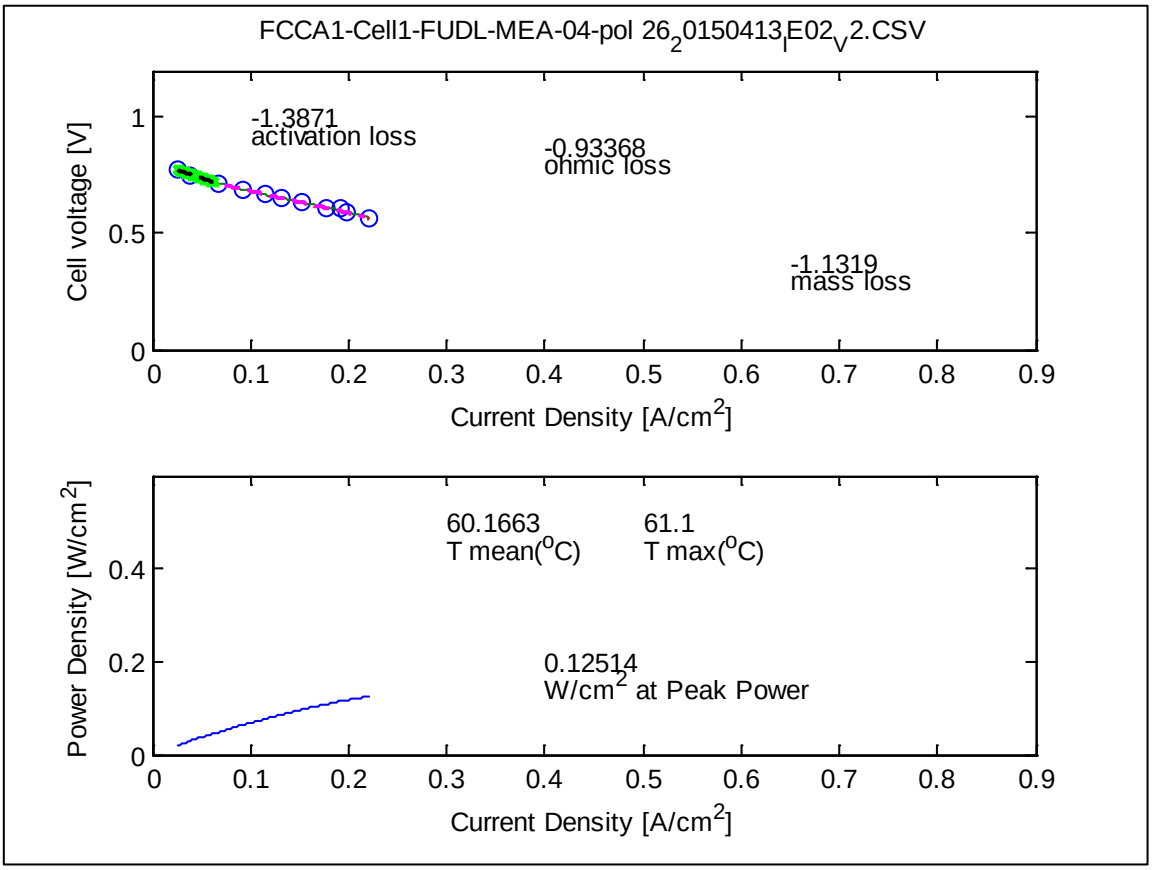

Figure 135: FUDL MEA 04 polarisation curve No. 26

As can be seen in Figure 135, for some polarisations curves this can give a slightly misleading under performance. In this case, it is likely that the MEA has yet to achieve true 'peak power level'. However, this error is uniform across all samples and, for the majority of samples, it is not a factor as the peak power is achieved well before the application of the full 3 Amp load. Having segregated the data, into the morning (AM) and afternoon (PM) sets of polarisation curves, it is now possible to begin to assess the datasets. The isolation of the PM results avoids the confusion caused by the lack of (reversabel) degradation in the morning results. Recall that the AM samples are impacted by the essential 'start up' sequence each day, which included nitrogen purging. Nitrogen purging that breifely removed the reversable degradation at the start of each day (as seen in Figure 132 and Figure 133). It was also found that isolation of PM results made identification of the improvement in

performance in the first half results which, when analysed as a linear plot, resulted in the unlikely outcome of an ever improving MEA as shown in Figure 129.

One-Amp (0.6Volts) measurements (rendered from here on as '$E1a_i$' for readings before the polarisation curve and '$E1a_f$' for those taken after), were taken before and after all polarisation curves, and the data compared, as were the open cell potential readings. Sample readings were taken four times a day for the square wave samples, and twice a day (at the start and end of each day) for the constant load experiments.

Figure 136 is a 'notched' box and whisker plot for MEA04 PM all polarisaiton cureve reuslts, showing the distribution of the potential readings for the open cell potential before and after polarisation curve (E_{ocvi} and E_{ocvi} respectivly) and the potnetial at amp load imedialty before and the polarisaiotn curve (E1Ai and E1Af respectivly). The 'notch' in the box plot indicates one standard deviaiotn around the mean point of the data. The red cross marks represent posible outlier data points.

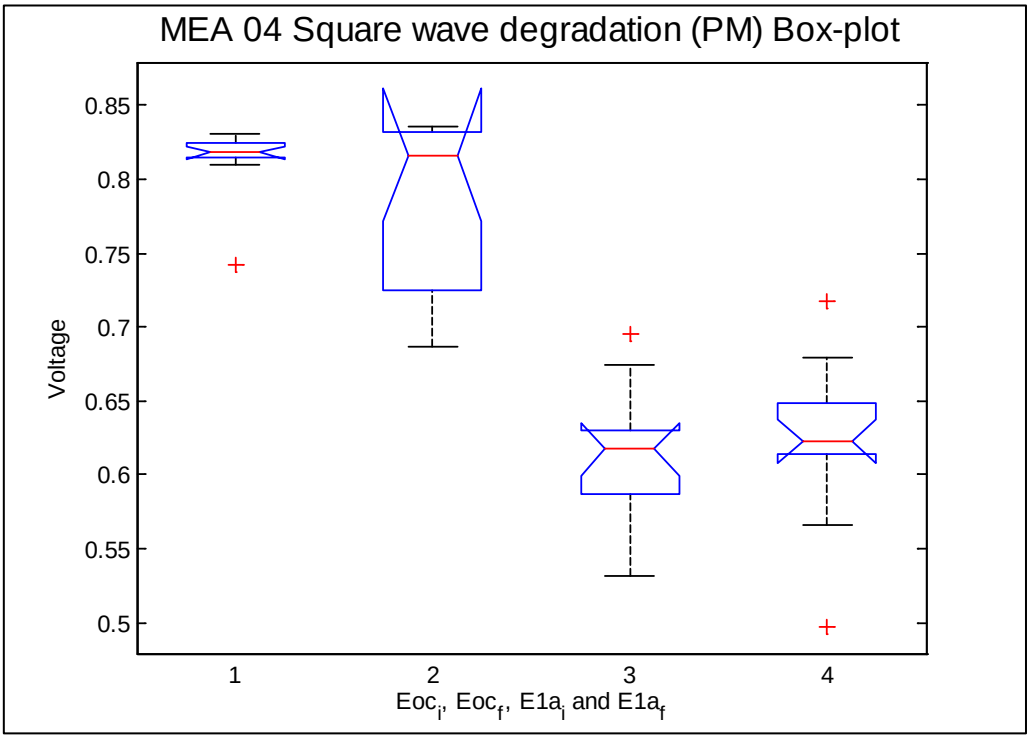

Figure 136: Boxplots for 'PM' FUDL#4

For at a typical sample, such as the one in Figure 136 (MEA#4 in the FUDL set), the mean potential for a given load is the same, to within in one standard deviation as visualised by the 'notch' either side of the mean before and after polarisation curves were carried out. Note that the 'twisted' notch feature of these box plots shows there is a great deal of deviation within each set. However, there were some difference in the pre and post open cell (open cell potential was recorded as Eoc_i and Eoc_f) and one-Amp load results. The act of carrying out a polarisation curve changes the performance of the cell slightly immediately afterwards. In the MEA04-PM case, the results are arguably not significant, but

for a handful of samples there was a measured difference in the pre and post polarising potential readings on a single cell. Because of these atypical before/after polarisation results only a single set (i.e. all Eoc_i results) should be considered together, and direct comparison between categories is not advised.

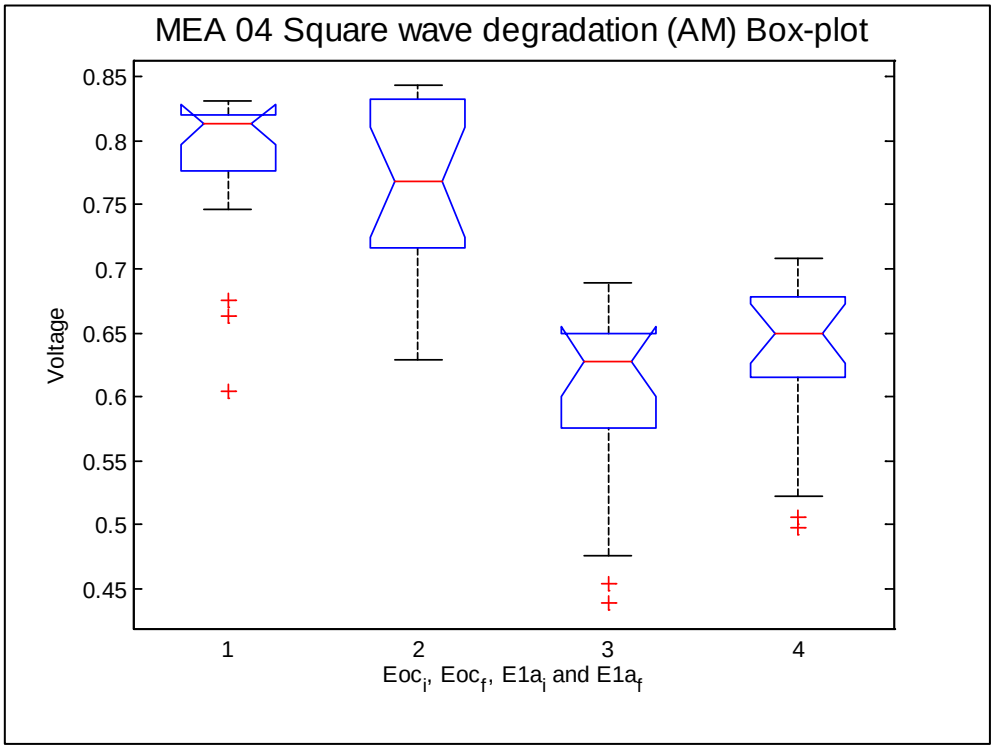

Figure 137: FUDL MEA04 'AM' box-plots

In Figure 137 the 'notch' in the box plot exceeds the upper bound, this is simply an indication of the number of samples being small, and so the 95% confidence bound for the mean point is beyond the middle 50% of the collected data. It also clear for this individual sample that it may be viable to pool polarisation curves for all polarisation curves of the same cell load (i.e. open circuit potential before and after the polarisation curve have the same median point (95% confidence level). It is also clear that it would be invalid to pool the readings across all samples (one-Amp load and open cell have a statistically significant mismatch in the median points). Once again, more sophisticated data analysis methods are advised.

6.5.1 Sample Selection and Alternate Fitting Procedures

In Figure 138 the 'morning' polarisation curves (the first one or two polarisation curves of the days testing) were fitted with a quadratic function, to assess if the improved performance detected in the linear fit is reasonable or not. As can be seen in all samples the quadratic has a far superior goodness of fit (r^2 value) compared to the linear plot earlier (see Figure 129).

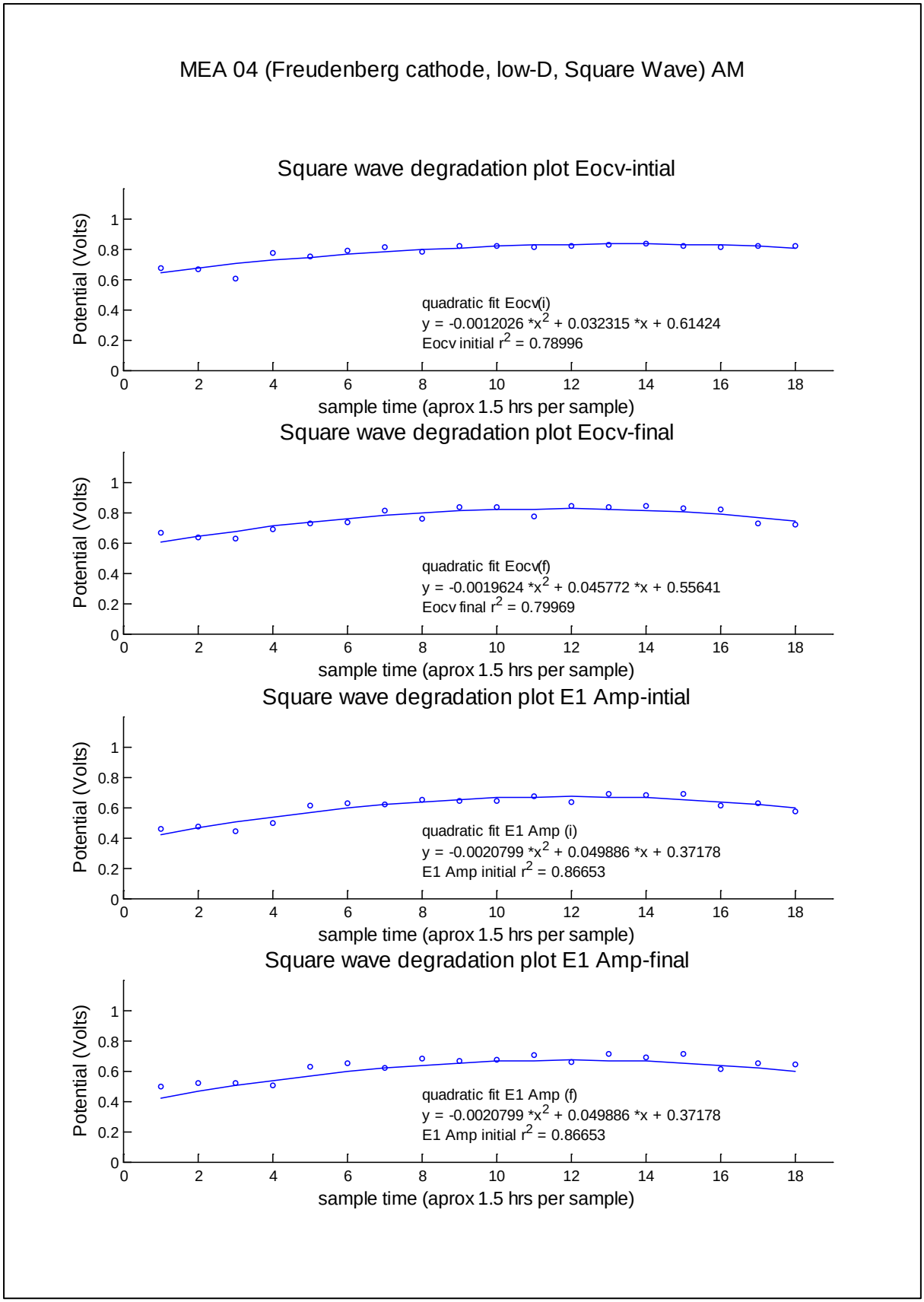

Figure 138: FUDL MEA 04 (AM) quadratic fit

If the tailing off of fuel cell performance, seen in Figure 138 for those data points beyond the peak of the fitted quadratic curve, is a true effect: Then a noise filter should also accentuate it. Too that end, a 'spline filter' was added to the data. The automated smoothing spline function provided by MATLAB is an average between the un-weighted cubic spline techniques and a direct linear fit between adjacent points. 85% of the spline fitted value was generated from the cubic spline approach, which interpolates a smooth curve between two points [178]: An integer value between data measurements was selected, giving a value of h=1 between measurements. (Hence time is given in units of variable length such 1.5 hours per unit as shown in Figure 139). For example; p = decimal percentage contribution of cubic function to Reduced Complexity spline fit.

$$p = \frac{1}{\left(1 + \frac{h^3}{6}\right)} \cong 0.857 \tag{6-13}$$

If a truly 100% cubic spline were used, there would be two possible solutions for every estimated arc between data points. Therefore, the software has designated this region (where 85% of the fitted curve comes from the cubic spline, and the rest comes from the least squares fit between three adjacent data points) 'the region of interest'. This region of interest approach avoids the quandary of deciding which of two possible cubic splines were selected as a fit for a given set of data. The generated spline values tracks between discrete regions with the larger data set and, and apply a best fit line between pairs of data points.

This spline fitting procedure generates a fit line that aids in the visual identification of features in a data set, and reduces the possibility of error that could arise from a simple peak value finding exercise. The spline fitted data, as seen in Figure 139, clearly identifies turning points between localised data points, and gives a clearer visual interpretation of the point where degradation effects are fully developed. In Figure 139, it can be seen that there was significant improvement in performance in all categories around sample number three to five (after 4.5 to 7.5 hours of testing), which is, arguably, in keeping with improved humidification of the system. It is likely that this is the major contributing factor in the improvement in the response detected. As the humidity of the system increases, the membrane (and any other water absorbing materials such as the PTFE based binder agents within the MEA), will take up water and swell. This increase in size will increase the clamping pressure slightly, and will, therefore, increase the contact pressure with the GDM. This in turn reduces the contact resistance between the current collector plate and the rest of the MEA [24,87,95].

Additionally, the uptake of water in the in the membrane materials will reduce its ionic resistance as well [24]. Recall however that this gradual improvement in performance is occurring at the same time

as the reversible degradation detected in the square wave performance charts (Figure 133) and that is seen each day. There is little surprise that a straight linear fit for degradation has been masked with these multiple effects taking place.

Figure 139 shows the 'smoothing spline fit' applied to the same data as that shown in Figure 138. This approach makes it easier to identify distinct regions of behaviour. So in Figure 139, it can be clearly seen that data points one to three show one mode of behaviour, data points four onwards seem to show another. Closer inspection, and the application of an understanding of likely degradation behaviour; indicates that there is a small improvement in performance up to data point 13 or 14, after which there is an inflexion and a small, but measurable, decrease in performance can now be measured. A linear fit to the data points beyond this point of inflexion can be used to generate a degradation rate for the MEA.

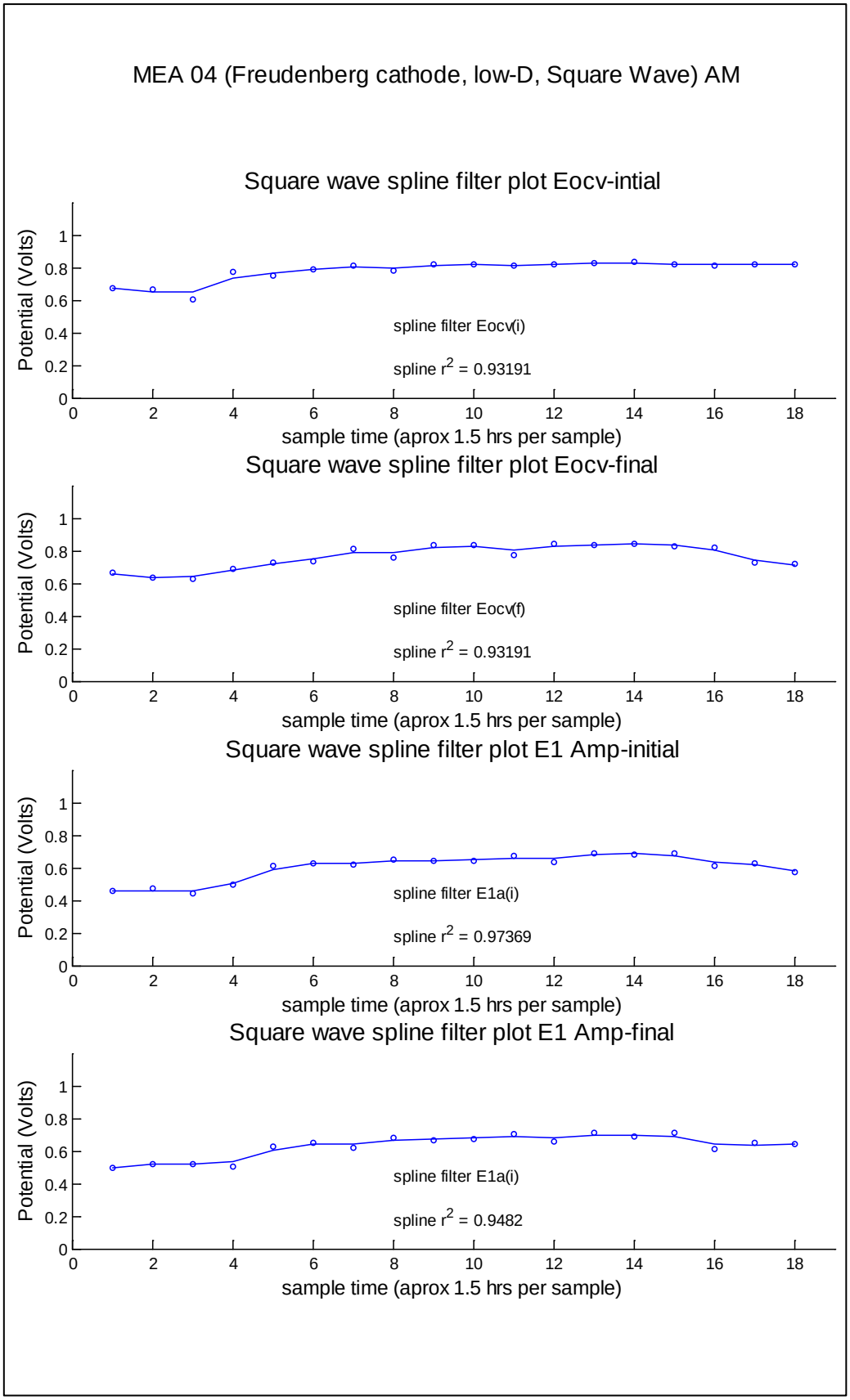

Figure 139: FUDL MEA 04 (AM) smoothing spline fit

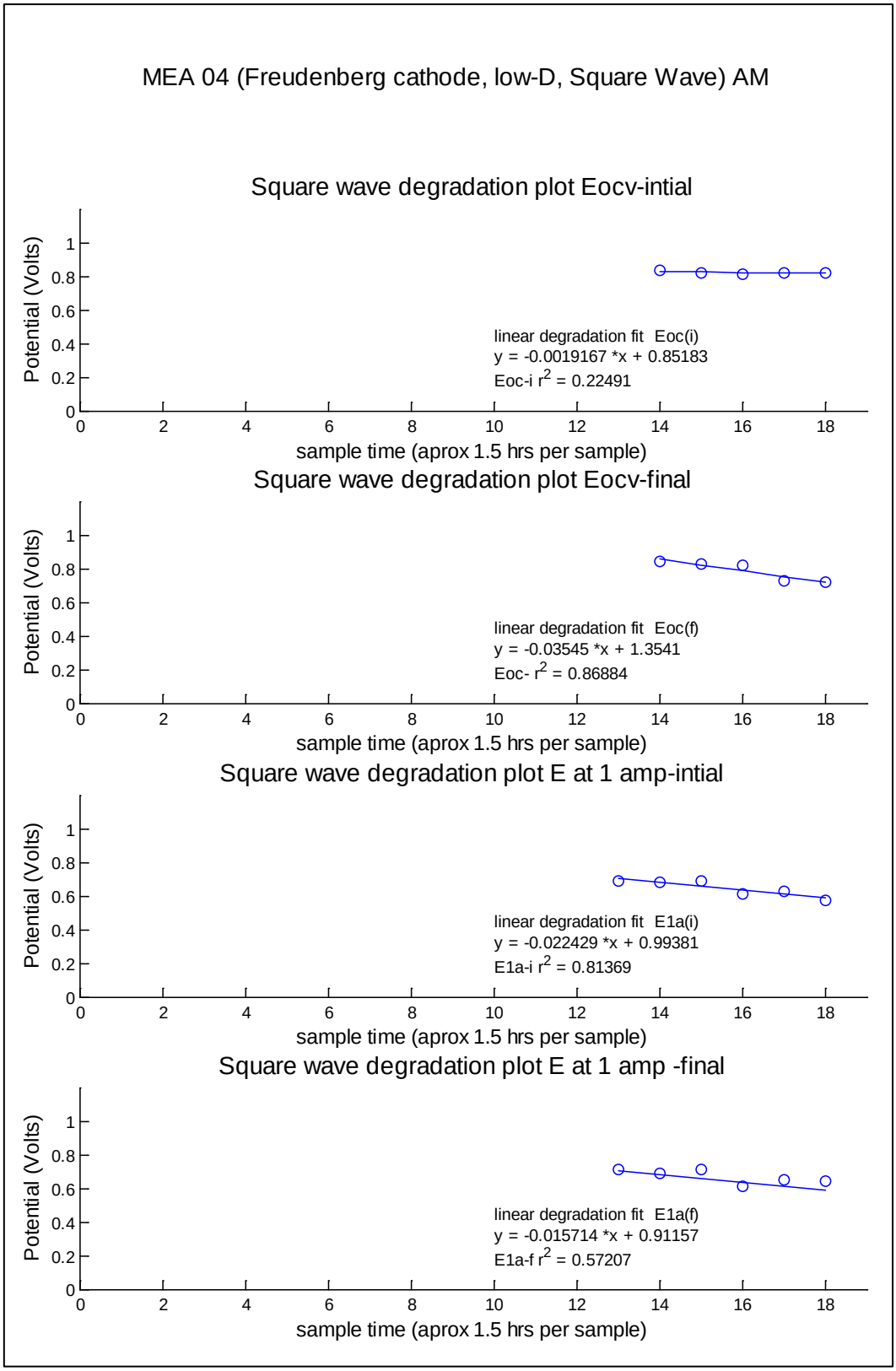

Figure 140: FUDL MEA 04 (AM) linear degradation

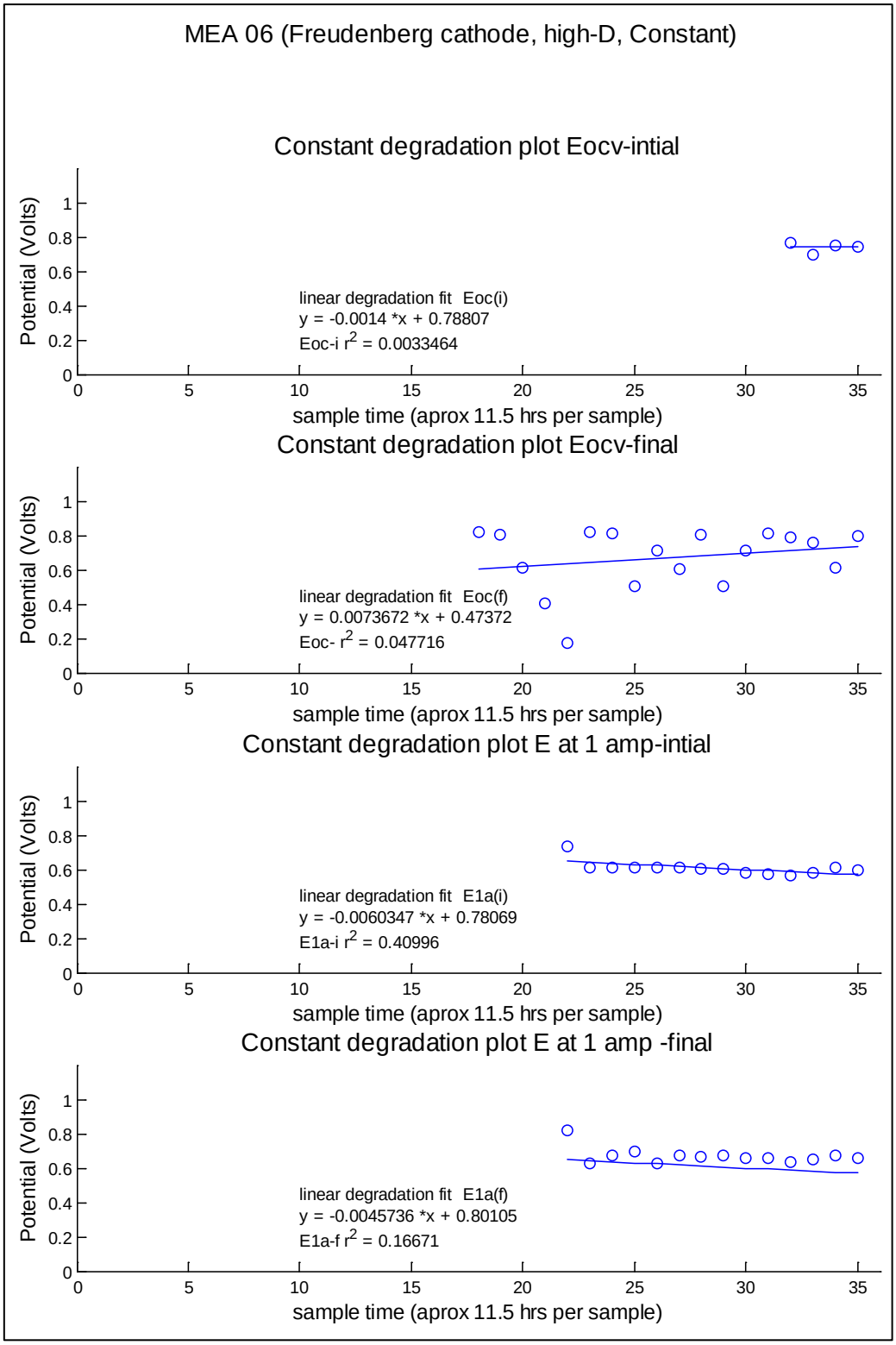

Figure 141: FUDL MEA 06 linear degradation

A comparative plot of linear fits to the region identified as undergoing degradation was generated for a constant load operationon MEA06 (Figure 141), where the sample was held under a 1Amp load, 24 hours a day. It can be seen that the open circuit potential, after completion of a polarising curve ($E_{ocv(f)}$), is no longer a good measure of performance.

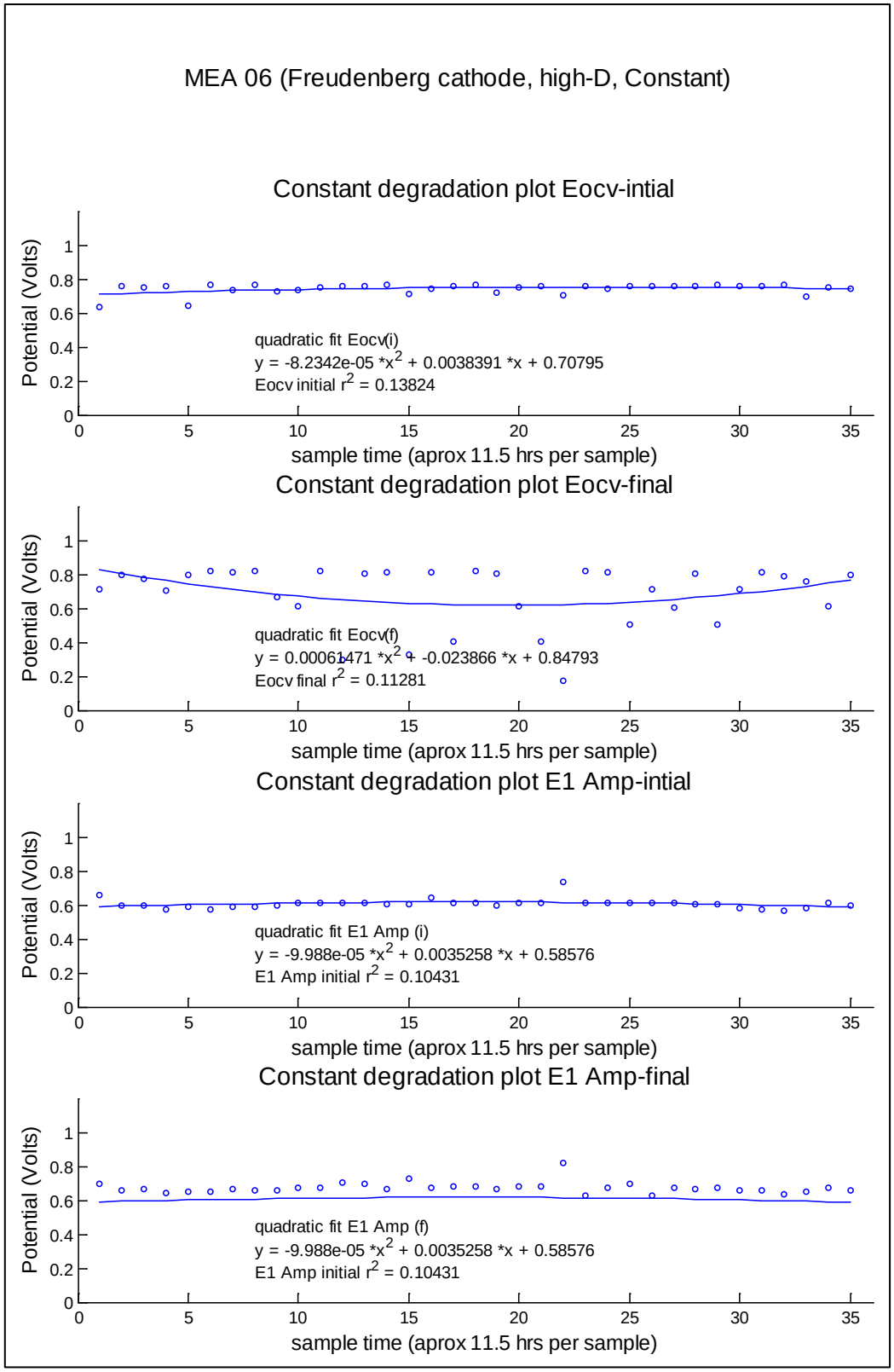

Figure 142: FUDL MEA 06 quadratic fit

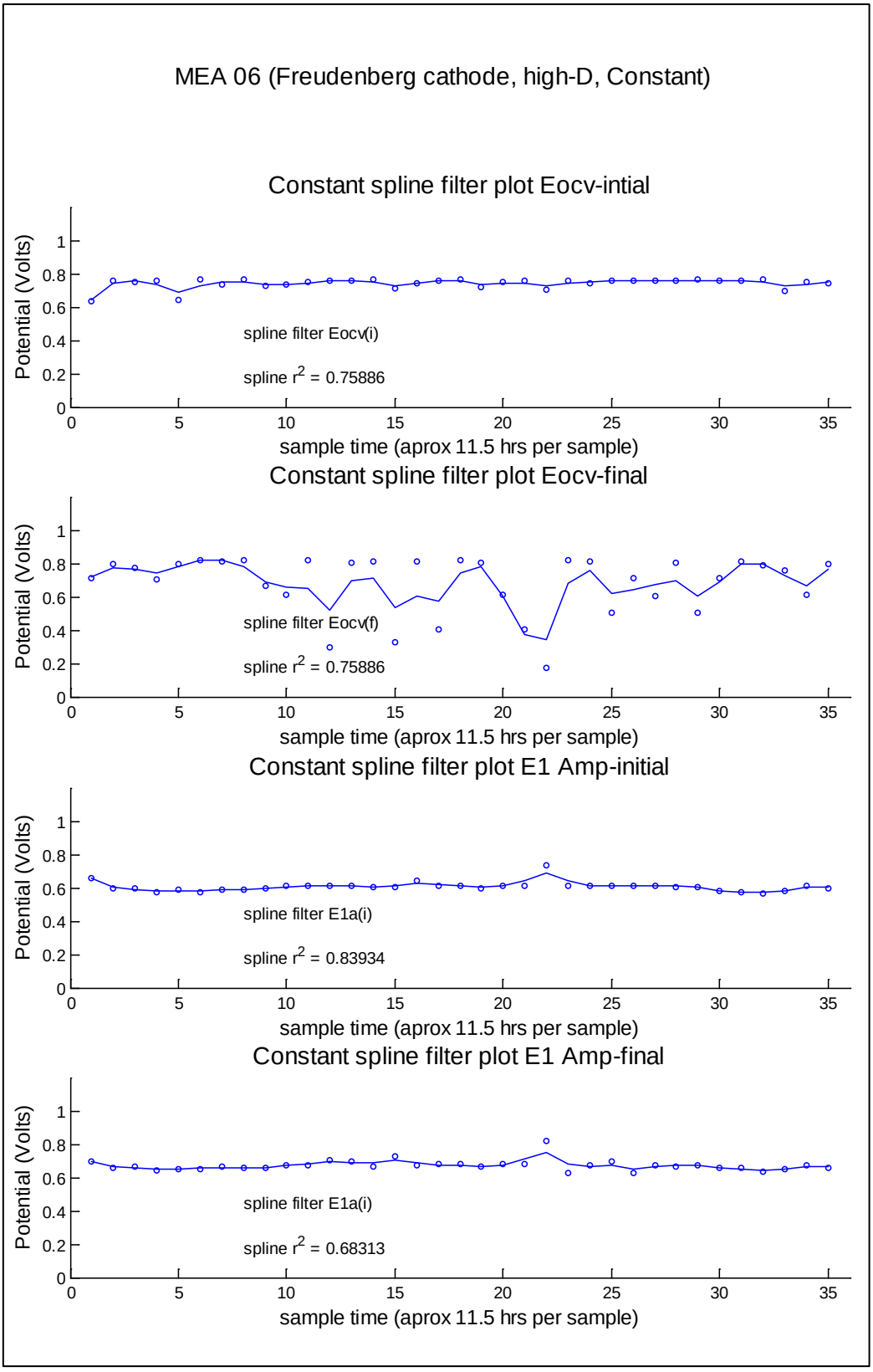

Figure 143: MEA 06 spline fit

Figure 142 shows the quadratic fit for the sake of comparison; though there is little to commend this approach for either square wave or constant load sample data. Figure 143 shows the spline fit for the constant load response. The stepwise improvement in open cell potential is, arguably, still visible between the first and second open cell potential readings before the polarisation of the cell. However, the one-Amp load plots (both before and after the polarisation curve), show a clear difference in the same region (the first two or three steps) with a drop in performance. This drop in cell potential is equivalent to the drop in performance seen in the AM to PM samples resulting from reversible degradation discussed earlier.

A full set of results, using the spline and degradation gradient approach just outlined, for the GDM, CL and degradation rate have already been reported in section 6.4.

6.6 Degradation rate calculations and validation

In Figure 140, a linear degradation fit from the data set maxima to the final reading was applied. Once again, adhering rigorously to the AM or PM data subsets, improvements in the goodness of fit (r^2) value for all measurements were gained. An improvement in fit is clearly visible in most categories, and more importantly, there is a measurable negative gradient for the first time. Multiplying this by the somewhat unusual time step (to facilitate a good fit to spline curves on the same plot) generates a degradation of:

$$-0.0019167 / 1.5 = -1.28 \times 10^{-3} \text{ Volts per hour}$$

or 1.28 mV per hour, which is over 110 times faster a derogation rate than anticipated, from comparison with other authors [148] variable duty cycles (from Table 46: 1.28×10^{-3} divided by 1.125×10^{-5} is approximately 113). Consider the constant load (Figure 141);

$$-0.0015/11.5 = -1.36 \times 10^{-4} \text{ Volts per hour.}$$

This gives a degradation rate over 12 times faster than expected compared, to the work of NEDC based degradation reported by Lin et al. (2014) [148] (from Table 46: 13.6×10^{-3} divided by 1.125×10^{-5} is approximately 12). It would be possible to track back along the data and measure the fall in gradient from an earlier point, and make the data match the expected degradation rate, but that is hardly good practice. The experiments carried out in this thesis, and those reported as a comparison from the literature ([70] and [148]), are broadly similar. Lin et al. (2014) [148] cite their MEA structure in another work [179], but this does not fully define the GDL and its hydrophobicity. As has been stated previously, the test sample fabrication method used by Zhang et al. (2015) [70] closely matches that used in the experiments that were completed for this thesis. However, the geometry of the samples used in that work [70] were not an ideal match. Between the two previous sets of experiments ([70] and [148]), the work completed for this thesis is comparable to both, though not an

exact match for either. Equally the MEA design, GDM selection and catalyst concentration, is broadly similar for MEA 04. The assumption has been made that these were suitable comparisons for the experimental results reported (see section 6.4). As reported in section 4.3.3, the Zhang et al. (2015) paper [70] was the starting point for creating the ink formulation used in creating the MEAs tested in this thesis**.** Zhang et al. (2015) [70] attribute reversible degradation to the formation, and subsequent carbon corrosion based removal, of CO layers previously evolved the catalyst surface. Lin et al. (2014) [148] state that longer term degradation impacts were caused by rapid changes in the duty cycle and changes in the overall geometry of the CL. Specific significance was attributed [148] to the reduction in mean pore size and uniformity of the porous structure of the CL, key components of fuel cell degradation, alongside a significant reduction of ECSA after 200 driving cycles. Zhang et al. (2015) [70] highlight permanent degradation resulting from the "…*agglomeration.*…" [70] (Ostwald ripening) of Pt deposits and the loss of carbon structures and their associated platinum catalyst sites (i.e. reduction of ECSA). The duty cycles in the work completed for this thesis were comparable to those reported by other authors ([70] and [148]).

Square or rectangular waves have been demonstrated to accelerate the loss of electrochemically active surface area [125,176] due to Ostwald ripening particle growth of the platinum catalyst; especially at potentials between 0.6 and 1.2 Volts, and with increased carbon carrion occurring in the range of 0.4 to 1.4 [sic] Volts [125,176]. In the FCCA system, voltages were not artificially induced to such high levels, but this extreme range of potentials may be reached during start or shut down cycles, though this will, of course, have no bearing on the constant load degradation study. Zhang et al. (2015) [70] report degradation rates in the order of $1.45x10^{-3}$ Volts per hour with a rapid polarisation cycling effect.

Table 46: Degradation rate comparison to literature

Test	Volts per hour loss	ref	Range (+/- to mean)	Standard Error (SE)
Square wave 0.15 to 0.8 Volts	$1.28x10^{-3}$	This research	$+/- 0.16x10^{-3}$	$0.533 x10^{-3}$
Constant load 0.6Volts	$13.6x10^{-3}$	This research	$+/- 1.13x10^{-3}$	$1.98 x10^{-3}$
Rapid potential cycle 0 to 1.2 Volts	$1.45x10^{-3}$	[70]	Not reported	Not reported
Constant load 1.5 Volts	$10.9 x10^{-3}$	[70]	Not reported	Not reported
Simplified drive cycle	$1.125 x10^{-5}$	[148]	Not reported	Not reported

It is evident that the results achieved in this set of experiments compare well with some results reported in the literature, but not all. In light of the reasonable agreement with the previous work [70], it is suggested that the reduced degradation rate in some findings is due the addition of hydrophobic coatings and MPLs, and the difference in duty cycle (NEDC instead of a square wave with very short wavelengths).

The electrode construction methods required for spinning disc electrochemical analysis [70] are fundamentally different to that required for the much larger MEAs, though the basic construction of carbon + platinum doped on carbon is not too dissimilar to the MEAs manufactured for this research. It is suggested that the broadly equivalent electrode construction, combined with the rapid cycle accelerated degradation, undertaken for both this thesis and in work completed by Zhang et al. (2015) [70], dominated any scaling issues between the very small (approximately 1cm diameter) rotating disc electrodes [70], and the larger MEAS (approximately 4cm diameter) used in work completed for this thesis: that demonstrated a similar degradation rates.

Making the assumption that the comparison between the slower degradation rate of the simplified drive cycles reported [148] and that the data is valid; it is possible to quantify the degree of 'acceleration degradation' the experiment has induced: That is to say, the ten-second wave legth square wave duty cycle used in work to complete this thesis, accelerates degradation by a factor of ~110 times compared to a standard duty (NEDC based) cycle. However, it would be preferable to validate this against MEAs of identical construction as those used in the simulated drive cycle, and against real world degradation measurements. From the discussion of results so far (see section 6.4 and section 6.5), it is reasonable to compare degradation rates after the 'peak' in performance and use the linear gradient after that point; to generate a degradation rate that is comparable to previous studies. This approach has been replicated across all samples in the designed experiment matrix, and the results are tabulated in Appendix 3 (all PM polarisaiton plots and fit data are in Appendix 4).

6.7 Numeric quantification of polarisation curves and degradation

The analysis of the designed experiment data, indicates there is no improvement to be gained from the multivariate example. The results were not statistically significant for co-varying inputs, based on the design space investigated. This lack of co-variance obviously counteracts somewhat the results from Chapter 4. There is a distinct possibility that the reduced order model, detailed previously (Figure 80), lacks sufficient power to investigate the design space for these more complex interactions. The existing design could, of course, be adapted to improve its resolution, by either completing the original design (though there would be a need to factor in a blocking effect for the elapsed time between experiments) or by including replicates of the existing, or if possible additional design points, if time permits. The findings are accepted as they stand, and it is concluded that there is no improvement in the DoE multifactorial model when compared to a simple mean of the results of

interest. It must be acknowledged, as discussed in section 2.2 and Chapter 3, that it is possible that a larger study, with increased numbers of samples, may detect higher order interactions (i.e. higher order effects with three or more input variables co-verying together). Such higher order interactions can be masked in the relatively small scale study undertaken in this chapter. Any such higher-order covariance, of three or more factors, that exist are likely to be quite subtle [82,85]. The work completed in this chapter has been analysed for two-factor covariance and was not been detected (i.e. the mean provides as good, or better, an estimate of the predicted result as any two level multivariate model). An increased study size may also be able to detect smaller two-factor interactions that may be too small for this set of experiments to detect. Though it is always possible to expend greater amounts of resource pursuing a definite answer to a given topic: Part of the utility of M-ANOVAR methods, is that they provide a degree of confidence in the negative result. Any two-factor effects that have not been detected in this set of experiments must be smaller than the error margin of the mean (discussed in more detail in section 6.7.2).

6.7.1 MEA performance improvements and reversible degradation

There were several improvements in performance that have had to be removed from the previous data analysis, to define a degradation rate that has a reasonable agreement with previous studies. This section discusses these increases in MEA performance in the early stage of the degradation testing in a little more detail, even though they do not form a major part of this investigation. The conditioning of fuel cells immediately after construction is a well-known requirement [180], and a standard conditioning cycle has been applied to all MEAs as discussed in section 4.3.7.

Previous work has identified performance improvements for up to fifteen hours in some MEAs [180], but nothing like the hundreds of hours required by some the samples tested in this research. Other factors such as reduced humidity and temperature can prolong the activation and conditioning process; but again the conditioning time would normally be expected to be in the order of tens of hours, not days. Examining the typical smoothing spline fits (Figure 139 and Figure 143) the improvement in performance is in fact broadly completed in a reduced period more in keeping with the times reported previously. However, adopting the approach that the flattening of the ‘smoothing spline fit’ at or around the 15 hours mark is the true peak performance [180]; the subsequent degradation results would not correspond as well as they have done with other degradation rates in the literature (see Table 46).

Likely sources of the improvement in MEA performance in early stages of testing:

- Humidification of membrane.
- Humidification of other PTFE structures.

- Reduced Ohmic resistance due to greater contact force between monopolar plates and the GDM as the membrane swells.
- Increased reactant and product flow due to changes in the CL structure [180].

As discussed previously (see sections 6.4, 6.5 and 6.5.1), the data analysed has been taken from the 'afternoon' polarising curves taken each day, to normalise the readings with regards to the reversible degradation effects that had been observed. Recall, the observed reversible degradation impacts the square wave duty cycle sample and significantly alters the results when comparing morning to afternoon samples (see section 6.5 and 6.5.1, with particular reference to Figure 136 and Figure 137). Once again, reversible degradation is a well-known phenomenon [70] and can be attributed to several effects. Platinum catalyst reaction sites can become blocked or poisoned by a variety of gases, often CO or CO_2. This build-up of passivating layers can be mitigated somewhat by encouraging its chemical evolution at certain potentials (as discussed earlier in Table 5): While prolonged periods of time at these potential will also oxidise the carbon-based supports and fibres present in the MEA, the materials coating the catalyst layer will also be removed, regenerating the available platinum surface area. Similarly, the nitrogen purge at the start and end of each days testing (square wave cycle) will strip surface adsorbed molecules from the platinum, as will brief periods of running pure hydrogen without generating current (Mench (2012) [95] and Whiteley (2016) [90]).

Another source of the performance recovery is the removal of excess water from pore structures. Running a two-minute nitrogen purge, without generating water as a reaction product, dries out the MEA to a certain degree, without excessively drying the membrane itself. This removal of water increases the total porosity available for reactants and products when the cell is next placed under a working load. This effect is, arguably, the best explanation for the short improvement and then collapse back that is clearly seen in of the morning square wave data logs (e.g. Figure 132 and Figure 131) and corresponds to effects reported by others [57,181].

Having utilised the spline fitting function to identify the point where degradation rates behave as expected, the decrease in performance that has been identified after reaching the maximum performance point is considered. The $E_{OCV\text{-}I}$ reading, identified as the maximum value, and confirmed through the spline fitting visual inspection as discussed in section 6.4, were the 'peak' or maximum reading after all improvement gains have been accrued in the test piece, and degradation rates were measured after this point in time.

Table 47 shows all results and measurements of the samples in the GDM, layered catalyst and degradation DoE study for Freudenberg non-woven (felt) GDM.

Table 48 shows all results and measurements of the samples in the GDM, layered catalyst and degradation DoE study for Toray (paper) GDM.

	Square Wave, daily, PM only										Eocv-i			
FCCA	mgPt/cm^2	cathode GDL	cycle	duration (days) each square set 1 day = 1 start/stop cycle as well	number of runs	# cycles	tot duty time (s)		MEA ID		E max	time step to E max		gradient loss per hour (volts per hour)
1	0.3 Low d	fberg	square	8	645	7740	77,400	21.5	Mea 04 PM		0.8300	9	13.82142857	-0.00339
1	0.4 high d	fberg	square	8	858	10296	102,960	28.6	mea 08 PM		0.8698	3	5.72	0.00157
1	0.35 uniform	fberg	square	7	1013	12156	121,560	33.8	mea 19 PM		0.8740	9	17.87647059	-0.00138
2	0.3 low d	fberg	sqaure	2	390	4680	46,800	13.0	MEA 27 all		0.6707	2	6.5	-0.00779
			Mean	6.25	727	8718	87180	24			0.8111	5.75	10.98	-0.00275
			stdev	2.87	270	3244	32441	9			0.0957	3.77	5.87	0.00393
			coef of d	0.46	0.37	0.37	0.37	0.37			0.1180	0.66	0.53	-1.43
			median	7.5	751.5	9018	90180	25.05			0.8499	6		-0.00238
FCCA	**1 Amp load constant**										Eocv-i			
1	0.4 high d	fberg	constant	17.5			1,512,000	420.0	mea 06		0.7690	32	373.33	-0.00012
2	0.3 low d	fberg	constant	5			432,000	120.0	mea02		0.7628	3	32.73	-0.00043
2	0.35 unifiorm	fberg	constant	8.5			734,400	204.0	mea 18		0.8548	11	149.60	-0.00114
			Mean	10.33			892800	248.0			0.7955	15.33	185.22	-0.00056
			stdev	6.45			557152	154.8			0.0514	14.98	173.07	0.00052
			coef of d	0.62			0.62				0.0646	0.98	0.93	-0.93
			Median	8.5			734400	204.0			0.769	11	149.6	-0.00043

Table 47: Freudenberg non-woven ('Felt') results

	Square Wave, daily, PM only										Eocv-i			
FCCA	mgPt/cm^2	cathode GDL	cycle	duration (days) each square set 1 day = 1 start/stop cycle as well	number of runs	# cycles	tot duty time (s)		MEA ID		E max	time step to E max		gradient loss per hour (volts per hour)
1	0.3 low d	torray	square	9	908	10896	108,960		Mea12 PM		0.8455	12	22.70	-0.00347
1	0.4 high d	torray	square	8	954	11448	114,480		mea 16 PM		0.8657	6	11.22	-0.01296
1	0.35 unifiorm	torray	sqaure	9	1043	12516	125,160		mea 23 PM		0.8500	6	12.27	-0.00074
			Mean	8.67	968	11620	116200				0.8537	8.00	15.40	-0.00572
			stdev	0.58	69	824	8236				0.0106	3.46	6.35	0.00641
			coef of d	0.07	0.07	0.07	0.07				0.0124	0.43	0.41	1.12
			median	9	954	11448	114480				0.85	6		-0.00347

	1 Amp load constant									Eocv-i			
1	0.4 high d	torray	constant	17.5			1,512,000	420.00	mea 14	0.8505	36	420.00	-0.00066
1	0.35 uniform	torray	constant	17.5			1,512,000	420.00	mea24	0.8960	29	338.33	-0.00033
2	0.3 low d	torray	constant	5			432,000	120.00	mea10	0.6573	6	120.00	0.00159
			Mean	13.33			1152000			0.8013	23.67	292.78	0.00020
			stdev	7.22			623538	173.21		0.1267	15.70	155.10	0.00122
			coef of d	0.54			0.54	0.00		0.1582	0.66	0.53	6.12
			Median	17.5			1512000			0.8505	29		-0.00033

Table 48: Toray paper results

Figure 144 compares the responses of each type of catalyst layer (uniform distribution at 0.35mg.cm$^{-2,}$ dual layered 0.3 mg.cm^{-2} and dual layered 0.4 mg.cm^{-2} on both paper (Toray) and non-woven (Freudenberg) GDMs) under a constant load. It is clear that the results for high concentration dual layer catalysts and uniform were very close together for the felt like material (F-Berg) for the constant result. At first glance, the uniform CL seems to indicate a separate result when applied to Toray papers, but closer analysis of the error bounds (see equation (6-16)) indicates an overlap with the Toray high dual layer readings as well. There is a marked difference in the performance of the low concentration dual layer, and it is clear to see that selection of the supporting substrate makes a significant difference. The high dual layer catalyst, can generate a broadly equivalent performance ($E_{OCV\text{-}I}$ = 0.855 Volts) regardless of which substrate it is deposited onto, though with a marginal decrease in performance for the non-woven GDM. The uniform concentration platinum layer on Toray (Pt=0.38mg.cm^{-2} (+/- 0.01)), is significantly poorer in performance ($E_{OCV\text{-}I}$ = 0.65 Volts) compared to its uniform counterpart on the non-woven Freudenberg GDM.

The reverse is true in the square wave duty cycle (Figure 145). There is no measurable difference in performance for the felt like Freudenberg materials in any category ($E_{OCV\text{-}I}$ = 0.855 Volts) this time, but the square wave performance of the paper (Toray) structured material is very poor in comparison ($E_{OCV\text{-}I}$ = 0.752 Volts). It seems clear that there is a structure and low dual layer interaction that is exacerbated by the duty cycle. Indeed the design expert Pro software had set a warning alert on the graph to point this out. Sadly the lack of data points means that the 'A-B-C' interaction indicated here cannot be quantified or reported with any reliability (there is a 50% probability that the effect is in fact due to experimental noise). In light of this, it is concluded there is no evidence for multivariate effect based on the data available, and with a 50% probability that the effect is a result of experimental noise; it is difficult to justify the resource allocation to research this further.

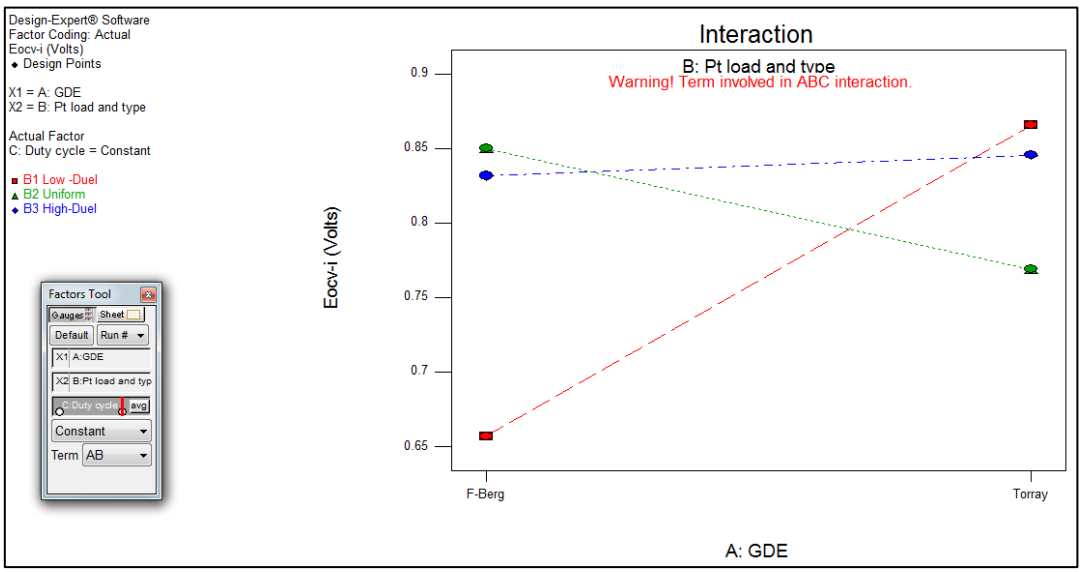

Figure 144: Constant load dual layer interactions

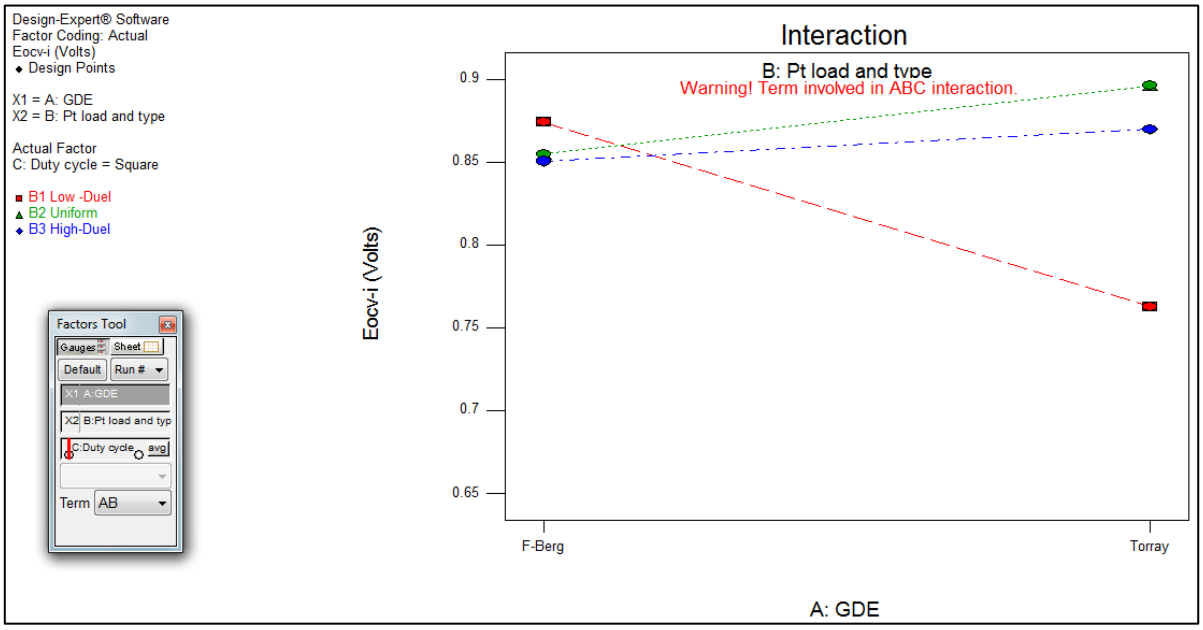

Figure 145: Square duty cycle dual layer interactions

The accrued data can be further analysed further to create the following table, to reduce the extraneous data, and gain a more detailed understanding of the data, as shown in Table 49.

Table 49: Dual layer interactions simplified data field

	constant						square				
Eocv-i	F-Berg	error		Torray	error	**Eocv-i**	F-berg	error		Torray	error
0.3 low-D	0.7628	0.0514		0.8505	0.127	0.3 low-D	0.8300	0.0957		0.8455	0.011
0.4 high -D	0.7690	0.0514		0.8960	0.127	0.4 high -D	0.8698	0.0957		0.8657	0.011
0.38 unifomr	0.8548	0.0514		0.6573	0.127	0.38 unifomr	0.8740	0.0957		0.8500	0.011
mean	0.7955			0.8013		mean	0.8579			0.8537	
stdev	0.0514			0.127		stdev	0.0243			0.011	
V/hr loss	F-Berg	error		Torray	error	**V/hr loss**	F-berg	error		Torray	error
0.3 low-D	-0.00043	0.00052		-0.00159	0.00065	0.3 low-D	-0.00034	0.03892		-0.00347	0.0064
0.4 high -D	-0.00012	0.00052		-0.00066	0.00065	0.4 high -D	0.00016	0.03892		-0.01296	0.0064
0.38 unifomr	-0.00114	0.00052		-0.00033	0.00065	0.38 unifomr	-0.00014	0.03892		-0.00074	0.0064
mean	-0.0006			-0.0009		mean	-0.0001			-0.0057	
stdev	0.0005			0.0007		stdev	0.0002			0.0064	
hours to Emax	F-Berg	error		Torray	error	**hours to Emax**	F-berg	error		Torray	error
0.3 low-D	32.73	173		120.00	155	0.3 low-D	13.82143	5.87		22.70	6.35
0.4 high -D	373.33	173		420.00	155	0.4 high -D	5.72	5.87		11.22	6.35
0.38 unifomr	149.60	173		338.33	155	0.38 unifomr	17.87647	5.87		12.27	6.35
mean	185			293		mean	12.4726			15.4	
stdev	173			155		stdev	6.1895			6.35	

Table 49 groups samples by the duty cycles the were exposed to, with constant one-Amp load test results on the left, and square wave duty cycles on the right. In each of these two groups is further broken down into sub categories of performance: The initial open circuit potential prior to conducting polarisation curves (E_{ocv-i}), the voltage loss per hour measured (V/hr loss) and the time in hours to reach the maximum potential (hours to Emax). It should be noted that the E_{ocv-i} reading corresponds to the E_{max} reading. Once segregated into these distinct families for both types of GDM, it is then

possible to conduct basic assessments of the data such as the mean, the standard deviation (6-15) and the standard error (6-16).

When measuring the open cell potential (E_{ocv-i}) there was no significant difference for either duty cycle. The voltage loss per hour results were far more telling, with Fberg (Freudenberg) samples performing well, except for the uniform catalyst distribution in a constant a 0.6 Volts. In all other circumstances, the felt like structure of the non-woven material consistently outperforms the paper GDM.

The time taken to achieve peak performance in a constant load gives the impression of being impacted by type and total presence of platinum, but in this analysis, the standard deviation is very large. This makes a case for removing the low concentration dual layer (referred to as low-d in Table 49, Table 50 and Table 51) sample from the data set, and treating it as a standalone result. Table 50 and Table 51 show the time to maximum E_{ocv-i} reading and the resultant mean and standard deviation (St.Dev), with the low concentration data excluded.

Table 50: Constant load time to Eocv-I(Max)

Hours to Emax	F-Berg	error		Toray	Error
~~0.3 low-D~~	~~33~~	~~173~~		~~120~~	~~155~~
0.4 high -D	373			420.	
0.38 uniform	150			338	
mean	261			379	
st.dev	158			58	

Table 51: Square cycle time to Eocv-I(Max)

Hours to Emax	F-berg	error		Toray	error
~~0.3 low-D~~	~~13.82~~	~~5.87~~		~~22.70~~	~~6.35~~
0.4 high -D	5.72			11.22	
0.38 uniform	17.88			12.27	
mean	11.80			11.7	
st.dev	8.60			0.74	

However, in manipulating the data in this fashion, it would no longer be possible to assign an accurate error values, as there would be only two measurements for that combination of factors in each duty cycle. Equations (6-15) and (6-16) both require the number of samples (n) in the set to be an integer value greater than three as they both includes the term ‘n-1’[80]. With that caveat aside, a claim

could be made for a measurable, significant, difference between the high and low concentration dual layer samples; though the more robust results presented in Table 49, and their standard deviation, call that into some doubt.

In Table 49, the high dual layer has a mean value of 373 hours (Fberg), with minus one standard deviation (St.Dev = 158 hours) giving a result of 215 hours as a minimum range, compared with the 33 hours of the low concentration dual layer (Fberg). It is highly likely that the low dual layer is reaching this peak performance much more quickly. To unpick this puzzle, a table of weighted (blocked) values was created to normalise experimental variability from the data set. This weighting and blocking technique has been discussed briefly in section 3.3.1, with a detailed example of the procedure demonstrated in section 4.7, specifically in Table 15. The original weighted tables (available in Appendix 3) were colour coded green to map the most desirable value in each weighted set. Note that in the 'time to reach maximum open cell potential' data set, it is not clear if shorter, or longer durations are preferred, and so a secondary colour (yellow) was used for the lowest value. The same procedure was repeated for the full set of data in Table 49, and the results of that weighting procedure are presented graphically in section 3.3.1.

6.7.2 Structure and catalyst interactions weighted values

When applying the weighting procedure to assess values (The full set of weighted results is available in Appendix 3), it is important to recall that the variance is

$$Variance = \frac{\sum(x - \bar{x})^2}{(n-1)} \qquad \textbf{(6-14)}$$

moreover, this relates to the error (set at one standard deviation) as

$$Standard\ Deviaiton\ = \sqrt{\frac{\sum(x - \bar{x})^2}{(n-1)}} \qquad \textbf{(6-15)}$$

Therefore any of the weighted values with a sufficiently small variance can now be considered valid data on which to make an assessment. This was achieved by arranging the data in such a way to ensure the number of specimens in each group is greater than two by utilising the three loadings catalyst materials.

This provides the requisite minimum sample size in each set to make the calculation of the standard error for the weighted results accordance with equation (6-16).

$$Standard\ error = \sqrt{\frac{1}{(n-2)}\left[\sum(y-\bar{y})^2 - \frac{[\sum(x-\bar{x})(y-\bar{y})]^2}{\sum(x-\bar{x})^2}\right]} \qquad \textbf{(6-16)}$$

The full spreadsheet of calculations is available in Appendix 3 (weighting tables). Those results where the weighted error indicates the results are significant are presented section 6.8.

6.8 Summary of Chapter 6

The preceding chapter has presented a case study of the application of the multivariate methods to an experimental case study on MEAs for PEMFCs. A wide range of input variables were identified as topics of interest in section 6.1, and a design of experiments procedure was undertaken for those inputs. The DoE originally included the three duty cells (constant, square and triangular). However, it became apparent that software security issues on the test apparatus prevented the use of the triangular wave duty cycle, and so this part of the work had to be abandoned. For this case study, the need to exclude triangular wave test cycles has been reported in this thesis, to demonstrate the flexibility of M-ANOVAR and DoE methods, so long as the researcher does not start from a 'bare minimum' complexity DoE. Anecdotally, the author can report experiencing a reluctance to adopt DoE experimental approaches in the wider fuel cell community (in the UK and EU), as they have been perceived as excessively time-consuming and inflexible. The designed experiments were robust enough to be adapted when practical experimental considerations required it: Combined with modern analytical software such as Design Expert Pro, it becomes a simple and straightforward procedure to reconfigure DoE plans, as was demonstrated in section 6.2.

The experiential method and sample parameters were detailed in section 6.3, with the completed experimental results presented in section 6.4 and its subsections. Analysis and discussion of the results were undertaken in Section 6.5. It was found that for the square wave duty cycle samples, it was difficult to fit trend lines to all data points. It became apparent that a simple linear degradation pattern was not occurring for the fit measurements, and that this was accompanied by variability between samples measured at the start and end of each day of experiments. In an effort to explain this difference between morning and afternoon experimental results, the author suggested that the variability and nonlinear degradation pattern was a result of a combination of factors:

- Nitrogen purge at the end of each days testing.
- Reversible degradation effects, such catalyst poisoning and excessive water build up, being impacted by the potential cycling and nitrogen purge procedures at the start and end of each day.
- Improvements in MEA performance due to a variety of factors including increased hydration of the membrane.

To achieve results that were comparable to pre-existing literature, and retain compatibility between samples sets, it was necessary to take a reading from the afternoon (PM) experimental results only. The one-Amp, constant load, samples were far less impacted by the morning and afternoon discrepancy. It was suggested that this was because of a high stoichiometry of the reactant gases (which reduces flooding effects by virtue of the higher through put of gas flow); and due to the constant one-Amp load test samples not requiring regular nitrogen purge and shut down procedures at the end of each day. However, experimental results for constant load samples were limited to the afternoon (PM) test data, to and retain compatibility between the two samples sets (constant-load and square-wave). Having isolated the afternoon polarisation curves from the rest of the data, the results were then analysed again, with a linear degradation fit, completed once the samples had stabilised and achieved a region of maximum performance. This was determined both numerically (single highest Eocv-i reading) and also with comparison to other measurable outputs such as the potential under a one Amp load. Lastly, a spline fitting procedure (detailed in section 6.5), was also carried out to aid visual inspection of the data, and ensure a region of maximum values had been achieved, and the degradation fit was not overly influenced by a single rogue measurement from the experimental process.

Having determined a degradation rate, comparable degradation results from the literature (which have utilised similar catalyst ink formulations, broadly equivalent GDMs and test parameters), were used to compare and validate the results generated in work completed for this thesis (see Table 46). It was determined that the square wave results were very similar to previously published rapid square wave cycles (see table 47) as were constant load one-Amp constant load. However, that longer term NEDC (see Chapter 2 for more informaiotn on the NEDC) based degradation rates were far less severe than the rapid duty cycle undertaken in both this work and the work of Zhang et al. (2015) [70]. It was shown that NEDC degradation rates were two orders of magnitude less (see section 6.6) than the rapid (10-seconds or less) square wave duty cycle, for both the work presented in Chapter 6, and the results reported by Zhang et al. (2015) [70]. It was further established that the test results in the DoE fail to pass the hypothesis test for multivariate analysis (F-values were greater than 0.05 in all cases). Therefore, it is appropriate to compare the samples by their mean values, as there is no strong evidence for co-varying factors. A basic analysis revealed a high degree of variability between the various sets of samples (non-woven, paper, constant, square wave, catalyst loading) that made direct comparison problematic. Therefore, a previously discussed blocking and weighting exercise (an example of which is shown in section 4.7, Table 15) was undertaken. The significant results of that analysis are presented here graphically (the full set of weighted results are available in Appendix 3).

Figure 146 shows the weighted results, with error bars as calculated from equation (6-16), for the maximum $E_{OCV\text{-}i}$ for all GDM, catalyst and degradation DoE samples, under a constant load. In the non-woven ‘felts’ (F-berg) samples, it can be seen that the degree of experimental error is such that no

conclusion can be drawn. In the paper (Toray) samples there is a clear reduction in the performance of the test sample. In the literature review (section 2.5) it was pointed out that Song, Wang, et al. (2005) [75] considered layered catalysts to be insignificant in comparison to concentration variation achieved through altering the Nafion® loading. Such an assertion seems to be in contradiction to the findings of other authors (e.g. Antione et al. (2000) [23]). It is suggested that the contradiction in results may, in fact, be influenced by the selection of GDM, with some materials (i.e. paper GDMs) not being well suited to layered catalyst methods.

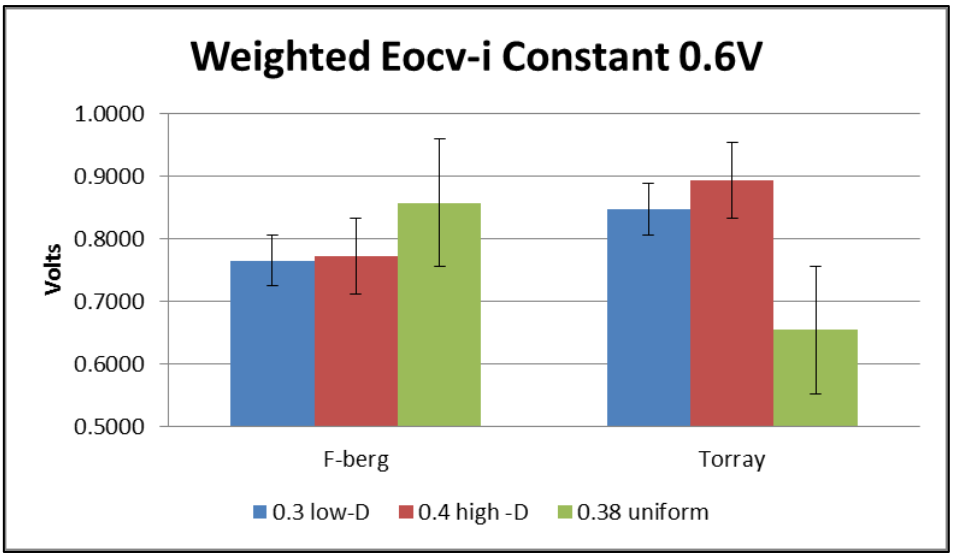

Figure 146: DoE Eocv-I

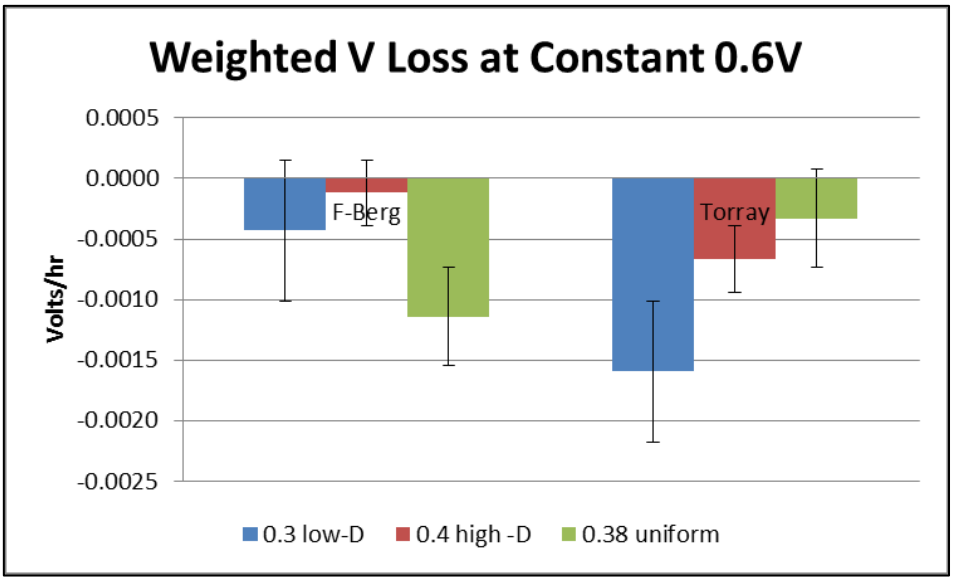

Figure 147: DoE loss rate at 0.6V

Figure 147 shows the weighted results, with error bars as calculated from equation (6-16), for the voltage loss rate after reaching peak $E_{OCV\text{-}i}$, under constant duty cycles, for all GDM, catalyst and degradation DoE samples. The error bar on the low concentration layered catalyst samples for the

non-woven materials is extremely large, and that data cannot be usefully analysed in these results. However, the remaining data clearly shows that reduced degradation rates (i.e. approaching zero) can be achieved more readily with a layered catalyst for both substrates. Referring to the apparent conflict in the literature mentioned previously; this too may be a factor. There is an improvement for non-woven materials (F-berg) with dual-layered high concentration catalyst layers showing a much slower degradation rate. Conversely, low concentration dual layers catalyst performs very poorly on a paper substrate, yet the higher concentration (in both the duel layer and the uniform distribution) have measurably lower degradation rates.

Figure 148 shows the weighted results, with error bars as calculated from equation (6-16), for the time taken to achieve peak $E_{OCV\text{-}i}$ under a constant duty cycle. It can be seen, that low concentration catalyst layers achieve their peak performance in the shortest period for both types of GDM. If previously published research test samples, and the models based upon those results, have undergone different conditioning cycles, or differing lengths of the long-term duty cycle (recall that degradation rates were only measured after the maximum performance of $E_{OCV\text{-}I}$ has been achieved): Then this too could indicate the conflict in the literature. Relatively new test samples, with shorter duration conditioning cycles, will perform differently to older samples. Great care must be taken in the future to consider this effect, when analysing catalyst coated substrate (CCS) GDMs.

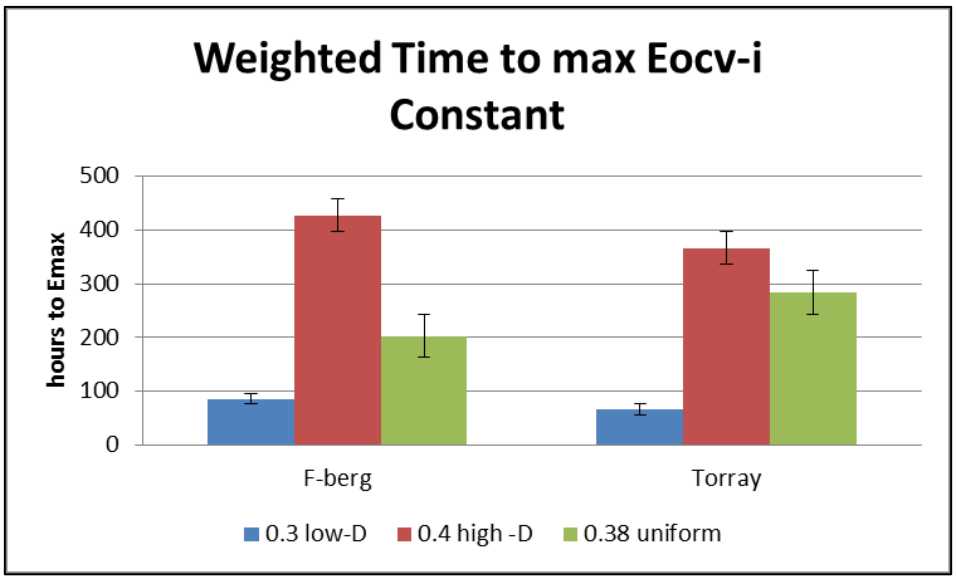

Figure 148: DoE max Eocv-i

Figure 149 shows the weighted results, with error bars as calculated from equation (6-16), for the voltage loss rate after reaching peak $E_{OCV\text{-}i}$, under ten-second square-wave duty cycles, for all GDM, catalyst and degradation DoE samples. It can be seen that the non-woven is insensitive to the type of catalyst applied for this set of results. The paper (Toray) sample, however, shows a marked difference between the various catalyst loadings: With the high concentration dual layer catalyst loading

showing a significant increase in voltage loss rate. It can be seen that high catalyst concentration layered catalyst structures on paper substrates are poorly suited to rapidly cycled operations. It is interesting to note the low concentration layered catalyst degraded at a much slower rate than the high concentration samples; so much so that the there is no measurable difference in degradation rate between low concentration dual layered catalyst at 0.3 $mg.cm^{-2}$, and the uniform concentration CL at 0.38 $mg.cm^{-2}$. Furthermore, the range of values on the low concentration dual layered Toray (paper) samples is significantly reduced. Based on these results it must be concluded that low concentration, dual layers CLs can offer on paper GDMs offers an opportunity to reduce catalyst loading. There was significant or measurable difference in square wave $E_{OCV\text{-}I}$ response for any samples.

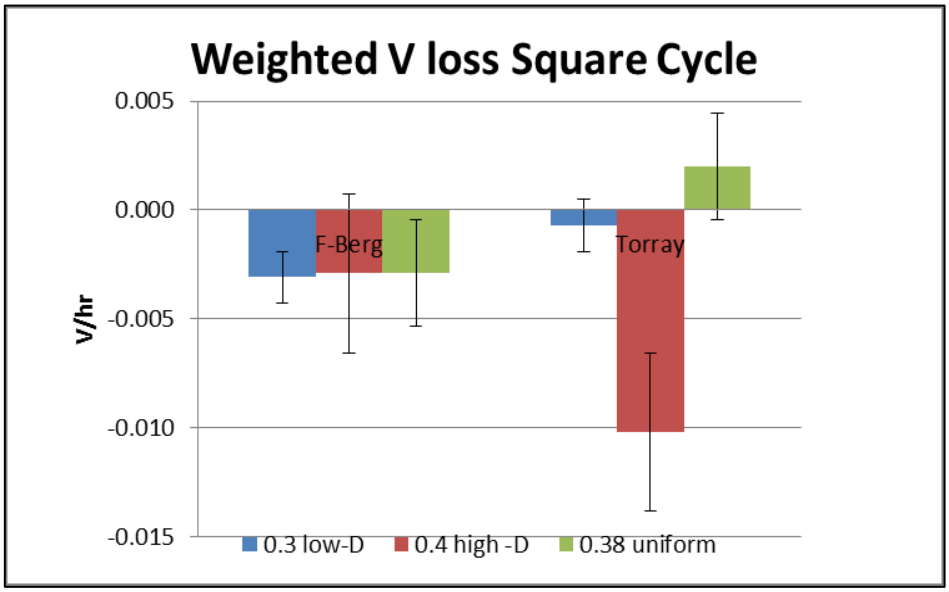

Figure 149: Loss rate Square cycle

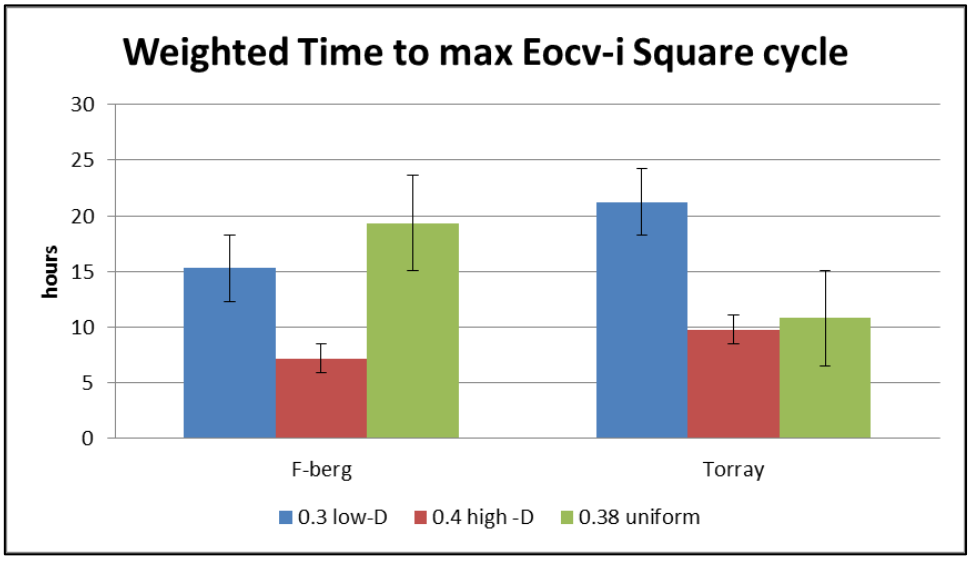

Figure 150: Time to max Eocv-i square cycle

Figure 150 shows the weighted results, with error bars as calculated from equation (6-16), for the time in hours to reach peak E_{OCV-i}, under a ten-second square-wave duty cycles, for all GDM, catalyst and degradation DoE samples. In this case, it is clear that high concentration dual layer samples take the least amount of time to achieve their peak performance on non-woven (F-berg) materials.

In Figure 146 to Figure 150 there are significant differences in the performance as follows:

- **Toray (Paper)**
    - Constant load:
        - Reduced E_{ocv-i} for uniform catalyst.
        - Decreased time to max E_{ocv-i} for low concentration dual layer catalyst.
        - Increased Voltage loss rate for low concentration dual layer catalyst.
    - Square cycle:
        - Increased Voltage loss rate for high concentration dual layer catalyst.
        - Reduced range of response for low concentration dual layer catalyst.
        - Increased time to maximum E_{ocv-i} performance for low concentration dual layer catalyst.

The paper system does not perform well in the constant load, and this is exacerbated by low dual layer catalysts (see Figure 147). Square duty cycles show increased voltage loss for high concentration dual layers. Low concentration dual layered samples exposed to rapid square wave duty cycles perform very well: To the extent that reduced catalyst loading could be achieved, compared to the uniform single layer catalyst.

- **Freudenberg (non-woven 'felt'):**
    - Constant load:
        - Decreased voltage loss rate for high concentration dual layer catalyst.
        - Decreased time to max E_{ocv-i} for low concentration dual layer catalyst.
    - Square Cycle Duty Load:
        - Decreased time to maximum E_{ocv-i} performance for high concentration dual layer catalyst.

Non-woven materials show improved performance for the high concentration dual layer in constant load, with a decreased time to achieve peak E_{ocv-i}.

The time to peak power in the square wave cycles were far lower, and there is no discernible pattern of behaviour; though it should be noted that high concentration dual layered catalysts on non-woven substrates demonstrated decreased time to peak power and comparable degradation loss rates to any

other configuration. The lack of similarity to the constant state time to peak power is somewhat concerning. Once again taking the, somewhat questionable, approach of stripping out the low concentration dual layer result for the Toray paper sample, there is a marked difference between it and the two high contrition samples. The low dual layer reached its peak performance much more slowly than the other two, the exact reverse of the non-woven material.

The absolute $E_{ocv\text{-}i}$ value reached is the same for all samples (see Appendix 3 Weighting Tables), and reduction in the voltage measurement from that point onwards is faster in the Torrey papers (with the notable exception of non-woven GDMs with a uniform catalyst distribution). This raises the prospect that whatever is causing the 'time to peak potential', also impacts the rate of degradation thereafter. Moreover, whatever is causing that effect is reversed in the two types of GDM.

This indicates there is a strong change in performance dependent on the structure of the GDM, but this is also highly dependent on the duty cycle the system is exposed to. Bearing in mind the known 'pore filling effect' [174] reported previously, it is surmised there is a difference in this pore filling effect for different GDMs used, and this is part of the reason different results for the two structures are detected. Recall that the two GDMs were selected to be as similar as possible in terms of overall porosity and through-plane thickness. The key difference between them is the 'planar' or stratified construction inherent in the paper system (see Figure 6), and the inclusion of 'through-plane' fibres in the non-wovens. It is suggested that the planar construction of the paper GDM is likely to have increased tortuosity. The nature of non-woven manufacture and its 'air needling' will create a direct pathway through the plane of the GDM sheet. This must play some role in the reduced loss of performance under constant load operation for layered catalyst on non-woven (see Figure 147). It is suggested that the creations of these 'needled' pathways in the non-woven manufacturing process reduce through-plane tortuosity, and this in turn plays to the strength of the duel layer catalyst approach (i.e. it increases the volume of space where catalysed reaction can take place). This effect is likely to be most marked in catalyst coated substrate (CCS) manufactured MEAs. The results reported by the author previously [47] and shown in Table 43, indicates that any MEA undergoing a heated pressing regime is likely to have a dispersed catalyst layers, and their associated PTFE based carrier components, away from the membrane. The degree of dispersal will depend on manufacturing regime and the type of GDM selected.

Returning to the original list of research questions the DoE was intended to answer:

I. Will variable wt% loading of Pt-on-C provide an equivalent performance to previous works that used a 'dilution' method to reduce the presence of catalyst sites in the low consecration layers?

a. Results are comparable to the uniform distribution in many if not all categories investigated, but the overall gain or loss in performance is highly influenced by the structure of the GDM it is deposited on.

II. Will reduced Pt loading overall of dual layer catalysts provide performance improvements?
    a. Paper-based substrates do benefit from a dual layered ink deposition in terms of the open cell potential, but non-woven 'felts' do not.

III. When applied as a CCS (catalyst coated substrate) will there be a difference between paper and 'felt' cathode GDMs?
    a. Yes, though there is equally important consideration as to the type of catalyst layer that is applied.

IV. Will there be a noticeable difference in degradation rate for dual layer catalyst or structures?
    a. Constant:
        i. Low concentration dual layers on paper degrade faster.
        ii. High concentration dual layers on non-woven degrade slower.
    b. Square wave:
        i. High concentration dual layers on paper degrade much faster.
        ii. Low concentration dual layers on paper GDMs perform as well as uniform catalyst layers, but with a decreased platinum loading.

V. What impact does constant, square wave (fast transit) or triangular (slower transit) load have?
    a. Work not completed due to software issues on test equipment.

VI. Will degradation be directly proportional to time spent at maximum load in the duty cycle?
    a. Work not completed due to software issues on test equipment.

VII. What, if any, factors co-vary in this data set?
    a. None detected.

7 Summary Discussion

After a brief outline of this thesis and the basics of fuel cells had been given in the introductory section (Chapter 1), several key aims and objectives were detailed for this thesis:

- Aims:
    a) Investigate if statistical methods, such DoE and multivariate-ANOVAR (M-ANOVAR) techniques, are applicable in fuel cell research.
    b) Demonstrate the application of such statistical methods and the reduction in total amount of time taken to conduct ageing and degradation studies in PEMFC research.
    c) Generate a thesis that will aid future fuel cell research scientists when applying statistical methods to their research.

- Objectives:
    g) Investigate the extent to which DoE and M-ANOVAR have already been utilised in fuel cell ageing/degradation research.
    h) Define a preferred statistical approach to apply in the next steps of the research.
    i) Identify several areas in PEMFC ageing/degradation research where multiple input and multiple output variables can be investigated simultaneously: reducing the total number of experiments required through the use of M-ANOVAR and DoE.
    j) Undertake a large scale set of experiments to act as a 'benchmarking' exercise and apply the identified statistical techniques from 'b'.
        - Consider appropriate software for the desired data analysis method.
    k) Utilise the 'benchmarking' exercise as an opportunity to validate selected statistical analysis methodology.
    l) Undertake a new study in which novel fuel cell assemblies are tested, and the results analysed using the newly validated method developed in objective 'j'.
        - Present this new study as a 'case study' on the use of DoE and M-ANOVAR methods.
        - Demonstrate the reduction in resources required to conduct the experiments.

In Chapter 2 (Literature review) key findings were reported, and quickly answered several of the points listed in the aims and objectives. Notably, that even basic statistical methods, such as confidence intervals or the reporting of standard error, were frequently absent from PEMFC literature. Additionally only a very small number of papers were found that had studied degradation rates in a controlled, DoE and M-ANOVAR, fashion. Furthermore, there were direct contradictions between some of these sources (see Chapter 2) that warranted further investigation, particularly in the field of layered catalyst structures.

If the DoE and M-ANOVAR approach were to be attempted for PEMFC studies, it was apparent that there were multiple possible input factors that must be considered when studying fuel cells. In general, the vast majority of published papers treat their research as a one factor at time (OFAT) problem. While this is rigorous, and has the advantage of simplifying the subsequent analysis, by definition the OFAT approach cannot be used to determine co-varying factors and their relationships. Furthermore, it is not possible to determine the standard error without at least three identical samples in the set. It was further identified that in-house manufacture of test cells should be utilised as far as possible. Direct comparison between researchers is often compromised by differences in the materials and construction methods used for the MEAs being tested. Even when standard MEAs from commercial suppliers are reported on, it was not uncommon to learn that manufacturer's products had changed over the time since the original research was completed. Comparisons between different

suppliers, or even different products from the same supplier, could not assure equivalent material properties for MEAs (e.g. type and mass percentage presence of hydrophobic coating in the GDM).

Even though degradation of PEMFCs is frequently reported in terms of multiple input factors (duty cycle, number of start-ups and shutdowns, temperature, pressure etc. to name but a few), and multiple outputs (peak power, E_{ocv}, hours to failure, degradation rate, loss of ECSA to name but a few), it was discovered that degradation studies are frequently limited to OFAT type investigation. One of the few rare exceptions, being the work by Song, Wang et al. (2005) [75], a lone example of co-varying analysis being used in fuel cell research. Even in the Song, Wang et al. (2005) [75] case, only two factors were considered (Pt loading and Nafion concentration), and the utility of multivariate analysis was not fully implemented. With the required length of time for degradation studies often taking hundreds, or even thousands of hours; it was suggested that degradation studies would benefit the most from the M-ANOVAR approach. Three key topics were provisionally identified as possibly co-varying and suitable for M-ANOVAR analysis:

- Type of GDM structure (Non-woven, paper and woven).
- Layered catalyst structures.
- Duty cycle.

Moreover, it was suggested that several possible outputs could be considered:

- Peak power.
- Degradation rate.
- Changes to the polarisation profile of the MEA.

As far as possible all other experimental variables were kept constant, and monitored. It was further noted that type of MEA manufacturing method used (deposition of catalyst inks onto the membrane or the GDM) might increase the probability of any covariance between the type of GDM and the catalyst ink.

The review of the literature indicates the investigation of multivariate methods in PEMFC degradation studies is well justified. There are several key gaps and conflicts in the literature that require further experimental study (see sections 2.2, 2.3, 2.5, and 2.7). Notably the failure to apply statistical methods correctly [33,37], and the conflicts in the results presented by different authors on the impact on degradation of fuel cells and the PTFE coatings applied to the GDM [40,43,44]. On the basis of this, and the observations from several authors that there is a lack of data on the performance and degradation of a wide variety of GDMs in the fuel cell literature [22,38,45]; it is suggested that the proposed work in this thesis is justified. At this stage of the thesis key objectives, ‘a’ and ‘c’ have been completed.

Chapter 3 (Statistical methods) went on to consider M-ANOVAR and DoE in greater depth. Starting with the basic principles of linear regression, and developing this into a generic matrix algebra approach for multiple input and multiple output statistical analysis of experimental data. This work was undertaken to explain the fundamental processes at work inside statistical software packages that are capable of such types of analysis. Whether it is Matlab® SSPS®, MiniTab®, Design Expert Professional® or some other bespoke software; all draw upon the same basic statistical methods. These methods have been used in a wide variety of engineering disciplines for many years, and a selection of references have been combined into a common nomenclature to present the information in a unified format. Other topics, such as ensuring a normal distribution of errors with Q-Q plots, and the need to transform non-normally distributed data sets into a normal format suitable for analysis, were briefly introduced. While it is certainly possible to use software packages such as Design Expert Pro® and their ilk without fully understanding of the mathematic at work inside the software, this is not a 'best practice' approach to take [29,81,82]. A more detailed explanation of the mathematics the software was based upon was presented. The background statistical theory presented in Chapter 3 was an amalgamation of knowledge from various sources [30,78-83]. ANOVAR and M-ANOVAR were introduced in detail, which in turn leads on to a discussion of response surface methods of modelling statistical data and generating designs of experiments.

Having introduced basic linear regression, Chapter 3 then went on to introduce DoE concepts such as factorial designs of experiments and ANOVAR analysis of single output experimental data. Having introduced this topic, it was then expanded upon to cover multiple input and multiple output data sets and the need to adapt ANOVAR methods (e.g. the Bonferroni Limit as discussed in section 3.6.2) to handle these more complex, multivariate, experimental results as a M-ANOVAR approach. A generic matrix algebra approach was provided, to help explain the calculations carried out by dedicated statistical software that is capable of handling these more complex sets of data. This included introduction of key concepts such as leverage (the ability of extreme data to skew the final result), and once again the ability to adapt data to cope with non-linear results was discussed briefly.

The need to simplify the created model, so that only the most useful and relevant factors are included (e.g. backwards elimination of non, or minimally, contributing factors as discussed in section 3.7) was introduced. This, in turn, was followed by a discussion of several different types DoE approach, where the total number of experiments to be conducted can be further reduced, without significant loss of accuracy on the final result (see section 3.8 and 3.9). Once again, the need to adapt basic linear regression theory to cope with such data sets was highlighted, this time concerning the need to understand variance inflation factors (VIF) for multiple co-varying inputs, and how they may inflate the error in the model to an unactable extent. It was suggested that a response surface method of analysis, adapted for categoric factors, would be well suited to studying PEMFCs: This achieved objective 'b'.

Chapter 3 considered the fundamental principles of the statistical methods utilised in the Design Expert Pro® software specifically. This software and the data analysis methods outlined previously were used in Chapters 4, 5, 6 and 8: Multivariate linear regression models, backwards elimination, and VIF were also used to a large extent. The general DoE for the work in Chapter 6, was an adaptation of the central composite response surface method (discussed in section 3.9) suitable for use with 'categoric data'.

The methods outlined in Chapter 3 are well understood, and recommended best practice in many fields of science and engineering [79,81,83,85]. Such multivariate methods have model validation built into their procedures. The quantification of residuals, and the inherent inclusion of ε_i values (residual error) at the most basic stages of the mathematical analysis, means that the linear regression models developed have been validated within their stated degree of accuracy, and within the limits and assumption of the original DoE [79,81,83,85].

In Chapter 4, a more detailed discussion of GDMs was undertaken, and this included the use of pre-existing models from Spiegel (2008) [87] and Beusher (2004) [88], adapted to reflect the geometry of the test apparatus used in experiments conducted for this thesis. A key part of this chapter, and reason for making use of the (Beusher inspired) Spiegel model (2008) [87] was to outline the importance of GDMs, to demonstrate the various roles they play inside the PEMFC, and some of the factors that impact those roles. A half-land-half-channel modelling approach was detailed. A GDM conceptual model of the half-land-half channel type was introduced (see Figure 18). The half-channel-half-land model can be the basis for creating a repeating segment, which can be expanded to model large areas of the fuel cell (though that is outside of the scope of the work in this thesis). However, for the work completed in this thesis, the basic unit model is used to illustrate reactant and product flow through the GDM. The inclusion of the Spiegel model [87] allowed the introduction several key concepts. Concepts such as the Darcy based diffusion speed of fluids through the GDM (equation 4-2 and equation 4-3) in section 4.2.1, the Steffen-Maxwell equation of gas phase transport (equation 4-4) and the concept of 'effective diffusion' (D_{eff}). The term 'perturbation factor' (θ) was also introduced to encapsulate several more components in understanding the flow of reactants and products through the GDM, such as wettability and tortuosity [87]. For this thesis, it was decided that this would be sufficient to explain the important role the GDM performs in the PEMFC, and why GDMs were selected as a topic of interest. Having introduced the model to be used, the first step of defining the steady state temperature in the GDM, was to map the deviation from the overall cell temperature (see Figure 20 in section 4.2.1). The steady state temperature variation and the height above the membrane layer it was located (i.e. peak temperature inside the GDM does not necessarily occur at the membrane surface), was a key input that informed the rest of the model and the final result. It was then possible to generate two-dimensional models of the temperature, oxygen concentration and water distribution (liquid and vapour) in the Spiegel PEMFC half-land half-channel model (within the limits

of the perturbation assumptions discussed previously) under steady state operation. The model was adapted as far as possible to match the geometry of the flow channels in the FCCA, and in this way, it was hoped that some understanding of the reactant and product flow rates in the cathode GDM could be understood more clearly. The creation of the model was also utilised to explain and understand some of the more fundamental mechanisms at work in an operating fuel cell. Having reproduced and adapted a published example of GDM modelling, and used that to gain an understanding of the processes taking place inside the GDM, the work in this thesis returned to its main area of interest, namely the use of statistical methods to produce statistical models.

Having developed an understanding of the fundamental factors which influence the movement of reactants, products and temperature distribution the GDM, a statistical data analysis of a large number of polarisation curves was completed. The polarisation curves being analysed were originally performed for a separate research project and as such constitute 'historic data' – i.e. their original purpose was not the completion of this research, but rather contributed to the work of others [15,16]. The original authors [15,16] had not utilised multivariate methods in their analysis, and it was suggested that more sophisticated statistical methods could be used to reveal new information from this large set of data. The basic experimental procedures were outlined, including ink formulation and other MEA manufacturing regime details in the creation of the original test pieces. Included in the DoE were input factors for the MPL, GDM structure and supplier (see Table 12). A detailed discussion of the polarisation curve comparison was given in section 4.4.2. The resulting data was then analysed using standard (OFAT) statistical methods such as matrix plots and box-and-whisker plots. The various categories and their impact on peak power were presented in Figure 36. It was clear from the combined box plots data that the range of the data points made the drawing of conclusions problematic.

The same data set was then analysed again using DoE and M-ANOVAR principles (i.e. using the methods outlined in Chapter 3). All data was assessed for the normality of the residuals (Q-Q plots), and initial response surface plots of the data were generated. A detailed discussion of the initial findings was presented, and then the refinement of the statistical model was carried out in accordance with the methods discussed in Chapter 3. The final results were presented in section 4.7 and 4.8, with a detailed breakdown of the coded factors. As the Design Expert Pro software does not directly apply the VIF or the Bonferroni limit, these calculations were completed by the author of this thesis and also reported in section 4.9. The results of the final model were validated using predicted, simulated results from the model plotted against experimental results: The linearity of the resultant plot indicating how well the model predicts reality [117]. Additional validation was completed through direct forecasting on additional test samples. Forecasting [81,87] is a validation method whereby additional samples are manufactured, and predictions are made based on the already created model on their performance. The accuracy with which the model predicts these additional values is used as a

measure of the validity of the model. This work was completed and the results reported in Table 40. As reported in Table 40, peak power output ($W.cm^{-2}$), was modelled with accuracy values approaching 1 (+/- 0.03), or a 3% margin of error. The gradients of the Ohmic loss region (gO) was modelled with an accuracy of +/- 0.26 (mean value), or a 26% margin of error. This indicates that the model for gO lacks the high degree of trueness seen in the peak power model. Table 32 (peak power or Wmax model M-ANOVAR assessment) has a reported 'p-value Prob > F', subsequently modified for VIF and the Bonferroni estimate of error, which generates a confidence interval (CI) of greater than 95%.

Table 21 (Gradient of the Ohmic loss region or gO model M-ANOVAR assessment) has reported p-value Prob > F, subsequently modified for modified for VIF and the Bonferroni estimate of error, which generates a confidence interval (CI) of greater than 95% (see section 3.6.2 and 4.6). This stage of the work completed objectives 'b', 'd' and 'e'.

The developed models were then analysed in detail, and several key observations were made (see section 4.9, 4.11, 4.12 and 4.13). The original objective had not been to elucidate new knowledge from the data presented (much of the data was already in the public domain and had been analysed by previous researchers using OFAT methods). Rather the objective was to validate the effectiveness of M-ANOVAR techniques by applying them to a historic data set and completing an assessment of the created model and its errors. In addition to achieving that aim (see section 4.10), it was found that the porosity had an impact on the performance of the peak power for the fuel cell. As a generalisation, this is to be expected in all GDM and fuel cell interactions. However, it was also found that in all cases, for all types of GDM (woven, non-woven 'felts' and paper), that there was a porosity dependent 'zone of stability'. A zone where operational parameters could be changed quite significantly and the power output of the fuel cell would be largely unaffected. It was also shown (see section 4.12), that each of the three types of GDM (woven, non-woven 'felts' and paper) should be modelled separately. The type of GDM selected would impact the final result of the experiment in a way that depended on their classification as a non-woven, paper or woven GDM (in addition to the normally reported input factors of porosity and through-plane thickness).

In all three cases, this region of stable peak power performance was found to be at approximately 42% porosity. In terms of the gradient of the Ohmic loss region of the modelled GDMs, it was found that the stability of the Ohmic loss regions was centred at approximately 52% porosity. As a general rule researchers have focused, rightly, on achieving peak performance for various designs of fuel cell. However, the ability to design GDMs with a region of stable operation under various conditions is also significant: At the very least GDM manufacturers would be able to offer improved guarantees of performance for GDMs with porosity levels of this value. To the knowledge of the author, this is the

first time this region of stable power output, relative to GDM through-plane thickness, for 42% porosity GDMs has been reported.

It was also found that distinctly different numeric values were required for non-woven, woven or paper GDM, verifying the need to classify GDMs in more than two categories (i.e. paper or woven) as has been the case in the past.

It should also be stated that the developed statistical model has also shown that the total power output for all three types of GDM did not follow the anticipated trend from the literature (see section 2.4). Typically woven GDMs are credited with being able to provide the best performance in high power and high humidity operation [21,56]. Paper GDMs are more often selected as a compromise solution that avoids the premium cost of woven carbon fibre and still provides adequate results if extreme humidification of the MEA is avoided. Wang et al. (2007) [21], have used numeric models to simulate paper and woven GDMs, and stated that paper GDMs would outperform woven GDM in low humidity operations, and woven GDMs are therefore superior in high demand, high humidity operational environments. The results from this thesis differ somewhat from this, as it was shown that high demand operations, based on 250-second polarisation curves, do not follow the same trend when hydrophobicity is identical for all samples (i.e. hydrophobic coating = 0wt%):

- 110µm thick woven GDM peak power = 0.473 $W.cm^{-2}$ (at 73.9^{o}C).
- 110µm thick paper peak power = 0.592 $W.cm^{-2}$ (at 73.9 ^{o}C).
- 110µm thick non-woven peak power = 0.562 $W.cm^{-2}$ (at 73.9 ^{o}C).

The peak power levels reported are lower than those often reported in the literature; it should be recalled from section 4.5.8, that it has been reported self-humidifying systems have reduced total outputs[116]. Based on these results (see section 4.12) it should be concluded that, for self-humidifying PEMFC systems, and in the relatively short duration operational window of a 250-second polarisation curve, that paper and non-woven felt materials outperform woven GDMs in high-performance duty cycles. To the knowledge of the author, this has not been reported previously. This result is significant in that it allows fuel cell suppliers to consider the end application and GDM selection in more detail. Where prolonged operating at higher humidity is not a significant part of the duty cycle, short-term transient duty cycles that require higher power densities may well be better served by paper or non-woven GDM materials. Combining this short term peak performance improvement, for non-humidified cells, along with the porosity and power relationship (i.e. no significant drop in peak power performance as thickness increases for 42% porosity GDMs as reported in section 4.12); the work carried using M-ANOVAR made it possible to define a lower cost, increased robustness GDM solution for fuel cell designers, manufacturers and suppliers.

Chapter 4 concludes with a return to the two-dimensional Spiegel (2008) [87] model and seeks to infer the most likely mechanisms at play in the reduced thickness system (see Figure 61 and Figure 62). It was suggested, on the basis of the Spiegel (2008) [87] model results, that there is a reduction in the relative number of pores that have been filled with liquid in the reduced thickness GDM, and this explains the overall performance improvement as far as mass transport in the GDM is concerned. This was based on the work undertaken by several authors [56,58,61,91,120,182-187] and also from the revised Spiegel model (see Figure 61 and Figure 62 in section 4.12). It is therefore suggested the changes in performance, which are correlated with porosity, are also linked to the closing of pores in some fashion. One likely consideration is that as the thickness of the GDM has increased; all other factors in the experimental set up have remained the same. It is suggested that changes in the thickness of the GDM system would result in the closing off of pore structures as cell geometry (i.e. gasket thickness), has not been altered to compensate. It is possible that the 42% porosity, and stable power outputs at various GDM through-plane thicknesses, indicates a region where the pore structure is either self-supporting (i.e. pores do not close down as rapidly when increased compression of the cell arises as a result of thermal and humidification events[24,87,95]), or that 42% porosity is a region where the balance between interconnected pore pathways is at its maximum (and so water transport pathways remain open even as compression effects close down open pore structures). However, continued investigation of this topic is outside the scope of this thesis (which focuses on the application of multivariate statistics in the hopes of accelerating PEMFC degradation studies), and would require the ability to manufacture bespoke porosity GDMs to verify (a very expensive and time-consuming set of experiments that it would be unfeasible to include in this thesis). The creation of novel and interesting results at this stage of the investigation, over and above the creation of the multivariate analysis and its validation for GDM types, is a highly desirable additional benefit of the work, but not a key objective.

It was concluded that the peak power model (referred to as ‘Wmax’) was highly suitable for analysing the data (see section 4.13). The gradient of the Ohmic loss region of the polarisation curve (referred to as ‘gO’) model was also a useful method for investigating GDM performance, though prone to a greater range of variability in the experimental results (see section 4.10.2). From Table 25, and the associated values for categoric values, the Ohmic loss gradient model for paper GDMs is shown in equation (4 30). The equivalent peak power model for paper GDMs is shown in equation (4 31). A brief summary of the f-distribution and resultant p-value probability of error was recapped in section 4.11, along with the key assumptions of the models to be analysed. The decision for which factors to map the response surface plots against were made using perturbation plots (e.g. Figure 51), and the limits of the model design were enumerated; both as bullet points and as 'design cube' results generated Design Expert Pro (Figure 54). The conclusions for the chapter were then detailed in section 4.12, where it was noted that porosity and thickness interactions in GDMs have a significant

impact on both the peak power performance and the gradient of the Ohmic loss region. The two-dimensional model reported in section 4.2 was once again utilised and adapted to more closely match the parameters of interest generated from the Wmax and gO models detailed in section 4.11 and 4.12. This then formed the basis of the discussion around likely causes for the various effects detected in the gO and Wmax reduced complexity M-ANOVAR models.

It was found that while peak power performance occurs for lower porosity GDMs regardless of type: GDMs have a key porosity value where their performance is more uniform over a variety of through-plane thicknesses. The Ohmic gradient shows a similar trend. In summary, the results were as follows:

- Wmax woven GDMs:
    - Peak power achieved with 110µm thick GDMs at 31.8% porosity (0.473 W.cm^-2). stable performance across a wide range of thickness is achieved with approximately 42% porosity GDMs.
- Wmax paper GDMs:
    - Peak power achieved with 110µm thick GDMs at 31.8% porosity (0.592 W.cm^-2). stable performance across a wide range of thickness is achieved with approximately 42 % porosity GDMs.
- Wmax non-woven GDMs:
    - Peak power achieved with 110µm thick GDMs at 31.8% porosity (0.562 W.cm^-2). stable performance across a wide range of thickness is achieved with approximately 42% porosity GDMs.

It should be noted that stable gO performance across a wide range GDM thicknesses were noted at approximately 50% porosity.

By this stage in the thesis, having completed all objectives, except ‘f’ and the requirement to demonstrate the reduction in testing time for objective ‘c’; it was decided to conduct a multivariate investigation into GDM structure, degradation cycles and layered catalyst structures. The completed multivariate investigation was reported in Chapter 6. The decision as to which possibly co-varying factors should be investigated was based on the findings of the historic data analysis completed in Chapter 4, and the finding of the literature review in Chapter 2. To showcase the power and effectiveness of multivariate methods, it was decided that possibly co-varying input factors be incorporated into the design of the experiments reported in Chapter 6. Furthermore, the number of outputs was also increased. The original work in Chapter 4 had only focused on a signal output – the polarisation curve. The multivariate method is not constrained to investigating a single output. Therefore, the single output of a polarisation curve was extended to include various aspects of the

polarisation curve (peak power, and the gradient of the three different regions of the polarisation curve). The measurement of a single output (i.e. the polarisation curve) was forced on the work carried out in Chapter 4, as it was the analysis of a database of historic results and previously published material. The original aim of the test data gathered was not to investigate GDM directly, but rather to assist colleagues from the University of Birmingham (UoB) by aiding them in accelerating the conditioning phase of the many samples under investigation in their work. The author of this thesis decided to save the polarisation data in case something of interest should become apparent during the testing, and satisfy colleagues at the UoB that the conditioning cycles had been carried out correctly if any anomalies in the data were detected. It was only after the fact when it was realised that an extensive database of results had been accumulated, that the collected data could be suitable for multivariate analysis. It was the availability of this historic dataset, and the results of the multivariate analysis, that inspired the idea to investigate GDMs in greater detail. The relationship between porosity and GDM structure, using multivariate methods, had not been investigated before in the literature, and so was prioritised as a topic of interest. To showcase the strength and flexibility of multivariate methods in PEMFC degradation research, it was identified that more input variables and more output variables would be desirable. It was decided to consider multiple degradation duty cycles (constant, square wave and triangular wave) based on reviews of degradation literature (see Chapter 2). It was also decided to expand the input variables to include not just GDM structural type, but also catalyst layers. Specifically to undertake a multivariate investigation of layered catalyst structures and uniform catalyst structures. The reasons to investigate catalyst structures were threefold:

1. It was known that catalyst layers are of critical importance to PEMFC research, and are frequently modelled and investigated by the PEMFC community.
2. It was known that layered catalyst structures had been a topic of interest, but there was a lack of experimental data on which to base accurate simulations.
3. It was hoped that multivariate methods would highlight previously unidentified covariate relationships. It was further suggested by the author that CCS manufacturing methods, where the ink is deposited directly onto the GDM were, perhaps, more likely to co-vary with the dual layered catalyst inks.

Before commencing this work on GDMs, degradation and dual layered catalyst; a more detailed investigation into catalyst layers was carried out. In much the same way that GDMs were detailed in accordance with good practice in Chapter 4. Chapter 5 went on to develop the understanding of catalyst layers in general, and dual layered catalyst in particular. In Chapter 5 the original literature review is expanded upon for catalyst materials. A particular focus is made on the time-dependent degradation of catalyst materials (see section 5.2.1 and Table 42), and the distinction is drawn between Ostwald ripening and the word ‘agglomerate’ to avoid possible confusion. A distinction is also made between reversible and irreversible degradation. In a similar process to that carried in

Chapter 4, the Spiegel (2008) [87] model of catalyst behaviours is presented in some detail (see section 5.3). The work by Spiegel [87] and Beusher [88] is reproduced, adapted to reflect the geometry of the test apparatus used in experiments conducted for this thesis (FCCA channel geometry). The Beusher-Spiegel model was used to outline the importance of catalyst layers, and to demonstrate the various roles they play inside the PEMFC and some of the factors that impact on these roles. Once again, as achieved in the previous chapter on GDMs, the intention is to frame the understanding of catalyst materials by utalising the model discussed. Key concepts such as the activation of catalyst layers and the diffusion of reactants around, and adjacent to, the catalyst particles as modelled by the Thiele modulus were introduced. The impact of these factors on the Butler-Volmer model of catalyst activation was presented graphically. The Spiegel model is well suited to modelling catalyses layers as single electrochemically active surface area (ECSA), and that too was presented graphically. It was shown how reductions in the ECSA could mimic degradation in the performance of the fuel cell (see Figure 68 through Figure 72) over time.

An attempt was made to model the possible impacts of layered catalyst structures. This required the completion of a set of practical experiments to define the likely thickness of discrete catalyst layers. As this work had not been carried out previously, the author developed a suitable fluorescent microscopy technique to measure such layers. This work was first reported by the author in the International Journal of Hydrogen Energy [47]. It was shown that the Spiegel model [87] was not well suited to modelling dual layers structures, and attempts to adapt it were inconclusive at best. For the avoidance of doubt – it was never the intention of this thesis to be yet another numeric simulation of theoretical models of catalyst layers in PEMFCs. That area of research is very well developed, and the interested reader is directed to the large number of other works that have already considered this topic in great depth over the decades [72,74,150,151,153-162,164,165,188-193]. The intention of this thesis is to highlight the need to accelerate practical investigation of fuel cell degradation through the use of more efficient experimental design and statistical data interpretations: A field of study sadly lacking in the PEMFC field (as discussed in the literature review in Chapter 2). To that end, the simulated Spiegel model [87] results were not validated in this thesis. The Spiegel model is published by an academic press and based upon published work by Beusher [88]. The validation work completed by Spiegel [87] and Beusher [88] in their original publications is accepted for the generic PEMFC model. It is the contention of this thesis that the agglomerate model is currently not well suited to the modelling of dual layered catalysts and that more experimental data is required. It was for this reason that the attempts to adapt the Spiegel model to simulate a two layered catalyst structure in section 5.3 and 5.4 were not successful. It is also suggested that the modelling of GDMs undertaken by Spiegel [87] and Beusher [88] (and by extension others in the PEMFC community), fails to take into account the impact that GDM structure can have on the performance of MEAs. This would be largely due to a lack of experimental evidence, especially if a catalyst coated substrate method has

been used in the fabrication of the MEA. To that end a statistical, regression-based model of experimental data was attempted in both Chapter 4 (modelling porosity, structure and temperature dependence of peak power and the gradient of polarisation regions, specificly the Ohmic loss region) and in Chapter 6 (GDM structure, layered catalyst structure and degradation duty cycle impacts, specifically constant load and square wave, on peak power and degradation rate). The work completed in Chapter 5 contributes to the work undertaken in Chapter 6 by providing a foundation of understanding that makes the formulation of research questions for Chapter 6, and the subsequent interpretation of results, possible.

As discussed previously (see section 2.2 and Chapter 3) any attempt to understand a system through detailed statistical methods, such as the ones proposed in this thesis, must be grounded on an understanding of the fundamentals of the object or process being studied. Having utilised a simple ECSA model to define the important parameters in layered catalyst structures, combined with an investigation into the real world likelihood of creating layered catalyst structures: It was possible to fully understand the requirements for a DoE on GDMs, degradation and layered catalyst structures. This, in turn, made it possible to formulate a set of research questions for the proposed DoE presented in Chapter 6.

Chapter 6 presents the DoE process and subsequent analysis in its entirety, including changes made to the experimental plan as a result of practical, experiential considerations. This meets one the core objectives and aims (see section 1.2) of the thesis; to provide a framework and knowledge base to encourage other fuel cell researchers to increase the use of M-ANOVAR and similar statistical methods. The starting point for any DoE exercise is to frame the research questions of interest. For work undertaken in this thesis, seven key research questions were considered, and the resultant DoE was designed in an attempt to answer them:

I. Will variable wt% loading of Pt-on-C provide an equivalent performance to previous works that used a ‘dilution’ method to reduce the presence of catalyst sites in the low consecration layers?
II. Will reduced Pt loading overall of dual layer catalysts provide performance improvements?
III. When applied as a CCS (catalyst coated substrate) will there be a difference between paper and ‘felt’ cathode GDMs
IV. Will there be a noticeable difference in degradation rate for dual layer catalyst or structures?
V. What impact does constant, square wave (fast transit) or triangular (slower transit) load cycling have
VI. Will degradation be directly proportional to time spent at maximum load in the duty cycle?
VII. What, if any, factors co-vary in this data set?

Following the same principle that statistical analyses is best carried out with a thorough understanding of the topic being studied; Chapter 4 developed the knowledge required to understand GDMs. Chapter 5 developed the knowledge required to understand dual layered catalysts. In chapter 6 these topics were combined, along with a degradation study (considered in detail in sections 2.3, 2.6, and 5.2.1), to create a case study of practical M-ANOVAR analysis in a field of interest for PEMFCs, namely: Dual Layer Catalyst Materials, Gas Diffusion Media and Degradation.

The anticipated input factors were:

- Dual layer catalyst concentration on the cathode:
    - Uniform catalyst layer (0.35mg.cm^2 of 30wt%Pt-on-C).
    - High concentration dual layer (0.4 mg.cm^2 of 40wt%Pt-on-C +10wt%Pt-on-C).
    - Low concentration dual layer (0.3 mg.cm^2 of 40wt%Pt-on-C +10wt%Pt-on-C).
- Duty cycles:
    - Constant.
    - Square wave.
- Types of GDM:
    - Paper.
    - Non-woven (felt).

The anticipated output factors were:

- Peak power.
- Degradation rate.
- Gradient of the Ohmic loss region.

A design of experiments process was carried out using Design Expert Pro, in accordance with the information provided in Chapters 2 and 3. The intended design of experiments was detailed in Table 44. This design had to be adapted away from the classic 'body centred cube' (see Figure 16 and Figure 17 in Chapter 3) construction typically discussed, as there were categoric factors to incorporate. To get a degree of replication around the nominal 'centre points'; the uniform catalyst layers were assigned the midpoint locations on the design cube. Effectively providing three replications of the centre point for each of two faces of the cube (see Figure 79). Practical experimental software difficulties were encountered at this point in the procedure. Typically such issues would not be reported. However, with the stated aim of promoting the wider use of M-ANOVAR (and similar statistical tools) in the PEMFC research community: The flexibility of DoE approaches was demonstrated by adapting the original design cube to a new set of parameters with a reduced number of test samples. Even in this reduced complexity design of experiments; it was still possible to retain two uniform catalyst layers as replication points on each face of the design cube (see Figure 80).

The final experimental parameters were detailed, and the results of the experiments were presented. Linear degradation rates did not occur immediately in the experimental results, and a spline fitting technique was used to verify the measured point from which to define the start of the degradation measurements (see section 6.5.1 and equation (6-13)). This use of a numeric spline fit ensured that the determination of the peak point would be consistent across all test results, and repeatable by other researchers in the future if required. The spline fits assisted in determining the point where degradation in performance could be detected. Before this point in each sample, improvements in performance were detected. As discussed previously (see section 6.5), it was suggested that increased hydration of the membrane had improved ionic conduction through the cell [24,87,95], and also the increased volume of the membrane (as a result of swelling of the Nafion® due to water uptake) [24,87,95]. This may have increased the contact pressure with the current collection plates of the fuel cell [24,87,95]. Both of these effects are likely to improve the overall performance of the test MEAs [24,87,95]. Additionally, it is possible that changes in the microstructure of the catalyst layers, and the hydrophobic PTFE solutions that were part of the catalyst ink formulation, may have evolved a more open structure during the test. It was suggested that these improvements in performance at the start of the experiment, were occurring at the same time as degradation loses (i.e. ECSA loss) may be occurring: however, the rate of improvement was greater than the rate of degradation in the early stages of testing.

It was also found that for the square wave duty cycle test pieces; there was a measurable and significant difference between polarisation curves taken in the morning (AM samples), and those taken at the end of the day (PM samples) (see section 6.5, 6.7 and 6.8). This was thought to be related to the need to stop and purge test pieces at the start and end of each day of square wave duty cycles. To make consistent, comparable, measurements only afternoon (PM) samples were analysed in depth. To make comparisons between constant load (continuous one-Amp load) and the ten-second wavelength square-wave duty cycles results; the constant load samples were also analysed in depth only for the afternoon results. This systematic approach to ensuring all test results were collected at the same time of day makes the grouping of the two sets of data (square wave and constant) for later types of analysis defensible. After the appropriate data transforms had been completed (see section (6.5, 6.7 and 6.6 for more details), it was found that square wave duty cycle test pieces were degrading at 1.28mV per hour (after reaching peak performance). It was also found that constant load test pieces were degrading at 0.136mV per hour (after reaching peak performance).

Direct comparisons with existing literature were difficult to find, but the most similar construction of GDM (i.e. one without any additional hydrophobic layer and broadly similar ink formulations) did have a comparable degradation rate (see Table 46 for more detail). It is worth noting that a broadly comparable MEA construction (similar ink formulations and GDM selections) performing the NEDC duty cycle degraded at a far slower rate, with nearly two orders of magnitude difference when

comparing hourly voltage losses for E_{ocv}. The work in this thesis helps to build towards the growing body of evidence that rapid, square wave duty cycles can effectively act as an accelerated stress test for PEMFCs. However exact replication of MEAs and test conditions are still required to confirm this.

Chapter 6 then moved on to discuss the comparison between the tested MEAs in more depth. It was quickly discovered that 'hypotheses 0' was not disproved (i.e. the M-ANOVAR results indicated that there was insufficient evidence to justify a multivariate approach, and that comparisons between of the means of the test sample sets were a valid approach to take). There is a possibility that the reduced order model detailed previously (Figure 80) lacked sufficient power to investigate the design space for these more complex, multivariate, interactions. The existing design could, of course, be adapted to improve its resolution, by either completing the original design (though there would be a need to factor in a blocking effect for the elapsed time between experiments) or by including replicates of the existing, or of possible additional, design points. For this thesis, the findings are accepted as they stand, and it is concluded that there is no improvement in the DoE multifactorial model when compared to a simple mean of the results of interest. It must be acknowledged, as discussed previously in section 2.2 and Chapter 3, that it is possible that a larger study, may detect higher order interactions (i.e. higher order effects with three or more input variables covering together) that can be masked in the study undertaken in this chapter. Any such higher-order co-variance of three or more factors that exist are likely to be quite subtle however, and have minimal influence on the final result [82,85] generated in the work completed for this thesis. The full sets of results were reported in Table 47, Table 48 and Table 49.

The fact that the DoE design has created sets of three samples means that groups of data can be created for which the standard deviation or standard error can be calculated in accordance with equation (6-15) and (6-16). Recall that both equations require the number of samples in a set (n) to be included as a value greater than 2 (as (n-1) or (n-2) features in each equation respectively.

Error analysis has been completed and discussed previously for both Chapter 4 and Chapter 6. In Chapter 4 each statistical regression model created was presented with a fully detailed M-ANOVAR error analysis table (see Table 18, Table 23, Table 28 and Table 34). IN each case, the M-ANOVAR error analysis considered the standard error (as per equations (6-15) and (6-16)), the upper and lower bounds of the test results that would conform to a 95% Confidence interval and applied the VIF in those cases where the Design Expert Pro software had failed to do so. Estimates of confidence interval were further reduced through the application of the Bonferroni principle (see section 3.6.2).

The results in Chapter 6 were shown not to benefit from Multivariate data analysis, and so more simplistic analysis was undertaken. To avoid biases between families or sets of data, a weighting and blocking procedure was carried out (see sections 3.3.1, 4.7 and 6.7.2 for more detail on this approach). This normalisation of the data across sets, makes the direct comparison between sets suitable, and so

equations (6-15) and (6-16) can be used to create a standard error assessment. In the graphical representation of the work completed in Chapter 6, error bars that were one standard error in length were in place. By definition, this means that true mean of the resultant values, depicted in the graphical results, were located within the range of the error bars with a 95% confidence interval [78,81,82,85]. As with all experimental work, this does not guarantee that the true value lies within the error bars shown in Figure 146 through Figure 150, but it is standard practice to accept that the error estimation procedure is correct 95% of the time [194].

If the same work had been created as a set of OFAT experiments; then to perform a similar error analysis, each set of data would require three separate samples for each variable – i.e. 15 samples in total (as shown in Table 52). It should also be reiterated that such a set of OFAT experiments could not be used to determine co-varying factors. The fact that co-varying factors were not discovered in the degradation model does not invalidate the effort to detect them. The elimination of possible covariance helps to establish that the standard error approach is a valid one to take in this case [82]. Furthermore combining results between the separate OFAT experiments, completed over a period, would be problematic; as it would require a blocking procedure (an example of which is available in chapter 4, section 4.7 and Table 15). Unless additional steps were taken to facilitate blocking across categories in the original design, and to ensure all samples were tested under identical conditions, such a blocking exercise would be difficult to justify. Recall that in work carried out in this thesis, that determination of the start of the degradation rate varied across samples, and that for square wave duty cycles it was required to utilise afternoon (PM) test results only to avoid the reversible degradation effects skewing the results compared to constant one-Amp duty test pieces. It seems unlikely that another researcher, considering similar research questions (i.e. the impacts of dual layer catalyst, GDM structure and duty cycle degradation rates) using the OFAT approach, would have been able to make direct comparison across all five separate experiments. Whereas this was achieved with ease using the DoE approach, even after it was discovered that M-ANOVAR was not required for this set of samples. This has clearly demonstrated that objective ‘i’ has been achieved.

Table 52: OFAT approximation of DoE

OFAT equivalent set of experiments	
Key factor of interest	Number of test pieces to calculate standard error
Degradation in felt GDMs	3
Degradation in paper GDMs	3
Impact of square wave degradation	3
Degradation in dual layer catalysts (high concentration)	3
Degradation in dual layer catalysts (low concentration)	3
Total number of experiments	15

The final DoE used in this thesis, using the reduced complexity design cube in Figure 80 achieved the same degree of error estimation and accuracy using only 12 test pieces: A 20% reduction in the materials costs, labour to create samples and total elapsed test time. Furthermore, by utilising statistical methods such as those outlined in Chapter 3, the improved efficiency in testing can be used across all types of tests. If the use of M-ANOVAR, and equivalent analysis techniques, can be promoted in the fuel cell research community, then more rapid advances in the technology can be accrued across a wide range of fuel cell research topics. Due to their prolonged test times of hundreds or even thousands of hours: Degradation studies, in particular, would benefit from the adoption of this approach.

For the results generated in the dual layer catalysts, GDM structure and degradation DoE carried out and reported in Chapter 6 of this thesis; a full weighting a blocking approach was carried out (available in Appendix three). The full sets of tabulated results were presented in Table 48 and Table 49. Those samples that showed a measurable difference greater than the standard error were reported graphically in section 6.7.2. It was shown that non-woven and paper substrates were broadly similar; except in a few key regards where they exhibited opposed behaviours:

Toray paper samples were shown to be far better suited to dual layer catalyst approach when under a constant load (Figure 146). Equally, it was shown that Toray papers with low concentration dual layer catalysts degraded at a higher rate (Figure 147). It was also shown (i.e. standard error bars do not overlap between categories; therefore the true mean between sets is unlikely to be the same with a

96% CI [29,78,81-83,195]) that high concentration dual layer Toray paper GDMs performed extremely poorly under the rapid square wave duty cycle (Figure 149).

The comparisons across all samples (with a measurable difference based on the standard error) can be summarised as follows:

- **Toray (Paper)**
  - Constant load:
    - Marginally reduced $E_{ocv\text{-}i}$ for uniform catalyst.
    - Decreased time to max $E_{ocv\text{-}i}$ for low concentration dual layer catalyst.
    - Increased Voltage loss rate for low concentration dual layer catalyst.
  - Square cycle:
    - Increased Voltage loss rate for high concentration dual layer catalyst.
    - Reduced range of response for low concentration dual layer catalyst.
    - Increased time to maximum $E_{ocv\text{-}i}$ performance for low concentration dual layer catalyst.

The paper system does not perform well in the constant load, and this is exacerbated by low dual layer catalysts (see Figure 147). Square duty cycles show increased voltage loss for high concentration dual layers. Low concentration dual layered samples exposed to rapid square wave duty cycles perform very well: To the extent that reduced catalyst loading could be achieved, compared to the uniform single layer catalyst.

- **Freudenberg (non-woven 'felt'):**
  - Constant load:
    - Decreased voltage loss rate for high concentration dual layer catalyst.
    - Decreased time to max $E_{ocv\text{-}i}$ for low concentration dual layer catalyst.
  - Square Cycle Duty Load:
    - Decreased time to maximum $E_{ocv\text{-}i}$ performance for high concentration dual layer catalyst.

Non-woven materials show marginal improved performance for the high concentration dual layer in constant load, with a decreased time to achieve peak $E_{ocv\text{-}I}$, without any measurable increase in degradation rate

It should be noted that, for rapid cycle square wave loading, high concentration, dual layered catalysts on non-woven substrates, demonstrated decreased time to peak power and comparable degradation loss rates to any other configuration. This may be considered an advantage in some circumstances. Considering Figure 147, it was concluded that in the case of self-humidifying PEMFCs, with MEAs

created using the CCS method: There is a measurable effect indicating low concentration, dual layered catalyst on paper substrates, can achieve equivalent open circuit potentials to uniform catalyst layers with significantly reduced platinum content (0.3mg.cm^{-2} Pt for low concentration dual layers on paper, and 0.38mg.cm^{-2} Pt for uniform, single layer CLs). Such low concentration, dual layer specimens have been shown to degrade more slowly (see Figure 149) under rapid square wave duty cycles. However, such low concentration, dual layer specimens also take longer to develop the maximum possible open cell potential (see Figure 150).

Returning to the original list of research questions:

I. Will variable wt% loading of Pt-on-C provide an equivalent performance to previous works that used a 'dilution' method to reduce the presence of catalyst sites in the low consecration layers?
    a. Results are comparable to the uniform distribution in many if not all categories investigated, but the overall gain or loss in performance is highly influenced by the structure of the GDM it is deposited onto.

II. Will reduced Pt loading overall of dual layer catalysts provide performance improvements?
    a. Paper-based substrates do benefit from a dual layered ink deposition in terms of the open cell potential, but non-woven 'felts' do not

III. When applied as a CCS (catalyst coated substrate) will there be a difference between paper and 'felt' cathode GDMs
    a. Yes, though there is equally important consideration as to the type of catalyst layer that is applied, and the type of GDM it is applied to

IV. Will there be a noticeable difference in degradation rate for dual layer catalyst or structures?
    a. Constant
        i. Low concentration dual layers on paper degrade at an accelerated rate
        ii. High concentration dual layers on non-woven degrade at a slower rate
    b. Square wave
        i. High concentration dual layers on paper degrade at an accelerated rate

V. What impact does constant, square wave (fast transit) or triangular (slower transit) load have?
    a. Work not completed due to software issues on test equipment

VI. Will degradation be directly proportional to time spent at maximum load in the duty cycle?
    a. Work not completed due to software issues on test equipment

VII. What, if any, factors co-vary in this data set?
    a. None detected

7.1.1 Novel contributions to the field

The following new information and novel contributions to the field of study have been made as a result of work on this thesis:

- DoE and M-ANOVAR techniques can be used successfully in PEMFC research, including the use of previously published data, to make new findings (see Chapter 4).
- Non-woven GDMs are not always reported as differing from paper GDMs in fuel cell research: M-ANOVAR based statistical models have shown non-woven GDMs are a different class of GDMs and, under certain circumstances, will alter the performance of the system being studied compared to paper or woven GDMs (see Chapter 4 and Chapter 6).
- GDMs of all types, within the limits of the experiments carried out in this work, have a 'zone of stability' at 42% porosity, that provides a constant performance regardless of the through-plane thickness of the GDM sheet (within the limits of the experimental region of the work completed in this thesis).
    - This in turn indicates that 42% porosity GDMs could be manufactured to a reduced through-plane thickness dimensional tolerance, and ensure a similar peak power performance for their customers. Such GDMs are also likely to be more tolerant of sub-optimal clamping forces arising during stack assembly or fuel cell operation.
- GDMs of all types, within the limits of the experiments carried out in this work, with a porosity of 52% tend to have a shallower gradient in the Ohmic loss region of the polarisation curve (within the limits of the experimental region of the work completed in this thesis).
    - For fuel cell applications where peak performance is less important than reliable performance over a broader range of potentials and load cycles; a 52% porosity GDM is likely to provide a wider window of suitable operational performance characteristics.
- Statistical linear regression models for the following types of MEA have been created for the first time (within the limits of the experimental region of the work completed in this thesis). These models are not tied to a specific supplier and can be used to estimate likely performances for a broad range of GDMs of similar fabrication types.
    - Peak power model (+/-3%, 95%CI) :
        - Carbon Fibre Woven GDM with MPL.
        - Carbon Fibre Woven GDM without MPL.
        - Carbon Fibre Non-Woven 'Felt' GDM with MPL.
        - Carbon Fibre Non-Woven 'Felt' GDM without MPL.
        - Carbon Fibre Paper GDM with MPL.
        - Carbon Fibre Paper GDM without MPL.

    - Gradient of the Ohmic loss region of the polarisation curve model (+/-26%, 95%CI):
        - Carbon Fibre Woven GDM with MPL.
        - Carbon Fibre Woven GDM without MPL.
        - Carbon Fibre Non-Woven 'Felt' GDM with MPL.
        - Carbon Fibre Non-Woven 'Felt' GDM without MPL.
        - Carbon Fibre Paper GDM with MPL.
        - Carbon Fibre Paper GDM without MPL.
- Fluorescence microscopy can be used to measure the thickness of separate PTFE layers in the MEA (as reported by the author previously [47]).
- Stratification in layered catalyst structures has been achieved through the use of two separate catalyst concentration loadings on carbon black – 40wt% Pt-on-C and 10wt%Pt-on-C - the work in this thesis is the first time this has been reported.
- There is no evidence to support the theory that layered catalyst structures, GDM type and degradation rates for PEMFCs co-vary.
- The effectiveness of DoE approaches in PEMFC remains valid, even when covariance is not detected; as well-designed M-ANOVAR experiments offer a large reduction in overall test time (20% within the limits of the experimental region of the work completed in this thesis) and still retain the ability to conduct standard error calculations.
- There is a measurable difference in the response of different types of GDM to dual layer catalysts. This may go some way to explaining conflicts in the literature that were reported in Chapter 2.
- Paper GDM materials, operating under rapidly cycles loads, may be better suited to dual layer catalyst carbon coated substrate manufacturing methods (within the limits of the experimental region of the work completed in this thesis):
    - Peak performance (as measured by open cell potential) is achieved more slowly.
    - Degradation rates are equivalent to uniform distribution single layer MEAs.
    - Platinum loading can be reduced by approximately 20% (0.3mg.cm^{-2} Pt for low concentration dual layers on paper, and 0.38mg.cm^{-2} Pt for uniform, single layer CLs).

8 Conclusions and Proposed Future Work

The aim of this thesis was to validate the use of multivariate statistical methods for fuel cell applications, to provide a guide for their use by other fuel cell researchers in the future, and to use these techniques to discover new information in the fuel cell field. All of these aims have been met.

Conflicts in the literature indicate that further research on aging of MEAs and an understanding of their performance with and without additional PTFE coatings and layers is required. There was some evidence that GDMs (with ostensibly similar levels of PTFE coating) may, in fact, have a significant difference in the performance of depending on the manufacturing method and/or the GDM substrate used: making comparison between different suppliers of pre-treated GDMs problematic. While the suppliers themselves were not a significant factor as such, differences in GDM construction and PTFE loadings must be factored in for accurate comparisons to be made.

Another possibly co-varying factor is the basic structure of the GDM, based on its manufacturing method. For CCS type MEAs, the choice of Paper, Woven or Non-woven GDMs have a bearing on the final performance of the fuel cell, and this has yet to be fully examined, and the number of degradation studies involving these factors have been woefully inadequate. Work in this thesis has shown that GDM structure (non-woven, paper or woven) is a significant factor in predicting peak performance even under relatively short duration test procedures, and all three systems should be modelled separately.

Another development in the optimisation of catalyst layers is by the use of a graded, through-plane, concentration, with the highest concentration at the surface closest to the membrane of the MEA. There is only a small pool of literature on this topic, and it has been largely focused on the variation of catalyst concentration by increasing PTFE content in the CL. It was identified that there is a need for an assessment of the layered CLs in terms of the basic structure using a more uniform carbon support to maintain electrical contact within the CL, its performance over time and its interactions with GDM structure, especially for CCS manufacturing methods.

As a result of these factors, the impact of these three input variables (GDM structure, layered catalysts and degradation) was in need of a great deal more research. Additionally, a far greater understanding of the impact of PTFE based coatings, to optimise water management, and its interaction with structure is still needed. Multiple analysis of variance techniques have been demonstrated as being well suited to analysing fuel cell experimental results. This research is the first to apply these methods in a rigorous fashion to cathode GDMs, duel layer catalyst and their duty cycle/degradation performance. Results indicate not only time savings but verify the approach is valid in a fuel cell context in general, with a very high degree of confidence in the final results.

8.1 Conclusions

The following conclusions are drawn

Historic 'data-mining' assessment on cathode GDMs.

- A novel 'gradient of regions' approach to comparing polarisation curves was developed and verified (+/-26%, CI = 95% or greater) as being a valid way of making direct comparisons between MEAs tested on the same equipment.
- Focusing on the gradient of the Ohmic region (gO) and the peak power outputs (Wmax) several significant findings were captured from previously existing data that had not been previously reported by the original authors.
    - There is a significant difference in the Ohmic behaviour of 'felt' like structures: The most likely explanation of this is the existence of 'through-plane' fibres that improve the conductivity of the sample. This is not necessarily a groundbreaking discovery, but the fact that the non-woven material outperform Woven structure materials in short term, high intensity, self-humidifying polarisation tests has not been reported before.
    - There is very strong evidence (greater than 95% CI) that the thickness and porosity of the GDM materials are interacting to alter the Ohmic performance of the sample. Lower thickness, lower porosity samples have the least Ohmic loss, as may be expected from a simple 'density and total resistance' interpretation: The more solid samples with the least through-plane material can be expected to offer the least electrical resistance in the system. What is not intuitively obvious was the impact of 52% porosity (which should arguably increase total performance through increased surface area and fluid pathways) and its interactions with through-plane thickness. The covariance of the two is not a simple linear effect and optimisation of GDMs requires careful consideration of the interplay of the two factors. 52% porosity GDMs have a stable Ohmic loss rate across a range of thicknesses. This effect has not been previously reported.
    - There is very strong evidence (+/- 3%, CI = 95% or greater) that the thickness and porosity of the GDM materials are interacting to alter the peak power performance of the sample. 42% porosity GDMs have a stable peak power output across a range of GDM thicknesses. This information could have a significant impact on GDM design and selection for applications where periods of high demand are very brief. This effect has not been previously reported.

DoE (CL layers, structure and degradation)

- The study presented is unique, and this combination of factors has not been examined before.
- Using normalised samples, with comparable through-plane thickness and porosity, co-variance between structures and other factors was not detected.
- Weighted analysis of the means did, however, determine notable differences between GDMs and their interactions with variable concentration catalyst layers and duty cycles.
    - Toray (Paper):
        - Constant Duty Load:
            - Reduced $E_{ocv\text{-}i}$ for uniform catalyst.
            - Decreased time to max $E_{ocv\text{-}i}$ for low dual layer catalyst.
            - Increased Voltage loss rate for low dual layer catalyst.
        - Square Cycle Duty Load:
            - Increased Voltage loss rate for high dual layer catalyst.
            - Increased time to maximum $E_{ocv\text{-}i}$ performance for low dual layer catalyst.
            - Low concentration dual layer catalyst performs as well as high concentration uniform catalyst layers.
    - Freudenberg (non-woven 'felt'):
        - Constant Duty Load.
            - Decreased voltage loss rate for high dual layer catalyst.
            - Decreased time to max $E_{ocv\text{-}i}$ for low dual layer catalyst.
        - Square Cycle Duty Load:
            - Decreased time to maximum $E_{ocv\text{-}i}$ performance for high dual layer catalyst.
- The GDM structure a catalyst layer is deposited onto impacts MEA ageing profile with low concentration dual layer paper GDMs degrading normally in highly cycled loads – this finding has not reported in the literature before now.
- Non-woven 'felt' based substrates show a reduced degradation rate under constant loads for high concentration dual layer catalyst in a way that Paper GDMs do not – this finding has not been reported in the literature before now.

8.2 Future work

Based on the results achieved to date these topics for future work are readily apparent.

- Complete a DoE study on the impact of MPL and catalyst structures in more detail. Due the poor water management of the MEAs created there was no scope for varying temperature and flow rates in the DoE for structure, a more comprehensive study of hydrophobicity, MPL formulations

and deposition techniques could build an understanding of the optimal MPL / CL fabrication process of CCS MEAs. Completing this research should make it possible to update the agglomerate model of catalyst layer usage with real world figure rather than assumed values of MPL thickness based on the mass of the deposited material. A proposed DoE for these topics reveals that 432 separate MEAs and experiments would need to be completed to address all these topics fully.

- Comparison of plasma treated hydrophobic coatings and their ageing effects compared to equivalent, commercially available hydrophobic treatments. This topic was identified as an alternate multivariate case study, but could not be perused with the equipment available in department at the time
- Further investigation of the impact of GDM porosity on PEMFC performance. If the ability to manufacture non-wovens, papers and weaves of carbon fibre, with control of the final porosity value were possible; then an extensive study into the optimum porosity of the GDM for a given duty cycle could be conducted.
- Undertake a programme of tuition and create a DoE and statistical analysis support tool specifically targeted at fuel cell researchers. This research, and other like it, can be used to show that multivariate DoE methodologies can and should be utilised in fuel cell research more often.
- Conduct a study into when, or if, woven GDMs outperform other cathode GDMs at high loads.
- Conduct analysis on humidified reactant streams and GDM type and porosity to determine if the same or similar ects hold true.

9 References

[1] Pachauri R.K. and Meyer L.A., "Climate Change 2014: Synthesis Report. Contribution of Working Groups I, II and III to the Fifth Assessment Report of the Intergovernmental Panel on Climate Change," IPCC, IPCC, Geneva, Switzerland, 2014.

[2] Barkery T., "The economics of avoiding dangerous climate change. An editorial essay on The Stern Review," *Climate Change* **89**(3):173-194, 2008.

[3] Calderon F., Oppenheim J., and Stern N., "New Climate Economy Report,", 2014.

[4] IEA, "Key World Energy Statistics 2011,", 2011.

[5] McKinsey & Company, "A portfolio of power-trains for Europe: a fact-based analysis: The role of Battery Electric Vehicles, Plug-in Hybrids and Fuel Cell Electric Vehicles,", 2011.

[6] Yang S., Lin X., Lewis W., Suyetin M., et al., "A partially interpenetrated metalic organic framework for selective hysteretic sorption of carbon dioxide," *Nat Mater* **advance online publication**, 2012.

[7] Tsouris C., Aaron D.S., and Williams K.A., "Is Carbon Capture and Storage Really Needed?1," *Environ.Sci.Technol.* **44**(11):4042-4045, 2010.

[8] Kanellos M., "Amprius Raises $25 Million: Is the Battery Component Market for Real?," http://www.greentechmedia.com/articles/read/amprius-raises-25-million-does-a-battery-component-market-exist/, 22/06/2012 2012.

[9] Halfacree G., "Graphene gets commercialised in new battery tech," http://www.bit-tech.net/news/hardware/2012/03/23/graphene-battery-tech/1, 22/06/2012 2012.

[10] Fehrenbacher K., " 13 Startups Working on Solar-Concentrating PV," http://gigaom.com/cleantech/13-startups-working-on-solar-concentrating-pv-1/, 22/06/2012 2012.

[11] Reisfeld R., "New developments in luminescence for solar energy utilization," *Optical Materials* **32**(9):850-856, 2010.

[12] Herman I., Yeo J., Hong S., Lee D., et al., "Nanoforest of hydrothermally grown hierarchical ZnO nanowires for a high efficiency dye-sensitized solar cell," *Nano Lett.* **11**(2):666, 2011.

[13] Millington B., Du S., and Pollet B.G., "The effect of materials on proton exchange membrane fuel cell electrode performance," *J.Power Sources* **196**(21):9013-9017, 2011.

[14] Prasanna M., Ha H.Y., Cho E.A., Hong S.-., et al., "Influence of cathode gas diffusion media on the performance of the PEMFCs," *J.Power Sources* **131**(1–2):147-154, 2004.

[15] El-kharouf A., Mason T.J., Brett D.J.L., and Pollet B.G., "Ex-situ characterisation of gas diffusion layers for proton exchange membrane fuel cells," *J.Power Sources* **218**(0):393-404, 2012.

[16] El-kharouf A. and Pollet B.G., "Chapter 4 - Gas Diffusion Media and their Degradation," In: Veziroglu M.M.M.C.K.N., editor. Polymer Electrolyte Fuel Cell Degradation, Academic Press, Boston, 2012, 215-247.

[17] Williams M.V., Begg E., Bonville L., Kunz H.R., et al., "Characterization of Gas Diffusion Layers for PEMFC," *Journal of The Electrochemical Society* **151**(8):A1173-A1180, 2004.

[18] Escribano S., Blachot J., Ethève J., Morin A., et al., "Characterization of PEMFCs gas diffusion layers properties," *J.Power Sources* **156**(1):8-13, 2006.

[19] Litster S. and McLean G., "PEM fuel cell electrodes," *J.Power Sources* **130**(1–2):61-76, 2004.

[20] Lim C. and Wang C.Y., "Effects of hydrophobic polymer content in GDL on power performance of a PEM fuel cell," *Electrochim.Acta* **49**(24):4149-4156, 2004.

[21] Wang Y., Wang C., and Chen K.S., "Elucidating differences between carbon paper and carbon cloth in polymer electrolyte fuel cells," *Electrochim.Acta* **52**(12):3965-3975, 2007.

[22] Yuan X., Li H., Zhang S., Martin J., et al., "A review of polymer electrolyte membrane fuel cell durability test protocols," *J.Power Sources* **196**(22):9107-9116, 2011.

[23] Antoine O., Bultel Y., Ozil P., and Durand R., "Catalyst gradient for cathode active layer of proton exchange membrane fuel cell," *Electrochim.Acta* **45**(27):4493-4500, 2000.

[24] O'hayre R., Cha S., Colella W., and Prinz F.B., "Fuel Cell Fundamentals," John Wiley and Son, New York, 2009.

[25] Barbir F., "PEM Fuel Cells: Theory and Practice," Academic press, Waltham MA, 2013.

[26] Larminie J.and Dicks A., "Fuel Cell Systems Explained," John Wiley & Sons Ltd, Chichester, 2006.

[27] Harrar S.W. and Bathke A.C., "Nonparametric methods for unbalanced multivariate data and many factor levels," *Journal of Multivariate Analysis* **99**(8):1635-1664, 2008.

[28] Manly B.F.J.1., "Multivariate statistical methods :a primer," Chapman & Hall/CRC, Boca Raton, Fla., ISBN 1584884142, 2005.

[29] Chatfield C., "Problem solving : a statistician's guide," Chapman & Hall, London, 1988.

[30] Roy R.K., "A primer on the Taguchi method," Van Nostrand Reinhold, New York, ISBN 0442237294, 1990.

[31] Yu W.L., "Parametric analysis of the proton exchange membrane fuel cell performance using design of experiments," *Int J Hydrogen Energy* **33**(9):2311-2322, 2008.

[32] Ferreira S.L.C., Bruns R.E., Ferreira H.S., Matos G.D., et al., "Box-Behnken design: An alternative for the optimization of analytical methods," *Anal.Chim.Acta* **597**(2):179-186, 2007.

[33] Carton J.G. and Olabi A.G., "Design of experiment study of the parameters that affect performance of three flow plate configurations of a proton exchange membrane fuel cell," *Energy* **35**(7):2796-2806, 2010.

[34] Bloom I., Walker L.K., Basco J.K., Malkow T., et al., "A comparison of Fuel Cell Testing protocols – A case study: Protocols used by the U.S. Department of Energy, European Union, International Electrotechnical Commission/Fuel Cell Testing and Standardization Network, and Fuel

Cell Technical Team," *J.Power Sources* **243**(0):451-457, 2013, doi:http://dx.doi.org/10.1016/j.jpowsour.2013.06.026.

[35] Dempster A.P., "An overview of multivariate data analysis," *Journal of Multivariate Analysis* **1**(3):316-346, 1971.

[36] Chatfield J.A., Draper E.A., Cochran K.D., and Herms D.A., "Evaluation of crabapples for apple scab at the Secrest arboretum in Wooster, Ohio," *Ohio Agricultural Research and Development Center Special Circular. Ornamental Plants: Annual Reports and Research Reviews*(177), 2000.

[37] Placca L., Kouta R., Candusso D., Blachot J., et al., "Analysis of PEM fuel cell experimental data using principal component analysis and multi linear regression," *Int J Hydrogen Energy* **35**(10):4582-4591, 2010.

[38] Secanell M., Wishart J., and Dobson P., "Computational design and optimization of fuel cells and fuel cell systems: A review," *J.Power Sources* **196**(8):3690-3704, 2011.

[39] Callister W.D.and Rethwisch D.G., "Materials science and engineering : an introduction," John Wiley and Son, New York, 2007.

[40] Wu J., Yuan X.Z., Martin J.J., Wang H., et al., "A review of PEM fuel cell durability: Degradation mechanisms and mitigation strategies," *J.Power Sources* **184**(1):104-119, 2008.

[41] Whiteley M., Dunnett S., and Jackson L., "Failure Mode and Effect Analysis, and Fault Tree Analysis of Polymer Electrolyte Membrane Fuel Cells," *Int J Hydrogen Energy*.

[42] Park S., Lee J., and Popov B.N., "A review of gas diffusion layer in PEM fuel cells: Materials and designs," *Int J Hydrogen Energy* **37**(7):5850-5865, 2012.

[43] Pei P., Yuan X., Chao P., and Wang X., "Analysis on the PEM fuel cells after accelerated life experiment," *Int J Hydrogen Energy* **35**(7):3147-3151, 2010.

[44] Chapuis O., Prat M., Quintard M., Chane-Kane E., et al., "
Two-phase flow and evaporation in model fibrous media Application to the gas diffusion layer of PEM fuel cells." *J Power Sources* **178**(258):68, 2008.

[45] Hiramitsu Y., Sato H., Kobayashi K., and Hori M., "Controlling gas diffusion layer oxidation by homogeneous hydrophobic coating for polymer electrolyte fuel cells," *J.Power Sources* **196**(13):5453-5469, 2011.

[46] Pai Y., Ke J., Huang H., Lee C., et al., "CF4 plasma treatment for preparing gas diffusion layers in membrane electrode assemblies," *J.Power Sources* **161**(1):275-281, 2006.

[47] McCarthy N., Chen R., Offer G., and Thring R., "PTFE mapping in gas diffusion media for PEMFCs using fluorescence microscopy," *Int J Hydrogen Energy*, 2016.

[48] Schmittinger W. and Vahidi A., "A review of the main parameters influencing long-term performance and durability of PEM fuel cells," *J.Power Sources* **180**(1):1-14, 2008.

[49] Sadeghifar H., Djilali N., and Bahrami M., "Effect of Polytetrafluoroethylene (PTFE) and micro porous layer (MPL) on thermal conductivity of fuel cell gas diffusion layers: Modeling and experiments," *J.Power Sources* **248**(0):632-641, 2014.

[50] Si X., Wang W., Hu C., and Zhou D., "Remaining useful life estimation – A review on the statistical data driven approaches," *Eur.J.Oper.Res.* **213**(1):1-14, 2011.

[51] Miller M. and Bazylak A., "A review of polymer electrolyte membrane fuel cell stack testing," *J.Power Sources* **196**(2):601-613, 2011.

[52] He Q., Joy D.C., and Keffer D.J., "Nanoparticle Adhesion in PEM Fuel Cell Electrodes," *J.Power Sources*(0), 2013.

[53] Glassman M., Omosebi A., and Besser R.S., "Repetitive Hot-Press Approach for Performance Enhancement of Hydrogen Fuel Cells," *J.Power Sources*(0), 2013.

[54] Mathias M.F., Roth J., Flemming J., and Lenhert W., "Diffusion media materials and characterisation,"Handbook of Fuel Cells, John Wiley & Sons Ltd, 2010.

[55] Jinuntuya F., "Numercial Investigation Of The Structural Effects On Water Trasportation In PEMFC Gas Diffusion Layers Using X-Ray Tomography Based Lattice Boltzman Method,", Loughbrough University, 2014.

[56] Williams M.V., Kunz H.R., and Fenton J.M., "Operation of Nafion®-based PEM fuel cells with no external humidification: influence of operating conditions and gas diffusion layers," *J.Power Sources* **135**(1–2):122-134, 2004.

[57] Park J., Oh H., Ha T., Lee Y.I., et al., "A review of the gas diffusion layer in proton exchange membrane fuel cells: Durability and degradation," *Appl.Energy* **155**(0):866-880, 2015.

[58] Lin J.F., Wertz J., Ahmad R., Thommes M., et al., "Effect of carbon paper substrate of the gas diffusion layer on the performance of proton exchange membrane fuel cell," *Electrochim.Acta* **55**(8):2746-2751, 2010.

[59] C¸ ec¸en A., Wargo E.A., Hanna A.C., Turner D.M., et al., "3-D Microstructure Analysis of Fuel Cell Materials: Spatial Distributions of Tortuosity, Void Size and Diffusivity ," *Journal of the Electrochemical Society* **159**(3):B299-B307, 2012.

[60] "The influence of micro structure of the GDL and MPL on the mass transport in PEFC," ECS Transactions, 2011.

[61] Kotaka T., Tabuchi Y., and Mukherjee P.P., "Microstructural analysis of mass transport phenomena in gas diffusion media for high current density operation in PEM fuel cells," *J.Power Sources* **280**(0):231-239, 2015.

[62] El-Hannach M. and Kjeang E., "Stochastic Microstructural Modeling of PEFC Gas Diffusion Media," *J. Electrochem. Soc.* **161**(9):F951-F960, 2014, doi:10.1149/2.1141409jes.

[63] Roshandel R. and Ahmadi F., "Effects of catalyst loading gradient in catalyst layers on performance of polymer electrolyte membrane fuel cells," *Renewable Energy* **50**(0):921-931, 2013.

[64] Morbidelli M., Gravriilidis A., and Varma A., "Catalyst Design: Optimal Distribution of Catalyst in Pellets, Reactors and Membranes," Cambridge University Press, Cambridge, 2001.

[65] Zhou K. and Li Y., "Catalysis Based on Nanocrystals with Well-Defined Facets," *Angewandte Chemie International Edition* **51**(3):602-613, 2012.

[66] Springer T.E., Zawodzinski T.A., and Gottesfeld S., "Polymer Electrolyte Fuel Cell Model," *Journal of the Electrochemical Society* **138**(8):2334-2342, 1991.

[67] Kim J., Lee S., Srinivasan S., and Chamberlin C.E., "Modeling of Proton Exchange Membrane Fuel Cell Performance with an Empirical Equation," *Journal of The Electrochemical Society* **142**(8):2670-2674, 1995.

[68] Jain P., "Multi-scale Modeling and Optimization of Polymer Electrolyte Fuel Cells,", CARNEGIE MELLON UNIVERSITY, 2009.

[69] ""Agglomerate" Merriam-Webster," http://www.merriam-webster.com/dictionary/agglomerate, 08/2/ 2016.

[70] Zhang Y., Chen S., Wang Y., Ding W., et al., "Study of the degradation mechanisms of carbon-supported platinum fuel cells catalyst via different accelerated stress test," *J.Power Sources* **273**(0):62-69, 2015.

[71] Cetinbas F.C., Advani S.G., and Prasad A.K., "Three dimensional proton exchange membrane fuel cell cathode model using a modified agglomerate approach based on discrete catalyst particles," *J.Power Sources* **250**(0):110-119, 2014.

[72] Cetinbas F.C., Advani S.G., and Prasad A.K., "An Improved Agglomerate Model for the PEM Catalyst Layer with Accurate Effective Surface Area Calculation Based on the Sphere-Packing Approach," *Journal of The Electrochemical Society* **161**(6):F803-F813, 2014.

[73] Xie Z., Navessin T., Shi K., Chow R., et al., "Functionally Graded Cathode Catalyst Layers for Polymer Electrolyte Fuel Cells: II. Experimental Study of the Effect of Nafion Distribution," *Journal of The Electrochemical Society* **152**(6):A1171-A1179, 2005.

[74] Wang Q., Eikerling M., Song D., Liu Z., et al., "Functionally Graded Cathode Catalyst Layers for Polymer Electrolyte Fuel Cells: I. Theoretical Modeling," *Journal of The Electrochemical Society* **151**(7):A950-A957, 2004.

[75] Song D., Wang Q., Liu Z., Eikerling M., et al., "A method for optimizing distributions of Nafion and Pt in cathode catalyst layers of PEM fuel cells," *Electrochim.Acta* **50**(16–17):3347-3358, 2005.

[76] Passalacqua E., Lufrano F., Squadrito G., Patti A., et al., "Nafion content in the catalyst layer of polymer electrolyte fuel cells: effects on structure and performance," *Electrochim.Acta* **46**(6):799-805, 2001.

[77] Yu X. and Ye S., "Recent advances in activity and durability enhancement of Pt/C catalytic cathode in PEMFC: Part I. Physico-chemical and electronic interaction between Pt and carbon support, and activity enhancement of Pt/C catalyst," *J.Power Sources* **172**(1):133-144, 2007.

[78] Ryan T.P., "Modern engineering statistics," Wiley-Interscience, Chichester, 2007.

[79] Harris R.J., "A primer of multivariate statistics," Lawrence Erlbaum Associates, Mahwah, N.J., 2001.

[80] Flury B., "A First Course in Multivariate Statistics," Springer-Verlag, New Yrok, 1997.

[81] Wadsworth, H,M, "Handbook of Statistical Methods for Engineers and Scientists," McGraw-Hill, New York, 1990.

[82] Anderson M.J.and Whitcomb P.J., "DOE Simplified: Practical Tools for Effective Experimentation," Productivity Press, New York, 2007.

[83] Moore D.S., McCabe G.P., and Craig B.A., " Introductin to the Practice of Statistics " Freeman, W. H. & Company, USA, 2012.

[84] Croft A.and Davison R., "Foundation Maths," Pearson Education Ltd., Harlow, 1997.

[85] Anderson M.J.and Whitcomb P.J., "RSM Simplified: Optimizing Processes Using Response Surface Methods for Design of Experiments," CRC press, Boca Raton, 2005.

[86] Box G. and Behnken D., "Some new three level designs for the study of quantitative variables," *Technometrics* **2**:455-475, 1960.

[87] Spiegel C., "PEM Fuel Cell Modeling and Simulation using MATLAB," Elsevier, Burlington, 2008.

[88] Beusher U., Bayram S., Broadbridge P., Driscoll T., et al., "Multi-Phase Flow in a Thin Porous Material," *Twentieth Annual Workshop on Mathematical Problems in Industry*, 2004.

[89] Placca L. and Kouta R., "Fault tree analysis for pem fuel cell degradation process modelling," *International Journal of Hydrogen Energy* **36**(19):12393, 2011.

[90] Whiteley M., "Advanced reliability analysis of polymer electrolyte membrane fuel cells in automotive applications,", Loughborough University, 2016.

[91] Park J., Oh H., Lee Y.I., Min K., et al., "Effect of the pore size variation in the substrate of the gas diffusion layer on water management and fuel cell performance," *Appl.Energy* **171**:200-212, 2016.

[92] Takahashi I. and Kocha S.S., "Examination of the activity and durability of PEMFC catalysts in liquid electrolytes," *J.Power Sources* **195**(19):6312-6322, 2010.

[93] Frey T. and Linardi M., "Effects of membrane electrode assembly preparation on the polymer electrolyte membrane fuel cell performance," *Electrochim.Acta* **50**(1):99-105, 2004.

[94] Marquis J. and Coppens M.-., "Achieving ultra-high platinum utilization via optimization of PEM fuel cell cathode catalyst layer microstructure," *Chemical Engineering Science* **102**(0):151-162, 2013.

[95] Mench M., Kumbur E.C., and T. Nejat Veziroglu T.N., "Polymer Electrolyte Fuel Cell Degradation," Elsevier, Oxford, 2012.

[96] Hartigan J.A., "Printer graphics for clustering," *Journal of Statistical Computation and Simulation* **4**(3):187-213, 1975.

[97] Mueller W.a., "Theory of the Polarisaiton curve technique for studying corrosion and electrochemical protection," *Canadian Journal of Chemistry* **38**:576-587, 1960.

[98] Santarelli M.G., Torchio M.F., and Cochis P., "Parameters estimation of a PEM fuel cell polarization curve and analysis of their behavior with temperature," *J.Power Sources* **159**(2):824-835, 2006.

[99] Bezmalinovic D., Simic B., and Barbir F., "Characterization of PEM fuel cell degradation by polarization change curves," *J.Power Sources* **294**(0):82-87, 2015.

[100] Al-Baghdadi M.A.R.S., "Modelling of proton exchange membrane fuel cell performance based on semi-empirical equations," *Renewable Energy* **30**(10):1587-1599, 2005.

[101] Wang H., Yuan X.Z., and Li H., "PEM Fuel Cell Diagnostic Tools," CRC press, BocaRaton, 2012.

[102] Wang Q., Dong H., Yu H., and Yu H., "Enhanced performance of gas diffusion electrode for electrochemical reduction of carbon dioxide to formate by adding polytetrafluoroethylene into catalyst layer," *J.Power Sources* **279**(0):1-5, 2015.

[103] Ito H., Abe K., Ishida M., Nakano A., et al., "Effect of through-plane distribution of polytetrafluoroethylene in carbon paper on in-plane gas permeability," *J.Power Sources* **248**(0):822-830, 2014.

[104] Koresawa R. and Utaka Y., "Improvement of oxygen diffusion characteristic in gas diffusion layer with planar-distributed wettability for polymer electrolyte fuel cell," *J.Power Sources* **271**(0):16-24, 2014.

[105] Latorrata S., Balzarotti R., Gallo Stampino P., Cristiani C., et al., "Design of properties and performances of innovative gas diffusion media for polymer electrolyte membrane fuel cells," *Progress in Organic Coatings*(0), 2014.

[106] Rohendi D., Majlan E.H., Mohamad A.B., Daud W.R.W., et al., "Effect of PTFE Content and Sintering Temperature on the Properties of a Fuel Cell Electrode Backing Layer," *Journal of Fuel Cell Science and Technology* **11**(4):041003-041003, 2014.

[107] Inoue G., Ishibe N., Matsukuma Y., and Minemoto M., "Understanding Mechanism of PTFE Distribution in Fibrous Porous Media," *ECS Transactions* **50**(2):461-468, 2013.

[108] Liu M., Wang C., Xie F., and Mao Z., "A polymer electrolyte fuel cell life test using accelerating degradation technique," *Int J Hydrogen Energy* **38**(25):11011-11016, 2013.

[109] Endoo S., "Identification of the key variables in membrane electrode preparation for PEM fuel cells by a factorial design," *Renewable Energy* **35**(4):807-813, 2010.

[110] Lin G. and Nguyen T.V., "Effect of Thickness and Hydrophobic Polymer Content of the Gas Diffusion Layer on Electrode Flooding Level in a PEMFC," *Journal of The Electrochemical Society* **152**(10):A1942-A1948, 2005.

[111] Sadeghifar H., Djilali N., and Bahrami M., "Effect of PTFE and micro porous layer on thermal conductivity of fuel cell gas diffusion layers: modeling and experiments," *J.Power Sources*(0).

[112] Mason T.J., Millichamp J., Neville T.P., El-kharouf A., et al., "Effect of clamping pressure on ohmic resistance and compression of gas diffusion layers for polymer electrolyte fuel cells," *J.Power Sources* **219**(0):52-59, 2012.

[113] Perng S., Wu H., and Shih G., "Effect of prominent gas diffusion layer (GDL) on non-isothermal transport characteristics and cell performance of a proton exchange membrane fuel cell (PEMFC)," *Energy* **88**:126-138, 2015.

[114] Millichamp J., Mason T.J., Neville T.P., Rajalakshmi N., et al., "Mechanisms and effects of mechanical compression and dimensional change in polymer electrolyte fuel cells – A review," *J.Power Sources* **284**:305-320, 2015.

[115] Hiramitsu Y., Kobayashi K., and Hori M., "Gas diffusion layer design focusing on the structure of the contact face with catalyst layer against water flooding in polymer electrolyte fuel cell," *J.Power Sources* **195**(22):7559-7567, 2010.

[116] Gerteisen D., Zamel N., Sadeler C., Geiger F., et al., "Effect of operating conditions on current density distribution and high frequency resistance in a segmented PEM fuel cell," *Int J Hydrogen Energy* **37**(9):7736-7744, 2012.

[117] Piñeiro G., Perelman S., Guerschman J.P., and Paruelo J.M., "How to evaluate models: Observed vs. predicted or predicted vs. observed?" *Ecol.Model.* **216**(3–4):316-322, 2008.

[118] Menditto A., Patriarca M., and Magnusson B., "Understanding the meaning of accuracy, trueness and precision," - *Accreditation and Quality Assurance* **12**(1):45-75, 2007.

[119] Benziger J., Blackwell D., Brennan T., and Itescu J., "Water flow in the gas diffusion layer of PEM fuel cells," *Journal of Membrane Science*(261):98-106, 2005.

[120] Kong C.S., Kim D., Lee H., Shul Y., et al., "Influence of pore-size distribution of diffusion layer on mass-transport problems of proton exchange membrane fuel cells," *J.Power Sources* **108**(1–2):185-191, 2002.

[121] Lee H., Park J., Kim D., and Lee T., "A study on the characteristics of the diffusion layer thickness and porosity of the PEMFC," *J.Power Sources* **131**(1–2):200-206, 2004.

[122] Jordan L.R., Shukla A.K., Behrsing T., Avery N.R., et al., "Diffusion layer parameters influencing optimal fuel cell performance," *J.Power Sources* **86**(1–2):250-254, 2000.

[123] Bae S.J., Kim S., Lee J., Song I., et al., "Degradation pattern prediction of a polymer electrolyte membrane fuel cell stack with series reliability structure via durability data of single cells," *Appl.Energy* **131**(0):48-55, 2014.

[124] Marcu A., Toth G., Pietrasz P., and Waldecker J., "Cathode catalysts degradation mechanism from liquid electrolyte to membrane electrode assembly," *Comptes Rendus Chimie*(0), 2014.

[125] Speder J., Zana A., Spanos I., Kirkensgaard J.J.K., et al., "Comparative degradation study of carbon supported proton exchange membrane fuel cell electrocatalysts – The influence of the platinum to carbon ratio on the degradation rate," *J.Power Sources* **261**(0):14-22, 2014.

[126] Wang F., Yang D., Li B., Zhang H., et al., "Investigation of the recoverable degradation of PEM fuel cell operated under drive cycle and different humidities," *Int J Hydrogen Energy*(0), 2014.

[127] Xiao S. and Zhang H., "The investigation of resin degradation in catalyst layer of proton exchange membrane fuel cell," *J.Power Sources* **246**(0):858-861, 2014.

[128] Yu J., Jiang Z., Hou M., Liang D., et al., "Analysis of the behavior and degradation in proton exchange membrane fuel cells with a dead-ended anode," *J.Power Sources* **246**(0):90-94, 2014.

[129] Cheng T.H., Wessel S., and Knights S., " Interactive Effects of Membrane Additives on PEMFC Catalyst Layer Degradation ," *Journal of the Electrochemical Society* **160**(1):F27-F33, 2013.

[130] Dillet J., Spernjak D., Lamibrac A., Maranzana G., et al., "Impact of flow rates and electrode specifications on degradations during repeated startups and shutdowns in polymer-electrolyte membrane fuel cells," *J.Power Sources*(0), 2013.

[131] Fairweather J.D., Spernjak D., Weber A.Z., Harvey D., et al., "Effects of Cathode Corrosion on Through-Plane Water Transport in Proton Exchange Membrane Fuel Cells," *Journal of The Electrochemical Society* **160**(9):F980-F993, 2013.

[132] Kreitmeier S., Lerch P., Wokaun A., and B¨uchi F.N., "Local Degradation at Membrane Defects in Polymer Electrolyte Fuel Cells," *Journal of the Electrochemical Society* **160**(4):F456-F463, 2013.

[133] Ous T. and Arcoumanis C., "Degradation aspects of water formation and transport in Proton Exchange Membrane Fuel Cell: A review," *J.Power Sources* **240**(0):558-582, 2013.

[134] Yu S., Li X., Li J., Liu S., et al., "Study on hydrophobicity degradation of gas diffusion layer in proton exchange membrane fuel cells," *Energy Conversion and Management* **76**(0):301-306, 2013.

[135] Kim J., Yi J.S., and Song T., "Investigation of degradation mechanisms of a high-temperature polymer-electrolyte-membrane fuel cell stack by electrochemical impedance spectroscopy," *J.Power Sources* **220**(0):54-64, 2012.

[136] Schiraldi D.A. and Savant D., "10.38 - Polymer Electrolyte Membrane Degradation," In: Editors-in-Chief: Krzysztof Matyjaszewski and Martin Möller, editors. Polymer Science: A Comprehensive Reference, Elsevier, Amsterdam, 2012, 767-775.

[137] Spernjak D., Fairweather J., Mukundan R., Rockward T., et al., "Influence of the microporous layer on carbon corrosion in the catalyst layer of a polymer electrolyte membrane fuel cell," *J.Power Sources* **214**(0):386-398, 2012.

[138] Bozzini B., Amati M., Boniardi M., Abyaneh M.K., et al., "Study of a proton exchange membrane fuel cells catalyst subjected to anodic operating conditions, by synchrotron-based scanning photoelectron microscopy (SPEM) and high lateral-resolution X-ray photoelectron spectroscopy," *J.Power Sources* **196**(5):2513-2518, 2011.

[139] Ishigami Y., Takada K., Yano H., Inukai J., et al., "Corrosion of carbon supports at cathode during hydrogen/air replacement at anode studied by visualization of oxygen partial pressures in a PEFC—Start-up/shut-down simulation," *J.Power Sources* **196**(6):3003-3008, 2011.

[140] Jung M. and Williams K.A., "Effect of dynamic operation on chemical degradation of a polymer electrolyte membrane fuel cell," *J.Power Sources* **196**(5):2717-2724, 2011.

[141] Sutharssan T., Montalvao D., Chen Y.K., Wang W., et al., "A review on prognostics and health monitoring of proton exchange membrane fuel cell," *Renewable and Sustainable Energy Reviews*.

[142] Baik K.D. and Kim M.S., "Characterization of nitrogen gas crossover through the membrane in proton-exchange membrane fuel cells," *Int J Hydrogen Energy* **36**(1):732-739, 2011.

[143] Casalegno A., Bresciani F., Groppi G., and Marchesi R., "Flooding of the diffusion layer in a polymer electrolyte fuel cell: Experimental and modelling analysis," *J.Power Sources* **196**(24):10632-10639, 2011.

[144] Hirata H., Shimotori S., and Aoki T., "Numerical study on the cathode flooding of direct humidified proton exchange membrane fuel cell," *J.Power Sources* **220**(0):383-390, 2012.

[145] Oh K., Kim W., Sung K.A., Choo M., et al., "A hydrophobic blend binder for anti-water flooding of cathode catalyst layers in polymer electrolyte membrane fuel cells," *Int J Hydrogen Energy* **36**(21):13695-13702, 2011.

[146] Casalegno A., Colombo L., Galbiati S., and Marchesi R., "Quantitative characterization of water transport and flooding in the diffusion layers of polymer electrolyte fuel cells," *J.Power Sources* **195**(13):4143-4148, 2010.

[147] Kannan A., Kabza A., and Scholta J., "Long term testing of start–stop cycles on high temperature PEM fuel cell stack," *J.Power Sources* **277**(0):312-316, 2015.

[148] Lin R., Xiong F., Tang W.C., Técher L., et al., "Investigation of dynamic driving cycle effect on the degradation of proton exchange membrane fuel cell by segmented cell technology," *J.Power Sources*(0), 2014.

[149] Pei P. and Chen H., "Main factors affecting the lifetime of Proton Exchange Membrane fuel cells in vehicle applications: A review," *Appl.Energy* **125**(0):60-75, 2014.

[150] Xing L., Song X., Scott K., Pickert V., et al., "Multi-variable optimisation of PEMFC cathodes based on surrogate modelling," *Int J Hydrogen Energy* **38**(33):14295-14313, 2013.

[151] Xing L., Mamlouk M., and Scott K., "A two dimensional agglomerate model for a proton exchange membrane fuel cell," *Energy* **61**:196-210, 2013.

[152] Xing L., Liu X., Alaje T., Kumar R., et al., "A two-phase flow and non-isothermal agglomerate model for a proton exchange membrane (PEM) fuel cell," *Energy* **73**:618-634, 2014.

[153] Moein-Jahromi M. and Kermani M.J., "Performance prediction of PEM fuel cell cathode catalyst layer using agglomerate model," *Int J Hydrogen Energy* **37**(23):17954-17966, 2012.

[154] Hu G., Li G., Zheng Y., Zhang Z., et al., "Optimization and parametric analysis of PEMFC based on an agglomerate model for catalyst layer," *Journal of the Energy Institute* **87**(2):163-174, 2014.

[155] Xing L., Mamlouk M., Kumar R., and Scott K., "Numerical investigation of the optimal Nafion® ionomer content in cathode catalyst layer: An agglomerate two-phase flow modelling," *Int J Hydrogen Energy* **39**(17):9087-9104, 2014.

[156] Zhang X., Ostadi H., Jiang K., and Chen R., "Reliability of the spherical agglomerate models for catalyst layer in polymer electrolyte membrane fuel cells," *Electrochim.Acta* **133**:475-483, 2014.

[157] Zhang X., Gao Y., Ostadi H., Jiang K., et al., "A proposed agglomerate model for oxygen reduction in the catalyst layer of proton exchange membrane fuel cells," *Electrochim.Acta* **150**:320-328, 2014.

[158] Molaeimanesh G.R. and Akbari M.H., "Agglomerate modeling of cathode catalyst layer of a PEM fuel cell by the lattice Boltzmann method," *Int J Hydrogen Energy* **40**(15):5169-5185, 2015.

[159] Yin K., Cheng B., and Chiang K., "Non-uniform agglomerate cathode catalyst layer model on the performance of PEMFC with consideration of water effect," *Renewable Energy* **95**:191-201, 2016.

[160] Madhusudana Rao R. and Rengaswamy R., "Dynamic characteristics of spherical agglomerate for study of cathode catalyst layers in proton exchange membrane fuel cells (PEMFC)," *J.Power Sources* **158**(1):110-123, 2006.

[161] Yin K.-., "Parametric Study of Proton-Exchange-Membrane Fuel Cell Cathode Using an Agglomerate Model," *Journal of The Electrochemical Society* **152**(3):A583-A593, 2005.

[162] Siegel N.P., Ellis M.W., Nelson D.J., and von Spakovsky M.R., "Single domain PEMFC model based on agglomerate catalyst geometry," *J.Power Sources* **115**(1):81-89, 2003.

[163] Jaouen F., Lindbergh G., and Sundholm G., "Investigation of Mass-Transport Limitations in the Solid Polymer Fuel Cell Cathode: I. Mathematical Model," *Journal of The Electrochemical Society* **149**(4):A437-A447, 2002.

[164] Sun W., Peppley B.A., and Karan K., "An improved two-dimensional agglomerate cathode model to study the influence of catalyst layer structural parameters," *Electrochim.Acta* **50**(16–17):3359-3374, 2005.

[165] Cetinbas F.C., Advani S.G., and Prasadz A.K., "A Modified Agglomerate Model with Discrete Catalyst Particles for the PEM Fuel Cell Catalyst Layer

," *Journal of the Electrochemical Society* **160**(8):F750-F756, 2013.

[166] Wu H., "A review of recent development: Transport and performance modeling of PEM fuel cells," *Appl.Energy* **165**:81-106, 2016.

[167] Wang Y. and Feng X., "Analysis of the Reaction Rates in the Cathode Electrode of Polymer Electrolyte Fuel Cells: II. Dual-Layer Electrodes," *Journal of The Electrochemical Society* **156**(3):B403-B409, 2009.

[168] Feng X. and Wang Y., "Multi-layer configuration for the cathode electrode of polymer electrolyte fuel cell," *Electrochim.Acta* **55**(15):4579-4586, 2010.

[169] Migliardini F., and Corbo P., "CV and EIS Study of Hydrogen Fuel Cell Durability in Automotive Applications," *Int. J. Electrochem. Sci.* **8**:11033-101047, 2013.

[170] White R.E., "Modern Aspects of Electrochemistry 40," Springer-Verlag, New York, 2007.

[171] Hou J., Song W., Yu H., Fu Y., et al., "Ionic resistance of the catalyst layer after the PEM fuel cell suffered freeze," *J.Power Sources* **176**(1):118-121, 2008.

[172] Chan S.H. and Tun W.A., "Catalyst Layer Models for Proton Exchange Membrane Fuel Cells," *Chemistry Engineering Technolgy* **24**(1):51, 2001.

[173] Secanell M., "Optimization of a proton exchange membrane fuel cell membrane electrode assembly," *Structural And Multidisciplinary Optimization* **40**(1-6):563-583, 2010.

[174] Yoon Y.-., Yang T.-., Park G.-., Lee W.-., et al., "A multi-layer structured cathode for the PEMFC," *J.Power Sources* **118**(1–2):189-192, 2003.

[175] Su H., Liang H., Bladergroen B.J., Linkov V., et al., "Effect of Platinum Distribution in Dual Catalyst Layer Structured Gas Diffusion Electrode on the Performance of High Temperature PEMFC," *Journal of The Electrochemical Society* **161**(4):F506-F512, 2014.

[176] Zana A., Speder J., Roefzaad M., Altmann L., et al., "Probing Degradation by IL-TEM: The Influence of Stress Test Conditions on the Degradation Mechanism

," *Journal of the Electrochemical Society* **160**(6):F608-F615, 2013.

[177] Kandlikar S.G., Lu Z., Lin T.Y., Cooke D., et al., "Uneven gas diffusion layer intrusion in gas channel arrays of proton exchange membrane fuel cell and its effects on flow distribution," *J.Power Sources* **194**(1):328-337, 2009.

[178] Rorres C. and Anton H., "Applications of Linear Algebra," John Wiley & Sons Inc, New York, 1984.

[179] Tang W., Lin R., Weng Y., Zhang J., et al., "The effects of operating temperature on current density distribution and impedance spectroscopy by segmented fuel cell," *Int J Hydrogen Energy* **38**(25):10985-10991, 2013.

[180] Yuan X., Sun J.C., Wang H., and Li H., "Accelerated conditioning for a proton exchange membrane fuel cell," *J.Power Sources* **205**:340-344, 2012.

[181] Dai W., Wang H., Yuan X., Martin J.J., et al., "A review on water balance in the membrane electrode assembly of proton exchange membrane fuel cells," *Int J Hydrogen Energy* **34**(23):9461-9478, 2009.

[182] Hu Z., Lin J., Zhang Y., and Hu G., "Study on modification of carbon fiber and performance of carbon paper as gas diffusion layer," *Gongneng Cailiao/Journal of Functional Materials* **47**(9):09112-09116, 2016.

[183] Prass S., Hasanpour S., Sow P.K., Phillion A.B., et al., "Microscale X-ray tomographic investigation of the interfacial morphology between the catalyst and micro porous layers in proton exchange membrane fuel cells," *J.Power Sources* **319**:82-89, 2016.

[184] Tötzke C., Gaiselmann G., Osenberg M., Bohner J., et al., "Three-dimensional study of compressed gas diffusion layers using synchrotron X-ray imaging," *J.Power Sources* **253**(0):123-131, 2014.

[185] Gostick J.T., "Random Pore Network Modeling of Fibrous PEMFC Gas Diffusion Media Using Voronoi and Delaunay Tessellations ," *Journal of the Electrochemical Society* **160**(8):F731-F743, 2013.

[186] Morgan J.M. and Datta R., "Understanding the gas diffusion layer in PEM fuel cells. I. How its structural characteristics affect diffusion and performance," *J.Power Sources*(0), 2013.

[187] Sun C., More K.L., Veith G.M., and Zawodzinski T.A., "Composition Dependence of the Pore Structure and Water Transport of Composite Catalyst Layers for Polymer Electrolyte Fuel Cells," *Journal of The Electrochemical Society* **160**(9):F1000-F1005, 2013.

[188] Shah A.A., Kim G., and Promislow K., "Mathematical modelling of the catalyst layer of a polymer electrolyte fuel cell," *IMA Journal of Applied Mathematics* **72**(3):302-330, June 2007.

[189] Lile J.R.D. and Zhou S., "Theoretical modeling of the PEMFC catalyst layer: A review of atomistic methods," *Electrochim.Acta* **177**:4-20, 2015.

[190] Weber A.Z., Borup R.L., Darling R.M., Das P.K., et al., "A Critical Review of Modeling Transport Phenomena in Polymer-Electrolyte Fuel Cells," *Journal of The Electrochemical Society* **161**(12):F1254-F1299, 2014.

[191] Hutzenlaub T., Becker J., Zengerle R., and Thiele S., "Modelling the water distribution within a hydrophilic and hydrophobic 3D reconstructed cathode catalyst layer of a proton exchange membrane fuel cell," *Journal of Power Sources* **227**:260, 2013, doi:10.1016/j.jpowsour.2012.11.065.

[192] Siroma Z. and Yasuda K., "Numerical simulation of the reaction and mass-transfer profiles in the two-layer catalyst of a PEMFC," *Electrochemistry* **79**(5):326-328, 2011.

[193] Eikerling M., "Water Management in Cathode Catalyst Layers of PEM Fuel Cells: A Structure-Based Model," *Journal of The Electrochemical Society* **153**(3):E58-E70, 2006.

[194] Neyman J., "Outline of a Theory of Statistical Estimation Based on the Classical Theory of Probability," *Philosophical Transactions of the Royal Society of London.Series A, Mathematical and Physical Sciences* **236**(767):333-380, 1937.

[195] Mendenhall W., Wackerly D., D., and Scheaffer R., L., " Mathematical statistics with applications," Boston, kent.

10 Appendices

Appendix 1: - Safety and data sheets & Agglomeration Definition

- OED definition of agglomeration
- Nafion date sheets
- Isopropanol MSDS
- GDM data sheets

Appendix 2: The Spiegel model

- Two dimensional GDM model from Spiegel

Appendix 3: Original data

- Matlab code for AeK pol curves and grad fitting
- All AeK data and NMcC results tables
- Included and excluded data for DoE
- M-ANOVA initial results
- Weighting tables

Appendix 4: Additional graphical versions of original data

- All FUDL ‘PM’ graphs and images

Appendix 5: Previously published work contributing to this thesis

- Journal paper
- Conference paper

Appendix 1: - Safety and Data sheets & Agglomeration Definition

The word agglomerate can be used as a verb, a noun and an adjective.

“Agglomerate” : OED Online, "Agglomerate, v, a and n"

(https://en.oxforddictionaries.com/definition/agglomerate, 18/12/2016 2016.)

- Verb – collect, or form into a mass
- Noun – a mass or collection of things
- Adjective – collected or formed into a mass

It is important to note that the term ‘agglomerate model’ does not, inherently, imply a transient time-dependent model, on the changes in the catalyst layer. In this thesis, it indicates that the type of catalyst being modelled consists of multiple phases clumped together (typically carbon black and platinum) into a broadly homogenised mass, with an ionically conductive phase at the surface. The term ‘agglomerate model’ can be easily be confused when referring to ‘agglomeration’. To clarify: A set of particles that is in the process of coming together to form a larger particle, is undergoing ‘agglomeration’ in the present tense. It is not uncommon, in fuel cell circles, to refer to a particle that is a combination of multiple phases as ‘an agglomeration’. For this reason is it recommended that Ostwald ripening [142] (see section 5.2) be used when referring to the active coalescing of particles of platinum, and the term ‘agglomeration’ be avoided.

Toray Carbon Fiber Paper "TGP-H"

Gas Diffusion Layer

Toray TGP-H is a Carbon-Carbon Composite Paper which has been used for PAFC and PEFC for decades and has proven durability. Its high mechanical strength, conductivity and gas permeability are suitable for use as a Gas Diffusion Layer (GDL) in fuel cell applications.

Characteristics

- High strength
- Excellent gas permeability and low electrical resistivity
- Good handling
- Minimal electrochemical corrosion

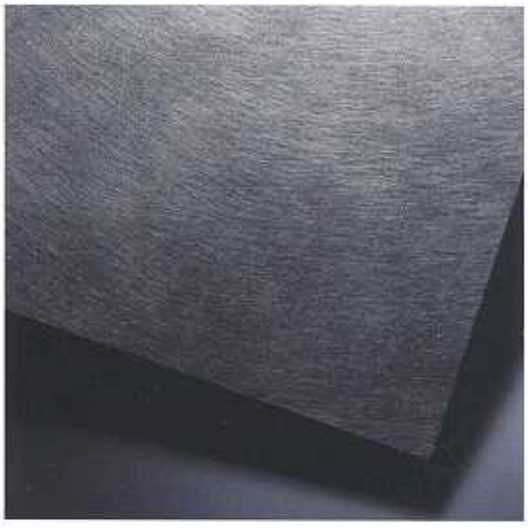

Structure

- TGP-H is made of PAN Carbon Fiber "TORAYCA" featuring high tensile strength and high modulus. Fibers are firmly connected by carbon.
- SEM (Scanning Electron Micrography) images on the right.

Surface 100μm

Cross section 10μm

Standard Sizes

- Thickness: TGP-H-030, 0.11mm
  TGP-H-060, 0.19mm
  TGP-H-090, 0.28mm
  TGP-H-120, 0.37mm
  Thicker materials available on request.
- Dimensions: 15"x15", 400mm x 400mm, 500mm x 500mm and 800mm x 800mm.
  800mm x 800mm board for TGP-H-030 is not available.

Basic Data

Properties	Unit	TGP-H-030	TGP-H-060	TGP-H-090	TGP-H-120
Thickness	mm	0.11	0.19	0.28	0.37
Bulk density	g/cm^3	0.40	0.44	0.44	0.45
Porosity	%	80	78	78	78
Surface roughness Ra	μm	8	8	8	8
Gas permeability	$ml \cdot mm/(cm^2 \cdot hr \cdot mmAq)$	2500	1900	1700	1500
Electrical resistivity					
through plane	mΩcm	80	80	80	80
in plane	mΩcm	–	5.8	5.6	4.7
Thermal conductivity					
through plane (room temp.)	W/ (m·k)	–	(1.7)	(1.7)	(1.7)
inplane (room temp.)	W/ (m·k)	–	21	21	21
inplane (100°C)	W/ (m·k)	–	23	23	23
Coefficient of thermal expansion					
in plane (25~100°C)	$x10^{-6}/°C$	-0.8	-0.8	-0.8	-0.8
Flexural strength	MPa	40	40	40	40
Flexural modulus	GPa	8	10	10	10
Tensile strength	N/cm	–	50	70	90

•The above data are experimental values and are not guaranteed.

FREUDENBERG GAS DIFFUSION LAYERS FOR PEMFC AND DMFC

TECHNICAL DATA

	H2315 I6	H2315 C2	H2315 C4	H2315 I4 C9	H2315 I2 C6	H2315 I2 C8	H2415 I2 C3	H2415 C5	H1410 I4 C9
HYDROPHOBIC TREATMENT	■			■	■	■	■		■
MICROPOROUS LAYER		■	■	■	■	■	■	■	■
Thickness @ 0.025 MPa (Internal) **in µm**	210	255	255	250	250	230	290	270	180
Thickness @ 1 MPa (Internal) **in µm**	175	215	215	210	210	200	230	215	150
Area weight (DIN EN ISO 29073-1) **in g/m²**	115	135	135	135	135	135	150	130	100
Compression Set @ 1 MPa (Internal) **in µm**	3	8	8	8	8	3	25	15	7
TP electrical resistance @ 1 MPa (Internal) **in mΩ·cm²**	7	10	8	8	8	8	9	9	7
IP electrical resistance (Internal) **in Ω**	0.8	0.8	0.8	0.7	0.7	0.8	0.6	0.7	1.0
TP air permeability* (DIN EN ISO 9237) **in l/m²·s**	160	–	–	–	–	–	–	–	–
TP air permeability acc. to Gurley (ISO 5636-5) **in s**	–	70	50	30	70	90	35	40	30
IP air permeability @ 1 MPa (Internal) **in µm²**	1.7	2.5	2.5	2.0	1.8	1.5	1.5	2.5	1.5
Tensile strength (DIN EN ISO 29073-3) **in N/50 mm**	80	80	60	70	70	70	110	70	70

* at 200 Pa pressure drop
TP = through-plane, IP = in-plane
(Rev. 04 – 13.02.2013)

All values represent averages which are subject to usual production tolerances. The values do not represent specifications.
Any warranty and liability is subject to Freudenberg FCCT SE & Co. KG's General Terms of Delivery and Payment applicable at the date of delivery.

FREUDENBERG GAS DIFFUSION LAYERS FOR PEMFC AND DMFC

GDL RECOMMENDATION FOR DIFFERENT LT-PEMFC APPLICATIONS

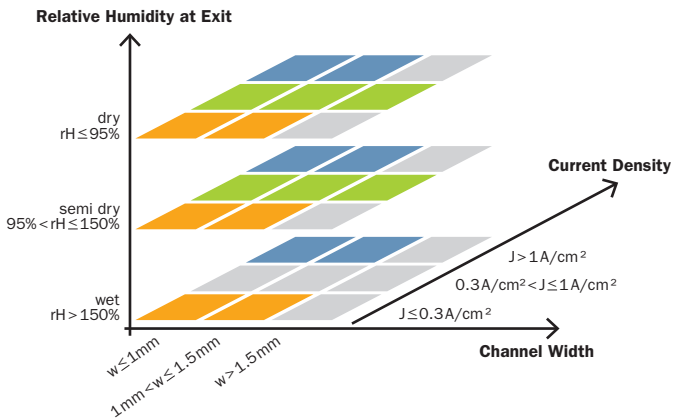

LT-PEMFC: (Auto)Motive	**H1410 I4 C9**	thin GDL substrate
	H2315 I4 C9	
	H2315 I2 C6	in particular suitable for GDE
	H2315 I2 C8	very smooth coating surface, suitable for GDE
LT-PEMFC: Stationary CHP High Humidification	**H2315 C2**	
	H2315 C4	in particular suitable for GDE
	H2315 I2 C6	
	H1410 I4 C9	thin GDL substrate
LT-PEMFC: Stationary CHP Low Humidification	**H2415 C5**	
	H2415 I2 C3	very dry operating conditions
LT-PEMFC: Back-up / Air-cooled / Off-Grid	**H2415 C5**	
	H2415 I2 C3	very dry operating conditions
HT-PEMFC	**H2315 C2**	
	H2315 C4	in particular suitable for GDE
Acitve DMFC	**H2315 C4**	in particular suitable for GDE
	H2315 I6	
Electrolysis	**H2315 I6**	

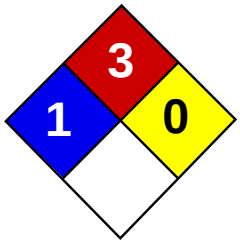

Material Safety Data Sheet
Isopropyl alcohol MSDS

Section 1: Chemical Product and Company Identification

Product Name: Isopropyl alcohol

Catalog Codes: SLI1153, SLI1579, SLI1906, SLI1246, SLI1432

CAS#: 67-63-0

RTECS: NT8050000

TSCA: TSCA 8(b) inventory: Isopropyl alcohol

CI#: Not available.

Synonym: 2-Propanol

Chemical Name: isopropanol

Chemical Formula: C3-H8-O

Contact Information:

Sciencelab.com, Inc.
14025 Smith Rd.
Houston, Texas 77396

US Sales: **1-800-901-7247**
International Sales: **1-281-441-4400**

Order Online: ScienceLab.com

CHEMTREC (24HR Emergency Telephone), call: 1-800-424-9300

International CHEMTREC, call: 1-703-527-3887

For non-emergency assistance, call: 1-281-441-4400

Section 2: Composition and Information on Ingredients

Composition:

Name	CAS #	% by Weight
Isopropyl alcohol	67-63-0	100

Toxicological Data on Ingredients: Isopropyl alcohol: ORAL (LD50): Acute: 5045 mg/kg [Rat]. 3600 mg/kg [Mouse]. 6410 mg/kg [Rabbit]. DERMAL (LD50): Acute: 12800 mg/kg [Rabbit].

Section 3: Hazards Identification

Potential Acute Health Effects:
Hazardous in case of eye contact (irritant), of ingestion, of inhalation. Slightly hazardous in case of skin contact (irritant, sensitizer, permeator).

Potential Chronic Health Effects:
Slightly hazardous in case of skin contact (sensitizer). CARCINOGENIC EFFECTS: A4 (Not classifiable for human or animal.) by ACGIH, 3 (Not classifiable for human.) by IARC. MUTAGENIC EFFECTS: Not available. TERATOGENIC EFFECTS: Not available. DEVELOPMENTAL TOXICITY: Classified Reproductive system/toxin/female, Development toxin [POSSIBLE]. The substance may be toxic to kidneys, liver, skin, central nervous system (CNS). Repeated or prolonged exposure to the substance can produce target organs damage.

Section 4: First Aid Measures

Eye Contact:
Check for and remove any contact lenses. In case of contact, immediately flush eyes with plenty of water for at least 15 minutes. Cold water may be used. Get medical attention.

Skin Contact:
Wash with soap and water. Cover the irritated skin with an emollient. Get medical attention if irritation develops. Cold water may be used.

Serious Skin Contact: Not available.

Inhalation:
If inhaled, remove to fresh air. If not breathing, give artificial respiration. If breathing is difficult, give oxygen. Get medical attention if symptoms appear.

Serious Inhalation:
Evacuate the victim to a safe area as soon as possible. Loosen tight clothing such as a collar, tie, belt or waistband. If breathing is difficult, administer oxygen. If the victim is not breathing, perform mouth-to-mouth resuscitation. Seek medical attention.

Ingestion:
Do NOT induce vomiting unless directed to do so by medical personnel. Never give anything by mouth to an unconscious person. Loosen tight clothing such as a collar, tie, belt or waistband. Get medical attention if symptoms appear.

Serious Ingestion: Not available.

Section 5: Fire and Explosion Data

Flammability of the Product: Flammable.

Auto-Ignition Temperature: 399°C (750.2°F)

Flash Points: CLOSED CUP: 11.667°C (53°F) - 12.778 deg. C (55 deg. F) (TAG)

Flammable Limits: LOWER: 2% UPPER: 12.7%

Products of Combustion: These products are carbon oxides (CO, CO2).

Fire Hazards in Presence of Various Substances:
Highly flammable in presence of open flames and sparks, of heat. Flammable in presence of oxidizing materials. Non-flammable in presence of shocks.

Explosion Hazards in Presence of Various Substances:
Risks of explosion of the product in presence of mechanical impact: Not available. Explosive in presence of open flames and sparks, of heat.

Fire Fighting Media and Instructions:
Flammable liquid, soluble or dispersed in water. SMALL FIRE: Use DRY chemical powder. LARGE FIRE: Use alcohol foam, water spray or fog.

Special Remarks on Fire Hazards:
Vapor may travel considerable distance to source of ignition and flash back. CAUTION: MAY BURN WITH NEAR INVISIBLE FLAME. Hydrogen peroxide sharply reduces the autoignition temperature of Isopropyl alcohol. After a delay, Isopropyl alcohol ignites on contact with dioxgenyl tetrafluorborate, chromium trioxide, and potassium tert-butoxide. When heated to decomposition it emits acrid smoke and fumes.

Special Remarks on Explosion Hazards:
Secondary alcohols are readily autooxidized in contact with oxygen or air, forming ketones and hydrogen peroxide. It can become potentially explosive. It reacts with oxygen to form dangerously unstable peroxides which can concentrate and explode during distillation or evaporation. The presence of 2-butanone increases the reaction rate for peroxide formation. Explosive in the form of vapor when exposed to heat or flame. May form explosive mixtures with air. Isopropyl alcohol + phosgene forms isopropyl chloroformate and hydrogen chloride. In the presence of iron salts, thermal decompositon can occur, whicn in some cases can become explosive. A homogeneous mixture of concentrated peroxides + isopropyl alcohol are capable of detonation by shock or heat. Barium perchlorate + isopropyl alcohol gives the highly explosive alkyl perchlorates.

It forms explosive mixtures with trinitormethane and hydrogen peroxide. It produces a violent explosive reaction when heated with aluminum isopropoxide + crotonaldehyde. Mixtures of isopropyl alcohol + nitroform are explosive.

Section 6: Accidental Release Measures

Small Spill:
Dilute with water and mop up, or absorb with an inert dry material and place in an appropriate waste disposal container.

Large Spill:
Flammable liquid. Keep away from heat. Keep away from sources of ignition. Stop leak if without risk. Absorb with DRY earth, sand or other non-combustible material. Do not touch spilled material. Prevent entry into sewers, basements or confined areas; dike if needed. Be careful that the product is not present at a concentration level above TLV. Check TLV on the MSDS and with local authorities.

Section 7: Handling and Storage

Precautions:
Keep away from heat. Keep away from sources of ignition. Ground all equipment containing material. Do not ingest. Do not breathe gas/fumes/ vapor/spray. Avoid contact with eyes. Wear suitable protective clothing. In case of insufficient ventilation, wear suitable respiratory equipment. If ingested, seek medical advice immediately and show the container or the label. Keep away from incompatibles such as oxidizing agents, acids.

Storage:
Store in a segregated and approved area. Keep container in a cool, well-ventilated area. Keep container tightly closed and sealed until ready for use. Avoid all possible sources of ignition (spark or flame).

Section 8: Exposure Controls/Personal Protection

Engineering Controls:
Provide exhaust ventilation or other engineering controls to keep the airborne concentrations of vapors below their respective threshold limit value. Ensure that eyewash stations and safety showers are proximal to the work-station location.

Personal Protection:
Splash goggles. Lab coat. Vapor respirator. Be sure to use an approved/certified respirator or equivalent. Gloves.

Personal Protection in Case of a Large Spill:
Splash goggles. Full suit. Vapor respirator. Boots. Gloves. A self contained breathing apparatus should be used to avoid inhalation of the product. Suggested protective clothing might not be sufficient; consult a specialist BEFORE handling this product.

Exposure Limits:
TWA: 983 STEL: 1230 (mg/m3) [Australia] TWA: 200 STEL: 400 (ppm) from ACGIH (TLV) [United States] [1999] TWA: 980 STEL: 1225 (mg/m3) from NIOSH TWA: 400 STEL: 500 (ppm) from NIOSH TWA: 400 STEL: 500 (ppm) [United Kingdom (UK)] TWA: 999 STEL: 1259 (mg/m3) [United Kingdom (UK)] TWA: 400 STEL: 500 (ppm) from OSHA (PEL) [United States] TWA: 980 STEL: 1225 (mg/m3) from OSHA (PEL) [United States]Consult local authorities for acceptable exposure limits.

Section 9: Physical and Chemical Properties

Physical state and appearance: Liquid.

Odor:
Pleasant. Odor resembling that of a mixture of ethanol and acetone.

Taste: Bitter. (Slight.)

Molecular Weight: 60.1 g/mole

Color: Colorless.

pH (1% soln/water): Not available.

Boiling Point: 82.5°C (180.5°F)

Melting Point: -88.5°C (-127.3°F)

Critical Temperature: 235°C (455°F)

Specific Gravity: 0.78505 (Water = 1)

Vapor Pressure: 4.4 kPa (@ 20°C)

Vapor Density: 2.07 (Air = 1)

Volatility: Not available.

Odor Threshold:
22 ppm (Sittig, 1991) 700 ppm for unadapted panelists (Verschuren, 1983).

Water/Oil Dist. Coeff.: The product is equally soluble in oil and water; log(oil/water) = 0.1

Ionicity (in Water): Not available.

Dispersion Properties: See solubility in water, methanol, diethyl ether, n-octanol, acetone.

Solubility:
Easily soluble in cold water, hot water, methanol, diethyl ether, n-octanol, acetone. Insoluble in salt solution. Soluble in benzene. Miscible with most organic solvents including alcohol, ethyl alcohol, chloroform.

Section 10: Stability and Reactivity Data

Stability: The product is stable.

Instability Temperature: Not available.

Conditions of Instability: Heat, Ignition sources, incompatible materials

Incompatibility with various substances: Reactive with oxidizing agents, acids, alkalis.

Corrosivity: Non-corrosive in presence of glass.

Special Remarks on Reactivity:
Reacts violently with hydrogen + palladium combination, nitroform, oleum, $COCl_2$, aluminum triisopropoxide, oxidants Incompatible with acetaldehyde, chlorine, ethylene oxide, isocyanates, acids, alkaline earth, alkali metals, caustics, amines, crotonaldehyde, phosgene, ammonia. Isopropyl alcohol reacts with metallic aluminum at high temperatures. Isopropyl alcohol attacks some plastics, rubber, and coatings. Vigorous reaction with sodium dichromate + sulfuric acid.

Special Remarks on Corrosivity: May attack some forms of plastic, rubber and coating

Polymerization: Will not occur.

Section 11: Toxicological Information

Routes of Entry: Absorbed through skin. Dermal contact. Eye contact. Inhalation.

Toxicity to Animals:
WARNING: THE LC50 VALUES HEREUNDER ARE ESTIMATED ON THE BASIS OF A 4-HOUR EXPOSURE. Acute oral toxicity (LD50): 3600 mg/kg [Mouse]. Acute dermal toxicity (LD50): 12800 mg/kg [Rabbit]. Acute toxicity of the vapor (LC50): 16000 8 hours [Rat].

Chronic Effects on Humans:
CARCINOGENIC EFFECTS: A4 (Not classifiable for human or animal.) by ACGIH, 3 (Not classifiable for human.) by IARC. DEVELOPMENTAL TOXICITY: Classified Reproductive system/toxin/female, Development toxin [POSSIBLE]. May cause damage to the following organs: kidneys, liver, skin, central nervous system (CNS).

Other Toxic Effects on Humans:
Hazardous in case of ingestion, of inhalation. Slightly hazardous in case of skin contact (irritant, sensitizer, permeator).

Special Remarks on Toxicity to Animals: Not available.

Special Remarks on Chronic Effects on Humans:
May cause adverse reproductive/teratogenic effects (fertility, fetoxicity, developmental abnormalities(developmental toxin)) based on animal studies. Detected in maternal milk in human.

Special Remarks on other Toxic Effects on Humans:
Acute Potential Health Effects: Skin: May cause mild skin irritation, and sensitization. Eyes: Can cause eye irritation. Inhalation: Breathing in small amounts of this material during normal handling is not likely to cause harmful effects. However, breathing large amounts may be harmful and may affect the respiratory system and mucous membranes (irritation), behavior and brain (Central nervous system depression - headache, dizziness, drowsiness, stupor, incoordination, unconciousness, coma and possible death), peripheral nerve and senstation, blood, urinary system, and liver. Ingestion: Swallowing small amouts during normal handling is not likely to cause harmful effects. Swallowing large amounts may be harmful. Swallowing large amounts may cause gastrointestinal tract irritation with nausea, vomiting and diarrhea, abdominal pain. It also may affect the urinary system, cardiovascular system, sense organs, behavior or central nervous system (somnolence, generally depressed activity, irritability, headache, dizziness, drowsiness), liver, and respiratory system (breathing difficulty). Chronic Potential Health Effects: May cause defatting of the skin and dermatitis and allergic reaction. May cause adverse reproductive effects based on animal data (studies).

Section 12: Ecological Information

Ecotoxicity: Ecotoxicity in water (LC50): 100000 mg/l 96 hours [Fathead Minnow]. 64000 mg/l 96 hours [Fathead Minnow].

BOD5 and COD: Not available.

Products of Biodegradation:
Possibly hazardous short term degradation products are not likely. However, long term degradation products may arise.

Toxicity of the Products of Biodegradation: The product itself and its products of degradation are not toxic.

Special Remarks on the Products of Biodegradation: Not available.

Section 13: Disposal Considerations

Waste Disposal:
Waste must be disposed of in accordance with federal, state and local environmental control regulations.

Section 14: Transport Information

DOT Classification: CLASS 3: Flammable liquid.

Identification: : Isopropyl Alcohol UNNA: 1219 PG: II

Special Provisions for Transport: Not available.

Section 15: Other Regulatory Information

Federal and State Regulations:
Connecticut hazardous material survey.: Isopropyl alcohol Illinois toxic substances disclosure to employee act: Isopropyl alcohol Rhode Island RTK hazardous substances: Isopropyl alcohol Pennsylvania RTK: Isopropyl alcohol Florida: Isopropyl alcohol Minnesota: Isopropyl alcohol Massachusetts RTK: Isopropyl alcohol New Jersey: Isopropyl alcohol New Jersey spill list: Isopropyl alcohol Director's list of Hazardous Substances: Isopropyl alcohol Tennesee: Isopropyl alcohol TSCA 8(b) inventory: Isopropyl alcohol TSCA 4(a) final testing order: Isopropyl alcohol TSCA 8(a) IUR: Isopropyl alcohol TSCA 8(d) H

and S data reporting: Isopropyl alcohol: Effective date: 12/15/86 Sunset Date: 12/15/96 TSCA 12(b) one time export: Isopropyl alcohol SARA 313 toxic chemical notification and release reporting: Isopropyl alcohol

Other Regulations:
OSHA: Hazardous by definition of Hazard Communication Standard (29 CFR 1910.1200). EINECS: This product is on the European Inventory of Existing Commercial Chemical Substances.

Other Classifications:

WHMIS (Canada):
CLASS B-2: Flammable liquid with a flash point lower than 37.8°C (100°F). CLASS D-2B: Material causing other toxic effects (TOXIC).

DSCL (EEC):
R11- Highly flammable. R36- Irritating to eyes. S7- Keep container tightly closed. S16- Keep away from sources of ignition - No smoking. S24/25- Avoid contact with skin and eyes. S26- In case of contact with eyes, rinse immediately with plenty of water and seek medical advice.

HMIS (U.S.A.):

Health Hazard: 2

Fire Hazard: 3

Reactivity: 0

Personal Protection: h

National Fire Protection Association (U.S.A.):

Health: 1

Flammability: 3

Reactivity: 0

Specific hazard:

Protective Equipment:
Gloves. Lab coat. Vapor respirator. Be sure to use an approved/certified respirator or equivalent. Wear appropriate respirator when ventilation is inadequate. Splash goggles.

Section 16: Other Information

References: Not available.

Other Special Considerations: Not available.

Created: 10/09/2005 05:53 PM

Last Updated: 05/21/2013 12:00 PM

The information above is believed to be accurate and represents the best information currently available to us. However, we make no warranty of merchantability or any other warranty, express or implied, with respect to such information, and we assume no liability resulting from its use. Users should make their own investigations to determine the suitability of the information for their particular purposes. In no event shall ScienceLab.com be liable for any claims, losses, or damages of any third party or for lost profits or any special, indirect, incidental, consequential or exemplary damages, howsoever arising, even if ScienceLab.com has been advised of the possibility of such damages.

Nafion® PFSA Membranes

Version 2.0
Revision Date 2011/02/01 Document no. 150000002917

This SDS adheres to the standards and regulatory requirements of China and may not meet the regulatory requirements in other countries.

Section 1 - Chemical and Enterprise Identification

Chinese name : Nafion® PFSA Membranes
Product name in English : Nafion® PFSA Membranes
Specifications : 115, 115FP, 117, 117FP, N115, N115FP, N117, N117FP, 1110, N1110

Manufacturer or supplier's details
Company : Du Pont China Holding Co., Ltd
Street address : China, Shanghai, 399 KeYuan Road, Bldg 11, Zhangjiang Hi-Tech Park, Pudong New District 201203

Telephone : 86 21 3862 2888
Telefax : 86 21 3862 2889

Emergency telephone number : 86 532 8388 9090

Recommended use of the chemical and restriction on use
Recommended use : sheets and shaped articles

Section 2 - Hazard Identification

GHS Hazard Category

Not a dangerous substance according to GHS.

Other hazards which do not result in classification or are not covered by the GHS

The thermal decomposition vapours of fluorinated polymers may cause polymer fume fever with flu-like symptoms in humans, especially when smoking contaminated tobacco.

Main Symptom and Emergency Summary After Contact

No information available.

Section 3 - Ingredients/Composition Information

Chemical nature : Substance

Components

Chemical Name	CAS-No.	Concentration
Perfluorosulfonic acid/TFE copolymer	31175-20-9	100 %

Section 4 - First-aid Measures

Never give anything by mouth to an unconscious person. No hazards which require special first aid measures. When symptoms persist or in all cases of doubt seek medical advice.

Inhalation	:	Move to fresh air in case of accidental inhalation of fumes from overheating or combustion. Consult a physician.
Skin contact	:	No hazards which require special first aid measures. Wash off with soap and water. Cool skin rapidly with cold water after contact with molten material. Do not peel polymer from the skin. Consult a physician.
Eye contact	:	Hold eyelids apart and flush eyes with plenty of water for at least 15 minutes. Get medical attention.
Ingestion	:	Not a probable route of exposure. However, in case of accidental ingestion, call a physician.
Most important symptoms/effects, acute and delayed	:	No information available.
Protection of first-aiders	:	No information available.
Notes to physician	:	No information available.

Section 5 - Fire-fighting Measures

Suitable extinguishing media	:	Carbon dioxide (CO2), Dry powder, Foam, Water
Specific hazards	:	Hazardous thermal decomposition products: Carbon oxides acid fluorides Fluorinated compounds Hydrogen fluoride Sulphur oxides Hydrogen fluoride, Carbon monoxide
Specific fire fighting methods and special protective equipment for fire fighters	:	In the event of fire, wear self-contained breathing apparatus. Wear suitable protective equipment. Wear neoprene gloves during cleaning up work after a fire. Protect from hydrogen fluoride fumes which react with water to form hydrofluoric acid. The solid polymer can only be burned with difficulty. Use extinguishing measures that are appropriate to local circumstances and the surrounding environment.

Section 6 - Leak Emergency Treatment

Protective measures, devices and emergency treatment procedure for workers	:	Ventilate the area. Refer to protective measures listed in sections 7 and 8. Material can create slippery conditions.
Environmental protection measures	:	No special environmental precautions required.
Collection of leaking materials, removal method and materials used for disposal	:	Use mechanical handling equipment.

Prevention of secondary hazards	:	No information available.

Section 7 - Operation Handling and Storage

Operation Handling

Technical measures/Precautions	:	When opening containers, avoid breathing vapours that may be emanating. Avoid breathing dust. Avoid contamination of cigarettes or tobacco with dust from this material. Provide appropriate exhaust ventilation at dryers, machinery and at places where dust or volatiles can be generated. For personal protection see section 8. In case of insufficient ventilation, wear suitable respiratory equipment.
Precautions for safe handling	:	Take necessary action to avoid static electricity discharge (which might cause ignition of organic vapours).
Hygiene measures	:	Regular cleaning of equipment, work area and clothing. Do not contaminate tobacco products. Wash hands before breaks and at the end of workday. General precaution for all plastics and elastomers: Do not breathe fumes evolved from hot polymer.

Storage

Suitable storage conditions	:	Keep in a dry, cool and well-ventilated place. Store in original container. Keep away from direct sunlight. Protect from contamination. Storage temperature: 10 - 30 °C Stable under recommended storage conditions.

Section 8 - Exposure Control and Personal Protection

Engineering controls	:	Ensure adequate ventilation, especially in confined areas. Good general ventilation should be provided to keep dust concentrations below the exposure limits. Local exhaust ventilation should be employed to minimize airborne contamination.

Occupational Exposure Limits

No information available.

Biological occupational exposure limits	:	No information available.

Personal protective equipment

Respiratory protection	:	When workers are facing concentrations above the exposure limit they must use appropriate certified respirators. Air purifying respirators may not provide adequate protection. In the case of hazardous fumes caused by overheating, wear self-contained breathing apparatus.
Hand protection	:	When handling hot material, use heat resistant gloves., Protective gloves (Type : Kevlar® - heat resistant, use possible until worn out)

Eye protection	:	Solid form, :, Safety glasses with side-shields Molten form, Wear coverall chemical splash goggles and face shield when the possibility exists for eye and face contact due to splashing or spraying of material.
Skin protection	:	If there is a potential for contact with hot/molten material wear heat resistant clothing and footwear.

Section 9 - Physical and Chemical Properties

Appearance (Physical state, form, colour, etc.)

Physical state	:	solid
Form	:	film
Colour	:	no data available

Odour : none

pH (specifed concentration) : no data available

Melting point/freezing point

no data available

Boiling point, initial boiling point and boiling range

no data available

Flash point : does not flash

Decomposition temperature : no data available

Autoignition temperature : no data available

Explosion limits

Upper explosion limit	:	no data available
Lower explosion limit	:	no data available

Vapour pressure : no data available

Vapour density : no data available

Density

no data available

Solubility(ies)

Water solubility	:	insoluble
Solubility in other solvents	:	no data available
Partition coefficient: n-octanol/water	:	no data available

Section 10 - Stability and Reactivity

Stability	:	Stable at normal temperatures and storage conditions.
Possible hazardous reactions under specific conditions	:	During drying, cleaning and moulding, small amounts of hazardous gases and/or particulate matter may be released. These may irritate eyes, nose and throat. Large molten masses may give off hazardous gases.
Conditions to avoid	:	To avoid thermal decomposition, do not overheat. Abnormally long processing time or high temperatures can produce irritating and toxic fumes. Stable under normal conditions.
Materials to avoid	:	Powdered metals, Finely divided aluminium, potent oxidizers like fluorine (F2)
Hazardous decomposition products	:	Decomposes with heat., Carbonyl fluoride, Hydrogen fluoride, Fluorinated hydrocarbons, acid fluorides, Sulphur oxides

Section 11 - Toxicological Information

Acute toxicity	:	Perfluorosulfonic acid/TFE copolymer: Oral: ALD/rat : > 20,000 mg/kg
Skin corrosion/irritation	:	Perfluorosulfonic acid/TFE copolymer: non-irritant
Eye irritation/corrosion	:	Perfluorosulfonic acid/TFE copolymer: non-irritant
Respiratory or skin sensitization	:	no data available
Germ cell mutagenicity	:	no data available
Carcinogenicity	:	no data available
Toxicity for reproduction	:	no data available

Specific Target Organs Toxicity (Single/Repeated)	:	no data available
Aspiration hazard	:	no data available
Other	:	Perfluorosulfonic acid/TFE copolymer: The substance is a polymer and is not expected to produce toxic effects.

Section 12 - Ecological Information

Ecotoxicity effects

Toxicity to fish	:	Perfluorosulfonic acid/TFE copolymer: The substance is a polymer and is not expected to produce toxic effects.
Persistence and degradation	:	no data available
Bioaccumulation	:	no data available
Mobility in soil	:	no data available
Other adverse effects	:	Nafion® PFSA Membranes: Toxicity is expected to be low based on insolubility in water.

Section 13 - Waste Disposal

Waste disposal methods	:	Like most thermoplastic plastics the product can be recycled. Where possible recycling is preferred to disposal or incineration. If recycling is not practicable, dispose of in compliance with local regulations. Can be landfilled, when in compliance with local regulations. Incinerate only if incinerator is capable of scrubbing out hydrogen fluoride and other acidic combustion products. Used package: Empty containers should be taken to an approved waste handling site for recycling or disposal.

Section 14 - Transport Information

Not classified as dangerous in the meaning of transport regulations.

Section 15 - Regulatory Information

not regulated

Nafion® PFSA Membranes

Version 2.0
Revision Date 2011/02/01 Document no. 150000002917

Section 16 - Other Information

References	:	not applicable
Other information	:	For further information contact the local DuPont office or DuPont's nominated distributors. The DuPont Oval Logo is a registered trademark of E.I. du Pont de Nemours and Company. Do not use DuPont materials in medical applications involving implantation in the human body or contact with internal body fluids or tissues unless the material has been provided from DuPont under a written contract that is consistent with DuPont policy regarding medical applications and expressly acknowledges the contemplated use. For further information, please contact your DuPont representative. You may also request a copy of the DuPont POLICY Regarding Medical Applications H-50103-3 and DuPont CAUTION Regarding Medical Applications H-50102-3.

Significant change from previous version is denoted with a double bar.

The information provided in this Safety Data Sheet is correct to the best of our knowledge, information and belief at the date of its publication. The information given is designed only as a guide for safe handling, use, processing, storage, transportation, disposal and release and is not to be considered a warranty or quality specification. The above information relates only to the specific material(s) designated herein and may not be valid for such material(s) used in combination with any other materials or in any process or if the material is altered or processed, unless specified in the text.

Appendix 2:- The Spiegel Model

```
%%%%%%%%%%%%%%%%%%%%%%%%%%%%%%%%

% Example 8-2: GDL Model

% C. Spiegel, PEM Fuel Cell Modeling and Simulation using MATLAB, Elsevier,
Burlington, (2008).

%%%%%%%%%%%%%%%%%%%%%%%%%%%%%%%%


% Assumptions

%water vapour at  Thermodynamic equilibrium and fully saturated
% no liquid water in the gas channel
% pure oxygen
% gas movement includes Fickean and  convective movement (Darcey)
% thermal conductivity is considered a linear effect from wet and dry
phases
% solid graphite cathode boundary


%%%%%%%%%%%%%%%%%

% Units

% T = kelvin
%P = atmospheres


clc
clear all
format long e


% define paramters

eps = 0.2; % perturbation parameter (h/l or y/(4*d) in this case) set to
0.2 simulates GDM pores

% define the number fo grid points in x & y directions

nx = 25; %101; % Number of grid points in direction 'x' - set to 25

ny = 17; %65;  % Number of grid points in direction 'y' - set to 17

% SOR parameters

omega = 1.4; % SOR parameter - Successive over relaxation iterative
solution method - set to 1.4

%%%
%capilary efects??
%%%
t = (2.0*cos(pi/(nx*ny)))^2; %???

% Calulate optimum value of SOR parameter
```

```
omega1 = 16.0+sqrt((256.0-(64.0*t)))/(2.0*t);

omega2 = 16.0-sqrt((256.0-(64.0*t)))/(2.0*t);

oopt= min(omega1,omega2);

if ((oopt<=1.0)||(oopt>=2.0))
    oopt=1.0;
end
omega = oopt;

% define domain dimensions

Lx = 2.0; % length of 'x' in the computation region

Ly = 1.0; % length of 'y' in the computation region

% Calcualte the mesh size

hx = Lx/(nx-1); % x direction grid spacing

hy = Ly/(ny-1); % y direction grid spacing


% generate the mesh grid

x(1) = -1.0;
y(1) = 0.0;

for i = 2:nx
    x(i) = x(i-1)+hx;
end

for j = 2:ny
    y(j)=y(j-1)+hy;
end

%%%%%%%%%%%%%%%%%

% Solve the temperature eqn.

% Initialize temperature field as zero

T=zeros(nx,ny);

% Max-norm Error {L-inf Error} initialised

%define 'Tolerance' - the degree of convergence of the iterative
%'Successive Over-Relaxation' matrix solution method

Tollerance = 1e-5;
Linf=1.0;
iteration=0;
while(Linf > Tollerance) %e-5 in the text
    iteration=iteration+1;
    %store the old values of T in 'told'
    Told=T;
```

```
    %Apply boundary conditions

    for i = 1:nx
        %BC for the bottom boundary
        T(i,1)=T(i,2)+hy;
        %BC for the top boundary

        if (x(i)<=0)
            T(i,ny)=1;
        else
            T(i,ny)=0;

        end
    end
    for j=1:ny
    %BC for the left boundary
    T(1,j)=T(2,j);
    %BC for the right boundry (NB - Says 'left' in the text...
    T(nx,j)=T(nx-1,j);
    end

    % Now compute interior domain using 2nd order finite difference
    for i=2:nx-1
        for j=2:ny-1

            % insert T= 60 deg (+ kelvin) for the first value fo 'T' then
            % re-writ eto avoid overwriting again
        Tterm1=((eps/hx)^2)*(T(i-1,j)+T(i+1,j));
        Tterm2=((1.0/hy)^2)*(T(i,j-1)+T(i,j+1));

        Tnum= Tterm1 + Tterm2;
        den=2.0*(((eps/hx)^2)+((1.0/hy)^2));

        Tgs=Tnum/den;
        T(i,j)=(omega*Tgs)+((1.0-omega)*Told(i,j));
        end
    end

% claculate error

Terr=abs(T-Told);
Linf=norm(Terr,2);


% Print the convergence history every 100 iterations

Tccheck = round(iteration/100)-(iteration/100);
if ((iteration==1)||(Tccheck==0))
    fprintf('%d \t%e \n',iteration,Linf); % ???
end

end %  in the text book here...

% plot the solutions

figure
[X,Y]=meshgrid(x,y);
```

```
clevel=[-1 -0.005 0 0.053 0.152 0.252 0.352 0.451 0.551 0.65 0.75 0.949
1.049 1.148 1.248 1.348 1.447 1.547 1.646 1.746 1.848 1.945 2.0 3.0];
contourf(X',Y',T,clevel)
colorbar
axis([-1.2 1.2 -0.8 1.8])
xlabel ('x across half channel / half land ','FontSize', 18)
ylabel ('y (through the GDL)' ,'FontSize', 18)
zlabel('T(x,y)')
title('Temperature through the Cathode GDL', 'FontSize', 18)
hold on
yi = [0.0:0.01:1];
xi=[zeros(length(yi))];
    plot (xi, yi, 'black')
    %print -djpeg figures\chap4\temperature



%%%%%%%%
%Save data to file
version = 0;
version = version +1;
filename = ['GDL_model_8_2_Temp_' num2str(version)];
save (filename)

%%
%%%%%%%%%%%%%%%%%%%%%%%%%%%%%%%%%%%%%%%%%%%%%%%%%%%%

% Solve the [O2 conc] eqn

%%%%%%%%%%%%%%%%%%%%%%%%%%%%%%%%%%%%%%%%%%%%%%%%%%%%

%omega=1.0 %SOR parameter  - should whole line be commented out??

% Initialise [O2 conc] as zero

u=zeros(nx,ny);

% NB copy and paste form above - check through!

% Max-norm Error {L-inf Error} initialised

Linf=1.0;
iteration=0;
while(Linf > Tollerance) %e-5 in the text
    iteration=iteration+1;
    %store the old values of U in 'Uold'
    uold=u;
    %Apply boundary conditions

    for i = 1:nx
        %BC for the bottom boundary
        u(i,1)=u(i,2)-(1.81*(eps^2)*hy);
        %BC for the top boundary

        if (x(i)<=0)
            u(i,ny)=1;
        else
            u(i,ny)=u(i,ny-1);
```

```
        end
    end

    for j=1:ny
    %BC for the left boundary
    u(1,j)=u(2,j);
    %BC for the right boundry (NB - Says 'left' in the text...)
    u(nx,j)=u(nx-1,j);
    end

    % Now compute interior domain using 2nd order finite difference
    for i=2:nx-1
        for j=2:ny-1
        uterm1=((eps/hx)^2)*(u(i-1,j)+u(i+1,j));
        uterm2=((1.0/hy)^2)*(u(i,j-1)+u(i,j+1));

        unum=uterm1 + uterm2;
        den=2.0*(((eps/hx)^2)+((1.0/hy)^2));

        ugs=unum/den;
        u(i,j)=(omega*ugs)+((1.0-omega)*uold(i,j));
        end
    end

% calculate error

uerr=abs(u-uold);
Linf=norm(uerr,2);

% plot the converegence history every 100 iterations
uccheck=round(iteration/100)-(iteration/100);
if ( iteration ==1)
    fighandle = figure;
    hold on
end

if (uccheck==0)
    fprintf('%d\t %e \n', iteration, Linf,'r.'); % ???
    hold on
end
end
close (fighandle);

% plot soluitons

figure
[X,Y] = meshgrid(x,y);
clevel = [-1 -0.5 -0.087 -0.031 0 0.025 0.08 0.136 0.192 0.247 0.303 0.359
0.415 0.47 0.526 0.582 0.693 0.749 0.805 0.86 0.916 0.916 0.972 1 3.0];

contourf(X', Y', u, clevel)
colorbar
axis([-1.2 1.2 -0.8 1.8])
xlabel ('x across half channel / half land ','FontSize', 12)
ylabel ('y (through the GDL)' ,'FontSize', 12)
zlabel('u(x,y)')
title('O2 conc. through the Cathode GDL','FontSize', 18)
hold on
yi=[0:0.01:1];
```

```
xi=zeros(length(yi));
plot (xi, yi, 'black')
 %print -djpeg figures\chap4\conctration

    %%%%%%%%
%Save data to file
version = 0;
version = version +1;
filename = ['GDL_model_8_2_O2Conc_' num2str(version)];
save (filename)

%%

%%%%%%%%%%%%%%%%%%%%%%%%%%%%%%%%%%%%%%%%%%%%%%%%%%%%%%%%%%%%

% Solve the [H2Og Conc'] eqn

%%%%%%%%%%%%%%%%%%%%%%%%%%%%%%%%%%%%%%%%%%%%%%%%%%%%%%%%%%%%

% Initlise H2Og vapour conc' field as zeros

v=zeros(nx,ny);

% max-norm error {L-inf error} initialised

Linf=1.0;
iteration=0;

while (Linf>Tollerance) %e-5 in the text
    iteration = iteration +1;
    % Store the old vluaes of v in vold
    vold=v;

    %apply the boundary ocnditions
    for i=1:nx
        %BC for the bottom boundry
        v(i,1)=v(i,2)+(0.755*(eps^2)*hy);

        %BC for top boundry
        if (x(i)<=0)
            v(i,ny)=1;
        else
            v(i,ny)=v(i,ny-1);
        end
    end

    for j=1:ny
        %BC for left boundary
        v(1,j)=v(2,j);

        %BC ofr right boundary

        v(nx,j) = v(nx-1,j);
    end

    % now compute interior domains using 2nd order finite difference

    for i = 2:nx-1
```

```
        for j=2:ny-1
            vterm1 = ((eps/hx)^2)*(v(i-1,j)+v(i+1, j));
            vterm2 = ((1.0/hy)^2)*(v(i,j-1)+v(i, j+1));

            vnum = vterm1 + vterm2;

            den=2.0*(((eps/hx)^2)+((1.0/hy)^2));

            vgs = vnum/den;

            v(i,j) = (omega*vgs)+((1.0-omega)*vold(i,j));
        end
    end


    % Calculate the error
    verr=abs(v-vold);
    Linf=norm(verr,2);

    %plot the converegence history every 100 iterations

    vccheck = round(iteration/100)-(iteration/100);
    if (iteration ==1)
        fighandle = figure;
        hold on
    end
    if (vccheck==0)
        fprintf('%d \t %e \n', iteration, Linf);
        plot(iteration,Linf,'b-',iteration,Linf, 'r.')
        hold on
    end
end
close (fighandle);

%plot solutions
figure
[X,Y]=meshgrid(x,y);
clevel=[0 1 1.012 1.035 1.058 1.082 1.105 1.128 1.152 1.175 1.198 1.222
1.245 1.268 1.291 1.315 1.338 1.361 1.385 1.408 1.431 3];
contourf(X',Y',v,clevel)
colorbar
axis([-1.2 1.2 -0.8 1.8])
xlabel ('x across half channel / half land ','FontSize', 12)
ylabel ('y (through the GDL)' ,'FontSize', 12)
zlabel('v(x,y)')
title('H2O vapour conc. through the Cathode GDL','FontSize', 18)
hold on
yi=[0:0.1:1];
xi=zeros(length(yi));
plot (xi,yi,'black')

%print djpeg figures chap4 etc etc

% save data to file
version = 0;
version = version +1;
filename = ['GDL_model_8_2_H2OConc_' num2str(version)];
save (filename)
```

```
%%%%%%%%%%%%%%%%%%

% Calculate the water vapour saturation
% and the 'S' variable form eqn 4.4  (NB wrong, its eqn 8-165 and eqns

%%%%%%
%thermodynamic 'lookup tabel' (aka 'steam table') calculations
%based on 80 deg c (353Kelvin)
%%%%%%

for i=1:nx
    for j=1:ny
        term1 = 710.0/((2.0*T(i,j))+353.0);
        term2 = (7.87e-2)*T(i,j);
        term3 = (5.28e-4)*(T(i,j)^2);
        term4 = (2.65e-6)*(T(i,j)^3);

        vsat(i,j) = term1*(exp((-0.869+term2 - term3 +term4)));
        S(i,j) = (v(i,j)-vsat(i,j))/vsat(i,j);
    end
end

% plot the solutions

figure
[X,Y]=meshgrid(x,y);
clevel = [-1 0 0.045 0.07 0.105 0.134 0.167 0.2 0.233 0.266 0.299 0.332
0.365 0.397 0.43 0.463 0.496 0.529 0.562 0.595 0.628 0.661 0.694 0.711 1.0];

contourf(X',Y',S,clevel)
colorbar
axis([-1.2 1.2 -0.8 1.8])
xlabel ('x across half channel / half land ','FontSize', 12)
ylabel ('y (through the GDL)' ,'FontSize', 12)
zlabel ('S(v,T)')
title('H2O saturation through the Cathode GDL','FontSize', 18)
hold on
yi=[0:0.1:1];
xi=zeros(length(yi));
plot(xi,yi,'black')

 %print -djpeg figures\chap4\saturation4


% save data to file
version = 0;
version = version +1;
filename = ['GDL_model_8_2_H2OConc_' num2str(version)];
save (filename)

%%%%%%%%%%%%%%%%%%
```

```
%%%%%%%%%%%%%%%%%%%%%%%%%%%%%%%%%%%%%%%%%%%%%

% EG 9_1 - Modelling catalyst layers

%model only valid up to 1.2 Amps load


Deff_O2_H_Nafion = 4e-15; % effective oxygen diffusivity in nafion times
henrys law constant
c_ref_H2 = 1.2e3; %mol per m^3)
c_ref_O2 = c_ref_H2/2;  %mol per m^3)
%%%%%%%%%%%%%%%%%%%%%%%%%%%%

% handling inhomegnous reactions

%

% Paramaters

A=11.34                       % Area of the FCCA test cell
F = 96487;                    % Faradays constant
R = 8.31434;                  % Ideal gas constant
R2 = 83.1434;                 % ideal gas constant
T = 333.15;                   % Temp (K)
Tc = T-273.15;                % Temp (C)
 Psi_O2_agg = 1.5e-11     % O2 permeation in agglomerates (= -
4*(pi)*n*F*R*Deff_O2*Cs_O2) from wang etal in Yang * P t chumani
                                %  in the chapter  "transport and
                                %  electrochemical phenomena" in Fuel cell
                                %  technology: reaching towards
                                %  commercialisation by N.Sammes (ed)

Psi_H2_agg =2e-11;       % H2 permeation in agglomerates
R_agg_an = 110e-5;            % agglomerate radius in anode
R_agg_cat = 110e-5;           % agglomerate radius in cathode
P_gas=1.5;                      % total gas pressure (atm)
P_H2 = 1.5;                     % hydrogen pressure (atm)
P_air = 1.5;                    % air pressure (atm)
S=0.6e-12;                    % Saturation (pressure)
x_O2_g =0.21;                 % mole fraction of O2 in the air-gas phase
x_H2_g = 1;                   % mole fraction of H2 in the H2 phase
alpha_a = 1;                  % anode transfer coef
alpha_c = 0.9;                % cathode transfer coef
R_ohm = 0.02;                 % constant ohmic resistance (ohm-cm^2)
il = 1.4;                     % limiting current density (re-calaualet for
FCCA?)
k = 1.1;                      % mass transport constant
Alpha_1 = 0.085;              % amplification constant (aka the fudge
factor...)
Gf_liq = -228170;             % Gibbs function in liquid form (J/mol)
for a120 =500:1125:5000                % electrode specific interfacial
area (1/cm)  - cyclovoltemtry for my MEAs?
volt = 0.14:0.00675:0.9567;    % voltage steps - edited to match experiment
i = 0:0.0021:0.252;              % current steps -A/cm2, 1.2 is maximum
                   % A.cm^2
Rcl=20e-3;
E0=0.875;
Ec1=Rcl.*i.^0.419;
Ec2=Rcl.*i.^0.581;
```

```
%%%%%%%%%%%%%%%%%%%%%%%%%%%%%%%%%%%%%%%%%%%%%

% Calculate partial pressures

% Calculate saturation pressure of water (steady state
% evaporation/condensation pressure at the given temperature)

x = -2.17994 + 0.02953.*Tc - 9.1837.*(10^-5).*(Tc.^2) + 1.4454.*(10^-
7).*(Tc.^3);

P_H2O = (10.^x); % sloved by taking the log value of x)

% partial Presure of H2

pp_H2 = 0.5.*((P_H2)./(exp(1.653.*i./(T.^1.334)))-P_H2O);

% partial presure of O2

pp_O2 = (P_air./exp(4.192.*i/(T.^1.334)))-P_H2O;

%%%%%%%%%%%%%%%%%%%%%%%%%%%%%%%%%%%%%%%%%%%%%%

% Reaction 1: H2O(liquid) generation

% exchange current density - from Butler volmer

i_orr = 1.0e-7.*exp((73269./R).*((1./303)-(1./T)));  % NB is thsi right ?
give i_oprr at e-6, and shoudl be e-3?close all


% kinetic portion of thiele modulus

k_O2 = a120.*i_orr./(4*F).*exp(((-alpha_c.*F)./(R.*T)).*(Ec1-Ec2-volt));

% Thiele modulus

phi_O2 = R_agg_cat.*sqrt(k_O2./Psi_O2_agg);

% effectiveness factor (as a result of mass transfer and reaction)

E_O2 = 3./phi_O2.^2.*(phi_O2./tanh(phi_O2)-1); % = original code

% E_O2 = (1./(3.*phi_O2.^2)).*(3.*phi_O2.*(coth(3.*phi_O2))-1); %= original
working out in text

% reaction rate of liquid water at cathode catalyst layers

rate_rx_H2Ol = k_O2.*x_O2_g.* P_gas .*(1-S).*E_O2;

%%%%%%%%%%%%%%%%%%%%%%%%%%%%%%%%%%%%%%%%%%%%

% Reaction 2:   Hydrogen oxidation

% Exchange current density (A/cm^2)
```

```
i_hor = 1e-3.*exp((9500./R).*((1./303)-(1./T)));

% kinetic portion o f thiele modulus


k_h = a120.*i_hor./(2.*F).*exp((alpha_a*F)./(R.*T).*volt);

% Thiele modulus

phi_H2 = R_agg_an.*sqrt(k_h./Psi_H2_agg);

% effectiveness factor due to mass transfer & reaction

E_H2 = 3./phi_H2.^2.*(phi_H2./tanh(phi_H2)-1);

i_h = exp(-(alpha_c.*F)./(R.*T).*volt)./exp((alpha_a.*F)./(R.*T).*volt);

% reaction rate of hydrogen  at anode catalyst layer

rate_rx_H2 = k_h.*(x_H2_g.*P_gas-i_h).*(1-S).*E_H2;

%%%%%%%%%%%%%%%%%%%%%%%%%%%%%%%%%%%%%%%%%%%%%%%%%%%%%%%%%%%%%%%%

% Calculate activation losses (Butler volmer method)

%activation loss (anode)

V_act_anode = ((R.*T)./((alpha_a + alpha_c).*F)).*log(i./(i_hor.*a120.*(1-
S).*(x_H2_g.*P_gas)));

% activation loss (cathode)

V_act_cathode = log(i./(-a120.*(1-S).*i_orr.*(x_O2_g.*P_gas)))*((R.*T)./(-
alpha_c.*F));

%total activation losses

V_act = V_act_anode + V_act_cathode;

% ohmic Losses
V_ohmic = -(i.*R_ohm);

% mass transport losses

term = (1-(i./il));
if term >0
    V_mass = Alpha_1.*(i.^k).*log(1-(i./il));
else
    V_mass = 0;
end

% Nernst voltage loss (equilibrium voltage - shouldn't really be used to
model systems with flowing current...)

E_nernst = -Gf_liq./(2.*F)-
((R.*T).*log(P_H2O./(pp_H2.*(pp_O2.^0.5)))./(2.*F);
```

```
% actual output voltage

V_out = E_nernst + V_ohmic  + V_act + V_mass;

if term <0
    V_mass = 0;
end
if V_out < 0
V_out = 0;
end

%plot Current Vs effectiveness factor

figure1 = figure ('color',[1 1 1]);

hdlp = plot(i , E_O2, i, E_H2);

title ('Cell Current Vs. Effectivenss Factor', 'FontSize', 18)
xlabel ('Cell Current (A/cm^2)','FontSize',12)
ylabel('Effectivenss Factor','FontSize',12)

set (hdlp,'lineWidth',1.5);
legend('Eff-O2','Eff-H2')

% axis ([0 1.4 0 0.7])
grid on;

%plot Current Vs Voltage (cell)

figure2 = figure ('color',[1 1 1]);
hdlp = plot(i,V_act);

title ('Cell Current (activation loss) Vs. Voltage', 'FontSize', 18)
xlabel ('Cell Current (A/cm^2)','FontSize',12)
ylabel('Voltage (volts)','FontSize',12)

set (hdlp,'lineWidth',1.5);

grid on;

% plot polarisation curve

figure3 = figure ('color',[1 1 1]);
hdlp = plot(i,V_out);

title ('Cell Current Vs. Voltage', 'FontSize', 18)
xlabel ('Cell Current (A/cm^2)','FontSize',12)
ylabel('Voltage (volts)','FontSize',12)

set (hdlp,'lineWidth',1.5);

grid on;



% plot flux density of hydrogen
```

```
figure4 = figure ('color',[1 1 1]);
hdlp = plot(i,rate_rx_H2);

title ('Superficial flux density of H2', 'FontSize', 18)
xlabel ('Cell Current (A/cm^2)','FontSize',12)
ylabel('Flux Density H2 (mol/cm^2 . s)','FontSize',12)

set (hdlp,'lineWidth',1.5);

grid on;


end
```

Appendix 3: - Original Data

Matlab Code for polarisation curve creation, and gradient of curve fitting

open_csv_files_1.m

```
%Creates 'structure' Array
CSVFiles = dir('*.CSV');
numfiles = length(CSVFiles);
mydata = cell(1, numfiles);

for k = 1:numfiles
  mydata{k} = xlsread(CSVFiles(k).name);
end

display 'finished'
```

Current_density_array4.m

```
 %%%%%%%%%%%%%%%
curve fitting for polarisaitn data generated by IE FCCA and then 'filtered'
through the 'Current_density_array4' matlab prgraame


    % run 'open_csv_files_1'

    %then run this file
%%%%%%%%%%%%%%%



    %A = active Area of GDL in cm^2
    %Pol = Current/voltage data
    %T=fuel cell test data file names
    %X = all AMPs measured data foem files
    %Y = all VOLTS measured data from files
    %c = count of files
    %fit =  GRA-Hong commands
    %k = iterative step
    %l = length of x
    %m= a number
    %mydata = all data files from analysis
    %n = numberfo files (differs for C how???)
    %normresid = curve fitting function
    %numfiles= number of files (cf 'c')
    %p=  a number
    %resids = curve  fitting function
    %x = last plot x data (A/cm^2)
    %y = last plot y data (V)
    %t=average temp during test

 for c=1:length(mydata);%each column in mydata
       A=11.64;
    Y(1:length(mydata{1,c}(:,2)),c)=mydata{1,c}(:,2);
    X(1:length(mydata{1,c}(:,3)),c)=mydata{1,c}(:,3)/A;
    Pol=[mydata{1,c}(:,3)/A,mydata{1,c}(:,2)];
    %%%%%%%%%%%%%%this next!!!----->>>
temp(1:length(mydata{1,c}(:2)=mydata{1,c}(:4);
    %%
```

```
    %****NEXT STEP TO CREATE POLARISATION PLOT****
    l=0; % l measures the start point of the last step change
    m=1; % m measures the number of times the current density steps
        for n=1:length(Pol)-1 % Steps through every value

            if Pol(n,1)<Pol(n+1,1)-0.02 %Threshold to determine 'step'
chnage in Amps
                mean_pol(m,1)=mean(Pol((l+1):n,1)); %Mean current between
last steps
                mean_pol(m,2)=mean(Pol((l+1):n,2)); %Mean voltage between
steps
                l=n; % Records point of step change in array for next
iteration
                m=m+1; % Records number of steps
            end
        end

        if m==1
            fprintf('Failed to read %6.2f \n',c);
            figure
        else
           % addding trend line, using the mean_pol data
           p = polyfit(mean_pol(:,1),mean_pol(:,2),3);
            x=linspace(min(mean_pol(:,1)),max(mean_pol(:,1)),100);
            y = polyval(p,x);

            %%


            %Plotting the mean pol data, trend line and tri-part gradients
together



            figure
            subplot(2,1,1)
            plot(mean_pol(:,1),mean_pol(:,2),'o',x,y)
            axis([0 0.9 0 1.2])
            xlabel('Current Density [A/cm^2]')
            ylabel('Cell voltage [V]')


            %get plot title from file Name
            T=getfield(CSVFiles(c,1),'name');
            title(T)
            %***NOTE - TITLE seqience to be checked! failed reading
disrputs sequience


        end

            hold on



try
```

```
    %stage 1 - find the gradient of the acitavion part of the polarisation
curve

    % Find x values for plotting the fit based on xlim
    axesLimits1 = xlim;


    xplot3 = linspace (x(1), x(20));
    %xplot1 = linspace(axesLimits1(1), axesLimits1(2));


     % Find coefficients for polynomial (order = 1) - Activation Losses
    fitResults3 = polyfit(x(1:20), y(1:20),1);
    % Evaluate polynomial
    yplot3 = polyval(fitResults3, xplot3);


    % Plot the fit
    fitLine3 = plot(xplot3,yplot3, 'g x','LineWidth',2);
    gA = fitResults3(1); %Gradientof fitted line for catalytic activation
losses



    % Plot the fit
    fitLine3 = plot(xplot3,yplot3, 'k --','LineWidth',2);
    gA = fitResults3(1); %Gradientof fitted line for catalytic activation
losses
    text (0.1, 1, num2str(gA)) % displays gradient of ohmic loss on the
chart

    text (0.1, 0.925, 'activation loss')


    l1=0; %l measures start point of last step change
    m1=1; % m measures number of times 'length-s' changes

    for n1=1:length(x)-1 %for every value of 'x'
               %%% need to iterate to find  'max(RSQyM)'

            % Find x values for plotting the fit based on xlim
            axesLimits1 = xlim;
            xplot1 = linspace (x(length(x)-n1), x(length(x))); %NB let n=25
to test code


            % Find coefficients for polynomial (order = 1) - Mass Losses
            fitResults1 = polyfit(x(length(x)-n1:length(x)), y(length(y)-
n1:length(y)),1);
            % Evaluate polynomial
            yplot1 = polyval(fitResults1, xplot1);

            %Find Coef of determination (R^2) as R^2= 1-SSresid/SStot
            yM = y(length(y)-n1:length(y));
            yresid = yM - xplot1(length(xplot1)-n1:length(xplot1));
            SSresid = sum(yresid.^2);
```

```
            SStot = (length(yM)-1*var(yM));
            RSQyM(n1) = 1-SSresid/SStot;
        end

    % having found maximum r^2, we now plot the fit line again, but this
time record the data on the plot
        [Y,n1] = max(RSQyM);

        % Find x values for plotting the fit based on xlim
    axesLimits1 = xlim;
    xplot1 = linspace (x(length(x)-n1), x(length(x))); %NB let n=25 to test
code


    % Find coefficients for polynomial (order = 1) - Mass Losses
    fitResults1 = polyfit(x(length(x)-n1:length(x)), y(length(y)-
n1:length(y)),1);
    % Evaluate polynomial
    yplot1 = polyval(fitResults1, xplot1);

    %Find Coef of determination (R^2) as R^2= 1-SSresid/SStot
    yM = y(length(y)-n1:length(y));
    yresid = yM - xplot1(length(xplot1)-n1:length(xplot1));
    SSresid = sum(yresid.^2);
    SStot = (length(yM)-1*var(yM));
    RSQyM(n1) = 1-SSresid/SStot;

    % Plot the fit
    fitLine1 = plot(xplot1,yplot1, 'r --','LineWidth',2);
    gM = fitResults1(1); %Gradientof fitted line for mass transport losses
    text (0.65, 0.375, num2str(gM)) % displays gradient of mass loss on the
chart
    text (0.65, 0.3, 'mass loss')



    %%

    axesLimits1 = xlim;
    xplot2 = linspace (x(25), x(length(x)-(n1+1)));
    %xplot1 = linspace(axesLimits1(1), axesLimits1(2));

     % Find coefficients for polynomial (order = 1) - Activation Losses
    fitResults2 =  polyfit(x(25:(length(x)-n1+1)), y(25:(length(y)-
n1+1)),1);
    % Evaluate polynomial
    yplot2 = polyval(fitResults2, xplot2);



    % Plot the fit
    fitLine2 = plot(xplot2,yplot2, 'm --','LineWidth',2);
    gO = fitResults2(1); %Gradient of fitted line for Ohmic losses
    text (0.4, 0.875, num2str(gO)) % displays gradient of ohmic loss on the
chart
    text (0.4, 0.8, 'ohmic loss')

catch
```

```
    %Create I/A Polarisation array from loaded workspace structure
    clear mean_pol
    c=c+1;


end
pow=x.*y;
            Wmax=max(pow);
            subplot(2,1,2)
            plot(x, pow)
            axis([0 0.9 0 0.6])
            xlabel('Current Density [A/cm^2]')
            ylabel('Power Density [W/cm^2]')


            text (0.4, 0.2, num2str(Wmax)) % displays peak power on the
chart

            text (0.4, 0.15, 'W/cm^2 at Peak Power')

            Tbar=mean(mydata{1,c}(:,4));
            Tmax=max(mydata{1,c}(:,4));


            text (0.3, 0.5, num2str(Tbar)) % displays mean temp on the
chart
            text (0.3, 0.45, 'T mean(^oC)')

            text (0.5, 0.5, num2str(Tmax)) % displays max temp on the chart
            text (0.5, 0.45, 'T max(^oC)')

%% need to rename files (eg to reflect 9 vs 09)
      Grad(c).Sample_ID = T;
      Grad(c).gA = gA;
      Grad(c).gO = gO;
      Grad(c).gM = gM;
      Grad(c).Tbar = Tbar;
      Grad(c).Tmax = Tmax;
      Grad(c).Current = x;
      Grad(c).Volts = y;
      Grad(c).Watts = pow;
      Grad(c).FCCA = str2num(T(5));
      Grad(c).Cell_Number = str2num(T(11));
      Grad(c).Aek_ID = str2num(T(17:18));
      %% this section adds in the month and day, assuming year is 201'X'
      Grad(c).month = str2num(T((findstr(T,'201')+4):(findstr(T,'201')+5)));
      Grad(c).day = str2num(T((findstr(T,'201')+6):(findstr(T,'201')+7)));




%Create I/A Polarisation array from loaded workspace structure
    clear mean_pol
    c=c+1;

 end
```

AeK & NMcC results (included and excluded)

random order	std order	T bar	Tmax	T amb	RH% amb	T dewpoint	PTFEwt%	Thickness	H2O angle	Mean pore sz	% porosity	FCCA	Cell#	MPL?	Structure	Supplier	gA	gO	gM	Wmax
26	1	65.93592232	67.2	20	78	16		185	96	769	64.9	2	4	yes	felt	E-Tek	-0.4967	-0.32539	-0.32539	0.41184
25	2	67.26168224	70.2	20	78	16	0.125	260	116	2998	60.2	2	3	yes	paper	Ballard	-0.70605	-0.57405	-0.57405	0.291079
120	3	71.99446494	74.1	6	86	4		370	120	1717	61.8	1	1	no	paper	Toray	-0.95484	-0.81947	-0.81947	0.232571
87	4	70.88235294	72.9	20	68	13		370	120	1717	61.8	1	1	no	paper	Toray	-0.74987	-0.60598	-0.60598	0.271828
35	5	71.78850174	73.6	18	68	11	0.125	210	116	859	44.8	2	2	yes	paper	Ballard	-1.07546	-0.55971	-0.55971	0.292917
123	6	69.04084507	70.2	8	79	5		280	138	3324	67.2	2	3	no	paper	Toray	-0.73623	-0.45697	-0.45697	0.259089
16	7	69.42	69.5	12	88	11		275	90	1055	31.8	1	2	yes	woven	E-Tek	-0.60181	-0.41027	-0.41027	0.356796
126	8	67.29836601	68.1	8	79	5		190	129	2631	63.1	1	4	no	paper	Toray	-0.85836	-0.75685	-0.75685	0.271305
41	9	69.33354037	71.2	18	68	11	0	250	61	1148	46.2	1	1	yes	felt	Freudenberg	-0.60076	-0.3242	-0.3242	0.407627
112	10	70.26109091	72.4	10	78	6	0	320	79	1631	71	1	3	no	woven	Tennex toho	-0.95318	-0.59866	-0.59866	0.226989
71	11	68.06521739	69.1	18	63	10	0.2	315	134	1593	40.8	2	2	yes	paper	Sigracet	-0.89463	-0.59714	-0.59714	0.298892
59	12	68.71263158	70	15	81	12	0.05	235	104	2450	40	2	3	yes	paper	Sigracet	-0.65247	-0.38796	-0.38796	0.355034
5	13	66.86724138	68.3	12	88	11		185	96	769	64.9	2	1	yes	felt	E-Tek	-0.62379	-0.42522	-0.42522	0.352303
4	14	62.36903226	64.1	14	86	11		275	90	1055	31.8	1	2	yes	woven	E-Tek	-0.6757	-0.5019	-0.5019	0.331536
118	15	71.55501859	73.1	6	86	4		280	138	3324	67.2	2	2	no	paper	Toray	-1.05484	-0.76863	-0.76863	0.236122
21	16	69.57110266	71.8	20	78	16	0	250	121	658	49.2	2	1	yes	felt	Freudenberg	-0.69993	-0.37941	-0.37941	0.337575
44	17	70.98960573	72.9	18	68	11	0	250	121	658	49.2	1	2	yes	felt	Freudenberg	-0.62048	-0.43682	-0.43682	0.360479
111	18	70.58055556	71.9	10	78	6	0	320	79	1631	71	1	3	no	woven	Tennex toho	-0.9654	-0.72827	-0.72827	0.226125
37	19	70.4537037	72	18	68	11	0	230	122	682	47	2	3	yes	felt	Freudenberg	-0.69788	-0.3504	-0.3504	0.371907
40	20	70.99429077	72.8	18	78	14			121	658	49.2	1	1	no	felt	Freudenberg	-0.63926	-0.35496	-0.35496	0.34664
78	21	67.81058394	70.2	18	63	10	0.05	420	122	2919	34.6	1	2	yes	paper	Sigracet	-0.54941	-0.43046	-0.43046	0.377988
69	22	68.47625418	69.5	18	72	12	0.2	315	123	1593	40.8	2	1	yes	paper	Sigracet	-0.79866	-0.60063	-0.60063	0.290312
101	23	73.95754717	75.2	10	78	6	0	266	126	2291	66.9	2	1	no	woven	Tennex toho	-0.73474	-0.64423	-0.64423	0.24465
125	24	66.59223301	67	8	79	5		190	129	2631	63.1	1	4	no	paper	Toray	-0.77224	-0.55642	-0.55642	0.296435
57	25	66.54594595	67.4	15	81	12	0.125	260	116	2998	60.2	2	2	yes	paper	Ballard	-0.91424	-0.57862	-0.57862	0.290152
117	26	71.03404255	72.1	6	86	4		280	138	3324	67.2	2	2	no	paper	Toray	-0.95568	-0.60779	-0.60779	0.257372
103	27	69.21326531	70.3	10	78	6	0.05	190		1705	66.2	2	2	no	paper	Sigracet	-0.88271	-0.68253	-0.68253	0.273462
13	28	70.01982759	71.7	12	88	11	0.05	235	112	842	36.5	1	1	yes		Sigracet	-0.56238	-0.3275	-0.3275	0.390078
8	29	69.275	70.8	12	88	11	0.05	235	104	2450	40	2	2	yes	paper	Sigracet	-0.7428	-0.35287	-0.35287	0.3764
79	30	70.4503876	71.5	18	70	12	0.125	260	116	2998	60.2	1	4	yes	paper	Ballard	-0.72727	-0.60125	-0.60125	0.308091
85	31	70.70029499	72.8	18	70	12			121	658	49.2	2	3	no	felt		-0.77761	-0.55131	-0.55131	0.320475
96	32	70.77003155	72.9	18	69	12	0.125	170	111	993	48.7	2	1	no		Ballard	-0.81283	-0.5245	-0.5245	0.305078
47	33	69.46846847	70.7	18	77	13	0	250	61	1148	46.2	2	1	yes	felt	Freudenberg	-0.46157	-0.33684	-0.33684	0.438713
46	34	70.44765101	72.2	18	68	11	0.125	180	114	1528	44.9	1	4	no	paper	Ballard	-1.08014	-0.552	-0.552	0.295196
38	35	71.69398496	74.2	18	68	11	0	230	122	682	47	2	3	yes	felt	Freudenberg	-0.61239	-0.3306	-0.3306	0.378642
114	36	66.03444444	66.4	6	91	4	0.05	300	123	2469	70.5	1	4	no	paper	Sigracet	-0.72914	-0.7271	-0.7271	0.240351
122	37	71.47086331	72.8	6	86	4		370	120	1717	61.8	1	2	no	paper	Toray	-1.00524	-0.92121	-0.92121	0.227683
1	38	68.57354086	71.1	14	86	11	0	250	121	658	49.2	2	1	yes	felt	Freudenberg	-0.69745	-0.47636	-0.47636	0.311354
83	39	70.69935275	72.8	20	68	13			121	658	49.2	2	2	no	felt		-0.75649	-0.38322	-0.38322	0.357601
28	40	68.98690476	71.5	20	78	16	0	230	122	682	47	1	1	yes	felt	Freudenberg	-0.75647	-0.54786	-0.54786	0.315333
119	41	72.09961538	73.8	6	86	4		370	120	1717	61.8	1	1	no	paper	Toray	-0.92658	-0.62114	-0.62114	0.250117
86	42	70.68	72.2	20	68	13		370	120	1717	61.8	1	1	no	paper	Toray	-0.66717	-0.50242	-0.50242	0.292309
36	43	71.88648649	72.8	18	68	11	0.125	210	116	859	44.8	2	2	yes	paper	Ballard	-0.82607	-0.53232	-0.53232	0.312744
56	44	64.49265734	67	16	71	11	0.05	235	112	842	36.5	2	1	yes	paper	Sigracet	-0.62722	-0.39207	-0.39207	0.368751
94	45	70.77003155	72.9	18	69	12	0.125	170	111	993	48.7	2	1	no		Ballard	-0.90476	-0.5245	-0.5245	0.305078
108	46	69.86569343	72.6	10	78	6	0.05	190	98	2208	73	1	1	no	paper	Sigracet	-0.58807	-0.59653	-0.59653	0.288869
23	47	68.27670251	70.6	20	78	16	0.05	315	126	2197	47.5	2	2	yes	paper	Sigracet	-0.77625	-0.49554	-0.49554	0.328364
10	48	70.32038835	71.8	12	88	11	0.05	315	126	2197	47.5	2	3	yes	paper	Sigracet	-0.57458	-0.3657	-0.3657	0.379998
124	49	66.20334572	67.1	8	79	5		280	138	3324	67.2	2	3	no	paper	Toray	-0.93454	-0.45036	-0.45036	0.249951
65	50	68.55090253	70.9	15	81	12	0.05	420	122	2919	34.6	1	4	yes	paper	Sigracet	-0.61822	-0.41138	-0.41138	0.348455
58	51	66.65234657	68.2	15	81	12	0.125	260	116	2998	60.2	2	2	yes	paper	Ballard	-0.83795	-0.58385	-0.58385	0.290489
63	52	66.91650485	68	15	81	12	0	235				1	2	yes		Sigracet	-0.83534	-0.6838	-0.6838	0.284018
116	53	67.0637037	68.9	6	86	4		190	129	2631	63.1	2	1	no	paper	Toray	-1.07529	-1.00169	-1.00169	0.203241
50	54	69.52722222	71.4	18	77	13	0	250	117	158	61	2	2	yes	felt	Freudenberg	-0.77452	-0.46508	-0.46508	0.299482
24	55	66.65	69.8	20	78	16	0.125	260	116	2998	60.2	2	3	yes	paper	Ballard	-0.83792	-0.69927	-0.69927	0.272239
105	56	70.71188119	71.9	10	78	6		110	133	2625	64.6	2	3	no	paper	Toray	-0.89042	-0.65616	-0.65616	0.270484
55	57	64.02043796	65.4	16	71	11	0.05	235	112	842	36.5	2	1	yes	paper	Sigracet	-0.58413	-0.35998	-0.35998	0.375896
31	58	69.51858407	70.4	20	78	16	0.125	170	111	993	48.7	1	4	no	paper	Ballard	-0.7876	-0.55547	-0.55547	0.301367
64	59	67.16176471	68.8	15	81	12	0	235				1	2	yes		Sigracet	-0.74172	-0.55956	-0.55956	0.289036
27	60	69.10188088	70.8	20	78	16	0	230	122	682	47	1	1	yes	felt	Freudenberg	-0.60755	-0.45944	-0.45944	0.34663
15	61	70.27272727	71.5	12	88	11		275	90	1055	31.8	1	2	yes	woven	E-Tek	-0.60181	-0.41027	-0.41027	0.356796
80	62	70.56814815	72.5	18	70	12	0.125	260	116	2998	60.2	1	4	yes	paper	Ballard	-0.84753	-0.66126	-0.66126	0.292236
67	63	70.41002865	72.6	18	72	12	0.05	420	122	2919	34.6	1	4	yes	paper	Sigracet	-0.78464	-0.41822	-0.41822	0.318525
30	64	70.71693122	72.9	20	78	16	0	250	117	158	61	1	2	yes	felt	Freudenberg	-0.4	-1.70798	-0.40018	0.309215
89	65	69.74067797	71.8	20	68	13		190	129	2631	63.1	1	2	no	paper	Toray	-4.46875	-0.11149	-3.78125	0.262493
92	66	69.60098039	70.8	18	69	12	0.125		107	2074	62.4	1	4	no	paper	Ballard	-0.63534	-0.44332	-0.44332	0.352449
51	67	69.30197628	70.7	18	77	13	0	250	61	1148	46.2	1	1	yes	felt	Freudenberg	-0.59725	-0.49349	-0.49349	0.355679
90	68	66.0887931	67	18	69	12	0.125	180	114	1528	44.9	1	2	no	paper		-0.72366	-0.69013	-0.69013	0.254484
61	69	70.51442308	71.8	16	71	11	0.05	325	118	2469	70.5	1	1	yes	paper	Sigracet	-0.62026	-0.45014	-0.45014	0.310196
49	70	68.94031008	69.9	18	77	13	0	250	117	158	61	2	2	yes	felt	Freudenberg	-0.85655	-0.4913	-0.4913	0.297628
52	71	69.7	72.3	18	77	13	0	250	61	1148	46.2	1	1	yes	felt	Freudenberg	-0.83104	-0.40297	-0.40297	0.316283
33	72	72.07575758	73.4	18	68	11	0.05	235	112	842	36.5	2	1	yes		Sigracet	-0.57964	-0.36922	-0.36922	0.393123
98	73	65.73728814	67.4	18	69	12		280	138	3324	67.2	2	2	no	paper	Toray	-1.07403	-0.8423	-0.8423	0.231224
100	74	70.18981132	72.3	18	69	12	0	356	68	3401	64.9	2	3	no	woven	Ballard	-0.8081	-0.56092	-0.56092	0.277946
48	75	66.9095941	68.2	18	77	13	0	250	61	1148	46.2	2	1	yes	felt	Freudenberg	-0.55301	-0.3594	-0.3594	0.403485
62	76	70.65248227	72.8	16	71	11	0.05	325	118	2469	70.5	1	1	yes	paper	Sigracet	-0.61106	-0.47629	-0.47629	0.303239
34	77	72	74.4	18	68	11	0.05	235	112	842	36.5	2	1	yes		Sigracet	-0.55602	-0.3739	-0.3739	0.383323
104	78	69.41967213	71.3	10	78	6	0.05	190		1705	66.2	2	2	no	paper	Sigracet	-0.89896	-0.69695	-0.69695	0.264169
19	79	71.42031662	75.2	20	61	12						1	4	yes			-0.5984	-0.47313	-0.47313	0.361817
17	80	64.3932387	74.1	20	61	12		275	90	1055	31.8	1	2	yes	woven	E-Tek	-0.74742	-0.33419	-0.33419	0.32824
11	81	69.11358491	70.7	20	61	12	0.125	210	116	859	44.8	2	4	yes	paper	Ballard	-0.78529	-0.44551	-0.44551	0.300323
29	82	70.08931298	71.5	20	78	16	0	250	117	158	61	1	2	yes	felt	Freudenberg	-0.64914	-0.41736	-0.41736	0.372647
39	83	71.24619718	73.9	18	78	14			121	658	49.2	1	1	no	felt	Freudenberg	-0.71393	-0.39285	-0.39285	0.328033
14	84	69.19577465	73.7	20	61	12	0.05	235	112	842	36.5	1	1	yes		Sigracet	-0.56215	-0.42927	-0.42927	0.375815
81	85	67.5578125	69.6	20	68	13						2	1	no			-2.57143	-0.5	-1.28571	0.342986
6	86	70.36215485	74.3	20	61	12		185	96	769	64.9	2	1	yes	felt	E-Tek	-0.4828	-0.55766	-0.55766	0.321892
66	87	68.66779661	69.8	15	81	12	0.05	420	122	2919	34.6	1	4	yes	paper	Sigracet	-0.63168	-0.41526	-0.41526	0.351207
18	88	70.55762712	71.7	12	88	11						1	4	yes			-0.62365	-0.41939	-0.41939	0.378449
76	89	70.53804348	73.2	18	63	10	0.05	325	118	2469	70.5	1	1	yes	paper	Sigracet	-0.51205	-0.40504	-0.40504	0.381586
113	90	68.13653846	68.9	6	91	4	0.05	300	123	2469	70.5	1	4	no	paper	Sigracet	-0.78162	-0.67698	-0.67698	0.254765
12	91	70.57400531	74	20	61	12	0.125	210	116	859	44.8	2	4	yes	paper	Ballard	-0.91963	-0.24503	-0.24503	0.30315
9	92	71.4860523	76.6	20	61	12	0.05	315	126	2197	47.5	2	3	yes	paper	Sigracet	-0.81367	-0.29534	-0.29534	0.348302
121	93	71.29	72.3	6	86	4		370	120	1717	61.8	1	2	no	paper	Toray	-0.81821	-0.75374	-0.75374	0.240992
43	94	70.91333333	72.1	18	68	11	0	250	121	658	49.2	1	2	yes	felt	Freudenberg	-0.60774	-0.43592	-0.43592	0.366334
106	95	70.55899281	72.5	10	78	6		110	133	2625	64.6	2	3	no	paper	Toray	-0.7959	-0.77073	-0.77073	0.263454
68	96	70.13259259	71.4	18	72	12	0.05	420	122	2919	34.6	1	4	yes	paper	Sigracet	-0.71206	-0.41375	-0.41375	0.32905
107	97	69.82692308	71.9	10	78	6	0.05	190	98	2208	73	1	1	no	paper	Sigracet	-0.68873	-0.73495	-0.73495	0.271926
102	98	73.93666667	75.5	10	78	6	0	266	126	2291	66.9	2	1	no	woven	Tennex toho	-0.7836	-0.67668	-0.67668	0.232315
91	99	66.4540146	68.3	18	69	12	0.125	180	114	1528	44.9	1	2	no	paper	Ballard	-0.75797	-0.74179	-0.74179	0.246999
75	100	69.90660377	71.8	18	63	10	0.05	325	118	2469	70.5	1	1	yes	paper	Sigracet	-0.53242	-0.37853	-0.37853	0.382384
74	101	69.27532051	71.9	18	63	10	0.125	210	116	859	44.8	2	3	yes	paper	Ballard	-0.78894	-0.18913	-0.18913	0.375527
53	102	70.68653846	71.9	18	77	13	0	250	117	158	61	1	4	yes	felt	Freudenberg	-0.65644	-0.43645	-0.43645	0.355322
73	103	68.73876404	70.4	18	63	10	0.125	210	116	859	44.8	2	3	yes	paper	Ballard	-0.65194	-0.29007	-0.29007	0.383809
54	104	70.28014706	72.4	18	77	13	0	250	117	158	61	1	4	yes	felt	Freudenberg	-0.59612	-0.48007	-0.48007	0.356794
95	105	70.52121212	71.9	18	69	12	0.125	170	111	993	48.7	2	1	no		Ballard	-0.74805	-0.54364	-0.54364	0.307896
20	106	70.04	71.4	20	78	16	0	250	121	658	49.2	2	1	yes	felt	Freudenberg	-0.72713	-0.43255	-0.43255	0.337341
88	107	69.17980759	70.5	20	68	13		190	129	2631	63.1	1	2	no	paper	Toray	-2.10019	-0.465	-0.465	0.22773
45	108	70.03961039	71	18	68	11	0.125	180	114	1528	44.9	1	4	no	paper	Ballard	-0.89522	-0.36304	-0.36304	0.332117
70	109	69.08284672	70.4	18	72	12	0.2	315	123	1593	40.8	2	1	yes	paper	Sigracet	-0.74853	-0.57945	-0.57945	0.292415
84	110	70.5748992	71.7	18	70	12			121	658	49.2	2	3	no	felt		-0.6499	-0.51141	-0.51141	0.341
97	111	65.14795918	66.2	18	69	12		280	138	3324	67.2	2	2	no	paper	Toray	-1.02541	-0.72818	-0.72818	0.241824
7	112	70.2131744	74	20	61	12	0.05	235	104	2450	40	2	2	yes	paper	Sigracet	-1.10012	-0.09676	-0.09676	0.330883
93	113	69.85481481	72.2	18	69	12	0.125		107	2074	62.4	1	4	no	paper	Ballard	-0.63198	-0.42876	-0.42876	0.349589
60	114	68.72618182	71.3	15	81	12	0.05	235	104	2450	40	2	3	yes	paper	Sigracet	-0.66642	-0.38119	-0.38119	0.355711
109	115	62.55391304	63.5	10	78	6	0.05	400				1	2	no	paper	Sigracet	-0.69197	-0.75673	-0.75673	0.208183
99	116	69.77	71.1	18	69	12	0		68	3401	64.9	2	3	no	woven		-0.72749	-0.56699	-0.56699	0.292696
22	117	65.87536946	69.2	20	78	16	0.05	315	126	2197	47.5	2	2	yes	paper	Sigracet	-0.80132	-0.50274	-0.50274	0.332261
82	118	70.27075472	71.5	20	68	13			121	658	49.2	2	2	no	felt		-0.74142	-0.40035	-0.40035	0.367182
72	119	68.62454212	70	18	63	10	0.2	315	134	1593	40.8	2	2	yes	paper	Sigracet	-0.85931	-0.61827	-0.61827	0.295414
3	120	69.4772766	72.6	14	86	11		275	90	1055	31.8	1	1	yes	woven	E-Tek	-0.60245	-0.47957	-0.47957	0.34452
110	121	63.96183486	65.8	10	78	6	0.05	400				1	2	no	paper	Sigracet	-0.69093	-0.71184	-0.71184	0.209428
2	122	60.3601043	62.9	14	86	11	0.05	315	126	2197	47.5	2	2	yes	paper	Sigracet	-0.86574	-0.54118	-0.54118	0.286431
42	123	70.20298913	72.7	18	68	11	0	250	61	1148	46.2	1	1	yes	felt	Freudenberg	-0.55014	-0.36625	-0.36625	0.383576
32	124	69.21402214	71.7	20	78	16	0.125	170	111	993	48.7	1	4	no	paper	Ballard	-0.75249	-0.52559	-0.52559	0.300912
77	125	68.29363636	69.4	18	63	10	0.05	420	122	2919	34.6	1	2	yes	paper	Sigracet	-0.58151	-0.43146	-0.43146	0.374685
115	126	66.27525773	67.3	6	86	4		190	129	2631	63.1	2	1	no	paper	Toray	-0.98352	-0.88928	-0.88928	0.212169

Initial M-ANoVAR (ManCoVar) results

Activation loss gradient multivariate analysis

The activation loss gradient is analysed for co varying factors in a backward step linear regression model. Note that the following results are taken directly from the Design Expert Pro ® software, as is the text in italics

ANOVA (Man-co-var) *for Response Surface Reduced 2FI Model, Analysis of variance table [Classical sum of squares - Type II]*

	Sum of		Mean	F	p-value	
Source	Squares	df	Square	Value	Prob > F	
Model	1.03942	20	0.05197	7.03990	< 0.0001	significant
A-Tbar	0.02746	1	0.02746	3.71985	0.0593	
B-Tmax	0.03084	1	0.03084	4.17731	0.0461	*
C-Ambient Tbar	0.00346	1	0.00346	0.46804	0.4970	
F-PTFE	0.01851	1	0.01851	2.50713	0.1195	
K-Porosity	0.02410	1	0.02410	3.26397	0.0767	
L-FCCA	0.07176	1	0.07176	9.71983	0.0030	***
M-Cell	0.11299	3	0.03766	5.10171	0.0037	**
N-MPL	0.05119	1	0.05119	6.93397	0.0112	**
P-Supplier	0.20157	3	0.06719	9.10143	< 0.0001	***
AM	0.10680	3	0.03560	4.82210	0.0050	**
BC	0.02169	1	0.02169	2.93817	0.0926	
BK	0.07488	1	0.07488	10.14323	0.0025	**
CL	0.03700	1	0.03700	5.01213	0.0296	**
CN	0.02332	1	0.02332	3.15917	0.0815	
Residual	0.37650	51	0.00738			
Cor Total	1.41593	71				

Table gA Regression

The Model F-value of 7.04 implies the model is significant. There is only a 0.01% chance that a "Model F-Value" this large could occur due to noise. Values of "Prob > F" less than 0.0500 indicate model terms are significant and marked with one or more asterisks (*) depending on their significance Values greater than 0.1000 indicate the model terms are not significant.

Std. Dev.	0.0859208	R-Squared	0.734095
Mean	-0.7282915	Adj R-Squared	0.629819
C.V. %	11.797579	Pred R-Squared	0.492552
PRESS	0.7185088	Adeq Precision	10.94973

Table gA summary

The "Pred R-Squared" of 0.4926 is in reasonable agreement with the "Adj R-Squared" of 0.6298. "Adeq Precision" measures the signal to noise ratio. A ratio greater than 4 is desirable. Your ratio of 10.950 indicates an adequate signal. This model can be used to navigate the design space.

	Coefficient		Standard	95% CI	95% CI		
Term	Estimate	df	Error	Low	High	VIF	sqrtVIF
Intercept	-6.16770	1	3.38592	-12.96523	0.62982		
A-Tbar	-0.03233	1	0.14283	-0.31908	0.25441	18.14981	4.26026
B-Tmax	0.00177	1	0.13856	-0.27639	0.27993	19.17069	4.37843
C-Ambient Tbar	0.00812	1	0.04566	-0.08355	0.09978	4.65255	2.15698
F-PTFE	-5.36992	1	3.39140	-12.17845	1.43861	3.83315	1.95784
K-Porosity	-0.04544	1	0.04120	-0.12815	0.03727	5.10274	2.25893
L-FCCA	0.00973	1	0.02702	-0.04453	0.06398	7.11710	2.66779
M[1]	-0.06865	1	0.03591	-0.14073	0.00344		
M[2]	-0.11575	1	0.02874	-0.17345	-0.05806		
M[3]	-0.01116	1	0.05311	-0.11779	0.09547		
N	-0.01677	1	0.03139	-0.07979	0.04624	6.02090	2.45375
P[1]	0.10839	1	0.02799	0.05221	0.16457		
P[2]	-0.33225	1	0.06670	-0.46616	-0.19834		
P[3]	0.09584	1	0.04171	0.01211	0.17958		
AM[1]	0.16362	1	0.07918	0.00466	0.32259		
AM[2]	0.15614	1	0.06997	0.01566	0.29662		
AM[3]	0.25159	1	0.13615	-0.02175	0.52493		
BC	-0.20319	1	0.11854	-0.44118	0.03479	7.17560	2.67873
BK	0.36380	1	0.11423	0.13448	0.59313	5.44620	2.33371
CL	-0.09107	1	0.04068	-0.17274	-0.00940	8.39792	2.89792
CN	-0.08231	1	0.04631	-0.17527	0.01066	4.96469	2.22816

Table gA regression error assessment

Final Equation in Terms of Coded Factors:

gA	=
-6.16770	
-0.03233	* A
0.00177	* B
0.00812	* C
-5.36992	* F
-0.04544	* K
0.00973	* L
-0.06865	* M[1]
-0.11575	* M[2]
-0.01116	* M[3]
-0.01677	* N
0.10839	* P[1]
-0.33225	* P[2]
0.09584	* P[3]
0.16362	* AM[1]
0.15614	* AM[2]
0.25159	* AM[3]
-0.20319	* BC
0.36380	* BK
-0.09107	* CL
-0.08231	* CN

Table gA coded factors

Ohmic loss gradient multivariate analysis

The Ohmic loss gradient is analysed for co varying factors in a backward step linear regression model.

Note that the following results are taken directly from the Design Expert Pro ® software, as is the text in italics

Note that the following results are taken directly from the Design Expert Pro ® software, as is the text in italics

ANOVA (Man-co-var) for Response Surface Reduced 2FI Model Analysis of variance table [Classical sum of squares - Type II] Stepwise Regression with Alpha to Enter = 0.100, Alpha to Exit = 0.100

Source	Sum of Squares	df	Mean Square	F Value	p-value Prob > F	
Model	1.18	9	0.13	5.25	< 0.0001	significant
D-Ambient RHbar	0.28	1	0.28	11.33	0.0013	***
F-PTFE	0.32	1	0.32	12.97	0.0006	***
K-Porosity	0.13	1	0.13	5.34	0.0242	**
L-FCCA	0.17	1	0.17	6.99	0.0103	**
M-Cell	0.22	3	0.074	2.98	0.0382	**
O-structure	0.2	2	0.098	3.93	0.0248	**
Residual	1.55	62	0.025			
Cor Total	2.72	71				

Table gO regression

The Model F-value of 5.25 implies the model is significant. There is only a 0.01% chance that a "Model F-Value" this large could occur due to noise. Values of "Prob > F" less than 0.0500 indicate model terms are significant. In this case D, F, K, L, M, O are significant model terms. Values greater than 0.1000 indicate the model terms are not significant.

Std. Dev.	0.16	R-Squared	0.4324
Mean	-0.49	Adj R-Squared	0.3501
C.V. %	31.95	Pred R-Squared	0.2527
PRESS	2.03	Adeq Precision	9.317

Table gO summary

The "Pred R-Squared" of 0.2527 is in reasonable agreement with the "Adj R-Squared" of 0.3501. Adeq Precision measures the signal to noise ratio. A ratio greater than 4 is desirable. Your ratio of 9.317 indicates an adequate signal. This model can be used to navigate the design space.

Term	Coefficient Estimate	df	Standard Error	95% CI Low	95% CI High	VIF	sqrtVIF
Intercept	-19.6	1	5.29	-30.18	-9.02		
D-Ambient RHbar	-0.14	1	0.042	-0.22	-0.057	1.26	1.12250
F-PTFE	-19.12	1	5.31	-29.74	-8.51	2.78	1.66733
K-Porosity	-0.093	1	0.04	-0.17	-0.013	1.44	1.20000

L-FCCA	0.064	1	0.024	0.016	0.11	1.68	1.29615
M[1]	0.02	1	0.032	-0.044	0.084		
M[2]	-0.096	1	0.032	-0.16	-0.031		
M[3]	0.023	1	0.042	-0.06	0.11		
O[1]	-0.13	1	0.058	-0.24	-9.80E-03		
O[2]	0.12	1	0.045	0.036	0.21		

Table 1 gO error assessment

Final Equation in Terms of Coded Factors:

gO	=
-19.6	
-0.14	* D
-19.12	* F
-0.093	* K
0.064	* L
0.02	* M[1]
-0.096	* M[2]
0.023	* M[3]
-0.13	* O[1]
0.12	* O[2]

Table gO coded factors

Mass loss gradient multivariate analysis

The mass loss gradient is analysed for co varying factors in a backward step linear regression model. Note that the following results are taken directly from the Design Expert Pro ® software, as is the text in italics

Note that the following results are taken directly from the Design Expert Pro ® software, as is the text in italics

Analysis of variance table [Classical sum of squares – Type II] II]

	Sum of		Mean	F	p-value	
Source	Squares	df	Square	Value	Prob > F	
Model	1.13	31	0.037	14.38	< 0.0001	significant
A-Tbar	1.50E-03	1	1.50E-03	0.59	0.4463	
C-Ambient Tbar	5.27E-03	1	5.27E-03	2.08	0.1575	
D-Ambient RHbar	0.029	1	0.029	11.49	0.0016	***
E-dew point T	1.42E-03	1	1.42E-03	0.56	0.4592	
F-PTFE	7.23E-03	1	7.23E-03	2.85	0.0993	*
G-Thickness	0.028	1	0.028	11.03	0.0019	***
H-H2O contact angle	0.017	1	0.017	6.51	0.0146	**
L-FCCA	0.018	1	0.018	7.01	0.0115	**
M-Cell	0.024	3	7.87E-03	3.1	0.0373	**
N-MPL	8.56E-04	1	8.56E-04	0.34	0.5648	
P-Supplier	0.03	3	9.95E-03	3.92	0.0152	**
AL	2.49E-03	1	2.49E-03	0.98	0.3276	
CD	0.039	1	0.039	15.55	0.0003	****
CH	8.97E-03	1	8.97E-03	3.53	0.0675	
DE	1.92E-03	1	1.92E-03	0.76	0.39	
DL	5.53E-03	1	5.53E-03	2.18	0.1478	
EG	1.72E-03	1	1.72E-03	0.68	0.4156	
EN	3.67E-03	1	3.67E-03	1.44	0.2365	
EP	0.03	2	0.015	5.9	0.0057	***
FN	1.94E-03	1	1.94E-03	0.76	0.3877	
LN	2.58E-04	1	2.58E-04	0.1	0.7517	
MN	9.27E-03	3	3.09E-03	1.22	0.3162	
E^2	3.48E-03	1	3.48E-03	1.37	0.2486	
H^2	0.063	1	0.063	24.88	< 0.0001	***
Residual	0.1	40	2.54E-03			
Cor Total	1.23	71				

Table gM regression

The Model F-value of 14.38 implies the model is significant. There is only a 0.01% chance that a "Model F-Value" this large could occur due to noise. Values of "Prob > F" less than 0.0500 indicate model terms are significant. In this case D, G, H, L, M, P, CD, EP, H++2+- are significant model terms. Values greater than 0.1000 indicate the model terms are not significant.

Std. Dev.	0.05	R-Squared	0.9177
Mean	-0.48	Adj R-Squared	0.8538
C.V. %	10.59	Pred R-Squared	N/A
PRESS	N/A	Adeq Precision	18.76

Table: gM Summary

Case(s) with leverage of 1.0000: Pred R-Squared and PRESS statistic not defined Adeq Precision measures the signal to noise ratio. A ratio greater than 4 is desirable. Your ratio of 18.760 indicates an adequate signal. This model can be used to navigate the design space.

Term	Coefficient Estimate	df	Standard Error	95% CI Low	95% CI High	VIF	sqrt(VIF)
Intercept	42.62	1	55.62	-69.8	155.03		
A-Tbar	0.033	1	0.07	-0.11	0.17	12.54	3.541186
C-Ambient Tbar	-0.21	1	0.17	-0.55	0.14	188.6	13.73317
D-Ambient RHbar	-0.099	1	0.11	-0.33	0.13	93.51	9.670057
E-dew point T	-0.085	1	0.37	-0.83	0.66	864.35	29.39983
F-PTFE	43.37	1	55.95	-69.72	156.46	3032.95	55.07223
G-Thickness	0.1	1	0.11	-0.12	0.32	55.89	7.475961
H-H2O contact angle	-0.027	1	0.1	-0.24	0.18	72.32	8.504117
L-FCCA	0.099	1	0.14	-0.19	0.38	560.58	23.67657
M[1]	0.054	1	0.082	-0.11	0.22		
M[2]	-0.19	1	0.17	-0.52	0.15		
M[3]	0.2	1	0.27	-0.34	0.74		
N	48.11	1	55.22	-63.48	159.71	5.42E+07	7358.668
P[1]	-2.83E-03	1	0.052	-0.11	0.1		
P[2]	-0.11	1	0.23	-0.57	0.35		
P[3]	0.015	1	0.097	-0.18	0.21		
AL	-0.07	1	0.071	-0.21	0.073	25.86	5.085273
CD	-0.38	1	0.096	-0.57	-0.18	30.15	5.490902
CH	-0.27	1	0.14	-0.57	0.021	85.93	9.269844
DE	0.22	1	0.25	-0.29	0.72	72.1	8.491172
DL	-0.05	1	0.034	-0.12	0.019	8.87	2.978255
EG	0.23	1	0.28	-0.34	0.81	68.18	8.257118
EN	0.11	1	0.093	-0.076	0.3	42.83	6.544463
EP[1]	0.25	1	0.14	-0.042	0.53		
EP[2]	-0.5	1	0.17	-0.85	-0.16		
EP[3] ALIASED Intercept, E, P[1], P[2], P[3], EP[1], EP[2]							
FN	48.55	1	55.6	-63.81	160.92	5.43E+07	7366.817
LN	0.041	1	0.13	-0.22	0.3	431.91	20.78244
M[1]N	0.069	1	0.084	-0.1	0.24		
M[2]N	-0.16	1	0.16	-0.49	0.18		
M[3]N	0.16	1	0.27	-0.38	0.71		
E^2	0.27	1	0.23	-0.2	0.74	203.85	14.2776
H^2	-0.32	1	0.064	-0.45	-0.19	7.63	2.762245

Table gM Regression error assessment

Final Equation in Terms of Coded Factors:

gM	=
42.62	
0.033	* A
-0.21	* C
-0.099	* D
-0.085	* E
43.37	* F
0.1	* G
-0.027	* H
0.099	* L
0.054	* M[1]
-0.19	* M[2]
0.2	* M[3]
48.11	* N
-2.83E-03	* P[1]
-0.11	* P[2]
0.015	* P[3]
-0.07	* AL
-0.38	* CD
-0.27	* CH
0.22	* DE
-0.05	* DL
0.23	* EG
0.11	* EN
0.25	* EP[1]
-0.5	* EP[2]
48.55	* FN
0.041	* LN
0.069	* M[1]N
-0.16	* M[2]N
0.16	* M[3]N
0.27	* E^2
-0.32	* H^2

Table: gM coded factors

Maximum Power multivariate analysis

The peak power is analysed for co varying factors in a backward step linear regression model. Note that the following results are taken directly from the Design Expert Pro ® software, as is the text in italics

Note that the following results are taken directly from the Design Expert Pro ® software, as is the text in italics

ANOVA for Response Surface Reduced Quadratic Model Analysis of variance table [Classical sum of squares - Type II]

	Sum of		Mean	F	p-value	
Source	Squares	df	Square	Value	Prob > F	
Model	0.1465	30	0.0049	26.6756	< 0.0001	significant
B-Tmax	0.0001	1	0.0001	0.8130	0.3725	
C-Ambient Tbar	0.0002	1	0.0002	1.0427	0.3132	
D-Ambient RHbar	0.0009	1	0.0009	4.9657	0.0314	*
E-dew point T	0.0005	1	0.0005	2.8026	0.1017	
F-PTFE	0.0129	1	0.0129	70.3322	< 0.0001	****
G-Thickness	0.0011	1	0.0011	6.2108	0.0168	*
H-H2O contact angle	0.0041	1	0.0041	22.2774	< 0.0001	****
K-Porosity	0.0016	1	0.0016	8.8374	0.0049	**
L-FCCA	0.0009	1	0.0009	4.8972	0.0325	*
M-Cell	0.0044	3	0.0015	7.9285	0.0003	**
N-MPL	0.0031	1	0.0031	17.1404	0.0002	***
BK	0.0001	1	0.0001	0.3798	0.5411	
CD	0.0028	1	0.0028	15.0878	0.0004	***
DE	0.0039	1	0.0039	21.4309	< 0.0001	****
DM	0.0075	3	0.0025	13.5996	< 0.0001	****
FN	0.0003	1	0.0003	1.7433	0.1940	
HL	0.0042	1	0.0042	23.1889	< 0.0001	****
HM	0.0028	3	0.0009	5.0343	0.0046	**
KN	0.0010	1	0.0010	5.4022	0.0251	*
LM	0.0021	3	0.0007	3.7561	0.0180	*
B^2	0.0026	1	0.0026	14.2595	0.0005	***
G^2	0.0001	1	0.0001	0.2916	0.5921	
Residual	0.0075	41	0.0002			
Cor Total	0.1540	71				

Table Wmax regression

The Model F-value of 26.68 implies the model is significant. There is only a 0.01% chance that a "Model F-Value" this large could occur due to noise. Values of "Prob > F" less than 0.0500 indicate model terms are significant. In this case D, F, G, H, K, L, M, N, CD, DE, DM, HL, HM, KN, LM, B++2+- are significant model terms. Values greater than 0.1000 indicate the model terms are not significant. If there are many insignificant model terms (not counting those required to support hierarchy), model reduction may improve your model.

Std. Dev.	0.0135		R-Squared	0.9513
Mean	0.3246		Adj R-Squared	0.9156
C.V. %	4.1692		Pred R-Squared	0.8492
PRESS	0.0232		Adeq Precision	22.3670

Table Wmax summary

The "Pred R-Squared" of 0.8492 is in reasonable agreement with the "Adj R-Squared" of 0.9156. "Adeq Precision" measures the signal to noise ratio. A ratio greater than 4 is desirable. Your ratio of 22.367 indicates an adequate signal. This model can be used to navigate the design space.

	Coefficient		Standard	95% CI	95% CI	
Term	Estimate	df	Error	Low	High	VIF
Intercept	-1.24	1	1.77	-4.81	2.33	
B-Tmax	0.01	1	0.01	-0.01	0.03	3.7056
C-Ambient Tbar	-0.06	1	0.04	-0.13	0.02	130.0481
D-Ambient RHbar	-0.04	1	0.02	-0.08	0.01	50.0860
E-dew point T	0.03	1	0.03	-0.03	0.10	96.1201
F-PTFE	-1.57	1	1.78	-5.16	2.02	42.5405
G-Thickness	-0.01	1	0.02	-0.05	0.04	30.8052
H-H2O contact angle	-0.03	1	0.02	-0.07	0.01	36.5337
K-Porosity	0.00	1	0.01	-0.02	0.03	17.8550
L-FCCA	0.00	1	0.00	-0.01	0.01	8.5242
M[1]	0.00	1	0.01	-0.02	0.02	
M[2]	-0.03	1	0.01	-0.06	0.00	
M[3]	-0.02	1	0.01	-0.05	0.01	
N	2.41	1	1.84	-1.32	6.13	838060.7944
BK	-0.01	1	0.02	-0.05	0.03	7.1192
CD	-0.09	1	0.02	-0.14	-0.04	25.8186
DE	0.16	1	0.03	0.09	0.23	19.0797
DM[1]	-0.05	1	0.01	-0.07	-0.03	
DM[2]	0.03	1	0.01	0.02	0.05	
DM[3]	0.00	1	0.01	-0.02	0.02	
FN	2.45	1	1.86	-1.30	6.20	839131.3980
HL	-0.02	1	0.01	-0.04	-0.01	3.4230
HM[1]	0.00	1	0.02	-0.04	0.04	
HM[2]	0.07	1	0.03	0.00	0.14	
HM[3]	0.06	1	0.03	0.00	0.11	
KN	0.03	1	0.01	0.00	0.06	19.3481
LM[1]	0.01	1	0.01	0.00	0.03	
LM[2]	0.00	1	0.01	-0.01	0.01	
LM[3]	0.01	1	0.01	0.00	0.03	
B^2	-0.04	1	0.01	-0.07	-0.02	2.0948
G^2	-0.02	1	0.04	-0.09	0.05	34.9987

Table Wmax regression error assessment

Final Equation in Terms of Coded Factors:

Wmax	=
-1.241236116	
0.006247576	* B
-0.058080436	* C
-0.037282953	* D
0.034538626	* E
-1.570635136	* F
-0.008918429	* G
-0.025993673	* H
0.001409558	* K
0.004266927	* L
-0.000592754	* M[1]
-0.031218396	* M[2]
-0.021007801	* M[3]
2.408608361	* N
-0.012675922	* BK
-0.092777661	* CD
0.159594237	* DE
-0.053828199	* DM[1]
0.034724819	* DM[2]
0.001080968	* DM[3]
2.450904592	* FN
-0.024938601	* HL
-0.001988837	* HM[1]
0.067757276	* HM[2]
0.055304047	* HM[3]
0.031951185	* KN
0.014508775	* LM[1]
-0.003672266	* LM[2]
0.011887253	* LM[3]
-0.043565502	* B^2
-0.018922243	* G^2

Table Wmax coded factors

Table: weighted response (key outputs)

constant	Family 1	Family 2		
Eocv-i	F-berg	Torray	within test mean	within test variance
0.3 low-D	0.7628	0.8505	0.8067	0.0038
0.4 high -D	0.7690	0.8960	0.8325	0.0081
0.38 uniform	0.8548	0.6573	0.7561	0.0195
mean	0.7955	0.8013	0.7984	=mean of means
difference of means	-0.002866667	0.002866667		
weighted values	Family 1	Family 2		
Eocv-i	F-berg	Torray	within test mean	within test variance
0.3 low-D	0.7657	0.8476	0.8067	0.0034
0.4 high -D	0.7719	0.8931	0.8325	0.0074
0.38 uniform	0.8577	0.6544	0.7561	0.0207
mean	0.7984	0.7984	0.7984	=mean of means
difference of means	0	0		

fberg	Family 1	Family 2		
Eocv-i	Constant	Square	within test mean	within test variance
0.3 low-D	0.7628	0.8300	0.7964	0.0023
0.4 high -D	0.7690	0.8698	0.8194	0.0051
0.38 uniform	0.8548	0.8740	0.8644	0.0002
mean	0.7955	0.8579	0.8267	=mean of means
difference of means	-0.0312	0.0312		
weighted values	Family 1	Family 2		
Eocv-i	Constant	Square	within test mean	within test variance
0.3 low-D	0.7940	0.7988	0.7964	0.0000
0.4 high -D	0.8002	0.8386	0.8194	0.0007
0.38 uniform	0.8860	0.8428	0.8644	0.0009
mean	0.8267	0.8267	0.8267	=mean of means
difference of means	0	0		

constant	Family 1	Family 2		
V/hr loss	F-Berg	Torray	within test mean	within test variance
0.3 low-D	-0.0004	-0.0016	-0.0010	0.0000
0.4 high -D	-0.0001	-0.0007	-0.0004	0.0000
0.38 uniform	-0.0011	-0.0003	-0.0007	0.0000
mean	-0.000563251	-0.00086178	-0.000712516	=mean of means
difference of means	0.000149265	-0.000149265		
weighted values	Family 1	Family 2		
V/hr loss	F-berg	Torray	within test mean	within test variance
0.3 low-D	-0.0006	-0.0014	-0.0010	0.0000
0.4 high -D	-0.0003	-0.0005	-0.0004	0.0000
0.38 uniform	-0.0013	-0.0002	-0.0007	0.0000
mean	-0.00071	-0.00071	-0.00071	=mean of means
difference of means	0	0		

fberg	Family 1	Family 2		
V/hr loss	constant	square	within test mean	within test variance
0.3 low-D	-0.0004	-0.0003	-0.0004	0.0000
0.4 high -D	-0.0001	-0.0002	-0.0001	0.0000
0.38 uniform	-0.0011	-0.0001	-0.0006	0.0000
mean	-0.00056	-0.00021	-0.000387145	=mean of means
difference of means	-0.000176107	0.00018		
weighted values	Family 1	Family 2		
V/hr loss	constant	square	within test mean	within test variance
0.3 low-D	-0.0003	-0.0005	-0.0004	0.0000
0.4 high -D	0.0001	-0.0003	-0.0001	0.0000
0.38 uniform	-0.0010	-0.0003	-0.0006	0.0000
mean	-0.00039	-0.00039	-0.000387145	=mean of means
difference of means	0	0		

constant				
hours to Emax	F-Berg	Torray	within test mean	within test variance
0.3 low-D	32.7	120.0	76.4	3808
0.4 high -D	373.3	420.0	396.7	1089
0.38 uniform	149.6	338.3	244.0	17810
mean	185.2	292.8	239.0	=mean of means
difference of means	-53.8	53.8		
weighted values	Family 1	Family 2		
hours to Emax	F-berg	Torray	within test mean	within test variance
0.3 low-D	86.5	66.2	76.4	206
0.4 high -D	427.1	366.2	396.7	1854
0.38 uniform	203.4	284.6	244.0	3295
mean	239.0	239.0	239.0	=mean of means
difference of means	0.0	0.0		

fberg	Family 1	Family 2		
Hours to max	constant	square	within test mean	within test variance
0.3 low-D	32.7	13.8	23.2744	179
0.4 high -D	373.3	5.7	189.5267	67570
0.38 uniform	149.6	17.9	83.7382	8676
mean	185.2	12.5	98.84641754	=mean of means
difference of means	86.4	-86.4		
weighted values	Family 1	Family 2		
Hours to max	constant	square	within test mean	within test variance
0.3 low-D	-53.6	100.2	23.2744	11834
0.4 high -D	287.0	92.1	189.5267	18986
0.38 uniform	63.2	104.3	83.7382	841
mean	98.8	98.8	98.84641754	=mean of means
difference of means	0	0		

Square	Family 1	Family 2		
Eocv-i	F-berg	Torray	within test mean	within test variance
0.3 low-D	0.8300	0.8455	0.8377	0.0001
0.4 high -D	0.8698	0.8657	0.8678	0.0000
0.38 uniform	0.8740	0.8500	0.8620	0.0003
mean	0.8579	0.8537	0.8558	=mean of means
difference of means	0.0021	-0.002103333		
weighted values	Family 1	Family 2		
Eocv-i	F-berg	Torray	within test mean	within test variance
0.3 low-D	0.8279	0.8476	0.8377	0.0002
0.4 high -D	0.8677	0.8678	0.8678	0.0000
0.38 uniform	0.8719	0.8521	0.8620	0.0002
mean	0.8558	0.8558	0.8558	=mean of means
difference of means	0	0		

torray	Family 1	Family 2		
Eocv-i	Constant	Square	within test mean	within test variance
0.3 low-D	0.8505	0.8455	0.8480	0.0000
0.4 high -D	0.8960	0.8657	0.8809	0.0005
0.38 uniform	0.6573	0.8500	0.7537	0.0186
mean	0.8013	0.8537	0.827496667	=mean of means
difference of means	-0.02623	0.02623		
weighted values	Family 1	Family 2		
Eocv-i	Constant	Square	within test mean	within test variance
0.3 low-D	0.8767	0.8193	0.8480	0.0017
0.4 high -D	0.9222	0.8395	0.8809	0.0034
0.38 uniform	0.6835	0.8238	0.7537	0.0098
mean	0.8275	0.8275	0.8275	=mean of means
difference of means	0	0		

Square	Family 1	Family 2		
V/hr loss	F-Berg	Torray	within test mean	within test variance
0.3 low-D	-0.0003	-0.0035	-0.0019	0.0000
0.4 high -D	-0.0002	-0.0130	-0.0066	0.0001
0.38 uniform	-0.0001	-0.0007	-0.0004	0.0000
mean	-0.0002	-0.0057	-0.0030	=mean of means
difference of means	0.0028	-0.0028		
weighted values	Family 1	Family 2		
V/hr loss	F-berg	Torray	within test mean	within test variance
0.3 low-D	-0.0031	-0.0007	-0.0019	0.0000
0.4 high -D	-0.0029	-0.0102	-0.0066	0.0000
0.38 uniform	-0.0029	0.0020	-0.0004	0.0000
mean	-0.0030	-0.0030	-0.0030	=mean of means
difference of means	0	0		

torray	Family 1	Family 2		
V/hr loss	constant	square	within test mean	within test variance
0.3 low-D	-0.0016	-0.0035	-0.0025	0.00000
0.4 high -D	-0.0007	-0.0130	-0.0068	0.00008
0.38 uniform	-0.0003	-0.0007	-0.0005	0.00000
mean	-0.0009	-0.0057	-0.0033	=mean of means
difference of means	0.0024	-0.0024		
weighted values	Family 1	Family 2		
V/hr loss	constant	square	within test mean	within test variance
0.3 low-D	-0.0040	-0.0010	-0.0025	0.00000
0.4 high -D	-0.0031	-0.0105	-0.0068	0.00003
0.38 uniform	-0.0028	0.0017	-0.0005	0.00001
mean	-0.0033	-0.0033	-0.0033	=mean of means
difference of means	0	0		

Square				
hours to Emax	F-Berg	Torray	within test mean	within test variance
0.3 low-D	13.82	22.70	18.26	39.41
0.4 high -D	5.72	11.22	8.47	15.14
0.38 uniform	17.88	12.27	15.07	15.71
mean	12.47	15.40	13.94	=mean of means
difference of means	-1.46	1.46		
weighted values	Family 1	Family 2		
hours to Emax	F-berg	Torray	within test mean	within test variance
0.3 low-D	15.28	21.24	18.26	17.72
0.4 high -D	7.18	9.76	8.47	3.32
0.38 uniform	19.34	10.81	15.07	36.39
mean	13.94	13.94	13.94	=mean of means
difference of means	0.00	0.00		

torray	Family 1	Family 2		
Hours to max	constant	square	within test mean	within test variance
0.3 low-D	120.00	22.70	71.35	4734
0.4 high -D	420.00	11.22	215.61	83549
0.38 uniform	338.33	12.27	175.30	53158
mean	292.78	15.40	154.09	=mean of means
difference of means	138.69	-138.69		
weighted values	Family 1	Family 2		
Hours to max	constant	square	within test mean	within test variance
0.3 low-D	-18.69	161.39	71.35	16214.36
0.4 high -D	281.31	149.91	215.61	8632.55
0.38 uniform	199.64	150.96	175.30	1185.02
mean	154.09	154.09	154.09	=mean of means
difference of means	0	0		

Appendix 4: - Additional graphical and tabulated data

This appendix presents the polarization load cycles and the curve fit and gradient measurement of the data gathered during polarisation curves.

Those with interest in the topic may use the digital data (in the. Fig files provided in the digital version fo the appendices) and the associated programme files, to manipulate and investigate the data in detail.

Each plot has an alphanumeric title to identify it:

e.g. FCCA1-Cell2-FUDL-MEA02-pol02-20150210|EO2.csv

This title identifies the following information:

Test apparatus (1 or 2)- test cell in that apparatus (1 to 4) – experiment code (FUDL) – Sample ID (e.g. MEA 02)- polarisation number – YearMonthDay|file save back up disc location and file type (.csv)

MEA 02

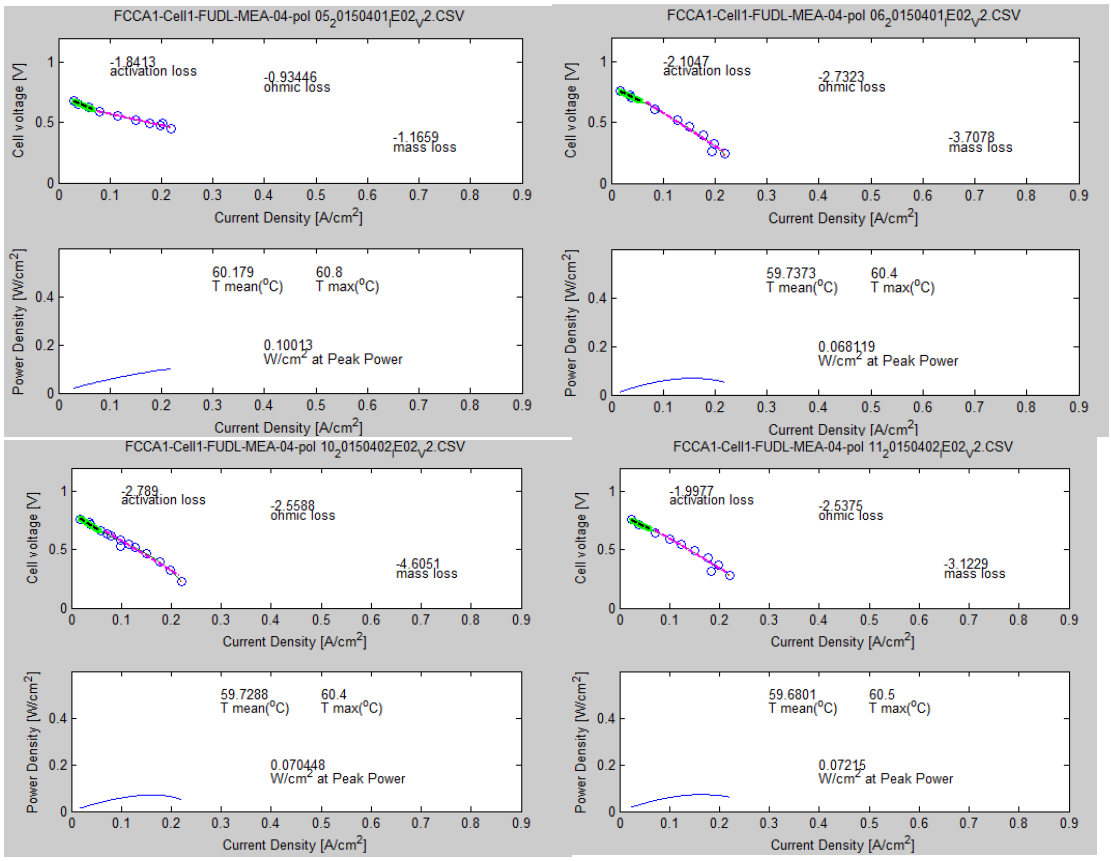

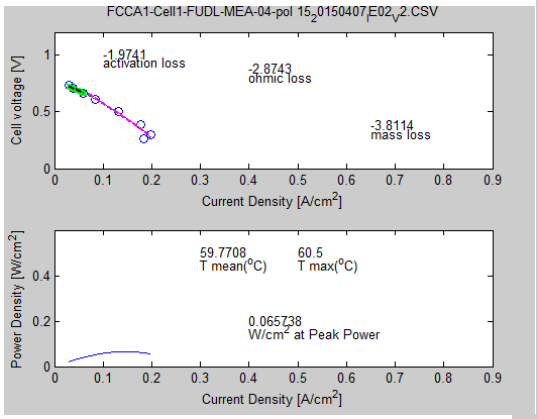
FCCA1-Cell1-FUDL-MEA-04-pol 15_20150407_E02_V2.CSV
-1.9741
activation loss
-2.8743
ohmic loss
-3.8114
mass loss
Cell voltage [V]
Current Density [A/cm2]
59.7708
T mean(°C)
60.5
T max(°C)
0.065738
W/cm2 at Peak Power
Power Density [W/cm2]
Current Density [A/cm2]

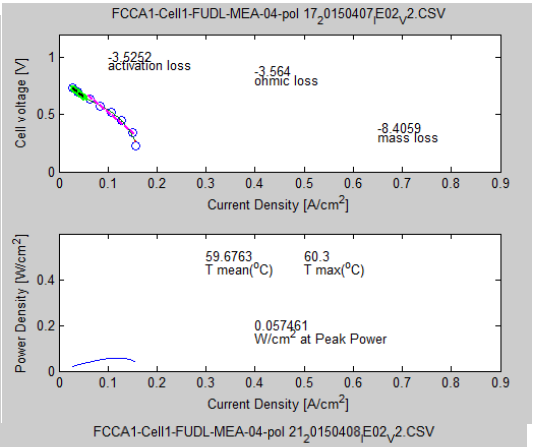
FCCA1-Cell1-FUDL-MEA-04-pol 17_20150407_E02_V2.CSV
-3.5252
activation loss
-3.564
ohmic loss
-8.4059
mass loss
Cell voltage [V]
Current Density [A/cm2]
59.6763
T mean(°C)
60.3
T max(°C)
0.057461
W/cm2 at Peak Power
Power Density [W/cm2]
Current Density [A/cm2]

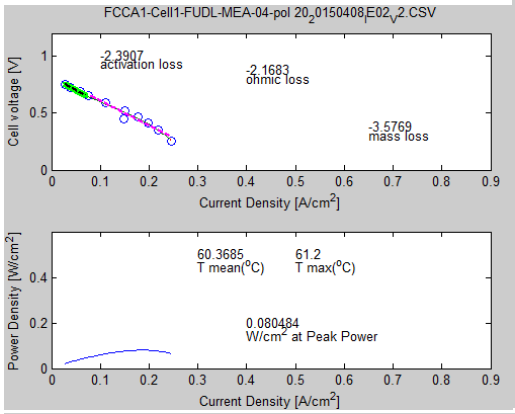
FCCA1-Cell1-FUDL-MEA-04-pol 20_20150408_E02_V2.CSV
-2.3907
activation loss
-2.1683
ohmic loss
-3.5769
mass loss
Cell voltage [V]
Current Density [A/cm2]
60.3685
T mean(°C)
61.2
T max(°C)
0.080484
W/cm2 at Peak Power
Power Density [W/cm2]
Current Density [A/cm2]

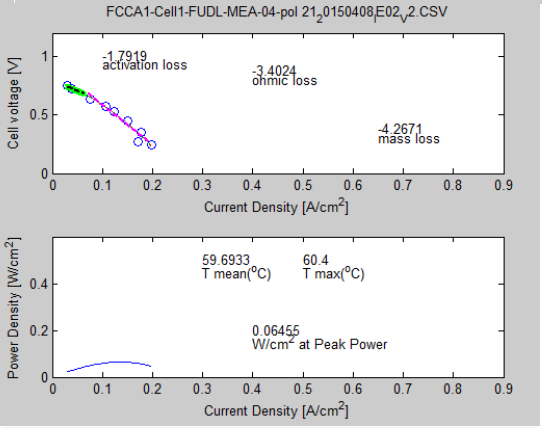
FCCA1-Cell1-FUDL-MEA-04-pol 21_20150408_E02_V2.CSV
-1.7919
activation loss
-3.4024
ohmic loss
-4.2671
mass loss
Cell voltage [V]
Current Density [A/cm2]
59.6933
T mean(°C)
60.4
T max(°C)
0.06455
W/cm2 at Peak Power
Power Density [W/cm2]
Current Density [A/cm2]

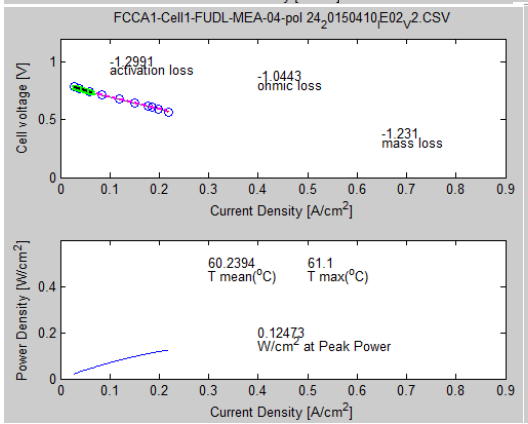
FCCA1-Cell1-FUDL-MEA-04-pol 24_20150410_E02_V2.CSV
-1.2991
activation loss
-1.0443
ohmic loss
-1.231
mass loss
Cell voltage [V]
Current Density [A/cm2]
60.2394
T mean(°C)
61.1
T max(°C)
0.12473
W/cm2 at Peak Power
Power Density [W/cm2]
Current Density [A/cm2]

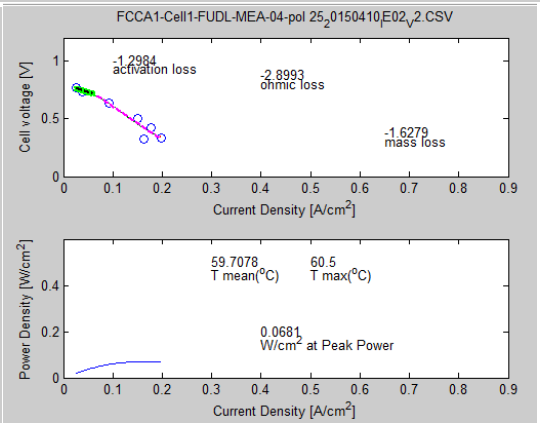
FCCA1-Cell1-FUDL-MEA-04-pol 25_20150410_E02_V2.CSV
-1.2984
activation loss
-2.8993
ohmic loss
-1.6279
mass loss
Cell voltage [V]
Current Density [A/cm2]
59.7078
T mean(°C)
60.5
T max(°C)
0.0681
W/cm2 at Peak Power
Power Density [W/cm2]
Current Density [A/cm2]

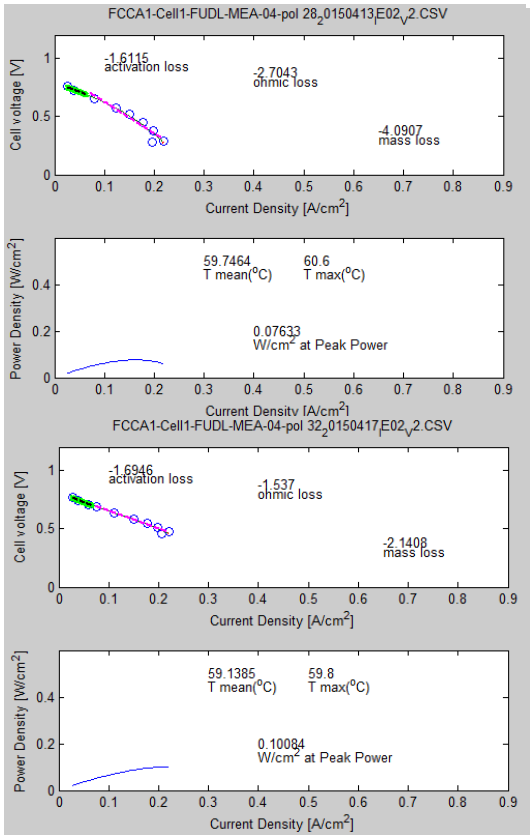
FCCA1-Cell1-FUDL-MEA-04-pol 28_20150413_E02_V2.CSV
-1.6115
activation loss
-2.7043
ohmic loss
-4.0907
mass loss
Cell voltage [V]
Current Density [A/cm2]
59.7464
T mean(°C)
60.6
T max(°C)
0.07633
W/cm2 at Peak Power
Power Density [W/cm2]
Current Density [A/cm2]

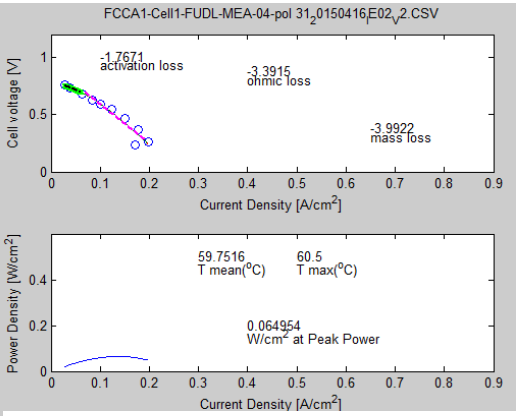
FCCA1-Cell1-FUDL-MEA-04-pol 31_20150416_E02_V2.CSV
-1.7671
activation loss
-3.3915
ohmic loss
-3.9922
mass loss
Cell voltage [V]
Current Density [A/cm2]
59.7516
T mean(°C)
60.5
T max(°C)
0.064954
W/cm2 at Peak Power
Power Density [W/cm2]
Current Density [A/cm2]

FCCA1-Cell1-FUDL-MEA-04-pol 32_20150417_E02_V2.CSV
-1.6946
activation loss
-1.537
ohmic loss
-2.1408
mass loss
Cell voltage [V]
Current Density [A/cm2]
59.1385
T mean(°C)
59.8
T max(°C)
0.10084
W/cm2 at Peak Power
Power Density [W/cm2]
Current Density [A/cm2]

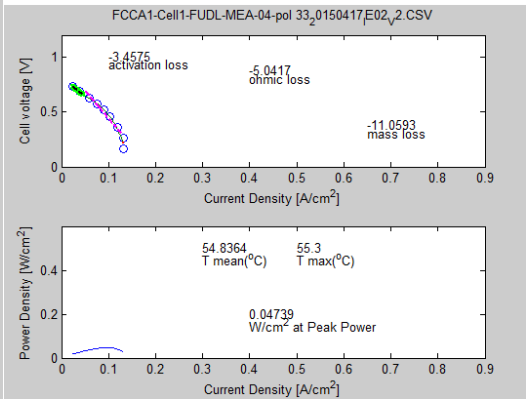
FCCA1-Cell1-FUDL-MEA-04-pol 33_20150417_E02_V2.CSV
-3.4575
activation loss
-5.0417
ohmic loss
-11.0593
mass loss
Cell voltage [V]
Current Density [A/cm2]
54.8364
T mean(°C)
55.3
T max(°C)
0.04739
W/cm2 at Peak Power
Power Density [W/cm2]
Current Density [A/cm2]

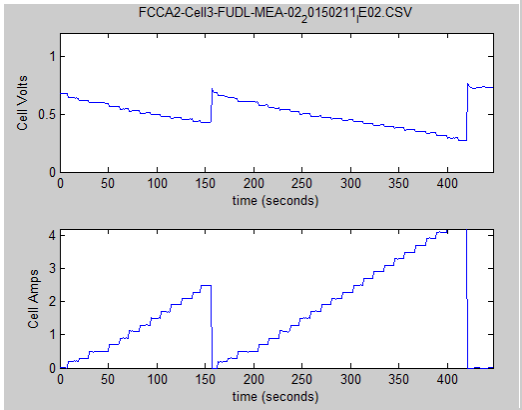
FCCA2-Cell3-FUDL-MEA-02_20150211_E02.CSV
Cell Volts
time (seconds)
Cell Amps
time (seconds)

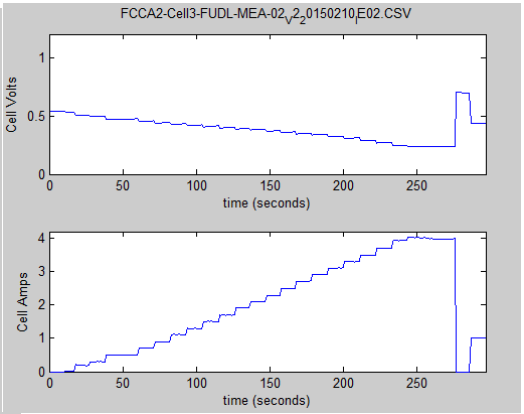
FCCA2-Cell3-FUDL-MEA-02_V2_20150210_E02.CSV
Cell Volts
time (seconds)
Cell Amps
time (seconds)

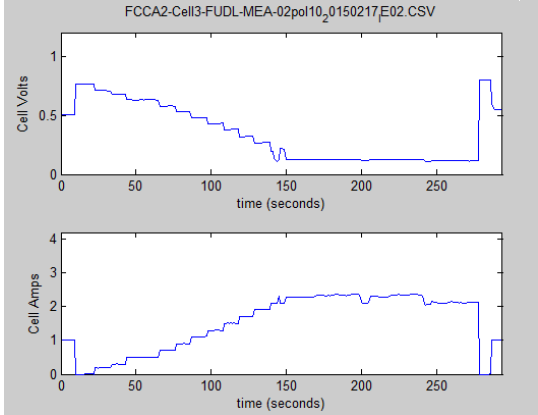
FCCA2-Cell3-FUDL-MEA-02pol10_20150217_E02.CSV
Cell Volts
time (seconds)
Cell Amps
time (seconds)

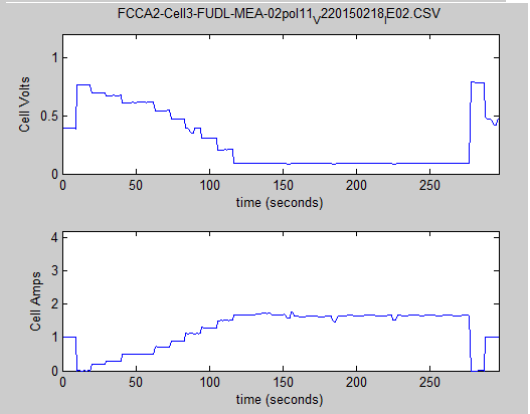
FCCA2-Cell3-FUDL-MEA-02pol11_V220150218_E02.CSV
Cell Volts
time (seconds)
Cell Amps
time (seconds)

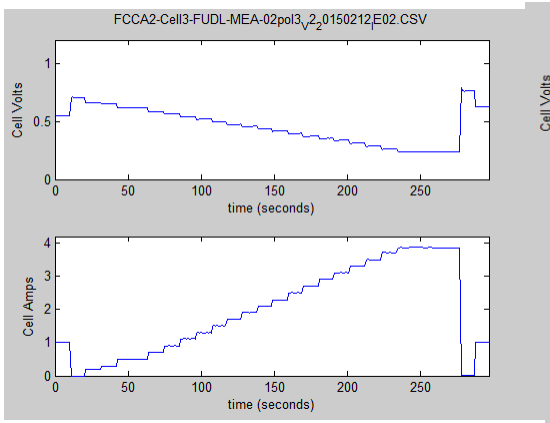
FCCA2-Cell3-FUDL-MEA-02pol3_V2_20150212_E02.CSV
Cell Volts
time (seconds)
Cell Amps
time (seconds)

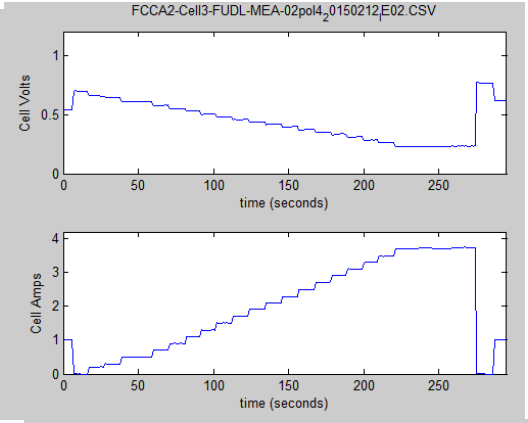
FCCA2-Cell3-FUDL-MEA-02pol4_2_20150212_E02.CSV
Cell Volts
time (seconds)
Cell Amps
time (seconds)

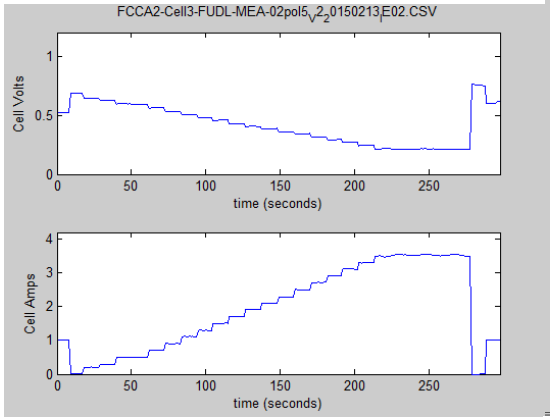
FCCA2-Cell3-FUDL-MEA-02pol5_V2_20150213_E02.CSV
Cell Volts
time (seconds)
Cell Amps
time (seconds)

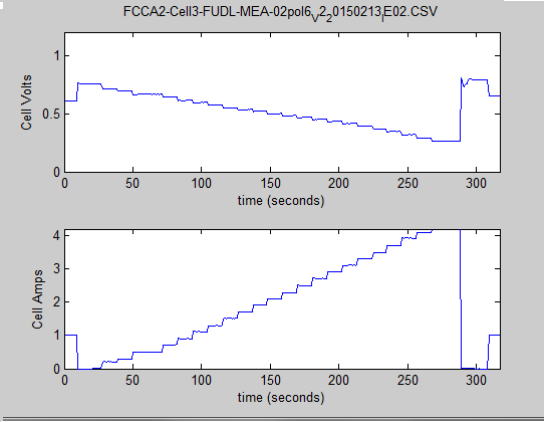
FCCA2-Cell3-FUDL-MEA-02pol6_V2_20150213_E02.CSV
Cell Volts
time (seconds)
Cell Amps
time (seconds)

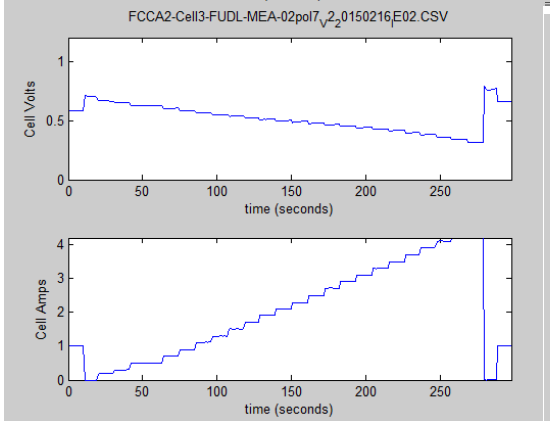
FCCA2-Cell3-FUDL-MEA-02pol7_V2_20150216_E02.CSV
Cell Volts
time (seconds)
Cell Amps
time (seconds)

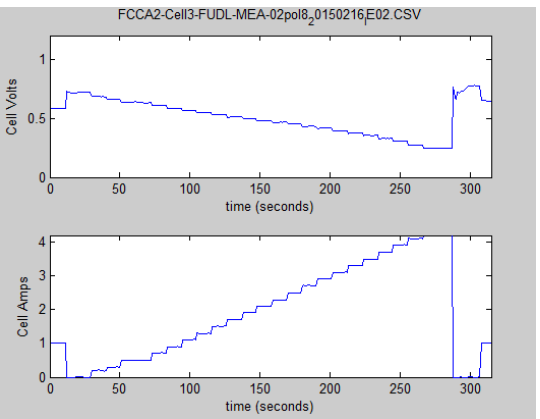
FCCA2-Cell3-FUDL-MEA-02pol8_2_20150216_E02.CSV
Cell Volts
time (seconds)
Cell Amps
time (seconds)

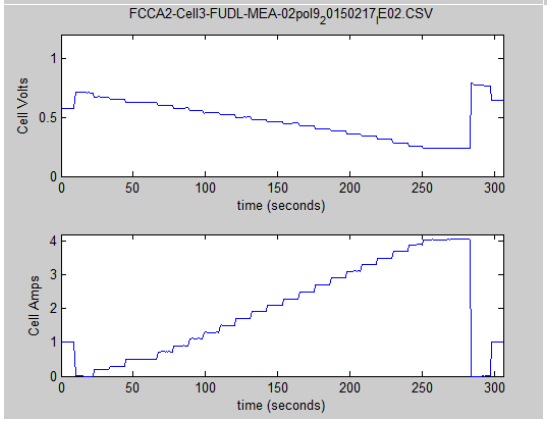
FCCA2-Cell3-FUDL-MEA-02pol9_2_20150217_E02.CSV
Cell Volts
time (seconds)
Cell Amps
time (seconds)

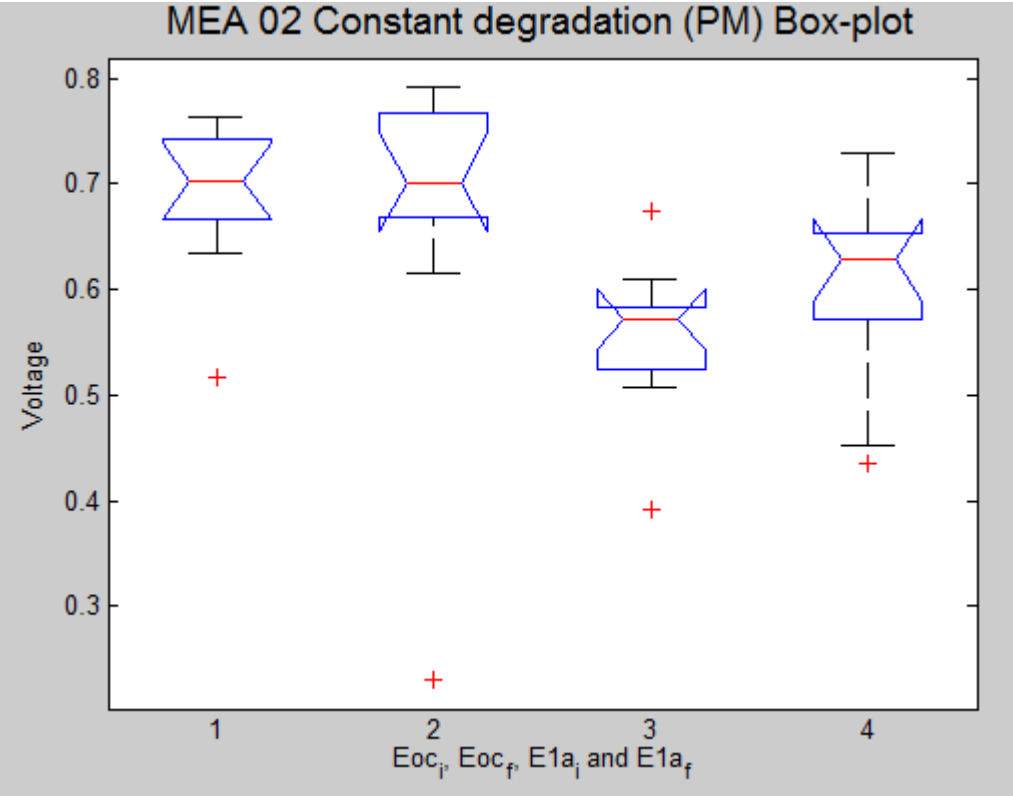
MEA 02 Constant degradation (PM) Box-plot
Voltage
0.8
0.7
0.6
0.5
0.4
0.3
1
2
3
4
Eoc$_i$, Eoc$_f$, E1a$_i$ and E1a$_f$

MEA 02 (Fberg, low-D, cathode, Uniform, Constant)PM

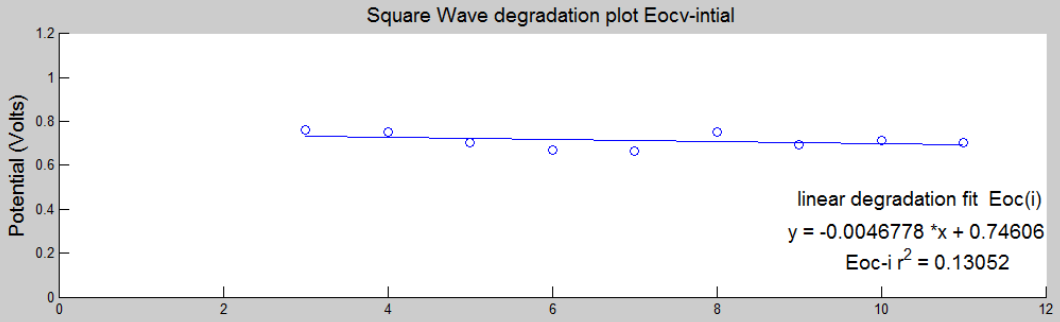

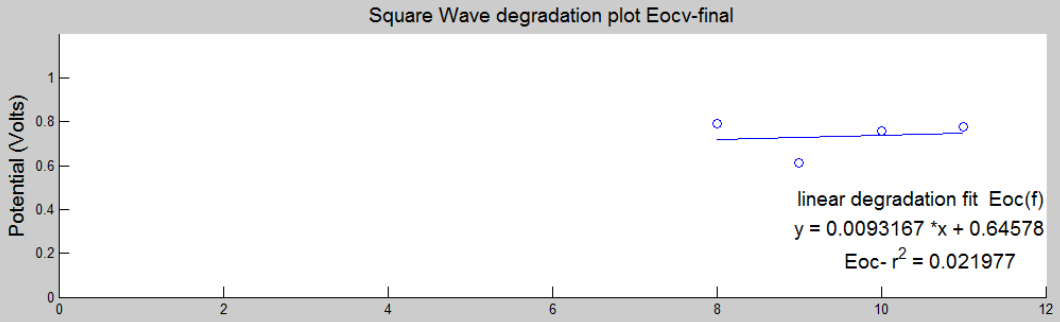

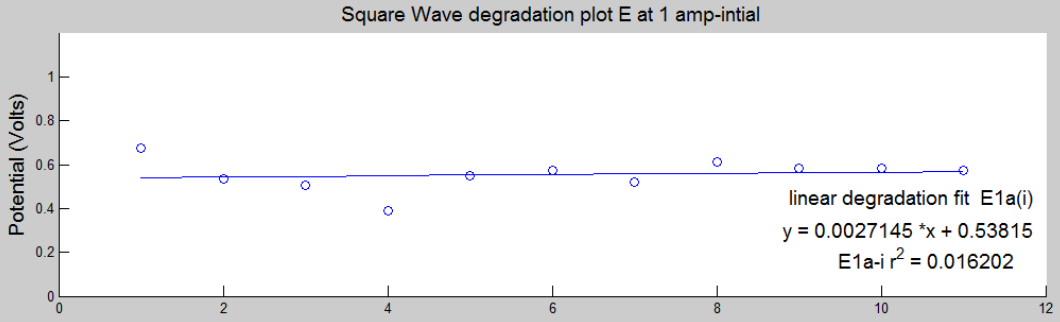

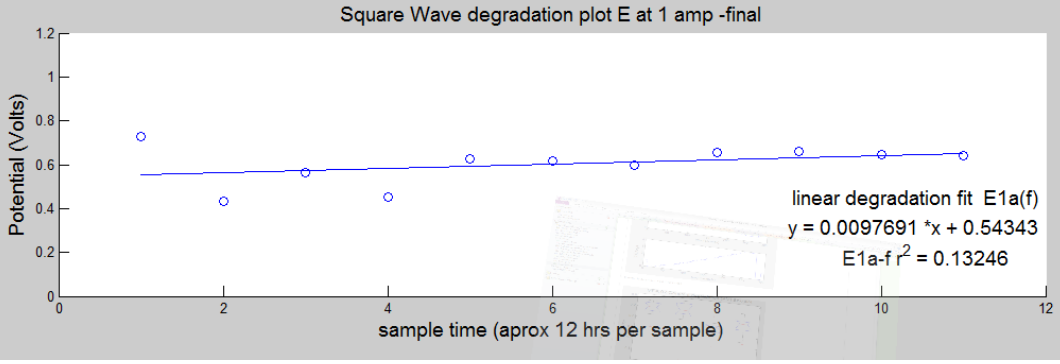

MEA 02 (Fberg, low-D, cathode, Uniform, Constant)PM

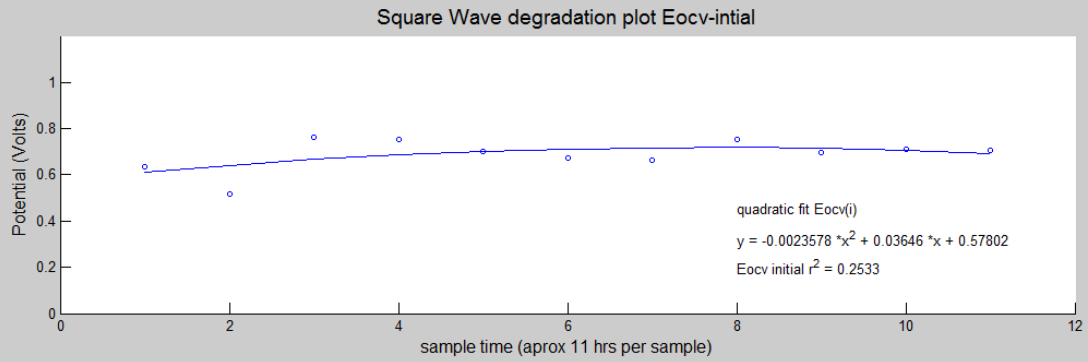

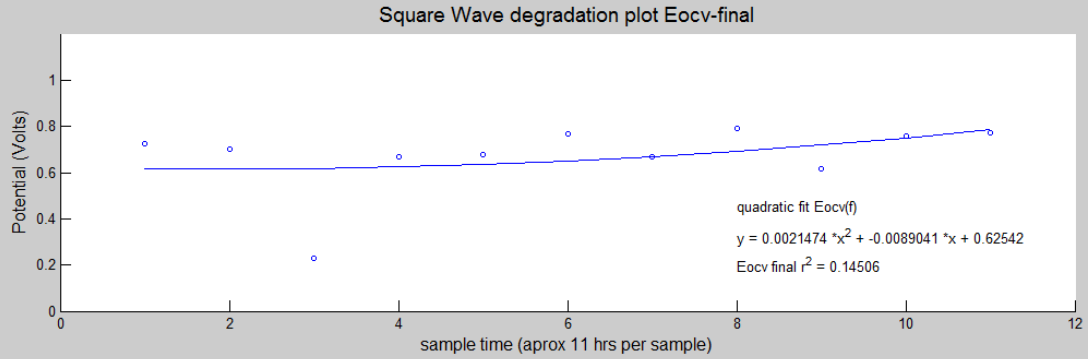

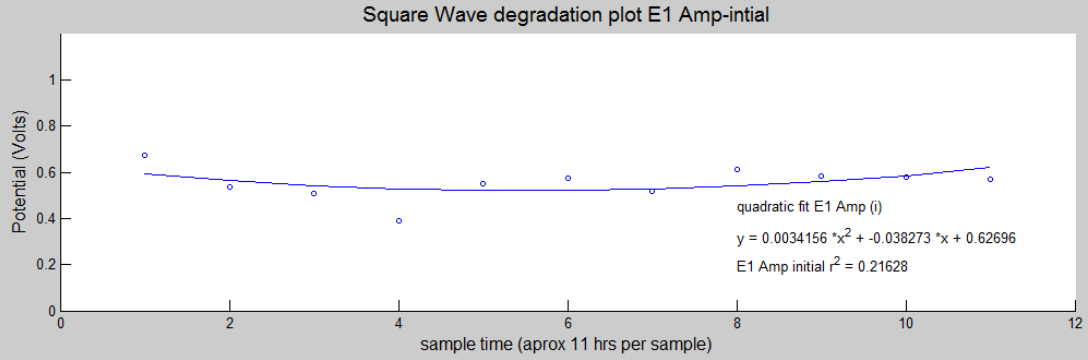

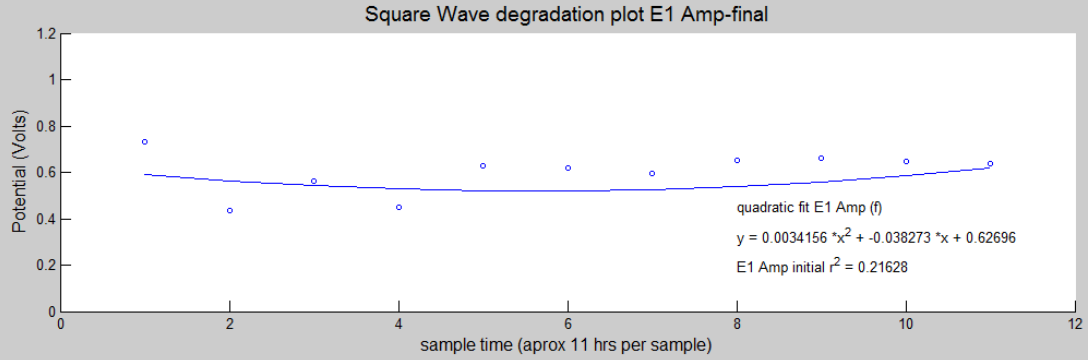

MEA 02 (Fberg, low-D, cathode, Uniform, Constant)PM

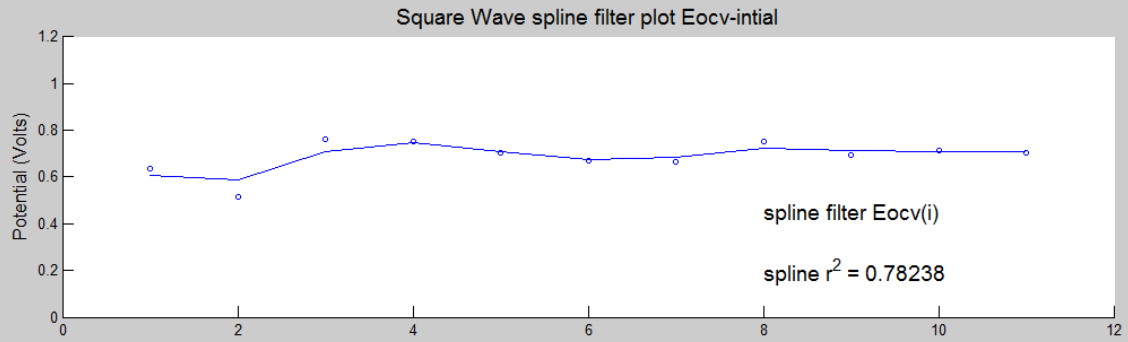

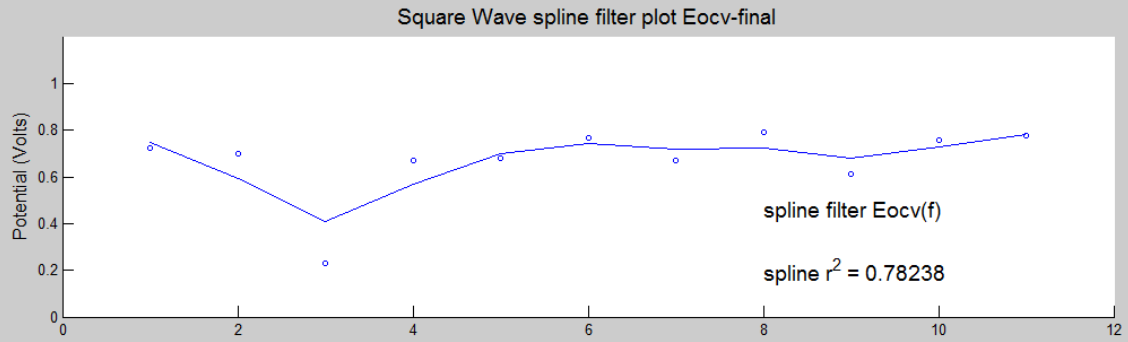

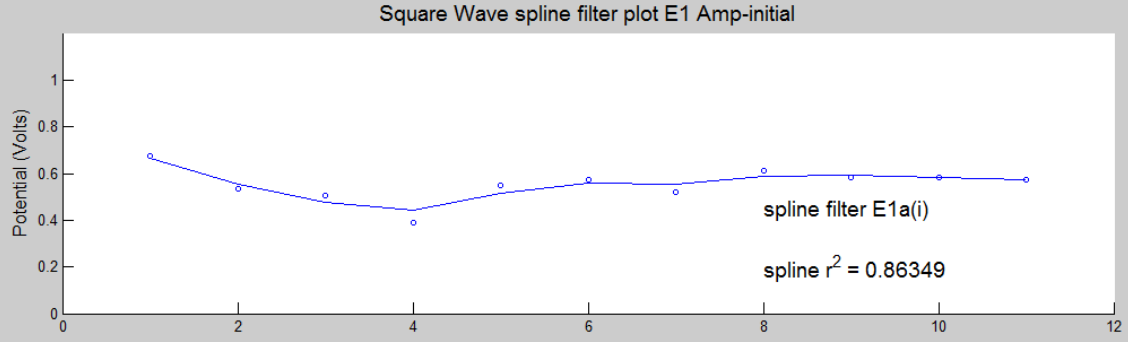

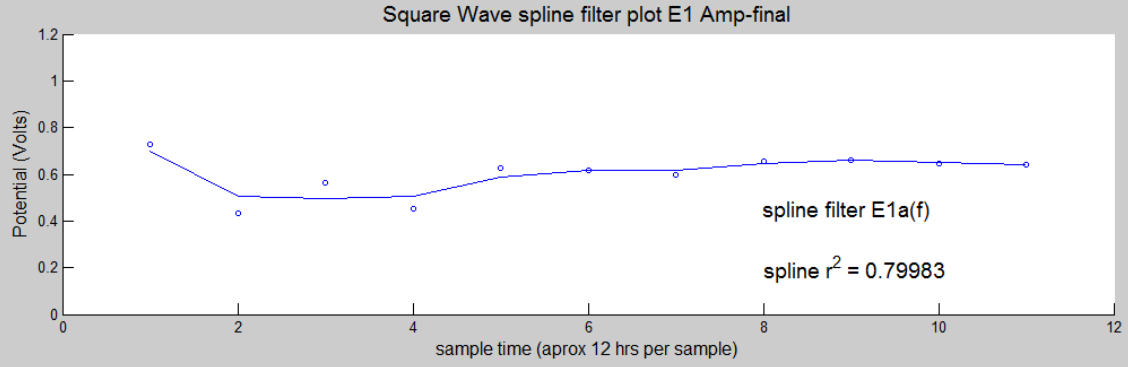

MEA 04

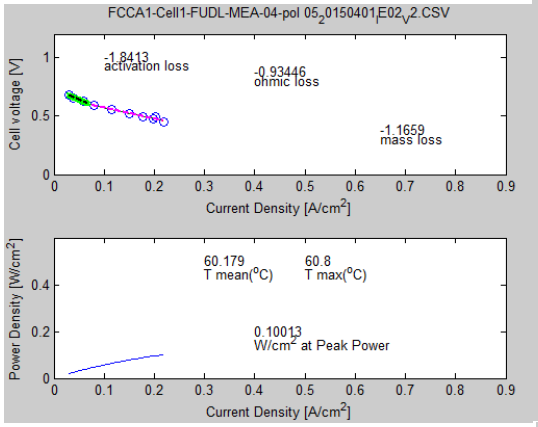
FCCA1-Cell1-FUDL-MEA-04-pol 05_0150401_E02_V2.CSV
-1.8413
activation loss
-0.93446
ohmic loss
-1.1659
mass loss
Cell voltage [V]
Current Density [A/cm²]
60.179
T mean(°C)
60.8
T max(°C)
0.10013
W/cm² at Peak Power
Power Density [W/cm²]
Current Density [A/cm²]

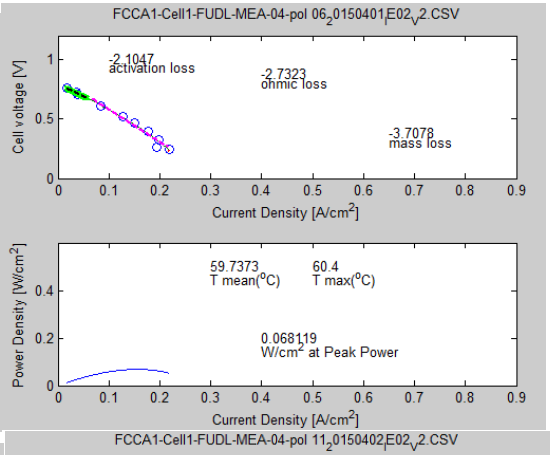
FCCA1-Cell1-FUDL-MEA-04-pol 06_0150401_E02_V2.CSV
-2.1047
activation loss
-2.7323
ohmic loss
-3.7078
mass loss
Cell voltage [V]
Current Density [A/cm²]
59.7373
T mean(°C)
60.4
T max(°C)
0.068119
W/cm² at Peak Power
Power Density [W/cm²]
Current Density [A/cm²]

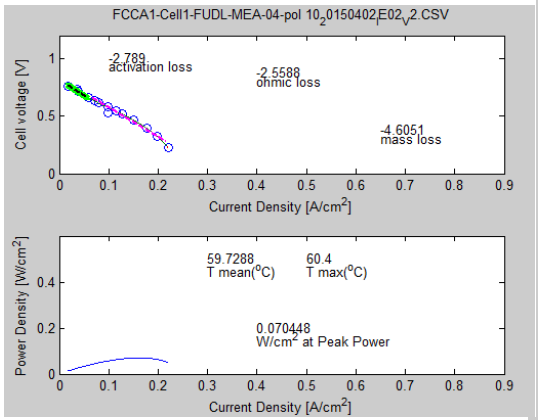
FCCA1-Cell1-FUDL-MEA-04-pol 10_0150402_E02_V2.CSV
-2.789
activation loss
-2.5588
ohmic loss
-4.6051
mass loss
Cell voltage [V]
Current Density [A/cm²]
59.7288
T mean(°C)
60.4
T max(°C)
0.070448
W/cm² at Peak Power
Power Density [W/cm²]
Current Density [A/cm²]

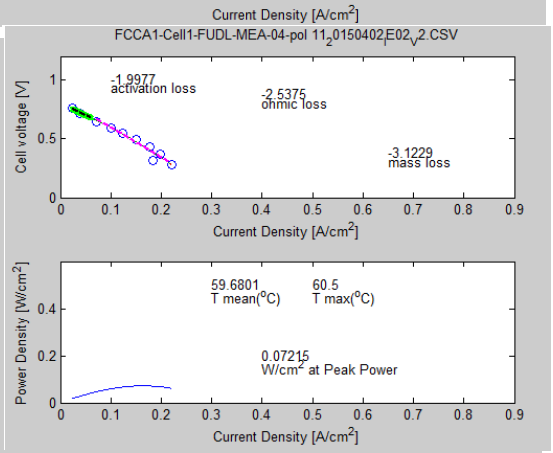
FCCA1-Cell1-FUDL-MEA-04-pol 11_0150402_E02_V2.CSV
-1.9977
activation loss
-2.5375
ohmic loss
-3.1229
mass loss
Cell voltage [V]
Current Density [A/cm²]
59.6801
T mean(°C)
60.5
T max(°C)
0.07215
W/cm² at Peak Power
Power Density [W/cm²]
Current Density [A/cm²]

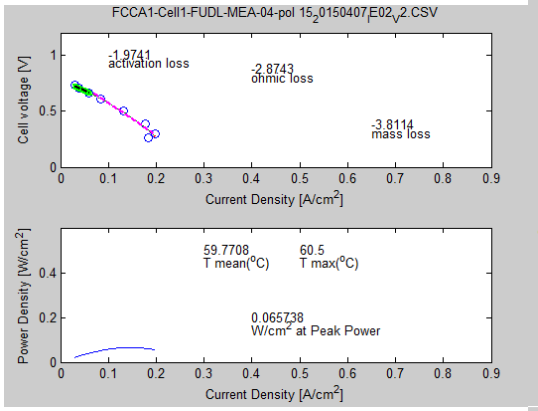
FCCA1-Cell1-FUDL-MEA-04-pol 15_0150407_E02_V2.CSV
-1.9741
activation loss
-2.8743
ohmic loss
-3.8114
mass loss
Cell voltage [V]
Current Density [A/cm²]
59.7708
T mean(°C)
60.5
T max(°C)
0.065738
W/cm² at Peak Power
Power Density [W/cm²]
Current Density [A/cm²]

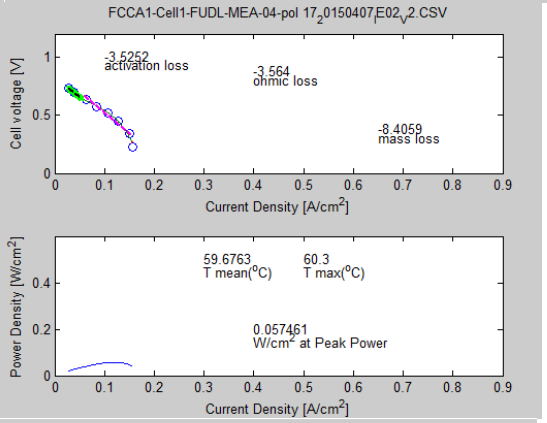
FCCA1-Cell1-FUDL-MEA-04-pol 17_0150407_E02_V2.CSV
-3.5252
activation loss
-3.564
ohmic loss
-8.4059
mass loss
Cell voltage [V]
Current Density [A/cm²]
59.6763
T mean(°C)
60.3
T max(°C)
0.057461
W/cm² at Peak Power
Power Density [W/cm²]
Current Density [A/cm²]

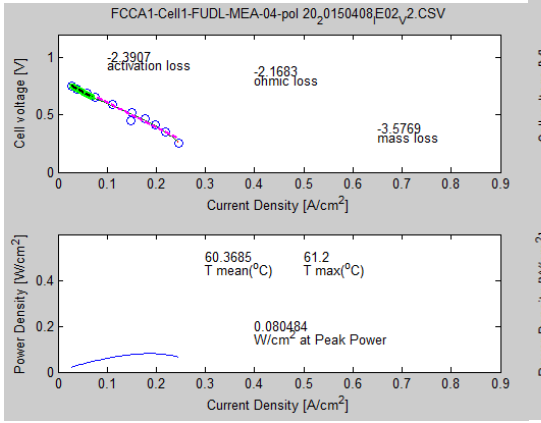
FCCA1-Cell1-FUDL-MEA-04-pol 20_0150408_E02_V2.CSV
-2.3907
activation loss
-2.1683
ohmic loss
-3.5769
mass loss
Cell voltage [V]
Current Density [A/cm²]
60.3685
T mean(°C)
61.2
T max(°C)
0.080484
W/cm² at Peak Power
Power Density [W/cm²]
Current Density [A/cm²]

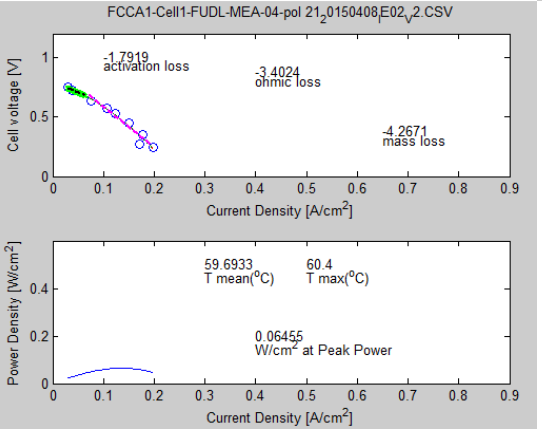
FCCA1-Cell1-FUDL-MEA-04-pol 21_0150408_E02_V2.CSV
-1.7919
activation loss
-3.4024
ohmic loss
-4.2671
mass loss
Cell voltage [V]
Current Density [A/cm²]
59.6933
T mean(°C)
60.4
T max(°C)
0.06455
W/cm² at Peak Power
Power Density [W/cm²]
Current Density [A/cm²]

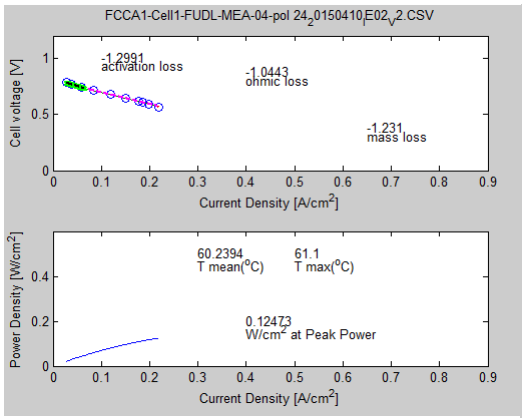
FCCA1-Cell1-FUDL-MEA-04-pol 24_20150410_E02_V2.CSV
-1.2991
activation loss
-1.0443
ohmic loss
-1.231
mass loss
Cell voltage [V]
Current Density [A/cm2]
60.2394
T mean(°C)
61.1
T max(°C)
0.12473
W/cm2 at Peak Power
Power Density [W/cm2]
Current Density [A/cm2]

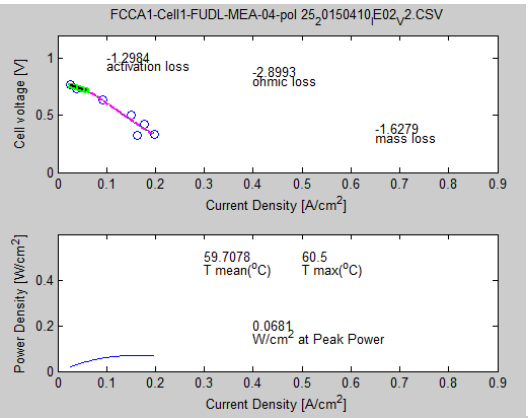
FCCA1-Cell1-FUDL-MEA-04-pol 25_20150410_E02_V2.CSV
-1.2984
activation loss
-2.8993
ohmic loss
-1.6279
mass loss
Cell voltage [V]
Current Density [A/cm2]
59.7078
T mean(°C)
60.5
T max(°C)
0.0681
W/cm2 at Peak Power
Power Density [W/cm2]
Current Density [A/cm2]

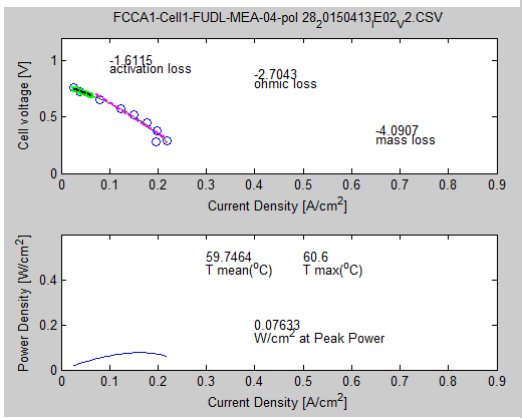
FCCA1-Cell1-FUDL-MEA-04-pol 28_20150413_E02_V2.CSV
-1.6115
activation loss
-2.7043
ohmic loss
-4.0907
mass loss
Cell voltage [V]
Current Density [A/cm2]
59.7464
T mean(°C)
60.6
T max(°C)
0.07633
W/cm2 at Peak Power
Power Density [W/cm2]
Current Density [A/cm2]

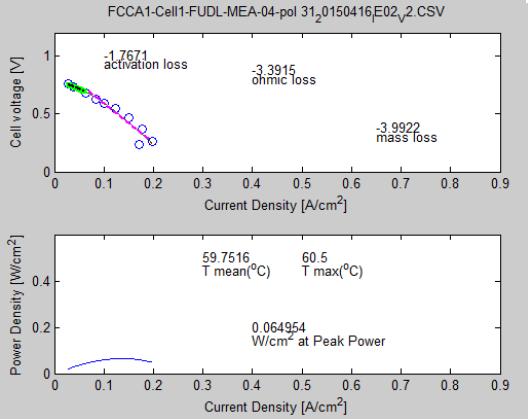
FCCA1-Cell1-FUDL-MEA-04-pol 31_20150416_E02_V2.CSV
-1.7671
activation loss
-3.3915
ohmic loss
-3.9922
mass loss
Cell voltage [V]
Current Density [A/cm2]
59.7516
T mean(°C)
60.5
T max(°C)
0.064954
W/cm2 at Peak Power
Power Density [W/cm2]
Current Density [A/cm2]

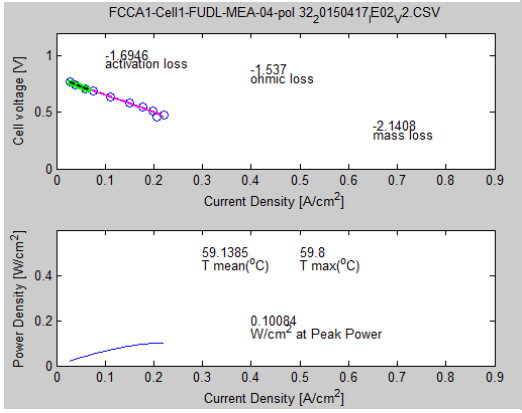
FCCA1-Cell1-FUDL-MEA-04-pol 32_20150417_E02_V2.CSV
-1.6946
activation loss
-1.537
ohmic loss
-2.1408
mass loss
Cell voltage [V]
Current Density [A/cm2]
59.1385
T mean(°C)
59.8
T max(°C)
0.10084
W/cm2 at Peak Power
Power Density [W/cm2]
Current Density [A/cm2]

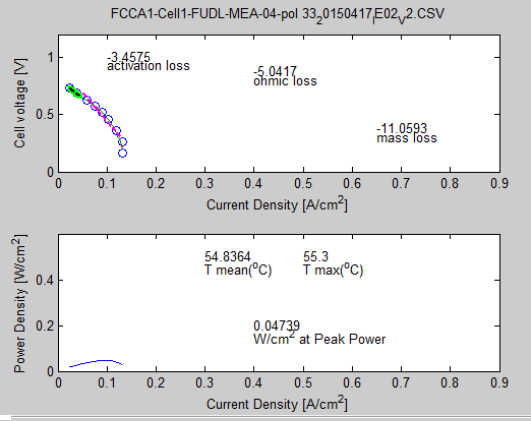
FCCA1-Cell1-FUDL-MEA-04-pol 33_20150417_E02_V2.CSV
-3.4575
activation loss
-5.0417
ohmic loss
-11.0593
mass loss
Cell voltage [V]
Current Density [A/cm2]
54.8364
T mean(°C)
55.3
T max(°C)
0.04739
W/cm2 at Peak Power
Power Density [W/cm2]
Current Density [A/cm2]

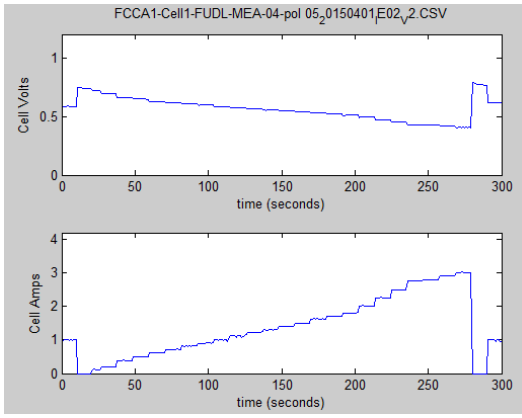
FCCA1-Cell1-FUDL-MEA-04-pol 05_20150401_E02_V2.CSV
Cell Volts
time (seconds)
Cell Amps
time (seconds)

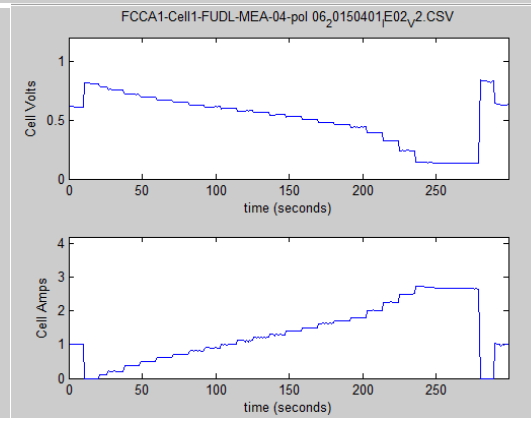
FCCA1-Cell1-FUDL-MEA-04-pol 06_20150401_E02_V2.CSV
Cell Volts
time (seconds)
Cell Amps
time (seconds)

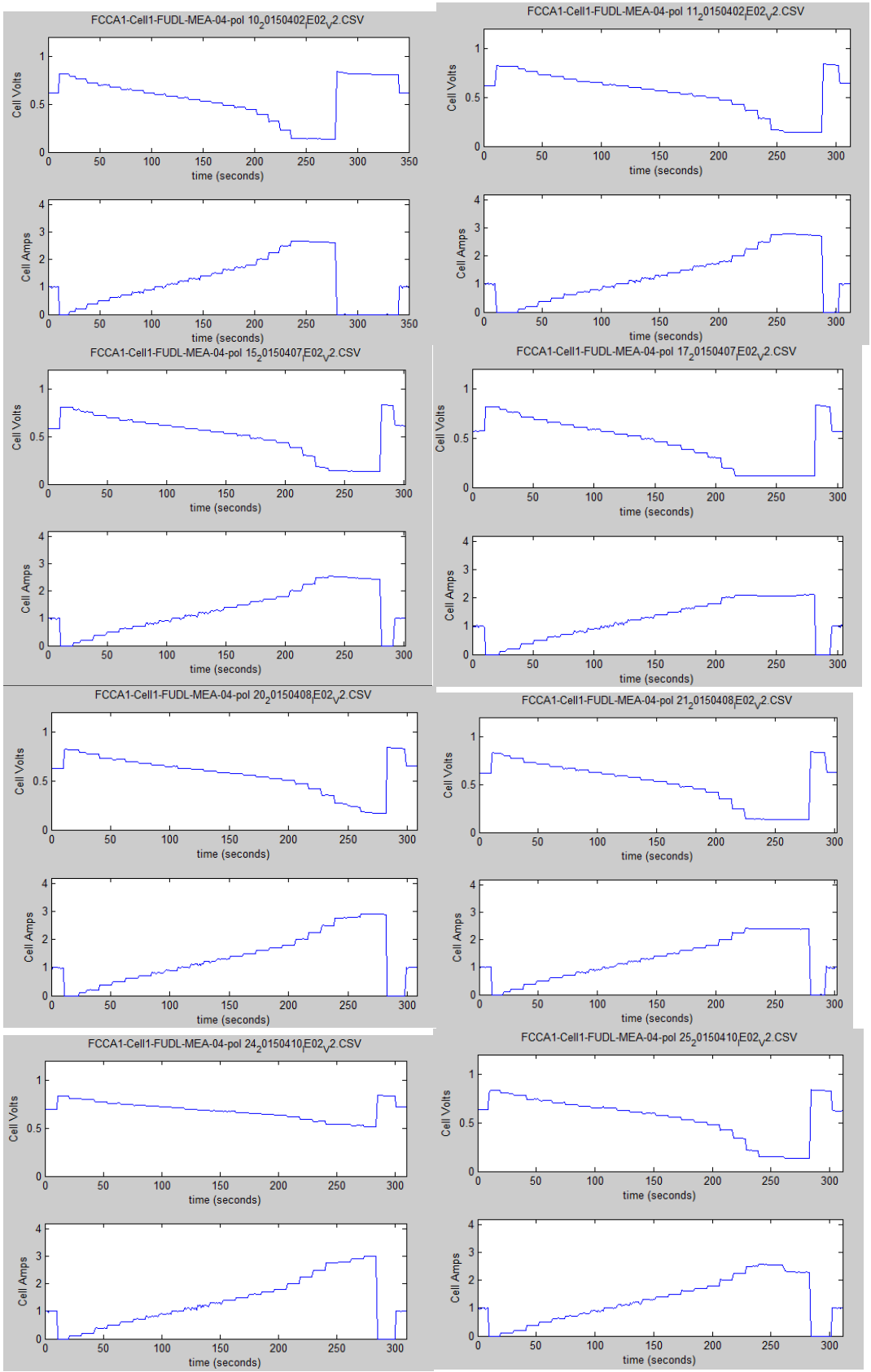
FCCA1-Cell1-FUDL-MEA-04-pol 10_20150402_E02_V2.CSV
FCCA1-Cell1-FUDL-MEA-04-pol 11_20150402_E02_V2.CSV
FCCA1-Cell1-FUDL-MEA-04-pol 15_20150407_E02_V2.CSV
FCCA1-Cell1-FUDL-MEA-04-pol 17_20150407_E02_V2.CSV
FCCA1-Cell1-FUDL-MEA-04-pol 20_20150408_E02_V2.CSV
FCCA1-Cell1-FUDL-MEA-04-pol 21_20150408_E02_V2.CSV
FCCA1-Cell1-FUDL-MEA-04-pol 24_20150410_E02_V2.CSV
FCCA1-Cell1-FUDL-MEA-04-pol 25_20150410_E02_V2.CSV
Cell Volts
Cell Amps
time (seconds)

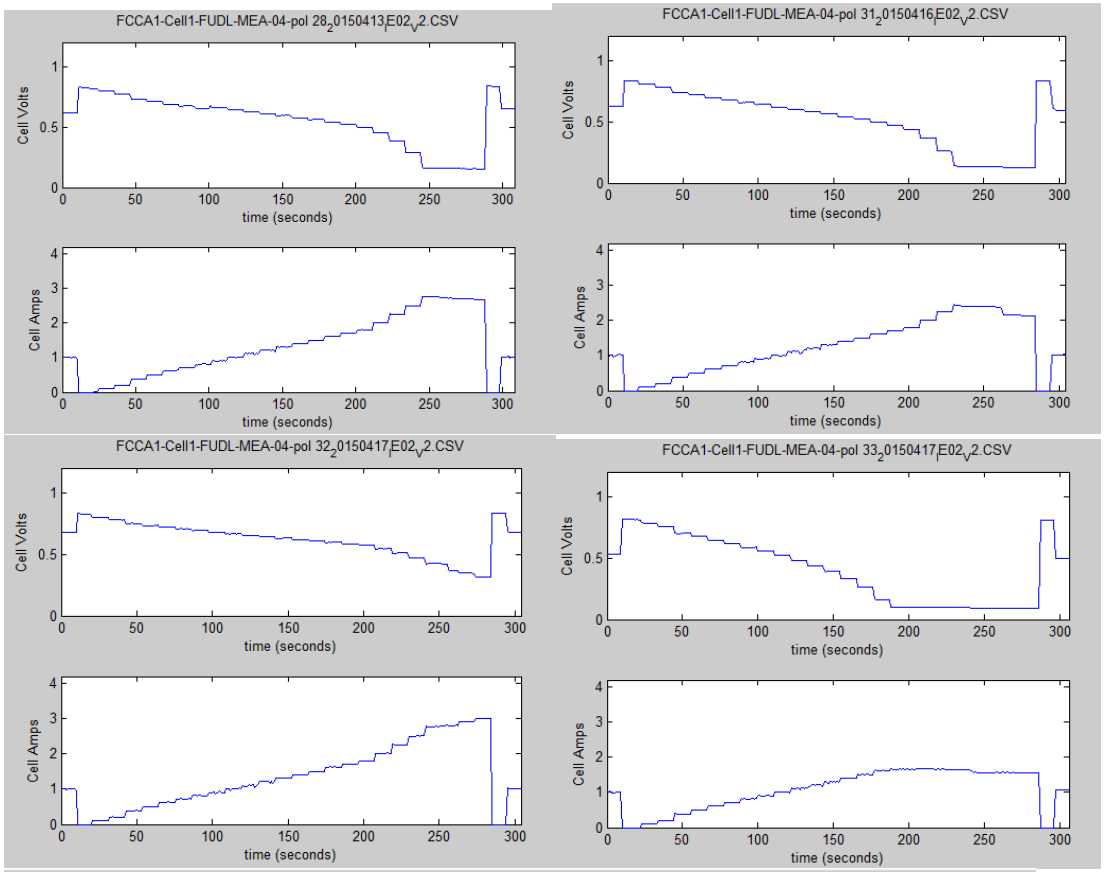
FCCA1-Cell1-FUDL-MEA-04-pol 28_0150413_E02_V2.CSV
FCCA1-Cell1-FUDL-MEA-04-pol 31_0150416_E02_V2.CSV
FCCA1-Cell1-FUDL-MEA-04-pol 32_0150417_E02_V2.CSV
FCCA1-Cell1-FUDL-MEA-04-pol 33_0150417_E02_V2.CSV
Cell Volts
Cell Amps
time (seconds)

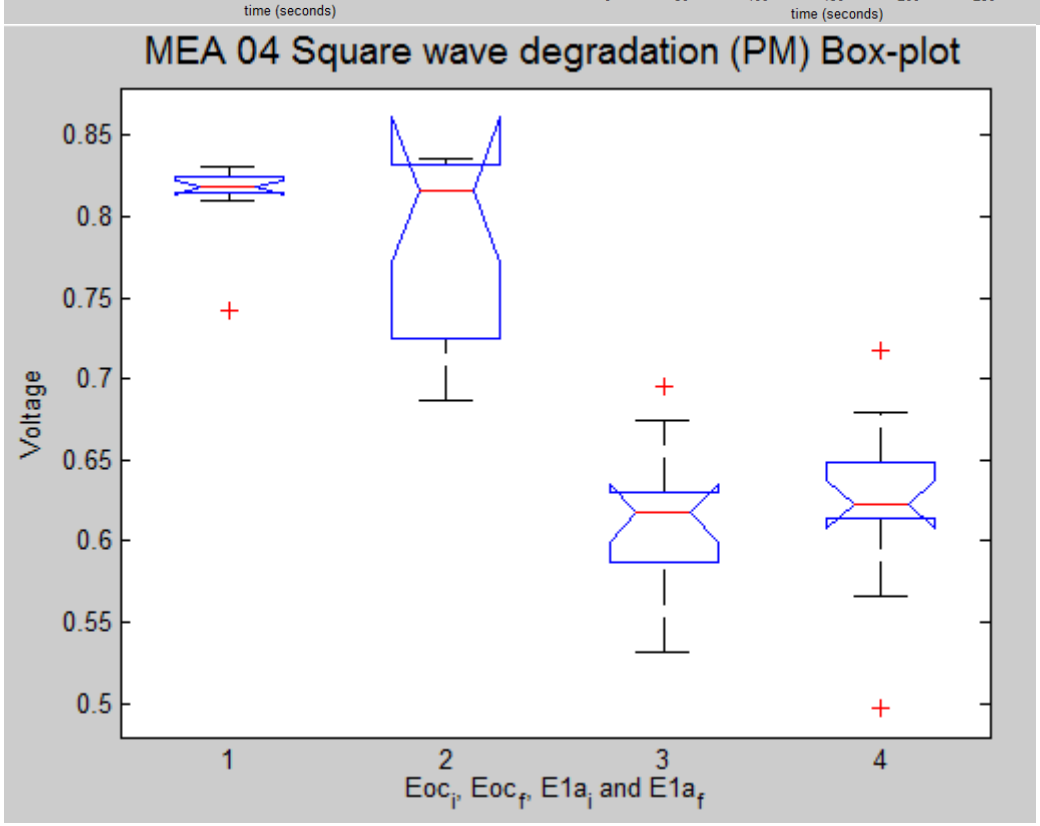
MEA 04 Square wave degradation (PM) Box-plot
Voltage
Eoc_i, Eoc_f, E1a_i and E1a_f

MEA 04 (Freudenberg cathode, low-D, Square Wave) PM

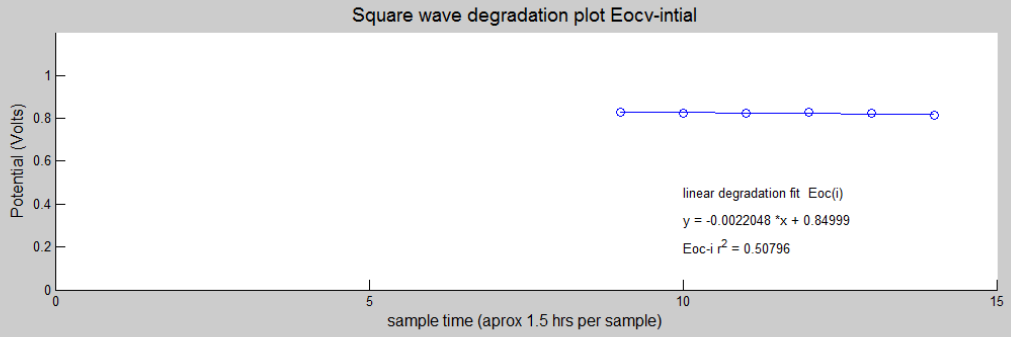

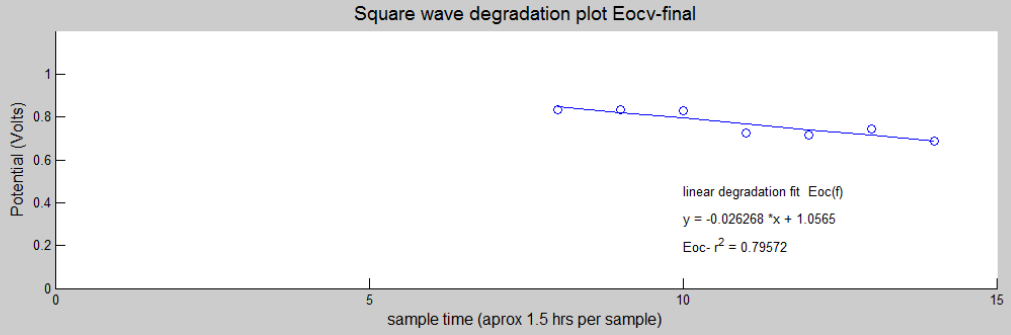

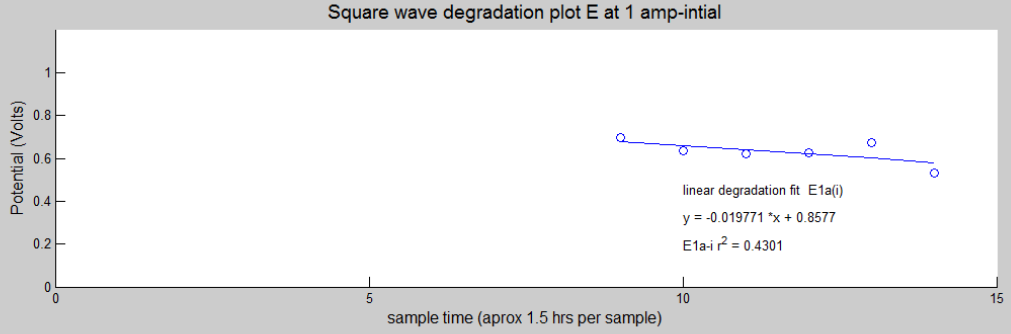

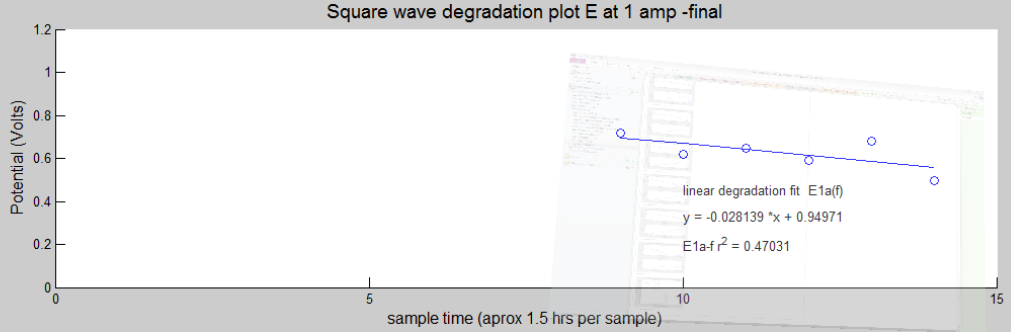

MEA 04 (Freudenberg cathode, low-D, Square Wave)PM

Square wave degradation plot Eocv-intial

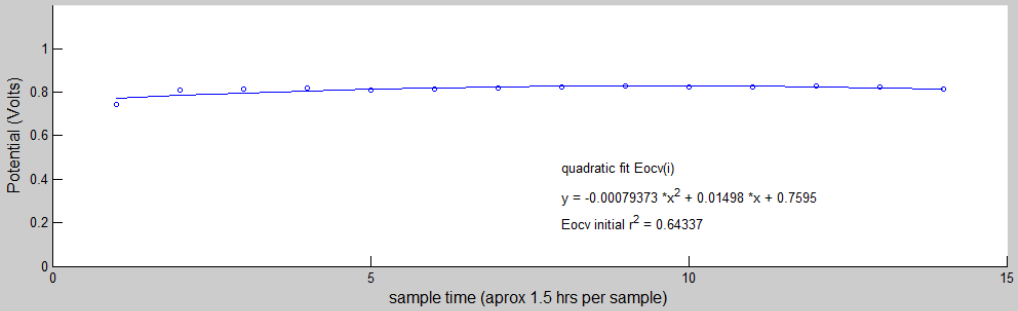

Square wave degradation plot Eocv-final

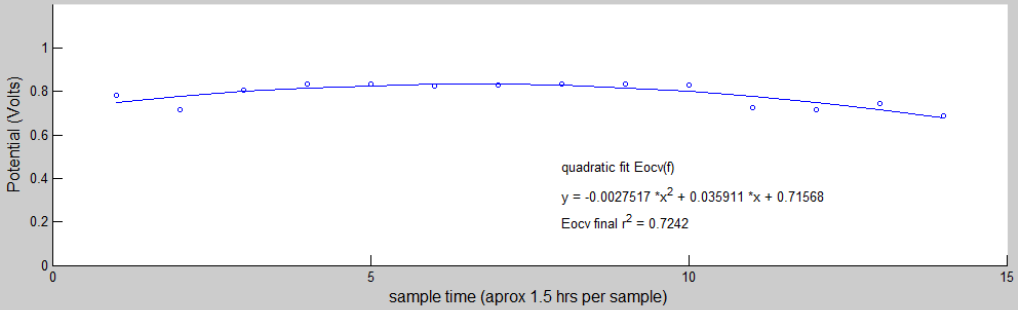

Square wave degradation plot E1 Amp-intial

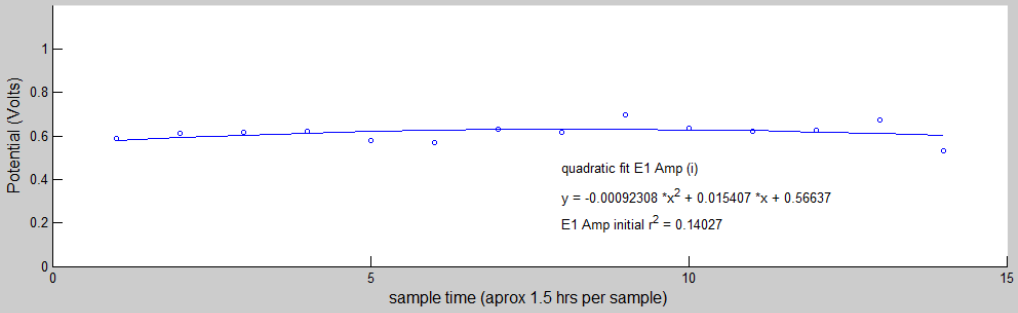

Square wave degradation plot E1 Amp-final

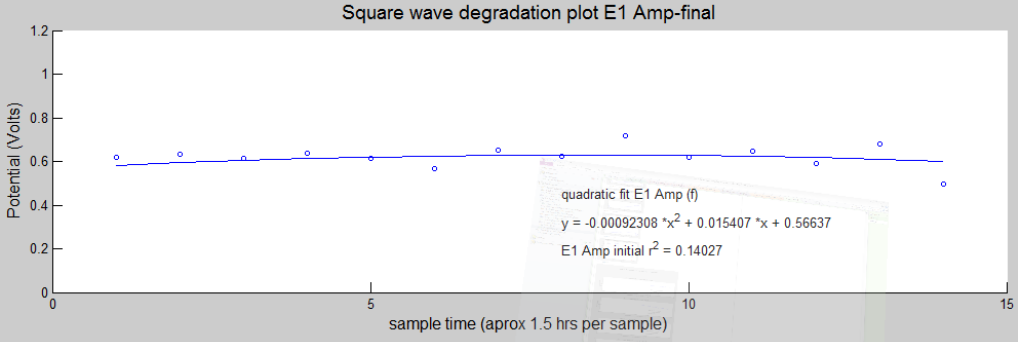

MEA 04 (Freudenberg cathode, low-D, Square Wave)PM

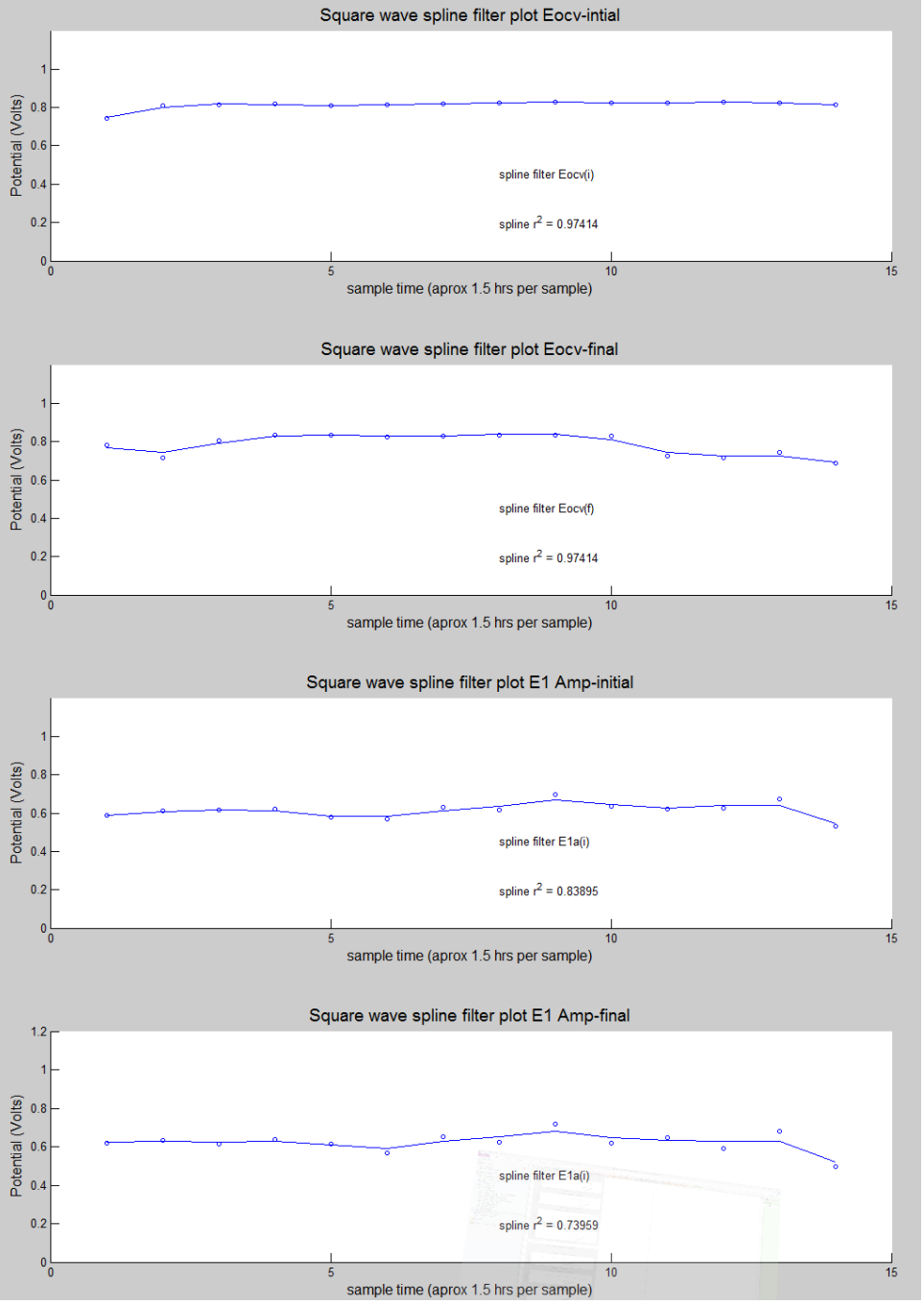

MEA 06

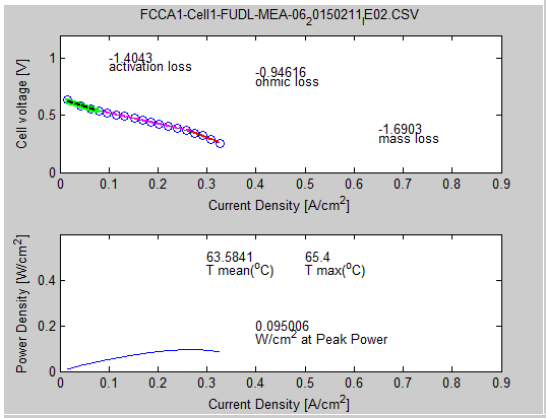
FCCA1-Cell1-FUDL-MEA-06_20150211_E02.CSV
-1.4043
activation loss
-0.94616
ohmic loss
-1.6903
mass loss
Cell voltage [V]
Current Density [A/cm2]
63.5841
T mean(°C)
65.4
T max(°C)
0.095006
W/cm2 at Peak Power
Power Density [W/cm2]
Current Density [A/cm2]

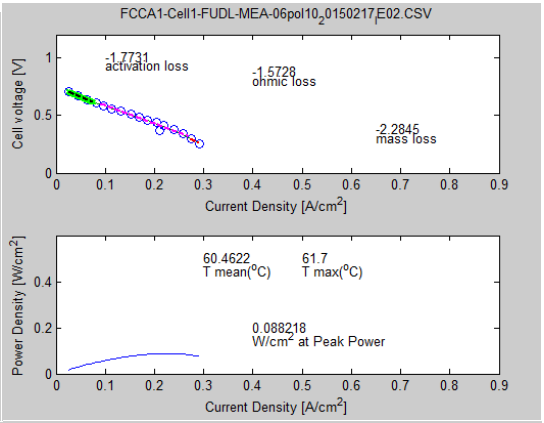
FCCA1-Cell1-FUDL-MEA-06pol10_20150217_E02.CSV
-1.7731
activation loss
-1.5728
ohmic loss
-2.2845
mass loss
Cell voltage [V]
Current Density [A/cm2]
60.4622
T mean(°C)
61.7
T max(°C)
0.088218
W/cm2 at Peak Power
Power Density [W/cm2]
Current Density [A/cm2]

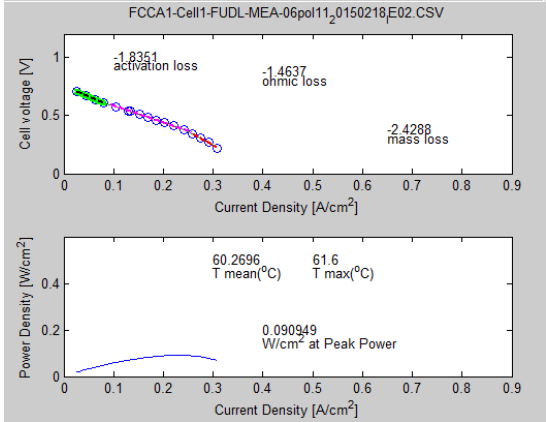
FCCA1-Cell1-FUDL-MEA-06pol11_20150218_E02.CSV
-1.8351
activation loss
-1.4637
ohmic loss
-2.4288
mass loss
Cell voltage [V]
Current Density [A/cm2]
60.2696
T mean(°C)
61.6
T max(°C)
0.090949
W/cm2 at Peak Power
Power Density [W/cm2]
Current Density [A/cm2]

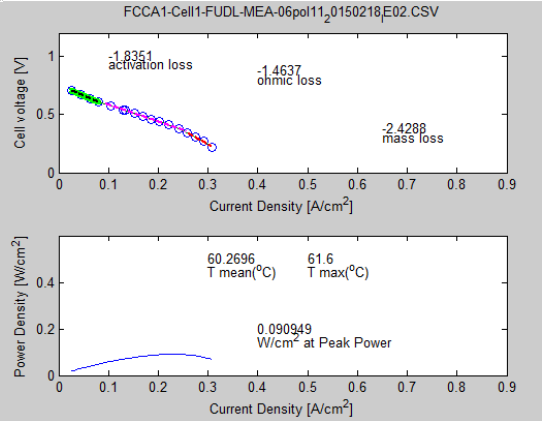
FCCA1-Cell1-FUDL-MEA-06pol11_20150218_E02.CSV
-1.8351
activation loss
-1.4637
ohmic loss
-2.4288
mass loss
Cell voltage [V]
Current Density [A/cm2]
60.2696
T mean(°C)
61.6
T max(°C)
0.090949
W/cm2 at Peak Power
Power Density [W/cm2]
Current Density [A/cm2]

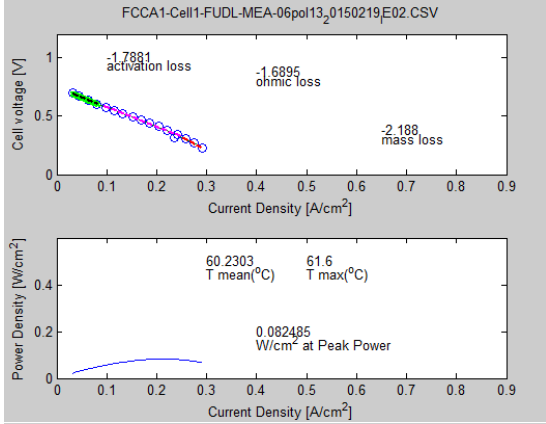
FCCA1-Cell1-FUDL-MEA-06pol13_20150219_E02.CSV
-1.7881
activation loss
-1.6895
ohmic loss
-2.188
mass loss
Cell voltage [V]
Current Density [A/cm2]
60.2303
T mean(°C)
61.6
T max(°C)
0.082485
W/cm2 at Peak Power
Power Density [W/cm2]
Current Density [A/cm2]

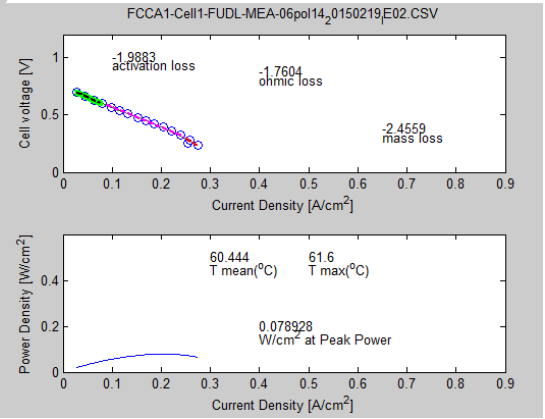
FCCA1-Cell1-FUDL-MEA-06pol14_20150219_E02.CSV
-1.9883
activation loss
-1.7604
ohmic loss
-2.4559
mass loss
Cell voltage [V]
Current Density [A/cm2]
60.444
T mean(°C)
61.6
T max(°C)
0.078928
W/cm2 at Peak Power
Power Density [W/cm2]
Current Density [A/cm2]

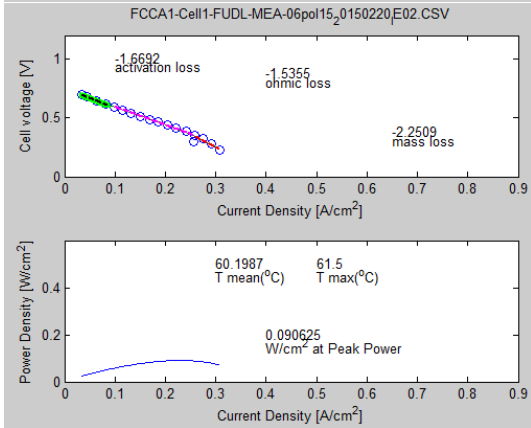
FCCA1-Cell1-FUDL-MEA-06pol15_20150220_E02.CSV
-1.6692
activation loss
-1.5355
ohmic loss
-2.2509
mass loss
Cell voltage [V]
Current Density [A/cm2]
60.1987
T mean(°C)
61.5
T max(°C)
0.090625
W/cm2 at Peak Power
Power Density [W/cm2]
Current Density [A/cm2]

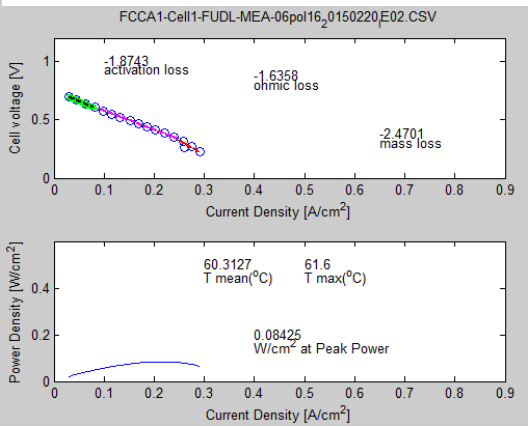
FCCA1-Cell1-FUDL-MEA-06pol16_20150220_E02.CSV
-1.8743
activation loss
-1.6358
ohmic loss
-2.4701
mass loss
Cell voltage [V]
Current Density [A/cm2]
60.3127
T mean(°C)
61.6
T max(°C)
0.08425
W/cm2 at Peak Power
Power Density [W/cm2]
Current Density [A/cm2]

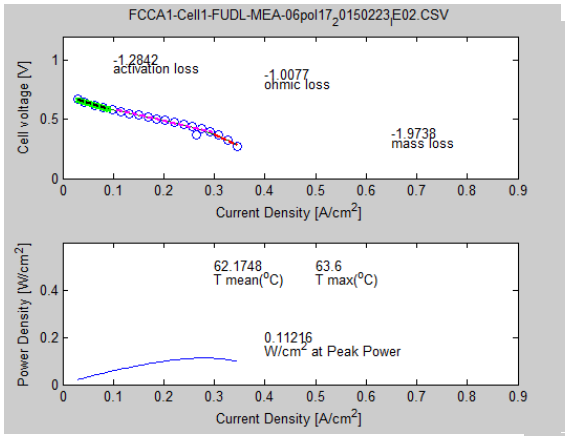
FCCA1-Cell1-FUDL-MEA-06pol17_0150223_E02.CSV
-1.2842
activation loss
-1.0077
ohmic loss
-1.9738
mass loss
Cell voltage [V]
Current Density [A/cm2]
62.1748
T mean(°C)
63.6
T max(°C)
0.11216
W/cm2 at Peak Power
Power Density [W/cm2]
Current Density [A/cm2]

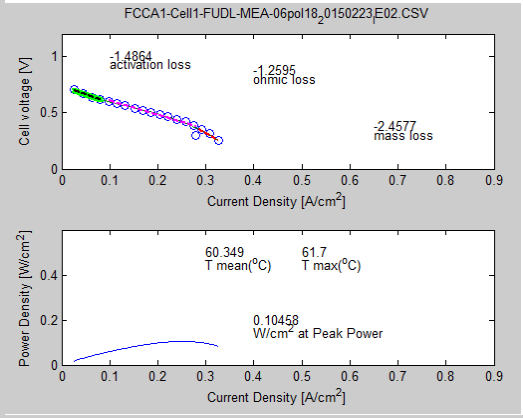
FCCA1-Cell1-FUDL-MEA-06pol18_0150223_E02.CSV
-1.4864
activation loss
-1.2595
ohmic loss
-2.4577
mass loss
Cell voltage [V]
Current Density [A/cm2]
60.349
T mean(°C)
61.7
T max(°C)
0.10458
W/cm2 at Peak Power
Power Density [W/cm2]
Current Density [A/cm2]

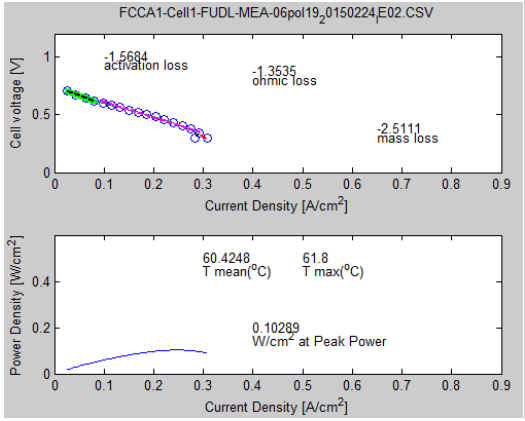
FCCA1-Cell1-FUDL-MEA-06pol19_0150224_E02.CSV
-1.5684
activation loss
-1.3535
ohmic loss
-2.5111
mass loss
Cell voltage [V]
Current Density [A/cm2]
60.4248
T mean(°C)
61.8
T max(°C)
0.10289
W/cm2 at Peak Power
Power Density [W/cm2]
Current Density [A/cm2]

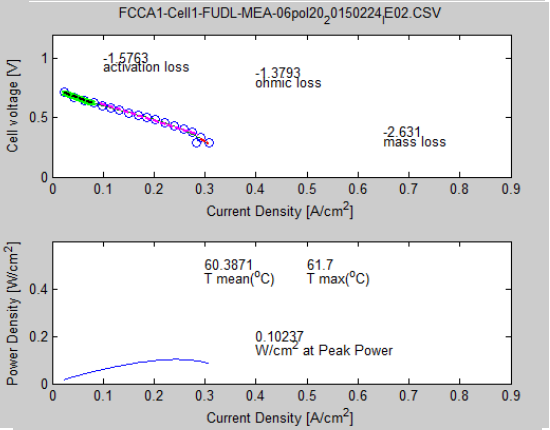
FCCA1-Cell1-FUDL-MEA-06pol20_0150224_E02.CSV
-1.5763
activation loss
-1.3793
ohmic loss
-2.631
mass loss
Cell voltage [V]
Current Density [A/cm2]
60.3871
T mean(°C)
61.7
T max(°C)
0.10237
W/cm2 at Peak Power
Power Density [W/cm2]
Current Density [A/cm2]

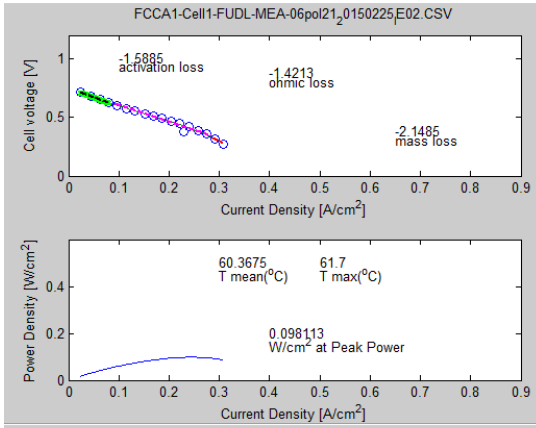
FCCA1-Cell1-FUDL-MEA-06pol21_0150225_E02.CSV
-1.5885
activation loss
-1.4213
ohmic loss
-2.1485
mass loss
Cell voltage [V]
Current Density [A/cm2]
60.3675
T mean(°C)
61.7
T max(°C)
0.098113
W/cm2 at Peak Power
Power Density [W/cm2]
Current Density [A/cm2]

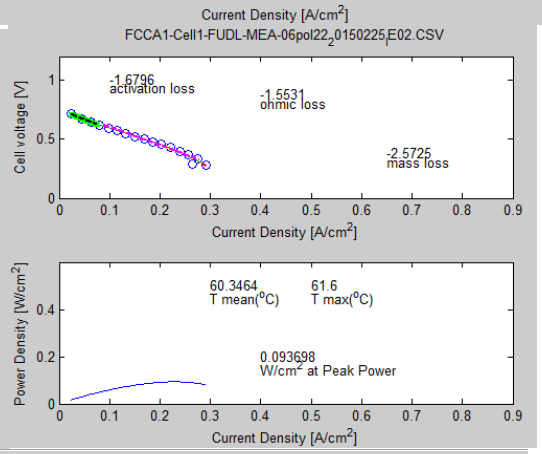
FCCA1-Cell1-FUDL-MEA-06pol22_0150225_E02.CSV
-1.6796
activation loss
-1.5531
ohmic loss
-2.5725
mass loss
Cell voltage [V]
Current Density [A/cm2]
60.3464
T mean(°C)
61.6
T max(°C)
0.093698
W/cm2 at Peak Power
Power Density [W/cm2]
Current Density [A/cm2]

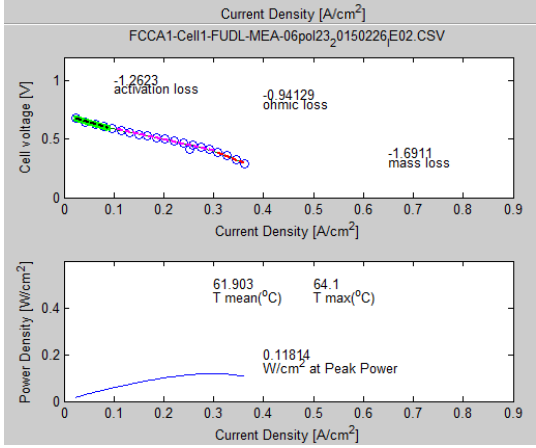
FCCA1-Cell1-FUDL-MEA-06pol23_0150226_E02.CSV
-1.2623
activation loss
-0.94129
ohmic loss
-1.6911
mass loss
Cell voltage [V]
Current Density [A/cm2]
61.903
T mean(°C)
64.1
T max(°C)
0.11814
W/cm2 at Peak Power
Power Density [W/cm2]
Current Density [A/cm2]

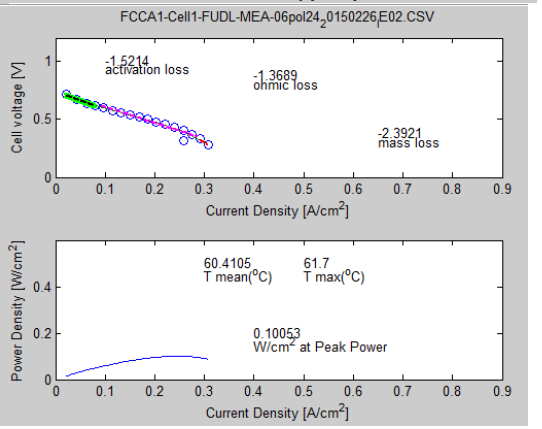
FCCA1-Cell1-FUDL-MEA-06pol24_0150226_E02.CSV
-1.5214
activation loss
-1.3689
ohmic loss
-2.3921
mass loss
Cell voltage [V]
Current Density [A/cm2]
60.4105
T mean(°C)
61.7
T max(°C)
0.10053
W/cm2 at Peak Power
Power Density [W/cm2]
Current Density [A/cm2]

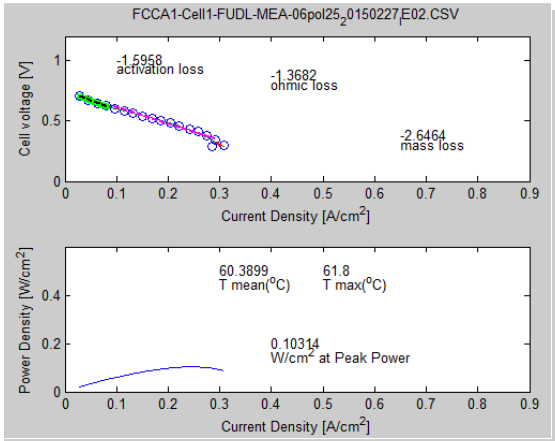
FCCA1-Cell1-FUDL-MEA-06pol25_2_0150227_E02.CSV
-1.5958
activation loss
-1.3682
ohmic loss
-2.6464
mass loss
Cell voltage [V]
Current Density [A/cm2]
60.3899
T mean(°C)
61.8
T max(°C)
0.10314
W/cm2 at Peak Power
Power Density [W/cm2]
Current Density [A/cm2]

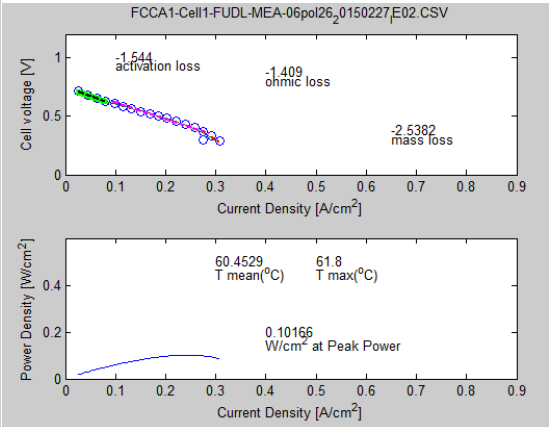
FCCA1-Cell1-FUDL-MEA-06pol26_2_0150227_E02.CSV
-1.544
activation loss
-1.409
ohmic loss
-2.5382
mass loss
Cell voltage [V]
Current Density [A/cm2]
60.4529
T mean(°C)
61.8
T max(°C)
0.10166
W/cm2 at Peak Power
Power Density [W/cm2]
Current Density [A/cm2]

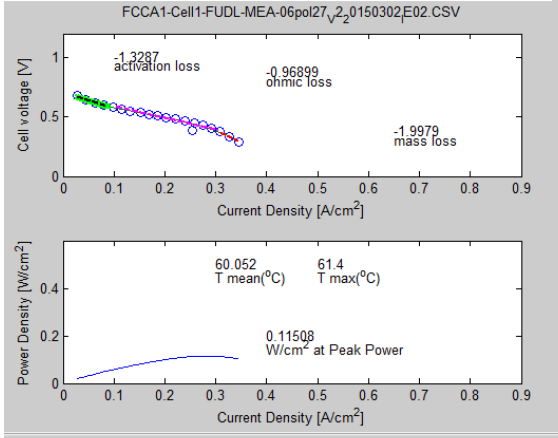
FCCA1-Cell1-FUDL-MEA-06pol27_V_2_0150302_E02.CSV
-1.3287
activation loss
-0.96899
ohmic loss
-1.9979
mass loss
Cell voltage [V]
Current Density [A/cm2]
60.052
T mean(°C)
61.4
T max(°C)
0.11508
W/cm2 at Peak Power
Power Density [W/cm2]
Current Density [A/cm2]

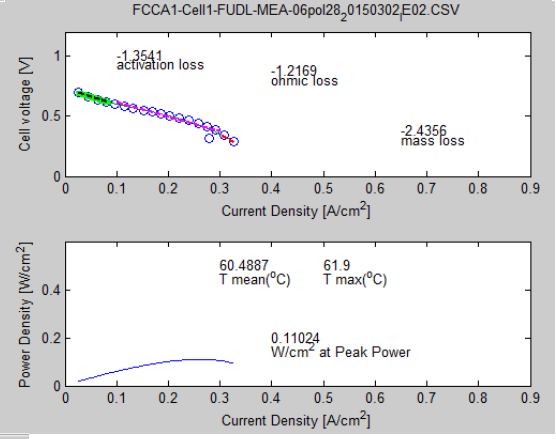
FCCA1-Cell1-FUDL-MEA-06pol28_2_0150302_E02.CSV
-1.3541
activation loss
-1.2169
ohmic loss
-2.4356
mass loss
Cell voltage [V]
Current Density [A/cm2]
60.4887
T mean(°C)
61.9
T max(°C)
0.11024
W/cm2 at Peak Power
Power Density [W/cm2]
Current Density [A/cm2]

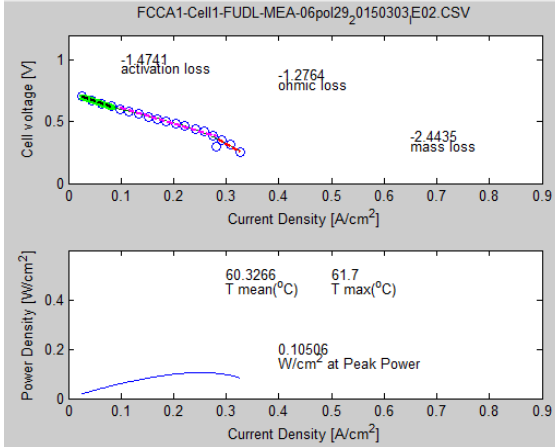
FCCA1-Cell1-FUDL-MEA-06pol29_2_0150303_E02.CSV
-1.4741
activation loss
-1.2764
ohmic loss
-2.4435
mass loss
Cell voltage [V]
Current Density [A/cm2]
60.3266
T mean(°C)
61.7
T max(°C)
0.10506
W/cm2 at Peak Power
Power Density [W/cm2]
Current Density [A/cm2]

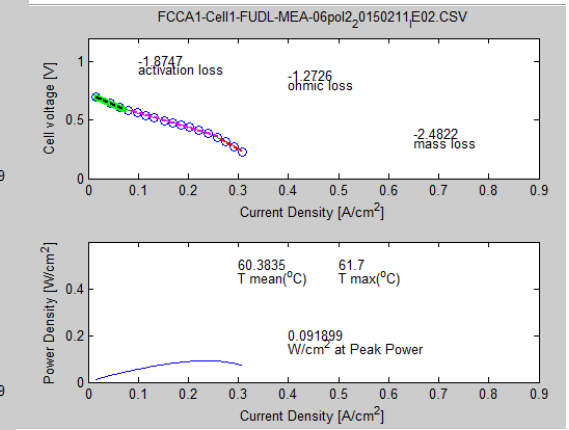
FCCA1-Cell1-FUDL-MEA-06pol2_2_0150211_E02.CSV
-1.8747
activation loss
-1.2726
ohmic loss
-2.4822
mass loss
Cell voltage [V]
Current Density [A/cm2]
60.3835
T mean(°C)
61.7
T max(°C)
0.091899
W/cm2 at Peak Power
Power Density [W/cm2]
Current Density [A/cm2]

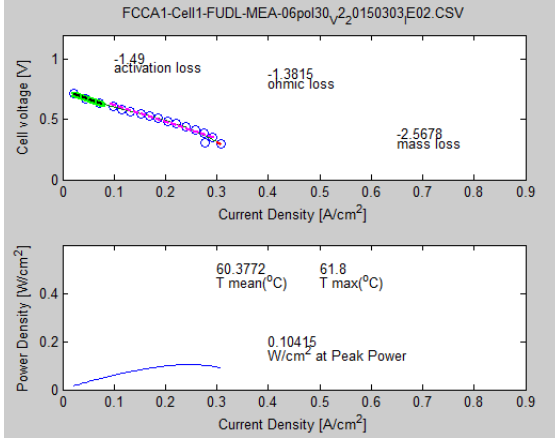
FCCA1-Cell1-FUDL-MEA-06pol30_V_2_0150303_E02.CSV
-1.49
activation loss
-1.3815
ohmic loss
-2.5678
mass loss
Cell voltage [V]
Current Density [A/cm2]
60.3772
T mean(°C)
61.8
T max(°C)
0.10415
W/cm2 at Peak Power
Power Density [W/cm2]
Current Density [A/cm2]

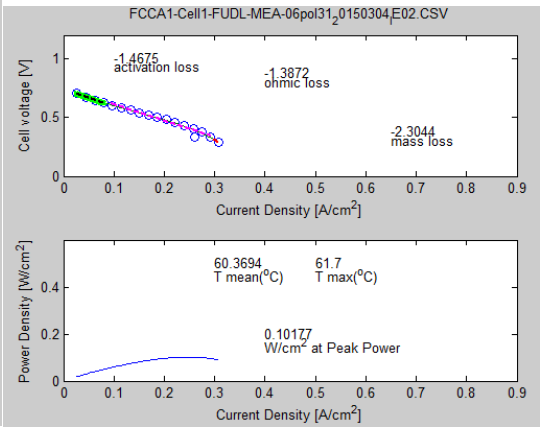
FCCA1-Cell1-FUDL-MEA-06pol31_2_0150304_E02.CSV
-1.4675
activation loss
-1.3872
ohmic loss
-2.3044
mass loss
Cell voltage [V]
Current Density [A/cm2]
60.3694
T mean(°C)
61.7
T max(°C)
0.10177
W/cm2 at Peak Power
Power Density [W/cm2]
Current Density [A/cm2]

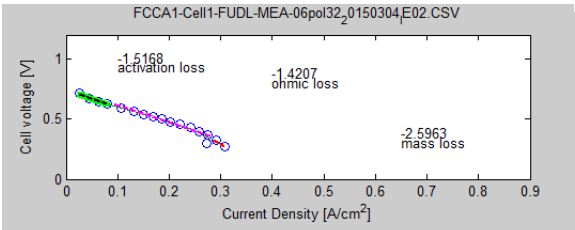
FCCA1-Cell1-FUDL-MEA-06pol32_20150304_E02.CSV
-1.5168
activation loss
-1.4207
ohmic loss
-2.5963
mass loss
Cell voltage [V]
Current Density [A/cm2]

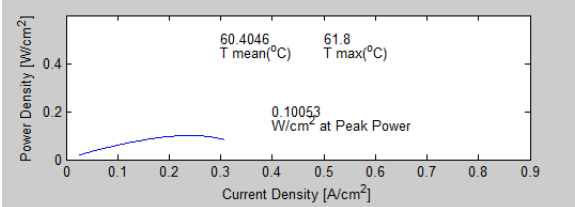
60.4046
T mean(°C)
61.8
T max(°C)
0.10053
W/cm2 at Peak Power
Power Density [W/cm2]
Current Density [A/cm2]

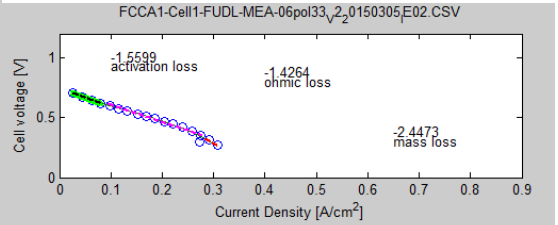
FCCA1-Cell1-FUDL-MEA-06pol33_V2_20150305_E02.CSV
-1.5599
activation loss
-1.4264
ohmic loss
-2.4473
mass loss
Cell voltage [V]
Current Density [A/cm2]

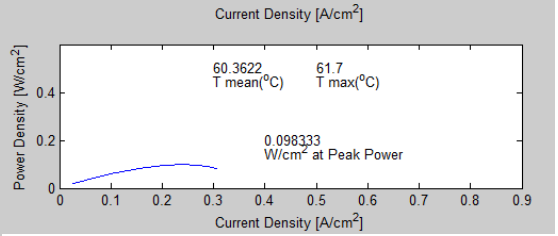
60.3622
T mean(°C)
61.7
T max(°C)
0.098333
W/cm2 at Peak Power
Power Density [W/cm2]
Current Density [A/cm2]

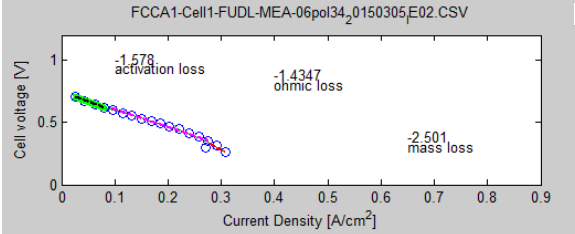
FCCA1-Cell1-FUDL-MEA-06pol34_20150305_E02.CSV
-1.578
activation loss
-1.4347
ohmic loss
-2.501
mass loss
Cell voltage [V]
Current Density [A/cm2]

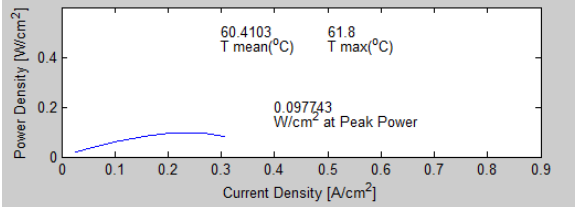
60.4103
T mean(°C)
61.8
T max(°C)
0.097743
W/cm2 at Peak Power
Power Density [W/cm2]
Current Density [A/cm2]

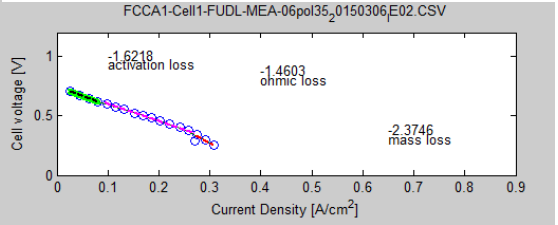
FCCA1-Cell1-FUDL-MEA-06pol35_20150306_E02.CSV
-1.6218
activation loss
-1.4603
ohmic loss
-2.3746
mass loss
Cell voltage [V]
Current Density [A/cm2]

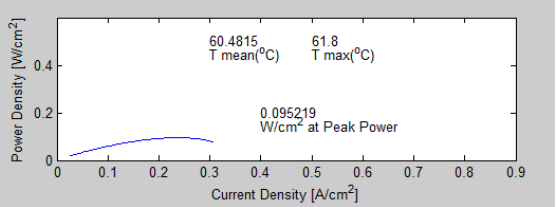
60.4815
T mean(°C)
61.8
T max(°C)
0.095219
W/cm2 at Peak Power
Power Density [W/cm2]
Current Density [A/cm2]

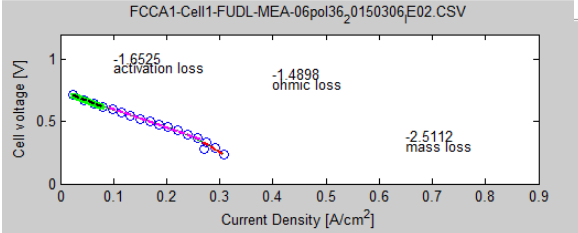
FCCA1-Cell1-FUDL-MEA-06pol36_20150306_E02.CSV
-1.6525
activation loss
-1.4898
ohmic loss
-2.5112
mass loss
Cell voltage [V]
Current Density [A/cm2]

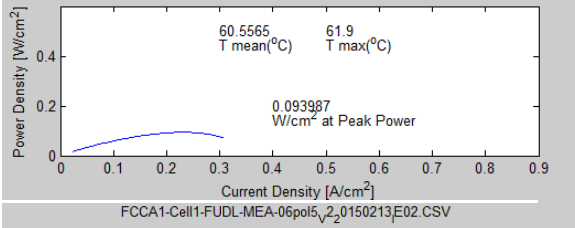
60.5565
T mean(°C)
61.9
T max(°C)
0.093987
W/cm2 at Peak Power
Power Density [W/cm2]
Current Density [A/cm2]

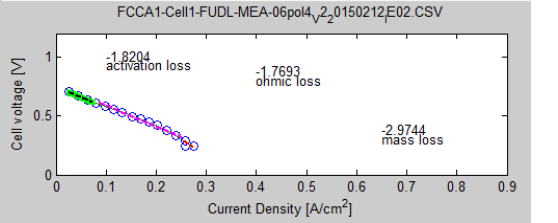
FCCA1-Cell1-FUDL-MEA-06pol4_V2_20150212_E02.CSV
-1.8204
activation loss
-1.7693
ohmic loss
-2.9744
mass loss
Cell voltage [V]
Current Density [A/cm2]

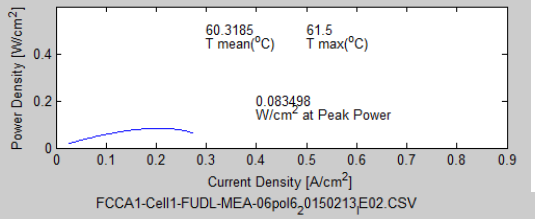
60.3185
T mean(°C)
61.5
T max(°C)
0.083498
W/cm2 at Peak Power
Power Density [W/cm2]
Current Density [A/cm2]

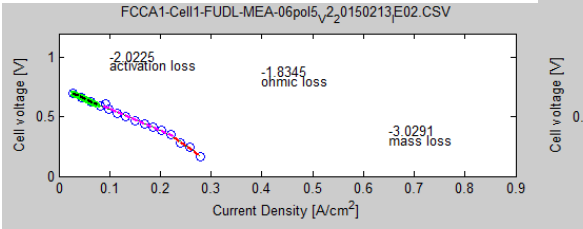
FCCA1-Cell1-FUDL-MEA-06pol5_V2_20150213_E02.CSV
-2.0225
activation loss
-1.8345
ohmic loss
-3.0291
mass loss
Cell voltage [V]
Current Density [A/cm2]

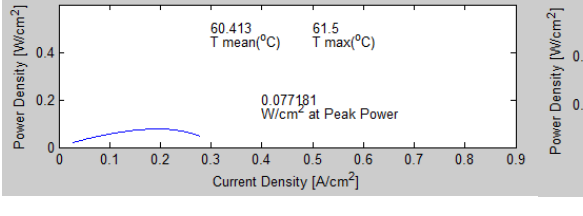
60.413
T mean(°C)
61.5
T max(°C)
0.077181
W/cm2 at Peak Power
Power Density [W/cm2]
Current Density [A/cm2]

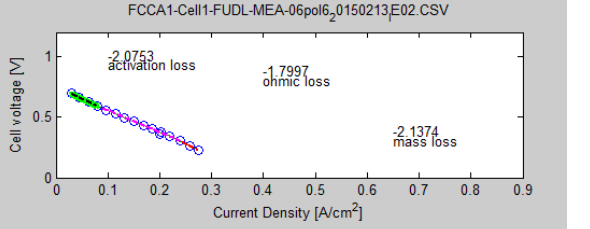
FCCA1-Cell1-FUDL-MEA-06pol6_20150213_E02.CSV
-2.0753
activation loss
-1.7997
ohmic loss
-2.1374
mass loss
Cell voltage [V]
Current Density [A/cm2]

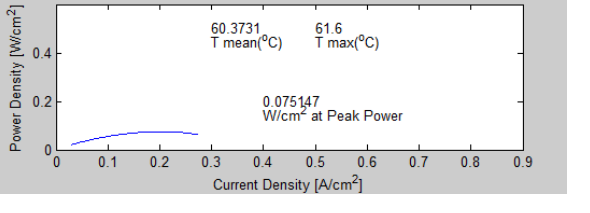
60.3731
T mean(°C)
61.6
T max(°C)
0.075147
W/cm2 at Peak Power
Power Density [W/cm2]
Current Density [A/cm2]

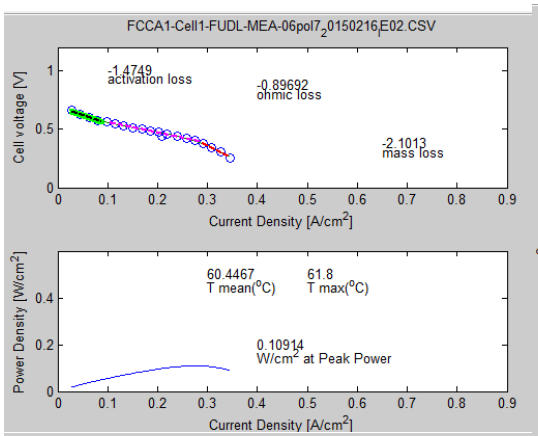
FCCA1-Cell1-FUDL-MEA-06pol7_2_0150216_E02.CSV
Cell voltage [V]
-1.4749
activation loss
-0.89692
ohmic loss
-2.1013
mass loss
Current Density [A/cm2]
Power Density [W/cm2]
60.4467
T mean(°C)
61.8
T max(°C)
0.10914
W/cm2 at Peak Power
Current Density [A/cm2]

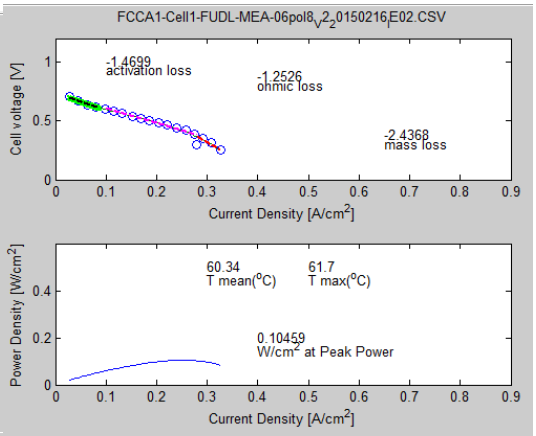
FCCA1-Cell1-FUDL-MEA-06pol8_V_2_0150216_E02.CSV
Cell voltage [V]
-1.4699
activation loss
-1.2526
ohmic loss
-2.4368
mass loss
Current Density [A/cm2]
Power Density [W/cm2]
60.34
T mean(°C)
61.7
T max(°C)
0.10459
W/cm2 at Peak Power
Current Density [A/cm2]

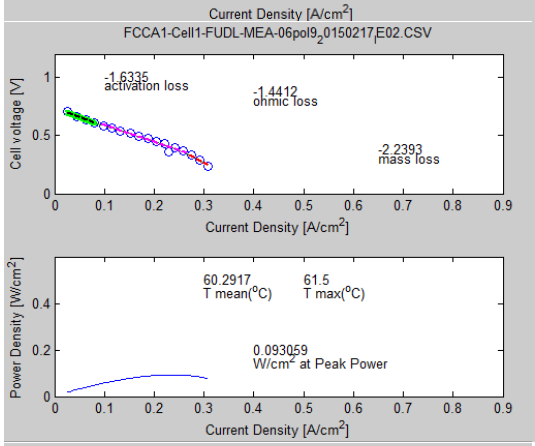
FCCA1-Cell1-FUDL-MEA-06pol9_2_0150217_E02.CSV
Cell voltage [V]
-1.6335
activation loss
-1.4412
ohmic loss
-2.2393
mass loss
Current Density [A/cm2]
Power Density [W/cm2]
60.2917
T mean(°C)
61.5
T max(°C)
0.093059
W/cm2 at Peak Power
Current Density [A/cm2]

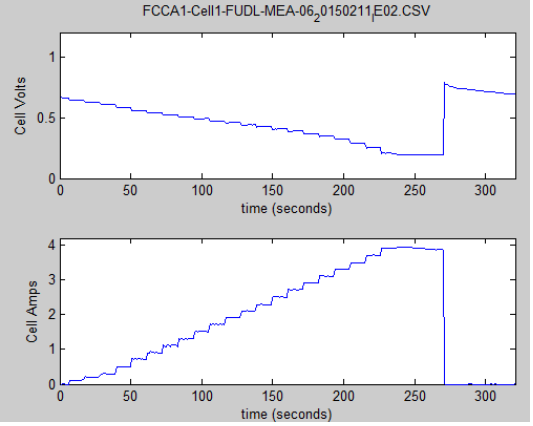
FCCA1-Cell1-FUDL-MEA-06_2_0150211_E02.CSV
Cell Volts
time (seconds)
Cell Amps
time (seconds)

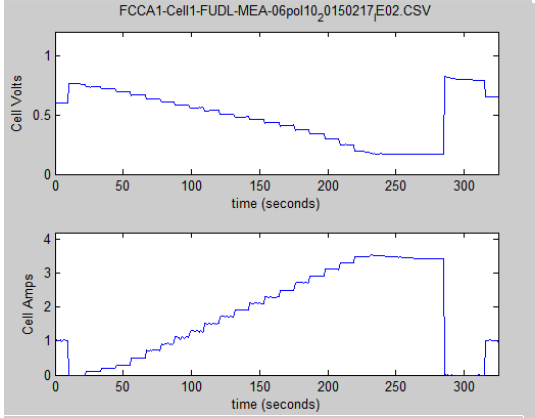
FCCA1-Cell1-FUDL-MEA-06pol10_2_0150217_E02.CSV
Cell Volts
time (seconds)
Cell Amps
time (seconds)

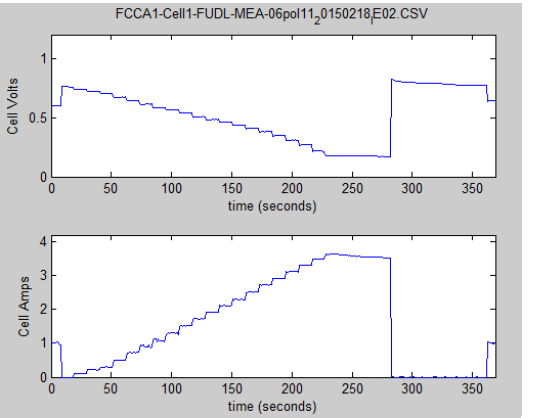
FCCA1-Cell1-FUDL-MEA-06pol11_2_0150218_E02.CSV
Cell Volts
time (seconds)
Cell Amps
time (seconds)

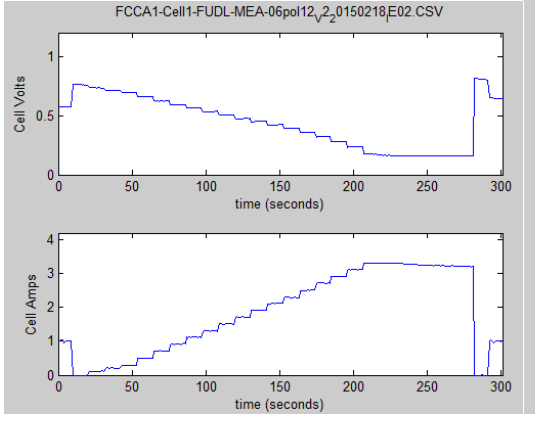
FCCA1-Cell1-FUDL-MEA-06pol12_V_2_0150218_E02.CSV
Cell Volts
time (seconds)
Cell Amps
time (seconds)

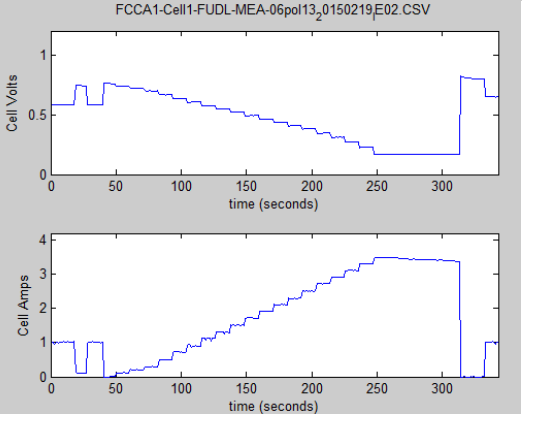
FCCA1-Cell1-FUDL-MEA-06pol13_2_0150219_E02.CSV
Cell Volts
time (seconds)
Cell Amps
time (seconds)

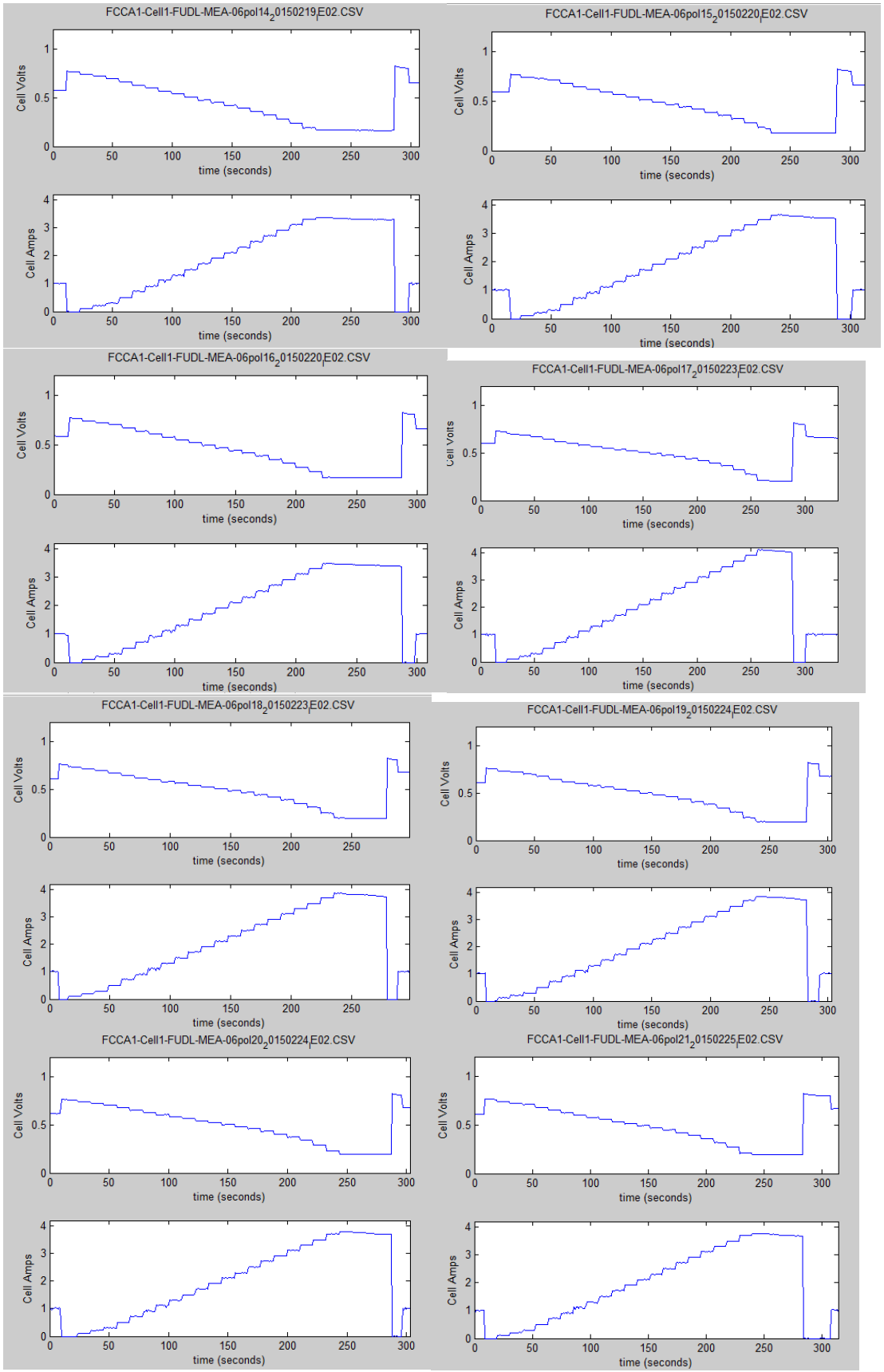
FCCA1-Cell1-FUDL-MEA-06pol14_20150219_E02.CSV
FCCA1-Cell1-FUDL-MEA-06pol15_20150220_E02.CSV
FCCA1-Cell1-FUDL-MEA-06pol16_20150220_E02.CSV
FCCA1-Cell1-FUDL-MEA-06pol17_20150223_E02.CSV
FCCA1-Cell1-FUDL-MEA-06pol18_20150223_E02.CSV
FCCA1-Cell1-FUDL-MEA-06pol19_20150224_E02.CSV
FCCA1-Cell1-FUDL-MEA-06pol20_20150224_E02.CSV
FCCA1-Cell1-FUDL-MEA-06pol21_20150225_E02.CSV
Cell Volts
Cell Amps
time (seconds)

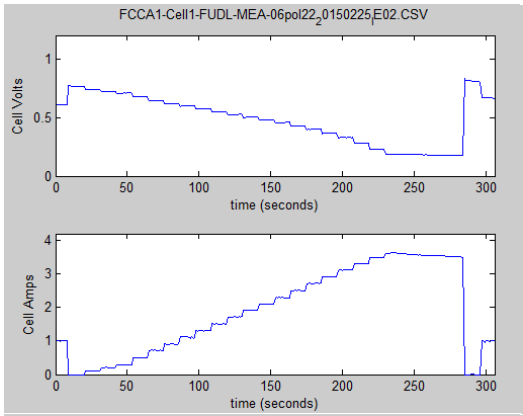
FCCA1-Cell1-FUDL-MEA-06pol22_20150225_E02.CSV
Cell Volts
time (seconds)
Cell Amps
time (seconds)

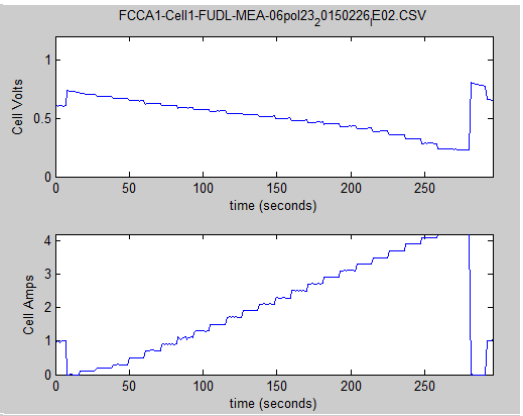
FCCA1-Cell1-FUDL-MEA-06pol23_20150226_E02.CSV
Cell Volts
time (seconds)
Cell Amps
time (seconds)

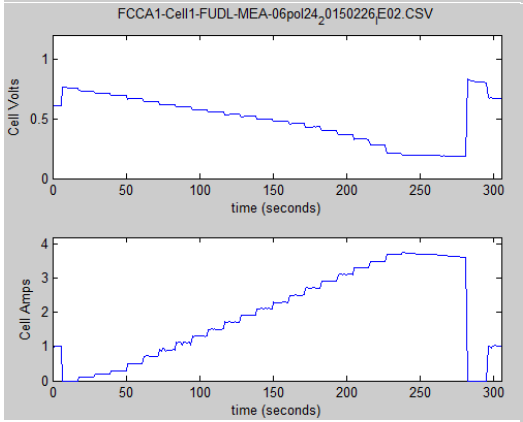
FCCA1-Cell1-FUDL-MEA-06pol24_20150226_E02.CSV
Cell Volts
time (seconds)
Cell Amps
time (seconds)

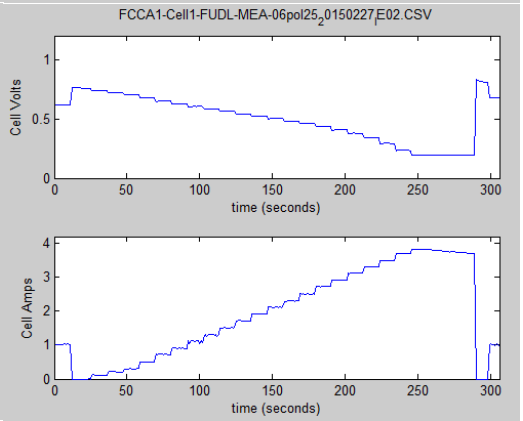
FCCA1-Cell1-FUDL-MEA-06pol25_20150227_E02.CSV
Cell Volts
time (seconds)
Cell Amps
time (seconds)

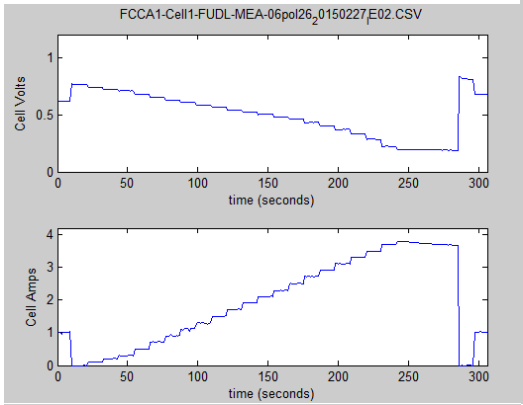
FCCA1-Cell1-FUDL-MEA-06pol26_20150227_E02.CSV
Cell Volts
time (seconds)
Cell Amps
time (seconds)

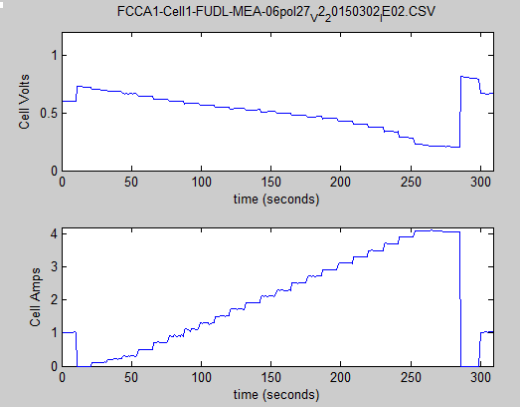
FCCA1-Cell1-FUDL-MEA-06pol27_v2_20150302_E02.CSV
Cell Volts
time (seconds)
Cell Amps
time (seconds)

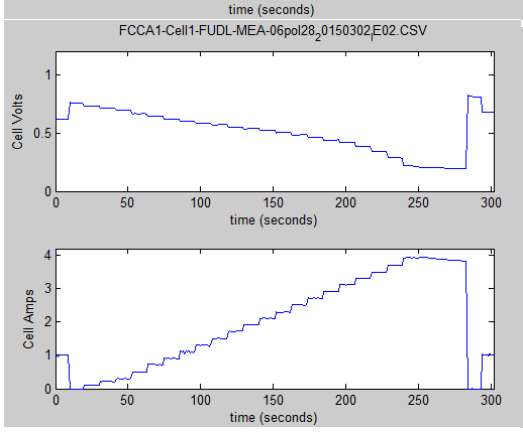
FCCA1-Cell1-FUDL-MEA-06pol28_20150302_E02.CSV
Cell Volts
time (seconds)
Cell Amps
time (seconds)

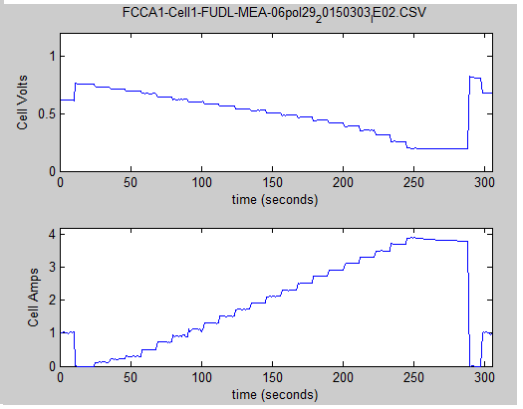
FCCA1-Cell1-FUDL-MEA-06pol29_20150303_E02.CSV
Cell Volts
time (seconds)
Cell Amps
time (seconds)

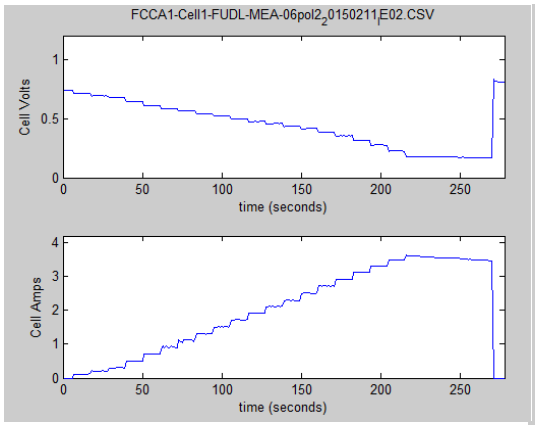
FCCA1-Cell1-FUDL-MEA-06pol2_0150211_E02.CSV
Cell Volts
time (seconds)
Cell Amps
time (seconds)

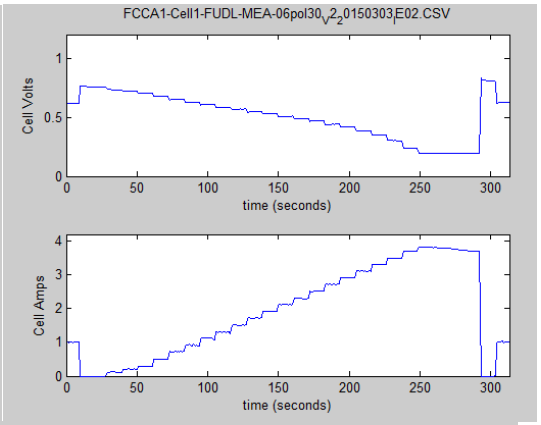
FCCA1-Cell1-FUDL-MEA-06pol30_V2_0150303_E02.CSV
Cell Volts
time (seconds)
Cell Amps
time (seconds)

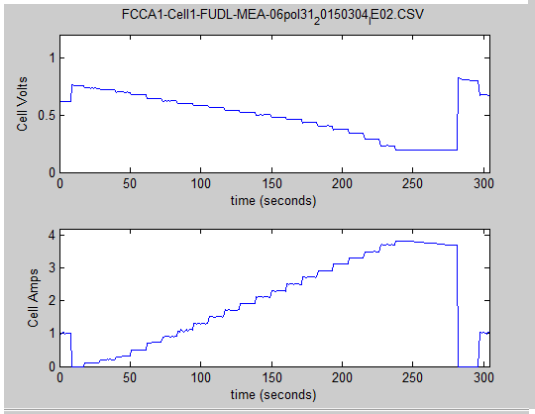
FCCA1-Cell1-FUDL-MEA-06pol31_0150304_E02.CSV
Cell Volts
time (seconds)
Cell Amps
time (seconds)

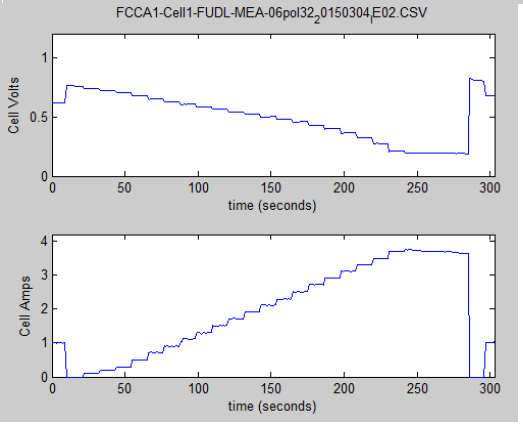
FCCA1-Cell1-FUDL-MEA-06pol32_0150304_E02.CSV
Cell Volts
time (seconds)
Cell Amps
time (seconds)

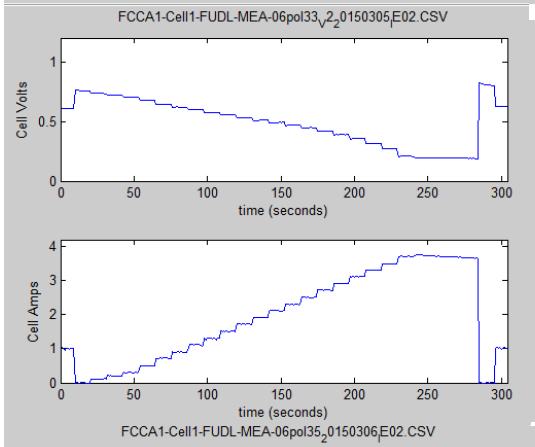
FCCA1-Cell1-FUDL-MEA-06pol33_V2_0150305_E02.CSV
Cell Volts
time (seconds)
Cell Amps
time (seconds)

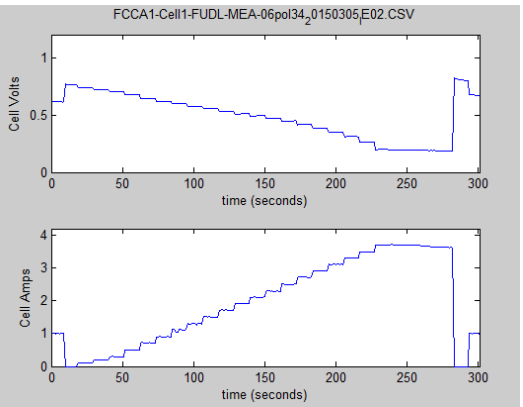
FCCA1-Cell1-FUDL-MEA-06pol34_0150305_E02.CSV
Cell Volts
time (seconds)
Cell Amps
time (seconds)

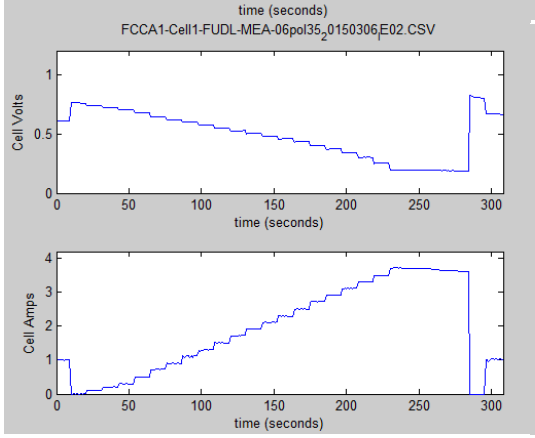
FCCA1-Cell1-FUDL-MEA-06pol35_0150306_E02.CSV
Cell Volts
time (seconds)
Cell Amps
time (seconds)

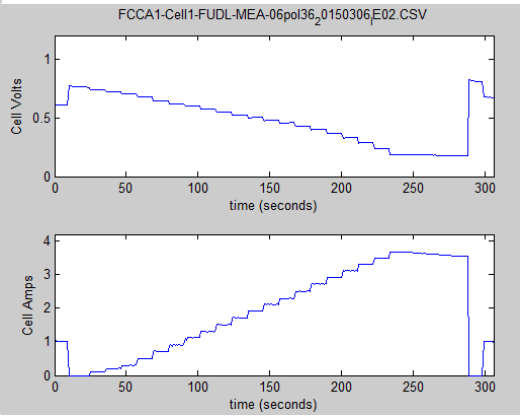
FCCA1-Cell1-FUDL-MEA-06pol36_0150306_E02.CSV
Cell Volts
time (seconds)
Cell Amps
time (seconds)

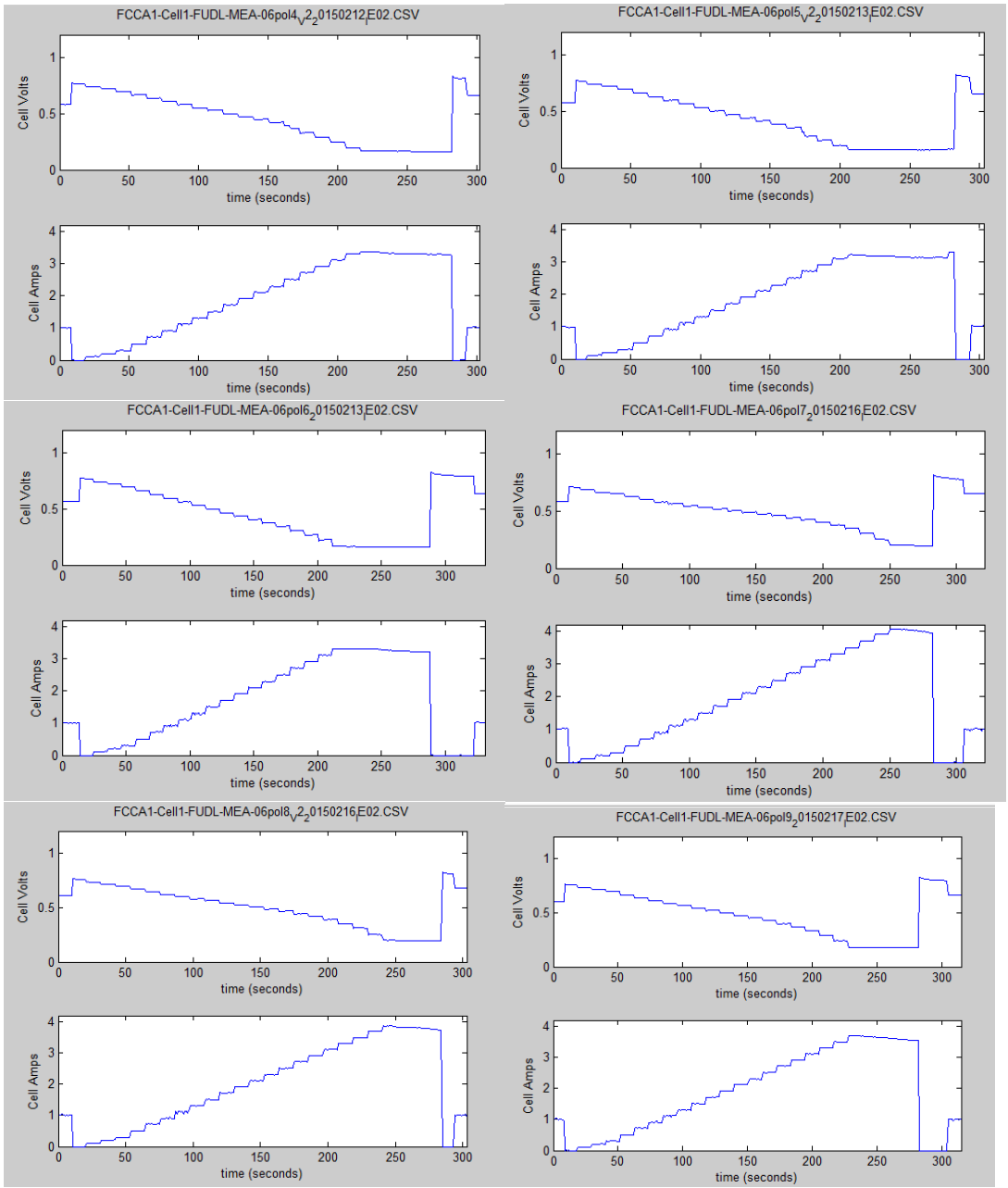
FCCA1-Cell1-FUDL-MEA-06pol4_V2_20150212_E02.CSV
FCCA1-Cell1-FUDL-MEA-06pol5_V2_20150213_E02.CSV
FCCA1-Cell1-FUDL-MEA-06pol6_20150213_E02.CSV
FCCA1-Cell1-FUDL-MEA-06pol7_20150216_E02.CSV
FCCA1-Cell1-FUDL-MEA-06pol8_V2_20150216_E02.CSV
FCCA1-Cell1-FUDL-MEA-06pol9_20150217_E02.CSV
Cell Volts
Cell Amps
time (seconds)

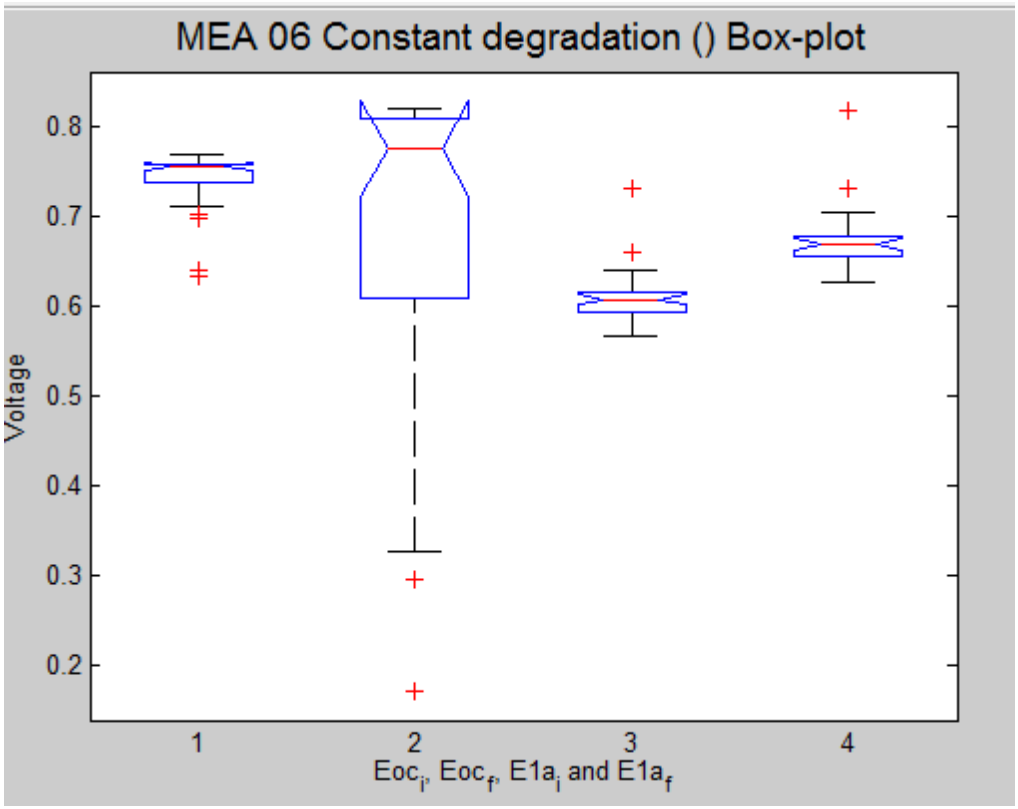
MEA 06 Constant degradation () Box-plot
Voltage
0.8
0.7
0.6
0.5
0.4
0.3
0.2
1
2
3
4
Eoc$_i$, Eoc$_f$, E1a$_i$ and E1a$_f$

MEA 06 (Freudenberg cathode, high-D, Constant)

Constant degradation plot Eocv-intial

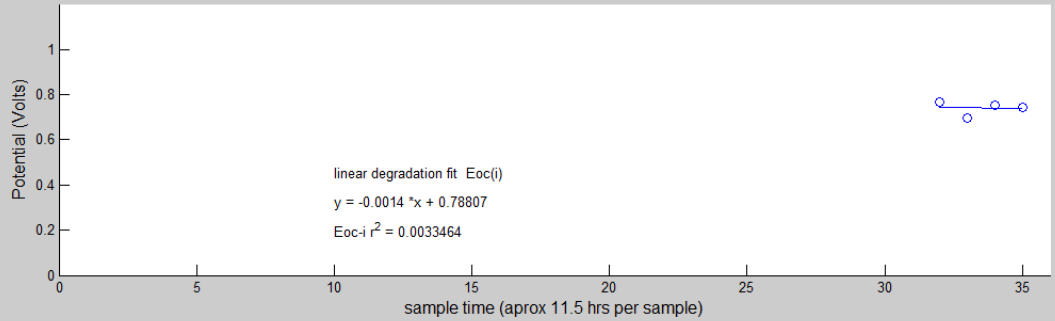

Constant degradation plot Eocv-final

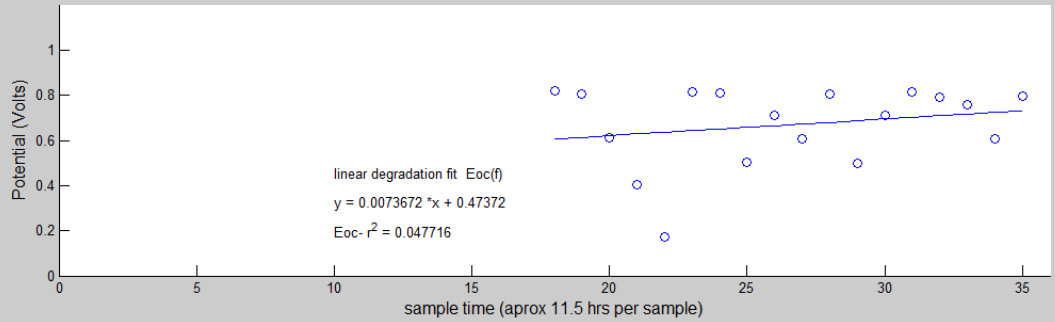

Constant degradation plot E at 1 amp-intial

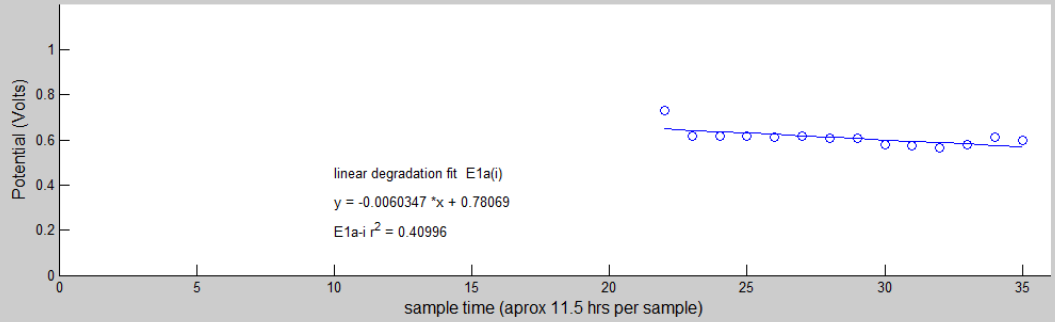

Constant degradation plot E at 1 amp -final

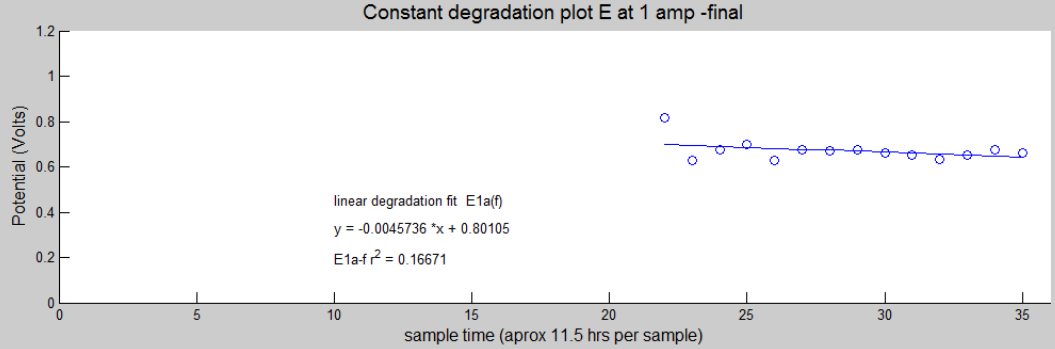

MEA 06 (Freudenberg cathode, high-D, Constant)

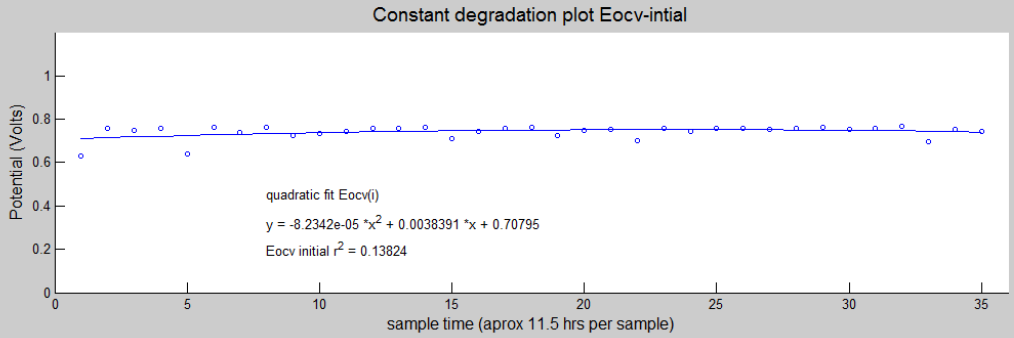

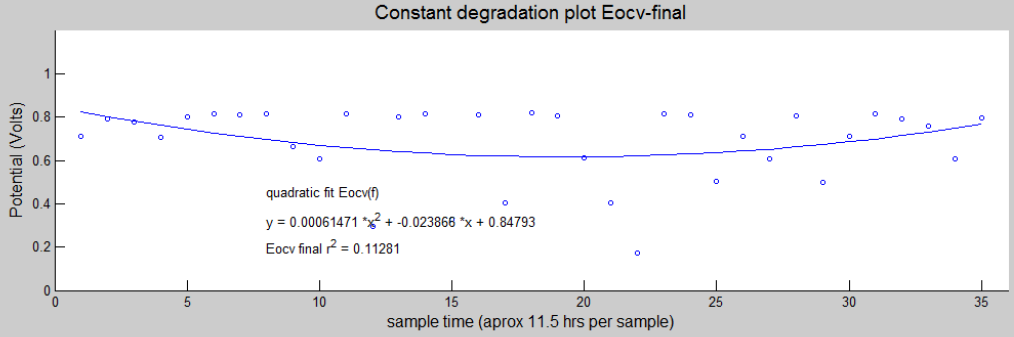

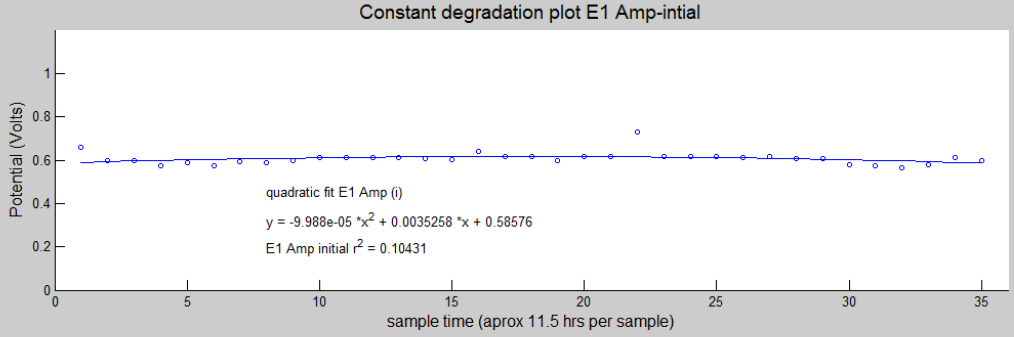

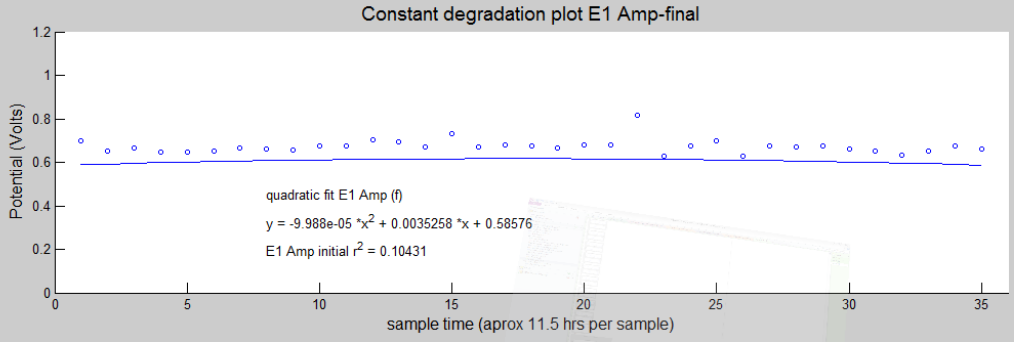

MEA 06 (Freudenberg cathode, high-D, Constant)

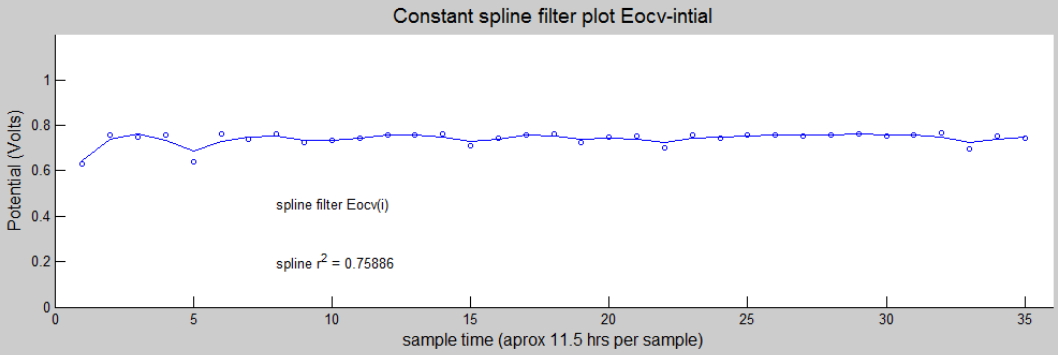

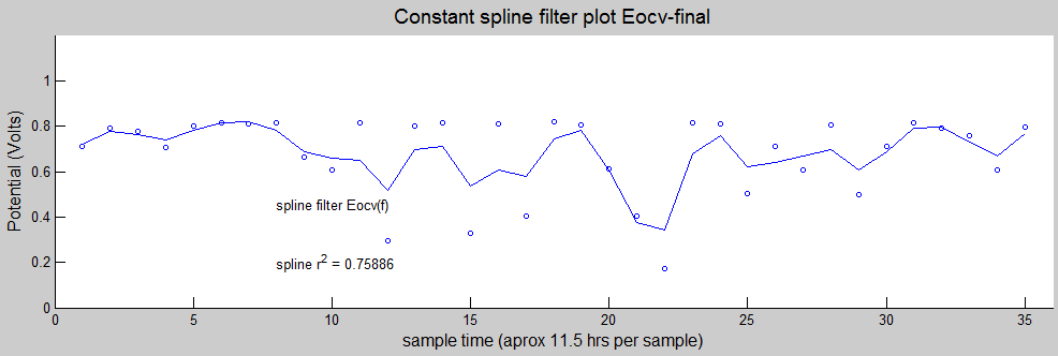

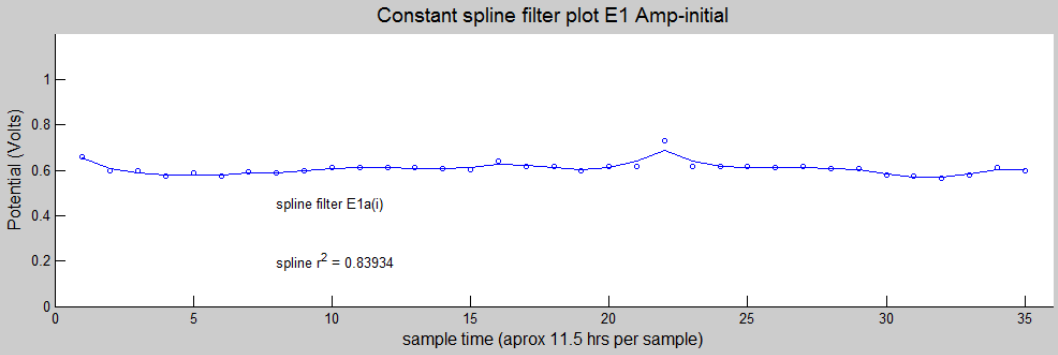

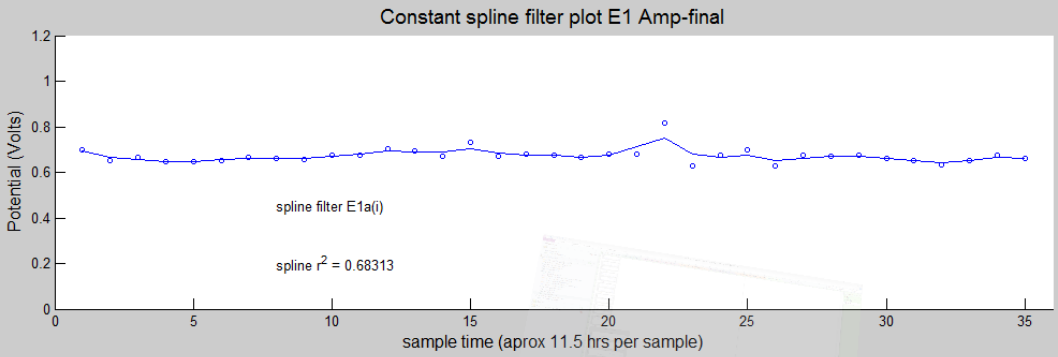

MEA 08

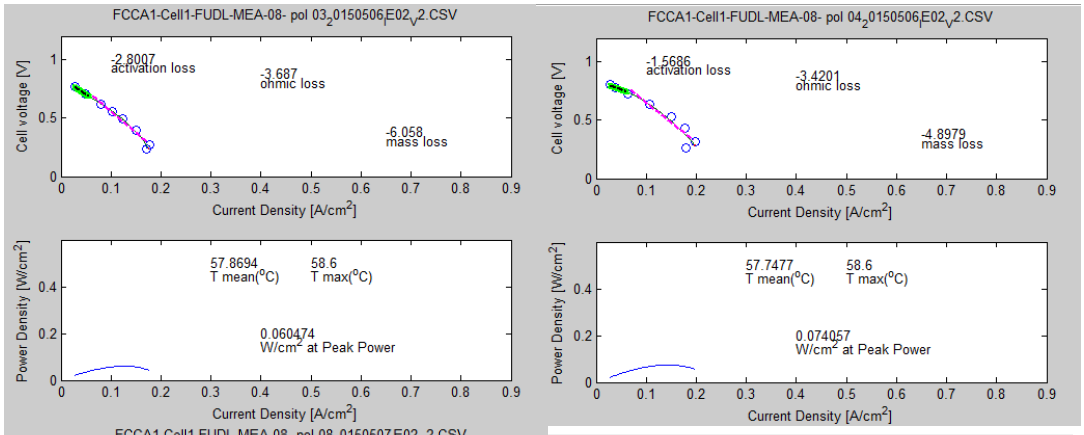
FCCA1-Cell1-FUDL-MEA-08- pol 03_0150506_E02_V2.CSV
-2.8007 activation loss
-3.687 ohmic loss
-6.058 mass loss
Cell voltage [V]
Current Density [A/cm²]
57.8694 T mean(°C)
58.6 T max(°C)
0.060474 W/cm² at Peak Power
Power Density [W/cm²]
FCCA1-Cell1-FUDL-MEA-08- pol 04_0150506_E02_V2.CSV
-1.5686 activation loss
-3.4201 ohmic loss
-4.8979 mass loss
57.7477 T mean(°C)
58.6 T max(°C)
0.074057 W/cm² at Peak Power

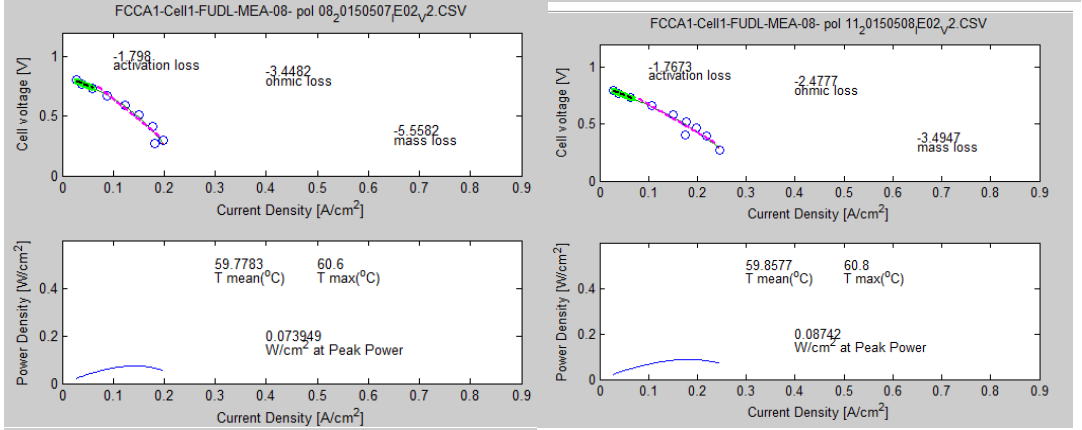
FCCA1-Cell1-FUDL-MEA-08- pol 08_0150507_E02_V2.CSV
-1.798 activation loss
-3.4482 ohmic loss
-5.5582 mass loss
59.7783 T mean(°C)
60.6 T max(°C)
0.073949 W/cm² at Peak Power
FCCA1-Cell1-FUDL-MEA-08- pol 11_0150508_E02_V2.CSV
-1.7673 activation loss
-2.4777 ohmic loss
-3.4947 mass loss
59.8577 T mean(°C)
60.8 T max(°C)
0.08742 W/cm² at Peak Power

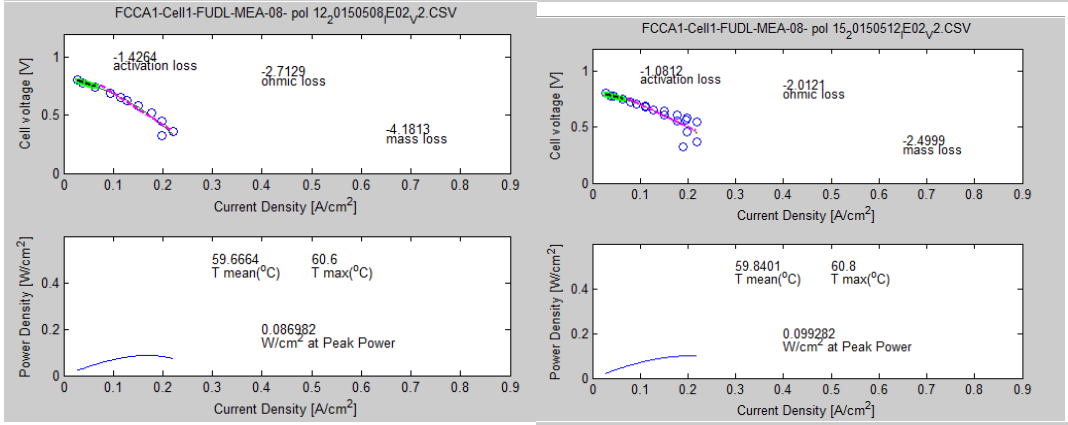
FCCA1-Cell1-FUDL-MEA-08- pol 12_0150508_E02_V2.CSV
-1.4264 activation loss
-2.7129 ohmic loss
-4.1813 mass loss
59.6664 T mean(°C)
60.6 T max(°C)
0.086982 W/cm² at Peak Power
FCCA1-Cell1-FUDL-MEA-08- pol 15_0150512_E02_V2.CSV
-1.0812 activation loss
-2.0121 ohmic loss
-2.4999 mass loss
59.8401 T mean(°C)
60.8 T max(°C)
0.099282 W/cm² at Peak Power

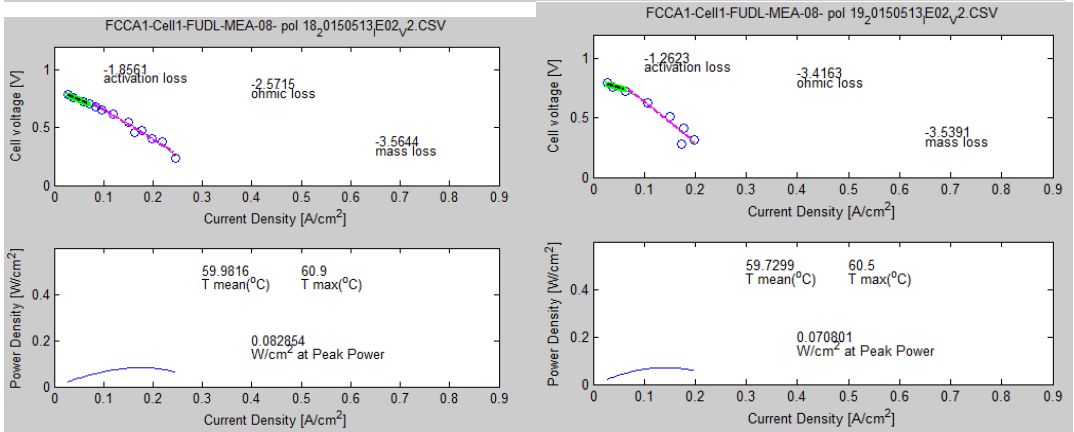
FCCA1-Cell1-FUDL-MEA-08- pol 18_0150513_E02_V2.CSV
-1.8561 activation loss
-2.5715 ohmic loss
-3.5644 mass loss
59.9816 T mean(°C)
60.9 T max(°C)
0.082854 W/cm² at Peak Power
FCCA1-Cell1-FUDL-MEA-08- pol 19_0150513_E02_V2.CSV
-1.2623 activation loss
-3.4163 ohmic loss
-3.5391 mass loss
59.7299 T mean(°C)
60.5 T max(°C)
0.070801 W/cm² at Peak Power

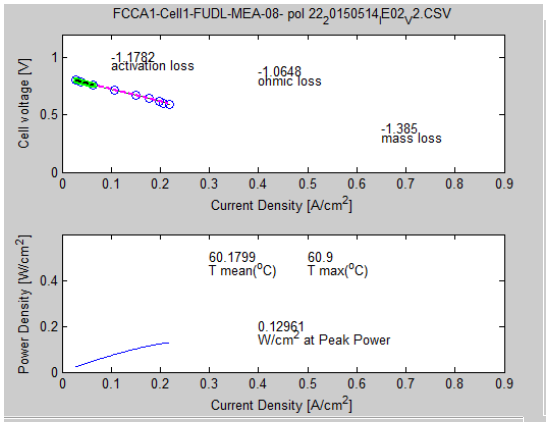
FCCA1-Cell1-FUDL-MEA-08- pol 22_0150514_E02_V2.CSV
-1.1782
activation loss
-1.0648
ohmic loss
-1.385
mass loss
Cell voltage [V]
Current Density [A/cm2]
60.1799
T mean(°C)
60.9
T max(°C)
0.12961
W/cm2 at Peak Power
Power Density [W/cm2]
Current Density [A/cm2]

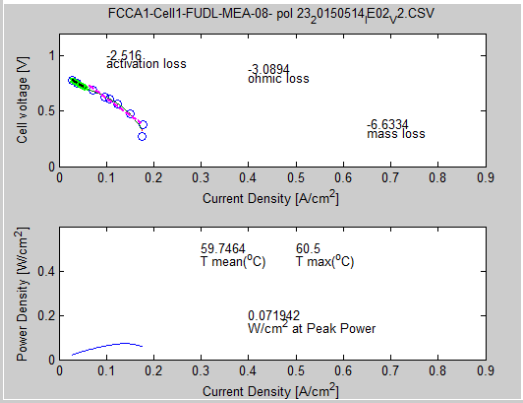
FCCA1-Cell1-FUDL-MEA-08- pol 23_0150514_E02_V2.CSV
-2.516
activation loss
-3.0894
ohmic loss
-6.6334
mass loss
Cell voltage [V]
Current Density [A/cm2]
59.7464
T mean(°C)
60.5
T max(°C)
0.071942
W/cm2 at Peak Power
Power Density [W/cm2]
Current Density [A/cm2]

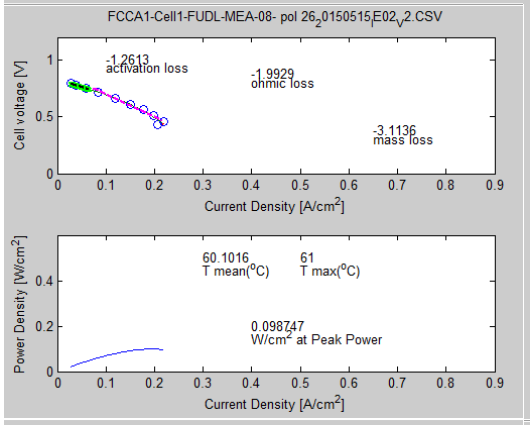
FCCA1-Cell1-FUDL-MEA-08- pol 26_0150515_E02_V2.CSV
-1.2613
activation loss
-1.9929
ohmic loss
-3.1136
mass loss
Cell voltage [V]
Current Density [A/cm2]
60.1016
T mean(°C)
61
T max(°C)
0.098747
W/cm2 at Peak Power
Power Density [W/cm2]
Current Density [A/cm2]

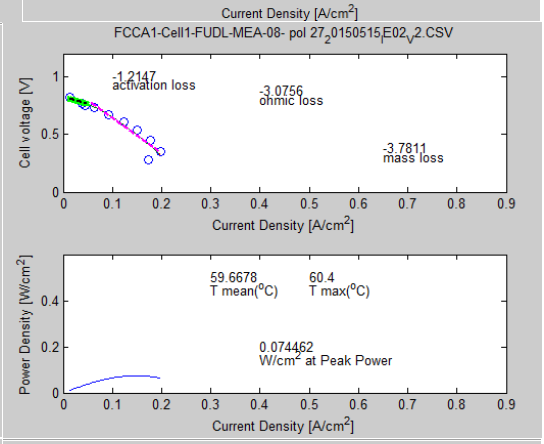
FCCA1-Cell1-FUDL-MEA-08- pol 27_0150515_E02_V2.CSV
-1.2147
activation loss
-3.0756
ohmic loss
-3.7811
mass loss
Cell voltage [V]
Current Density [A/cm2]
59.6678
T mean(°C)
60.4
T max(°C)
0.074462
W/cm2 at Peak Power
Power Density [W/cm2]
Current Density [A/cm2]

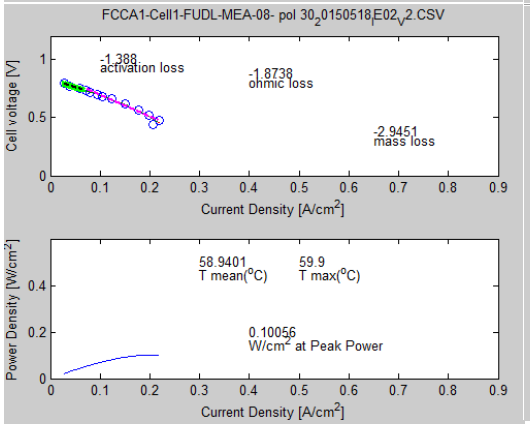
FCCA1-Cell1-FUDL-MEA-08- pol 30_0150518_E02_V2.CSV
-1.388
activation loss
-1.8738
ohmic loss
-2.9451
mass loss
Cell voltage [V]
Current Density [A/cm2]
58.9401
T mean(°C)
59.9
T max(°C)
0.10056
W/cm2 at Peak Power
Power Density [W/cm2]
Current Density [A/cm2]

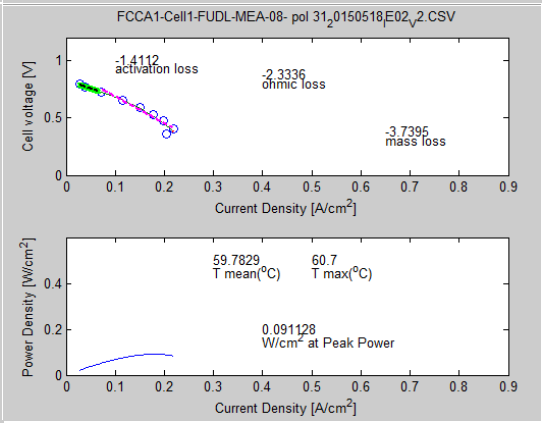
FCCA1-Cell1-FUDL-MEA-08- pol 31_0150518_E02_V2.CSV
-1.4112
activation loss
-2.3336
ohmic loss
-3.7395
mass loss
Cell voltage [V]
Current Density [A/cm2]
59.7829
T mean(°C)
60.7
T max(°C)
0.091128
W/cm2 at Peak Power
Power Density [W/cm2]
Current Density [A/cm2]

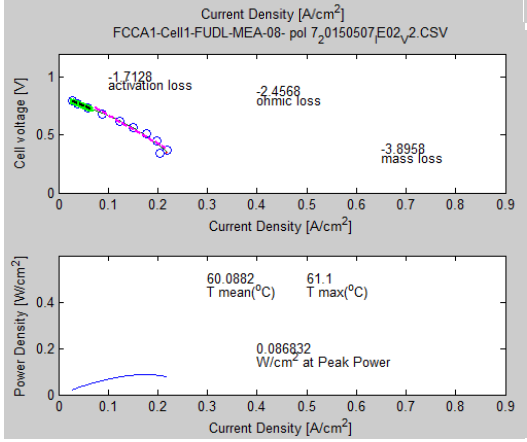
FCCA1-Cell1-FUDL-MEA-08- pol 7_0150507_E02_V2.CSV
-1.7128
activation loss
-2.4568
ohmic loss
-3.8958
mass loss
Cell voltage [V]
Current Density [A/cm2]
60.0882
T mean(°C)
61.1
T max(°C)
0.086832
W/cm2 at Peak Power
Power Density [W/cm2]
Current Density [A/cm2]

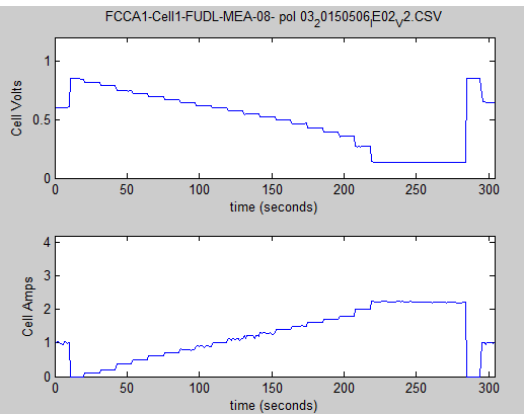
FCCA1-Cell1-FUDL-MEA-08- pol 03_0150506_E02_V2.CSV
Cell Volts
time (seconds)
Cell Amps
time (seconds)

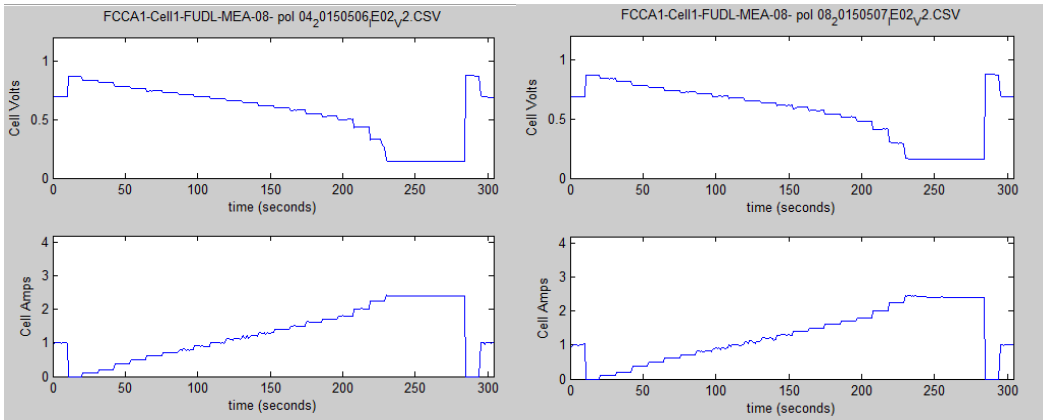
FCCA1-Cell1-FUDL-MEA-08- pol 04_20150506_E02_V2.CSV
Cell Volts
time (seconds)
Cell Amps
time (seconds)

FCCA1-Cell1-FUDL-MEA-08- pol 08_20150507_E02_V2.CSV
Cell Volts
time (seconds)
Cell Amps
time (seconds)

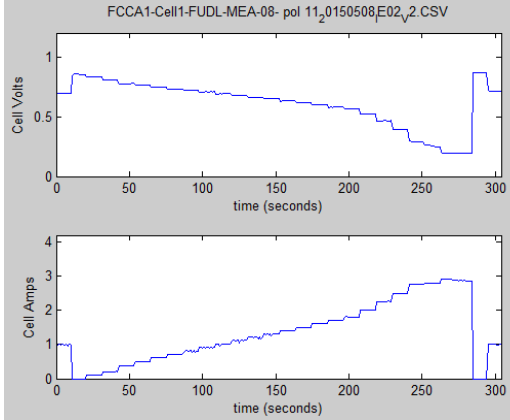
FCCA1-Cell1-FUDL-MEA-08- pol 11_20150508_E02_V2.CSV
Cell Volts
time (seconds)
Cell Amps
time (seconds)

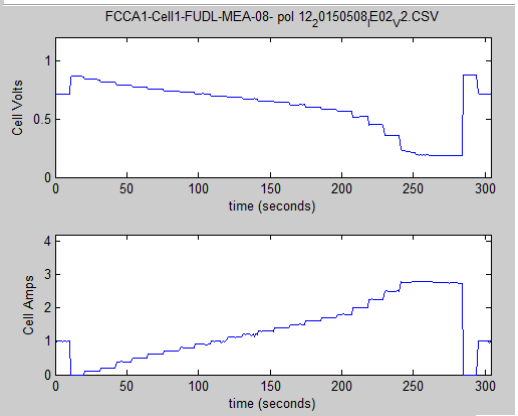
FCCA1-Cell1-FUDL-MEA-08- pol 12_20150508_E02_V2.CSV
Cell Volts
time (seconds)
Cell Amps
time (seconds)

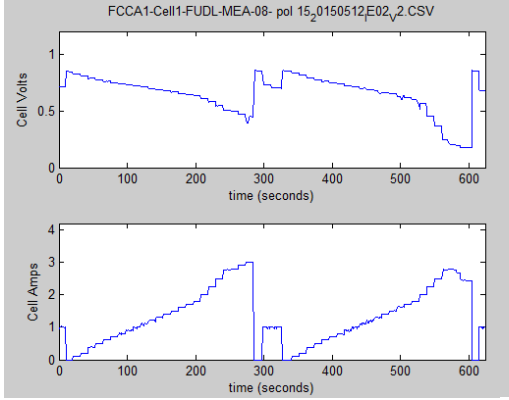
FCCA1-Cell1-FUDL-MEA-08- pol 15_20150512_E02_V2.CSV
Cell Volts
time (seconds)
Cell Amps
time (seconds)

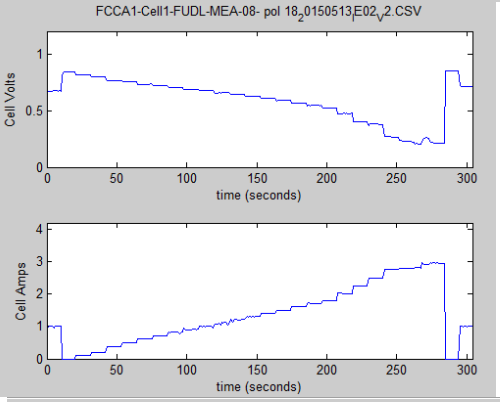
FCCA1-Cell1-FUDL-MEA-08- pol 18_20150513_E02_V2.CSV
Cell Volts
time (seconds)
Cell Amps
time (seconds)

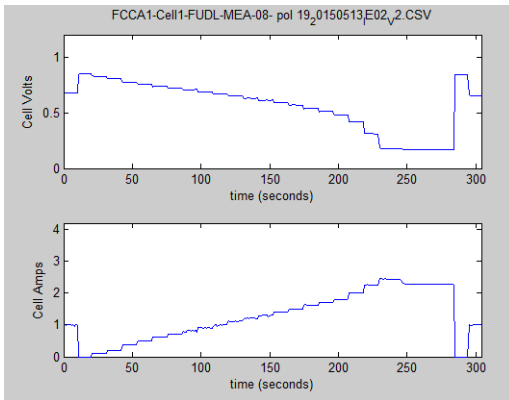
FCCA1-Cell1-FUDL-MEA-08- pol 19_20150513_E02_V2.CSV
Cell Volts
time (seconds)
Cell Amps
time (seconds)

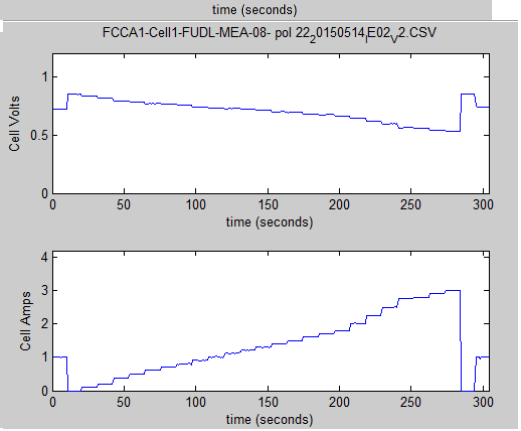
FCCA1-Cell1-FUDL-MEA-08- pol 22_20150514_E02_V2.CSV
Cell Volts
time (seconds)
Cell Amps
time (seconds)

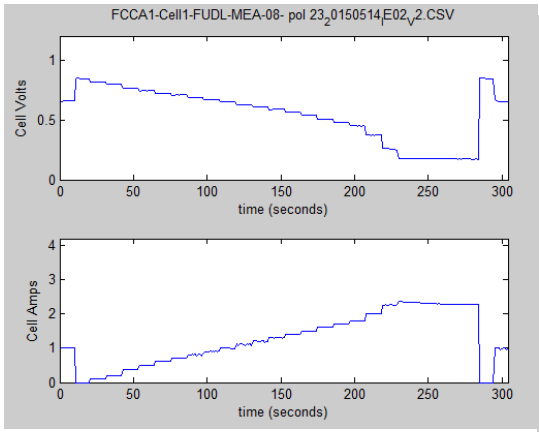
FCCA1-Cell1-FUDL-MEA-08- pol 23_20150514_E02_V2.CSV
Cell Volts
time (seconds)
Cell Amps
time (seconds)

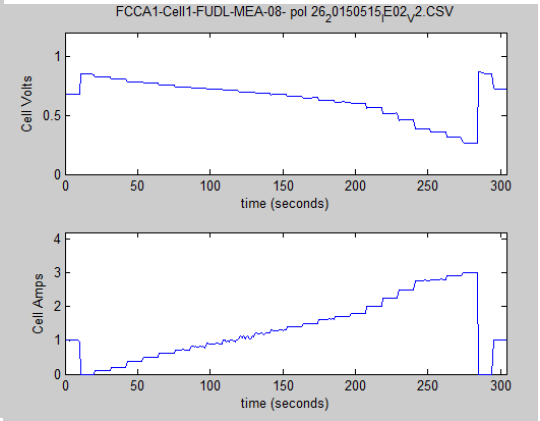
FCCA1-Cell1-FUDL-MEA-08- pol 26_20150515_E02_V2.CSV
Cell Volts
time (seconds)
Cell Amps
time (seconds)

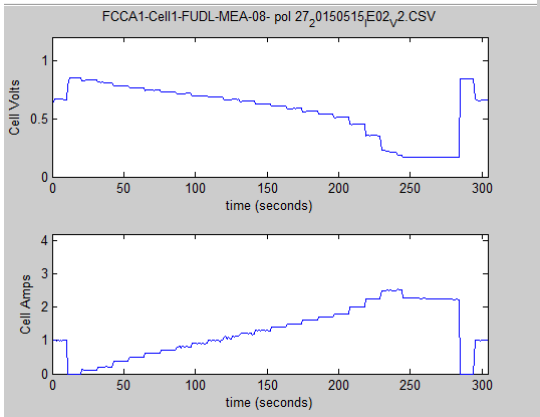
FCCA1-Cell1-FUDL-MEA-08- pol 27_20150515_E02_V2.CSV
Cell Volts
time (seconds)
Cell Amps
time (seconds)

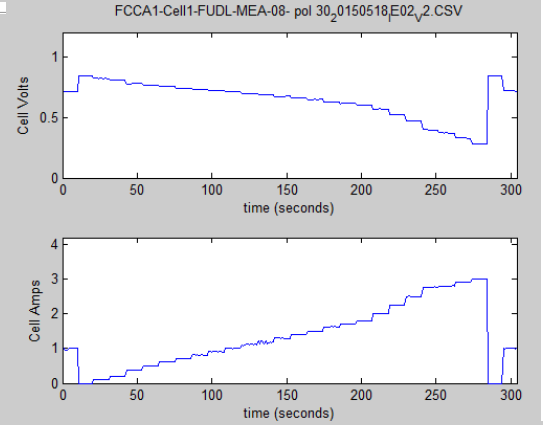
FCCA1-Cell1-FUDL-MEA-08- pol 30_20150518_E02_V2.CSV
Cell Volts
time (seconds)
Cell Amps
time (seconds)

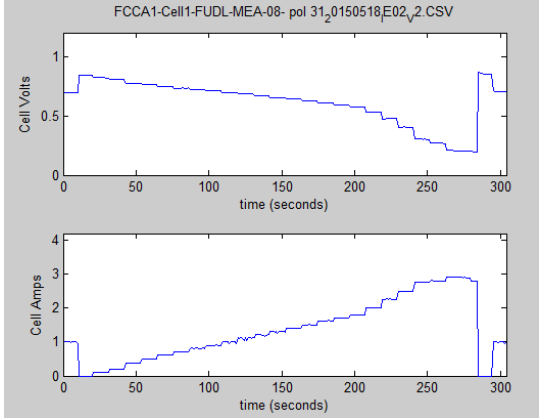
FCCA1-Cell1-FUDL-MEA-08- pol 31_20150518_E02_V2.CSV
Cell Volts
time (seconds)
Cell Amps
time (seconds)

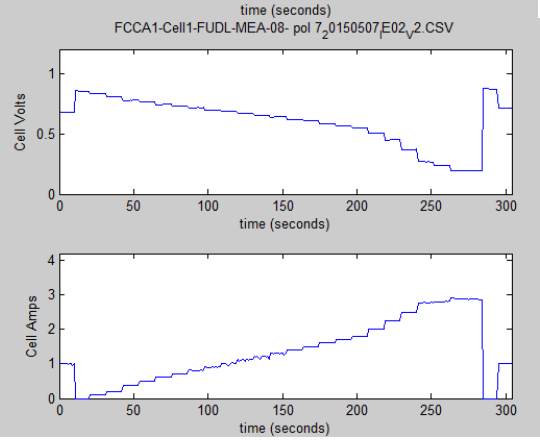
FCCA1-Cell1-FUDL-MEA-08- pol 7_20150507_E02_V2.CSV
Cell Volts
time (seconds)
Cell Amps
time (seconds)

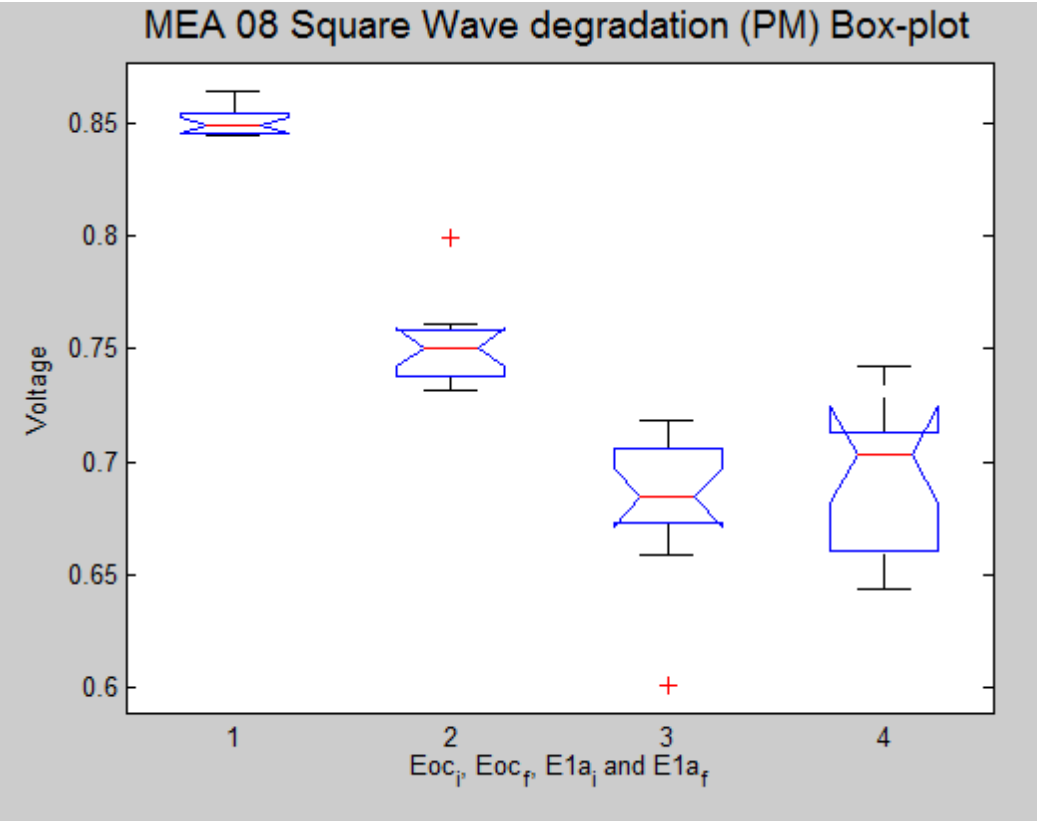
MEA 08 Square Wave degradation (PM) Box-plot
Voltage
0.85
0.8
0.75
0.7
0.65
0.6
1
2
3
4
Eoc$_i$, Eoc$_f$, E1a$_i$ and E1a$_f$

MEA 08 (Freudenberg cathode, high-D, Square Wave)PM

Square Wave degradation plot Eocv-intial

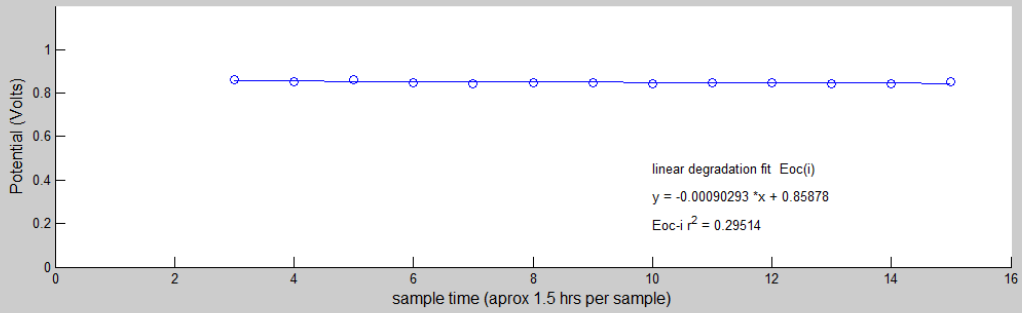

Square Wave degradation plot Eocv-final

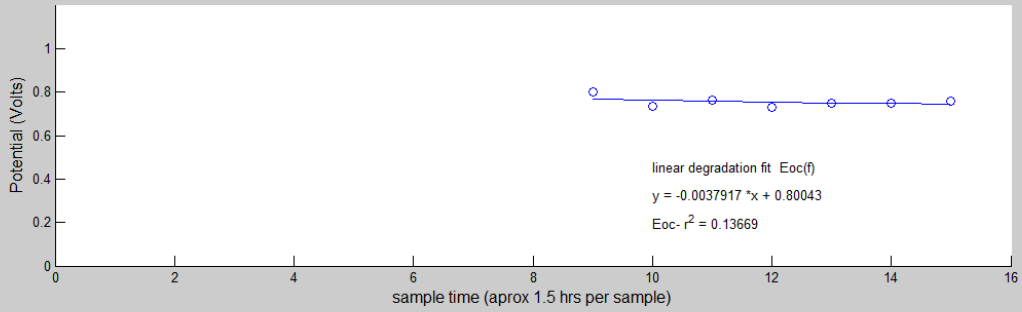

Square Wave degradation plot E at 1 amp-intial

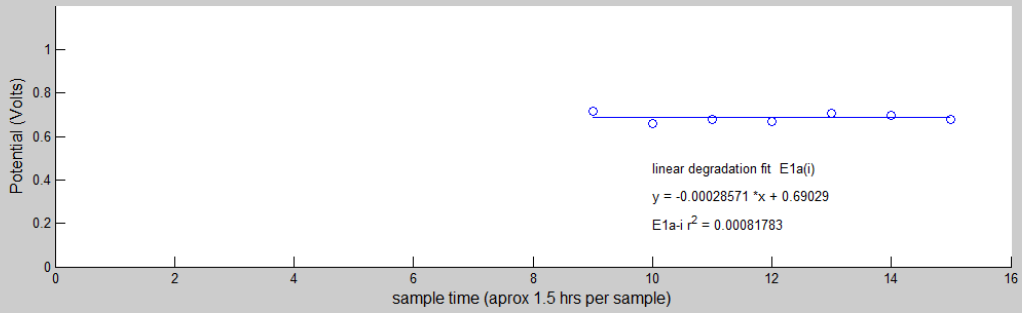

Square Wave degradation plot E at 1 amp -final

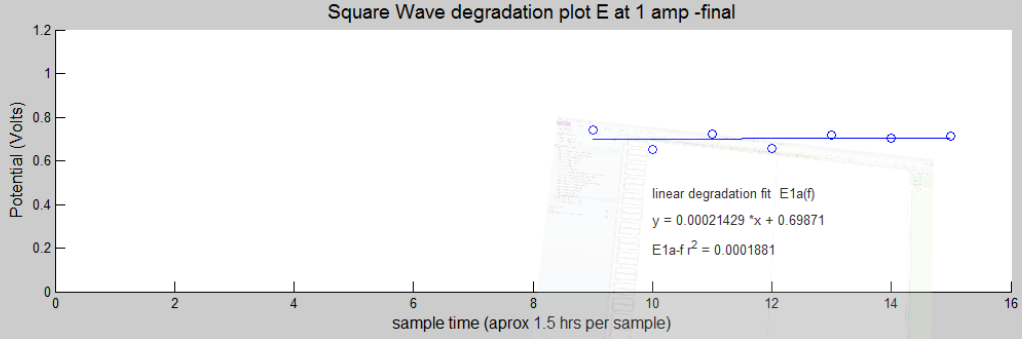

MEA 08 (Freudenberg cathode, high-D, Square Wave)PM

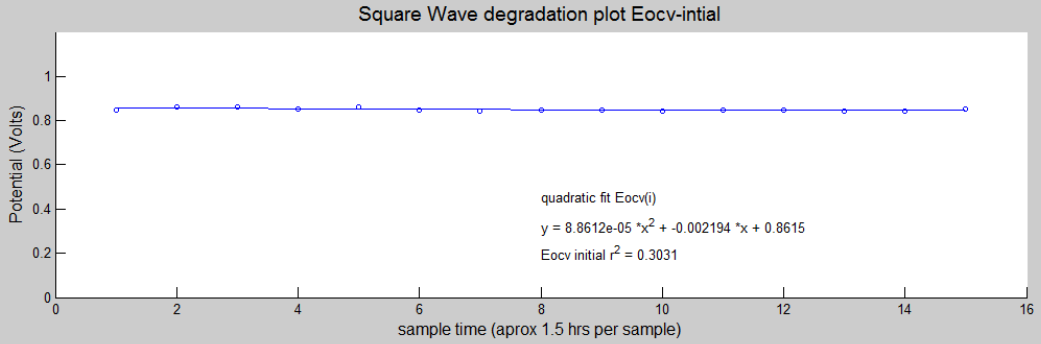

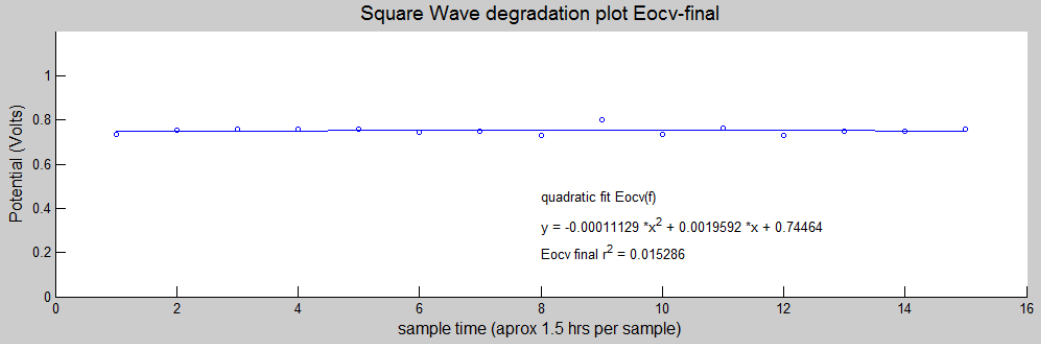

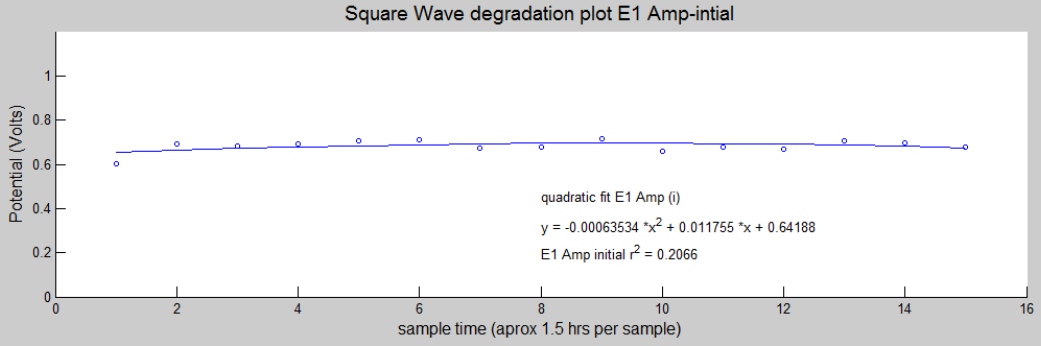

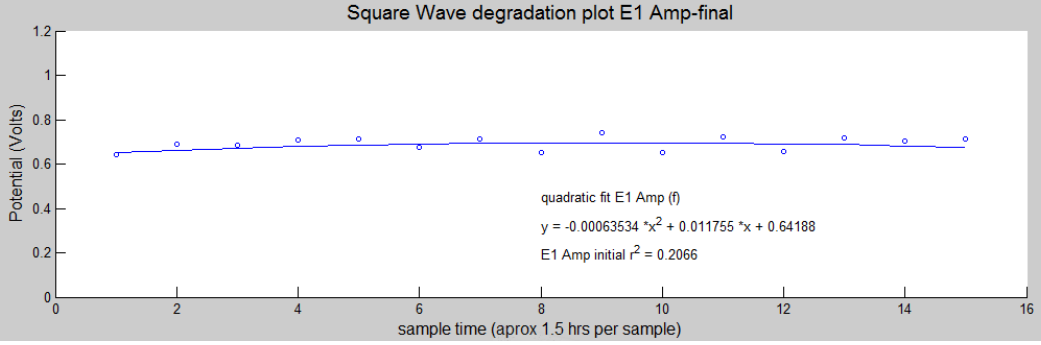

MEA 08 (Freudenberg cathode, high-D, Square Wave)PM

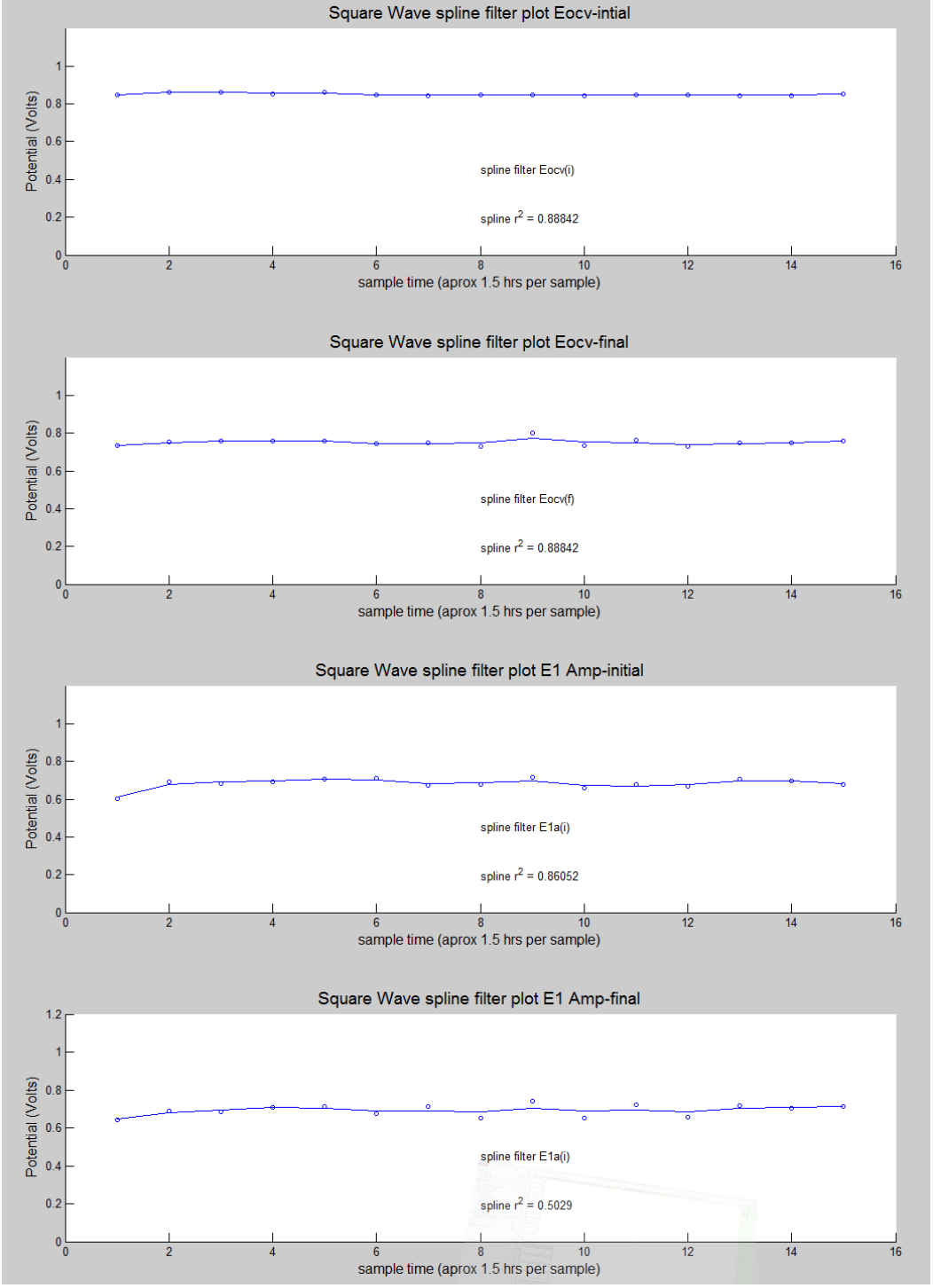

MEA 10

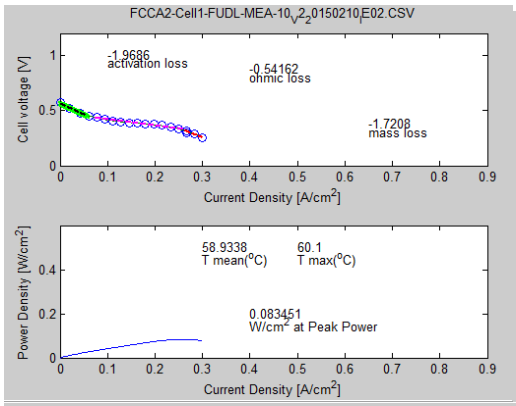
FCCA2-Cell1-FUDL-MEA-10_V2_20150210_E02.CSV
-1.9686
activation loss
-0.54162
ohmic loss
-1.7208
mass loss
Cell voltage [V]
Current Density [A/cm2]
58.9338
T mean(°C)
60.1
T max(°C)
0.083451
W/cm2 at Peak Power
Power Density [W/cm2]
Current Density [A/cm2]

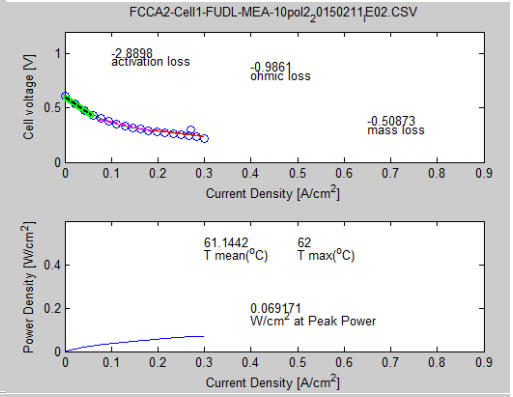
FCCA2-Cell1-FUDL-MEA-10pol2_20150211_E02.CSV
-2.8898
activation loss
-0.9861
ohmic loss
-0.50873
mass loss
Cell voltage [V]
Current Density [A/cm2]
61.1442
T mean(°C)
62
T max(°C)
0.069171
W/cm2 at Peak Power
Power Density [W/cm2]
Current Density [A/cm2]

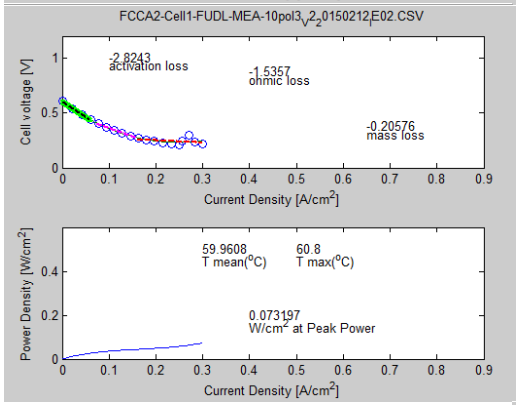
FCCA2-Cell1-FUDL-MEA-10pol3_V2_20150212_E02.CSV
-2.8243
activation loss
-1.5357
ohmic loss
-0.20576
mass loss
Cell voltage [V]
Current Density [A/cm2]
59.9608
T mean(°C)
60.8
T max(°C)
0.073197
W/cm2 at Peak Power
Power Density [W/cm2]
Current Density [A/cm2]

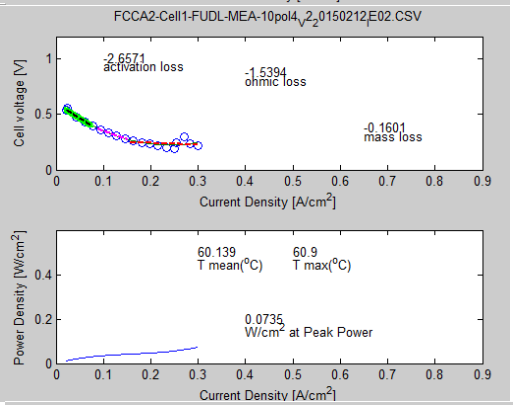
FCCA2-Cell1-FUDL-MEA-10pol4_V2_20150212_E02.CSV
-2.6571
activation loss
-1.5394
ohmic loss
-0.1601
mass loss
Cell voltage [V]
Current Density [A/cm2]
60.139
T mean(°C)
60.9
T max(°C)
0.0735
W/cm2 at Peak Power
Power Density [W/cm2]
Current Density [A/cm2]

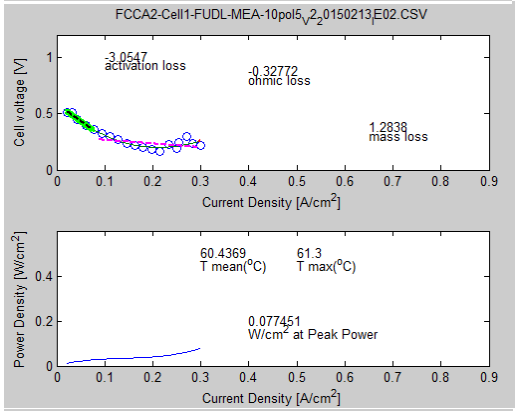
FCCA2-Cell1-FUDL-MEA-10pol5_V2_20150213_E02.CSV
-3.0547
activation loss
-0.32772
ohmic loss
1.2838
mass loss
Cell voltage [V]
Current Density [A/cm2]
60.4369
T mean(°C)
61.3
T max(°C)
0.077451
W/cm2 at Peak Power
Power Density [W/cm2]
Current Density [A/cm2]

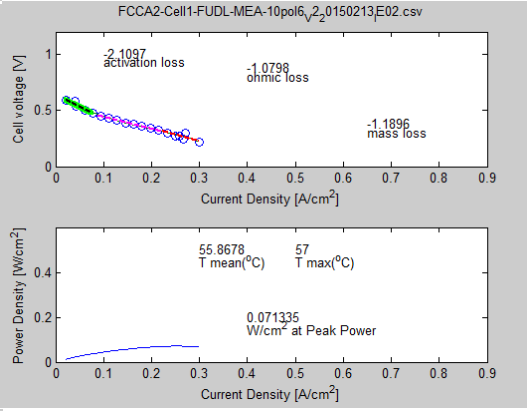
FCCA2-Cell1-FUDL-MEA-10pol6_V2_20150213_E02.csv
-2.1097
activation loss
-1.0798
ohmic loss
-1.1896
mass loss
Cell voltage [V]
Current Density [A/cm2]
55.8678
T mean(°C)
57
T max(°C)
0.071335
W/cm2 at Peak Power
Power Density [W/cm2]
Current Density [A/cm2]

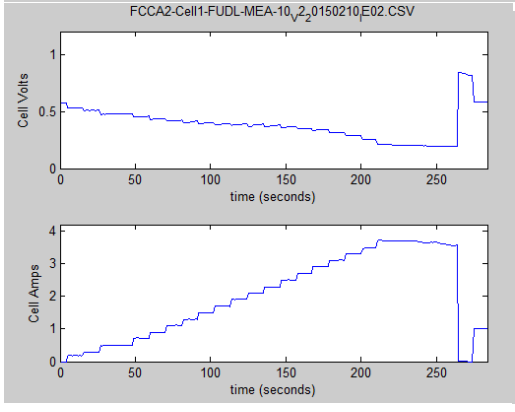
FCCA2-Cell1-FUDL-MEA-10_V2_20150210_E02.CSV
Cell Volts
time (seconds)
Cell Amps
time (seconds)

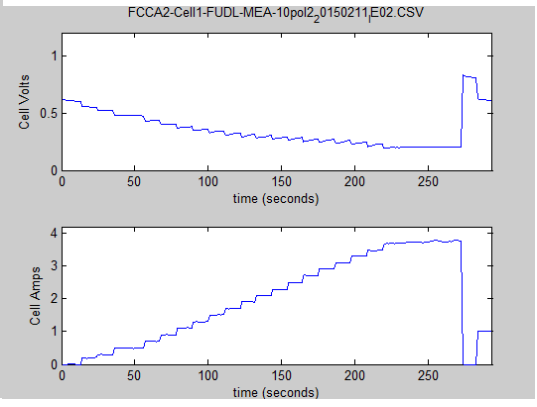
FCCA2-Cell1-FUDL-MEA-10pol2_20150211_E02.CSV
Cell Volts
time (seconds)
Cell Amps
time (seconds)

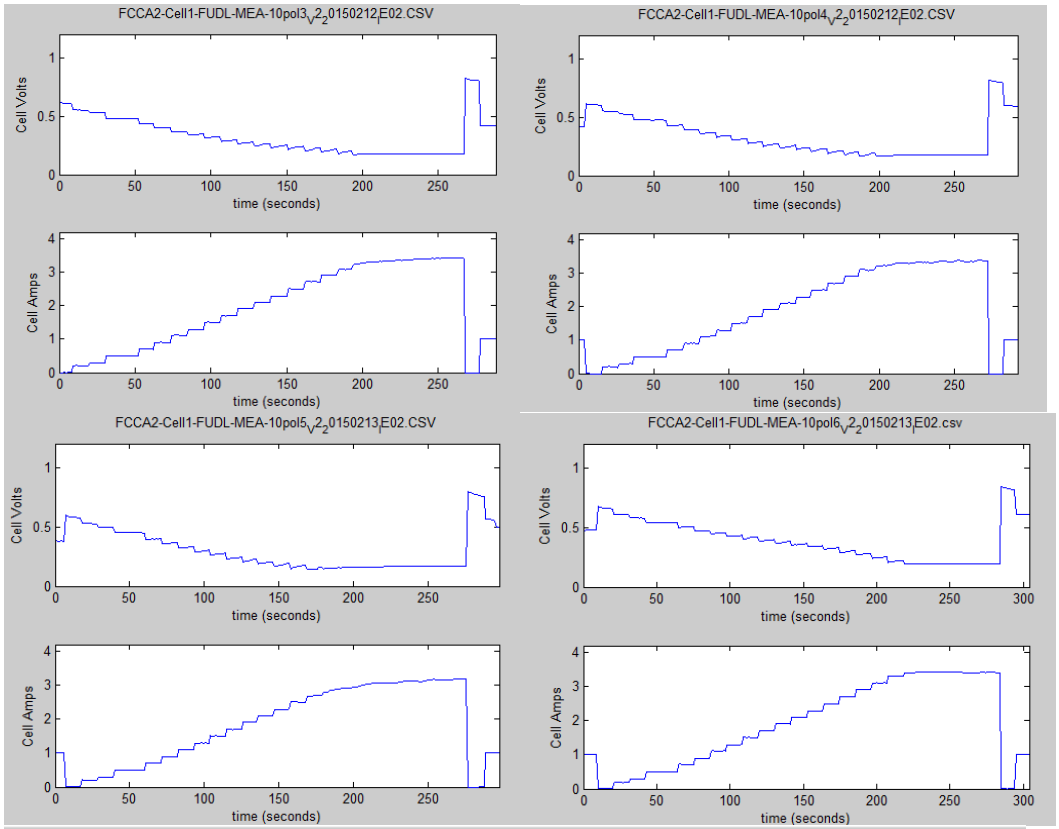
FCCA2-Cell1-FUDL-MEA-10pol3_V2_20150212_E02.CSV
FCCA2-Cell1-FUDL-MEA-10pol4_V2_20150212_E02.CSV
FCCA2-Cell1-FUDL-MEA-10pol5_V2_20150213_E02.CSV
FCCA2-Cell1-FUDL-MEA-10pol6_V2_20150213_E02.csv
Cell Volts
Cell Amps
time (seconds)

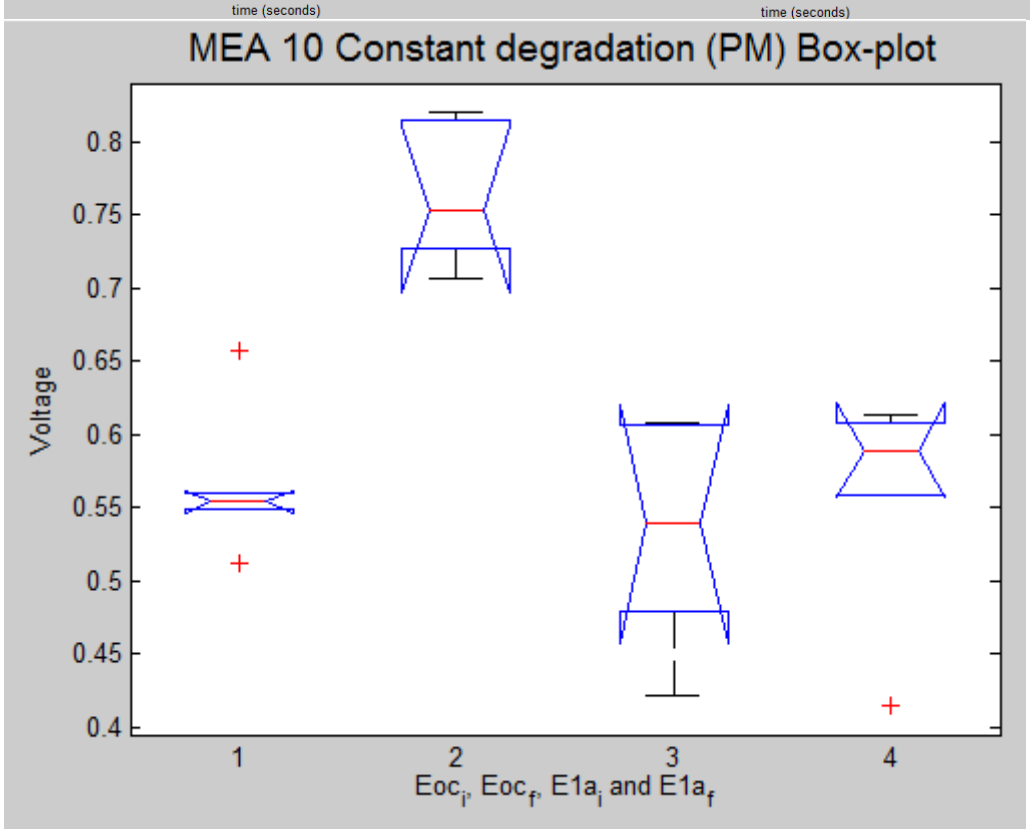
MEA 10 Constant degradation (PM) Box-plot
Voltage
Eoc$_i$, Eoc$_f$, E1a$_i$ and E1a$_f$

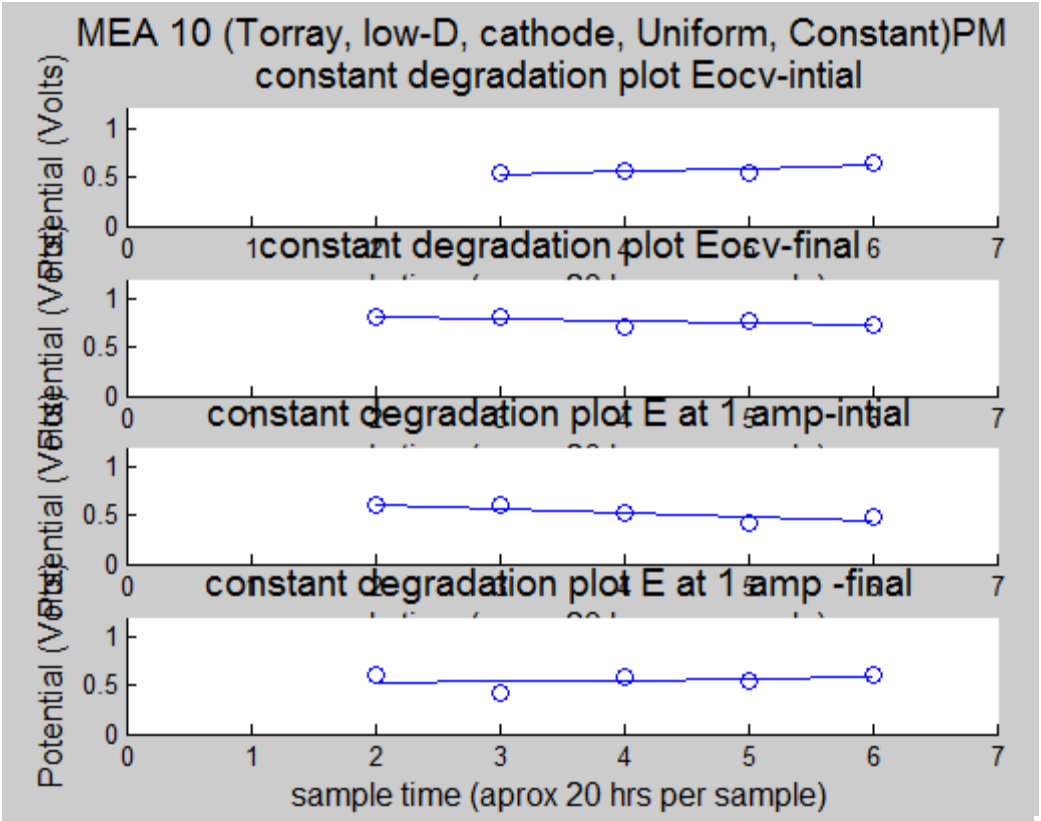
MEA 10 (Torray, low-D, cathode, Uniform, Constant)PM
constant degradation plot Eocv-intial
constant degradation plot Eocv-final
constant degradation plot E at 1 amp-intial
constant degradation plot E at 1 amp -final
Potential (Volts)
sample time (aprox 20 hrs per sample)

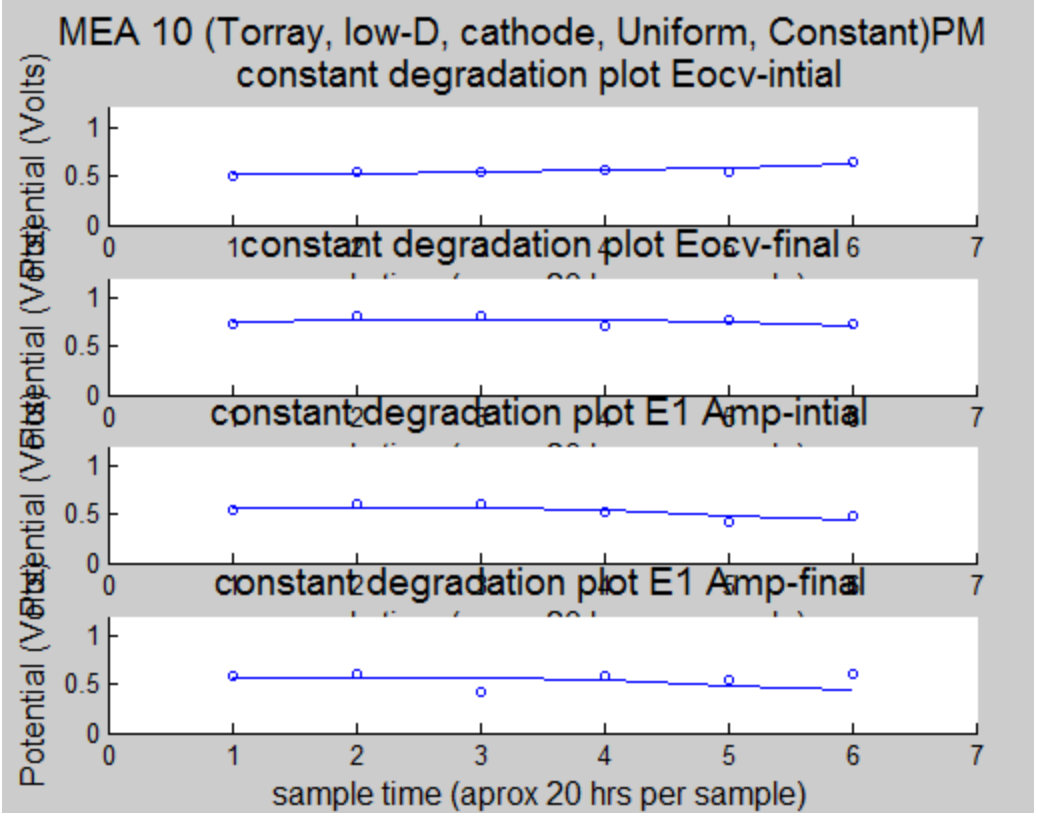
MEA 10 (Torray, low-D, cathode, Uniform, Constant)PM
constant degradation plot Eocv-intial
constant degradation plot Eocv-final
constant degradation plot E1 Amp-intial
constant degradation plot E1 Amp-final
Potential (Volts)
sample time (aprox 20 hrs per sample)

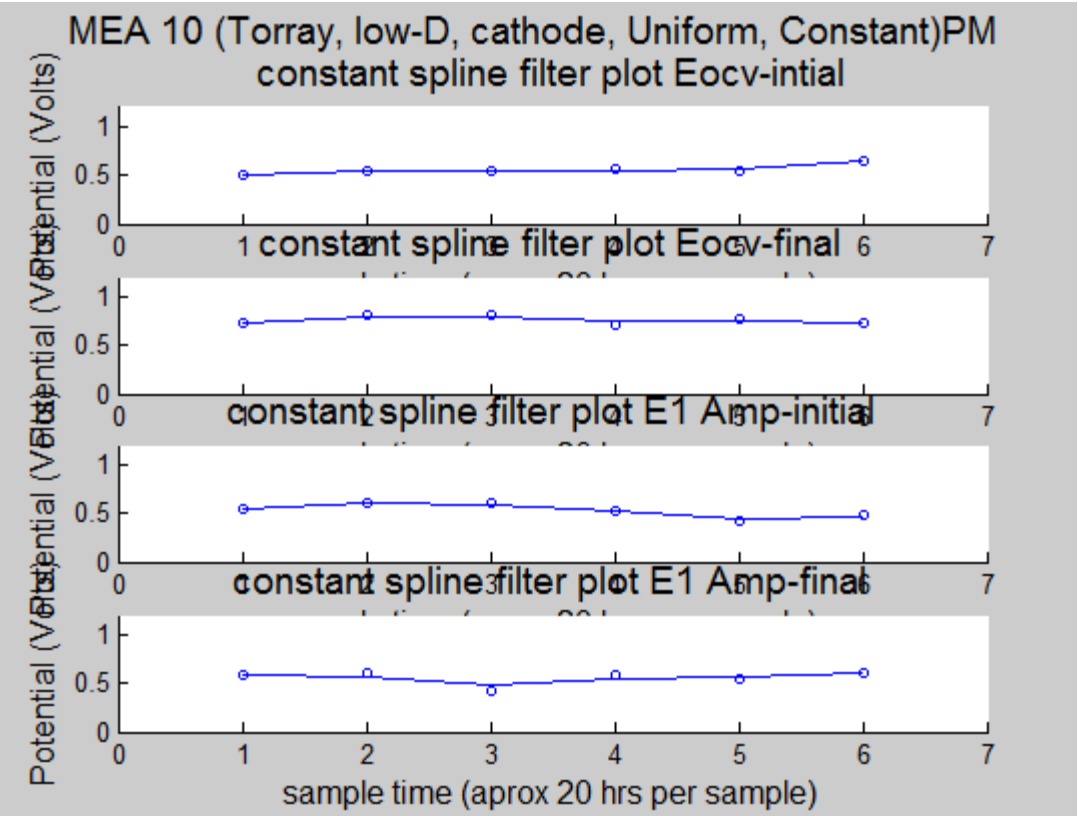
MEA 10 (Torray, low-D, cathode, Uniform, Constant)PM
constant spline filter plot Eocv-intial
constant spline filter plot Eocv-final
constant spline filter plot E1 Amp-initial
constant spline filter plot E1 Amp-final
Potential (Volts)
sample time (aprox 20 hrs per sample)

MEA 12

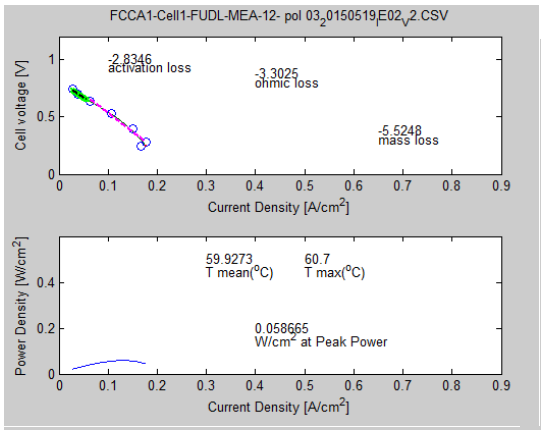
FCCA1-Cell1-FUDL-MEA-12- pol 03_20150519_E02_V2.CSV
-2.8346
activation loss
-3.3025
ohmic loss
-5.5248
mass loss
Cell voltage [V]
Current Density [A/cm²]
59.9273
T mean(°C)
60.7
T max(°C)
0.058665
W/cm² at Peak Power
Power Density [W/cm²]
Current Density [A/cm²]

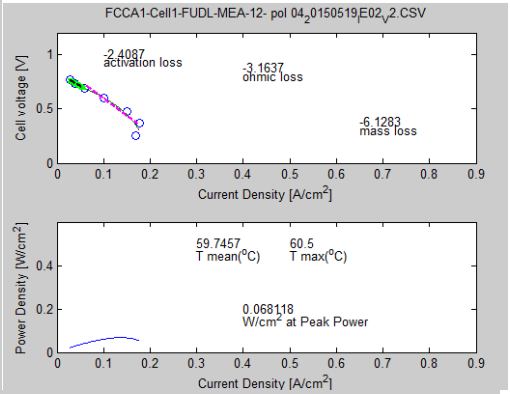
FCCA1-Cell1-FUDL-MEA-12- pol 04_20150519_E02_V2.CSV
-2.4087
activation loss
-3.1637
ohmic loss
-6.1283
mass loss
Cell voltage [V]
Current Density [A/cm²]
59.7457
T mean(°C)
60.5
T max(°C)
0.068118
W/cm² at Peak Power
Power Density [W/cm²]
Current Density [A/cm²]

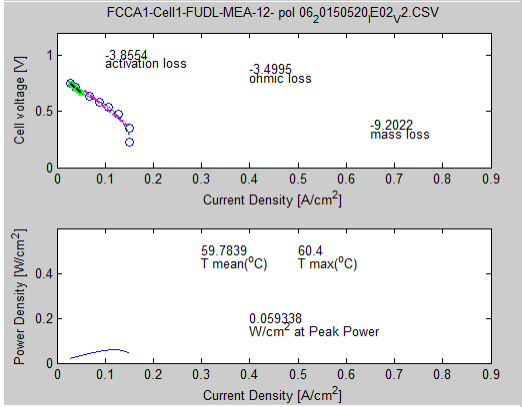
FCCA1-Cell1-FUDL-MEA-12- pol 06_20150520_E02_V2.CSV
-3.8554
activation loss
-3.4995
ohmic loss
-9.2022
mass loss
Cell voltage [V]
Current Density [A/cm²]
59.7839
T mean(°C)
60.4
T max(°C)
0.059338
W/cm² at Peak Power
Power Density [W/cm²]
Current Density [A/cm²]

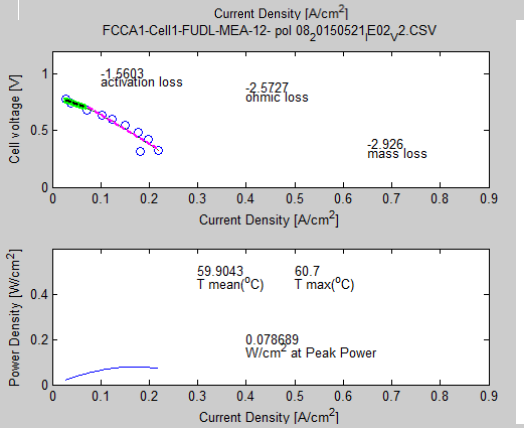
FCCA1-Cell1-FUDL-MEA-12- pol 08_20150521_E02_V2.CSV
-1.5603
activation loss
-2.5727
ohmic loss
-2.926
mass loss
Cell voltage [V]
Current Density [A/cm²]
59.9043
T mean(°C)
60.7
T max(°C)
0.078689
W/cm² at Peak Power
Power Density [W/cm²]
Current Density [A/cm²]

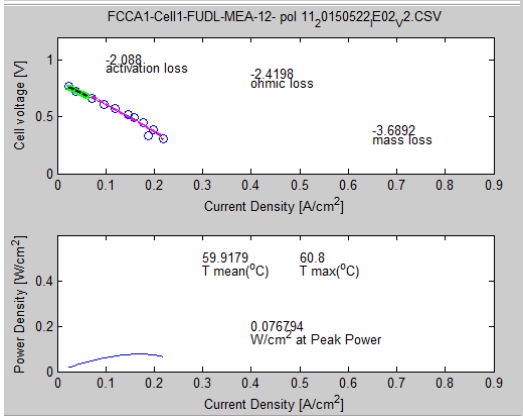
FCCA1-Cell1-FUDL-MEA-12- pol 11_20150522_E02_V2.CSV
-2.088
activation loss
-2.4198
ohmic loss
-3.6892
mass loss
Cell voltage [V]
Current Density [A/cm²]
59.9179
T mean(°C)
60.8
T max(°C)
0.076794
W/cm² at Peak Power
Power Density [W/cm²]
Current Density [A/cm²]

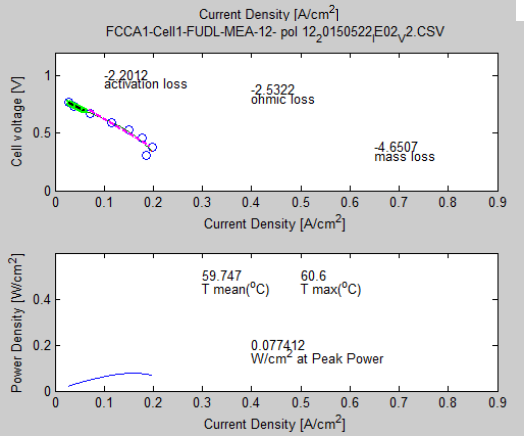
FCCA1-Cell1-FUDL-MEA-12- pol 12_20150522_E02_V2.CSV
-2.2012
activation loss
-2.5322
ohmic loss
-4.6507
mass loss
Cell voltage [V]
Current Density [A/cm²]
59.747
T mean(°C)
60.6
T max(°C)
0.077412
W/cm² at Peak Power
Power Density [W/cm²]
Current Density [A/cm²]

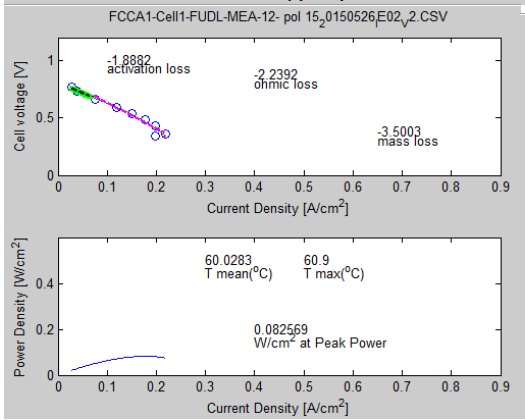
FCCA1-Cell1-FUDL-MEA-12- pol 15_20150526_E02_V2.CSV
-1.8882
activation loss
-2.2392
ohmic loss
-3.5003
mass loss
Cell voltage [V]
Current Density [A/cm²]
60.0283
T mean(°C)
60.9
T max(°C)
0.082569
W/cm² at Peak Power
Power Density [W/cm²]
Current Density [A/cm²]

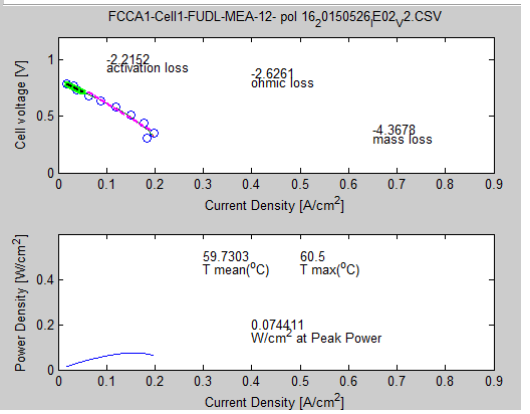
FCCA1-Cell1-FUDL-MEA-12- pol 16_20150526_E02_V2.CSV
-2.2152
activation loss
-2.6261
ohmic loss
-4.3678
mass loss
Cell voltage [V]
Current Density [A/cm²]
59.7303
T mean(°C)
60.5
T max(°C)
0.074411
W/cm² at Peak Power
Power Density [W/cm²]
Current Density [A/cm²]

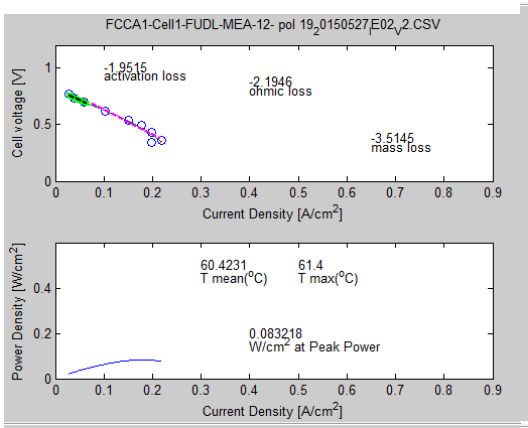
FCCA1-Cell1-FUDL-MEA-12- pol 19_20150527_E02_V2.CSV
-1.9515
activation loss
-2.1946
ohmic loss
-3.5145
mass loss
Cell voltage [V]
Current Density [A/cm2]
60.4231
T mean(°C)
61.4
T max(°C)
0.083218
W/cm2 at Peak Power
Power Density [W/cm2]
Current Density [A/cm2]

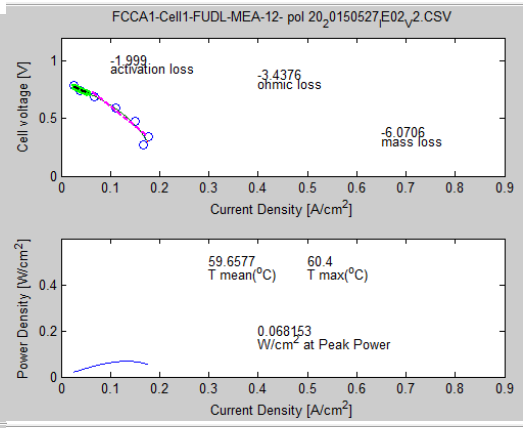
FCCA1-Cell1-FUDL-MEA-12- pol 20_20150527_E02_V2.CSV
-1.999
activation loss
-3.4376
ohmic loss
-6.0706
mass loss
Cell voltage [V]
Current Density [A/cm2]
59.6577
T mean(°C)
60.4
T max(°C)
0.068153
W/cm2 at Peak Power
Power Density [W/cm2]
Current Density [A/cm2]

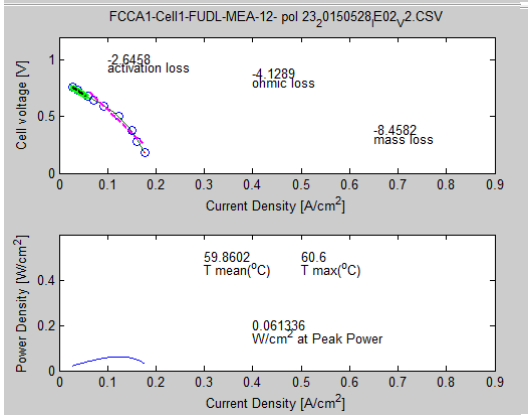
FCCA1-Cell1-FUDL-MEA-12- pol 23_20150528_E02_V2.CSV
-2.6458
activation loss
-4.1289
ohmic loss
-8.4582
mass loss
Cell voltage [V]
Current Density [A/cm2]
59.8602
T mean(°C)
60.6
T max(°C)
0.061336
W/cm2 at Peak Power
Power Density [W/cm2]
Current Density [A/cm2]

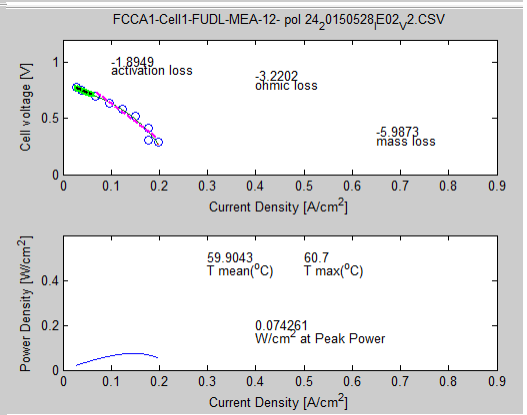
FCCA1-Cell1-FUDL-MEA-12- pol 24_20150528_E02_V2.CSV
-1.8949
activation loss
-3.2202
ohmic loss
-5.9873
mass loss
Cell voltage [V]
Current Density [A/cm2]
59.9043
T mean(°C)
60.7
T max(°C)
0.074261
W/cm2 at Peak Power
Power Density [W/cm2]
Current Density [A/cm2]

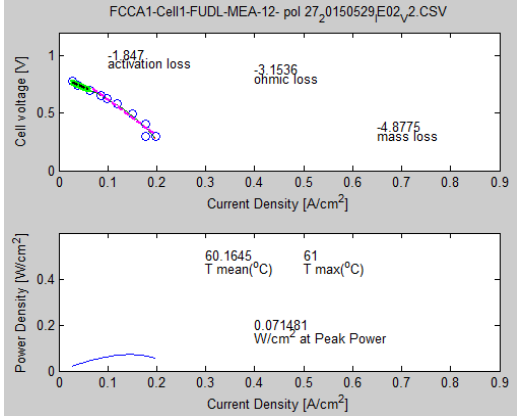
FCCA1-Cell1-FUDL-MEA-12- pol 27_20150529_E02_V2.CSV
-1.847
activation loss
-3.1536
ohmic loss
-4.8775
mass loss
Cell voltage [V]
Current Density [A/cm2]
60.1645
T mean(°C)
61
T max(°C)
0.071481
W/cm2 at Peak Power
Power Density [W/cm2]
Current Density [A/cm2]

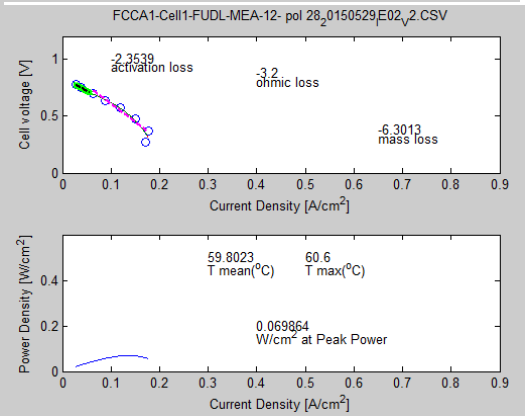
FCCA1-Cell1-FUDL-MEA-12- pol 28_20150529_E02_V2.CSV
-2.3539
activation loss
-3.2
ohmic loss
-6.3013
mass loss
Cell voltage [V]
Current Density [A/cm2]
59.8023
T mean(°C)
60.6
T max(°C)
0.069864
W/cm2 at Peak Power
Power Density [W/cm2]
Current Density [A/cm2]

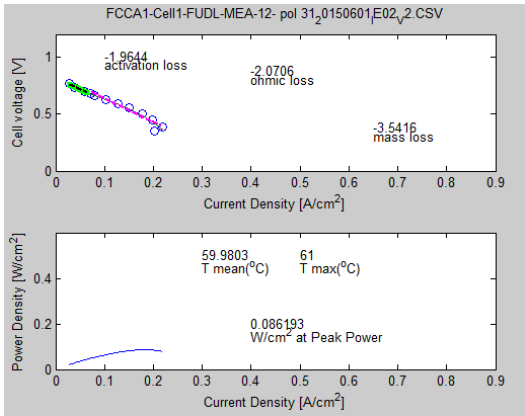
FCCA1-Cell1-FUDL-MEA-12- pol 31_20150601_E02_V2.CSV
-1.9644
activation loss
-2.0706
ohmic loss
-3.5416
mass loss
Cell voltage [V]
Current Density [A/cm2]
59.9803
T mean(°C)
61
T max(°C)
0.086193
W/cm2 at Peak Power
Power Density [W/cm2]
Current Density [A/cm2]

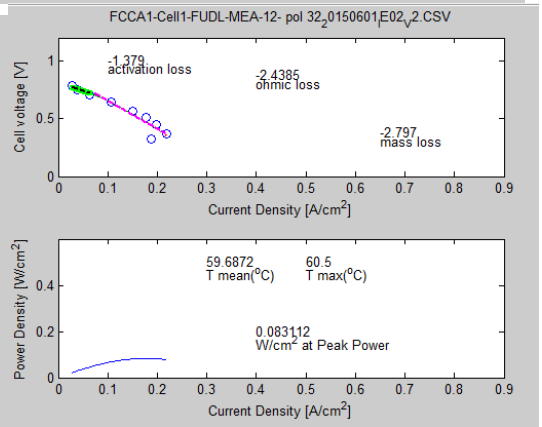
FCCA1-Cell1-FUDL-MEA-12- pol 32_20150601_E02_V2.CSV
-1.379
activation loss
-2.4385
ohmic loss
-2.797
mass loss
Cell voltage [V]
Current Density [A/cm2]
59.6872
T mean(°C)
60.5
T max(°C)
0.083112
W/cm2 at Peak Power
Power Density [W/cm2]
Current Density [A/cm2]

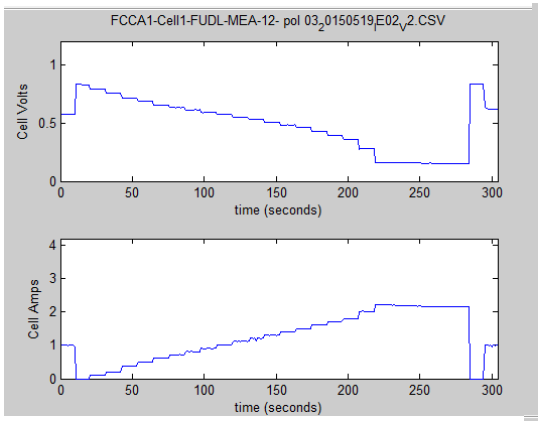
FCCA1-Cell1-FUDL-MEA-12- pol 03_20150519_E02_V2.CSV
Cell Volts
time (seconds)
Cell Amps
time (seconds)

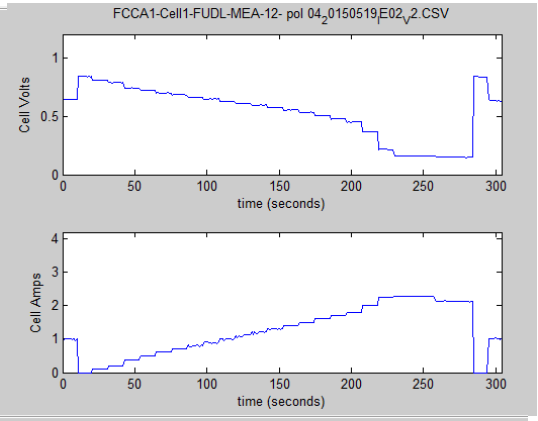
FCCA1-Cell1-FUDL-MEA-12- pol 04_20150519_E02_V2.CSV
Cell Volts
time (seconds)
Cell Amps
time (seconds)

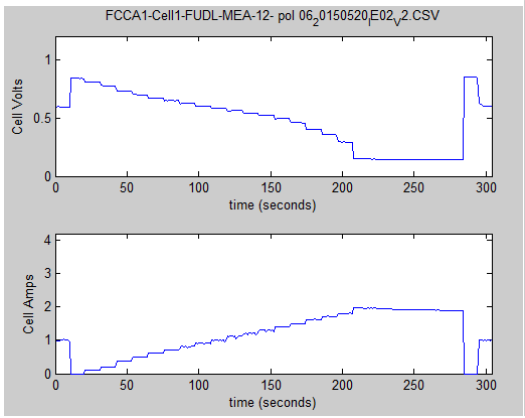
FCCA1-Cell1-FUDL-MEA-12- pol 06_20150520_E02_V2.CSV
Cell Volts
time (seconds)
Cell Amps
time (seconds)

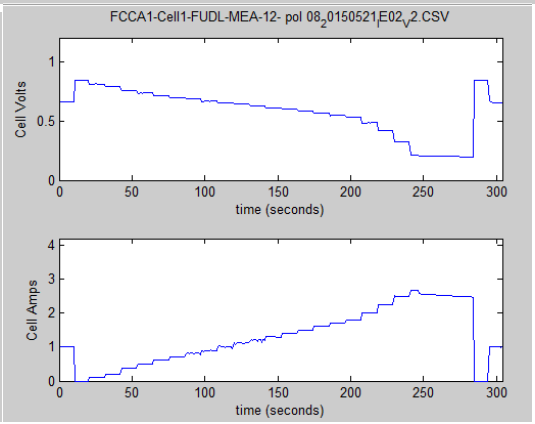
FCCA1-Cell1-FUDL-MEA-12- pol 08_20150521_E02_V2.CSV
Cell Volts
time (seconds)
Cell Amps
time (seconds)

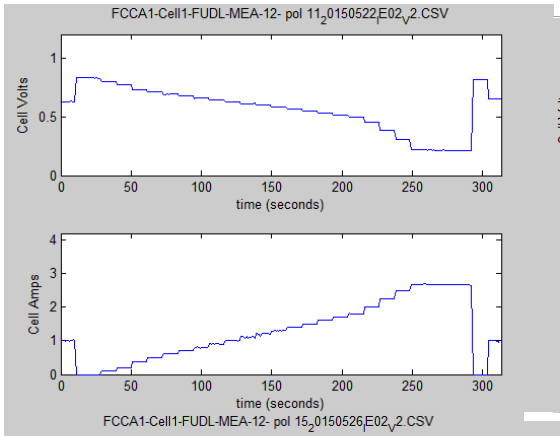
FCCA1-Cell1-FUDL-MEA-12- pol 11_20150522_E02_V2.CSV
Cell Volts
time (seconds)
Cell Amps
time (seconds)

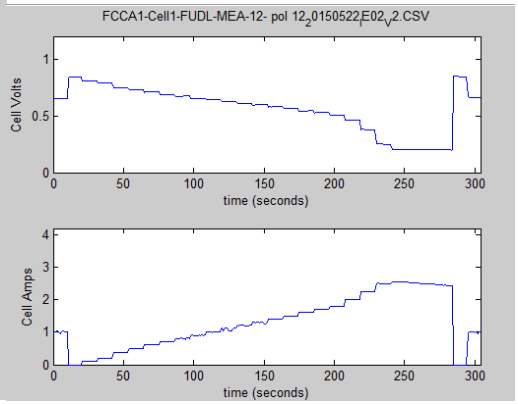
FCCA1-Cell1-FUDL-MEA-12- pol 12_20150522_E02_V2.CSV
Cell Volts
time (seconds)
Cell Amps
time (seconds)

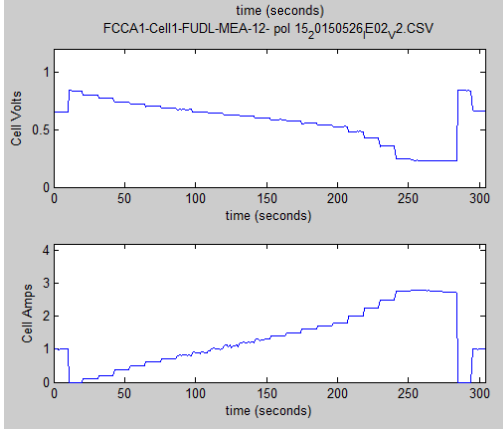
FCCA1-Cell1-FUDL-MEA-12- pol 15_20150526_E02_V2.CSV
Cell Volts
time (seconds)
Cell Amps
time (seconds)

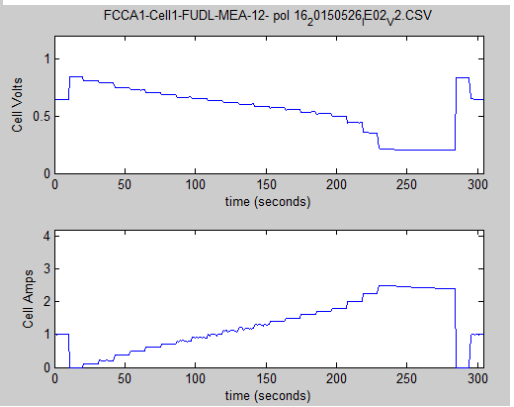
FCCA1-Cell1-FUDL-MEA-12- pol 16_20150526_E02_V2.CSV
Cell Volts
time (seconds)
Cell Amps
time (seconds)

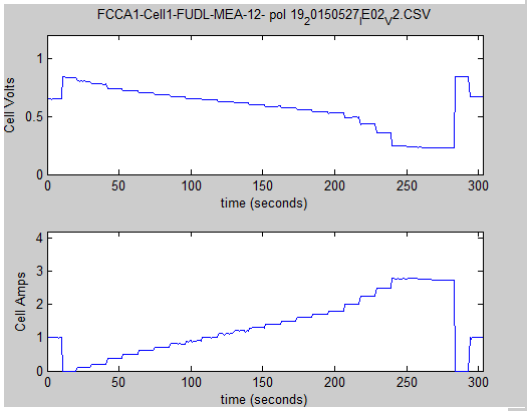
FCCA1-Cell1-FUDL-MEA-12- pol 19_20150527_E02_V2.CSV
Cell Volts
time (seconds)
Cell Amps
time (seconds)

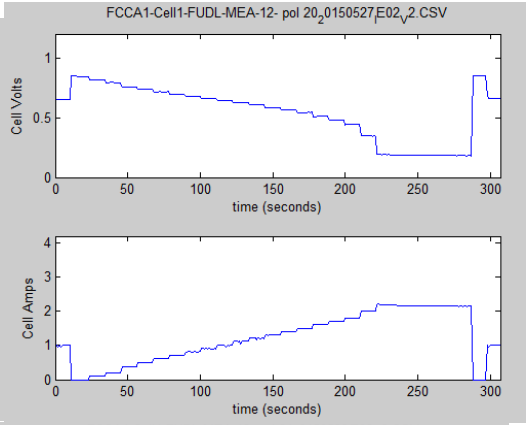
FCCA1-Cell1-FUDL-MEA-12- pol 20_20150527_E02_V2.CSV
Cell Volts
time (seconds)
Cell Amps
time (seconds)

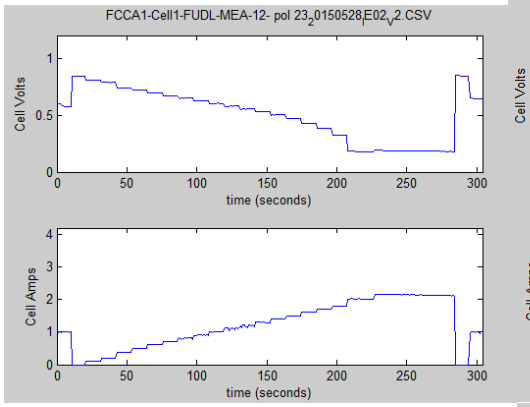
FCCA1-Cell1-FUDL-MEA-12- pol 23_20150528_E02_V2.CSV
Cell Volts
time (seconds)
Cell Amps
time (seconds)

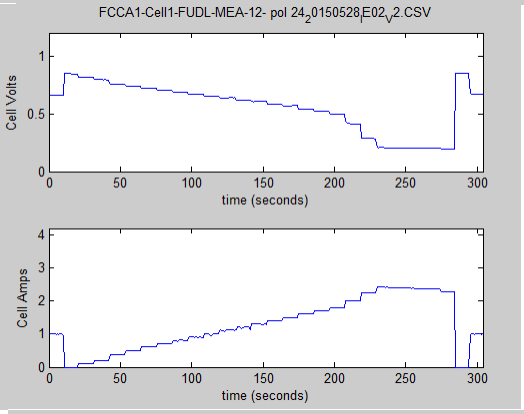
FCCA1-Cell1-FUDL-MEA-12- pol 24_20150528_E02_V2.CSV
Cell Volts
time (seconds)
Cell Amps
time (seconds)

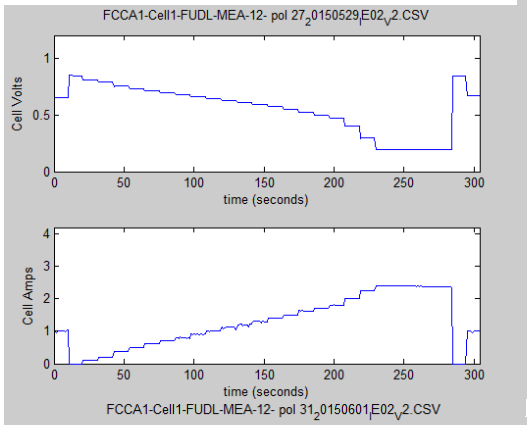
FCCA1-Cell1-FUDL-MEA-12- pol 27_20150529_E02_V2.CSV
Cell Volts
time (seconds)
Cell Amps
time (seconds)

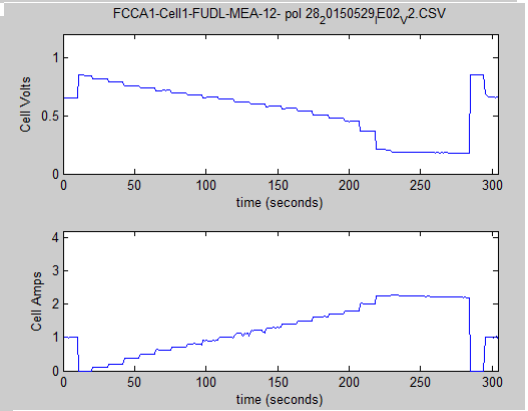
FCCA1-Cell1-FUDL-MEA-12- pol 28_20150529_E02_V2.CSV
Cell Volts
time (seconds)
Cell Amps
time (seconds)

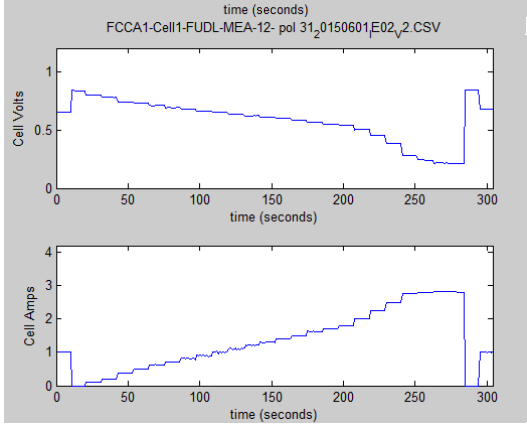
FCCA1-Cell1-FUDL-MEA-12- pol 31_20150601_E02_V2.CSV
Cell Volts
time (seconds)
Cell Amps
time (seconds)

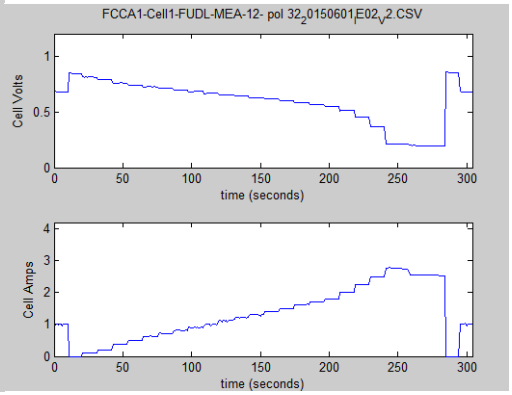
FCCA1-Cell1-FUDL-MEA-12- pol 32_20150601_E02_V2.CSV
Cell Volts
time (seconds)
Cell Amps
time (seconds)

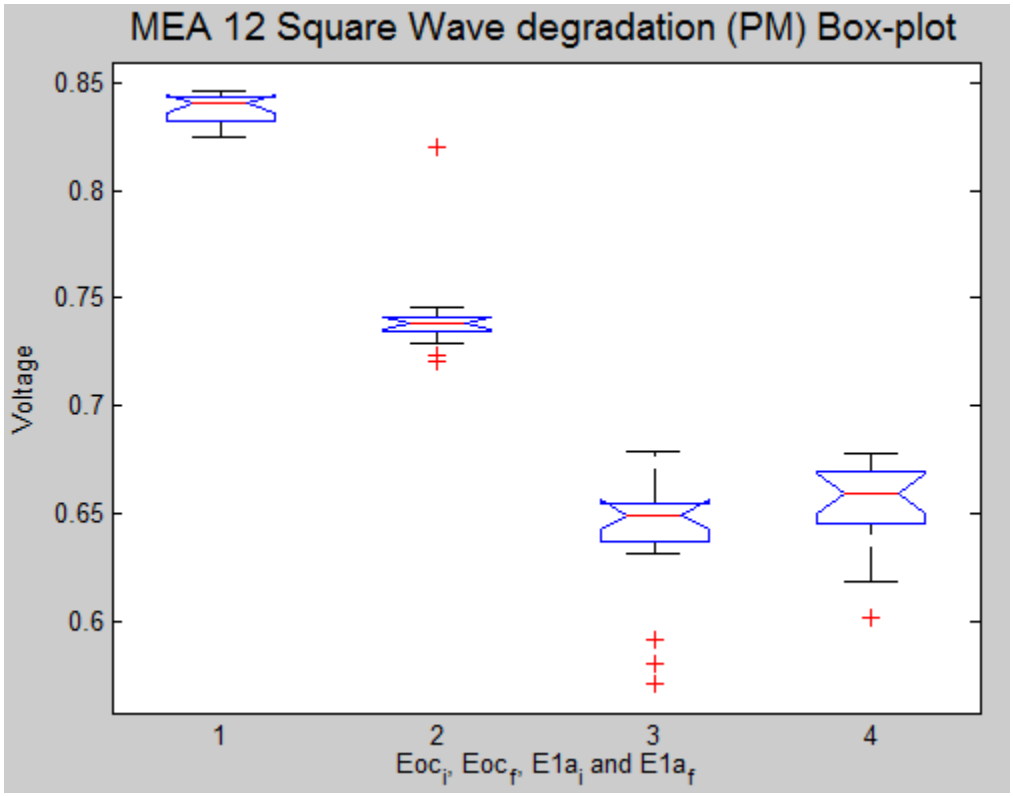
MEA 12 Square Wave degradation (PM) Box-plot
Voltage
0.85
0.8
0.75
0.7
0.65
0.6
1
2
3
4
Eoc$_i$, Eoc$_f$, E1a$_i$ and E1a$_f$

MEA 12 (Freudenberg cathode, high-D, Square Wave)PM

Square Wave degradation plot Eocv-intial

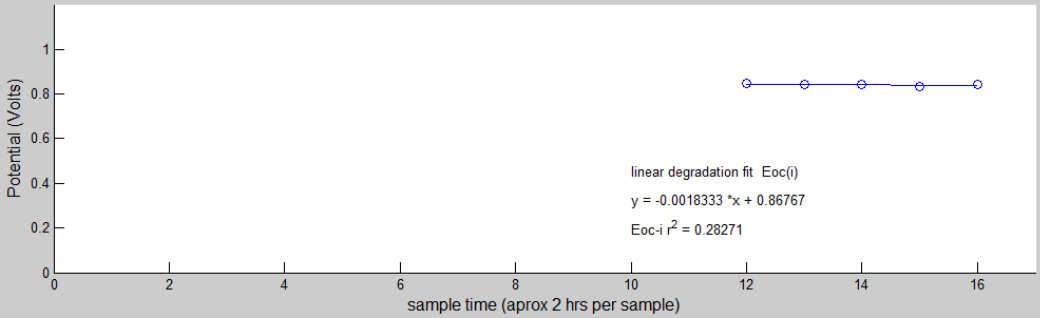

Square Wave degradation plot Eocv-final

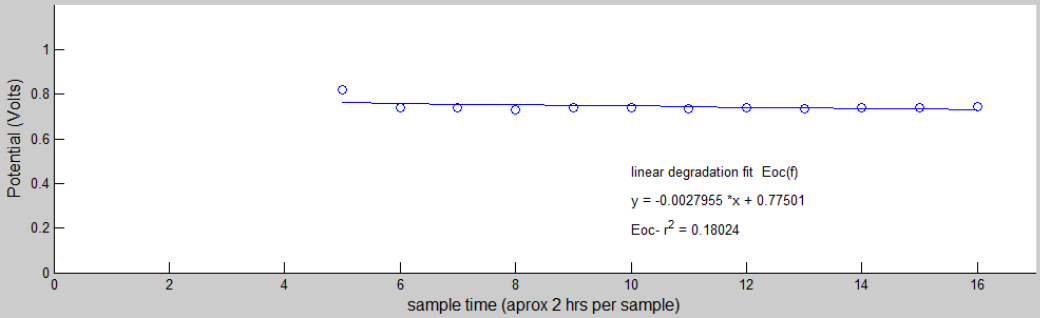

Square Wave degradation plot E at 1 amp-intial

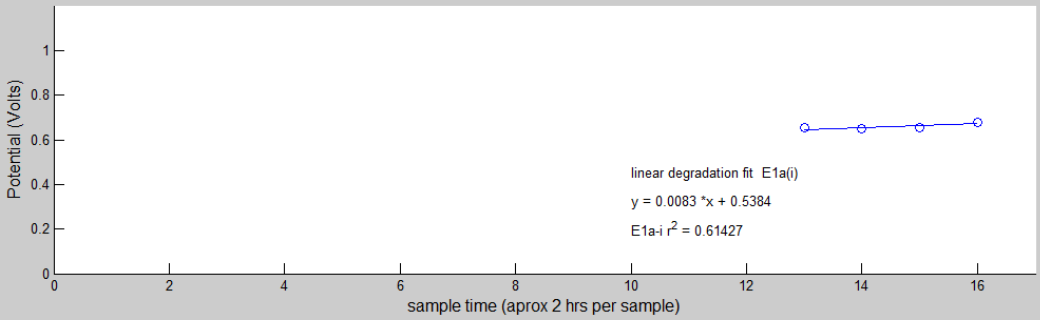

Square Wave degradation plot E at 1 amp -final

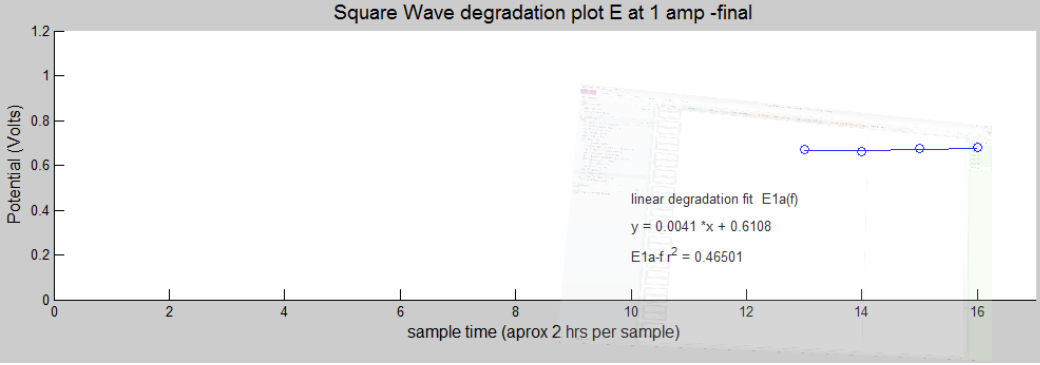

MEA 12 (Freudenberg cathode, high-D, Square Wave)PM

Square Wave degradation plot Eocv-intial

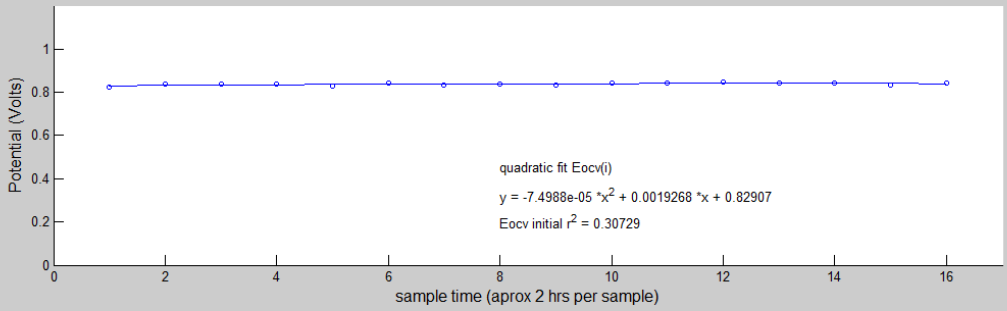

Square Wave degradation plot Eocv-final

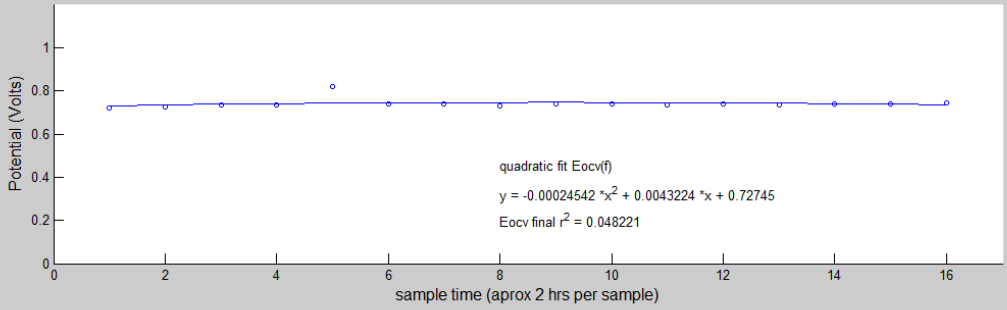

Square Wave degradation plot E1 Amp-intial

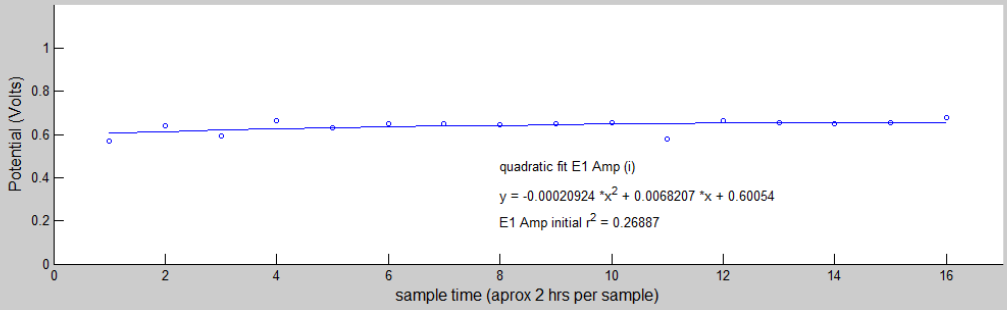

Square Wave degradation plot E1 Amp-final

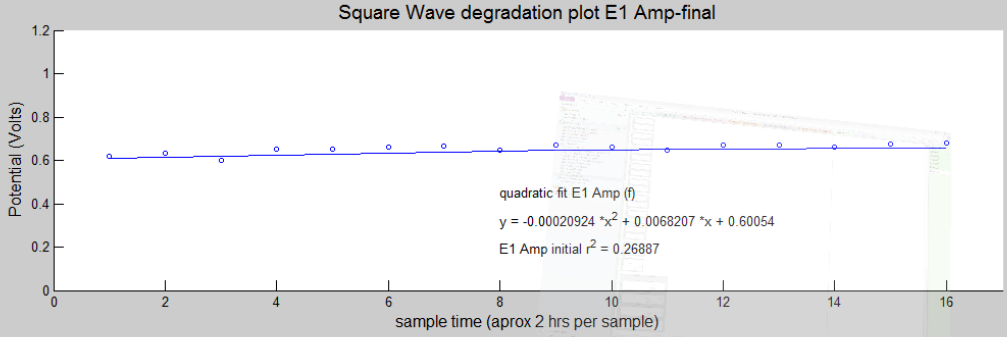

MEA 12 (Freudenberg cathode, high-D, Square Wave)PM

Square Wave spline filter plot Eocv-intial

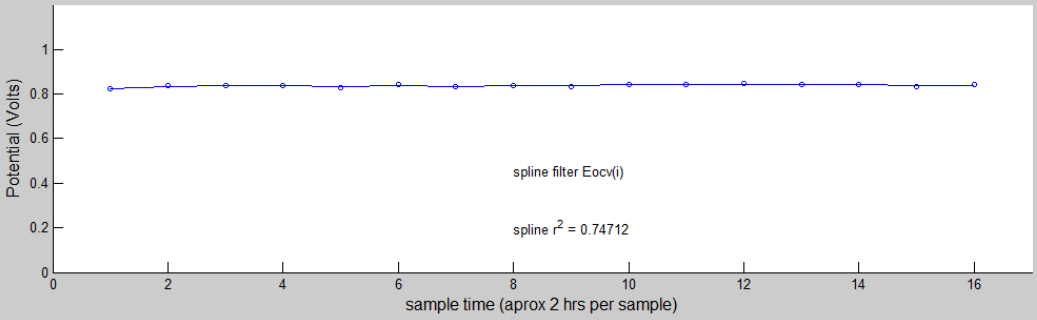

Square Wave spline filter plot Eocv-final

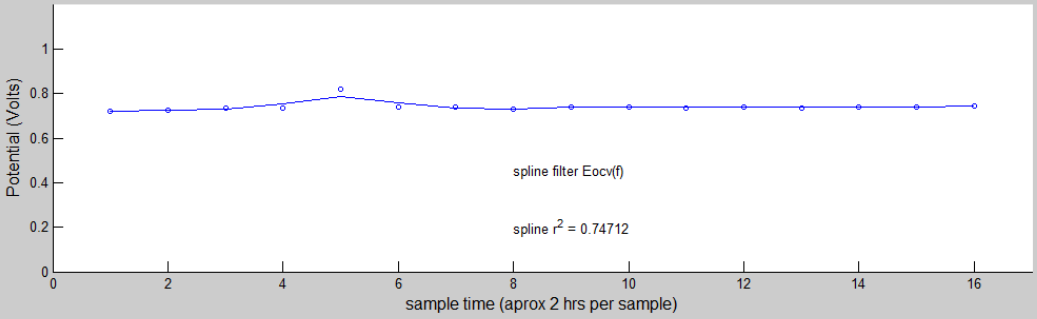

Square Wave spline filter plot E1 Amp-initial

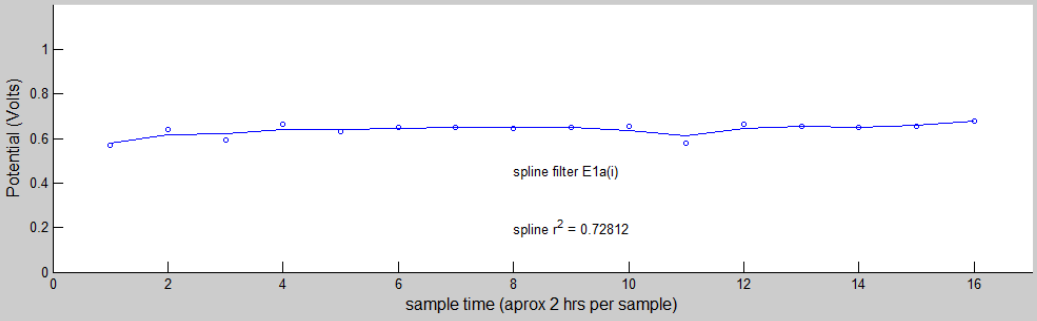

Square Wave spline filter plot E1 Amp-final

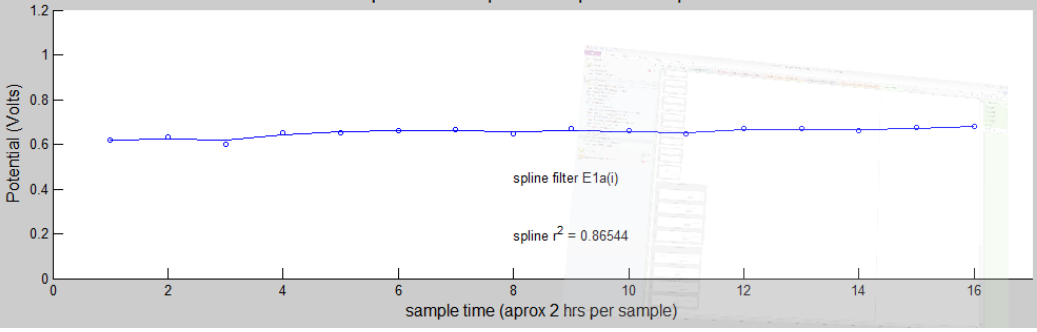

MEA 14

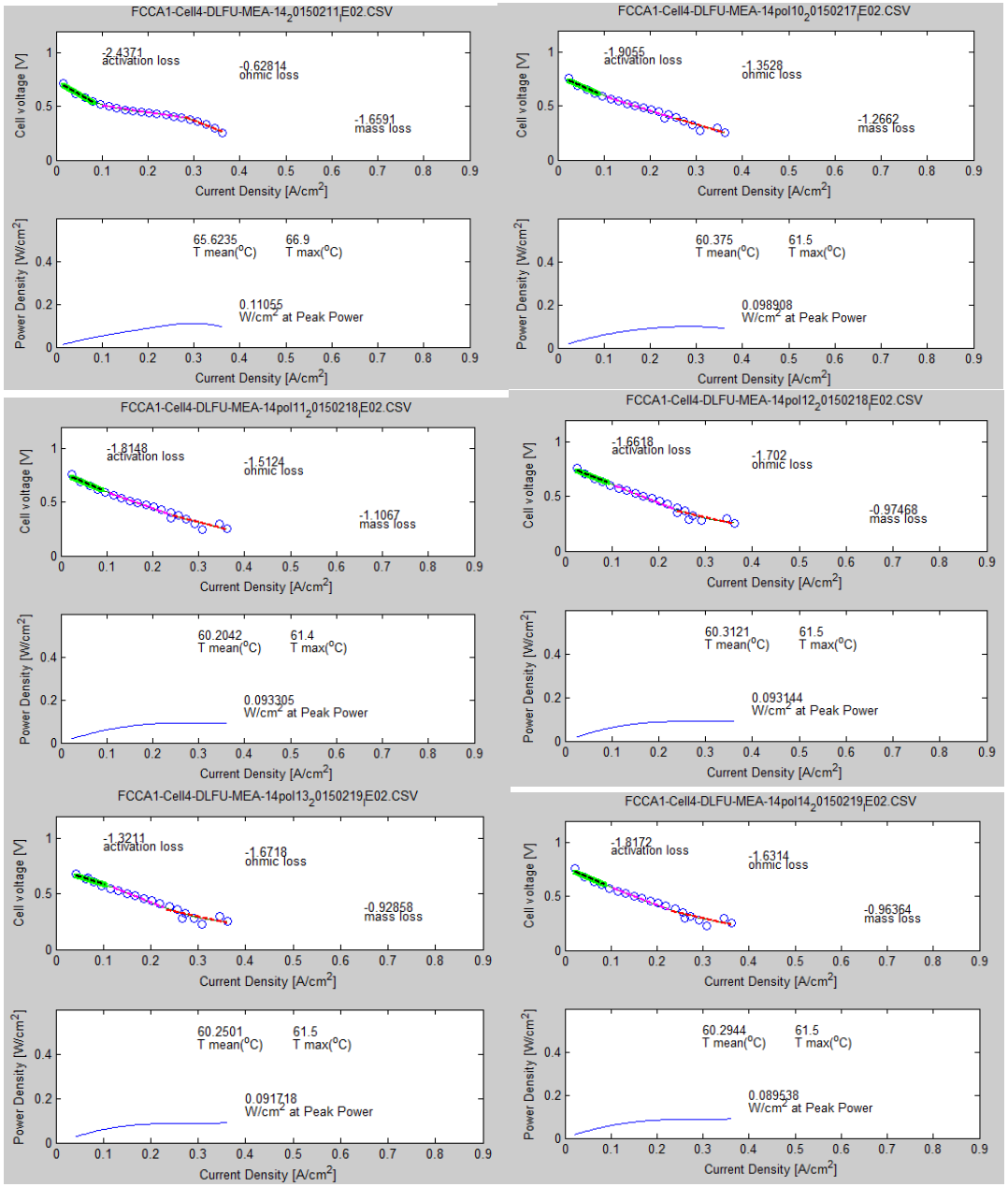
FCCA1-Cell4-DLFU-MEA-14_20150211_E02.CSV
-2.4371
activation loss
-0.62814
ohmic loss
-1.6591
mass loss
Cell voltage [V]
Current Density [A/cm2]
65.6235
T mean(°C)
66.9
T max(°C)
0.11055
W/cm2 at Peak Power
Power Density [W/cm2]
FCCA1-Cell4-DLFU-MEA-14pol10_20150217_E02.CSV
-1.9055
activation loss
-1.3528
ohmic loss
-1.2662
mass loss
60.375
T mean(°C)
61.5
T max(°C)
0.098908
W/cm2 at Peak Power
FCCA1-Cell4-DLFU-MEA-14pol11_20150218_E02.CSV
-1.8148
activation loss
-1.5124
ohmic loss
-1.1067
mass loss
60.2042
T mean(°C)
61.4
T max(°C)
0.093305
W/cm2 at Peak Power
FCCA1-Cell4-DLFU-MEA-14pol12_20150218_E02.CSV
-1.6618
activation loss
-1.702
ohmic loss
-0.97468
mass loss
60.3121
T mean(°C)
61.5
T max(°C)
0.093144
W/cm2 at Peak Power
FCCA1-Cell4-DLFU-MEA-14pol13_20150219_E02.CSV
-1.3211
activation loss
-1.6718
ohmic loss
-0.92858
mass loss
60.2501
T mean(°C)
61.5
T max(°C)
0.091718
W/cm2 at Peak Power
FCCA1-Cell4-DLFU-MEA-14pol14_20150219_E02.CSV
-1.8172
activation loss
-1.6314
ohmic loss
-0.96364
mass loss
60.2944
T mean(°C)
61.5
T max(°C)
0.089538
W/cm2 at Peak Power

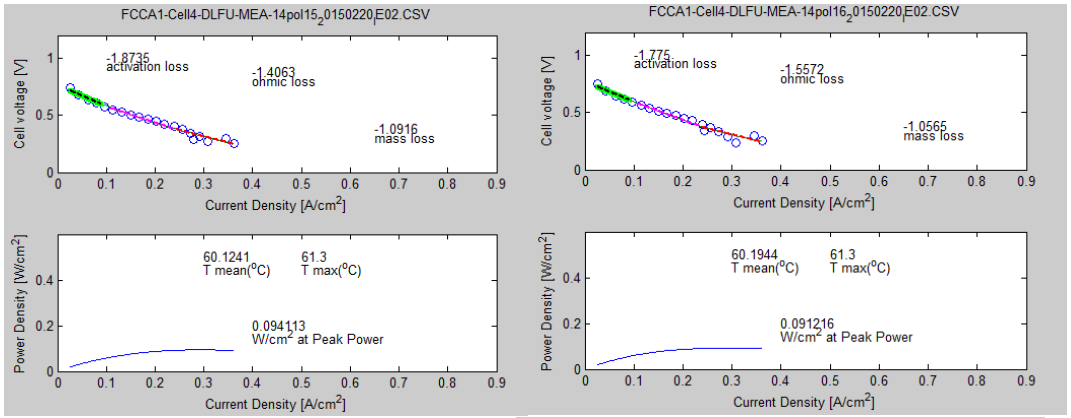
FCCA1-Cell4-DLFU-MEA-14pol15_20150220_E02.CSV
-1.8735
activation loss
-1.4063
ohmic loss
-1.0916
mass loss
Cell voltage [V]
Current Density [A/cm2]
60.1241
T mean(°C)
61.3
T max(°C)
0.094113
W/cm2 at Peak Power
Power Density [W/cm2]
Current Density [A/cm2]

FCCA1-Cell4-DLFU-MEA-14pol16_20150220_E02.CSV
-1.775
activation loss
-1.5572
ohmic loss
-1.0565
mass loss
Cell voltage [V]
Current Density [A/cm2]
60.1944
T mean(°C)
61.3
T max(°C)
0.091216
W/cm2 at Peak Power
Power Density [W/cm2]
Current Density [A/cm2]

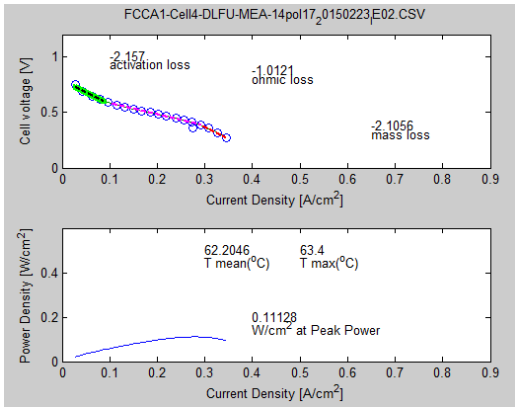
FCCA1-Cell4-DLFU-MEA-14pol17_20150223_E02.CSV
-2.157
activation loss
-1.0121
ohmic loss
-2.1056
mass loss
Cell voltage [V]
Current Density [A/cm2]
62.2046
T mean(°C)
63.4
T max(°C)
0.11128
W/cm2 at Peak Power
Power Density [W/cm2]
Current Density [A/cm2]

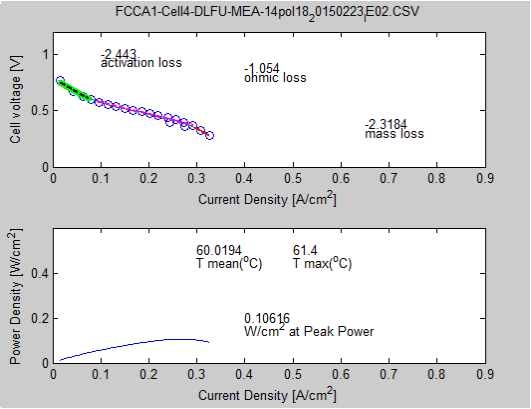
FCCA1-Cell4-DLFU-MEA-14pol18_20150223_E02.CSV
-2.443
activation loss
-1.054
ohmic loss
-2.3184
mass loss
Cell voltage [V]
Current Density [A/cm2]
60.0194
T mean(°C)
61.4
T max(°C)
0.10616
W/cm2 at Peak Power
Power Density [W/cm2]
Current Density [A/cm2]

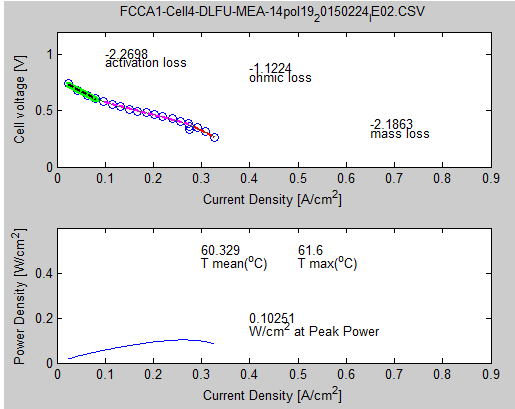
FCCA1-Cell4-DLFU-MEA-14pol19_20150224_E02.CSV
-2.2698
activation loss
-1.1224
ohmic loss
-2.1863
mass loss
Cell voltage [V]
Current Density [A/cm2]
60.329
T mean(°C)
61.6
T max(°C)
0.10251
W/cm2 at Peak Power
Power Density [W/cm2]
Current Density [A/cm2]

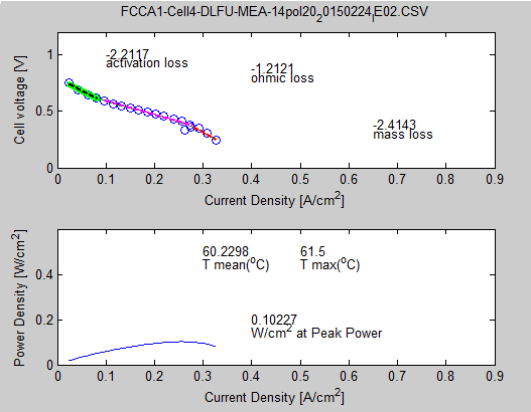
FCCA1-Cell4-DLFU-MEA-14pol20_20150224_E02.CSV
-2.2117
activation loss
-1.2121
ohmic loss
-2.4143
mass loss
Cell voltage [V]
Current Density [A/cm2]
60.2298
T mean(°C)
61.5
T max(°C)
0.10227
W/cm2 at Peak Power
Power Density [W/cm2]
Current Density [A/cm2]

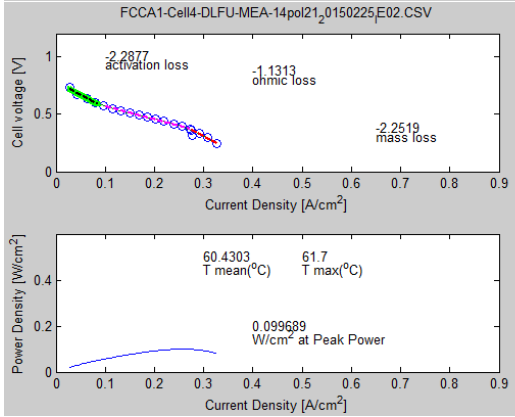
FCCA1-Cell4-DLFU-MEA-14pol21_20150225_E02.CSV
-2.2877
activation loss
-1.1313
ohmic loss
-2.2519
mass loss
Cell voltage [V]
Current Density [A/cm2]
60.4303
T mean(°C)
61.7
T max(°C)
0.099689
W/cm2 at Peak Power
Power Density [W/cm2]
Current Density [A/cm2]

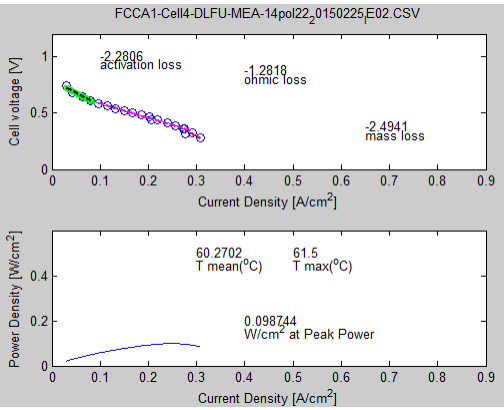
FCCA1-Cell4-DLFU-MEA-14pol22_20150225_E02.CSV
-2.2806
activation loss
-1.2818
ohmic loss
-2.4941
mass loss
Cell voltage [V]
Current Density [A/cm2]
60.2702
T mean(°C)
61.5
T max(°C)
0.098744
W/cm2 at Peak Power
Power Density [W/cm2]
Current Density [A/cm2]

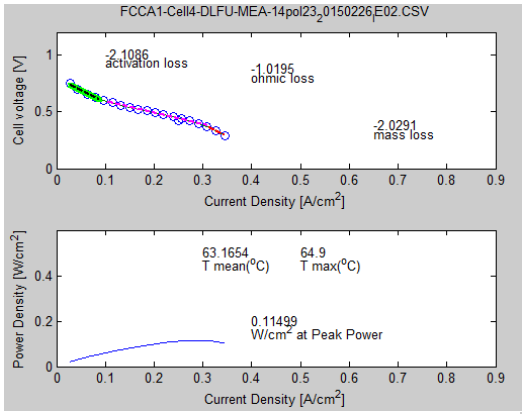
FCCA1-Cell4-DLFU-MEA-14pol23_0150226_E02.CSV
-2.1086
activation loss
-1.0195
ohmic loss
-2.0291
mass loss
Cell voltage [V]
Current Density [A/cm2]
63.1654
T mean(°C)
64.9
T max(°C)
0.11499
W/cm2 at Peak Power
Power Density [W/cm2]
Current Density [A/cm2]

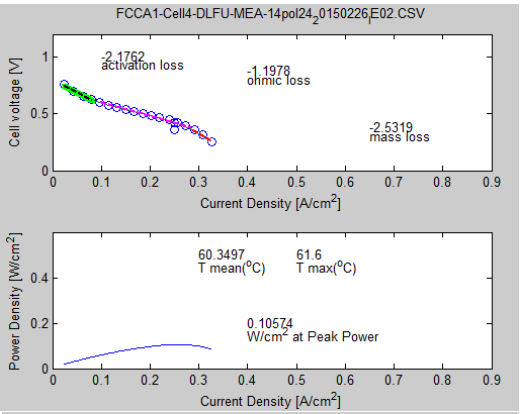
FCCA1-Cell4-DLFU-MEA-14pol24_0150226_E02.CSV
-2.1762
activation loss
-1.1978
ohmic loss
-2.5319
mass loss
Cell voltage [V]
Current Density [A/cm2]
60.3497
T mean(°C)
61.6
T max(°C)
0.10574
W/cm2 at Peak Power
Power Density [W/cm2]
Current Density [A/cm2]

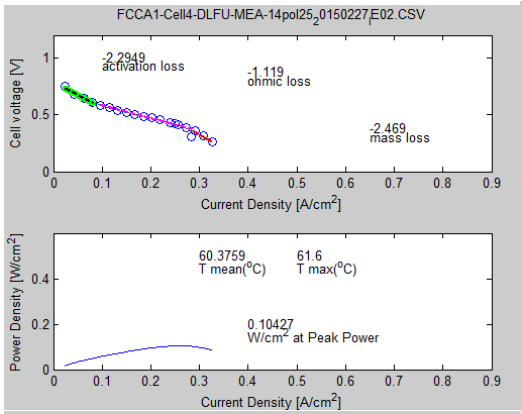
FCCA1-Cell4-DLFU-MEA-14pol25_0150227_E02.CSV
-2.2949
activation loss
-1.119
ohmic loss
-2.469
mass loss
Cell voltage [V]
Current Density [A/cm2]
60.3759
T mean(°C)
61.6
T max(°C)
0.10427
W/cm2 at Peak Power
Power Density [W/cm2]
Current Density [A/cm2]

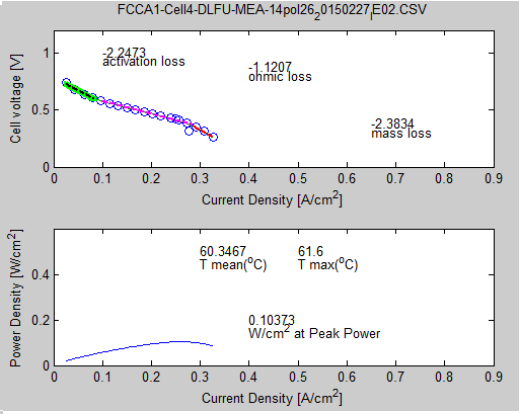
FCCA1-Cell4-DLFU-MEA-14pol26_0150227_E02.CSV
-2.2473
activation loss
-1.1207
ohmic loss
-2.3834
mass loss
Cell voltage [V]
Current Density [A/cm2]
60.3467
T mean(°C)
61.6
T max(°C)
0.10373
W/cm2 at Peak Power
Power Density [W/cm2]
Current Density [A/cm2]

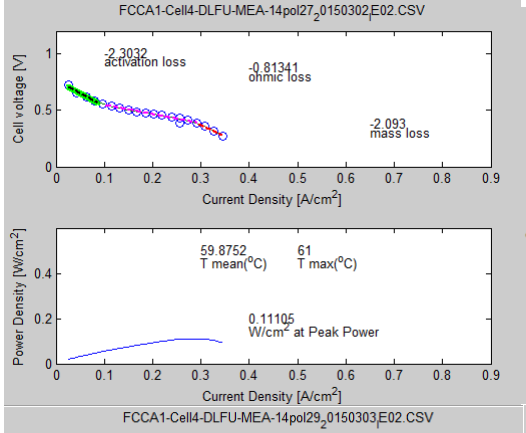
FCCA1-Cell4-DLFU-MEA-14pol27_0150302_E02.CSV
-2.3032
activation loss
-0.81341
ohmic loss
-2.093
mass loss
Cell voltage [V]
Current Density [A/cm2]
59.8752
T mean(°C)
61
T max(°C)
0.11105
W/cm2 at Peak Power
Power Density [W/cm2]
Current Density [A/cm2]

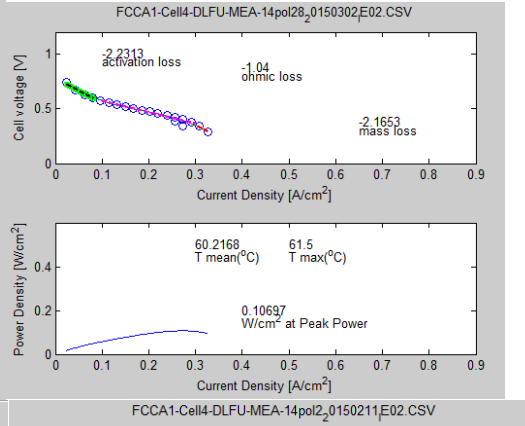
FCCA1-Cell4-DLFU-MEA-14pol28_0150302_E02.CSV
-2.2313
activation loss
-1.04
ohmic loss
-2.1653
mass loss
Cell voltage [V]
Current Density [A/cm2]
60.2168
T mean(°C)
61.5
T max(°C)
0.10697
W/cm2 at Peak Power
Power Density [W/cm2]
Current Density [A/cm2]

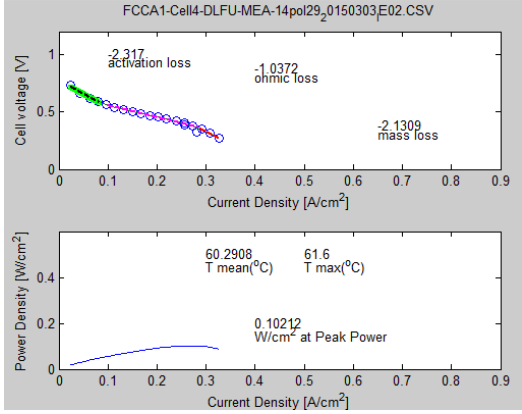
FCCA1-Cell4-DLFU-MEA-14pol29_0150303_E02.CSV
-2.317
activation loss
-1.0372
ohmic loss
-2.1309
mass loss
Cell voltage [V]
Current Density [A/cm2]
60.2908
T mean(°C)
61.6
T max(°C)
0.10212
W/cm2 at Peak Power
Power Density [W/cm2]
Current Density [A/cm2]

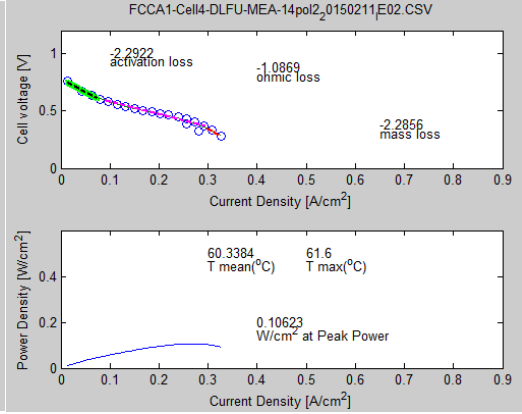
FCCA1-Cell4-DLFU-MEA-14pol2_0150211_E02.CSV
-2.2922
activation loss
-1.0869
ohmic loss
-2.2856
mass loss
Cell voltage [V]
Current Density [A/cm2]
60.3384
T mean(°C)
61.6
T max(°C)
0.10623
W/cm2 at Peak Power
Power Density [W/cm2]
Current Density [A/cm2]

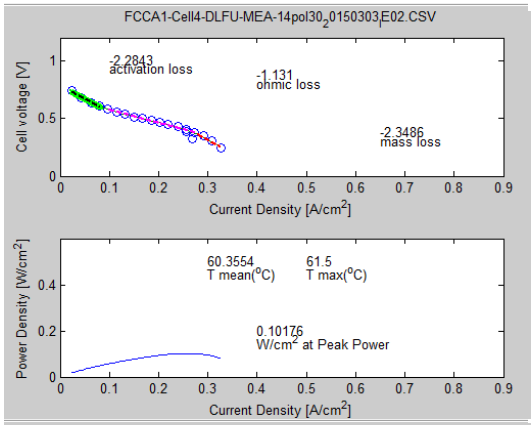
FCCA1-Cell4-DLFU-MEA-14pol30_0150303_E02.CSV
-2.2843
activation loss
-1.131
ohmic loss
-2.3486
mass loss
Cell voltage [V]
Current Density [A/cm2]
60.3554
T mean(°C)
61.5
T max(°C)
0.10176
W/cm2 at Peak Power
Power Density [W/cm2]
Current Density [A/cm2]

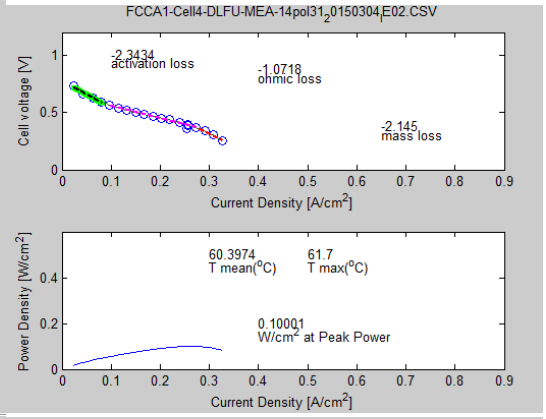
FCCA1-Cell4-DLFU-MEA-14pol31_0150304_E02.CSV
-2.3434
activation loss
-1.0718
ohmic loss
-2.145
mass loss
Cell voltage [V]
Current Density [A/cm2]
60.3974
T mean(°C)
61.7
T max(°C)
0.10001
W/cm2 at Peak Power
Power Density [W/cm2]
Current Density [A/cm2]

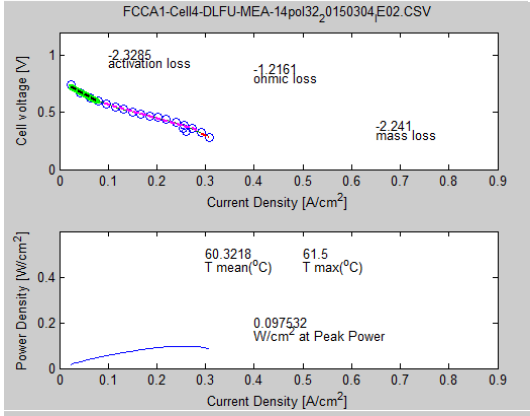
FCCA1-Cell4-DLFU-MEA-14pol32_0150304_E02.CSV
-2.3285
activation loss
-1.2161
ohmic loss
-2.241
mass loss
Cell voltage [V]
Current Density [A/cm2]
60.3218
T mean(°C)
61.5
T max(°C)
0.097532
W/cm2 at Peak Power
Power Density [W/cm2]
Current Density [A/cm2]

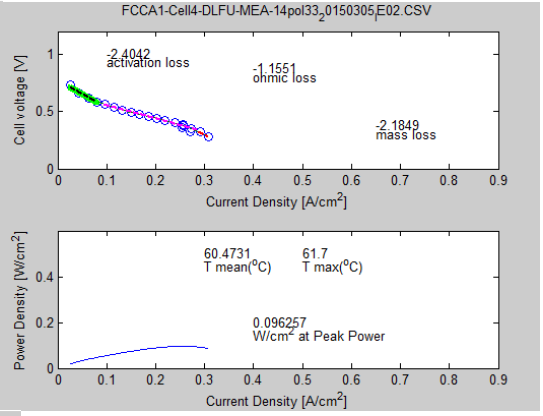
FCCA1-Cell4-DLFU-MEA-14pol33_0150305_E02.CSV
-2.4042
activation loss
-1.1551
ohmic loss
-2.1849
mass loss
Cell voltage [V]
Current Density [A/cm2]
60.4731
T mean(°C)
61.7
T max(°C)
0.096257
W/cm2 at Peak Power
Power Density [W/cm2]
Current Density [A/cm2]

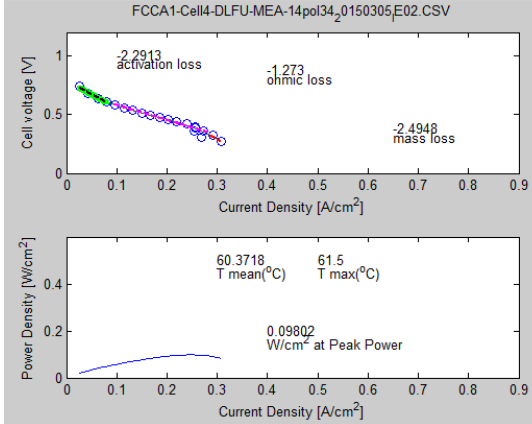
FCCA1-Cell4-DLFU-MEA-14pol34_0150305_E02.CSV
-2.2913
activation loss
-1.273
ohmic loss
-2.4948
mass loss
Cell voltage [V]
Current Density [A/cm2]
60.3718
T mean(°C)
61.5
T max(°C)
0.09802
W/cm2 at Peak Power
Power Density [W/cm2]
Current Density [A/cm2]

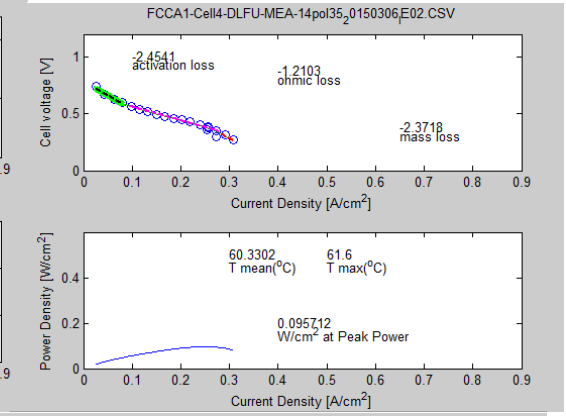
FCCA1-Cell4-DLFU-MEA-14pol35_0150306_E02.CSV
-2.4541
activation loss
-1.2103
ohmic loss
-2.3718
mass loss
Cell voltage [V]
Current Density [A/cm2]
60.3302
T mean(°C)
61.6
T max(°C)
0.095712
W/cm2 at Peak Power
Power Density [W/cm2]
Current Density [A/cm2]

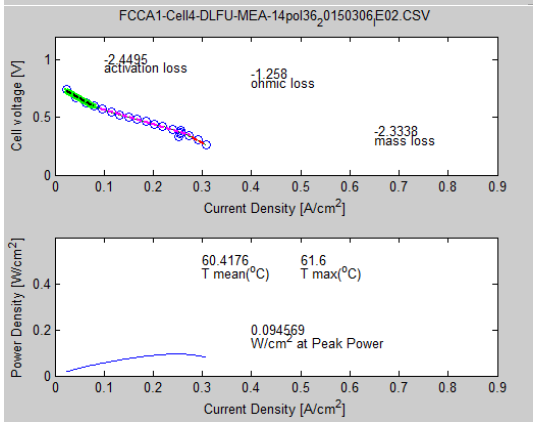
FCCA1-Cell4-DLFU-MEA-14pol36_0150306_E02.CSV
-2.4495
activation loss
-1.258
ohmic loss
-2.3338
mass loss
Cell voltage [V]
Current Density [A/cm2]
60.4176
T mean(°C)
61.6
T max(°C)
0.094569
W/cm2 at Peak Power
Power Density [W/cm2]
Current Density [A/cm2]

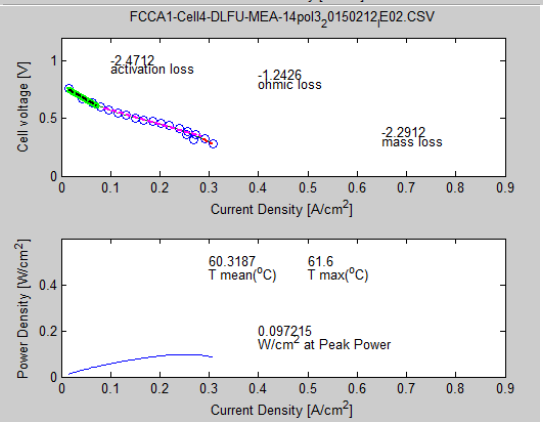
FCCA1-Cell4-DLFU-MEA-14pol3_0150212_E02.CSV
-2.4712
activation loss
-1.2426
ohmic loss
-2.2912
mass loss
Cell voltage [V]
Current Density [A/cm2]
60.3187
T mean(°C)
61.6
T max(°C)
0.097215
W/cm2 at Peak Power
Power Density [W/cm2]
Current Density [A/cm2]

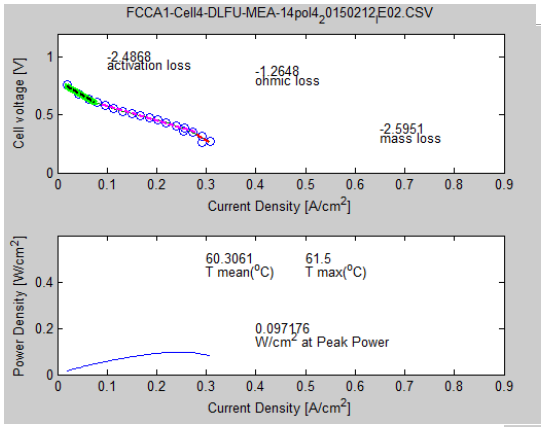
FCCA1-Cell4-DLFU-MEA-14pol4_20150212_E02.CSV
-2.4868
activation loss
-1.2648
ohmic loss
-2.5951
mass loss
Cell voltage [V]
Current Density [A/cm2]
60.3061
T mean(°C)
61.5
T max(°C)
0.097176
W/cm2 at Peak Power
Power Density [W/cm2]
Current Density [A/cm2]

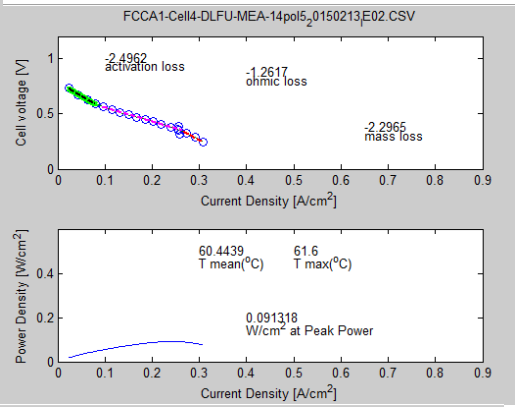
FCCA1-Cell4-DLFU-MEA-14pol5_20150213_E02.CSV
-2.4962
activation loss
-1.2617
ohmic loss
-2.2965
mass loss
Cell voltage [V]
Current Density [A/cm2]
60.4439
T mean(°C)
61.6
T max(°C)
0.091318
W/cm2 at Peak Power
Power Density [W/cm2]
Current Density [A/cm2]

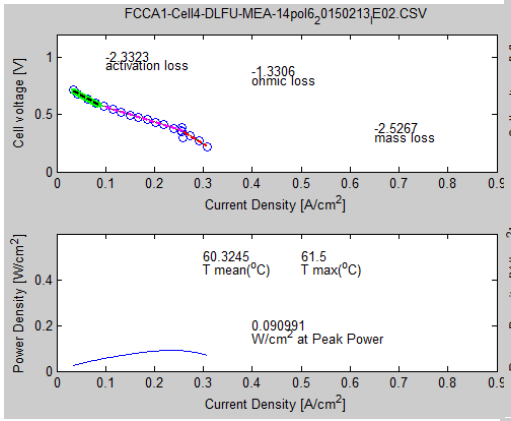
FCCA1-Cell4-DLFU-MEA-14pol6_20150213_E02.CSV
-2.3323
activation loss
-1.3306
ohmic loss
-2.5267
mass loss
Cell voltage [V]
Current Density [A/cm2]
60.3245
T mean(°C)
61.5
T max(°C)
0.090991
W/cm2 at Peak Power
Power Density [W/cm2]
Current Density [A/cm2]

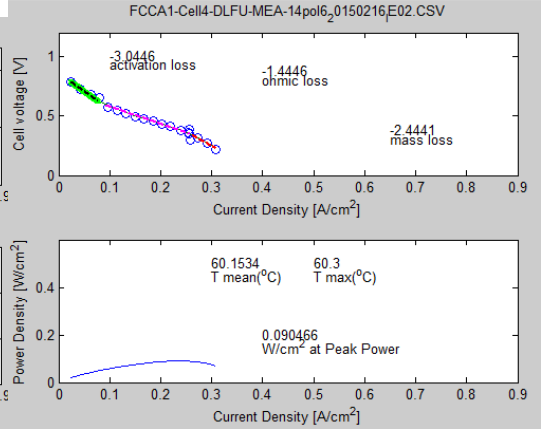
FCCA1-Cell4-DLFU-MEA-14pol6_20150216_E02.CSV
-3.0446
activation loss
-1.4446
ohmic loss
-2.4441
mass loss
Cell voltage [V]
Current Density [A/cm2]
60.1534
T mean(°C)
60.3
T max(°C)
0.090466
W/cm2 at Peak Power
Power Density [W/cm2]
Current Density [A/cm2]

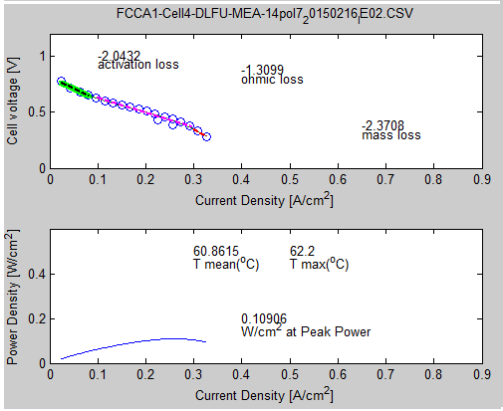
FCCA1-Cell4-DLFU-MEA-14pol7_20150216_E02.CSV
-2.0432
activation loss
-1.3099
ohmic loss
-2.3708
mass loss
Cell voltage [V]
Current Density [A/cm2]
60.8615
T mean(°C)
62.2
T max(°C)
0.10906
W/cm2 at Peak Power
Power Density [W/cm2]
Current Density [A/cm2]

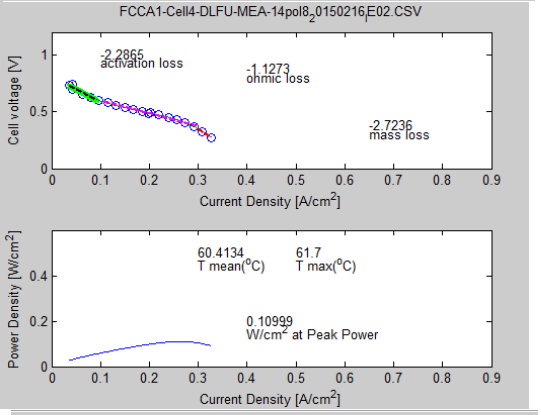
FCCA1-Cell4-DLFU-MEA-14pol8_20150216_E02.CSV
-2.2865
activation loss
-1.1273
ohmic loss
-2.7236
mass loss
Cell voltage [V]
Current Density [A/cm2]
60.4134
T mean(°C)
61.7
T max(°C)
0.10999
W/cm2 at Peak Power
Power Density [W/cm2]
Current Density [A/cm2]

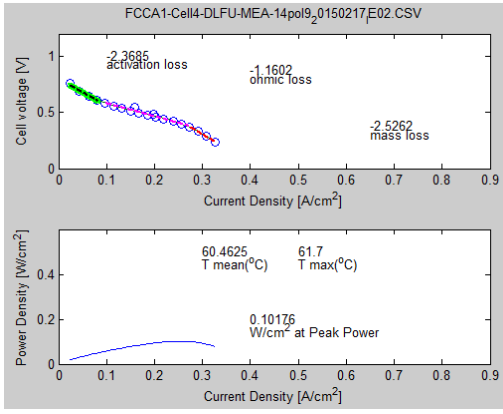
FCCA1-Cell4-DLFU-MEA-14pol9_20150217_E02.CSV
-2.3685
activation loss
-1.1602
ohmic loss
-2.5262
mass loss
Cell voltage [V]
Current Density [A/cm2]
60.4625
T mean(°C)
61.7
T max(°C)
0.10176
W/cm2 at Peak Power
Power Density [W/cm2]
Current Density [A/cm2]

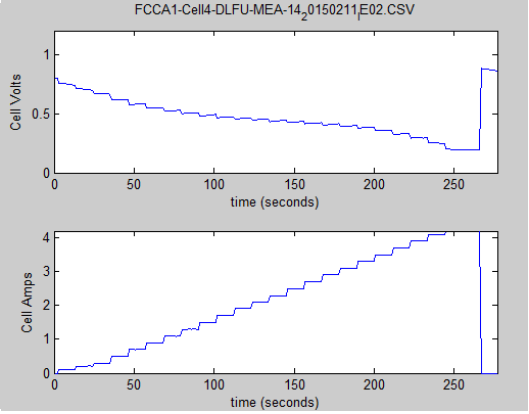
FCCA1-Cell4-DLFU-MEA-14_20150211_E02.CSV
Cell Volts
time (seconds)
Cell Amps
time (seconds)

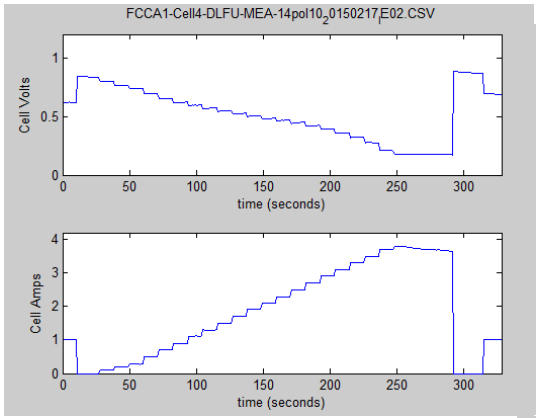
FCCA1-Cell4-DLFU-MEA-14pol10_20150217_E02.CSV
Cell Volts
time (seconds)
Cell Amps
time (seconds)

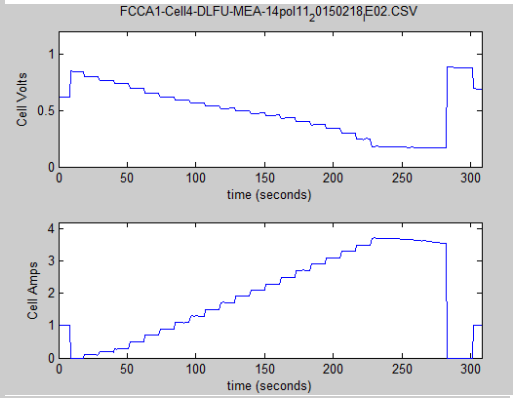
FCCA1-Cell4-DLFU-MEA-14pol11_20150218_E02.CSV
Cell Volts
time (seconds)
Cell Amps
time (seconds)

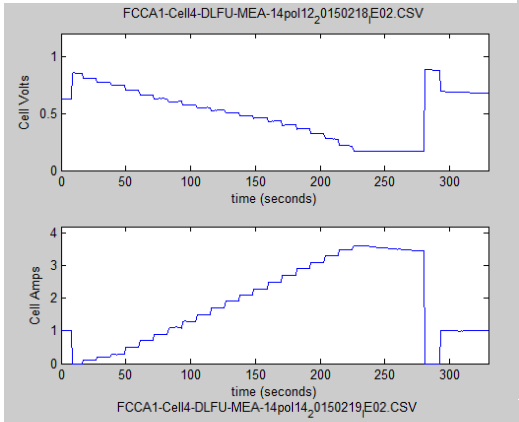
FCCA1-Cell4-DLFU-MEA-14pol12_20150218_E02.CSV
Cell Volts
time (seconds)
Cell Amps
time (seconds)

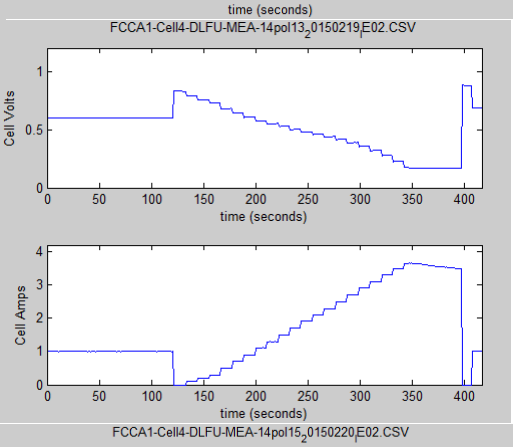
FCCA1-Cell4-DLFU-MEA-14pol13_20150219_E02.CSV
Cell Volts
time (seconds)
Cell Amps
time (seconds)

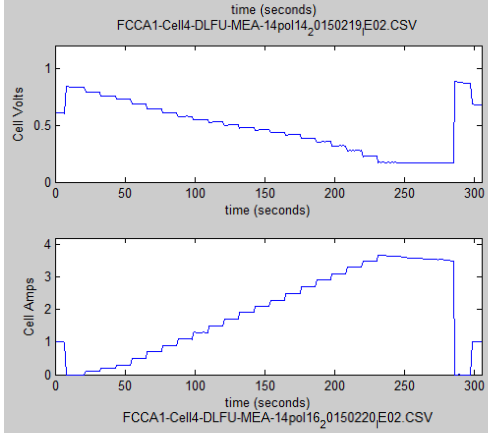
FCCA1-Cell4-DLFU-MEA-14pol14_20150219_E02.CSV
Cell Volts
time (seconds)
Cell Amps
time (seconds)

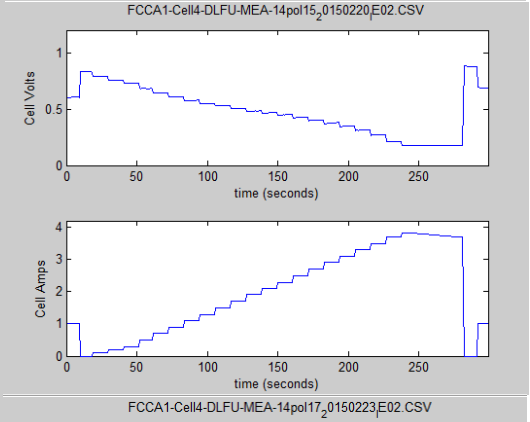
FCCA1-Cell4-DLFU-MEA-14pol15_20150220_E02.CSV
Cell Volts
time (seconds)
Cell Amps
time (seconds)

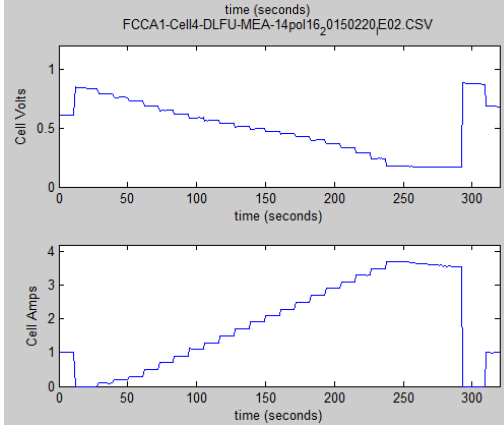
FCCA1-Cell4-DLFU-MEA-14pol16_20150220_E02.CSV
Cell Volts
time (seconds)
Cell Amps
time (seconds)

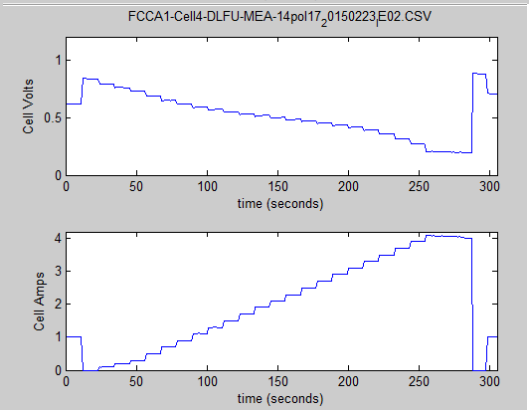
FCCA1-Cell4-DLFU-MEA-14pol17_20150223_E02.CSV
Cell Volts
time (seconds)
Cell Amps
time (seconds)

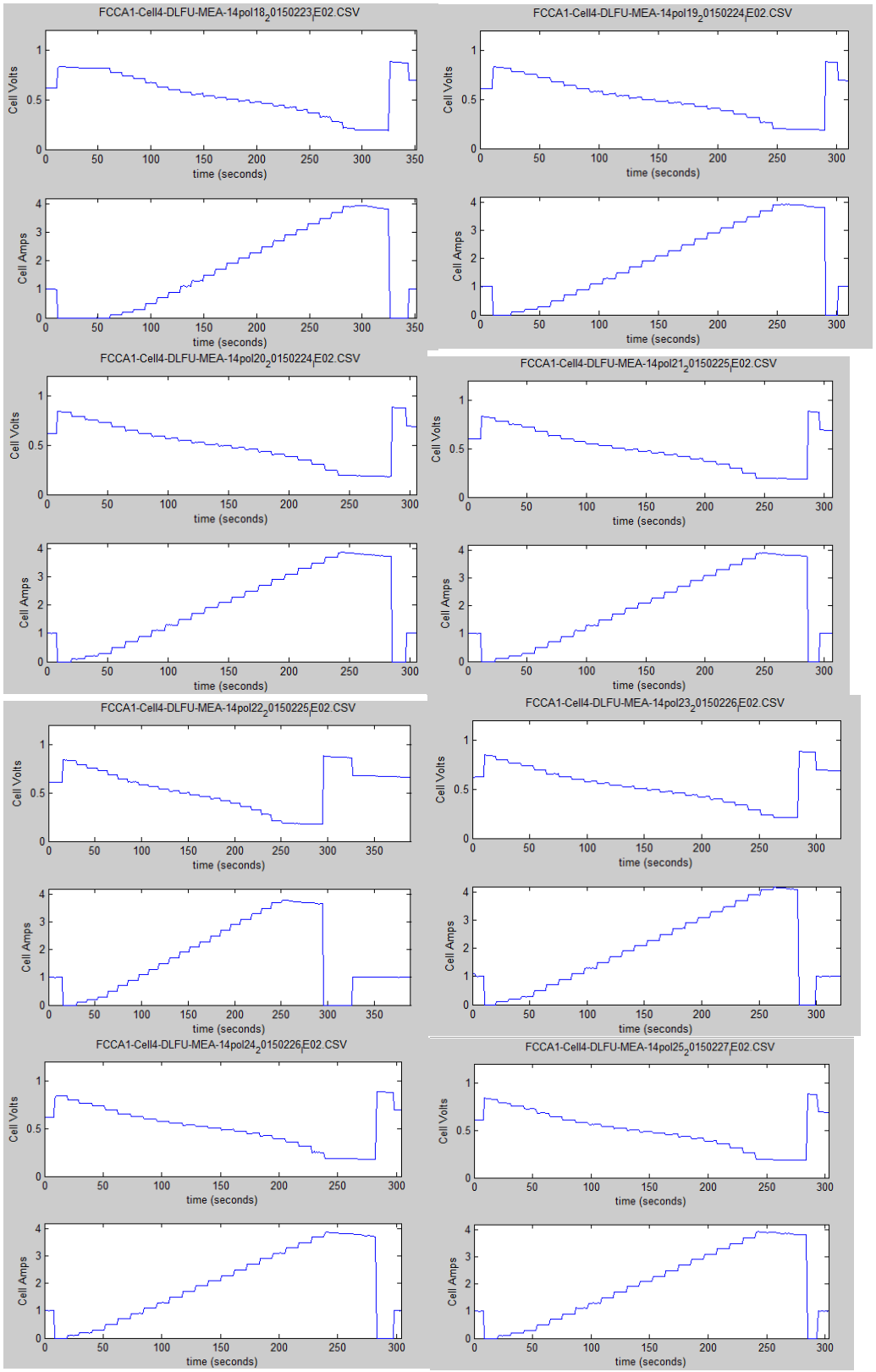
FCCA1-Cell4-DLFU-MEA-14pol18_20150223_E02.CSV
FCCA1-Cell4-DLFU-MEA-14pol19_20150224_E02.CSV
FCCA1-Cell4-DLFU-MEA-14pol20_20150224_E02.CSV
FCCA1-Cell4-DLFU-MEA-14pol21_20150225_E02.CSV
FCCA1-Cell4-DLFU-MEA-14pol22_20150225_E02.CSV
FCCA1-Cell4-DLFU-MEA-14pol23_20150226_E02.CSV
FCCA1-Cell4-DLFU-MEA-14pol24_20150226_E02.CSV
FCCA1-Cell4-DLFU-MEA-14pol25_20150227_E02.CSV
Cell Volts
Cell Amps
time (seconds)

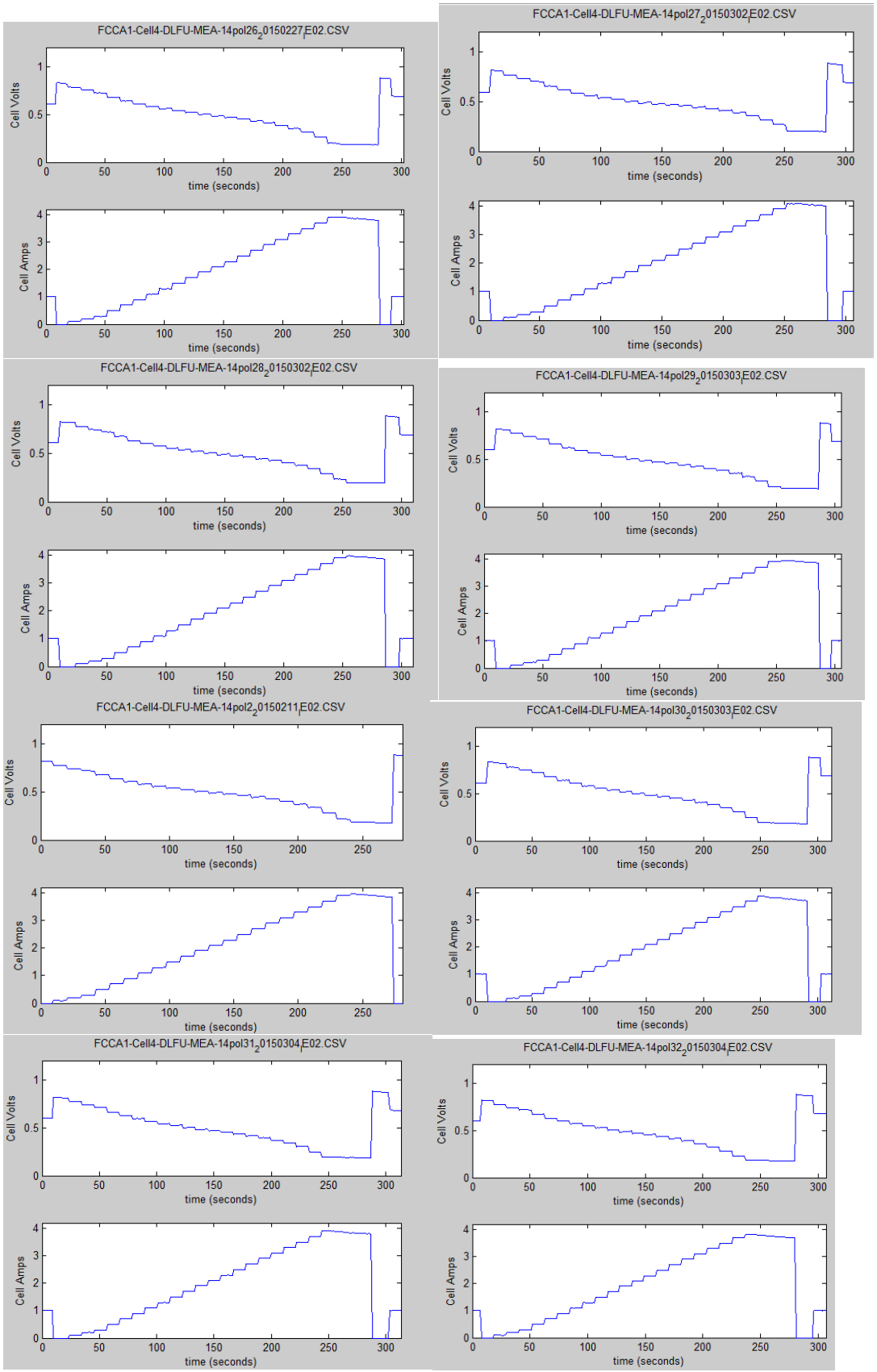
FCCA1-Cell4-DLFU-MEA-14pol26_20150227_E02.CSV
Cell Volts
time (seconds)
Cell Amps
time (seconds)
FCCA1-Cell4-DLFU-MEA-14pol27_20150302_E02.CSV
Cell Volts
time (seconds)
Cell Amps
time (seconds)
FCCA1-Cell4-DLFU-MEA-14pol28_20150302_E02.CSV
Cell Volts
time (seconds)
Cell Amps
time (seconds)
FCCA1-Cell4-DLFU-MEA-14pol29_20150303_E02.CSV
Cell Volts
time (seconds)
Cell Amps
time (seconds)
FCCA1-Cell4-DLFU-MEA-14pol2_20150211_E02.CSV
Cell Volts
time (seconds)
Cell Amps
time (seconds)
FCCA1-Cell4-DLFU-MEA-14pol30_20150303_E02.CSV
Cell Volts
time (seconds)
Cell Amps
time (seconds)
FCCA1-Cell4-DLFU-MEA-14pol31_20150304_E02.CSV
Cell Volts
time (seconds)
Cell Amps
time (seconds)
FCCA1-Cell4-DLFU-MEA-14pol32_20150304_E02.CSV
Cell Volts
time (seconds)
Cell Amps
time (seconds)

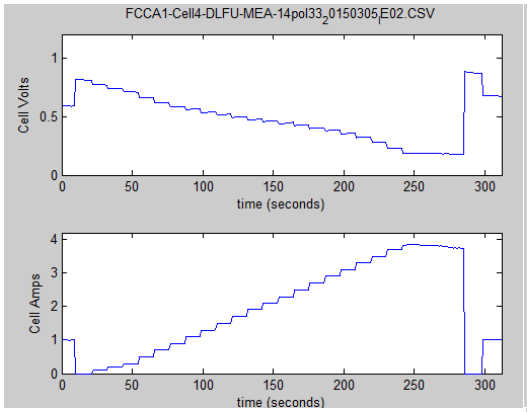
FCCA1-Cell4-DLFU-MEA-14pol33_20150305_E02.CSV
Cell Volts
time (seconds)
Cell Amps
time (seconds)

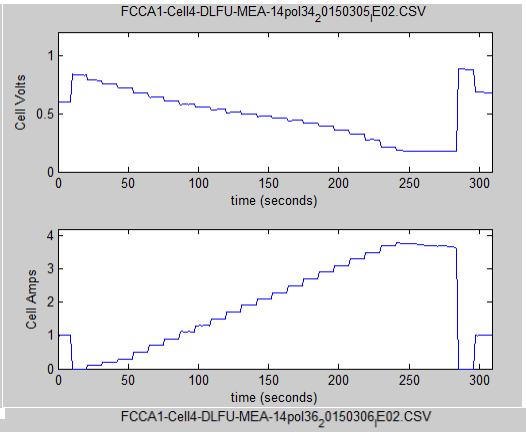
FCCA1-Cell4-DLFU-MEA-14pol34_20150305_E02.CSV
Cell Volts
time (seconds)
Cell Amps
time (seconds)

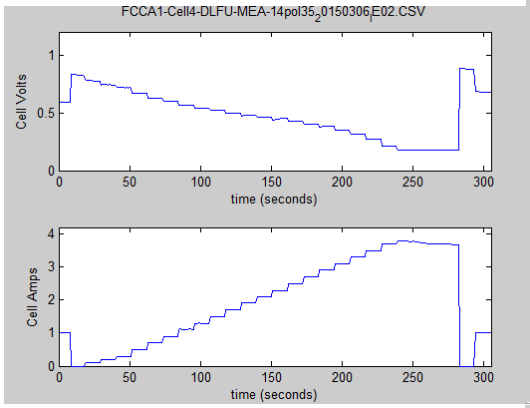
FCCA1-Cell4-DLFU-MEA-14pol35_20150306_E02.CSV
Cell Volts
time (seconds)
Cell Amps
time (seconds)

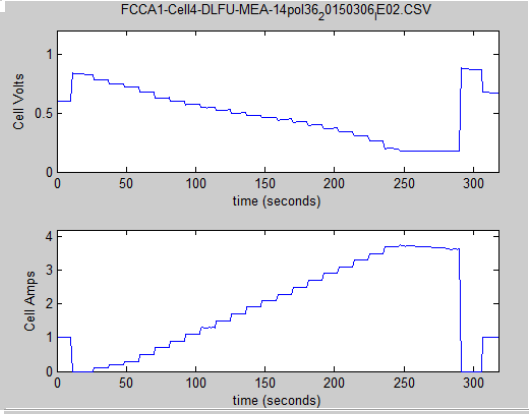
FCCA1-Cell4-DLFU-MEA-14pol36_20150306_E02.CSV
Cell Volts
time (seconds)
Cell Amps
time (seconds)

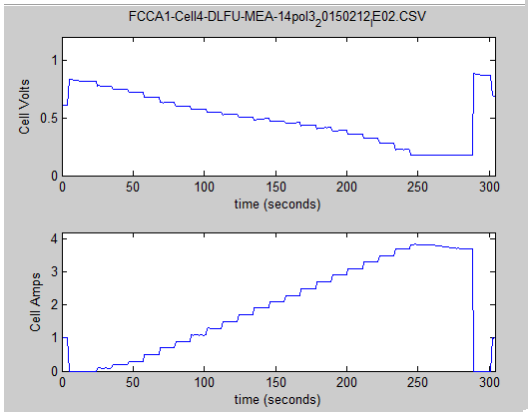
FCCA1-Cell4-DLFU-MEA-14pol3_20150212_E02.CSV
Cell Volts
time (seconds)
Cell Amps
time (seconds)

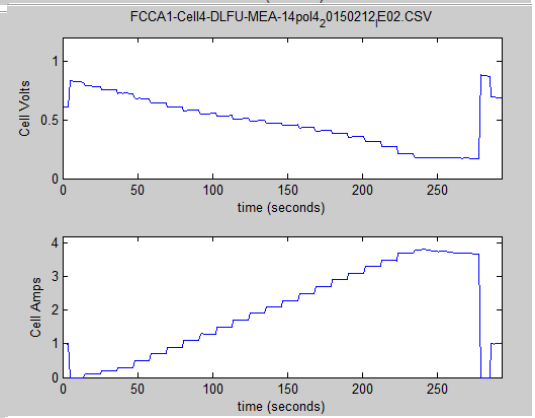
FCCA1-Cell4-DLFU-MEA-14pol4_20150212_E02.CSV
Cell Volts
time (seconds)
Cell Amps
time (seconds)

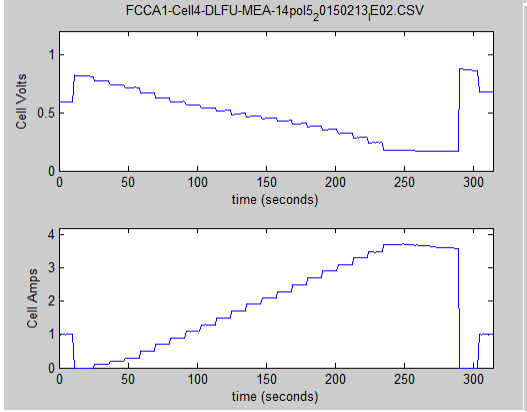
FCCA1-Cell4-DLFU-MEA-14pol5_20150213_E02.CSV
Cell Volts
time (seconds)
Cell Amps
time (seconds)

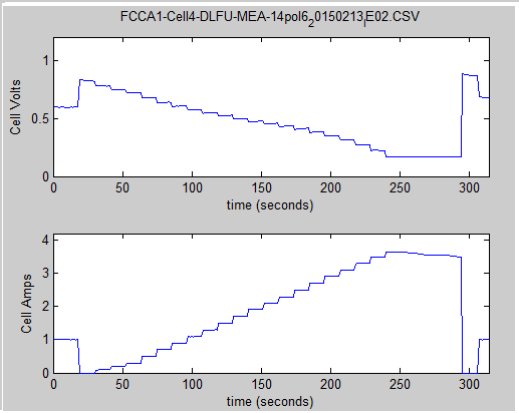
FCCA1-Cell4-DLFU-MEA-14pol6_20150213_E02.CSV
Cell Volts
time (seconds)
Cell Amps
time (seconds)

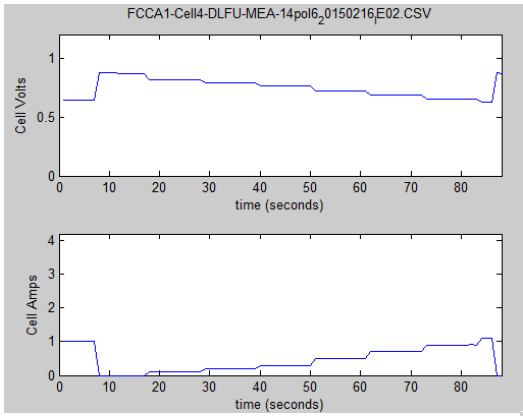
FCCA1-Cell4-DLFU-MEA-14pol6_20150216_E02.CSV
Cell Volts
time (seconds)
Cell Amps
time (seconds)

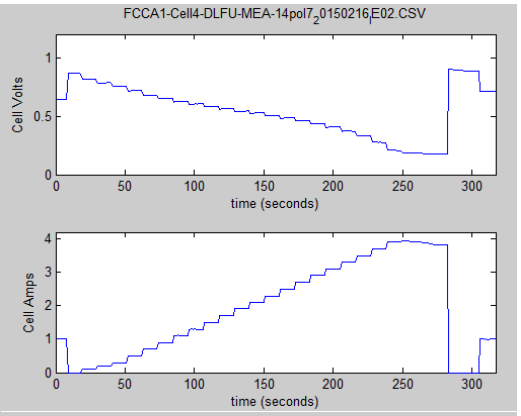
FCCA1-Cell4-DLFU-MEA-14pol7_20150216_E02.CSV
Cell Volts
time (seconds)
Cell Amps
time (seconds)

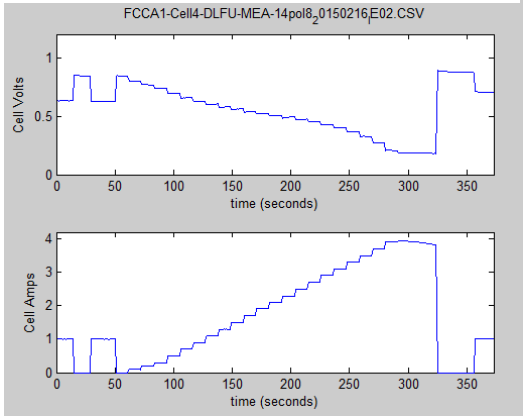
FCCA1-Cell4-DLFU-MEA-14pol8_20150216_E02.CSV
Cell Volts
time (seconds)
Cell Amps
time (seconds)

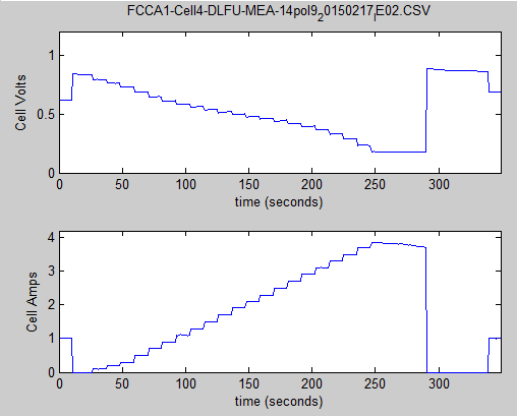
FCCA1-Cell4-DLFU-MEA-14pol9_20150217_E02.CSV
Cell Volts
time (seconds)
Cell Amps
time (seconds)

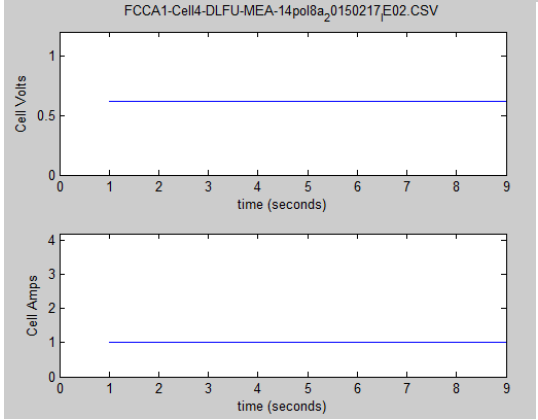
FCCA1-Cell4-DLFU-MEA-14pol8a_20150217_E02.CSV
Cell Volts
time (seconds)
Cell Amps
time (seconds)

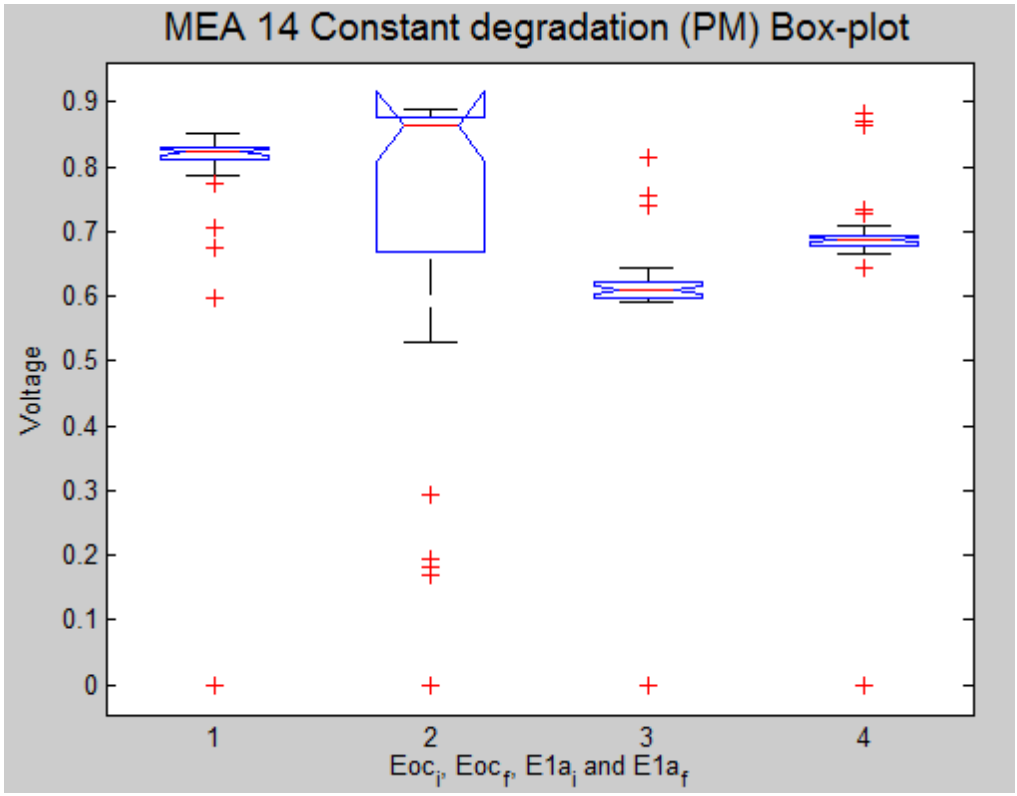
MEA 14 Constant degradation (PM) Box-plot
Voltage
0.9
0.8
0.7
0.6
0.5
0.4
0.3
0.2
0.1
0
1
2
3
4
Eoc$_i$, Eoc$_f$, E1a$_i$ and E1a$_f$

MEA 14(Torray Cathode, High D, Constant)

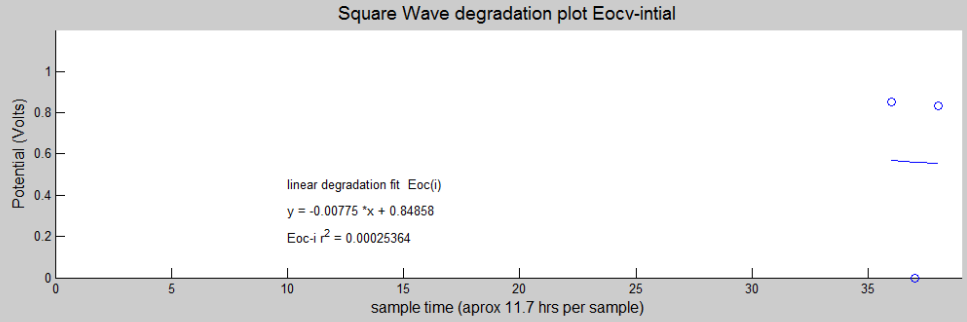

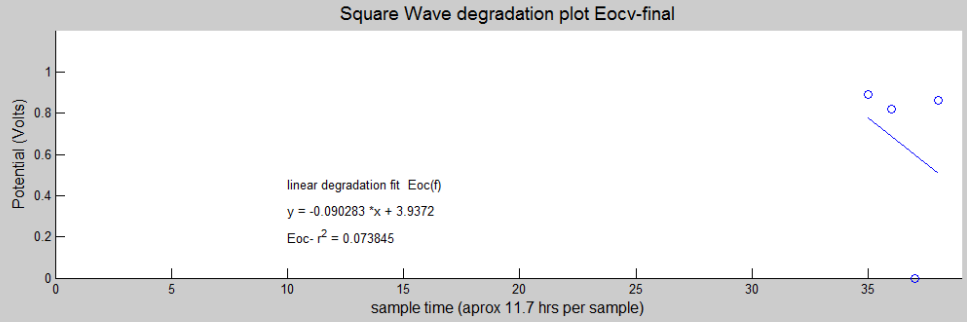

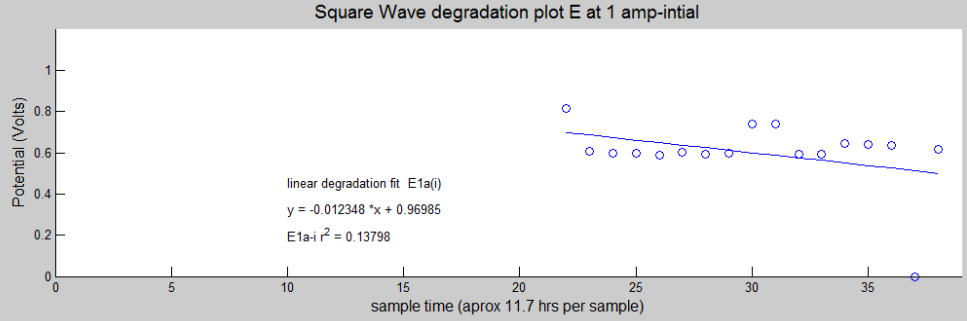

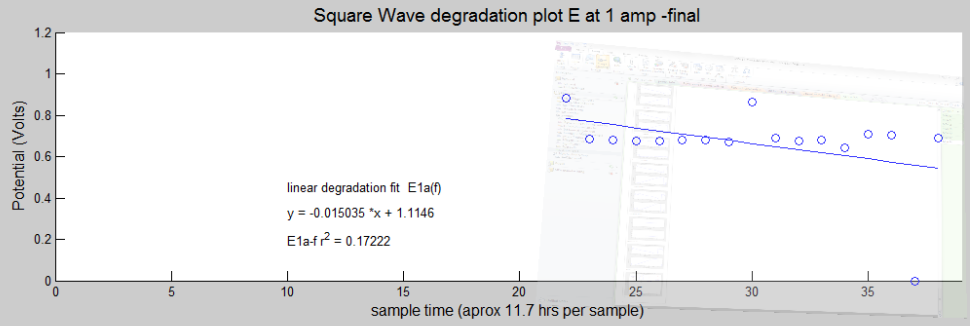

MEA 14(Torray Cathode, High D, Constant)

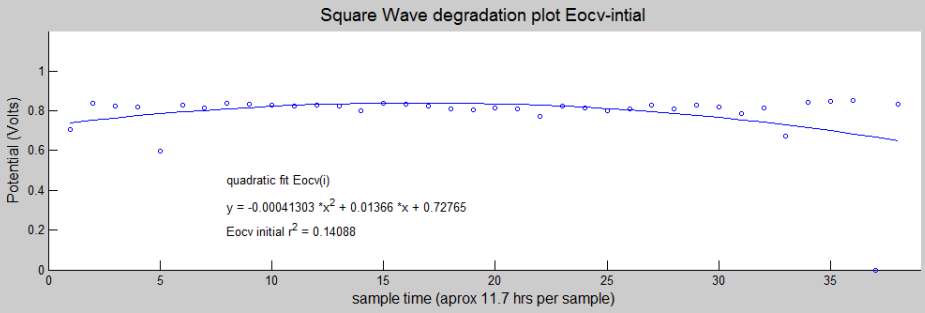

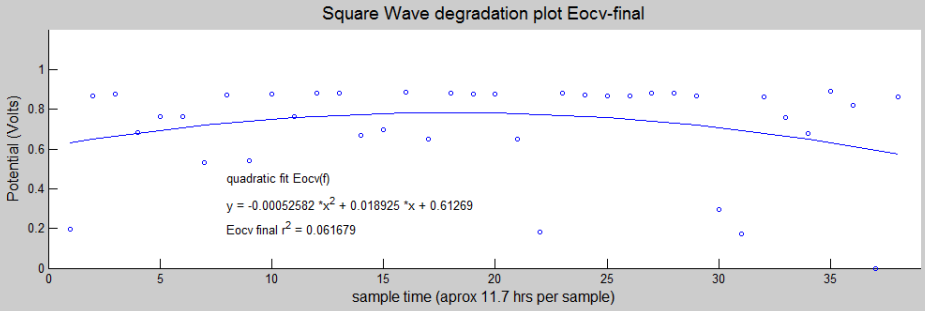

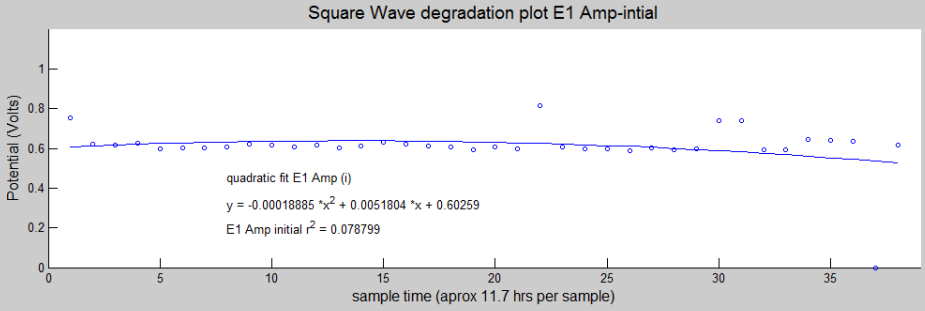

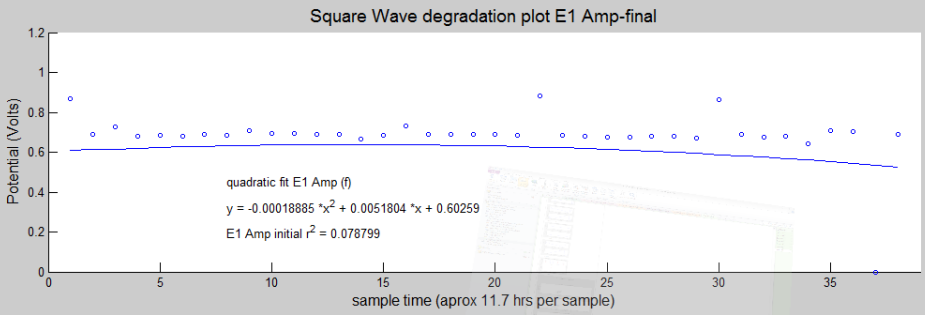

MEA 14(Torray Cathode, High D, Constant)

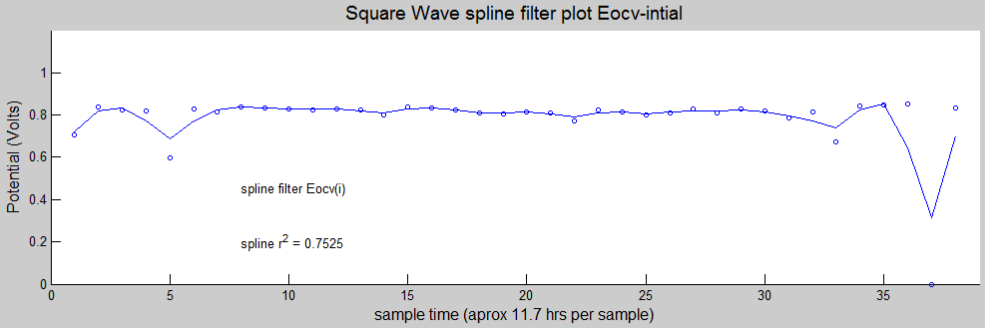

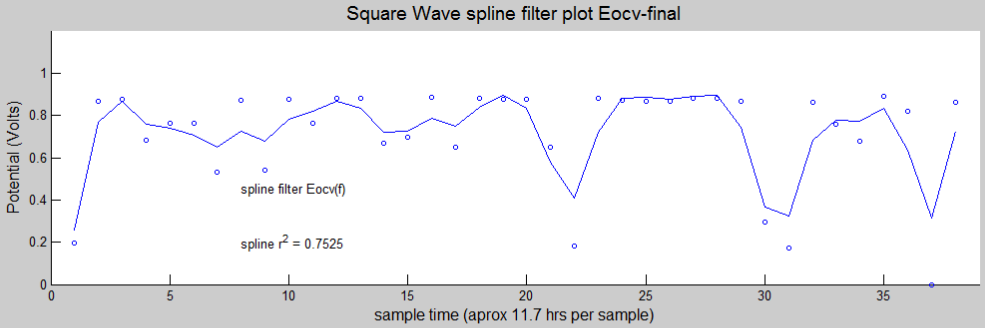

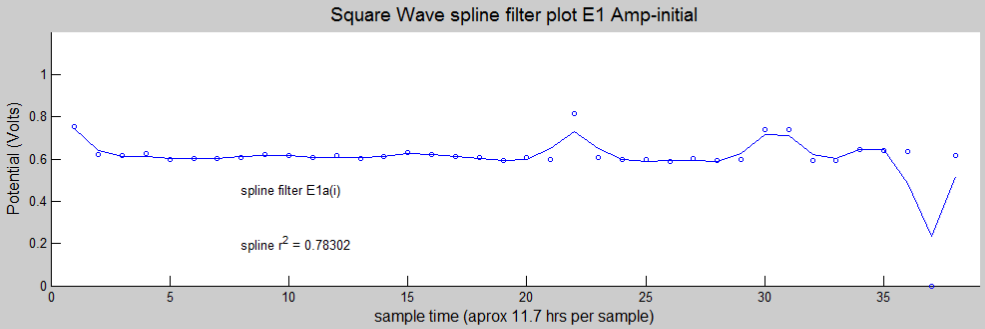

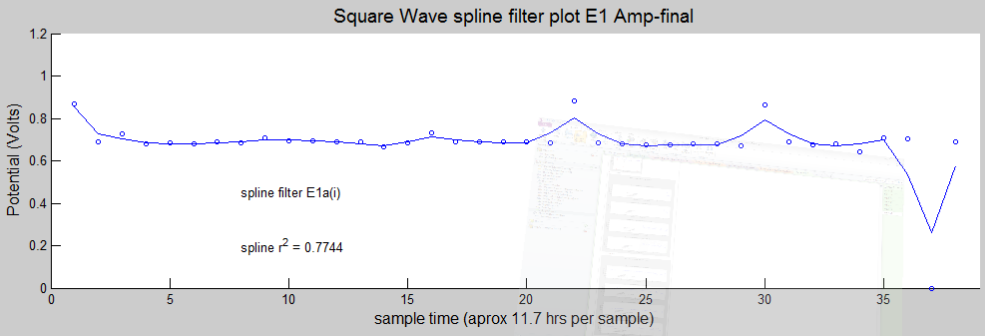

MEA 16

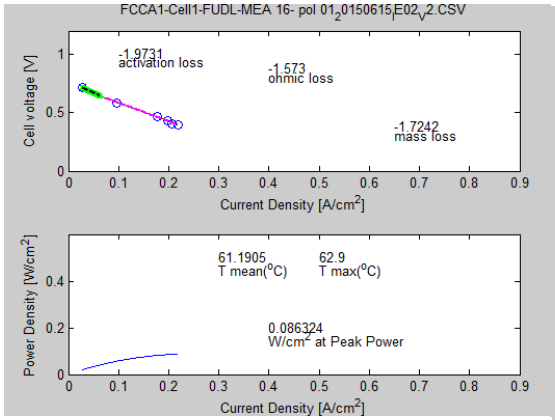
FCCA1-Cell1-FUDL-MEA 16- pol 01_20150615_E02_V2.CSV
-1.9731
activation loss
-1.573
ohmic loss
-1.7242
mass loss
Cell voltage [V]
Current Density [A/cm2]
61.1905
T mean(°C)
62.9
T max(°C)
0.086324
W/cm2 at Peak Power
Power Density [W/cm2]
Current Density [A/cm2]

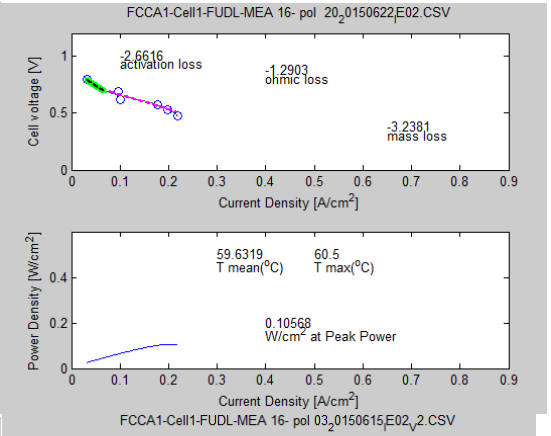
FCCA1-Cell1-FUDL-MEA 16- pol 20_20150622_E02.CSV
-2.6616
activation loss
-1.2903
ohmic loss
-3.2381
mass loss
Cell voltage [V]
Current Density [A/cm2]
59.6319
T mean(°C)
60.5
T max(°C)
0.10568
W/cm2 at Peak Power
Power Density [W/cm2]
Current Density [A/cm2]

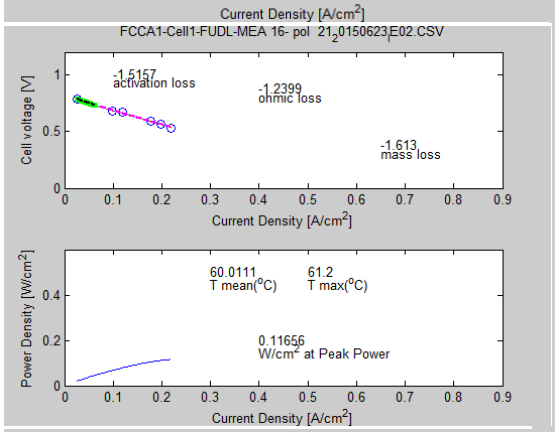
FCCA1-Cell1-FUDL-MEA 16- pol 21_20150623_E02.CSV
-1.5157
activation loss
-1.2399
ohmic loss
-1.613
mass loss
Cell voltage [V]
Current Density [A/cm2]
60.0111
T mean(°C)
61.2
T max(°C)
0.11656
W/cm2 at Peak Power
Power Density [W/cm2]
Current Density [A/cm2]

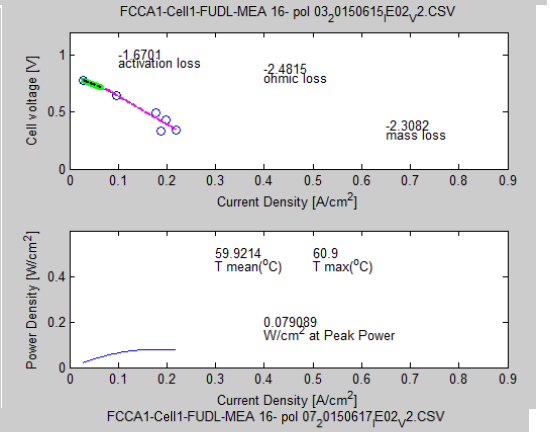
FCCA1-Cell1-FUDL-MEA 16- pol 03_20150615_E02_V2.CSV
-1.6701
activation loss
-2.4815
ohmic loss
-2.3082
mass loss
Cell voltage [V]
Current Density [A/cm2]
59.9214
T mean(°C)
60.9
T max(°C)
0.079089
W/cm2 at Peak Power
Power Density [W/cm2]
Current Density [A/cm2]

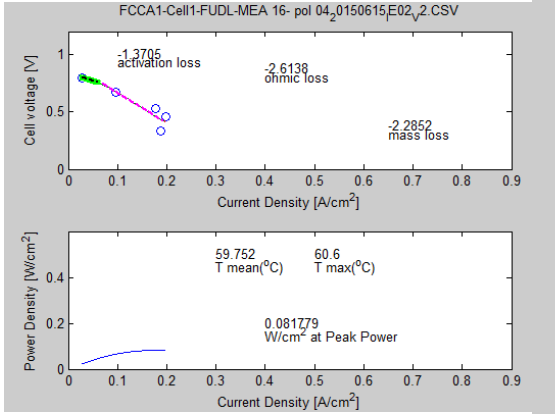
FCCA1-Cell1-FUDL-MEA 16- pol 04_20150615_E02_V2.CSV
-1.3705
activation loss
-2.6138
ohmic loss
-2.2852
mass loss
Cell voltage [V]
Current Density [A/cm2]
59.752
T mean(°C)
60.6
T max(°C)
0.081779
W/cm2 at Peak Power
Power Density [W/cm2]
Current Density [A/cm2]

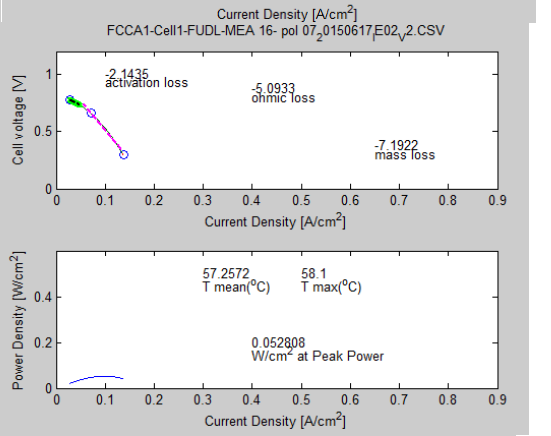
FCCA1-Cell1-FUDL-MEA 16- pol 07_20150617_E02_V2.CSV
-2.1435
activation loss
-5.0933
ohmic loss
-7.1922
mass loss
Cell voltage [V]
Current Density [A/cm2]
57.2572
T mean(°C)
58.1
T max(°C)
0.052808
W/cm2 at Peak Power
Power Density [W/cm2]
Current Density [A/cm2]

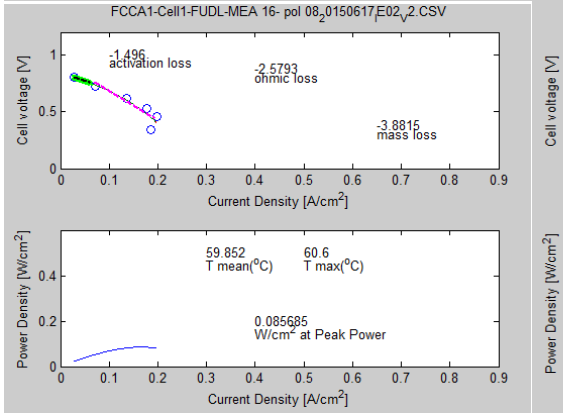
FCCA1-Cell1-FUDL-MEA 16- pol 08_20150617_E02_V2.CSV
-1.496
activation loss
-2.5793
ohmic loss
-3.8815
mass loss
Cell voltage [V]
Current Density [A/cm2]
59.852
T mean(°C)
60.6
T max(°C)
0.085685
W/cm2 at Peak Power
Power Density [W/cm2]
Current Density [A/cm2]

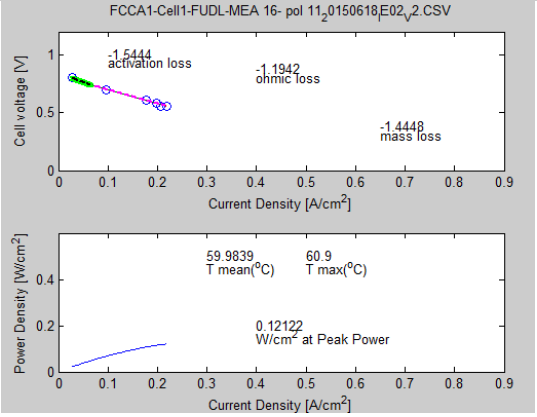
FCCA1-Cell1-FUDL-MEA 16- pol 11_20150618_E02_V2.CSV
-1.5444
activation loss
-1.1942
ohmic loss
-1.4448
mass loss
Cell voltage [V]
Current Density [A/cm2]
59.9839
T mean(°C)
60.9
T max(°C)
0.12122
W/cm2 at Peak Power
Power Density [W/cm2]
Current Density [A/cm2]

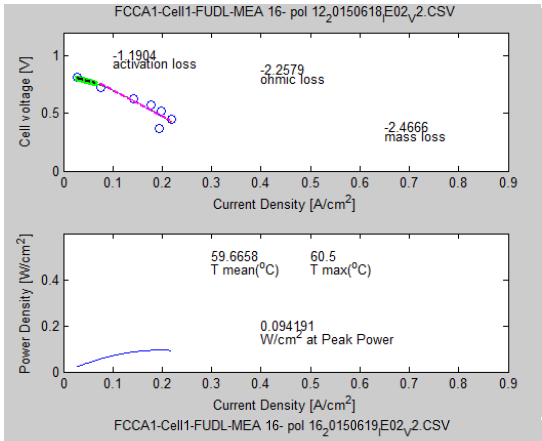
FCCA1-Cell1-FUDL-MEA 16- pol 12_20150618_E02_V2.CSV
-1.1904
activation loss
-2.2579
ohmic loss
-2.4666
mass loss
Cell voltage [V]
Current Density [A/cm2]
59.6658
T mean(°C)
60.5
T max(°C)
0.094191
W/cm2 at Peak Power
Power Density [W/cm2]
Current Density [A/cm2]

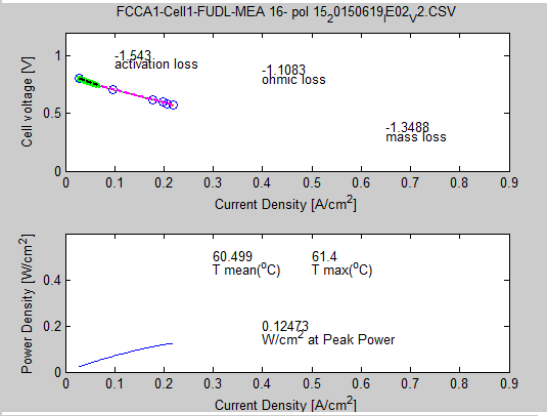
FCCA1-Cell1-FUDL-MEA 16- pol 15_20150619_E02_V2.CSV
-1.543
activation loss
-1.1083
ohmic loss
-1.3488
mass loss
Cell voltage [V]
Current Density [A/cm2]
60.499
T mean(°C)
61.4
T max(°C)
0.12473
W/cm2 at Peak Power
Power Density [W/cm2]
Current Density [A/cm2]

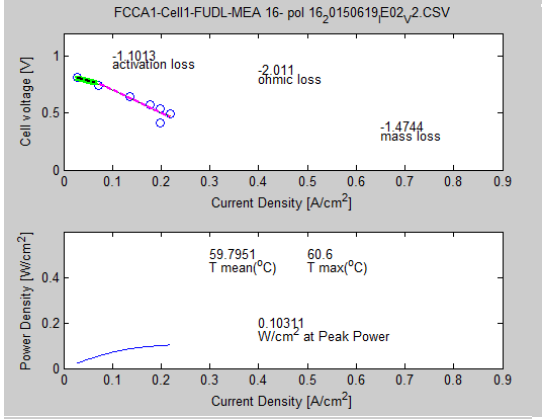
FCCA1-Cell1-FUDL-MEA 16- pol 16_20150619_E02_V2.CSV
-1.1013
activation loss
-2.011
ohmic loss
-1.4744
mass loss
Cell voltage [V]
Current Density [A/cm2]
59.7951
T mean(°C)
60.6
T max(°C)
0.10311
W/cm2 at Peak Power
Power Density [W/cm2]
Current Density [A/cm2]

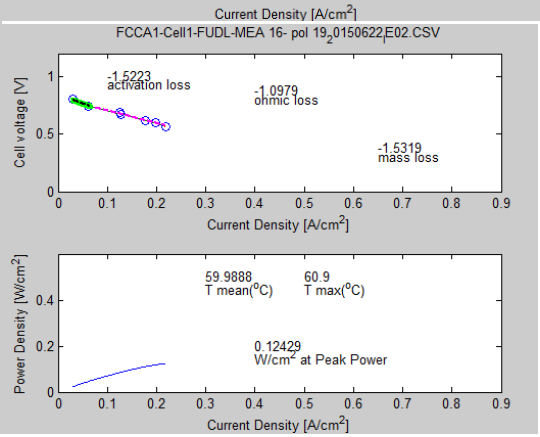
FCCA1-Cell1-FUDL-MEA 16- pol 19_20150622_E02.CSV
-1.5223
activation loss
-1.0979
ohmic loss
-1.5319
mass loss
Cell voltage [V]
Current Density [A/cm2]
59.9888
T mean(°C)
60.9
T max(°C)
0.12429
W/cm2 at Peak Power
Power Density [W/cm2]
Current Density [A/cm2]

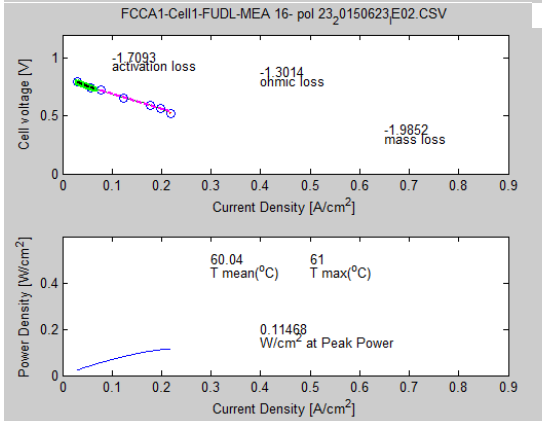
FCCA1-Cell1-FUDL-MEA 16- pol 23_20150623_E02.CSV
-1.7093
activation loss
-1.3014
ohmic loss
-1.9852
mass loss
Cell voltage [V]
Current Density [A/cm2]
60.04
T mean(°C)
61
T max(°C)
0.11468
W/cm2 at Peak Power
Power Density [W/cm2]
Current Density [A/cm2]

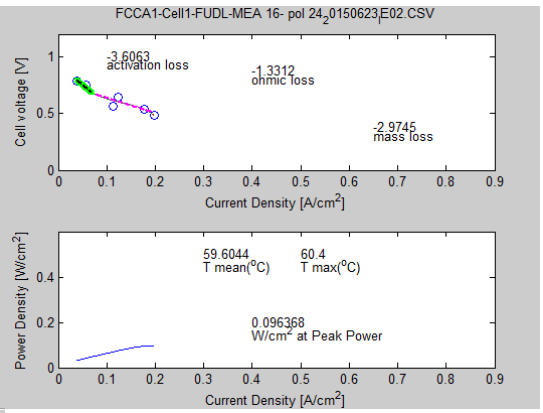
FCCA1-Cell1-FUDL-MEA 16- pol 24_20150623_E02.CSV
-3.6063
activation loss
-1.3312
ohmic loss
-2.9745
mass loss
Cell voltage [V]
Current Density [A/cm2]
59.6044
T mean(°C)
60.4
T max(°C)
0.096368
W/cm2 at Peak Power
Power Density [W/cm2]
Current Density [A/cm2]

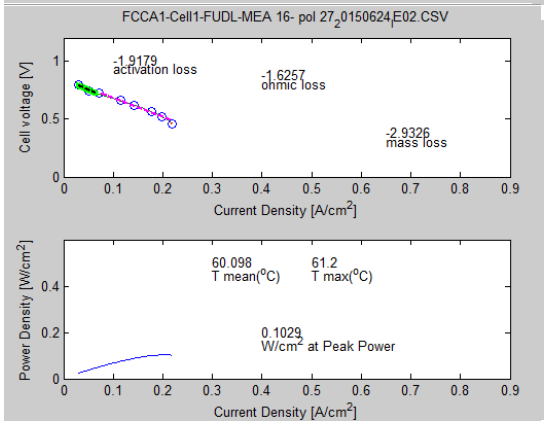
FCCA1-Cell1-FUDL-MEA 16- pol 27_20150624_E02.CSV
-1.9179
activation loss
-1.6257
ohmic loss
-2.9326
mass loss
Cell voltage [V]
Current Density [A/cm2]
60.098
T mean(°C)
61.2
T max(°C)
0.1029
W/cm2 at Peak Power
Power Density [W/cm2]
Current Density [A/cm2]

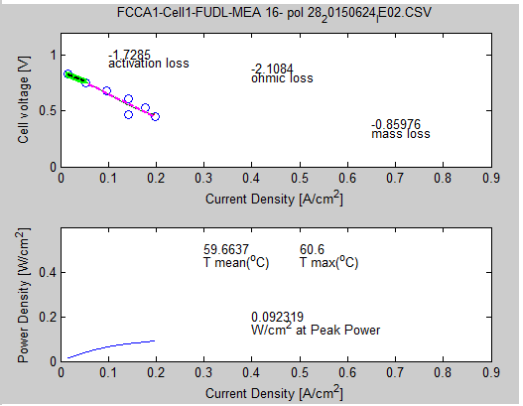
FCCA1-Cell1-FUDL-MEA 16- pol 28_20150624_E02.CSV
-1.7285
activation loss
-2.1084
ohmic loss
-0.85976
mass loss
Cell voltage [V]
Current Density [A/cm2]
59.6637
T mean(°C)
60.6
T max(°C)
0.092319
W/cm2 at Peak Power
Power Density [W/cm2]
Current Density [A/cm2]

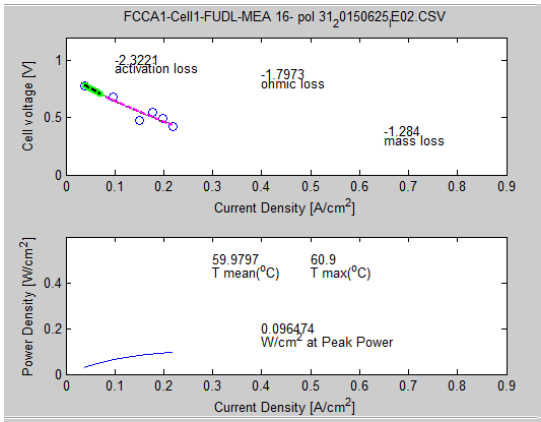
FCCA1-Cell1-FUDL-MEA 16- pol 31_20150625_E02.CSV
-2.3221
activation loss
-1.7973
ohmic loss
-1.284
mass loss
Cell voltage [V]
Current Density [A/cm2]
59.9797
T mean(°C)
60.9
T max(°C)
0.096474
W/cm2 at Peak Power
Power Density [W/cm2]
Current Density [A/cm2]

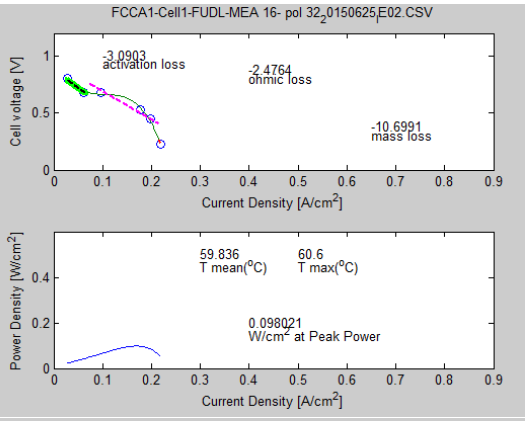
FCCA1-Cell1-FUDL-MEA 16- pol 32_20150625_E02.CSV
-3.0903
activation loss
-2.4764
ohmic loss
-10.6991
mass loss
Cell voltage [V]
Current Density [A/cm2]
59.836
T mean(°C)
60.6
T max(°C)
0.098021
W/cm2 at Peak Power
Power Density [W/cm2]
Current Density [A/cm2]

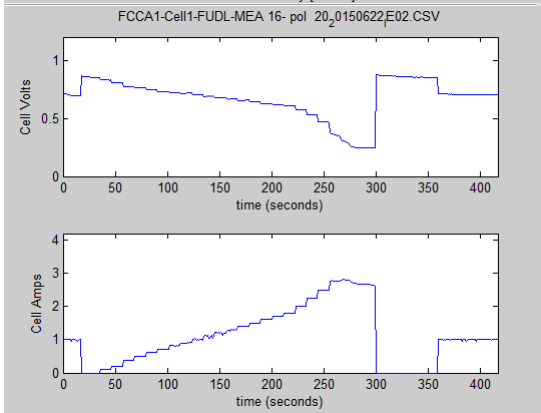
FCCA1-Cell1-FUDL-MEA 16- pol 20_20150622_E02.CSV
Cell Volts
time (seconds)
Cell Amps
time (seconds)

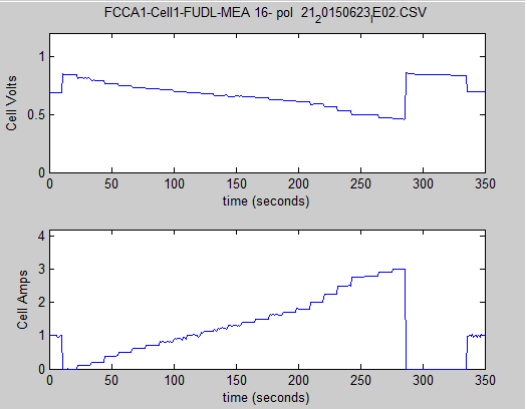
FCCA1-Cell1-FUDL-MEA 16- pol 21_20150623_E02.CSV
Cell Volts
time (seconds)
Cell Amps
time (seconds)

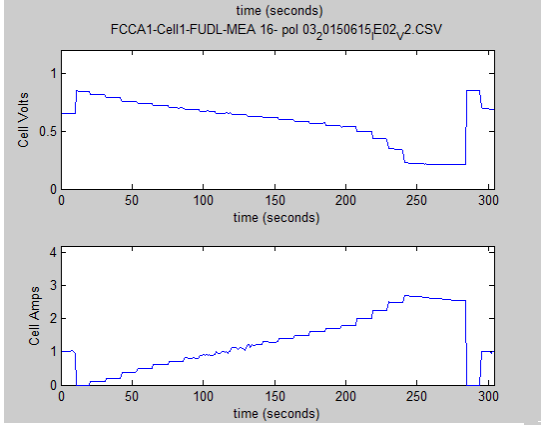
FCCA1-Cell1-FUDL-MEA 16- pol 03_20150615_E02_V2.CSV
Cell Volts
time (seconds)
Cell Amps
time (seconds)

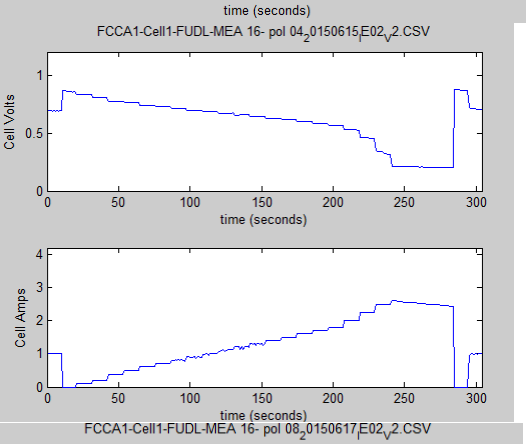
FCCA1-Cell1-FUDL-MEA 16- pol 04_20150615_E02_V2.CSV
Cell Volts
time (seconds)
Cell Amps
time (seconds)

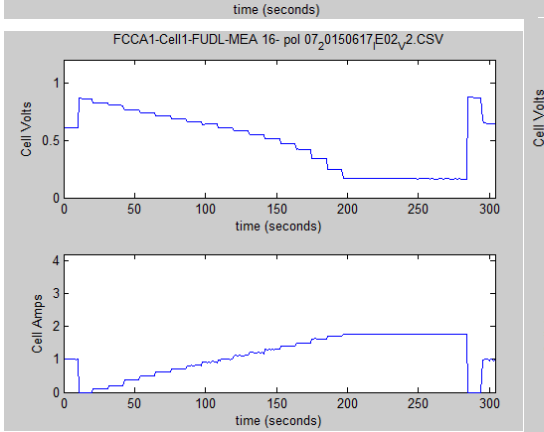
FCCA1-Cell1-FUDL-MEA 16- pol 07_20150617_E02_V2.CSV
Cell Volts
time (seconds)
Cell Amps
time (seconds)

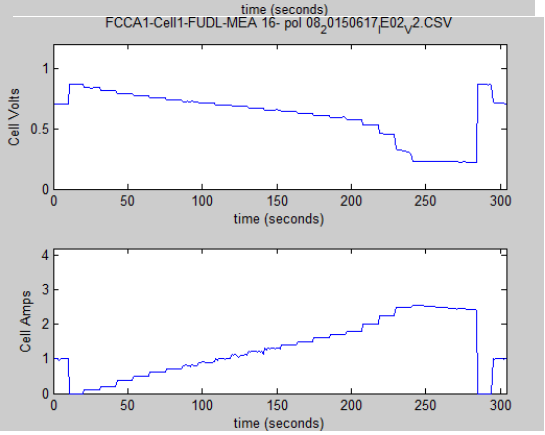
FCCA1-Cell1-FUDL-MEA 16- pol 08_20150617_E02_V2.CSV
Cell Volts
time (seconds)
Cell Amps
time (seconds)

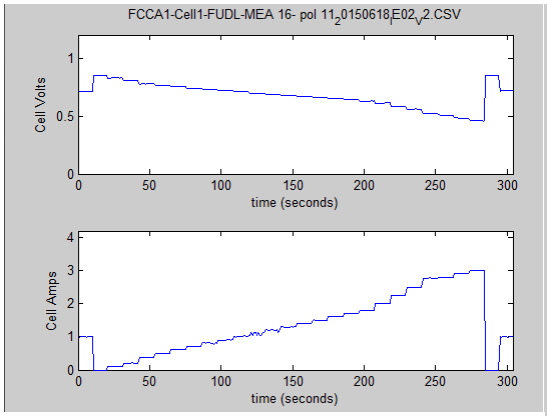
FCCA1-Cell1-FUDL-MEA 16- pol 11_20150618_E02_V2.CSV
Cell Volts
time (seconds)
Cell Amps
time (seconds)

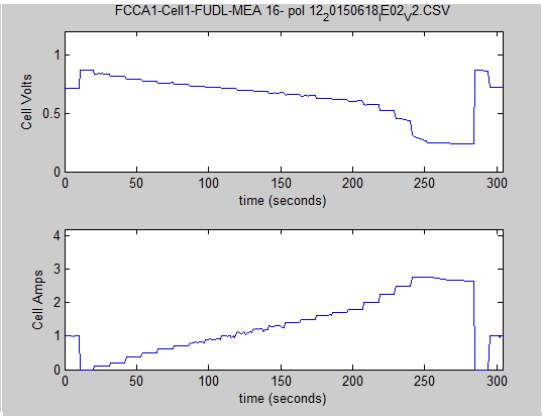
FCCA1-Cell1-FUDL-MEA 16- pol 12_20150618_E02_V2.CSV
Cell Volts
time (seconds)
Cell Amps
time (seconds)

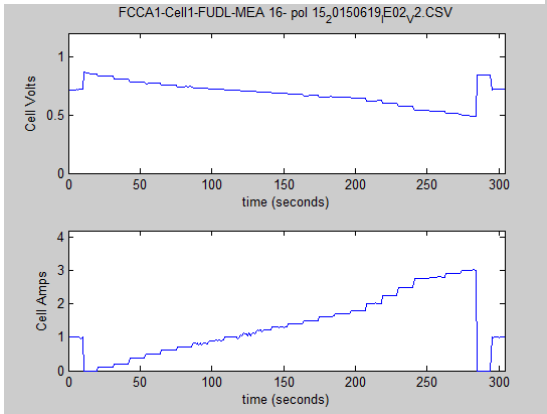
FCCA1-Cell1-FUDL-MEA 16- pol 15_20150619_E02_V2.CSV
Cell Volts
time (seconds)
Cell Amps
time (seconds)

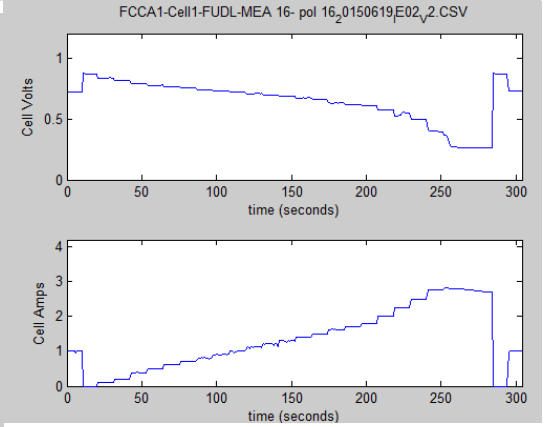
FCCA1-Cell1-FUDL-MEA 16- pol 16_20150619_E02_V2.CSV
Cell Volts
time (seconds)
Cell Amps
time (seconds)

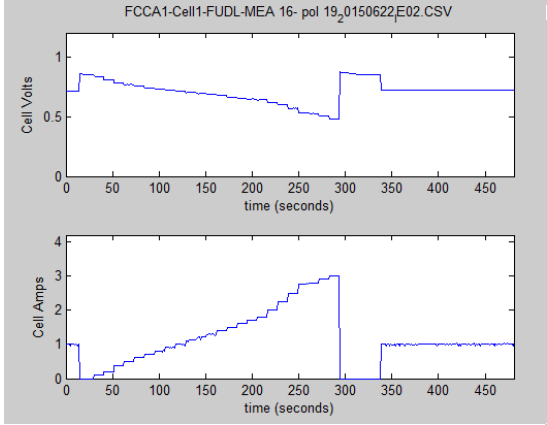
FCCA1-Cell1-FUDL-MEA 16- pol 19_20150622_E02.CSV
Cell Volts
time (seconds)
Cell Amps
time (seconds)

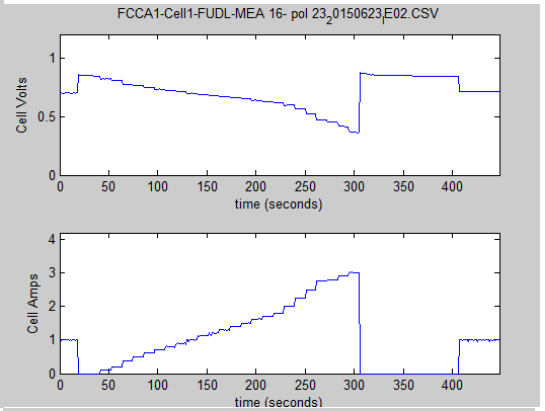
FCCA1-Cell1-FUDL-MEA 16- pol 23_20150623_E02.CSV
Cell Volts
time (seconds)
Cell Amps
time (seconds)

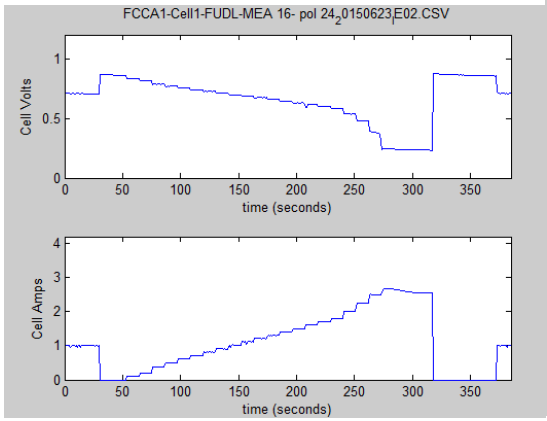
FCCA1-Cell1-FUDL-MEA 16- pol 24_20150623_E02.CSV
Cell Volts
time (seconds)
Cell Amps
time (seconds)

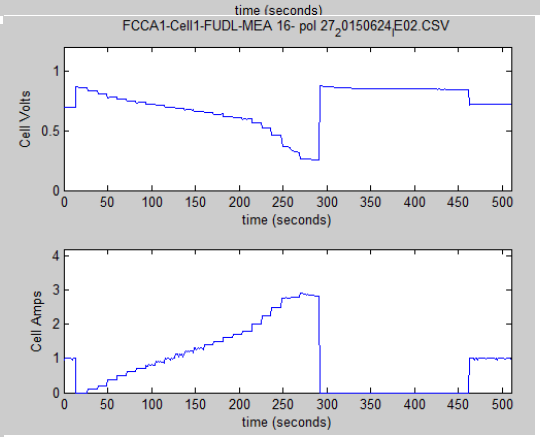
FCCA1-Cell1-FUDL-MEA 16- pol 27_20150624_E02.CSV
Cell Volts
time (seconds)
Cell Amps
time (seconds)

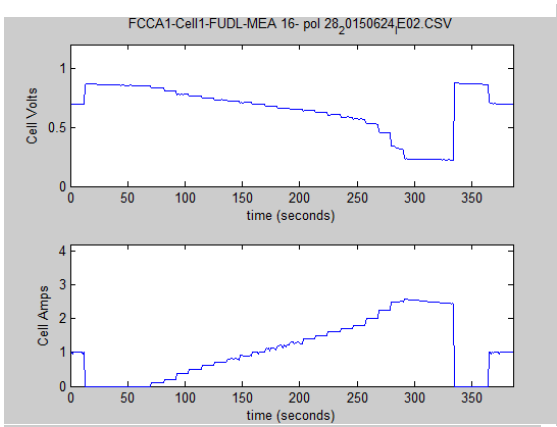
FCCA1-Cell1-FUDL-MEA 16- pol 28_20150624_E02.CSV
Cell Volts
time (seconds)
Cell Amps
time (seconds)

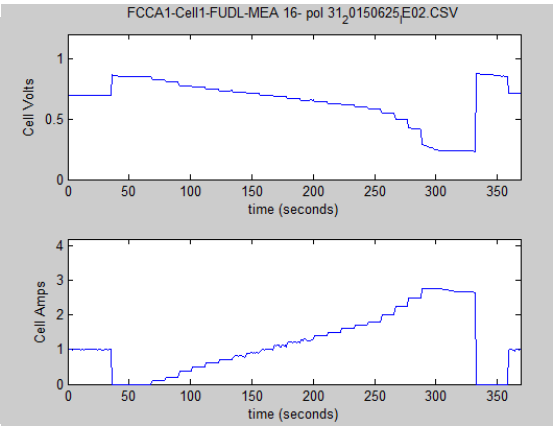
FCCA1-Cell1-FUDL-MEA 16- pol 31_20150625_E02.CSV
Cell Volts
time (seconds)
Cell Amps
time (seconds)

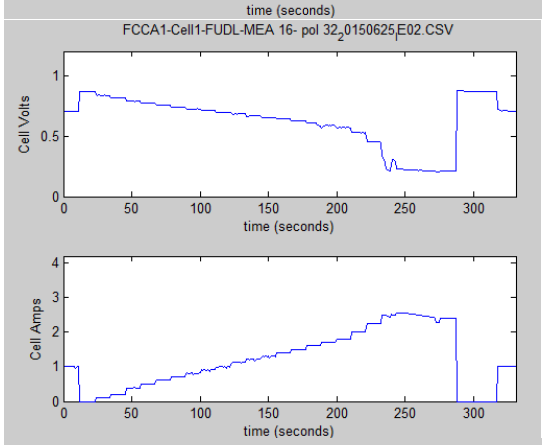
FCCA1-Cell1-FUDL-MEA 16- pol 32_20150625_E02.CSV
Cell Volts
time (seconds)
Cell Amps
time (seconds)

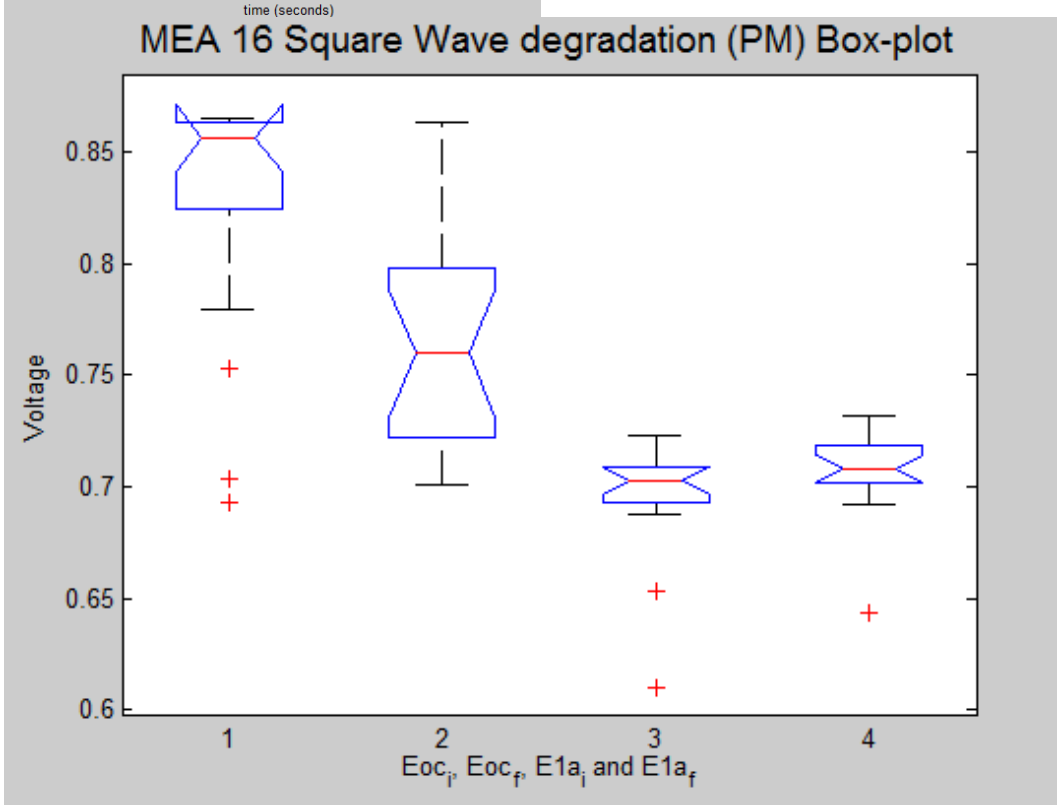
MEA 16 Square Wave degradation (PM) Box-plot
Voltage
Eoc_i, Eoc_f, E1a_i and E1a_f

MEA 16 (Torray cathode, high-D, Square Wave)PM

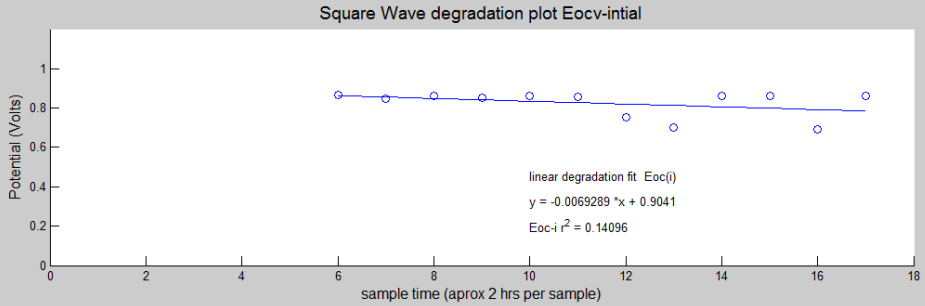

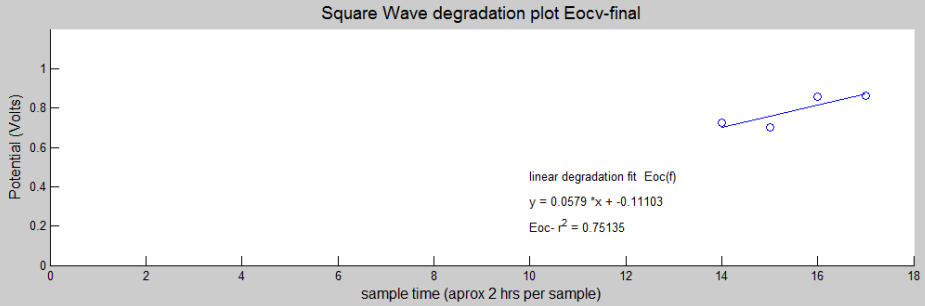

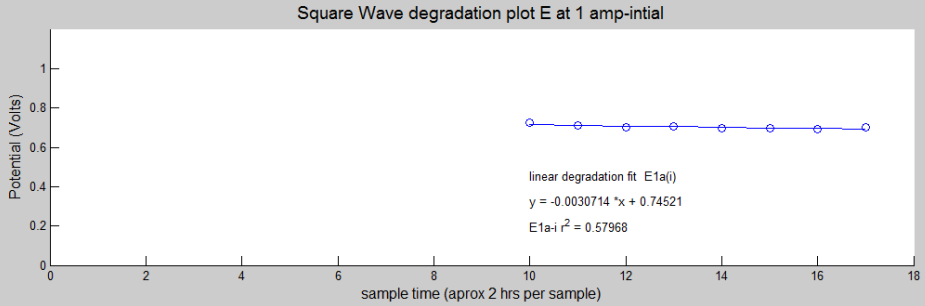

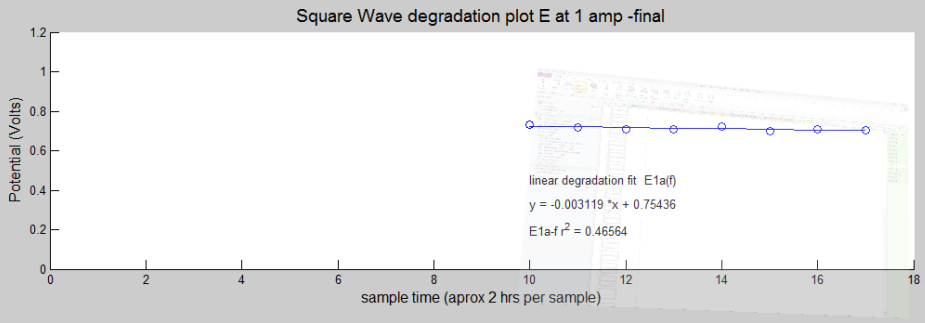

MEA 16 (Torray cathode, high-D, Square Wave)PM

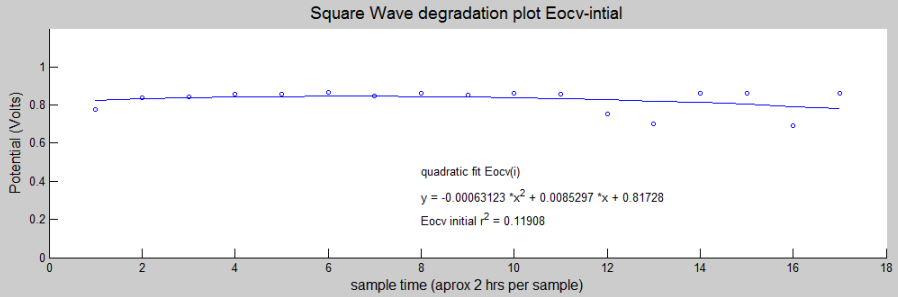

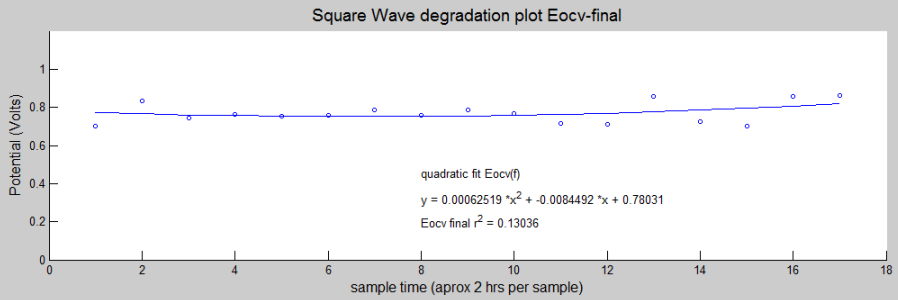

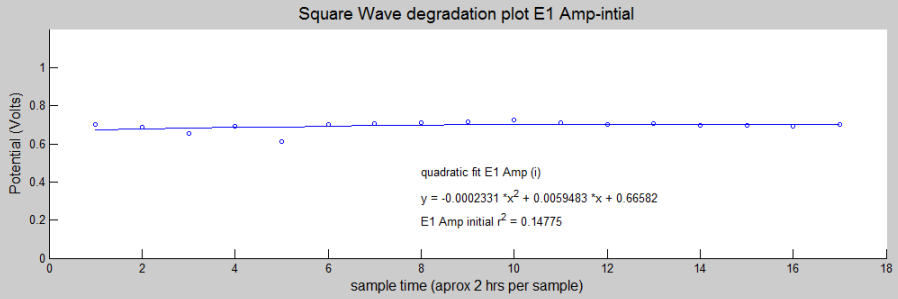

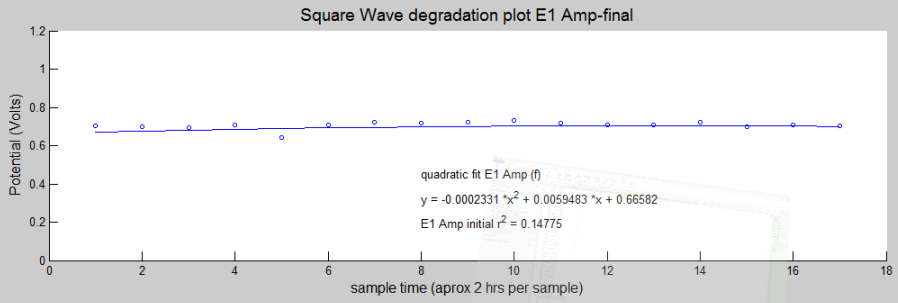

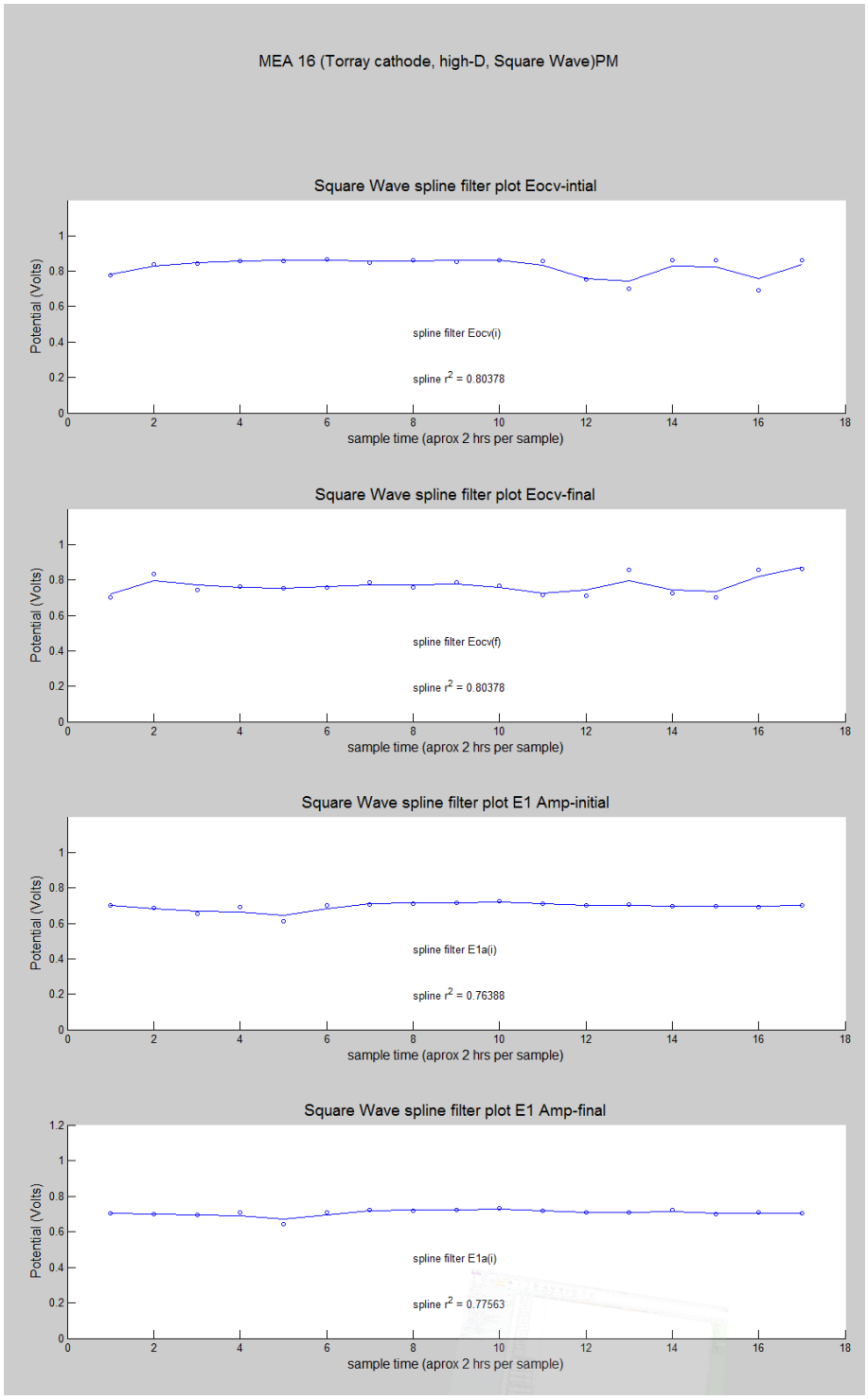
MEA 16 (Torray cathode, high-D, Square Wave)PM
Square Wave spline filter plot Eocv-intial
Potential (Volts)
spline filter Eocv(i)
spline r2 = 0.80378
sample time (aprox 2 hrs per sample)
Square Wave spline filter plot Eocv-final
Potential (Volts)
spline filter Eocv(f)
spline r2 = 0.80378
sample time (aprox 2 hrs per sample)
Square Wave spline filter plot E1 Amp-initial
Potential (Volts)
spline filter E1a(i)
spline r2 = 0.76388
sample time (aprox 2 hrs per sample)
Square Wave spline filter plot E1 Amp-final
Potential (Volts)
spline filter E1a(i)
spline r2 = 0.77563
sample time (aprox 2 hrs per sample)

MEA 18

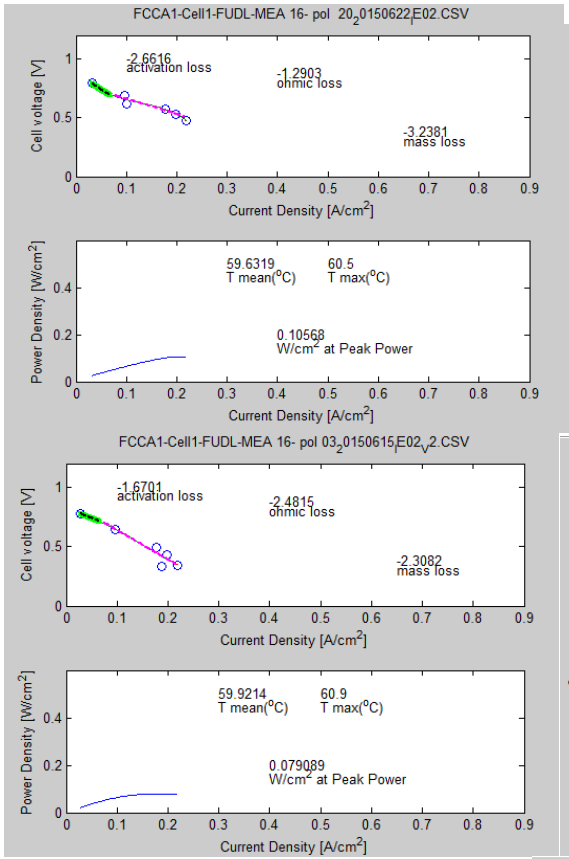
FCCA1-Cell1-FUDL-MEA 16- pol 20_20150622_E02.CSV
-2.6616
activation loss
-1.2903
ohmic loss
-3.2381
mass loss
Cell voltage [V]
Current Density [A/cm2]
59.6319
T mean(°C)
60.5
T max(°C)
0.10568
W/cm2 at Peak Power
Power Density [W/cm2]
Current Density [A/cm2]

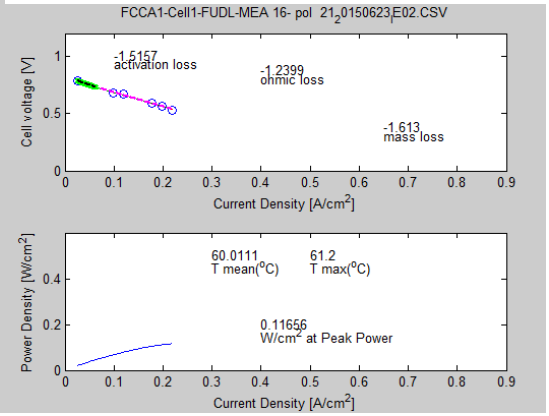
FCCA1-Cell1-FUDL-MEA 16- pol 21_20150623_E02.CSV
-1.5157
activation loss
-1.2399
ohmic loss
-1.613
mass loss
Cell voltage [V]
Current Density [A/cm2]
60.0111
T mean(°C)
61.2
T max(°C)
0.11656
W/cm2 at Peak Power
Power Density [W/cm2]
Current Density [A/cm2]

FCCA1-Cell1-FUDL-MEA 16- pol 03_20150615_E02_V2.CSV
-1.6701
activation loss
-2.4815
ohmic loss
-2.3082
mass loss
Cell voltage [V]
Current Density [A/cm2]
59.9214
T mean(°C)
60.9
T max(°C)
0.079089
W/cm2 at Peak Power
Power Density [W/cm2]
Current Density [A/cm2]

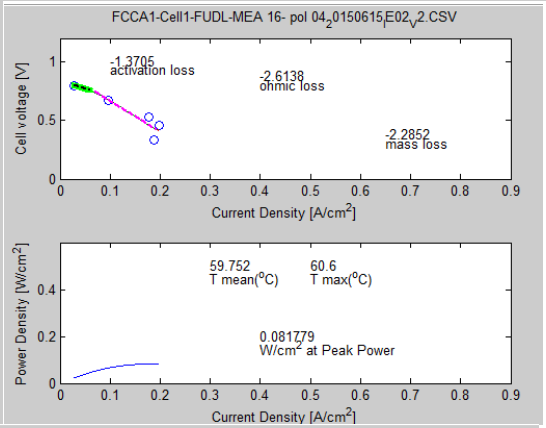
FCCA1-Cell1-FUDL-MEA 16- pol 04_20150615_E02_V2.CSV
-1.3705
activation loss
-2.6138
ohmic loss
-2.2852
mass loss
Cell voltage [V]
Current Density [A/cm2]
59.752
T mean(°C)
60.6
T max(°C)
0.081779
W/cm2 at Peak Power
Power Density [W/cm2]
Current Density [A/cm2]

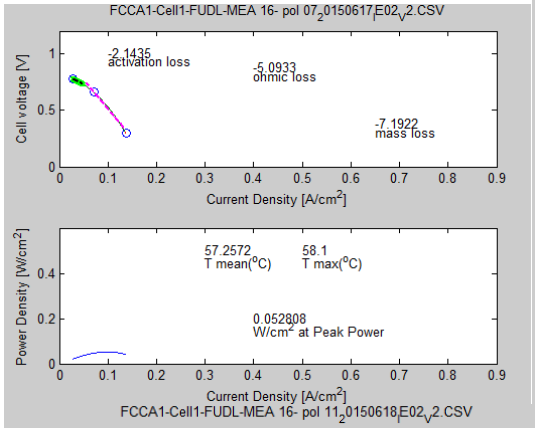
FCCA1-Cell1-FUDL-MEA 16- pol 07_20150617_E02_V2.CSV
-2.1435
activation loss
-5.0933
ohmic loss
-7.1922
mass loss
Cell voltage [V]
Current Density [A/cm2]
57.2572
T mean(°C)
58.1
T max(°C)
0.052808
W/cm2 at Peak Power
Power Density [W/cm2]
Current Density [A/cm2]

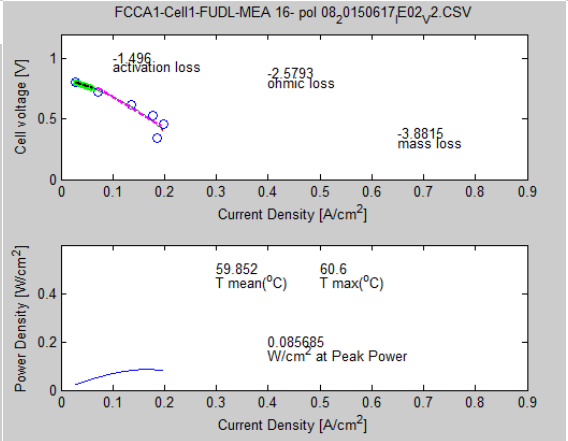
FCCA1-Cell1-FUDL-MEA 16- pol 08_20150617_E02_V2.CSV
-1.496
activation loss
-2.5793
ohmic loss
-3.8815
mass loss
Cell voltage [V]
Current Density [A/cm2]
59.852
T mean(°C)
60.6
T max(°C)
0.085685
W/cm2 at Peak Power
Power Density [W/cm2]
Current Density [A/cm2]

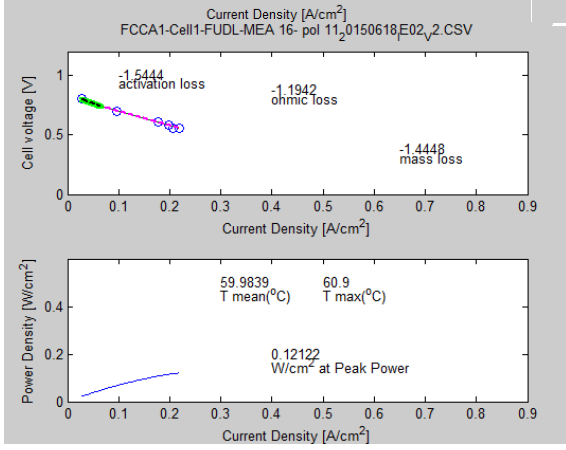
FCCA1-Cell1-FUDL-MEA 16- pol 11_20150618_E02_V2.CSV
-1.5444
activation loss
-1.1942
ohmic loss
-1.4448
mass loss
Cell voltage [V]
Current Density [A/cm2]
59.9839
T mean(°C)
60.9
T max(°C)
0.12122
W/cm2 at Peak Power
Power Density [W/cm2]
Current Density [A/cm2]

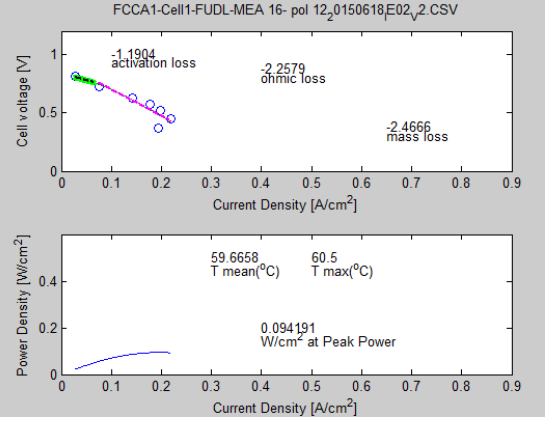
FCCA1-Cell1-FUDL-MEA 16- pol 12_20150618_E02_V2.CSV
-1.1904
activation loss
-2.2579
ohmic loss
-2.4666
mass loss
Cell voltage [V]
Current Density [A/cm2]
59.6658
T mean(°C)
60.5
T max(°C)
0.094191
W/cm2 at Peak Power
Power Density [W/cm2]
Current Density [A/cm2]

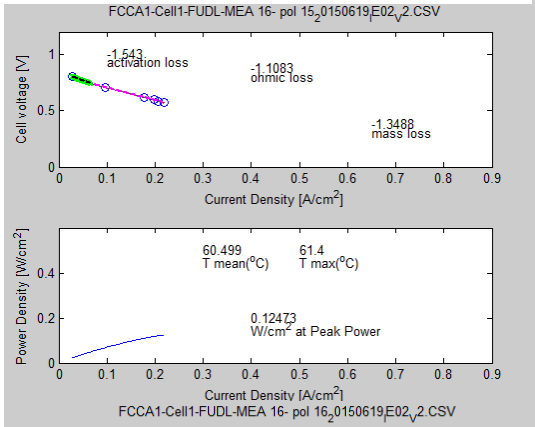
FCCA1-Cell1-FUDL-MEA 16- pol 15_20150619_E02_V2.CSV
-1.543
activation loss
-1.1083
ohmic loss
-1.3488
mass loss
Cell voltage [V]
Current Density [A/cm2]
60.499
T mean(°C)
61.4
T max(°C)
0.12473
W/cm2 at Peak Power
Power Density [W/cm2]
Current Density [A/cm2]

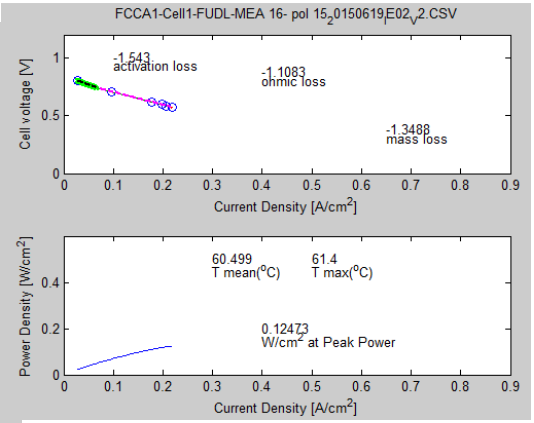
FCCA1-Cell1-FUDL-MEA 16- pol 15_20150619_E02_V2.CSV
-1.543
activation loss
-1.1083
ohmic loss
-1.3488
mass loss
Cell voltage [V]
Current Density [A/cm2]
60.499
T mean(°C)
61.4
T max(°C)
0.12473
W/cm2 at Peak Power
Power Density [W/cm2]
Current Density [A/cm2]

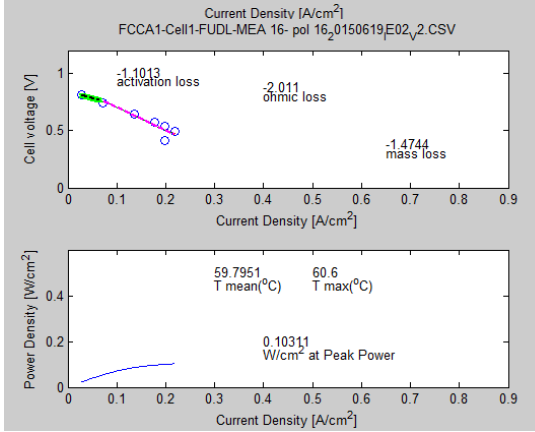
FCCA1-Cell1-FUDL-MEA 16- pol 16_20150619_E02_V2.CSV
-1.1013
activation loss
-2.011
ohmic loss
-1.4744
mass loss
Cell voltage [V]
Current Density [A/cm2]
59.7951
T mean(°C)
60.6
T max(°C)
0.10311
W/cm2 at Peak Power
Power Density [W/cm2]
Current Density [A/cm2]

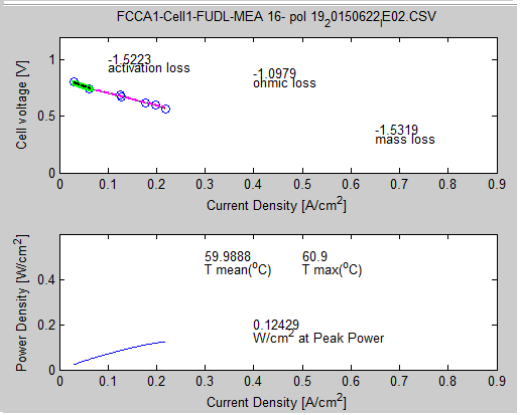
FCCA1-Cell1-FUDL-MEA 16- pol 19_20150622_E02.CSV
-1.5223
activation loss
-1.0979
ohmic loss
-1.5319
mass loss
Cell voltage [V]
Current Density [A/cm2]
59.9888
T mean(°C)
60.9
T max(°C)
0.12429
W/cm2 at Peak Power
Power Density [W/cm2]
Current Density [A/cm2]

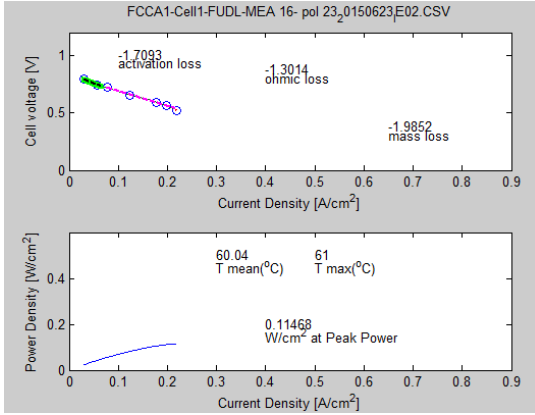
FCCA1-Cell1-FUDL-MEA 16- pol 23_20150623_E02.CSV
-1.7093
activation loss
-1.3014
ohmic loss
-1.9852
mass loss
Cell voltage [V]
Current Density [A/cm2]
60.04
T mean(°C)
61
T max(°C)
0.11468
W/cm2 at Peak Power
Power Density [W/cm2]
Current Density [A/cm2]

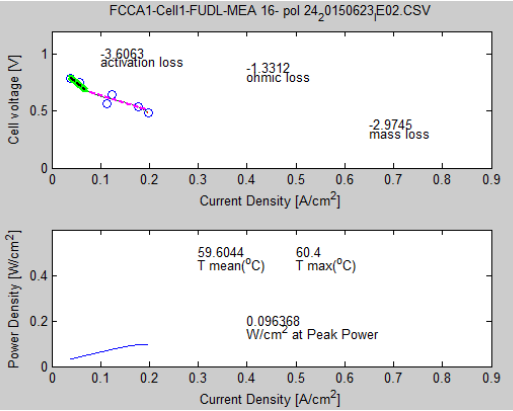
FCCA1-Cell1-FUDL-MEA 16- pol 24_20150623_E02.CSV
-3.6063
activation loss
-1.3312
ohmic loss
-2.9745
mass loss
Cell voltage [V]
Current Density [A/cm2]
59.6044
T mean(°C)
60.4
T max(°C)
0.096368
W/cm2 at Peak Power
Power Density [W/cm2]
Current Density [A/cm2]

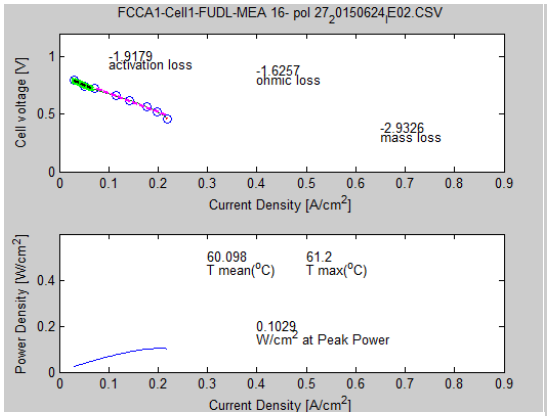
FCCA1-Cell1-FUDL-MEA 16- pol 27_20150624_E02.CSV
-1.9179
activation loss
-1.6257
ohmic loss
-2.9326
mass loss
Cell voltage [V]
Current Density [A/cm2]
60.098
T mean(°C)
61.2
T max(°C)
0.1029
W/cm2 at Peak Power
Power Density [W/cm2]
Current Density [A/cm2]

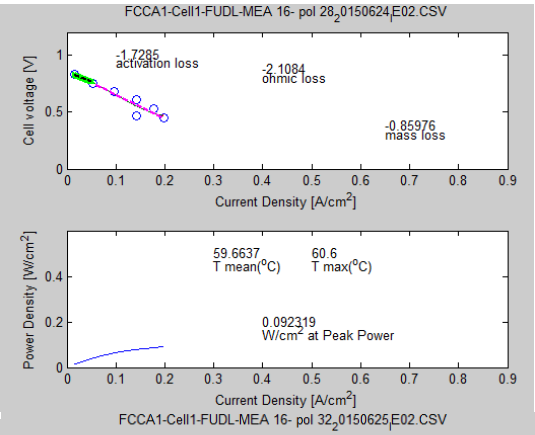
FCCA1-Cell1-FUDL-MEA 16- pol 28_20150624_E02.CSV
-1.7285
activation loss
-2.1084
ohmic loss
-0.85976
mass loss
Cell voltage [V]
Current Density [A/cm2]
59.6637
T mean(°C)
60.6
T max(°C)
0.092319
W/cm2 at Peak Power
Power Density [W/cm2]
Current Density [A/cm2]

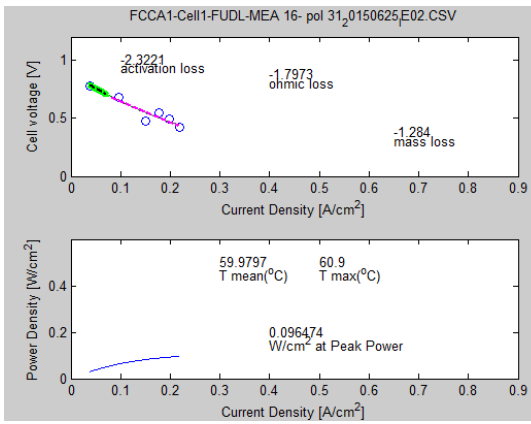
FCCA1-Cell1-FUDL-MEA 16- pol 31_20150625_E02.CSV
-2.3221
activation loss
-1.7973
ohmic loss
-1.284
mass loss
Cell voltage [V]
Current Density [A/cm2]
59.9797
T mean(°C)
60.9
T max(°C)
0.096474
W/cm2 at Peak Power
Power Density [W/cm2]
Current Density [A/cm2]

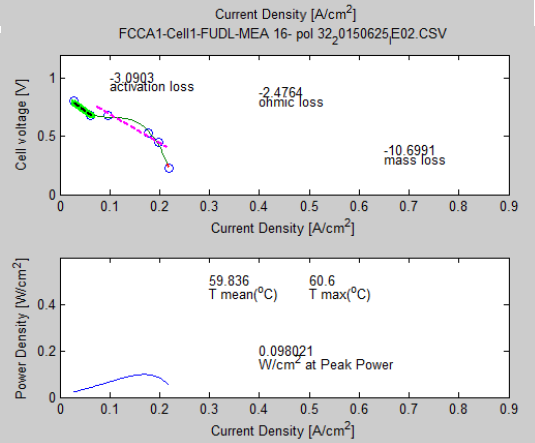
FCCA1-Cell1-FUDL-MEA 16- pol 32_20150625_E02.CSV
-3.0903
activation loss
-2.4764
ohmic loss
-10.6991
mass loss
Cell voltage [V]
Current Density [A/cm2]
59.836
T mean(°C)
60.6
T max(°C)
0.098021
W/cm2 at Peak Power
Power Density [W/cm2]
Current Density [A/cm2]

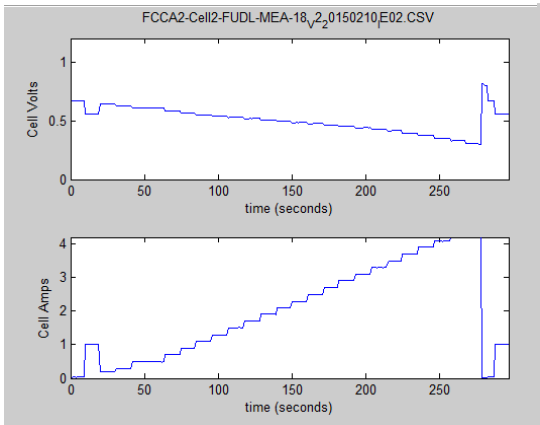
FCCA2-Cell2-FUDL-MEA-18_V2_20150210_E02.CSV
Cell Volts
time (seconds)
Cell Amps
time (seconds)

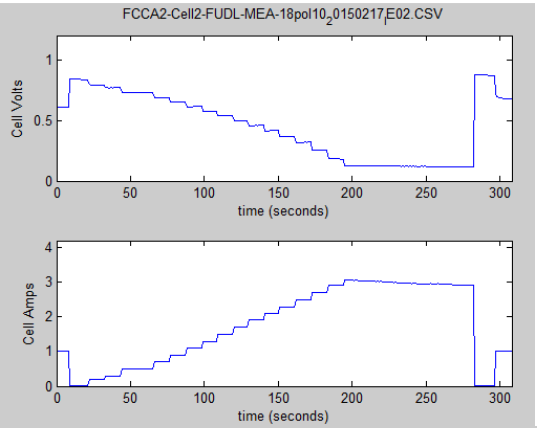
FCCA2-Cell2-FUDL-MEA-18pol10_20150217_E02.CSV
Cell Volts
time (seconds)
Cell Amps
time (seconds)

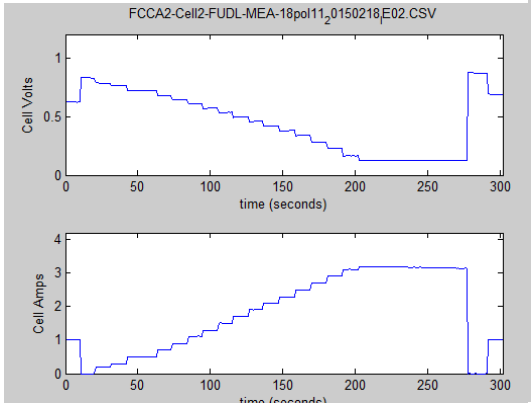
FCCA2-Cell2-FUDL-MEA-18pol11_20150218_E02.CSV
Cell Volts
time (seconds)
Cell Amps
time (seconds)

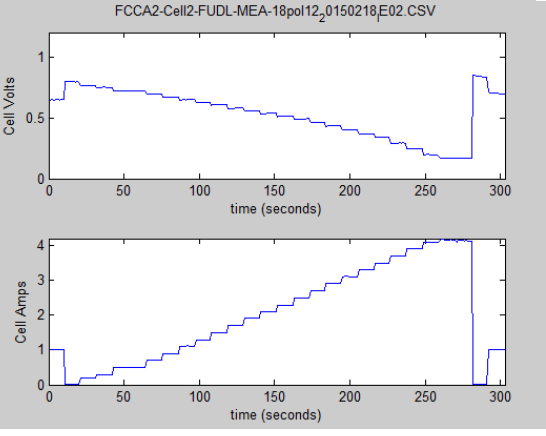
FCCA2-Cell2-FUDL-MEA-18pol12_20150218_E02.CSV
Cell Volts
time (seconds)
Cell Amps
time (seconds)

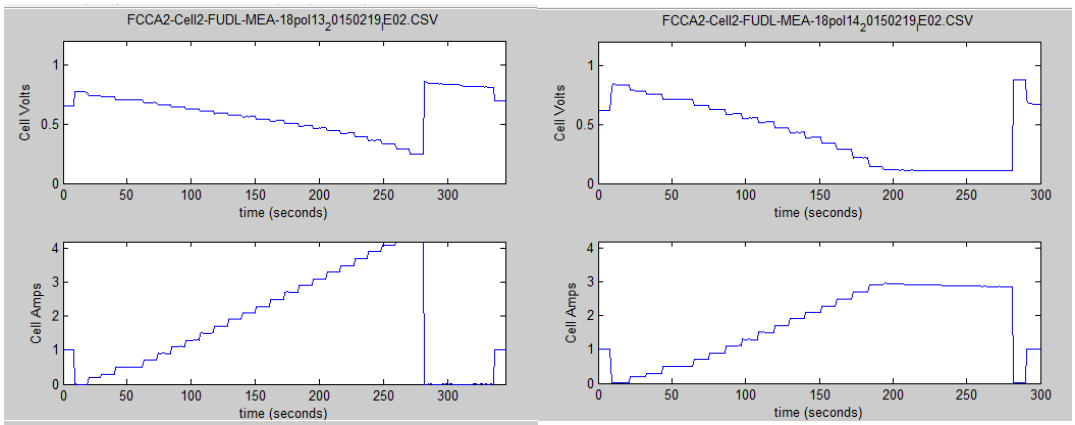
FCCA2-Cell2-FUDL-MEA-18pol13_20150219E02.CSV
Cell Volts
time (seconds)
Cell Amps
time (seconds)

FCCA2-Cell2-FUDL-MEA-18pol14_20150219E02.CSV
Cell Volts
time (seconds)
Cell Amps
time (seconds)

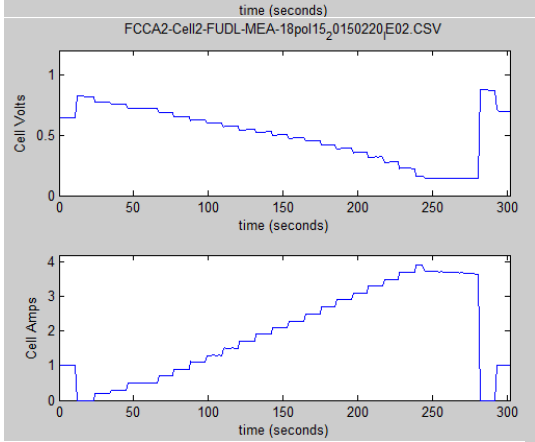
FCCA2-Cell2-FUDL-MEA-18pol15_20150220E02.CSV
Cell Volts
time (seconds)
Cell Amps
time (seconds)

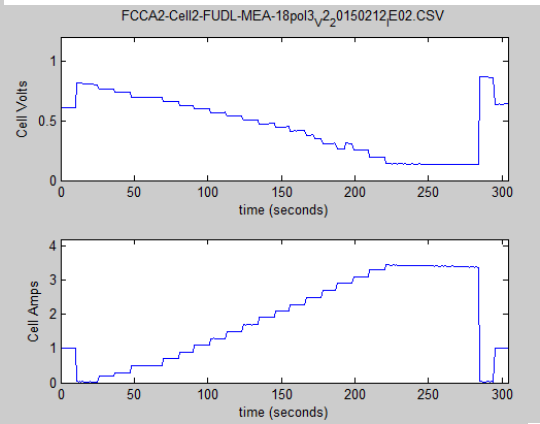
FCCA2-Cell2-FUDL-MEA-18pol3_V2_20150212E02.CSV
Cell Volts
time (seconds)
Cell Amps
time (seconds)

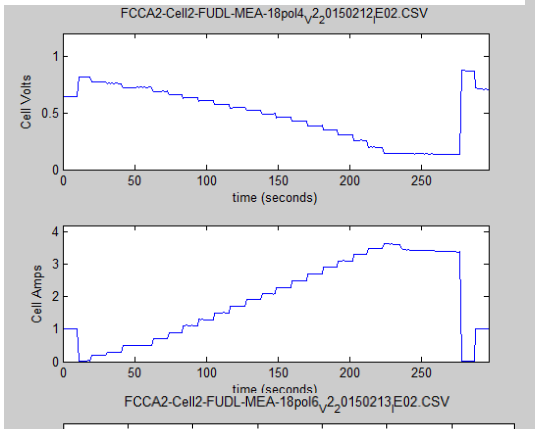
FCCA2-Cell2-FUDL-MEA-18pol4_V2_20150212E02.CSV
Cell Volts
time (seconds)
Cell Amps
time (seconds)

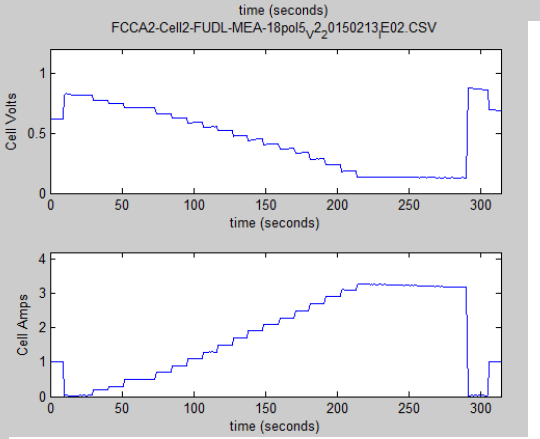
FCCA2-Cell2-FUDL-MEA-18pol5_V2_20150213E02.CSV
Cell Volts
time (seconds)
Cell Amps
time (seconds)

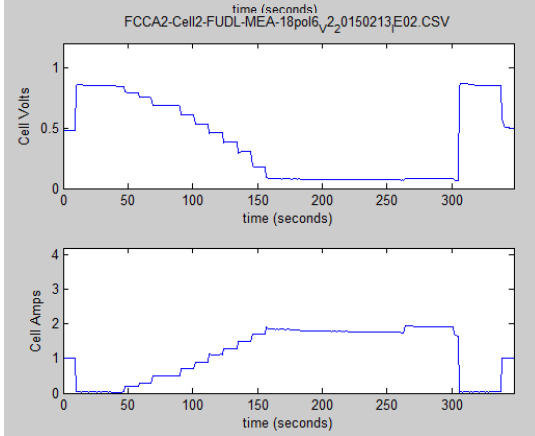
FCCA2-Cell2-FUDL-MEA-18pol6_V2_20150213E02.CSV
Cell Volts
time (seconds)
Cell Amps
time (seconds)

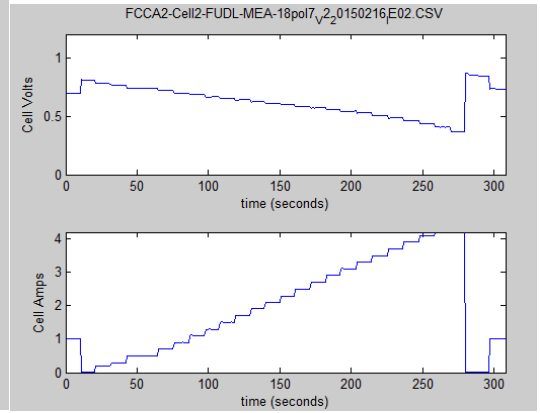
FCCA2-Cell2-FUDL-MEA-18pol7_V2_20150216E02.CSV
Cell Volts
time (seconds)
Cell Amps
time (seconds)

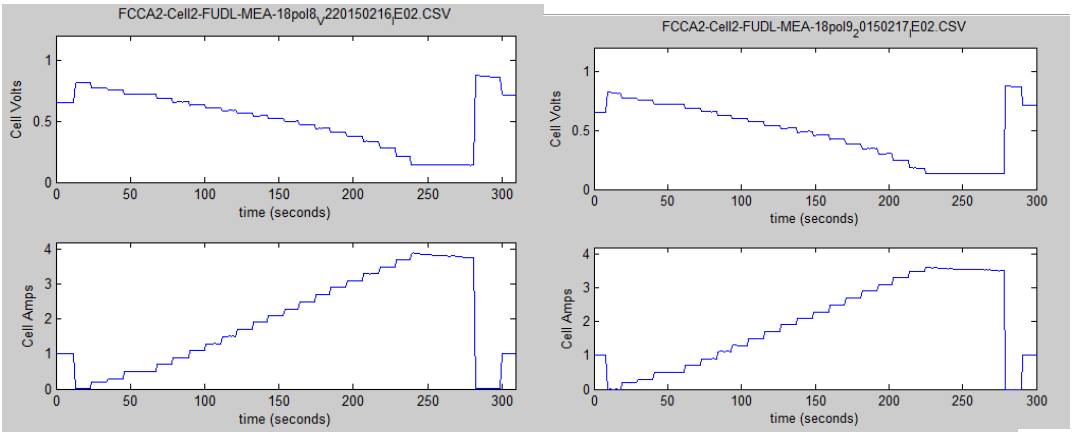
FCCA2-Cell2-FUDL-MEA-18pol8_V220150216_E02.CSV
FCCA2-Cell2-FUDL-MEA-18pol9_20150217_E02.CSV
Cell Volts
Cell Amps
time (seconds)

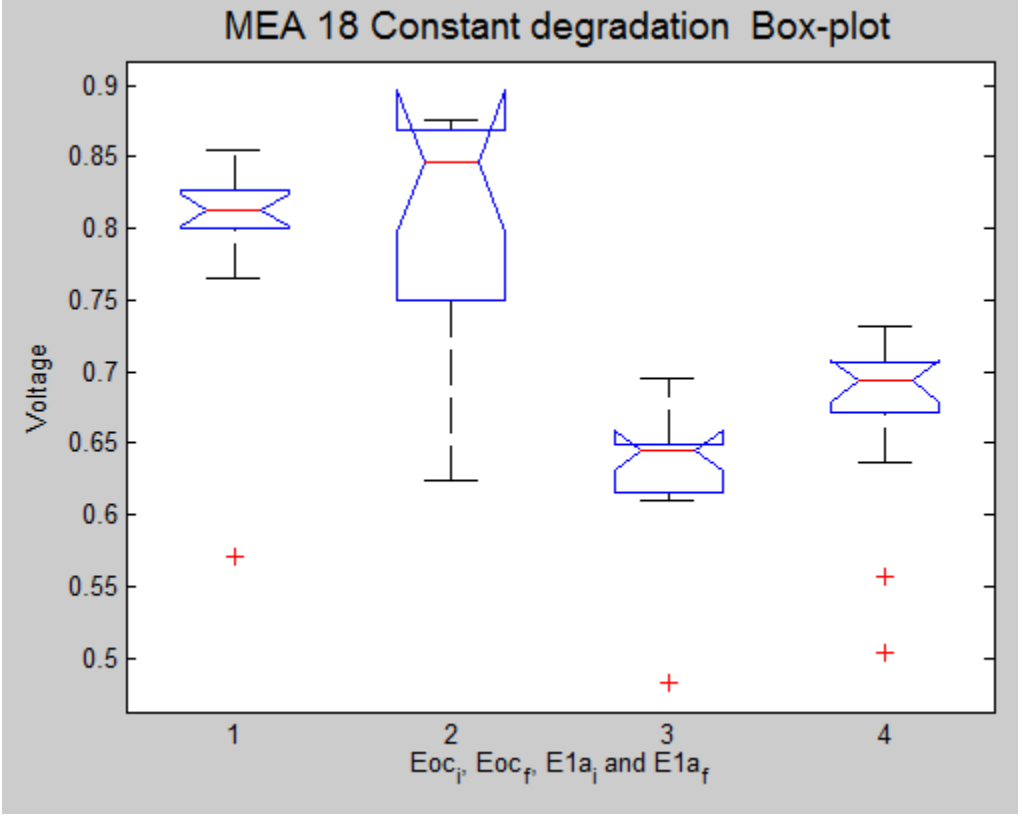
MEA 18 Constant degradation Box-plot
Voltage
Eoc_i, Eoc_f, E1a_i and E1a_f

MEA 18 (Fberg, Uniform cathode, Constant)PM

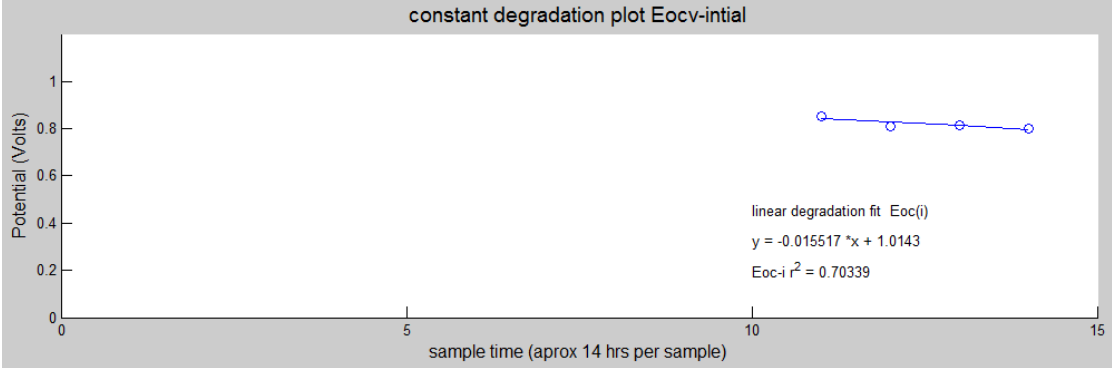

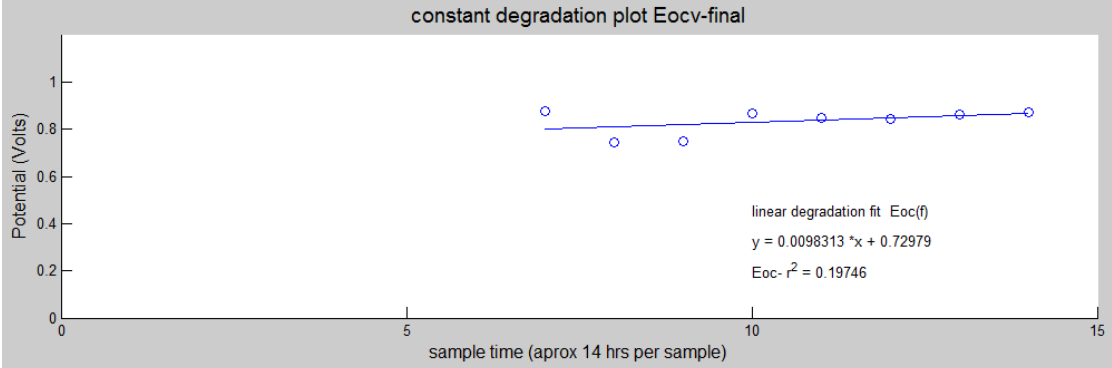

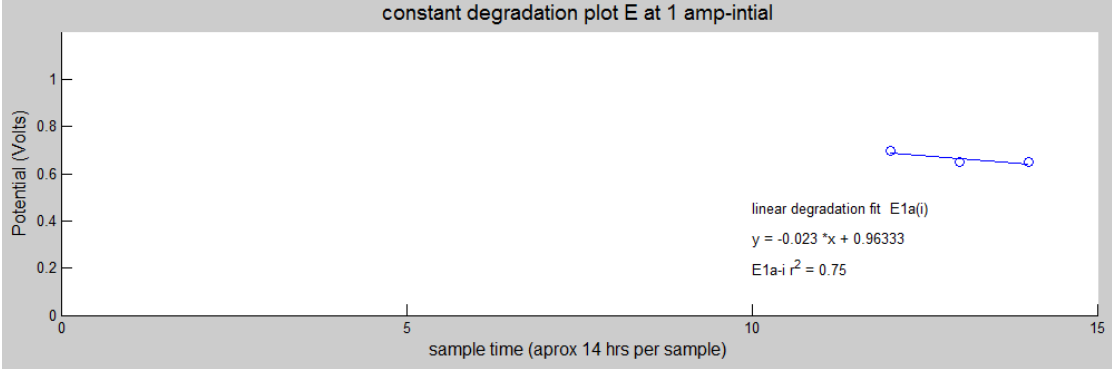

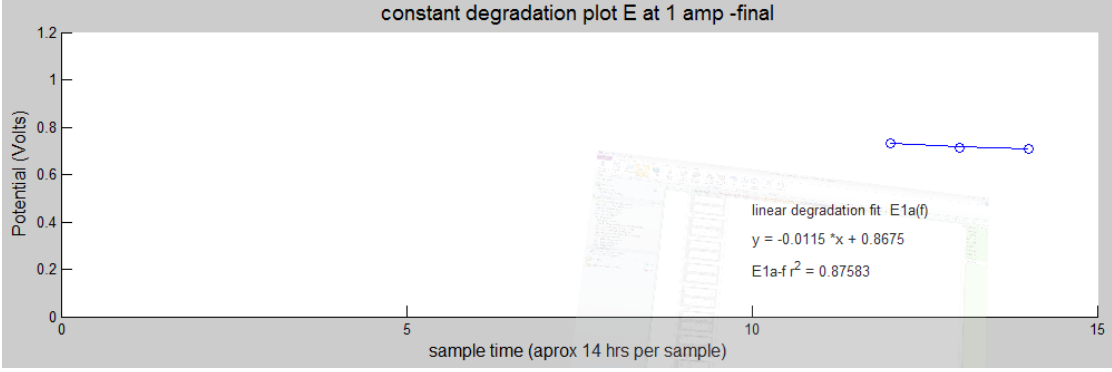

MEA 18 (Fberg, Uniform cathode, Constant)PM

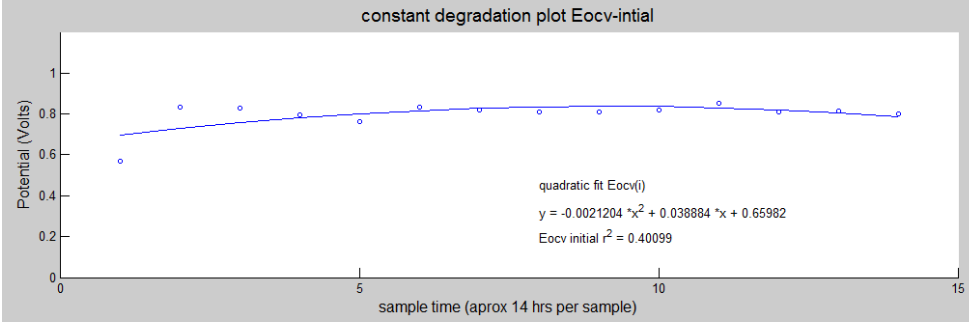

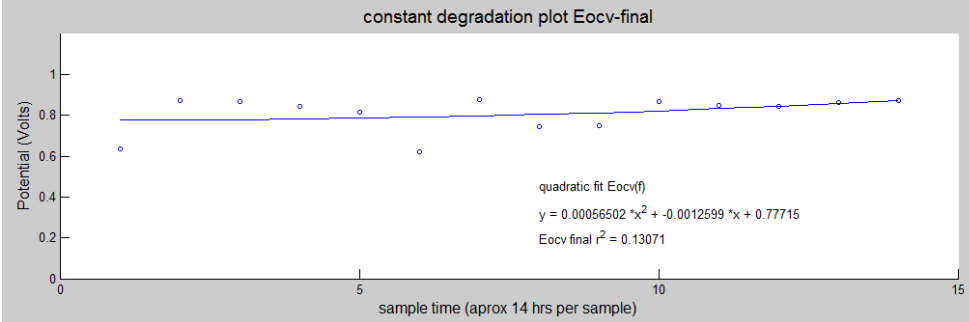

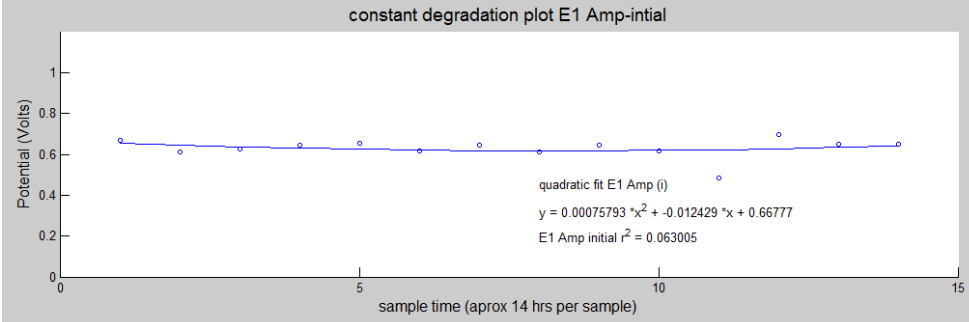

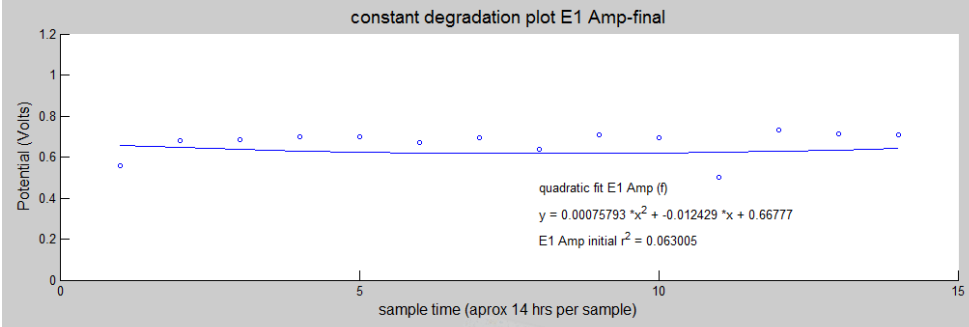

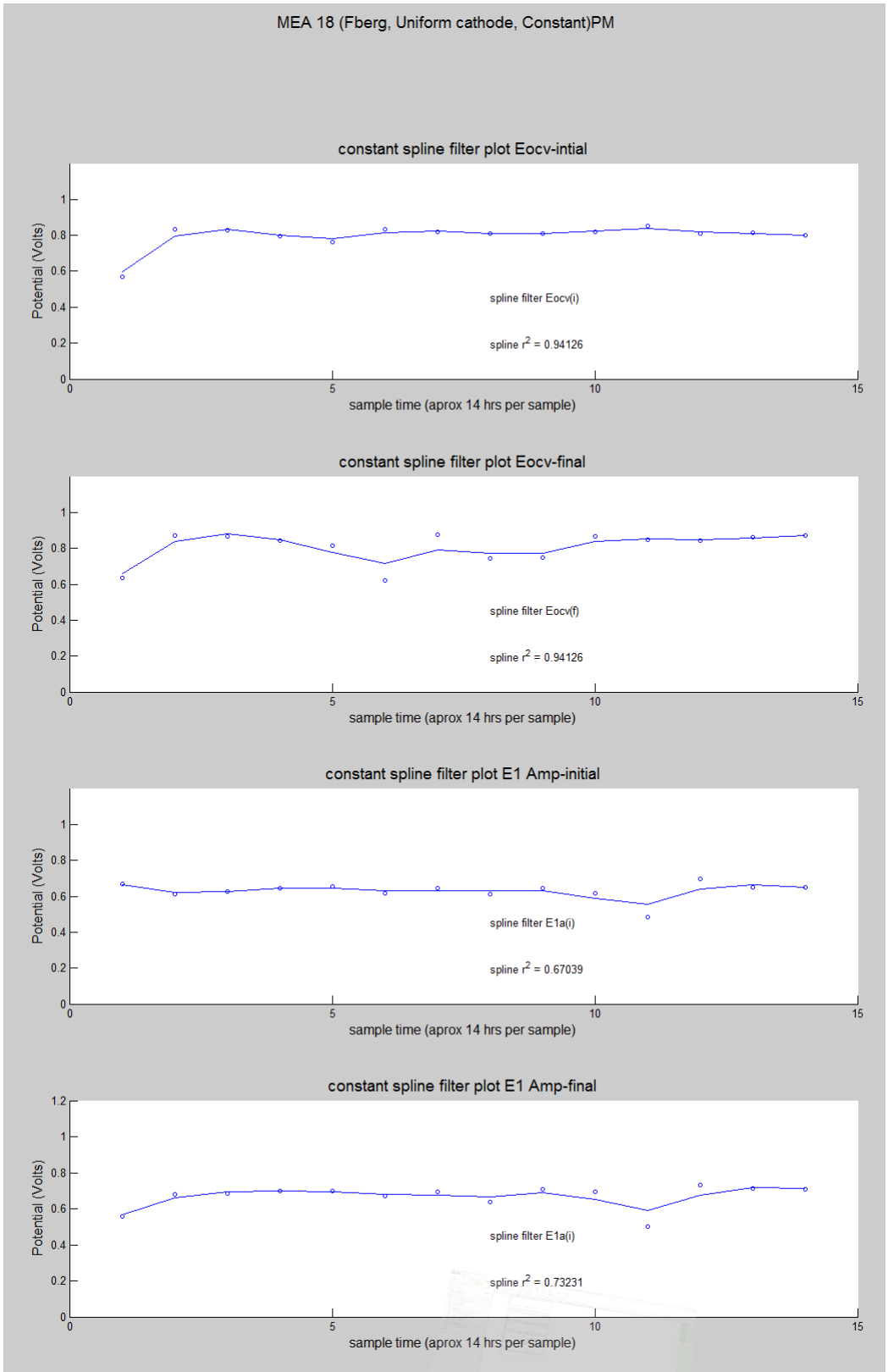
MEA 18 (Fberg, Uniform cathode, Constant)PM
constant spline filter plot Eocv-intial
Potential (Volts)
spline filter Eocv(i)
spline r2 = 0.94126
sample time (aprox 14 hrs per sample)
constant spline filter plot Eocv-final
Potential (Volts)
spline filter Eocv(f)
spline r2 = 0.94126
sample time (aprox 14 hrs per sample)
constant spline filter plot E1 Amp-initial
Potential (Volts)
spline filter E1a(i)
spline r2 = 0.67039
sample time (aprox 14 hrs per sample)
constant spline filter plot E1 Amp-final
Potential (Volts)
spline filter E1a(i)
spline r2 = 0.73231
sample time (aprox 14 hrs per sample)

MEA 19

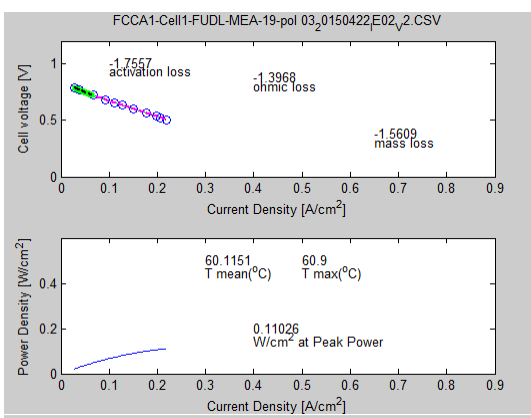
FCCA1-Cell1-FUDL-MEA-19-pol 03_20150422_E02_V2.CSV
-1.7557
activation loss
-1.3968
ohmic loss
-1.5609
mass loss
Cell voltage [V]
Current Density [A/cm2]
60.1151
T mean(°C)
60.9
T max(°C)
0.11026
W/cm2 at Peak Power
Power Density [W/cm2]
Current Density [A/cm2]

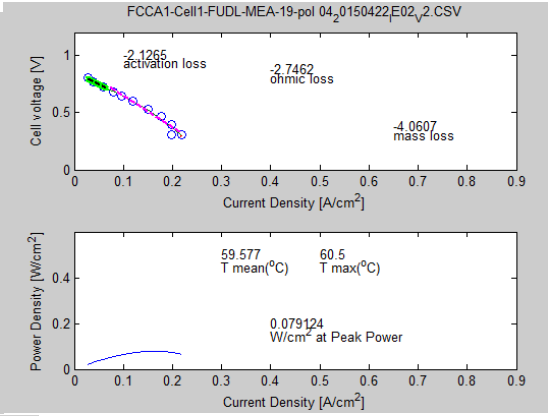
FCCA1-Cell1-FUDL-MEA-19-pol 04_20150422_E02_V2.CSV
-2.1265
activation loss
-2.7462
ohmic loss
-4.0607
mass loss
Cell voltage [V]
Current Density [A/cm2]
59.577
T mean(°C)
60.5
T max(°C)
0.079124
W/cm2 at Peak Power
Power Density [W/cm2]
Current Density [A/cm2]

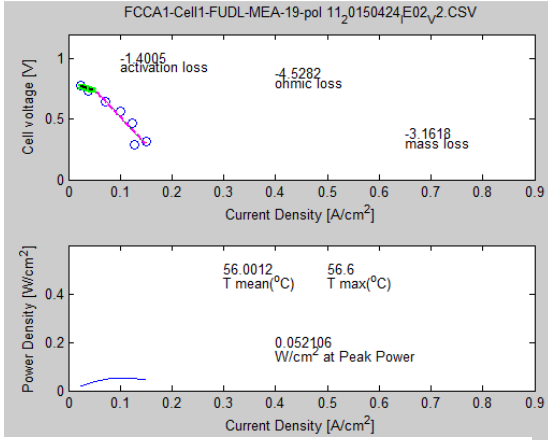
FCCA1-Cell1-FUDL-MEA-19-pol 11_20150424_E02_V2.CSV
-1.4005
activation loss
-4.5282
ohmic loss
-3.1618
mass loss
Cell voltage [V]
Current Density [A/cm2]
56.0012
T mean(°C)
56.6
T max(°C)
0.052106
W/cm2 at Peak Power
Power Density [W/cm2]
Current Density [A/cm2]

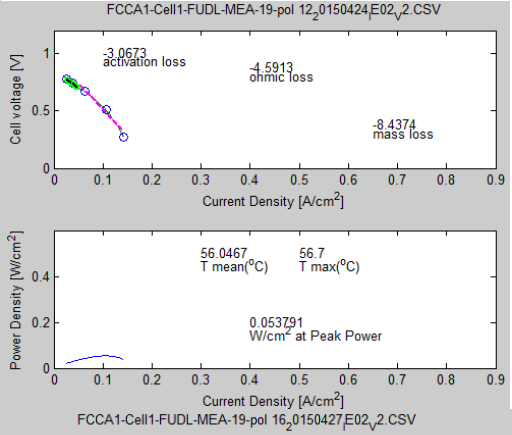
FCCA1-Cell1-FUDL-MEA-19-pol 12_20150424_E02_V2.CSV
-3.0673
activation loss
-4.5913
ohmic loss
-8.4374
mass loss
Cell voltage [V]
Current Density [A/cm2]
56.0467
T mean(°C)
56.7
T max(°C)
0.053791
W/cm2 at Peak Power
Power Density [W/cm2]
Current Density [A/cm2]

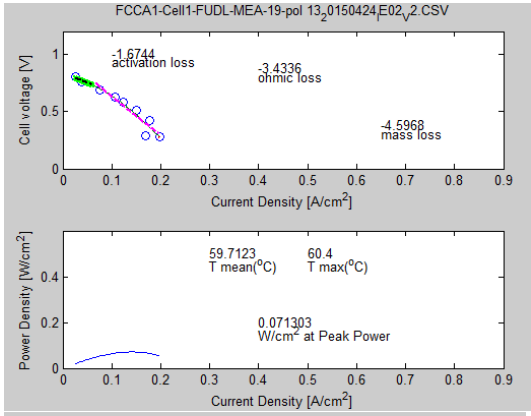
FCCA1-Cell1-FUDL-MEA-19-pol 13_20150424_E02_V2.CSV
-1.6744
activation loss
-3.4336
ohmic loss
-4.5968
mass loss
Cell voltage [V]
Current Density [A/cm2]
59.7123
T mean(°C)
60.4
T max(°C)
0.071303
W/cm2 at Peak Power
Power Density [W/cm2]
Current Density [A/cm2]

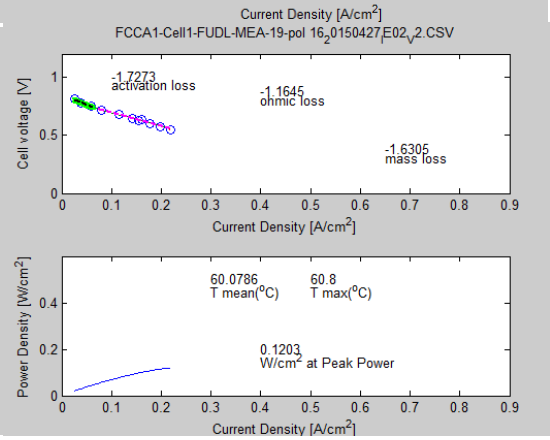
FCCA1-Cell1-FUDL-MEA-19-pol 16_20150427_E02_V2.CSV
-1.7273
activation loss
-1.1645
ohmic loss
-1.6305
mass loss
Cell voltage [V]
Current Density [A/cm2]
60.0786
T mean(°C)
60.8
T max(°C)
0.1203
W/cm2 at Peak Power
Power Density [W/cm2]
Current Density [A/cm2]

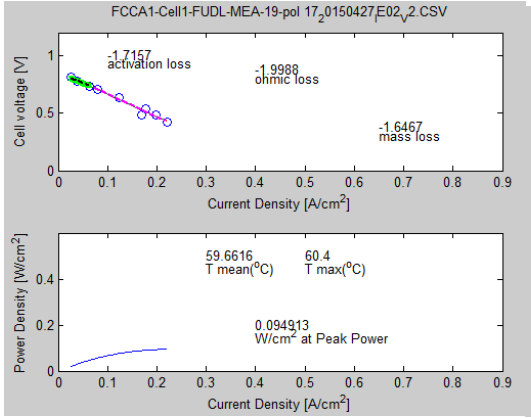
FCCA1-Cell1-FUDL-MEA-19-pol 17_20150427_E02_V2.CSV
-1.7157
activation loss
-1.9988
ohmic loss
-1.6467
mass loss
Cell voltage [V]
Current Density [A/cm2]
59.6616
T mean(°C)
60.4
T max(°C)
0.094913
W/cm2 at Peak Power
Power Density [W/cm2]
Current Density [A/cm2]

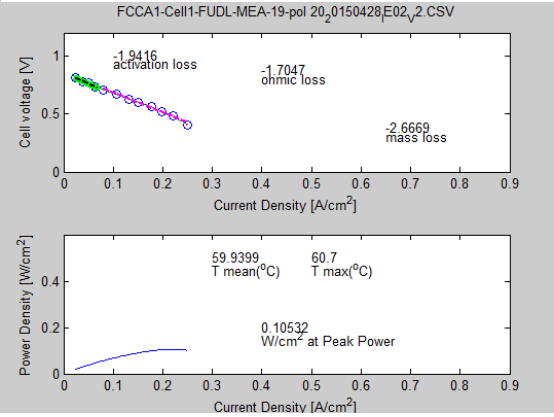
FCCA1-Cell1-FUDL-MEA-19-pol 20_20150428_E02_V2.CSV
-1.9416
activation loss
-1.7047
ohmic loss
-2.6669
mass loss
Cell voltage [V]
Current Density [A/cm2]
59.9399
T mean(°C)
60.7
T max(°C)
0.10532
W/cm2 at Peak Power
Power Density [W/cm2]
Current Density [A/cm2]

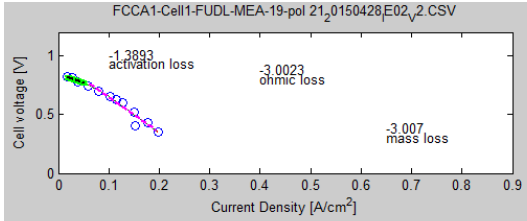
FCCA1-Cell1-FUDL-MEA-19-pol 21_0150428_E02_V2.CSV
-1.3893
activation loss
-3.0023
ohmic loss
-3.007
mass loss
Cell voltage [V]
Current Density [A/cm²]

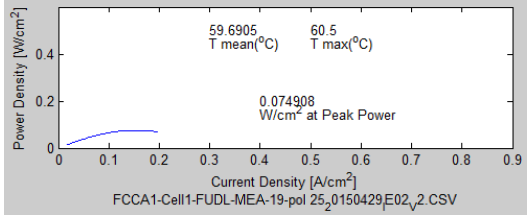
59.6905
T mean(°C)
60.5
T max(°C)
0.074908
W/cm² at Peak Power
Power Density [W/cm²]
Current Density [A/cm²]

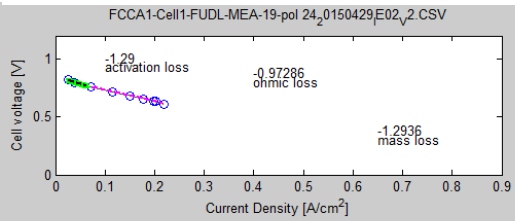
FCCA1-Cell1-FUDL-MEA-19-pol 24_0150429_E02_V2.CSV
-1.29
activation loss
-0.97286
ohmic loss
-1.2936
mass loss
Cell voltage [V]
Current Density [A/cm²]

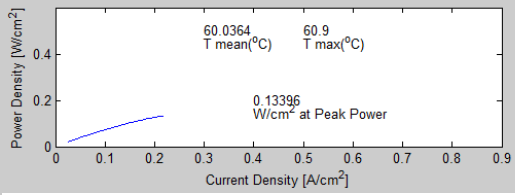
60.0364
T mean(°C)
60.9
T max(°C)
0.13396
W/cm² at Peak Power
Power Density [W/cm²]
Current Density [A/cm²]

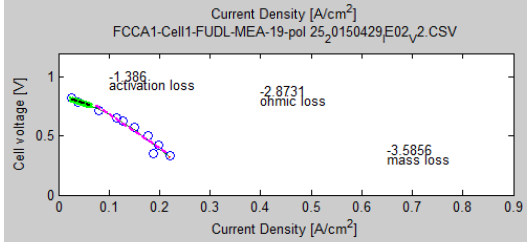
FCCA1-Cell1-FUDL-MEA-19-pol 25_0150429_E02_V2.CSV
-1.386
activation loss
-2.8731
ohmic loss
-3.5856
mass loss
Cell voltage [V]
Current Density [A/cm²]

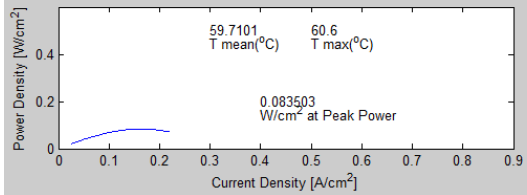
59.7101
T mean(°C)
60.6
T max(°C)
0.083503
W/cm² at Peak Power
Power Density [W/cm²]
Current Density [A/cm²]

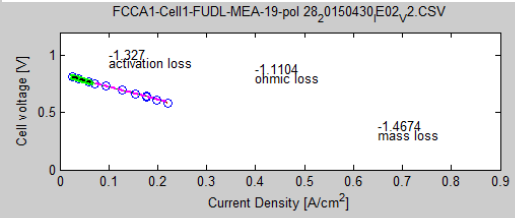
FCCA1-Cell1-FUDL-MEA-19-pol 28_0150430_E02_V2.CSV
-1.327
activation loss
-1.1104
ohmic loss
-1.4674
mass loss
Cell voltage [V]
Current Density [A/cm²]

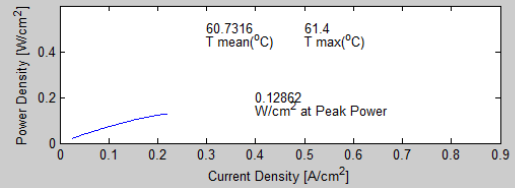
60.7316
T mean(°C)
61.4
T max(°C)
0.12862
W/cm² at Peak Power
Power Density [W/cm²]
Current Density [A/cm²]

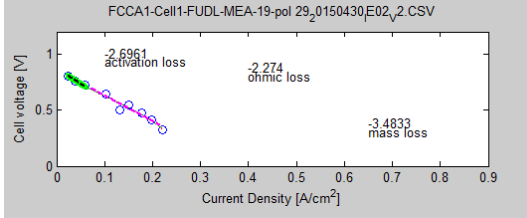
FCCA1-Cell1-FUDL-MEA-19-pol 29_0150430_E02_V2.CSV
-2.6961
activation loss
-2.274
ohmic loss
-3.4833
mass loss
Cell voltage [V]
Current Density [A/cm²]

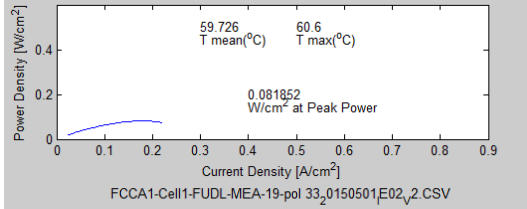
59.726
T mean(°C)
60.6
T max(°C)
0.081852
W/cm² at Peak Power
Power Density [W/cm²]
Current Density [A/cm²]

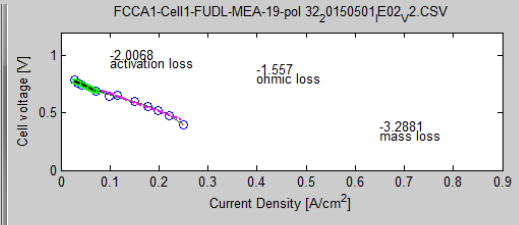
FCCA1-Cell1-FUDL-MEA-19-pol 32_0150501_E02_V2.CSV
-2.0068
activation loss
-1.557
ohmic loss
-3.2881
mass loss
Cell voltage [V]
Current Density [A/cm²]

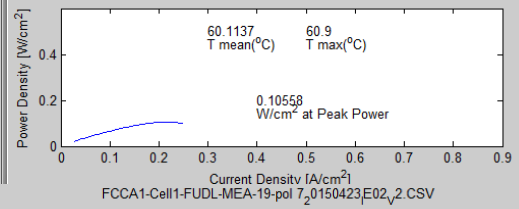
60.1137
T mean(°C)
60.9
T max(°C)
0.10558
W/cm² at Peak Power
Power Density [W/cm²]
Current Density [A/cm²]

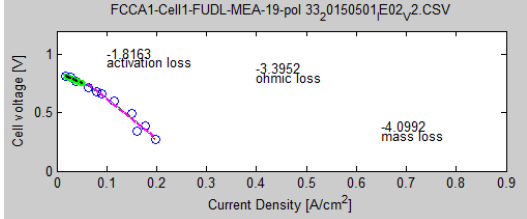
FCCA1-Cell1-FUDL-MEA-19-pol 33_0150501_E02_V2.CSV
-1.8163
activation loss
-3.3952
ohmic loss
-4.0992
mass loss
Cell voltage [V]
Current Density [A/cm²]

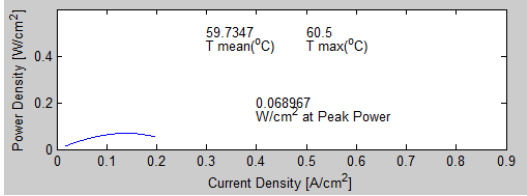
59.7347
T mean(°C)
60.5
T max(°C)
0.068967
W/cm² at Peak Power
Power Density [W/cm²]
Current Density [A/cm²]

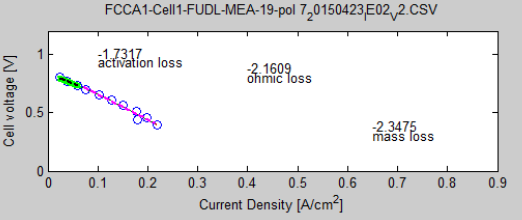
FCCA1-Cell1-FUDL-MEA-19-pol 7_0150423_E02_V2.CSV
-1.7317
activation loss
-2.1609
ohmic loss
-2.3475
mass loss
Cell voltage [V]
Current Density [A/cm²]

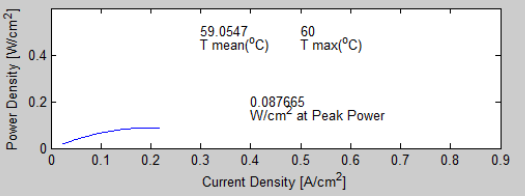
59.0547
T mean(°C)
60
T max(°C)
0.087665
W/cm² at Peak Power
Power Density [W/cm²]
Current Density [A/cm²]

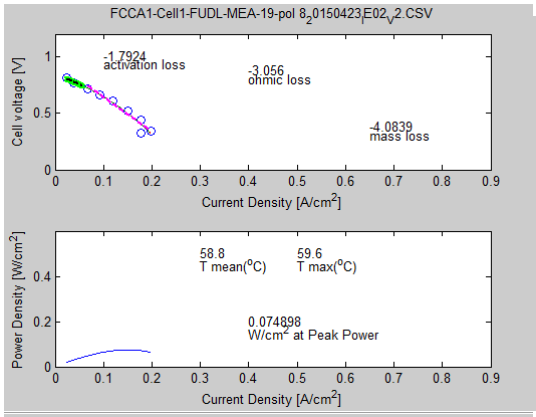
FCCA1-Cell1-FUDL-MEA-19-pol 8_0150423_E02_V2.CSV
Cell voltage [V]
-1.7924
activation loss
-3.056
ohmic loss
-4.0839
mass loss
Current Density [A/cm2]
Power Density [W/cm2]
58.8
T mean(°C)
59.6
T max(°C)
0.074898
W/cm2 at Peak Power
Current Density [A/cm2]

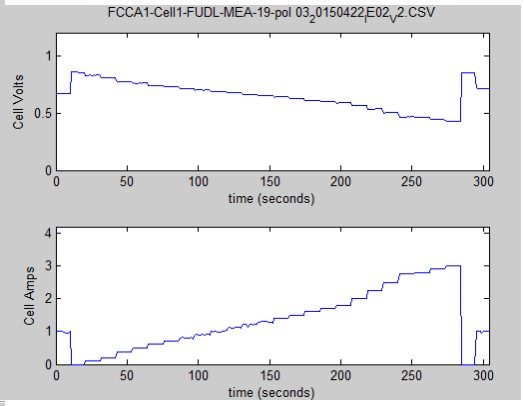
FCCA1-Cell1-FUDL-MEA-19-pol 03_0150422_E02_V2.CSV
Cell Volts
time (seconds)
Cell Amps
time (seconds)

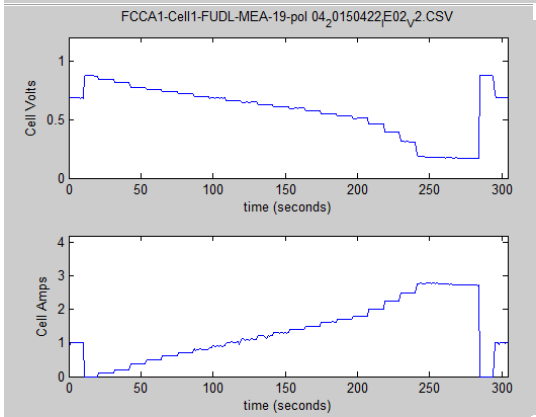
FCCA1-Cell1-FUDL-MEA-19-pol 04_0150422_E02_V2.CSV
Cell Volts
time (seconds)
Cell Amps
time (seconds)

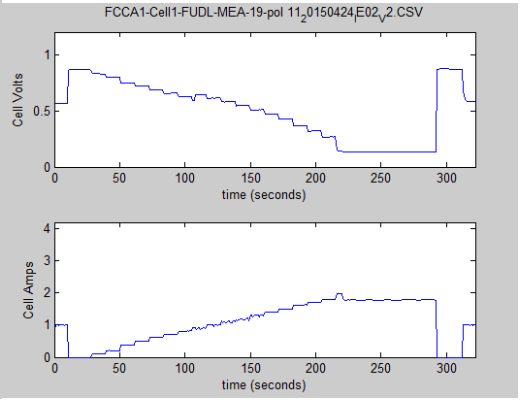
FCCA1-Cell1-FUDL-MEA-19-pol 11_0150424_E02_V2.CSV
Cell Volts
time (seconds)
Cell Amps
time (seconds)

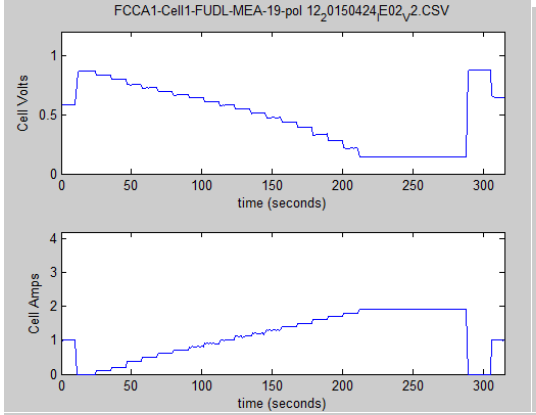
FCCA1-Cell1-FUDL-MEA-19-pol 12_0150424_E02_V2.CSV
Cell Volts
time (seconds)
Cell Amps
time (seconds)

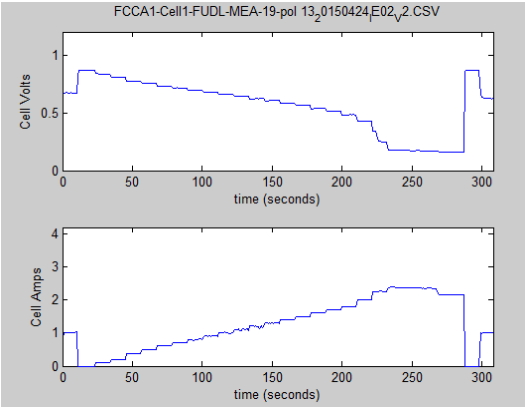
FCCA1-Cell1-FUDL-MEA-19-pol 13_0150424_E02_V2.CSV
Cell Volts
time (seconds)
Cell Amps
time (seconds)

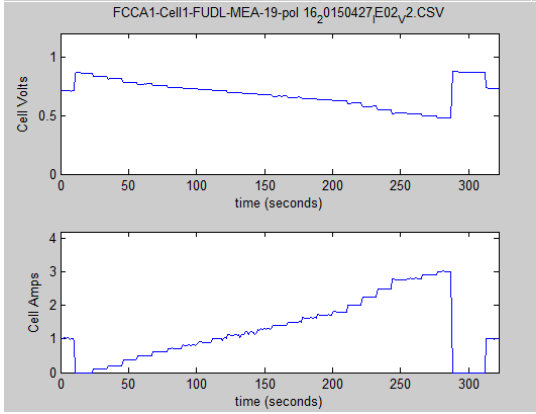
FCCA1-Cell1-FUDL-MEA-19-pol 16_0150427_E02_V2.CSV
Cell Volts
time (seconds)
Cell Amps
time (seconds)

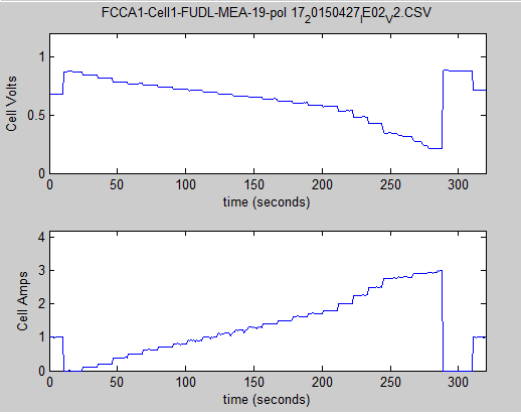
FCCA1-Cell1-FUDL-MEA-19-pol 17_0150427_E02_V2.CSV
Cell Volts
time (seconds)
Cell Amps
time (seconds)

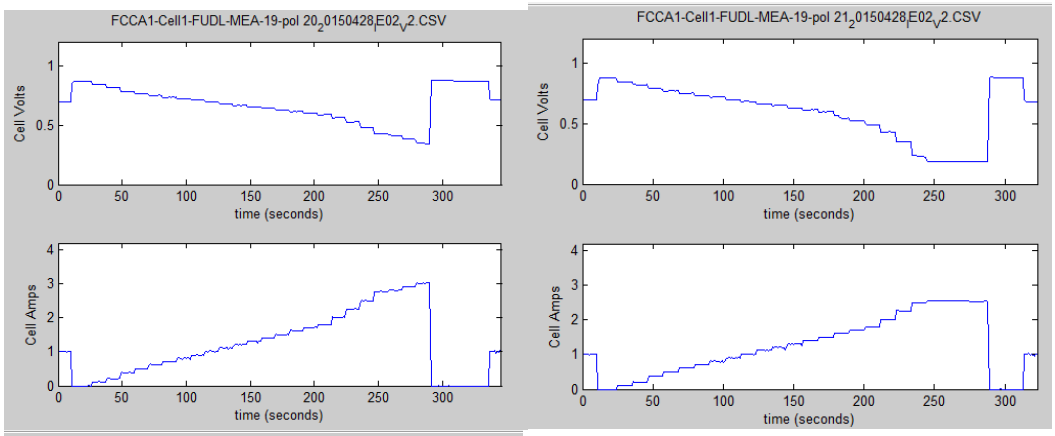
FCCA1-Cell1-FUDL-MEA-19-pol 20_20150428_E02_V2.CSV
FCCA1-Cell1-FUDL-MEA-19-pol 21_20150428_E02_V2.CSV
Cell Volts
Cell Amps
time (seconds)

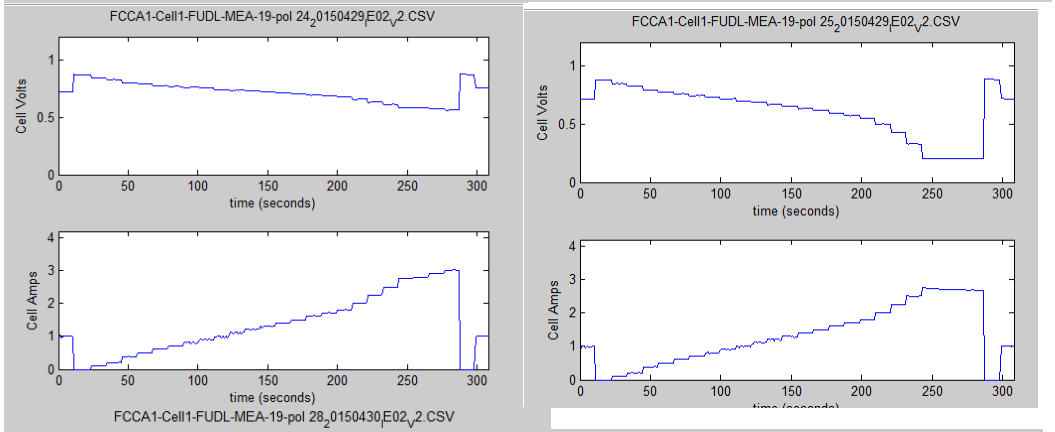
FCCA1-Cell1-FUDL-MEA-19-pol 24_20150429_E02_V2.CSV
FCCA1-Cell1-FUDL-MEA-19-pol 25_20150429_E02_V2.CSV
Cell Volts
Cell Amps
time (seconds)

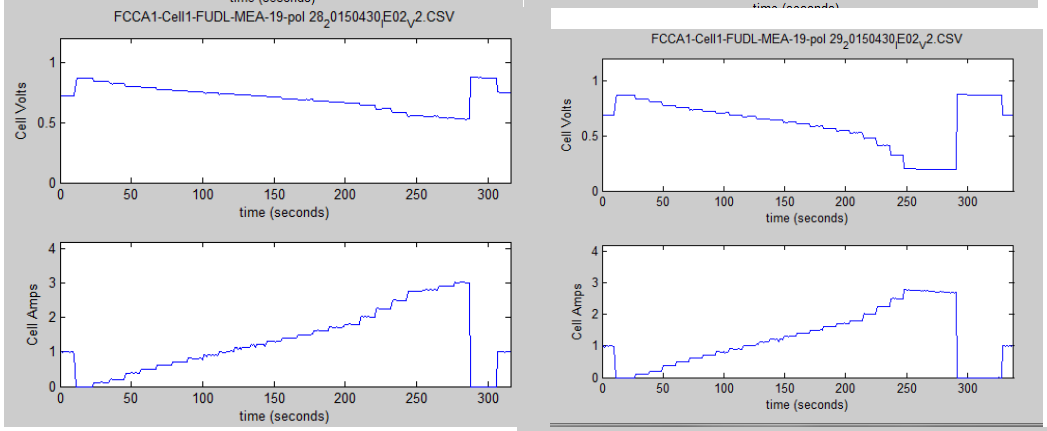
FCCA1-Cell1-FUDL-MEA-19-pol 28_20150430_E02_V2.CSV
FCCA1-Cell1-FUDL-MEA-19-pol 29_20150430_E02_V2.CSV
Cell Volts
Cell Amps
time (seconds)

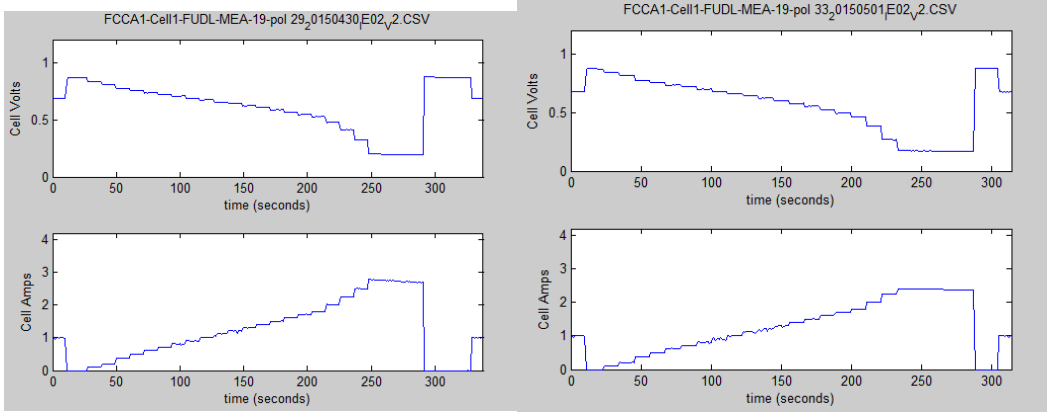
FCCA1-Cell1-FUDL-MEA-19-pol 29_20150430_E02_V2.CSV
FCCA1-Cell1-FUDL-MEA-19-pol 33_20150501_E02_V2.CSV
Cell Volts
Cell Amps
time (seconds)

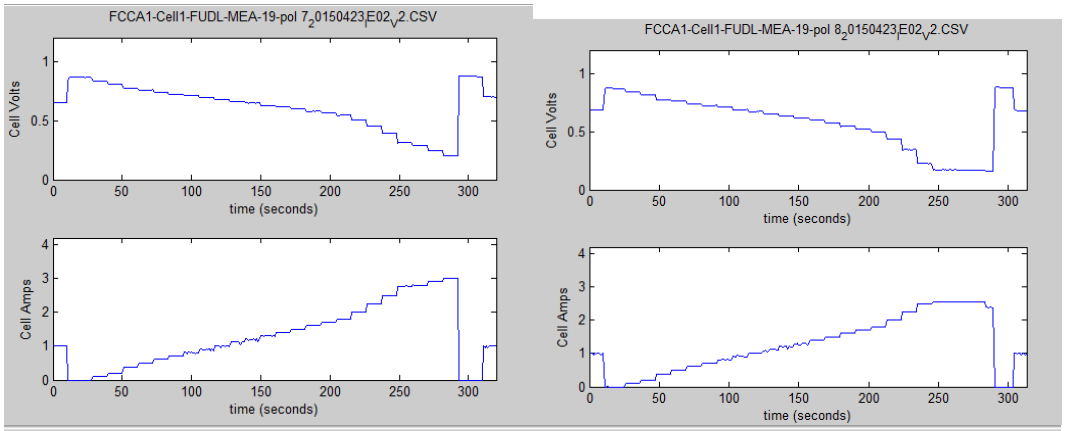
FCCA1-Cell1-FUDL-MEA-19-pol 7_20150423_E02_V2.CSV
Cell Volts
time (seconds)
Cell Amps
time (seconds)
FCCA1-Cell1-FUDL-MEA-19-pol 8_20150423_E02_V2.CSV
Cell Volts
time (seconds)
Cell Amps
time (seconds)

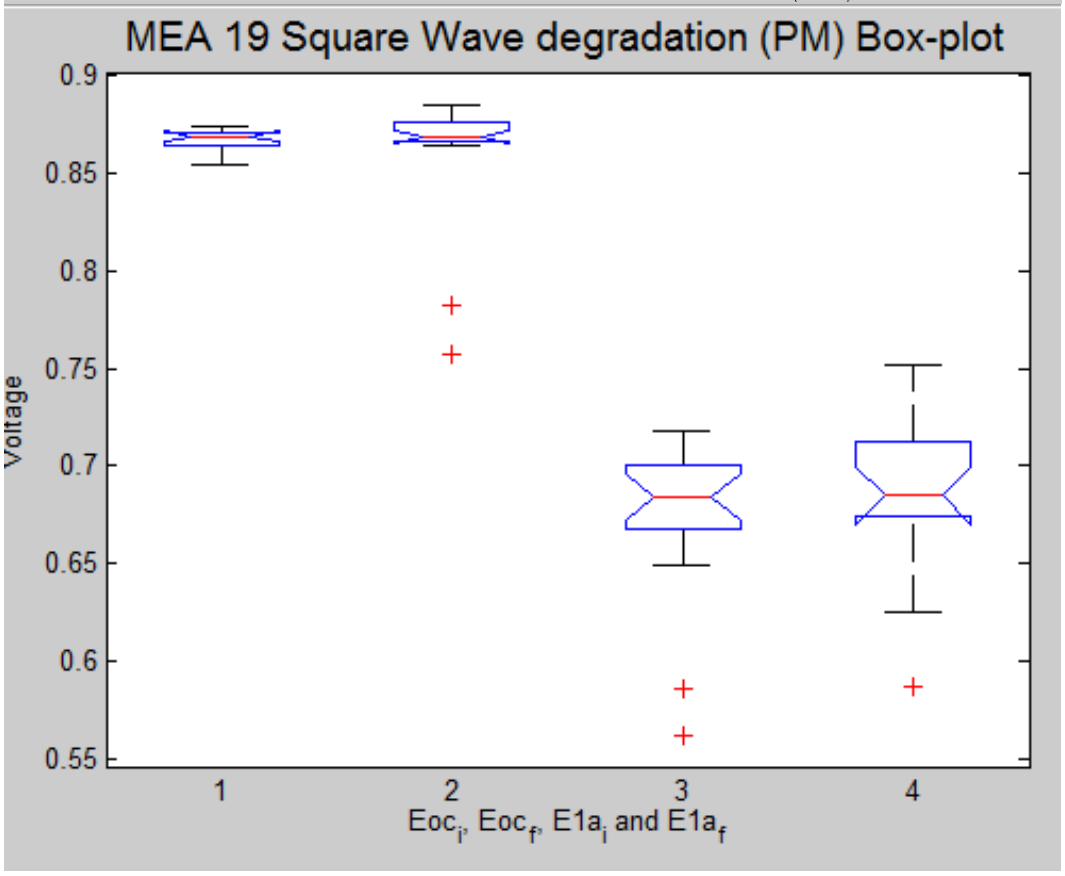
MEA 19 Square Wave degradation (PM) Box-plot
Voltage
Eoc_i, Eoc_f, E1a_i and E1a_f

MEA 19 (Freudenberg cathode, Uniform, Square Wave)PM

Square Wave degradation plot Eocv-intial

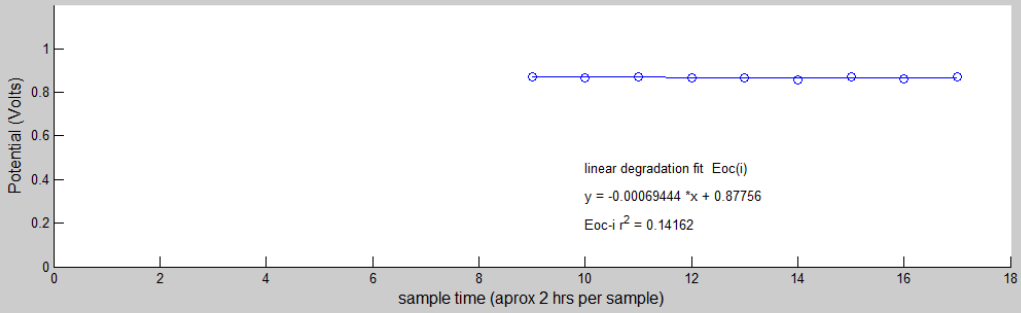

Square Wave degradation plot Eocv-final

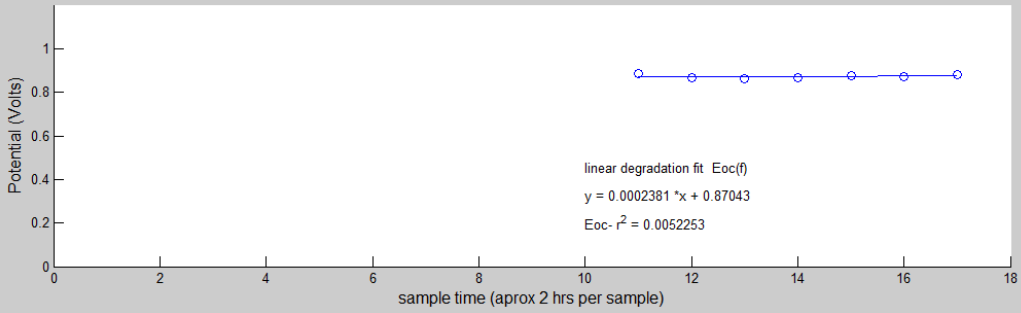

Square Wave degradation plot E at 1 amp-intial

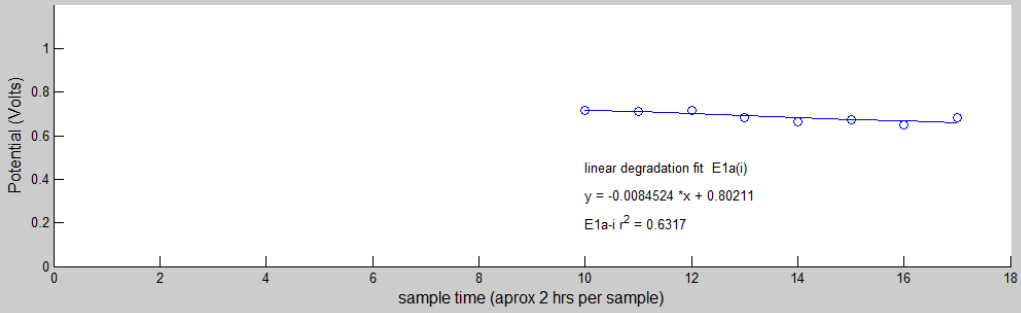

Square Wave degradation plot E at 1 amp -final

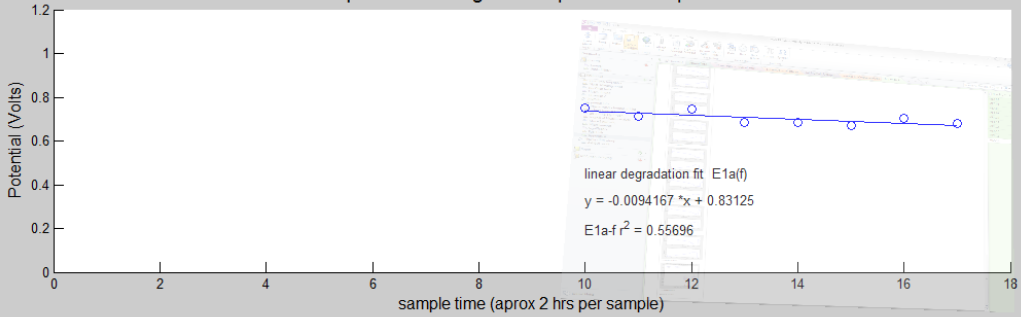

MEA 19 (Freudenberg cathode, Uniform, Square Wave)PM

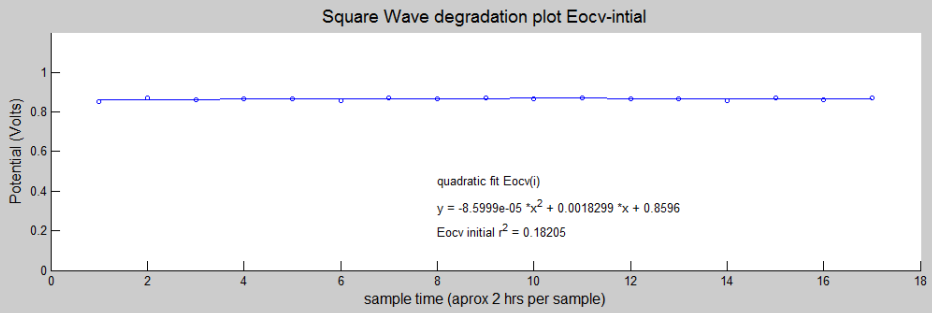

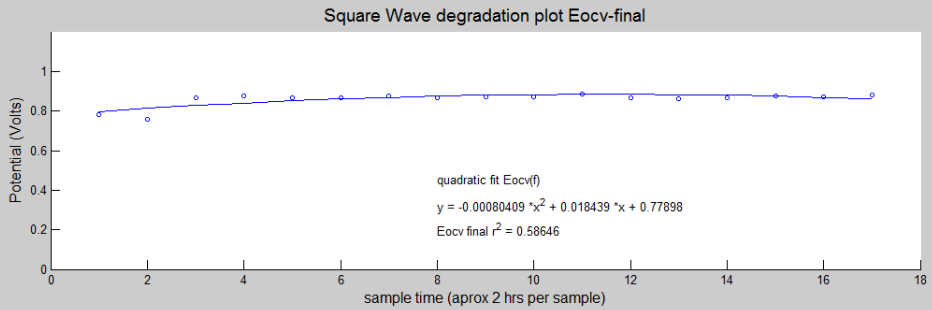

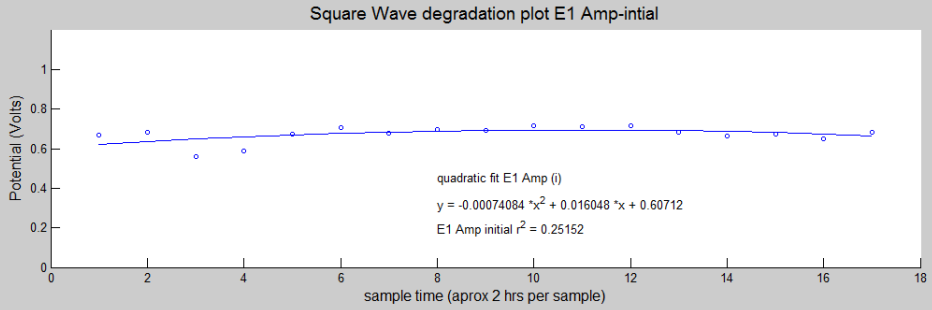

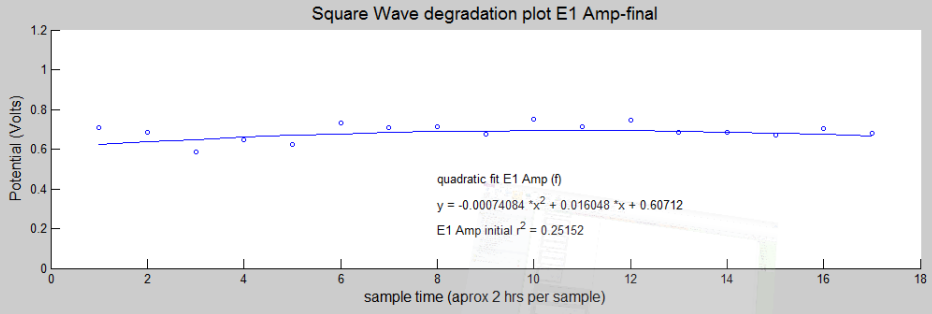

MEA 19 (Freudenberg cathode, Uniform, Square Wave)PM

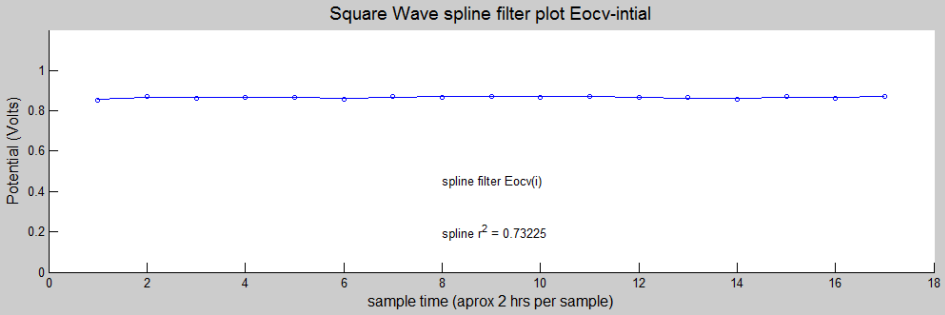

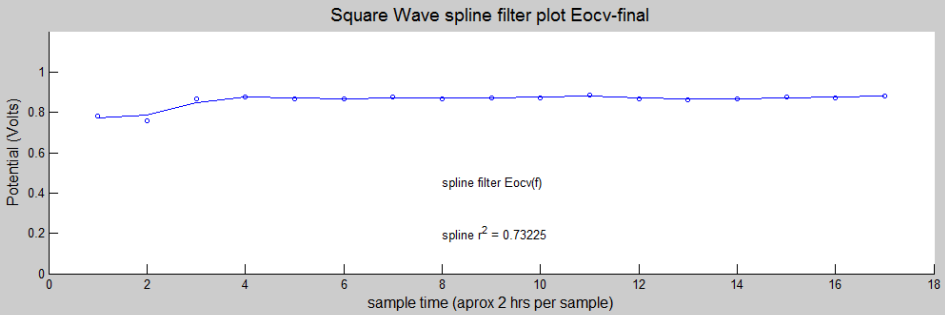

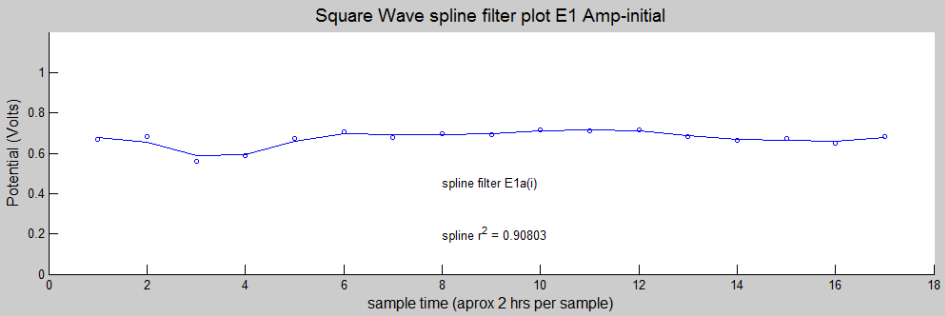

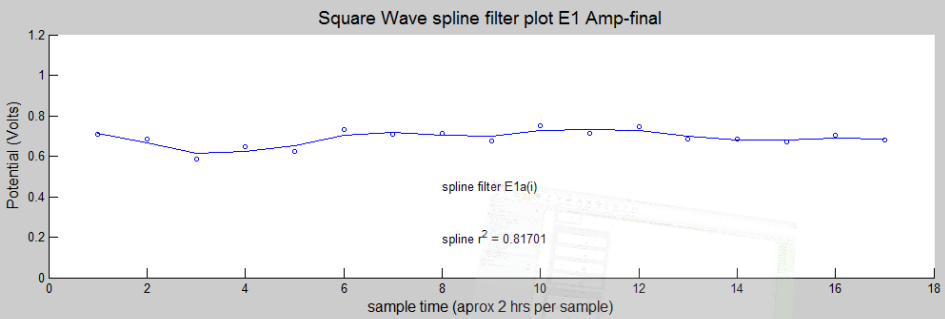

MEA 23

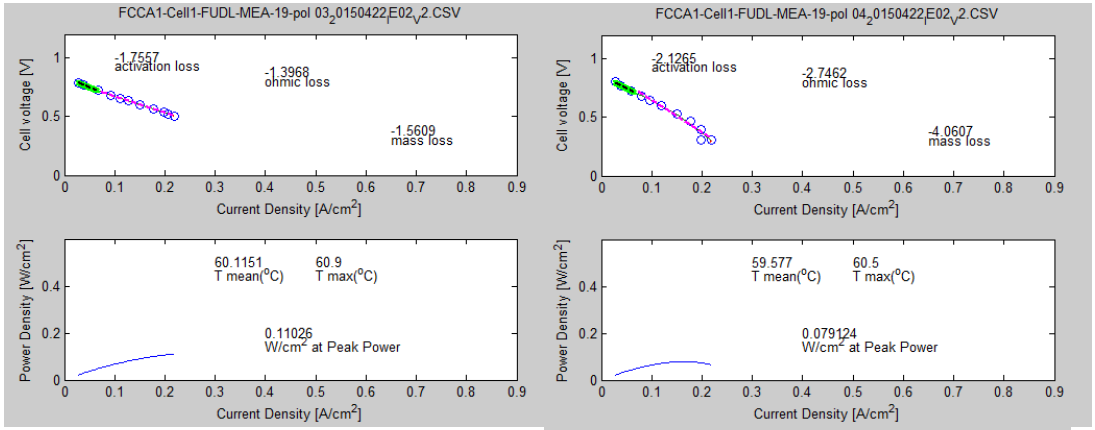
FCCA1-Cell1-FUDL-MEA-19-pol 03_20150422_E02_V2.CSV
-1.7557
activation loss
-1.3968
ohmic loss
-1.5609
mass loss
Cell voltage [V]
Current Density [A/cm²]
60.1151
T mean(°C)
60.9
T max(°C)
0.11026
W/cm² at Peak Power
Power Density [W/cm²]
Current Density [A/cm²]
FCCA1-Cell1-FUDL-MEA-19-pol 04_20150422_E02_V2.CSV
-2.1265
activation loss
-2.7462
ohmic loss
-4.0607
mass loss
Cell voltage [V]
Current Density [A/cm²]
59.577
T mean(°C)
60.5
T max(°C)
0.079124
W/cm² at Peak Power
Power Density [W/cm²]
Current Density [A/cm²]

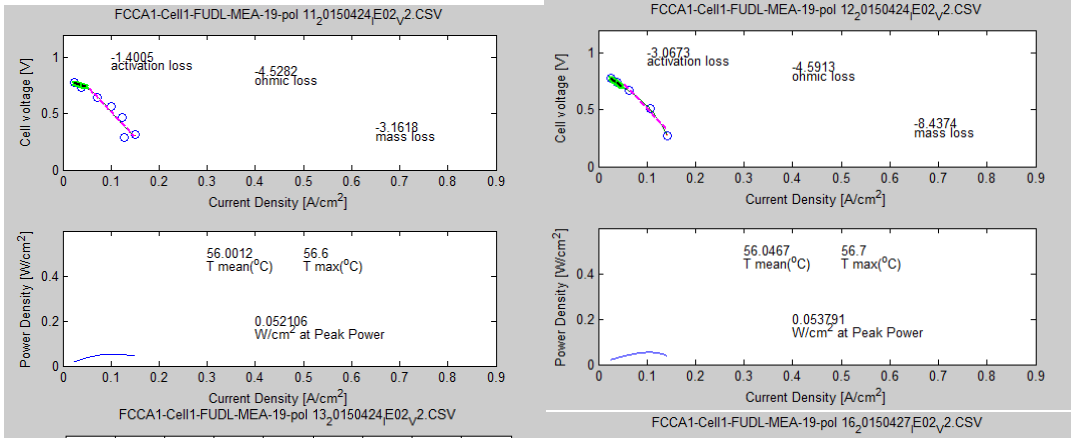
FCCA1-Cell1-FUDL-MEA-19-pol 11_20150424_E02_V2.CSV
-1.4005
activation loss
-4.5282
ohmic loss
-3.1618
mass loss
Cell voltage [V]
Current Density [A/cm²]
56.0012
T mean(°C)
56.6
T max(°C)
0.052106
W/cm² at Peak Power
Power Density [W/cm²]
Current Density [A/cm²]
FCCA1-Cell1-FUDL-MEA-19-pol 12_20150424_E02_V2.CSV
-3.0673
activation loss
-4.5913
ohmic loss
-8.4374
mass loss
Cell voltage [V]
Current Density [A/cm²]
56.0467
T mean(°C)
56.7
T max(°C)
0.053791
W/cm² at Peak Power
Power Density [W/cm²]
Current Density [A/cm²]

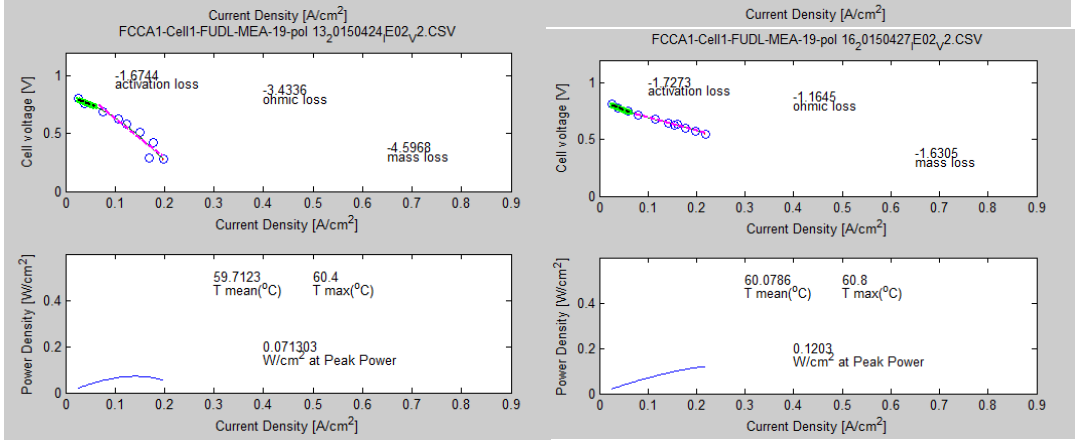
FCCA1-Cell1-FUDL-MEA-19-pol 13_20150424_E02_V2.CSV
-1.6744
activation loss
-3.4336
ohmic loss
-4.5968
mass loss
Cell voltage [V]
Current Density [A/cm²]
59.7123
T mean(°C)
60.4
T max(°C)
0.071303
W/cm² at Peak Power
Power Density [W/cm²]
Current Density [A/cm²]
FCCA1-Cell1-FUDL-MEA-19-pol 16_20150427_E02_V2.CSV
-1.7273
activation loss
-1.1645
ohmic loss
-1.6305
mass loss
Cell voltage [V]
Current Density [A/cm²]
60.0786
T mean(°C)
60.8
T max(°C)
0.1203
W/cm² at Peak Power
Power Density [W/cm²]
Current Density [A/cm²]

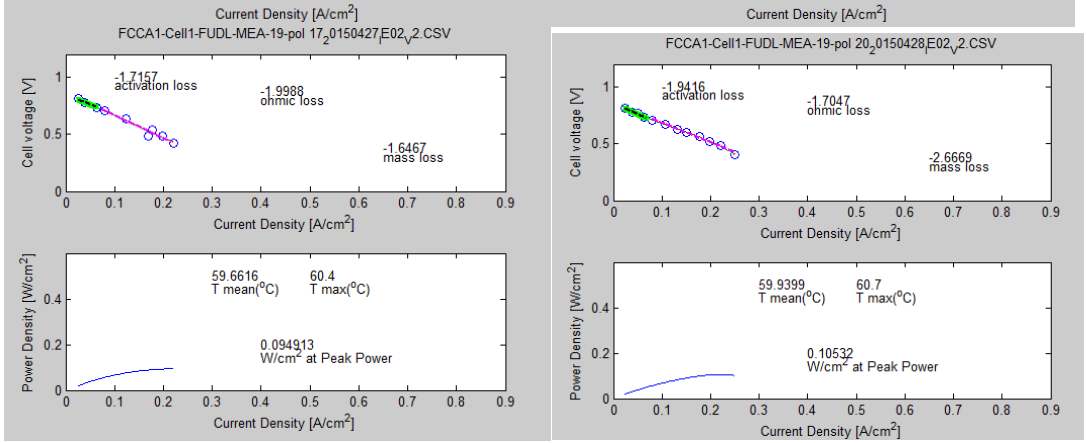
FCCA1-Cell1-FUDL-MEA-19-pol 17_20150427_E02_V2.CSV
-1.7157
activation loss
-1.9988
ohmic loss
-1.6467
mass loss
Cell voltage [V]
Current Density [A/cm²]
59.6616
T mean(°C)
60.4
T max(°C)
0.094913
W/cm² at Peak Power
Power Density [W/cm²]
Current Density [A/cm²]
FCCA1-Cell1-FUDL-MEA-19-pol 20_20150428_E02_V2.CSV
-1.9416
activation loss
-1.7047
ohmic loss
-2.6669
mass loss
Cell voltage [V]
Current Density [A/cm²]
59.9399
T mean(°C)
60.7
T max(°C)
0.10532
W/cm² at Peak Power
Power Density [W/cm²]
Current Density [A/cm²]

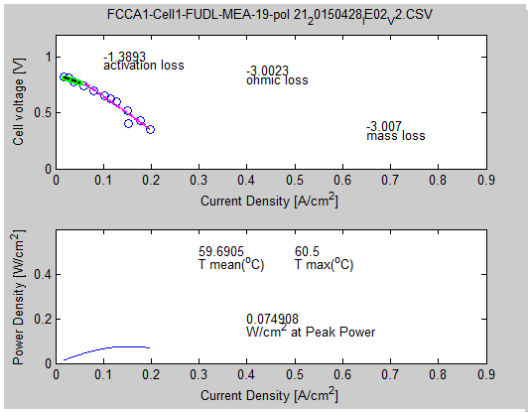
FCCA1-Cell1-FUDL-MEA-19-pol 21_20150428_E02_V2.CSV
-1.3893
activation loss
-3.0023
ohmic loss
-3.007
mass loss
Cell voltage [V]
Current Density [A/cm²]
59.6905
T mean(°C)
60.5
T max(°C)
0.074908
W/cm² at Peak Power
Power Density [W/cm²]
Current Density [A/cm²]

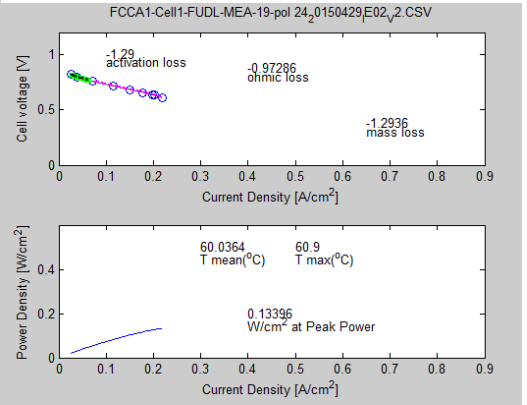
FCCA1-Cell1-FUDL-MEA-19-pol 24_20150429_E02_V2.CSV
-1.29
activation loss
-0.97286
ohmic loss
-1.2936
mass loss
Cell voltage [V]
Current Density [A/cm²]
60.0364
T mean(°C)
60.9
T max(°C)
0.13396
W/cm² at Peak Power
Power Density [W/cm²]
Current Density [A/cm²]

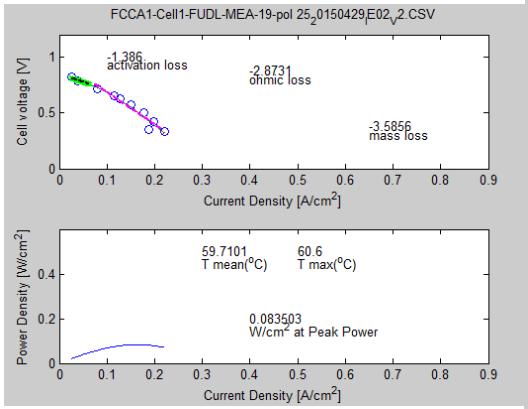
FCCA1-Cell1-FUDL-MEA-19-pol 25_20150429_E02_V2.CSV
-1.386
activation loss
-2.8731
ohmic loss
-3.5856
mass loss
Cell voltage [V]
Current Density [A/cm²]
59.7101
T mean(°C)
60.6
T max(°C)
0.083503
W/cm² at Peak Power
Power Density [W/cm²]
Current Density [A/cm²]

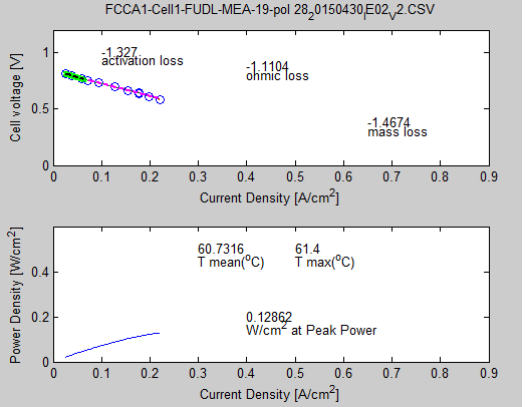
FCCA1-Cell1-FUDL-MEA-19-pol 28_20150430_E02_V2.CSV
-1.327
activation loss
-1.1104
ohmic loss
-1.4674
mass loss
Cell voltage [V]
Current Density [A/cm²]
60.7316
T mean(°C)
61.4
T max(°C)
0.12862
W/cm² at Peak Power
Power Density [W/cm²]
Current Density [A/cm²]

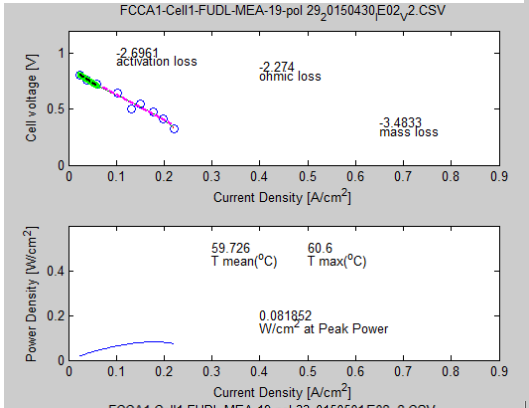
FCCA1-Cell1-FUDL-MEA-19-pol 29_20150430_E02_V2.CSV
-2.6961
activation loss
-2.274
ohmic loss
-3.4833
mass loss
Cell voltage [V]
Current Density [A/cm²]
59.726
T mean(°C)
60.6
T max(°C)
0.081852
W/cm² at Peak Power
Power Density [W/cm²]
Current Density [A/cm²]

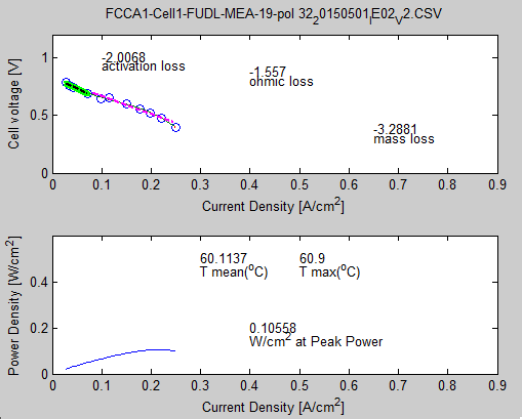
FCCA1-Cell1-FUDL-MEA-19-pol 32_20150501_E02_V2.CSV
-2.0068
activation loss
-1.557
ohmic loss
-3.2881
mass loss
Cell voltage [V]
Current Density [A/cm²]
60.1137
T mean(°C)
60.9
T max(°C)
0.10558
W/cm² at Peak Power
Power Density [W/cm²]
Current Density [A/cm²]

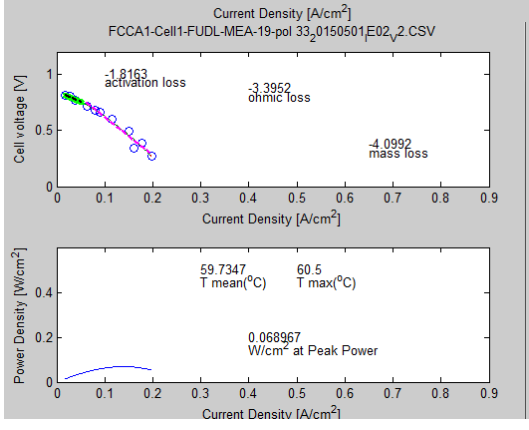
FCCA1-Cell1-FUDL-MEA-19-pol 33_20150501_E02_V2.CSV
-1.8163
activation loss
-3.3952
ohmic loss
-4.0992
mass loss
Cell voltage [V]
Current Density [A/cm²]
59.7347
T mean(°C)
60.5
T max(°C)
0.068967
W/cm² at Peak Power
Power Density [W/cm²]
Current Density [A/cm²]

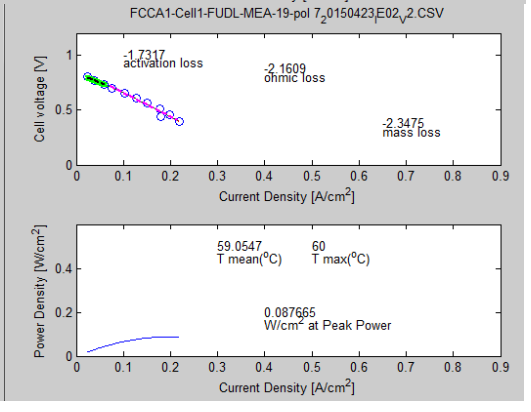
FCCA1-Cell1-FUDL-MEA-19-pol 7_20150423_E02_V2.CSV
-1.7317
activation loss
-2.1609
ohmic loss
-2.3475
mass loss
Cell voltage [V]
Current Density [A/cm²]
59.0547
T mean(°C)
60
T max(°C)
0.087665
W/cm² at Peak Power
Power Density [W/cm²]
Current Density [A/cm²]

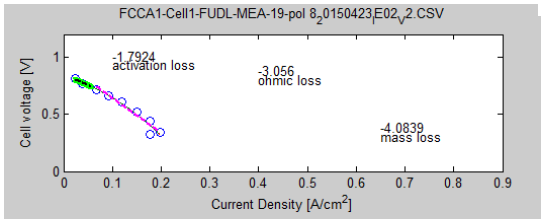
FCCA1-Cell1-FUDL-MEA-19-pol 8_0150423_E02_V2.CSV
-1.7924
activation loss
-3.056
ohmic loss
-4.0839
mass loss
Cell voltage [V]
Current Density [A/cm2]

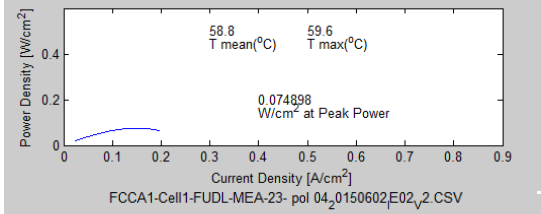
58.8
T mean(°C)
59.6
T max(°C)
0.074898
W/cm2 at Peak Power
Power Density [W/cm2]
Current Density [A/cm2]

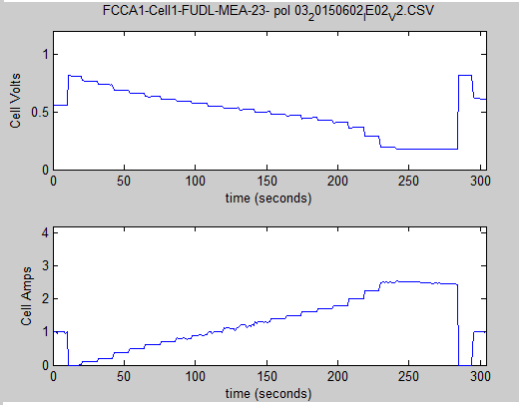
FCCA1-Cell1-FUDL-MEA-23- pol 03_0150602_E02_V2.CSV
Cell Volts
time (seconds)
Cell Amps
time (seconds)

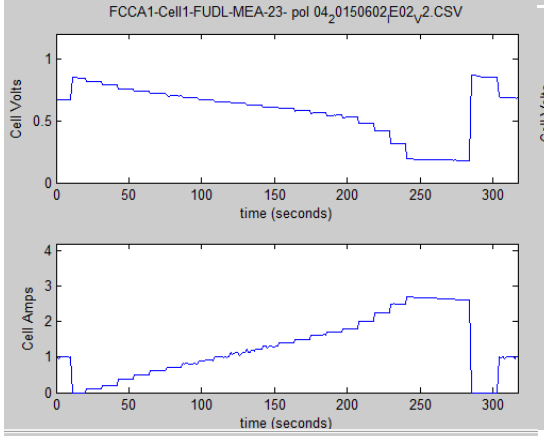
FCCA1-Cell1-FUDL-MEA-23- pol 04_0150602_E02_V2.CSV
Cell Volts
time (seconds)
Cell Amps
time (seconds)

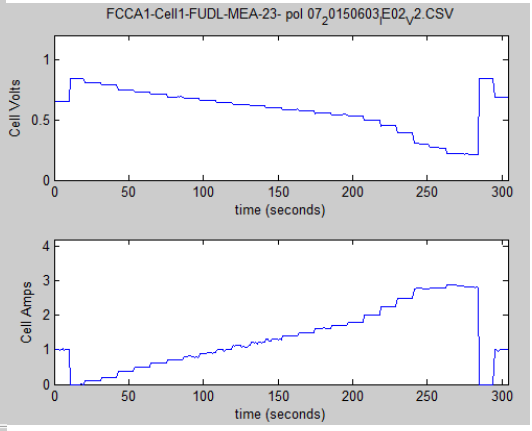
FCCA1-Cell1-FUDL-MEA-23- pol 07_0150603_E02_V2.CSV
Cell Volts
time (seconds)
Cell Amps
time (seconds)

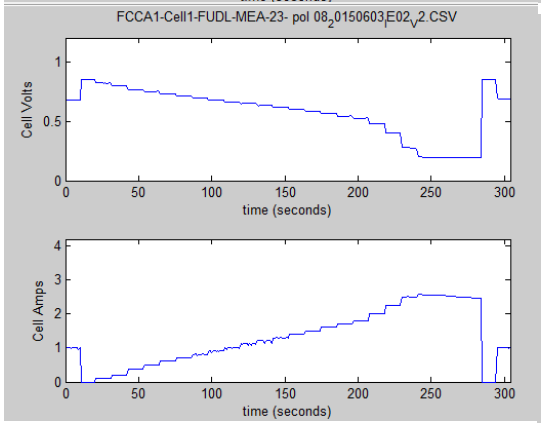
FCCA1-Cell1-FUDL-MEA-23- pol 08_0150603_E02_V2.CSV
Cell Volts
time (seconds)
Cell Amps
time (seconds)

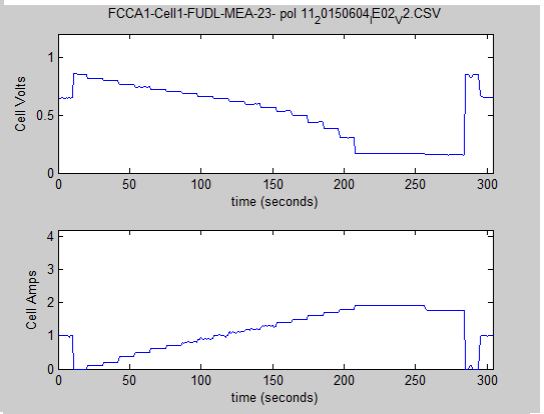
FCCA1-Cell1-FUDL-MEA-23- pol 11_0150604_E02_V2.CSV
Cell Volts
time (seconds)
Cell Amps
time (seconds)

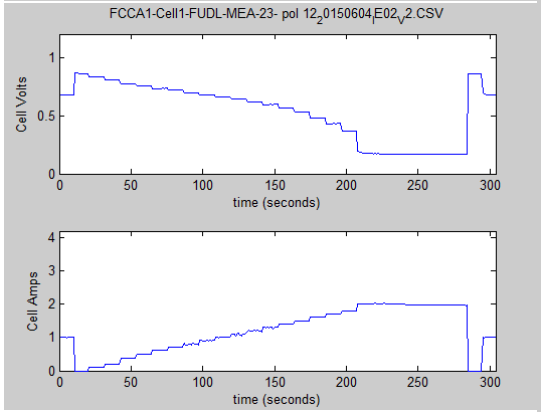
FCCA1-Cell1-FUDL-MEA-23- pol 12_0150604_E02_V2.CSV
Cell Volts
time (seconds)
Cell Amps
time (seconds)

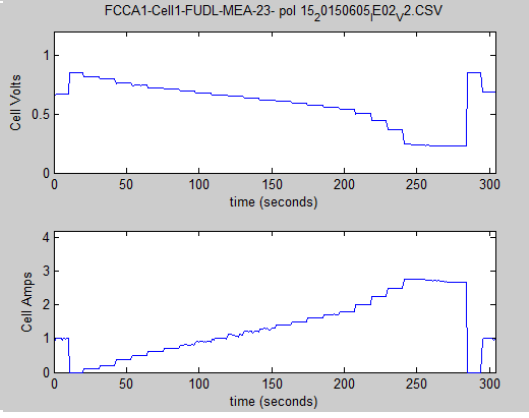
FCCA1-Cell1-FUDL-MEA-23- pol 15_0150605_E02_V2.CSV
Cell Volts
time (seconds)
Cell Amps
time (seconds)

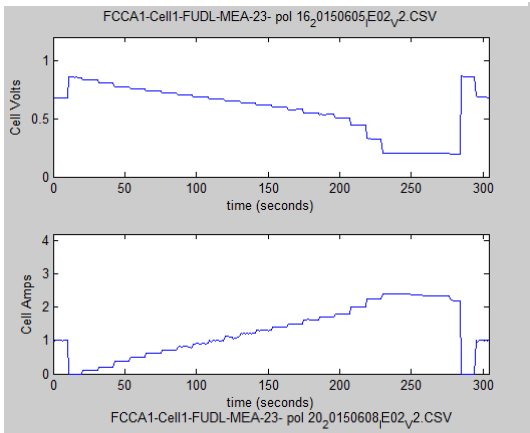
FCCA1-Cell1-FUDL-MEA-23- pol 16_20150605_E02_V2.CSV
Cell Volts
time (seconds)
Cell Amps
time (seconds)

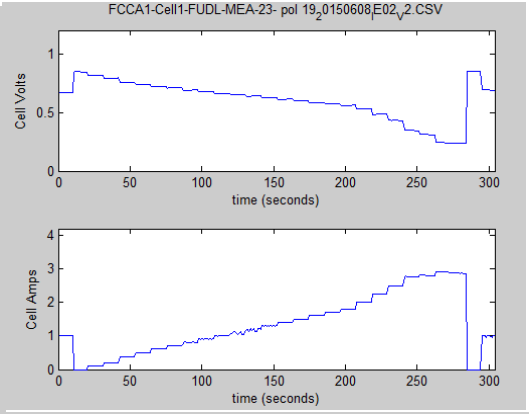
FCCA1-Cell1-FUDL-MEA-23- pol 19_20150608_E02_V2.CSV
Cell Volts
time (seconds)
Cell Amps
time (seconds)

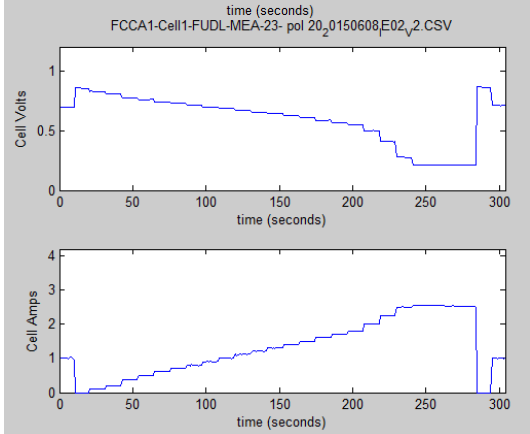
FCCA1-Cell1-FUDL-MEA-23- pol 20_20150608_E02_V2.CSV
Cell Volts
time (seconds)
Cell Amps
time (seconds)

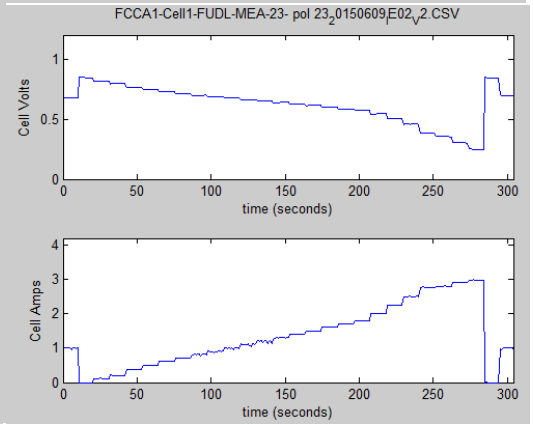
FCCA1-Cell1-FUDL-MEA-23- pol 23_20150609_E02_V2.CSV
Cell Volts
time (seconds)
Cell Amps
time (seconds)

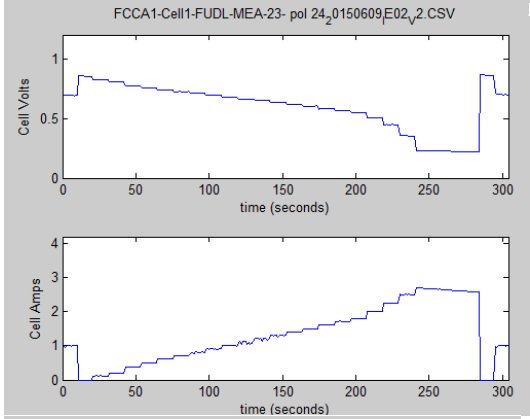
FCCA1-Cell1-FUDL-MEA-23- pol 24_20150609_E02_V2.CSV
Cell Volts
time (seconds)
Cell Amps
time (seconds)

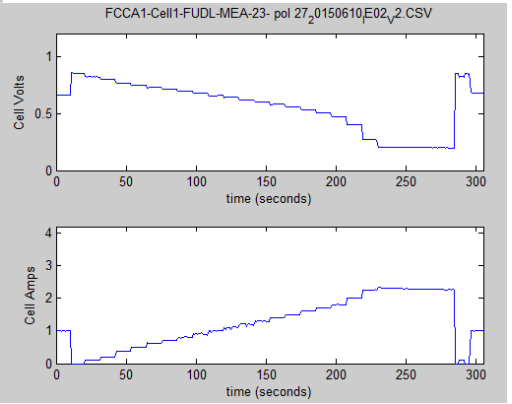
FCCA1-Cell1-FUDL-MEA-23- pol 27_20150610_E02_V2.CSV
Cell Volts
time (seconds)
Cell Amps
time (seconds)

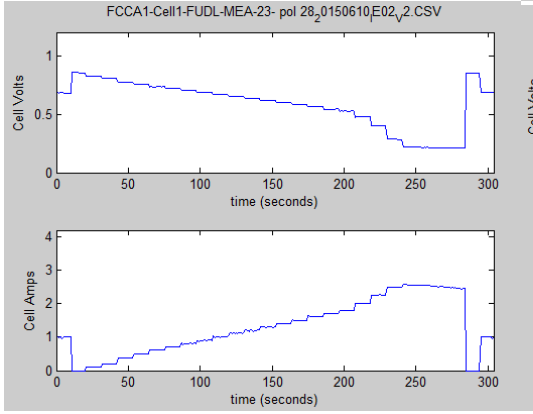
FCCA1-Cell1-FUDL-MEA-23- pol 28_20150610_E02_V2.CSV
Cell Volts
time (seconds)
Cell Amps
time (seconds)

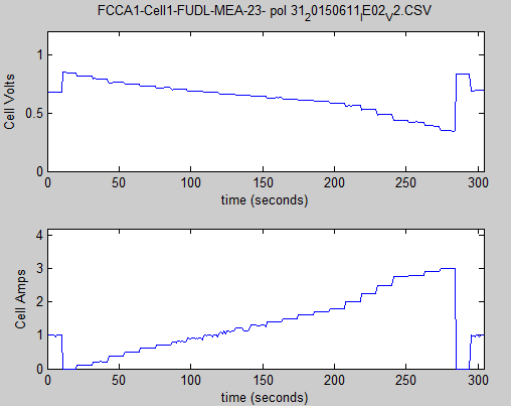
FCCA1-Cell1-FUDL-MEA-23- pol 31_20150611_E02_V2.CSV
Cell Volts
time (seconds)
Cell Amps
time (seconds)

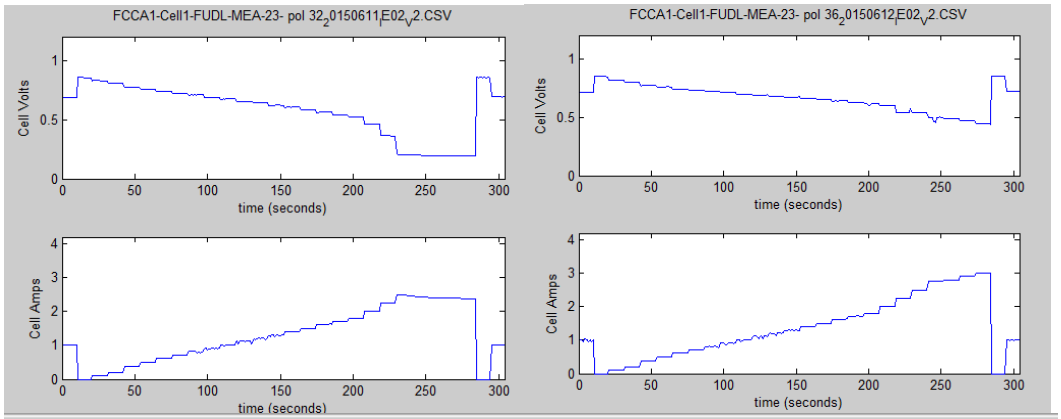
FCCA1-Cell1-FUDL-MEA-23- pol 32_20150611_E02_V2.CSV
FCCA1-Cell1-FUDL-MEA-23- pol 36_20150612_E02_V2.CSV
Cell Volts
Cell Amps
time (seconds)

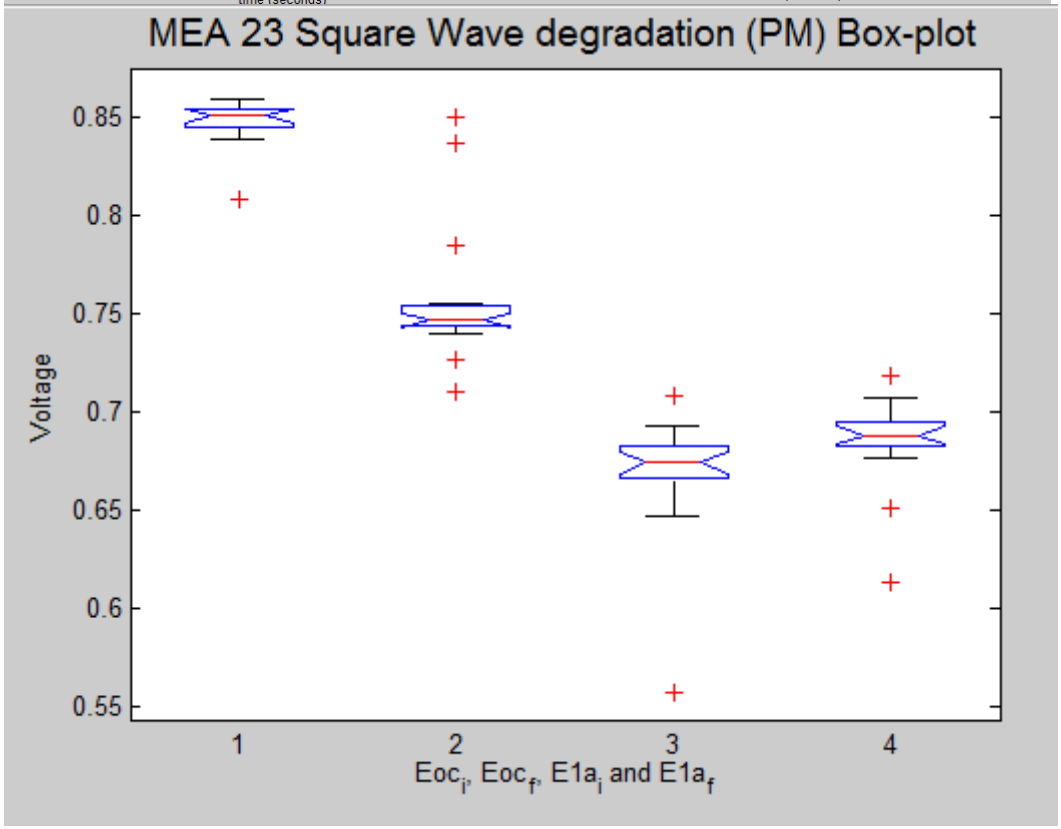
MEA 23 Square Wave degradation (PM) Box-plot
Voltage
0.85
0.8
0.75
0.7
0.65
0.6
0.55
1
2
3
4
Eoc_i, Eoc_f, E1a_i and E1a_f

MEA 23 (Torray cathode, Uniform, Square Wave)PM

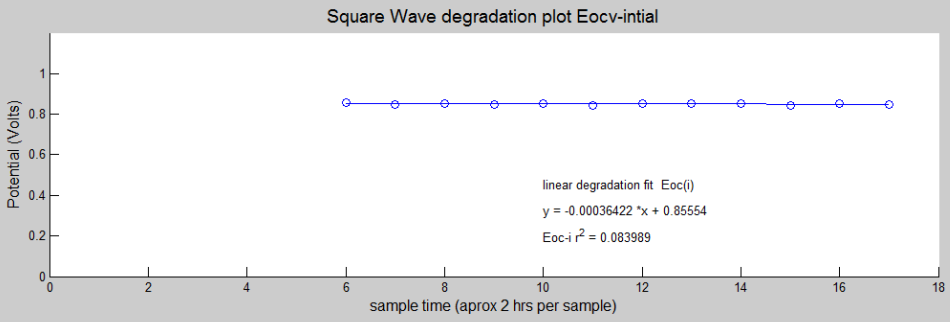

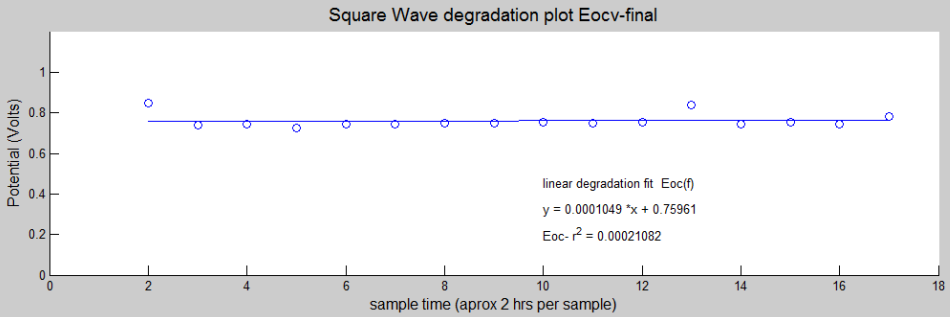

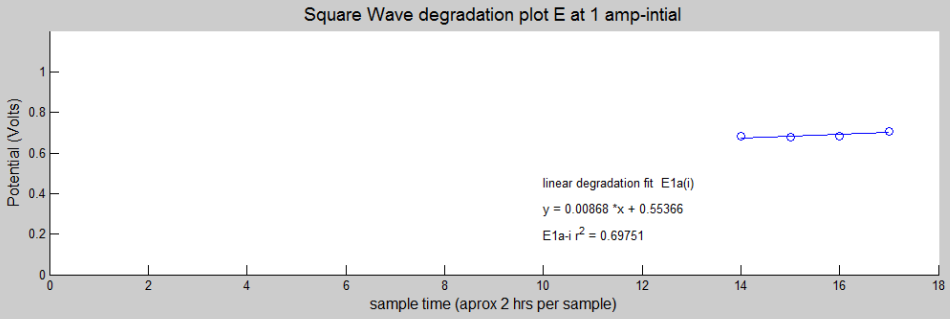

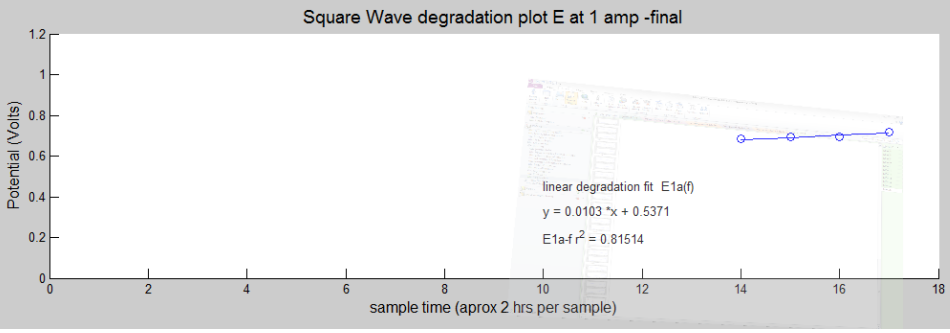

MEA 23 (Torray cathode, Uniform, Square Wave)PM

Square Wave degradation plot Eocv-intial

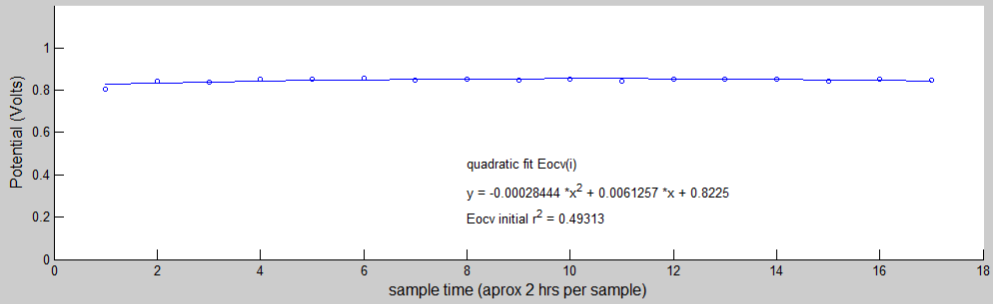

Square Wave degradation plot Eocv-final

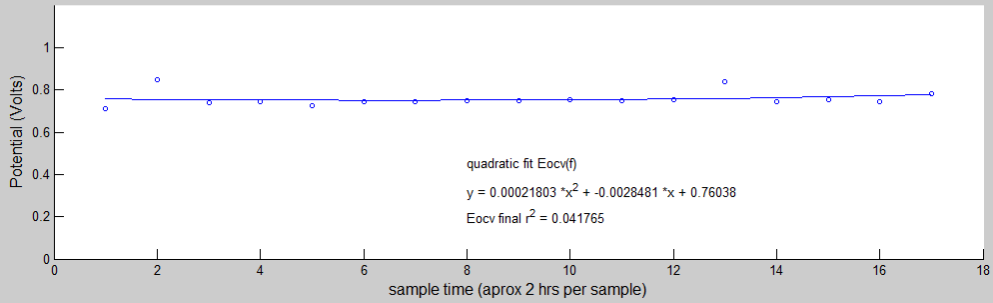

Square Wave degradation plot E1 Amp-intial

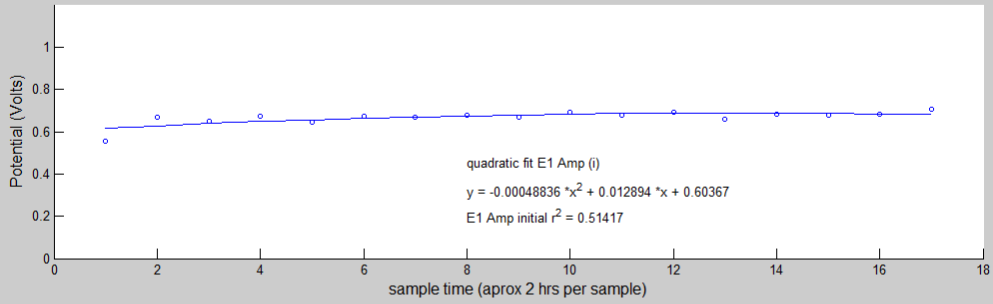

Square Wave degradation plot E1 Amp-final

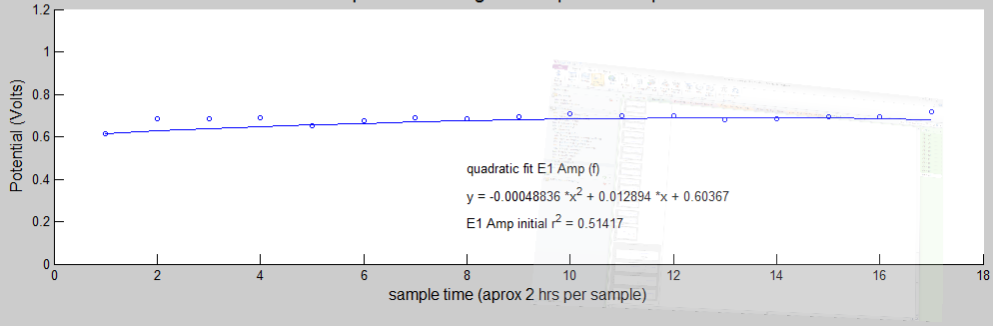

MEA 23 (Torray cathode, Uniform, Square Wave)PM

Square Wave spline filter plot Eocv-intial

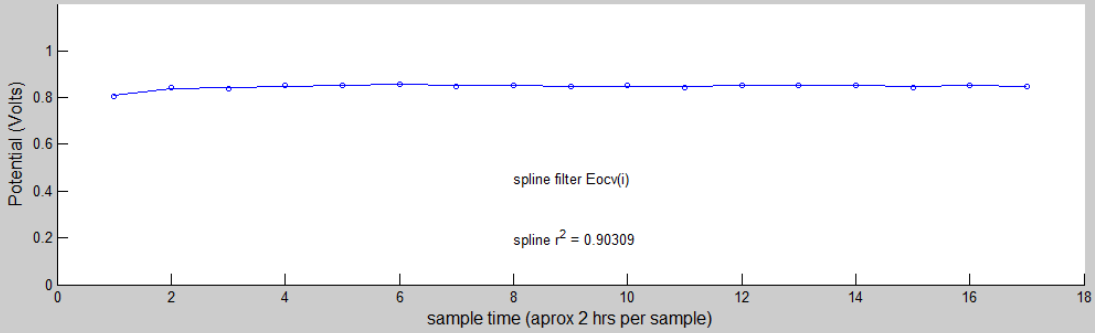

Square Wave spline filter plot Eocv-final

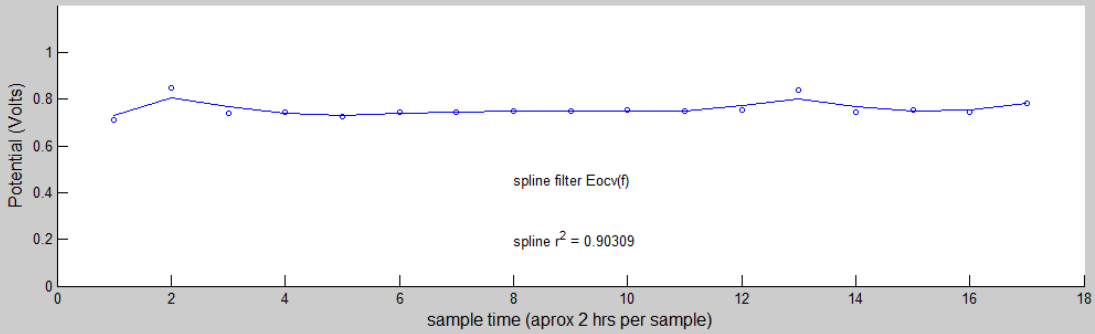

Square Wave spline filter plot E1 Amp-initial

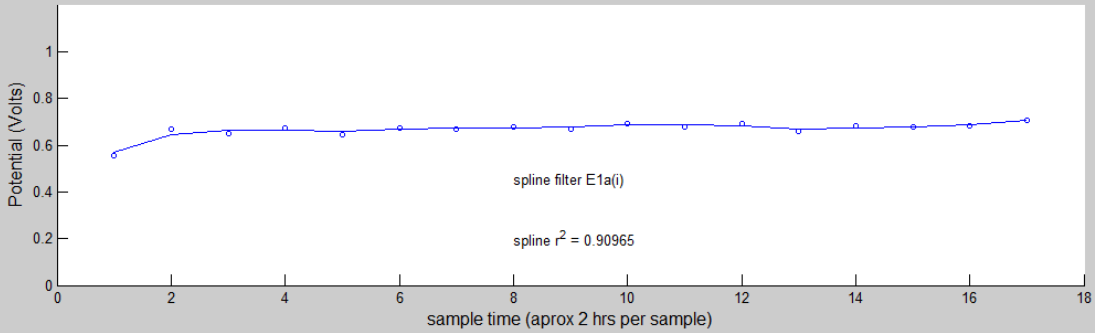

Square Wave spline filter plot E1 Amp-final

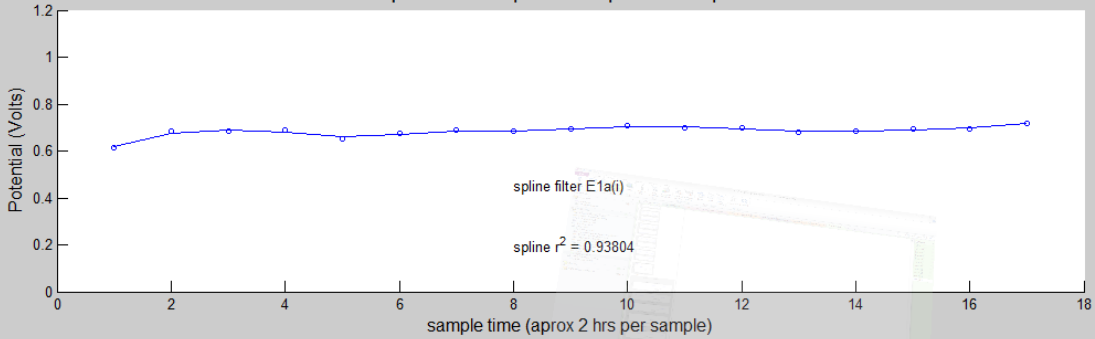

MEA 24

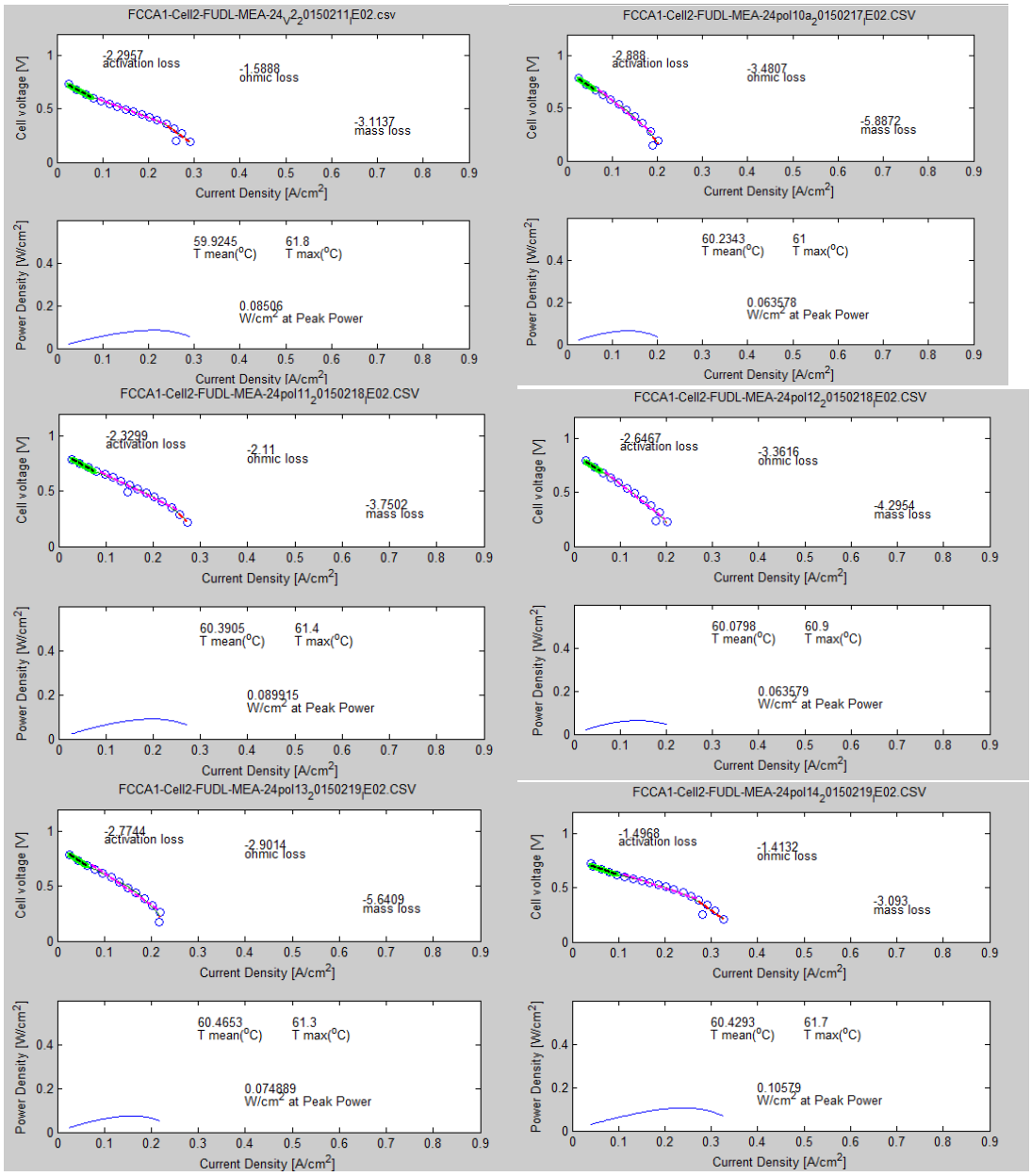
FCCA1-Cell2-FUDL-MEA-24_V_2_0150211_E02.csv
-2.2957 activation loss
-1.5888 ohmic loss
-3.1137 mass loss
Cell voltage [V]
Current Density [A/cm2]
59.9245 T mean(°C)
61.8 T max(°C)
0.08506 W/cm2 at Peak Power
Power Density [W/cm2]
FCCA1-Cell2-FUDL-MEA-24pol10a_2_0150217_E02.CSV
-2.888 activation loss
-3.4807 ohmic loss
-5.8872 mass loss
60.2343 T mean(°C)
61 T max(°C)
0.063578 W/cm2 at Peak Power
FCCA1-Cell2-FUDL-MEA-24pol11_2_0150218_E02.CSV
-2.3299 activation loss
-2.11 ohmic loss
-3.7502 mass loss
60.3905 T mean(°C)
61.4 T max(°C)
0.089915 W/cm2 at Peak Power
FCCA1-Cell2-FUDL-MEA-24pol12_2_0150218_E02.CSV
-2.6467 activation loss
-3.3616 ohmic loss
-4.2954 mass loss
60.0798 T mean(°C)
60.9 T max(°C)
0.063579 W/cm2 at Peak Power
FCCA1-Cell2-FUDL-MEA-24pol13_2_0150219_E02.CSV
-2.7744 activation loss
-2.9014 ohmic loss
-5.6409 mass loss
60.4653 T mean(°C)
61.3 T max(°C)
0.074889 W/cm2 at Peak Power
FCCA1-Cell2-FUDL-MEA-24pol14_2_0150219_E02.CSV
-1.4968 activation loss
-1.4132 ohmic loss
-3.093 mass loss
60.4293 T mean(°C)
61.7 T max(°C)
0.10579 W/cm2 at Peak Power

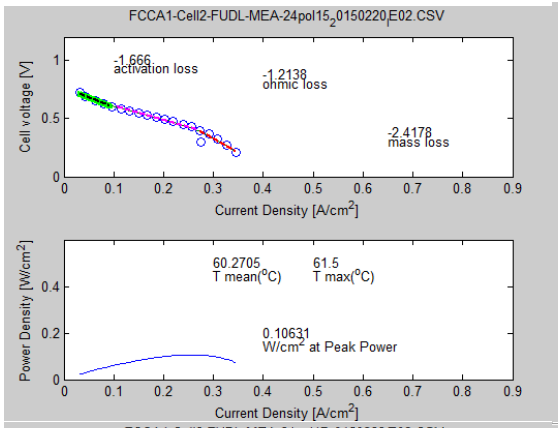
FCCA1-Cell2-FUDL-MEA-24pol15_0150220_E02.CSV
-1.666
activation loss
-1.2138
ohmic loss
-2.4178
mass loss
Cell voltage [V]
Current Density [A/cm2]
60.2705
T mean(°C)
61.5
T max(°C)
0.10631
W/cm2 at Peak Power
Power Density [W/cm2]
Current Density [A/cm2]

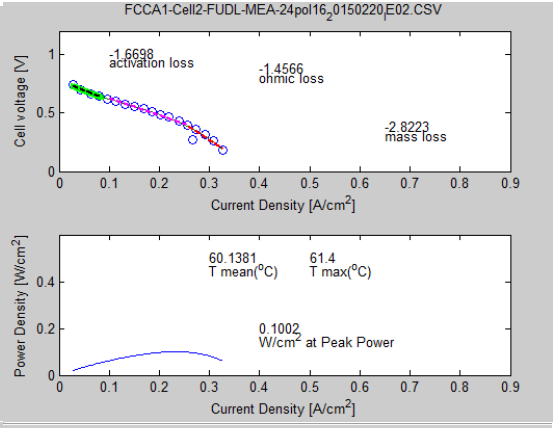
FCCA1-Cell2-FUDL-MEA-24pol16_0150220_E02.CSV
-1.6698
activation loss
-1.4566
ohmic loss
-2.8223
mass loss
Cell voltage [V]
Current Density [A/cm2]
60.1381
T mean(°C)
61.4
T max(°C)
0.1002
W/cm2 at Peak Power
Power Density [W/cm2]
Current Density [A/cm2]

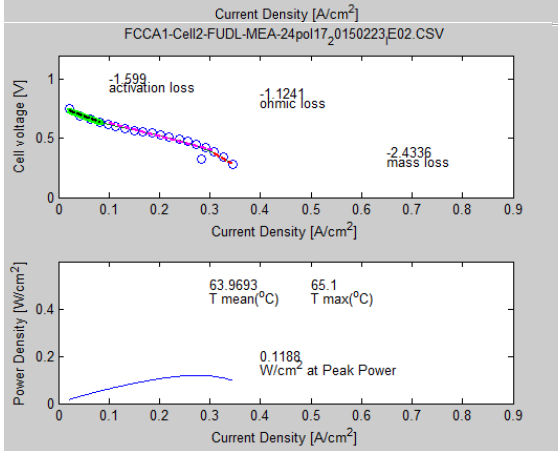
FCCA1-Cell2-FUDL-MEA-24pol17_0150223_E02.CSV
-1.599
activation loss
-1.1241
ohmic loss
-2.4336
mass loss
Cell voltage [V]
Current Density [A/cm2]
63.9693
T mean(°C)
65.1
T max(°C)
0.1188
W/cm2 at Peak Power
Power Density [W/cm2]
Current Density [A/cm2]

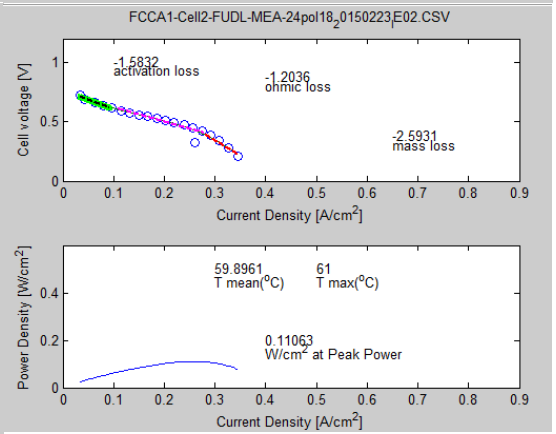
FCCA1-Cell2-FUDL-MEA-24pol18_0150223_E02.CSV
-1.5832
activation loss
-1.2036
ohmic loss
-2.5931
mass loss
Cell voltage [V]
Current Density [A/cm2]
59.8961
T mean(°C)
61
T max(°C)
0.11063
W/cm2 at Peak Power
Power Density [W/cm2]
Current Density [A/cm2]

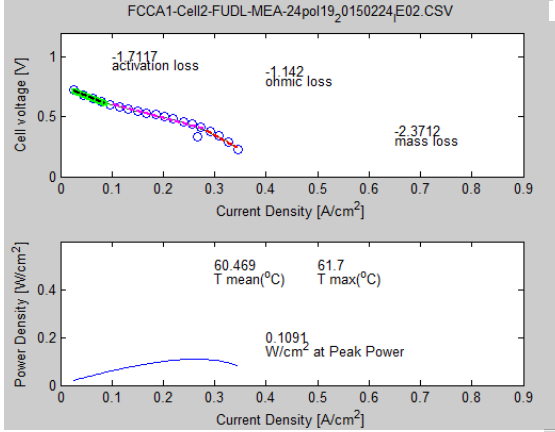
FCCA1-Cell2-FUDL-MEA-24pol19_0150224_E02.CSV
-1.7117
activation loss
-1.142
ohmic loss
-2.3712
mass loss
Cell voltage [V]
Current Density [A/cm2]
60.469
T mean(°C)
61.7
T max(°C)
0.1091
W/cm2 at Peak Power
Power Density [W/cm2]
Current Density [A/cm2]

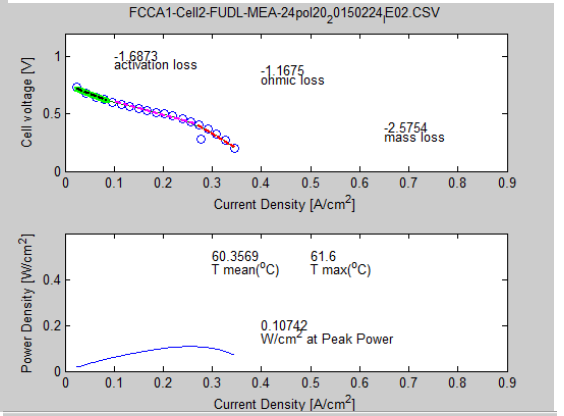
FCCA1-Cell2-FUDL-MEA-24pol20_0150224_E02.CSV
-1.6873
activation loss
-1.1675
ohmic loss
-2.5754
mass loss
Cell voltage [V]
Current Density [A/cm2]
60.3569
T mean(°C)
61.6
T max(°C)
0.10742
W/cm2 at Peak Power
Power Density [W/cm2]
Current Density [A/cm2]

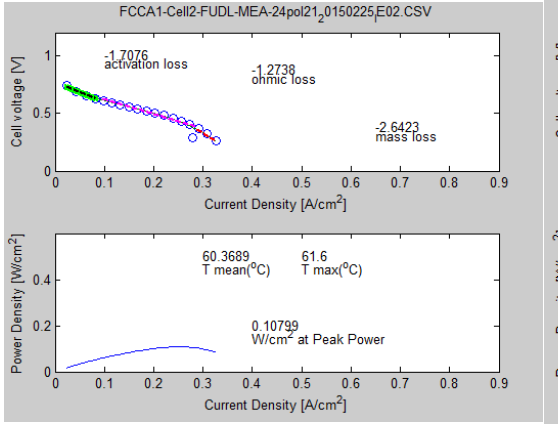
FCCA1-Cell2-FUDL-MEA-24pol21_0150225_E02.CSV
-1.7076
activation loss
-1.2738
ohmic loss
-2.6423
mass loss
Cell voltage [V]
Current Density [A/cm2]
60.3689
T mean(°C)
61.6
T max(°C)
0.10799
W/cm2 at Peak Power
Power Density [W/cm2]
Current Density [A/cm2]

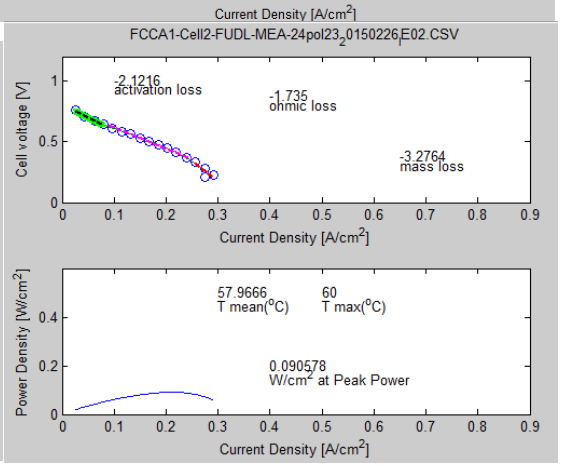
FCCA1-Cell2-FUDL-MEA-24pol23_0150226_E02.CSV
-2.1216
activation loss
-1.735
ohmic loss
-3.2764
mass loss
Cell voltage [V]
Current Density [A/cm2]
57.9666
T mean(°C)
60
T max(°C)
0.090578
W/cm2 at Peak Power
Power Density [W/cm2]
Current Density [A/cm2]

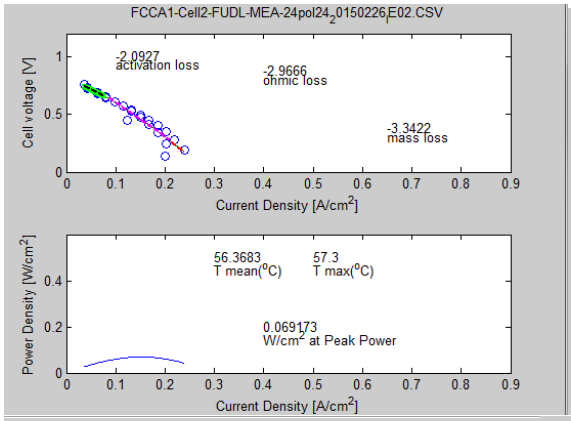
FCCA1-Cell2-FUDL-MEA-24pol24_20150226_E02.CSV
-2.0927
activation loss
-2.9666
ohmic loss
-3.3422
mass loss
Cell voltage [V]
Current Density [A/cm2]
56.3683
T mean(°C)
57.3
T max(°C)
0.069173
W/cm2 at Peak Power
Power Density [W/cm2]
Current Density [A/cm2]

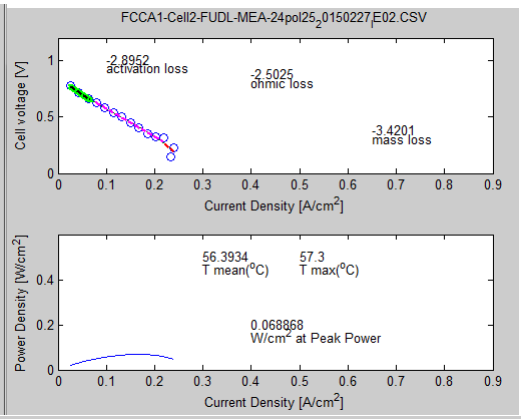
FCCA1-Cell2-FUDL-MEA-24pol25_20150227_E02.CSV
-2.8952
activation loss
-2.5025
ohmic loss
-3.4201
mass loss
Cell voltage [V]
Current Density [A/cm2]
56.3934
T mean(°C)
57.3
T max(°C)
0.068868
W/cm2 at Peak Power
Power Density [W/cm2]
Current Density [A/cm2]

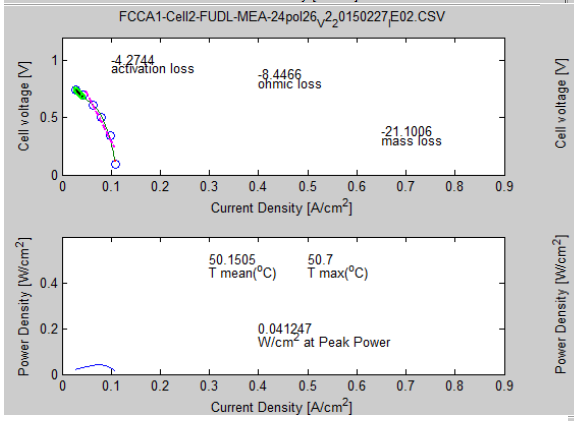
FCCA1-Cell2-FUDL-MEA-24pol26_v2_20150227_E02.CSV
-4.2744
activation loss
-8.4466
ohmic loss
-21.1006
mass loss
Cell voltage [V]
Current Density [A/cm2]
50.1505
T mean(°C)
50.7
T max(°C)
0.041247
W/cm2 at Peak Power
Power Density [W/cm2]
Current Density [A/cm2]

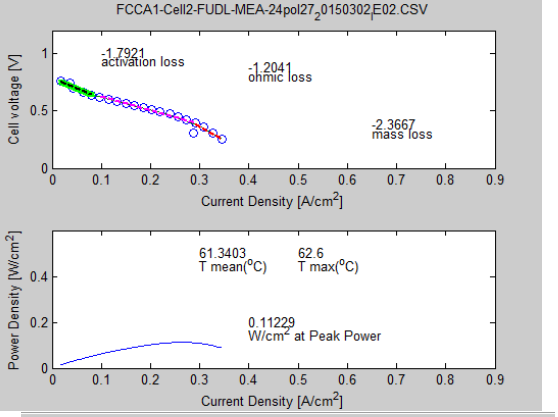
FCCA1-Cell2-FUDL-MEA-24pol27_20150302_E02.CSV
-1.7921
activation loss
-1.2041
ohmic loss
-2.3667
mass loss
Cell voltage [V]
Current Density [A/cm2]
61.3403
T mean(°C)
62.6
T max(°C)
0.11229
W/cm2 at Peak Power
Power Density [W/cm2]
Current Density [A/cm2]

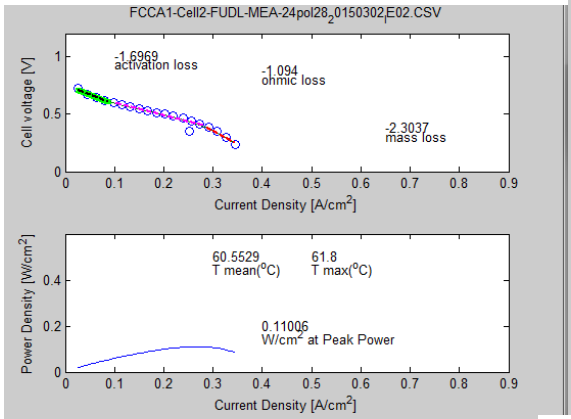
FCCA1-Cell2-FUDL-MEA-24pol28_20150302_E02.CSV
-1.6969
activation loss
-1.094
ohmic loss
-2.3037
mass loss
Cell voltage [V]
Current Density [A/cm2]
60.5529
T mean(°C)
61.8
T max(°C)
0.11006
W/cm2 at Peak Power
Power Density [W/cm2]
Current Density [A/cm2]

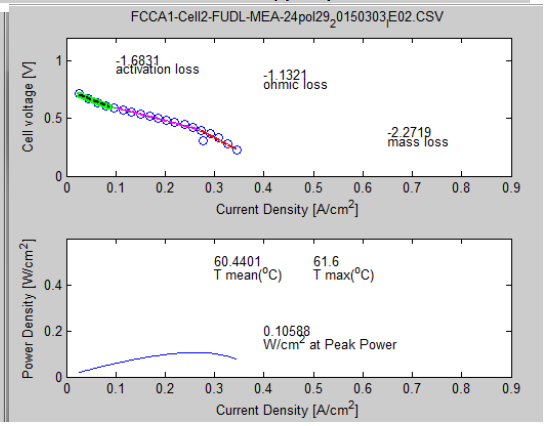
FCCA1-Cell2-FUDL-MEA-24pol29_20150303_E02.CSV
-1.6831
activation loss
-1.1321
ohmic loss
-2.2719
mass loss
Cell voltage [V]
Current Density [A/cm2]
60.4401
T mean(°C)
61.6
T max(°C)
0.10588
W/cm2 at Peak Power
Power Density [W/cm2]
Current Density [A/cm2]

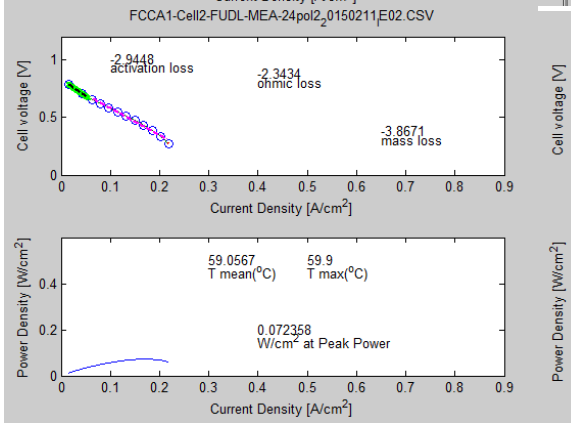
FCCA1-Cell2-FUDL-MEA-24pol2_20150211_E02.CSV
-2.9448
activation loss
-2.3434
ohmic loss
-3.8671
mass loss
Cell voltage [V]
Current Density [A/cm2]
59.0567
T mean(°C)
59.9
T max(°C)
0.072358
W/cm2 at Peak Power
Power Density [W/cm2]
Current Density [A/cm2]

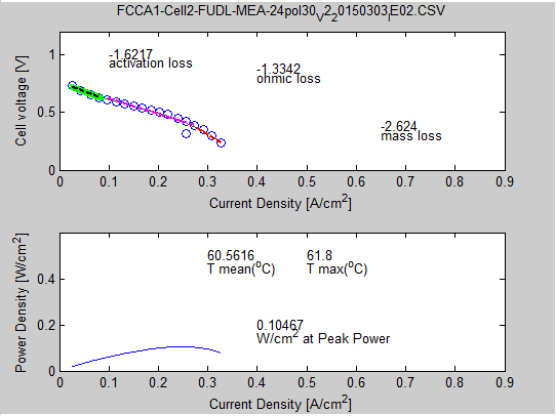
FCCA1-Cell2-FUDL-MEA-24pol30_v2_20150303_E02.CSV
-1.6217
activation loss
-1.3342
ohmic loss
-2.624
mass loss
Cell voltage [V]
Current Density [A/cm2]
60.5616
T mean(°C)
61.8
T max(°C)
0.10467
W/cm2 at Peak Power
Power Density [W/cm2]
Current Density [A/cm2]

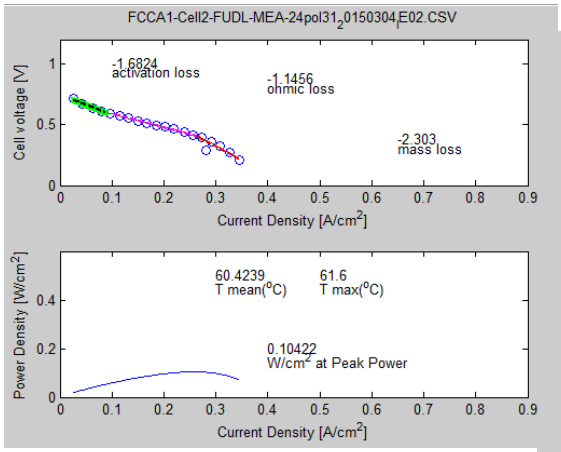
FCCA1-Cell2-FUDL-MEA-24pol31_20150304_E02.CSV
-1.6824
activation loss
-1.1456
ohmic loss
-2.303
mass loss
Cell voltage [V]
Current Density [A/cm2]
60.4239
T mean(°C)
61.6
T max(°C)
0.10422
W/cm2 at Peak Power
Power Density [W/cm2]
Current Density [A/cm2]

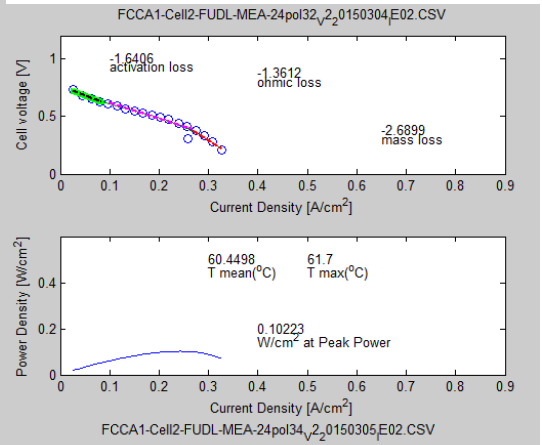
FCCA1-Cell2-FUDL-MEA-24pol32_V2_20150304_E02.CSV
-1.6406
activation loss
-1.3612
ohmic loss
-2.6899
mass loss
Cell voltage [V]
Current Density [A/cm2]
60.4498
T mean(°C)
61.7
T max(°C)
0.10223
W/cm2 at Peak Power
Power Density [W/cm2]
Current Density [A/cm2]

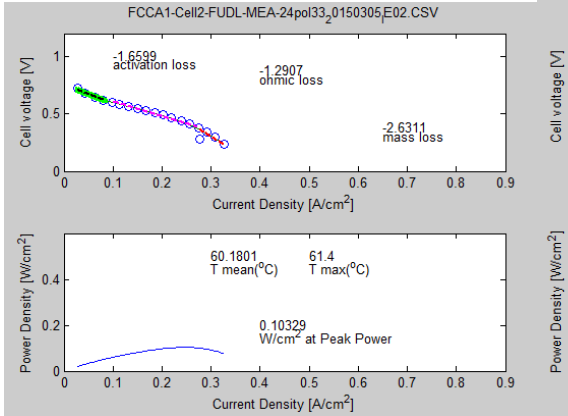
FCCA1-Cell2-FUDL-MEA-24pol33_20150305_E02.CSV
-1.6599
activation loss
-1.2907
ohmic loss
-2.6311
mass loss
Cell voltage [V]
Current Density [A/cm2]
60.1801
T mean(°C)
61.4
T max(°C)
0.10329
W/cm2 at Peak Power
Power Density [W/cm2]
Current Density [A/cm2]

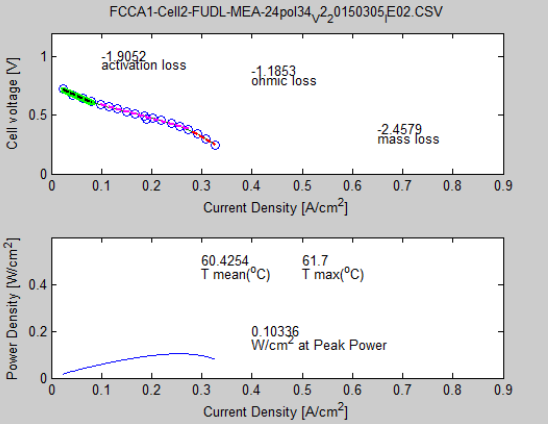
FCCA1-Cell2-FUDL-MEA-24pol34_V2_20150305_E02.CSV
-1.9052
activation loss
-1.1853
ohmic loss
-2.4579
mass loss
Cell voltage [V]
Current Density [A/cm2]
60.4254
T mean(°C)
61.7
T max(°C)
0.10336
W/cm2 at Peak Power
Power Density [W/cm2]
Current Density [A/cm2]

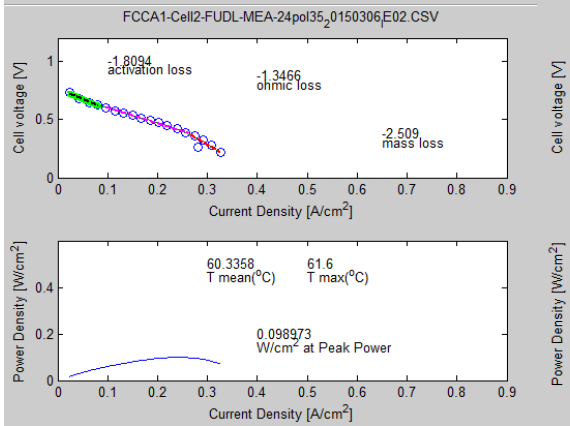
FCCA1-Cell2-FUDL-MEA-24pol35_20150306_E02.CSV
-1.8094
activation loss
-1.3466
ohmic loss
-2.509
mass loss
Cell voltage [V]
Current Density [A/cm2]
60.3358
T mean(°C)
61.6
T max(°C)
0.098973
W/cm2 at Peak Power
Power Density [W/cm2]
Current Density [A/cm2]

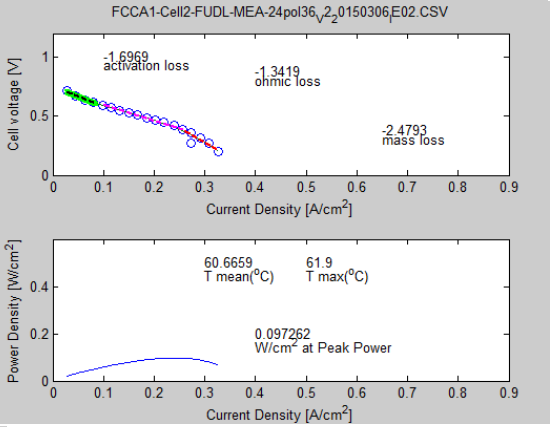
FCCA1-Cell2-FUDL-MEA-24pol36_V2_20150306_E02.CSV
-1.6969
activation loss
-1.3419
ohmic loss
-2.4793
mass loss
Cell voltage [V]
Current Density [A/cm2]
60.6659
T mean(°C)
61.9
T max(°C)
0.097262
W/cm2 at Peak Power
Power Density [W/cm2]
Current Density [A/cm2]

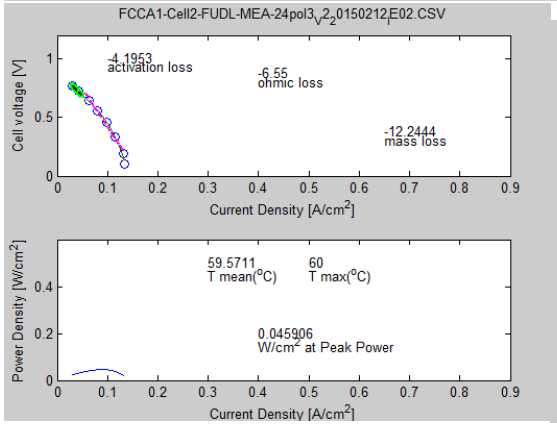
FCCA1-Cell2-FUDL-MEA-24pol3_V2_20150212_E02.CSV
-4.1953
activation loss
-6.55
ohmic loss
-12.2444
mass loss
Cell voltage [V]
Current Density [A/cm2]
59.5711
T mean(°C)
60
T max(°C)
0.045906
W/cm2 at Peak Power
Power Density [W/cm2]
Current Density [A/cm2]

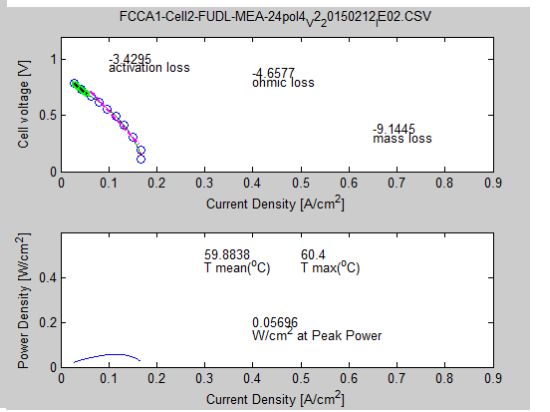
FCCA1-Cell2-FUDL-MEA-24pol4_V2_20150212_E02.CSV
-3.4295
activation loss
-4.6577
ohmic loss
-9.1445
mass loss
Cell voltage [V]
Current Density [A/cm2]
59.8838
T mean(°C)
60.4
T max(°C)
0.05696
W/cm2 at Peak Power
Power Density [W/cm2]
Current Density [A/cm2]

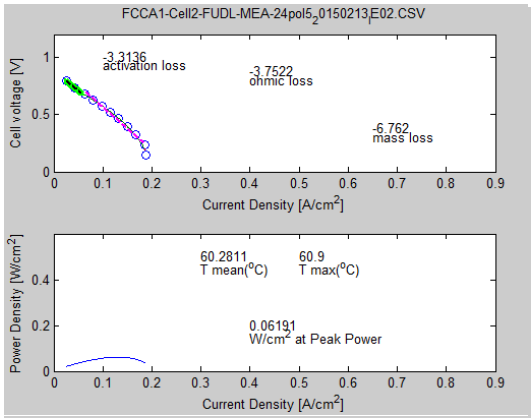
FCCA1-Cell2-FUDL-MEA-24pol5_2_0150213_E02.CSV
-3.3136
activation loss
-3.7522
ohmic loss
-6.762
mass loss
Cell voltage [V]
Current Density [A/cm2]
60.2811
T mean(°C)
60.9
T max(°C)
0.06191
W/cm2 at Peak Power
Power Density [W/cm2]
Current Density [A/cm2]

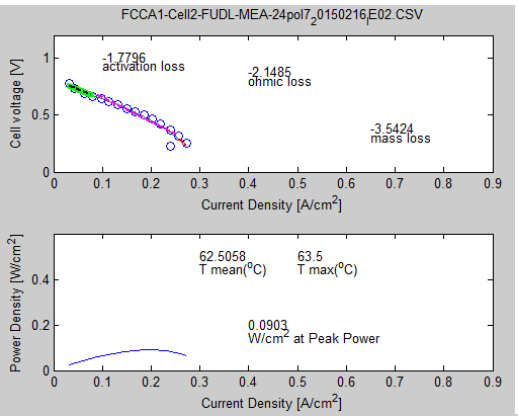
FCCA1-Cell2-FUDL-MEA-24pol7_2_0150216_E02.CSV
-1.7796
activation loss
-2.1485
ohmic loss
-3.5424
mass loss
Cell voltage [V]
Current Density [A/cm2]
62.5058
T mean(°C)
63.5
T max(°C)
0.0903
W/cm2 at Peak Power
Power Density [W/cm2]
Current Density [A/cm2]

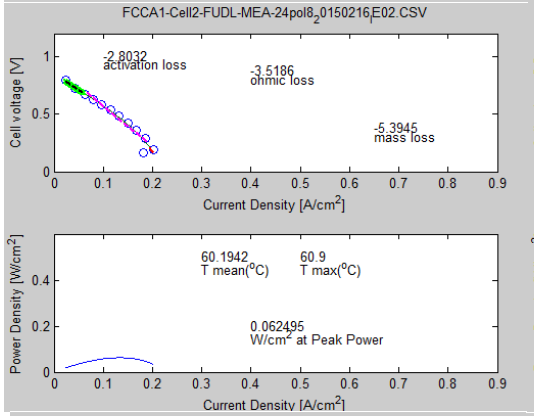
FCCA1-Cell2-FUDL-MEA-24pol8_2_0150216_E02.CSV
-2.8032
activation loss
-3.5186
ohmic loss
-5.3945
mass loss
Cell voltage [V]
Current Density [A/cm2]
60.1942
T mean(°C)
60.9
T max(°C)
0.062495
W/cm2 at Peak Power
Power Density [W/cm2]
Current Density [A/cm2]

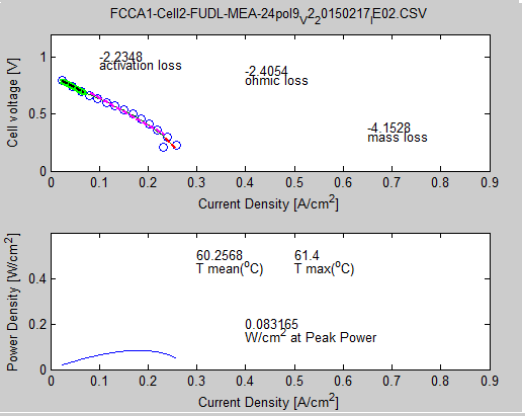
FCCA1-Cell2-FUDL-MEA-24pol9_V2_2_0150217_E02.CSV
-2.2348
activation loss
-2.4054
ohmic loss
-4.1528
mass loss
Cell voltage [V]
Current Density [A/cm2]
60.2568
T mean(°C)
61.4
T max(°C)
0.083165
W/cm2 at Peak Power
Power Density [W/cm2]
Current Density [A/cm2]

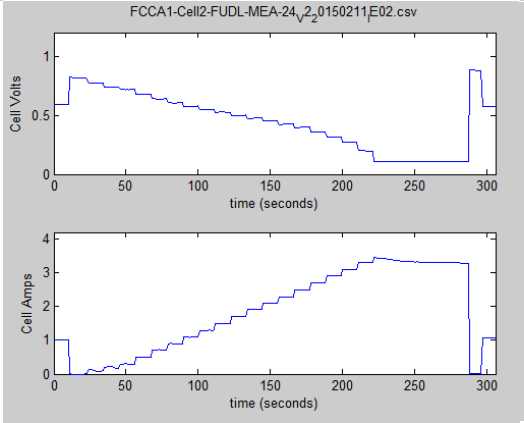
FCCA1-Cell2-FUDL-MEA-24_V2_2_0150211_E02.csv
Cell Volts
time (seconds)
Cell Amps
time (seconds)

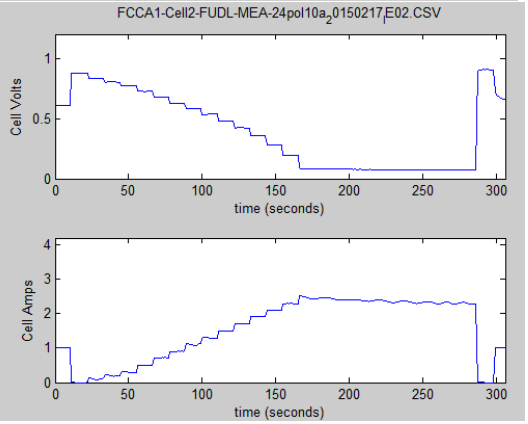
FCCA1-Cell2-FUDL-MEA-24pol10a_2_0150217_E02.CSV
Cell Volts
time (seconds)
Cell Amps
time (seconds)

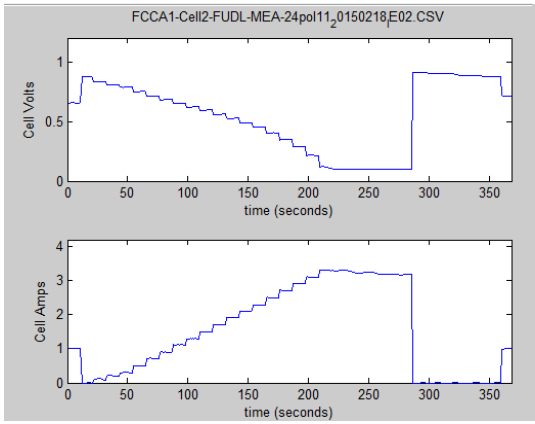
FCCA1-Cell2-FUDL-MEA-24pol11_2_0150218_E02.CSV
Cell Volts
time (seconds)
Cell Amps
time (seconds)

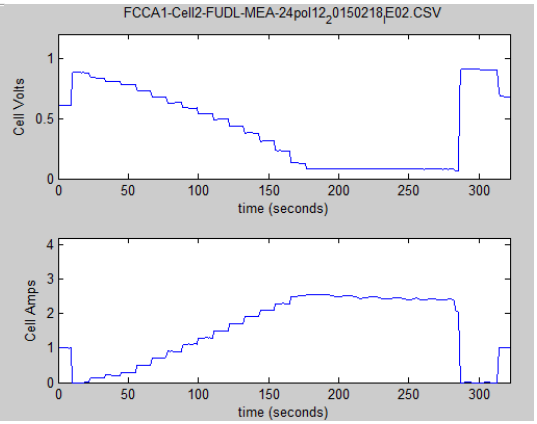
FCCA1-Cell2-FUDL-MEA-24pol12_2_0150218_E02.CSV
Cell Volts
time (seconds)
Cell Amps
time (seconds)

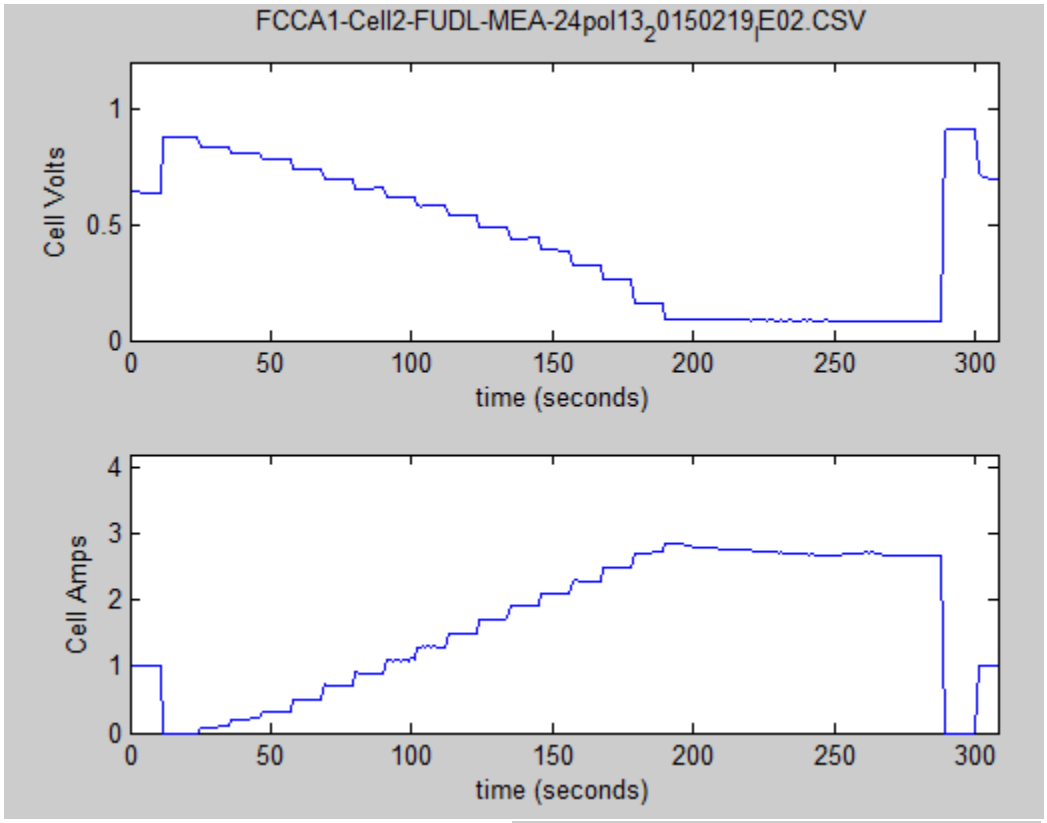
FCCA1-Cell2-FUDL-MEA-24pol13_20150219_E02.CSV
Cell Volts
time (seconds)
Cell Amps
time (seconds)

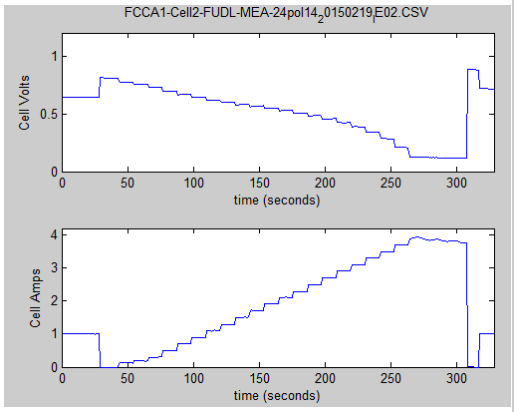
FCCA1-Cell2-FUDL-MEA-24pol14_20150219_E02.CSV
Cell Volts
time (seconds)
Cell Amps
time (seconds)

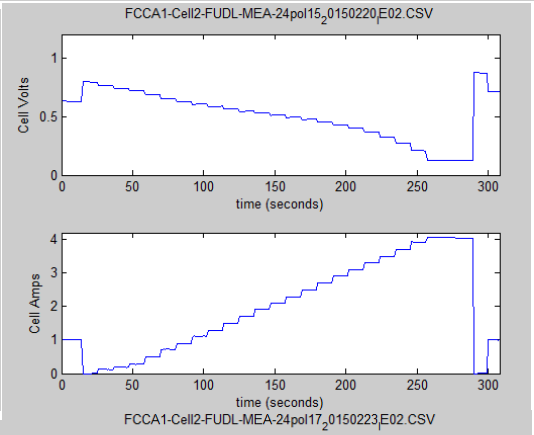
FCCA1-Cell2-FUDL-MEA-24pol15_20150220_E02.CSV
Cell Volts
time (seconds)
Cell Amps
time (seconds)

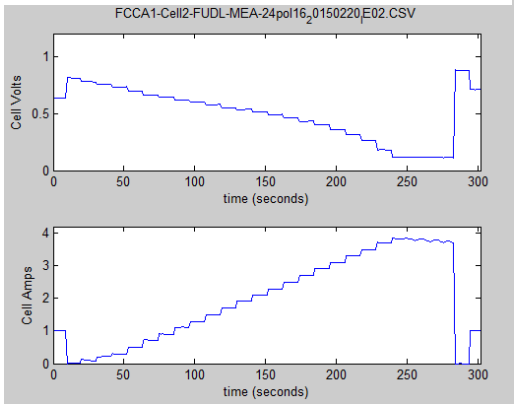
FCCA1-Cell2-FUDL-MEA-24pol16_20150220_E02.CSV
Cell Volts
time (seconds)
Cell Amps
time (seconds)

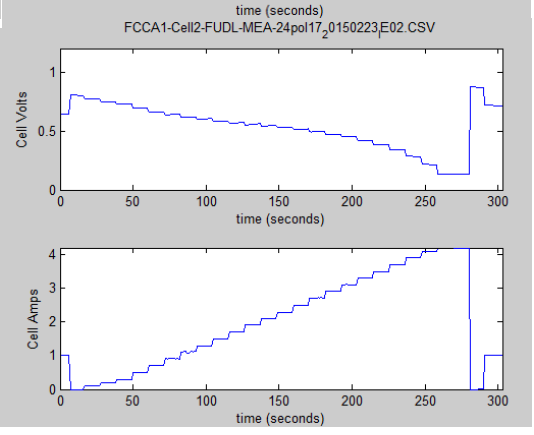
FCCA1-Cell2-FUDL-MEA-24pol17_20150223_E02.CSV
Cell Volts
time (seconds)
Cell Amps
time (seconds)

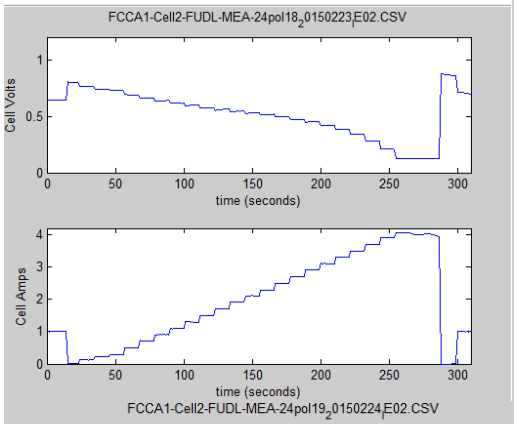
FCCA1-Cell2-FUDL-MEA-24pol18_20150223_E02.CSV
Cell Volts
time (seconds)
Cell Amps
time (seconds)

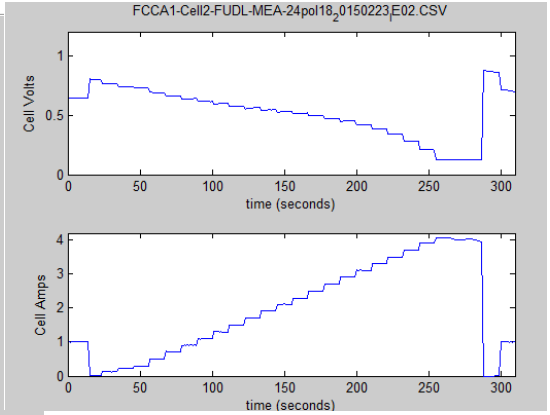
FCCA1-Cell2-FUDL-MEA-24pol18_20150223_E02.CSV
Cell Volts
time (seconds)
Cell Amps
time (seconds)

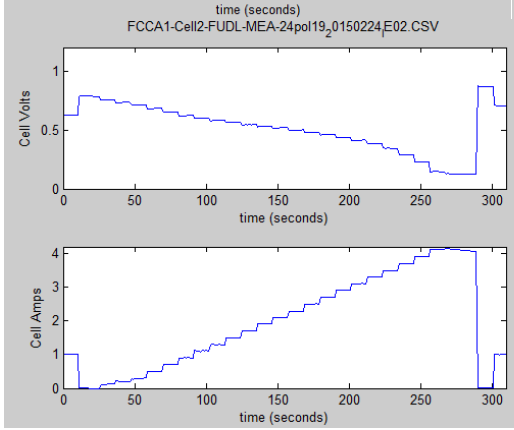
FCCA1-Cell2-FUDL-MEA-24pol19_20150224_E02.CSV
Cell Volts
time (seconds)
Cell Amps
time (seconds)

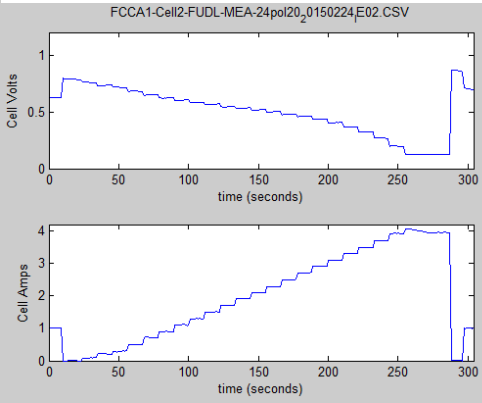
FCCA1-Cell2-FUDL-MEA-24pol20_20150224_E02.CSV
Cell Volts
time (seconds)
Cell Amps
time (seconds)

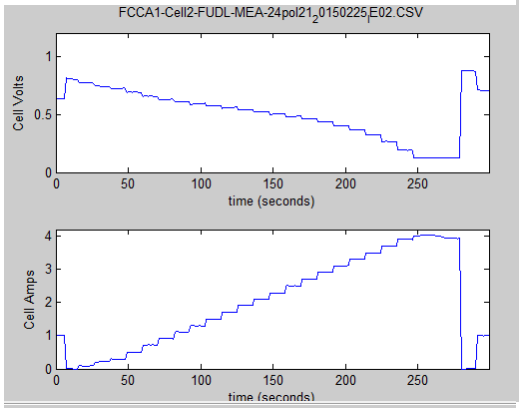
FCCA1-Cell2-FUDL-MEA-24pol21_20150225_E02.CSV
Cell Volts
time (seconds)
Cell Amps
time (seconds)

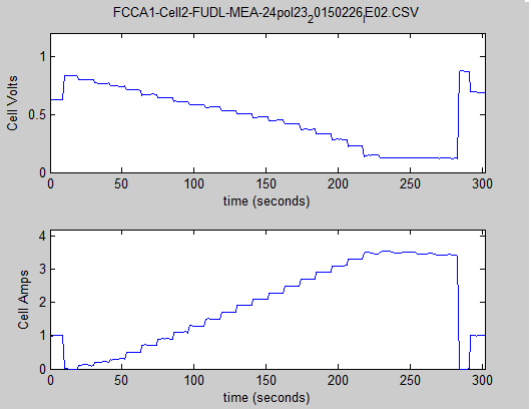
FCCA1-Cell2-FUDL-MEA-24pol23_20150226_E02.CSV
Cell Volts
time (seconds)
Cell Amps
time (seconds)

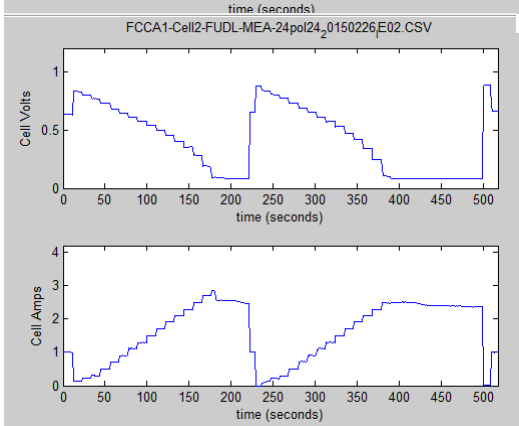
FCCA1-Cell2-FUDL-MEA-24pol24_20150226_E02.CSV
Cell Volts
time (seconds)
Cell Amps
time (seconds)

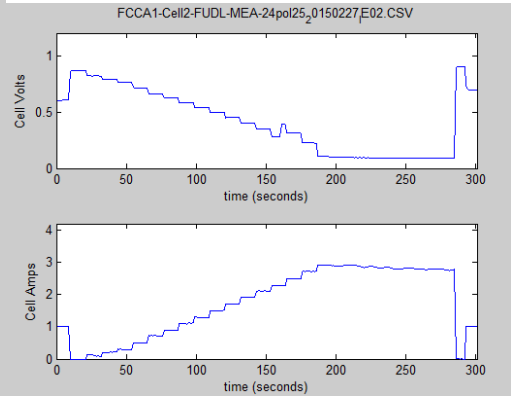
FCCA1-Cell2-FUDL-MEA-24pol25_20150227_E02.CSV
Cell Volts
time (seconds)
Cell Amps
time (seconds)

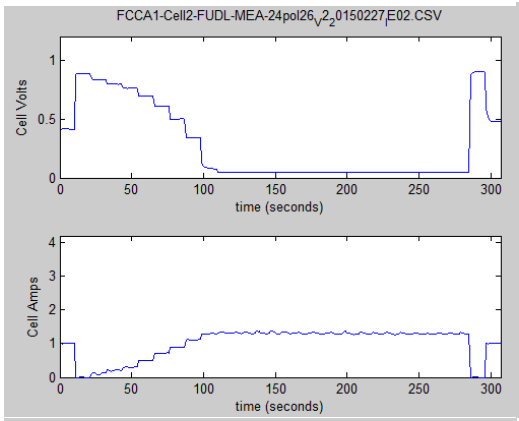
FCCA1-Cell2-FUDL-MEA-24pol26_V2_0150227_E02.CSV
Cell Volts
time (seconds)
Cell Amps
time (seconds)

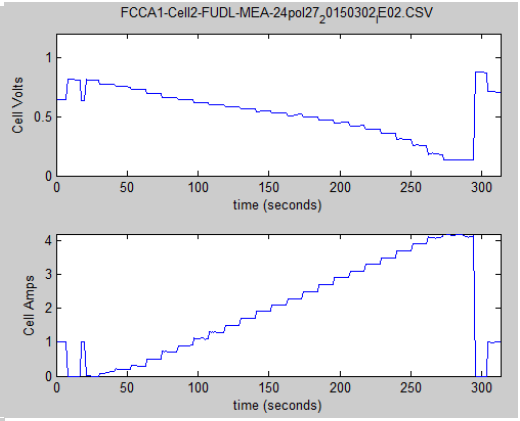
FCCA1-Cell2-FUDL-MEA-24pol27_2_0150302_E02.CSV
Cell Volts
time (seconds)
Cell Amps
time (seconds)

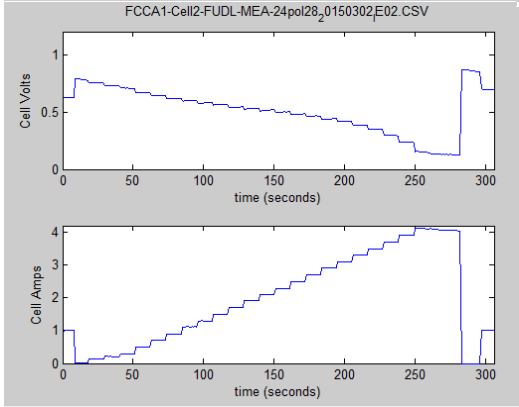
FCCA1-Cell2-FUDL-MEA-24pol28_2_0150302_E02.CSV
Cell Volts
time (seconds)
Cell Amps
time (seconds)

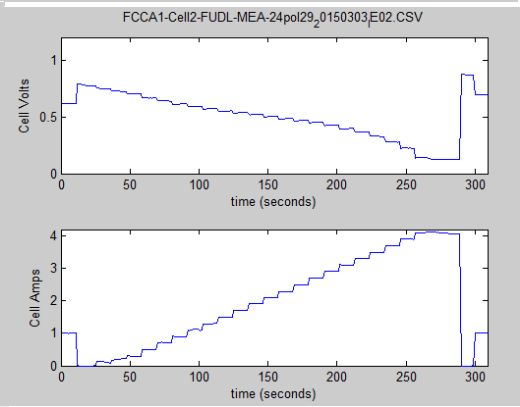
FCCA1-Cell2-FUDL-MEA-24pol29_2_0150303_E02.CSV
Cell Volts
time (seconds)
Cell Amps
time (seconds)

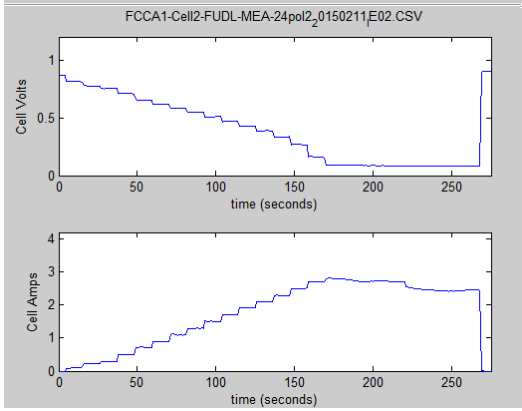
FCCA1-Cell2-FUDL-MEA-24pol2_2_0150211_E02.CSV
Cell Volts
time (seconds)
Cell Amps
time (seconds)

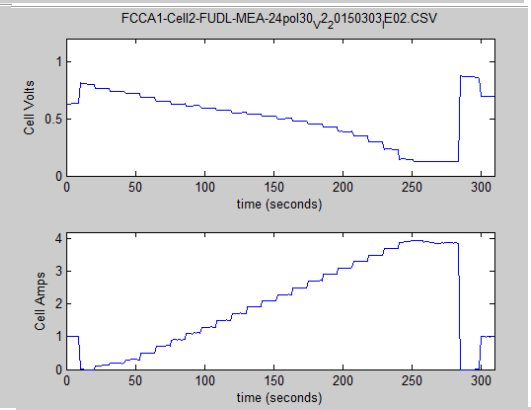
FCCA1-Cell2-FUDL-MEA-24pol30_V2_0150303_E02.CSV
Cell Volts
time (seconds)
Cell Amps
time (seconds)

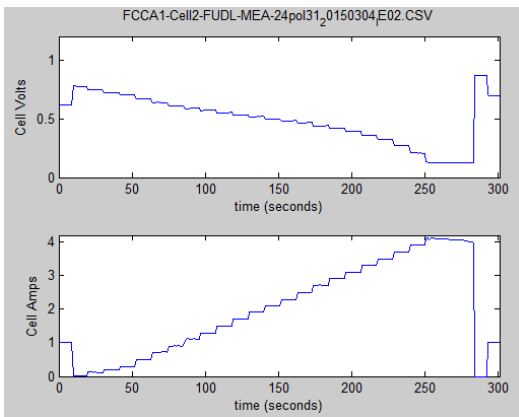
FCCA1-Cell2-FUDL-MEA-24pol31_2_0150304_E02.CSV
Cell Volts
time (seconds)
Cell Amps
time (seconds)

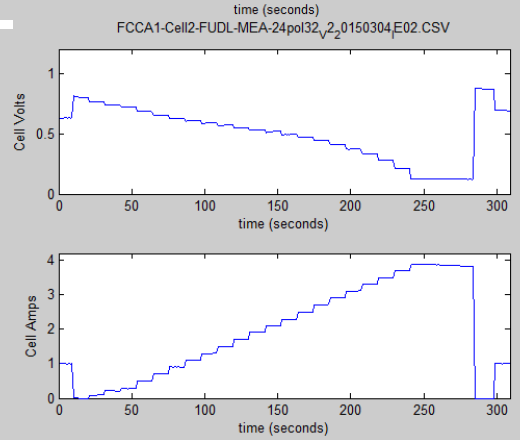
FCCA1-Cell2-FUDL-MEA-24pol32_V2_0150304_E02.CSV
Cell Volts
time (seconds)
Cell Amps
time (seconds)

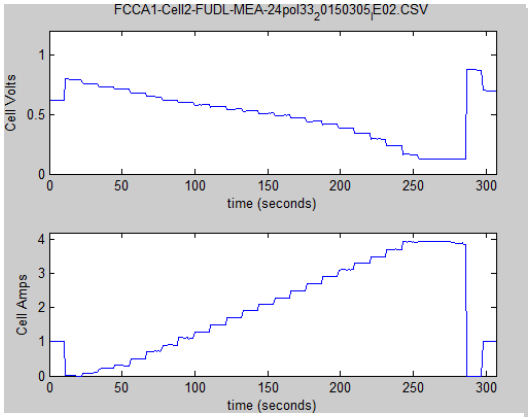
FCCA1-Cell2-FUDL-MEA-24pol33_20150305_E02.CSV
Cell Volts
time (seconds)
Cell Amps
time (seconds)

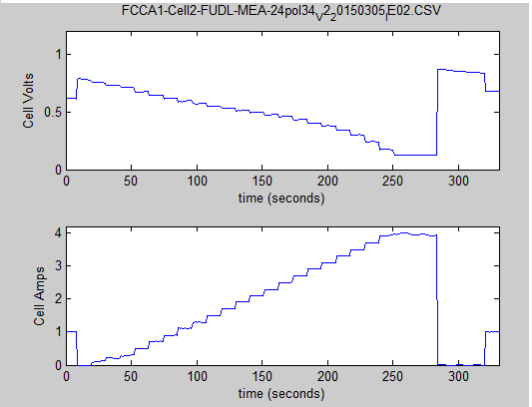
FCCA1-Cell2-FUDL-MEA-24pol34_V2_20150305_E02.CSV
Cell Volts
time (seconds)
Cell Amps
time (seconds)

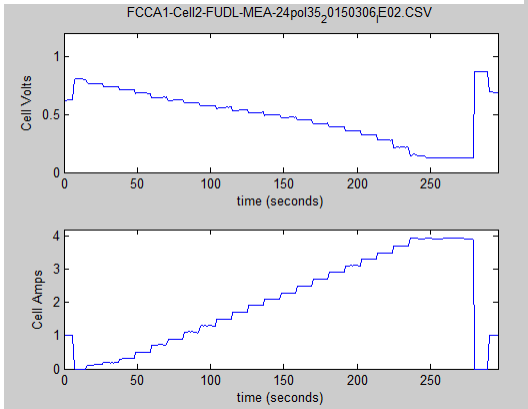
FCCA1-Cell2-FUDL-MEA-24pol35_20150306_E02.CSV
Cell Volts
time (seconds)
Cell Amps
time (seconds)

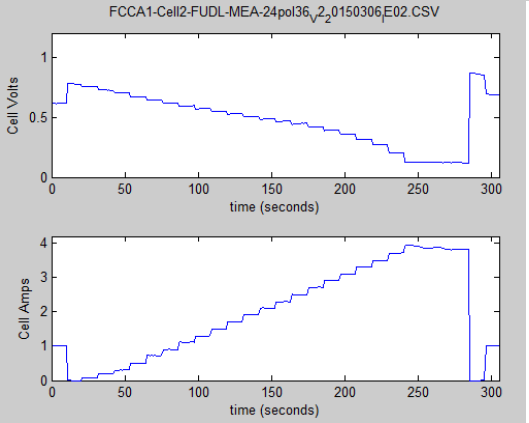
FCCA1-Cell2-FUDL-MEA-24pol36_V2_20150306_E02.CSV
Cell Volts
time (seconds)
Cell Amps
time (seconds)

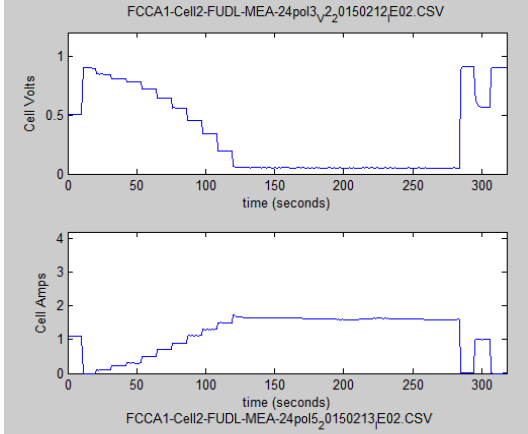
FCCA1-Cell2-FUDL-MEA-24pol3_V2_20150212_E02.CSV
Cell Volts
time (seconds)
Cell Amps
time (seconds)

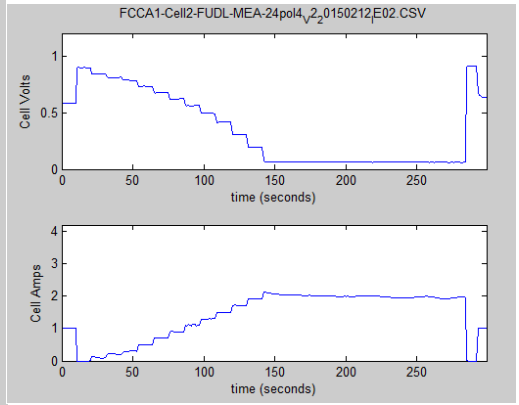
FCCA1-Cell2-FUDL-MEA-24pol4_V2_20150212_E02.CSV
Cell Volts
time (seconds)
Cell Amps
time (seconds)

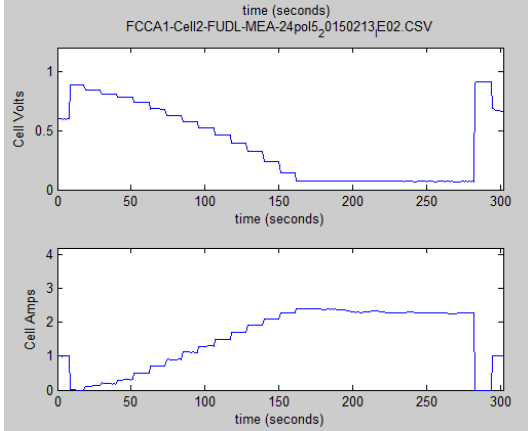
FCCA1-Cell2-FUDL-MEA-24pol5_20150213_E02.CSV
Cell Volts
time (seconds)
Cell Amps
time (seconds)

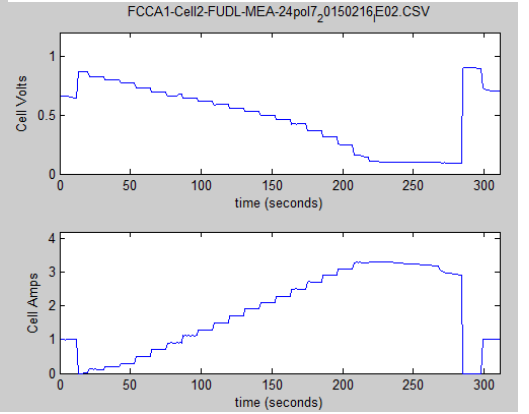
FCCA1-Cell2-FUDL-MEA-24pol7_20150216_E02.CSV
Cell Volts
time (seconds)
Cell Amps
time (seconds)

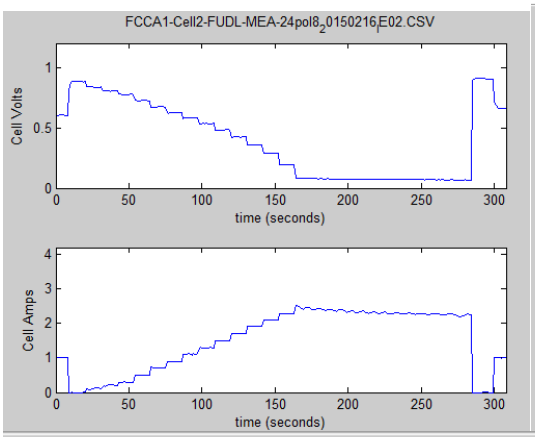
FCCA1-Cell2-FUDL-MEA-24pol8_20150216_E02.CSV
Cell Volts
time (seconds)
Cell Amps
time (seconds)

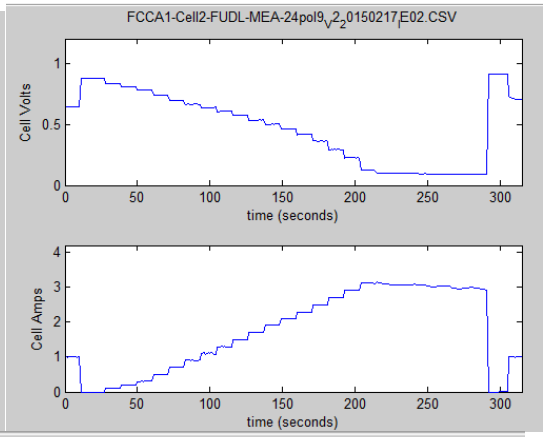
FCCA1-Cell2-FUDL-MEA-24pol9_V2_20150217_E02.CSV
Cell Volts
time (seconds)
Cell Amps
time (seconds)

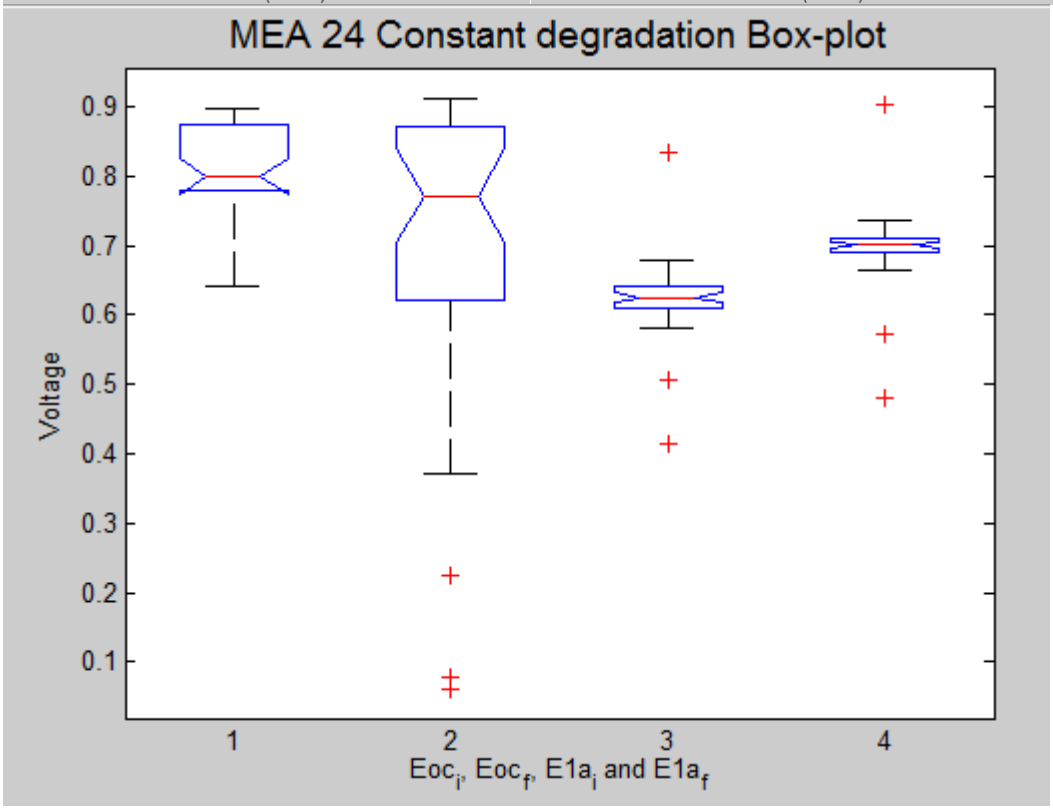
MEA 24 Constant degradation Box-plot
Voltage
Eoc_i, Eoc_f, E1a_i and E1a_f

MEA 24 (Torray cathode, Uniform, Constant)

Constant degradation plot Eocv-intial

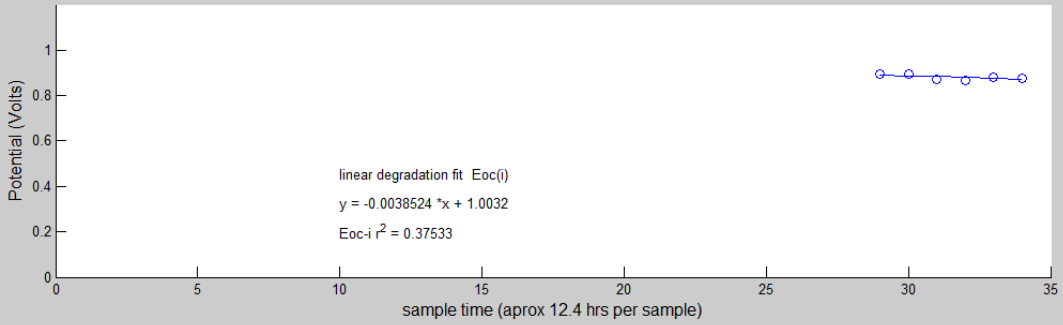

Constant degradation plot Eocv-final

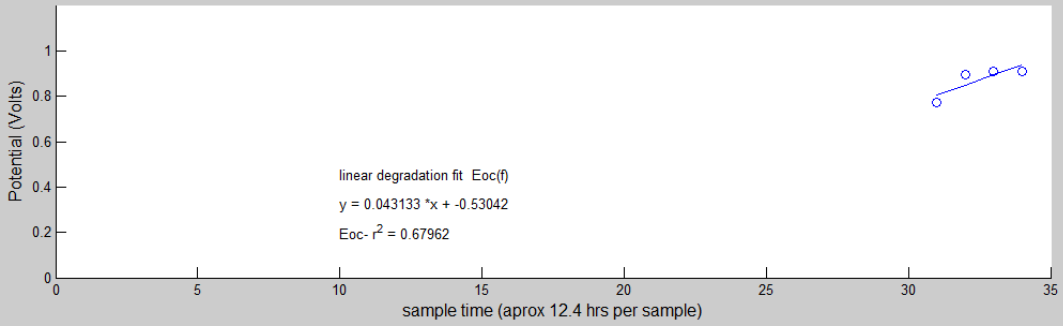

Constant degradation plot E at 1 amp-intial

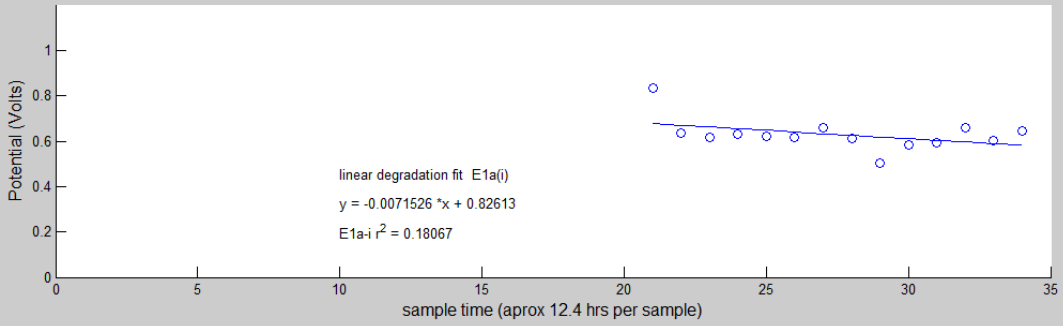

Constant degradation plot E at 1 amp -final

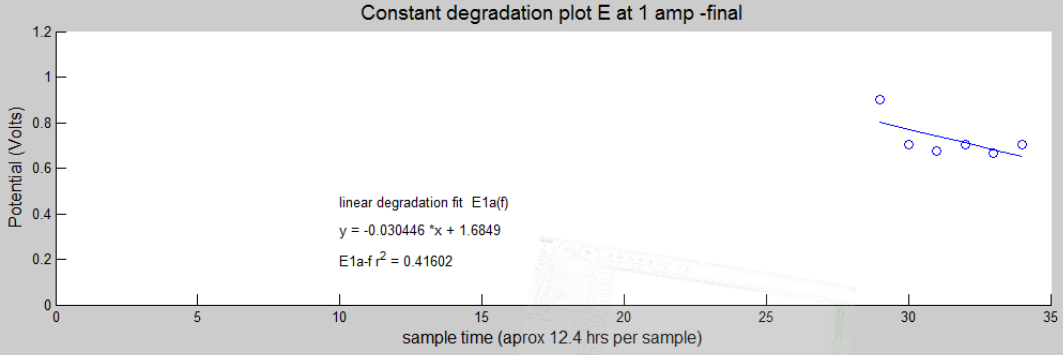

MEA 24 (Torray cathode, Uniform, Constant)

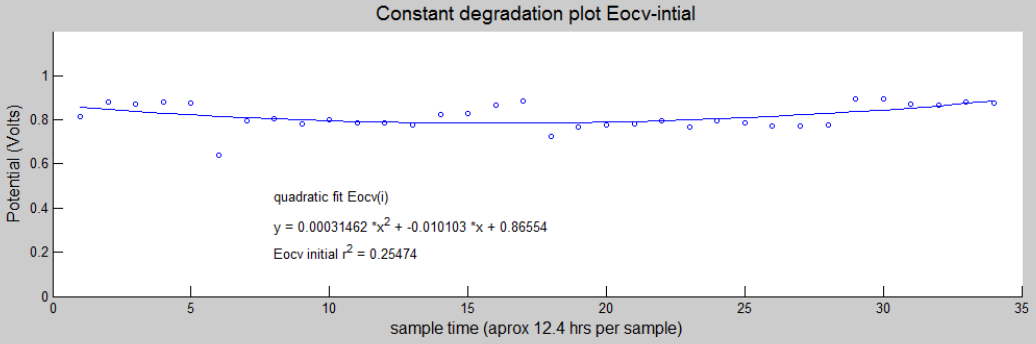

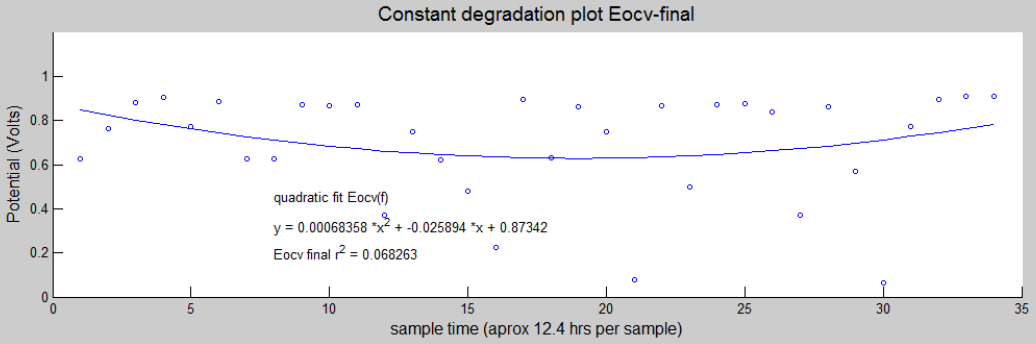

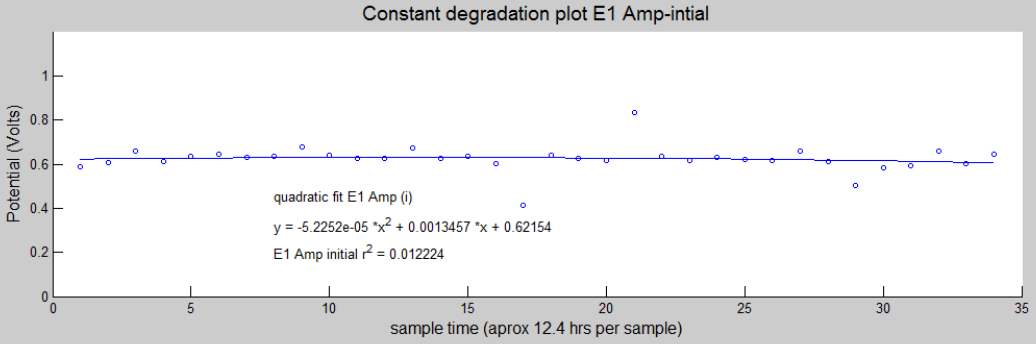

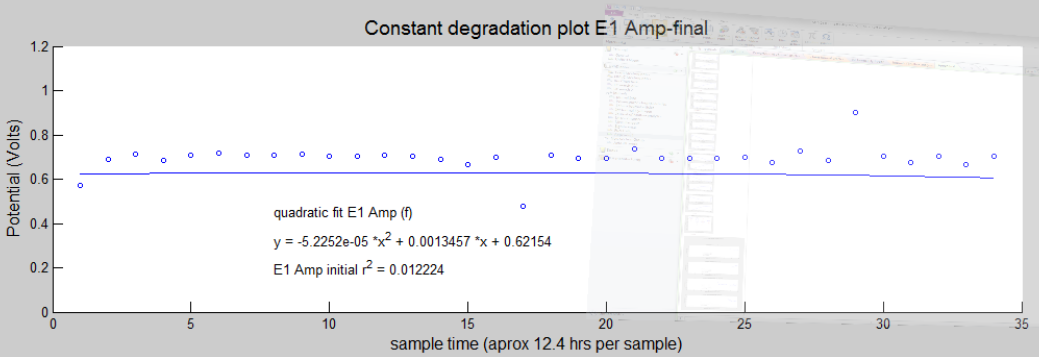

MEA 24 (Torray cathode, Uniform, Constant)

Constant spline filter plot Eocv-intial

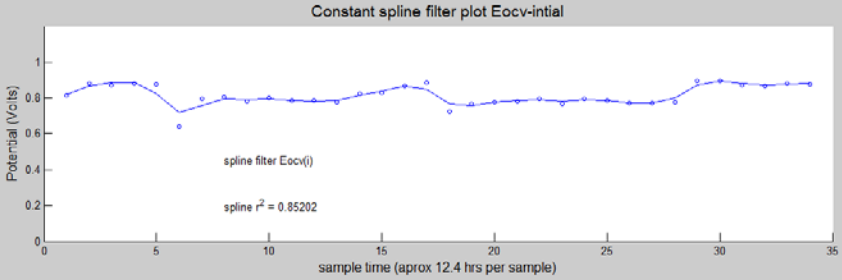

Constant spline filter plot Eocv-final

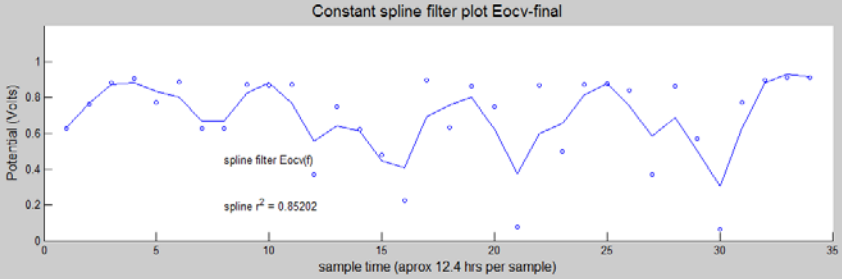

Constant spline filter plot E1 Amp-initial

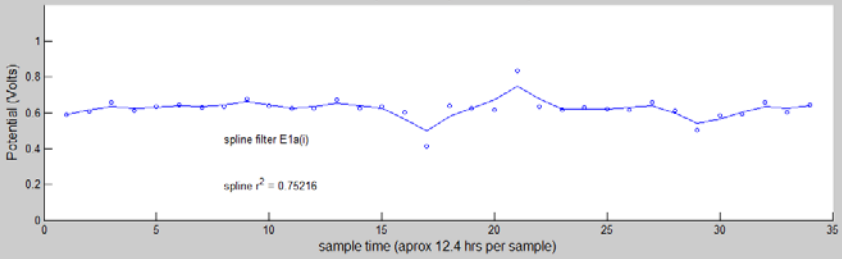

Constant spline filter plot E1 Amp-final

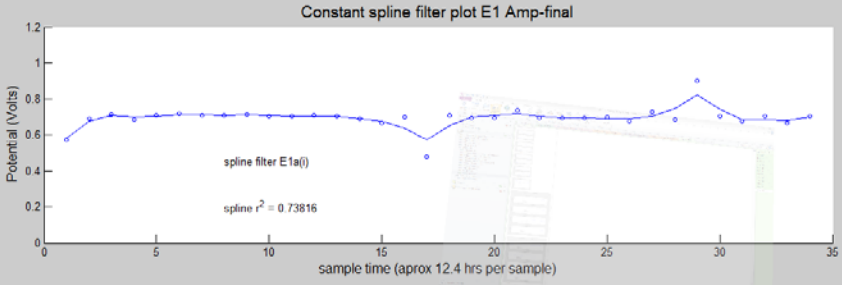

Appendix 5: Published papers

Journal paper:

McCarthy et al. (2016): PTFE mapping in gas diffusion media for PEMFCs using fluorescence microscopy: International Journal of Hydrogen Energy: **41**, 39, 17631–17643

Conference paper:

McCarthy et al. (2012): The impact of cathode gas diffusion structure on fuel cell performance: ABAF XIII, Burno, Czech Republic

The Impact of Cathode Gas Diffusion Layer Structure on Fuel Cell Performance

Nicholas McCarthy*, Ahmad El-kharouf**, Rui Chen*, Waldemar Bujalski**

* Dept. Aeronautical and Automotive Engineering, Loughborough University, LE11 3TU, U.K. ** PEM Fuel Cell Research Group, Centre for Hydrogen and Fuel Cell Research, School of Chemical Engineering, The University of Birmingham, Edgbaston, Birmingham B15 2TT, UK

Abstract

Four gas Diffusion Layer (GDL) materials have been investigated. Each Membrane Electrode Assembly (MEA) was manufactured with identical catalyst and binder loadings. MEAs were tested in-situ using a 'Fuel Cell Component Analyser' and polarisation curves produced and compared. GDL properties obtained in a previous work were considered for the analysis of the results. Results show differences in the polarisation response for different GDL structures; indicating changes in resistance loss, mass transport loss, and the flooding effects on fuel cells due to GDL structure.

Introduction

Polymer Electrolyte Membrane Fuel Cells (PEMFCs) offer the potential of efficient, sustainable power solutions for the future. A key element in these devices is the Gas Diffusion Layer (GDL). It is critical for the transport of reactants to the catalyst active sites, the transport of charge into and out of the cell, and water management in the MEA. The variation in performance for different GDLs has been reported in the literature [1, 2]. The difference is explained by the variation in the characteristics of the samples tested, however, due to the many variables in the GDL materials properties, explaining the variation in GDL performance can prove to be challenging. Some studies have focused on testing GDL properties in order to achieve a better understanding of GDLs behaviour and the relationship between the different properties [3] [4] [5].

Usually, a GDL consists of a carbon fibre substrate that is carbonised and teflonated. Commonly GDLs have a Micro-Porous Layer (MPL) painted on one side of the substrate to enhance water transport away from the catalyst layer, and provide a smooth surface with lower contact resistance for the catalyst layer. Different fibre structures are used for GDLs, namely; woven cloths, non-woven straight fibres paper, and non-woven felt paper. The fibre structure of the substrate in the GDL plays an important role in its

function and therefore affects the performance of the cell. Previous work has indicated that woven carbon GDLs have higher power densities [6], [7] and are more efficient at higher humidity [8]. In comparison non-woven carbon fibres, 'Papers' and 'Felts', are competitive on price, easier to work with, and mechanically stiffer.

This paper discusses preliminary results to date of in-situ testing for MEAs of different GDLs with the variation of structure and bulk density.

Method

Two, Intelligent Energy Ltd (I.E. Ltd), Fuel Cell Component Analysers (FCCA) were used to establish baseline measurements on a wide variety of commercially available GDLs. Both consist of four test chambers, each with independent anode and cathode gas flow and pressure control. Cell humidification is achieved through a humidification membrane supplied by the exhaust gases form the cell reaction, achieving 100% relative humidity once a steady state is established[9].

The fabricated MEAs active surface area is 11.34 cm^2.The mono-polar plates used are graphite, with a circular, single serpentine, flow field.

The Gas Diffusion Electrode (GDE) anode material was held constant. Commercial JM electrode ELE00165 is used with a catalyst loading of 0.4 $mg.cm^{-2}$. A variety of other GDLs were tested on the cathode side. TKK Pt/C catalyst based ink was hand painted on the GDLs to achieve a loading of 0.4 ±0.05 $mg.cm^{-2}$. Nafion 212 Polymer Electrolyte Membranes (PEM) are used. The electrodes and the membrane are hot pressed at 125^{O}C and 1800kg. The following cathode materials are presented in this paper. All cathode GDLs had a Micro Porous Layer (MPL) on one side of the GDL.

- E-TEK LT1200N (Non-woven carbon paper)
- E-TEK LT1200W (Woven carbon cloth)
- Sigracet SGL 24 BC (Non-woven carbon paper)
- Sigracet SGL 25 BC (Non-woven carbon paper)
- Sigracet SGL 34 BC (Non-woven carbon paper)
- Sigracet SGL 35 BC (Non-woven carbon paper)

Three MEAs of each cell type were fabricated to limit any errors resulting from MEA fabrication and during testing.

product code	manufacturer data			measured data																		
	microns thick	area wt g/cm^2	bulk densityg. cm^2	real density	±		bulk density	surface roughness SA	±		surface roughness SQ	±		%porosity	tortuosity	mean pore diameter	permeability Hg	water contact angle	±		-	-	in plane resistivity
LT1200N	185	75	0.41	2.053	±	0.004	0.39	17	±	2	22	±	0.8	64.9	2.74	769	6.45E-12	90	±	6	-	-	2.93E-04
LT1200W	275	200	0.73	1.906	±	0.002	0.5	-	-	-	-	-	-	31.8	2.74	1055	4.98E-12	96	±	1	-	-	1.03E-04
GDL 24 BC	235	100	0.44	2.01	±	0.003	0.44	13.3	±	0	18.3	±	0.8	40	3	2450	5.09E-12	104	±	4	-	-	2.51E-03
GDL 25 BC	235	86	-	2.009	±	0.007	0.34	23	±	4	32	±	3	36.5	2.92	842	5.64E-12	112	±	12	-	-	-
GDL 34 BC	315	140	-	1.987	±	0.001	0.41	23.9	±	1	30.8	±	0.2	47.5	2.47	2197	8.97E-12	126	±	7	-	-	2.22E-03
GDL 35 BC	325	110	-	1.98	±	0.007	0.31	36	±	2	46	±	5	52.6	1.94	1467	1.72E-11	118	±	11	-	-	3.67E-03

Table 1: Selected materials data for GDLs [3]

The study will focus on the samples LT1200W and LT1200N to study the effect of structure, and SGL 24BC and SGL 25BC to study the effect of substrate bulk density. Samples SGL 34BC and SGL 35BC are also analysed in this paper.

The MEAs were soaked in deionised water (resistivity = 18MΩ.cm) overnight to accelerate the membrane activation process. The MEAs were then randomly assigned to one of seven test chambers for in-situ testing, under the following operating, set point, conditions:

- H_2 flow rate: 80 sccm
- Air flow rate: 200 sccm
- Back pressure: 2 Bar
- Cell temperature: 70 ^{O}C
- Data logging rate: 1 Hertz
- Relative humidity: 100%

MEA 'conditioning' was achieved by holding the cells at variable current load to induce a potential of 0.6 ± 0.03 V for a period of three hours. Once completed the MEA was subjected to 25 'rapid' polarisation curves. A three second time step was initiated, with 25 current settings increasing to the maximum current load achievable by the MEA. Polarisation curve number 25 of the sequence was recorded. A further polarisation curve with a 10 second step time was also carried out and recorded. Polarisation curves are plotted by averaging the V / I values across each time step.

Results

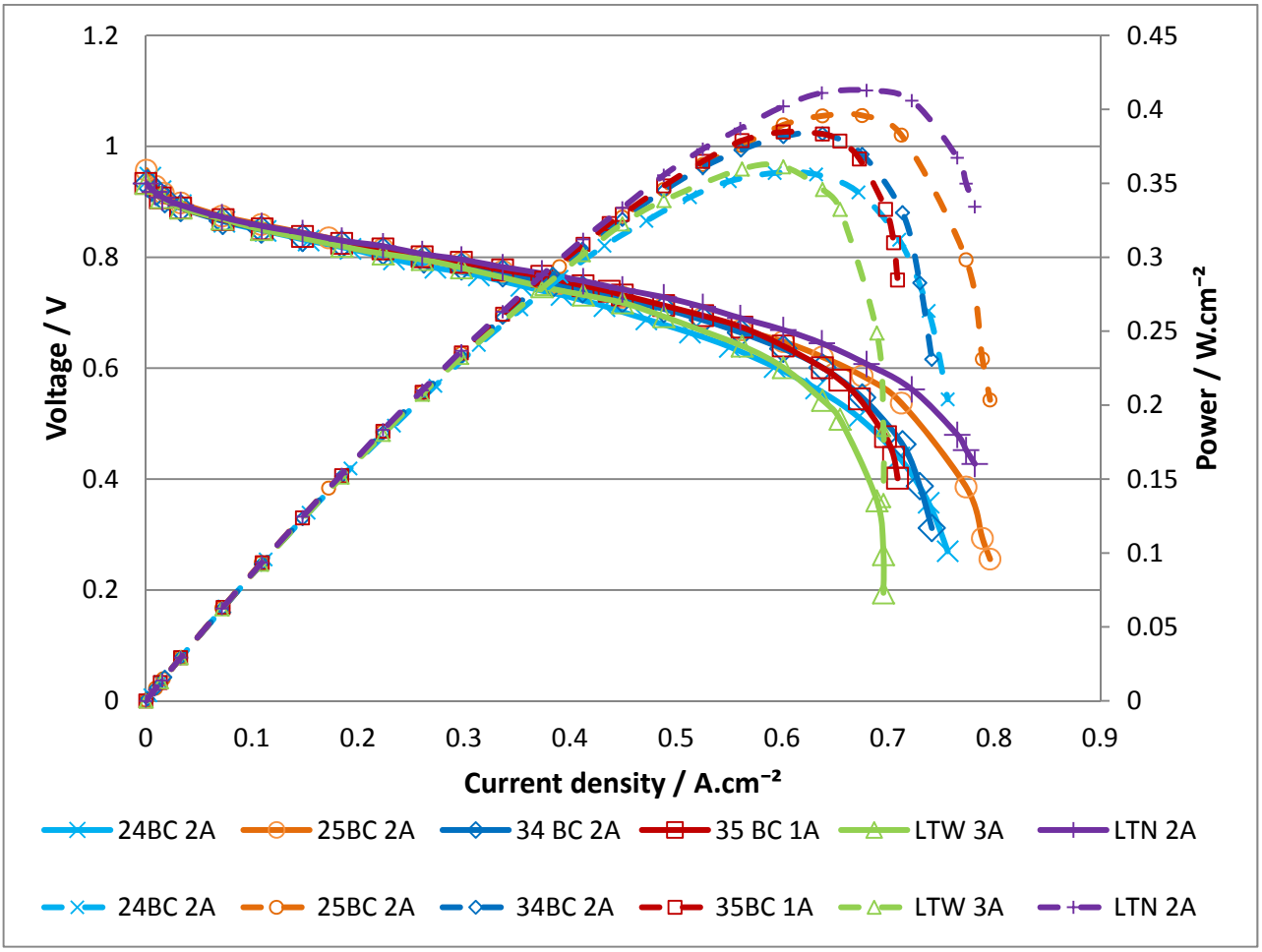

Figure 1: polarisation curves for all GDLs with peak power

Figure 1 shows the result of the polarisation curve from the best, representative, test sample from each material.

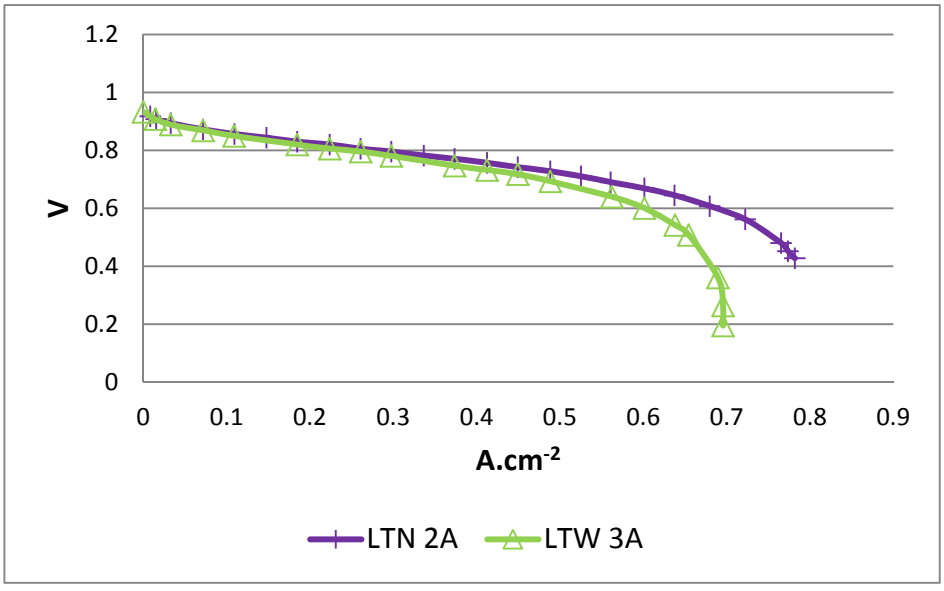

Figure 2: Comparison of LT1200W and LT1200N samples

Figure 2 shows a higher performance for the non woven LT1200N compared to the woven LT1200W. Comparison of the nonwoven (LTN 2A) variant to the woven (LTW 3A) shows that the non-woven GDL outperforms the woven sample in rate of Ohmic loss in the polarisation curve, the onset of mass transportation losses in the final third of the curve, in the rate of mas transport loss and also in the peak current drawn. Figure 1 also reveals that peak power is superior for the non-woven LTN 2A test piece. Closer examination of the temperature during testing shows that the non-woven GDL was actually tested at a significantly lower temperature (65.9^{o}C for LTN 2A, compared to 70.2^{o}C for the LTW 3A test sample). This leads to the conclusion that the improved performance of the LTN sample has actually been suppressed by the test conditions. Comparison to Table 1 shows that hydrophobicity (indicated by water contact angle), resistivity and permeability values are similar. Density, thickness, porosity and mean pore diameter are all significantly different. It should be kept in mind that the test cells have undergone uniform clamping pressures, and gasket heights have not been optimised for each GDL. The increased thickness for the woven sample (LTW) could limit the effective porosity of the material still further through excessive clamping force.

The non-woven material is superior in this instance, and the reduced mean pore size, combined with the increased total porosity, offers a possible mechanism to explain this. The increased total pore volume requires a greater volume of liquid water to fill before significant limits to the flow of reactants around and through the GDL are detected. The reduced mean pore size may also play a role in accelerating liquid water away from the reaction surfaces.

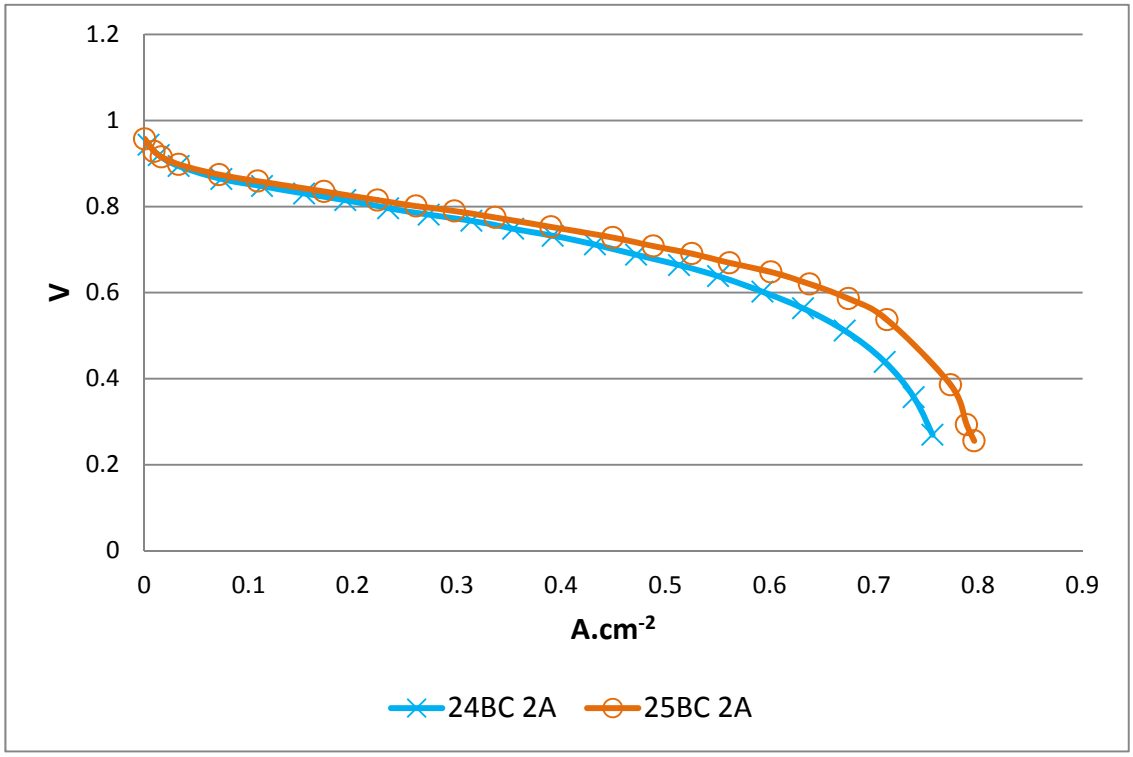

Figure 3: Comparison of 24BC and 25BC samples

In Figure 3 we see a reduced performance for the 25BC variant of GDL

The 24 and 25 BC GDLs are examined in Figure 3 and in this case there is a similarity in the GDL thickness, however porosity, density mean pore diameter and water contact angle differ. In the BC tests, both samples have been tested in a narrower temperature range (68.7 ^{o}C and 72.1^{o}C respectively). If we refer to the previous results for the LT woven and non-woven materials; we see that smaller mean pore diameter and a greater porosity volume are linked to improved performance, as discussed previously. Examination of the material properties for the 24BC 2A and 25BC 2A test pieces reveals a similar relationship. The most significant difference in properties between the two samples is mean pore size: The 24BC GDL materials have a measured mean porosity 2.450 µm, and the 25BC have a mean pore diameter 0.842µm.

25BC 2A outperforms 24BC 2A in rate of Ohmic loss in the polarisation curve, the onset of mass transportation losses in the final third of the curve, and also in the peak current drawn. Figure 1 also reveals that peak power is marginally superior for the 25BC 2A test piece. The fact that the rate of mass transport loss is slightly inferior (i.e. steeper) in the 25BC variant is interesting, and suggests that mean pore diameter is not dominant in this section of the curve, though more testing is required to confirm this to a reasonable degree of certainty.

Once again we suggest that the reduced mean pore size, combined with the increased total porosity, of 25 BC 2A when compared to 24BC 2A, offers an explanation for the improved performance of 25BC 2A, through the same mechanisms discussed earlier.

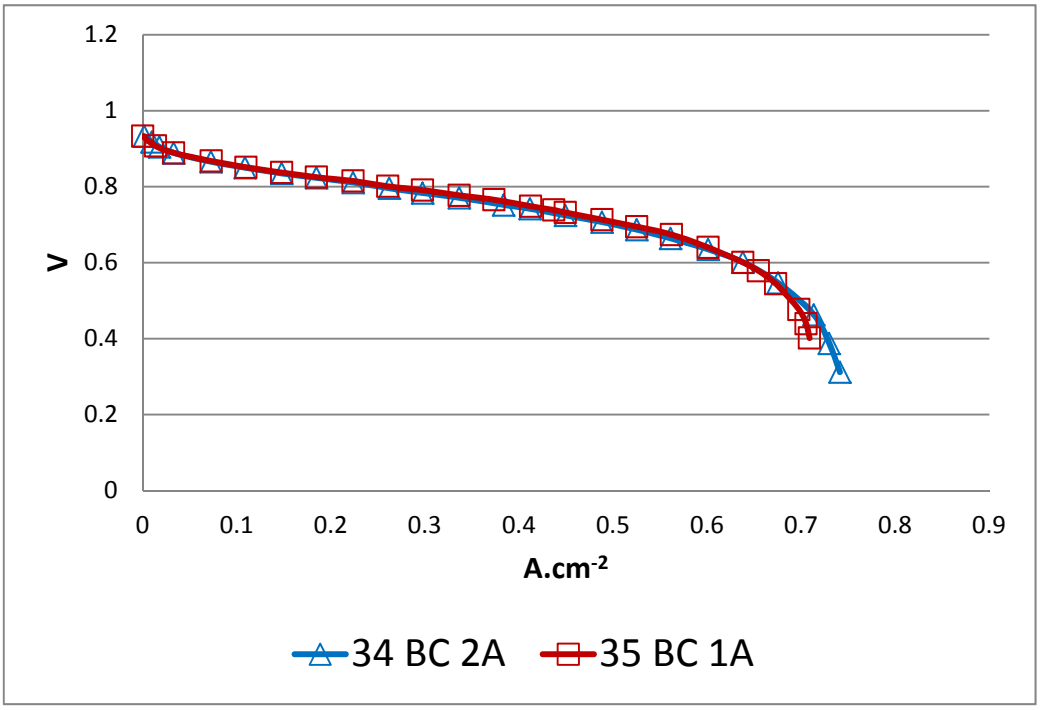

Figure 4: Comparison of 34BC and 35BC samples

Figure 4 shows a more uniform performance from the two GDLs, with 34BC being marginally better, especially in the mass transport section of the curve

In the 34 BC and 35 BC GDLs we can examine the mean pore diameter and total porosity. Table 1 reveals a smaller mean pore diameter and a larger total pore volume in 35 BC. From our recent discussion we would expect to see 35 BC outperforming the 34BC GDL. However comparison to Figure 4 at first glance indicates that 34 BC is marginally superior. The test temperature for the two samples was extremely uniform, with 70.3°C for the 34 BC and 69.9°C . This narrow temperature range should not have a significant impact based on our previous observations. The thickness of the sample is also at the higher end of the ranges tested, with 35 BC being the thickest of all the GDLs tested. The compression force experienced in the test cell will be greatest for this material. Plotting the peak power for these two samples, shows a very close match between the two, and the highest recorded peak power in this set is 0.3847W.cm^{-2} for sample 35 BC, exactly as predicted. We suggest that the effect could be even more pronounced if the gasket height were optimised for both of these samples (thereby eliminating excessive compression forces from 'closing off' the porous structure).

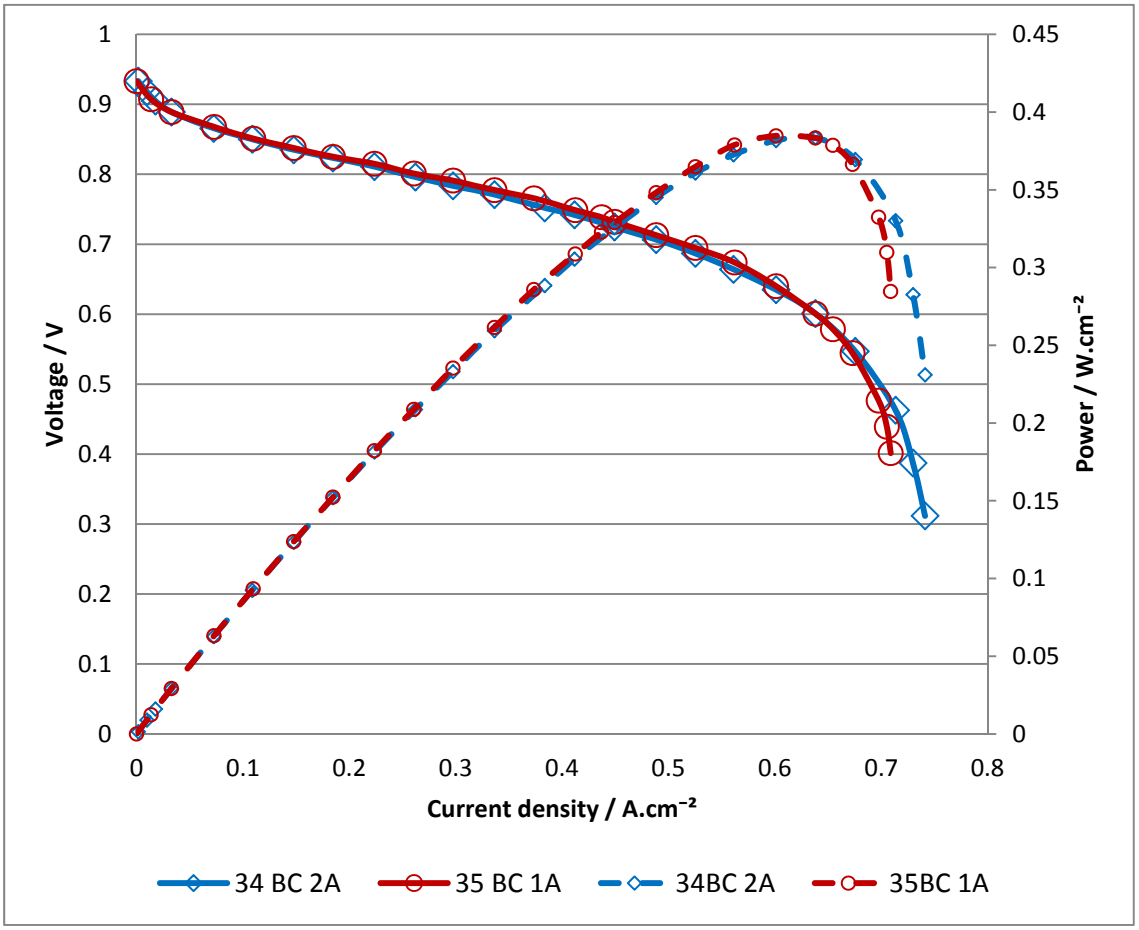

Figure 5: Peak power 34 BC and 35 BC

Initial Observations:

Based on the tests to date (55 of 90 test specimens completed):

- Woven structures do not out-perform non-woven materials in these tests
  - This may be due to the lack of cell optimisation for the increased through plane thickness of the woven sample used
- Reduced mean pore size and increased total porosity dominate in determining peak power output for MEA assemblies

	24BC 2A	25BC 2A	
temperature during test	68.7	72.1	^{o}C
mean pore D	2.45	0.84	microns
% porosity	40.0	36.5	%
Ohmic Loss	-0.4456	-0.4109	Ohms
Rate of Mass transport Loss	-2.2769	-2.305	Ohms
maximum current	0.7561	0.7961	A.cm^{-2}
Peak power	0.3570	0.3958	W.cm^{-2}
	LTW 3A	LTN 2A	
temperature during test	70.2	65.9	^{o}C
mean pore size	1.06	0.77	microns
% porosity	34.0	65.0	%
Ohmic Loss	-0.4046	-0.353	Ohms
Rate of Mass transport Loss	-3.9527	-1.7455	Ohms
maximum current	0.6955	0.7817	A.cm^{-2}
Peak power	0.3613	0.4128	W.cm^{-2}
	34 BC 2A	35 BC 1A	
temperature during test	70.3	69.9	^{o}C
mean pore size	2.20	1.47	microns
% porosity	47.5	52.6	%
Ohmic Loss	-0.4017	-0.4084	Ohms
Rate of Mass transport Loss	-2.1787	-3.659	Ohms
maximum current	0.7411	0.7088	A.cm^{-2}
Peak power	0.3835	0.3847	W.cm^{-2}

Table 2: Key material properties and measured outputs

Acknowledgements

Without the aid of the following organisations, this work would not have been possible: Doctorial Training Centre in Applied Hydrogen and Fuel cell Technologies, Midland Energy Consortium, Engineering and Physical Sciences Research Council, and Intelligent Energy Ltd

References

1 B. Millington, S. Du and B. G. Pollet, *J. Power Sources,* **196**, 9013-9017, (2011).

2 M. Prasanna, H. Y. Ha, E. A. Cho, S. -. Hong and I. -. Oh, *J. Power Sources,* **131**, 147-154, (2004).

3 A. El-kharouf, T. J. Mason, D. J. L. Brett and B. G. Pollet, *J. Power Sources,* **218**, 393-404, (2012).

4 M. V. Williams, E. Begg, L. Bonville, H. R. Kunz and J. M. Fenton, *Journal of The Electrochemical Society,* **151**, A1173-A1180, (2004).

5 S. Escribano, J. Blachot, J. Ethève, A. Morin and R. Mosdale, *J. Power Sources,* **156**, 8-13, (2006).

6 S. Litster and G. McLean, *J. Power Sources,* **130**, 61-76, (2004).

7 C. Lim and C. Y. Wang, *Electrochim. Acta,* **49**, 4149-4156, (2004).

8 Y. Wang, C. Wang and K. S. Chen, *Electrochim. Acta,* **52**, 3965-3975, (2007).

9 Intelligent Energy Ltd, *Fuel Cell Component Analyser: Version 3 DRAFT Sept 2007*, Intelligent Energy Ltd, Loughborough, (2007).

Available online at www.sciencedirect.com

ScienceDirect

journal homepage: www.elsevier.com/locate/he

PTFE mapping in gas diffusion media for PEMFCs using fluorescence microscopy

Nicholas McCarthy [a], Rui Chen [a,*], Gregory Offer [b], Robert Thring [a]

[a] Department of Aeronautical and Automotive Engineering, Loughborough University, Loughborough, LE11 3TU, UK
[b] Department of Mechanical Engineering, South Kensington Campus Imperial College London, London, SW7 2AZ, UK

ARTICLE INFO

Article history:
Received 4 May 2016
Received in revised form
26 July 2016
Accepted 31 July 2016
Available online 20 August 2016

Keywords:
Fuel cell
MEA
PTFE
Microscopy
Fluorescence
GDL

ABSTRACT

Differentiating between the various polytetrafluoroethylene based structures inside polymer electrolyte membrane fuel cells with a degree of certainty is necessary to optimize manufacturing processes and to investigate possible degradation mechanisms. We have developed a novel method using fluorescence microscopy for distinguishing the origin and location of PTFE and/or Nafion® in Membrane Electrode assemblies and the gas diffusion media from different sources and stages of processing. Fluorescent material was successfully diffused into the PTFE based structures in the GDM by addition to the 'ink' precursor for both the microporous layer and the catalyst layer; this made it possible to map separately both layers in a way that has not been reported before. It was found that hot pressing of membrane coated structures resulted in physical dispersion of those layers away from the membrane into the GDM itself. This fluorescence technique should be of interest to membrane electrode assembly manufacturers and fuel cell developers and could be used to track the degradation of different PTFE structures independently in the future.

Introduction

Polytetrafluoroethylene (PTFE) based polymers play several important roles in polymer electrolyte membrane fuel cells (PEMFCs). A sulphonated variant is the backbone of the most commonly used solid electrolyte in the form of Nafion® membranes. PTFE based polymers are also used as hydrophobic coatings on carbon fibers, binder agents for catalyst layer (CL) inks, to provide structural integrity for microporous layers (MPL) and as an adhesive binder for the various layers that form the final membrane electrode assembly (MEA). By using PTFE based polymers for these differing functions, improved adhesion between the various structures is promoted by their broadly similar chemistry. For some types of MEAs the various coatings and functional layers are applied directly to the membrane, and in others the coatings are applied to the gas diffusion media (GDM) adjacent to the membrane. These are generally applied as a liquid suspension, and the impregnation of these PTFE solutions into the GDM make a significant impact on the final porosity of the completed MEA.

The hydrophobicity (water contact angle) of GDMs has been commented on and studied extensively by a wide array

* Corresponding author.
E-mail addresses: n.mccarthy@lboro.ac.uk (N. McCarthy), r.chen@lboro.ac.uk (R. Chen), gregory.offer@imperial.ac.uk (G. Offer), R.H.Thring@lboro.ac.uk (R. Thring).

http://dx.doi.org/10.1016/j.ijhydene.2016.07.270

of authors [1–5], who all agree that the coatings applied, to modify the hydrophobicity of the GDM, is an important factor in determining its overall performance of the fuel cell. Comprehensive reviews of this topic [6] and other GDM issues [7] agree that water contact angle has a significant impact on the fuel cell performance. Typically the control of the wetting angle on the carbon fibers is achieved by the addition of a PTFE based polymers to the carbon fibers during the manufacture of the GDM, and in some cases this coating is an important part of the GDM fabrication method, binding together non-woven structures. In other cases the hydrophobic polymer content is added solely to change the water transport properties of the GDM. This additional polymer coating is, like many engineering solutions, a compromise between increased hydrophobicity to facilitate water transport and a decrease in the available pore volume for fluid transport in the GDM.

When it comes to the fundamental understanding of reactant and product mass transport mechanisms in the fuel cell, the through plane thickness, total volume or percentage surface coverage of these various layers can be a significant consideration. Typically an examination of 'Spatially-Varying' performance of fuel cells will consider the MEA as a plane. These studies seek to understand localized performance variations across the plane of the MEA, usually as a result of reactant and product concentration changes, along the length of the gas flow channels [8–10]. Some work in this area has investigated the variation in the fuel cell through the plane of the MEA [11], focusing on the distribution of water through the plane of the GDM; not the direct measurement of PTFE structures through the plane of the GDM.

For example, in agglomerate models of catalyst layers an estimation of the thickness of CL is a key factor. This is often done by determining the total mass of catalyst material applied, and then assuming a uniform, monolayer distribution. For layered catalyst structures this estimation is done iteratively for each subsequent level [12,13]. For the catalyst coated substrate (CCS) manufacturing method – where the CL is applied to the GDM and not the membrane – this is also used. However, the validity of this through plane thickness assumption becomes questionable as mass gain is no longer an accurate indication of the dimensions of each layer applied to the complex, porous surface of the carbon fiber GDM. This same principle applies to other PTFE based surface treatments such as the addition of microporous layers. In many cases these PTFE based layers, and their exact dimensions, cannot be defined with any certainty when the GDM has been pretreated with a hydrophobic (PTFE based) coating. Energy Dispersive X-ray (EDX, or 'EDaX') techniques and secondary backscatter electron imaging have all been used in conjunction with Scanning Electron Microscopy to map various chemical species in the MEA [14]. Heavier atomic weight molecules and atoms show up as a brighter contrast to lighter species in the standard image with the induced emission of x-rays (of a specific energy and frequency) being used to identify the individual chemical species. This makes chemical species that are largely composed of carbon difficult to distinguish between. It is this brightness value and species identity that is used to generate chemical composition maps such as those in Fig. 1(c) where the Fluorine response has been highlighted in red, and to distinguish it from the other adjacent carbon based structures. For a comparison between the graphitized carbon fibers of a typical GDM, and the largely carbon based PTFE species present in the system, fluorine detection is typically recommended. The limitation of this technique is that it is impossible to distinguish the fluorine content of two different PTFE sources. For example if a MPL layer has a PTFE based dispersive agent, and the catalyst ink is applied with a 10wt% solution aqueous Nafion solution, both will give an equal response in fluorine mapping with EDX analysis. Fig. 1 (c & d) show a typical fluorine map generated from EDX. As can be clearly seen there is no way to numerically differentiate the fluorine in the image between the various PTFE based polymers (ink, MPL, CL and hydrophobic coatings on fibers) in the MEA that generate a fluorine response.

In the case where SEM/EDX mapping of the MPL layer was desirable, a low concentration of 10 weight percent of platinum on carbon (10wt% Pt-on-C) can be deposited in the same way as an MPL. This low concentration of heavy metals is an attempt to differentiate between various layers of the MEA. This is reliant on the assumptions that the platinum doped carbon particles are uniformly spread through region of interest, and that the PTFE based polymers used in the MPL 'ink' are dispersed throughout the material in the same way. This 'functionalized' MPL is equivalent to the dual layer catalyst systems suggested by some researchers [15–18], and according to their finding it must be acknowledged that fuel cell performance is changed by this approach. Furthermore by taking this approach we have now in turn made it impossible to clearly differentiate between the MPL and CL. Additionally this low concentration of Platinum approach cannot be used at the same time for other PTFE structures in the MEA such as the PTFE based hydrophobic coatings, especially for comparisons with standard GDMs used in fuel cell research. There has been a great deal of work using novel imaging techniques such as X-ray tomography (XRT) to aid the conceptualization of the internal structures of the GDM and its impact on the performance of performance of fuel cells [19,20]. Synchrotron or neutron based imaging techniques can also be used to visualize the water generation and flow inside a working fuel cell in real time [21–24]. These processes require specialist equipment, and in the case of XRT a significant level of expertise and computer processing time to process the captured images. Whist these techniques can demonstrate the overall impact of water flow (neutron imaging), or identify the totality of the combined structure of fibers and PTFE additions (XRT); both suffer the same limitations as EDX and cannot differentiate between multiple sources of PTFE content in the GDM.

An alternate methodology is needed for mapping the distribution of these various layers and coatings in the MEA. A system that will not change the performance of the MEA under operating conditions would obviously be preferred. With this in mind the following work was undertaken to determine if fluorescence based microscopy could be used to differentiate between different polymeric materials within the GDM; with the intention that this can be used to optimize GDM/PTFE interactions. In this paper we present the use of a fluorescent dye doped directly into the PTFE component of a layer of interest, and map the PTFE distribution in a CL and MPL separately in multiple MEAs.

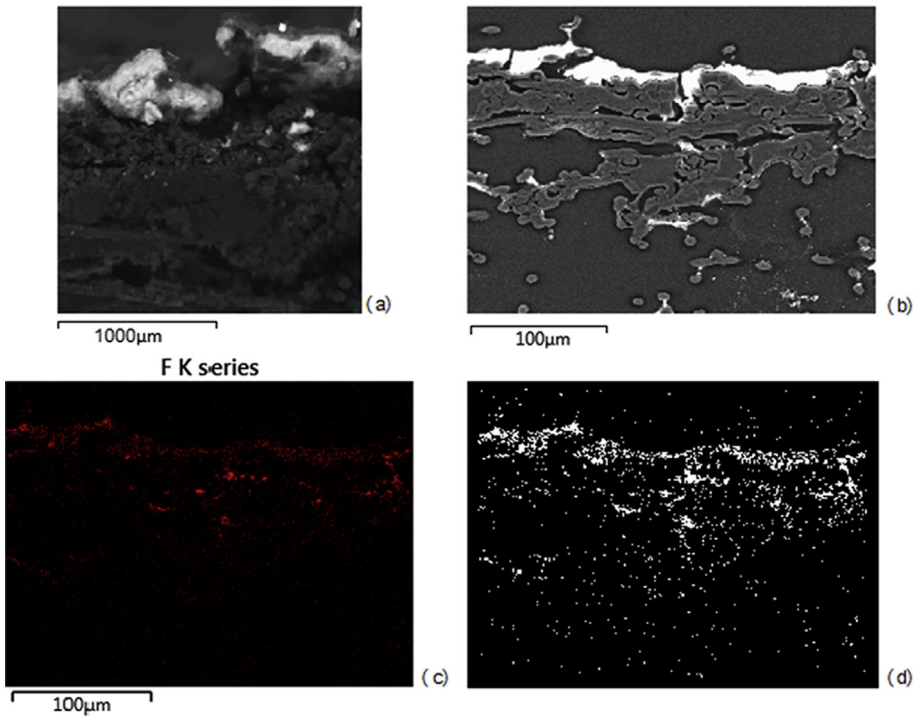

Fig. 1 – SEM of standard cathode GDM (a) optical image, (b) SEM image, (c) Back scatter map of Fluorine, Black and White processing of 'c' (d).

Litster et al. [25] in 2006 utilized fluorescent water impregnation to characterize the liquid penetration time through GDM and also to gain greater understanding of the pathways for water penetration through the material. Their work provided the inspiration for this work to consider the possibility of faster and more cost effective ways of assessing the PTFE distributions in the GDM in the CL and MPL. To date there has been no work done to assess the interaction of catalyst ink formulations and their impact on PTFE distributions in the GDM or CCS type fuel cell assemblies. This is due to the inability of SEM/EDX techniques in generating clear separation of the elemental species in the carbon based fibers, the carbon based catalyst inks, the carbon (PTFE) based GDM binder agents and the Carbon (PTFE) based catalyst ink suspensions. This inability to distinguish chemically similar phases in a sample is not unique to the field of fuel cells. Fluorescence in degradation products is well known in the food sciences, yet they are often difficult to distinguish for different stages of the ripening/decomposition process. As highlighted by Croptova et al. [26] it is possible to correlate with a high degree of confidence (95% confidence level easily achieved in their study) the emitted fluorescence of a single phase of interest in a chemically complex system, especially if the filter system used in the experimental set up is optimized. Le Duigou et al. [27] have also used fluorescence microscopy to differentiate between optically similar samples in their confocal microscopy analysis; mapping resin impregnation into the fibrous structures of an epoxy-flax composite. This is a very similar environment to the PTFE impregnated carbon fibers for the GDM. Whittman et al. [28] examined the impact of organic fluorescent dye on PTFE type materials, and indicated that, with the correct heat treatment regime, the fluorescent dye can alter the structure of the PTFE materials, and form a PTFE/copolymer composite material. This provides solid evidence that the proposed concept – that a fluorescent dye will mix with the PTFE component of a catalyst ink formulation and make it possible to track its distribution through the GDM – is worthy of further investigation.

Experimental

Five fluorescent dye concentrations were investigated. Concentrations between 0.5 and 10 wt% of EpoDye™ added prior to sonication of the ink formulation in each case. EpoDye™ is a propriety brand of 'Brilliant yellow 43' ($C_{20}H_{24}N_2O_2$), which typically has its highest stimulation frequencies in the 275 nm–450 nm wavelengths, comfortably in the Ultraviolet spectrum and so well suited to fluorescence microscopy with mercury lamp illumination. The use of 2-propanol in the ink formulation described in this paper indicates this solvent dye should be suitable. The 1wt% EpoDye™ loading was found to achieve the maximum luminescent response with the least amount of material added, and was in line with the manufacturers recommended dosing levels. The 0.5wt% doped fluorescent samples (Fig. 2 (b)) could, after a prolonged exposure time, generate a usable image, and were very well suited to generating sufficient contrast to examine the fiber structure of the GDM. Higher weight percentages generated a more complete coverage of the GDM surface as shown in figures (c & d).

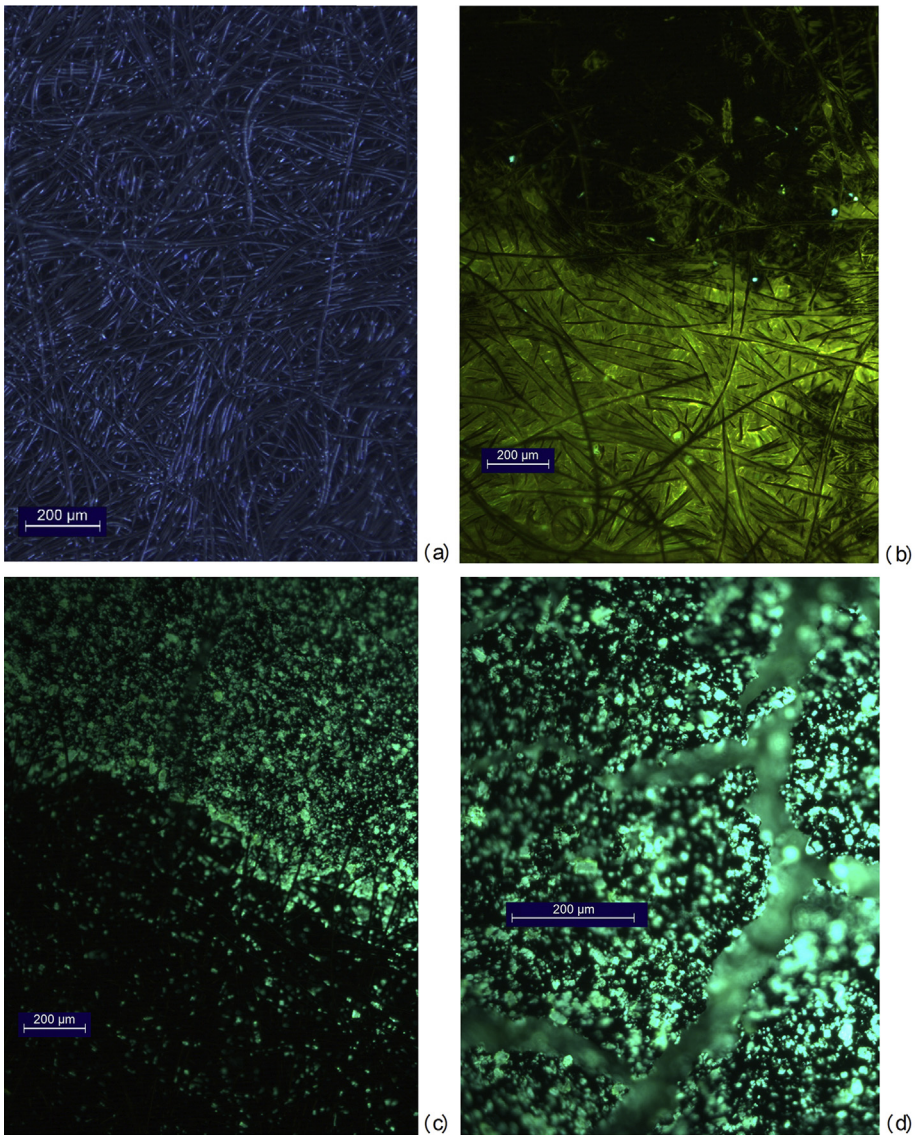

Fig. 2 – (a) Auto-fluorescence of cathode carbon fibers, (b) 0.5wt% EpoDye™ doped cathode carbon fibers, (c) 1.0wt% EpoDye™ doped cathode carbon fibers, (d) 400× magnification image of Microporous layer structure.

Catalyst ink formulations

Various ink formulations in the literature [29–31] were adapted until a stable ink manufacturing procedure was developed. DI water, and 30 'weight percent' (30wt%) of platinum (Pt) on carbon (C)[1] and 10wt% aqueous Nafion® solution, and 1 M 2-propanol solution (IPA) are sonicated together for 1 h. To determine the total amount of aqueous Nafion® solution required (in μL) for the ink; the mass of carbon desired (catalyst weight not included) in mg is divided by the percentage Nafion solution strength (expressed as a decimal).

$$Nafion_{soln.}(\mu l) = \frac{m_{Carbon}(mg)}{\%_{soln.}(asdecimal)} \quad (1)$$

[1] Carbon black catalyst support was 'Vulcan carbon black' according to the suppliers.

5.31 times this value derived in Eq. (1) gives the volume of 2-propanol required

DI water with a volume equal to 10% of the measured out volume of 2-propanol (isopropanol) is first added to the Pt on C to reduce the possibility of combustion during mixing. The whole mixture is then sonicated at room temperature for one hour immediately before application. Single layers of ink are painted on, and then allowed to dry for eight hours (or overnight). The MEAs are weighed, and the process repeated until the desired catalyst loading is achieved. The ink preparation is sonicated for twenty minutes immediately prior to application if it has been left static for a significant period of time (more than three hours).

MPL equivalent inks were manufactured in much the same way, but with carbon particles with no platinum, or in the case where EDX mapping of the MPL dimensions was required with a 10wt% Pt-on-C loading.

Fluorescent dye study

Due to the lack of contrast between the carbon based ink and the carbon fiber support; typical optical microscopy of the CCS active surface results in a more or less uniform 'black field' image that has little or no discernible features that can be effectively imaged. Non-woven fibers with a hydrophobic coating and without carbon based ink coatings could, with extremely long exposure times under UV light, induce any PTFE present to emit characteristic auto fluorescence (Fig. 2 (a)). All microscopy images were captured using a Leica DMRX fluorescent microscope equipped with a Leica DFC480 5 Mega pixel digital color camera. Surface images of MEAs with fluorescent dye doped inks demonstrate a characteristic 'green' color (Fig. 2 (b,c &d)) as a result of the use of a violet/blue filter cube: an 'E4' band pass filter from Leica. This reduces the overall intensity of the light emitted, but also reduces the signal to noise ratio by filtering out much of the visible light except for the 436/7 nm wavelength, and a proportion of those frequencies at or above 513 nm. This can be used beneficially to image the mixed blue light (436/7 nm) with the yellow/green light emitted from the EpoDye™ in solution with the PTFE in the ink: Making it possible to differentiate between the yellow florescence of the doped PTFE component in the catalyst ink and the naturally 'blue' fluorescence of the (untreated, PTFE based) binder agents, the phobicity controlling surface treatments of the GDM itself.

Having completed the conditioning and initial polarization curves, samples were edge mounted and cross sectioned for microscopy. In order to maintain the GDM structure great care was taken over the polishing procedure, as it was found more aggressive polishing recipes resulted in fiber pull out and disrupted the GDM structure. To maintain GDM structural integrity in the polishing stage, all samples were mounted in low viscosity epoxy resin (EpoFix™) and vacuum impregnation was used to support the carbon fibers during the polishing process. The resin was then left to set for 24 h and polishing of samples for optical microscopy was carried out.

MEA fabrication and test cell dimensions

The fabricated MEAs active surface area is 11.34 cm^2. Graphite current collection plates are used, with a single serpentine circular ('disc-like') flow field. The GDM anode material was Toray TGP-H-120 with a catalyst loading of 0.3 mg cm^{-2} (±0.02 mg cm^{-2}). The cathode material was much the same with 0.35 mg cm^{-2} (±0.02 mg cm^{-2}) of catalyst. Nafion 212 Polymer Electrolyte Membranes (PEMs) are used. The electrodes and the membrane are hot pressed at 125^{O}C and 1.0 MPa for two minutes.

Two sets of MEA were fabricated. In order to analyze not only the applicability of the fluorescence technique, but to also determine how small a resolution of the PTFE distribution could be effectively analyzed; a mixed application cathode (MAC) manufacturing technique was used. A high Pt concentration layer (40wt% Pt-on-C) was deposited directly onto the membrane in one layer, and a low concentration (10wt% Pt-on-C) was deposited directly onto the GDM in another layer. This lower concentration layer acting as the effective MPL, but with additional heavy metal in the hopes of aiding SEM image capture at a later stage.

These two mixed application catalyst samples were identified as MAC1 and MAC2. In MAC1 the fluorescent dye is in the catalyst layer, and in 'MAC2' it is the MPL that has been doped with fluorescent dye. In this way we hope to see what the minimum resolution of this technique could be. Recall in this work the layer furthest away from the membrane is the low concentration platinum layer and can be considered as a MPL rather than as a true CL.

Having determined the mass loading for each layer as described previously, the ink solutions were hand painted on. The MEA was then fabricated up in the usual way. MAC1 has 1wt% EpoDye™ on the membrane side of the MAC assembly. Mac 2 has 1wt% EpoDye™ on the GDM side of the assembly.

Polarization performance

Having established the feasibility of the approach, MEAs were fabricated and tested under operational conditions. All MEAs were conditioned at 0.6 V (+/−0.05 V) for three hours at 60 °C. Twenty polarization curves were then run on each sample. After this conditioning cycle was completed an additional set of polarizing curves were undertaken. All samples were tested at 65 °C (+/−2 °C) at 100% relative humidity with a hydrogen flow rate of 60sccm and an air flow rate of 150sccm. All gases were at 150 kPa absolute and the fuel cell clamping assembly was tightened down to 2Nm of torque per bolt on a three bolt system (circular geometry). The test apparatus is a 'self −humidifying' system that does not make use of pre-humidified or pre-heated reactant gas streams. Such self-humidifying systems result in an anticipated reduction in the overall performance [32] of the cell when compared to pre-humidified and pre-heated gas stream results.

The performance of the EpoDye™ doped fuel cells was very poor, indicating the dye inhibits the system. For the 'MAC2' sample getting any sort of polarization curve at all took several attempts, and the conditioning regime had to use a significantly reduced load to achieve the twenty 'conditioning' polarization curves. A comparative MEA without fluorescent dye (un-doped) is also shown (Fig. 3) labeled as control.

Results & discussion

SEM and EDX study

Images in Fig. 1 were taken with a Cambridge Instruments Stereoscan 360 Tungsten Filament SEM. In Fig. 1(b) the standard SEM image of a prepared GDM in cross section can be seen. The lighter, brighter section in the grey scale image represents heavier atomic mass elements. EDX was used to generate the map shown in Fig. 1(c). However, as shown in Fig. 1(d) the ability of the technique to map the distribution of the fluorine molecules (the only way to differentiate the PTFE based Nafion® from the remaining carbon based structures) is extremely limited. The F k series response in Fig. 1(d), gives no clear demarcation between the various layers. Numeric assessment of the two separate PTFE layers (MPL and CL) in this sample was impossible when based on Fluorine

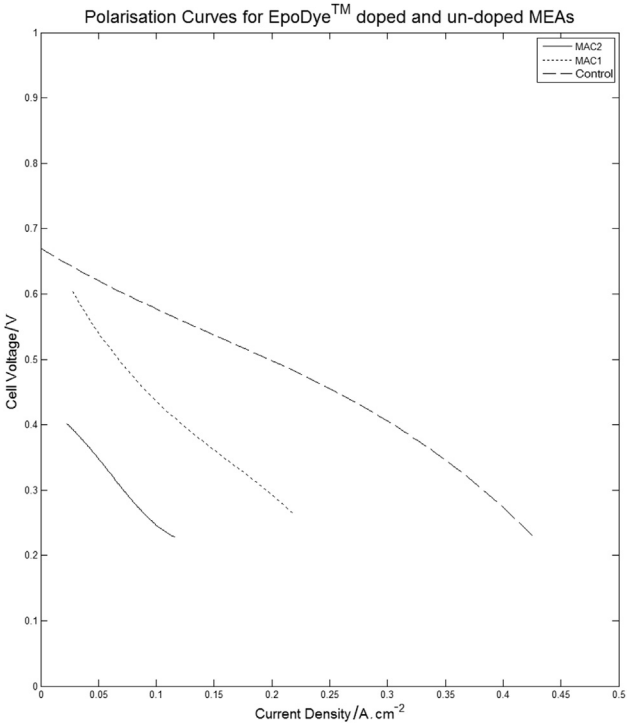

Fig. 3 – Polarization response of MEAs with and without fluorescent dye.

distribution only. When examining a GDM that has been pre-treated with a hydrophobic layer, the ability to distinguish PTFE based layers through fluorine molecule mapping becomes indeterminable (Fig. 1(c)).

In order to process such images the threshold has to be 'turned up' to the point where when running a standard image analysis tests (using MatLab®) the simplified black and white image as shown in Figs. 1(d) and 4(a) is produced. In this case the threshold level used to decide if a given pixel should be converted to 'black' or 'white' is set at 50% of the total brightness of all pixels in the equivalent grayscale image. Fig. 4(a) shows two distinct regions of PTFE distribution, with the histogram (Fig. 4(b)) showing the centroid point of each discrete point mapped. Therefore it is not possible to answer the question: has the CL or MPL added to this GDM actually penetrated ~200 μm into the body of the GDM, or has the image processing software incorrectly identified the pre-existing hydrophobic coating in the GDM fibers instead? Traditional EDX cannot answer this question.

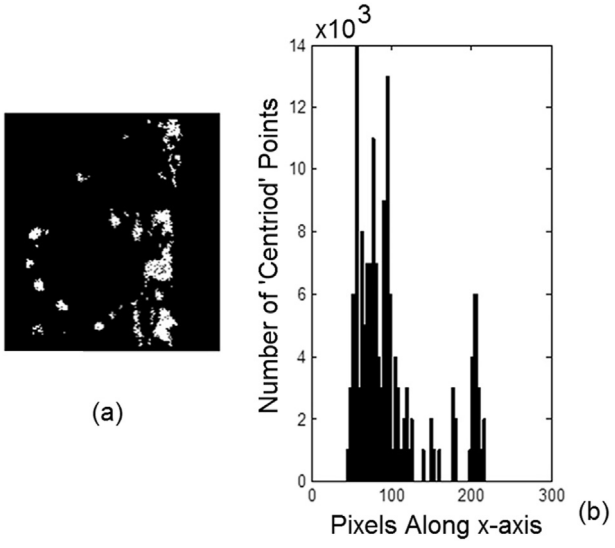

Fig. 4 – (a) Black and white processed image of standard GDM cathode Fluorine content, (b) 'centroid point' locations of individual particles in 'a'.

As stated previously, a low Pt loading system is used to help identify through scanning electron microscopy (SEM/EDX) the likely distribution of the MPL. Comparison to Fig. 1(d) the fluorine response is far superior in mapping the distribution of the PTFE based MPL, and the addition of a small amount of Platinum is needed to define the boundaries of the MPL itself.

Fluorescent dye study

Fig. 2(a) shows an 'as received' GDM material yet to be coated with catalyst ink. Note the light blue highlights as a result of the inherent PTFE based hydrophobic coating in the GDM fluorescing as is common for many organic molecules ("*auto-fluorescence*" [33]). The time taken to create this image was extremely long; well in excess of 60 s. This is impractical for the significant numbers of pictures used in large scale imaging studies and automated quality control in mass production lines. The fluorescent image could only be generated at 100× magnification or greater. This reduces the field of view for the surface of the GDM, and would again limit the utility for catalyst optimization studies for larger surface area GDMs. This long exposure time increases significantly the excitation of fluorophores that are out of focus (beyond the depth of field of the captured image as detailed in Table 1). Therefore whilst the image contrast is increased by increased exposure times, the amount of in–focus information is not increased at the same rate and excess exposure can reduce the overall value of a given fluorescent image. Therefore additional fluorescent material is required to reduce the exposure time, and improve image capture at lower magnifications.

It was found that at higher magnifications it was possible to view the open structure of the MPL itself (note that in image Fig. 2(d) the MPL has been dried overnight and the full development of MPL structure as a result of hot pressing is not represented here). Prior to MEA assembly, sample sections of GDM were coated with the fluorescent catalyst ink, and it proved possible to examine the CCS active surface in excellent detail.

In the cross section (Fig. 5) of the same GDM in Fig. 1(a) we clearly see florescence from the untreated PTFE binders, and

Table 1 – Depth of field at various magnifications.

Total magnification through camera	50×	100×	400×
Numeric Aperture (NA)	0.15	0.30	0.75
Focal Lens	5×	10×	40×
Depth of field (UV light source mean λ = 350 nm)	15.5/μm	3.9/μm	0.6/μm

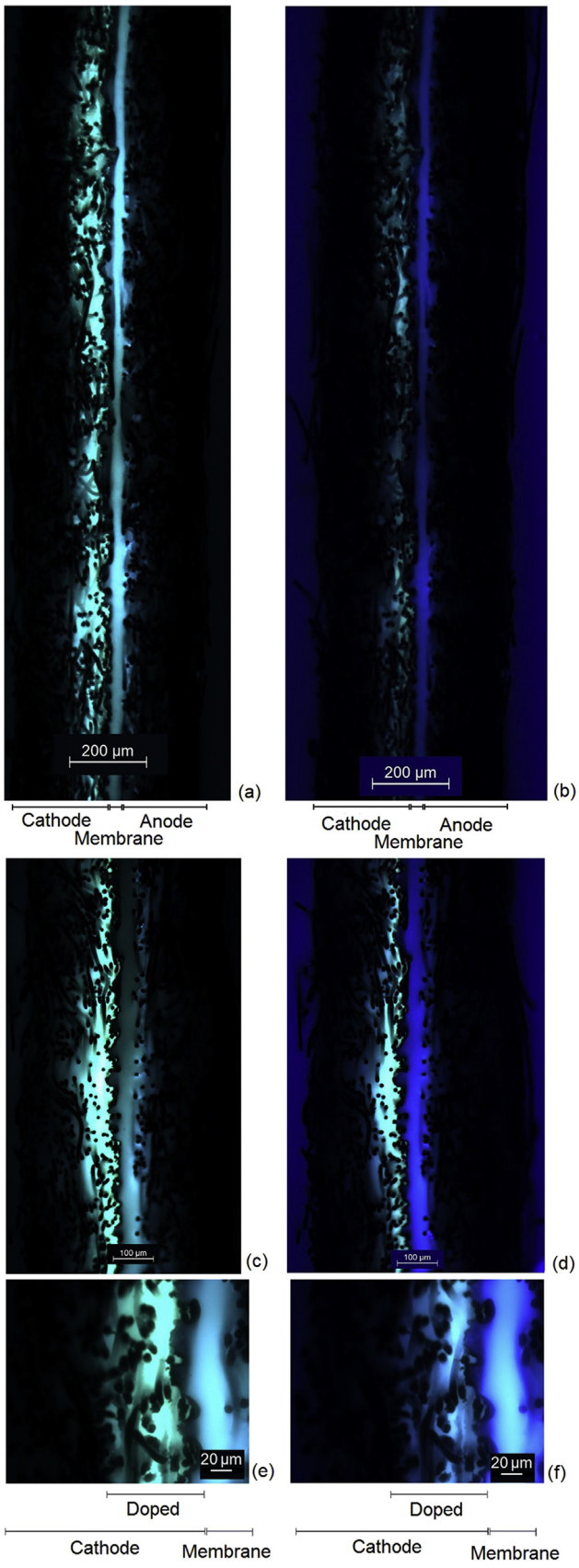

Fig. 5 – Comparison of unfiltered (left) and filtered (right) MEA cross sections at various magnifications (a) 100×, (b) 100× filtered, (c)200×, (d)200× filtered, (e)400×, (f)400× filtered.

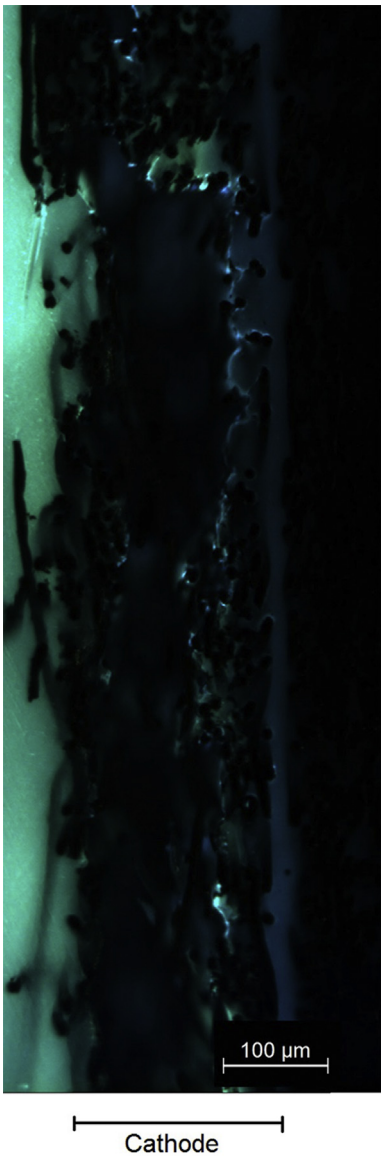

Fig. 6 – Observed 'bright region' on in MAC2 indicating delamination of membrane and GDM.

ink carrier solution, that can be imaged as the blue response. It is not possible to differentiate with any confidence the multiple sources of PTFE based autofluorescence.

The 1wt% EpoDye™ treated samples were able to produce a very strong fluorescence response immediately they were illuminated with a suitable ultra violet (UV) source. The illumination level does reduce the ability to identify specific fibers on the surface of the GDM, but the decreased image capture time makes this an attractive option.

The higher concentrations of fluorescent dye made no improvements to the images captured. Typically the MPL surface can be difficult to image with its characteristic 'black powder on black fiber' lack of contrast. Fig. 2(c) shows the active surface area of a 'proof of concept' test sample before MEA fabrication began. The fluorescence time is far less, and it is for this reason the texture of the fiber substrate in those

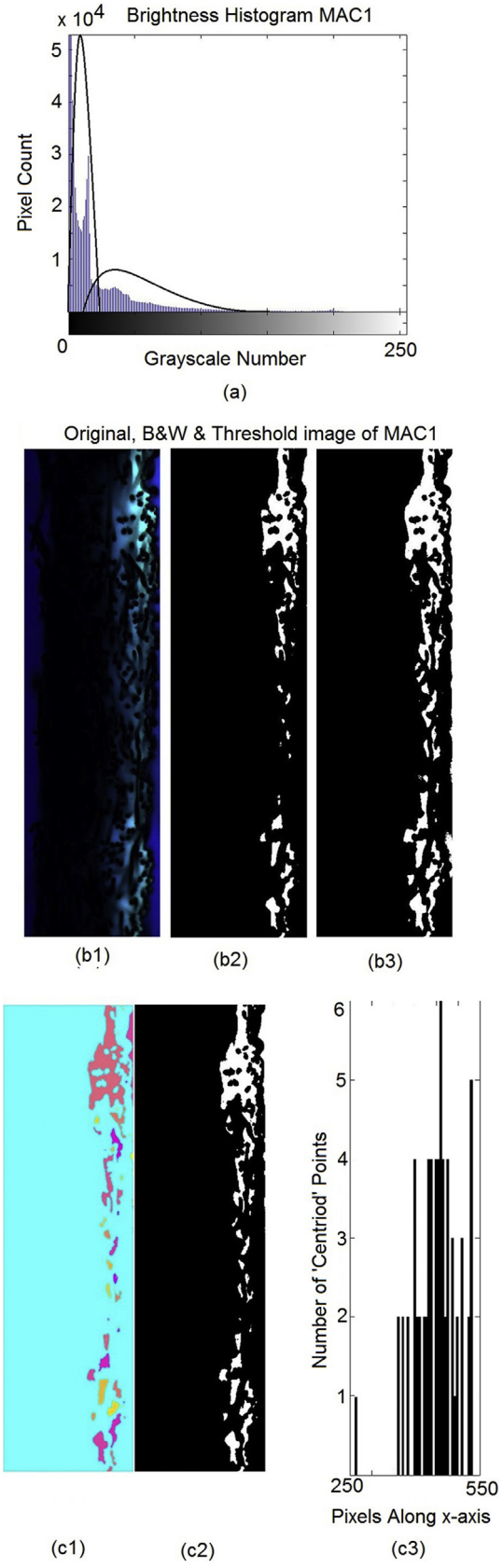

Fig. 7 – MAC1 Cathode image processing example (a) brightness histogram, (b1) filtered 200× fluorescent image, (b2) Black and white image transform, (b3) Otsuo image transform, (c1) PTFE region map for all particles, (c2) Otsuo transform, (c3) centroid point locations of individual particles in 'c2'.

areas not coated in catalyst ink is lost. This is the first time this type of image has been reported in a fuel cells context. The edge of the ink coated region is clearly visible, and there are notable features in the painted catalyst surface, with clear fissures in the surface of the active area leading deeper into the GDM. This test sample highlights the ability of this technique to quickly and easily asses the uniformity of catalyst coating for CCS fabrication procedures, and may prove useful in ink deposition optimization studies in the future. Once again we believe this is the first time it has been possible to distinguish PTFE added as part of the ink formulation on GDMs that have been pre-treated with a PTFE based hydrophobic coating.

The left hand images in Fig. 5 shows the standard response for a fluorescence doped MAC-MEA (left). It is immediately apparent that the characteristic 'blue' emission of the untreated PTFE is shifted to a green color, and also the characteristic 'yellow' response of the EpoDye™ is also shifted to the green as the two emitted frequencies 'mix'. By the addition an E4 filter the green response from the yellow EpoDye™ can be increased and the range of auto-fluorescence frequencies interfering with our understanding of the image can be limited. The ability to reduce the intensity of the response from the untreated PTFE in the Nafion® membrane, and the untreated hydrophobic coating of the GDM, greatly increases the contrast between phases, as can be seen in the right hand images in Fig. 5.

Applying this same approach at 100× magnification produces images that can be characterized digitally.

At this level it is still is possible to differentiate the segregation of PTFE layers in the GDM as a result of variable doping with EpoDye™ if additional image processing is used. At higher magnification still (400×) the flaring of the emitted light through the transparent mounting resin (used in the vacuum impregnation process) makes it impossible to differentiate between any PTFE based structures with confidence (Fig. 5 (e) and (f)).

The MAC 2 samples (where the MPL or 'CCS portion' of the ink is EpoDye™ loaded) again showed no significant variation in the emitted intensity response compared to those already studied. It is not possible to differentiate the order in which the fluorescent layers were painted on at any magnification 'by eye'. There is a degree of reflection and refraction through the doped PTFE, the un-doped hydrophobic coatings and the transparent epoxy resin mounting system vacuum impregnated into the GDM. It is possible that these light effects are causing difficulty in imaging the exact presence of the PTFE in the two separate ink layers. The depth of field may also be a factor. The depth of field of the images is clearly defined as follows for each magnification.

$$\frac{\lambda}{NA^2} = d_{field}(2) : \text{Depth of field}$$

Litster et al. [25] stated that the "... *observable range of the surface height ... is 30 μm ...*". Whilst our depths of field calculations are slightly less than theirs, we can reasonably expect

Table 2 – MAC1 PTFE region area (top) and centroid point location (bottom) along x-axis for MAC1 images.

Area per object	Section 1 (pixels)	Section 4 (pixels)	Section 5 (pixels)	Mean of means (μ)	StDev (σ)	(σ/μ)
Mean	7.61E+03	7.65E+03	7.82E+03	7.69E+03	1.10E+02	1.43%
Centroid 'x' coordinate	Section 1 (pixels)	Section 4 (pixels)	Section 5 (pixels)	Mean of means (μ)		
Mean	388	406	401	398.3	9.29	2.33%

to image fluorescent responses at a depth of 15 μm for the 50× magnification as our approaches are similar. However the washing out of the collected florescent light at high magnifications (and therefore reduced depth of field) indicate that emitted light from even further into the body of the sample than this assumed depth is being gathered. In order to overcome this limitation in the higher magnifications; several attempts were made at microtoming very thin slices of the MEA. Both the EpoFix™ epoxy mounting and standard epoxy filler mounting were extensively tested in this fashion but no specimens suitable for microscopy could be produced with the time and resources available. Therefore the technique of fluorescent doping, at its present stage of development, is only well suited to images that are in the 50 to 100 times magnification range.

One area observed in the fluorescence microscopy of the MAC 2 sample was notably different to the rest. In Fig. 6 there is a highly defined region with significantly increased emission. This 'lightening flash' may be a feature brought about by poor vacuum impregnation and represent light passing up through air gaps in the GDM. However the fact that the MAC2 sample gave such a very poor response when attempting to generate polarization curves gives rise to the far more likely possibility that this was a pre-existing defect in the MEA itself, and the fluorescent dye has congregated in the void space. In all probability this is a delamination effect (separation of the membrane and the catalyst/GDM layers from each other). It is unclear if the addition of the EpoDye™ is the cause of the delamination or not; but the reduced performance in both samples compared to the control sample could well be explained by a reduction in the adhesion of the various layers brought about by the addition of the fluorescent dye. If a more chemically compatible fluorescent dye, that does not reduce fuel cell performance, can be developed in the future; then there is an interesting possibility that this fluorescence microscopy method could be used for defect detection in MEA manufacturing techniques in the future.

Digital image analysis

Whilst it may not be possible to differentiate the layers separation visually, as can be seen in Fig. 7, the gathered data is amenable to image processing. Standard black and white conversion (Fig. 7 (b2)) leaves much to be desired. Setting the

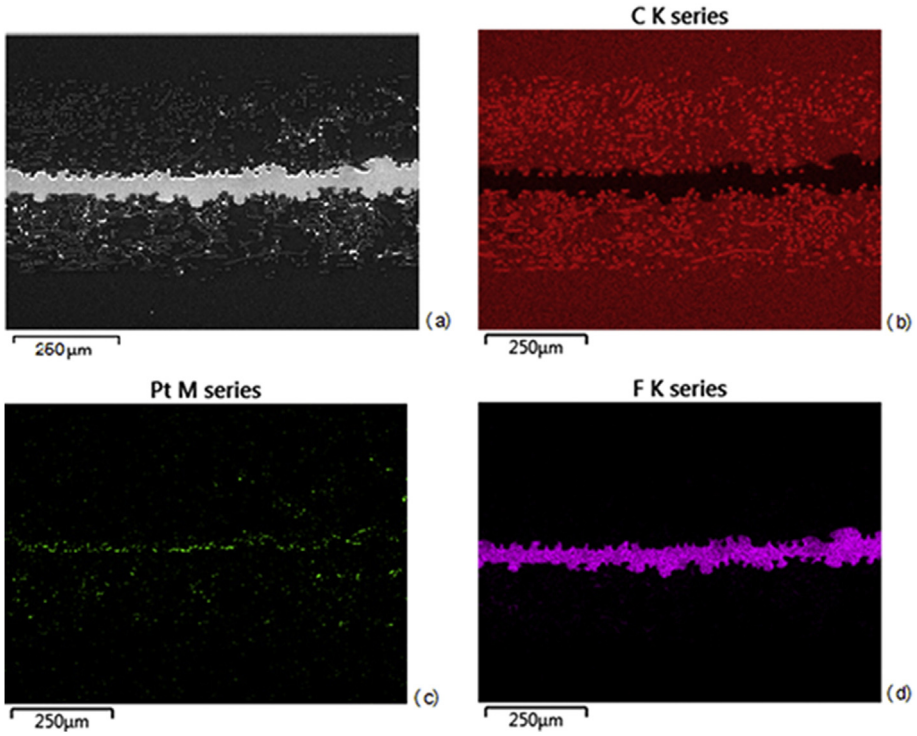

Fig. 8 – FEG-SEM of standard cathode GDM (a) FEG-SEM image, (b) back scatter carbon map, (c) back scatter platinum map, (d) back scatter fluorine map.

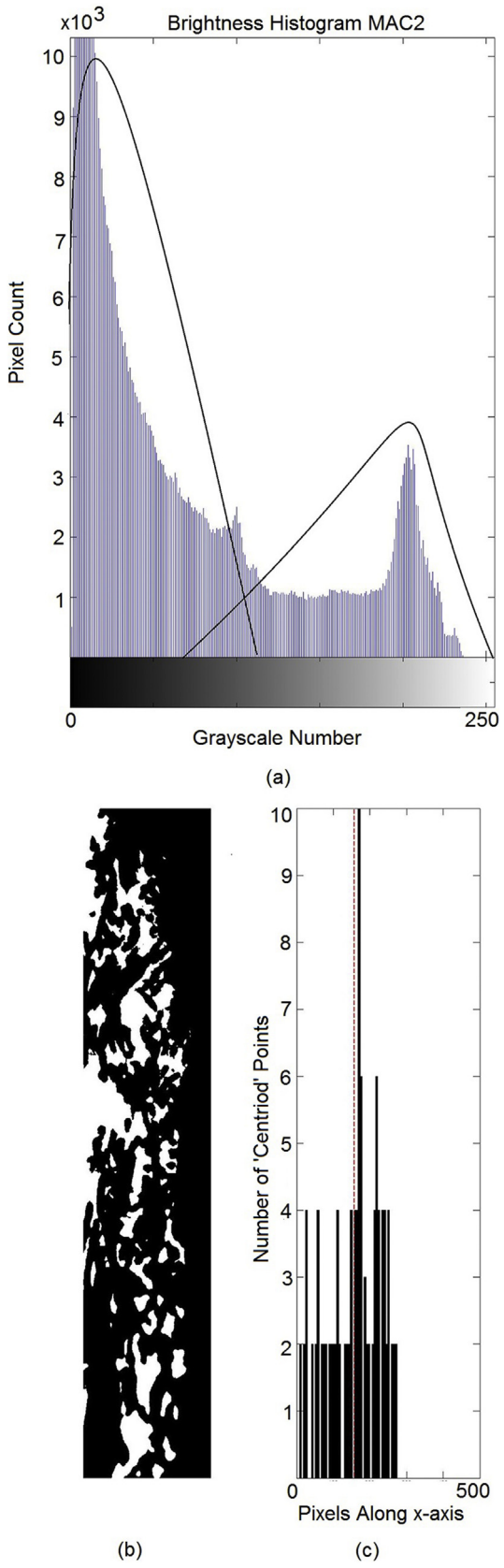

Fig. 9 – MAC2 Cathode image processing example (a) bimodal brightness histogram, (b) Otsuo transform, (c) centroid point of each particle distribution.

threshold at the mean point of all brightness in the original image results in the loss of too much information (Fig. 7(b2)), and so another method is required. The use of Otsu's method [34,35] (through the 'Graythresh' command in Matlab) shown in Fig. 7 (b3) does an acceptable conversion of the image for further analysis. For this approach to be valid the following assumptions must be true:

(i) Histograms (and therefore the image) are bi-modal
(ii) There is no relevant structure or geometry that needs to be specifically included
(iii) Illumination is uniform across the image and so bi-modality is a function of the time imaged and not a lighting effect

A bi-modal brightness distribution was achieved by cropping the field of view down to the point where only the Cathode GDM was largely visible (excluding as much of the Nafion membrane layer as was feasible). It is now possible to quantify the data (see Table 2). The 'graythresh' command in Matlab® automatically applies Otsuo's method to the selected image, and is applicable in this case. Fig. 7(a) assesses this, and whilst the bi-modal nature of the image could, ideally, be greater; it is strong enough that Otsu's method improves the number of PTFE regions in the GDM identified (as shown in Fig. 7 (b3)).

'Particle' identification

Having completed the converting of the image from the grayscale to black and white, the inbuilt image analysis functions in Matlab® can be used. It is simple to detect and quantify all the identified regions that are continuous with each other (the 'particle' effect) and those regions can be defined in several ways. Fig. 7(c1) shows the discretized 'continuous' regions as identified by the analysis parameters created from Otsu's Method.

As in all image analysis a certain degree of caution must be exercised when viewing the data, giving due consideration to the relative intensity for all possible test samples, lighting conditions and fluorescent responses. With care and practice the methodology can be applied with confidence of achieving consistent, repeatable results. Utilizing the inbuilt capabilities of the MatLab® program we can accurately return the area of all identified PTFE 'particle' or regions, their mean size, measure the perimeter of each particle or determine the 'centroid point' of each particle. As a measure of the distribution of the Nafion added into the GDM by the catalyst ink (or its MPL equivalent) the centroid point approach has been selected for this study.

Fig. 7 (c3) shows the histogram of doped PTFE regions and their position along the x axis of the image as defined by the centroid point.

In Fig. 7 (b2 and c2) we can see a region of depleted PTFE content approximately in the middle third of the image. This highlights the usefulness of this technique. Using this fluorescent methodology it is clear that we are failing to achieve a uniform distribution of PTFE based polymers in the CL (in the case the 'MAC1' test sample). In future work we could now optimize out catalyst deposition and MEA fabrication methods to reduce or eliminate the variation in the PTFE

Table 3 – MAC2 PTFE region Area (top) and Centroid Point location (bottom) along x-axis for MAC2 images.

Area per object	Section 3 (pixels)	Section 4 (pixels)	Section 7 (pixels)	Mean of means (μ)	StDev (σ)	(σ/μ)
Mean	5.97E+03	5.86+03	5.72 E+03	5.85E+03	1.27E+02	2.17%
Centroid 'x' coordinate	Section 1 (pixels)	Section 4 (pixels)	Section 5 (pixels)	Mean of means (μ)		
Mean	178	158	200	178.7	21.01	11.76%

component of the CL, and seek to optimize the performance of the MEA over time. Recall that Otsuo's method assigns pixels into one of two 'bins' and the automated thresholding procedure has excluded a significant amount of information from the original image in the central region of the image. The unprocessed image gave a false impression of a uniform PTFE distribution due to the refracted/reflected light traveling up through the transparent areas in the GDM. The automated image analysis now excludes light from the center of the image as it is not sufficiently bright to originate the within our depth of field study area (approx. 15 μm or less) surface of the sample.

Recall that in manufacturing sample 'MAC1', the non-doped MPL was applied directly to the GDM, and the doped CL was applied directly to the Membrane layer. The fluorescent dye has clearly moved away from the surface of the membrane. Utilizing a SEM (Fig. 8 was captured using a Leo (Carl Zeiss) 1530VP FEG-SEM (Germany) fitted with an Oxford Instruments X-Max 80 mm EDS detector (England) in the hope of improving PTFE image capture. As can be seen in Fig. 8 this did not prove to be the case.

Comparison to the PTFE distribution in Fig. 5 (d) and the processed images in Fig. 7, and the platinum distribution (Fig. 8 c) it is clear that the Pt has largely remained near the surface of the membrane, but that the PTFE suspension media of the catalyst ink has tracked up into the body of the GDM. It is equally clear that the EDX map for PTFE tracking in Fig. 8(d) has failed to identify this (the bright fluorine response from the Nafion membrane has 'swamped' the less bright fluorine response in other structures). The movement of the PTFE binder (with its dissolved fluorescent dye) up into the GDM fibers can only have happened at the time when the various parts of the MEA (MPL coated GDM and catalyzed membrane) were hot pressed together to form a single, fully adhered, unit. This is the first time it has been established that the PTFE component of a catalyst ink formulation can segregate away from the heavy metal component during MEA hot pressing. In the future it should be possible to utilize this fluorescent microscopy technique to optimize the MEA manufacturing technique and the degree of separation of Pt and PTFE required for optimum performance.

The addition of a small amount of platinum into the 'MPL' equivalent low concentration CL helps to map its distribution, and Fig. 8 (c) shows the MPL layer has penetrated a large way into the GDM (almost completely through in some places). Each pixel in the analyzed image space for the transformed images is 1.84 μm wide. In MAC 2, the (very low Pt concentration) 'MPL' applied to the GDM first was doped with the EpoDye™ and the subsequent CL applied to the membrane was not. A typical Otsuo transform and PTFE distribution for sample MAC2 is shown in Fig. 9. Table 3 shows a typical assessment of the PTFE regions within the GDM. The PTFE map using fluorescent microscopy and Otsuo's image analysis generates a similar depth of penetration. i.e. the both the PTFE and low concentration platinum 'tracker' have moved together through the GDM.

The layer thickness for CL and MPL, based on these results for the two separate MEAs can now be accurately determined as shown in Table 4. Note that in Fig. 10 the x plane represents the thickness of the GDM, with the value of '0' being the point furthest away from the membrane and the catalyst layer.

Conclusion and outlook

A new method for distinguishing the origin and location of PTFE in gas diffusion media as a result of catalyst ink or MPL applications is reported for the first time and report the following findings

a) It is possible to use Fluorescence microscopy to map the penetration of PTFE based products in the Catalyst Layer (CL) inks or Microporous layers (MPL) or applied to a substrate, and their penetration into the GDM itself.
b) The PTFE component of a catalyst ink formulation can track into the body of the GDM during the hot pressing stage of MEA manufacture.
c) Fluorescence based PTFE tracking is well suited to mapping the location of MPLs applied as a coated substrate directly to the GDE
d) The proposed system of fluorescence microscopy on Epo-Dye™ doped MEAs is accurate, with a low variance (less

Table 4 – Catalyst layer thickness estimation.

MAC1	Mean layer location (pixels)	Mean layer thickness (pixels)	Mean layer location along x (μm)	Standard error (μm)	Mean layer thickness (μm)	Standard error (μm)
Layer 1 (CL)	398.3	228.3	733	9.9	420	49.6
MAC 2	Mean layer location (pixels)	Mean layer thickness (pixels)	Mean layer location along x (μm)	Standard error (μm)	Mean layer thickness (μm)	Standard error (μm)
Layer 2 (MPL)	178.7	316.7	329	22.4	583	52.7

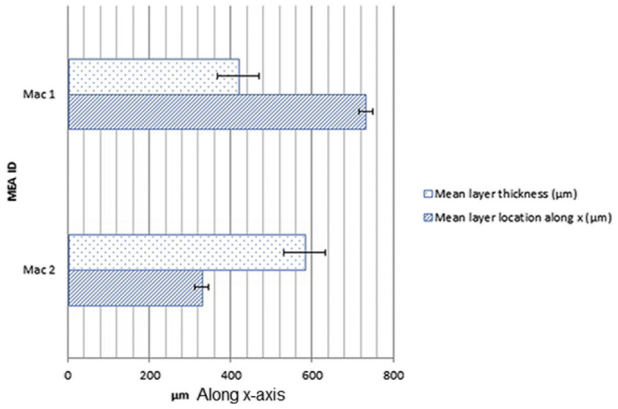

Fig. 10 – Mean centroid location and mean layer thickness comparison for MAC1 (CL) and MAC2 (MPL).

than 12% of the measured value in any image captured; typically much less) and distinct separation between the standard errors for each region (380 µm between mean locations of individual layers in the GDM).

e) The total area of the two samples ('MAC1' a Membrane Coated layer and 'MAC2' a GDM coated layer) shows a similar degree of separation – with the 'Fluorescent CL layer' (MAC1) having the largest area of the two samples

This is the first time it has been possible to differentiate between the likely distributions of PTFE in the GDM added as a result of catalyst ink or MPL applications and subsequent manufacturing processes. Whilst the distribution of some atomically heavier materials in the GDM can be tracked through X-ray techniques, these methods cannot distinguish between carbon structures. It has been until now difficult to differentiate with certainty between fibers and the binder agents present. . Fluorine mapping using scanning electron microscopy techniques such as EDX to map fluorine distribution ineffective. It cannot reliably differentiate between different sources of PTFE present in the GDM (e.g. those found in Nafion, CL ink, MPL binder or hydrophobic coating on GDM fibers).

The use of common digital analyses techniques, such as Otsu's method, utilized in the Matlab® command 'graythresh', is effective and produces quantifiable results that are of use in a research context when combined with fluorescence microscopy. The depth of field for the fluorescence images generated means the technique is best suited to cross sectional images of MEAs in the 50 to 100 times magnification range.

Further developments in the compatibility of fluorescent dyes with PTFE based binder agents for use in PEMFCs, so that the PEMFC can work normally, is required. This would be a significant body of work, that would make possible direct observation of degradation effects on PTFE based structures in the GDM over its working life. If several different frequency responses could be developed (i.e. different colored fluorescent dyes that do not negatively impact the performance the completed MEA), individual PTFE structures such as the hydrophobic coating, the MPL and the binder agents for the CL could all be analyzed separately in a single MEA. Their contribution to losses in performance over time could then be calculated directly and optimization of fuel cell performance could be advanced.

Acknowledgments

The technical support from Mr. Shawn Fowler and Dr Keith Yendall (Department of Materials, Loughborough University) was crucial to the successful completion of this work.

This work could not have been completed without the help and support of the EPSRC through its funding of the Doctorial training Centre (DTC) for Hydrogen, Fuels Cells and Their Applications at the University of Birmingham (EPSRC Grant EP/G037116/1), and also the FUTURE vehicles project (EPSRC Grant EP/I038586/1). The supporting research data for this article can be found at http://dx.doi.org/10.17028/rd.lboro.3562128.v1.

Nomenclature

T	threshold brightness
W	Brightness intensity 'weighting'
n	A number (of pixels)

Greek

μ	mean value
σ^2	variance

Subscripts

b	background
f	foreground

REFERENCES

[1] Lim C, Wang CY. Effects of hydrophobic polymer content in GDL on power performance of a PEM fuel cell. Electrochim Acta 2004;49:4149–56.

[2] Hiramitsu Y, Sato H, Kobayashi K, Hori M. Controlling gas diffusion layer oxidation by homogeneous hydrophobic coating for polymer electrolyte fuel cells. J Power Sources 2011;196:5453–69.

[3] Hiramitsu Y, Kobayashi K, Hori M. Gas diffusion layer design focusing on the structure of the contact face with catalyst layer against water flooding in polymer electrolyte fuel cell. J Power Sources 2010;195:7559–67.

[4] Chapuis O, Prat M, Quintard M, Chane-Kane E, Guillot O, Mayer N. Two-phase flow and evaporation in model fibrous media application to the gas diffusion layer of PEM fuel cells. J Power Sources 2008;178:68.

[5] Lin G, Nguyen TV. Effect of thickness and hydrophobic polymer content of the gas diffusion layer on electrode flooding level in a PEMFC. J Electrochem Soc 2005;152:A1942–8.

[6] Park S, Lee J, Popov BN. A review of gas diffusion layer in PEM fuel cells: materials and designs. Int J Hydrogen Energy 2012;37:5850–65.

[7] Park J, Oh H, Ha T, Lee YI, Min K. A review of the gas diffusion layer in proton exchange membrane fuel cells: durability and degradation. Appl Energy 2015;155:866–80.

[8] Weng F, Hsu C, Li C. Experimental investigation of PEM fuel cell aging under current cycling using segmented fuel cell. Int J Hydrogen Energy 2010;35:3664–75.

[9] Tang W, Lin R, Weng Y, Zhang J, Ma J. The effects of operating temperature on current density distribution and impedance spectroscopy by segmented fuel cell. Int J Hydrogen Energy 2013;38:10985–91.
[10] Lin R, Cao C, Ma J, Gülzow E, Andreas Friedrich K. Optimizing the relative humidity to improve the stability of a proton exchange membrane by segmented fuel cell technology. Int J Hydrogen Energy 2012;37:3373–81.
[11] Wang Y, Chen KS. Effect of spatially-varying GDL properties and land compression on water distribution in PEM fuel cells. J Electrochem Soc 2011;158:B1292–9.
[12] Wang Y, Feng X. Analysis of the reaction rates in the cathode electrode of polymer electrolyte fuel Cells: II. Dual-Layer electrodes. J Electrochem Soc 2009;156:B403–9.
[13] Feng X, Wang Y. Multi-layer configuration for the cathode electrode of polymer electrolyte fuel cell. Electrochim Acta 2010;55:4579–86.
[14] Newbury DE, Ritchie NWM. Elemental mapping of microstructures by scanning electron microscopy-energy dispersive X-ray spectrometry (SEM-EDS): extraordinary advances with the silicon drift detector (SDD). J Anal At Spectrom 2013:973–88.
[15] Antoine O, Bultel Y, Ozil P, Durand R. Catalyst gradient for cathode active layer of proton exchange membrane fuel cell. Electrochim Acta 2000;45:4493–500.
[16] Xie Z, Navessin T, Shi K, Chow R, Wang Q, Song D, et al. Functionally graded cathode catalyst layers for polymer electrolyte fuel cells: II. Experimental study of the effect of nafion distribution. J Electrochem Soc 2005;152:A1171–9.
[17] Wang Q, Eikerling M, Song D, Liu Z, Navessin T, Xie Z, et al. Functionally graded cathode catalyst layers for polymer electrolyte fuel cells: I. Theoretical modeling. J Electrochem Soc 2004;151:A950–7.
[18] Song D, Wang Q, Liu Z, Eikerling M, Xie Z, Navessin T, et al. A method for optimizing distributions of Nafion and Pt in cathode catalyst layers of PEM fuel cells. Electrochim Acta 2005;50:3347–58.
[19] Rama P, Liu Y, Chen R, Ostadi H, Jiang K, Zhang X, et al. An X-ray tomography based lattice Boltzmann simulation study on gas diffusion layers of polymer electrolyte fuel cells. J Fuel Cell Sci Technol 2010;7. 031015–031015.
[20] Gao Y, Zhang X, Rama P, Chen R, Ostadi H, Jiang K. Lattice Boltzmann simulation of water and gas flow in porous gas diffusion layers in fuel cells reconstructed from micro-tomography. Comput Math Appl 2013;65:891–900.
[21] Manke I, Hartnig C, Grünerbel M, Lehnert W, Kardjilov N, Haibel A, et al. Investigation of water evolution and transport in fuel cells with high resolution synchrotron x-ray radiography. Appl Phys Lett 2007;90:174105.
[22] Zhang J, Kramer D, Shimoi R, Ono Y, Lehmann E, Wokaun A, et al. In situ diagnostic of two-phase flow phenomena in polymer electrolyte fuel cells by neutron imaging: part B. Material variations. Electrochim Acta 2006;51:2715–27.
[23] Tötzke C, Gaiselmann G, Osenberg M, Bohner J, Arlt T, Markötter H, et al. Three-dimensional study of compressed gas diffusion layers using synchrotron X-ray imaging. J Power Sources 2014;253:123–31.
[24] Lee J, Hinebaugh J, Bazylak A. Synchrotron X-ray radiographic investigations of liquid water transport behavior in a PEMFC with MPL-coated GDLs. J Power Sources 2013;227:123–30.
[25] Litster S, Sinton D, Djilali N. Ex situ visualization of liquid water transport in PEM fuel cell gas diffusion layers. J Power Sources 2006;154:95–105.
[26] Cropotova J, Tylewicz U, Cocci E, Romani S, Dalla Rosa M. A novel fluorescence microscopy approach to estimate quality loss of stored fruit fillings as a result of browning. Food Chem 2016;194:175–83.
[27] Le Duigou A, Kervoelen A, Le Grand A, Nardin M, Baley C. Interfacial properties of flax fibre–epoxy resin systems: existence of a complex interphase. Compos Sci Technol 2014;100:152–7.
[28] Wittmann JC, Meyer S, Damman P, Dosière M, Schmidt H. Preparation and characterization of side-chain liquid crystalline polymer thin films aligned on PTFE friction-transferred layers. Polymer 1998;39:3545–50.
[29] Takahashi I, Kocha SS. Examination of the activity and durability of PEMFC catalysts in liquid electrolytes. J Power Sources 2010;195:6312–22.
[30] Frey T, Linardi M. Effects of membrane electrode assembly preparation on the polymer electrolyte membrane fuel cell performance. Electrochim Acta 2004;50:99–105.
[31] Marquis J, Coppens M-. Achieving ultra-high platinum utilization via optimization of PEM fuel cell cathode catalyst layer microstructure. Chem Eng Sci 2013;102:151–62.
[32] Gerteisen D, Zamel N, Sadeler C, Geiger F, Ludwig V, Hebling C. Effect of operating conditions on current density distribution and high frequency resistance in a segmented PEM fuel cell. Int J Hydrogen Energy 2012;37:7736–44.
[33] Ploem JS, Walter F. Multi-wavelength Epi-illumination in fluorescence microscopy, 2015. 2001.
[34] Otsu N. A threshold selection method from gray-level histograms, systems, man and cybernetics. IEEE Trans 1979;9:62–6.
[35] Greensted A. Otsu thresholding, 2015. 2010.